Materials for Advanced Power Engineering 2014

Jacqueline Lecomte-Beckers, Olivier Dedry, John Oakey, Bernd Kuhn (Ed.)

Materials for Advanced Power Engineering 2014

Jacqueline Lecomte-Beckers, Olivier Dedry, John Oakey,
Bernd Kuhn (Ed.)

Foreword

The 10th Liege Conference on Materials for Advanced Power Engineering presents the achievements of international materials related research for high efficiency, low-emission power plants. Furthermore the new demands of the transition of electricity supply towards more and more regenerative power sources are reported.

Resource preservation and maximization of economic success by improved plant efficiency were the driving forces in past materials and power plant technology development. Fossil fuels will still play a considerable role for future energy security, even if renewables gain rising importance. The integration of fluctuating renewable energy technologies poses great future challenges in terms of load flexibility, thermal cycling capability and downtime corrosion resistance for the materials employed in new concentrated solar power, biomass fired or gas to liquid plants and the backing conventional fossil fired power plants. In order to balance erroneous availability forecasts of fluctuating regenerative power sources (wind, solar) and vice versa to bridge short periods of low conventional power demand, the minimum load capability of conventional power plants will have to be decreased, while on the other hand start-up times and load ramps will have to be increased to ensure grid stability. Above all improved efficiency of plant, implying rising process temperatures and pressures remains of the utmost importance to ensure economic prosperity. All these issues will create even stronger demands for future materials research and development.

The series of Liège Conferences on Materials for Advanced Power Engineering reflects the necessity of joint international material research and component development for critical components of power generation equipment by bringing together material scientists, design engineers, alloy producers and component manufacturers. To put European efforts into an international framework there are several invited research and review papers covering materials, component and process development in the USA and Asia. In addition there are more than 75 contributed papers from 22 countries which are presented as posters at the conference.

The Conference Proceedings are organised as follows:

- Materials for Advanced Steam Power Plants;

- New materials;

- Manufacturing, Processing and Examination;

- Gas Turbine Materials;

- Corrosion, Thermomechanical Fatigue and Modelling;

- Materials for Advanced Nuclear Power Plants;

- New Power Plant Cycles and Flexible Operation.

The Organization Committee and Editorial Board members would like to express their gratitude to all the authors for their contributions and the scientific advisory board members for their considerable help in reviewing of the submitted papers.

Forschungszentrum Jülich GmbH

"Forschungszentrum Jülich pursues cutting-edge interdisciplinary research addressing the pressing issues of the present. With its competence in materials science and simulation, and its expertise in physics, nanotechnology, and information technology, as well as in the biosciences and brain research, Jülich is developing the basis for the key technologies of tomorrow. In this way, Forschungszentrum Jülich helps to solve the grand challenges society is facing in the fields of energy and environment, information, and brain research.

Forschungszentrum Jülich is also exploring new avenues in strategic partnerships with universities, research institutions, and industry in Germany and abroad. With more than 5,000 employees, Jülich - a member of the Helmholtz Association - is one of the large interdisciplinary research centres in Europe."

University of Liège (ULg)

The University of Liège devotes more than half of its annual budget to high-level research, recognized throughout the world. Its activities extend from fundamental to applied research. More than 2000 people- lecturer/researchers, scientists and technicians- are involved in its research programmes. The moderate size of the University encourages inter-disciplinary research and, more generally, contacts between scientists from various disciplines. There exist numerous partnerships with the industrial sector and the University plays an active role in enhancing the creation of spin-off companies and guiding their development.

In terms of research, the University of Liège offers several possibilities for

- companies or organisations from both the public and private sectors who wish to set up partnerships or subcontract research tasks;

- master's graduates wishing to engage in research while pursuing a doctorate;

- post-doctoral researchers seeking to broaden the scope of their activities as part of one of our reputed research teams;

- experienced researchers interested in an academic position enabling them to combine teaching activities with top range research activities.

The ULg has chosen inter-disciplinarity and partnership of the research units in order to develop a quality collaborative research, rich in diversity and differences, by also favouring the critical size through forming research centres to have access to international partnerships of high quality. It encourages researchers in particular to create spin-offs on the basis of their research findings and to guide their development.

The ULg has been resolute in its desire to become involved in a Free Access policy, by putting PhD theses of its students online on the Internet (BICTEL/e Project), by inviting members of the ULg to deposit their scientific publications in order to enable the free circulation of them over the Internet (Digitheque Project ORBI) and by creating a publication portal of scientific periodicals of the ULg. Furthermore, it wishes to make science available to the general public through the scientific popularisation website Reflections.

10th Liege Conference : Materials for Advanced Power Engineering 2014
edited by J. Lecomte-Beckers, O. Dedry, J. Oakey and B. Kuhn.

Cranfield University

Cranfield University is an exclusively postgraduate university that has global reach in its education and research activities in technology and management. Located at the heart of the UK, we provide transformational research, premier learning, impact and influence for over 750+ organisations working with us from around the world.

Cranfield produces the highest number of Engineering and Technology postgraduates in the UK and is ranked number one in the UK for its Customised Executive Education. We are among 1% of business schools globally with Triple Accreditation and we are a three times winner of the prestigious Queen's Anniversary Prize. 94% of our graduates achieve relevant employment or further study within six months of graduation, securing jobs in some of the world's best known companies including Nissan, Oxfam, Airbus, Johnson & Johnson, Williams F1, Water-Aid, PricewaterhouseCoopers, Rolls-Royce, Shell, Affinity Water, Kraft and GlaxoSmithKline.

Our transformational research is aimed at meeting the needs of business, government and the wider society. Cranfield is one of the top five research-intensive universities in the UK and is recognised as one of the world's strongest universities in Mechanical, Aeronautical & Manufacturing Engineering. We are informing policy for governments, providing management best practice and producing new technologies and products for the world of commerce. Global warming, flood prevention, food production, safer transport and national security, are just a few areas in which we apply our research and teaching to real-world problems.

Technology development and the engineering of viable energy systems is a major theme, combining established research strengths in conventional and renewable power generation; oil and gas; offshore wind/wave/tidal energy systems; CO2 capture, use and storage; resource management and biomass/waste energy systems. Materials and coatings development and reliability in service represent major capabilities in our Centre for Power Engineering. Close industrial links have allowed us to develop specialist facilities and equipment to assist our clients and support our research and teaching activities. Many are industrial-scale, pushing the boundaries of current operating practice and are unique to Cranfield.

For more information please visit www.cranfield.ac.uk or contact business@cranfield.ac.uk`

International Advisory Board

Technical and Editorial Board

Lecomte-Beckers, J. (chief editor)	Université de Liège	Belgium
Dedry, O. (co-editor)	Université de Liège	Belgium
Mertens, A.	Université de Liège	Belgium
Kuhn, B. (co-editor)	Forschungszentrum Jülich	Germany
Oakey, J. (co-editor)	Cranfield University	UK

Organisation of Sessions

Introducing session	Kuhn, B.
Dissemination session EU-project "NextGenPower"	Oakey, J.
Steam power plant materials	Hald, J.
New materials	Kuhn, B.
Innovative processes and load flexibility	Beck, T.
Gas turbine materials	Singheiser, L.
Perspectives of energy supply on international / national level	Lecomte-Beckers, J.
Closing session	Kuhn, B.

Local Organizing Committee

Kuhn, B. (chairman)	Forschungszentrum Jülich	Germany
Adamczak, J. (co-ordinator)	Forschungszentrum Jülich	Germany
Singheiser, L.	Forschungszentrum Jülich	Germany
Kuhn-Stassar, S.	Forschungszentrum Jülich	Germany
Lecomte-Beckers, J.	Université Liège	Belgium
Dedry, O.	Université Liège	Belgium
Mertens, A.	Université Liège	Belgium
Pirson, R.	Université Liège	Belgium
Oakey, J.	Cranfield University	UK

Contents

Contributed Papers 379

D Gas Turbine Materials

Part A

Materials for Advanced Steam Power Plants

CO-ORDINATION OF EUROPEAN RESEARCH IN STRUCTURAL MATERIALS FOR POWER GENERATION EQUIPMENT

Christof Sommitsch[a], Rod Vanstone[b], Torsten-Ulf Kern[c], Peter Barnard[d], Peter Mayr[e], Rachel Thomson[f], Alina Agüero[g]

[a]Institute for Materials Science and Welding, Graz University of Technology, Kopernikusgasse 24, 8010 Graz, Austria, christof.sommitsch@tugraz.at
[b]Alstom Power, Newbold Road, Rugby, CV21 2NH, UK, rod.vanstone@power.alstom.com
[c]Siemens AG, Energy Sector, Rheinstr. 100, 45478 Muelheim an der Ruhr, Germany, torsten-ulf.kern@siemens.com
[d]Doosan Babcock, Birmingham New Road, Tipton, West Midlands, DY4 8YY, UK, peter.barnard@doosan.com
[e]Institut für Füge- und Montagetechnik, Technische Universität Chemnitz, Reichenhainer Strasse 70, 09126 Chemnitz, Germany, peter.mayr@mb.tu-chemnitz.de
[f]School of Aeronautical, Automotive, Chemical and Materials Engineering, Department of Materials, Loughborough University, Loughborough, Leicestershire, LE11 3TU, UK, R.C.Thomson@lboro.ac.uk
[g] Área de Materiales Metálicos, INTA, Ctra. de Ajalvir Km 4, 28850 Torrejón de Ardoz, Spain, agueroba@inta.es

Abstract

Over the last 25-30 years, the main focus for development of improved steels for power generation equipment (boilers, steam turbines, pipework systems) has been the concerted actions of COST 501, 522 and 536. These actions have been very successful. Steels were developed and have been applied to critical components such as boiler tubing, pipework and turbine castings and rotor forgings. These enabled an increase in steam parameters from 540-565ºC to 600-620ºC, bringing benefits in reduced fuel costs and lower emissions.

A new framework for co-ordination of this effort was launched in 2012. KMM-VIN (Knowledge-based Multi-functional Materials Virtual Institute), is a legal entity established in 2007 with membership of mainly academic institutes. In 2012 it experienced significant expansion as around 40 participants, including many industrial companies from the power generation industry and its supply chain, with long history of working together within the COST Actions, joined the organisation. An Energy Materials Working Group (WG2) has been formed and has adopted a work programme for the further improvement of steels for power generation plant. One of the main goals for this work programme EMEP (Engineered Micro- and nanostructures for Enhanced long-term high-temperature materials Performance) is the industrial-scale demonstration of components using the advanced MARBN steel concept, steels with potential to allow increase of operating temperatures from 600-620ºC to 650ºC. The authors of this paper are leading work topics within this work programme.

In the same way that the COST Concerted Actions provided a framework for collaboration between projects funded by many different agencies, WG2 has already fostered collaboration between projects funded by the European Commission Framework Programme, e.g MACPLUS and POEMA, projects funded by national governments, e.g the UK IMPACT project, projects funded by academic funding agencies, e.g EPSRC, and projects funded privately by WG2 industrial partners.

Keywords: Steam power plant, efficiency improvement, alloy design, microstructure modelling and process simulation, ferritic-martensitic steels, steam oxidation, coatings

1 Background

1.1 General background

Clean coal power is one of the most challenging technologies in the light of ongoing discussions on climate change versus the security of a steady affordable electricity supply to the fast growing world population. Coal power supplies 40% of world electricity and is growing fast in highly populated areas such as China and India because of its high energy density per commissioned unit compared to the renewable energy types available today. Efficiency increase of coal fired steam power plants is an indispensable technology step towards clean coal power since it is economical, it enables enormous direct reductions of CO_2 emissions and it compensates part of the efficiency loss from carbon capture and storage (CCS) technologies.

The efficiency of steam power plants is limited by the availability of new stronger high-temperature materials with improved temperature capability, which allows the construction of plants operating at increased steam pressure and temperature. Extended long-term integrity of steam power plant components for 30 years of reliable operation at high temperature requires both resistance to microstructure degradation and to oxidation in steam as well as for boiler parts at fireside. Currently developed steels allow steam parameter up to 300bar and 600-620°C.

Targeted material development will enable further reductions of emissions and improved planned economy. Improved steels for 325bar and 650°C will permit an increase of efficiency of affordable steel based steam power plants from today's maximum of 46% up to a value close to 50%, equivalent to 8% reduction of specific CO_2 emissions.

The present Working Program aims to achieve such a steel development in an open networking between European partners across the whole power plant materials sector, including universities, research institutes, manufacturers of steel components, power plant manufacturers and power plant operators. The defragmentation of universities and industry know-how enabling the advance of competitiveness relative to other economic areas in the world is a key factor to maintain Europe's standard of living in future.

The unique cross-sector network of KMM-VIN WG2 Materials for Energy is highly effective both for directing university research towards "hot topics" and for fast implementation of results by industrial partners (both large and small).

This great advantage by using the KMM-VIN WG2 Materials for Energy open networking approach cannot be realized in other research frameworks such as ESF, ESA, EUREKAS or the EU Framework program. During the running program, further partners can join without any obstacles and introduce their knowledge to widen the expertise range and achieve the challenging goal of network development.

1.2 Current state of knowledge

Because of their combination of high creep and fatigue strength, toughness, oxidation resistance and moderate costs the ferritic-martensitic steels are potential materials for operation in fossil power plants with increased steam parameters.

The European material development includes steels for thick section boiler parts, piping and turbine components, which are key components in the steam power plant, where better material is needed in order to advance the steam parameters. Long-term laboratory testing of the new materials has been carried out up to 100,000h after screening tests of a larger number of testing melts. Specimens from pilot components (rotors, valve bodies, thin and thick walled parts) tested in different ways have confirmed the transferability of properties from 50-500kg melts to full size 30t parts. The application of the newly developed steels in 23 new steam power plants with advanced steam parameters up to 275bar/600-620°C, built by European steam plant manufacturers demonstrates the success of such a development path for new steels.

Microstructure investigations (XRD, LM, SEM, FIB, TEM, EFTEM, 3D APFIM, etc.) of specimens of virgin condition and after long-term creep testing of base material and welds identified precipitation strengthening as the key mechanism to stabilize the tempered martensitic structure against creep. Microstructure and creep modelling based on thermodynamic equilibrium and multi-component diffusion modelling using software such as Thermocalc, DICTRA, and MatCalc, have supported the understanding of microstructure - property relationships of this class of steels. However, the definition of new alloy compositions has not significantly advanced beyond a trial-and-error approach.

Over the past three decades, the development of new ferritic-martensitic 9Cr steels with improved creep strength led by Europe and Japan has enabled advances in steam conditions from subcritical 180bar/540°C to supercritical 300bar/600-620°C corresponding to about 30% reduction in specific CO_2 emissions. Long-term oxidation tests up to 300bar/650°C in steam environment in laboratory as well as field tests in a steam plant up to 57,000h have demonstrated that steels with 9%Cr do not have sufficient oxidation resistance for a steam temperature of 650°C. Such steels will need surface coatings at temperatures higher than 600-620°C. Steam oxidation of a number of coatings (Al slurries, thermal spraying, CVD siliconizing and nickel plating) has demonstrated the feasibility of coatings to improve the oxidation resistance.

Oxidation and creep tests of steels modified from 12%Cr steels have demonstrated that such a Cr content provide sufficient oxidation resistance for steam temperatures up to 650°C at least under atmospheric pressure. However, all attempts to develop 12% Cr steels with sufficient creep strength for 325bar/650°C steam condition have failed due to microstructure instabilities leading to a breakdown of long-term strength. It is now evident that the breakdown is caused by the increase of the Cr content from 9 to 12%, which is found to accelerate the transformation of fine vanadium and niobium based nitrides into coarse Z-phase nitrides (Cr(V,Nb,)N) resulting in a severe loss of precipitation strengthening. Moreover, recent oxidation testing carried out under supercritical steam conditions at 650º C indicates lack of sufficient oxidation resistance.

Similar development projects were run by individual companies in Japan and led to many steel compositions with high Cr and Co contents. This resulted in unstable microstructures in the long-term range, caused by the formation of Z-phase at the expense of MX-nitrides. In addition, a government funded 15-year research project was carried-out in Japan at the National Institute for Materials Science (NIMS) aiming at the development of stronger ferritic-martensitic heat resistant steels. A well balanced composition of boron and nitrogen in the steel led to the strongest available steel i.e., a 9%Cr-3%W-3%Co-VNbBN ferritic-martensitic alloy, which seems to have the potential for 630-640°C application from creep strength point of view. It will, however, still require surface coating against steam oxidation. The mechanism for the strong effect of boron to improve creep strength is still not fully understood. Some modern power plants with steam parameters of up to 280bar/605°C based on newly developed 9%Cr steels are in service or under construction in Japan. There is a strong interest and growing research activities in the development of new high temperature steels of the present class in the Asian economies Korea and China as well in India.

The present Research Program is addressing the development of improved steels and coatings in an innovative way. Recent advantages in micro-nanostructure characterizations techniques (Cs-corrected High Resolution TEM, 3D Atom Probe analysis 3D electron tomography and FIB targeted sample preparation) and novel modelling tools (improved kinetic and microstructure and atomistic modelling, together with improved process modelling) which are available at network partner institutes and universities are used in combination with the manufacturing and testing capabilities available at industrial partners. This unique network facilitates a streamlined development of innovative steels and coatings based on advances in the understanding and predictability of relationships between their micro/nanostructure and properties. This approach is termed "Engineered Micro- and nanostructures for Enhanced long-term high temperature materials Performance – EMEP".

1.3 Reasons for the Working Program

The realization of improvements of the properties of heat resistant 9-12%Cr steels requires extensive knowledge, experience and equipment of participating universities, institutes and manufacturers of steels, components, boilers and turbines as well as power plant operators which will be merged by the cross sectional network of the experts of these organizations.

The planned added value of this KMM-VIN WG2 Materials for Energy network is a reduction of the CO_2 emission of around 8% by the increase of the steam parameters of the nowadays level of 275bar/600°C to 325bar/650°C of coal-fired steam power plants at limited investment costs. Continued use of coal will also improve the security and affordable steady electricity supply due to widespread low-cost, long lasting (150+ years) global coal reserves. It is estimated that replacement of old inefficient power plants and implementation of state-of-the-art technology in all new-built plants could lead to annual global savings up of to 1.7 Gigatons CO_2, equivalent to 5.5% of the global emissions (IEA 2008).

This KMM-VIN WG2 Materials for Energy network is aimed at European economic/societal needs as well as at scientific /technological advances of Europe. The results of this development will ensure worldwide competitiveness and maintain a high employment rate in European countries such as steel and metal plants, producers of large forgings, foundries, boiler makers, and turbine manufacturers. Finally, the defragmentation of university and

industry know-how and experience will promote the economic and scientific position of Europe.

1.4 Complementarity with other research programmes

The need to decrease CO_2 emissions has initiated further activities in research and development in Europe.

In Germany, the national COORETEC program (CO_2 REduction TEChnologies) is run to support the development and improvement of energy supply technologies with the focus on CO_2 reduction. In the UK, there is a running project IMPACT to further strengthen the steel research for the energy and power plant industry. The application of steels for coal fired, nuclear power, or natural gas fired power plants is regarded as a prerequisite to be able to develop economic solutions for the future. European projects, such as CRESTA, AUSPLUS, Z-ULTRA, NextGenPower, POEMA and MACPLUS dealt or are also dealing with the development of high temperature materials.

KMM-VIN is already a platform of interaction with these research projects to ensure that new technical developments and research work is integrated in the working topics of EMEP.

2 Objectives and Benefits

2.1 Aim

The aim of EMEP is to enhance process efficiency and reduce greenhouse gas (particularly CO_2) emissions in thermal power generation by developing innovative ferritic-martensitic steel grades and their coatings that facilitate operation at steam temperatures of 650°C or higher; and to verify the required temperature capability of the new steels to serve as critical components, in particular headers, steam lines and turbines.

2.2 Objectives

The targeted improvement in the process efficiency is 20%, in comparison with the current average efficiency level in Europe and the rest of the world (maximum steam temperatures of 580-610°C in new plant), with a corresponding reduction of CO_2 and other emissions. The solutions for use with steam temperatures up to 650°C will be realized using a novel approach which considers the mechanisms influencing the steel below the grain scale and the impact on the macroscopic structure. This Research Program exhibits broad alloying concepts, developing these through modelling of the micro/nanostructure development during processing leading to the prediction of the properties of interest. In addition to suitable mechanical and fabrication properties, the ability to survive in aggressive environments, such as high-pressure steam, is also critically important. EMEP aims to develop radically new methods of surface engineering through microstructure and coating routes to protect the alloys. The candidate alloys and surface solutions are validated first through testing in small-scale batches and then demonstration for large-scale components. Key objectives to meet are:
- Identification of innovative alloying concepts, promising steel compositions and surface engineering solutions for elevated temperature service
- Identification of coating systems capable of withstanding long term steam oxidation

resistance at 650º C
- Evaluation of most promising surface engineering solutions
- Production of small scale melts (<100kg), to be selected for satisfactory properties in fabrication (welding, casting, forming, heat treatment, non-destructive inspection, coating, etc.) and improved performance under service conditions (mechanical and environmental resistance)
- Characterisation of material (coatings and materials) microstructures down to a nanoscale. Tailoring materials micro/nanostructure for desired properties. Optimisation of the processing route, if necessary.
- Production of the best alloys and protective solutions in the scale of prototype components (approx. 10 tons)
- Development and qualification of welding consumables and joining strategies for new alloys
- Testing and verification of the new materials systems in terms of the life-limiting long-term performance (creep, fatigue, oxidation, etc.) towards acceptance for new plant design.

In recent years, the steel and power generation industries have suffered from a perception that they are in decline and unadventurous, dirty and lacklustre. Consequently, there have been noticeable difficulties in attracting fresh graduates with the inevitable result that there is now both an ageing workforce and a gender imbalance within the industry. To address this, EMEP has a set of secondary objectives, which are:
- to attract fresh bright graduates in the research on challenging new materials for future power generation
- to improve the image of the steel and power generation industries highlighting the challenges and rewards from careers in these industries
- to promote the competitive research, micro/nanostructure characterisation- and modelling methods and expertise for materials development activities within the scientific partnership network including the collaborating universities and research institutes
- to develop solutions withstanding higher temperatures than any earlier alternatives which advance competiveness of European companies providing materials, components, equipment, design and systems.

2.3 How networking within EMEP yields the objectives

KMM-VIN WG2 Materials for Energy comprises a network of research institutes, the material supply chain, OEM´s and generators from across Europe. The combined expertise and scientific facilities within the network encompass all the required know-how and technologies required to achieve the prime objective, including material characterization, modelling, processing and testing. Each activity within EMEP comprises an optimum mix of these groups that will enable precise delivery of the objectives without losing focus or becoming unwieldy.

The network also exposes, thorough collaborative activities, interactions, workshops and meetings, early stage researchers at universities to industrial companies and encourage them to consider future careers in the power generation industry after achieving their qualifications.

2.4 Potential impact of EMEP

A key component within the range of measures to reduce CO_2 and other emissions is to increase the efficiency of fossil fuelled power stations. This has both an intrinsic benefit and also enables the economic introduction of carbon capture technology into the plants. As a direct benefit the steels developed within EMEP will enable the construction of high efficiency plants with operational flexibility and with reduced costs compared to the introduction of Ni-base alloys. These new power plants will produce environmental benefits and energy security in Europe.

Indirect benefits of the Research Program will be an increase in industrial competitiveness in Europe through the knowledge generated and the strengthening of the R&D capability. An additional benefit will come through the stimulation of early stage and female researchers and an increased interest in the industries involved in EMEP.

2.5 Target groups/end users

The output from EMEP is used through the entire supply chain including material producers (steelmakers), material fabricators (e.g. forgemasters), coating companies, OEMs and end users (power generating companies). Involvement in this Research Program benefits universities and research institutes, extending their knowledge and expertise through building links with industrial companies, facilitating future collaboration and scientific innovation. Both stakeholders and end users were strongly involved in the preparation of the proposal.

3 Objectives and Benefits

3.1 Scientific focus

The degradation of long-term creep strength and oxidation resistance accelerates with increasing temperature and thereby limits the temperature capability and lifetime of components fabricated from ferritic-martensitic steels.

Creep degradation of the ferritic-martensitic steels is controlled by the stability of the tempered martensite microstructure against the plastic deformation at high temperature. High microstructure stability is mainly obtained by precipitation strengthening from numerous micro- or nano-sized hard particles of carbides, nitrides or intermetallic phases, which nucleate and grow in the microstructure mainly during the final quality heat treatment of the steels. During service loading, the precipitate particles coarsen, and their strengthening effect is gradually lost. Furthermore, new precipitates can nucleate and grow during service exposure or existing precipitates can dissolve or transform into other precipitate types. Control of the precipitate particles to form a distribution of numerous fine particles, which remain stable (fine) during long-term exposure to high temperature will enable increased creep strength of these steels. It is estimated, that the temperature at which the 100,000 hour creep rupture strength is 100MPa will limit the temperature capability of a given steel.

Steam oxidation of the ferritic-martensitic steels results in the formation of metal-oxide layers on components exposed to hot steam. If the oxide formation rate becomes too high it might result in spallation of oxide layers from the exposed surfaces, which could lead to blockings

and erosion damage in steam cycle components. The Cr content in the steels primarily controls the oxidation rate of the martensitic 9-12%Cr steels. It has been found that a Cr content of 9% will result in oxidation rates, which limit the temperature capability of the steels to 600-620°C. Further, in laboratory atmospheric pressure steam oxidation testing it has been found that, a Cr content of 12% or higher is needed to obtain oxidation rates, which will increase the temperature capability up to 650°C. However, in recent high-pressure tests, also carried out in the laboratory under supercritical conditions, higher Cr alloys such as VM12 (12 wt% in Cr) or even austenic steels such as 316LN (16.8 wt% in Cr) do not exhibit the required oxidation resistance. In fact, little is known about the effects of pressure in the stability of protective oxide scale.

3.1.1 Strength enhancements

The previous developments of new martensitic steels capable of temperatures up to 600°C were mainly based on the optimization of minor alloying contents of vanadium, niobium and nitrogen, which resulted in precipitation of finely dispersed (V,Nb)N nitrides along with $Cr_{23}C_6$ carbides. Further improvements were targeted by additions of tungsten, leading to the formation of Fe_2W intermetallic Laves phase and the addition of 20-150ppm of boron, which increases the long-term creep strength of the steels. The underlying mechanism of boron strengthening is still unknown, and will be targeted in this Research Program. Special emphasis will be put on an optimum balance of the boron and nitrogen contents in the steels. This development has high potential to meet the requirements for strength enhancement and to increase the temperature capability of ferritic-martensitic steels up to 650°C. However, the lack of understanding of the strengthening mechanism by boron currently only leads to new developments based on a trial-and-error approach. By contrast, the different strengthening mechanisms and influencing parameters, supported by modelling activities, will be studied in detail here.

So far, it has not been possible to obtain sufficient creep strength at 650°C of 12%Cr steels simply by (V,Nb)N nitrides or boron. Still, more stable coarse Cr(V,Nb)N Z-phase particles form with time in expense of finely distributed (V,Nb)N and result in a loss of precipitation strengthening and a breakdown of the long-term creep strength. An increased Cr content, necessary for improved oxidation resistance, accelerates this formation of Z-phase nitrides. One approach is to use the more stable Z-phase itself as a strengthening phase and promote a finely dispersed precipitation of Z-phase. Other strengthening phases like intermetallic phases or yttrium dispersoids in ODS alloys will be investigated. Based on different strengthening mechanisms and computer simulations, new steels with improved creep strength will be developed.

3.1.2 Surface engineering

Radically new methods of surface engineering are required to modify the surfaces of candidate structural materials such that their oxidation properties are improved with no deficit to the strength. Surfaces can be 'engineered' in a number of ways, but in general the methods fall into two categories, namely microstructure and coatings.

Microstructure modification can be achieved in a number of ways, through heat treatment, mechanical treatment, alloying etc. Better understanding and control of the effect of microstructure modification is needed. EMEP aims to conduct fundamental investigations on the oxidation resistance and oxidation mechanisms of different ferritic-martensitic steels after

selected surface treatments have been performed. This will include the microanalysis of the internal stresses present in the surface layers as a function of the depth, investigation of the microstructure at the surface and in the near surface area (by cross-sectional SEM and FIB-TEM) as well as the surface topography (by AFM) as this will affect the diffusion paths and consequently the oxidation rate. In parallel a thorough metallographic investigation will be carried out on 9%Cr steels that showed unexpectedly high steam oxidation resistance at 650ºC in order to understand the causes. In addition treatments such as shot peening are known to improve oxidation resistance, however, the processes must be made more reliable and reproducible. Clarification of the microstructure mechanisms of corrosion and the means to curb the oxidation mechanism will also be investigated. In addition the effect of higher temperatures, non-isothermal and thermal transient conditions will be a subject for fundamental, mechanistic and laboratory development. EMEP will support modelling activities and will contribute to validate any produced models.

Whilst microstructure control and surface modification (such as peening) would be the preferred method for increasing the range of applicability of conventional alloys, the use of coatings is a promising option for providing oxidation and corrosion control for alloys which lack the oxidation resistance whilst having sufficient mechanical properties. New coating systems will be applied based on multi-step processes, if required including depositions techniques such as electroless, hot-dipping, thermal spray, slurry application anodic oxidation, etc. Understanding the degradation of coatings, application method and tailoring the coating composition and microstructure is vital to the success of coating technology. The Research Program will focus on these aspects and has consequently identified key areas of interest that will be addressed. These include basic research on the microstructure stability of the coating in supercritical steam and fireside environments, the effect of the coating on the mechanical properties of the alloy as well as the optimization of already developed coatings and the development of new ones. Figure 1 shows the steam oxidation behavior at 650ºC of an aluminide coating developed during the previous COST action. The coating protects P92 and has already reached more than 70,000 h of exposure without signs of substrate attack. Moreover, not only the typical Al and Cr based coatings, but also the behaviour of intermetallics and alloys formed with the substrate and other elements will be explored. Care will be taken when selecting coatings and coatings processes so that non-toxic or environmentally unfriendly species are formed. Other aspects include surface preparation prior to application of the coating, optimization of the diffusion treatment (temperature and time steps) when required and developing models to predict the performance of the coating in service. Components, which are likely to need coatings, will be defined and the most adequate coating deposition method will be selected for each specific component. Finally, a very important issue that will be addressed is the definition of new steam oxidation testing parameters that better reflect real operation conditions. Most laboratories have been testing under atmospheric flowing steam or steam/Ar mixtures isothermally, but recent results have shown that the laboratory observed spallation behaviour of uncoated substrates is significantly different from that in a steam turbine at 150 bar. Moreover, access to high-pressure laboratory rigs will establish the presently not fully understood effect of pressure on oxide scales, Cr, Si and Al based. Finally, the synergy between steam oxidation, wear and/or erosion of coatings and new materials will be studied specifically for valve seats.
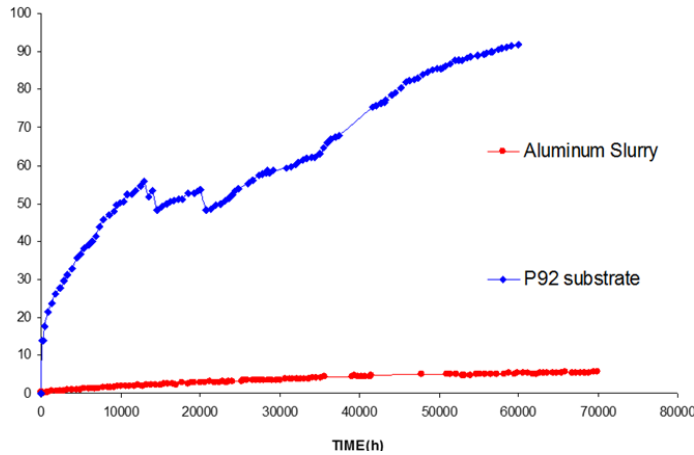
Figure 1: Mass change of a slurry aluminide coating deposited on P92 when exposed to flowing steam at 650º C in the laboratory.

3.1.3 Microstructure characterization and modelling

For both strength enhancements and surface engineering the strategy for improvement of temperature capability of this group of materials is to focus on replacing the trial-and-error approaches with engineered micro- and nanostructures for optimum performance by science-based modelling approaches, i.e. to optimize compositions, heat treatment schedules or manufacturing techniques in order to stabilize microstructures over an extended period of time. This is based on improved understanding of mechanisms of the essential degradation processes of creep and steam oxidation by detailed characterization and modelling of microstructure evolution.

Microstructure characterization methods have advanced significantly in recent years. In addition to well-known metallographic techniques, advanced high-resolution and analytical transmission electron microscopy (EFTEM, EDS with SDD detectors, precession electron diffraction, Cs corrected STEM/HAADF and HRTEM, 3D electron tomography) as well as Focused Ion Beam (FIB) sampling are now available at many partner institutes. This allows unprecedented details of crystal defects or local chemistry of precipitate particles to be revealed on a sub-nano scale. The latest generation 3D atom probe equipment provides much faster analysis on the atomic scale, which can widen the range of this powerful characterization technique. Atom probe in combination with localized sampling by FIB is the most useful technique to locate boron in the microstructure, and thus help to clarify the mechanism of ppm additions of this element to strongly enhance creep strength. Recently, a new possibility for unambiguous characterization of three-dimensional shape and real size distribution of the strengthening precipitates is given by electron tomography (EFTEM, HAADF and FIB tomography). Experience has shown that it is essential to investigate laboratory samples exposed for very long times (5-10 years) in order to draw the right conclusions. Industrial partners in EMEP will share such unique samples.

Microstructure stability and creep modelling are absolutely necessary to evaluate the combined influence of up to 10 alloying elements on microstructure stability in order to optimize chemical compositions and heat treatment schedules. Thermodynamic equilibrium

and multi-component diffusion modelling using software such as Thermocalc, MatCalc and DICTRA has advanced significantly. This will be used to evaluate influences of chemical composition on precipitate phase formations and interdiffusion between coatings and substrate, as well as effects of shot peening on oxidation rates. Novel software such as MatCalc can evaluate influence of composition and heat treatment on the rate of nucleation, growth and coarsening processes for precipitates. Generated microstructure data will be used to validate the modelling as well as to refine underlying thermodynamic and kinetic databases to include critical phases such as e.g. boron containing precipitates. Figure 2 shows an example of a thermodynamic equilibrium calculation for a MarBN steel.
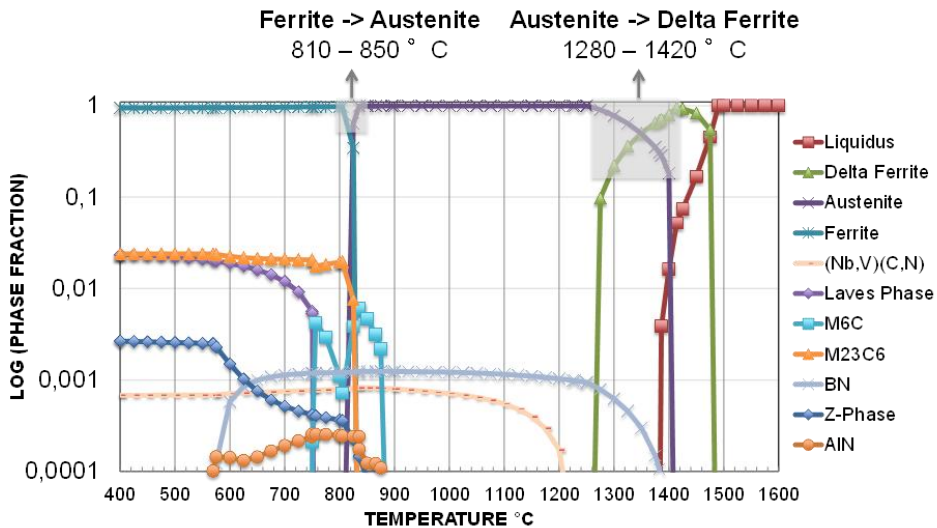
Figure 2: Thermodynamic equilibrium calculations of a MarBN steel using the software MatCalc.

Ab-initio modelling can also generate basic thermodynamic and kinetic data as enthalpy of formation for precipitates and atomic jump ratios in specific crystal systems. Neural network approaches will provide a broader view of influential factors, which might otherwise not be recognized.

3.1.4 Manufacture and validation of trial materials and components
Steelmakers, forgemasters and foundries will manufacture trial melts of 50-100kg size with optimised compositions and heat treatment resulting from the microstructure characterization and modelling exercises. Mechanical and oxidation testing including long-term tests will be made at partner laboratories in order to validate the properties of the developed materials.
Welding of pipes and other components is known to lead to a loss in creep strength of the heat affected zone (HAZ), which has an adverse effect on components lifetime in power plants. New welding consumables will be developed and tested along with the materials solutions for base materials. Recent results indicate that in 9%Cr steels an appropriate balance of boron and nitrogen could suppress the strength loss of the weld HAZ in an innovative way. This will be thoroughly tested in the Working Program by manufacture and testing of welded joints. Figure 3 shows a macrograph of a MARBN crossweld creep tested at 650°C and 70MPa (a)

and corresponding hardness map (b). Simulation of the lifetime of welded components under creep loading based on finite element methods will be carried out.
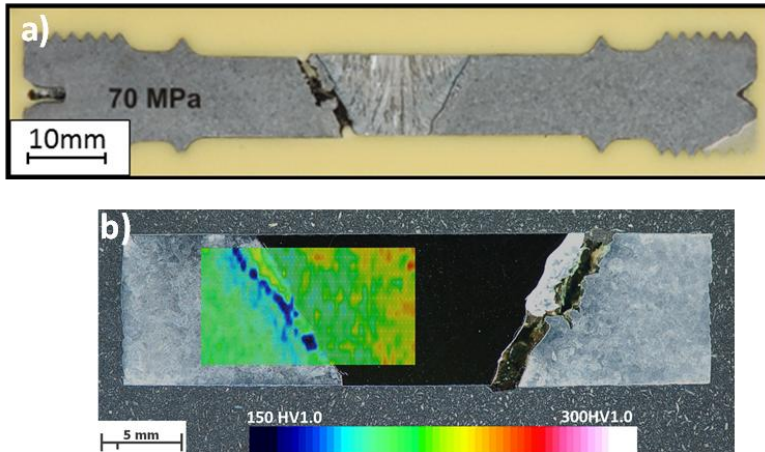
Figure 3: a) Cross-section of a MARBN crossweld sample tested at a stress level of 70MPa at 650°C and b) corresponding hardeness map including weld metal, damaged area in the HAZ and base metal.

Manufacture of large components weighing up to 30t by casting or forging may produce microstructures, which deviate from the ideal laboratory case. E.g. segregation and non-ideal precipitate distributions may lead to reduced creep strength, or grain structures in the centre of large forgings may reduce the possibility for ultrasonic inspections. This seems to be of particular interest for boron alloyed steels. EMEP will implement simulation tools to optimize manufacturing processes in order to minimize such deviations. Forgemasters and foundries will supply components for validation of simulation tools to predict effects of solidification and forging processes on segregation and residual stresses in large components, forging of trial samples are shown in Figure 4.

Figure 4: Forging of MarBN Trial Billets.

Industrial partners will manufacture full-size demonstration components of steam pipes, cast valves and full size trial rotors from successful trial melt compositions. Figure 5 shows MarBN tubes for insertion in power plant for long term testing. These components will be thoroughly tested to validate their properties for plant application prior to installiation in commercial operating plant.

14

Figure 5: MarBN Tubes samples ready for insertion in power plant for long term testing.

Figure 6: MarBN cast bonnet manufactured by Goodwin Steel Castings Ltd within the UK IMPACT project. The reason of a sectioning a 30° cross sectional slice out from the bonnet was to conduct mechanical testing.

An example of the collaboration fostered within the KMM-VIN/EMEP framework is the development of MARBN castings. A casting (Figure 6) was manufactured by Goodwin Steel Castings Ltd. within the IMPACT project part funded by the UK government. The casting was 3.5tonne to pour (around 1.75tonne after method removal) and was part of a 9tonne AOD refined melt. Short term testing within IMPACT has indicated a 25-30 degree C increase in temperature capability compared with current state-of-the-art high temperature casting steels

but longer term testing is necessary to confirm this potential. Samples from the casting are therefore being distributed to other partners in KMM-VIN who have offered to carry out the required long term testing. Further scale-up of this casting technology is planned within a UK funded project starting in April 2014 and it is again anticipated that longer term testing will be conducted within KMM-VIN/EMEP.

4 Economic Dimension

The benefit for the European industry after successful performance of the project will be given by availability of cost effective material solutions for different power plant applications covering all activities for high temperature power plants and Carbon Capture and Storage (CCS) technologies.
The benefit for European science is predicted to be a new kind of networking, a continuous transfer of knowledge to young researchers, and stronger interaction of academia and industry to enable a faster transformation of new solutions into practice. This will strengthen the international importance of European research community.

5   Summary

Despite the indisputable results in implementing new environmentally friendly energy production technologies and fuels, the coal will remain the major fuel source for global electricity production. Unfortunately, coal combustion leads to relatively high CO2 emissions per kWh, which is a highly imminent and challenging task for the mitigation of climate changes. Employing Carbon Capture and Storage together with increased net efficiency in all newly built power plants will lead to meet the EC 20-20-20 target. However, new stronger high temperature steels and coatings for boilers, steam lines and turbines, are required.
This Research Program will develop innovative materials solutions based on detailed understanding and modelling of high-temperature microstructure degradation processes and surface protection against steam oxidation, and on simulation of manufacturing processes for large components to ensure optimal properties during scale up from laboratory samples to industrial use.
KMM-VIN / WG2-EMEP is conducted by a unique network representing universities, research institutes, steel producers power plant component manufacturers and power plant operators. This will enable defragmentation of European research efforts, interdisciplinary education of early stage researchers both from science and industry, and lay solid foundations upon which Europe can build future networks and maintain its leading position in this highly competitive field.

6   References

[1]   R. Blum et al.: The European Perspective and Advancements for Advanced USC Steam Power Plants, *EPRI Sixth International Conference on Advances in Material Technology for Fossil Power Plants*, Santa Fe, New Mexico, USA, (2010).
[2]   M. Fukuda: Advanced USC Technology Development in Japan, *9th Liège Conference*

on Materials for Advanced Power Engineering, Liège, Belgium, p. 5, (2010).

[3]   T. U. Kern et al.: The European Efforts in Development of new High Temperature Rotor Materials – COST 536, *9th Liège Conference on Materials for Advanced Power Engineering*, Liège, Belgium, p. 29, (2010).

[4]   J. Hald: Development Status and future Possibilities for Martensitic Creep Resistant Steels, *9th Liège Conference on Materials for Advanced Power Engineering*, Liège, Belgium, p. 55, (2010).

[5]   A. T. Fry et al.: Steam Oxidation and the Evaluation of Coatings and Material Performance through Collaborative Research, *9th Liège Conference on Materials for Advanced Power Engineering*, Liège, Belgium, p. 935, (2010).

[6]   F. Abe: Boundary and Sub-Boundary Hardening in Tempered Martensitic 9Cr Steel during Long-Term Creep at 650°C, *9th Liège Conference on Materials for Advanced Power Engineering*, Liège, Belgium, p. 330, (2010).

[7]   P. Mayr, I. Holzer, F. Mendez-Martin, M. Albu, S. Mitsche, V. González, A. Agüero: Improved Creep and Oxidation Behavior of a Martensitic 9Cr Steel by the Controlled Addition of Boron and Nitrogen, *Materials for Advanced Power Engineering 2010*, p. 351-361, (2010).

[8]   R. Hanus: Steel Castings for the Next Generation of Power Plants, International Steel Casting Conference, Dresden, Germany, (2010).

[9]   P. Mayr, C. Schlacher, S. Mitsche: Critical issues with creep-exposed ferritic-martensitic welded joints for thermal power plants, *International Conference of the IIW,* Chennai, India*,* pp. 417 - 425, (2011).

[10]   C. Schlacher et al.: Creep and damage investigation of improved 9%Cr steel welded joints, *9th International Conference on Trends in Welding Research*, pp. 376 – 381, Chicago, USA, (2012).

[11]   P. Mayr et al.: Analysis of low-stress creep testing data and its implication on the life-time prediction for 9-12% Cr steels, *12th Int. Conf. on Creep and Fracture of Engineering Materials and Structures,* Kyoto, Japan, pp. C24 - C25, (2012).

[12]   C. Gupta et al.: Analysis of creep cavitation in advanced 9-12%Cr steels using 3-D characterization, *12th International Conference on Creep and Fracture of Engineering Materials and Structures*, Kyoto, Japan, pp. C17 – C18, (2012).

[13]   C. Schlacher et al.: Study of creep damage in creep exposed matensitic high chromium steel weldments, *International Conference on Advances in Materials Technology for Fossil Power Plants*, Hawaii, USA, in Press, (2013).

[14]   S. Vujic et al.: Modelling and optimizing precipitation in creep resistant austenitic steel 25Cr-20Ni-Nb-N, *International Conference on Advances in Materials Technology for Fossil Power Plants*, Hawaii, USA, in Press, (2013).

[15]   S. Vujic et al.: Microstructure evolution and Precipitation modeling in Ni-based alloy C-263, *THERMEC,* in Press, (2013).

[16]   Baumgartner et al: Flux Cored Wires for Welding Ad - vanced 9-10% Cr Steels, *International Conference on Advances in Materials Technology for Fossil Power Plants*, Hawaii, USA, in Press, (2013).

[17]   A. Golpayegani, H. O. Andren, H. K. Danielsen, J. Hald: A study on Z-phase nucleation in martensitic chromium steels, *Materials Science and Engineering* A, 489, p. 310, (2008).

[18]   J. Hald, L. Korcakova, H. K. Danielsen, K. V. Dahl: Thermodynamic and kinetic modelling: creep resistant materials, *Materials Science and Technology*, 24, p. 149, (2008).

[19]   H. K. Danielsen, J. Hald: Tantalum-containing Z-phase in 12%Cr martensitic steels, *Scripta Materialia*, 60, p. 811, (2009).

[20]   L. Cipolla, H. K. Danielsen, D. Venditti, P. E. Nunzio, J. Hald, M. A. J. Somers: Conversion of MX nitrides to Z-phase in a martensitic 12%Cr steel, *Acta Materialia*, 58, p. 669, (2010).

[21]   L. Cipolla, H. K. Danielsen, P. E. Nunzio, D. Venditti, J. Hald, M. A. J. Somers: On the role of Nb in Z-phase formation in a 12% Cr steel, *Scripta Materialia*, 63, p. 324, (2010).

[22]   T. H. Hyde, W. Sun, A. A. Becker, S. B. Leen, P. H. Shipway, Y. Zhang, R.C. Thomson, A. H. Yaghi, J. Sanchez-Hanton: A Holistic Approach to Structural Integrity of High Temperature Welds in Power Plants, *Energy Materials*, 4, p. 17-22, (2009).

[23]   G. West, R.C. Thomson: Combined EBSD/EDS Tomography in a Dual-Beam FIB/FEG-SEM, *Journal of Microscopy*, 233(3), p. 442-450, (2009).

[24]   U. Hermosilla, M. Karunaratne, I. A. Jones, T. H. Hyde, R. C. Thomson: Modelling the High Temperature Behaviour of TBCs using Sequentially Coupled Microstructural-Mechanical FE Analysis, *Materials Science and Engineering* A, 513-514, p.302-310, (2009).

[25]   R.C. Thomson: Future for Fossils, *Materials World*, 178, p. 28-30, (2009).

[26]   A. Agüero, V. González, M. Gutiérrez, R. Knödler, R. Muelas, S. Straub: Comparison between Field And Laboratory Steam Oxidation Testing on Aluminide Coatings on P92, *Materials and Corrosion*, available on line, (2010).

[27]   P. Mayr, F. Mendez Martin, M. Albu, H.-H. Cerjak: Correlation of creep strength and microstructural evolution of a boron alloyed 9Cr3W3CoVNb steel in as-received and welded condition, *Materials at high temperatures 27*, p. 67-72, (2010).

[28]   P. Mayr, T. A. Palmer, J. W. Elmer, E. D. Specht, S. M. Allen: Formation of Delta Ferrite in 9 wt.% Cr Steel Investigated by In Situ X-ray Diffraction Using Synchrotron Radiation, *Metallurgical and materials transactions* / A 41A, 10, p. 2462 – 2465, (2010).

[29]   K. Sawada, M. Bauer, F. Kauffmann, P. Mayr, A. Klenk: Microstructural change of 9% Cr-welded joints after long-term creep, *Materials science and engineering*, A 527, p. 1417-1426, (2010).

[30]   M. Albu, F. Mendez Martin, G. Kothleitner, B. Sonderegger: Compositional characterisation and thermodynamic modelling of nitride precipitates in a 12 % Cr steel, *International journal of materials research = Zeitschrift für Metallkunde 4*, p. 422-427, (2008).

[31]   B. Sonderegger, S. Mitsche, H. Cerjak: Microstructural analysis on a creep resistant martensitic 9-12% Cr steel using the EBSD method, *Materials science and engineering* / A, p. 466 - 470, (2008).

[32]   S. Vujic et al.: Numerical modelling and validation of precipitation kinetics in advanced creep resistant austenitic steel, *Computer methods in materials science = Informatyka w technologii materiałów 12 (2012) 3*, pp. 175 – 182, (2012).

[33]   C. Gupta, et al.: Study of Creep damage in a 10.86% Cr Heat Resistant Steel using Synchrotron X-ray Microtomography, *Advanced materials research 794*, pp. 476 - 483, (2013).

[34]   C. Gupta et al.: Study of creep cavitation behavior in tempered martensitic steel using synchrotron micro-tomography and serial sectioning techniques, Materials science and engineering / A A564, pp. 525 – 538, (2013).

CREEP-FATIGUE INTERACTION IN STEAM POWER PLANT MATERIALS

Stuart Holdsworth

EMPA: Swiss Federal Laboratories for Materials Science and Technology
Überlandstrasse 129, CH-8600 Dübendorf, Switzerland (stuart.holdsworth@empa.ch)

Abstract

Current knowledge relating to the development of creep-fatigue damage in a number of steam power plant materials has been reviewed. The classical understanding of creep-fatigue interaction is mostly based on evidence gathered for low alloy ferritic and austenitic steels, and is not always reflected by newer advanced alloys with significantly different deformation and oxidation responses. In particular, the implications of the high influences of creep on cyclic softening and cyclic plasticity on creep properties of the 9-11%Cr steels are examined.

Based on evidence presented in the form of damage summation diagrams, the extent of creep-fatigue interaction exhibited by the advanced 9-11%Cr steels is apparently significantly greater than for low alloy ferritic or austenitic steels, although cyclic/hold creep-fatigue crack initiation endurances exhibited by a range of turbine steels appear not to substantiate these observations. The reasons for this apparent anomaly are explored.

The creep-fatigue characteristics of a Ni-based alloy adopted for advanced super critical power plant applications are compared with those for 1CrMoV and 9-11%Cr steels.

Keywords: Creep-fatigue, damage, deformation, power plant materials

1. Background and Introduction

The classical understanding of creep-fatigue interaction mainly relates to the enhancement of slip induced fatigue crack development by the presence of physical creep damage at grain boundaries. This mainly originated from observations of crack development at high temperatures in low alloy ferritic and austenitic stainless steels. In the advanced martensitic stainless steels now widely adopted in steam power plant, consideration of creep-fatigue deformation interactions (determined by changes at a microstructural level) are just as important as any interaction between creep and fatigue damage. In addition to the microstructural evidence, the extent of deformation interactions in the advanced 9-11%Cr steels is reflected by the higher respective influences of creep on cyclic softening and cyclic plasticity on creep resistance than experienced in traditional lower alloy power plant steels [1].

Critical locations in high temperature power plant components may be subject to the combined accumulation of cyclic damage arising from strain transients generated during start-up and shut-down operation, and creep damage arising from primary (directly applied) and

19

secondary (self equilibrating) stresses during operation. The development of creep-fatigue damage in most power plant steels depends on temperature, strain range, strain rate, hold time, and the creep strength and ductility of the material (e.g. [2-4]). In the absence of a significant hold time (or relatively high strain rates, or both), crack initiation and growth are fatigue dominated, even at high application temperatures (Figure 1a). With increasing hold time (or decreasing strain rate, or both) at high temperatures, the creep damage condition within the structure becomes increasingly influential, to the limit beyond which crack development becomes completely creep dominated (Figure 1b). At intermediate hold times and strain rates, fatigue cracking interacts with creep damage, developing 'consequentially' or 'simultaneously', resulting in accelerated crack propagation (Figure 1c,d), the extent of any interaction increases with decreasing creep ductility [3]. Creep-fatigue deformation interactions are also influential, and in a dominant way for a number of alloys under certain conditions [1,5].
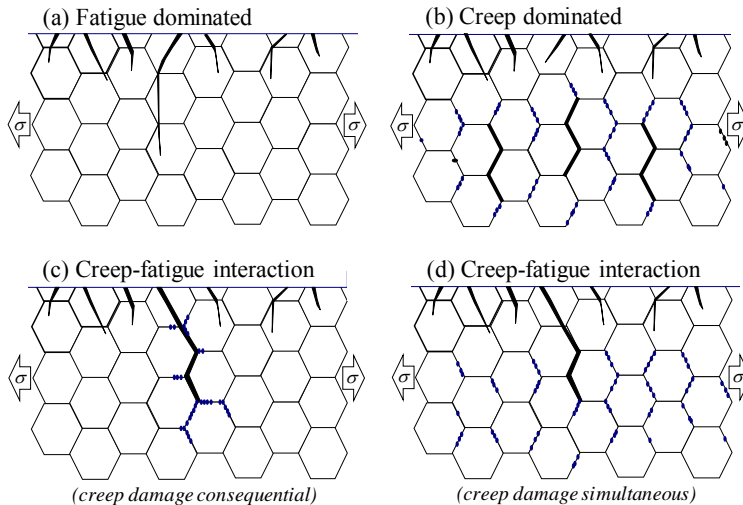
Figure 1: Creep-fatigue cracking mechanisms: (a) fatigue dominated, (b) creep dominated, (c) creep-fatigue interaction (due to 'consequential' creep damage accumulation), and (d) creep-fatigue interaction (due to 'simultaneous' creep damage accumulation)

Depending on the component type and the purpose of the analysis, a defect-free or defect assessment procedure (or both) is undertaken to assess fitness.

2. Creep-Fatigue Assessment of Defect-Free Components

Various published and in-house procedures are adopted to assess the integrity of defect-free components subjected to creep-fatigue loading, a number of which can be represented by the generic flow diagram shown in Figure 2 [6-9]. Other approaches are possible (e.g. [10-13]), but these are not so widely adopted. An important step in all creep-fatigue assessment procedures is determination of the state of stress and strain at critical locations in the component. This requires knowledge of the external forces and thermal transients

experienced by the component during service, and representations of cyclic and creep deformation properties of the material(s) of construction. Irrespective of whether the local stress/strain state is determined by approximate analytical solutions or finite element analysis, the test sources of material property data are generally the same [14]. Having established the stress/strain history at critical locations, cyclic and creep damage fractions are determined by reference to the appropriate material endurance property data (Figure 2). Fatigue (D_F) and creep (D_C) damage fractions are finally compared with, for example, the crack initiation locus in a creep-fatigue damage summation diagram, and the risk of cracking is evaluated.
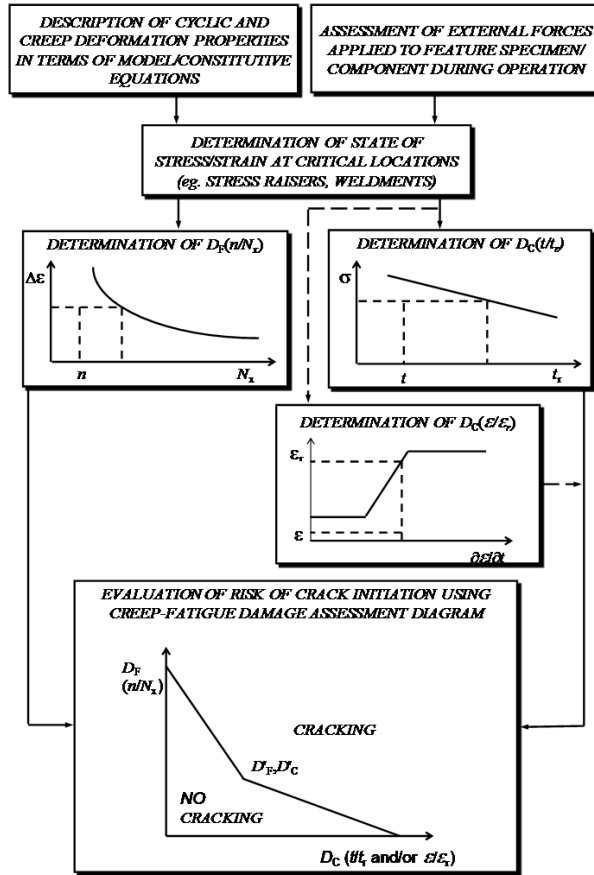
Figure 2: Generic flow diagram representing analysis route adopted by a number of 'defect-free' creep-fatigue assessment procedures (e.g. [6-9])

Fatigue damage fraction is typically determined with reference to the $N_i(\Delta\varepsilon)$ crack initiation endurance, i.e. $D_F = N_{CF}/N_i(\Delta\varepsilon)$, where N_{CF} is the number of creep-fatigue cycles. Creep-fatigue assessment procedures are broadly differentiated by the way creep damage fraction is determined. Time-fraction methods are still currently the most widely used to determine the

creep-fatigue damage accumulated (e.g. [6-8]), whereby creep usage is determined as a function of the creep rupture time, i.e. $t_r(\sigma)$ for the stress, temperature and material under consideration.

$$D_{C(t)} = N_{CF}.\int^{t_h} dt/t_r(\sigma) \tag{1}$$

where t_h is the hold time in a cyclic/hold creep fatigue test or the steady running period during component operation. The best known approach for the determination of creep damage in terms of strain-fraction (or ductility exhaustion) is that adopted in the R5 procedure [9], i.e.

$$D_{C(\varepsilon)} = N_{CF}.\int^{t_h} \dot{\varepsilon}_c.dt/\varepsilon_r(\dot{\varepsilon}_c) \tag{2}$$

where ε_r is the creep-rupture ductility relating to the acting creep strain rate ($\dot{\varepsilon}_c$) conditions. Creep and fatigue may then be summed with reference to a creep-fatigue damage summation diagram (Figure 2), whereby bilinear damage loci as used in Refs. 7 and 8 may be modelled using:

$$D_F = 1 - D_C.(1 - D'_F)/D'_C \qquad \text{for } D_C < D'_C \tag{3}$$
$$D_F = (1 - D_C).D'_F/(1 - D'_C) \qquad \text{for } D_C > D'_C$$

where $D'_F(D'_C)$ defines the intersection co-ordinate [15]. For linear damage accumulation, $D'_F(D'_C) = 0.5(0.5)$. Elsewhere $D'_F(D'_{C(t)})$ values of 0.3(0.3), 0.25(0.25) and 0.1(0.01) are respectively adopted for 17Cr12Ni [7,8], 1CrMoV [15] and 9CrMoVNb [8] steels, while recognising that the intersection co-ordinate is not only a function of material and temperature, but also the assessment procedures employed to determine D'_F and D'_C.
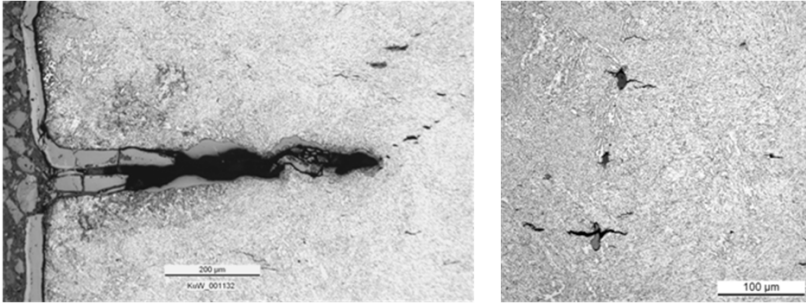
Figure 3: Creep fatigue crack development in a creep ductile 2%Cr steam turbine rotor steel for which $D'_F(D'_C) = 0.5(0.5)$ [16]

3. Creep-Fatigue Crack Development

Figure 1 represents the classical view developed from observations relating to low alloy ferritic and austenitic steels. In these cases, fatigue cracking is typically transgranular, and creep cracking is intergranular due to the nucleation and growth of cavities on prior austenite grain boundaries (PAGBs). Once crack development has moved onto the PAGBs in such materials, it becomes difficult from the examination of appearance alone to differentiate

between propagation due to creep-fatigue interaction, and that purely due to creep. The consequence of this type of interaction is typically associated with $D'_F(D'_C) < 0.5(0.5)$.

Creep-fatigue crack development can be transgranular in creep ductile steels when creep damage is generated due to particle matrix decohesion, e.g. Figure 3. The consequence of this type of independent damage accumulation is typically associated with $D'_F(D'_C) \geq 0.5(0.5)$.
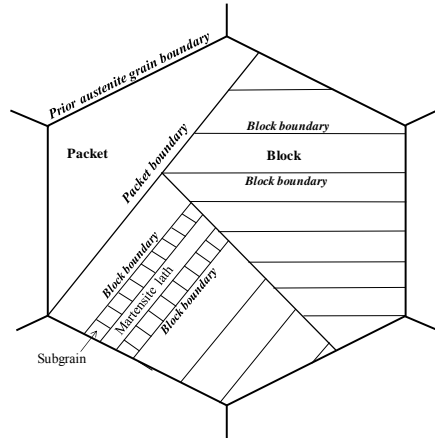
Figure 4: Schematic representation of microstructure of 9-11%Cr martensitic steels [17]
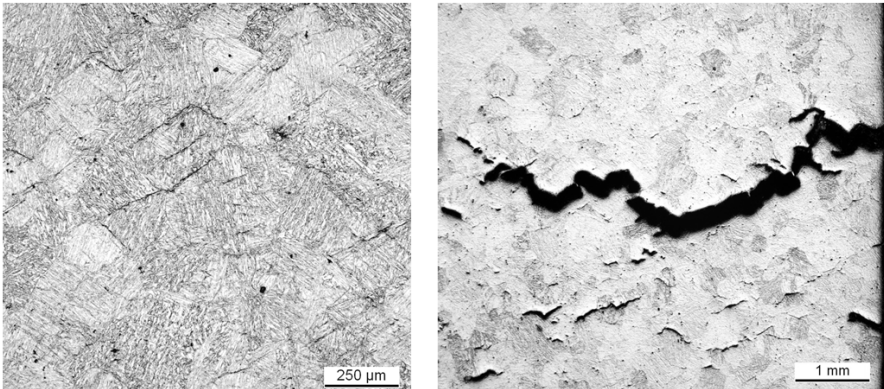
Figure 5: Creep fatigue crack development in a 9%Cr steam turbine rotor steel for which
$D'_F(D'_C) \sim 0.1(0.1)$ [16]

In advanced 9-11%Cr steels, creep voids/cavities do not exclusively form on PAGBs. The martensitic structure of such steels comprises a number of blocks (or packets) of laths of similar orientations within a single PAG (Figure 4). Small creep voids/cavities can also form on lath and block boundaries as well as PAGBs in these steels. This is responsible for the creep-fatigue crack development behaviour shown in Figure 5, with $D'_F(D'_C) \sim 0.1(0.1)$.

Another important feature of the advanced 9-11%Cr steel microstructures is the sub-grain structure of which the martensitic laths are composed (e.g. Figure 4).
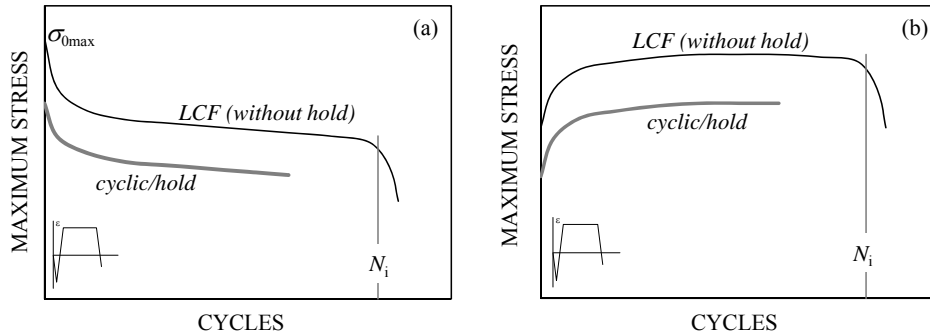
Figure 6: Schematic representations of variation of maximum stress with cycle number for strain-controlled LCF and cyclic/hold creep-fatigue tests at elevated temperature involving materials which (a) cyclic soften, and (b) cyclic harden

4. Creep-Fatigue Deformation Response

The cyclic/hold creep-fatigue tests typically used to determine deformation and crack initiation endurance properties for power plant materials also reveal important information concerning the effects of creep on cyclic plasticity, and cyclic plasticity on creep deformation response [1,5].

The maximum stress response during strain controlled LCF (without hold time) loading may reduce (soften) or increase (harden) with increasing cycle number. Figure 6a is typical of many precipitation strengthened alloys which cyclic soften at elevated temperature whereas Figure 6b represents the cyclic hardening behaviour of many solution strengthened austenitic alloys. Low alloy ferritic steels (such as 1CrMoV at 550°C) typically soften to $0.8.\sigma_{0max}$ at the mid-life cycle, where softening is due to dynamic recovery of the fine dislocation microstructure (e.g. [18]). Figure 6a also represents the behaviour exhibited by the advanced 9-11%Cr martensitic steels, although the extent of softening exhibited by these materials at the mid-life cycle is more of the order of 0.5 to $0.6.\sigma_{0max}$ (e.g. [16]). In contrast, solution strengthened austenitic alloys (such as NiCr23Co12Mo at 500-750°C) can harden to $1.4.\sigma_{0max}$ at the mid-life cycle [19], where hardening is due to the generation of a dislocation sub structure (e.g. [20]).

Figure 6 also illustrates the variation with cycle number of maximum stress in cyclic/hold creep-fatigue tests. The cyclic/hold peak stress responses reflect the influence of creep deformation on cyclic flow properties, which is significantly more notable for 9-11%Cr

24

martensitic steels than for low alloy creep resistant steels, e.g. [16]. The results of cyclic/hold tests can also reveal the influence of cyclic plasticity on creep resistance and again, the effects are significantly more notable for 9-11%Cr steels relative to low alloy ferritic steels [1,5,21].
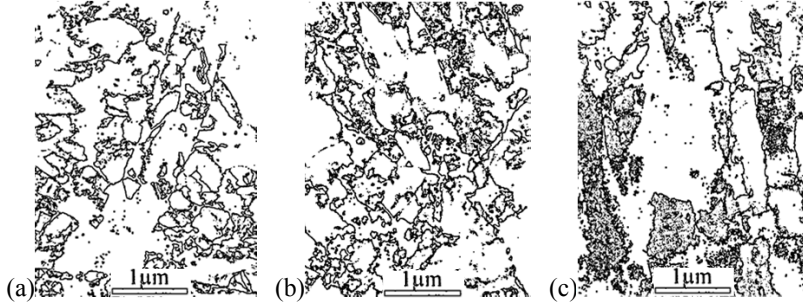
Figure 7: Comparison of sub-grain sizes in a 9%Cr steel, (a) as-received, (b) pure fatigue cycled, and (c) creep-fatigue cycled at the same cyclic strain

The evolution of the sub-grain size (the extent of dynamic recovery) is significantly enhanced during cyclic/hold (tensile hold) creep-fatigue tests. Sub grain sizes resulting from creep-fatigue deformation exceed those due to pure creep loading (and in much shorter time), and are significantly greater than those generated in pure cyclic tests (Figure 7) [22].
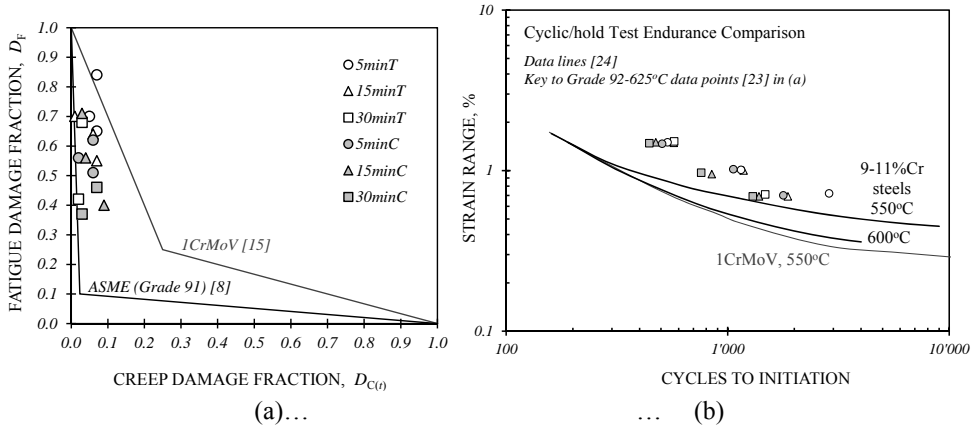
Figure 8: Comparison of cyclic/hold creep-fatigue test results for P92 steel at 625°C [23] with properties for 1CrMoV and 9-11%Cr steels, in terms of (a) $D'_F(D'_{C(t)})$ co-ordinates, and (b) crack initiation endurances

5. Creep-Fatigue Crack Initiation Endurance

The determination of creep damage in terms of a time fraction calculation (Eqn. 1) is not unreasonable for materials for which the creep strength is not significantly influenced by the effects of cyclic plasticity. For materials which are, the creep damage fraction determined as a function of conventional t_r properties (unaffected by cyclic plasticity) can be a significant

underestimation of actual $D_{C(t)}$ for a given cyclic/hold creep-fatigue test endurance. This results in the type of damage summation diagram for the 9%Cr steels (e.g. Grade 91) shown in Figure 8a, implying a low creep-fatigue crack initiation resistance, despite the fact that the associated crack initiation endurances at 600°C [24] and 625°C [23] are significantly superior to those of 1CrMoV rotor steel at 550°C [24], Figure 8b. Care is therefore required in the use of damage summation diagrams to make material comparisons on the basis of creep-fatigue cracking when the analytical procedures for determining D_F and D_C, and the respective creep-fatigue deformation resistances of the materials, are different.

For 9-11%Cr steels at temperatures above ~525°C, the most damaging cyclic/hold conditions are when hold times are at peak strain in compression, i.e. when the main interaction is with oxidation rather than creep [22]. The effect is discernable in the data for P92 at 625°C in Figure 8b, although it becomes less dominant at higher temperatures as the effects of creep become more influential.

6. Nickel Alloys

Solid solution strengthened and precipitation strengthened nickel-base alloys are increasingly being adopted for application in advanced ultra super critical steam power plant. It has been mainly solution strengthened alloys such as NiCr23Co12Mo which have received attention in terms of their creep-fatigue properties for such applications (in both unwelded and welded conditions, e.g. [19,25]). Despite the fact that creep-fatigue cracking in NiCr23Co12Mo at 700°C is predominantly intergranular (e.g. Figure 9a), there is not the analytical evidence for strong interaction characteristics in terms of the $D'_F(D'_C)$ co-ordinates (i.e. 0.5(0.5) [19]).
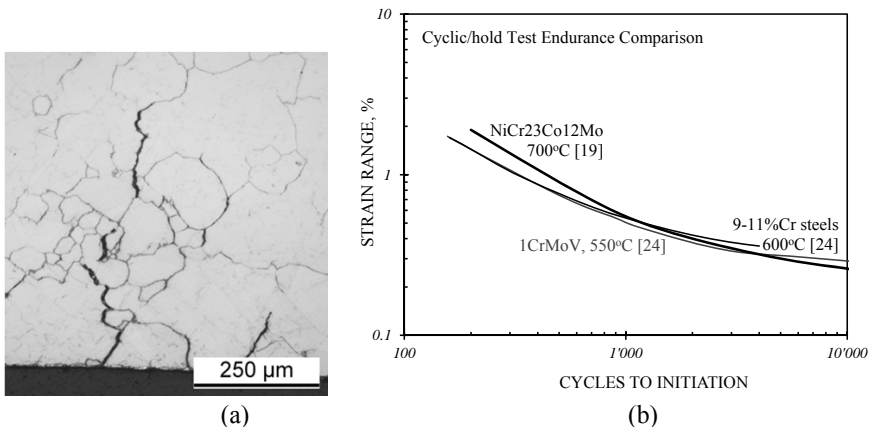
Figure 9: Strain-controlled cyclic/hold creep-fatigue in NiCr23Co12Mo at 700°C, (a) appearance of cracking, and (b) comparison of crack initiation endurance with other turbine rotor steels (30min hold time at peak strain in tension)

Cyclic/hold creep-fatigue crack initiation endurances for NiCr23Co12Mo at 700°C appear to be directly comparable with those for 9-11%Cr steels at 600°C and 1CrMoV steel at 550°C (Figure 9b).

7. Concluding Remarks

Current knowledge relating to the development of creep-fatigue damage in a number of steam power plant materials has been reviewed. The classical understanding of creep-fatigue interaction is mostly based on evidence gathered for low alloy ferritic and austenitic steels, and is not always reflected by newer advanced alloys with significantly different deformation and oxidation characteristics. In particular, the high influences of creep on cyclic softening and cyclic plasticity on creep properties of the 9-11%Cr steels have been examined.

Creep-fatigue crack initiation endurances for NiCr23Co12Mo at 700°C are similar to those for 9-11%Cr steels at 600°C and 1CrMoV steel at 550°C.

8. References

[1] Holdsworth, SR, 'Component assessment data requirements from creep-fatigue tests', *J. ASTM International*, 8(3), pp. 1-14 (2011).
[2] Thomas, G. & Dawson, RAT., 'The effect of dwell period and cycle type on high strain fatigue properties of 1CrMoV rotor forgings at 500-550°C', *in Proc. Intern. Conf. on Engineering Aspects of Creep*, Sheffield, 15-19.9.80, I.Mech.E., pp. 167-173 (1980).
[3] Miller, D., Priest, RH. & Ellison, EG., 'A review of material response and life prediction techniques', *High Temperature Material Processes*, 6(3/4), pp. 155-194 (1984).
[4] Bicego, V., Fosati, C. & Ragazonni, S., 'Low cycle fatigue characterisation of a HP-IP steam turbine rotor', *in Low Cycle Fatigue, ASTM STP 942*, pp.1237-1260 (1988).
[5] Holdsworth, SR., 'Creep-fatigue in steam turbine materials', *in Proc. 6th Intern. Conf. on Advances in Materials Technology for Fossil Power Plants*, Santa Fe, 31.8-3.9.10, EPRI/ASM, pp. 487-503 (2010).
[6] TRD 301, Annex I, *Design: Calculation for Cyclic Loading due to Pulsating Pressure or Combined Changes of Internal Pressure and Temperature Rules for Steam Boilers*, Technische Regeln für Dampfkessel (1978).
[7] RCC-MR, *Design and Construction Rules for Mechanical Components of FBR Nuclear Islands, Section I - Nuclear - Islands*, AFCEN (1985).
[8] ASME, *Rules for Construction of Nuclear Facility Components, Class 1 Components in Elevated Temperature Service, Boiler and Pressure Code, Section III, Division I - Subsection NH*, American Society of Mechanical Engineers (2001).
[9] R5, *An Assessment Procedure for the High Temperature Response of Structures*, EDF Energy, Barnwood (2003).
[10] Halford, GR. & Manson, SS., 'Life prediction of thermal mechanical fatigue using strain range partitioning', *in Thermal Fatigue of Materials and Components, ASTM STP 612*, pp. 239-254 (1976).

[11] Hoffelner, W., 'Creep-fatigue life determination of Grade 91 steel using strain-range separation method', *in Proc. ASME Pressure Vessel and Piping Conf. on Sustainable Energy for the Third Millennium*, Prague, 26-30.7.09, American Society of Mechanical Engineers, (2009).

[12] Prager, M., 'Extend low chrome steel fatigue rules', *Report No. STP-PT-027, ASME Standards Technology* (2009).

[13] Holmström, S. & Auerkari, P., 'A robust model for creep-fatigue life assessment', *Materials Science & Engineering A*, 559, pp. 333-335 (2013).

[14] Holdsworth, SR, 'A knowledge based system for creep-fatigue assessment', *Nuclear Engineering & Design*, 188, pp. 289-301 (1999).

[15] Holdsworth, SR., 'Prediction of creep-fatigue behaviour at stress concentrations in 1CrMoV steel', *in Proc. Conf. on Life Assessment and Life Assessment and Life Extension of Engineering Plant Structures and Components*, Churchill College, Cambridge, 09.96, EMAS, pp. 137-147 (1996).

[16] Radosavljevic, M., 'Creep-fatigue assessment of high temperature steam turbine rotors', *DSc Thesis DISS ETH No. 19880* (2011).

[17] Kitahara, H., Ueji, R., Tsuji, N. & Minamino, Y., ' Crystallographic features of lath martensite in low-carbon steel', Acta Materialia, 54(5), pp. 1279-1288 (2006).

[18] Holdsworth, SR., Maschek, AKF, Binda, L. & Mazza, E., 'Effect of prior cyclic damage removal on high temperature low cycle fatigue endurance', *Procedia Engineering*, 2, pp. 379-386 (2010).

[19] Ehrhardt, F., 'Thermo-mechanical lifetime assessment of components for 700°C steam turbine applications', *DSc Thesis DISS ETH* (2014).

[20] Pham, MS., Solenthaler, C., Janssens, KGF. & Holdsworth, SR., 'Dislocation structure evolution and its effects on cyclic deformation response of AISI 316L steel', *Materials Science & Engineering*, A528, pp. 3261-3269 (2011).

[21] Holdsworth, S.R., 2012, 'Influence of prior fatigue on creep properties', *Proc. 12th Intern. Conf. on Creep and Fracture of Engineering Materials and Structures (CREEP 2012)*, Kyoto, 27-31.May (2012).

[22] Fournier, B., 'Fatigue - fluage des aciers martensitiques à9-12%Cr. Comportement et endommagement', *PhD Thesis, Ecole des Mines de Paris* (2007)

[23] Sato, M. et al, 'Creep-fatigue characteristics of advanced high strength Cr-W steels for power boiler applications', *in Proc. Conf. on Advanced Heat Resistant Steels for Power Generation*, IOM, UK, pp. 298-308 (1999).

[24] Holdsworth, SR., 'Creep-fatigue of high temperature turbine steels', *Materials at High Temperatures*, 18(4), pp. 261-265 (2001).

[25] Ehrhardt, F., Holdsworth, S.R., Kühn, I. & Mazza, E., 'Creep-fatigue crack development in dissimilar metal welded joints between steels and a nickel base alloy', *Materials Research Innovations*, 17(5), pp. 327-331 (2013).

ADVANCED FERRITIC ASTM GRADE 23: MECHANICAL, CREEP PROPERTIES AND WELDABILITY PERFORMANCE

P. Mariani[1,a], G. Cumino[1,b], E. Escorza[1,c]

[1]TenarisDalmine, Piazza Caduti 6 Luglio 1944 no.1, 24044 Dalmine (BG), Italy
[a]pmariani@tenaris.com, [b]DCOCUG@dalmine.it, [c]EESCORZA@TENARIS.COM

Abstract

ASTM Grade 23 is a 2.25Cr-0.3Mo-1.5W-V-Nb-B steel derived from ASTM Grade 22 by addition of W, V, Nb and B and optimization of C and Mo content to enhance the creep resistance and ensure an easier weldability.
This steel, regulated by the main International Standards like ASME/ASTM and EN, is widely used for the fabrication of boiler components for the recent USC Power Plants and for HRSG; it combines high creep resistance, enhanced oxidation and corrosion resistance and good weldability.
Microstructural, mechanical, and creep properties of seamless tubes and pipes after normalising and tempering heat treatment are compared with those obtained after cold bending and hot induction bending.
The creep resistance is achieved through the precipitation (after normalizing and tempering) of Cr and W carbides along the grain boundaries and fine V and Nb-carbides inside the grains.
TEM investigations on crept samples have been carried out to assess the evolution of the microstructure and its phases after long term high-temperature exposure, in terms of chemical composition, size and distribution of precipitates.
Among the weldability issues, the sensitivity to stress-relief cracking has been thoroughly investigated.

Keywords: Grade 23, mechanical properties, creep, microstructure, stress relief cracking

1. Introduction

Grade 23 is a low alloy steel widely applied for the fabrication of boiler components such as waterwalls, waterpanels, headers, steam pipes, superheaters and reheaters for the heat recovery steam generator (HRSG) and for the advanced super-critical (SC) and ultra-super-critical (USC) coal fired boilers.
Grade 23 is selected for such demanding applications because it combines good creep resistance and a relatively easy weldability [1, 2].

The effects of cold deformation and of hot induction bending on creep resistance have been investigated and compared with the behaviour of the base material.
Long term creep tests and advanced microstructural investigations have been carried out on samples in the as-treated condition as well as after long term exposure at high temperature: the evolution of the microstructure and its precipitates in terms of size, distribution and chemical composition has been assessed.

Stress Relief Cracking (SRC) of Tenaris Grade 23 was deeply investigated in Laboratory because has been indicated in literature as a reason for possible failures for welded components made of low alloy steels.
The results of the study showed that Tenaris Grade 23 is not sensitive to this phenomenon.

2. Material properties

Seamless pipes and tubes in Grade 23 are regulated by the ASTM standards A335 (P23) and A213 (T23) [3, 4] and by EN10216-2 (7CrWVMoNb9-6) [5]. This steel, as per the Code Case 2199-6, is also in accordance to the ASME requirements for the construction of boilers and pressure equipment.

Grade 23 is a low alloyed steel (2.25%Cr-1.5%W) derived from the well known ASTM Grade 22 by partial substitution of the Mo with W and by addition of Nb, V and B [6].
Compared to Grade 22, the chemistry of Grade 23 has been optimized to enhance its creep resistance: Mo and W act as solution strengtheners of the metal matrix; W, V, Nb and Ti form fine and diffuse precipitates (mainly carbides) which obstacle the dislocation movement, thus increasing the mechanical and creep resistance of the material; B improves the hardenability and stabilizes the precipitates against coarsening, which is a detrimental phenomenon for the creep resistance.

The chemical composition of this steel, according to ASTM and ASME, is summarized in Table 1.

Grade	C	Mn	P	S	Si	Cr	Mo	W	Cb	V	B	Ti	N	Al	Ni	Others
22	0.05 0.15	0.30 0.60	0.025 max	0.025 max	0.50 max	1.90 2.60	0.87 1.13	-	-	-	-	-				-
23	0.04 0.10	0.10 0.60	0.030 max	0.010 max	0.50 max	1.90 2.60	0.05 0.30	1.45 1.75	0.02 0.08	0.20 0.30	0.0010 0.006	0.005 0.060	0.015 max	0.030 max	0.040 max	Ti/N>3.5

Table 1: Chemical Composition (wt%) of Grade 23 according to ASTM A213 and A335, compared with Gr 22 (T22 ASTM A213)

In TenarisDalmine and TenarisSilcotub Grade 23 seamless pipes and tubes are produced in three different mills, starting from solid billets. In the rolling process the billets are pre-heated in a rotary furnace and then pierced by Mannesmann process to obtain a hollow, which is subsequently rolled in a mandrel mill. After an intermediate re-heating, the tubes/pipes are sized to the final dimensions.

In the continuous mill, it is also possible to produce small boiler tubes with outside diameter (OD) up to 88.9 mm and with lengths up to 26 meters, particularly suitable for the fabrication of panels for HRSG.
The heat treatment is the critical and basic process to achieve the final microstructure, the mechanical properties and creep resistance. In particular the tubes are normalized (N) and tempered (T), while the pipes with large wall thickness are quenched (Q) and tempered (T), following the indications of the relevant standards.

Continuous cooling transformation curves (CCT, see Figures 1 a) and b)) are typically used, taking into consideration the size of the tubes/pipes and the cooling systems, to define the minimum cooling rate to obtain a full bainitic microstructure after cooling from the austenitizing temperature.
This CCT was obtained at the Research and Development Laboratory of TenarisDalmine by means of a Gleeble machine from Tenaris Grade 23 material.

The austenitisation temperature range is 1040°C-1070°C, sufficiently high to put into solution most of carbide forming elements. The tempering is carried out between 750°C and 780°C, in order to ensure optimum creep strength and good toughness properties.

a)

b)
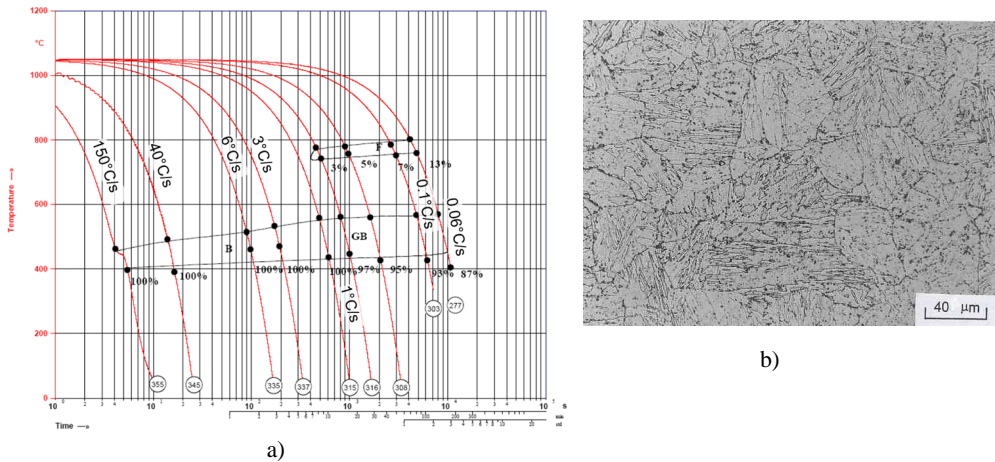
Figure 1: a) CCT diagram of Grade 23 and b) its microstructure after cooling at about 1°C/s.

Examples of the microstructures of respectively a pipe and a tube are shown in the Figures 2 and 3 by light microscope (LM) and scanning electron microscope (SEM): the microstructure consists of tempered bainite.

a)

b)
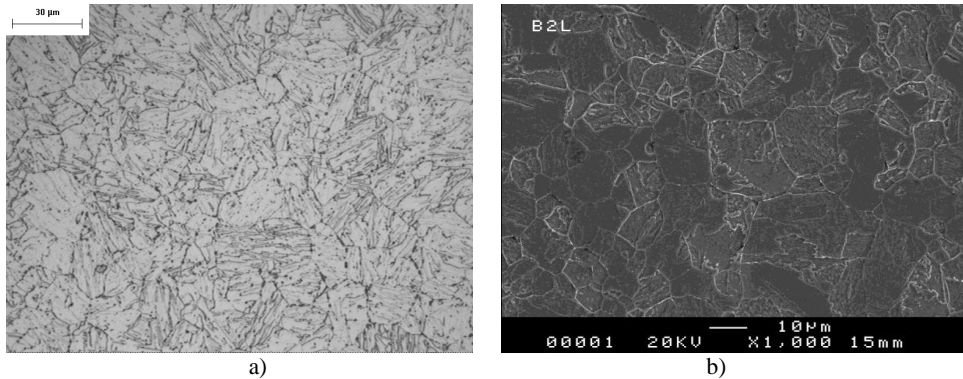
Figure 2: Tempered bainitic microstructure of a Grade 23 pipe (OD x WT 219 x 31.75mm) after Q+T by (a) LM and (b) SEM

31

a)   *b)*
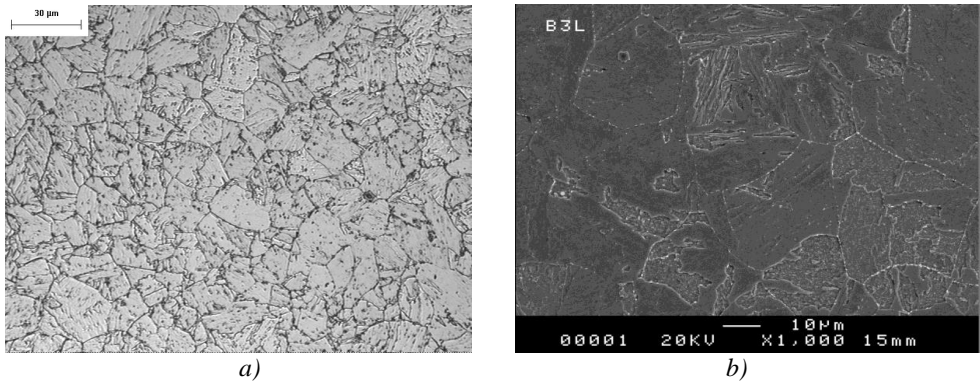
Figure 3: Tempered bainitic microstructure of a Grade 23 tube (OD x WT 38 x 3.8mm) after N+T by (a) LM and (b) SEM

Figures 4 a) and b) shows the distribution of mechanical properties (YS and UTS) over more than 350 industrial batches of T23 tubes. Both YS and UTS are well above the minimum requirements provided by ASTM A213, which are summarized in Table 2.

a)   *b)*
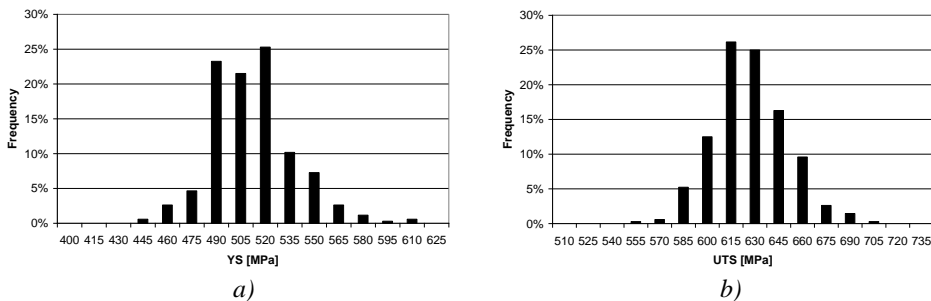
Figure 4: Statistical distribution of YS (a) and UTS (b) of Tenaris ASTM A213 T23 tubes

Steel	YS [MPa]	UTS [MPa]	Elongation [%]	Hardness [HV]
T23	Min 400	Min 510	Min 20	Max 230

Table 2: Mechanical Properties according to ASTM A213

A broad creep test program is ongoing out on both tubes and pipes (but mainly on tubes), with test temperatures 500°-550°-600°C. Figure 5 shows the status of broken (black) and running (white) tests.

It can be noted that the maximum reached times for creep data are, up to now, between 55,000 and 70,000 hours. We have several tests running and some of them are expected to reach 90,000-100,000 hours.

The dotted lines are interpolating the data of the broken specimens; the extrapolation to 100000 hours is the one theoretically expected but shall be updated as further tests will be completed.

No correction factors, in consideration of the scale formation at 600°C, were applied.

At present no international reference data (e.g. from ECCC) are available.

ASME Code Case 2199-6 (which provides allowable stress values and not creep data) is under discussion in ASME for a possible revision (of the chemistry).
EN 10216-2 edition 2013 supplies (Annex A) creep data as information: the values for Grade 23 (EN 7CrWVMoNb9-6) at 100,000 hours are obtained by 3 times extrapolation.
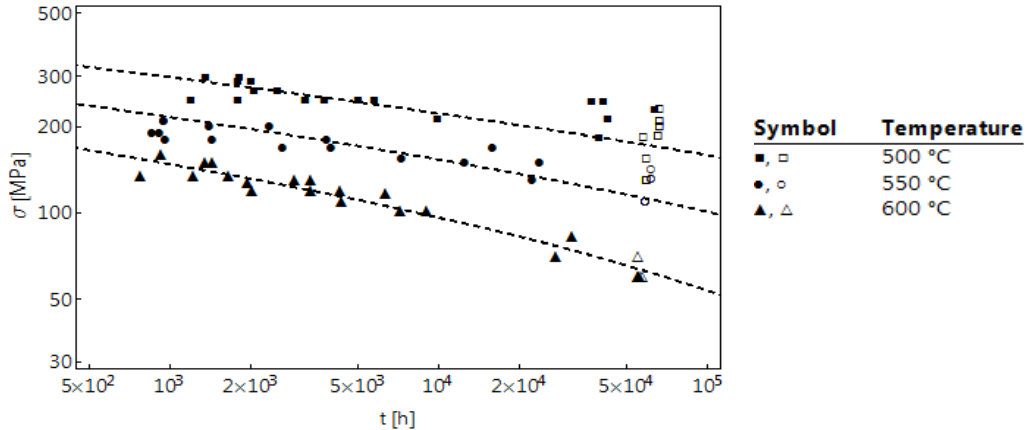
Figure 5: Tenaris Grade T/P23 creep data

During boiler fabrication, tubes and pipes are often subjected to many forming operations such as cold bending, swaging or hot induction bending, the effect of plastic deformation on microstructural, mechanical and creep properties has been widely investigated [7]. Cold bends were produced starting from small diameter tubes, while hot induction bends were produced from big diameter pipes; creep specimens were machined from real bends at intrados, extrados and neutral axis.

Results of creep tests performed on samples extracted from the intrados and extrados of T23 cold bends (OD x WT 76 x 12.5 mm, R/OD=4.5) fall in the lower scatter band of the base material average line, as shown in Figure 6 a). Differences of creep-rupture ductility between extrados and intrados have been found: intrados portions of cold bends show higher values of reduction of area to rupture compared to extrados portions of the same bend.

Creep tests have been also carried out on specimens machined from the intrados and extrados of P23 hot induction bends (OD x WT 219 x 31.75 mm, R/OD=5): creep results are in line with those of base material; the optimization of the bending parameters as well as the carrying out of an accelerated cooling and tempering heat treatment after the bending process have the effect of restoring optimal microstructure and creep properties; the results are shown in Figure 6 b).

a)   b)
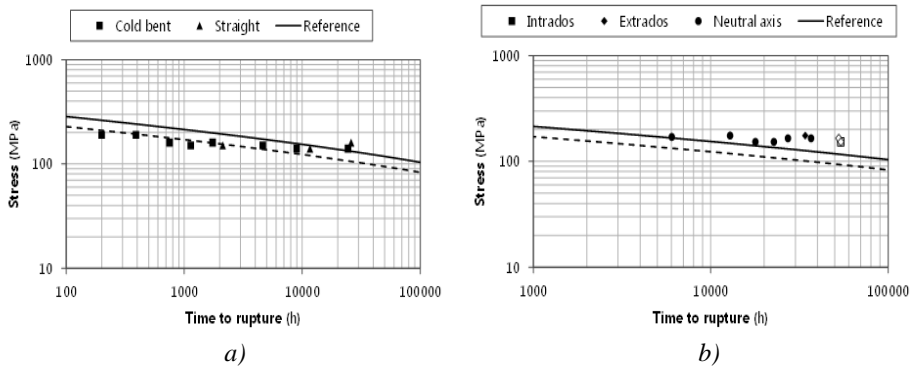
Figure 6: Results of creep tests from (a) cold bends and (b) hot induction bends. Open points are running tests

3. Long term microstructure evolution

3.1. Microstructure after industrial heat treatment

Selected samples after normalising and tempering heat treatment as well as from crept specimens were investigated by SEM, transmission electron microscopy (TEM) and X-Ray powder diffraction (XRD).

Figure 7 a) shows the X-ray diffractogram of the extracted precipitates from as-treated Grade 23 after tempering at 760°C. The same precipitates were identified by TEM diffractions and EDS chemical analysis: the phases present are mainly carbides ($M_{23}C_6$, M_7C_3 and M_6C type) located at grain boundaries and along bainitic laths, while smaller MC carbides are finely distributed inside the grain. Figure 7 b) shows the W-(Cr+Fe)-(Ti+V+Nb) ternary diagram, where the analysed precipitates of as-treated sample are grouped into M_7C_3, M_6C, $M_{23}C_6$ and MC (mainly based on V, W, Nb).

a)   b)
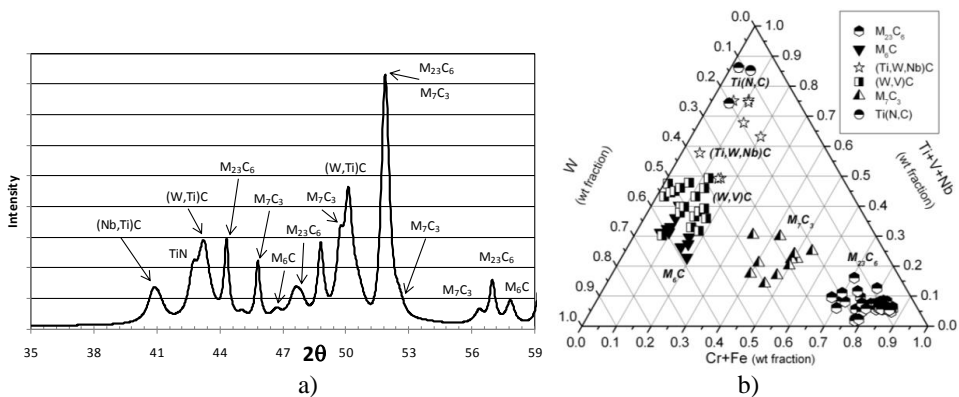
Figure 7: Phases in P23 as-treated sample after tempering at 760°C; identification by a) XRD and b) EDS-TEM

3.2. Microstructure after long term exposure

The microstructural evolution after long term high-temperature exposure was investigated especially on two selected samples: P23 exposed at 550°C for around 20,000 hours (20.61 points in terms of the Larson Miller Parameter (LMP) value with LM constant (LMC) equal to 20) and P23 exposed at 600°C for about 52,000 hours (LMP value of 21.58).

Figures 8 a) and b) show the microstructure of a Grade 23 pipe after 20,000 hours at 550°C, respectively by LM and SEM.

Figures 9 a) and b) show the microstructure of a Grade 23 pipe after 52,000 hours at 600°C, respectively by LM and SEM.

Both aged microstructures consist of tempered bainite; grain boundaries are decorated mainly by M_6C.

a)   *b)*
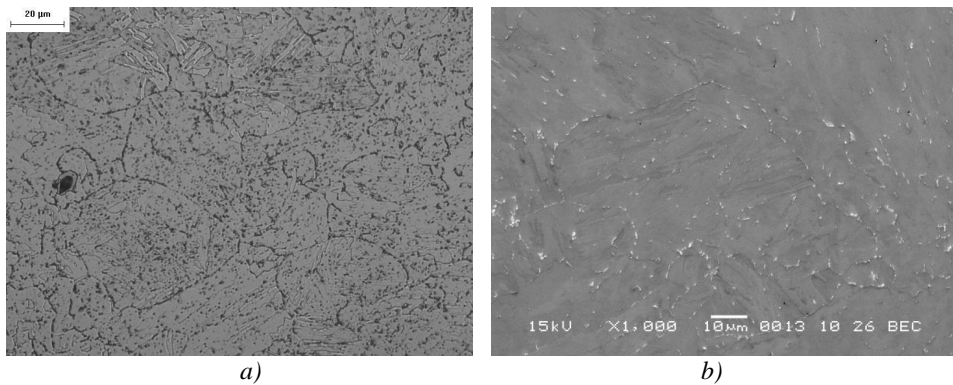
Figure 8: Grade 23 pipe after approx. 20,000 hours at 550°C, respectively by a) LM and b) SEM

a)   *b)*
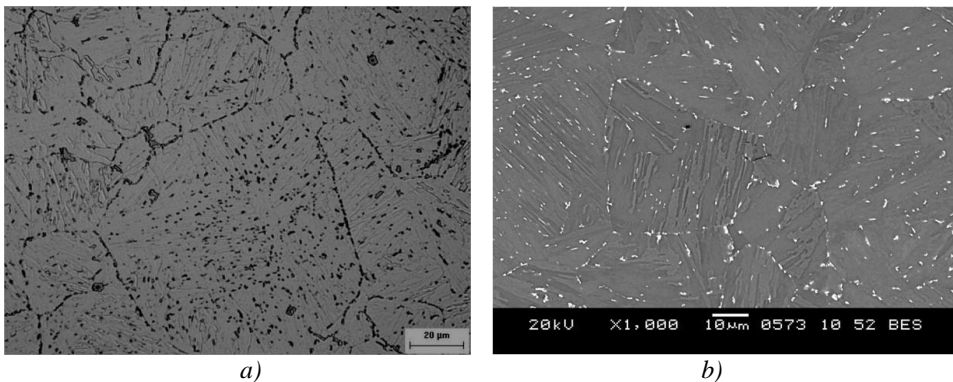
Figure 9: Grade 23 pipe after approx. 52,000 hours at 600°C, respectively by (a) LM and (b) SEM

TEM and XRD investigations of aged samples show that M_7C_3 and $M_{23}C_6$ are not thermodynamically stable in the temperature range of creep service and that a new population of fine M_6C particles precipitates with increasing exposure, while the M_6C formed during the

initial tempering tend to coarsen with increasing time/temperature exposure. The existing MC particles are stable against coarsening in all the analysed conditions.

Figure 10 a) shows the microstructure of the 600°C/52kh aged sample by TEM thin foil; the precipitates along triple joint are mainly M_6C carbides. The same sample was investigated by extraction replica, also: Figure 10 b) shows a triple joint decorated by $M_{23}C_6$ and M_6C, identified by their EDS chemical composition (wt%) reported in the attached table. A network of fine and diffuse carbides is present in the background of the Figure 10 b).

Figure 11 shows the microstructure of 550°C/20kh aged sample observed at high magnification by extraction replica. The fine MC particles were identified by their EDS chemical composition (wt%), and the results are shown in the attached table.

Table 3 summarises the evolution of the average diameter of the different precipitates from the as-treated condition to the two aged stages (550°C/20kh and 600°C/52kh).

wt%

Spectrum	Ti	V	Cr	Fe	Nb	Mo	W
Sp.21	75	6	1	1	10	0	7
Sp.22	0	1	5	22	0	3	69
Sp.23	0	1	36	43	0	1	19
Sp.24	0	2	5	21	0	3	70
Sp.25	0	1	36	45	0	1	17
Sp.26	0	1	36	44	0	0	19
Sp.27	0	2	6	22	0	3	67
Sp.28	0	2	6	20	0	3	68

a)　　　　　　　　　　　　　　b)
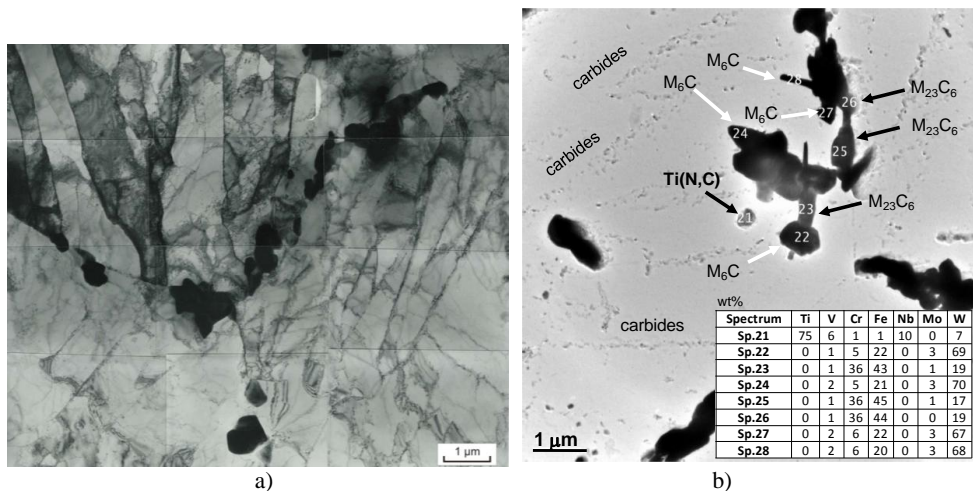
Figure 10: P23 after approx. 52,000h at 600°C by (a) thin foil and (b) extraction replica

Spectrum	Ti	V	Cr	Fe	Nb	Mo	W
Sp.29	12	14	7	3	18	0	45
Sp.30	22	4	5	4	37	1	27
Sp.31	1	32	7	3	2	2	54
Sp.32	17	8	5	3	28	0	39
Sp.33	10	21	6	3	15	1	45
Sp.34	2	37	8	4	4	0	45
Sp.35	2	15	11	6	3	2	61
Sp.36	2	27	7	3	4	3	54
Sp.37	3	23	9	3	4	1	56
Sp.38	2	31	8	3	2	4	49
Sp.39	7	24	8	3	10	1	46
Sp.40	19	9	5	2	28	2	35
Sp.41	5	28	8	3	8	2	45
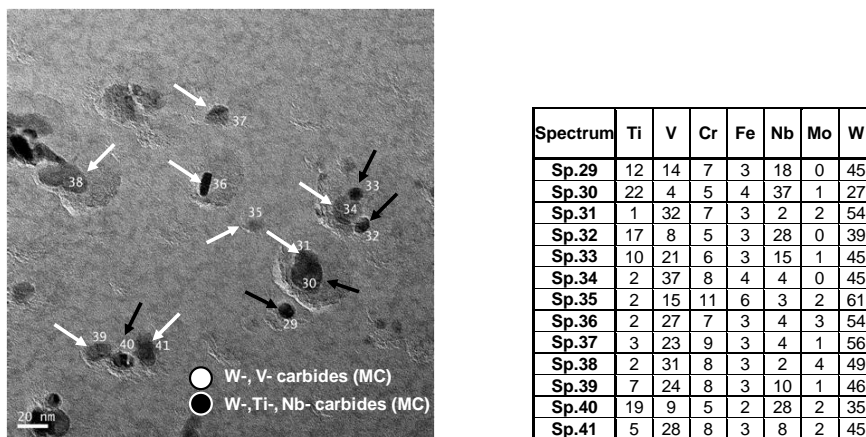
Figure 11: Extraction replica of 575°C/20kh aged sample; fine MC carbides were identified by EDS chemical analysis (in attached table)

	Average Diameter (nm)		
	As treated	550°C/20kh (LMP 20.61)	600°C/52kh (LMP 21.58)
M_7C_3	40	38	dissolving
M_6C	37	165	257
$M_{23}C_6$	158	138	91 - dissolving
TiN	210*	110*	76
(W,V)C	45	55	61
(Ti,W,Nb)C	96	80	89

* Few particles found. Data are not statistically reliable

Table 3: Average diameters of identified phases in as-treated and aged samples. Values obtained by TEM investigations over a population of about 200 particles from each sample

4. Weldability: Studies on the sensitivity to Stress Relief Cracking

The welding tubes and pipes of Grade 23 can be performed with all the conventional welding techniques. Thin sections (<= 7 mm) could be welded without pre-heating or post-weld heat treatment, but these basic rules can be changed according to the specific type and conditions of the welded components. For thicker sections pre-heating and post-weld heat treatment are necessary.
Pre-heating shall be carried out with temperatures between 150°C and 200°C, while interpass temperature should range between 200°C and 300°C. PWHT can be performed in the range of 710-740°C for at least 1.5 hours.

Stress Relief Cracking (SRC) is defined as an intergranular cracking in the heat affected zone or weld metal that occurs during exposure of welded assemblies to postweld heat treatments (PWHT) or high-temperature service [8, 9]. Coarse grained heat affected zone (CGHAZ) is the area most critical for SRC. The sensitivity of Tenaris grade 23 steel to stress-relief cracking has been studied using the procedure developed by the Belgian Welding Institute (BWI). First of all a CGHAZ microstructure has been simulated by means of a thermal cycle simulator (Gleeble) imposing a thermal cycle based on industrial welding procedures. The parameters were:
− heat input of 0.88 kJ/mm
− current of 50-80A for 2.5 mm electrodes and of 65-100A for 3.2 mm electrode and voltage of 20-24 V
− welding speed of 120-180 mm/min

Both single-pass and multi-pass (3 passes) microstructures were simulated to study the tempering effect of single- and multi-bead welding techniques. The samples were then subjected to low strain rate ($10^{-5}s^{-1}$) tensile tests until rupture at different temperatures: at room temperature, at service (540°C) and at PWHT temperature (710°C and 740°C). The tests at room temperature has been used to simulate the behaviour of the material without PWHT during erection on site; the tests at service temperature was instead defined to verify the behavior of material fabricated without PWHT during the actual service in the power station;

finally the two tests at PWHT temperature were used to simulate the effect of two different PWHT conditions on SRC. According to BWI guidelines, the material is considered not susceptible to SRC if the reduction of area exceeds 20%.

Results of SRC tests are shown in table 4, while Figure 12 shows the thermal cycles used to simulate the CGHAZ microstructure.

Temperature [°C]	Simulated welding cycle	Z %	Result
RT	Single Pass	74	Not susceptible
540	Single Pass	36	Not susceptible
710	Single Pass	30	Not susceptible
740	Single Pass	57	Not susceptible
RT	Multi Pass	75	Not susceptible
540	Multi Pass	54	Not susceptible
710	Multi Pass	82	Not susceptible
740	Multi Pass	63	Not susceptible

Table 4: Experimental results of SRC sensitivity tests on simulated CGHAZ

a)   *b)*
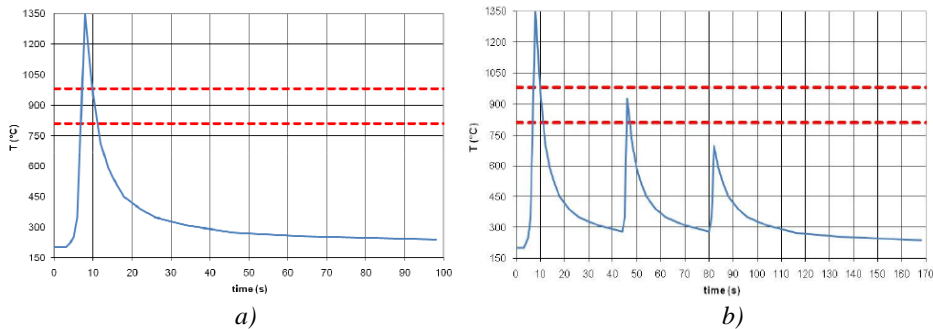
Figure 12: Thermal cycles used to simulate the CGHAZ: left: single pass welding technique; right: multi-pass welding technique

The experimental results, in all the tested conditions, show a reduction of area well above the minimum threshold of 20%, indicating that grade 23 steel produced by Tenaris is not sensitive to SRC phenomena. As suggested by the literature, multi-pass welding techniques have a beneficial effect on the final ductility of the CGHAZ.

5. Conclusions

Microstructural and mechanical properties of Grade 23 have been presented and discussed. Creep results obtained in the temperature range 500°C-600°C show that Grade 23 exhibits higher creep resistance compared to traditional low alloy steels (i.e. ASTM Grade 22). The effect of plastic deformation on the creep properties has also been investigated. Creep resistance after cold deformation lies in the lower scatter band of base material, while creep resistance of hot induction bends is in line with that of unbent material.

The evolution of the microstructure after long term high-temperature exposure has been assessed: M_6C and MC carbides are stable phases, which enable a long lasting precipitation strengthening of the material. Their evolution in terms of size, distribution and chemical analysis has been also investigated.
Slow strain rate tensile tests carried out at different temperatures have shown that grade 23 is not sensitive to SRC. The combination of high creep strength, easy weldability and the results shown on its long term microstructural stability demonstrates that Grade 23 is a strong candidate for demanding components of USC and combined cycle power plants.

6. References

[1] G. Cumino, A. Poli, S. Caminada, E. Bauné et al., Grade 23 tubes, pipes and welded joints production: materials, consumables and process developments, *EPRI Welding and Repair for Power Plants Conference*, (2006)
[2] G. Cumino, S. Caminada, E. Bauné, E. Galand et al., Weldability and long term performances of advanced grades for power generation, *3rd International Conference "Integrity of High Temperature Welds"*, (2007).
[3] ASTM A335-11, *Standard Specification for Seamless Ferritic Alloy-Steel Pipe for High-Temperature Service,* (2013).
[4] ASTM A213-11a, *Standard Specification for Seamless Ferritic and Austenitic Alloy-Steel Boiler, Superheater, and Heat-Exchanger Tubes,* (2013).
[5] EN10216-2: 2013, *Seamless steel tubes for pressure purposes Technical delivery conditions - Part 2: Non-alloy and alloy steel tubes with specified elevated temperature properties,* (2013).
[6] N. Komai, F. Masuyama, M. Igarashi, 10-year experience with T23 (2.25Cr-1.6W) and T122 (12Cr-0.4Mo-2W) in a power boiler, *Journal of Pressure Vessel Technology*, Volume 127, (2005).
[7] S.Caminada, L.Cipolla, G.Cumino, A.Di Gianfrancesco, Cold bending of advanced ferritic steels: ASTM grades T23, T91, T92, *International Journal of Pressure Vessels and Piping*, Volume 86, Issue 12, pages 853-861, (2009).
[8] J. G. Nawrocki, J. N. Dupont, C. V. Robino and A. R. Marder: The Mechanism of Stress-Relief Cracking in a Ferritic Alloy Steel, *Welding Research Supplement*, (2003).
[9] P. Nevasmaa, J. Salonen, S. Holmström and S. Caminada: Heat-affected zone toughness behaviour and reheat cracking susceptibility of thermally simulated microstructures in new P23 (7CrWVMoNb9-6) steel, *VTT report VTT-R-03109-06.*

EXPERIENCE IN MANUFACTURE AND BEHAVIOURS OF HIGH CHROMIUM FORGED ROTOR STEELS

A. Di Gianfrancesco, S. Budano, P. Lombardi, M. Paura: Centro Sviluppo Materiali, Roma, Italy

S. Neri, M. Calderini, N. Longari: Società delle Fucine, Terni, Italy

a.digianfrancesco@c-s-m.it

Abstract

The target to increase the steam parameters, temperature and pressure, in the new power generation plants for reduction of CO_2 emission generated the development of enhanced high Chromium steels with improved creep behaviours and stability at service temperature.

After several years of research activities in Europe currently the composition Rotor E, developed in the frame of COST programs (501, 522 and 536), become a commercial product.

This forged steel is mainly produced by remelting of ingot by Electro Slag Remelting (ESR), but this paper demonstrate that also the conventional route, without ESR, can be also used to produce successfully large rotor components using tailored process control of the production steps.

This paper describes the current production of Società delle Fucine for Rotor E steel grade by conventional process route, based on ladle furnace and vacuum degassing, and the mechanical and creep behaviours of the forged products.

Società delle Fucine (SdF) produced also a FB2 prototype rotor using a conventional process route. In fact in the COST 522 the best candidate, coded FB2 - a 10%Cr steel with additions of Co and B, without W - was selected for scale-up from laboratory trial to full industrial component. In fact the addition of Boron was successfully adopted to increase the stability of the microstructure and as consequence to improve the creep behaviour of the new enhanced martensitic steels.

Also the update of the long term characterization program of trial rotor made by FB2 steel grade will be also presented.

Keywords: COST 501-522-536, 10%Cr Steels, High Temperature Application, Creep strength, microstructural evolution, Boron effect.

1. Introduction

The energy production is faced with the introduction of more and more stringent emission regulations to safeguard health and to preserve the environment for the future generations.

The thermal efficiency is influenced by several factors, but the adoption of ultrasupercritical (USC) conditions by increasing steam temperatures and pressures plays a key role. On the other hand, the increase of steam parameters from 600°C up to 650°C/300bar will generate an efficiency improvement of 8-10% with a corresponding CO_2 reduction [1]. These very high temperatures and pressures make mandatory the use of steels suitable for these severe conditions [2]. In fact these advanced steam parameters require materials with adequate creep strength and resistance to oxidation. Experience with austenitic materials was unsatisfactory showing considerably restrictions in the operational flexibility of the plants due to the difference in the thermal expansion between austenitic and ferritic components and the consequent stresses [1]. The class of the 9-12% Cr steels offers the highest potential to meet the required creep resistance level for the critical components in steam power plants.

In Europe the main efforts to improve the 9-12%CrMoV steels were concentrated in the COST (CO-operation in Science and Technology) Programmes: COST501 (1986-1997), COST 522 (1997-2003) [1-5]. In these programmes new ferritic steels for forging, casting and pipework were developed and characterised to increase the operating steam temperatures:
- from the subcritical plant: with live steam pressure (PLS) of 166bar, live steam temperature (TLS) of 540°C and reheat steam temperature (TRH) of 540°C,
- to the supercritical plant: PLS 250bar, TSL 540°C, TRH 560°C,

- to the first generation of USC plants PLS 270bar, TLS 580°C, TRH 600°C,
- up to the second generation USC plants: PLS 300bar, TLS 600°C, TRH 620°C.

The qualifications of these materials are still on-going after the end of COST 536 Programme (2004-2009), in to the KMM-VIN, WG2 EMEP.

2. Materials development for 600°C turbine rotor applications

In COST 501 forged and cast 9 to 10%Cr steels were developed with additions of 1.5%Mo (type E) or a combination of 1%Mo and 1%W. They showed much improved creep strength, resistance to embrittlement in operation and weldability [1]. In addition samples from production components were subjected to low cycle fatigue and long term creep testing permitting a statistical evaluation of the results. They are in use at temperatures up to 600°C.

The trend to even higher steam conditions was the subject of the COST 522 programme which explored the possibilities of stabilising the tempered martensitic microstructure through addition of small quantities of Boron [1]. These are the steels (forged steel FB2 and cast steel CB2) now being employed in orders currently being executed in Germany and the USA.

Within COST 501 a series of advanced steels for forgings, castings and pipe/tube application as given in Table 1 was qualified and currently the Type E composition is utilized for rotor manufacture.

After the good results obtained in the COST 501 on composition E, F and B a new modified steel called "FB2" was produced as trial melt. Furthermore the promising properties of the trial melt, at the beginning of the new COST 522; it was decided to scale up FB2 steel to industrial heat in order to manufacture a trial forged rotor. Boehler/Austria has manufactured a full-size rotor forging with a final weight of 17tons. The steel making process was Boehler-BEST, consisting in a pouring process with special measures to improve the homogeneity of the ingot [7].

COST	Forged Steels	C	Cr	Mo	W	V	Ni	Nb	N	B	100MPa 100.000h	Status
	1CrMoV	0.25	1.0	1.0		0.25					550°C	Long term operating
	12CrMoV	0.23	11.5	1.0		0.25					570°C	Long term operating
501	Type F	0.1	10	1.0	1	0.2	0.7	0.05	0.05		597°C	Operating in plant
501	Type E	0.1	10	1.5		0.2	0.6	0.05	0.05		597°C	Operating in plant
501	Type B	0.2	9.0	1.5		0.2	0.1	0.05	0.02	0.01	620°C	
522	Type FB2 (SdF)	0.13	9.32	1.47		0.2	0.16	0.05	0.019	0.085		Trial rotor manufactured

Table 1: Compositions of improved ferritic steels developed in COST 501 and operating temperature for 100MPa/100.000h. [2]

A second proposal for a FB2 trial rotor manufacturing was brought into COST522 by the Italian Società delle Fucine (SdF) in Terni; it produced a 52tons ingot by conventional steel making (Ladle Furnace and Vacuum Degassing) with a final rotor weight of 28tons [2].

One more trial rotor has been produced by ESR remelting of 57tons ingot in Saarschmiede [8].

3. The manufacture of FB2 trial rotor at Società delle Fucine (SdF)

The aim of the investigations is to qualify the different steelmaking processes for this class of Boron containing 10CrMoCoVB alloys. One of the main tasks is how to increase and optimise the composition homogeneity and the properties of the final rotor forging are.

Figure 1 shows the lay-out of the SdF manufacture route: from the melting shop to the final machining. Due to the characterisation work on experimental rotor the component machining was stopped at the step of NDT control after quality heat treatment.

The chemical composition of the SdF trial rotor is based on the FB2 trial melt from COST 501. Table 2 shows the chemical analysis of the cast product. Very good agreement with the aimed composition has been obtained with very low content of residual elements.

FB2	C	Si	Mn	P	S	Cr	Mo	Ni	Al	B	Co	N	Nb	V
min	0.12	-	0.3	-	-	9.0	1.45	0.1	-	0.006	1.2	0.015	0.04	0.18
max	0.14	0.006	0.4	0.01	0.005	9.5	1.55	0.2	0.008	0.009	1.4	0.030	0.06	0.22
cast	0.14	0.032	0.32	0.007	0.003	9.1	1.5	0.14	0.001	0.009	1.23	0.015	0.046	0.2

Table 2: Required and obtained chemical composition of FB2 trial forged rotor

(residual elements: H_2= 1,2ppm; Sb= 0,001%; Sn=0,001%; As=0,006%; Cu=0,035%; W <0.01%)

The final dimensions of the trial component are shown in Figure 2. After forging the trial rotor has been treated as follows:
- Austenitizing: 1100°C/ 17h/oil quenched;
- 1st Tempering: 570°C/ 24h/ air cooled;
- 2nd Tempering: 700°C/ 24h/ air cooled.

The trial component in as treated condition and after preliminary machining has been subject to NDT ultrasonic inspection (US) with a 2MHz source. The maximum defects discovered (flat bottom hole equivalent) in the different positions are summarised in Table 3 [9]. Figure 2 show the trial component after final forging and heat treatment during the NDT control tests.
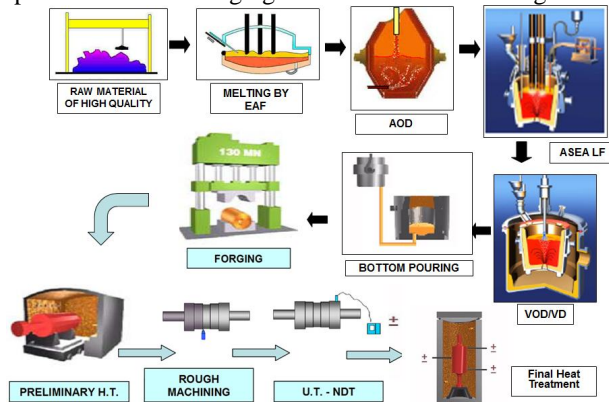
Figure 1: Flow chart of rotor manufacturing route at SdF

FB2 SdF Trial rotor	Total (L1+L2+L3)	D1	D2	D3
Dimensions (mm)	4380	925	1110	790
Max Defect discovered (mm)		1.0	1.5	1.5

Table 3: Results of the US inspection on SdF trial rotor

42

3.1 Product characterisations

In order to verify the homogeneity of the properties of the trial rotor, the specimens for chemical analysis and mechanical tests have been obtained from different parts of the component positions from the core. The chemical analysis (Table 4) shows a very good homogeneity in the composition of the main alloy elements as well as for the Boron and Nitrogen content that could be critical for their distribution in a large component processed without remelting.
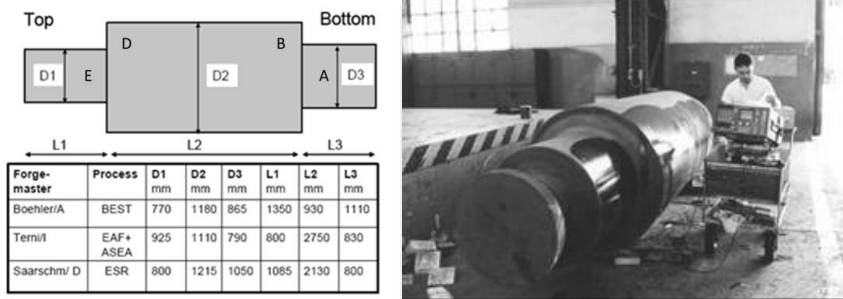
Figure 2: COST trial rotor forgings (type FB2) dimensions [9]; SdF rotor during US NDT control.

The chemical composition of FB2 steel guarantees a fully martensitic structure. Also with very low cooling rate, corresponding to claim air, no traces of ferritic transformation appear. In fact the microstructural analysis performed after the final heat treatment (normalizing + tempering) shows a typical tempered martensitic structure with a 0-2 ASTM grain size. The prior austenite and the martensitic lath boundaries are decorated by a typical precipitation of $M_{23}C_6$ carbides. The microstructure contains a high dislocation density.

Conventional mechanical tests have been performed in different positions and orientation. The results, just discussed in previous papers [10-11], shown a quite good homogeneity of the obtained values in term of YS, UTS and ductility: elongation and reduction of area.

Position/Element	A	B	D	E	FB2 trial melt
C	0,12	0,13	0,13	0,15	0,13
Cr	9,08	9,13	9,11	9,02	9,32
Mo	1,57	1,59	1,59	1,62	1,47
Ni	0,14	0,14	0,14	0,14	0,16
V	0,21	0,21	0,21	0,22	0,20
Nb	0,054	0,054	0,054	0,060	0,05
B	0,0095	0,0096	0,010	0,012	0,0085
N	0,015	0,016	0,015	0,014	0,019
Co	1,28	1,27	1,27	1,29	1.23

Table 4: Chemical composition (wt%) of forged trial rotor in different positions compared with the nominal composition.

3.2. Microstructural characterisations

In the KMM-VIN WG2 EMEP Alloy Design Group discussion it is still open on the effect of B addition not only as $M_{23}C_6$ and grain boundary stabiliser, but also on the correct amounts of B and N to avoid the formation of BN particles as defined by Abe & Co-workers [12] in

Figure 3. The formation of these particles have the double negative effect to reduce the amount of B available in solution and able to diffuse into the $M_{23}C_6$ and otherwise to form particles reducing the ductility in creep as demonstrate for the FB2 trial melt.

The FB2 material from SdF it is on the border line of the equilibrium (red point in the Figure 3) and therefore BN formation could be present.

Then investigations have been made by FEG-SEM +EDS on RT tensile test specimens fracture surface: no BN pure particles have been identified, but some dimples appears sometime associated with particles identified as complex inclusions that contain also BN particles:

- Figure 4a shows a BN particles jointly with a MnO inclusion,
- Figure 4b shows a BN associated with other complex oxide
- Figure 5 shows a sulphide inclusion with BN particle.

As conclusion of these analyses the following consideration can be made: SdF FB2 seems have a quite good balancing of B and N, because pure particles have not been discovered and the dimensions of the discovered BN particles are very small. The SdF FB2, conventionally processed without remelting, shows small sulphide and oxide inclusion where sometime BN can nucleate.
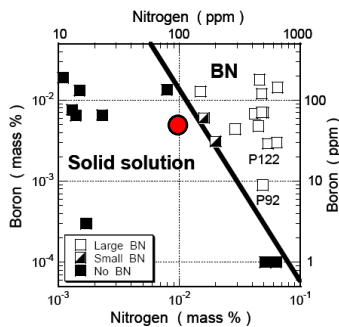
Figure 3: BN equilibrium diagram [12]: circle point is the FB2 from SdF

Figure 4: a) BN + MnO on FB2 tensile specimen; b) BN plus MnO, Al and Ti on FB2 tensile specimen

Figure 5: Particle of BN plus MnS on FB2 tensile specimen
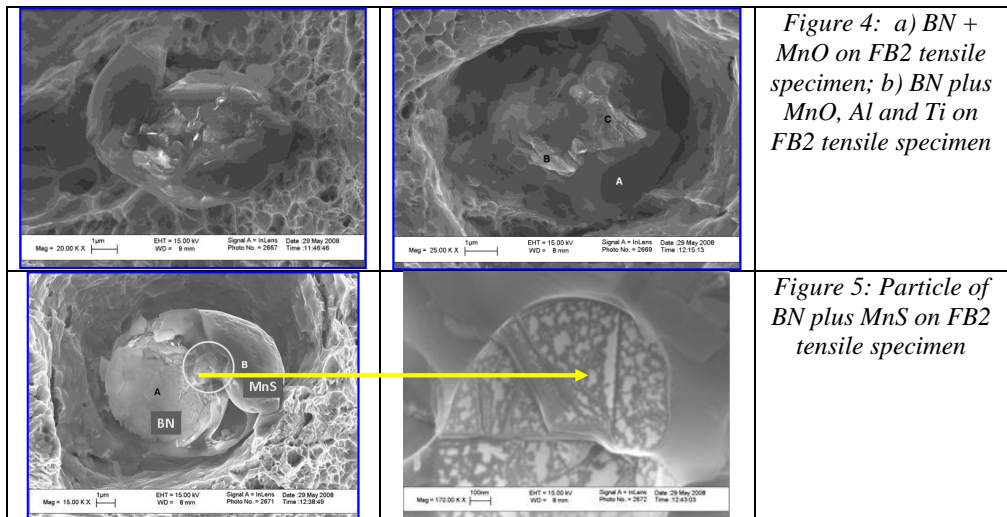
3.3 Creep properties

A large creep test programme was defined in the Turbine Working Group of COST 536 to qualify the trail rotor and the tests have been carried out by CSM. Notched and un-notched specimens have been machined from different positions and tested in the temperature range 600-650°C with continuous strain measurements. Some tests have been planned to reach the rupture in 100.000 hours. The creep results obtained on the SdF trial rotor confirm with the behaviour of the 500kg trial melt [9]. Figure 6 summarises the current status of the tests compared with the master curves (Larson-Miller) of COST 501 rotors E, F and B2. Some specimens are still running: 3 at 625°C currently in the range of 34.000 hours and 1 notched specimen at 600°C 130MPa it is recently broken after 84.000 hours.

It is possible to observe that the results of FB2 SdF trial rotor are in the upper band of the previous trial rotors and the ductility of the creep specimens broken up to now it is very good both in term of elongation and reduction of area without evidence of ductility drop for the longer tests at the different temperatures.

Figure 6: Creep master curve of tests of SdF FB2 trial rotor (open point = specimens running) compared with B2 and E + F rotors curves [15]
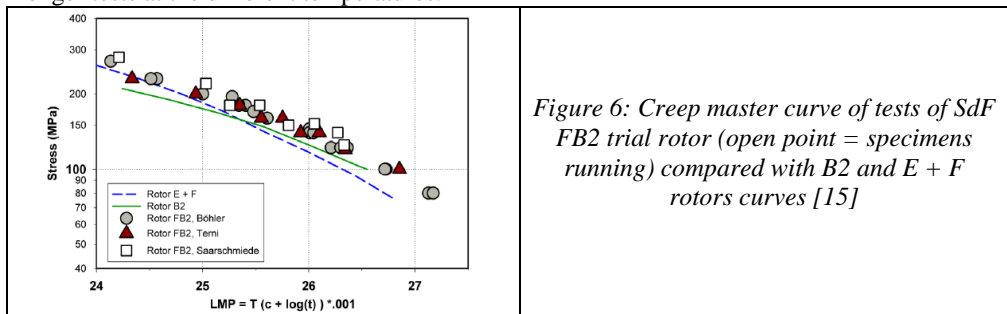
3.4 Microstructural evolution

In parallel with the mechanical and creep tests a programme to investigate the microstructural evolution of the FB2 steel is started. The thermodynamic tools predict, at equilibrium the main presence of $M_{23}C_6$ carbides and M(C,N), Laves phase and a little amount of Z-phase. As well known the Z-phase appearance has been identified as the main reason of the drop of the creep properties of all the recently developed 10-12%Cr steels [12]. The microstructural investigations have been carried out by TEM quantitative investigation with EDS analysis on the as treated material and on specimens after aging at different temperatures.

The forged material after heat treatment is characterised by a fine precipitation of $M_{23}C_6$ and, in the meantime, by a low amount of larger particles of MX: their dimensions and mean chemical compositions is reported in Table 5 and can be summarised as:
-   No fine MX are present after heat treatment,
-   The large MX are bigger then MX in 9%Cr steels,
-   $M_{23}C_6$ are 20-40% smaller then $M_{23}C_6$ in 9% grades,
-   $M_{23}C_6$ frequency is much higher than the in 9% grades.

Precipitates/ Dimen. (nm)	FB2 SdF	Grade 92 1070+780	Grade 911 1060+760	Grade 91 1070+780	Frequency (%)	Cr (%)	Mo (%)	V (%)	Nb (%)	Fe (%)
MX	180	45	50	35	4	17	5	3	68	6
$M_{23}C_6$	98	125	130	139	96	56	14	1,5	4	22

Table 5: Mean dimension of precipitates present in N+T forged FB2 compared with the other and quantitative analysis (% in weight) of FB2 precipitates [13-14]

3.5 Microstructural analysis on aged specimens

Microstructural analysis by SEM+ EDS and STEM+EDS started on crept aged specimens in order to investigate the evolution of the precipitates: the first 2 specimens have been selected after 23.576 hours at 625°C and after 10.026 hours at 650°C (Figure 7).
It was possible to observe that in aging condition there are:
- still a relevant amount of small $M_{23}C_6$ particles without appearance of coarsening process,
- the precipitation of some small MX particles, not present in the as treated condition,
- the appearance of Laves phase in the specimen aged at 625°C,
- the start of transformation of the bigger MX in to Z-phase (1 particle analysed) (Figure 8).
The $M_{23}C_6$ dimensions in FB2 aged specimens have been compared with the dimension of the precipitates in the grade 91: it was observed that the coarsening phenomena are strongly reduced [14-18]. This effect could be related to the introduction of B in the chemical composition, that seems have a stabilising effect on the $M_{23}C_6$ and on grain boundary [19-21], but this item is still under discussion worldwide.

4. Type E Rotor

After this quite good results on this experimental steel in year 2001 Società delle Fucine decided to made some other forged rotors in Steel X12CrMoVWNb10-1-1 (COST Type E), following Technical Specification suggested by COST program. The ingots have been melted in ThyssenKrupp Acciai Speciali Terni.
An example of the chemical composition (%wt) obtained in one delivered rotor is reported in Table 6. It is possible to observe that all the elements in the component are in the range the standard. The other residual elements analyses are: Cu<0.06%; Sn <0.003%; As <0.004%.
Manufacturing process for Rotor E components is the same of FB2, described in the scheme just illustrated in Figure 2.

Figure 7: Microstructure after 23576 hours at 625°C and after 10026 hours at 650°C
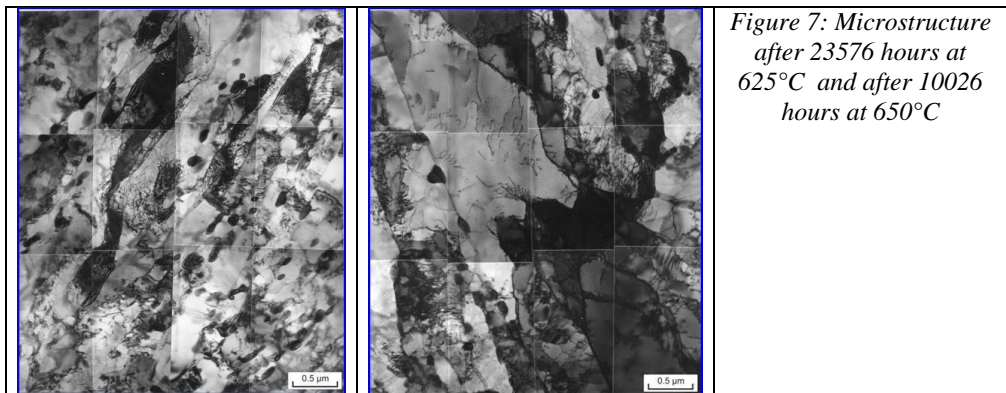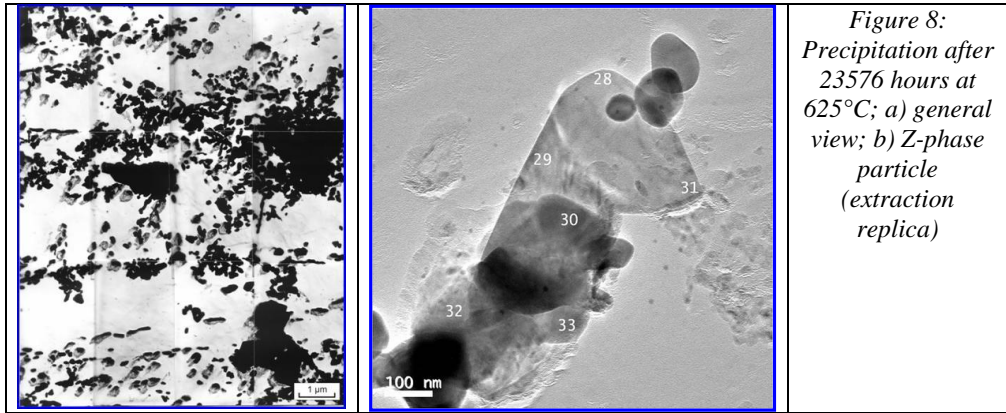
Figure 8: Precipitation after 23576 hours at 625°C; a) general view; b) Z-phase particle (extraction replica)

	Wt %	C	Mn	P	S	Si	Ni	Cr	Mo	Nb	W	Al	N	V
X12CrMoVWNb1 0-1-1 / COST E	min	0,11	0,4			0,05	0,7	10,2	1,02	0,04	0,95		0,04	0,17
	max	0,13	0,5	0,015	0,005	0,15	0,8	10,8	1,1	0,06	1,1	0,04	0,06	0,22
SdF Rotor E		0,12	0,45	0,01	0,001	0,07	0,78	10,6	1,04	0,06	1,01	0,001	0,05	0,20

Table 6: Chemical composition of a rotor produced with Steel X12CrMoVWNb10-1-1 (COST Type E)

After completion of the first rough machining, the forging rotors were subject to quality heat treatment, for instance, as follow:
- Austenitizing at T=1070°C; oil quenching;
- 1st Tempering at T=520°C, and air cooling;
- 2nd tempering at T=710°C, and air cooling.

Tempered martensite microstructure of one rotor component has been obtained in all the different positions of the components.

An example of the basic mechanical characteristics of Rotor E components are shown in Table 7. The scattering of strength values are quite low: these results confirm the good heat treatment practises and the homogeneous mechanical properties. [23].

The FATT value has been evaluated as 38°C. Tensile tests have been carried also in the temperature up to 620°C.

The material strength values are in the range of nominal values of the Rotor E 23.

No recordable indications were found by NDT control in all the forging components.

In order to have a full qualification of the material Rotor E a large and comprehensive testing program including tests on smooth and notched specimens, cracked and un-cracked specimens were planned as follows:
- Creep program: 550-600-650°C,
- high cyclic fatigue tests (HCF), Low cycle fatigue tests at high temperature (LCF), Thermo-mechanical fatigue tests (TMF),
- Crack growth tests at high temperatures and static loads and under isothermal conditions (CG),
- Fatigue and creep/fatigue crack growth (CCG/FCG) characterisation of crack propagation on CT specimens under TMF condition.

		Typical requested values		SdF	
		min	max	nim	max
UTS	MPa	800	900	824	880
YS	MPa	700		706	740
El.	%	15		17	19
RoA	%			54	63
KCV	Joule	30		35	96

Table 7: Example of Tensile tests results on forged components

The creep test program has been planned at 550-600-650°C. In Figure 9 have shown the creep results at three temperatures, which are in agreement with the Cost E mean lines: the red symbols with arrows represent the still running tests over 30.000 hours. The tests have been performed with strain measurements and shows the strain/time curves currently still in secondary stage.
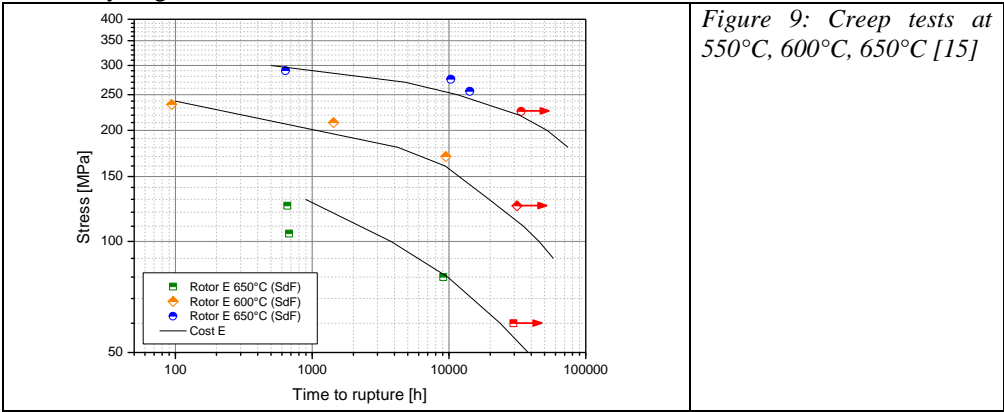
Figure 9: Creep tests at 550°C, 600°C, 650°C [15]

5. Summary and Conclusions

The result obtained up to now on FB2 trial rotor and on Steel X12CrMoVWNb10-1-1 (COST Type E) produced at Società delle Fucine, without ingot remelting, demonstrate that it is possible to realise full scale forged components by conventional process route with very good homogeneity of chemical analysis, mechanical behaviour and creep properties.

The FB2 from SdF has a quite good balancing of the B and N content, therefore a very low amount of BN that are present and there are always in connection with MnS or inclusion oxides particles.

In term of creep behaviour FB2 seems to offer a significant improvement over the parent E-F-B type steels and it could be suitable for 625°C applications. In fact the experience gained during the last few years seems guarantee that the 9%Cr are more stable materials from the microstructural evolution point of view [12,13], and suggests that the formation of some Z-phase precipitates may not significantly affect by mean of the long term creep behaviour of this steel. Obviously these results have to be confirmed with longer creep tests in order to generate a more consistent database, assessment and extrapolation. Tests still running are planned to reach more than 50-70.000 hours life.

The TEM investigation on long term aged specimens shown that the microstructural evolution is significantly different respect to the other 9%Cr steels: the dimension of the $M_{23}C_6$ seems not slightly affected by time and temperature precipitates and few Z-phase particles have been found in FB2 after 23.576 hours at 625°C.

If the slower coarsening of the $M_{23}C_6$ particles will confirmed by the analysis of the more aged specimens, these will be an experimental confirmation of the positive effect the Boron on the microstructural stability of this steel and therefore on the creep behaviours. Other microstructural investigations are planned for the longer time aged crept specimens.

Also the parent Steel X12CrMoVWNb10-1-1 (COST Type E) has been successfully produced in Società delle Fucine and the microstructural analysis, mechanical and creep tests shown properties in agreement with the literature values. Currently about 20 rotor components have been produced in Società delle Fucine starting from a maximum ingot of 75tons: the dimension of the components have a maximum delivered weight of 27 tons and a maximum diameter of 1200mm.

Acknowledgement

REFERENCES

1. T.U. Kern, K. Wieghardt, H. Kirchner: Material and design solutions for advanced steam power plants, EPRI Fourth International Conference on Advanced in Materials Technology for Fossil Power Plants; October 25-28, 2004, Hilton Head Island, South Carolina USA
2. R.W. Vanstone, Alloy design and microstructural control for improved 9-12%Cr power plant steels, Annex A, COST 522 Steam Power Plant, Final Report, 1998-2003
3. B. Scarlin and others: Materials developments for Ultrasupercritical Steam Turbines, As reference [1]
4. B. Scarlin, T-U. Kern, M. Staubli: The European efforts in material development for 650°C USC power plants – cost522, Ibidem
5. Y. Tanaka, T. Azuma, K. Miki: Development of steam turbine rotor forging for high temperature application high temperature steel forgings for power generation, Ibidem
6. P. Peel, B. Scarlin, R.Vanstone: From materials development to advanced steam turbines: PARSONS 2007: 7th International Charles Parsons Turbine Conference, Power Generation in an Era of Climate Change, 11-13 September 2007, Univ. of Strathclyde, Glasgow, UK.
7. G. Zeiler, W. Meyer, K. Spiradek, J. Wosik: Experiences in manufacturing and long-term mechanical & microstructural testing on 9-12 % chromium steel forgings for power generation plants,: as reference [1]
8. N. Blaes, B. Donth, K.H. Schönfeld, D. Bokelmann: High temperature steel forgings for power generation, Ibidem
9. T.U. Kern, M. Stabli, K.H. Mayer, B. Donth, G. Zeiler, A. Di Gianfrancesco: The European effort in development of new high temperature rotor materials – COST 536: Int. Conf. Materials for Advanced Power Engineering, 19-21 September 2006 Liege, Belgium
10. T.-U. Kern, B. Scarlin, B. Donth, G. Zeiler, A. Di Gianfrancesco: The European COST536 project for the development of new high temperature rotor materials: 18° International Forgemaster Meeting: 3-6 November 2008 Santander, Spain
11. A. Di Gianfrancesco, L. Cipolla, D. Venditti, S.Neri, M. Calderini: High Temperature Properties and Creep Behaviour of a CrMoCoB (FB2) Steel Trial Rotor, Ibidem
12. F. Abe: Alloy Design of Creep and Oxidation Resistant 9Cr Steels for Thick Section Boiler Components Operating at 650°C: As reference [1]
13. A. Di Gianfrancesco, L. Cipolla, D. Venditti, S.Neri, M. Calderini: Creep Behaviour and microstructural stability of FB2 (CrMoCoB) Steel Trial Rotor Sixth International Conference on Advances in Materials Technology for Fossil Power Plants August 31–September 3, 2010 Santa Fe, New Mexico, USA
14. L. Cipolla, S. Caminada, D. Venditti, H. K. Danielsen, A. Di Gianfrancesco: Microstructural evolution of ASTM P91 after 100,000 hours exposure at 550°C AND 600°C: 9th Liège Conference on Materials, for Advanced Power Engineering: September 27th – 29th, 2010, Liège • Belgium

15. T.-U. Kern, K.H. Mayer, B. Donth, G. Zeiler, A. Di Gianfrancesco:The European efforts in development of new high temperature rotor materials – COST536: ibidem
16. A. Di Gianfrancesco and others: Long term creep properties and microstructural evolution of IN718 prototype forged disk: 18th International Forgemasters Meeting: September 12-16, 2011 Pittsburgh, PA, USA
17. J. Hald, H. Danielsen: Z-phase in 9-12%cr steels: As reference [1]
18. S. Caminada, G. Cumino L. Cipolla, A. Di Gianfrancesco: Long term creep behaviour and microstructural evolution of ASTM grade 91 steel; ibidem
19. Fujio Abe: Effect of boron on creep deformation behaviour of 9cr steel for USC boilers at 650°C: PARSONS 2007: 7th International Charles Parsons Turbine Conference, Power Generation in an Era of Climate Change, 11-13 September 2007, Univ. of Strathclyde, Glasgow, UK.
20. H.O. Andren, A. Golpayegani: Microstructure of a high boron chromium steel for steam turbine applications: ibidem
21. H.O. Andren, A. Golpayegani: Creep resistant high boron 9-12% chromium steels for steam power plants: Int. Conf. New Developments on Metallurgy and Applications of High Stregth Steels: Buenos Aires, Argentina 26-28 May 2008
22. P. Lombardi and others: Development of methods for the characterisation, fracture assessment and life prediction of new high strength steels under variable temperature operating conditions: DELOC: RFSR CT 2007-00021; 01/01/2007 – 30/06/2010, Final Report
23. Y. Wakeshima, M. Mikami, manufacturing of trial rotor forgings of cost e steel (x12crmowvnbn10-1-1), IFM 2006, 16th International Forgemasters Meeting,15 – 19 October 2006, Cutlers' Hall, Sheffield, UK

DEVELOPMENT OF IMPROVED HIGH TEMPERATURE BOILER MATERIALS FOR THE INDIAN ADVANCED ULTRA SUPER-CRITICAL THERMAL POWER PLANT TECHNOLOGY

T. Jayakumar, A.K. Bhaduri and S.C. Chetal[$]

Indira Gandhi Centre for Atomic Research, Kalpakkam 603102, India
[$]Office of the Principal Scientific Adviser to the Govt. of India, New Delhi 110011, India
Email: tjk@igcar.gov.in; bhaduri@igcar.gov.in; chetalsc@gmail.com

Abstract

As part of the mission programme initiated in India for design and establishment of an 800 MWe Advanced Ultra Supercritical (AUSC) thermal power plant with steam parameters of 710°C/720°C/ 310 bar, focused R&D is in progress for indigenous development and qualification of 304HCu stainless steel and modified nickel-base Alloy 617 boiler tubes and their welding consumables for use in sections operating above 530°C in the AUSC boiler. For this purpose, stage-wise characterization approach was adopted to establish the optimised process route for manufacturing 52 mm diameter seamless tubes of 304HCu SS and Alloy 617M with wall thickness of 9.5 and 11.9 mm, respectively. These involved detailed characterisation of thermo-physical properties, microstructure, heat treatment response and evaluation of thermo-mechanical processing. Welding procedure specifications have also been developed for TIG welding of 304HCu SS and Alloy 617M tubes, including dissimilar 304HCu SS/Alloy 617M tubes. Detailed evaluation of tensile, creep, low-cycle fatigue, impact, quasi-static fracture, and creep and fatigue crack growth of both the tube materials and their weld joints have confirmed that these properties are comparable to internationally reported values and the codified values in VdTÜV standard.

Keywords: 304HCu stainless steel; Alloy 617M, AUSC technology; Welding procedures; Mechanical property evaluation

1. Introduction

Coal fired power plants will continue to contribute a significant part of the supply of electric power for India in the near future. Significant efforts are being made today towards enhancing the plant efficiency and reducing the carbon-dioxide emissions. To achieve higher efficiency, it is necessary that the power plants be operated at higher steam temperatures. Towards this, a mission programme has been initiated in India towards evolving a design for an 800 MWe capacity Advanced Ultra Supercritical (AUSC) plant with steam parameters of 710°C/720°C/ 310 bar to achieve high efficiency. To implement this programme, advanced materials that show good performance and life under such conditions are required. Currently plants worldwide are working with superheater and reheater temperatures of up to about 660°C. However, further significant efficiency increase is being considered with steam temperatures above 700°C. This paper provides the details of efforts made in India towards development of high temperature materials for realisation of this goal. As part of the mission programme, two high temperature materials 304HCu austenitic stainless steel (304HCu SS) and modified nickel-base Alloy 617 (Alloy 617M) have been identified for development for boiler tubes operating at temperatures beyond 530°C.

For development of indigenous 304HCu SS and Alloy 617M, a stage-wise characterization approach was adopted to establish optimised process route for obtaining quality tubes. Detailed characterisation of thermo-physical properties, microstructure, heat treatment response and evaluation of thermo-mechanical processing map enabled necessary

understanding of the behaviour of these materials during mechanical working and heat treatment. Welding filler wires of matching composition to 304HCu SS and Alloy 617M were manufactured indigenously, and used for development of procedures for tungsten inert gas (TIG) welding of 304HCu SS and Alloy 617M tubes, including their dissimilar metal tubes welds. Detailed evaluation of mechanical properties, viz. tensile, creep, fatigue, impact, quasi-static fracture, and creep and fatigue crack growth of the tube materials and their weld joints were carried out to qualify these materials for use in the Indian AUSC power plant boilers.

2. Manufacture of 304HCu SS and Alloy 617M boiler tubes

The chemical compositions (Table 1) and mechanical properties requirements of 304HCu SS [UNS S30432] and Alloy 617M tubes were prepared by suitably modifying the composition within the ASME Code Case 2328-1 and ASME SB 167 (2010: Sec-II Part-B) specifications, respectively. Based on the detailed microstructure characterisation after each stage of manufacturing, the process flow-sheet was revised to ensure high quality of the tubes produced. The heat treatment temperature and time for solutionising, intermediate and final heat treatments were optimised by carrying out detailed laboratory studies involving multiple heat treatments, over different combinations of temperature and time, in order to dissolve the coarse primary Nb-rich carbides and carbonitrides in 304HCu SS and Cr- and Mo-rich inter-granular precipitates in Alloy 617M. Calorimetry study was also carried out to establish the various reactions that take place during heating and cooling. These studies indicated that, for 304HCu SS, heat treatment at 1270°C and above is beneficial as the size range and volume fraction of Nb-rich precipitates are significantly reduced; while for Alloy 617M, intermediate annealing at 1160–1180°C controls grain size. These 304HCu SS and Alloy 617M tubes met the specifications for all the mechanical properties and grain size requirements, as also non-destructive testing involving ultrasonic examination with defect sensitivity of 3% of nominal wall thickness, which is more stringent than the 5% notch depth specified in ASME SE-213.

Table 1: Chemical composition specifications for 304HCu SS and Alloy 617M boiler tubes

Element	304HCu SS		Alloy 617M	
(wt%)	Indian AUSC	ASME	Indian AUSC	ASME
Aluminium	0.003-0.030	0.003-0.030	0.8-1.3	0.8-1.5
Boron	0.002-0.006	0.001-0.010	0.002-0.005	0.006 max
Carbon	0.07-0.13	0.07-0.13	0.05-0.08	0.05-0.15
Chromium	17.00-19.00	17.00-19.00	21.0-23.0	20.0-24.0
Cobalt	–	–	11.0-13.0	10.0-15.0
Copper	2.50-3.50	2.50-3.50	0.5 max	0.5 max
Iron	Balance	Balance	1.5 max	3.0 max
Manganese	1.00 max	1.00 max	0.3 max	1.0 max
Molybdenum	–	–	8.0-10.0	8.0-10.0
Nickel	8.00-10.00	7.50-10.50	Balance	44.5 min
Niobium	0.30-0.60	0.30-0.60	*For record*	–
Nitrogen	0.07-0.12	0.05-0.12	0.05 max	–
Phosphorous	0.030 max	0.040 max	–	–
Silicon	0.30 max	0.30 max	0.3 max	1.0 max
Sulphur	0.010 max	0.010 max	0.008 max	0.015 max
Titanium	–	–	0.3-0.5	0.6 max

To optimize the strain rate and temperature combination for manufacturing of the 304HCu SS and Alloy 617M tubes, compression tests were carried out in Gleeble thermo-mechanical simulator over a wide range of temperatures and strain rates, and the experimental data were used to develop processing maps based on Dynamic Materials Model followed by extensive microstructural investigations to validate the domains exhibited by the processing maps. The results from the processing maps and microstructural investigations reveal that the temperature range of 1200–1250ºC and strain rate range of 1–50 s^{-1} is the optimum window for thermo-mechanical processing of 304HCu SS, while the domain bounded within the temperature range of 1110–1250ºC and strain rate range of 0.01–0.2 s^{-1} is found to be the suitable domain for hot working of Alloy 617M.

3. Welding of 304HCu SS and Alloy 617M tubes

Specifications for appropriate filler wires, of both matching and non-matching chemistry were finalised, including indigenous development of 304HCu SS and Alloy 617M filler wires. Matching composition ER304HCu filler wires and two nickel-base alloys filler wires, ER625 (AWS ERNiCrMo-3) and ER617 (AWS ERNiCrCoMo-1) were used for TIG welding of 304HCu SS, while ER617 filler wires were used for TIG welding of Alloy 617M tubes and 304HCu SS/Alloy 617M dissimilar tubes.

During the initial trials for welding of 304HCu SS using ER625 and ER617 consumables, weld defects like root-cracks, hot-cracks and crater-cracks were observed due to the poor fluidity of Ni-base filler metals. Figure 1(a) shows a typical hot-crack observed during one of the initial trials. These problems were overcome by suitably altering weld joint design and optimising the welding heat input, and weld procedure qualification (WPQ) was carried out using the optimised welding parameters. Figures 1(b) and 1(c) show the acceptable 304HCu SS tube weld joints made with optimised parameters using ER625 and ER617 filler wires, respectively. WPQ was also carried out for 304HCu SS joints with matching chemistry ER304HCu filler wires, and with ER617 filler wires for the Alloy 617M joints and the 304HCu SS/Alloy 617M dissimilar joints. All the similar and dissimilar tube weld joints passed the soundness evaluation tests as per ASME Section IX, viz. dye-penetrant and X-ray radiography examinations, the face-bend and root-bend tests,
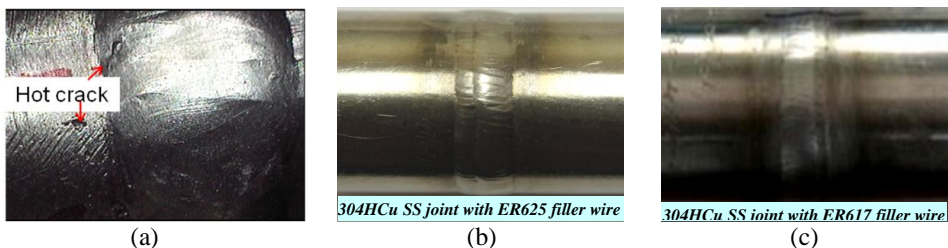
Figure 1: Macrographs of 304HCu SS weld joints: (a) hot crack in initial trials using ER625 filler wire; and WPQ weld joints made using (b) ER625 and (c) ER617 filler wires

4. Tensile properties of 304HCu SS and Alloy 617M tube materials and their weld joints

Comparison of tensile properties of the indigenous 304HCu SS tube material with internationally reported values [1-3] (Fig. 2) showed that while the yield strength (YS) at all

test temperatures are higher than those reported in literature (Fig. 2a), the ultimate tensile strength (UTS) is generally comparable with internationally reported values at all temperatures (Fig. 2b). Compared to the tensile properties of Alloy 617 reported in literature [4], the indigenous Alloy 617M shows higher YS and UTS at all the test temperatures while its tensile ductility is lower below 600ºC and higher above 600ºC (Fig. 3). Thus, for both the indigenously developed materials, the YS and UTS are comparable to or better than the minimum specified in the VdTÜV (German) standards. The transverse-weld tensile properties of the similar and dissimilar weld joints of 304HCu SS and Alloy 617M are given in Table 2.

(a)   (b)
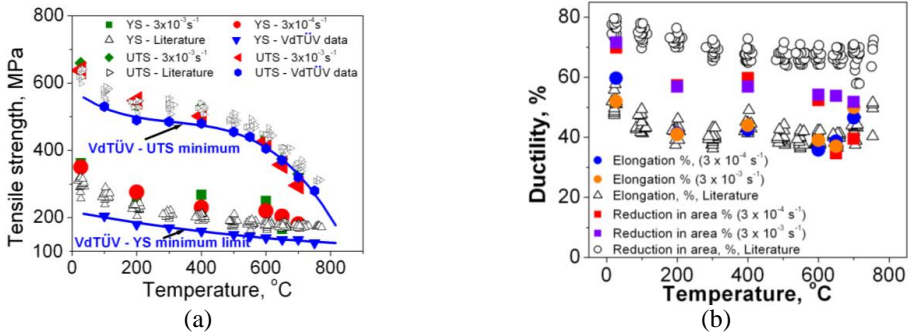
Figure 2: Variation of tensile properties with test temperature of indigenous 304HCu SS tube material: (a) tensile strength; and (b) tensile ductility

(a)   (b)
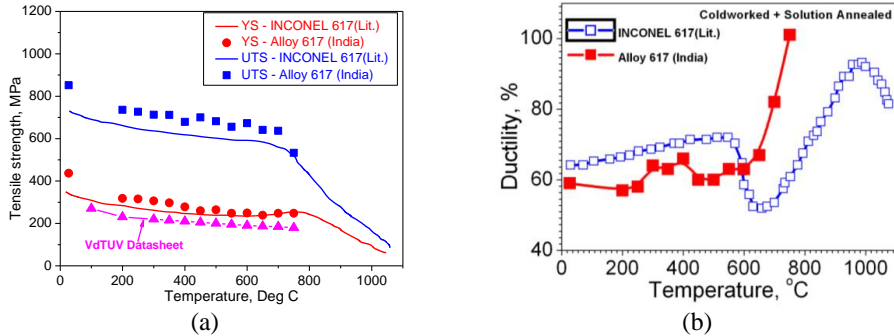
Figure 3: Variation of tensile properties with test temperature of indigenous Alloy 617M tube material: (a) tensile strength; and (b) tensile ductility

Table 2: Tensile properties of tube materials and transverse-weld joints of tubes

Tube Material	Filler wire	YS (MPa)	UTS (MPa)	Failure Location
304HCu SS Tube		311	635	–
304HCu SS	ER625	479	688	Base metal
304HCu SS	ER617	424-436	651-762	Base metal
304HCu SS	ER304HCu	428-457	637-694	Base metal / Weld metal
Alloy 617M Tube		331-339	783-813	–
Alloy 617M	ER617	418-443	747-798	Base / Weld metal / HAZ
304HCu SS/Alloy617M	ER617	455	706	Base metal

5. Creep properties of 304HCu SS and Alloy 617M tube materials and their weld joints

Compared with internationally reported data [1-3], creep-rupture strength of the indigenous 304HCu SS tube material, based on short-term creep tests, (Fig. 4), is within the ±20% scatter band and is similar to the VdTÜV and ASME average values. Compared to the creep-rupture life of the base material at 650°C, the 304HCu SS joint welded using ER625 filler wire shows lower creep rupture life and ductility while the one welded with ER304HCu filler wire shows higher creep rupture life and ductility (Figs. 4a and 5a) along with lower steady-state creep rate (Fig. 5b). The variation of creep-rupture life of the Alloy 617M tube material with applied stress at different temperatures, based on short-term creep tests, compared with internationally reported data [4] (Fig. 6) shows very encouraging trends with the indigenously produced tubes showing better creep properties. Long-term creep tests are in progress.
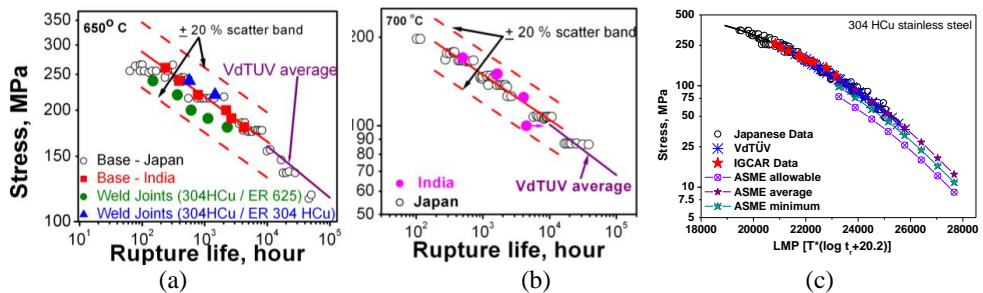
Figure 4: Variation with applied stress of creep-rupture life of 304HCu SS at (a) 650ºC (including for weld joints) and (b) 700ºC, and (c)of Larsen-Miller parameter
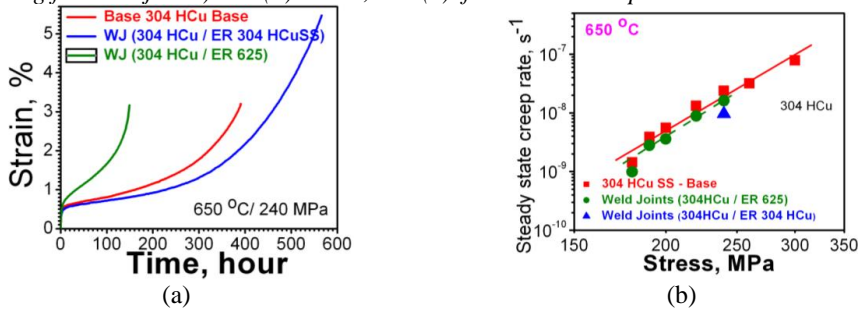
Figure 5: Comparison of creep behaviour at 650ºC of 304HCu SS and its weld joints: (a) creep rupture ductility; and (b) steady state creep rate at different stress levels.
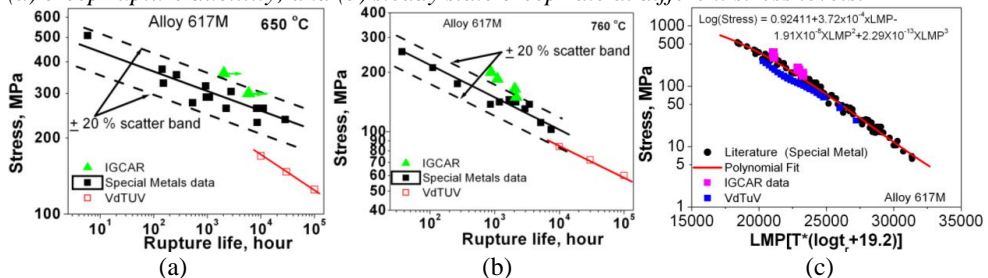
Figure 6: Variation with applied stress of creep-rupture life of Alloy 617M at (a) 650ºC and (b) 760ºC, and (c)of Larsen-Miller parameter

6. Low cycle fatigue properties of 304HCu SS and Alloy 617M tube materials

Continuous cycling tests on 304HCu SS was carried out at 650 and 700ºC (923 and 973K) using a strain rate of 3×10^{-3} s^{-1} at strain amplitudes of ±0.4, ±0.6 and ±1.0%. Figure 7 shows the cyclic stress response (Fig. 7a), the strain-life plot (Fig. 7b) and the effect of tension hold on fatigue life (Fig. 7c) for the indigenous 304HCu SS tube material.

(a)   (b)   (c)
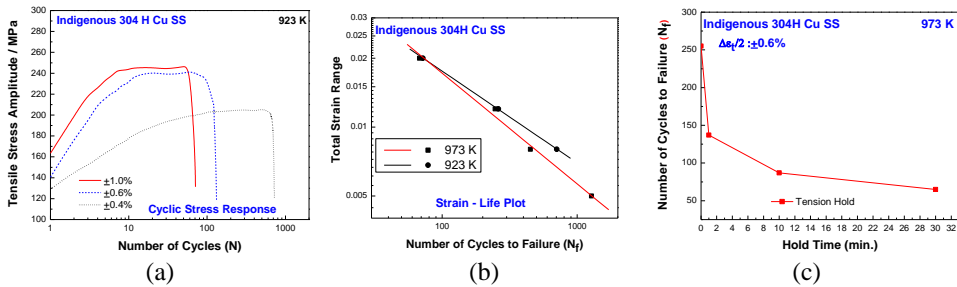
Figure 7: (a) Cyclic stress response at 650ºC (923K), (b) strain-life plots at 650 and 700ºC (923 and 973K) and (c) variation of fatigue life with hold time for 304HCu SS tube material

Continuous cycling tests on Alloy 617M were carried out at 700 and 750ºC (973 and 1023K) using a strain rate of 3×10^{-3} s^{-1} with strain amplitudes of ±0.25, ±0.40 and ±0.60%. Figure 8 shows the cyclic stress response (Fig. 8a) and the strain-life plots (Fig. 8b) for the Alloy 617M tube material, and Table 3 summarises the low cycle fatigue test results. The fatigue lives of the Alloy 617M tubes developed indigenously and those obtained from an international manufacturer are comparable with results available in international literature [5].

(a)   (b)
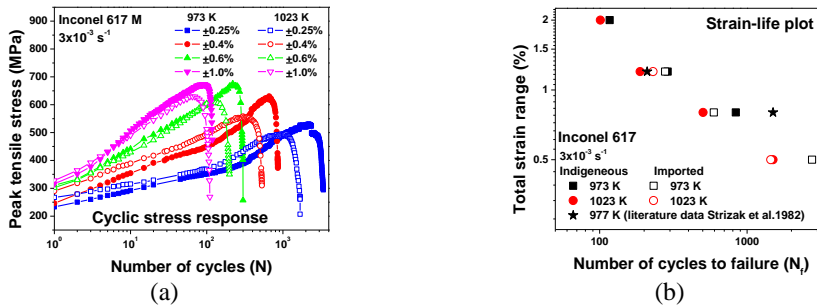
Figure 8: (a) Cyclic stress response at 700ºC (973K), and (b) strain-life plot at 700-750ºC (973-1023K) for Alloy 617M tube material

Table 3: Low cycle fatigue results for Alloy 617M tested at a strain rate of 3×10^{-3} s^{-1}

Temperature	Strain amplitude (%)	No. of cycles to failure (N$_f$)	1st cycle Stress (MPa)	Stress at Half life (MPa)	Half life plastic strain range (%)
700°C	±0.25	3145	225	508	0.08
	±0.40	595	259	560	0.31
	±0.60	278	299	631	0.68

7. Fracture properties 304HCu SS and Alloy 617M tube materials

7.1. Charpy impact testing of 304HCu SS and Alloy 617M tube materials

The Charpy impact test specimen blanks were extracted from the 52 mm diameter tubes, and the specimens were fabricated with two different notch orientations, viz. Type-A and Type-B having notch orientation to ensure crack propagation along the circumferential and radial directions, respectively (Fig. 9). In accordance with ASTM E23 guidelines, the size of the finished Charpy V-notch impact test specimens obtained was $5 \times 5 \times 55$ mm^3 with V-notch depth of 1 mm for the 304HCu SS tubes (of 9.5 mm wall thickness), and $10 \times 10 \times 55$ mm^3 with V-notch depth of 2 mm for the Alloy 617M tubes (of 11.9 mm wall thickness). The results of the Charpy V-notch impact tests at ambient temperature (Table 4) show that the Charpy energy is in the similar range for both types of specimen orientations for 304HCu SS. However, for Alloy 617M, the Charpy energy in the circumferential direction (Type-A) is higher compared to that in the radial direction (Type-B). Also, for 304HCu SS, the Charpy energy obtained from sub-size specimens has been converted to full-size (FS) equivalent using empirical formula: $C_v(full) = K*C_v(sub)$, with K=8 [6]; the converted full-size equivalent Charpy energy is also given in the Table 4.
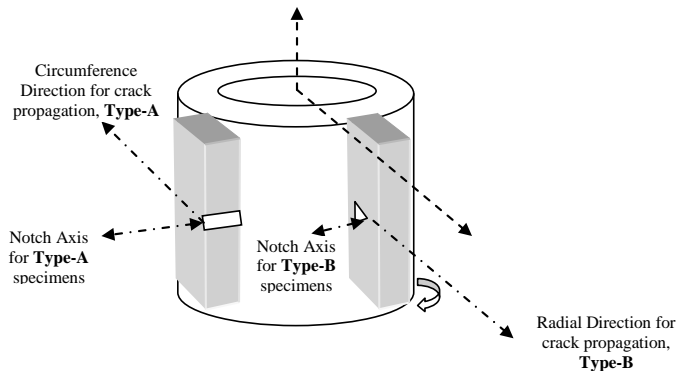
Figure 9: Schematic layout of specimen fabrication from the tubes, along with notch axis

Table 4: Results of Charpy V-notch impact test at ambient temperature for 304HCu SS and Alloy 617M tube materials

Material	Specimen size (mm)	Notch Orientation	Charpy Energy (Joules)
304HCu SS	$5 \times 5 \times 55$ (notch: 1 mm)	Type-A (circumferential)	33.0 ± 1.0, FS: 272 ± 6
		Type-B (radial)	34.0 ± 1.0, FS: 276 ± 4
Alloy 617M	$10 \times 10 \times 55$ (notch: 2 mm)	Type-A (circumferential)	327.5 ± 0.5
		Type-B (radial)	269.5 ± 4.5

After the ageing of 304HCu SS tubes at 700°C for 1000h and Alloy 617M tubes at 750°C for 1000h, Charpy impact test specimen blanks with two different notch orientations, viz. Type-A and Type-B, were extracted from the aged tubes as detailed before (Fig. 9). The results of the Charpy V-notch impact tests at ambient temperature, including the converted to full size equivalent for 304HCu SS, (Table 5) show that, for both the materials, substantial degradation

in Charpy energy occurs on ageing. While orientation dependence on Charpy energy is not evident for 304HCu SS, in Alloy 617M, the Charpy energy is lower for crack growth in the radial direction. The trends are similar in both as-received and aged conditions.

Table 5: Results of Charpy V-notch impact test at ambient temperature for the indigenous 304HCu SS and Alloy 617M tube materials after ageing

Aged material	Specimen size (mm)	Notch Orientation	Charpy Energy (Joules)
304HCu SS (700°C/1000h)	5×5×55 (notch: 1 mm)	Type A (circumferential)	21 ± 0, FS: 168.0 ± 2.0
		Type-B (radial)	22 ± 3, FS: 175.5 ± 4.5
Alloy 617M (750°C/1000h)	10×10×55 (notch: 2 mm)	Type-A (circumferential)	133.0 ± 3.0
		Type-B (radial)	121.5 ± 1.5

7.2. Quasi-static fracture and fatigue crack growth behaviour

Both the 304HCu SS and Alloy 617M tube materials were evaluated for their elasto-plastic fracture toughness and fatigue crack growth (FCG) behaviour. Compact tension (CT) specimens were fabricated according to ASTM E1820 standards, with the dimensions of the tube necessitating use of ¼ CT specimens with 6.25 mm thickness (B) and 25 mm width (W). The specimens were machined in the C-L orientation; i.e. with the crack plane normal to the circumferential direction for crack growth in the longitudinal direction, as this is the expected orientation for the lowest crack growth resistance. For crack growth measurement during testing, a fully calibrated direct current potential drop (DCPD) measurement device was used, with the DCPD calibration being carried out using specimens of the same geometry as the test samples but with cracks of different lengths machined using wire EDM. The DCPD calibration constants thus estimated were used for online crack length measurements during fracture and FCG testing. These were further validated using data from post-test optical measurements of the crack lengths. The quasi-static fracture and FCG tests as per the ASTM E1820 and E647 standards have thus far been carried out at ambient temperature on the as-received materials.

Ambient temperature (25ºC) quasi-static fracture toughness evaluated for 304HCu SS tube materials exhibits very similar J–Δa curves, with the elastic-plastic fracture toughness ($J_{0.2}$) for the indigenous material of 210–253 kJ.m^{-2} (Fig. 10a), being comparable (235 kJ.m^{-2}) to the material obtained from an international manufacturer.

Quasi-static fracture toughness testing has also been carried out at ambient temperature (25ºC) for the indigenous Alloy 617M tube material, and the J-R curve is presented in Fig. 10(b). The indigenous Alloy 617M is found to have a $J_{0.2}$ value of 417 kJ.m^{-2}. This has been compared with an equivalent grade of Alloy 617 [7] whose J_{Ic} values are reported as 250–439 kJ.m^{-2} depending on the method of estimation (J_{Ic} values are 250 kJ.m^{-2} by potential drop method, 390 kJ.m^{-2} by simplified ASTM normalization method, 408 kJ.m^{-2} by ASTM normalization method, and 439 kJ.m^{-2} by unloading compliance method). As the potential drop method gives a lower J-R curve, the present results for the indigenous Alloy 617M tube material obtained using DCPD for crack growth measurement may be considered as conservative, but are still comparable with the reported values.
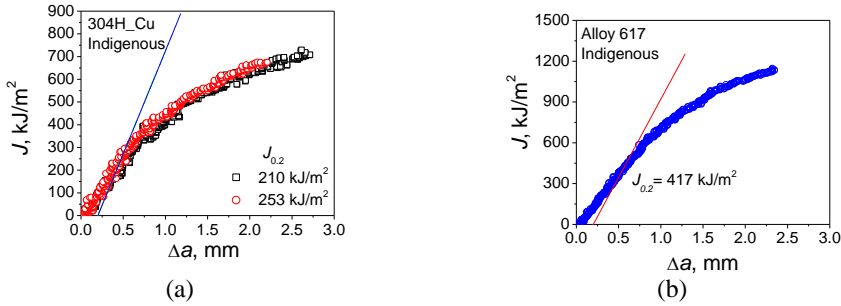
Figure 10: J-R curve at ambient temperature for as-received indigenous tube materials: (a) 304HCu SS; and (b) Alloy 617M

FCG tests have been carried out at ambient temperature (25ºC) on ¼ CT specimens of 304HCu SS extracted from indigenous tubes and also tubes obtained from an international manufacturer, with the crack growth oriented along the length of the tube. Preliminary results, without crack closure correction, indicate that the FCG behaviour of both the tube materials is comparable (Fig. 11). The tubes from the international manufacturer are with smaller grain size of ASTM no. 9 and the roughness-induced crack closure is expected to be smaller compared to that in the indigenous tube material with grain size of ASTM no. 7-8. The crack closure analyses and testing at elevated temperatures are in progress. Also, the oscillations observed in Fig. 11 are typical of the high-resolution crack length measurements, and represent intermittent microstructural barriers like grain boundaries.
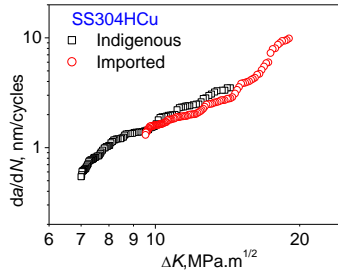
Figure 11: Fatigue crack growth plots for 304HCu SS tube materials tested at 25ºC, using 15Hz frequency and load ratio of 0.1

8. Concluding Remarks

(1)   Based on the inputs from stage-wise metallurgical characterisation during manufacturing, the process flow sheet was optimised for successfully manufacturing 52 mm diameter seamless tubes of 304HCu SS and Alloy 617M, with wall thickness of 9.5 and 11.9 mm, respectively.

(2)   The welding procedures were developed and qualified for welding of 304HCu SS tubes using ER625, ER617 and ER304HCu filler wires, of Alloy 617M tubes using ER617 filler wires, and dissimilar welding of 304HCu SS tubes to Alloy 617M tubes using ER617 filler wires.

(3)   Tensile, creep, low-cycle fatigue, impact, quasi-static fracture and fatigue crack
        growth properties have been evaluated for both the indigenously developed 304HCu
        SS and Alloy 617M tube materials and their weld joints. The results of mechanical
        properties of both the tube materials and their weld joints indicate that these properties
        are comparable to the internationally reported values as also the codified values in the
        VdTÜV (German) standard.

Acknowledgements

References

[1]   H.Okada, Y.Sawaragi, F.Masuyama and N.Komai, *Mechanical properties and
      microstructure of 0.1C-18Cr-9Cr-3Cu-Nb-N steel tube after long term exposures in a
      power boiler*, Proc. 7th Intnl. Conf on Creep and Fatigue at Elevated Temperatures,
      Tsukuba, Japan, The Japan Society of Mechanical Engineers (2001).
[2]   Y.Sawaragi, K.Ogawa, S.Kato, A.Natori and S.Hirano, *Development of the economical
      18-8 stainless steel (Super 304H) having high elevated temperature strength for fossil
      fired boilers*, The Sumitomo Research, No. 48, , Sumitomo Metal Industries, Ltd.,
      Osaka & Tokyo, Japan (January 1992)
[3]   DMV 304HCu, Salzgitter Mannesmann Stainless Tubes, Germany
[4]   Inconel 617, Special Metals, USA
[5]   J.P. Strizak, C.R. Brinkman, M.K. Booker, P.L. Rittenhouse, *The influence of
      temperature, environment, and thermal aging on the continuous cycle fatigue behavior
      of Hastelloy X and Inconel 617*, Report No. ORNL/TM-8130, Oak Ridge National
      Laboratory, Oak Ridge, TN, USA (April 1982)
[6]   G.E.Lucas, G.R.Odette, J.W.Sheckherd, P.McConnel, J.Perrin, *Sub-sized bend and
      Charpy V notch specimens for irradiated testing*, in: The Use of Small Scale Specimens
      for Testing Irradiated Material, ASTM STP 888, Eds. W.R.Corwin and G.E.Lucas
      (1986) pp.305-324
[7]   R.K. Nanstad, M.A. Sokolov, Lizhen Tan, Xiang Chen, *Fracture Toughness of High
      Temperature Alloys for Advanced Reactor Applications*, Materials Science and
      Technology Division, Oak Ridge National Laboratory, DOE-NE Materials Crosscut
      Coordination Webinar, In the Ether (28 August 2012)

DETERMINATION OF THE MAXIMUM ALLOWABLE NUMBER OF SUBSEQUENT POST WELD HEAT TREATMENTS ON EX-SERVICE GRADE 91 MATERIAL

De Bruycker E., Manssouri F., Huysmans G., Vanderlinden F.

Laborelec GDF SUEZ, Rodestraat 125, B-1630 Linkebeek, Belgium,
evy.debruycker@laborelec.com

Abstract

Martensitic Grade 91 steel is a high strength material developed and intensively used for tubes and pipes in new ultra super critical power plants and refurbishment projects for components subject to temperatures up to 600°C. This advanced martensitic material has high strength at high temperature, and more specifically high creep rupture strength, which is only guaranteed if the correct microstructure, tempered martensite with fine precipitates, is achieved. Hence, the chemical composition and the received heat treatment are essential parameters.

A critical manufacturing step is welding. After welding and after each repair weld, a Post Weld Heat Treatment (PWHT) is required in order to restore the properties of the material. However, subsequent heat treatments on the same base material adjacent to the weld can have a detrimental effect on its properties, so the total number of PWHT's should be limited. There is no consensus yet as to where this limit lays.

The objective of the investigation was to determine the maximum number of PWHT's that a base material can undergo without a significant negative impact on its properties (yield strength, tensile strength, ductility, fracture toughness, hardness, creep strength, etc.). Therefore, simulations of a single and multiple PWHT's were performed in a furnace on an ex-service Grade 91 material. Mechanical properties of the material were characterized before and after each simulation. Finally, the results were reviewed and the maximum allowable number of PWHT's was determined.

Keywords: multiple PWHT, Grade 91, creep strength

1. Introduction

Martensitic Grade 91 steel is widely used in refurbishment projects and new power plants for components subject to temperatures up to 600°C. The Grade 91 steel owes its strength largely to the presence of fine precipitates in a martensitic structure. This structure has a high tensile strength at high temperatures and a high creep resistance. Failure to achieve the optimum microstructure during original steel production or to maintain this microstructure during subsequent component fabrication, plant construction or component repair, will significantly impair the mechanical properties of the alloy and can lead to premature failures. Hence, the chemical composition and the received heat treatments are essential parameters.

A critical manufacturing step is welding. After welding untempered martensite is formed in the weld and HAZ. Therefore after each weld or repair weld, a Post Weld Heat Treatment (PWHT) is required in order to obtain a tempered martensite and to restore the properties of

the material. During the lifetime of piping components, repair welds are often performed for different reasons, with as a consequence that another PWHT needs to be performed. However, subsequent heat treatments on the same base metal surrounding the weld (Heat Affected Zone, HAZ) can have a detrimental effect on its properties, so the total number of PWHT's on the same material should be limited.

The influence of multiple PWHT's has been studied before, however, there is no consensus yet as to where exactly the limit lays. The effect of multiple PWHT's on mechanical properties has been studied by Dey et al. [1] on real weld joints. The samples were subjected to a single PWHT at 760°C during variable holding times, up to 12 hours, which represents about 3 PWHT's. This heat treatment has been found to have no adverse effect on the tensile properties and impact toughness of the weld joint. This was confirmed by microstructural examinations and hardness measurements. Spiegel [2] showed that a heat treatment at 770°C during 14 hours had no effect on the hardness (HV10) of a P91 base metal and no significant effect on the yield strength. The conservative rule of thumb that is currently used in industry is a maximum of 3 PWHT's.

The objective of this investigation was to determine the maximum number of PWHT's that the base metal can undergo without a significant negative impact on its properties (yield strength, tensile strength, fracture toughness, hardness and creep rupture strength). Therefore, simulations of single and multiple PWHT's were performed on an ex-service P91 pipe. Mechanical and creep properties of the material were characterized before and after simulation of different numbers of PWHT's. The results were reviewed and the maximum allowable number of PWHT's was determined.

2. Experimental set-up

2.1. Material

An ex-service P91 pipe, which had been in service for about 39500h at an average temperature of 570°C was used. The chemical composition and mechanical properties of the material are shown in Table 1.

Table 1: Chemical composition and mechanical properties of the used ex-service P91 material

Time in operation [h]		39 500
Average metal temperature in operation[°C]		570
Chemical composition measured with ICP spectroscopy [wt%]	**C**	0.1
	Mn	0.36
	Si	0.34
	S	0.004
	P	0.015
	Cr	8.7
	Ni	0.16
	Mo	0.98
	Cu	0.14
	V	0.2
	Nb	0.09
	Al	0.01
	N	0.04
Mechanical properties measured in the longitudinal direction		
Yield strength [MPa]		631
Tensile strength [MPa]		760
Elongation [%]		46
Impact energy [J]		106
Hardness [HV10]		209

2.2. Post Weld Heat Treatment (PWHT) simulations

Typical PWHT temperatures for P91 are between 740 and 760°C. The duration at the PWHT temperature depends on the thickness of the component. Holding times of 1h/25mm thickness are recommended with a minimum of 2h for Shielded Metal Arc Welding (SMAW) and 4h for Submerged Arc Welding (SAW). For the simulation of the PWHT's, a temperature of 760°C was chosen, representing a worst case concerning material degradation. Each sample was introduced in a furnace for a global heat treatment at 760°C for specific holding times ranging from 3h to 21h, hence simulating up to 7 subsequent PWHT's of 3h:

- − step 1: Heating up to 400°C
- − step 2: Slow heating at maximum heating rate of 150°C/hour
- − step 3: Annealing at 760°C during "a multiple of" 3 hours holding time
- − step 4: Slow cooling at a maximum cooling rate of 150°C/hour

2.3. Determination of properties after PWHT's

2.3.1. Mechanical properties
For each sample tensile tests (ISO 6892-1:2009) in the transversal direction and impact toughness tests (Charpy V-notch, ISO 148:2010) have been performed at room temperature.

2.3.2. Microstructure

The microstructure of the samples was checked with an Olympus PMG3 Light Optical Microscope (LOM) on embedded cross sections after etching with Villella.

2.3.3. Hardness

For each sample Vickers Hardness (HV10) was determined with a Struers Duramin A300 table-top hardness tester as the average of 20 measurements on embedded cross sections.

2.3.4. Creep strength

Short term creep tests at 650°C and 100MPa were carried out on selected samples on a single specimen direct weight creep tester with continuous strain monitoring.

3. Results

3.1. Mechanical properties

The evolution of the tensile strength, yield strength, elongation and toughness in function of the number of PWHT's is shown in Figure 1 and Figure 2. According to the EN 10216-2:2007, the minimum ultimate tensile strength is 630 MPa, the minimum yield strength is 450 MPa and the minimum elongation in the transversal direction is 17%. Based on thresholds for tensile strength and yield strength, the maximum acceptable holding time at 760°C is 18 hours. The elongation is above minimum requirements for all analyzed samples. Impact toughness was close to 200J for all samples up to 18h holding time at 760°C and started to decrease after 21h.

(a)   (b)
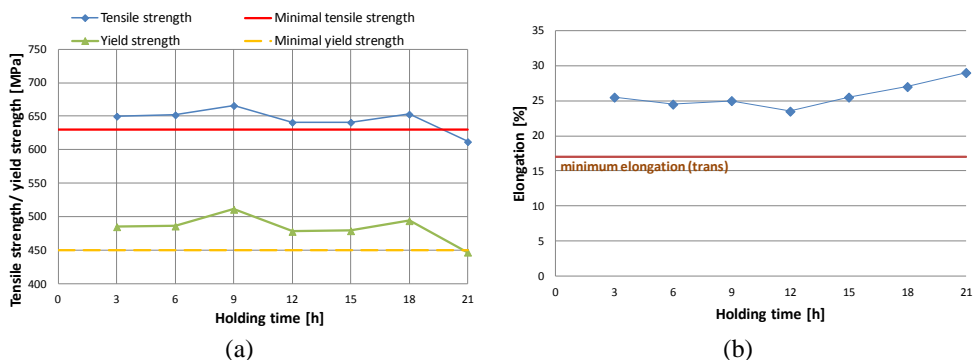
Figure 1: Evolution of the mechanical properties in the transversal direction as a function of the holding time at 760°C. a) Tensile and yield strength; b) elongation.
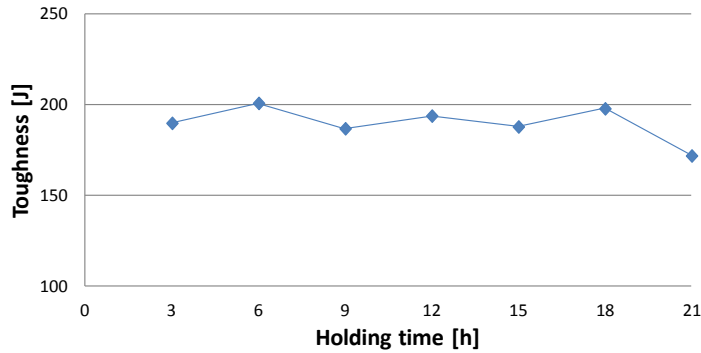
Figure 2: Evolution of the Charpy V-notch toughness at room temperature as a function of the holding time at the PWHT temperature of 760°C.

3.2. Microstructure

Figure 3 shows the evolution of the microstructure after several simulated PWHT's. The original microstructure is tempered martensite, with a clearly visible lath structure. The annealing at the PWHT temperature of 760°C causes an agglomeration and coarsening of carbide precipitates and a fading of the lath structure. This can already be observed after 6h of annealing (equivalent of 2 PWHT's). After 21 h at 760°C (equivalent of 7 PWHT's) the microstructure is clearly over-tempered martensite.

(a)

(b)

(c)

(d)
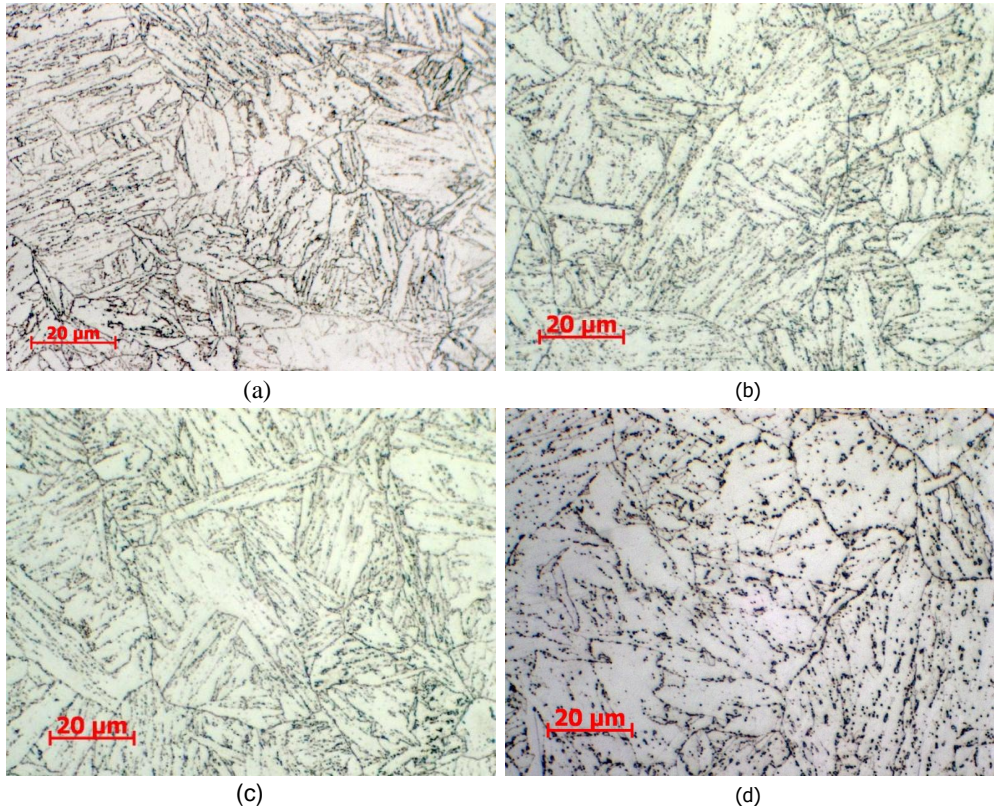
Figure 3: LOM micrographs after etching with Villella showing the evolution of the microstructure after several PWHT's. a) Before PWHT; b) after 6h at 760°C; c) after 15h at 760°C d) after 21h at 760°C

3.3. Hardness

Figure 4 shows the evolution of the hardness in function of the number of PWHT's. The hardness shows a sharp decrease after 18 hours holding time at 760°C. Recommended hardness for Grade91 components entering service is between 200-290 HV10. Generally, a hardness that is lower than 190 HV10 is not acceptable [3].
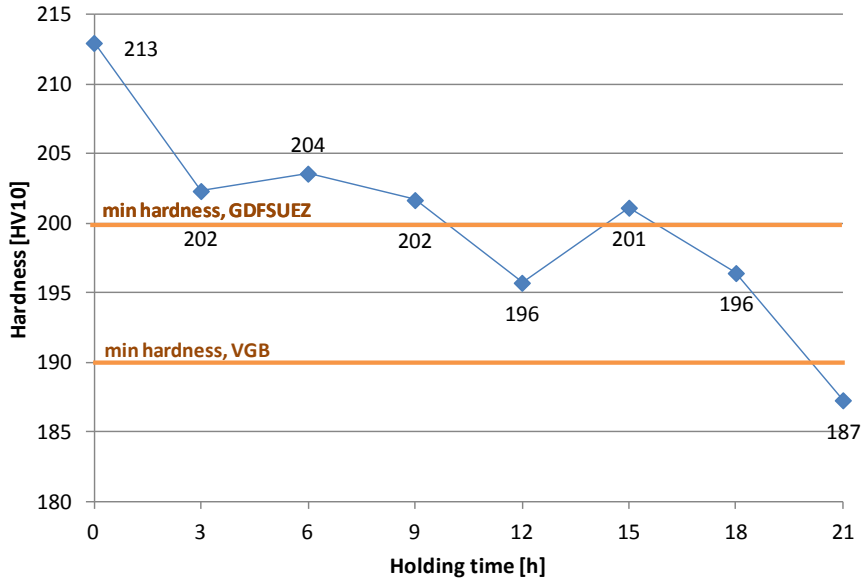
Figure 4: Evolution of the hardness as a function of the holding time at 760°C.

3.4. Creep strength

Based on the results of the mechanical tests and microstructural investigation the samples that were annealed at 760°C for 15h and 21h were selected for the creep testing. Results of the short term creep tests are shown in Figure 5. The creep strength of the ex-service material with no PWHT is still slightly above the average value for Grade 91. After 15h at 760°C, creep strength is lower, but still within the +/-20% scatterband. After 21h at 760°C, however, creep strength has dropped below the -20% curve. Since the time to rupture of the tests was very limited (<200h for the post PWHT's samples), it is advisable to confirm these results with longer term creep tests.
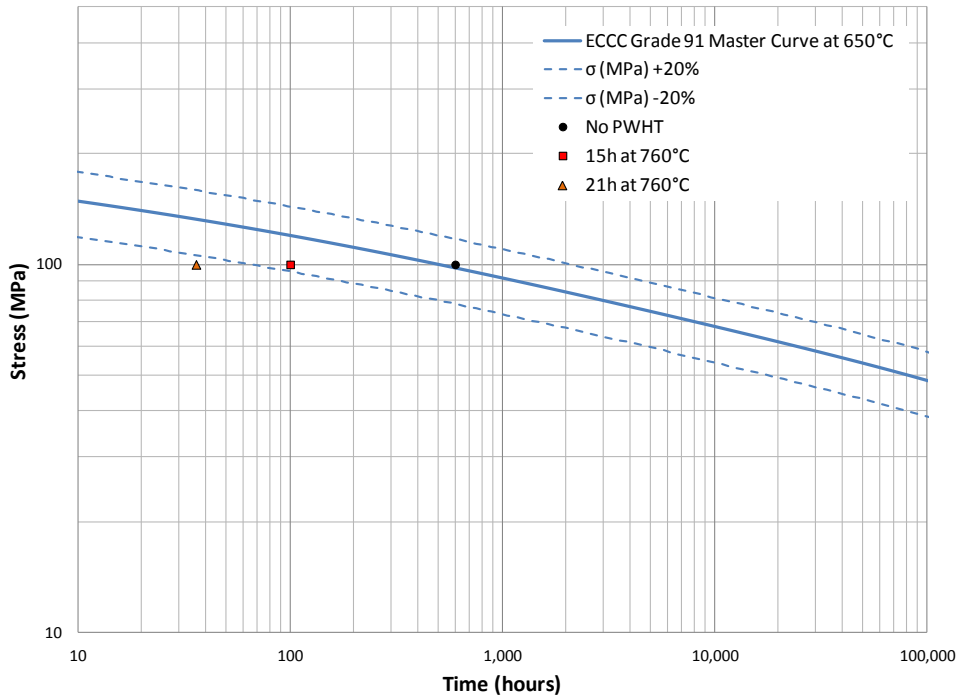
Figure 5: Creep test results at 650°C compared with the ECCC master curve for Grade 91 material [4].

4. Discussion

Based on the results of the mechanical testing, microstructural investigation, hardness measurements and short term creep tests, the investigated Grade 91 material can undergo up to 15h of annealing at 760°C, without a significant negative impact on its properties. However, when trying to translate these results into a general guideline for the maximum allowed number of PWHT's, several considerations have to be made.

The used material had an average creep strength to start with. For material with a creep strength closer to the lower boundary, the total allowed number of hours at 760°C could be lower. The initial creep strength depends on the exact chemical composition and the received normalising and tempering conditions.

Both the PWHT temperature and holding time can vary in practice. Temperatures will typically vary between 740°C and 760°C, so the simulations are conservative. The duration at the PWHT temperature depends on the thickness of the component and can be more than 4 h for thick-walled components. Holding times of 1h/25mm thickness are recommended with a

minimum of 2h for Shielded Metal Arc Welding (SMAW) and 4h for Submerged Arc Welding (SAW).

The simulation of multiple PWHT's was done by increasing the holding time at 760°C. The heating up and cooling down was only done once. Since some degradation will take place during these heating and cooling periods, the influence of real multiple PWHT's will be slightly larger. In order to estimate the importance of this heating and cooling period the Larson Miller Parameter (LMP) was used:

$$LMP\,(t,T) = T[K](31 + \log(t[h])$$

As illustrated in Figure 6 the heating and cooling curves were approached by a series of small time intervals at constant temperatures. For each temperature the equivalent time at 760°C was determined by using the LMP. The sum of all these contributions gives the time needed at 760°C to have the same degradation as during the heating and cooling period. For the PWHT simulation in the furnace this equivalent time at 760°C was determined to be 0.2h.
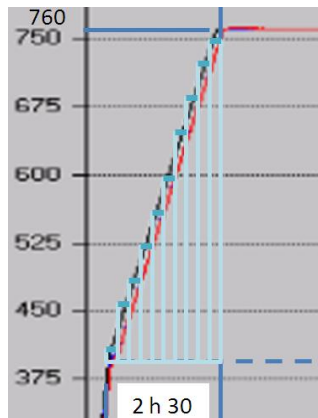
Figure 6: Illustration of how the heating curve was approached by subsequent time steps at constant temperature.

If repair is carried out after several years of service some material ageing has already taken place and hence the total amount of hours at 760°C before significant influence on the properties will be lower, compared to what is allowed on new material. The same LMP approach can be used to estimate this influence. For the tested material, the 39500h at 570°C corresponds to an equivalent time at 760°C of only 0.01h. As an example, 100 000h operating at 580°C corresponds to 0.05h at 760°C and 100 000h operating at 600°C corresponds to 0.27h at 760°C. This shows that, although there is an influence of the service time, this influence is small compared to the influence of a PWHT.

In practice, the complete history of the component that needs to be repaired has to be taken into account (service life, previous repairs, etc.) when evaluating if an extra PWHT can be

done. An equivalent LMP for the component can be calculated and compared with the LMP of 33244 for the 15h holding at 760°C.

5. Conclusion

The current investigation revealed that for Grade 91, based on PWHT's of 4 hours at 760°C, maximum 3 PWHT's are acceptable.

If longer PWHT times are necessary (e.g. for thicknesses>100mm) or if the initial creep strength of the material is close to the lower boundary, the number of PWHT's should be limited to 2.

In practice, the complete history of the component that needs to be repaired has to be taken into account (service life, previous repairs, etc.) when evaluating if an extra PWHT can be done. An equivalent LMP for the component can be calculated. If the sum of this LMP and the equivalent LMP of the planned PWHT is still below 33244, the repair will have no significant influence on the properties of the surrounding base material.

Long term creep tests in order to confirm these results are planned. In addition, confirmation tests on real welds are ongoing to check the exact failure locations.

6. Acknowledgement

This work was made possible through financial support from GDF Suez.

7. References

[1] H.C.Dey et al, Effect of Post Weld Heat Treatment (PWHT) Time and Multiple PWHT on Mechanical Properties of Modified 9Cr-1Mo Steel Weld Joints, *IIW*, Doc.No.IX-2442-13 (2013).
[2] M.Spiegel,. Glühbehandlung an P91/P92 – Ergebnisse, *Salzgitter Mannesmann Forschung* (2012).
[3] Material specification for components under pressure in fossil-fired power plants, *VGB R-109*, p.47 (2012).
[4] W. Bendick, L. Cipolla, J. Gabrel and J. Hald, New ECCC Assessment of Creep Rupture Strength for Steel Grade X10CrMoVNb9-1 (Grade 91), *ECCC Creep Conference*, p. 56-67 (2009).

MICROSTRUCTURE CHARACTERIZATION OF TWO Z-PHASE STRENGTHENED 12%CHROMIUM STEELS

Masoud Rashidi*, Fang Liu, Hans-Olof Andrén

Department of Applied Physics, Chalmers University of Technology, SE-412 96 Göteborg, Sweden
*Contact author, masoud.rashidi@chalmers.se

Abstract

The microstructure of two Z-phase strengthened steels was characterized in different heat treatment conditions, as-tempered and after 1000 hours ageing at 650°C. A high Cr content together with Ta and N additions were used to stimulate the formation of a fine distribution of Z-phase as strengthening particles in both alloys. Atom probe tomography, transmission electron microscopy, and scanning electron microscopy were employed for a detailed characterization of the microstructure. The A1 steel contained very little carbon, which resulted in a fast transformation from MX to Z-phase. In the A2 steel that contained a higher carbon content and an addition of Cu, the MX to Z-phase transformation was slower. The Cu addition to the A2 steel improved Laves-phase distribution and morphology.

Keywords: 9-12% chromium steels; precipitation hardening; APT; TEM.

1. Introduction

In steam power plants, higher thermal efficiency and lower fuel consumption is achievable at higher steam temperatures and pressure. Developments in heat-resistant steels with better creep strength have contributed to a major increase in the efficiency of steam power plants. Martensitic 9-12% Cr steels have been playing an important role during the last decades towards achieving higher efficiency. At higher temperature and pressure, both improved creep strength and improved corrosion resistance are required to avoid material failures [1].

Several attempts towards improving the creep resistance of steels with high corrosion resistance (11-12% Cr) at least for 100,000 hours at 650°C have resulted in better creep strength only up to 10,000 hours. For longer creep times, the material experienced a dramatic loss of creep strength due to the transformation of fine MX (M = V, Nb, Ta; X = C, N) precipitates into coarse Z-phase (CrMN, M = V, Nb, Ta) particles [2].

By considering the fact that Z-phase is thermodynamically more stable at 650°C, John Hald and Hilmar Danielsen suggested to use Z-phase as strengthening phase instead of MX [3]. In the present study, Atom Probe Tomography (APT), Transmission Electron Microscopy (TEM), and Scanning Electron Microscopy (SEM) were employed to characterize the microstructure evolution during ageing of two trial Z-phase strengthened alloys.

2. Experimental methods

2.1 Materials

The chemical composition of two experimental steels received from the Technical University of Denmark is provided in Table 1. These steels are supposed to form small Ta containing Z-

phase (CrTaN) since it is believed that Ta results in a finer distribution of Z-phase compared to Nb-based Z-phase [2]. The main differences between the two experimental steels are in their carbon and copper content.

The A1 steel was austenitized at 1150°C for 1 hour and tempered at 650°C for 24 hours. The A2 steel was austenitized at 1150°C for 1 hour and then underwent double step tempering of 6 hours at 650°C followed by 6 hours at 740°C. The A1 steel was studied in the as-tempered condition and after 981 hours ageing at 650°C. The A2 steel was studied in the as-tempered condition and after 1000 hours ageing at 650°C. The Charpy V-notch impact toughness of the two steels in the as-tempered condition was determined at room temperature to 2.3 J and 76.3 J for A1 and A2 steels, respectively.

Table 1. Composition of Z-phase strengthened steel A1 and A2 (Fe in balance).

Steel		Ni	Co	Cr	W	Ta	C	B	N	Si	Mn	Cu
Steel A1	at%	0.48	7.01	12.84	0.89	0.12	0.02	0.02	0.13	0.60	0.49	0
	wt%	0.50	7.30	11.79	2.90	0.39	0.005	0.004	0.033	0.30	0.48	0
Steel A2	at%	0.18	3.35	13.13	0.76	0.11	0.28	0.03	0.20	0.62	0.22	1.73
	wt%	0.19	3.50	12.10	2.47	0.36	0.06	0.006	0.049	0.31	0.21	1.95

2.2. Specimen preparation

TEM specimens were prepared by electropolishing in 10% perchloric acid + 90% methanol. Note that this electrolyte preferentially etches away Cu particles and subsequently holes are left in the TEM specimens. Thus in the HAADF (high angle annular dark field) micrographs obtained from the electropolished specimens, most of the black contrast (holes) within the steel matrix are footprints of Cu particles.

Standard grinding and polishing process was employed to prepare specimens for SEM analysis. Sample preparation for APT was done according to the method reported by Liu et al. [4].

2.3. Electron microscopy

A Leo Ultra 55 Field Emission Gun SEM (FEG-SEM) equipped with an Oxford Inca Energy Dispersive X-ray Spectrometry (EDS) system, and a FEI Tecnai LaB$_6$ gun TEM equipped with an EDAX X-ray detector and the TIA EDS software, were employed for a detailed characterization of the microstructure of both steels. For SEM several accelerating voltages between 5 and 20 kV were used. The TEM was operated at 200 kV.

2.4 Atom Probe Tomography

APT is by far the most powerful analytical method to study the chemical composition of different phases at an atomic level. It determines the chemical composition based on counting the number of atoms of each type. An Imago LEAP 3000X HR local electrode APT was employed to study the chemical composition of precipitates smaller than 50 nm. During analysis the specimen was held at a temperature of 55-56 K. The instrument was operated in pulsed laser mode with a laser pulse energy of 0.3 nJ. The data collected by the instrument was further analyzed using the IVAS 3.4.6 software.

3. Results

The microstructure of the two experimental steels at different heat treatment condition was investigated by using SEM, TEM, and APT.

3.1 Steel A1

Decreasing the C content to 0.02 atomic % aimed at making the system simple and easy to study by excluding $M_{23}C_6$ and MX carbonitrides, and to test whether a dense Z-phase distribution could be obtained. If so, it would be a proof of concept of the idea of Z-phase strengthening.

3.1.2 Steel A1 in the as-tempered condition

Figure 1 shows backscattered electron (BSE) micrographs obtained by SEM from the A1 steel in the as-tempered condition. The contrast obtained in these micrographs is mainly due to the difference in atomic number. EDS point analyses showed that the bright phases are rich in W, suggesting they are Laves-phase (Fe_2W). It worth noticing that some Laves-phase particles appear continuously along prior austenite grain boundaries (PAGB) and inside grains. The prior austenite grain size was determined to 114 μm.
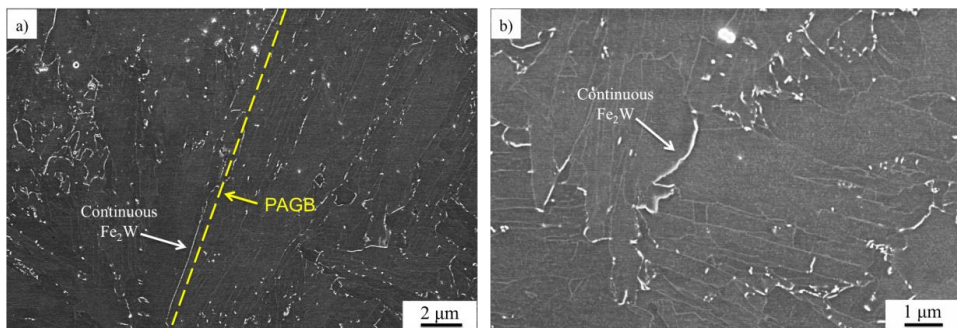
Figure 1. SEM/BSE micrographs of the A1 steel in the as-tempered condition at two different magnifications. Note that at some areas, an almost continuous Laves-phase formed along the PAGBs.

Figure 2 shows a reconstruction of an APT data set obtained for the A1 steel in the as-tempered condition. In this image, each purple dot is a TaN ion. Chemical composition of these particles varies depending on their size. They mainly contain Ta, Cr, and N. Thus, already after tempering a dense distribution of what appears to be Z-phase was obtained.
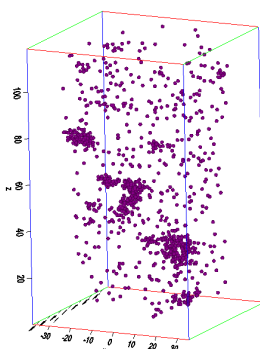
Figure 2. Reconstruction of an APT data set obtained from the A1 steel in the as-tempered condition. Purple dots are TaN ions (box size: $120 \times 70 \times 70$ nm^3).

3.1.2 Steel A1 aged for 981 hours at 650°C

Figure 3 shows SEM/BSE micrographs of the A1 steel after 981 hours ageing at 650°C. At this stage, continuous Laves-phase still exists at PAGBs. Besides we can see Laves-phase of equiaxed morphology inside PAGs and at lath boundaries. SEM/EDS elemental mapping of the A1 steel after 981 hours ageing at 650°C is provided in Figure 4, which illustrates the Laves-phase distribution via the W map. Considering the very small amount of C in this alloy, it is not surprising that in all our SEM analyses we could find only one relatively big particle rich in Cr, which might be a $M_{23}C_6$ particle. Z-phase particles are still smaller than the detection limit of SEM/EDS even after 981 hours ageing at 650°C.
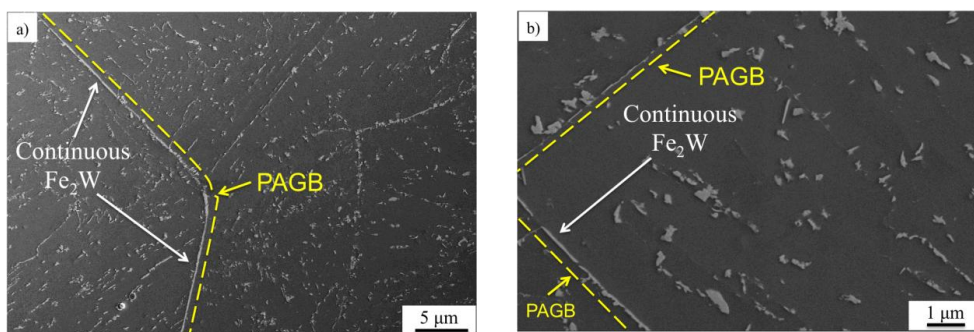
Figure 3. SEM/BSE micrographs of the A1 steel aged at 650°C for 981 hours.

Using APT a dense distribution of small nitride precipitates was found. The chemical composition of one of these precipitates obtained from APT is provided in Table 2. It is obvious from the nitrogen content and the high Cr content that Z-phase has formed.

Table 2. Chemical composition (at%) of a Z-phase precipitate in the A1 steel aged at 650°C for 981 hours.

	Ta	Cr	N	C	W	V	Fe
Z-phase	25.5	35.4	33.9	0.5	0.3	1.1	1.3

74
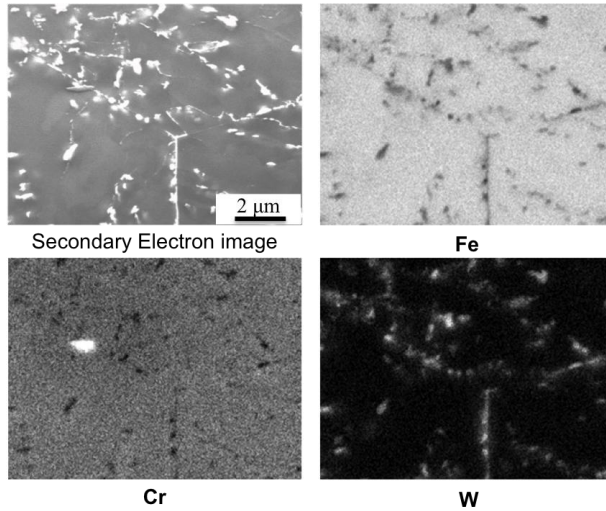
Figure 4. SEM/EDS elemental mapping of the A1 steel aged at 650°C for 981 hours.

3.2 Steel A2

The A2 steel contains more carbon compared to the A1 steel. This addition of C might affect the Z-phase formation process. This was studied in detail in the as-tempered condition and after 1000 hours ageing at 650°C. In addition, how Cu addition in the A2 steel affects the microstructure was also studied in detail.

3.2.1 Steel A2 in the as-tempered condition
Figure 5 shows a rather big BN particle with irregular morphology as well as a spherical primary TaC particle. TaC precipitates exist in different sizes ranging from 300 nm to 1 μm. The EDS spectra obtained from aforementioned particles are provided in Figure 5.
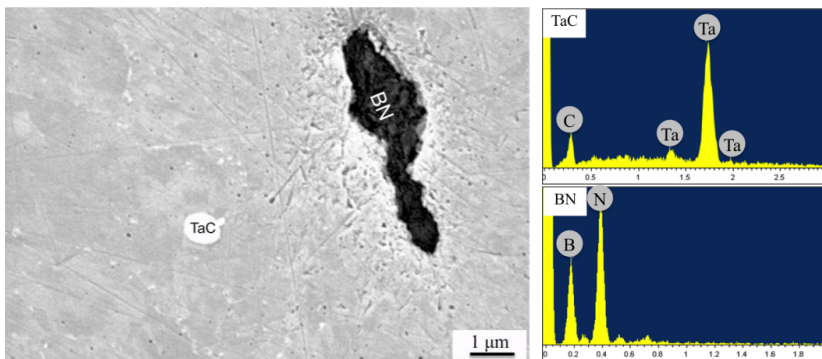
Figure 5. SEM secondary electron micrograph of the A2 steel in the as-tempered condition together with EDS spectra from the TaC and BN particles.

Figure 6 shows HAADF-STEM micrographs of the A2 steel in the as-tempered condition. It can be seen that Laves-phase particles (bright contrast), a few hundred nm in size and equiaxed in shape, are mostly distributed at PAGBs. This is also true for $M_{23}C_6$ precipitates (gray contrast), while Cu ''particles'' (black contrast) are distributed at PAGBs, lath boundaries and inside laths. The prior austenite grain size was 50 μm.
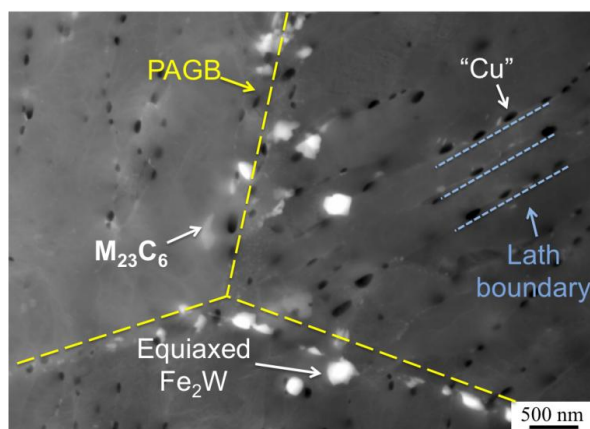
Figure 6. HAADF-STEM image of the A2 steel in the as-tempered condition showing Laves-phase (bright contrast), $M_{23}C_6$ (gray contrast) mostly at PAGBs, and footprints of Cu particles (black contrast) at PAGBs, lath boundaries and inside laths.

For the A2 steel in the as-tempered condition, a total volume of 2.2×10^6 nm^3 was investigated using APT. Two relatively big (≈ 40 nm) Cr+N-rich particles were found. They contain roughly 75% Cr and 22% N (in atomic percentage) and the concentration of other elements are low. The chemical composition suggests Cr_2N.

In the APT analysis, a Ta(C, N) particle was identified. The chemical composition of this particle is provided in Table 3. The high amount of C might make it harder for these particles to transform to Z-phase. One 15 nm Z-phase precipitate was analyzed by using APT. The chemical composition of this particle is also provided in Table 3.

Table 3. Chemical composition (at%) of particles in the A2 steel obtained by APT. The results were obtained from one particle of each type.

		Cr	Ta	N	C	B	V	Fe
A2 (as-tempered)	Ta(C, N)	13.1	38.1	16.7	25.9	-	-	4.2
A2 (1000 h aged)	Ta(C, N)	4.7	50.0	11.8	29.4	-	0.7	2.7
A2 (as-tempered)	Z-phase	36.6	25.1	24.8	2.4	0.7	0.7	9.1
A2 (1000 h aged)	Z-phase	40.8	25.8	24.5	0.6	-	0.8	7.0

3.2.2 Steel A2 aged for 1000 hours at 650°C
In Figure 7, SEM/BSE micrograph of the A2 steel aged for 1000 hours is shown. It shows that particles do not only exist at PAGBs but also at lath boundaries and inside laths after ageing for 1000 hours. Further EDX analysis showed that these particles are Laves-phase and $M_{23}C_6$.
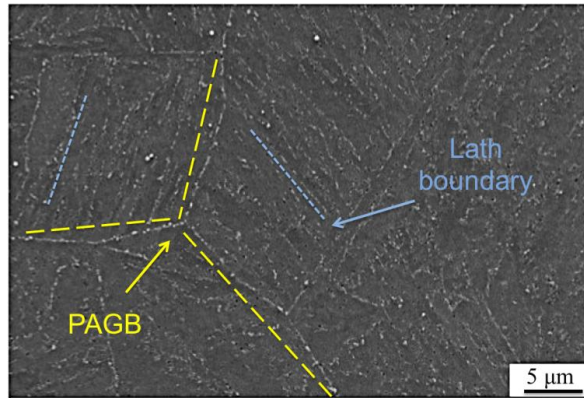
Figure 7. SEM/BSE micrographs of the A2 steel aged for 1000 hours at 650°C.

In Figure 8, STEM/EDS elemental mapping shows different particles in the A2 steel after 1000 hours ageing at 650°C. Laves-phase (W map), $M_{23}C_6$ (Cr and C maps) are shown as well as one particle rich in Cr and N approximately 400 nm in size (marked by red arrow). Black contrast is footprint of Cu particles. As is highlighted in Figure 8, we can see Laves-phase precipitates adjacent to Cu particles.
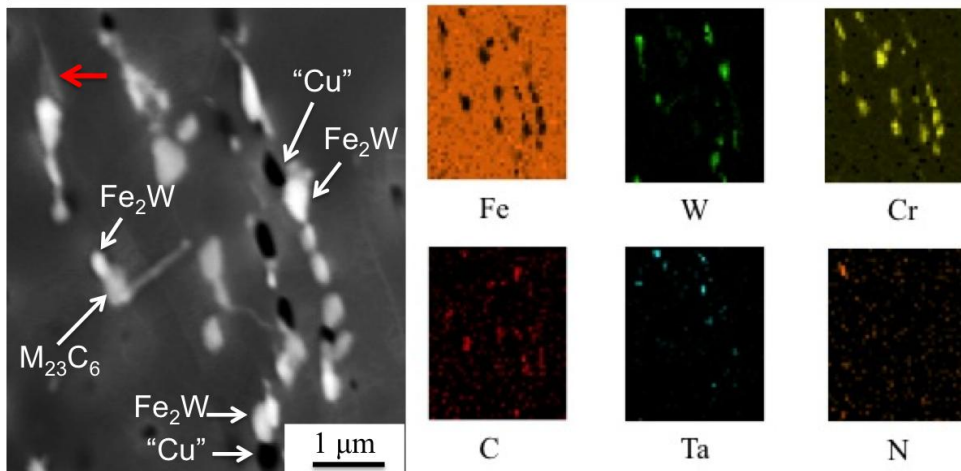
Figure 8. HAADF-STEM/EDS elemental mapping of the A2 steel aged for 1000 hours at 650°C showing Laves-phase, $M_{23}C_6$, and Cr+N-rich particles (red arrow).

In Figure 9, STEM/EDS elemental mapping of small particles (<100nm) shows that they are enriched in Ta and Cr. EDS is not an accurate method for quantifying the light elements N and C. Therefore, using EDS it was not possible to distinguish if the particles are Z-phase or Ta(C, N).
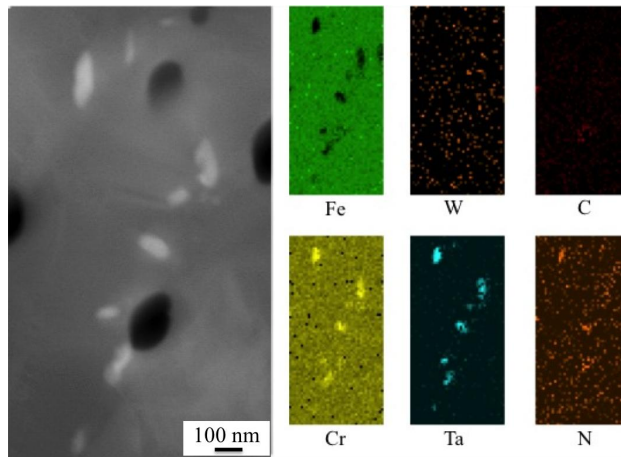
Figure 9. HAADF-STEM/EDS elemental mapping of the A2 steel aged for 1000 h at 650°C.

For The A2 steel aged for 1000 hours at 650°C a total volume of 2.07×10^6 nm^3 was investigated using APT. One Ta(C, N) particle of 30 nm was analyzed. The chemical composition of this particle is provided in Table 3. This kind of particle was also seen in the A2 steel in the as-tempered condition. Z-phase precipitates were observed in the APT analysis. The chemical composition of Z-phase particle is provided in Table 4.

4. Discussion

4.1 Primary particles

Two families of primary particles were characterized: BN and TaC particles. BN particles were found in the A2 steel. They may separate first from the melt during casting and consume both beneficial B and N. Boron has the effect of hindering the $M_{23}C_6$ coarsening [4] and N was supposed to form nitrides and Z-phase. An optimum relation between B and N concentrations to avoid BN formation was suggested by Abe [5]. Thus the B and N content of the A2 steel needs to be modified.

Primary TaC particles exist in both alloys. TaC consumes Ta, which was supposed to participate in Z-phase formation. However, TaC particles can lock PAGBs and restrict grain coarsening during the austenitization process. The A2 steel contains much more C compared to A1, thus in A2 there are more TaC particles that pin the grain boundaries and decrease grain growth. The prior austenite grain size in A2 is approximately half of the prior austenite grain size in A1.

4.2 Laves-phase

Laves-phase is an important precipitate in 9-12% Cr steels that significantly affects the microstructure and mechanical properties. Some authors believe that Laves-phase formation is detrimental to materials performance mainly due to depletion of W from matrix and subsequently decreased solid solution strengthening of W [6], while some other authors have

shown that formation of fine Laves-phase at sub-grain boundaries and grain boundaries retards the recovery of these boundaries [7]. Thus Laves-phase distribution and morphology must be controlled in order to improve the creep strength of the material. In the A1 steel we have continuous precipitation of Laves-phase along some of the PAGBs, which resulted in poor impact toughness. The morphology and distribution of Laves-phase have been modified in the A2 steel. There might be two reasons for this modification. Firstly, in A2, Cu was added to the steel. It is believed that Cu particles form during the first step of tempering and act as nucleation sites for Laves-phase particles [8]. This is shown in Figure 8 where we can see Laves-phase particles closely connected to Cu particles. Secondly, formation of $M_{23}C_6$ will result in regions depleted in Cr adjacent to $M_{23}C_6$ and subsequently high amounts of W are left in this region, and this is beneficial for Laves-phase formation [7].

4.3 Z-phase vs. MX

It is known that Z-phase is formed by transformation from MX precipitates [9]. In the A1 steel, a high Cr content together with Ta and N resulted in a fast transformation from MX particles to Z-phase. Thus a fine distribution of Z-phase is achieved even in the as-tempered condition. A high Co content is also believed to accelerate the formation of Z-phase [3]. By considering the fact that Z-phase is thermodynamically the most stable nitride phase in 9-12% Cr steel at 650°C, it is believed that this fine distribution of Z-phase obtained in the as-tempered condition will not be transformed to any other phases during ageing and subsequently will contribute greatly to the creep strength of the alloy.

In the A2 steel, the high amount of C resulted in formation of $M_{23}C_6$ and secondary Ta(C, N) that both attract Cr (see Table 3). Both particles consume some Cr and subsequently less Cr is left in the matrix to form Z-phase. However, in A2 steel APT analysis proved the existence of Z-phase in the as-tempered condition together with Ta(C, N). By considering the existence of Ta(C, N) in the aged specimen of A2 for 1000 hours, it is believed that phase transformation from MX to Z-phase in the A2 steel, which contains a high amount of C, is not as fast as phase transformation in the A1 steel.

In the A1 steel a fine distribution of Z-phase was achieved, while in the A2 steel, the distribution of Z-phase in not as dense as in the A1 steel.

4.4 $M_{23}C_6$ and M_2X

The very small amount of carbon in the A1 steel resulted in a high matrix concentration of Cr to form Z-phase. However in the A2 steel containing more C, we can see that already in the as-tempered condition $M_{23}C_6$ formed in equiaxed morphology along PAGB and after ageing, also at lath boundaries and inside grains. $M_{23}C_6$ particles improve the creep strength of the material by particle strengthening and by retarding the sub-grain growth [7]. The presence of B decreases the coarsening rate of $M_{23}C_6$ [2], which increases creep resistance of the steel.

The chemical composition of Cr+N-rich particles suggests that they are M_2X particles. In four random APT analyses, two M_2X precipitates were found, however S(T)EM/EDS investigations show very small amount of these particles in the A2 steel.

5. Conclusions

In the A1 steel a high Cr content together with Ta and N additions, high amounts of Co and very little C resulted in a fast transformation from MX particles to Z-phase during tempering. In the A2 steel with 0.06 wt. % C, this transformation is much slower. Thus the concept of Z-phase strengthened 12% Cr steels was shown to work in practice, at least for low C contents.

In the A1 steel (no Cu and very little C) some Laves-phase formed continuously along PAGBs resulting in poor impact toughness. In the A2 steel the distribution of Laves-phase was affected by Cu particles that act as nucleation sites for Laves-phase particles. This results in separate equiaxed precipitates a few hundred nm in size and a good toughness.

Acknowledgments

References

[1] A.Golpayegani, H-O.Andrén, H.Danielsen, J.Hald, A study on Z-phase nucleation in martensitic chromium steels, *Materials science and engineering A*, 489, 310-318, (2008).
[2] F.Liu, H-O.Andrén, Initial study on Z-phase strengthened 9-12% Cr steels by atom probe tomography, In "Materials for Advanced Power Engineering 2010", Eds. J.Lecomte-Beckers, O.Contrepois, T.Beck and B.Kuhn, Schriften Forschungszentrum Jülich GmbH, Reihe Energitechnik, Part III pp 107-116 (2010).
[3] H.Danielsen, J.Hald, Influence of Z-phase on Long-term Creep Stability of Martensitic 9 to 12 % Cr Steels, *VGB PowerTech 5/2009,* 68-73, (2009).
[4] F.Liu, D.H.R.Fors, A.Golpayegani, H-O.Andrén, G.Wahnström, Effect of boron on carbide coarsening at 873 K (600 °C) in 9 to 12 pct chromium steels, *Metallurgical and Materials Transactions A*, 43, 4053-4062, (2012).
[5] K.Sakuraya, H.Okada, F.Abe, Coarse size BN type inclusions formed in boron bearing high Cr ferritic heat resistant steel, *4th international conference on advances in materials technology for fossil power plants*, R.Viswanathan, D.Gandy, K.Coleman, Eds., ASM International, Hilton Head Island, SC, 1270-1279, (2004).
[6] J.Lee, H.G.Armaki, K.Maruyama. T.Muraki, H.Asahi, Causes of breakdown of creep strength in 9Cr–1.8W–0.5Mo–VNb steel, *Mater. Sci. Eng. A*, 428, 270-275, (2006).
[7] O.Prat, J.Garcia, D.Rojas, G.Sauthoff, G.Inden, The role of Laves-phase on microstructure evolution and creep strength of novel 9%Cr heat resistant steels, *Intermetallics*, 32, 362-372, (2013).
[8] F.Liu, H-O.Andrén, Effect of copper addition on the toughness of new Z-phase strengthened 12% chromium steels, *7th international conference on advanced in materials technology for fossil power plants*, Hawaii, (2013).
[9] H.Danielsen, J.Hald, M.Somers, Atomic resolution imaging of precipitate transformation from cubic TaN to tetragonal CrTaN, *Scripta Materialia*, 66,261-264, (2012).
[10] F.Abe, Effect of Boron on Microstructure and Creep Strength of Advanced Ferritic Power Plant Steels, *Procedia Engineering*, 10, 94-99, (2011).

PERFORMANCE OF WELDED JOINTS IN LOW-ALLOY STEELS T/P23 AND T/P24 FOR CHALLENGING HIGH-TEMPERATURE APPLICATIONS

Pertti Auerkari[1], Stefan Holmström[2], Pekka Nevasmaa[1], Jorma Salonen[1]

[1]VTT Technical Research Centre of Finland, Espoo Finland; firstname.surname@vtt.fi
[2]EC, JRC Petten, The Netherlands; firstname.surname@ec.europa.eu

Abstract

Increasing thermal loads, temperatures and pressures in boilers and steam systems is attractive to improve the efficiency and operational economy of power and process plants. The adoption of new high strength, modified 2% Cr steels can be an option, provided that these will perform for the required component life. Challenges have arisen when using new high strength T/P23 and T/P24 steels for waterwalls, superheaters and steam lines. This paper reviews the recent understanding of the applicability and limitations of these steels in welded components. A range of causative reasons are proposed for the not entirely successful application of the P/T23 and P/T24 particularly in waterwalls and steam lines. The complexity of optimising weld properties is demonstrated in view of unforgiving material response especially at weld defects, as well as of high weldment hardness and limited ductility. Selection of filler metal type and composition is elucidated with respect to propensity to low weld metal ductility, such as low creep ductility damage or reheat cracking. The role of structural rigidity and actual constraint conditions in real components is discussed, as it comes to adopting filler metals with the aim of either increasing weld creep strength or ensuring adequate creep ductility, as well as to whether to conduct or omit the subsequent PWHT. One of the most persistent remaining challenging issues concerns welded thick-wall applications for high temperature headers, steam pipes or turbines, where the weld metal tends to show very limited creep ductility. More recently, setbacks have been seen in the attempts to use T24 in welded water walls of large boiler plants. Multiple causes have been proposed for the observed early waterwall cracking, and again, the problems concentrate on welds that tend to exhibit reduced creep ductility.

Keywords: power plant, high-temperature, T/P23 steel, T/P24 steel, creep, ductility, cracking

1. Introduction

In principle, efficiency and operational economy of power and process plants can be improved, and equipment size reduced by increasing thermal loads, temperatures and pressures of the process. As this has been well known for a long time and the allowable high temperature material strength levels only gradually increased, the improvement has been relatively slow [1]. A more emerging challenge is the increasingly variable supply from other renewable sources of power than hydro, as in the remaining thermal power plants of the grid life of major components can be reduced by the more fluctuating operation. In addition, when higher strength material is selected for optimised process and to limit section size and sensitivity to more fluctuating operation, other complications may intervene from e.g. unfavourable creep ductility, thermal properties, or weld behaviour. This paper compares conventional and newer creep resistant steels in terms of expected and observed properties and suitability for the changing modes of operation. The selected examples include the

experience and suggested limitations with e.g. welded T/P23 and T/P24 in comparison with conventional low alloy steels.

Low-alloy Cr-Mo steels like T22 (10CrMo9-10) are widely used since 1940's at steam temperatures up to 540–565°C. The steel shows fair weldability and ductility, but only modest creep strength. For strength improvement at similar temperature range, modified low-alloy steels have been developed with small additions of elements that improve hardenability and form strengthening precipitates. Early versions of such grades like 0.5CMV (14MoV6-3) steel were successful in considerably improving the uniaxial creep strength at modest operating temperatures, but were also found to suffer from lower creep ductility than Cr-Mo steels, resulting in relatively short mean time to creep cavitation and cracking in the plant inspection statistics [2]. More recently, newer modified grades P/T23 (7CrWVMoNb9-6) and P/T24 (7CrMoVTiB10-10) have been introduced with higher hardenability, small additions of precipitation forming elements such as V, Ti, Nb, W, B and/or N and more complex tempered bainitic to martensitic (Figure 1) microstructure [3, 4]. Again, limitations and operational setbacks have been observed when aiming to benefit from the improved creep strength in waterwalls or steam lines. These have been associated with sensitivity to microstructure, weld quality control and/or defects and operating environment, and have resulted in premature failures in service [5]. Any increase in parent material creep strength is hence of little use if it is not reasonably matched by sufficient ductility and properties of welds. As a result, the modified 2% Cr steels are not yet common in waterwalls or steam lines, but mainly used in a narrow range of applications, such as superheaters. These limitations are now obstacles in applying materials that once appeared to be cost effective solutions for a supercritical plant.
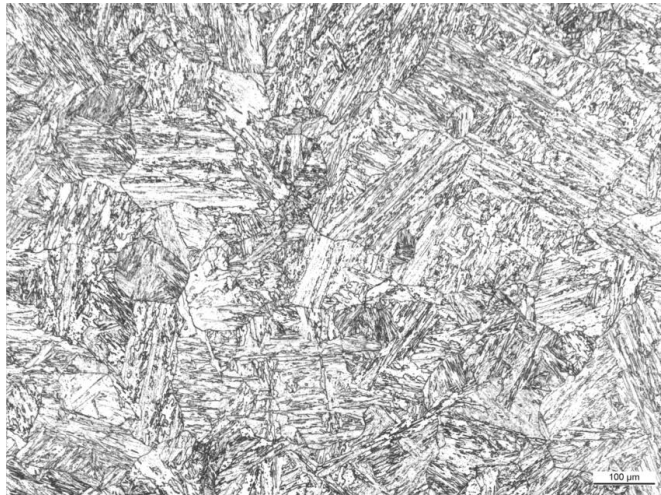
Figure 1: As-new parent microstructure of P24 steel [6].

2. Materials and experiments

The standard compositions [7, 8] of the ferritic steels 0.5CMV, T/P22, T/P23, T/P24 and X20 are shown in Table 1.

Table 1: Composition of selected conventional and modified pipe and tube steels [7, 8].

Steel	C	Cr	Ni	Mo	W	V	Nb	Ti	Other
14MoV63 0.5CMV	0.10 0.15	0.30 0.60	0.30	0.50 0.70	-	0.22 0.28	-	-	-
10CrMo9-10 T22	0.08 0.14	2.00 2.50	0.30	0.90 1.10	-	-	-	-	-
7CrWVMoNb9-6 T23	0.04 0.10	1.90 2.60	-	0.05 0.30	1.45 1.75	0.20 0.30	0.02 0.08	-	N ≤ 0.03 B 0.0005…0.006
7CrMoVTiB10-10 T24	0.05 0.10	2.20 2.60	-	0.90 1.10	-	0.20 0.30	-	0.05 0.10	N ≤ 0.010 B 0.0015…0.007
X20CrMoV11-1 X20	0.17 0.23	10.0 12.5	0.30 0.80	0.80 1.20	-	0.25 0.35	-	-	Al ≤ 0.040

The arc welding consumables are mostly of roughly matching composition, with some compensation for arc burn losses. In case of P/T24, for example, the arc loss of Ti can be so extensive and difficult to control that Nb instead of Ti may be selected (i.e. the approximate composition of the P/T23 consumable). On the other hand, higher levels of elements like V, Nb and B will increase creep strength but this can be at the expense of ductility and resistance to cracking [9-15]. For higher ductility and toughness in the weld metal, undermatching consumables corresponding to P/T22 could be used. This may work when the welds are not fully loaded and/or are partly strengthened via dilution by the parent metal for additional alloying (i.e. relatively thin sections and butt-welds with narrow grooves), but the approach is less effective for multipass welds of thick-wall sections. As an example, SMAW butt weld made with Thermanit 24 consumables on Ø 400 x 30 mm P24 pipe was subjected to cross-weld creep testing after passing weld qualification tests (NDE, hardness, tensile, bending, impact and reheat cracking tests), and metallography to show no deviations or damage [6].
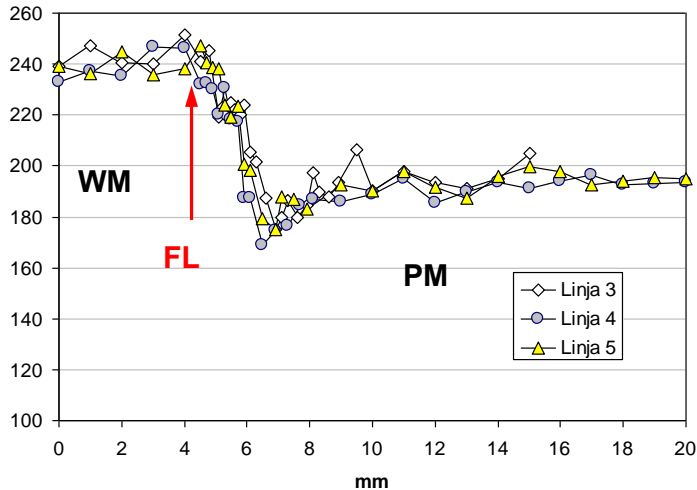
Figure 2: Vickers (HV1) hardness profile across the P24 weldment [6].

An example of the P24 weldment hardness profile in Figure 2 shows that the Nb-alloyed P24 type SMAW weld metal exhibits hardness level equivalent to the grain-coarsened HAZ, and

that satisfactorily low weldment maximum hardness (<< 300 HV) is obtained in the PWHT condition (740°C/2 h).

3. Weld integrity and creep performance

The creep testing results of the example P24 component and its weldment are shown in Figure 3 as a Wilshire plot; for modelling and formulation for this purpose, see [6]. A comparison is also shown to the expected parent metal (P24) mean strength, given as three interpretations, as well as to a lower bound line of a weld strength factor WSF = 0.64; WSF is the ratio of (cross)-welded and parent metal rupture strength for the same temperature and time to rupture. It is seen that there is no clear difference between cross-weld and (longitudinal) weld metal test results. This was confirmed in inspection, showing grain boundary creep failures in the weld metal (Figure 4) with elongation of less than 10%. Hence even when the parent alloys remain quite ductile, creep ductility is considerably reduced in welded P/T23 and P/T24 [10]. Like in many low alloy steels, creep ductility may pass through a minimum by decreasing first and then growing again with increasing time to fracture. Overall, however, the ductility levels of welded P/T24 are lower than in the conventional Cr-Mo steels, perhaps somewhat similar to 14MoV6-3.
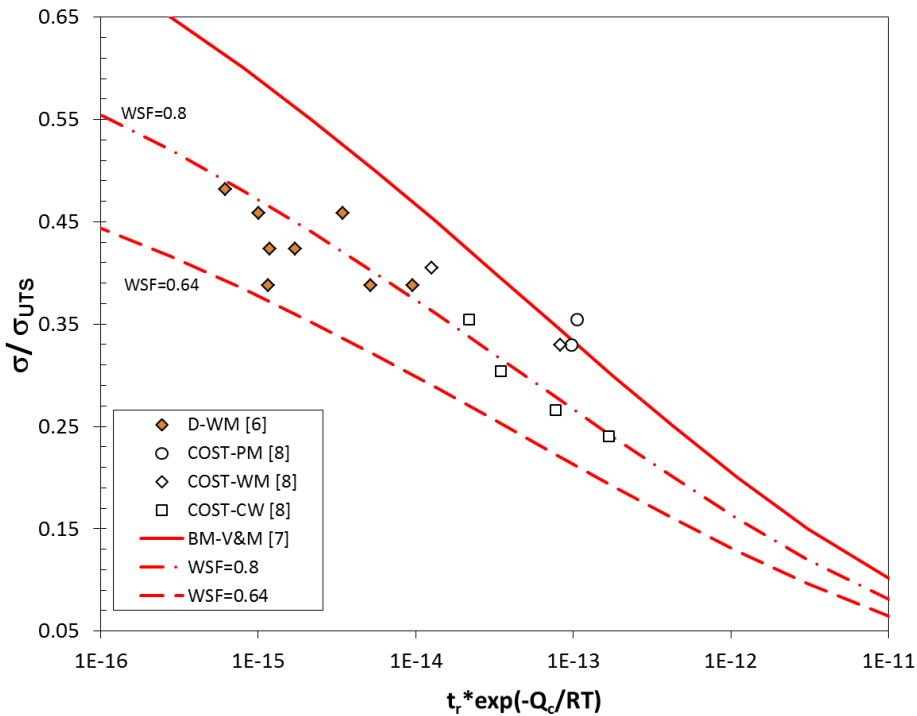
Figure 3: P24 cross-weld (CW) and weld metal (WM) data in comparison with PM and WSF models.
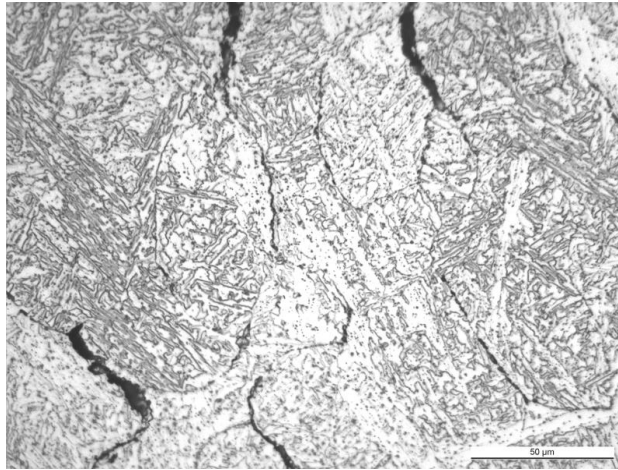
Figure 4: Grain boundary cracking of weld metal after CW creep test of P24 [6].

4. Indicators and mitigation of low ductility

It is common observation that increasing material strength tends to reduce its ability to deform and yield without damage like cracking or fracture. This certainly applies to low-alloy Cr-Mo steels and many other steels, and one of the early lessons was with the steel 0.5CMV (14MoV63) that like P/T23 and P/T24 contains vanadium for precipitate (MX) strengthening. In spite of showing better creep strength than P22, this steel has fallen into disuse in new plants partly because of its propensity to creep cavitation and cracking in welded joints. The difference to P22 appears as lower elongation and reduction of area (RA) under nearly any testing conditions including those in standard qualification tests [4]. However, details will also matter, and detrimental features can include even partially martensitic weldment microstructure that can be sensitive to hydrogen damage and stress corrosion cracking, simultaneously with the increased likelihood of crack extension from weld defects [3, 5].

Material's low ductility can be indicated by high hardness, but the often quoted limit of 350 HV may not be sufficiently restrictive to guarantee safe, crack-free welds. In practice this will frequently mean requirements to use preheating for welding (e.g. 150°C), possibly followed by PWHT [5, 9-11]. Unfortunately, PWHT will compromise one of the major original advantages of low-alloy Cr-Mo steel tubes, i.e. the option to assemble large scale structures without mandatory PWHT. The compounding effects related to, or indicated by low ductility will be further aggravated by the effects of ageing that can further reduce ductility and toughness. Even if the impact of ageing were temporary and largely removed by long term service at sufficiently high temperature [11], this will not help if the period of low ductility will already introduce damage to a component. Any attempt to repair such damage can start the low ductility cycle from the beginning and therefore may not be of much help without removal or mitigation of the original challenge. The complexity of optimising weld properties was clearly demonstrated in a recent work [17, 18] on thick-section tube multipass welds in P23 (Table 2): while the as-welded condition exhibited excessive weld metal hardness (well above 350 HV) and poor impact toughness (less than 10 J at RT), the subsequent PWHT resulted in reheat cracking in the weld metal irrespective of simultaneously improved

toughness and decreased weld hardness. In this context, it was found that reheat cracking sensitivity of P23 weld metal can be reduced by selecting a filler material with its chemical composition more closely matching to T/P24, and that T/P24 is obviously much less susceptible to reheat cracking than T/P23 (see Table 3).

Table 2: Hardness of P23 weldment, simulated HAZs and Gleeble re-heated welds [17, 18].

Weld/simulated microstructure	Condition	Hardness (HV5)
actual weld metal	as-welded (final bead)	313 ; 328
actual weld metal	as-welded	315 – **353**
actual weld metal	re-heated (softened) (*	288 – 312
actual weld metal	reheated (coarse-grained) (*	**353 – 384**
actual CGHAZ	close to fusion boundary	341 – **368**
actual FGHAZ	≈ 1.5 mm from fusion boundary	324
actual ICHAZ	≈ 2.0 mm from fusion boundary	285
Gleeble-reheated weld metal	FG(R)-CG(R)-WM (**	**358 – 371**
Gleeble-reheated weld metal	SC(R)-CG(R)-WM (**	**374 – 385**
Gleeble_CGHAZ	as-simulated	**356**
Gleeble_CGHAZ	PWHT	216
Gleeble_FGHAZ	as-simulated	311
Gleeble_FGHAZ	PWHT	190
Gleeble_IC(R)-CGHAZ	as-simulated	291
P23 grade steel	as-delivered	194 – 203

(* Note: reheated by repetitive thermal cycles caused by multiple-pass welding.
(** Note: reheated by multiple thermal Gleeble simulation cycles c.f. Table 3.

Any measures to reduce local hardness and improve toughness and ductility can be of assistance, for example by shifting details of parent metal and weld composition, and the process of fabrication and heat treatments for better plasticity. In the case of the example P24 weld, selecting the Nb-alloyed consumable for welding P24 was enough to result in satisfactory as-fabricated properties and to remove any cracking indications from the welded joint before creep testing. However, low ductility damage and cracking in weld metal reappeared when subjected to medium term creep loading (up to about 10 000 h). Further improvement through extended process optimization does not seem to be particularly easy. Alternatively, an improved and more ductile weld metal, i.e. a new consumable, could be sought. Previous experience has shown [15] that maximising the weld metal creep strength at the expense of creep ductility, for instance by adding large amounts of Nb and B into P23 consumable, can recoil on increased propensity to weld metal reheat cracking (Table 3). A compromise with creep strength is possible, for example there is no reason to assume better than 80% of parent creep strength for the cross-weld case. All-weld metal P24 specimens extracted in the direction of the weld beads were not significantly more ductile than the cross-weld specimens in creep, although the all-weld metal specimens showed a longer creep life in uniaxial testing.

Overall, low ductility makes material unforgiving against straining under constraint (e.g. in rigid, high-restraint structures), and against any crack-like defects. Therefore low creep ductility may translate into poor performance of welded components that are subjected to more realistic loading conditions than the same material in uniaxial creep testing. Time to

failure in cross-weld specimens can correspond closely to the 80% strength level of the mean parent material strength, but may fall slightly lower when compared to the actual parent material strength (see Figure 2). In addition to weld metal, also the coarse-grained heat affected zone (CGHAZ) can show low ductility and significant sensitivity to damage.

Table 3: BWI Reheat Cracking Test results for the thermally re-heated microstructures of P23 (high-Nb-Ti-B) and P24 (Ni-Nb-Ti-free) grade multipass weld metals [17, 18].

Weld metal specimen / Case	Weld configuration	Specimen orientation	Reduction of area RA (%)
P23 weldment; high-Nb –W–Ti–B type filler metal B323(experimental)			
CG(R)-WM_10	circumferential pipe butt-weld	transverse	**3.0** **3.0**
	welded pad	longitudinal	**1.7** **1.4**
FG(R)-CG(R)-WM_10	circumferential pipe butt-weld	transverse	15 15
	welded pad	longitudinal	16 17
'P24' weldment; Ni–Nb–Ti-free type filler metal intended for P24 steel grade			
CG(R)-WM_10	circumferential pipe butt-weld	transverse	18 15
	welded pad	longitudinal	19 19
FG(R)-CG(R)-WM_10	circumferential pipe butt-weld	transverse	28 28
	welded pad	longitudinal	33 32
IC(R)-CG(R)-WM_10	welded pad	longitudinal	43 42
SC(R)-CG(R)-WM_10	welded pad	longitudinal	19 16

Note: CG(R)-WM: Tp1 = 1340°C ; FG(R)-CG(R)-WM: Tp1 = 1340°C & Tp2 = 1020°C ; IC(R)-CG(R)-WM: Tp1 = 1340°C & Tp2 = 900°C ; SC(R)-CG(R)-WM: Tp1 = 1340°C & Tp2 = 675°C ; t8/5 = 10 sec.; PWHT = 760°C / 2 h (P23 weldment) and 740°C / 2 h ('P24' weldment).

The lessons from X20 steam lines have been more positive: even when creep damage will appear after extensive time in service, it does not appear without fair early warning as observable indicators (Figure 5). With respect to the limitations being obstacles for a more widespread use of low-alloy Cr-Mo steels, it is interesting to compare their behaviour to vintage high-chromium vanadium-bearing martensitic steel X20. This steel is quite brittle in as-welded state before tempering, but appears to behave relatively well in long term service as thick-wall pipe and headers [2]. In spite of low ductility in as-welded as-new condition, and considerable embrittlement by in-service aging even after proper post-weld heat treatment, the long term creep ductility of this steel appears to remain quite satisfactory [20]. It is less clear whether the future will show similarly pleasant experience for the newer martensitic 9% Cr steels P91 and P92.
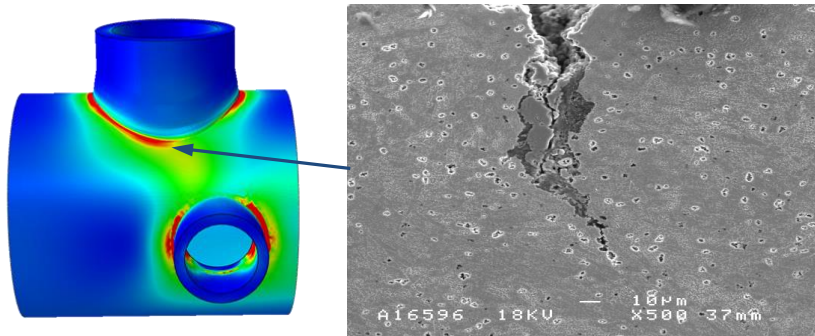
Figure 5: Creep cavitation and cracking in a branch weld heat affected zone at a saddle point position of a X20 steam line header after 135 000 h of service at 530°C [20].

5. Discussion and conclusions

A range of causative reasons and explanations have been proposed for the not entirely successful application of the modified 2% Cr steels P/T23 and P/T24 in power plants, particularly in waterwalls and steam lines. One root cause is *high hardenability*, resulting in high hardness and low ductility in welded joints (c.f. Tables 2 and 3), depending on details in chemical composition, fabrication, welding and heat treatments. For example, variations in the parent steel carbon content within the permitted standard range (0.05–0.10%) will notably affect the as-welded hardness, especially at comparatively low heat inputs typical in fillet welds and one-sided butt welds of boiler tubes. This applies also to weld metal, as the carbon content in the T/P23 and T/P24 materials can sometimes be greater in the weld metal than the parent steel (c.f. Figure 2), which then manifests itself as not only high HAZ, but also weld metal, hardness. This is the case for the thick section P23 steel weldment in Table 2 where the multiple thermal cycles have resulted in excessive local hardening in the reheated weld metal regions. In case of P/T23, *high weld hardness* and *poor toughness* without PWHT (i.e. the as-welded condition) may also be difficult to balance with the *risk of reheat cracking* during subsequent PWHT (Table 3).

Particular challenges appear when mitigating PWHT is needed for large panel assemblies. Further *ductility and toughness reduction* can be expected after subsequent ageing, as well as *reduced creep strength/ductility* in welds (reduced WSF), also in thick-wall pipes or headers. Relatively *unforgiving material response* to quality deviations, structural constraint and local stresses add to the challenge particularly at defects from welding or environmental impact. For instance, one-side welding of thin-wall tubes in all-around-the-clock positions is technically very demanding and can easily lead to weld defects, such as either incomplete or excess root penetration, end crater pipe, lack of (root / side-wall) fusion, and root concavity.

Complex microstructures responsible for the combined strength and ductility of parent material are difficult to sustain in the CGHAZ and weld metal. The *welding procedure and weld process parameters* therefore become much more important than for conventional Cr-Mo steels, and need even further optimisation in the case of modified 2% Cr steels. The available experience suggests that *welding techniques* maximising the thermal (normalising)

effect of successive weld passes (e.g. thinner weld layers) are beneficial in limiting the CGHAZ and weld metal hardness and associated detrimental phenomena. In general it remains a challenge to keep the *metallurgical design of welding consumables* in pace with that of the new parent steels, and the challenges evidently increase with the section thickness. The benefit from good creep strength of T23 and T24 is currently realised mainly in superheaters, i.e. in flexible structures with butt joints only and with typical wall thickness not exceeding 10–12 mm. The implied limitations from structural restraint to integrity will require attention to weld design, but high weld creep strength at the expense of ductility can nevertheless prevent the use of such steels in stiff, rigid or heavy sections. This suggests that structural design, weld joint design, welding procedures, filler metal compositions and adoption/omission of PWHT should all be tailored case-specifically, depending on the stiffness and rigidity of the structure and component in question.

The observed limitations with modified 2% Cr steels imply that higher alloy steels like P91 remain attractive for thick-wall high-pressure pipes and headers even at modest operating temperatures. The proposed improvements like steel variants with even higher creep strength, such as new 3% Cr steels [6, 12–14] will not solve the challenge before the issue of weld performance is settled, but any fair progress could launch the use of such steels in further applications. While the conventional X20 steel has demonstrated quite satisfactory long term creep ductility (in spite of its low ductility in as-welded as-new condition), it is not yet clear whether the service experience will be similar for 9% Cr steels P91 and P92.

References

[1] Mayer, K.-H., Masuyama, F. "The development of creep-resistant steels". In *Creep-resistant steels* (ed. by F. Abe, T-U Kern, R. Viswanathan), Woodhead Publishing, Cambridge, pp. 15-77.

[2] Auerkari, P. *et al.* "Evaluation of creep damage from replica inspection results". Nordtest project 1306-96, *VTT VAL B 211*. 33 p, (1996)

[3] Vaillant, J.C. *et al.* "T/P23, 24, 911 and 92: New grades for advanced coal-fired power plants - Properties and experience", *International Journal of Pressure Vessels and Piping*, Vol. 85, pp. 38-46, (2008).

[4] Auerkari P., Salonen J., Nevasmaa P. "2%CrMo(W)V steels for welded high temperature applications", VTT Research Report TUO74055258 (Espoo, 2005).

[5] Nowack R., Götte C., Heckmann S. "Quality management at RWE using T24 boiler material as an example", *VGB Powertech* (2011) 5 p.

[6] Auerkari P., Holmström S., Rantala J., Nevasmaa P., Salonen J. Assessment of the performance of welded P24 (7CrMoVTiB10-10). Final Report, Welding Group (FI-1), COST 536. VTT, Espoo, 2008. 12 p.

[7] EN 10216-2:2002+A2:2007. Seamless steel tubes for pressure purposes. Technical delivery conditions. Part 2: Non-alloy and alloy steel tubes with specified elevated temperature properties. 1+78 p.

[8] EN 10216-5:2004. Seamless steel tubes for pressure purposes. Technical delivery conditions. Part 5: Stainless steel tubes with specified elevated temperature properties. 1+84 p.

[9] Nevasmaa P., Laukkanen A., Häkkilä J. "Evaluation of weld metal hydrogen cracking risk in a 2.25-1Mo-0.25V-TiB (T24) boiler steel". *Baltica VI*, vol 2, 2004. VTT Symposium 234, pp. 393-407.

[10] Dhooge A., Vekeman J. "New generation 21/4 Cr steels T/P23 and T/P24 weldability and high temperature properties", *Welding in the World* Vol. 49 (2005), pp. 75-93.

[11] Bendick, W. *et al*. New low alloy heat resistant ferritic steels T/P23 and T/P24 for power plant application. *International Journal of Pressure Vessels and Piping*, Vol. 84 (2007). pp. 13-20.

[12] Mohyla P., Foldyna V. "Improvement of reliability and creep resistance in advanced low-alloy steels", *Materials Science and Engineering A* Vol. 510-511 (2009), pp. 234-237.

[13] Whittaker M.T., Wilshire B. "Advanced procedures for long-term creep data prediction for 2.25 chromium steels", *Metallurgical and Materials Transactions*, Vol. 44A (2013), pp. S136-S153.

[14] Klueh R.L. *et al*. "Creep-rupture behavior of 3Cr-3W-V bainitic steels", *International Journal of Pressure Vessels and Piping* Vol. 84 (2007), pp. 29-36.

[15] Abe F. "Bainitic and martensitic creep-resistant steels", *Current Opinion in Solid State and Materials Science* Vol. 8 (2004), pp. 305-311.

[16] Klueh R.L., Nelson A.T. "Ferritic/martensitic steels for next-generation reactors", *Journal of Nuclear Materials* Vol. 371 (2007), pp. 37-52.

[17] Nevasmaa, P., Salonen, J. "Reheat cracking susceptibility and toughness of 2%CrMoWVNb (P23) steel welds", *Welding in the World* Vol. 52 (2008), pp. 68-78.

[18] Nevasmaa, P. *et al*. "Reheat cracking susceptibility of P23 (7CrWVMoNb9-6) steel welds made using matching and mis-matching filler metals", *Proc 9th Liege Conference on Materials for Advanced Power Engineering*, Liege, Sept. 2010. 10 p.

[19] Auerkari, P. *et al*. "Performance of welded low-alloy steels T/P23 and T/P24 for power plant applications", IIW Congress, Singapore, 8-10 July 2013. 4 p.

[20] Auerkari, P. *et al*. "Creep damage in X20CrMoV11-1 – ex-service experience and a case study", Värmeforsk project M08-830, Report VTT-R-07168-10, Espoo 2010. 40 p.

ALLOY DESIGN FOR SUPPRESSION OF TYPE IV FRACTURE IN 9Cr STEEL WELDS AT 650 °C

Fujio Abe, M. Tabuchi and S. Tsukamoto

National Institute for Materials Science, 1-2-1 Sengen, Tsukuba 305-0047, Japan

E-mail : ABE.Fujio@nims.go.jp

Abstract

The degradation in creep life of Gr.92 after the A_{C3} thermal cycle shows that it is not caused by the grain refinement but that the reduction of boundary and subboundary hardening is the most important. The 9Cr-boron steel exhibits substantially the same microstructure as the base metal even after the A_{C3} thermal cycle and hence substantially the same time to rupture at 650 °C as the base metal. Soluble boron is essential for the change in α/γ transformation behavior during heating of welding and for the production of same microstructure as the base metal. For suppression of Type IV fracture in HAZ of 9Cr steel welds, the elimination of tempering before welding or the retention of soluble boron are proposed to obtain enough $M_{23}C_6$ carbides at PAGBs, lath and block boundaries during PWHT. 9Cr-3W-3Co-0.2V-0.05Nb steel with 120-150 ppm boron and 60-90 ppm nitrogen (MARBN) exhibits not only much higher creep rupture strength of base metal than P92 but also substantially no Type IV fracture in HAZ of welded joints at 650 °C.

Keywords: 9Cr steel, welded joint, creep strength, boundary hardening, $M_{23}C_6$ carbide, boron, Type IV fracture

1. Introduction

In 9 to 12Cr steels, softening zone and fine-grained zone are produced in the heat-affected-zone (HAZ) of welded joints, which accelerates damage development during creep at elevated temperature, especially above 600 °C. This is called Type IV fracture and significantly reduces the creep life of welded joints [1]. The suppression of Type IV fracture is one of the critical issues to increase the maximum allowable temperature of ferritic steels above 600 °C.

We have revealed that the multi-axial stress condition in HAZ with lower creep strength, resulting from mechanical constrain effect by the surrounding weld metal and base metal with higher creep strength, is essential for the formation of creep voids and brittle Type IV fracture in HAZ of conventional 9 to 12Cr steel welded joints [2]. We have also revealed that the addition of boron to 9Cr steel produces roughly the same microstructure in HAZ as the base metal, which effectively suppresses the Type IV fracture [3-6].

In this paper, using simulated-HAZ specimens, we investigate the mechanisms responsible for the lower creep strength of HAZ in Gr.92 welded joints than its base metal and also the boron effects on the microstructure evolution in HAZ of 9Cr steel welded joints during heating of welding. The alloy design for suppression of Type IV fracture in 9Cr steel welds is also proposed.

2. Experimental procedure

The steels examined were Gr.92 (0.09C-8.73Cr-0.45Mo-1.87W-0.21V-0.06Nb-0.050N-0.002B) [7] and 9Cr-boron steel (0.08C-9Cr-3W-3Co-0.2V-0.05Nb in nominal) [4-5] containing 90 and 130 ppm boron. Nitrogen was not added in the 9Cr-boron steel to avoid the formation of boron nitrides during normalizing heat treatment. The Gr.92 was normalized at

1070 °C for 1 h and then tempered at 780 °C for 1 h, while the 9Cr-boron steel was normalized at 1080 °C for 1 h and then tempered at 800 °C for 1 h. The preparation of simulated-HAZ specimens are described elsewhere [6]. At a heating rate of 100 K s^{-1}, the A_{C1} temperature was found to be 817 and 841 °C for P92 and the 9Cr-boron steel containing 90 ppm boron, respectively, while the A_{C3} temperature was 912 and 920 °C for P92 and the 9Cr-90 ppm B steel, respectively. The specimens were kept for 0.5 s at various peak temperatures between 810 and 1125 °C and then cooled to room temperature. Finally, the post weld heat treatment (PWHT) was carried out for each specimen including the base metal at 740 °C for 4.7 h. The preparation of welded joints is described elsewhere [4].

Creep tests were carried out at 650 °C, using specimens of 6 mm gauge diameter and 30 mm gauge length for the simulated-HAZ specimens and of 17.5 x 5mm cross section and 100 mm gauge length for the welded joints. Creep tests for the base metals were also carried out at 650 °C, using specimens of 10 mm gauge diameter and 50 mm gauge length.

3. Results and discussion

3.1 Effect of grain size and boundary hardening on creep strength of simulated-HAZ specimens

Figure 1 shows the time to rupture of the simulated-HAZ specimens of Gr.92, Gr.92N, Gr.92NN and the 9Cr-90 ppm B steel at 650 °C and 110 MPa, as a function of peak temperature in the thermal cycle. Gr.92 was subjected to normalizing and tempering heat treatment, while Gr.92N was subjected to only normalizing but no tempering before the thermal cycle, Table 1. Gr.92NN was subjected to sub-zero treatment in liquid nitrogen after normalizing but no tempering before the thermal cycle. In Fig.1, Gr.92 exhibits a significant decrease in time to rupture after the thermal cycle to a peak temperature near A_{C3}. On the other hand, the time to rupture of Gr.92N, Gr.92NN and the 9Cr-boron steel is substantially the same as that of their base metals, independent of peak temperature in the thermal cycle.

Figure 2 shows the grain size and distribution of $M_{23}C_6$ carbides along prior austenite grain boundaries (PAGBs) in Gr.92, Gr.92N and Gr.92NN after the thermal cycle to a peak temperature of 950 °C, just above the A_{C3} temperature. Gr.92 is observed to be the fine-grained microstructure having a prior austenite grain size of smaller than 10 μm after the A_{C3}
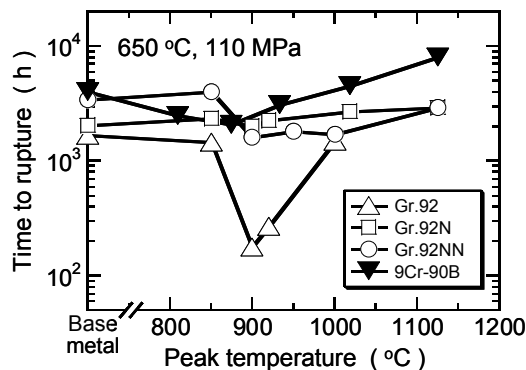
*Fig.1 Time to rupture of simulated-HAZ specimens at 650 °C and 110 MPa,
as a function of peak temperature in thermal cycle.*

*Table 1 Heat treatment conditions before A$_{C3}$ thermal cycle for
Gr.92, Gr.92N and Gr.92NN and microstructure after PWHT*

	Heat treatment	Grain size after PWHT	GB M$_{23}$C$_6$ after PWHT
Gr.92	Normalizing → Tempering → Thermal cycle	fine grains	poor
Gr.92N	Normalizing → Thermal cycle	coarse grains	enough
Gr.92NN	Normalizing → Sub-zero → Thermal cycle	fine grains	enough

Normalizing : 1070 ^{o}C x 0.5 h, Tempering : 780 ^{o}C x 1 h, Sub-zero : immersed in liquid nitrogen,
Thermal cycle : Peak Temp. 950 ^{o}C → PWHT (740 ^{o}C x 4.7 h)

thermal cycle, while Gr.92N exhibits the coarse-grained microstructure even after the A$_{C3}$ thermal cycle, substantially the same prior austenite grain size as the base metal [4]. The average prior austenite grain size of the base metals of Gr.92 and Gr.92N is roughly 50 μm. Gr.92NN exhibits the fine-grained microstructure after the A$_{C3}$ thermal cycle, similar as Gr.92. Figure 3 shows the transmission electron micrographs inside the grains of the specimens shown in Fig.2.   Very few precipitates are formed along PAGBs in the fine-grained microstructure of Gr.92 and the lath-block subgrain structure is not clearly seen inside the grains, suggesting that the boundary and subboundary hardening is significantly reduced in the Gr.92 after the A$_{C3}$ thermal cycle.   Inside the grains, the Gr.92 consists of equiaxed subgrains with low density of dislocations and sparse distributions of large carbides.   The subboundary hardening, which is inversely proportional to the width of lath and block, has been shown to be the most important strengthening mechanism in creep of tempered martensitic steels and is enhanced by fine dispersions of precipitates along lath and block boundaries.   In the Gr.92N and Gr.92NN, not only PAGBs but also lath and block boundaries are covered by enough M$_{23}$C$_6$ carbides even after the A$_{C3}$ thermal cycle, similar as the base
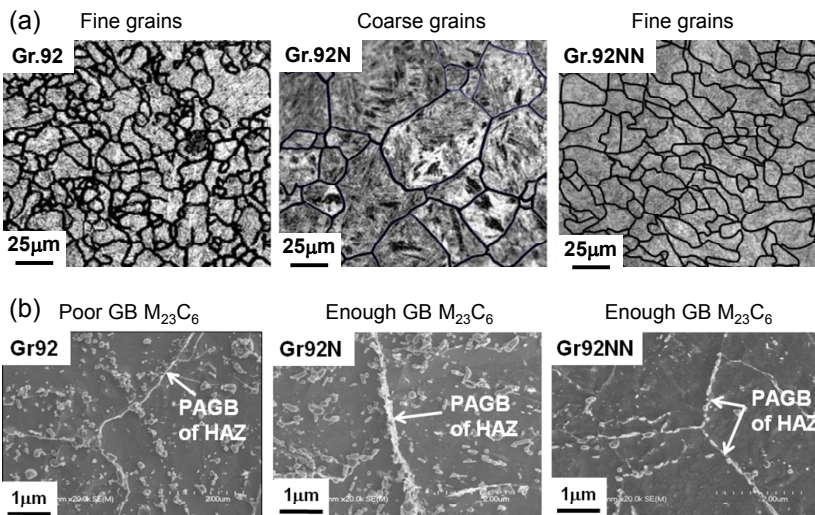
Fig.2 (a) optical and (b) scanning electron micrographs of Gr.92, Gr.92N and Gr.92NN after thermal cycle to a peak temperature of 950 ^{o}C, just above A$_{C3}$.
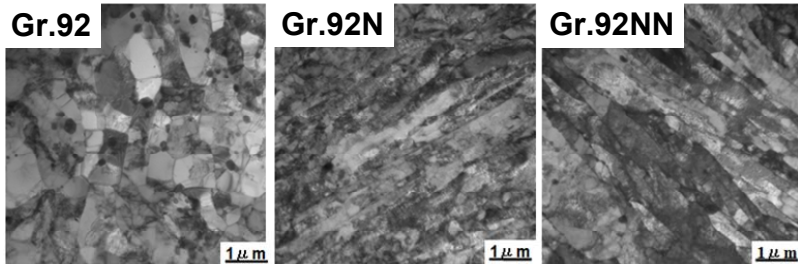
Fig.3 Transmission electron micrographs of Gr.92, Gr.92N and Gr.92NN
after thermal cycle to a peak temperature of 950ºC, just above A$_{C3}$.

metal, irrespective of coarse-grains or fine-grains.

It should be noted in Fig.1 that the time to rupture of Gr.92NN is substantially the same as that of base metal, in spite of fine grains. Therefore, the degradation in creep life in Gr.92 after the A$_{C3}$ thermal cycle shows that it is not caused by the grain refinement but that the reduction of boundary and subboundary hardening is the most important.

The 9Cr-boron steel basically consists of coarse grains of roughly 200 to 300 μm after the A$_{C3}$ thermal cycle, which is substantially the same as that of base metal, and of fine grains of 10 to 50 μm along PAGBs of coarse grains, Fig. 4. PAGBs of the coarse grains are covered
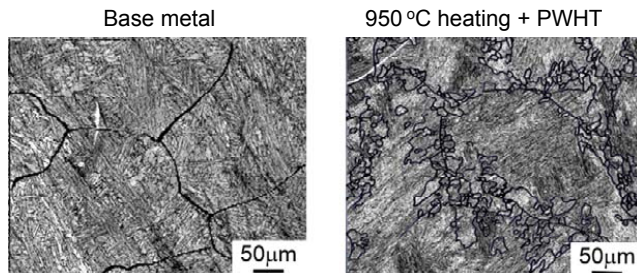
Fig.4 Optical micrograph of 9Cr-90 ppm boron steel base metal and that
after thermal cycle to a peak temperature of 950ºC, just above A$_{C3}$.
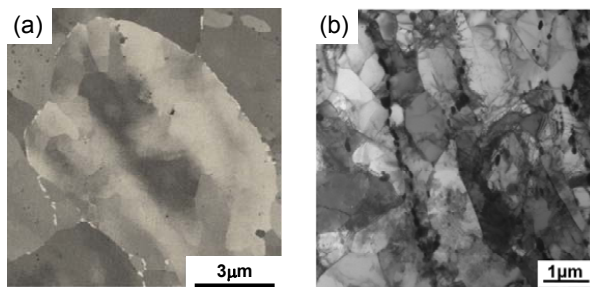
Fig.5 (a) precipitation of Fe$_7$W$_6$-μ phase at GBs of fine grains and
(b) tempered martensitic microstructure inside grain of 9Cr-90 ppm boron steel
after heat cycle to a peak temperature of 950ºC and subsequent PWHT.

94

by enough $M_{23}C_6$ carbides even after the A_{C3} thermal cycle, substantially the same as the base metal. It should be noted that a large number of Fe_7W_6-μ phase precipitates at grain O boundaries of the fine grains during PWHT, Fig. 5(a) [6]. Inside the grains, the tempered martensitic microstructure substantially consists of blocks, Fig. 5(b). Therefore, the boundary and subboundary hardening is enough in the 9Cr-boron steel even after the A_{C3} thermal cycle, resulting in no reduction of creep strength in the A_{C3}- HAZ.

3.2 Creep deformation behavior of simulated-HAZ specimens

Figure 6 shows the creep rate versus time curves for the A_{C3} simulated-HAZ specimens of Gr.92, Gr.92N and Gr.92NN at 90 and 110 MPa at 650 °C, comparing with those for the Gr.92 base metal. The creep rate curves consist of the primary or transient creep region, where the creep rate decreases with time, and of the tertiary or acceleration creep region, where the creep rate increases with time after reaching a minimum creep rate. There is no steady-state region. The onset of acceleration creep takes place at earlier times in the A_{C3} simulated-HAZ specimens of Gr.92 than in the other specimens, resulting in higher minimum creep rates and shorter time to rupture.
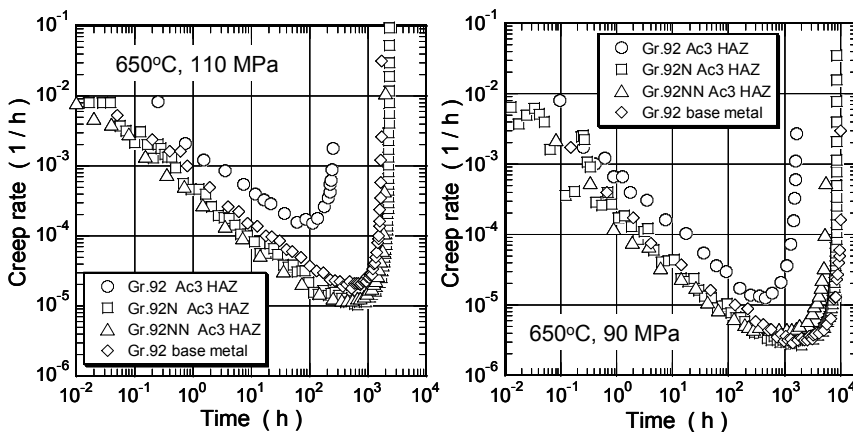
Fig. 6 Creep rate versus time curves of A_{C3} simulated-HAZ specimens of Gr.92, Gr.92N and Gr.92NN at 650°C, 110 and 90 MPa, comparing with those of Gr.92 base metal.

Figure 7 shows the change in kernel average misorientation (KAM) and boundary length in an area of 120 x 120 μm for the A_{C3} simulated-HAZ specimens of Gr.92, Gr.92N, Gr.92NN and 9Cr-90ppm boron before and after creep at 650 °C and 110 MPa [7]. The decrease in KAM reflects the recovery of dislocations during creep, while the decrease in boundary length reflects the coarsening of laths, blocks and packets inside the grains. The present results indicate the microstructure recovery during creep is more significant in the A_{C3} simulated-HAZ specimens of Gr.92 than in those of Gr.92N, Gr.92NN and 9Cr-boron steel.

The equiaxed subgrains with low density of dislocations and sparse distributions of large carbides in the Gr.92 after the A_{C3} thermal cycle shown in Fig.3 suggest a lower resistance to creep deformation in the initial stage of creep than the lath martensitic microstructure with enough $M_{23}C_6$ carbides at lath boundaries in the Gr.92N and Gr.92NN. This results in higher creep rates in the transient region in the A_{C3} simulated-HAZ specimens of Gr.92, which
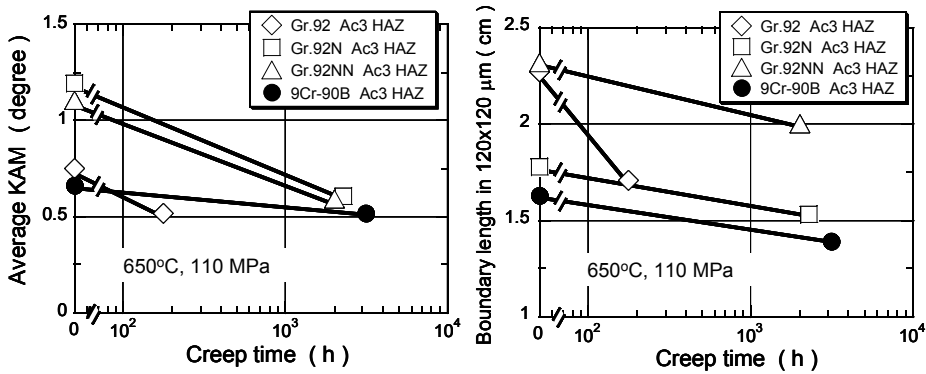
*Fig. 7 Change in KAM and boundary length for Gr.92, Gr.92N, Gr.92NN
and 9Cr-90ppm boron by creep at 650 ^{o}C and 110 MPa.*

promotes the microstructure recovery during creep and hence promotes the onset of acceleration creep.

The creep rate curves of the A_{C3} simulated-HAZ specimens of 9Cr-boron steel are substantially the same as those of the base metal.

3.3 Microstructure evolution in HAZ during heating of welding

In Gr.92, the nucleation and growth of γ phase by diffusive transformation take place during heating, producing the fine-grained microstructure when the peak temperature is not so high, as shown in Fig. 8. Carbonitrides such as $M_{23}C_6$ also become dissolved during heating but cannot dissolve completely, when the peak temperature is not so high. The dissolved carbon atoms precipitate again as $M_{23}C_6$ carbides during PWHT at 740 ^{o}C. Whether new grain boundaries are covered by enough $M_{23}C_6$ carbides or not depends on the amount of new grain boundaries and dissolved carbon atoms. When the peak temperature is not so high, at around A_{C3} temperature, the amount of dissolved carbon atoms is only a little bit, while a large number of new grain boundaries is produced, Fig.8. This causes the very few $M_{23}C_6$ carbides along new grain boundaries in the Gr.92 after the heating to a peak temperature near A_{C3} followed by PWHT. It should be noted that the temperature range for the formation of fine-grained microstructure in the Gr.92 is overlapped with that for the very few $M_{23}C_6$ carbides along new grain boundaries, Fig.8. This suggests that the observations of fine-grained HAZ provide us an indication of very few $M_{23}C_6$ carbides along new grain boundaries, suggesting the reduction of boundary and sub-boundary hardening.

The reconstitution of original austenite grain structure in Gr.92N is due to an austenite memory effect. Shirane et al. observed 3 vol% retained austenite in Gr.92 after normalizing [8]. The austenite memory effect has been shown to be a consequence of the growth of thin films of retained austenite in starting martensitic microstructure during subsequent heating [9-10]. The growing thin films of retained austenite coalesce on impingement, which leads to the reconstitution of original austenite grain structure and reproduces the same grain size as the original austenite. In Gr.92NN, the 3 vol% retained austenite present after normalizing completely transforms to martensite during sub-zero treatment in liquid nitrogen. This sugegst that no austenite memory effect is available in Gr.92NN during heating and that the nucleation and growth of γ phase by diffusive transformation takes place during heating,
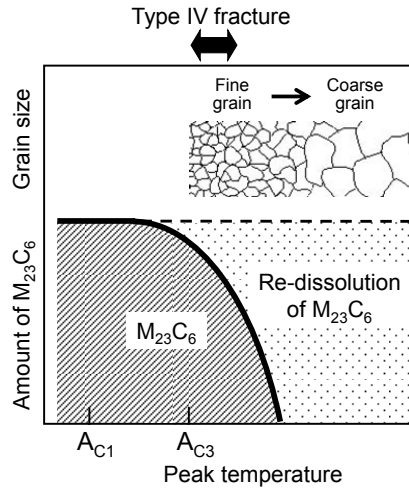
Fig. 8 Schematics of change in grain size and amount of $M_{23}C_6$ carbides
in Gr.92 during heating.

resulting in fine-grained microstructure, similar as Gr.92.

In the Gr.92N and Gr.92NN, no $M_{23}C_6$ carbide presents before the thermal cycle and all the carbon atoms are in solution, because of no tempering, Table 1. Therefore, the precipitation of enough $M_{23}C_6$ carbides takes place preferentially at PAGBs, lath and block boundaries during PWHT.   The PHWT for Gr.92N and Gr.92NN corresponds to a temepring heat treatment at low temperature of 740 °C.

The direct observation of the 9Cr-130 ppm boron steel surface using a confocal scanning laser microscope during heating clearly shows a high surface relief, suggesting that martensitic transformation takes place in the 9Cr-boron steel during heating [4-5].   The martensitic transformation introduces a high density of dislocations during heating, but recrystallization cannot take place, because boron retards recrystallization.   This suggests no production of new grain boundaries.   Therefore, the resultant microstructure of 9Cr-boron steel after PWHT exhibits enough $M_{23}C_6$ carbides along PAGBs and block boundaries, which is substantially the same as that of the original microstructure.

The formation of fine grains along PAGBs of coarse grains shown in Fig.4 suggests that at first the nucleation of γ phase by diffusive transformation takes place preferentially at GBs during heating but martensitic transformation takes place inside the grain. The nucleation of γ phase is promoted at GBs, because strained regions at GBs enable nuclei to be formed with a much smaller free energy.   On the other hand, the grain boundary segregation of boron reduces the interfacial energy $\sigma_{\alpha\alpha}$ for α/α boundary and makes the α/α boundaries less effective as heterogeneous nucleation sites for γ phase.   This retards diffusive α/γ transformation, and hence martensitic reverse transformation by shear can take place during heating, similar as maraging steel. Using a binding energy of 62.7 kJ/mol [11] between boron and grain boundary reported for type 316 stainless steel, the grain boundary segregation of boron is estimated to be several % to 10 % at 950 °C [4-5]. We think that the driving force for diffusive α/γ transformation during heating is a little bit larger at PAGBs than the retardation effect by boron near GBs but that the formation of fine grains is limited near PAGBs of coarse grains by the retardation effect due to boron, Fig.9(a). The driving force for diffusive α/γ

transformation is considered to be much smaller inside the grain than near PAGBs, because strained regions are limited near GBs. The retardation effect by boron is also smaller inside the grain than near PAGBs, because of no GB segregation of boron inside the grain. The present results that the martensitic α/γ transformation takes place inside the grain during heating suggest that the retardation effect by boron is larger inside the grain than the driving force for nucleation of γ by diffusive α/γ transformation, Fig.9(a). The soluble boron concentration in the matrix is estimated to be about 20 ppm, as shown in Fig.9(c), by assuming the initial boron concentration is 100 ppm, the enriched boron concentration in $M_{23}C_6$ carbides is 0.5% (Fig.9(b)) and the mole fraction of $M_{23}C_6$ carbides is 0.0016 by thermo-calc. We think that the soluble boron concentration of 20 ppm in the matrix is enough to retard the diffusive α/γ transformation and hence the martensitic α/γ transformation takes place inside the grain during heating.
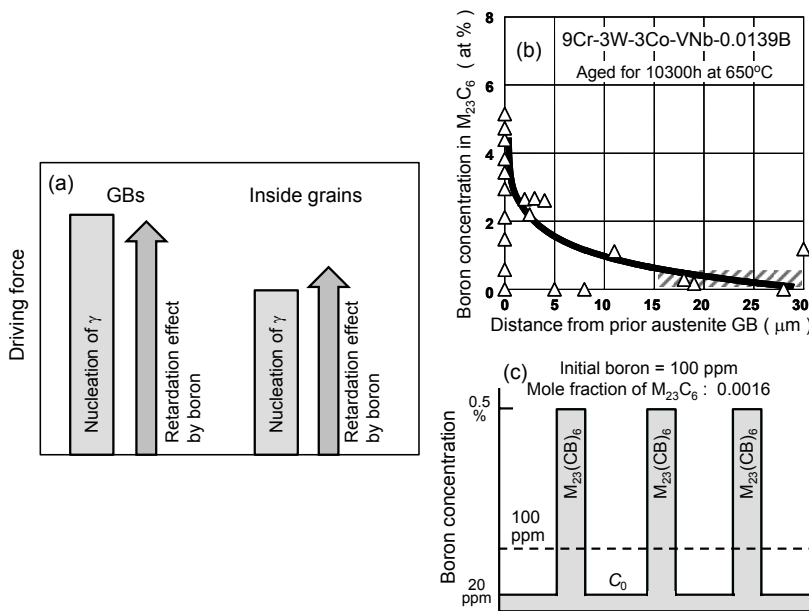
Fig. 9 (a) driving force for diffusive transformation and retardation effect by boron, (b) enrichment of boron in $M_{23}C_6$ near PAGBs and (c) boron distribution in 9Cr-boron steel.

3.4 Alloy design for suppression of Type IV fracture in 9Cr steel welds

In order to suppress the Type IV damage in HAZ of Gr.92 welded joints, the elimination of tempering heat treatment before welding is proposed. The elimination of tempering causes the precipitation of enough $M_{23}C_6$ carbides at PAGBs, lath and block boundaries during PWHT, which resdults in no reduction of boundary hardening and hence no degradation in creep strength of HAZ, as shown for Gr.92NN. The present scenario can also be applied to Gr.91 and Gr.122.

With respect to Gr.91 welded joints, recently a new pre-weld heat treatment at lower temperature was proposed by Yu et al [12] to mitigate the Type IV damage. A welded joint specimen subjected to tempering at lower pre-weld tempering temperature (LTT) of 650 ºC

exhibits a significantly lower steady-state creep rate and a significantly longer creep life at 650 ºC than the specimen subjected to tempering at the higher pre-weld tempering temperature (HTT) of 760 ºC. Poor $M_{23}C_6$ carbides are distributed along new grain boundaries (GBs) of fine-grained HAZ in the HTT specimen after PWHT, while enough $M_{23}C_6$ carbides are observed along new GBs of fine-grained HAZ in the LTT specimen. Their results provide one solution to extending the life of Gr.91 welded joints by control of carbide distributions at GBs in HAZ.

The soluble boron is essential for the martensitic reverse transformation in 9Cr-boron steel during heating of welding. Excess addition of boron and nitrogen promotes the formation of boron nitrides during normalizing heat treatment, which significantly reduces soluble boron and soluble nitrogen concentrations. We observed a large number of boron nitrides of several μm in Gr.92, examined in the present work, which contained 20 ppm boron and 0.05 % (500 ppm) nitrogen. This suggests substantially no boron effect in Gr.92.

Based on the suppression of Type IV fracture using boron and the improvement of long-term creep strength of base metal by using both boron and MX nitride without any formation of boron nitrides during normalizing heat treatment, a 9Cr-3W-3Co-0.2V-0.05Nb steel containing 120-150 ppm boron and 60-90 ppm nitrogen was alloy-designed. The steel is denoted MARBN, which means _mar_tensitic 9Cr steel strengthened by _b_oron and MX _n_itrides. Figure 10 shows the creep rupture data for the base metal and welded joints of MARBN at 650 ºC, together with those for P92 [14]. MARBN exhibits not only much higher creep rupture strength of base metal than P92 but also substantially no degradation in creep rupture strength of welded joints compared with base metal, indicating no Type IV fracture.
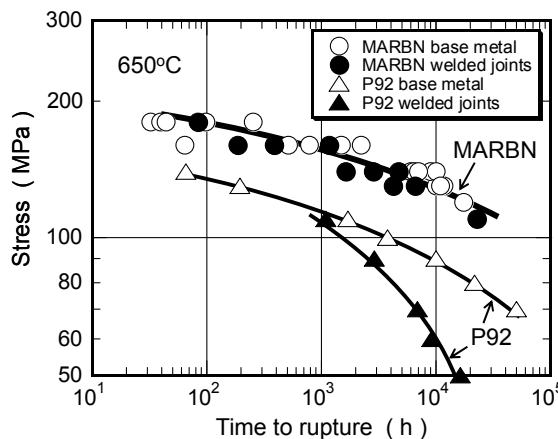
Fig. 10 Creep rupture data for base metal and welded joints of MARBN and P92 at 650ºC.

4. Summary

(1) The simulated-HAZ specimens of Gr.92 exhibit the fine-grained microstructure after the A_{C3} thermal cycle, where very few precipitates are formed along PAGBs and the lath-block subgrain structure is not clearly seen inside the grain. The degradation in creep life in Gr.92 after the A_{C3} thermal cycle is not caused by the grain refinement but that the reduction of boundary and sub-boundary hardening is the most important.

(2) The simulated-HAZ specimens of 9Cr-boron steels exhibit substantially the same microstructure as the base metal even after the A_{C3} thermal cycle and hence substantially the same time to rupture as the base metal, independent of peak temperature.

(3) For suppression of Type IV fracture in HAZ of 9Cr steel welds, the elimination of tempering before welding or the retension of soluble boron are proposed to obtain enough $M_{23}C_6$ carbides at PAGBs, lath and block boundaries during PWHT.

(4) 9Cr-3W-3Co-0.2V-0.05Nb steel with 120-150 ppm boron and 60-90 ppm nitrogen (MARBN) exhibits not only much higher creep rupture strength of base metal than P92 but also substantially no degradation in creep strength due to Type IV fracture in HAZ of welded joints at 650 °C.

References

[1] J. A. Francis, W. Mazur and H. K. D. H. Bhadeshia, 'Type IV cracking in ferritic power plant steels', Mater. Sci. Technol., 22, 1387-1395 (2006).

[2] F. Abe and M. Tabuchi, 'Microstructural and Creep Strength of Welds in Advanced Ferritic Power Plant Steels', Materials Science and Technology of Welding and Joining, 9, 22-30 (2004).

[3] M. Tabuchi, M. Kondo, T. Watanabe, H. Hongo, F. Yin and F. Abe, 'Improvement of Type IV Cracking Resistance of 9Cr Heat Resisting Steel Weldment by Boron Addition', Acta Metallurgica Sinica, 17, 331-337 (2004).

[4] F. Abe, M. Tabuchi, S. Tsukamoto and T. Shirane, 'Microstructure Evolution in HAZ and Suppression of Type IV Fracture in Advanced Ferritic Power Plant Steels', Intern. J. Pessure Vessels and Piping, 87, 598- 604 (2010).

[5] F. Abe, M. Tabuchi and S. Tsukamoto, 'Mechanisms for boron effect on microstructure and creep strength of ferritic power plant steels', Energy Materials, 4, 166-175 (2012).

[6] Y. Liu, S. Tsukamoto, K. Sawada and F. Abe, 'Role of Boundary Strengthening on Prevention of Type IV Failure in High Cr Ferritic Heat-Resistant Steels', Metall. Mater. Trans. A, 45A, 1306-1314 (2014).

[7] Y. Liu, S. Tsukamoto, T. Shirane and F. Abe, 'Formation Mechanism of Type IV Failure in High Cr Ferritic Heat-Resistant Steel-Welded Joint', Metall. Mater. Trans. A, 44, 4626-4633 (2013).

[8] T. Shirane, S. Tsukamoto, K. Tsuzaki, Y. Adachi, T. Hanamura, M. Shimizu and F. Abe, 'Ferrite to austenite reverse transformation process in B containing 9%Cr heat resistant steel HAZ', Sci. Technol. of Welding and Joining, 14, 698-707 (2009).

[9] S.T. Kimmins and D.J. Gooch, 'Austenite memory effect in 1Cr-1Mo-0.75V(Ti,B) steel', Metal Science, 17, 519-32 (1983).

[10] R.K. Shiue, K.C. Lan and C. Chen, 'Toughness and austenite stability of modified 9Cr-1Mo welds after Tempering', Mater. Sci. Eng., A287, 10-16 (2000).

[11] L. Karlsson and H. Norden, 'Non-equilibrium grain boundary segregation of boron in austenitic stainless steels', Acta Metall., 36, 13-27 (1988).

[12] X. Yu, S. S. Babu, H. Terasaki, Y. Komizo, Y. Yamamoto and M. L. Santella, 'Correlation of precipitate stability to increased creep resistance of Cr-Mo steel welds', Acta Materialia, 61, 2194–2206 (2013).

[13] K. Sakuraya, H. Okada and F. Abe, 'BN type inclusions formed in high Cr ferritic heat resistant steel', Energy Materials, 1, 158-166 (2006).

[14] F. Abe, 'Effect of Boron on Long-term Stability of 9Cr Steel for 650°C Boilers', Proc. of 38th MPA-Seminar, Stuttgart, October 1 and 2, 2012, CD-ROM (2012).

CREEP STRENGTH OF DISSIMILAR WELDED JOINTS USING HIGH B-9CR STEEL FOR A-USC BOILER

M. Tabuchi, H. Hongo and F. Abe

National Institute for Materials Science
(1-2-1 Sengen, Tsukuba, 305-0047 Japan – TABUCHI.Masaaki@nims.go.jp)

Abstract

Research project aiming to commercialize 700°C class pulverized coal advanced ultra-supercritical (A-USC) pressure power generation has been conducted in Japan. In the A-USC boiler, Ni or Ni-Fe base alloys are used for high temperature parts at 650-700˚C, and advanced high Cr ferritic steels are planning to be used at lower temperature parts than 650˚C. In the dissimilar welds between Ni base alloy and high Cr steels, Type-IV failure and creep-fatigue are the major concerns. Because the high B-9Cr steel developed in National Institute for Materials Science (NIMS) has improved creep strength in weldments, it is one of the candidate materials for A-USC boilers. In the present paper, creep tests were conducted on the dissimilar welded joints between Ni base alloys and high B-9Cr steels. Microstructures and creep damages in the dissimilar welded joints were investigated. In the heat affected zone (HAZ) of the high B-9Cr steels, fine-grained microstructures were not formed and the grain size of the base metal was retained. Consequently, the creep rupture life of the dissimilar welded joints using high B-9Cr steel was 5-10 times longer than that of the conventional 9Cr steel welded joints at 650˚C.

Keywords: A-USC boiler, High B-9Cr steel, Dissimilar welded joint, Creep

1. Introduction

Research project aiming to commercialize 700°C class pulverized coal advanced ultra-supercritical (A-USC) pressure power generation has been conducted from 2008 in Japan. By raising the current USC steam conditions of 600 ˚C and 25MPa to A-USC conditions of 700 ˚C and 35MPa, the net thermal efficiency is improved from 42% to 46-48% and CO_2 emissions can be reduced by more than 10%. In the A-USC boiler, Ni or Ni-Fe base alloys such as Alloy 617, Alloy 263, Alloy 740, Alloy 141 and HR6W would be used for the high temperature parts at 650-700 ˚C. At temperatures lower than 650 ˚C, advanced high Cr ferritic steels would be used in order to reduce the costs of materials. High boron 9Cr (high B-9Cr) steel, low carbon 9Cr (LC-9Cr) steel and SAVE12AD steel are candidate high-Cr steels [1]. In the A-USC research project, creep rupture, fatigue, oxidation, corrosion, welding and bending tests are being conducted on the above alloys and steels. In the dissimilar welds between Ni base alloy and high Cr steel, Type-IV failure and thermal-fatigue (creep-fatigue) are concerns. Since the 9Cr-3W-3Co-VNb steel containing about 0.01% boron and low nitrogen (high B-9Cr steel) developed in National Institute for Materials Science (NIMS) has

improved creep strength not only in the base metal but also in the welded joint [2, 3], it is one of the candidate materials for the Japanese A-USC boiler [1].

In the present paper, creep tests of the dissimilar welded joints between high B-9Cr steels and Ni base alloys for A-USC boilers were conducted at 650 ˚C. Microstructures and creep damages in the dissimilar welded joints were investigated. Creep damage was evaluated using damage mechanics for comparison with the experimental results.

2. Experimental procedure

2.1. Materials

Two kinds of the high B-9Cr steels; MARBN10 steel (9Cr-3W-3Co-VNb-0.01B-0.003N) and MARBN12 steel (9Cr-2.6W-3Co-VNb-0.01B-0.007N) were prepared. The chemical compositions are shown in Table 1. Figure 1 shows the solubility product for boron nitride (BN) at normalizing temperatures 1000-1050 ˚C [4]. In the present steels, 0.01% boron was added to maximize the grain boundary strengthening effect of boron. Nitrogen content was lower than 0.01 % to avoid the formation of boron nitride (BN). The MARBN12 steel contains more nitrogen than the MARBN10 steel. Plate thickness was 25 mm. These steel plates were normalized at 1100 ˚C for 1 h and tempered at 800 ˚C for 1 h.

Table 1: Chemical compositions of the present high B-9Cr steels (wt. %).

	C	Si	Mn	P	S	Cr	W	Mo	Co	Ni	V	Nb	N	O	B	Sol.Al
MARBN10	0.078	0.29	0.54	0.003	0.001	9.11	3.13	<0.01	3.03	<0.01	0.21	0.052	0.0030	0.003	0.010	0.001
MARBN12	0.081	0.30	0.53	0.001	0.001	9.09	2.62	<0.01	3.02	<0.01	0.21	0.052	0.0072	0.003	0.011	0.001
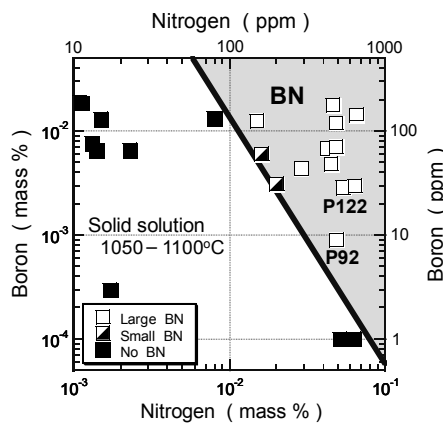
Figure 1: Solubility product for boron nitride (BN) at normalizing temperatures 1050-1100 ˚C [4]

2.2. Welding

Four kinds of dissimilar welded joints between high B-9Cr steels (MARBN10 steel and MARBN12 steel) and Ni base alloys for A-USC boilers (Alloy 617 and Alloy 263) were prepared by gas tungsten arc (GTA) welding using Inconel 82 filler wire, as shown in Figure 2. These welded joints had a U-groove with a 20 ° groove angle. All dissimilar welded joints were given post weld heat treatment (PWHT) at 740 ˚C for 4 h. Weld defects were not detected in the radiographic examination and magnetic particle testing.

2.3. Creep tests

Creep tests of the base metals were conducted using round bar-type specimens 6 mm in diameter and 30 mm in gauge length. Creep tests of the dissimilar welded joints were conducted at 650 ˚C using the smooth plate type specimens 17.5×5 mm in section and 100 mm in gauge length as shown in Figure 3.
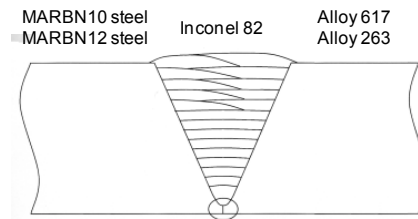
Figure 2: Dissimilar welded joints used in the present study.
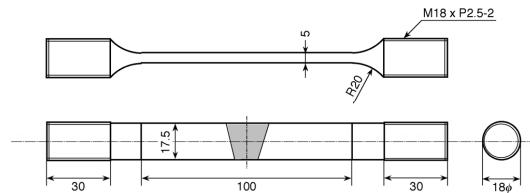
Figure 3: Creep test specimen for the dissimilar welded joint.

3. Results and discussion

3.1. Microstructures of HAZ of high B-9Cr steel

Figure 4 shows the crystallographic orientation distribution maps for the normal direction of the specimen and the grain boundary maps of the base metal and HAZ of the high B-9Cr steel in the dissimilar welded joint (MARBN10 steel-Alloy 263 weld) obtained by the electron

103

back-scattered diffraction (EBSD) analysis. EBSD analysis was conducted using a hexagonal grid at steps of 2 μm. In the grain boundary maps, grain boundaries with misorientation from 15 ˚ to 48 ˚ were drawn and their length was measured. Kernel average misorientation (KAM) at points with misorientation from 0 ˚ to 5 ˚ was calculated in order to investigate the changes of dislocation structures.

The base metal of the present steel shows tempered martensitic structures having a grain boundary length per unit area of 28.7 mm^{-1} and KAM of 1.83 (Figure 4(a)). In the conventional high Cr steels, HAZ at 1.5 mm from the fusion boundary correspond to fine-grained HAZ with average grain size of about 5 μm. In the present high B-9Cr steel, however, the fine-grained microstructures were not formed at a distance of 1.5 mm from the fusion boundary. In this region, the grain size of the base metal was retained and small grains were formed only on the prior-austenite grain boundaries (Figure 4(b)). The grain boundary length per unit area was 82.9 mm^{-1} and KAM was 1.94 for Figure 4(b). At a distance of 0.5 mm from the fusion boundary, recrystallization occurred and the grain size was more than several tens of micrometers (Figure 4(c)). The grain boundary length per unit area was 68.4 mm^{-1} and KAM was 2.22 for Figure 4(c).

Orientation distribution map	Orientation distribution map	Orientation distribution map
Grain boundary map	Grain boundary map	Grain boundary map
(a) Base metal	(b) HAZ at 1.5mm from fusion boundary	(c) HAZ at 0.5mm from fusion boundary
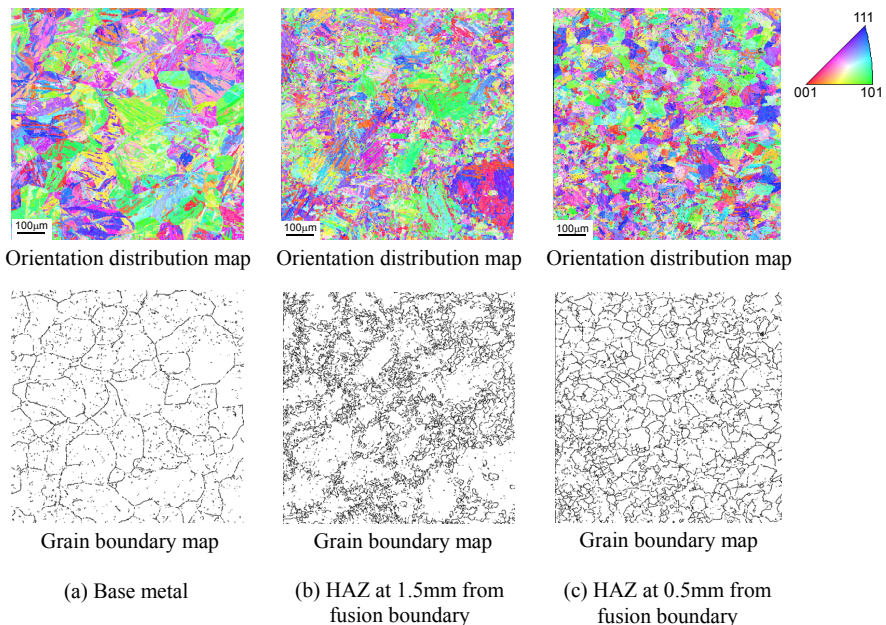
Figure 4 : Crystallographic orientation distribution maps for the normal direction and grain boundary maps (15-48˚) of the base metal and HAZ of the high B-9Cr steel in the dissimilar welded joint (MARBN10 steel-Alloy 263 weld).

In the conventional high Cr steel welds, Type-IV creep damages form in the fine-grained HAZ with average grain size of about 5 μm; consequently, the creep strength of welds decreases more than that of base metals [5, 6]. These results in Figure 4 confirm that the HAZ microstructures of high B-9Cr steel are considerably different from those of the conventional high Cr ferritic steels, and soluble free boron is essential in suppressing grain refinement during weld thermal cycle. We consider that the free boron decreases the grain boundary energies, and suppresses the nucleation of γ phase from the grain boundaries by diffusional transformation, causing the martensitic reverse transformation. Similar phenomena of the martensitic reverse transformation where the original grain size and crystal orientation were retained after heating up to A_{C3} transformation temperature have also been reported in the maraging steels [7] and 12Cr turbine rotor steels containing boron [8].

3.2. Creep test results of the similar welded joints

We have also conducted the creep tests of simulated HAZ and similar welded joints of high B-9Cr steels. The simulated HAZ specimens were produced using a weld simulator (Gleeble test machine) by heat treatment: rapid heating to a peak temperature of 950 ˚C followed by gas cooling. A similar welded joint of the high B-9Cr steel was also prepared using 9Cr filler wire. Figure 5 shows the creep rupture times of the base metal, simulated HAZ and similar welded joint of the present high B-9Cr steel (MARBN12 steel) at 650 ˚C. All of the base metal, simulated HAZ and similar welded joint of the high B-9Cr steel showed higher creep strength than those of the conventional 9Cr steel (Gr.92 steel). The similar welded joints of the high B-9 Cr steel fractured in the 9Cr weld metal, not in the HAZ (Type-IV). These results mean that the creep strength of the HAZ of the high B-9Cr steel was considerably improved; it is higher than that of the conventional 9Cr weld metal.
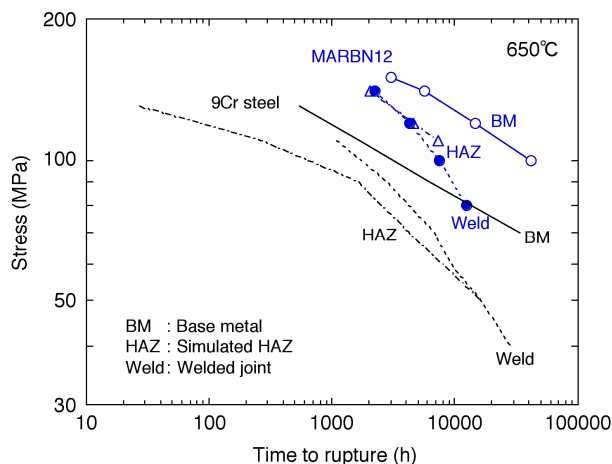
Figure 5: Creep rupture times of the base metal, simulated HAZ and similar welded joint using the 9Cr wire for the present high B-9Cr steel (MARBN12 steel) at 650 ˚C.

3.3. Creep strength of the dissimilar welded joints for A-USC

Figure 6 shows the relations between stress and creep rupture times of the base metals of high B-9Cr steels and four kinds of the present dissimilar welded joints at 650 ˚C. Open symbols show the rupture times of the base metals and solid symbols show those of the dissimilar welded joints. The creep strength of the base metal of the high B-9Cr steels was higher than that of the conventional 9Cr steel (Gr.92 steel) due to the grain boundary strengthening effect of boron. The creep strength of base metal of the MARBN12 steel with 0.007 % N was higher than that of the MARBN10 steel with 0.003 % N.

Creep rupture tests of the dissimilar welded joints were conducted at 650 ˚C for 160, 140, 120 and 100 MPa. The dissimilar welded joints using the high B-9Cr steels showed creep rupture times 5-10 times longer than that of the Gr.92 steel welded joint at 100 MPa. The differences of the creep strength between dissimilar welded joints and base metals are small up to 20000h at 650 ˚C, and we are now investigating the creep strength at lower stress conditions of 90 and 80 MPa.

The dissimilar welded joints fractured in the base metal of high B-9Cr steel under the higher stress conditions, and in the fusion boundary between high B-9Cr steel and Ni base weld metal (Inconel 82) under the lower stress conditions. None of the present dissimilar welded joints using high B-9Cr steels showed Type-IV failure in the HAZ, and their creep rupture lives were much longer than those of the conventional 9Cr steel welded joints that showed Type-IV failure at the present creep test conditions. This means that the microstructures and creep strength of the HAZ were considerably improved in the high B-9Cr steel, which
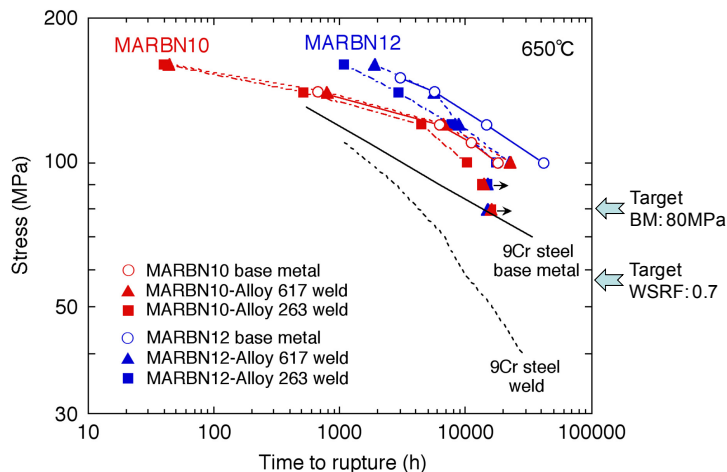
Figure 6: Creep rupture times of the base metals of the high B-9Cr steels and the dissimilar welded joints between high B-9Cr steels and Ni base alloys for A-USC boiler at 650 ˚C.

106

contains 0.01 % boron and low nitrogen (<0.01 %), due to the effect of soluble boron. The grain boundary strengthening of boron is effective not only in the base metal but also in the HAZ of welded joints.

We have investigated the microstructures and creep damages in the creep ruptured dissimilar welded joints. Figure 7 shows the specimen (MARBN12 steel-Alloy 617 weld) that ruptured at 650 ˚C and 140 MPa for 5619h, and its microstructures and creep damages in the HAZ. It was observed that a creep crack formed and propagated along the fusion boundary at the bottom surface of the U-groove, and then plastic collapse occurred in the high B-9Cr steel. In the HAZ at about 1.5 mm from the fusion boundary, a small number of creep voids were observed, as shown in Figure 7. This area corresponds to Figure 4(b) where the grain size of the base metal was retained and small grains formed only on the prior-austenite grain boundaries. Creep voids in the HAZ of high B-9Cr steel were observed on the prior-austenite grain boundaries with large grain size. It is considered that the void coalescence and crack formation, which causes Type-IV failure, are suppressed and, consequently, the life of welded joints is improved in these HAZ microstructures of high B-9Cr steel compared with the fine-grained HAZ microstructures of conventional high Cr steels.
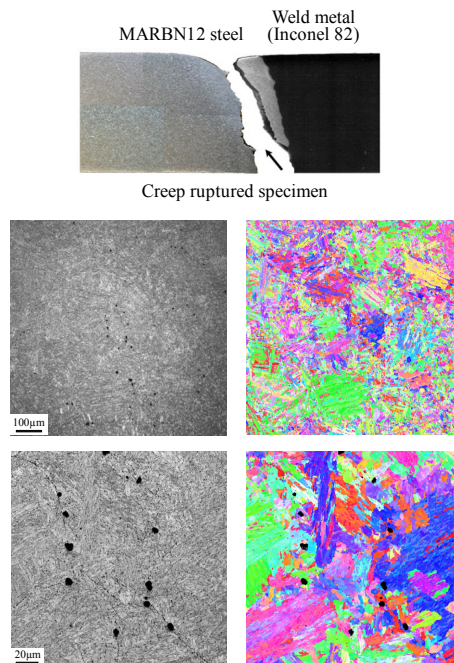
Figure 7: Dissimilar welded specimen (MARBN12 steel-Alloy 617 weld) ruptured at 650 ˚C and 140 MPa for 5619h, and its microstructures and creep damages in the HAZ.

3.4. Damage analysis of the dissimilar welded joint

We have also conducted the creep damage analysis for the present dissimilar welded joint. The following equations were used [9, 10].

$$\varepsilon = \varepsilon_e + \varepsilon_p + \varepsilon_t + \varepsilon_c \tag{1}$$

$$\varepsilon_t = \beta\Delta T \tag{2}$$

$$\frac{d\varepsilon_c}{dt} = \frac{3}{2} A \left[\frac{\sigma_{eq}}{1-\omega}\right]^n \frac{S_{ij}}{\sigma_{eq}} t^m \tag{3}$$

$$\frac{d\omega}{dt} = \frac{M\left[\alpha\sigma_1 + (1-\alpha)\sigma_{eq}\right]^{\chi}}{(1+\phi)\,(1-\omega)^{\phi}} t^m \tag{4}$$

where β is the coefficient of thermal expansion, σ_1 is the maximum principal stress, σ_{eq} is the equivalent stress, ω is the damage variable, and A, n, m, M, ϕ and χ are the material constants for creep. α is the parameter that describes material behaviour in a multiaxial stress state. These material constants were decided to fit the experimental uniaxial creep curves of the base metal and the simulated HAZ of high B-9Cr steel and Alloy 617 at 650˚C. Since the creep data of weld metal, Inconel 82, was not obtained, it was substituted by that of Alloy 617.
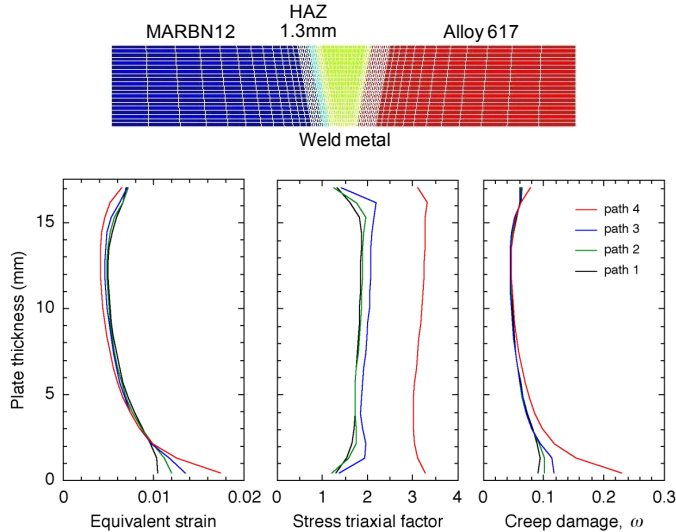
Figure 8: Variations in equivalent strain, stress triaxial factor and creep damage along the path in the HAZ of the dissimilar welded joint (MARBN12 steel-Alloy617 weld) after 10000h creep at 650˚C and 100MPa.
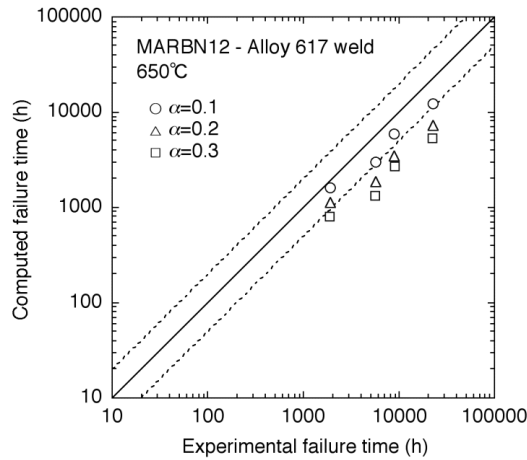
Figure 9: Comparison of the computed rupture times and experimental rupture times of the present dissimilar welded joint.

We have investigated the creep damage distribution using the three-dimensional finite-element (FE) model of the dissimilar welded joint. Figure 8 shows the variations in equivalent strain, stress triaxial factor (*TF*) and creep damage (*ω*) in the HAZ of the high B-9Cr steel along the plate thickness direction of the dissimilar welded joint (MARBN12 steel-Alloy617 weld) after 10000h creep at 650°C and 100MPa. Creep damage was higher near the fusion boundary at the bottom surface of the U-groove due to the mechanical constraint effect of Ni base weld metal. Computed failure times, when creep damage of one element reaches 1.0, also correspond well to the experimental rupture times as shown in Figure 9. These computed results confirm that the experimental results of failure location and creep rupture times of the dissimilar welded joints were reasonable.

4. Conclusions

In the present paper, creep tests of the dissimilar welded joints between high B-9Cr steels and Ni base alloys, which will be used in the 700 °C class pulverized coal power system (A-USC), were conducted. The results can be summarized as follows:

1) For the high B-9Cr steels, fine-grained microstructures observed in the conventional high Cr steels were not formed in the HAZ. Free soluble boron on the grain boundaries is considered to decrease the grain boundary energy and change the mechanisms of the α-γ transformation during the weld thermal cycle.

2) The creep rupture lives of the present dissimilar welded joints between high B-9Cr steels and Ni base alloys were 5-10 times longer than those of the conventional 9Cr steel welded joints at 650 °C.

3) The failure location of dissimilar welded joints was the base metal or fusion boundary. A small number of creep voids were observed in the HAZ with large grain size; however, Type-IV failure did not occur after about 20000 h at 650°C. The grain boundary strengthening effect of boron is useful not only in the base metal but also in the HAZ for high B-9Cr steel.

4) The computed results using the damage mechanics equations confirm that the experimental results of failure location and creep rupture times of the present dissimilar welded joints were reasonable.

Acknowledgment

References

[1]   M. Fukuda, Advanced USC power generation technology., *Journal of the Japan Society of Mechanical Engineers*, Vol. 114, pp.244-247, (2011) (in Japanese).

[2]   M. Tabuchi, M. Kondo, H. Hongo, T. Watanabe, F. Yin and F. Abe, Improvement of creep properties of high Cr steel weldment by boron addition., *Journal of the Society of Materials Science Japan*, Vol. 54, pp.162-167, (2005) (in Japanese).

[3]   S.K. Albert, M. Kondo, M. Tabuchi, F. Yin, K. Sawada and F. Abe, Improving the creep properties of 9Cr-3W-3Co-NbV steels and their weld joints by the addition of boron., *Metallurgical and Materials Transactions A*, Vol. 36A, pp.333-343, (2005).

[4]   F. Abe, M. Tabuchi, S. Tsukamoto and T. Shirane, Microstructure evolution in HAZ and suppression of Type IV fracture in advanced ferritic power plant steels., *International Journal of Pressure Vessels and Piping*, Vol. 87, pp. 598-604, (2010).

[5]   H. Hongo, M. Tabuchi an T. Watanabe, Type IV creep damage behavior in Gr.91 steel welded joints., *Metallurgical and Materials Transactions A*, Vol. 43A, pp.1163-1173, (2012).

[6]   M. Tabuchi and H. Hongo, Evaluation of long-term creep damage in high Cr ferritic steel welds., *Materials at High Temperatures*, Vol. 28, pp.172-180, (2011).

[7]   T. Maki, H. Morimoto and I. Tamura, Recrystallization of the austenite transformed reversely and structure of martensite in 18Ni maraging steel., *Tetsu-To-Hagane*, Vol.65, pp.1598-1606, (1979) (in Japanese).

[8]   T. Azuma, K. Miki, Y. Tanaka and T. Ishiguro, Effect of B on the behavior of austenite formation and recrystallization in high Cr ferritic heat resistant steel., *Tetsu-To-Hagane*, Vol.86, pp.667-673, (2000) (in Japanese).

[9]   T.H. Hyde, W. Sun, and A.A. Becker, Creep crack growth in welds: a damage mechanics approach to predicting initiation and growth of circumferential cracks., *International Journal of Pressure Vessels and Piping*, Vol. 78, pp.765-771, (2001).

[10] S.T. Tu, P. Segle and J.M. Gong, Creep damage and fracture of weldments at high temperature., *International Journal of Pressure Vessels and Piping*, Vol. 81, pp.199-209, (2004).

MICROSTRUCTURAL CHANGES AND TYPE-IV DAMAGE EVOLUTIONS DURING CREEP IN HIGH CR FERRITIC STEEL WELDS

H. Hongo and M. Tabuchi

National Institute for Materials Science
(1-2-1 Sengen, Tsukuba, 305-0047 Japan – HONGO.Hiromichi@nims.go.jp)

Abstract

High Cr ferritic steels have been used in the 600˚C class ultra-super critical (USC) thermal power plants. More than a decade has passed from the application of high Cr steels to USC power plants in Japan, and the Type-IV creep damages in heat-affected zone (HAZ) of welded components are concerns. In the present study, microstructural changes and damage evolution behaviours in HAZ during creep were investigated for the ASME Gr.91 and Gr.122 steel weld joints. Creep voids formed at an early stage of life and coalesced to form a macro crack at 0.8 of life for the Gr.91 steel weld. On the other hand, for the high strengthened Gr.122 steel weld, a small amount of Type-IV creep voids formed at 0.5 of life, increased slightly until 0.9 of life and rapid crack growth occurred after that. Kernel average misorientation (KAM) and grain boundary length of fine-grained HAZ obtained by EBSD decreased and saturated till 0.2 of life in the Gr.91 steel weld, whereas they decreased after 0.5 of life in the Gr.122 steel weld. It was found that the recovery of dislocation structures in HAZ was completed at early stage of life for the Gr.91 steel weld, whereas it occurred after recrystallization at the later stage of life for the Gr.122 steel weld. These differences of microstructural changes was considered to relate to the differences of Type-IV creep damage behaviour; early initiation of creep voids at 0.2 of life in the Gr.91 steel weld and later damage evolution after 0.5 of life in the Gr.122 steel weld. From these results, remaining life assessment methods for high Cr steel welds were discussed.

Keywords: High Cr ferritic steel, Weld, Creep, Type-IV damage, Microstructural change

1. Introduction

In order to improve the efficiency of thermal power plant, the pressure and temperature conditions of steam have been continuously increased. In 1990s, the high Cr ferritic heat resisting steels were applied to the boiler components in 600 ˚C class ultra super critical (USC) thermal power plants in Japan. The base metals of these steels with tempered martensite structures have excellent high temperature strength; however, fine-grained structures without lath-martensite are formed in the heat-affected zone (HAZ) during weld thermal-cycle and the creep strength of welds decreases than the base metals. The Type-IV failure along the inter-critical and fine-grained HAZ of weld joints is caused through the nucleation and growth of creep voids and cracks during long-term services at elevated temperatures [1-8]. Recently, it was recommended to take the weld strength reduction factor (WSRF) into account for the high temperature design using high Cr steels [9, 10]. It is

important to understand the microstructural changes and damage evolutions in HAZ during creep for the remaining life assessment of weld components.

In the present paper, aiming to contribute to the remaining life assessment methods for high Cr steel welds, we have investigated the Type-IV creep damage evolutions and microstructural degradations through interrupting creep tests using the large-scale welded joint specimens. Remaining life assessment methods of high Cr steel welds were discussed based on the experimental results.

2. Experimental procedure

2.1. Materials and welding

The materials investigated are the Gr.91 steel (9Cr-1Mo-VNb steel) plate with a thickness of 25mm and the Gr.122 steel (11Cr-0.4Mo-2W-CuVNb steel) plate with a thickness of 30mm. Their chemical compositions are shown in Table 1. These plates were welded by gas tungsten arc (GTA) welding using a double U groove. The filler wires with matching compositions were used for GTA welding. Cross sectional view of the welded joints for the Gr. 91 and Gr. 122 steels are shown in Figure 1. After welding, a post-weld heat treatment (PWHT) was conducted at 745 ˚C for 60 min for the Gr.91 steel weld and for 75 min for the Gr.122 steel weld. The simulated fine-grained HAZ (f-HAZ) specimens were produced using a weld simulator (a Gleeble testing machine) by rapid heating to a peak temperature of 900 ˚C for the Gr.91 steel and 950 ˚C for the Gr.122 steel, respectively.

2.2. Creep tests

Creep tests of the base metal and simulated f-HAZ were conducted using smooth bar specimens and those of the welded joints were conducted using smooth plate type specimens

Table 1: Chemical compositions of material used (mass%).

	C	Si	Mn	P	S	Cu	Ni	Cr	W	Mo	V	Nb	Al	N	B
Gr. 91	0.10	0.25	0.43	0.006	0.002	0.012	0.06	8.87	-	0.93	0.19	0.07	0.014	0.060	-
Gr. 122	0.11	0.28	0.62	0.015	0.002	0.98	0.39	10.54	1.82	0.32	0.19	0.05	0.001	0.063	0.003

Gr. 91 welded joint   Gr. 122 welded joint
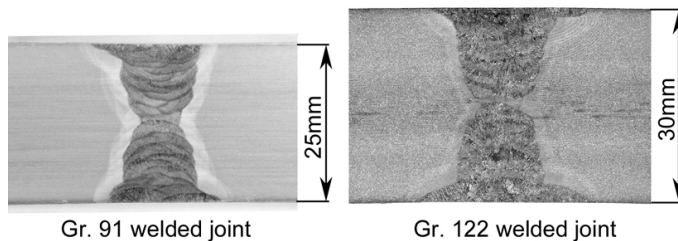
Figure 1: Cross sectional view of the welded joints for the Gr. 91 and Gr. 122 steels.

of 17.5×5 mm^2 in cross-section and 100 mm in gauge length (S-welded joint) at 550, 600 and 650 ˚C [7]. Creep interruption tests were conducted using a large-scale thick plate type specimen (L-welded joint) of 21×21 mm^2 in cross-section and 100 mm in gauge length for the Gr.91 steel weld, and of 24.5×24.5 mm^2 in cross-section and 120 mm in gauge length for the Gr.122 steel weld, which included the full original plate thickness close to the structural components [7, 8]. Creep test specimens for the simulated HAZ and L-welded joint of the Gr.122 steel are shown in Figure 2.

Creep tests were conducted using several L-welded joint specimens at 600 ˚C and interrupted at several time steps. Because creep voids formed inside the specimen, we cut the specimens in the centre of the specimen width after interruption of creep tests, and observed the Type-IV creep voids in HAZ using SEM or laser-microscope. The number and size of creep voids were measured using the image processing software. Changes of microstructures in fine-grained HAZ were investigated by measuring Kernel average misorientation (KAM) and grain boundary length using EBSD (Electron backscatter diffraction). KAM was measured as a parameter to evaluate dislocation density [11].
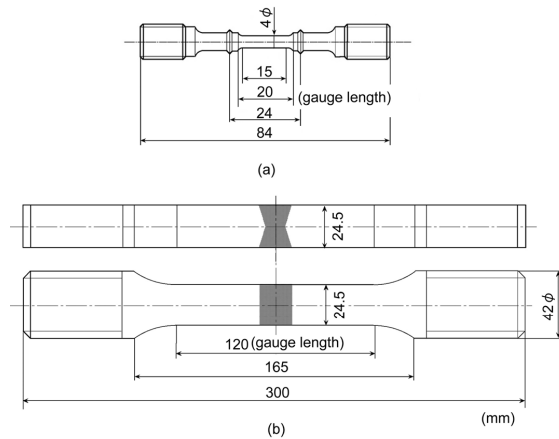
Figure 2: Creep test specimens for the (a) simulated HAZ and (b) welded joint of the Gr.122 steel.

3. Results and discussion

3.1. Creep strength of welded joints

Figure 3 and 4 shows the relations between stress and creep rupture times for the base metal, simulated f-HAZ and welded joints of the Gr.91 and Gr.122 steels, respectively. Figure 5 compares the creep rupture ductility (reduction of area) for the base metal and simulated f-HAZ of the Gr.91 and Gr.122 steels. The failure locations of the welded joint specimens are

indicated with the subscripts attached to the plots, where BM means failure in base metal, HAZ means Type-IV failure in the fine-grained HAZ and WM means failure in weld metal.

In the Gr.91 steel weld, the Type-IV failure occurred after 10,000h at 550 ˚C and 1,000h at 600 ˚C. The differences in creep rupture times between welded joint and base metal tended to widen with decreasing stress at all temperatures. The creep rupture times of the simulated f-HAZ were more than one order shorter than those of the base metal for the same stresses.
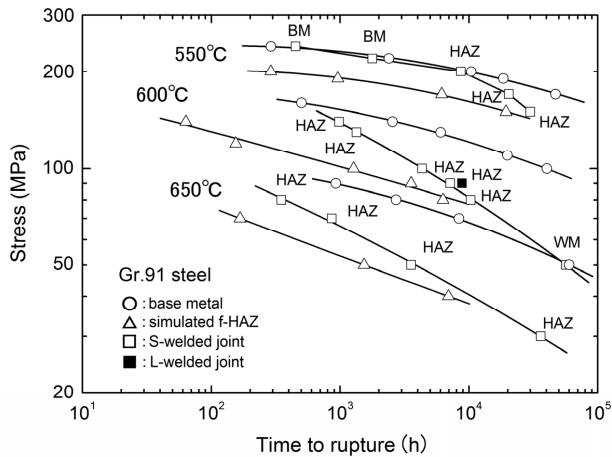
Figure 3: Creep rupture times of the base metal, simulated f-HAZ and welded joints of the Gr.91 steel.
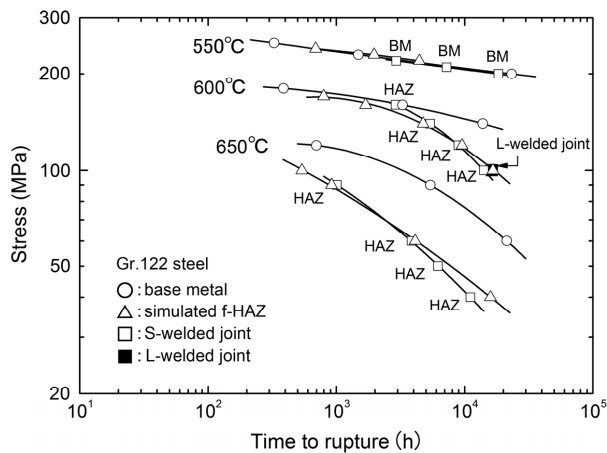
Figure 4: Creep rupture times of the base metal, simulated f-HAZ and welded joints of the Gr.122 steel.

114

For the Gr.122 steel welds, Type-IV failure did not occur at 550 ˚C within this test conditions (<20,000h). It occurred after 5,000 h at 600 ˚C. The creep rupture times of the simulated f-HAZ were nearly the same as the base metal at 550 ˚C within this test range; they decreased than the base metal after 5,000 h at 600 ˚C. The differences in creep rupture times between base metal and simulated f-HAZ were large at all test conditions for the Gr.91 steel, whereas they appeared at lower stress conditions than 140 MPa at 600 ˚C for the Gr.122 steel. At these test conditions, the simulated f-HAZ of the Gr.122 steel revealed void-type intergranular failure and its creep ductility decreased from 75% to 35% as shown in Figure 5.
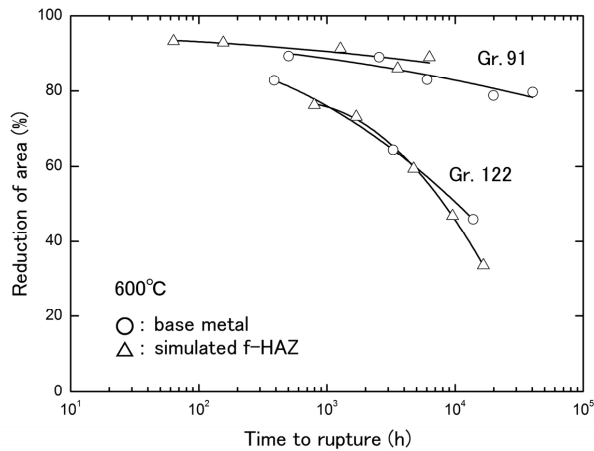
*Figure 5: Creep rupture ductility of the base metal and simulated f-HAZ
of the Gr.91 and Gr.122 steel.*

3.2. Evolution of Type-IV creep damage

Creep rupture times of the L-welded joints were 8,853 h at 600 ˚C and 90 MPa for the Gr.91 steel, and 16,340 h at 600 ˚C and 100 MPa for the Gr.122 steel; they also showed the Type-IV failure and their rupture times were slightly longer than the S-welded joints as shown in Figures. 3 and 4. We have conducted the creep interruption tests using the L-welded joints for both steels at these test conditions and investigated the processes of Type-IV damage and fracture. Figure 6 shows the binary images of creep voids and cracks observed in HAZ of the central cross-section of the L-welded joints of the Gr.91 steel creep-interrupted at 600 ˚C and 90 MPa. It was found that a small number of creep voids formed at about 0.2 of creep rupture life, and the number of voids increased with time, and then coalesced to form a crack at 0.8 of life. Creep voids and cracks were mostly observed in the area about 20% below the plate surfaces.

The area fraction of creep voids in the HAZ of the Gr.91 and Gr.122 steel welds are plotted against the life ratio (t/t_r) in Figure 7. In this figure, the area fraction of creep voids in the area about 20% below the plate surfaces, where the creep voids mostly formed, are plotted. It was
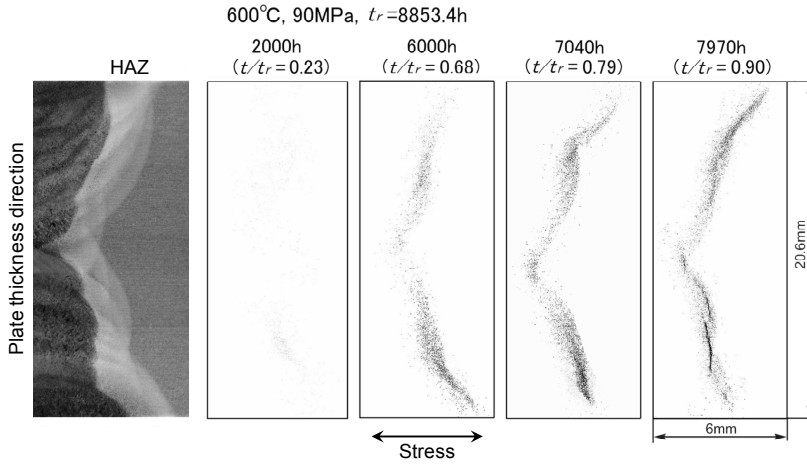
Figure 6: Binary images of creep voids and cracks observed in the HAZ of a central cross-section of the L-welded joints for the Gr.91 steel crept at 600 ˚C and 90 MPa.
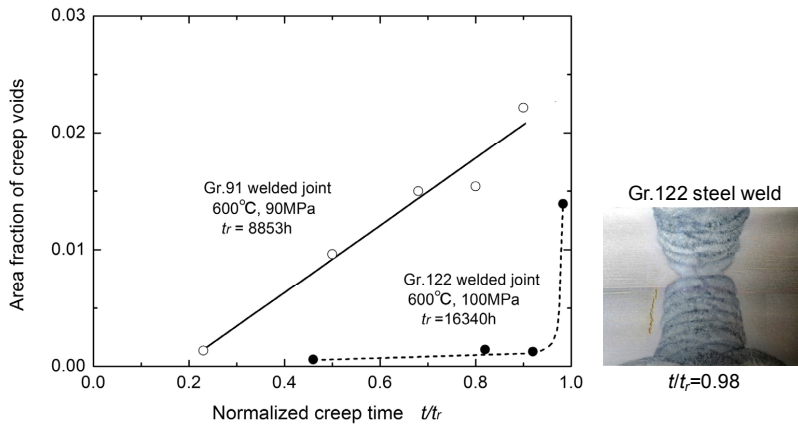
Figure 7: Changes of the area fraction of creep voids in HAZ during creep of the Gr.91 and Gr.122 steel welds at 600 ˚C.

found that the Type-IV damage behaviour and amounts of creep voids were considerably different for both steel welds. In the Gr.91 steel weld, Type-IV creep voids formed at the early stage 0.2 of creep life and increased gradually with elapse of time. On the other hand, in the Gr.122 steel weld, only a small amount of creep voids formed at 0.5 of creep life and slightly increased till 0.92 of life. Type-IV cracks did not form still at 0.92 of life; it was observed in the specimen interrupted at 0.98 of life as shown in the photo of Figure 7.

The formation and growth of creep voids were suppressed during steady-state condition; however, the crack growth rate in the accelerated stage was high for the high strengthened

Gr.122 steel. The lower creep ductility of the Gr.122 steel shown in Figure 5 is related to these damage behaviours.

3.3. Microstructural changes in HAZ

Changes of microstructures in HAZ of the creep-interrupted L-welded joints were observed using SEM, TEM and EBSD. Hardness measurement and microstructural observation were conducted on the cross-section about 30% below the plate surface. KAM and grain boundary length were calculated from the EBSD data. Figure 8 shows the changes in the grain boundary length in the fine-grained HAZ during creep for both steel welds. Here, length of grain boundaries with misorientation from 5° to 65° is plotted as prior austenitic boundaries. For the f-HAZ in the Gr.91 steel weld, the grain boundary length decreased till 0.2 of life and saturated after that. On the other hand, for the f-HAZ in the Gr.122 steel weld, the grain boundary length increased till 0.5 of life, and then decreased after that. The decrease of grain boundary length occurs due to the recovery of microstructures during creep.

Figure 9 shows the changes in the micro-hardness and KAM during creep in the fine-grained HAZ of both steel welds. Here, average value of KAM is plotted excluding the points whose misorientation is larger than 5° in order to investigate the changes of dislocation structures. For the fine-grained HAZ in the Gr.91 steel weld, hardness and KAM decreased till 0.2 of life and saturated to constant value. In the Gr.122 steel weld, however, they did not change till 0.5 of life and then decreased after that. The decrease of KAM and hardness occurs due to the recovery of dislocation structures. Because the grain boundary length increased without changing KAM and hardness till 0.5 of life, dynamic recrystallization was considered to be occurred in the fine-grained HAZ of the Gr.122 steel. Figure 10 compares the grain boundary structure before creep with that after creep for 0.46 of rupture time. It was observed that the gain refinement occurred after creep due to dynamic recrystallization.

These differences of microstructural changes are considered to relate to the differences of creep damage behaviour for these two steels. In the Gr.91 steel weld, the recovery of dislocation structures of fine-grained HAZ occurs at early stage of life, and then early initiation and evolution of Type-IV creep voids occur as shown in Figure 7. In the Gr.122 steel weld, the recovery of dislocation structures occurs after recrystallization of the fine-grained HAZ, and then damage evolution occurs at the later stage of life.

From these experimental results, we consider about the methods for the residual life assessment of welded components of high Cr steels as follows. For the Gr.91 steel weld, ultrasonic nondestructive testing is available for residual life assessment because creep voids and cracks increase gradually inside the plate thickness. Creep damage can be detected at 0.7 of life for the present Gr.91 steel weld using phased array ultrasonic testing [12]. Hardness measurement and microstructural observation are not available because their changes saturate in the early stage of life. Local necking on the specimen surface in HAZ is also available

because the creep ductility is high for the Gr.91 steel. For the Gr.122 steel weld, ultrasonic testing may be difficult to detect Type-IV creep damages because the amount of voids are small and crack grows rapidly after 0.9 of life. Evaluation of hardness and dislocation structures (KAM) is considered to be available because they change in the latter half of life. Local necking on the specimen surface was scarcely observed for the Gr.122 steel weld with low creep ductility. Since changes in hardness and dislocation density during creep might be smaller at the plate surfaces than that inside the plate thickness with creep damages, further attention would be necessary.
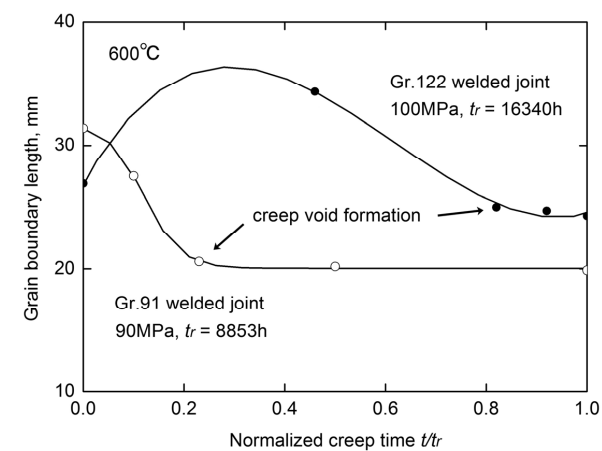
Figure 8: Changes in the grain boundary length in the fine-grained HAZ during creep for the Gr.91 and Gr.122 steel welds measured by EBSD.
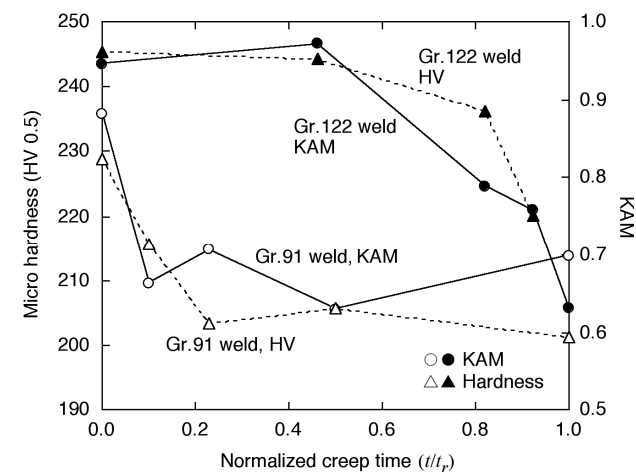
Figure 9: Changes in the micro hardness and KAM in the fine-grained HAZ during creep for the Gr.91 and Gr.122 steel welds measured by EBSD.

118

(a) before creep   (b) $t/t_r = 0.46$
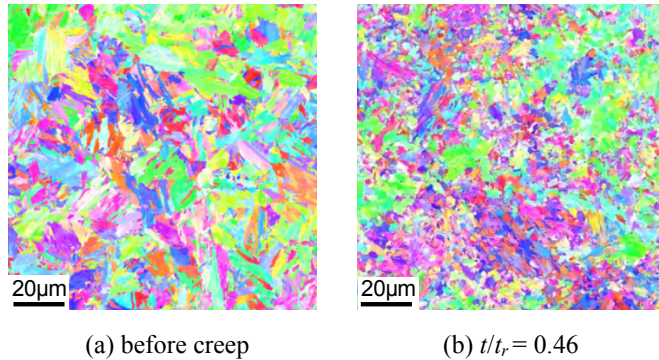
Figure 10: Grain boundary structures (a) before creep and (b) after creep for 0.46 of rupture time for the HAZ of Gr.122 steel welds.
Dynamic recrystallization was observed in Figure 10(b).

4. Conclusions

In the present paper, creep strength, Type-IV damage evolution and microstructural change during creep in the Gr.91 and Gr.122 steel welds were investigated quantitatively using the large-scale welded joint specimens. The results are summarized as follows:

1) In the Gr.91 steel weld, the Type-IV failure occurred after 10,000h at 550 ˚C and 1,000h at 600 ˚C. In the Gr.122 steel weld, Type-IV failure did not occur at 550 ˚C within this test range (<20,000h); it occurred after 5,000 h at 600 ˚C.

2) Type-IV creep voids in the Gr.91 steel weld formed at the early stage 0.2 of creep life, increased with elapse of time, and then coalesced to form a macro crack after 0.8 of life.

3) In the Gr.122 steel weld, a small number of Type-IV creep voids formed at 0.5 of life, increased slightly till 0.9 of life, and then rapid crack growth occurred after that. The area fraction of creep voids in the Gr.122 steel weld was much smaller than that in the Gr.91 steel weld.

4) In the Gr.91 steel weld, the recovery of dislocation structures of fine-grained HAZ occurred at early stage 0.2 of life, and was followed by early initiation and evolution of Type-IV creep voids. In the Gr.122 steel weld, the recovery of dislocation structures occurred after recrystallization of fine-grained HAZ, and then damage evolution occurred at the later stage of life.

5) From the above experimental results, for the Gr.91 steel weld; it is considered that ultrasonic nondestructive testing etc. is available for the residual life assessment because creep voids and cracks increase gradually inside the plate thickness. Hardness measurement and microstructural observation of fine-grained HAZ are not available because their changes saturate in the early stage of life.

6) For the Gr.122 steel weld, ultrasonic testing is considered to be difficult to detect Type-IV creep damages because the amount of voids are small and crack grows rapidly after 0.9 of life. Evaluation of hardness and dislocation structures (KAM) is considered to be available for the residual life assessment because they change after 0.5 of life.

Acknowledgment

References

[1] G. Eggeler, A. Ramteke, M. Coleman, B. Chew, G. Peter, A. Burblies, J. Hald, C. Jefferey, J. Rantala, M. deWitte and R. Mohrmann, Analysis of creep in a welded P91 pressure vessel., *International Journal of Pressure Vessels and Piping*, Vol. 60, pp.237-257, (1994).

[2] J.A. Francis, W. Mazur, H.K.D.H. Bhadeshia, Review-Type IV cracking in ferritic power plant steels., *Materials Science and Technology*, Vol. 22, pp.1387-1395, (2006).

[3] F. Masuyama, Creep degradation in welds of Mod.9Cr-1Mo steel., *International Journal of Pressure Vessels and Piping*, Vol. 83, pp.819-825, (2006).

[4] Y. Hasegawa, T. Muraki, M. Ohgami, Identification and formation mechanism of a deformation process determining microstructure of Type-IV creep damage of the advanced high Cr containing ferritic heat resistant Steel., *Tetsu-to Hagane*, Vol. 92, pp.609-617, (2006) (in Japanese).

[5] K. Kubushiro, S. Takahashi and K. Morishima, Degradation of microstructures during creep in high Cr steel weldment., *Journal of the Society of Materials Science, Japan*, Vol. 59, pp.840-845, (2010) (in Japanese).

[6] T. Ogata, T. Sakai and M. Yaguchi, Damage assessment method of P91 steel welded tube under internal pressure creep based on void growth simulation., *International Journal of Pressure Vessels and Piping*, Vol. 87, pp.611-616, (2010).

[7] H. Hongo, M. Tabuchi and T. Watanabe, Type IV creep damage behaviour in Gr.91 steel welded joints., *Metallurgical and Materials Transactions A*, Vol. 43A, pp.1163-1173, (2012).

[8] M. Tabuchi and H. Hongo, Evaluation of long-term creep damage in high Cr ferritic steel welds., *Materials at High Temperatures*, Vol. 28, pp.172-180, (2011).

[9] M. Tabuchi and Y. Takahashi, Evaluation of creep strength reduction factors for welded joints of modified 9Cr-1Mo steel., *Transactions of the ASME*, *Journal of Pressure Vessel Technology*, Vol. 134, pp.031401-1-6, (2012).

[10] Y. Takahashi and M. Tabuchi, Evaluation of creep strength reduction factors for welded joints of Grade 122 steel., *Transactions of the ASME*, *Journal of Pressure Vessel Technology*, Vol.133, pp.021401-1-5, (2011).

[11] K. Fujiyama, K. Mori, D. Kaneko, H. Kimachi, T. Saito, R. Ishii and T. Hino, Creep damage assessment of 10Cr-1Mo-1W-VNbN steel forging through EBSD observation, *International Journal of Pressure Vessels and Piping*, Vol. 86, pp. 570-577 (2009).

[12] Y. Takahashi, H. Fukutomi and N. Miura, Creep strength of welded joints of high-chromium steel and damage detection by ultrasonic testing, Proc. M&M2008, The Japan Society of Mechanical Engineers, OS1306, (2008).

STRESS RELAXATION MODELLING BY USING CREEP DATA

G. Angella[a], D. Della Torre[a], R. Donnini[a], M. Maldini[a,1], D. Ripamonti[a],
F. Pero[b], E. Poggio[b], A. Riva[b,2], A. Sanguineti[b]

[a] Institute for Energetics and Interphases (IENI) - CNR, Via R. Cozzi 53, 20125 Milan, Italy
[b] Ansaldo Energia S.p.A, Corso Perrone 118, 16161 Genoa, Italy

[1] maldini@ieni.cnr.it
[2] andrea.riva@aen.ansaldo.it

Abstract

Bolts in gas turbine units are often subjected to severe work conditions at high service temperatures, for which the relaxation of the initial stress, generated by the tightening couples, can become significant. Besides, since in such conditions re-tightening operations become necessary, the stress trend must be accurately calculated and predicted in order to avoid inappropriate value before every maintenance interval of the turbine.

A constitutive equation based on the Continuum Damage Mechanics (CDM) formalism, describing the creep and stress relaxation behaviour of a martensitic steel, has been developed and evaluated. Creep tests were performed at 520°C with applied stresses producing a strain $\varepsilon = 1$ % in a time range of 1000-10000 h. The stress relaxation tests were performed at 520°C, with initial stress at 300 MPa corresponding to a strain in the range of 0.2 %. The specimens were reloaded several times in order to simulate the aforesaid service conditions of bolts. In this work it is proposed a set of equations, with parameters obtained by creep tests interpolation, able to accurately reproduce and well predict the experimental relaxation behaviour of the steel under investigation. The model, fitted on creep tests, includes a term accounting for the internal stress, entailing the capability to foresee the changes in stress relaxation during successive reloading of the same specimens (or, alternatively, during successive re-tightening of the same bolt).

The advantage of such approach (i.e. calculating relaxation data from creep tests) consists mainly in the possibility to perform evaluations and assessments even without stress relaxation data, which are more expensive to collect experimentally and rarer to find in literature.

Keywords: creep, stress relaxation, constitutive equation, gas turbine components, martensitic steel

1. Introduction

Most of the theoretical and practical studies on creep phenomena are often limited to analyze a few features of the creep curves as functions of the test parameters: usually the minimum strain rate, the time to achieve a determined strain level ($\varepsilon = 1$ % for instance), the time to rupture and the strain at failure. High temperature components are usually designed on the basis of these parameters: however such design procedures results in being very conservative. This is because most of such design approaches cannot properly predict the stress redistribution that occurs on the components during the operational conditions because of creep deformation mechanisms. In order to avoid over-conservative design, but at the same time ensuring the proper safety and reliability of the components, it would be more useful to take into account constitutive equations able to describe the evolution of creep strain as a

function of time, for a given set of test conditions. Furthermore, these equations are requested to be able to predict stresses beyond the experimentally investigated ones, and accurately describe the behavior of the material subjected to complex experimental conditions, like non-constant stresses and temperatures along time, as it occurs in operating components.

By a practical point of view the parameters of these equations developed for creep tests, relatively inexpensive and easy to perform, can be suitable to predict also the stress relaxation behaviour, omitting to carry out an high number of expensive and difficult stress relaxation tests.

In this work a constitutive equation is proposed, based on the Continuum Damage Mechanics (CDM) formalism, able to well interpolate the experimental creep curves of a martensitic steel for bolts in gas turbine units. The proposed equation can predict correctly also the behavior of the considered steel during stress relaxation. Furthermore, the possibility to describe satisfactorily also the stress relaxation during subsequent reloading on the same material is showed, thus simulating the usual bolts re-tightening during maintenance. A careful calculation of its value is indeed necessary to avoid inappropriate operations for the following maintenance intervals.

2. Experimental

Creep tests at constant stress have been carried out at 520°C with stress values between 150 and 300 MPa on cylindrical specimens having 5.6 mm gauge diameter and 28.0 mm gauge length. The elongation has been continuously monitored using two capacitive transducers connected, outside the furnace, to extensometers clamped to the ridges delimiting the specimen gauge length. After assembling the specimens on creep instrumentation, they have been partially loaded at room temperature and at the test temperature to calculate the Young modulus of the material and to verify the assembly of the test and the absence of applied bending on the specimen. Before the actual start of the test, the specimens have been maintained at least an hour at the test temperature. This temperature and its gradient along the specimen length have been continuously monitored by three R-type thermocouples applied along the gauge length of the specimen.

In this paper all strains are true strains, defined by $\varepsilon = ln(1+\Delta l/l_o)$ with $\Delta l = l - l_o$, where l_o and Δl are the initial length and the elongation of the specimen gauge length during creep, respectively. The creep tests have been generally interrupted when a strain of 1 % has been achieved. Stress relaxation tests have been carried out on specimens with the same geometry as that for the creep tests at the temperature of 520°C, using an electromechanical servo-assisted test machine. The imposed strain $\varepsilon \sim 0.19$ %, corresponding to an initial stress of 300 MPa, have been achieved in 60 s. After a relaxation time of about 200 hours, the sample has been reloaded at 300 MPa, re-starting the stress relaxation stress on the same specimen. This procedure has been repeated several times.

The material considered for the experimental tests is a martensitic steel for bolts in turbines power plants.

3. Results

3.1 Experimental data

The experimental creep curves are showed in Figure 1, whilst the Norton plot, i.e. minimum creep rate vs. applied stress, is reported in Figure 2.

In Figure 3, a stress relaxation test consisting of two subsequent reloading after the first one is reported: the stress relaxation rate is very fast during the first loading on the as-received specimen and it is slower during the subsequent ones for the hardened material. Note that all three stress relaxation tests have been carried out with an initial stress of 300 MPa corresponding to an initial elastic strain of about 0.19%.
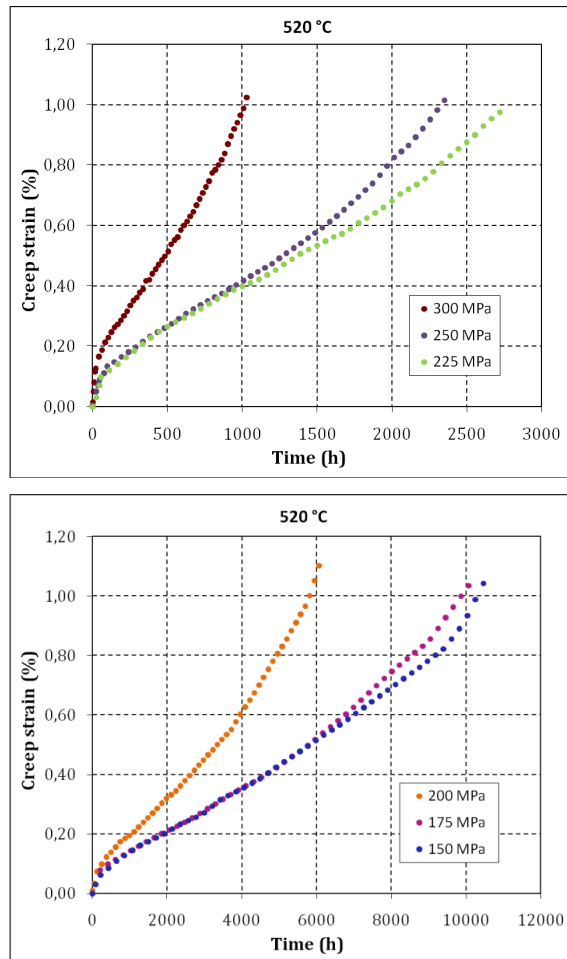
Figure 1: Creep tests carried out at 520°C for a) σ = 300, 250, 200 MPa and b) σ = 200, 175, 150 MPa.
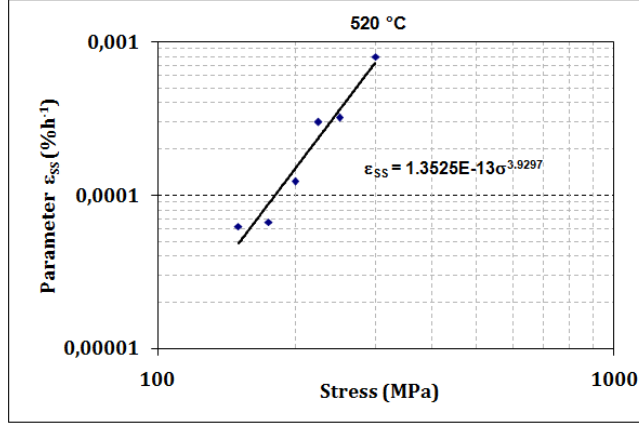
Figure 2: Experimental values for the minimum creep rates $\dot{\varepsilon}_{ss}$.
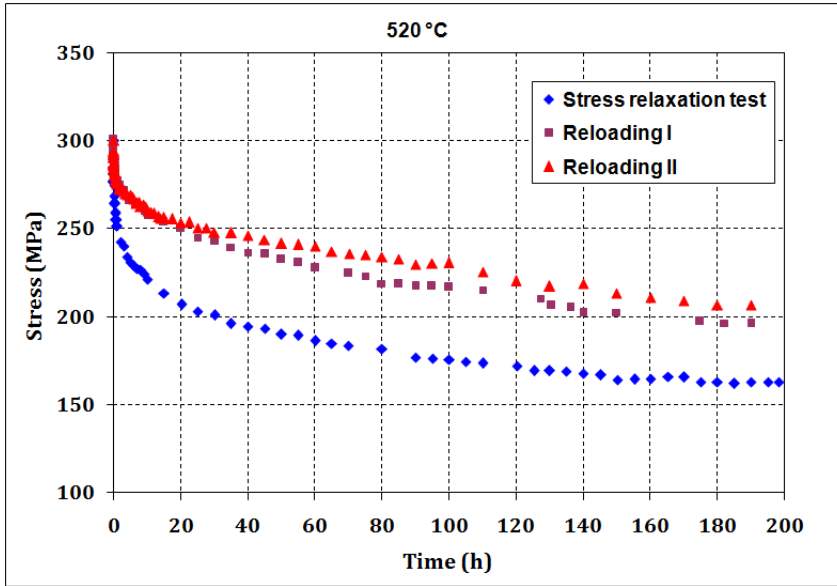
Figure 3: Stress relaxation test with two reloadings after the first loading carried out on the same specimen.

3.2 Modelling

In stress relaxation tests the imposed strain ε_0 is defined as:

$$\varepsilon_0 = \sigma(t)/E + \varepsilon_{pl} + \varepsilon_c(t) \tag{1}$$

with E the Young modulus, σ the applied stress, ε_{pl} the instantaneous plastic strain at the loading time (if the applied stress is lower than the elastic limit, then $\varepsilon_{pl} = 0$) and $\varepsilon_c(t)$ the time-dependent strain because of the creep mechanisms. Differentiating Eq.(1) with respect to time, it gives:

$$\dot{\sigma} = -E\dot{\varepsilon}_c \tag{2}$$

At the beginning of the test $\sigma = \sigma_0$ and $\varepsilon_c = 0$. Increasing t the activation of the creep mechanisms produces an increase of strain ($\dot{\varepsilon}_c > 0$) and so a decrease of the stress σ according to Eq.(2). Assuming that the constitutive equation of creep is the Norton's typical equation:

$$\dot{\varepsilon}_c = A\sigma_c^n \tag{3}$$

A and n are constants independent of stress on first approximation, whilst A depends on temperature. Substituting Eq.(3) in Eq.(2), after integration the following relationship is found [1]:

$$t = \frac{1}{EA(n-1)\sigma^{n-1}} \left(1 - \left(\frac{\sigma}{\sigma^\circ} \right)^{(n-1)} \right) \tag{4}$$

Eq.(4) represents the time needed for reaching a stress σ starting from an initial stress σ_0. In engineering applications Eq.(4) is also used to indicate the dependence of relaxed stress on an average strain rate, defined as the ratio of a fixed strain, $\varepsilon = 1\%$ for instance, to the time requested to achieve it, that is $t_{(\varepsilon=1\%)}$: the average rate will be $1\%/t_{(\varepsilon=1\%)}$. This average creep rates can be interpolated by Eq.(3), resulting in values of A and n different from those obtained by fitting the minimum creep rates of secondary creep stage. This leads to new (and less conservative) predictions of Eq.(4). In Figure 4 the experimental data from the stress relaxation test carried out on the as-received material are compared with the predictions calculated by Eq.(4) with the parameters A and n obtained from the minimum creep rates (Figure 2) and the average strain rates ($1\%/t_{(\varepsilon=1\%)}$ and $0.2\%/t_{(\varepsilon=0.2\%)}$).

In Figure 4 it is clear that the use of Eq.(4) leads to a no good prediction for the experimental stress relaxation rate, whatever strain rate is used in Eq.(3). Note that the average rate for strain $\varepsilon = 0.2\%$ well describes the beginning of the test, because it is more similar to the actual strain rate at low creep strains, namely during the primary stage of the creep curve. It is noteworthy that in stress relaxation tests, the initial elastic strain partly becomes, with time, plastic strain because of the creep processes. The accumulating plastic strains are small, having a value lower than the loaded elastic strain, that is $\varepsilon_c < \sigma_0/E$. Therefore, the operating creep mechanisms regard the primary stage, when the strain rate is significantly higher than both the minimum rate and the aforesaid average rates. A better modelling can be thus obtained by taking into account the actual creep curve during the primary regime of creep curves. Furthermore, the approach of Eq.(4) results insensitive to the reloading conditions on the same specimen (i.e. the simulation of a second relaxation curve after re-tightening will be identical to the first relaxation, which is not what happens experimentally, see Fig. 3).
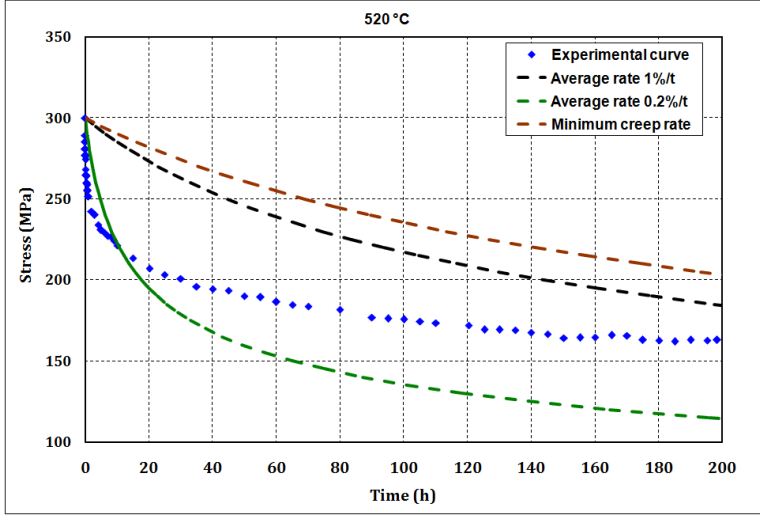
Figure 4: Comparison between the stress relaxation curve and the modelling by eq.(4) using the minimum creep rates, and the average strain rates (1%/t$_{(\varepsilon = 1\%)}$ and 0.2%/t$_{(\varepsilon = 0.2\%)}$).

In order to describe the primary stage for engineering alloys, the following differential equation system has been proposed [2]:

$$\begin{cases} \dot{\varepsilon}_c = \dot{\varepsilon}_i(1-s) \\ \dot{s} = H\dot{\varepsilon}_c - Rs \end{cases} \tag{5}$$

The first equation describes the creep strain rate $\dot{\varepsilon}_c$ as a function of the variable s, correlated to the occurrence of an internal stress in the material. The second one represents the evolution rate for s with time. Such variable is equal to zero at the test start, increasing up to a constant saturation value s_{ss} when the minimum creep rate is achieved. By interpolating the creep curves for different stresses and temperatures, the value of three parameters $\dot{\varepsilon}_i$, H and R are determined as functions of the test conditions, namely

$$\dot{\varepsilon}_i = \dot{\varepsilon}_i(\sigma,T)$$
$$H = H(\sigma,T) \tag{6}$$
$$R = R(\sigma,T)$$

Including these relationship into Eq.(5), the creep curves can be predicted for any stress and temperature condition. It is noteworthy that Eq.(5) and (6) can model tests with varying stress and/or temperature, through updating the parameters in Eq.(6) to the new values of stress and temperature.

Interpolating creep curves with Eq.(5) to obtain the aforesaid three parameters can be complicated. However, such difficulties can be easily overcome by considering the analytical solution of Eq.(5):

$$\varepsilon_c = \varepsilon_P \left[1 - exp(-rt) \right] + \dot{\varepsilon}_{SS} t \tag{7}$$

ε_P, r and $\dot{\varepsilon}_{SS}$ are functions of the parameters of Eq.(5):

$$\varepsilon_P = \frac{\left(H \dot{\varepsilon}_i^2 \right)}{\left(H \dot{\varepsilon}_i + R \right)^2} \qquad \text{dimension of the primary stage of the creep curve}$$

$$r = \left(H \dot{\varepsilon}_i + R \right) \qquad \text{characteristic curvature radius of the primary stage of the creep curve} \tag{8}$$

$$\dot{\varepsilon}_{SS} = \frac{\left(R \dot{\varepsilon}_i \right)}{\left(H \dot{\varepsilon}_i + R \right)} \qquad \text{identifying the steady state of the creep curve}$$

ε_P, r and $\dot{\varepsilon}_{SS}$ can be determined from a single creep curve as reported in Figure 5.
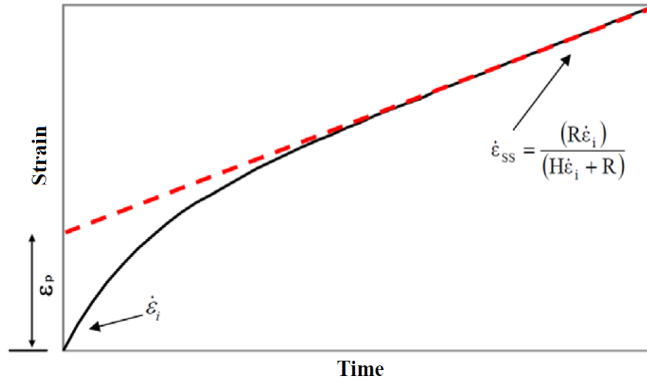
Figure 5: Typical creep curve with a decelerating primary stage followed by a secondary steady state: ε_P is the strain due to the primary stage, $\dot{\varepsilon}_i$ the initial strain rate and $\dot{\varepsilon}_{SS}$ the minimum creep rate (slope of the red broken line).

Note that Eq.(7) represents the typical primary stage describe by McVetty-Garofalo [3,4], whilst Eq.(5) and the analytical solution of Eq.(7) are equivalent. The first one is more suitable for finite elements calculations or to simulate test conditions at variable stress and/or temperature, e.g. tensile test or stress relaxation. The analytical solution can be useful to obtain the parameter values ε_P, r and $\dot{\varepsilon}_{SS}$ that interpolate the experimental creep curves, to calculate successively the parameters $\dot{\varepsilon}_i$, H and R by the following relationships:

$$\dot{\varepsilon}_i = \varepsilon_p r + \dot{\varepsilon}_{SS}$$

$$R = \frac{\dot{\varepsilon}_{SS} r}{\varepsilon_p r + \dot{\varepsilon}_{SS}}$$
$$\tag{9}$$

$$H = \frac{\varepsilon_p r^2}{\left(\varepsilon_p r + \dot{\varepsilon}_{SS}\right)^2}$$

3.3 Comparison between the experimental data and the proposed modelling

The interpolation of the creep curves by Eq.(7) allows to determine the dependence of parameters ε_p, r and $\dot{\varepsilon}_{ss}$ on the test conditions:

$$\varepsilon_p = \varepsilon_p(\sigma, T)$$

$$r = r(\sigma, T) \tag{10}$$

$$\dot{\varepsilon}_{SS} = \dot{\varepsilon}_{SS}(\sigma, T)$$

Since the plastic strain during the relaxation test is very small, only the first part of the creep curves has been interpolated, up to a strain of 0.4%, i.e. when the primary stage is finished and the strain rate can be considered constant. In this approach, the creep curves have not been interpolated with Eq.(7) through the ordinary least squares methods to have the best fit, but ε_p and $\dot{\varepsilon}_{ss}$ have been graphically obtained as showed in Figure 5, whilst r has been chosen in order to have the best interpolation. Figure 2 and Figure 6 show the parameter values obtained for the single creep curves. Through their interpolation versus σ, a power law for $\dot{\varepsilon}_{ss}$ and r, and a linear relationship for ε_p, have been found:

$$\varepsilon_p = 4.64 \cdot 10^{-4} \sigma - 1.77 \cdot 10^{-2}$$

$$r = 1.58 \cdot 10^{-11} \sigma^{-4.02} \tag{11}$$

$$\dot{\varepsilon}_{SS} = 1.35 \cdot 10^{-13} \sigma^{3.93}$$
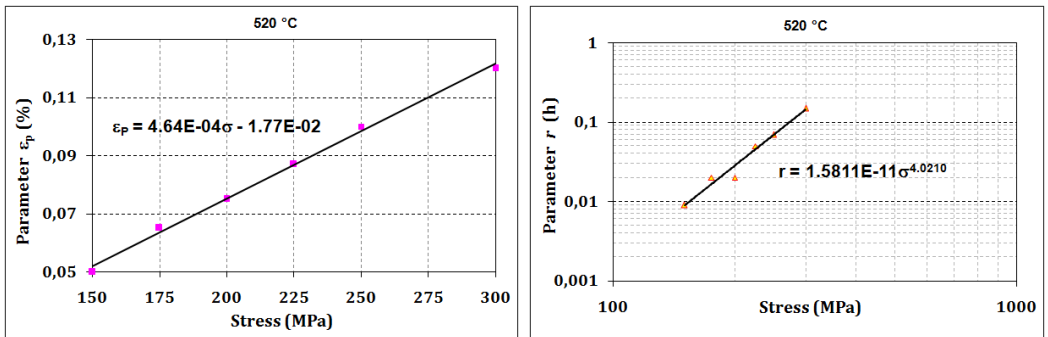
Figure 6: Experimental values for the parameters ε_p and r with their interpolation by Eq.(11).

In Figure 7 the primary stage of the experimental creep curves are compared with the curves predicted by Eq.(5), with parameters values calculated according to Eq.(11).
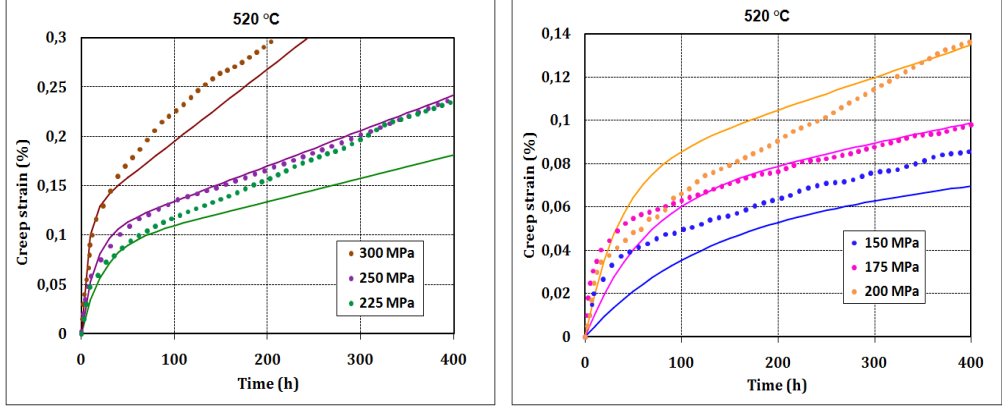
Figure 7: Experimental creep curves compared with Eqs.(5) and the parameters by Eqs.(11) (continuous outline curves), focused on the primary stage and the initial part of steady state.

The relationships in Eq.(11) are used to determine the dependence of the parameters $\dot{\varepsilon}_{SS}$, R and H on stress and temperature through Eqs. (9). To sum up, considering Eq.(2) and (5) in a single system as follows:

$$\begin{cases} \dot{\sigma} = -E\dot{\varepsilon}_c \\ \dot{\varepsilon}_c = \dot{\varepsilon}_i (1-s) \\ \dot{s} = H\dot{\varepsilon}_c - Rs \end{cases} \tag{12}$$

and using the relationships by Eq.(6) obtained from the creep curves, it is possible to predict the stress relaxation curves. The experimental stress relaxation tests are compared with the predictions by the numerical integrations of the Eq.(12) in Figure 8.

At the beginning of the first relaxation test, the parameter associated to the internal stress s is equal to zero, then it increases according to Eq.(12). In the subsequent reloading on the same specimen, since the material has been already subjected to stress relaxation, the initial s will be the value achieved at the end of the previous relaxation test. Note that the presented model describes experimental data more accurately than the procedures based on minimum/average creep test, being able to well describe the repeated stress relaxation.

129
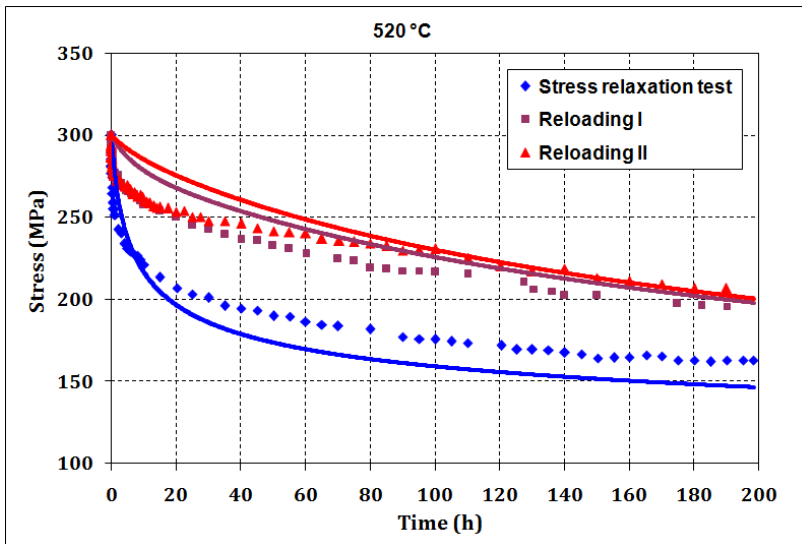
Figure 8: Experimental stress relaxation tests with two repeated strain reloadings: comparison with the proposed modelling (continuous outline curves).

3. Conclusion

The presented work aims at describing a modelling procedure for stress relaxation behavior. Unlike conventional methods, where the conventional minimum/average creep rates are used, the presented model takes into account the primary stage of the creep curves (since it concerns the strain levels typical of the relaxation phenomena) and an internal stress parameter (to account for the evolution of primary creep deformation in a scenario of multiple re-loadings). The model parameters as functions of stress σ and temperature T have been determined through interpolation of the creep curves by equations that can describe the aforesaid primary stage. Such parameters are used in the construction of the interpolation model for the stress relaxation test. The proposed method can predict the relaxation behavior significantly better than the conventional ones. Furthermore, the model can adequately describe repeated reloading on the same specimen, which cannot be done by the conventional models.

References

[1] R. K. Penny and D.L. Marriott, in *Design for creep*, McGraw-Hill, London, 1971.
[2] J. C. Ion, A. Barbosa, M.F. Ashby, B.F. Dyson and M. McLean, NPL report DMA A 115, Teddington, UK, April 1986.
[3] P.G. McVetty, Working stresses for high temperature service, *Mechanical Engineering*, Vol. 56, 1934, p. 149.
[4] F. Garofalo, in *Fundamentals of Creep and Creep-Rupture in Metals*, Macmillan, New York, 1965.

INFLUENCE OF AGEING PROCESS ON MICROSTRUCTURE AND MECHANICAL PROPERTIES OF 9%Cr CAST STEEL

Adam Zieliński[1], Grzegorz Golański[2], Anna Zielińska-Lipiec[3], Joanna Jasak[2], Cezary Kolan[2]

[1]Institute for Ferrous Metallurgy, K. Miarki 12-14, 44-100 Gliwice, Poland
[2]Institute of Materials Engineering, Czestochowa University of Technology,
Armii Krajowej 19, 42 – 200 Czestochowa, Poland
[3]Faculty of Metals Engineering and Industrial Computer Science,
University of Science and Technology, Mickiewicza 30, 30-059 Cracow, Poland

Abstract

The paper presents results of research on the influence of long term ageing at times up to 20 000 hours and the temperature of 600°C on the microstructure and mechanical properties of GX12CrMoVNbN91 (GP91) cast steel. A detailed microstructural research of the GP91 cast steel after ageing process was carried out with TEM and included: analysis of secondary phases morphology, changes in the dislocation substructure (dislocation density and mean diameter of subgrains). Whereas mechanical properties of the cast steel included a hardness test, static tensile test and impact energy measurements. In the microstructure of the GP91 cast steel after ageing, the processes of recovery and polygonization of matrix, and coagulation of $M_{23}C_6$ carbides were observed. Ageing of the investigated cast steel resulted in a slight decrease in the strength properties (YS, TS, HV30), which was accompanied by significant decrease in impact energy.

Key words: 9%Cr cast steel, ageing, microstructure, TEM, mechanical properties

1. Introduction

Environmental requirements connected with the EU directives on limiting the emission of CO_2, SO_2, NO_x into the atmosphere, as well as the economic requirements that aim for reducing fuel consumption and increasing the power efficiency, force the power industry to raise the thermal efficiency of power units. Increasing the thermal efficiency of power units (up to around 50% as a target) and limiting the emission is directly related to the application of high parameters of steam, the so-called supercritical parameters. Higher steam parameters require introducing new grades of steels and cast steels in the power industry, that have an increased resistance to creeping and oxidation at the temperature of ca. 600°C. The steels used so far did not fulfill the requirements set for high-temperature creep resisting materials [1, 2]. The new steels for power industry were developed as a result of modification in the chemical composition of the previously used creep-resisting steels. Thus, a number of new grades of high-chromium martensitic steels have been found, including: P/T91, P/T92, E911, VM12. Apart from the high-chromium martensitic steels, also new grades of cast steels are being introduced into the power industry. The new high-chromium martensitic cast steels have been developed to replace the so far used low alloy Cr–Mo or Cr–Mo–V cast steels. Martensitic cast steels are formed on the basis chemical composition of martensitic steels, for example, the GX12CrMoVNbN9-1 (GP91) cast steel is based on the chemical composition of X10CrMoVNbN9-1 (P/T91) steel, whilst the GX12CrMWVNbN10-1-1 (GX12) cast steel - on the chemical composition of E911 steel. The above cast steels are designed for work in the creeping conditions at the temperature not higher than 600ºC [3, 4].

The behaviour of high mechanical properties of martensitic cast steels during the service depends on the stability of their microstructure at elevated temperature. One of the methods of estimating the changes that run in the microstructure and in the morphology of precipitates, and their influence on the properties is performing long-term ageing at the temperature similar to the temperature of the expected service [3, 5-8]. Such simulation allows understanding the mechanisms of microstructure degradation in high-temperature creep resisting materials and is a highly significant issue when estimating and forecasting the time of safe operation of the appliances.

2. Material and methodology of research

The material for research was high-chromium GX12CrMoVNnN9-1 (GP91) cast steel of chemical composition presented in Table 1.

Table 1.Chemical composition of GX12CrMoVNbN9–1 (GP91) cast steel, %mass

C	Mn	Si	P	S	Cr	Mo	V	Nb	N
0.12	0.47	0.31	0.014	0.004	8.22	0.90	0.12	0.07	0.04

The research was carried out on the GP91 cast steel in the as-received condition (after heat treatment - 1040°C/12h/oil, 760°C/12h/air 750°C/8h/furnace) and after 20 000 hours of ageing at the temperature of 600°C. The influence of heat treatment on the microstructure and mechanical properties of GP91 cast steel is shown inter alia in [9]. The study of the microstructure was carried out using the transmission electron microscope JEOL JEM 200CX and TITAN 80-300 with the use of thin foils. The morphology of precipitates was determined by means of extraction carbon replicas and thin foils using the selective electron diffraction. The tests of mechanical properties included the following: static test of tension, impact strength tests performed on the standard Charpy „v" test pieces and measurement of hardness with the Vickers method with the microindenter load of 30 kG.

3. Microstructure and mechanical properties of GP91 cast steel in the as-received state

In the as-received state (after the heat treatment) the GP91 cast steel is characterized by a microstructure of lath tempered martensite with numerous precipitations.
In the microstructure, not only the retained lath substructure of martensite was observed, but also the areas of polygonized ferrite (Fig. 1). After the heat treatment, the dislocation density inside subgrains and the mean width of subgrains amounted to: 2.95×10^{14} m^{-2} and 0.708 μm, respectively [8].
The microstructure of the examined cast steel is a „typical" microstructure for the hardened and tempered creep resisting steels/cast steels containing 9-12% Cr [7, 10-12]. Performed identifications of carbide phases have shown two types of precipitates in the microstructure of GP91 cast steel in the as-received state: $M_{23}C_6$ carbides and precipitates of the MX type (Fig. 2).
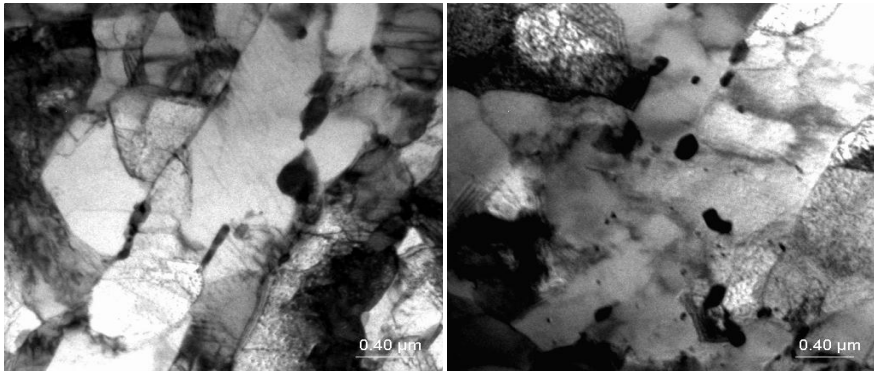
Fig. 1. Microstructure of GP91 cast steel in the as-received condition, TEM, thin foil

The $M_{23}C_6$ carbides of diverse morphology were mostly revealed on the boundaries of prior austenite grain and the boundaries of martensite laths. In the examined cast steel, two morphology types of the MX precipitates were observed: the spherical shaped ones, rich in niobium − NbC and lamellar precipitates, rich in vanadium − VX. The precipitates of the MX type were revealed mostly inside the laths of martensite on the dislocations and on the boundaries of subgrains. The vanadium-rich fine-dispersive secondary MX precipitates strengthen the examined cast steel (precipitation strengthening), however the role of the primary niobium-rich MX precipitates is actually limited to impeding the grain growth during austenitizing [13]. The MX precipitates are characterized by very high stability, they anchor the dislocations and impede their movement, at the same time providing high resistance to creeping. Whilst the $M_{23}C_6$ carbides stabilize the subgrain microstructure of martensite, impeding the movement of dislocation boundaries [11]. The mean diameters of $M_{23}C_6$ carbides and MX precipitates in the examined cast steel in the as-received condition amounted to: 127 nm and 19 nm, respectively[8].
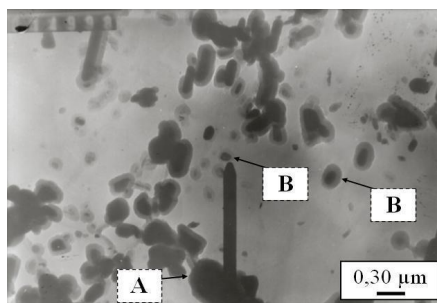
Fig.2. Morphology of precipitates in the GP91 cast steel in the as-received condition:
A) $M_{23}C_6$; B) MX; TEM, extraction carbon replica

Literature data [11, 12] also show that in the high-chromium steels/cast steels, the precipitations called „*V – wings*" can occur. They consist of a spherical NbX precipitate and

the lamellar nitride precipitates VX, nucleating on the NbX precipitate. In the examined cast steel, however, such a type of complex precipitations was not observed.

Mechanical properties of the investigated cast steel determined at room temperature and the minimum requirements [14] are shown in Table 2.

Table 2. Mechanical properties of GP91 cast steel in the as-received condition

YS, MPa	TS, MPa	El., %	KV, J	HV30
468	632	26	154	209
min. 450	*min. 600*	*min. 15*	*min. 30*	---

Mechanical properties of GP91 cast steel in the as-received state determined with the static test (yield strength – YS; tensile strength – TS, elongation – El.) fulfilled the minimum requirements for this grade of material. The examined cast steel was characterized by high fracture energy KV amounting to 154 J, similar to the ductility of other grades of steels/cast steels used in the power industry [5, 7, 10]. High fracture energy KV > 100 J of the examined cast steel in the as-received state is necessary, since as the literature data show, e.g.[15, 16], during long-term service of low alloy steels/cast steels at elevated temperature, the decreasing of impact strength KV runs faster compared to the mechanical properties. The fall of impact strength KV is accompanied by a shift of the nil ductility temperature (NDT) to a positive temperature.

4. Microstructure and mechanical properties of GP91 cast steel after ageing

An example of the microstructure of GP91 cast steel after 20 000 hours of ageing at the temperature of $600^{o}C$ is presented in Fig. 2.
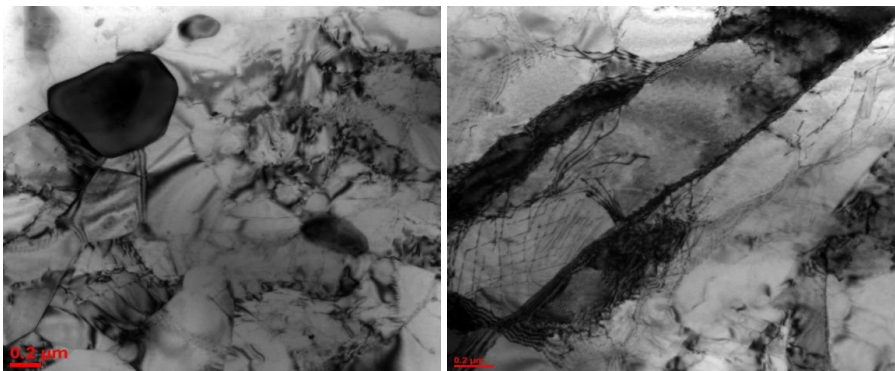
Fig. 2. Microstructure of GP91 cast steel after long-term ageing, TEM, thin foil

After 20 000 hours of ageing at the temperature of $600^{0}C$, the microstructure of the investigated cast steel was similar to the as-received condition, that is both were observed: the

retained lath substructure of tempered martensite with large density of dislocations, as well as the polygonized ferrite substructure. The microareas observed in the microstructure permeated one other.
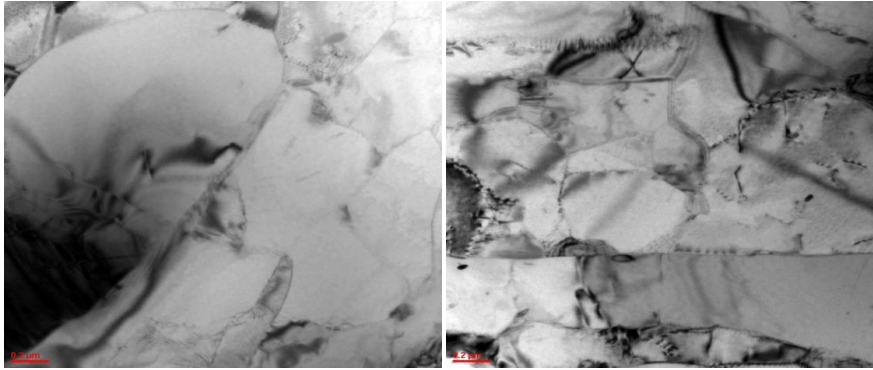
Fig. 3. Microstructure recovery in GP91 cast steel after ageing, TEM, thin foil

However, long-term ageing at the temperature of 600°C contributed to a gradual disappearance of lath microstructure of tempered martensite, as a result of the processes of recovery and polygonization of the matrix (Fig. 3). The effect of the above processes was the observed decrease in the dislocation density to the level of 2.36 10^{14} m^{-2} and growth of the subgrain width – 0.805 μm.

Performed identifications in the aged cast steel showed the occurrence of $M_{23}C_6$ and MX precipitates, as well as the precipitations of the intermetallic Laves phase (Fig. 4).
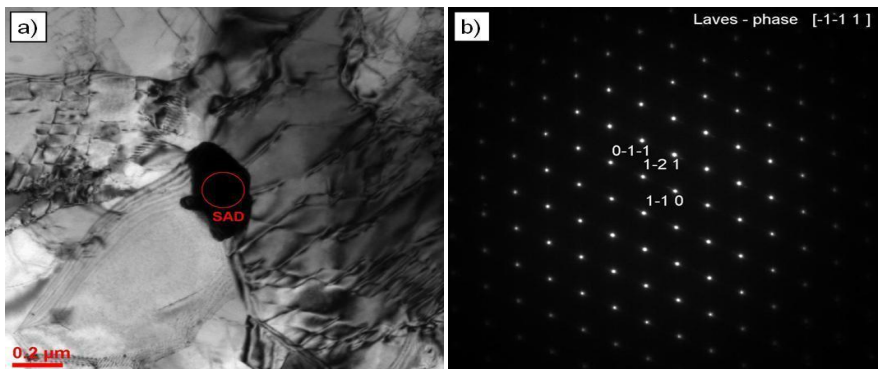
Fig. 4. Precipitation of the Laves phase in the cats steel after the ageing process (a), solved electron diffractogram of the Laves phase (b), TEM, thin foil

In the case of the $M_{23}C_6$ and MX precipitates, similarly as in the as-received state, they were respectively revealed: on the boundaries of grains/laths and inside the grains/laths. The precipitations of the Laves phase were mostly observed on the boundaries of grains, often

near the $M_{23}C_6$ carbides. The calculated mean diameter of $M_{23}C_6$ carbides and the Laves phase in the cast steel after ageing amounted to: 107 and 267 nm, respectively.

The amount of $M_{23}C_6$ carbides, with their size smaller than the average, amounted to 38% for the as-received state, and 80% of the whole population after ageing. Moreover, after ageing, the $M_{23}C_6$ carbides were seen several times as big, compared to the mean diameter (Fig. 2), which constituted around 12% of the population. In the Authors' view, this explicitly indicates that the process of coagulation of $M_{23}C_6$ carbides is running.

The influence of Laves phase on the microstructure and mechanical properties of high-chromium steels/cast steels is clearly negative. The precipitation and growth of Laves phase causes matrix depletion of substitution elements (chromium, molybdenum) as a result of their diffusion from the matrix to this phase, which leads to the quickening of the processes of recovery and polygonization of the matrix. At the same time, matrix depletion of alloy elements, which are also the components of $M_{23}C_6$ carbides, slows down the processes of coagulation of these carbides. Additionally, the Laves phase precipitating on the boundaries has a negative influence on the ductility of the investigated cast steel. According to studies [17], the precipitations of Laves phase with the mean diameter larger than 130 nm contribute to the change of the mechanism of cracking in the creep resisting steel, from the ductile to the brittle one (transcrystalline fissile). Moreover, they are the main cause for a rapid decrease in the creep resistance of the 9% Cr type steel.

Apart from the above-mentioned precipitates in the microstructure of the examined cast steel also single precipitates of NbCrN (Z phase) were revealed – Fig. 5. The mean diameter of these precipitates amounted to 61.43 nm. Precipitation of the Z phase in high-chromium steels/cast steels is connected with the transformation of metastable precipitates of the MX type into more thermodynamically stable precipitates of compound nitride. This causes a disappearance of the precipitation strengthening with MX type particles, which in martensitic steels containing at least 10% Cr results in a very rapid decrease in the creep strength and is the main mechanism of degradation of these steels, serviced at the temperature above 600°C [18]. In steels/cast steels containing on average 9% Cr, according to the literature data [18, 19], the precipitations of the Z phase were observed at the earliest after 10^5 h. The presence of single NbCrN precipitates in the microstructure of the examined cast steel should probably be associated with the microsegregation of chemical composition occurring in the cast steel, which can locally cause favourable conditions for the formation of his phase. Nevertheless, the revealed precipitations of Z phase in the GP91 cast steel after 20 000 hours of ageing require further research.

Performed research on the mechanical properties of GP91 cast steel, after the process of isothermal ageing at the temperature of 600°C, has shown that the properties determined for the examined material by means of the static test of tension and hardness HV30 practically did not decrease, or that the drop of a given parameter value did not exceed 5% (Fig. 6a-6c). Similar course of changes in mechanical properties of aged high-chromium steels was observed inter alia in the works [5, 7]. Similar strength properties – TS and YS, as well as hardness HV30 of the investigated cast steel in the as-received condition and after ageing, suggest that the observed process of softening of the matrix, as a result of the recovery and

polygonization processes, is partly compensated by other processes, such as the precipitation of secondary phases.
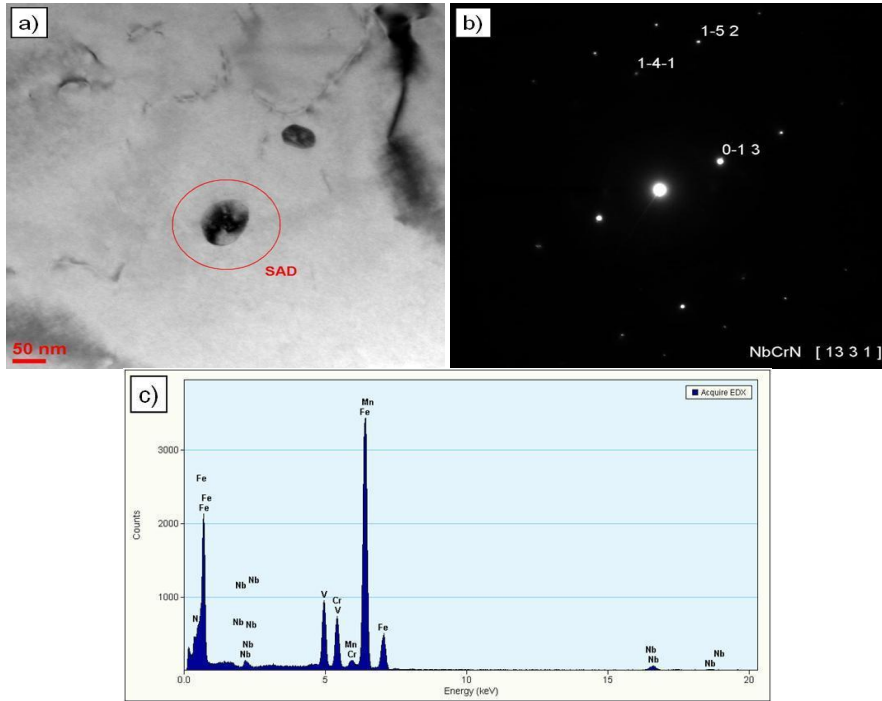
Fig. 5. Precipitations of NbCrN phase (Z phase) in the examined cast steel (a), solved electron diffractogram of Z phase (b), EDS spectrum from the analysed Z phase (c)
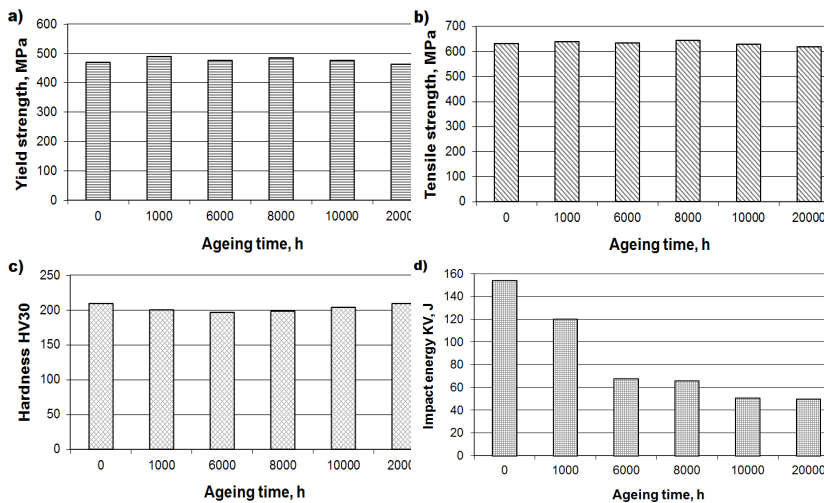
Fig. 6. Influence of the ageing time on mechanical properties of GP91 cast steel: a) YS; b) TS; c) HV30; d) KV

The fracture energy KV of the GP91 cast steel in the as-received state (after the heat treatment) amounted to 154 J (Table II), whilst after 20 000 hours of ageing at the temperature of 600°C, it decreased to the level of 50 J (Fig. 6d). This indicates around 70% reduction of crack resistance of the examined cast steel compared to the as-received state. The main reason for the reduction of the impact strength KV of the investigated cast steel should be seen not only in the precipitation and growth of Laves phase, as suggested by other researchers as well [9, 17, 20]. It should also be seen in the growth of the amount of $M_{23}C_6$ carbides precipitated on the boundaries of grains, forming the so-called „continuous grid of precipitates" in some areas (Fig. 7), and in the disappearance of lath microstructure of tempered martensite (Fig. 2, 3).
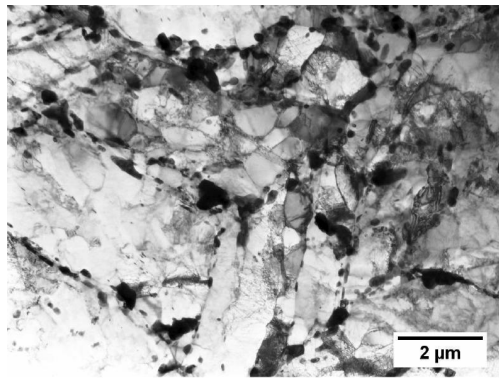
Fig. 7. Grid of $M_{23}C_6$ carbides on grain boundaries in the microstructure of GP91 cast steel after the ageing process [8]

Another possible cause influencing the decrease in ductility of the examined cast steel can be perceived in the segregation of atoms of additions, such as, for example, phosphorus to the grain boundaries or packet boundaries, which was not investigated in this study. However, the study results presented inter alia in [21] show that such a process is possible. The considerable decrease in impact strength KV of the examined cast steel is probably a resultant of the above processes running in the microstructure during ageing.

5. Conclusions

1. Long-term ageing of GP91 cast steel leads to a gradual disappearance of the lath microstructure of tempered martensite in favour of the more thermodynamically stable microstructure of polygonized ferrite. The ageing process also contributes to the precipitation of Laves phase. Moreover, in the microstructure of the examined cast steel, single precipitates of NbCrN phase were observed.
2. The process of long-term ageing has a little influence on the changes in strength properties (YS, TS) and hardness HV30, which shows that the process of matrix softening is partly compensated by the precipitation of secondary phases.

3.   A significant decrease in impact strength KV should be mostly associated with the precipitation of Laves phase on the boundaries of grains. Moreover, the impact strength decrease is also influenced by the precipitation of $M_{23}C_6$ carbides and the disappearance of lath microstructure of martensite. This indicates the need to aim for increasing the stability of precipitations of Laves phase and $M_{23}C_6$ carbides, and the subgrain microstructure of martensite.

6. Literature

[1]   R. Viswanathan, W. T. Bakker, Materials for Ultra Supercritical Coal Power Plants, Boilers Materials: Part 1, and Turbine Materials: Part 2, *J. Mater. Eng. Perfor.*, 10, 1, 81-100, (2001).

[2]   K. Hidaka, M. Shiga, S. Nakamura, Y. Fukui, N. Shimizu, R. Kaneko, Y. Watanabe, Development of 12Cr steel for 650ºC USC steam turbine rotors, *Materials for advanced power engineering*, Kluwer Academics Publishers, 309-316, (1994).

[3]   K. H. Mayer, H. Cerjak, P. Hofer, E. Letofsky, F. Schuster, Evolution of microstructure and properties of 10%Cr steel castings, Microstructural development and stability in high chromium ferritic power plant steels, Edited by A. Strang and D. J. Gooch *The Institute of Materials*, 105-122, (1997).

[4]   F. A. Schuster, R. Hanus, H. Cerjak, Foundry experience in large turbine casings and valve bodies made of steel castings P91 and G-X12CrMoWVNbN10–11, *IMechE* 11 – 20, (1996).

[5]   H.-S. Bong, S.-Ch. Cheng, Z.-D. Liu, S.-P. Tan, Aging precipitates and strengthening mechanism of T122 boiler steel, J. *Iron Steel Research Inter.*, 17(2), 67-73, (2010).

[6]   M. Tamura, K. Shinozuka, H. Esaka, S. Sugimoto, K. Ishizawa, K. Masamura, Mechanical properties of 8Cr-2WVta steel aged for 30 000 h, *J. Nucl. Mater*, 283-287, 667-671, (2000).

[7]   J. Dobrzański, A. Zieliński, M. Sroka, The influence of simultaneous impact of temperature and time on the properties and structure of X10CrWMoVNb9-2 steel, *J. Achiev. Mater. Manufact. Eng.*, 34/1. 7-14, (2009).

[8]   G. Golański, J. Kępa, The effect of ageing temperature on microstructure and mechanical properties of GX12CrMoVNbN9-1 (GP91) cast steel, *Arch. Metall. Mater.*, 57, 2, 575-582, (2012).

[9]   G. Golański, Mechanical properties of GX12CrMoVNbN9-1 (GP91) cast steel after different heat treatment, *Materials Science,* 48, 3, 384-391, (2012).

1.   V. T. Paul, S. Soroja, M. Vijayakshmi, Microstructural stability of modified 9Cr-1Mo steel during long term exposures at elevated temperatures*, J. Nucl. Mater*, 378, 273-281, (2008).

[10] P. J. Ennis, A. Zielińska – Lipiec, O. Wachter, A. Czyrska – Filemonowicz, Microstructural stability and creep rupture strength of martensitic steel P92 for advanced power plant, *Acta Mater.*, 45, 12, 4901-4907, (1997).

[11] A. Zielińska – Lipiec, T. Kozieł, A. Czyrska – Filemonowicz, Quantitative characterisation of the microstructure high chromium steel with boron for advanced steam power plants*, J. Achiev. Mater. Manufact. Eng., 43/1, 200-204, (2010).

[12] G. Golański, Evolution of Secondary Phases in GX12CrMoVNbN9-1 Cast Steel after Heat Treatment, *Arch. Mater. Sci. Eng*., 48/1, 12-18, (2011).

[13] ECCC Data Sheet 2005.

[14] A. Zieliński, J. Dobrzański, G. Golański, Estimation of the residual life of L17HMF cast steel elements after long-term service, *J. Achiev. Mater. Manufact. Eng., 34/2, 137-144, (2009).

[15] G. Golański, Microstructure and Mechanical Properties of G17CrMoV5-10 Cast Steel After Regenerative Heat Treatment. *J. Press. Vessel Techn*., 132, 6, 064503-1 – 064503-5, (2010).

[16] J. S. Lee, H. G. Armaki, K. Maruyama, T. Muraki, H. Asahi, Causes of breakdown of creep strength in 9Cr-1.8W-0.5Mo-VNb steel, *Mater. Sc. Eng. A,* 428, 270-275, (2006).

[17] H. K. Danielsen, J. Hald, Influence of Z-phase on long-term creep stability of martensitic 9 to 12% Cr steel *VGB PowerTech*, 5, 68-73, (2009).

[18] Kaibyshev R. O., Skorobogatykh V. N., Shchenkova I. A.: Formation of the Z-phase and prospects of martensitic steels with 11%Cr for operation above 590°C. *Metal Sci. and Heat Treatment*, 52, 90-99, (2010).

[19] P. Hu, W. Yan, W. Sha, W. Wang, Z.-L. Guo, V.-Y. Shan, K. Yang, Study on Laves phase in an advanced heat treatment heat-resistant steel, Front., *Mater., Sci. China*, 3(4), 434-441, (2009).

[20] M. Mackenbrock, H. J. Grabke, Grain boundary segregation and diffusion of phosphorus in 12Cr-Mo-V steel, *Mater. Sc. Techn*., 8, 6, 541-545, (1992).

IMPROVEMENT OF CREEP PROPERTIES OF MODIFIED 9CR-1MO STEEL WELDMENTS THROUGH A THERMO-MECHANICAL TREATMENT

Yukinori Yamamoto[1*], Sudarsanam Suresh Babu[2], Benjamin Shassere[2], Xinghua Yu[1]

[1] Materials Science and Technology Division, Oak Ridge National Laboratory, Oak Ridge, TN 37831, USA

[2] Department of Mechanical, Aerospace, and Biomedical Engineering, the University of Tennessee, Knoxville, TN 37996, USA

E-mail: yamamotoy@ornl.gov (*corresponding author)

Abstract

Cross-weld creep performance in Grade 91 (Modified 9Cr-1Mo, ASTM A387) steel weldments has successfully been improved through a thermo-mechanical treatment (TMT) process prior to welding. Aus-forging/-rolling combined with subsequent aus-aging were applied into the Grade 91 steel in order to promote precipitation kinetics of MX in the base metal which increased the creep resistance drastically. Such pre-existing MX precipitates are also expected to be stable during welding process at the FGHAZ and contribute to prevent degradation of creep resistance at the FGHAZ region. Dense carbide dispersion was observed in the optimized TMT sample, which effectively contributed to an improved cross-weld creep properties compared to that of the standard heat-treated sample, after post-weld heat treatment. The base metal also showed sufficient room-temperature toughness comparable to the standard heat-treated samples, indicating that the optimized TMT could be one of the solutions to minimize Type IV failure of the CSEF steels without sacrificing the balanced properties.

Keywords: Grade 91, thermo-mechanical treatment, weld, creep

1. Introduction

Creep strength-enhanced ferritic (CSEF) steels containing 9-12Cr are widely used as high temperature structural components, such as coal-fired boilers, heat-recovery steam generators, and piping systems in newly developed high-efficiency fossil power plants, because of their excellent creep properties at elevated temperatures as well as relatively inexpensive material costs [1,2]. However, there were numerous reports that the CSEF steel weldments exhibited unexpected, short creep-rupture lives compared to the base metals, which was due to the formation of non-equilibrium, weakened microstructure in fine grained heat affected zone (FGHAZ) [3-10]. Such premature failures of welded components at FGHAZ, so-called "Type-IV failures", could result in lowering the weld strength reduction factor (WSRF) of the materials as low as 40-50%, especially in the test/service conditions above 550 °C [11,12]. Therefore, minimizing or eliminating such weakened microstructure formation at FGHAZ would be the key to improve the performance of CSEF steels.

In late 1980's, it was reported that a Grade 91 steel (modified 9Cr-1Mo with V, Nb, and N, ASTM A387) applied relatively lower temperature pre-weld tempering (e.g. 621 °C) showed improved cross-weld creep properties after post weld heat treatment (PWHT) compared to that of the materials applied a standard pre-weld tempering (e.g. 760 °C) [13]. This result indicated a potential solution to minimize Type IV failure problem through non-standard pre-weld heat treatment. Present authors recently reported an *in-situ* high energy X-ray diffraction study of the HAZ simulating heat-treated Grade 91 samples [14,15], which revealed that the standard heat-treated sample (tempered at 760 °C) showed incomplete dissolution of $M_{23}C_6$ (M: mainly Cr) in the heating and cooling process simulating the FGHAZ region during welding. Coarsening of the residual $M_{23}C_6$ at the FGHAZ took place predominantly during PWHT, which caused reducing the creep strength significantly. On the other hand, the non-standard heat-treated sample (tempered at 650 °C) exhibited less $M_{23}C_6$ formation in the base metal which allowed complete dissolution of the $M_{23}C_6$ at the FGHAZ during welding, and then redistribution of fine $M_{23}C_6$ precipitates occurred during PWHT to increase the resistance of creep deformation. The improvement of cross-weld creep property of Grade 92 (9Cr-2W base) steels was also reported through the elimination of pre-weld tempering process, which resulted in re-distribution of $M_{23}C_6$ onto prior austenite grain boundaries and sub-boundaries after PWHT to maintain the creep resistance at FGHAZ similar to the base metal [16,17]. These results indicate that FGHAZ strengthening after PWHT is the key to improve the cross-weld creep properties of the CSEF steels.

Klueh et al. [18,19] reported a breakthrough concept for improving creep properties of 9-12Cr CSEF steels through a thermo-mechanical treatment (TMT) with aus-rolling combined with aus-aging. This process enhances the formation of the stable MX carbo-nitrides (M: mainly Nb and V) at austenitizing temperatures by applying hot-work (e.g. rolling or forging) to introduce dislocations which act as nucleation sites of the MX. The following aus-aging resulted in a dense MX precipitation before the austenite matrix transformed either to ferrite at high temperature or to martensite during cooling. The resulting material exhibited almost two to three orders of magnitude longer creep life at 650 °C and 138 MPa [18]. Since MX precipitates were stable and would not be dissolved into the matrix at FGHAZ during welding [14,15], the aus-forging/rolling + aus-aging could be worthwhile trying for a potential improvement of high temperature creep properties at the FGHAZ.

The objective of this study is to investigate the optimization of the TMT process onto the Grade 91 steel suitable for the improvement of the cross-weld creep properties via introduction of stable MX. It should be noted that the non-standard heat treatment described above also resulted in raising the ductile-brittle transition temperature (DBTT) of the base metal above room temperature (RT) [20, 21]. Therefore, the improvement of RT toughness of the base metal is also a major concern, and it has been attempted through a standard tempering applied after the TMT process.

2. Experimental Procedures

The chemistry of the Grade 91 steel used in the present study is shown in Table 1. Several small pieces (50-100 mm x 150-250 mm x 25 mm) were sectioned from a 25 mm-thickness hot-rolled plate prepared in the previous study [13]. Aus-forging/rolling and subsequent aus-aging were applied to the Grade 91 steel plates in various conditions to find an optimized, stable MX dispersion in a martensitic microstructure. The samples were heated to 1050°C and held for 1 h in Ar gas atmosphere, followed by air-cooling to an intermediate temperature in the range between 700 °C and 900 °C (just below or above the A_{e1} and A_{e3} at ~820 and 860 °C, respectively, and significantly higher than the M_s at ~400 °C). Once the intermediate temperature was achieved a 7-17% thickness reduction was applied by forging or rolling with only one action or pass. The plates were subsequently placed in a furnace for 1 h at the same temperature that the hot-working was performed, and then air-cooled to RT. The samples were then tempered at 760 °C for 2 h. Figure 1 shows the temperature profiles of the Grade 91 samples during the TMT at 700, 800, and 900 °C. Manual gas tungsten arc weld (GTAW) was applied to the TMT + tempered plates with or without the filler metal shown in Table 1, and then PWHT at 760 °C for 2 h was performed.

Table 1. Chemical compositions of the Grade 91 base metal and filler metal (balanced Fe).

(wt%)	C	Mn	Si	Cr	Mo	Ni	V	Nb	N	B
Base metal	0.08	0.27	0.11	8.61	0.89	0.09	0.21	0.07	0.06	<0.001
Filler metal	0.08	0.41	0.31	8.62	0.92	0.15	0.24	0.08	0.04	<0.001

Cross-sectional samples of as-TMT, TMT + tempered, and GTAW + PWHT samples were prepared by using a conventional metallographic sample preparation, and characterized by using a light optical microscope (OM). A carbon extraction replica technique was also used for the detailed characterization of the second-phase (MX) dispersion in selected as-TMT samples, and the high magnification observation was conducted by using a scanning electron microscope equipped with a scanning-transmission electron microscope (STEM) mode with an accelerate voltage of 30 kV.

Micro-Vickers hardness measurements were conducted on cross-sections of the GTAW + PWHT samples, using a 300g load and automated stage motion, measuring hardness in 50-100 μm steps on a traverse across the base metal, heat affected zone, and weld metal. Standard cross-weld tensile specimens with a cylindrical gauge section (ASTM E8, shown in Figure 2) were machined from the GTAW + PWHT samples, and then creep-rupture tested at 600 °C and 100 MPa in laboratory air. Charpy V-notch impact testing (ASTM E23) was conducted at room temperature on a standard size specimens (10 mm x 10 mm x 55 mm, with a 2 mm depth V-notch) machined from a TMT + tempered sample.
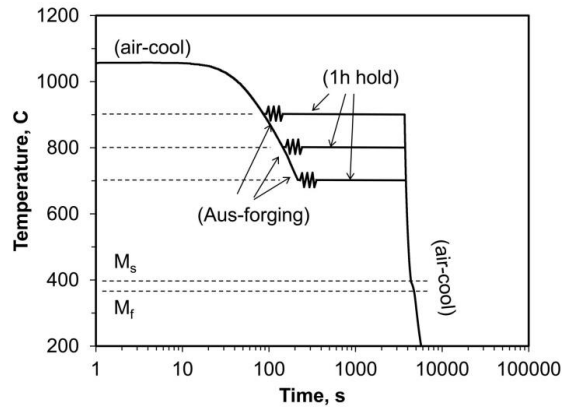
Figure 1: Temperature profiles of the thermo-mechanical heat treatments studied (after references 20 and 21).
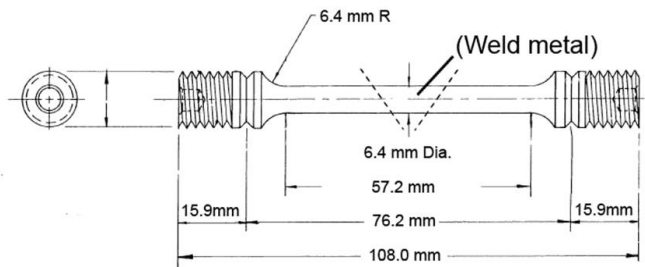
Figure 2. A drawing of tensile creep-rupture specimen used in this study.

3. Results and Discussion

3.1. Thermo-mechanical treatments

Figure 3 shows microstructure of as-TMT and TMT + tempered samples which were aus-forged with 7% thickness reduction and then aus-aged at 900, 800, and 700 °C for 1 h. Hereafter, they are called as "TMT9", "TMT8", and "TMT7", respectively, unless otherwise noticed. Martensitic microstructure was observed in the as-TMT9 and as-TMT8 samples (3a and 3b), and they were macroscopically very similar to each other. The microstructures after tempering (3d and 3e) exhibited a typical tempered martensite of Grade 91 steels. The detailed observation indicated that a small amount of ferrite grains formed in as-TMT8 sample. On the other hand, no martensite but ferrite + pearlite mixed microstructure was observed in as-TMT7 sample (3c) and no drastic changes after tempering (3f). These results indicate that in order to obtain martensitic microstructure the TMT process needs to be conducted above 800 °C, in the case of applying aus-aging for 1 h.
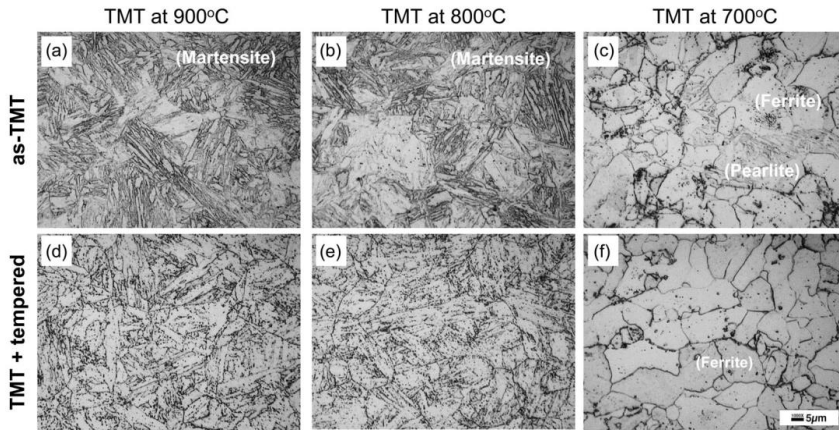
Figure 3. OM pictures showing microstructure of as-TMT (a-c) and TMT + tempered (d-f) samples; the aus-forged and aus-aged temperatures were at 900 °C(a,d), 800 °C (b,e), and 700 °C (c,f).

Figure 4 represents high-angle annular dark-field (HAADF) STEM images of the carbon extraction replicas taken from as-TMT9 (4a) and as-TMT8 (4b), showing the dispersions of nano-scale, high-Z element enriched second-phase particles, possibly MX, inside a martensite lath. It clearly shows that dense particles with the size of 1-3 nm disperse in as-TMT8 sample which looks very similar to the report by Klueh et al. [18,19], whereas relatively small number of the particles can be seen in as-TMT9 sample. This result indicates that the kinetics of MX formation during TMT process can be drawn as a C-curve with a nose close to 800 °C in a time-temperature-transformation (TTT) diagram, and 900 °C is close to the upper limit temperature to expect the MX formation after aus-aging.
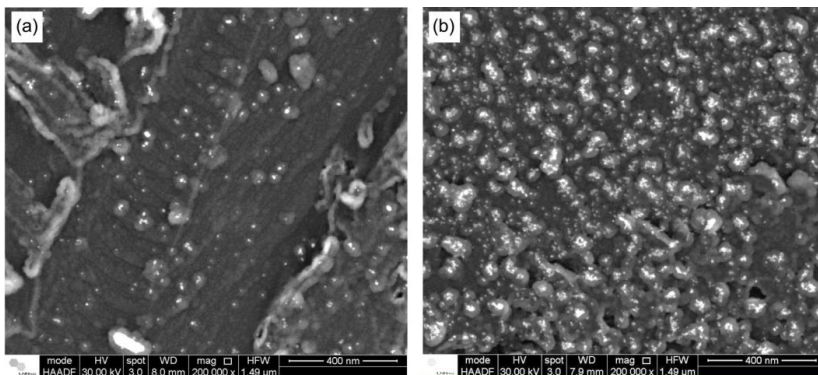
Figure 4. HAADF STEM images of carbon extraction replicas taken from the Grade 91 steel applied (a) TMT at 900 °C and (b) at 800 °C, showing precipitate dispersions inside martensite laths.

3.2. Gas tungsten arc weld

Figure 5 illustrates cross-sectional views of autogenous bead-on-plate GTAW plates applied a standard heat treatment (5a, normalized at 1050 °C and tempering at 760 °C [20,21]), TMT9 + tempering (5b), and TMT8 + tempering (5c) prior to the welding, together with the micro-Vickers hardness color maps super-imposed onto the corresponding measured areas. The cross-sectional microstructures consist of the weld metal, the heat affected zone, and the base metal, and there are no significant differences in the configurations among the samples. The standard heat-treated samples showed a distinct soft zone on the FGHAZ which corresponded to the area showing the coarse $M_{23}C_6$ formation [14]. Creep-rupture of the cross-welded specimens also took place typically in this area [20, 21]. The TMT9 + tempered sample also showed the same hardness distribution with a distinct soft zone on the FGHAZ, indicating that the TMT process at 900 °C was not beneficial to improve the mechanical properties at FGHAZ compared to the standard heat-treated sample. On the other hand, the TMT8 + tempered sample exhibited very high hardness in the base metal together with relatively low hardness reduction at the FGHAZ. This was presumably due to the dense MX formation lifting up the hardness of both the base metal and the FGHAZ. Previous study by the authors revealed that the RT hardness profile could reflect the high temperature creep resistances [21], so that improved creep properties would also be expected in the TMT8 + tempered sample.

3.3. Creep-rupture testing

Figure 6 shows pictures of the as-welded TMT + tempered plates (6a), and the machined tensile creep specimens after applying PWHT (6b). The TMT + tempered plates with 11mm-thickness were machined to make a bevel single U-shape groove, and then the groove was filled by multi-pass GTAW with a matching Grade 91 filler metal shown in Table 1. Leftover materials after the specimen machining were used for the microstructure characterization as well as hardness measurements of the multi-pass GTAW, which showed similar results to the Figure 5 [21].

Figure 7a represent the creep-rupture curves of both TMT + tempered samples after GTAW and PWHT, together with those of the standard and non-standard heat-treated samples [20, 21], tested at 600 °C and 100 MPa. The appearances of the creep-ruptured specimens of both TMT + tempered samples are also shown in Fig. 7b. The TMT8 + tempered sample showed significant improvement of the cross-weld creep properties with almost doubled creep-life compared to the standard heat-treated sample, and it was comparable to that of the non-standard heat-treated sample. The TMT9 + tempered sample, on the other hand, exhibited very little improvement compared to the standard heat-treated one. The creep-rupture of both TMT + tempered samples took place at FGHAZ as shown in Fig. 7b, indicating that the creep properties at FGHAZ dominated the creep deformation of these samples. It should be noted that the microstructure factors such as prior austenite grain size and average martensite block width did not show a significant difference between the standard heat-treated sample and the

146

TMT samples. Therefore, it is concluded that the improvement of the cross-weld creep properties is attributed to the formation of dense MX dispersion through the TMT process at 800 °C.
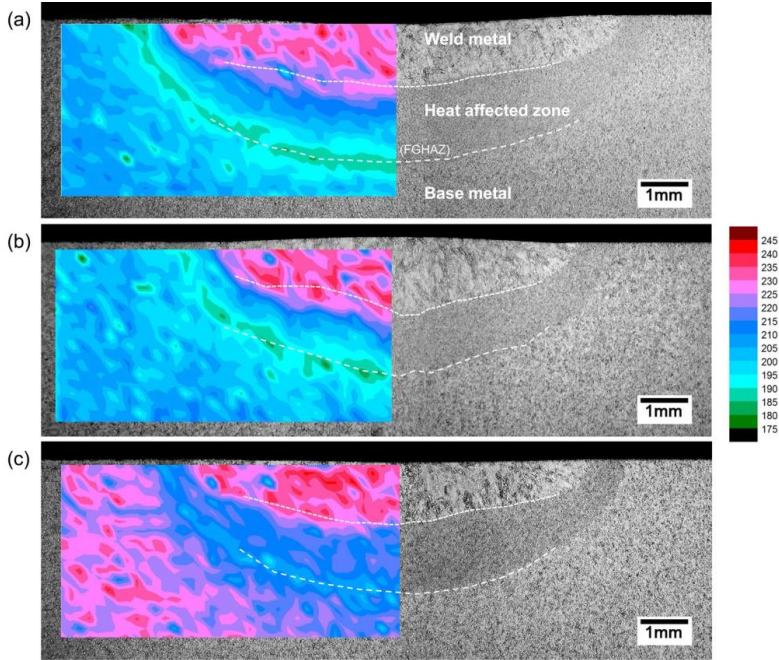
Figure 5. Cross sectional microstructure of the Grade 91 steel after (a) standard normalization and tempering, (b) TMT at 900 °C + tempering, or (c) TMT at 800 °C + tempering, followed by autogenous bead-on-plate GTAW + PWHT. The hardness color maps measured across the base metal, heat affected zone, and weld metal, were super-imposed on the corresponding areas (after references 20 and 21).
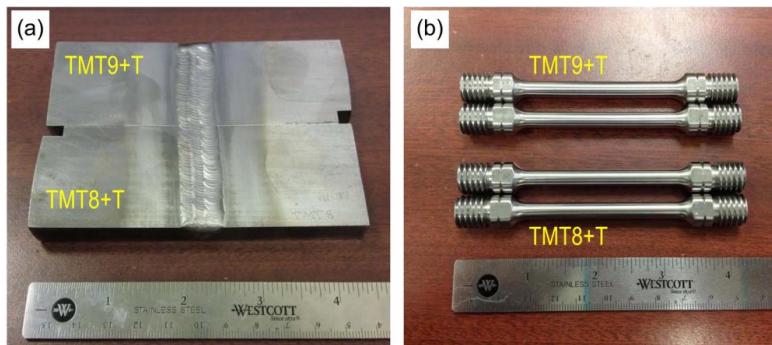
Figure 6. (a) Appearance of the TMT + tempered plates after GTAW on a single-V groove, and (b) the tensile creep specimens machined from the welded plates after applying PWHT.
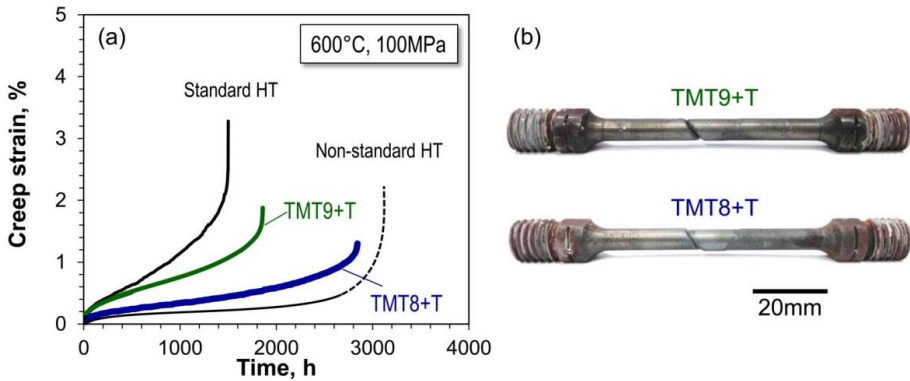
Figure 7. (a) Creep-rupture curves at 600 °C and 100 MPa of the Grade 91 steel applied thermo-mechanical treatments, together with those with standard and non-standard heat treatment (after references 20 and 21), and (b) appearance of the creep-ruptured specimens.

3.4. Room temperature toughness

The base metal of the TMT8 + tempered sample also showed improved RT toughness, as shown in Figure 8. The sample used in the Charpy impact test was aus-rolled at 800 °C with 17% thickness reduction, followed by aus-aged at 800°C for 1h. The average Charpy impact absorbed energy of the TMT8 + tempered sample was more than 150 J which was comparable to the standard heat-treated sample, and significantly higher than that of the non-standard heat-treated sample [20,21]. Therefore, the TMT process at 800 °C combined with a standard tempering can be described as an optimized TMT process to achieve improved cross-weld creep properties together with sufficient RT toughness of the base metal.
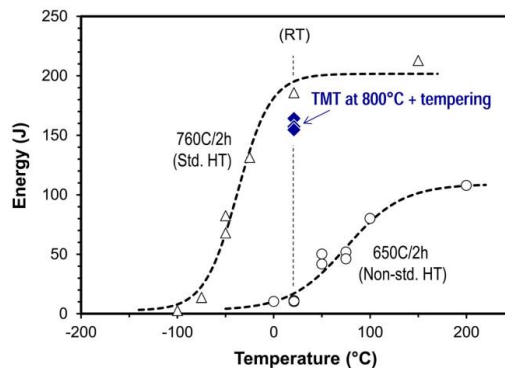
Figure 8. Charpy impact test results of the Grade 91 steel applied TMT at 800 °C + tempering, together with those of the standard and non-standard heat-treated samples (after references 20 and 21).

Preliminary hardness analysis of the TMT + tempered sample after GTAW + PWHT revealed that the higher thickness reduction (= higher amount of hot-working) during the TMT process resulted in increasing the hardness of both base metal and FGHAZ, indicating that the higher amount of MX formation could be expected in the sample. The detailed microstructure characterization of the TMT samples as a function of the thickness reduction during the TMT process is currently in progress, in order to find further optimized condition of the TMT process, and the results will be presented elsewhere.

4. Summary

Thermo-mechanical treatment of the Grade 91 (Modified 9Cr-1Mo, ASTM A387) steel has been studied in order to improve the cross-weld creep performance. Aus-forging/-rolling combined with subsequent aus-aging were applied to the Grade 91 steel which successfully promoted MX precipitation in the base metal when the process was conducted at 800 °C. Such pre-existing MX precipitates contributed to increase the resistance creep deformation at the FGHAZ region, resulting in improving the cross-weld creep properties compared to that of the standard heat-treated sample, after post-weld heat treatment. The base metal also showed sufficient room-temperature ductility comparable to the standard heat-treated samples. The optimized TMT process could be one of the solutions to minimize Type IV failure of the CSEF steels without sacrificing the balanced properties.

5. Acknowledgements

References

[1]   D. G. Cole, "Design of Heat-Resistant Steels for Small Power Plant," *Doctoral Dissertation*, University of Cambridge, UK (2000)

[2]   F. Abe, "Precipitate design for creep strengthening of 9% Cr tempered martensitic steel for ultra-supercritical power plants," *Science and Technology of Advanced Materials*, vol. 9, p. 013002 (2008).

[3]   I.A. Shibli, *OMMI*, 1 (2002) 1

[4]   J.F. Henry. *Combined Cycle Journal*, First Quarter (2005) 8

[5]   www.ommi.co.uk/etd/ETD-EPRI-%20P91%20Failures.pdf

[6]   F. J. Berte, *Combined Cycle Journal*, Second Quarter (2007) 52

[7]   J.A. Francis, W. Mazur, H. K. D. H. Bhadeshia, *Mater. Sci and Technol.* 22 (2006) 1387

[8]   F. Abe, M. Tabuchi, *Mater Sci and Technol.*, 9 (2004) 22

[9]   H. Hirata, K. Ogawa, *Weld. Int*, 19 (2005) 37

[10]   H. Hirata, K. Ogawa, *Weld. Int*, 19 (2005) 118

[11]   S.K. Albert, M. Matsui, T. Watanabe, H. Hongo, K. Kubo, M. Tabuchi, *Int. J. Press. Vessel. Pip.*, 80 (2003) 405

[12]   M. Yaguchi, T. Matsumura, K. Hoshino, *Proceedings of the ASME 2012 Pressure Vessels & Piping Conference, PVP 2012*, July 15-19, 2012, Ontario, Canada, ASME (2014), PVP2012-78393

[13]   C.R. Brinkman, V.K. Sikka, J.A. Horak, M.L. Santella, *ORNL/TM-10504* (1987)

[14]   Yu, X, "Multi-Scale Characterization of Heat-Affected Zone in Martensitic Steels", *Doctor of Philosophy Dissertation,* Columbus, Ohio: The Ohio State University (2012)

[15]   X. Yu, S.S. Babu, H. Terasaki, Y. Komizo, Y. Yamamoto, M.L. Santella, *Acta Mater.*, 61 (2013) 2194

[16]   Y. Liu, S. Tsukamoto, T. Shirane, F. Abe, *Met. Mat. Trans. A* 44 (2011) 4626

[17]   F. Abe, M. Tabuchi, S. Tsukamoto, *Materials at High Temperatures*, 28-2 (2011) 85

[18]   R.L. Klueh, N. Hashimoto, P.J. Maziasz, *Scripta Mater.*, 53 (2005) 275

[19]   R.L. Klueh, N. Hashimoto, P.J. Maziasz, *J. Nuc. Mater.*, 367-370 (2007) 48

[20]   Y. Yamamoto, M.L. Santella, X. Yu, S.S. Babu, *Proceedings of the 7th International Conference on Advances in Materials Technology for Fossil Power Plants* (Oct. 22-25, 2013, Waikoloa, HI), eds. D. Gandy and J. Shingledecker, ASM International, Materials Park, OH (2014) 1016

[21]   Y. Yamamoto, X. Yu, S.S. Babu, *Proceedings of the ASME Symposium on Elevated Temperature Application of Materials for Fossil, Nuclear, and Petrochemical Industries*, (March 25-27, 2014, Seattle, WA), ASME (2014), S2-1 ETS 2014-1009

THE STEAM OXIDATION AND CREEP BEHAVIOUR OF A FERRITIC-MARTENSITIC STEEL COATED WITH A SLURRY ALUMINIDE COATING

M. Seraffon, A. T. Fry, D. M. Laing

National Physical Laboratory, Teddington, Middlesex, TW11 0LW, UK

Abstract

Commercial, regulatory and social pressures have led the energy industry to seek improvements in power plant efficiency by increasing the combustion plant operating temperatures from 540 to 700 °C (European targets, 750 °C in the US) and steam pressures from 180 to 300 bar. These increased operating conditions place current conventional materials in extremely aggressive environmental conditions. Current ferritic-martensitic steels do not possess the high temperature corrosion resistance necessary for long term use, with a temperature limit of ~620 °C. Thus, aluminide coatings to protect against steam side oxidation have been developed for use on ferritic steels with encouraging results. These coatings combine good high temperature oxidation resistance through the growth of an Al_2O_3 scale and, in the case of Al slurry, the possibility to apply the coating on an industrial scale at moderate cost. Whilst there is information on the oxidation properties of the coating there is little information and understanding of the effect of aluminide coatings on the mechanical behaviour of the ferritic substrate. Main concerns lie with cracks developing in the coating and the possible penetration of cracks into the substrate, the loss of creep strength caused by the diffusion of Al into the substrate and the formation of AlN precipitates. The purpose therefore of the work reported here was to examine and generate the necessary data on the microstructural evolution of Al slurry coated P91 alloy subjected to oxidising atmosphere of 100% flowing steam at 650 °C for times up to 5000 hours at atmospheric pressure. These test pieces were then used to evaluate the creep properties of as coated and aged samples using creep stresses up to 120MPa. Results show that the coating prevented breakaway oxidation as expected, thereby showing its protective potential and the creep results showed that whilst the coated samples entered the tertiary creep zone earlier than the uncoated ones, cracking and creep of the coating remained confined to the surface of the specimen and that the ultimate creep rupture time remained within the accepted experimental scatter for this alloy. Examples of the creep data, microstructure and damage mechanisms are presented.

Keywords: steam oxidation, creep, T91, aluminide, slurry, coating

1. Introduction

The power generation industry is facing the challenge to follow strict regulations to reduce its environmental impact whilst meeting the increasing demand for power, plant reliability, availability and maintainability. Improving power plant efficiency by increasing operating temperatures (by up to 50 °C) is a way to achieve this goal. In facilities using steam turbines, higher steam temperatures significantly influence the performance of materials used for boiler components by accelerating the oxidation rate and degrading the mechanical properties. Current ferritic-martensitic steels have a temperature limit of ~620 °C [1]. The development of high temperature creep resistant alloys has resulted in a lowering the Cr content in these alloys which has led to unacceptable high rates of oxidation and spalling [2]. These thick oxide scales on tube walls cause overheating while exfoliation and spallation reduces the steam flow because of blockages and the erosion of components located down-stream [3]. Plans to reach steam operating temperatures of 650 to 760 °C will require the development of new oxidation resistant alloys or the use of expensive Ni- based alloys [1, 4-5]. Surface engineering of more cost effective materials, like the commonly used ferritic-martensitic steels, would be a more economical solution [6].

Promising research [2, 6-9] was carried out on aluminide coatings which combine good high temperature oxidation resistance and, in the case of an Al slurry, the possibility to apply the deposition technique to an industrial scale at moderate cost [2]. Most studies have concentrated on the ferritic substrates, especially the commonly used T/P22, T/P23 (2.25wt% Cr ferritic steels) [2], T/P91 and T/P92 (9wt% Cr ferritic-martensitic steels) [2, 6, 7,9]. On a ground and degreased substrate, the Al slurry is usually applied by brush followed by a curing heat treatment [6]. A further heat treatment (reported to be in Ar at 700 °C for 10 hours), produces the desired Al_5Fe_2 layer which forms the protective Al_2O_3 upon exposure accompanied by a thin FeAl layer close to the substrate. When exposed in steam, the thickness of the FeAl layer increases to the detriment of the Al_5Fe_2 because of the growth of the Al_2O_3 layer and the inward diffusion of Al in the substrate [6-8]. AlN precipitation occurs in the Al diffusion zone in substrates containing a minimum amount of N in their initial composition. These precipitates can also form when N from the environment diffuses inwardly through the coating toward the substrate [2]. Laboratory tests undertaken on coated P92 have shown that diffusion aluminide coatings are protective for at least 60,000 hours of exposure to steam at 650 ºC [2]. Failure of the aluminide coatings is due (a) to the formation of cracks because of the coefficient mismatch between the Fe-Al intermetallic phases and the substrate [7,8] and (b) to the diffusion of Al into the substrate, leading to the formation of rich Al precipitates, Kirkendal voids at the coating/substrate interface and the inability to repair the Al_2O_3 layer [2].

The progressive formation of AlN precipitates deeper into the substrate as the exposure time increases through the diffusion of Al from the coating has been one of the main factors against the application of these coating on an industrial scale. Indeed, it is believed that the loss of soluble N, that is added to ferritic-martensitic steels to improve their high temperature mechanical properties, might affect the materials long term creep properties. Creep tests performed in air on 9wt% Cr ferritic-martensitic steels with as deposited slurry aluminide coatings showed that a slight loss in creep strength was caused by the weak creep properties of the FeAl phase and the decrease of these steels' mechanical properties at temperatures as high as 650 °C. No evident detrimental effect of the AlN precipitates was reported [10,11]. However, no data on the effect of a prolonged exposure to steam on the creep behaviour of the steel substrate could be found in the literature.

The purpose therefore of the work presented in this paper is to examine and generate the necessary data on the microstructural evolution of Al slurry coated P91 alloy subjected to oxidising atmosphere of 100% flowing steam at 650 °C for times up to 5000 hours at atmospheric pressure. These test pieces were then used to evaluate the creep properties of as coated and aged (for up to 3000 hours) samples using creep stresses up to 120MPa.

2. Experimental details

The slurry coating applied to the T91 substrate comprised of fine aluminium power dispersed in a binder. To obtain the desired even aluminide layer on materials with high oxidation rates it is advised for the samples to be heat-treated in an atmosphere free of oxygen (preferably vacuum + Ar) at temperatures below the tempering temperature of the steel (760 °C for T91). The presence of oxygen in the atmosphere causes the growth of undesirable Fe oxides which then act as diffusion barrier for the aluminide coating to form. It is also highly recommended to grind the surface of the samples before coating them with an Al slurry. If the surface is grit-

blasted, embedded grit particles prevent the diffusion coating from forming a continuous layer. The coated T91 samples were heat-treated at 750 °C for 2 hours in vacuum+Ar and slow cooling.

Two forms of sample geometries were used : (a) curved coupons were machined from coated tubes (15 mm long and 1/6th of the tube circumference wide) that had been previously ground and (b) flat strips of T91 were electro discharge machines from a section of tube, coated and then cut into 10 x 10 x 3 mm coupons. Because of the different curvature of the substrate, different amount of Al slurry was initially deposited on the surface (Figures 1(a) and (b)) which resulted in aluminide coatings with different thicknesses after heat-treatment. The aluminide coating thickness was ~25 µm on the curved sample and ~15 µm on the flat ones (Figure1 1(c) and (d)). A selection of samples remained uncoated for comparison purposes.
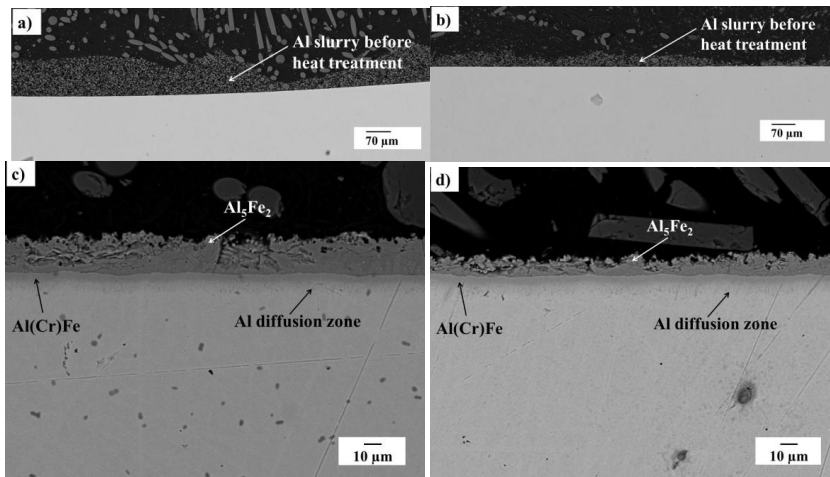
Figure 1 SEM images of cross-section through Al slurry coated (a) curved and (b) flat T91 substrate before heat-treatment and (c) (d) resulting aluminide coatings respectively after heat-treatment at 750 °C for 2 hours in vacuum + Ar.

The coated samples were exposed to 100% flowing steam environments at 650 ±5 °C, for durations of 300, 1000, 3000 and 5000 hours. On removal from the furnace the samples were nickel coated, sectioned and mounted in Bakelite resin and metallographically polished to a 1um diamond surface finish. A Camscan MX2500 SEM fitted with an Oxford Instruments EDX detector was subsequently used to examine the cross-sectioned samples.

Creep tests were performed using a W.H. Mayes Uniaxial Creep frame which subjects specimens to a constant stress whilst holding them under an isothermal temperature via a cylindrical furnace surrounding the load train. Automated load levelling, temperature control and displacement logging is provided. The creep testing of the slurry aluminide coating deposited on T91 was performed at 650 ±4 °C in air at uniaxial stress values of 80, 100 and 120 MPa. The cylindrical creep test specimens had a parallel gauge length of 40 mm with a 8 mm diameter. Before testing some test specimens were exposed to 100% flowing steam at 650 ±5 °C for 1000 and 3000 hours (Table I). Some specimens were removed prior to failure in an attempt to localise the early formation of voids or cracks in the steels.

Sample	Ageing time in steam (at 650°C, hours)	Creep temperature in air (°C)	Creep stress (MPa)	Removal time (hours)
AETI041	none	650	120	92 (entered tertiary)
AETI042	none	650	80	2098 (rupture)
AETI043	1000	650	120	63 (rupture)
AETI044	1000	650	100	377 (entered tertiary)
AETI045	1000	650	80	3504 (rupture)
AETI046	3000	650	80	2174 (rupture)
AETI047	3000	650	100	On-going
AETI048	3000	650	120	On-going

Table I Experimental condition for creep testing of Al slurry coated P91

3. Results

3.1. Steam oxidation of slurry aluminide coated T91

Curved and flat samples of T91 were oxidised in steam at 650 ^{o}C for 5000 hours (Figure 2). A thick duplex oxide comprising of an outer Fe_3O_4 and inner Fe-Cr spinel layer was formed and reached an average thickness of 250 μm on the uncoated T91 samples (Figure 2 (a) and (c)). On the aluminide slurry coated samples (Figure 2(b) and (d)), observation of cross-sections made through the samples before and after exposure showed the presence of three main phases: Al_5Fe_2, Al(Cr)Fe and Al diffusion zone. Upon exposure to steam, the Al(Cr)Fe and Al diffusion layer thicknesses increased due to diffusion of Al into the substrate and the formation of an Al_2O_3 scale. After 1000 hours on the flat samples (thinner coating) and 5000 hours on the curved ones (thicker coating), the Al_5Fe_2 phase was completely replaced by Al(Cr)Fe. The coating prevented the growth of Fe oxides on the ground samples where the Al-Fe intermetallic layer was continuous after heat-treatment.

The evolution of the different phases present in the aluminide coating is presented in Figure 3. The graphs shows the gradual disappearance of the Al_5Fe_2 phase to be replaced by Al(Cr)Fe and the growth of the Al diffusion zone with exposure time. The depth of Al penetration was measured from the interface between the Al(Cr)Fe phase and the Al diffusion zone to the boundary after which no Al was detected in the substrate using EDX analysis. It is also recognisable by the presence of AlN precipitates. Despite the different initial coating thicknesses, the depth of the Al diffusion zone was similar on both curved and flat samples and reached average depths of 25, 45 and 55 μm after 1000, 3000 and 5000 hours respectively. However, after 5000 hours exposure, the amount of Al remaining the Al(Cr)Fe phase was ~ 35 at% in the initially thicker coating and ~20 at% in the thinner one.
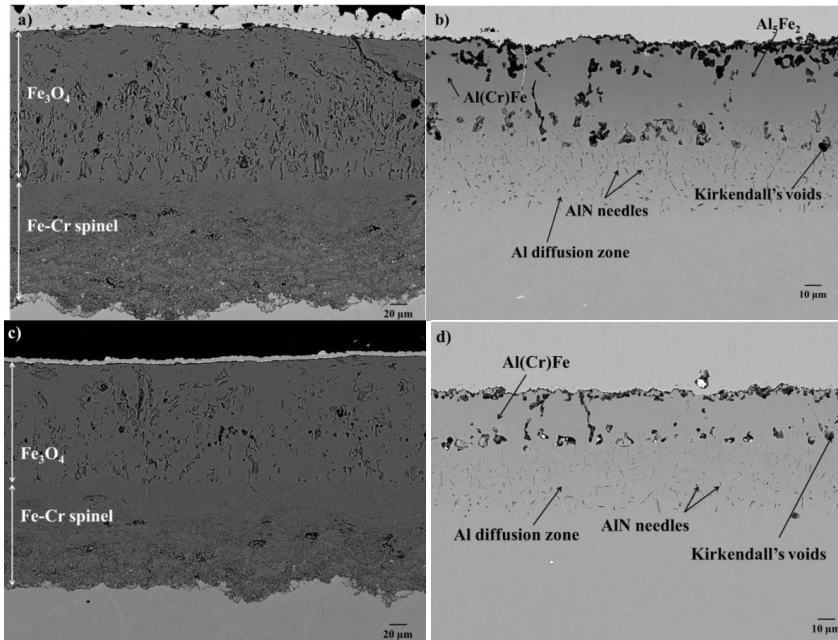
Figure 2 SEM images of cross-sections through the (a) uncoated and (b) coated curved T91 samples and (c) the uncoated and (d) coated flat T91 samples after 5000 hours at 650 °C in steam.
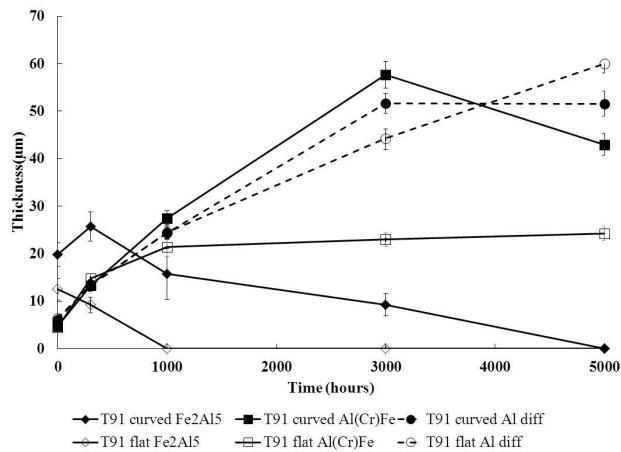
Figure 3 Thickness of Fe2Al5 (diamonds), Al(Cr)Fe (squares) and Al diffusion zone (circles) measured on curved (closed symbols) and flat (open symbols) Al slurry coated T91.

3.2 Creep testing of slurry aluminide coated T91

The hardness of the coated specimen was measured before and after heat-treatment, and after the aging in steam to ensure that the mechanical integrity of the steels was not affected by exposure to high temperature. The hardness (Hv30) values obtained were ~224HV for the substrate before heat-treatment, ~219HV after heat-treatment at 700 °C, ~216HV after 1000 hours in steam and ~216HV after 3000 hours in steam.

The rupture lifetimes (or times of removal from test after having entered tertiary) of the uniaxial creep testing as a function of applied stress are shown in Figure 4. The creep rupture strain levels obtained were ~21-24%. The values obtained for the coated T91 creep specimens are compared to time to fracture values obtained in the literature after the creep testing in air at 650 °C of uncoated T91 [12]. As expected, increasing the applied stress decreases the creep life of the specimen. In general, the creep rupture strength of the Al slurry coated T91 samples was slightly lower than for the uncoated T91 alloy. For the tests performed at 80 MPa, aging the sample in steam and thus increasing the depth of Al diffusion also decreased the rupture time. However, the specimen tested under a load of 80 MPa experienced the opposite phenomena with the aged samples lasting longer than the as-received one even when considering a standard uncertainty of 2.3% for the rupture time value [13].

Metallographic characterisation of the failed samples under the different conditions showed typical creep damage with rupture occurring because of the formation of voids and cracks within the T91 substrate itself rather than because of the presence of the Al slurry coating (Figure 5). Larger voids were observed on the samples crept under lower stress loads, as there was more time for the coalescence of the creep voids to occur. Etching the sample with a Vilella's reagent revealed an elongation of the martensitic laths close to the rupture location while the microstructure remained unchanged away from fracture.
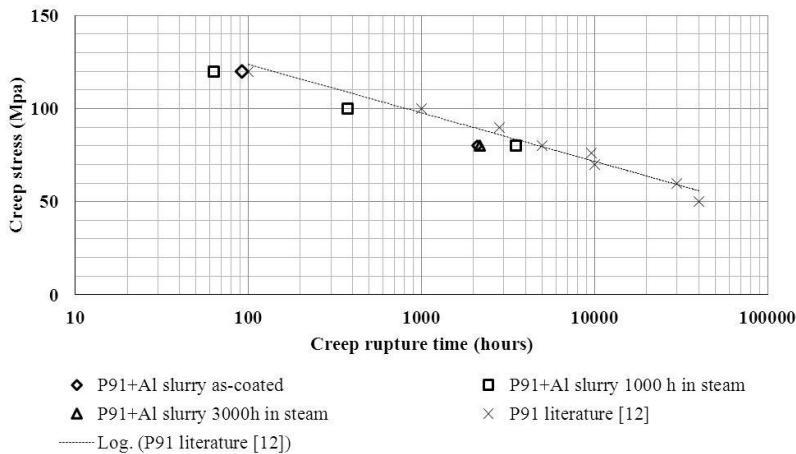
Figure 4 Creep testing results of Al slurry coated T91 with and without aging. Additional data for the uncoated T91 were found in the literature [12].
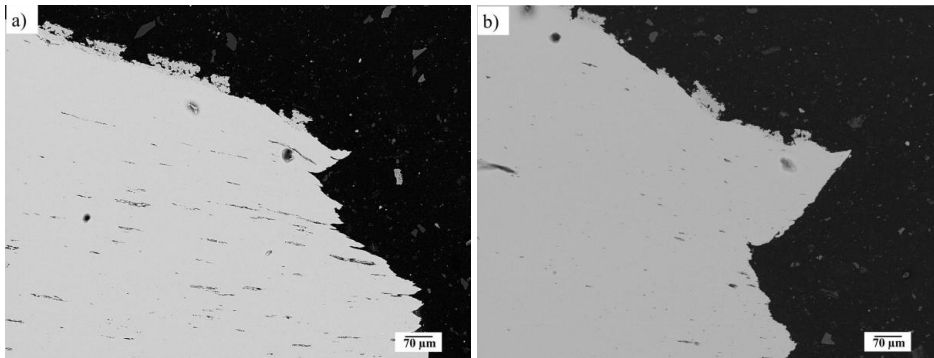
Figure 5 SEM images of cross-sections through al slurry coated T91 after creep test at 650 °C (a) under 80 MPa as-coated, (b) under 120 MPa after 1000 hours aging (AETI042 and AETI043 respectively).

The images in Figure 6 show the cracks present in the different layers of the coating on the samples crept under different conditions. The as-received sample crept at 120 MPa was removed as it just entered the tertiary creep phase (Figure 6(a)). As a result only few vertical cracks were present in the coating and no significant strain was recorded or observed. Wide cracks were located and extended along the thickness of the Fe_2Al_5 layer. Below them in the Al(Cr)Fe layer, fine cracks propagated until reaching the Al diffusion zone. Few pores were present at the interface between the coating and the substrate. The Al diffusion zone was as thick as an unexposed sample and did not experience any thinning during creep. Figure 6(b) shows the aluminide coating close to the failure location on a sample crept under a load of 120 MPa after having been aged for 1000 hours in steam. The sample was removed after rupture which happened after 63 hours. Fe-Al aluminides having very low strength, the coating sustained extensive damage under creep. Away from the failure area, the microstructure of the aluminide coating was similar to the one observed on the samples aged isothermally in steam. Close to the failure area, long wide cracks were located in the Al(Cr)Fe phase and Al diffusion zone without propagating into the substrate. Large voids could be seen in the Al diffusion zone. This layer was found to have accommodated the strain through plastic deformation better than the less ductile Al(Cr)Fe layer which experienced more cracking. Indeed the Al diffusion zone which has after 1000 hours in steam a ~45 μm thickness was only ~18 μm thick close to failure. The sample crept under a 100 MPa load after being aged in steam for 1000 hours, shown in Figure 6(c) was removed from the creep test after having entered the tertiary phase (after 377 hours). A slight necking was observed on the specimen and under the SEM, small voids were found in the centre of the T91 substrate. In the necked area, widening cracks were observed in the Al(Cr)Fe layer of the coating. These cracks connected with pores appearing in the Al diffusion zone. Some Kirkendal voids were also present at the interface between the coating and the substrate. Slight thinning of the Al diffusion zone was measured. Figure 6(d) shows the condition of the aluminide coating away from the rupture area of the sample crept under a load of 80 MPa in as-received condition which was removed after failure (after 2098 h). Again wide cracks were present in the Al(Cr)Fe phase. These cracks seem to propagate by the coalescence of voids appearing it the layer. Few voids were present in the Al diffusion zone.
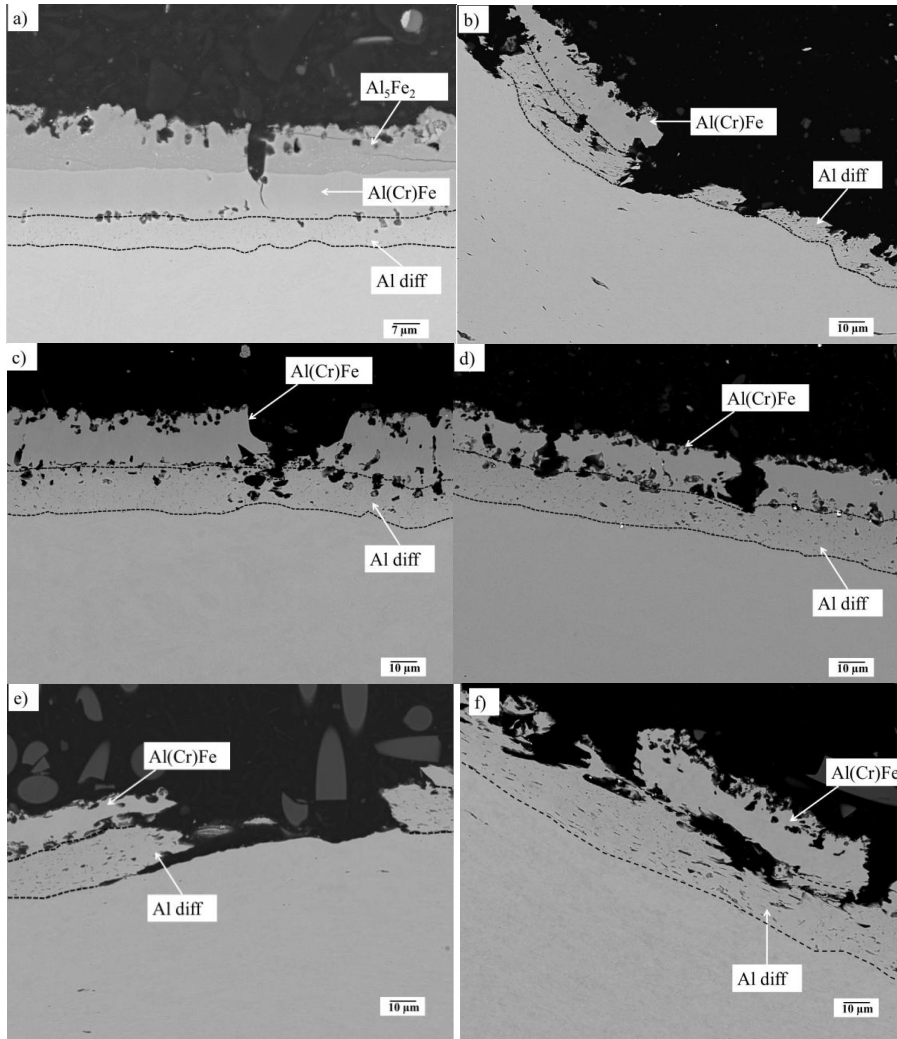
Figure 6 SEM images of cross-sections through al slurry coated T91 after creep test at 650 °C (a) under 120 MPa as-coated, (b) under 120 MPa after 1000 hours aging, (c) under 100 MPa after 1000 hours aging, (d) under 80 MPa as-coated, (e) under 80 MPa after 1000 hours aging and (f) under a 80 MPa load after 3000 hours aging (AETI042, AETI044, AETI045, AETI042, AETI045 and AETI046 respectively).

In Figure 6(e), an image close to the failure area on the sample crept under a 80 MPa load after aging in steam for 1000 hours shows how large horizontal cracks propagate at the interface between the Al free substrate and the Al diffusion zone rather than vertically into the substrate. The thickness of the Al diffusion zone decreased from ~55 to ~30 μm. Under a similar load but an exposure in steam for 3000 h, as depicted in Figure 6(f), a similar mode of

failure was observed. Wide cracks were present in the Al(Cr)Fe layer and larger Kirkendal voids were able to elongate and grow during the creep test at the interface between the coating and the substrate. In the Al diffusion zone, AlN particles acted as preferential sites for void formation which then elongate parallel to the loading axis. This seems to have helped the cracks to propagate horizontally rather than vertically into the Al free substrate. The depth of the Al diffusion zone decreased from ~65 to ~26 µm in areas away and close to rupture respectively.

4. Discussion

The measurements reported in this paper show that the presence of the aluminide slurry coating reduced the creep strength of the batch of T91tested,compared to values for uncoated T91 found in literature. The loss of mechanical strength was by the coating and the Al diffusion zone, which were less load bearing than the ferritic-martensitic steel itself. This effect will only be limited to a small portion of the tube thickness as the diffusion follows a parabolic law and has been seen to slow down after a certain amount of time in steam (Figure 3). However, there could be issues caused by the formation of cracks in the creeping coating which could expose unprotected steel to steam oxidation. The failure mechanism of the coating under a mechanical load was observed to start by the formation of a vertical crack in the Fe_2Al_5 or Al(Cr)Fe layers of the coating because of thermal expansion coefficient mismatch or the formation of voids caused by the applied stress. These cracks then widen under the constant load. In parallel, the Al diffusion zone becomes thinner with time. Kirkendal voids appear because of the fast diffusion of Al into the substrate and under widening cracks other voids are created because of the mechanical load. However these vertical cracks do not propagate into the substrate. Instead, large voids appear between portions of the coating which gradually detach from the substrate by horizontal cracks travelling beneath the Al diffusion zone.

The presence of the Fe_2Al_5 phase on as-received samples could be detrimental to a coating under mechanical loading at elevated temperatures. The difference of coefficient of thermal expansion between Fe_2Al_5 and Fe(Cr)Al promotes the formation of vertical cracks in the top surface of the coating which can then easily widen and expose the substrate to the oxidising environment.

5. Conclusion

The aluminide slurry coating deposited on T91 prevented breakaway oxidation after 5000 hours exposure, thereby showing its protective potential. Creep results showed that whilst the coated samples entered the tertiary creep zone earlier than the uncoated ones, cracking and creep of the coating remained confined to the surface of the specimen and that the ultimate creep rupture time remained within the accepted experimental scatter for this alloy.

6. Ackowledgments

7. References

[1] Wright I.G. and Dooley R.B., "A review of the oxidation behaviour of structural alloys in steam", *International Materials Review*, Vol. 55, pp. 129-167, (2010).

[2] Agüero A., González V., Gutiérrez M., Knödler R., Muelas R, Straub S., "Comparison between field and laboratory steam oxidation testing on aluminde coatings on P92", *Materials and Corrosion*, vol. 62, pp. 561-568, (2011).

[3] Wright I.G., Tortorelli P.F., Schütze M., "Oxide Growth and Exfoliation on Alloys Exposed to Steam," EPRI Report No. 1013666, (2007).

[4] Di Gianfrancesco A., "ENCIO project: An European approach to 700 °C power plant", Advances in Materials Technology for Fossil Power Plants Proceedings from the 7th International Conference, October, pp. 9-23, (2014).

[5] Shingledecker J., Purgert R., Rawls P., "Current status of the U.S. DOE/OCDO A-USC materials technology research and development program", Advances in Materials Technology for Fossil Power Plants Proceedings from the 7th International Conference, October, pp. 41-52 (2014).

[6] Agüero A, Muelas R., Pastor A, Osgerby S., "Long exposure steam oxidation testing and mechanical properties of slurry aluminide coatings for steam turbine components", *Surface and Coatings Technology*, Vol. 200, pp. 1219-1224, (2005).

[7] Bates B.L., Wang Y.Q., Zhang Y., Pint B.A., "Formation and oxidation performance of low-temperature pack aluminide coatings on ferritic-martensitic steels", *Surface and Coatings Technology*, Vol. 204, pp. 766-770, (2009).

[8] Wang C.J., Badaruddin M., "The dependence of high temperature resistance of aluminized steel exposed to water-vapour oxidation", *Surface and Coatings Technology*, Vol. 205, pp. 1200-1205, (2010).

[9] Durham R.N, Singheiser L., Quadakkers W.J., "Identification of degradation mechanisms in coatings for supercritical steam applications", *Materials and Corrosion*, Vol. 59, pp. 402-408, (2008).

[10] Dryepont S, Pint B.A., Zhang Y., "Creep and corrosion behaviours of bare and aluminized ferritic-martensitic substrates", NACE international Corrosion 2007 Conference & Expo, pp. 11-15, (2007).

[11] Agüero A.,Muelas R., Gutiérrez M., Van Vulpen R., Osgerby S., Banks J.P., "Cyclic oxidation and mechanical behaviour of slurry aluminide coatings for steam turbine components", *Surface and Coating Technology*, vol. 201, pp.6253-6260 (2007).

[12] Abe F. et al. in Haney E.M., Dalle F., Sauzay M., Vincent L., Tournié I., Allais L., Fournier B., " Macroscopic results of long-term creep on a modifier 9Cr-1Mo steel (T91)", *Materials Science and Engineering A*, Vol 510-511, pp. 99-103, (2009).

[13] Foster D.J., "The determination of uncertainties in creep testing to European standard prEN 10291, *Manual of codes of practice for the determination of uncertainties in mechanical tests on metallic materials*, code of practice n°10, (2000).

MICROSTRUCTURE EVOLUTION AFTER LONG TERM HIGH TEMPERATURE EXPOSURE OF 22-25Cr AUSTENITIC STAINLESS STEELS

Oriana Tassa[1a]**,** Susanna Matera[1b,] **,** R. Sandstrom[2], Joanna Zurek[3], Muhammad Farooq[2]

[1]Centro Sviluppo Materiali, Via di Castel Romano 100-102, 00128 Castel Romano, Italy

[2]Materials Science and Engineering, KTH Royal Institute of Technology, Stockholm SE-100 44 Sweden

[3]Forschungszentrum Jülich, Wilhelm Johnen Strasse, 52425 Jülich, Germany

[1a]o.tassa@c-s-m.it; [1b]s.matera@c-s-m.it; [2] rsand@kth.se [3]; j.zurek@fz-juelich.de

Abstract

Austenitic steel 22Cr-25NiNb-W-Cu (San25) and two austenitic 25Cr-20NiNbN (DMV 310N and HR3C) steels are candidates to be used in reheater and superheater tubing, which are the hottest parts of coal-fired power generation plants operating at 700/720°C. In this work the microstructural evolution of samples exposed in test loops for time up to 22,000 hours, as well as isothermal laboratory aged samples for temperature in the range 650°C to 750°C, for times up to 10,000 hours, have been investigated with the aim to improve the understanding of microstructure stability under severe service conditions. The investigations have been performed in the framework of the ECSC MACPLUS project. They were carried out by light Microscopy, Scanning Electron Microscopy (SEM), Transmission Electron Microscopy (TEM) equipped with Energy Dispersive Spectroscopy (EDS) combined with Selected Area Diffraction (SAD). Hardness has been also related to the ageing conditions. For DMV 310N and HR3C steels, CrNbN nitride (Z phase), Cr,Fe σ phase, $M_{23}C_6$ carbide, Nb(C,N) carbonitride, and $CR_3Ni_2Si(C,N)$ carbo-nitride (P phase) phase were likely to be present on all the samples that were aged for long time. For San25 steel the common phases were CrNbN nitride (Z phase), Laves (Fe,W,Cr) phase, $M_{23}C_6$ carbide, Nb(C,N) carbo-nitride, (Cr,Fe,W) σ phase, and Cu-rich phase. San25 steel is characterised by the highest precipitate fraction, particularly the sample with the most severe exposition conditions (678ºC ~22,000 hours). The precipitation state evolution combined with the presence of Cu precipitates in San25 is associated with the highest creep strength and hardness values.

Keywords: austenitic stainless steels, power plant, microstructure evolution, precipitation

1. Introduction

The continuous trend in efficiency improving in advanced ultrasupercritical (AUSC) coal-fired power plants for power generation needs an increase in temperature and pressure of the critical components, namely boiler and turbine. The target is to reach efficiency up to 60% through an increase of steam temperature up to 750°C and pressure in the range of 350-375 bar. Advanced austenitic steels have been currently used in reheater and superheater tubing which are the hottest part of coal-fired power generation plants, and where corrosion/oxidation conditions (coupled with creep strength requirements) are most severe.

The design principles for advanced austenitic steels are to achieve stable microstructure, high strength by precipitation strengthening and solution hardening through elements W and Mo, high corrosion resistance with high Cr content. Ni and N, that can suppress the formation of sigma phase, are added to reach sufficient structural stability and good fabricability.

High temperature strength and high creep rupture strength mainly depend on precipitate strengthening through fine and uniformly dispersed particles of Nb(C, N) (MX), NbCrN (Z phase). Addition of copper (about 3% wt) to form Cu phase has been found to significantly improve the creep-rupture ductility. Cr carbides, $M_{23}C_6$, reduce the grain boundary sliding and the surface cracks that increase the creep strength. The formation and stability of Cr carbides can be increased by addition of Mo.

Long term microstructural stability depends on microstructure evolution which can occur under severe service conditions for long times. Coarsening of Z phase, evolution of $M_{23}C_6$ towards coarse $Cr_3Ni_2Si(C,N)$ carbo-nitrides (P phase) and the occurrence of coarse σ phases $(Cr,Fe,(W))$ and Laves (Fe_2W) can have an important role in degrading creep strength, ductility and corrosion resistance .

In this work microstructure evolution, in terms of hardness and evolution of the precipitation state, of 25Cr-20NiNbN (DMV310N and HR3C) and 22Cr-25NiNbWCu (San25) austenitic steels have been investigated after exposition in test loops as well as laboratory isothermal ageing treatments. Precipitation state characterization in terms of size, morphology, location (grain boundary, within grains) and chemical composition of main phases: MX, $M_{23}C_6$, P , Z carbo-nitrides, Cu and intemetallic phases Laves, and σ has been used for monitoring relevant modifications which can affect long term microstructure stability.

2. Materials and Methods

Austenitic 25Cr-20NiNbN (DMV 310N and HR3C) 22Cr 25NiWCuNbN (San25) steels have been used for the investigation. The standard chemical compositions of the austenitic steel grades are outlined in Table 1.

grade			C	Si	Mn	Cr	Ni	W	Nb	Cu	Co	N
DMV 310N 25Cr 20Ni		min	0.05	0.30	1.0	24.0-	20.8	0.60-	0.4			0.18-
		max	0.07	0.50	1.4	25.0	21.5	1.50	0.5			0.24
HR3C 25Cr 20NiNbN		min	0.04			24.0-	17.0		0.20			0.15
		max	0.10	0.75	2.0	26.0	23.0		0.60			0.35
San25 22Cr 25NiWCuNbN*		max 0.1	0.2	0.5	22.5-	25.0	3.6-	0.5	3.0	1.5	0.23

Table 1: Standard chemical composition (wt%, Fe balance) of investigated austenitic steels (*nominal composition).

Samples from exposed tubes in test loops (COMTES 700 and ETR) and laboratory isothermal aged samples (from tube and plate) have been used for microstructural assessment. Samples from tube and plate products in solubilized conditions have been also investigated as reference materials. In laboratory isothermal annealing, temperature were in the range 600÷750°C for time from 1,000 up to 10,000 hours. In service, the exposure temperature was not constant, but the materials were subjected to a thermal cycle. For the analysis of results

the high temperature exposure ranges are generally given, with the associated exposure time: to explain, for a total exposure time of 32000 hours, the sample was exposed at the highest temperature range for about 22,000 hours.

Metallographic investigations have been carried out on not exposed (solution treated) and aged samples by Light Microscopy (LM) and Hardness Tests (HV_{10}) have also been performed. Scanning Electron Microscopy (SEM, SEM-FEG), Transmission Electron Microscopy (TEM-FEG) equipped with Energy Dispersive Spectroscopy (EDS) combined with Selected Area Diffraction (SAD) analysis have been performed to assess precipitation state evolution. TEM observations were carried out on thin foils prepared from aged samples. TEM-EDS analysis on extraction replicas was also performed to estimate chemical composition and the quantitative assessment of geometrical parameters (size distributions, mean size) of the second phases..

3. Results
3.1. Microstructure characterization

LM analysis showed an austenitic matrix constituted by equiaxed grains. Grain size have been measured on solution treated, laboratory aged samples and exposed tubes. Average grain size in some exposed tube samples varied from a minimum of 26 μm in San25 steel (ETR test loop at T_{max} 678°C for service time ~22,000 hours) up to 80 μm DMV310N steel (COMTES test loop at 586÷612°C ~ 22,000 hours). These differences have been associated to previous different thermomechanical cycle of the tube/plate products. As expected for all investigated austenitic steels, the effect of ageing temperature and time on grain size is likely to be small in both isothermal treatment and exposure service conditions.
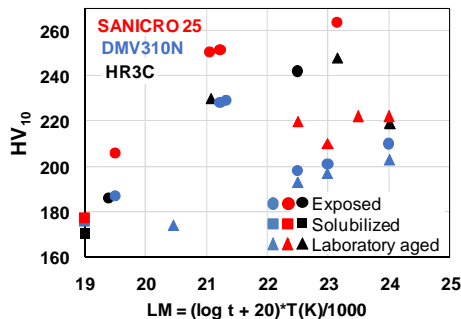
Figure 1 Hardness, HV_{10}, values in isothermal laboratory aged and exposed samples as function of Larson Miller (LM) parameter of austenitic steels HR3C; DMV310N; and Sanicro25

Hardness measurements (HV_{10}) have been performed on as received materials (solution treated condition), laboratory isothermal aged samples and exposed tubes. In Figure 1, the

163

hardness values are reported as function of Larson Miller (LM) parameter: t: LM=(log+20)T(K)/1000 where t is time and T is temperature (K). In the exposed sample T is the maximum temperature of the high temperature exposure range.

Starting from material in the solution treated condition, hardness increases as LM parameter is increased. Hardness increase of exposed samples is higher than that of laboratory aged samples, as particularly evident on San25 steel. Hardness values measured on San25 exposed samples, in the range between $220 \div 264 HV_{10}$, are higher than those of HR3C and DMV310N, $180 \div 240 \ HV_{10}$ respectively. Hardness values for laboratory aged San25 resulted lower than that measured for test loop samples: this difference can be explained considering that exposed materials are tubes whereas aged samples were taken from plates.

3.2. Precipitation state

Grain boundaries in all samples after solution treatment are particle-free. Coarse spherical and elongated precipitates with round edges, having sizes from 0.2 up to 2 µm were observed within grains. They were identified as MX, of type (Nb)(C,N). This phase was observed in all materials and was present also in the aged samples.
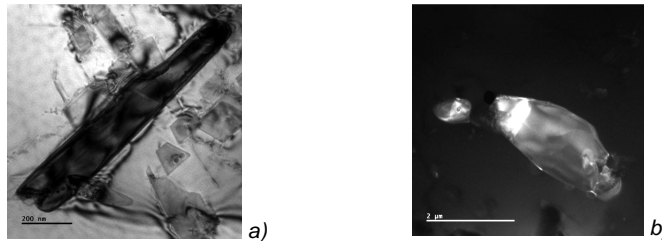
Figure 2 TEM micrograph of σ phase on thin foils. a) DMV310N exposed sample at $590 \div 616°C \sim 22,000$ hours. b). Sanicro25 exposed sample at T_{max} $678°C \sim 22,000$ hours

In laboratory isothermally aged samples and exposed tubes grain boundaries (GB) were continuously surrounded by elongated precipitates with round edges and size in the range $100 \div 600$ nm. They were identified as GB $M_{23}C_6$ carbides of type $(Cr,Fe)_{23}C_6$ in HR3C and DMV310N alloys and $(Cr,W)_{23}C_6$ in San25. $M_{23}C_6$ carbides having cuboidal, platelike and spherical morphology were also distributed within grains. Coarsening of $M_{23}C_6$ precipitates located at grain/twin boundaries and within grains was observed in all the investigated alloys after long term aging. Fine particles of NbCrN nitrides (Z phase) having cuboidal and platelike morphology were distributed within grains. This nitride was often associated to (Nb)(C,N). Coarse particles of Z phase, elongated with round edges morphology, were also present. Particles of σ (Cr,Fe) phase particles (wt% 51 Cr, 36 Fe, 13 Ni), platelike and elongated with round edges were observed in DMV310N (Figure 2a). In the case of San25 (Figure 2b) , W enrichment, was analyzed in σ (Cr,Fe,W) (wt% 42 Cr, 38 Fe , 10 Ni, 10 W) phase particles.

Coarse $Cr_3Ni_2Si(C,N)$ (P phase) and large sharp-edged Laves (Fe_2W) phase precipitates have been found in HR3C (DMV310N) and San25 steels respectively (Figure 3).

Figure 3 TEM micrograph of extraction replica: a) $Cr_3Ni_2Si(C,N)$ carbo-nitrides in DMV310N (586÷612°C): b) Laves (Fe_2W) in Sanicro25 (579÷605°C) .
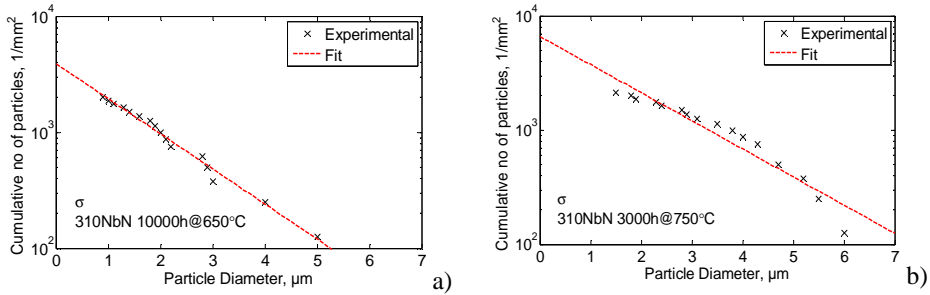
Figure 4. Cumulative particle distribution of σ phase in DMV310N laboratory aged samples: a) 650°C for 10,000 h b) 750°C for 3,000 h.
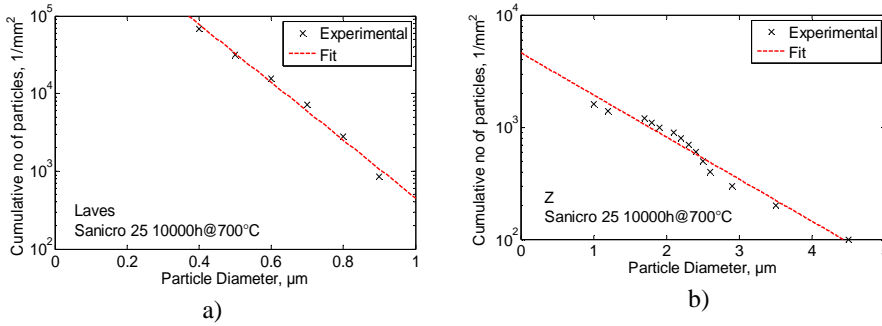
Figure 5. Cumulative particle distribution of phases in San25 laboratory aged sample at 700°C for 10,000 h a) Laves phase b) Z phase

The cumulative size distribution of different particles types has been assessed for some laboratory aged samples. The distributions are fitted to the exponential function: $F = Ne^{-kd}$, where N is the total number of particles per unit area, k the slope of the distribution, and d the equivalent area diameter of the particles. The experimental results for σ particles in DMV310N

and Laves and Z phase in San25 are shown in Figure 4 and 5 respectively. The typical chemical composition of phases in laboratory aged samples HR3C and Sanicro25 are shown in Tables 2 and 3.

Aging temp.	Aging Time (h)	Phase	Cr		Nb		Ni		Si	
			Cr_{min}	Cr_{max}	Nb_{min}	Nb_{max}	Ni_{min}	Ni_{max}	Si_{min}	Si_{max}
750	10000	Z	9	32.2	18.2	70.1	0.9	14.3	0.1	0.2
		σ	35	43.6	0.1	2.4	8.6	13.1	0.2	0.9
		$M_{23}C_6$	11.8	78.2	0	4.6	5	26.1	0	3.7
		η	23.8	37.8	0	5.1	24.6	45.8	3.3	7.8
		Nb (C,N)	5	30.6	14.4	86.2	0.1	4.5	0.8	7.7
		Cr Nitride	30.6	54	0	0	0	0	0	0
650	10000	Z	25	31.5	30	63.5	0.9	11.7	0.1	0.3
		σ	38.1	44.6	0.6	2.6	8	18.1	0.5	2.1
		$M_{23}C_6$	28.7	43.2	0.4	5	10.4	27.6	0.4	3.6

Table 2: Chemical composition (wt%) by SEM-EDS of different phases in HR3C laboratory aged samples for long holding times.

Aging Temp. ºC	Aging Time hours	Phase	Cr		Nb		Ni		Si		W	
			Cr_{min}	Cr_{max}	Nb_{min}	Nb_{max}	Ni_{min}	Ni_{max}	Si_{min}	Si_{max}	W_{min}	W_{max}
As received	As received	Z	24	29.5	11.6	60.5	1.2	19.4	0.1	0.1		
700	10000	Z	27.4	31	46.5	57	1.1	5.3	0.1	0.1	4	6.2
		Laves	16.6	19.2	0	1.4	4.6	10.4	0	0	37.6	51
		Cr_2N	54.4	88.5	0	2.2	0	14.2	0	0	0	1.3
650	10000	Z	26.6	28	9.7	63.9	1.9	22.9	1.5	1.8		
		Laves	15.5	26.8	0.8	2	5	23.5	0.1	0.1	30.3	50.5
		Cr_2N	35	60	0.3	7.1	21.3	23.3	0.5	1.6	3.6	5

Table 3: Chemical composition (wt%) of different phases in Sanicro25 laboratory aged samples for long holding times.

In Figure.6 isothermal precipitation diagrams are roughly drafted for DMV310N and Sanicro25 steels respectively on the base experimental evidence of phases observed in laboratory aged samples.
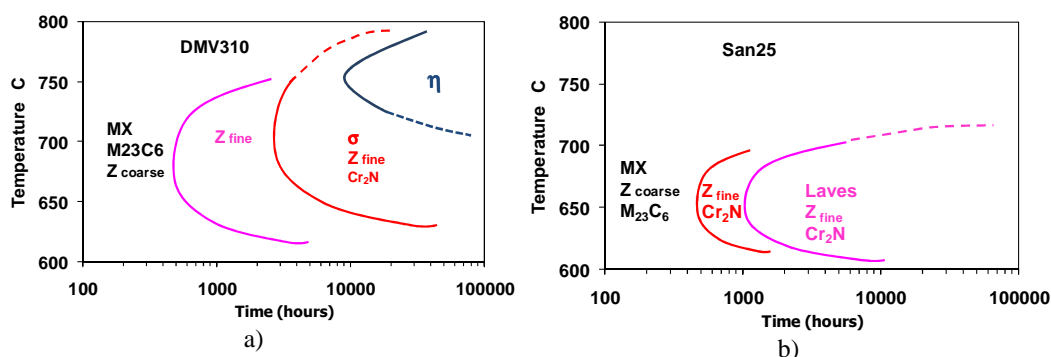
Figure 6: Isothermal precipitation diagrams in steels: a) DMV310N; b) San25.

Precipitates with high Cu content up to 50-55 (wt%), having mainly spherical morphology, size in the class range 20÷140 nm and average size 75 nm, were observed on thin foils of Sanicro25 samples, within grains and located on dislocations (Figure 7a, b, c). The amount of Fe, Cr, Ni and W in the average chemical composition was due to matrix contribution because of their quite small thickness resulting in a grey contrast. SAD image and computing (Figure 7c) was consistent with the crystal structure (face centred cubic) and lattice parameter (0.3615 nm) of Cu element.
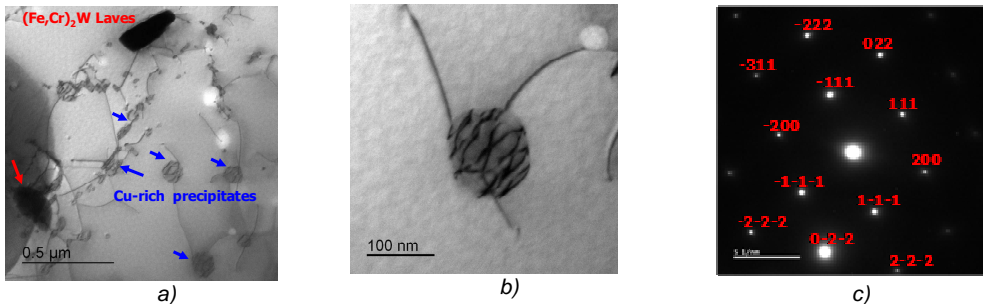
Figure 7 TEM micrograph on thin foil of San25 exposed (678°C/ ~22,000 hour)s:
a) b) Cu rich particles; c) SADp analysis Cu FCC: a: 0.3615 nm·, zone axis [0 1 -1]

4. Discussion

In this work laboratory aged and test loop exposed materials have been investigated. In comparing the results it has to be taken in account that for samples from the test loops, the exposure temperature was not constant, but the materials were subjected to a thermal cycle.
Microstructural modifications, which can affect long term microstructure stability, have been revealed in the present investigation in spite of the limited aging time: 22,000 hours.
At the level of macroscopic investigation, all alloys showed quite similar hardness variations with increasing temperature and aging time. Starting from material in the as solution treated condition, hardness increases with increasing LM parameter due to the intense precipitation that increases with the ageing conditions.

All the investigated steels shows a very complex evolution of precipitate state, according to literature [1-6], that can be summarised as follow:

- San25 steel, characterised by the presence of intragranular precipitates: Laves phase, Z nitride (Figure 5). $M_{23}C_6$, Nb(C,N), σ (Figure 2b) and Cu-rich phase (Figure 6) were also observed.

- Z, σ, $M_{23}C_6$, Nb(C,N), are present for different temperature time conditions in DMV310N and HR3C steels

The comparison of size distributions of the whole precipitate population clearly shows a shift in the distribution peak towards longer sizes as the ageing temperature is increased. The

broadest size distributions are observed in San25 indicating a fast formation of particles below 150 nm (Figure 8). Particles in this size range give a significant contribution to the precipitation hardening and it explains why San25 has such a high creep strength.
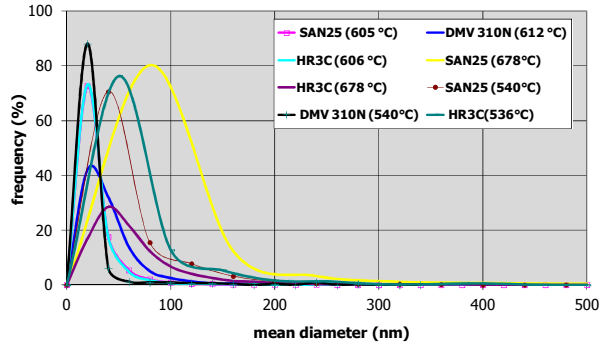
Figure 8 Size distribution of total amount of precipitates (TEM) of exposed samples at different T_{max} temperatures for long time (~22,000 hours).

The precipitate evolution can be interpreted with the help of thermodynamic phase diagrams: The equilibrium phase diagrams of HR3C and San25 steels, calculated by JMatPro software (JMatPro 4.1, Stainless Steels DB) are shown in Figure 9. Precipitate fractions increase strongly for temperatures from 600°C up to 750°C, which have been reached during service exposure.

Complex precipitation involving many phases is predicted for San25 steel as well as for HR3C, as confirmed by experimental analyses. Sigma phase is very stable in HR3C with phase fraction up to ~20% (wt%): on the contrary calculated sigma phase fraction is relatively low in Sanicro steel that is characterised by a large Laves phase fraction, due to W content.
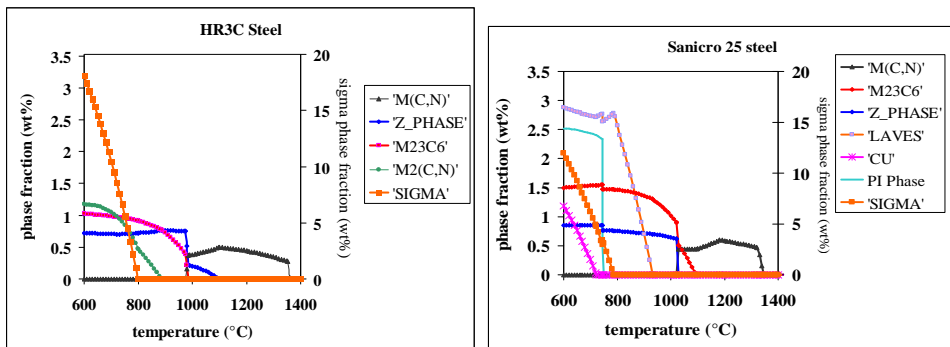
Figure 9 Equilibrium phase diagrams of HR3C and San25 steels calculated by JMatPro

According to [4] the following precipitation sequence can be considered for the investigated 25Cr austenitic steels:

$$MX \rightarrow MX+M23C6 \rightarrow MX+M23C6+Z \text{ phase} \rightarrow MX+M23C6+Z \text{ phase}+Cr3Ni2SiN$$
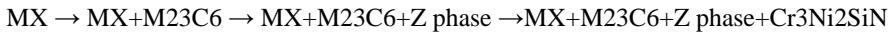
For 22Cr San25 steel the following precipitation sequence can be suggested:

$$MX \rightarrow MX+M23C6 \rightarrow MX+M23C6+Z \text{ phase} \rightarrow MX+M23C6+Z \text{ phase}+Laves$$
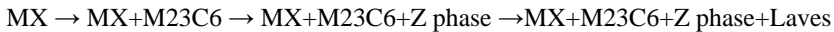
It was observed that Z phase was often formed by nucleating and growing on niobium carbonitrides: this can be explained by considering that Nb (C,N), formed at high temperature during fabrication process, is unstable at the exposition/ageing temperatures and it's transformed into stable Z phase nitride.

Coarse precipitates influence the room temperature mechanical properties. The precipitate status evolution including the presence of Cu precipitates in San25 is associated with the highest hardness values (Figure 1). The high amount of the brittle phases is generally associated with a reduction of ductility that can be the cause of failure of austenitic steels used at high temperature [7-10].

The complex precipitation sequence during ageing has been simulated both for DMV 310N and San25 using MatCalc and the results of the present work have been used for set up of model parameters [11]. For DMV 310N six different precipitates $M_{23}C_6$, Cr_2N, σ-phase, Z-phase, P-phase ($Cr_3Ni_2Si(C,N)$) and Nb(C,N) were modelled. Five precipitate types in San25 $M_{23}C_6$, Z-phase, Nb(C,N), Laves and Cr_2N were covered [12]. The time dependence of the particle radius and the phase fractions was analysed. The contribution of the different precipitates to the creep strength has been studied elsewhere[13]. An accurate prediction of the total strength could be achieved.

5. Conclusion

The experimental results of this work gave evidence of relevant microstructural modifications in austenitic steel after long term exposition up to 22,000 hours.

The precipitation and growth σ phase appeared the most dangerous microstructural modifications. These phases can affect microstructure stability and cause reduction in creep ductility. San25 steel is characterised by the highest precipitate fraction, particularly the sample with more severe exposition conditions (T_{max} 678ºC ~22, 000 hours) exhibited the highest amount of intragranular precipitates (Laves phase, Z phase, σ phase). The precipitation state evolution combined with the presence of Cu precipitates in San25 is associated with the highest hardness values.

ACKNOWLEDGMENT

Clean Coal Technologies. The authors wish also to thank: COMTES700 Partners and Coordinator (VGB) and for their kind support to supply exposed materials

REFERENCE

[1] Masuyama F., New developments in steels for power generation boilers, Editors R. Viswanathan and R. Nutting, editors, *Advanced heat resistant steels for power generation*, The Institute of Materials, London, 1998, pp. 33 – 47

[2] Plau R. L.., A Short Review on Wrought Austenitic Stainless Steels at High Temperatures: Processing, Microstructure, Properties and Performance, *Materials Research*, 10, (2007), pp. 453-460

[3] Shima J. H., Kozeschnik E., Jung W. S., Lee S. C., Kima D., Suha J. Y., Lee Y. S., Choa Y. W.: Numerical simulation of long-term precipitate evolution in austenitic heat-resistant steels, *CALPHAD Computer Coupling of Phase Diagrams and Thermochemistry* 34 (2010), pp.105–112

[4] Sourmail T., Bhadeshia H.K.D.H.: Microstructural Evolution in Two Variants of NF709 at 1023 and 1073K; *Mater. Sci. Technol.*; 2001; vol. 17, pp. 1-14

[5] Trillo E., Murr L., Effects of carbon content, deformation, and interfacial energetics on carbide precipitation and corrosion sensitization in 304 stainless steel, *Acta Mater.* 1999, 47(1), pp.235–45.

[6] Yae K. A., Tavares SSM, Pardal JM, Souza JA: Microstructure and intergranular corrosion resistance evaluation of AISI 304 steel for high temperature service. *Mater. Charact.* 2008; 59, pp.651-5

[7] Semba H., Okada H., Yonemura M., Igarashi M.: Creep Properties and Microstructure of HR6W and Ni-base Super alloys for Advanced USC Boilers, *3rd Symposium on Heat Resistant Steels and Alloys for High Efficiency USC Power Plants*; June 2 - 4, 2009

[8] Tavares S.S.M., Moura V., V.C. da Costa, Ferreira M.L.R., Pardal J.M, Microstructural changes and corrosion resistance of AISI 310S steel exposed to 600–800°C, *Materials characterization,* 60 (2009) 573–578

[9] Swindeman R. W., Maziasz P. J.: Evaluation of Advanced Austenitic Alloys Relative to Alloy Design Criteria for Steam Service; Part 2-20 to 30% Chromium Alloys; *Oak Ridge National Laboratory Report*; 1991; 30

[10] Sandström R, Farooq M, Ivarsson B, Influence of particle formation during long time ageing on mechanical properties in the austenitic stainless steel 310, Mater High Temp, 29 (2012) 1-7.

[11] Vujic S, Farooq M, Sonderegger B, Sandstrom R, Sommitsch C, Numerical modelling and validation of precipitation kinetics in advanced creep resistant austenitic steel, Computer Methods in Materials Science, 12 (2012) 175-182.

[12] Vujic S, Beal C, Sommitsch C, Farooq M, Sandström R, Zurek J, Modelling and optimizing precipitation in creep resistant austenitic steel 25Cr-20Ni-Nb-N, in: 7th Int. Conf. on Advances in Materials and Technology for Fossil Power Plants, Hawaii, 2013.

[13] Sandström R, Farooq M, Zurek J, Basic creep models for 25Cr20NiNbN austenitic stainless steels, Materials Research Innovations, 17 (2013) 355-359.

INFLUENCE OF NICKEL ON THE MECHANICAL PROPERTIES OF A CREEP RESISTANT CB2 FLUX CORED WIRE WELD METAL

S. Baumgartner[1], M. Schuler[2], R. Schnitzer[1], N. Enzinger[2]

[1] voestalpine Böhler Welding Austria GmbH, Böhler-Welding-Str. 1, 8605 Kapfenberg, Austria
susanne.baumgartner@voestalpine.com

[2] Institute for Materials Science and Welding, Technical University of Graz, Kopernikusgasse 24, 8010 Graz, Austria

Abstract

Within the European COST programs the modified 9Cr-1.5Mo-1Co steel with boron addition designated as "CB2" has evolved as the most promising candidate for cast components, which are already used for service temperatures up to 620°C. A matching flux cored wire for welding these cast components has been developed.
Nickel is often added to filler metals to increase the toughness of the weld metal at room temperature. On the other hand Nickel is reported to be detrimental for long term creep properties of martensitic 9%Cr steels.
This paper discusses the influence of Nickel on the mechanical properties of the weld metal. The results of tensile tests and impact tests of all-weld metal with different Ni-content are compared and microstructural investigations were performed. Creep rupture tests of a matching joint at 625°C show differences even after short times.

Keywords:CB2, Flux Cored Wire

1. Introduction

The modified 9Cr-1.5Mo-1Co cast alloy with additional boron, which was developed during the European COST programs and designated as "CB2", is utilized for large cast components used at steam temperatures up to 620°C [1]. To come up with the demand for a highly productive welding process a matching filler wire has been developed. Originally the chemical composition of all-weld metal was close to the chemical composition of the base material, only the Boron content was reduced to decrease hot cracking susceptibility and to meet the toughness requirements [2]. To enhance impact energy at ambient temperature a modified version of the flux cored wire with increased Ni-content was developed. Due to the fact that Nickel is reported to be detrimental to long term creep properties [3] the high Ni-content version was highly controversial.

The aim of this paper is to investigate the influence of Nickel on mechanical properties and creep rupture strength at 625°C and to evaluate the effect of post weld heat treatment (PWHT) on tensile strength and impact energy.

171

2. Experimental

The influence of nickel on microstructure and its mechanical properties were investigated. Two different CB2 flux cored wires with a Ni-content of 0.2 wt% and 0.7 wt%, respectively, were used to perform welding tests. The chemical composition of all-weld metal is listed in Table 1.

Table 1: Nominal chemical composition of CB2 flux cored wire all-weld metal [wt%].

	C	Si	Mn	Cr	Mo	Co	Ni	V	Nb	N	B
Low Ni	0.1	0.2	0.9	9.0	1.5	1.0	0.2	0.2	0.03	0.02	0.005
High Ni	0.1	0.2	0.7	9.0	1.4	1.0	0.7	0.2	0.03	0.02	0.006

2.1 Welding Procedure of All-Weld Metal Samples

All-weld metal samples were welded according to EN ISO 15792-1 and tensile samples and impact samples were produced. The welding parameters are listed in Table 2. PWHT was varied from 710 °C to 760 °C and from 4 h to 48 h (see Table 3).

Table 2: Welding Parameters for All-Weld Metal Samples.

Shielding Gas	Ar+18% CO_2, 16 l/min
Wire Feed Rate	13 m/min
Voltage	29 V
Current	240 A
Preheating	200 °C
Interpass Temperature	260 °C
Welding Speed	30 cm/min
Heat Input	1.4 kJ/mm
$t_{8/5}$	12 s

Table 3: PWHT for All-Weld Metal Samples.

	4 h	8 h	12 h	24 h	48 h
710 °C		x	x	x	
720 °C		x	x	x	
730 °C		x	x	x	x
740 °C		x			
760 °C	x				

2.2 Matching Joints

As the flux cored wire is used for welding of cast components the influence of nickel on mechanical properties was also tested on matching joints. Seam preparation and layer sequence are shown in Figure 1. Welding parameters are listed in Table 4.
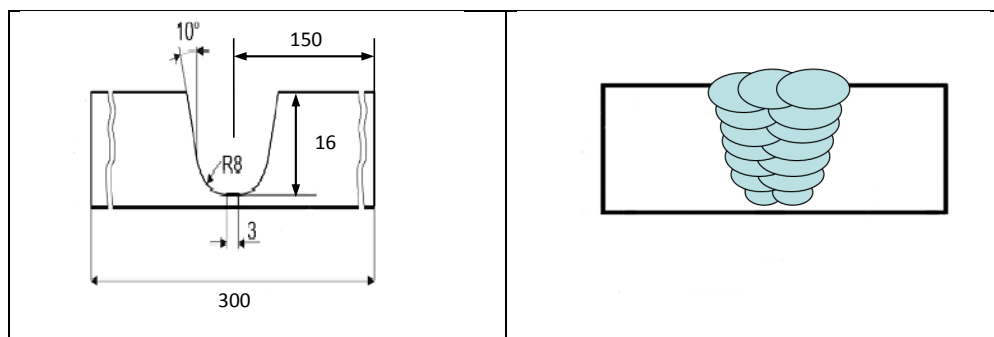
Figure 1: Seam preparation (left) and layer sequence (right) of CB2 matching joint.

Table 4: Welding Parameters of matching CB2 joints.

	first pass	intermediate and final passes
Filler metal	Böhler CB 2 Ti-FD	
Diameter [mm]	1.2	
Wire feeding rate [m/min]	11	13
Voltage [V]	28	29
Current [A]	215	245
Preheating/interpass temp.	250 °C/260 °C	
Welding position	PA (G1)	
Shielding gas	Ar+18%CO$_2$, 16 l/min	
PWHT	730 °C/8 h, 730 °C/24 h	
Base metal	CB2	

Cross weld samples as well as longitudinal tensile samples and charpy V-notch samples of the weld metal were prepared. Cross sections for light optical microscopy and hardness measurements were taken.

Besides, creep rupture tests with cross weld samples and longitudinal weld metal samples with PWHT 730 °C/24 h were performed at 625 °C with a load of 120 MPa and 100 MPa, respectively.

3. Results and Discussion

3.1 Microstructure and Transformation Temperatures

Table 5 shows the transformation temperatures A_{c1} and A_{c3} measured according to ASTM A1033-10.

Table 5: Transformation temperatures A_{c1} and A_{c3} of CB2 flux cored wire weld metals acc. ASTM A1033-10.

	Ac_1 [°C]	Ac_3 [°C]
0.2 wt% Ni	817	890
0.7 wt% Ni	785	878

The transformation temperatures were lower in samples with higher Ni-content. That corresponds to published investigations, that the Mn+Ni-content has a very strong effect on A_1 temperature in P91 steel grades [4].

Grain size measurements of the weld metal revealed an average grain size of 50 µm in the annealed regions of the multi-pass weld for 0.2 wt% Nickel and 40 µm for 0.7 wt% Nickel, which coincides to the grain refining effect of Nickel [5].

3.2. Mechanical Properties of All-Weld Metal at Ambient Temperature

3.2.1 Influence of PWHT

Figure 2 shows the influence of PWHT on tensile properties of CB2 flux cored wire weld metal at ambient temperature. The trend lines show that the yield strength and tensile strength decrease. With higher Ni-content, yield strength is a little higher while there is no significant difference in tensile strength.
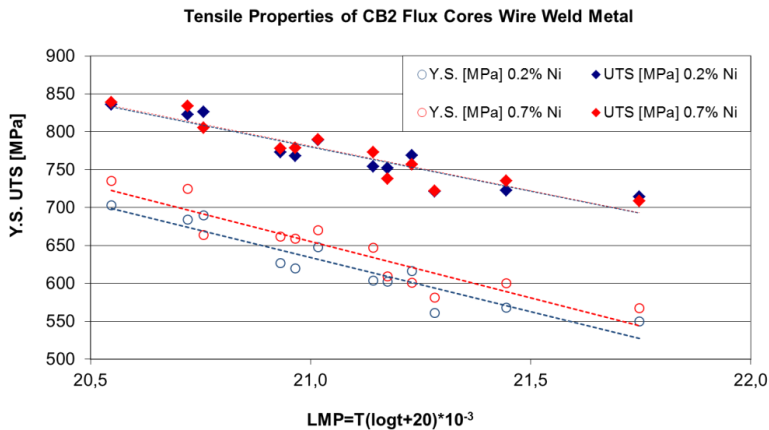
Figure 2: Influence of PWHT on tensile properties of CB2 flux cored wire weld metals.

174

However, with higher annealing temperature and longer annealing time increasing impact energy can be observed (see Figure 3). The influence of temperature on the results is more pronounced than the influence of time. This effect is more significant with higher Ni-content.
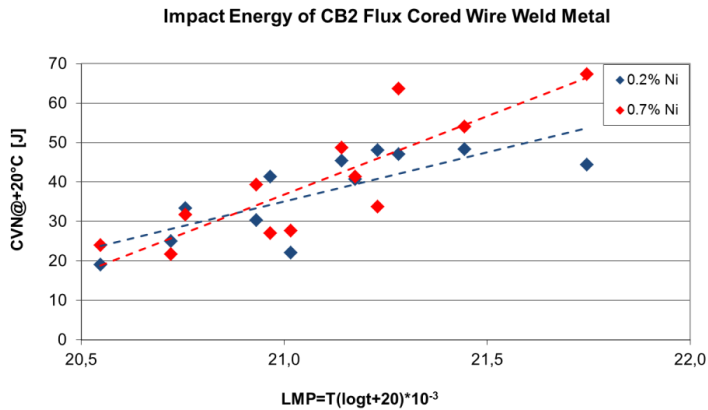
Figure 3: Influence of PWHT on impact energy of CB2 flux cored wire weld metals.

3.2 Matching Joints

3.2.1 Mechanical Properties

Cross tensile samples and longitudinal samples of the weld metal were tested at ambient temperature. All cross tensile specimens fractured in the base material. The results of the longitudinal samples are shown in Figure 4. Yield strength and tensile strength decrease with longer annealing time and elongation increases. Similar to all-weld metal tests, the yield strength is slightly higher with higher Ni-content, tensile strength and elongation seem to be unaffected by the Ni-content.
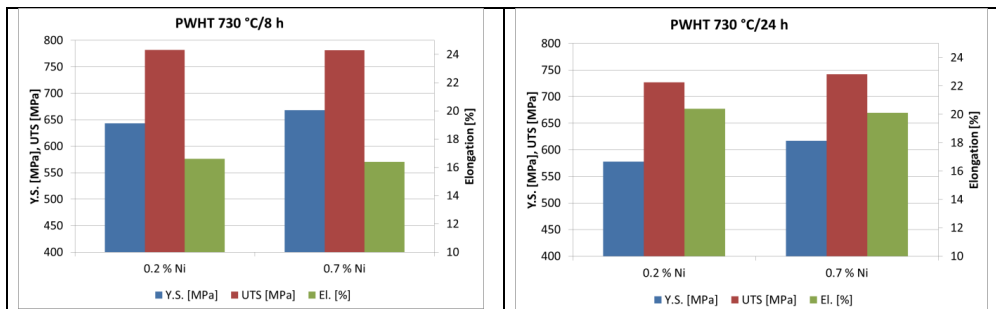
Figure 4: Results of longitudinal tensile tests of CB2 Weld Metal
with PWHT 730 °C/8 h (left) and 730 °C/24 h(right).

175

Figure 5 shows the A_v/T-curves of both weld metals with PWHT of 730 °C/8 h and 730 °C/ 24 h, respectively. With higher Ni-content impact energy at ambient temperature is a little bit higher and the transition temperature is slightly shifted to lower temperatures, but above 150 °C the upper shelf level of more than 100 J is reached even with low Ni-content and short PWHT.
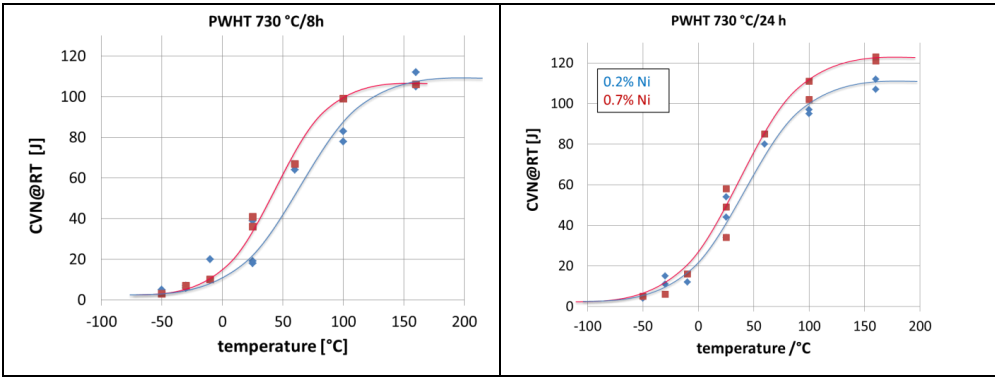
Figure 5: Impact energy of CB2 Weld Metal with PWHT 730°C/8h (left) and 730°C/24h(right).

Figure 6 shows hardness mappings of the matching CB2 joints after PWHT 730 °C/8 h and 730 °C/24 h, respectively. There is no significant difference regarding the Ni-content. With longer annealing time the hardness of the weld metal slightly decreases, the hardness peak at the fusion line is reduced and the hardness drop in HAZ seems to be wider.
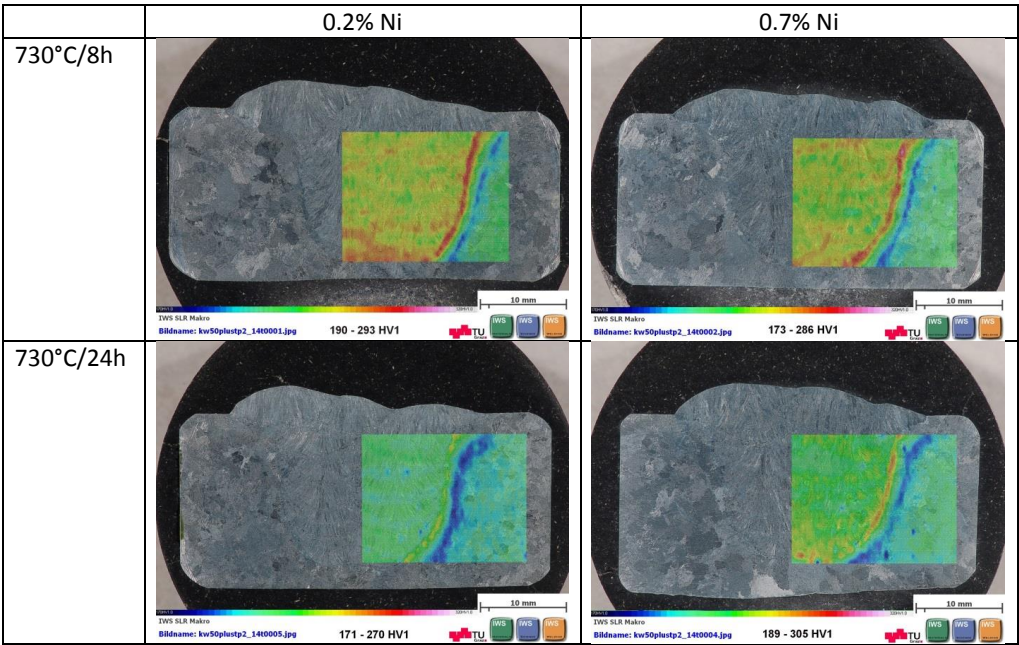
Figure 6: Hardness mappings of matching CB2 joints.

3.2.2 Creep Rupture Tests

Creep rupture tests of cross weld and weld metal samples up to 6,500 h were performed at 625 °C. The results are shown in Figure **7**. The fracture location is specified for cross weld specimens.
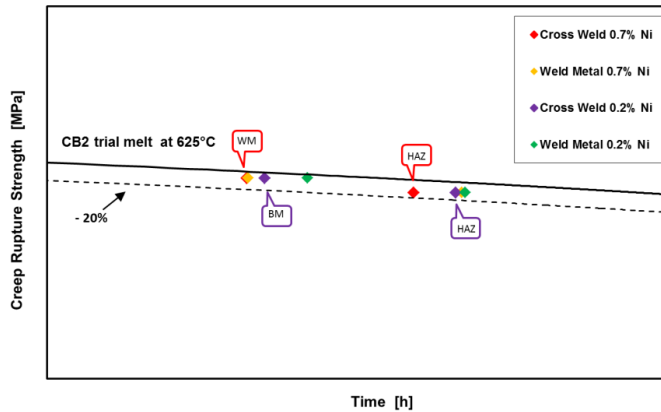
Figure 7: Creep Rupture Tests at 625°C.

Weld metal samples with lower Ni-content achieved longer fracture times compared to the high Ni samples, but all samples tested at 625°C fractured within the -20% scatterband of the CB2 trial melt. Figure 8 shows the fracture location of the cross weld samples with lower Ni-content. The 120 MPa specimen fractured in the base material and the 100 MPa specimen fractured in HAZ. The 100 MPa cross weld sample with 0.7 % Ni also fractured in the HAZ, whereas the 120 MPa Sample fractured in the weld metal (see Figure 9). Investigation of microstructure of the broken specimen revealed no significant differences. However, calculations with the thermokinetic software MatCalc predicted a slightly different evolution of precipitates with higher phase fraction of $M_{23}C_6$ and MX particles in the low nickel weld metal, and lower mean radius of laves phase[6].
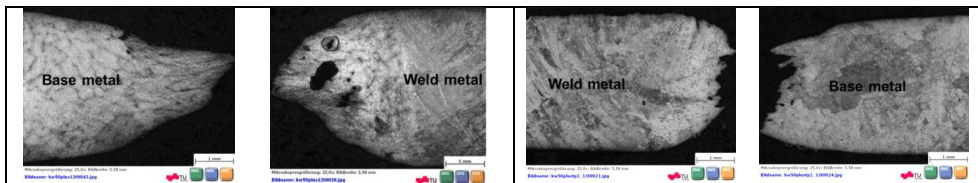
Figure 8: Fracture location of cross weld specimen 0.2 % Ni: 120 MPa (left), 100 MPa (right).
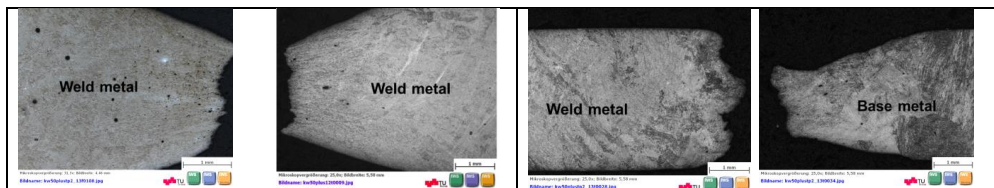
Figure 9: Fracture location of cross weld specimen 0.7 % Ni: 120 MPa (left), 100 MPa (right).

177

4. Summary

Tensile tests and charpy-V-notch-tests at ambient temperature were performed with all-weld metal samples after varied PWHT with 0.2 wt% Ni and 0.7 wt% Ni, respectively. Furthermore, tensile tests and charpy-V-notch-tests from -50 °C to 160 °C of matching joints with PWHT of 730 °C/8 h and 730 °C/24 h, respectively, were done. The tensile properties decreased and the impact energy increased with increased PWHT.

Regarding the Ni-content, the investigation of all-weld metal and matching joint weld tests confirmed that Nickel increases toughness but decreases creep rupture strength also in a CB2 flux cored wire weld metal.

A detailed analysis reveals that a Ni-content of 0.2 wt% in the flux cored wire weld metal, which is in the same range as the content of the base material, leads to the following results compared to a Ni-content of 0.7 wt%:

1) The transition temperatures A_{c1} and A_{c3} are approximately 30 °C higher with lower Ni-content.

2) The grain size in the annealed region of the multi-pass weld is larger compared to the weld metal with higher Ni-content.

3) Yield strength is slightly lower, but tensile strength seems to be unaffected by the Ni-content.

4) Impact energy at room temperature is a little lower and the transition temperature is slightly higher, but above 150 °C the upper shelf level of more than 100 J is reached even with PWHT of 730 °C/8 h.

5) Creep rupture tests up to 6,500 h at 625 °C show that weld metal samples with lower Ni-content achieved longer times. Cross weld samples fractured in HAZ.

Regarding the importance of long term behaviour at service temperature, the increase of Ni-content should be considered carefully.

Literature

[1] C. Lochbichler, E. Schmidtne-Kelity, S. Baumgartner, Latest Developments of Cast Materials and Welding Consumables for Coalfired Steam Turbines Com-ponents / Nickel-base Alloy A625 and CB2 Steel for the A-USC Technology, *Power Gen.* (2013).

[2] S. Baumgartner, G. Posch, P. Mayr, Welding advanced martensitic creep-resistant steels with boron containing filler metal, *Welding in the World* 56 (2012), 2-9.

[3] Kimura, K., Sawada, K., Kushima, H., Toda, Y., Microstructural Stability and Long-term Creep Strength of Grade 91 Steel, *Energy Materials: Materials Science and Engineering for Energy Systems,* Vol. 4, No. 4 , 8th Charles Parsons Turbine Conference (2011), pp. 176-183

[4] B. Alexandrov, L. Wang, J. Siefert, J. Tatman, J. Lippold, Phase Transformation in Creep Strength Enhanced Ferritic Steel Welds*, Machines, Technologies, Materials,* 4 (2012), pp. 33-36

[5] E. Letofsky, Das Verhalten von Schweißverbindungen moderner Kraftwerkswerkstoffe, Thesis TU Graz (2001)

[6] M. Schuler, S. Baumgartner, R. Schnitzer, N. Enzinger, Creep investigation and simulation of CB2 joints using similar rutile CB2 flux-cored wire, *Welding in the World,* DOI 10.1007/s40194-014-0169-0

MICROSTRUCTURE FOR AN OPTIMIZED CREEP RUPTURE STRENGTH OF HIGH CR STEELS

Ernst Plesiutschnig[1,a], Coline Beal[1,b], Stefan Paul[2,c], Günter Zeiler[2,d], Stefan Mitsche[3,e], Christof Sommitsch[1,f]

[1]Institute for Materials Science and Welding, Graz University of Technology, Kopernikusgasse 24, 8010 Graz, Austria

[2]Böhler Edelstahl GmbH & Co KG, Mariazellerstraße 25, 8605 Kapfenberg, Austria

[3]Institute for Electron Microscopy, Graz University of Technology,   Steyrergasse 17, 8010 Graz, Austria

[a]ernst.plesiutschnig@tugraz.at, [b]coline.beal@tugraz.at, [c]stefan.paul@bohler-edelstahl.at, [d]guenter.zeiler@bohler-edelstahl.at, [e]stefan.mitsche@felmi-zfe.at, [f]christof.sommitsch@tugraz.at

Abstract

Increasing the efficiency of modern steam power plants requires raising the inlet fluid temperature and pressure. To fulfill these conditions, the materials of cast, rolled and forged parts such as the case, pipes and rotor, need to be improved.

Variations within the chemical composition of the material as well as appropriate processing steps are of crucial importance to meet an optimized microstructure for creep exposure. In this work, the influence of heat treatment on the microstructure of a MARBN and a modified FB2 steel was investigated. Systematic LOM, SEM and EBSD investigations were performed in order to characterize the microstructure before and after creep testing. Comparative creep tests carried out at 650°C show that, by applying appropriate heat treatment, creep rupture time can be increased by more than 100%.

Keywords: MARBN steels, creep, open die forging, rotor, steam turbine, SEM, EBSD

1. Introduction

Over the last decades a lot of effort has been performed to improve the creep behavior of ferritic 9% Cr martensitic steels. Over decades Böhler Edelstahl GmbH & Co KG has been a premium supplier of forged components for the power generation industry, e.g. discs, centre shafts, turbine shafts, shaft components and accessories for gas and steam turbines. Within the European COST framework (1987 – 2008) a lot of knowledge has been created within materials development such as optimizing chemical composition, grain refinement and homogeneity of large-scale forgings. Within the Austrian framework of KW50+ the concept, ideas and the knowledge are passed to the next decade. Development of the material runs hand-in-hand with increasing efficiency of modern state of the art steam power plants.

To further improve the behavior of high Cr steels, investigation of microstructure evolution during manufacturing as well as in service is essential. Recent developments over the past 15 years in microstructure characterization of high Cr steels by means of the Electron Backscatter Diffraction (EBSD) technique mounted with a Scanning Electron Microscope (SEM) [1], extensively used by [2], [3] permits to analyze the substructure after the γ to α' transformation. One other main development is the software package MatCalc by Kozeschnik and co workers to describe the evolution of microstructure during heat treatment (HT) and service [4], [5].

Martensite as a sum of all four hardening mechanism [6] is very complex to understand and to simulate. The evolution of the four hardening mechanisms is not just time related but also interdependent. For instance considering one time step if solid solution hardening decreases (matrix loses alloying elements on regular lattice positions) causing either the formation of new precipitates or precipitate coarsening (i.e. precipitation hardening in- or decreases) at areas of high dislocation density which act as the nucleation sites and pathways (mobility decreases) leads to a strong interaction within each hardening mechanism.

2. Experimental

Two chemical compositions of open die forged 9%Cr steels were supplied by Böhler Edelstahl GmbH & Co KG, see Table.1.

Table.1 Chemical composition of investigated steels.

	COST	C	Mn	Cr	Mo	Co	W	V	Nb	N	B	Fe
T570	FB2-2-LN	0.16	0.31	8.81	1.43	0.97	0.05	0.2	0.04	0.011	0.015	bal.
T516	NPM1-LN	0.07	0.50	8.96	0.05	2.86	2.95	0.2	0.05	0.009	0.010	bal.

Four different prior austenite grain (PAG) sizes of 50µm, 100µm, 300µm and 700µm were created using 2 different hardening times (30min and 3 hours) at 2 different temperature levels (1150°C and 1100°C), in order to study their influence on creep behavior. After hardening, the samples were annealed two times at 700°C for 3h.

Light optical microscopy (LOM) after heat treatment was used to evaluate the PAG sizes. The software package OIM from EDAX [7] was further used to analyze the microstructure after phase transformation. After heat treatment (HT), creep samples were machined to a diameter of 7.07mm and creep exposed with 150MPa at 650°C.

3. Results and Discussion

The PAG size after the HT was analyzed on a polished and etched sample, using the linear interception method. Two different obtained grain sizes of T570 are shown in Fig. 1.
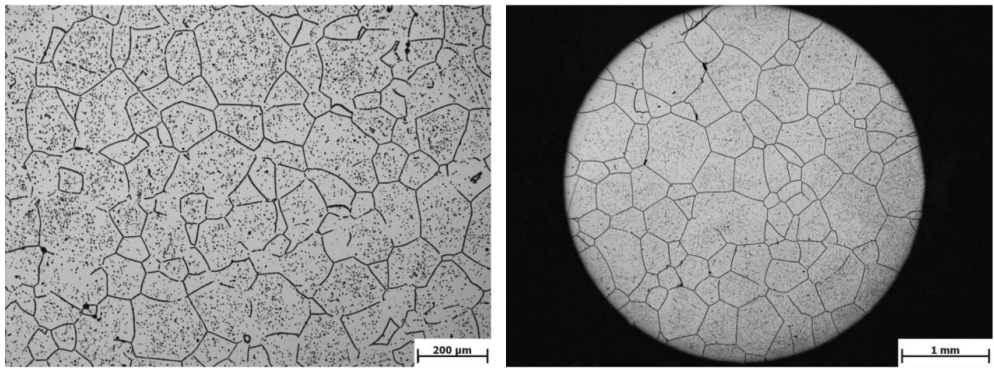
a.) T570 with 50µm grain size. b.) T570 with 300µm grain size.
Fig. 1 LOM for T570 after etching.

After EBSD measurements, the pole figures (PF) in Fig. 1 were analyzed with a specific software [7] from a selected area inside one PAG. Overlapping with the calculated PF from the orientation relationship according to Kurdjumov-Sachs (K-S) for the γ to α' transformation, four different colors highlight the signals from the (4x6) 24 variants of the four parent austenite {111}γ planes (also known as packets), each consisting out of six separate variants (also known as blocks) separated by high angle grain boundaries [8], [9].

The PF in Fig. 2 show that all 24 variants are present within one PAG for T516 and T570. The light intensity of the variants in Fig. 2 b.) is due to the lager block size in T516 which is discussed later.
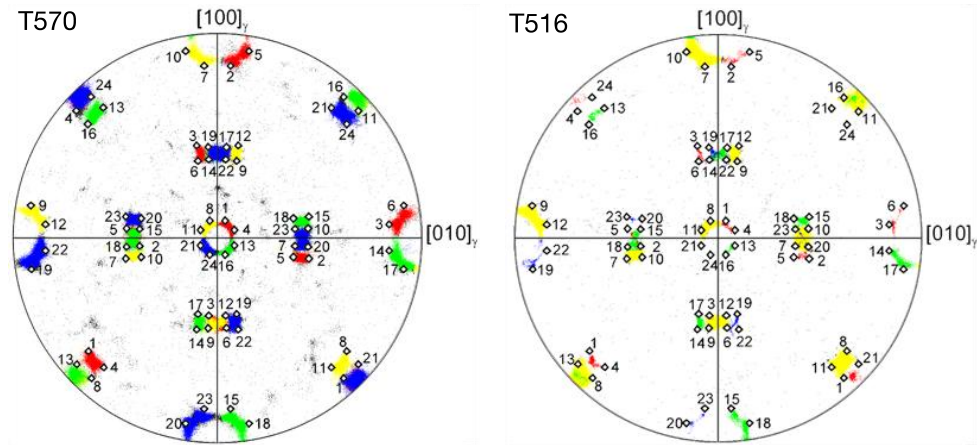
a.) Pole figure (PF) for T570.   b.) Pole figure (PF) for T516.

Fig. 2 obtained K-S relationship for T516 and T570.

As an example, the Inverse Pole Figure (IPF) maps in Fig. 3 is related to the PF for T570 in Fig. 2 a.) and illustrate the packets 1 - 4 within one PAG. Analysis of their size for comparison was not a feasible option, therefore the grain boundaries from the IPF were classified according to their misorientation (MO).
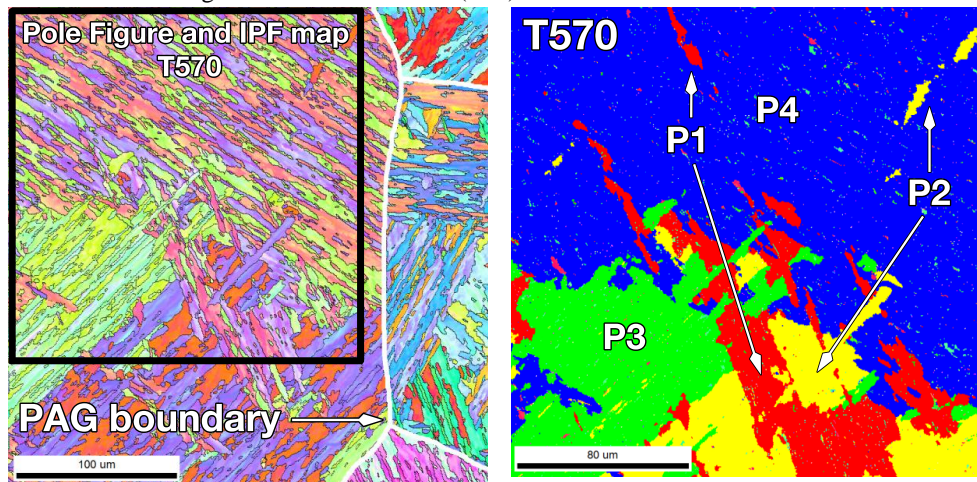
a.) Selected area for PF analysis corresponding to Fig. 2 a.) and Fig. 3 b.).

b.) IPF map for T570 from the black-framed area in a.).

Fig. 3 IPF maps for T570 as an example for packet analysis.

Fig. 4 shows comparative IPF maps (section of 300x300px with step size of 0.5µm) at the same PAG size for T570 in Fig. 4 a.), for T516 in Fig. 4 b.). The difference of the block size is evident.
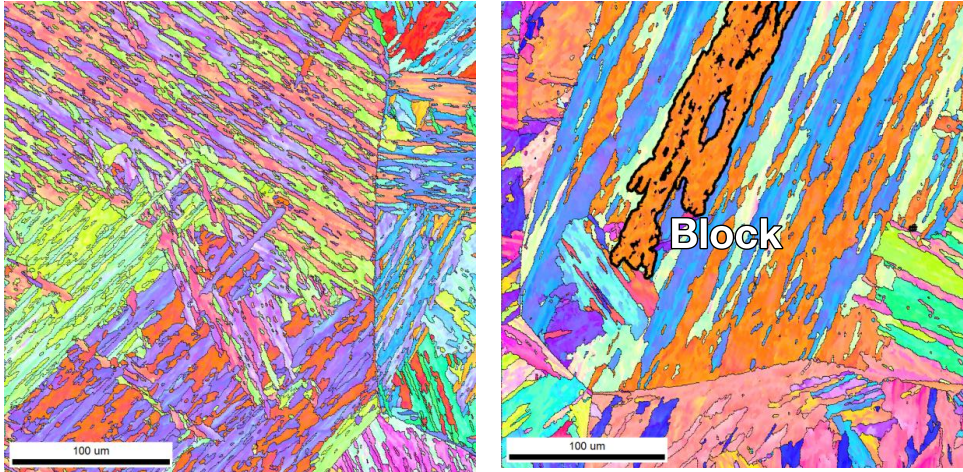
a.) IPF map for T570.   b.) IPF map for T516.
Fig. 4 Comparative IPF maps for T516 and T570.

The grain boundaries were split according their MO into 3 classes to measure their length and are shown as a histogram in Fig. 5 a.). Class 5°-15° are sub-grain boundaries, showing slight differences and will not be further discussed. The misorientation angle (MOA) class between 15°-50° is of small amount and mainly refers to PAG [10]. The class between 50°-65° [10], [11] mainly refers to high angle block boundaries. It exhibits the highest amount and show a difference of factor 2 between the two steels.
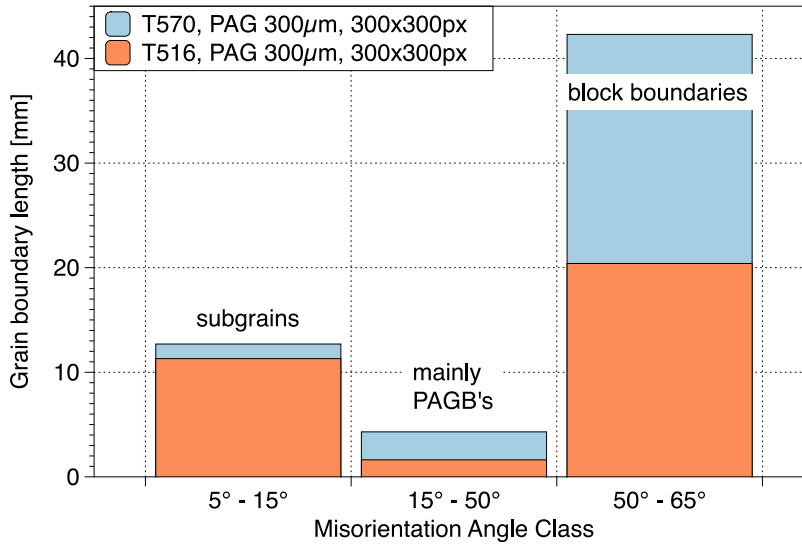
Fig. 5 MOA in the as HT condition for T570 and T516 at a PAG size of 300μm.

The creep behavior of T516 and T570 is shown in Fig. 6 a.). Comparing the PAG sizes for T570, it was found that a grain size of 300μm leads to the best creep behavior. Specimen 700μm T570 ruptured before 300μm T570 on a statistical basis of four creep tests for each condition. LOM observations on the fracture surfaces revealed show an intergranular fracture mechanism with a creep rupture strain of about 10%. From the creep curves, it can further be seen, that increasing the PAG size leads to a loss of the creep rupture ductility. Regardless of the PAG sizes, T570 shows shorter less creep rupture time t_r than T516. Comparing a PAG size of 50μm, T516 shows a five times longer t_r than T570. T516 specimen with PAG sizes of 100μm, 300μm and 700μm are still running.

Fig. 6 b.) displays the log creep rupture strain (ε_r) on the first- and the log Reduction of Area (RA) on the second y-axis versus the log PAG size for T570. Regression is carried out for ε_r of T570, suggesting a power law dependency of $\varepsilon_r = c\gamma^a$, where γ is the PAG size, c is a material constant and a is depending on the PAG size between 50μm – 700μm. From regression, the exponent a=-0.428 has been found which is close to -0.5 according to Hall-Petch.

185

By comparing Fig. 6 a.) with b.), it can be seen that the PAG size has the main influence on the ε_r (for $t_r < 3{,}000$h). For the RA, regression is not representative because RA approximates two times asymptotically the minimum and maximum ε_r.
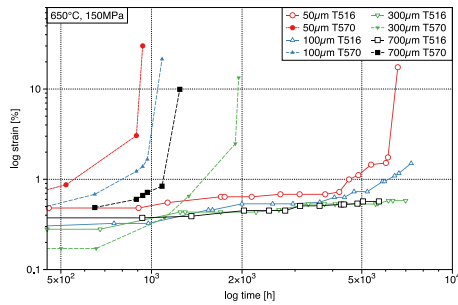
a.) Evolution of creep strain measured during interrupted creep tests at 650°C and 150MPa. T516 with 100µm, 300µm and 700µm are still running.
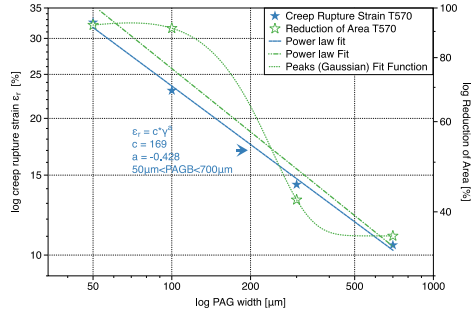
b.) Creep rupture ductility, and RA for different PAG sizes for ruptured specimen of T570.

Fig. 6 creep data comparison between T516 and T570.

Plotting the t_r versus the PAG size in Fig. 7 a.) shows that a PAG size of T570 between 200µm – 600µm leads to the longest t_r for T570. No conclusion can be drawn for the T516 as tests are still running but a similar behavior with much higher t_r can be expected.
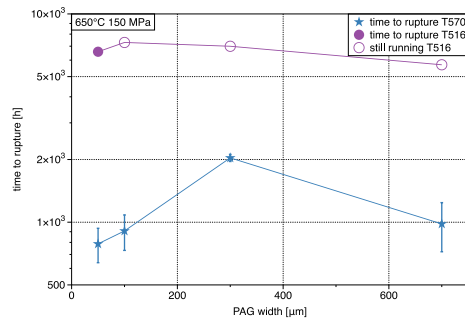
a.) Time to rupture versus PAG width.
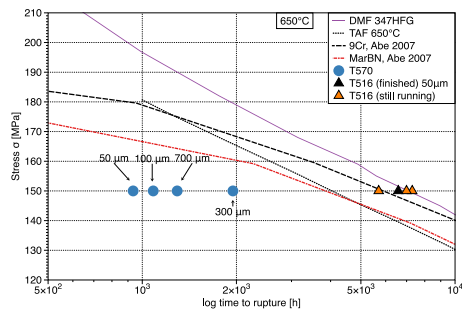
b.) T570, T516, TAF [12], 9Cr [13] and the MARBN [14] compared to Austenite DMF 347 HFG [15].

Fig. 7 Creep data comparison between T516 and T570.

Fig. 7 b.) compares the creep behavior at 650°C and 150MPa of different steels: a fine grained Austenite DMF 347HFG from [15], the TAF steel [12], [16], a low carbon and nitrogen optimized martensitic steel 9Cr–3W–3Co–V-Nb–0.05N [13], one of the latest developments of NIMS, and the two investigated T570, T516 steels. The comparison shows that T570 has a lower creep rupture strength of the classical MARBN steel of [14]. However, T516 reaches the DMF 347HFG at each PAG size, outperforming all other 9%Cr steels.

4. Summary and Conclusion

Two chemical compositions of MARBN steel from Böhler Edelstahl, namely T570 and T516 were heat treated with variations on the hardening time and temperature, producing four different PAG sizes. After the hardening, the samples were tempered two times at 700°C for 3h. The microstructure of T516 and T570 specimens was systematically analyzed with EBSD before creep exposure at 650°C and 150MPa.

The results show that:

i.)   T516 exhibits a lower grain boundary length, corresponding to lager block sizes than T570 which is mainly responsible for the improved creep rupture time.

ii.)   Creep rupture strain mainly depends on the PAG size (measured for t_r<3,000h), following a Hall-Petch type relationship.

iii.)   Creep rupture time t_r increases with increasing PAG size, with the maximum between 200µm<PAG size<600µm for steel T570.

iv.)   The MARBN steel T516 outperforms most comparable steels in the literature at each PAG size in the uniaxial creep test at 650°C and 150MPa.

v.)   T516 shows better creep rupture time at 650°C and 150MPa than the austenitic alloy DMV 347HFG, used for boilers.

T516 shows very promising results when compared to other creep resistant 9% Cr MARBN steels. Further creep tests at different temperatures and stress levels are needed to confirm the outstanding behavior.

5. Bibliography

[1]   A. J. Schwartz, M. Kumar, B. L. Adams, and D. P. Field, Eds., *Electron Backscatter Diffraction in Materials Science*, 2nd ed. Boston, MA: Springer US, 2009, p. 403.

[2]   S. Morito, H. Tanaka, R. Konishi, T. Furuhara, and T. Maki, "The morphology and crystallography of lath martensite in Fe-C alloys," *Acta Mater.*, vol. 51, no. 6, pp. 1789–1799, Apr. 2003.

[3]   H. Kitahara, R. Ueji, N. Tsuji, and Y. Minamino, "Crystallographic features of lath martensite in low-carbon steel," *Acta Mater.*, vol. 54, no. 5, pp. 1279–1288, Mar. 2006.

[4]   I. Holzer, *Modelling and Simulation of Strengthening in Complex Martensitic 9-12 % Cr Steel and a Binary Fe-Cu Alloy*, 2nd ed., no. May. Graz: Verlag d. Technischen Universität Graz, 2010, p. 165.

[5]   E. Kozeschnik, J. Svoboda, P. Fratzl, and F. D. Fischer, "Modelling of kinetics in multi-component multi-phase systems with spherical precipitates," *Mater. Sci. Eng. A*, vol. 385, no. 1–2, pp. 157–165, Nov. 2004.

[6]   S. Morito, H. Yoshida, T. Maki, and X. Huang, "Effect of block size on the strength of lath martensite in low carbon steels," *Mater. Sci. Eng. A*, vol. 438–440, pp. 237–240, Nov. 2006.

[7]   EDAX, "OIM." EDAX, Mahwah, N.J., USA, pp. 1–3, 2013.

[8]   H. Bhadeshia and R. Honeycombe, *Steels: Microstructure and Properties*, 3rd ed. Elsevier Ltd, 2006, p. 360.

[9]   S. Morito, X. Huang, T. Furuhara, T. Maki, and N. Hansen, "The morphology and crystallography of lath martensite in alloy steels," *Acta Mater.*, vol. 54, no. 19, pp. 5323–5331, Nov. 2006.

[10]   B. Sonderegger, "Charakterisierung der Substruktur in modernen 9-12% Cr Stählen mittels der EBSD Methode," 2005.

[11]   B. Sonderegger, S. Mitsche, and H. Cerjak, "Martensite laths in creep resistant martensitic 9–12% Cr steels — Calculation and measurement of misorientations," *Mater. Charact.*, vol. 58, no. 10, pp. 874–882, Oct. 2007.

[12]   F. Abe, T. Kern, and R. Viswanathan, *Creep-resistant steels*, 1st ed. Woodhead Publishing Limited, 2008, p. 700.

[13]   F. Abe, M. Taneike, and K. Sawada, "Alloy design of creep resistant 9Cr steel using a dispersion of nano-sized carbonitrides," *Int. J. Press. Vessel. Pip.*, vol. 84, no. 1–2, pp. 3–12, Jan. 2007.

[14]   F. Abe, "Precipitate design for creep strengthening of 9% Cr tempered martensitic steel for ultra-supercritical power plants," *Sci. Technol. Adv. Mater.*, vol. 9, no. 1, p. 013002, Mar. 2008.

[15]   S. M. S. T. GmbH, "DMF 347 HFG," 2008. [Online]. Available: http://www.smst-tubes.com/fileadmin/media/pdf_datasheets/smst_booklet_347HFG_2008.pdf. [Accessed: 01-Apr-2014].

[16]   M. Svoboda, A. Dlouhý, and I. Podstranská, "Microstructural changes in creep of TAF 650 steel at 650°C," in *Mezinárodní metalurgická konference*, 2000, pp. 2–9.

SIMULATION OF MICROSTRUCTURE AND MODELLING OF MECHANICAL PROPERTIES OF CB2 FLUX CORED WIRES WELD METAL

Authors: Schuler M.[1], Ramskogler C.[1], Baumgartner S.[2], Schnitzer R.[2], Enzinger N.[1]

Affiliations: [1]Institute for Materials Science and Welding, Technical University of Graz, Kopernikusgasse 24, 8010 Graz, Austria;
Email: monika.schuler@tugraz.at
claudia.ramskogler@tugraz.at
[2]voestalpine Böhler Welding Austria, Böhler-Welding-Straße 1, 8605 Kapfenberg, Austria;
Email: susanne.baumgartner@voestalpine.com

Abstract

The cast steel GX13CrMoCoVNbNB10-1-1 (CB2) developed in the European COST Projects shows the most promising properties for operating temperatures up to 620°C. Matching flux cored wires, mainly rutile with additional basic slag forming components, for welding this creep resistant steel, have been developed, too. Not only the creep properties but also the mechanical properties like impact toughness and tensile strength are of great importance for the qualification and application of the material in thermal power plants. These mechanical properties are in a close relationship to microstructural parameters like precipitates, dislocations or voids. Two different nickel content variants of the weld metal and two different post weld heat treatments have been investigated with regard to their impact on mechanical properties and microstructure. Results are presented in the paper.

Keywords: CB2 weld metal, flux-cored-wire, creep resistant steel, toughness, strength

1. Introduction

There is a large growth in the worldwide electricity demand and fossil energy is predicted to be one of the most important sources for power generation [1]. The 'International Energy Agency' has published in the 'World Energy Outlook 2013' different forecasts, how the energy demand in the next 20 years will develop – they are shown in Figure 1. It takes into account only policies enacted as of mid-2013. The 'New Policies Scenario' takes account of existing policies and declared policy intentions; and the '450 Scenario' shows an energy pathway compatible with a 50% chance of limiting the long-term increase in average global temperature to 2°C.

The report shows further that the transition away from fossil fuels will take considerable time to achieve [1]. Until then a proper improvement of efficiencies in fossil fuel power plants is not only to cover economical interest, but should also decrease the emissions of CO_2.
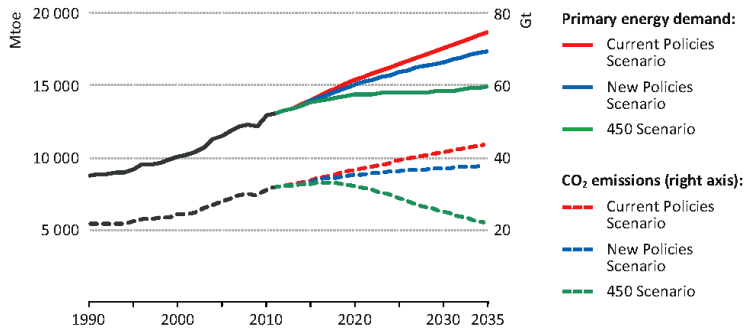
Note: Mtoe = Million tonnes of oil equivalent; Gt = gigatonnes.

Figure 1 : World primary energy demand and related CO$_2$ emissions by different scenario [1]

The power generation industry is in charge to take materials which allow higher steam temperature and pressure, to reach these aims. Through improvements in the group of the 9% Cr steels during the COST project [2], steam temperatures up to 620°C in the family of creep resistant steels, are nowadays states of the art.

For the production of heavy castings for power stations, welding processes are an important part of the manufacturing procedure. A rutile, matching CB2 flux-cored wire was developed for this purpose. It has to reach the excellent creep properties of the cast base material where among other microstructural features a large PAG (prior austenite grain size) assures the creep resistance. The weld metal of the flux cored wire and its creep properties in 'short- and midterm tests' have been investigated. Results considering a variation of the nickel content are published in welding in the world [3].

The focus of this contribution is the simulation of microstructure and on first attempts of modelling mechanical properties based on experimental data. A varying Ni-content is taken into account as well as the development of the microstructure of the weld metals. Tensile tests at room temperature and impact toughness tests in a broad temperature range for this martensitic 9% Cr weld metals have been carried out, because sufficient impact toughness must be achieved for material qualification processes.

2. Material

2.1. Chemical Composition

Mechanical properties tests of the base material CB2 and of two filler metal compositions with different nickel contents have been carried out. The chemical composition of a CB2 trial melt has been taken from the PhD Thesis Schaffernak [4] and is listed in the first line of Table 1. The nominal chemical composition of the weld metals are listed in lines two and three of the same table [3]. The nickel content of the weld metal was varied to investigate its influence on the mechanical properties with focus on the Charpy-V-impact toughness.

Material	C	Mn	Cr	Mo	Si	Ti	Ni	Nb	N	V	Co	B
CB2	0.12	0.88	9.20	1.49	0.20	0.002	0.17	0.06	0.02	0.21	0.98	0.011
WM 1	0.10	0.90	9.0	1.50	0.20	0.03	0.2	0.03	0.02	0.2	1.0	0.005
WM 2	0.10	0.70	9.0	1.40	0.20	0.03	0.7	0.03	0.02	0.2	1.0	0.006

Table 1 : Chemical composition of the CB2 base metal and the nominal chemical composition of two different weld materials, all values in wt%

2.2. Welding Procedure

CB2 base metal plates of 20 mm thickness with U shaped weld preparation were filled with two different CB2 flux-cored-wires by multilayer welding. The new formed weld metals thereby were produced as joining weld (neglecting a root pass). The used welding parameters are given in [5].

Samples were taken in 'as welded' condition and after post weld heat treatment of 730 C/8h and 730°C/24h, respectively. The sample grid is shown in Figure 2.
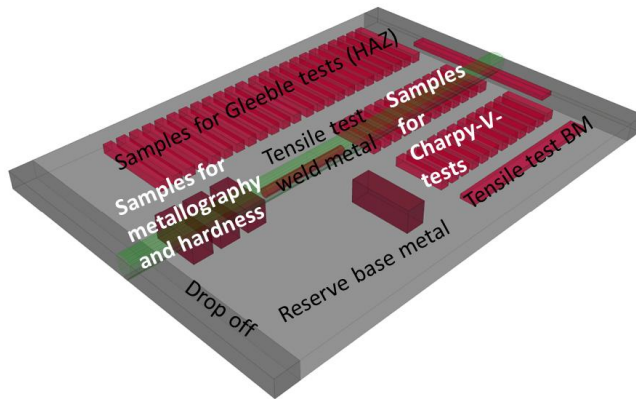
Figure 2 : Schematic view of welded plate with sample grid.

The Gleeble tests for simulating the heat affected zone (HAZ) and for studying the influence of welding parameters on the mechanical properties of HAZ were conducted in the frame of the diploma thesis of Sarić [6].

3. Experiments and Results

All tests performed on the two weld metals and on base metal are shown in Table 2. To avoid confusion, the Gleeble-simulated HAZ tests are not listed in this table.

Microscopic investigations and MatCalc simulations of the BM in different creep conditions have been done by Ramskogler [7]. Comparisons between BM, HAZ and WM1 of the crept samples are already published [8].

Material	"as welded"	PWHT short (730°C/8h)	PWHT long (730°C/24h)	Crept samples (625°C/~6500h)
CB2 Base metal (BM)	Mech. tests, LOM, SEM, MatCalc			LOM, SEM, EDX, MatCalc [7]
Weld metal 1	Mech. tests, LOM, SEM, TEM, MatCalc			LOM, SEM, EDX, TEM, MatCalc
Weld metal 2				

Table 2 : Test matrix of base metal and the two weld metals under different treatment conditions. LOM...light optical microscopy; SEM...scanning electron microscopy, EDX... energy dispersive X-ray spectroscopy, TEM... transmission electron microscopy; MatCalc [9]...numerical precipitation simulations

The focus for the next pages is to compare the two different weld metals in two different PWHT states.

3.1. Mechanical tests

In general, the 'as welded state' is not comparable to the 'finished' heat treated material or the base material in regard to the mechanical testing, because the fresh martensitic structures without any tempered regions are extremely hard and brittle. For that reasons, weld metal without treatment, for creep resistant steels, cannot be used in industrial applications.

3.1.1. Tensile Tests

A comparison of the two weld metals with base metal after PWHT is depicted in Figure 3. Just three measurements of the BM are compared; the two with the shorter fracture elongation were measured after a long PWHT and that one with the highest strength were measured after a short PWHT.
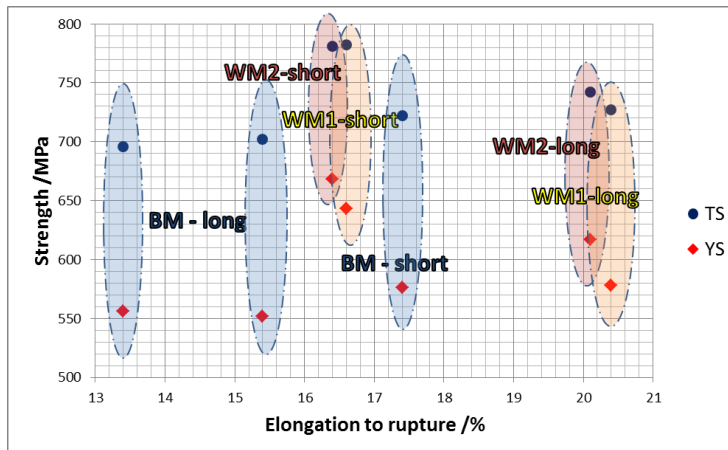
Figure 3 : Tensile strength (TS) and yield strength (YS) on y-axis of base metal and weld metals, in relation to their elongation to rupture values on x-axis

Weld metals with short treatment show less fracture elongation and have higher strength values compared to weld metals with longer PWHT. The tested base metal has the lowest fracture elongation as well as the lowest strength level. Exception is the base metal sample

with short treatment. Here, the tensile strength and the yield strength are on the same level as on sample WM1-long and the fracture elongation is even higher, as it is on short treated weld metal samples. The differences in fracture elongation between the two weld metals are rather small, but a longer treatment shifts the fracture elongation - systematically to higher values.

3.1.2. Toughness tests

Toughness was mainly measured by using the Charpy-V-impact-test procedure. The used testing apparatus (300J max energy) is instrumented. Instrumentation details: In the hammer fin inside, resistance strain gauges (RSG) are implicated. The received signal is forwarded into the bridge circuit of a transient recorder with a measuring rate of 1MS/s (MegaSamples/second), transformed into a load value and recorded. Displacement measurement is positioned directly under the sample position and carried out through an eddy current sensor; these data are also recorded from the transient recorder.

Charpy-V-tests have been done for a broad range of testing temperatures, because it's well known, that the martensitic-ferritic bcc (body-centred-cubic) structure has a distinct transition region. This means that the amount of energy, the material can absorb and convert into plastic deformation before it breaks, is much lower at low temperatures. In Figure 4 (left), four measured Charpy-V-test series from -50°C to +160°C and their approximated sigmoidal shaped curves [10] are shown. Weld metals 1 and 2 in the two different post weld heat treatment conditions (short and long) are compared.

As expected, the highest impact values and the lowest transition temperatures are reached with a longer post weld heat treatment (PWHT). Additionally, it can be seen, that in all two PWHT cases, the higher Ni-variant (WM2) reveals higher impact values and lower transition temperatures compared to WM1.
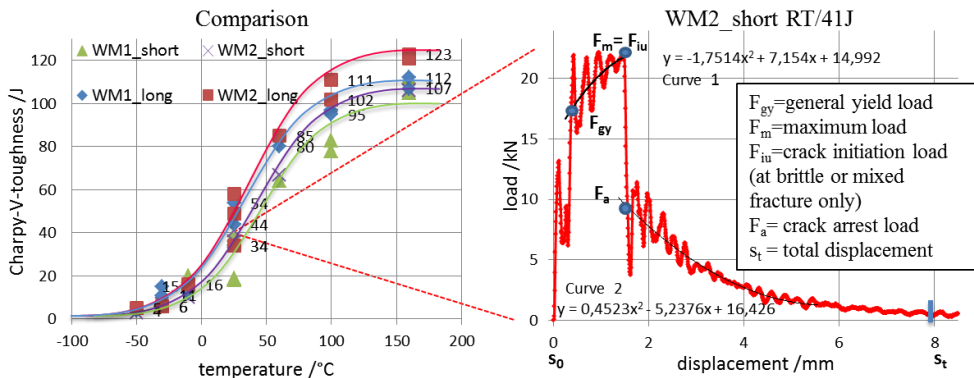
Figure 4 : (Left): Impact toughness values of WM1 (weld metal 1) with low nickel content and WM2 (weld metal 2) with high nickel content and two different PWHT conditions (8h/730°C – short; 24h/730°C – long) are compared over a temperature range from -50°C to 160°C. (Right): One instrumented measurement at RT with 41J, evaluated acc. [11]

The toughness improving nature of nickel is well known [10]; one possible reason for this effect is the grain and structure fining behaviour of this element. Grain size measurements of

the normalized regions of the weld metals, show a difference of 25% between the weld metals; WM1 is coarser than WM2. The finer the grain is, the higher the toughness rises.

During all Charpy-V tests, load-displacement curves have been recorded and evaluated – see Figure 4 (right). Evaluation of characteristic forces was carried out according EN ISO 14556 [11]. So, more information about fracture behaviour than in a regular Charpy-V test can be obtained [12]. The integral under the curve represents also the absorbed energy. Additionally, a relation to the crack initiation and crack arrest can be drawn [13].

In weld metals with long heat treatment, fracture toughness tests with single-edge bend (SEB) samples according ASTM E 1820-08 [14] have been carried out. These results are already presented [15].

3.2. Metallography

In addition to light optical microscopy (LOM) also different electron microscopy investigations have been done. Several pictures of LOM are published in [3]. Under the light microscope no significant differences can be found related to nickel content or PWHT.

3.2.1. Scanning electron microscopy (SEM), energy dispersive X-ray spectroscopy (EDX)
On the one hand, polished and etched microsections have been investigated and on the other hand, fracture surfaces of broken Charpy-V-samples were studied in detail under the scanning electron microscope. The most ductile and tough specimen (test at 160°C sample temperature) of both weld metals are depicted in Figure 5 and Figure 6.
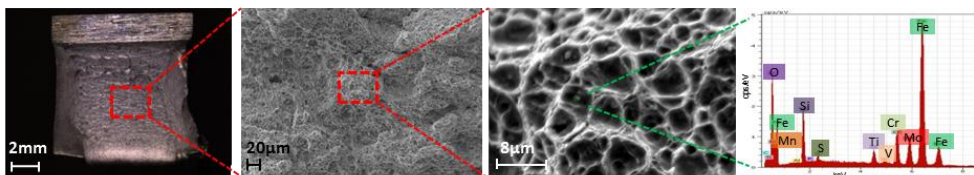
Figure 5 : Fracture Surface of WM1-short tested at 160°C with SEM studies of the very ductile fracture and an EDX scan of a representative particle, Charpy-V-toughness: 105 J
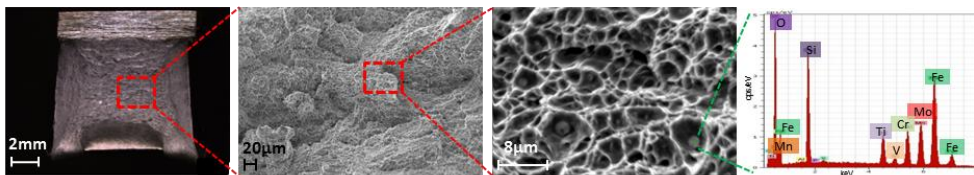
Figure 6 : Fracture Surface of WM2-short tested at 160°C with SEM studies of the very ductile fracture and an EDX scan of a representative particle; Charpy-V-toughness: 106 J

All samples tested at high temperatures, show a ductile fracture with macroscopic shear lips and dimples on the fracture surface. In these dimples particles or inclusions can be seen. EDX spectroscopy revealed that they are mostly oxides with background iron signals. SiO_2 as well as mixed oxides with Mn, Si and Ti [16] were found in the fracture dimples.

3.2.2. Transmission electron microscopy (TEM),

The TEM investigations have been carried out with the energy filtered (EFTEM) method. Additionally, EDX and EELS investigations were performed for characterisation of precipitates. Some EFTEM images of the 'as welded' WM1 are depicted in Figure 7.
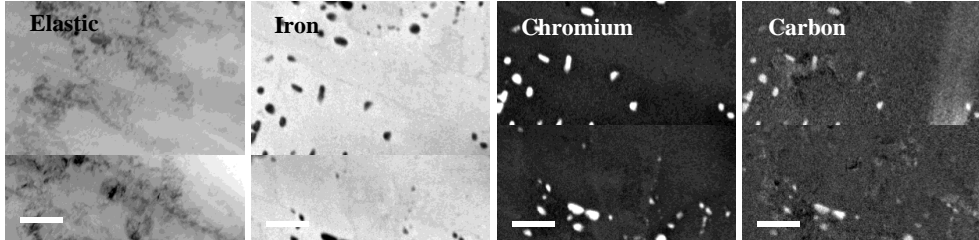
Figure 7 : EFTEM Images of WM1 in the as welded condition with Cr-carbides

First image is of elastic scattered electrons. With the possibility to filter the energy-wavelength the different elements can be distinguished. The matrix consists of iron – this can be seen on the bright 'iron-image'. The precipitates are Cr-carbides, as it can be seen on the chromium and carbon image. In this contribution, just the as welded condition is shown, because the work is still in progress.

3.3. Simulation

The precipitate evolution can be simulated with the thermo-kinetic software MatCalc [9]. The used CALPHAD based thermo-dynamic databases for equilibriums and kinetic simulations are a development 'prebeta' product from the MatCalc team [17] at the Technical University Vienna. Calculation results are discussed and compared with experimental findings in the next section.

4. Discussion and Comparison

4.1.1. Microstructure WM1 simulated and TEM investigated after welding

The precipitation evolution simulation of the welding process of WM1 is depicted in Figure 8 and compared with the evaluated TEM measurements.
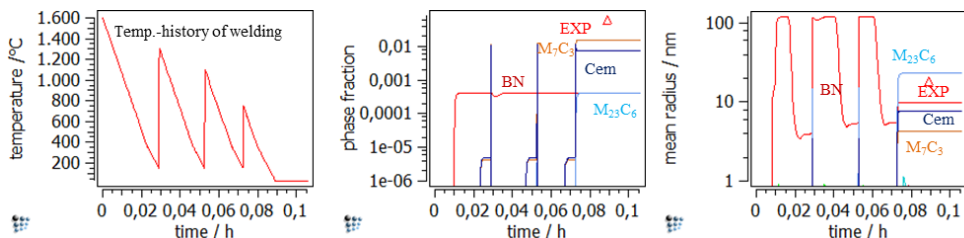
Figure 8 : Precipitation simulation of multilayer welding, WM1 with comparison of the measured Cr-carbide values (red triangles), concerning the phase fraction and the mean radius of precipitates

The calculation underestimates the phase fraction a bit, or the measured and evaluated TEM data overestimate the Cr-carbide phase fraction, because only very small regions are investigated using TEM, questioning the statistical significance. The mean radius is in a good correlation. Experimentally a mean radius of 18.5 nm was measured whereas the calculated value of $M_{23}C_6$ is 23 nm. After welding simulation, most of the precipitates are carbides ($M_{23}C_6$, M_7C_3 and cementite), just a small amount of boron-nitrides reveals.

4.1.2. Microstructure WM1 and WM2 after PWHT

After PWHT, the cementite has dissolved completely but the M_7C_3 carbides are still stable. The $M_{23}C_6$ carbides grow during heat treatment in quantity (from 0.04 to 0.54 – WM1) and in extension (from 23nm to 384 nm – WM1), as it can be seen in Table 3.

Phase fraction /%	$M_{23}C_6$	M_7C_3	BN	NbC	VN	Matrix (ferrite)
WM1	0.54	1.78	0.04	0.01	0.00	97.62
WM2	1.46	0.63	0.07	0.00	0.00	97.84
Mean radius /nm						
WM1	384	196	121	179	0	
WM2	319	160	195	163	0	

Table 3 : Comparison of phase composition and mean radius of precipitates of the two weld metals after long PWHT

There are differences between the two weld metals in forming and developing carbides. The MX precipitates have small quantities; they grow and coarsen slowly in both weld metals. BN is neither large nor in great quantities, in both metals, but it has a tendency to coarsen fast. In simulation BN arise in small quantities, but the ongoing experimental investigations show no indication for boron nitrides in these weld metals at all.

5. Conclusion

Based on the observations presented in this contribution, the following conclusions can be drawn:

5.1.1. Strength and fracture elongation
Weld metals with short PWHT have higher strength values and less fracture elongation compared to weld metals with longer PWHT.

5.1.2. Toughness
- Highest impact values and lowest transition temperatures are reached with a longer PWHT. Also a higher Ni-content (WM2) reveals higher impact values and lower transition temperatures, compared to the lower Ni-content (WM1).
- The finer the grain size of the matrix is, the higher the toughness rises.
- Experimental values of regular and instrumented Charpy-V-tests have been evaluated, some connections with the microstructural behaviour has been shown, e.g.dimples with inclusions in ductile fracture surfaces.

5.1.3. Microstructure

In the 'as welded' state of WM1, EFTEM investigations revealed a dominance of Cr-carbides. Numerical precipitate simulations executed with MatCalc, confirmed this development.

6. Outlook

- The relation between precipitate-status and yield strength, based on precipitation strengthening and solid solution strengthening, is well known and discussed in literature [18, 19]. So in a next step, with trustworthy simulations, some strength parameters can be derived in this ongoing work.
- Through known damage and toughness models from literature [20-22] and new approaches, connections between microstructural parameters as precipitates, inclusions and dislocations will be drawn and a prediction of the toughness should be enabled.
- Microstructural precipitate considerations will not sufficiently describe the material in view to toughness considerations. Here, in a 'next' approach, other parameters as dislocations must be taken into account.

7. Acknowledgement

8. Literature

[1] IEA, *World Energy Outlook 2013*, 2013.

[2] M. Staubli, R. Hanus, T. Weber, Mayer K-H., Kern T-U., *The European efforts in development of new high temperature casting materials, COST 536* Proceedings of the 8th Liège Conference. European Commission, Université de Liège, (Part II), vol. Vol. 53, pp. 855-870, 2006.

[3] M. Schuler, S. Baumgartner, R. Schnitzer, N. Enzinger, *Creep investigation and simulation of CB2 joints using similar rutile CB2-flux cored wire;* Welding in the World, DOI: 10.1007/s40194-014-0169-0, 2014.

[4] B. Schaffernak, *Charakterisierung von 9 - 12 % Cr-Stählen mittels thermodynamischer Modell-rechnungen,* PhD Thesis, Graz University of Technology, pp. 227 Bl., 2000.

[5] S. Baumgartner, M. Schuler, R. Schnitzer, N. Enzinger, *Influence of Nickel on the Mechanical Properties of a CB2 Flux Cored Wire Weld Metal,* Proceedings of the 10th Liège Conference, 2014.

[6] A. Sarić, *Charakterisierung der Wärmeeinflusszone von Mehrlagenschweißungen,* TU-Graz, IWS, diploma thesis, 2014.

[7] C. Ramskogler, *KW50+ Untersuchungsberichte zu den Arbeitspaketen,* interne Untersuchungs-dokumentation, Graz, vol. J1U1, 2013.

[8] S. Baumgartner, M. Schuler, C. Ramskogler, E. Schmidtne-Kelity, A. Sarić, R. Schnitzer, C. Lochbichler and N. Enzinger, *Mikrostrukturentwicklung von CB2 Fülldraht-Schweißungen, 36. Vortragsveranstaltung; Düsseldorf, am 22.11*.2013

[9] E. Kozeschnik, *http://matcalc.tuwien.ac.at/ Documentation and Examples* Vienna, vol. 2013.

[10] G. Hofer, C.C. Hung and Ü. Günes, *Eine mathematische Funktion für die Beschreibung der Ergebnisse aus Kerbschlagbiegeversuchen*, Materialwissenschaft und Werkstofftechnik, vol. 8, no. 4, pp. 109-111, 1977.

[11] ÖNORM EN ISO 14556, *Stahl - Kerbschlagbiegeversuch nach Charpy (V-Kerb) - Instrumentiertes Prüfverfahren,* ON-K 021, Stahl und Eisen, vol. EN ISO 14556, 2007.

[12] S. Münstermann, W. Bleck, P. Langenberg, *Mikromechanische Modellierung der Hochlagenzähigkeit von normalisierten und vergüteten hochfesten Feinkornbaustählen.* 20. Aachener Stahlkolloquium Werkstofftechnik "Zukunft für Stahl - Stahl ist Zukunft", 17.-18.03.2005, Aachen, pp. 145-157, 2005.

[13] W. Böhme, *Möglichkeiten und Grenzen des instrumentierten Kerbschlagbiegeversuchs ? Ergebnisse eines Ringtests*, Materialwissenschaft und Werkstofftechnik, vol. 32, no. 6, pp. 520-524. 2001.

[14] ASTM E 1820-08, *Standard Test Method for Measurement of Fracture Toughness,* ASTM International, vol. E 1820-08, 2008.

[15] M. Schuler, S. Baumgartner, R. Schnitzer, N. Enzinger, *Modelling mechanical properties of 9% chromium weld metals,* IIW Intermediate Meeting, Doc. II-C-465-14, 2014.

[16] K. Seo, Y.-M. Kim, G.M. Evans, H.-J. Kim, C.-H. Lee, *Formation of Mn-depleted zone in Ti-containing weld metal,* IIW Intermediate Meeting, Doc. IX-L-1122-14, 2014.

[17] E. Povoden-Karadeniz, *Thermodynamic and diffusion mobility databases mc_fe_v2.019.tdb and mc_fe_v2.005.ddb for thermokinetic precipitation simulations using MatCalc.* Vienna, unpublished results, 2014.

[18] I. Holzer, *Modelling and simulation of strengthening in complex martensitic 9-12% Cr steel and a binary Fe-Cu alloy*, PhD Thesis, Graz University of Technology, 2010.

[19] B. Sonderegger, *Charakterisierung der Substruktur in modernen Kraftwerkswerkstoffen mittels der EBSD Methode,* PhD Thesis, Graz University of Technology, pp. 306 S., 2005.

[20] V. Tvergaard, A. Needleman, *Effect of material rate sensitivity on failure modes in the Charpy V-notch test*, J.Mech.Phys.Solids, vol. 34, no. 3, pp. 213-241. 1986.

[21] F.M. Beremin, *Cavity formation from inclusions in ductile fracture of A508 steel,* Metall Trans A, Phys Metall Mater Sci, vol. 12 A, pp. 723. 1981

[22] G. Rousselier, *Ductile fracture models and their potential in local approach of fracture*, Nucl.Eng.Des., vol. 105, no. 1, pp. 97-111. 1987

EFFECT OF TEMPERING CONDITION ON CREEP STRENGTH AND MICROSTRUCTURE IN HIGH CR STEEL ROTOR FORGINGS FOR STEAM TURBINES

M. Mikami [1), K. Sawada [2), S. Kobayashi [2), T. Hara [2), and K. Kimura [2)

[1) Japan Casting & Forging Corporation
46-59 Nakabaru Sakinohama, Tobata-ku Kitakyushu, Fukuoka 804-8555, Japan,
masato_mikami@jcf.co.jp
[2) National Institute for Materials Science
1-2-1 Sengen, Tsukuba, Ibaraki 305-0047, Japan

Abstract

In order to investigate a possibility of improvement in long-term creep strength of high Cr steel rotor forgings by means of higher temperature tempering treatment, creep rupture tests and microstructural investigations were performed with specimens taken from a COST type "E", X12CrMoWVNbN 10-1-1, material large forging subjected to normalizing and tempering heat treatments with final tempering at 690 °C with and without additional tempering at 730 °C. Creep rupture strength of the specimens subjected to the additional tempering heat treatment is lower than that of the samples without the additional tempering over the stress range examined. As the results of microstructural investigations, cell-like structures considered to be caused by progress in recovery of tempered martensitic microstructure was appeared prominently in the steel subjected to the additional tempering in comparison with the steel without the additional tempering. Microstructural evolution during creep exposure and corresponding creep deformation behaviour is influenced by such differences in initial microstructure in the as heat treated condition. Regarding precipitates, number density of M_2X particles was reduced by the additional tempering in contrast to increase in that of VX particles, and the size of both precipitates was increased with the additional tempering. Formation of Z-phase was recognized after creep exposure about 10,000 h at 600 °C in the specimens subjected to the additional tempering whereas the precipitation was not found after creep exposure for about 28,000 h at 600 °C in the materials without the additional tempering. Formation and growth of Z-phase is also considered to be influenced by such difference in proportion of the precipitates in the as heat treated condition.

Keywords: 9-12%Cr steels; turbine rotors; forgings; heat treatment; microstructure

1. Introduction

High chromium steel rotor forgings are very important components relevant to stable service as well as thermal and electric power generating efficiency in fossil fuel power plants. A lot of research activities on alloy design of those steels has been conducting for further improvements in creep strength, with the aim of reducing CO_2 emissions and fuel consumption [1,2]. While manufacturing process, particularly heat treatment conditions control the microstructure of those materials, nevertheless influences of the processes on microstructure and creep strength are still unclear. In the case of 12Cr steel boiler materials, Iseda et al. reported that a higher temperature tempering treatment suppresses remarkable

deterioration of microstructure during creep exposure, thereby improving long-term creep strength [3]. Based on the results, the present work is intended to investigate a possibility of improvement in long-term creep strength of high Cr steel rotor forgings by means of higher temperature tempering conditions. We have examined creep rupture tests and microstructural evolution with the specimens taken from a COST type "E", X12CrMoWVNbN 10-1-1 steel large trial forging manufactured through the process similar to the products. Those samples were subjected to various additional tempering heat treatments for our study. This paper describes the results of those investigations and discussion on the effects of higher temperature tempering conditions on creep strength and microstructural change during creep exposure.

2. Experimental procedures

A trial rotor forging for investigations was made from an ingot with the weight of 69.5 metric ton [4]. Specimens examined were taken from the center position of the forging barrel having 1290 mm in diameter after quality heat treatments. Chemical composition of the samples is shown in Table 1. In the quality heat treatment process, the forging was solution treated at 1090 °C and quenched in oil followed by double tempering at 570 °C and 685 °C. After sampling and primary mechanical tests, final tempering heat treatment at 690 °C was decided to adjust the target 0.2% yield stress of about 750 MPa. Additional tempering treatment at 730 °C was done to investigate a possibility of improvement in creep strength by means of higher temperature tempering treatment. Materials for tests were subjected to these two type further tempering conditions, one consists of final tempering heat treatment at 690 °C (steel FT), and the another is composed of the final tempering treatment followed by the additional tempering at 730 °C (steel AT). Those heat treatment cycles for the specimens including the quality heat treatments for the trial rotor forging are shown in Figure 1. Tensile properties of the materials tested after those tempering heat treatments are summarized in Table 2.

Table 1: Chemical composition of materials studied. (mass %)

C	Si	Mn	P	S	Ni	Cr	Mo	W	V	Nb	N
0.13	0.07	0.44	0.009	0.001	0.78	10.52	1.07	1.03	0.20	0.052	0.054
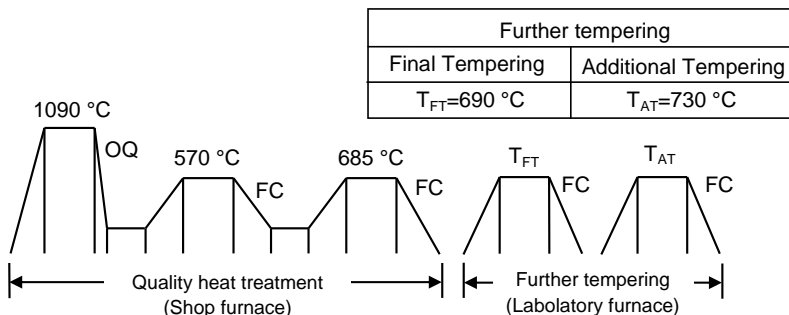
Figure 1: Heat treatment cycles of specimens examined.

Dimension of creep test specimen is 5.5 mm – 7.1 mm in diameter and 25 mm in gage length, the testing temperature is 600 °C. Microstructural observation was performed by optical microscope, transmission electron microscope (TEM) and scanning electron microscope (SEM) equipped with electron back scattered diffraction (EBSD) system. Analyses of precipitates with carbon extracted replicas were examined by scanning transmission electron microscope (STEM) with energy dispersion X-ray (EDX) analyzer.

Table 2 : Results of tensile tests on materials examined.

Steel	Testing temperature	0.02%YS (MPa)	0.2%YS (MPa)	TS (MPa)	El (%)	RA (%)
FT	RT	650	744	870	19	57
	600 °C	292	368	451	25	81
AT	RT	474	535	712	29	69
	600 °C	221	274	346	32	88

3. Results and discussion

3.1 Creep strength of the steels

Figure 2 provides a comparison of creep rupture strength and rupture ductility on the both steels. Change in slope of the stress versus time to rupture curve to be steeper in the long-term is observed on both steels, and that is observed at higher stress level for the steel FT in accordance with the difference in 0.2% yield stress of the steels, while the difference in creep rupture strength is reduced with decrease in applied stress. Ductility of the steel AT is higher than that of the steel FT and the difference also decreases with increase in creep exposure time, though remarkable drop in ductility observed in high Cr steel boiler materials is not recognized for the both steels.
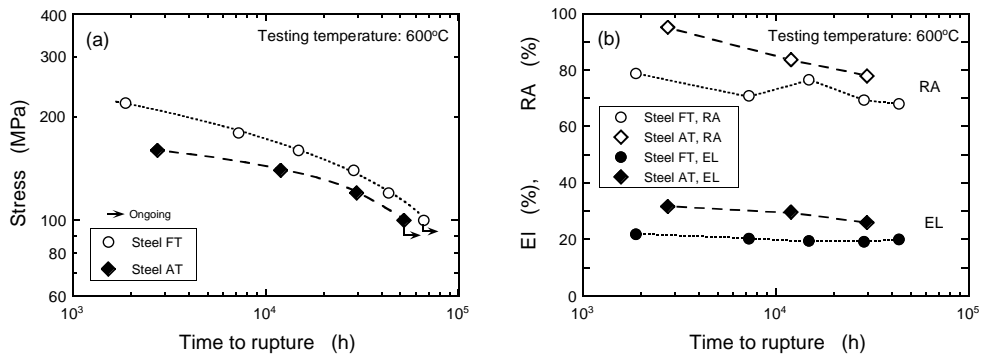
Figure 2 : Comparison in creep strength and creep rupture ductility between steel FT and AT.

201

3.2. Microstructure after heat treatments

Figure 3 demonstrates the optical micrographs of the specimens after the final tempering with and without the additional tempering heat treatments. Tempered martensitic structures are observed and no delta and proeutectoid ferrite is found on them. Prior austenite grain size numbers are 1.9 for both steels according to the ASTM method. TEM images of thin foils after the final tempering with and without additional tempering heat treatments are shown in Figure 4. Fine martensitic lath structures containing high density and uniformly distributed dislocations are recognized in the steel FT, while coarsened lath, partially cell-like sub-grain structures and lower dislocation density due to higher temperature tempering treatments are found on the steel AT. There are large oval shape lath boundary particles about 50 to 200 nm in diameter.
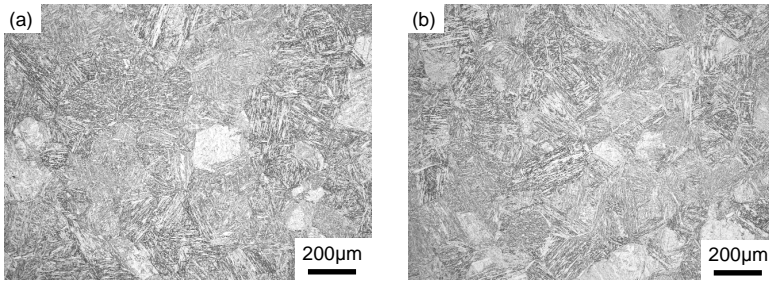
Figure 3 : Optical micrographs of specimens after final tempering treatment in steel FT (a) and additional tempering treatment in steel AT (b).
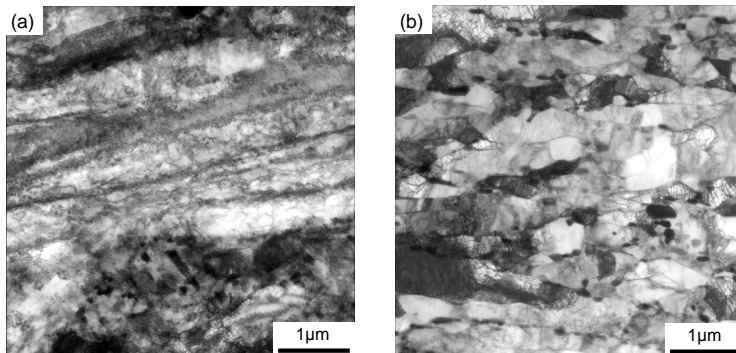
Figure 4: TEM bright field images of thin foils after final tempering treatment in steel FT (a) and additional tempering treatment in steel AT (b).

Figure 5 displays the bright field images and composite elemental maps of extracted replicas after the final tempering with and without the additional tempering heat treatments. The composite maps are obtained from the elemental maps for Cr, V and Nb, thereby indicating $(Fe,Cr)_{23}C_6$ in red color, $(Cr,V)_2X$ pink, NbX green and VX blue as shown in Figure 5 (b) and

(d). There are a lot of $M_{23}C_6$ particles, a few M_2X and vanadium rich VX precipitates and no fine niobium rich NbX on both steels. Table 3 is summary of average diameter of these particles and number ratio of VX to M_2X observed on the replicas. Sizes of $M_{23}C_6$ are almost same for both steels, whereas those of M_2X and VX in the steel FT are smaller in comparison with the steel AT. In addition, number fraction of VX to M_2X in the steel AT is higher than that in the steel FT, and additional tempering temperature has an influence on the precipitation behaviour. These microstructural investigations results in that the additional tempering at 730 °C promotes progression of martensitic lath recovery, precipitation of VX and coarsening of M_2X.
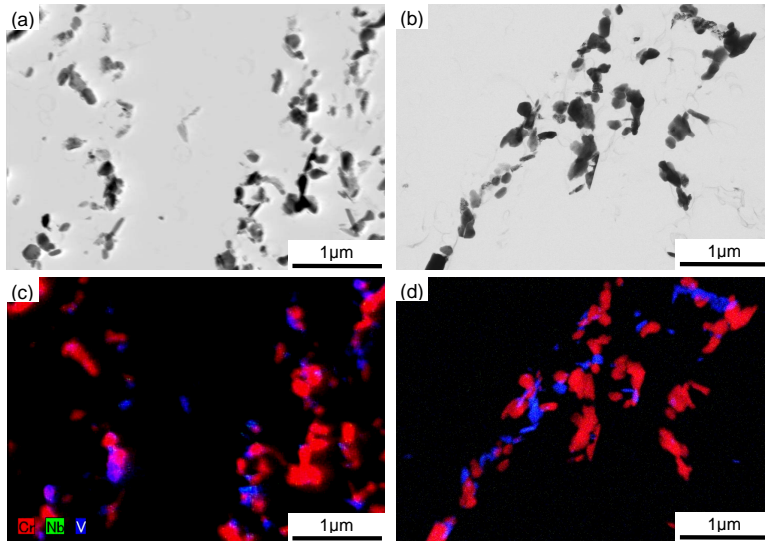
Figure 5 : TEM bright field images and elemental maps with extract replicas after final tempering treatment in steel FT (a), (c) and additional tempering treatment in steel AT (b), (d).

Table 3 : Summary of average diameter of particles and number ratio of VX to M_2X observed on the replicas after additional tempering heat treatments.

Steel	Average diameter (nm)			Number ratio
	$M_{23}C_6$	M_2X	VX	$N_{VX}/(N_{VX}+N_{M2X})$
FT	197	58	38	0.24
AT	194	86	51	0.64

3.3. Microstructure after creep exposure

Figure 6 shows TEM images of the thin foils after creep rupture. Martensitic laths widths and cell-like sub-grain sizes increase and dislocation densities gradually decrease with increase in creep exposure time for both steels. Figure 7 demonstrates preferential recovery of the lath

structure observed in the specimens creep-ruptured for the both steels. Coarsened sub-grains with the width of about 2 μm are found in the sub-micro size martensitic lath structure as indicated with arrows in Figure 7, and the martensitic lath recovery, hence, progresses accompanying the preferential recovery with increase in creep exposure time.

(a) Steel FT, t_r =28,500h

(b) Steel FT, t_r =43,300h

(c) Steel AT, t_r =11,900h

(d) Steel AT, t_r =29,500h
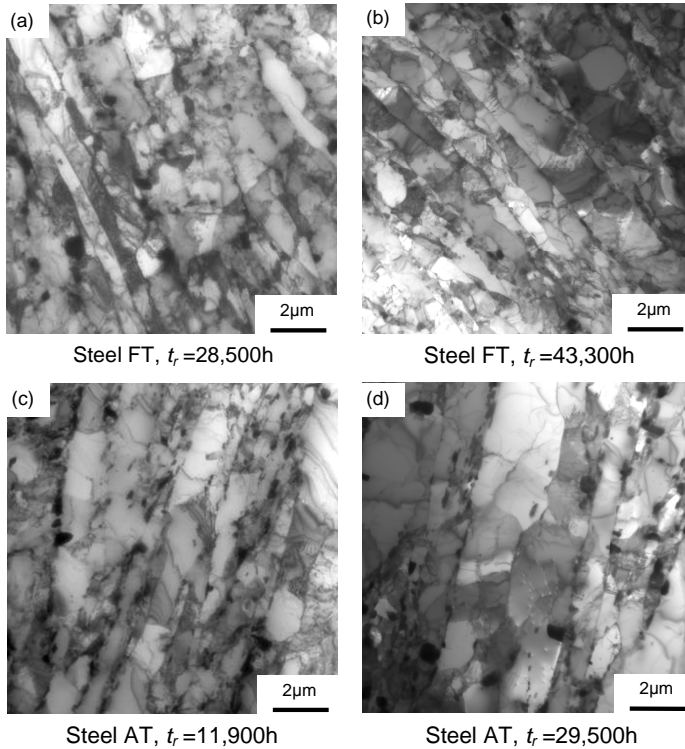
Figure 6 : TEM bright field images of thin foils after creep rupture for both steels.
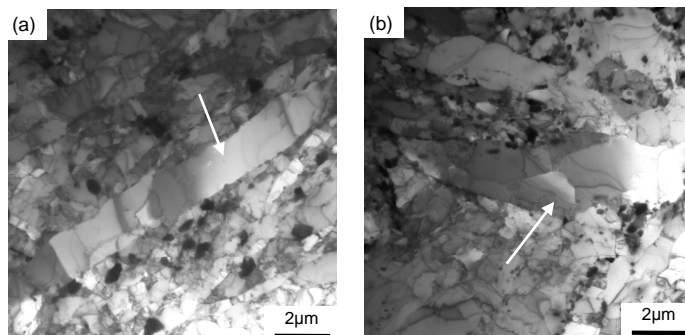
Figure 7 : Preferential recovery of lath structures in specimens creep ruptured at 43,300 h on steel FT (a) and at 29,500 h on steel AT (b).

We performed the microstructural observations with EBSD mounted on SEM to investigate the behaviour of lath structure recovery in the large areas. Figure 8 shows boundary maps on the specimens after creep rupture under the applied stress conditions of 120 MPa for both steels. A line in white and that in yellow indicate the boundary with lower angle ranging from 0.5° to 5° and higher angle 5° or more, respectively, thereby describing an area with dense white lines as a region having fine martensitic lath structures and black areas with low density white lines as a region where martensitic lath recovery progressed. Fraction of black area extended towards interior of prior austenite grains in the steel AT is higher than that in the steel FT. In addition, there are some black areas where preferential recovery seems to exist near the prior austenite grain boundaries and the proportion of those black regions in the steel AT is also larger than that in the steel FT. Recovery of martensitic lath structure, therefore, is encouraged under the influence of initial microstructure in the as heat treated condition.
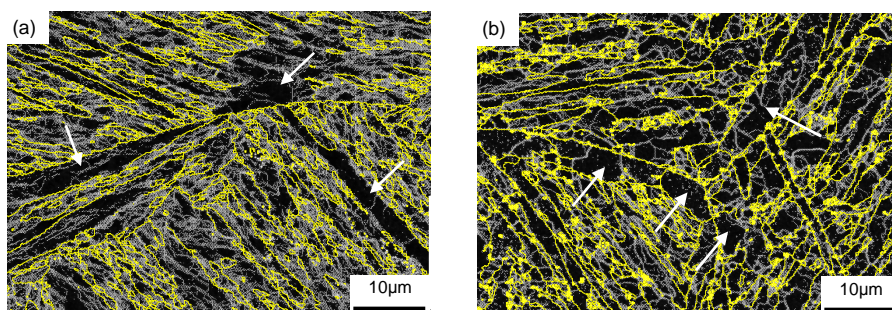
Figure 8 : Boundary maps after creep exposure for 43,300h in steel FT (a) and for 29,500 h in steel AT (b).

Figures 9 and 10 show TEM bright field images and elemental maps of the extract replicas after creep rupture for the both steels. Elemental maps of Fe and W are overlaid on the composite maps, thereby Laves phase is indicated by yellow. Laves phase are already detected in the specimens ruptured after about 1,000 h for both steels. M_2X particles in pink still exist at 43,300 h and 29,500 h for steel FT and AT, respectively, and the size of the particles gradually increases up to approximately 350 nm in average diameter in the case of the steel FT. Number density of VX precipitates in blue seems to increase with creep exposure time for both steels, but some of them are particles in pale blue as indicated with arrows in Figures 9 (c), 9 (d) and 10 (d). Those particles have been identified as Z-phase by comparing the amount ratios of Nb, V and Cr obtained with EDX analyses. Formation of Z-phase is recognized on the specimen creep ruptured at 11,900 h of the steel AT. Although Z-phase is found on the specimen creep ruptured after 43,300 h of the steel FT, it is not observed on the specimen creep ruptured after 28,500 h. Figure 11 displays the ternary diagram of M_2X, VX and Z-phase detected on the specimens after creep rupture under the applied stress condition of 140 MPa for both steels. Distinction in chemical composition between Z-phase and VX is obvious as shown in this figure, and the composition of Z-phase in the present work is almost similar to that in 9-12Cr steels boiler materials [5]. Sawada et al.

have reported that a lower temperature tempering treatment provides precipitation of M_2X particles instead of VX and presence of those M_2X retard Z-phase formation, thereby improving the creep strength in the case of Grade 91 boiler materials [6]. It is confirmed in this microstructural investigation that precipitation of Z-phase in the specimens subjected to the higher temperature additional tempering heat treatment is faster than that in the materials without the additional tempering one whereas M_2X particles still exist during long-term creep exposure for both steels. In addition, there is a possibility of that Z-phase formation behaviour having some relevance to preferential recovery of martensitic lath structures in the vicinity of the prior austenite grain boundaries since fraction of area where preferential recovery occurs near the prior austenite grain boundaries in the steel AT which Z-phase appears earlier is larger in comparison with the steel FT as shown in Figure 8. It also corresponds to the case of 9Cr-1Mo steel [7]. In the present study, the tempering temperature has influences on initial microstructure, progress in recovery during creep exposure and Z-phase formation, therefore, it has been concluded that higher temperature tempering is detrimental to the creep strength up to 40,000 h at 600 °C from a viewpoint of microstructural stability. Further long-term creep rupture data and detailed investigations on microstructure, however, are required to evaluate the efficacy of high temperature tempering treatments in the practical operating condition.

$t_r = 28,500h$ $t_r = 43,300h$
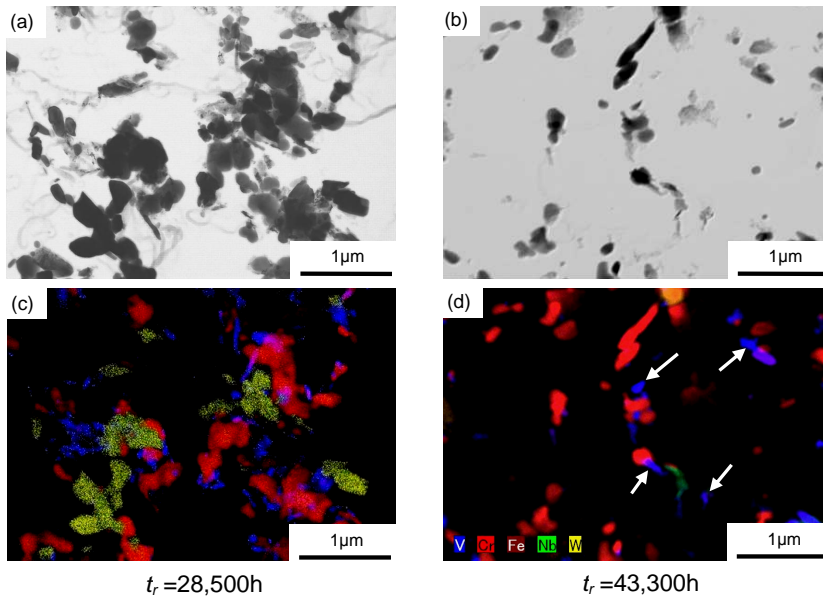
Figure 9 : TEM bright field images and elemental maps of specimens ruptured at 28,500h in (a), (c) and at 43,300 h (b), (d) in steel FT.

t_r =11,900h t_r =29,500h
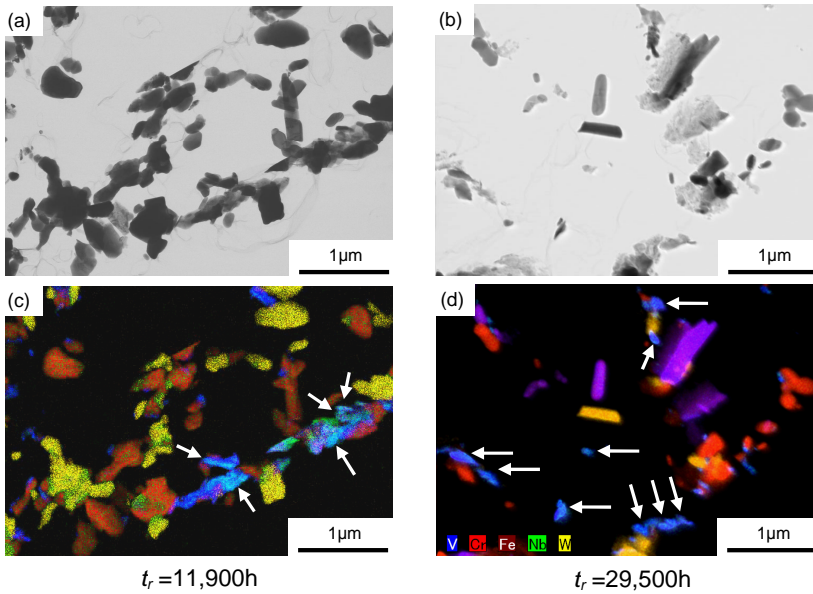
Figure 10 : *TEM bright field images and elemental maps of specimens ruptured at 11,900h in (a), (c) and at 29,500 h (b), (d) in steel AT.*
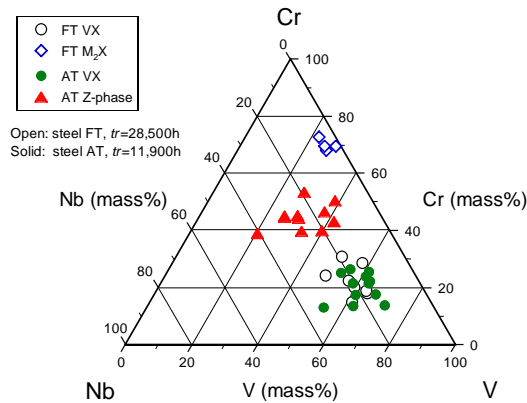
Figure 11 : *Ternary diagram of precipitates found in specimens creep ruptured at 28,500 h on steel FT and at 11,900 h on steel AT.*

4. Conclusions

Creep rupture tests and microstructural investigations were performed with specimens taken from a COST type "E", X12CrMoWVNbN 10-1-1, material large forging subjected to normalizing and tempering heat treatments containing final tempering at 690 °C with and without additional tempering at 730 °C. The results obtained are as follows.

207

- The creep rupture strength of the specimens subjected to the additional tempering heat treatment is lower than that of the samples without the additional tempering over the applied stress range from 160 to 120 MPa, while the difference diminishes with increase in time.
- Fine martensitic lath structures containing high density dislocations are observed on the specimens without the additional tempering treatment, while coarsened lath, partially cell-like sub-grain structures with lower dislocation density are found on the samples with the additional tempering. Number density of M_2X particles is reduced by the additional tempering treatment in contrast to increase in that of VX precipitates.
- Martensitic lath recovery progresses accompanying the preferential recovery during creep exposure for both materials and is promoted by the influence of initial microstructure in the as heat treated condition. Higher temperature tempering treatment hastens formation of Z-phase due to presence of VX. which has some relevance to preferential recovery martensitic lath structures.
- Tempering temperature has influences on initial microstructure, progress in recovery during creep exposure and precipitation of Z-phase, therefore, it has been concluded that higher temperature tempering is detrimental to the creep strength up to about 40,000 h at 600 °C from a viewpoint of microstructural stability.

References

[1] K.-H. Mayer and F. Masuyama, The Development of Creep-Resistant Steels, *Creep-resistant steels*, Woodhead Publishing Ltd. (Cambridge England, 2008), 15.

[2] F. Masuyama, History of Power Plants and Progress in Heat Resistant Steels, *ISIJ Int.*, 41, (2001), 612.

[3] A. Iseda, H. Teranishi and F. Masuyama, Effects of Chemical Compositions and Heat Treatments on Creep Rupture Strength of 12 wt%Cr Heat Resistant Steels for Boiler, *Tetsu-to Hagané*, 76, (1990), 1076.

[4] M. Mikami, Y. Wakeshima, T. Miyata and K. Kawano, Manufacturing Experiences and Investigation of Properties of 12%Cr Steel Forgings for Steam Turbines, *Proc. of 5th Int. Conf. on Advances in Materials Technology for Fossil Power Plants*, Marco Island Florida USA (2007).

[5] K. Sawada, H. Kushima and K. Kimura, Phase Formation during Creep and Aging in 9-12% Cr Heat Resistant Steels, *ISIJ Int.* 46, (2006), 769.

[6] K. Sawada, K. Suzuki, H. Kushima, M. Tabuchi and K. Kimura, Effect of tempering temperature on Z-phase formation and creep strength in 9Cr-1Mo-V-Nb-N steel, *Mater. Sci. and Eng.*, A 480, (2008), 558.

[7] K. Suzuki, S. Kumai, H. Kushima, K. Kimura and F. Abe, Heterogeneous Recovery and Precipitation of Z Phase during Long Term Creep Deformation of Modified 9Cr-1Mo steel, *Tetsu-to-Hagané.* 86, (2000), 550.

IMPRESSION CREEP TESTING FOR MATERIAL CHARACTERIZATION IN DEVELOPMENT AND APPLICATION

S J Brett[1], B Kuhn[2], J H Rantala[3], C J Hyde[1]

[1]Dept. Mechanical, Materials & Manufacturing Engineering
University of Nottingham
Contact e-mail: steve.brett456@btinternet.com

[2]Forschungszentrum Jülich GmbH, Institute for Energy and Climate Research
Microstructure and Properties of Materials (IEK-2)
Contact e-mail: b.kuhn@fz-juelich.de

[3]VTT Technical Research Centre of Finland, Materials and Manufacturing
Contact e-mail: juhani.rantala@vtt.fi

Abstract

The current status of the application of small scale sampling and impression creep testing to material characterization at the University of Nottingham, Forschungszentrum Jülich and the VTT Technical Research Centre of Finland is reviewed. Most of the practical experience gained to date at these has been obtained on two particular paths: Acquisition of data from in-service materials (Nottingham / VTT: ½CrMoV, grade 91 / 2.25Cr1Mo, grade 91) and data obtained from novel (mostly small quantity) trial alloys (Forschungszentrum Jülich, IEK-2: Crofer® 22 H and trial steels from Crofer® 22 H development).

Keywords: Impression creep testing, equipment, ex-service and experimental alloys, ceramic loading set-up

1. Introduction

At Nottingham University impression creep testing (ICT) focused on ½CrMoV steel, which is widely used for steam pipework systems on the UK's coal-fired power stations. Because some systems have operated well beyond their design life failure of the parent material must be taken into account. Small scale sampling and impression creep testing allows for comparisons to be made between the creep strength distributions of different stations and different components. The steel grade 91 is used for retrofitting and construction of new plants. There is an increasing need for creep life assessment of parent and particularly of aberrant grade 91 parent material, which entered service in an incorrectly heat treated condition. Demostration projects have been run for 2.25Cr1Mo and P91 materials at the VTT Technical Research Centre of Finland with the aim to apply impression creep for power plant assesments. Small scale sampling and impression creep testing allows for both creep strength ranking and an estimate of absolute creep strength for individual materials and components. Recommendations for the practical application of this technique to power plant have been provided elsewhere [1].

In most cases research is left with trial material quantities insufficient to suit all the characterization and qualification tasks arising during the development of a new steel grade. In case of novel high chromium Laves phase strengthened ferritic steels (derived from the

commercial steel grade Crofer® 22 H, developed at IEK-2 in cooperation with Outokumpu VDM), which are under development at FZ Jülich, the thermomechanical treatment history has a tremendous impact on the initial dislocation density, which in turn affects precipitation kinetics and particle morphology and thus creep strength of the material. For this reason production process optimization by thermomechanical treatment simulation is considered to be a mandatory element of future successful alloy development. The specimens typically utilized in thermomechanical treatment simulators only provide small quantities of homogenously deformed material for subsequent mechanical characterization. In this case small scale sampling (e.g. by spark erosion) and impression creep testing allows for the ranking of alloy compositions and thermomechanical processing routes with extremely small amounts of material. Application of impression creep testing for material development at VTT has concentrated on demonstration of the method for power plant life assessment purposes and on validation of testing methods for the materials of advanced nuclear reactors.

Examples of the practical application of this testing approach are given along with correlation of results to conventional creep testing and a brief summary of the differing testing set-ups.

2. Experimental

2.1. Materials

2.1.1. Commercial materials

The chemical composition and heat treatment parameters of the investigated materials are given in Tab. 1 and Tab. 2. In case of Crofer® 22 H ITC specimens were taken from plate material in hot-rolled / solution annealed condition.

Tab.1: Chemical compositions of the materials tested at Nottingham University and Forschungszentrum Jülich

Batch-ID:	C	N	Cr	W	Nb	Si	Mn	Ni	Ti	Mo	V
P91 (NU/FZJ)	0.1	0.073	8.70	0.02	0.07	0.27	0.43	0.32	<0.005	1.08	0.24
Crofer® 22 H	0.007	0.015	22.93	1.94	0.51	0.21	0.43	0.3	0.07	-	-

Tab.2: Heat-treatment parameters of the materials

Batch-ID:	Hot rolling:	Solution annealing:	Cooling:	Tempering:
P91 (NU/FZJ)		1060°C / 45 Min	Air	760°C / 120 Min
Crofer® 22 H (SA)	X	1075°C / 22 Min.	Air	none
Crofer® 22 H (HR)	X	none	Air	none

2.2. Experimental set-ups and testing procedures

ICT test samples are relatively easy to manufacture, using, for example, spark erosion, grinding and polishing processes. In general, creep tests are carried out under constant load conditions and either dead-weight or servo-electric (or servo-hydraulic) loading methods can be used (the authors have a preference for servo-electric test equipment because the effects of frictional contacts in linear bearings, temperature fluctuations etc. can be eliminated).

2.2.1. Nottingham University

Schematic diagrams of the specimen geometry (a), principal loading arrangement (b) and the testing set-up at Nottingham University (c) are shown in Fig. 1. Typical specimens dimensions are w×b×h = 10×10×2.5mm for use with an indenter of d = 1mm, or w×b×h = 8×8×2mm for use with an indenter of d = 0.8mm.
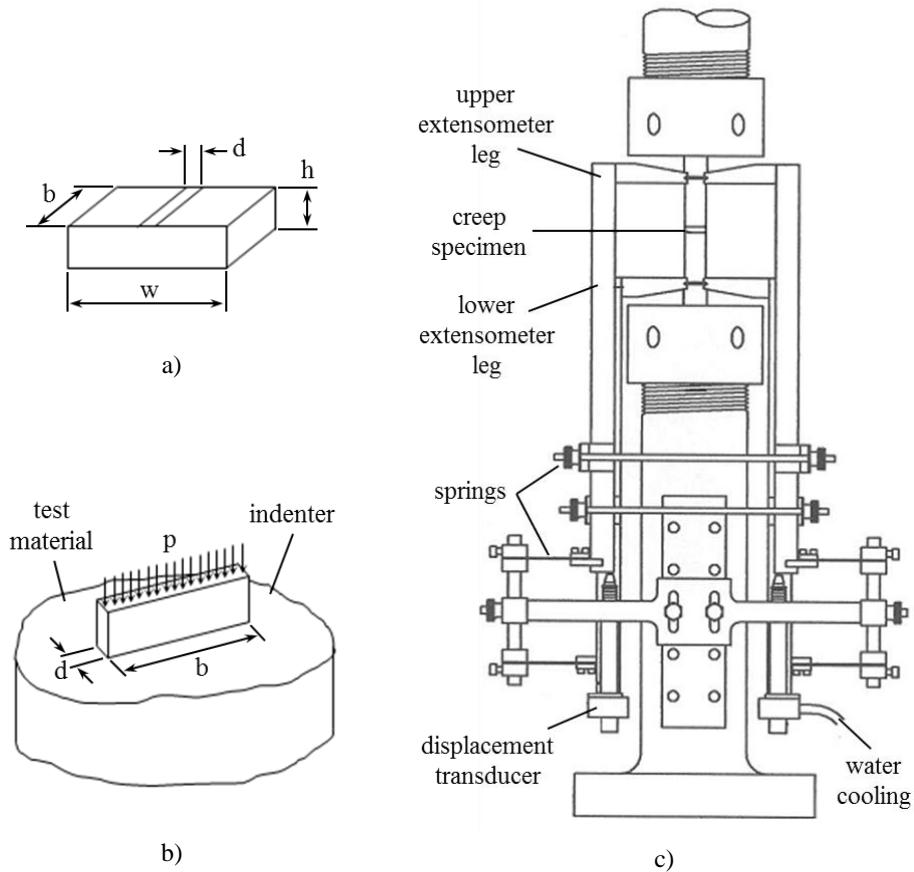
Figure 1: Typical impression creep specimen (a), indenter geometry (b) and schematic of the impression creep testing set-up at Nottingham Universtiy

Load-line displacements can be measured using extensometry of the type shown in Fig. 1 [2] and LVDTs. The choice of extensometry and transducers is not of critical importance but control of the temperature inside the furnace and within the laboratory is of particular importance. Water cooling of the extensometer legs, for example, can be helpful. Alignment of specimens is important. The contacting surfaces should be flat and parallel and the indenters should be re-ground at regular intervals.

2.2.2. Forschungszentrum Jülich

At Forschungszentrum Jülich impression creep specimens are produced by spark erosion, grinding to a grit 1200 surface finish and subsequent ultrasonic cleaning in ethanol. The experimental set-up consists of an Instron electromechanical testing machine, equipped with a resistance furnace and an all ceramic loading and displacement measurement set-up (Fig. 2). Two individual LVDTs with a minimum resolution of 0.1 µm are utilized for displacement measurement via a ceramic table / cross-head / rod arrangement.

a)   b)
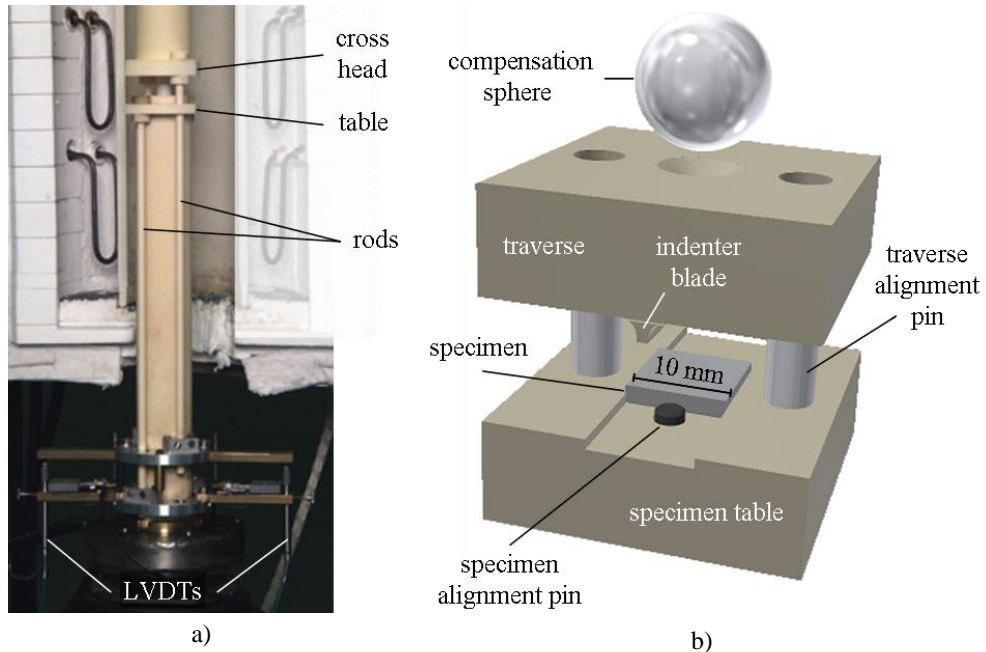
Figure 2: Impression creep set-up at Forschungszentrum Jülich, consisting of a) ceramic loading-train and displacement measurement set-up and b) all ceramic testing jig

A ceramic (Al_2O_3) testing jig, consisting of the specimen table, the traverse and pins for specimen/table and table/traverse alignment (cf. Fig. 2), was designed for impression creep testing. The specimen is put into a groove in the ceramic specimen table and positioned by the specimen alignment pin. The indenter blade is machined into the bottom side of the traverse, which is put on the specimen and aligned with the table by the traverse alignment pins. A conical clearance is machined into the upper side of the traverse to keep the compensation sphere.

After positioning of the specimen in the testing jig, the jig is placed on the machine table, aligned, pre-loaded with a controlled force of 10 N and the traverse alignment pins are removed to reduce friction. The whole testing set-up is then subjected to several constant force-rate loading cycles (up to the intended testing force or close to the elastic limit of the tested material in order to avoid work hardening) at ambient temperature until the hysteresis between the cyclic loading and unloading curves becomes minimized. This procedure reduces "noise" in the displacement signal during the early stages of testing by reducing microscopic

misalignment caused by the surface roughness of all the individual parts of the testing set-up. A type S (Pt/RhPt) thermocouple is inserted into the testing jig and placed at the side face of the specimen. The arrangement is then heated up under a controlled pre-load of 10 N to the designated testing temperature. After thermal equilibrium is reached the specimen is constant force-rate loaded to the testing force within 30 s. During the creep phase load and relative displacement (evaluated from the arithmetic mean value of the two extensometers) are recorded.

2.2.3. VTT Technical Research Centre

The VTT set up consists of Nimonic tools with a cylindrical part allowing the indenter to rotate and settle parallel to the specimen surface. A similar hysteris check as at Forschungszentrum Jülich is carried out to verify frictionless operation of the extensometry. The displacement measurement set up is a ceramic tube + rod type of device with a digital displacement transducer (resolution of 20 nm). Instead of a resistance furnace two mineral insulated heating cables with an integrated thermocouple are used to heat the upper and lower tool separately. The temperature of the heating cable is kept constant within +/-0.2°C resulting in a very good stability of the specimen temperature (+/-0.2°C) and displacement signal (typically +/-0.5μm).

The improvement achieved in the measured strain rate evolution during the test is demonstrated by comparison of two identical tests of the same material (2.25Cr1Mo, 540°C, 95MPa, Fig. 3). The improved stability result was achieved by controlling the heating cable temperature, while the scattered result was obtained without. Note also that in an impression creep test the strain rate does not reach a constant value but is decreasing continuously. Therefore some criterion has to be decided when to read the "minimum strain rate" corresponding to the uniaxial minimum strain rate.
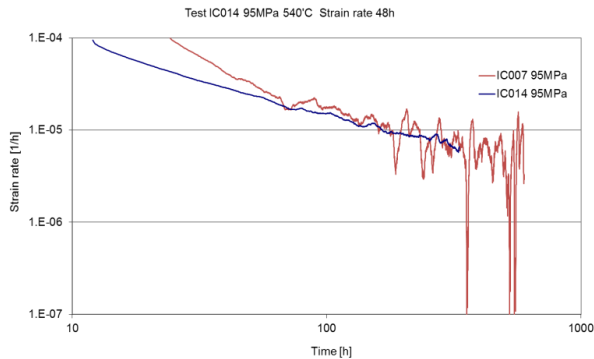
Figure 3: Examples of the effect of temperature control on the stability of the measured strain rate.

3. Results and Discussion

3.1. Grade 91

Grade 91 material was tested at Nottingham University and compared to uniaxial testing data and the mean value derived from the Cipolla equation [3] giving reasonable correlation (Fig.

4). Examples from testing of ex-service materials and application of the acquired testing data to creep strength evaluation are given in [4, 5]. As a first step towards interlaboratory comparability evaluation grade 91 material for comparative testing at FZ Jülich was supplied by Nottingham University via ECCC WG1.3 (Miniaturised Creep Testing). Two experiments were carried out as stepped stress tests (110, 120, 130 MPa). As outlined in section 2.2.3, the criterion used to evaluate the "minimum strain rate" is an important issue. This is especially true in stepped stress tests if reliable results need to be obtained in reasonably short time. As a practical approach the strain rate at each stress level was calculated from the slope of a linear approximation when the recorded curve remained within a +/- 0.5 % (relative value) deviation from its approximation for a time period of 100 hours. After this the testing stress was raised to the next level.
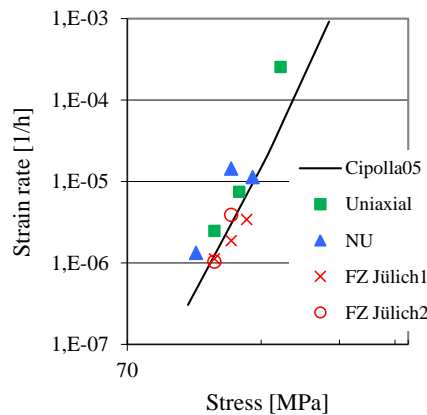
Figure 4: Stress / strain rate relations for grade 91 at 600 °C obtained from impression creep and uniaxial creep testing at Nottingham University (NU) and Forschungszentrum Jülich (FZJ) in comparison to the mean values derived from the Cipolla 2005 assessment [3].

Test #1 yielded good correlation to the Cipolla mean data at the lowest stress level, but increasingly deviated with rising stress. Increasing friction because of non-parallelism of specimen and indenter blade was caused by damage of the ceramic indenter blade by poor specimen surface quality. The specimen utilized in test #2 was prepared to a lower roughness surface finish (as outlined in section 2.2.2.) which is better suited for a ceramic indenter. In combination with a reconditioned indenter blade and the compensation sphere (cf. Fig. 2) the second test yielded satisfactory results.

3.2. Crofer® 22 H

The use of an all ceramic set up at Forschungszentrum Jülich enables testing up to very high temperatures, but it is crucial that oxide scale growth on the specimen surface does not interfere with accurate displacement measurement. For this reason the maximum testing temperature is more or less governed by the oxidation resistance of the investigated material. In terms of Crofer® 22 H the highest temperature applied so far was 900 °C. Fig. 5 gives a comprehensive view of the ICT and uniaxial creep testing results of Crofer® 22 H (uniaxial 700 °C and 800 °C data replotted from [6]).
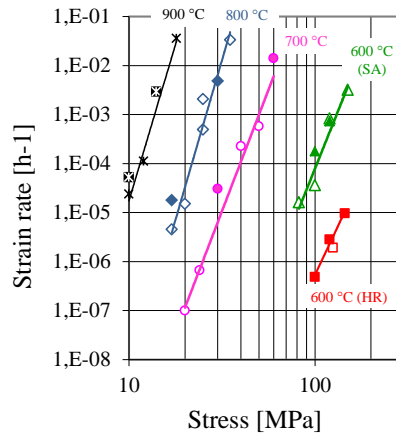
Figure 5: Stress / strain rate relations for Crofer® 22 H at various temperatures obtained from impression creep testing (filled symbols) and uniaxial creep (open symbols) at Forschungszentrum Jülich.

The trend lines for the individual temperatures were fitted to the uniaxial data only. Like it is demonstrated by the concordance of the results, ICT prove to be reliable in a wide temperature and stress / strain rate range. Currently the reliability limit of the set-up is marked by the 100 MPa test of the hot-rolled (HR) Crofer® 22 H material at 600 °C at approximate strain rates of $5 \cdot 10^{-7} h^{-1}$. Because hot-rolled material from the first commercial batches was scarce only one uniaxial creep test was performed at 600 °C. Under these circumstances ICT is a valuable method to evaluate stress / creep rate relations even with the smallest amounts of material available. In fact the ICT specimens were manufactured from the cut-offs from uniaxial tensile specimen manufacturing.

4. Conclusion and Outlook

Impression creep testing is a practical tool to generate data from small quantities of material. Its application to standard, ex-service, under development and differently thermomechanically treated materials was successfully demonstrated. It may thus be considered a valuable tool for both remaining life assessment and development of new materials.

Comparability of ICT results to uniaxial data was successfully proven at different laboratories applying various testing set-ups. The experience gained at Nottingham University, VTT Technical Research Center and Forschungszentrum Jülich shows that special care has to be taken in achieving exact temperature control in both furnace and laboratory. Implementation of ceramic testing set-ups might enable future testing of superalloys, but special care has to taken about matching surface roughness of specimen and a ceramic indenter as well as proper chamfering of the specimen edges to avoid damage of the indenter blade. High stiffness of all ceramic loading trains may cause undesirable load fluctuation when closed loop testing machines are used, which might require integration of attenuators into the loading train.

For this and the reason of cost it would be desirable to transfer the gained know-how to dead weight loaded (low-cost) testing set-ups. Furthermore a reliable criterion has to be developed for evaluating the "minimum strain rate" corresponding to the uniaxial minimum strain rate. A practical approach was outlined in the present paper, but has to be checked for applicability for a broader range of materials and testing parameters in the future.

Acknowledgement

Supply of Crofer® 22 H material by Outokumpu VDM is greatly appreciated.

References

[1]   ECCC Recommendations 2014; Vol. 3, Part III, Appendix 3

[2]   T. H. Hyde, W. Sun, C. J. Hyde: An overview of small specimen creep testing. IUTAM Symposium on Advanced Materials Modelling for Structures, Paris, 23-27 April (2012)

[3]   L. Cipolla, J. Gabrel: New Creep Rupture Assessment of Grade 91. ETD Conference on Industry and Research Experience in the Use of P/T91 in HRSGs/Boilers, IOM3, London, 7-8 December (2005)

[4]   S. J. Brett: Small Scale Sampling and Impression Creep Testing Applied to Aged ½CrMoV Steam Pipework Systems. EPRI International Conference on Advances in Condition and Remaining Life Assessment for Fossil Power Plants – Coal, Gas and HRSG, Hilton Head Island, South Carolina, 17- 19 October (2012)

[5]   S. J. Brett: The Practical Application of Small Scale Sampling and Impression Creep Testing to Grade 91 Components. EPRI - 7th International Conference on Advances in Materials Technology for Fossil Power Plants, Hawaii, 22-25 October (2013)

[6]   B. Kuhn, C. Asensio Jimenez, L. Niewolak, T. Hüttel, T. Beck, H. Hattendorf, L. Singheiser, W.J. Quadakkers : Effect of Laves phase strengthening on the mechanical properties of high Cr ferritic steels for solid oxide fuel cell interconnect application. Materials Science and Engineering A, Volume 528, Issue 18, 5888–5899, (2011)

MODELLING THE CONTRIBUTION FROM SOLID SOLUTION HARDENING TO THE CREEP STRENGTH OF AUSTENITIC STAINLESS STEELS

Rolf Sandström, Pavel Korzhavyi

Department of Materials Science and Engineering, KTH Royal Institute of Technology, SE-100 44 Stockholm, Sweden. Email: rsand@kth.se

Abstract

In recent years, important progress in the modelling of creep properties of austenitic stainless has taken place. It is now possible to compute the creep strength of creep resistant steels without the use of adjustable parameters. In this way, a fully basic modelling has been established that allows the prediction not only for existing steels but also for new grades. The present paper focuses on the role of solid solution hardening. In addition, precipitation hardening and dislocation strengthening must be handled. These contributions are analysed in other papers. Elements like W and Cu appear partially or fully in solid solution. They show a strong interaction to the dislocations. Cottrell atmospheres of the solutes are formed around the dislocations. This creates a solute drag effect that slows down the dislocations. This contribution to the creep strength in the austenitic stainless steel 23Cr25NiWCuCo (Sanicro 25) is computed. The elements W, Cu and Nb are considered.

Keywords: creep strength, solid solution hardening, austenitic stainless steel, model

1. Introduction

High-alloy austenititic stainless have been developed for use in superheaters and re-heaters of advanced coal-firing steam boilers. One such steel is 23Cr25NiWCuCo. Its designation is UNS S31035 and its trade name is Sandvik Sanicro 25 [1]. The composition of the steel is 22.5% Cr, 25% Ni, 3.6% W, 1.5% Co, 3% Cu, 0.5% Nb, 0.06% C and 0.23% N (wt.%). The material has a very high creep strength combined with good oxidation resistance. An extrapolation analysis of the creep strength at 700 ℃ has given a rupture strength at 100 000 h of 97 MPa, which is close to the target at that temperature of 100 MPa [2].

To obtain high creep strength for 23Cr25NiWCuCo precipitation hardening, solid solution hardening, and dislocation hardening have been combined. The present paper will focus on the solid solution hardening. The origin of the solid solution hardening is the lattice mismatch between the solutes and the matrix atoms.

In the past, no attempts seem to have been made to develop basic models of the solid solution hardening contribution to creep strength of austenitic stainless steels. Models are however, available for other alloy systems. The effect of W and Cr has been investigated for 9% Cr steels [3]. The influence of 50 ppm phosphorus in copper was studied by Sandstrom and Andersson [4]. A similar approach will be used for 23Cr25NiWCuCo. The basic assumption

in these models is that solute clouds are formed around the dislocations and that these clouds slow down the motion of the dislocations.

To model solid solution hardening, the influence of the elements in solid solution on the lattice parameter must be known. The rate of change of the lattice parameter with composition is referred to as the lattice misfit parameter. For binary alloys, the lattice misfit parameters are readily available in the literature. Since austenitic stainless steels always have large amounts of several alloying elements, binary alloys cannot be used as a starting point. Instead first-principles calculations of the lattice parameter of Fe-Cr-Ni-based alloys as a function of concentration have been performed to find the misfit parameters. The following solute elements: Cu, Nb, and W have been considered. It is the aim of the present paper to derive lattice misfit parameters of 23Cr25NiWCuCo and to apply them to the modelling of solid solution hardening of the steel.

2. Computation method for lattice misfit parameter

Density functional theory (DFT) [5] and the exact muffing-tin orbital (EMTO) method [6] were used to calculate the electronic structure. To consider the substitutional and magnetic disorder in the austenitic steel, the coherent potential approximation (CPA) [7],[8] was applied. The calculations were performed at 1000 K. The magnetic entropy in the high-temperature paramagnetic state due to the temperature-dependent spin moments of the host and solute atoms was modelled using the disordered local moment (DLM) approach [9]. The free energy contribution from the electron gas at a finite temperature was taken into account by Fermi-Dirac smearing of the level occupancy [10].

Previously, this type of finite-temperature modelling has been applied successfully to elastic properties of austenitic [11] and ferritic steels [12],[13], stacking faults in austenitic steels [14], structural and thermodynamic properties of sigma phase [15],[16]. Since CPA is involved a requirement is that the atoms should be at their ideal positions of the fcc lattice. The present results concerning largely oversized solute atoms (Nb and W) should be treated with some caution.

Some further details in the computations should be mentioned. Exchange and correlation effects in the electron gas were considered in the generalized gradient approximation (GGA) with PBE parameterization [17]. The full charge density technique (FCD) [18] was applied for calculating the total energies. Screening corrections to the electrostatic potential and energy within the CPA were included [19],[20].

The computations were initiated with a Fe-rich alloy composition (50% Fe, 25% Cr, and 25%Ni). In this alloy a small fraction (1.56%) of Fe atoms was replaced by one of the alloying elements (Cr, Ni, Cu, Nb, and W). For each of these 6 alloy compositions (host without and with the solute elements), the equilibrium lattice parameter was determined by minimizing the calculated free energy. The free energy took into account the electronic and magnetic entropy contributions evaluated at 1000 K.

3. Results for lattice misfit

6 alloys were considered, starting with the Fe-rich one with the designation $i = \{\text{Fe, Cr, Ni, Cu, Nb, W}\}$. A fraction Δc of Fe atoms is substituted in the first composition. y fractions are introduced such that $y_{\text{Fe}} = 0.5 - \Delta c$, $y_{\text{Cr}} = y_{\text{Ni}} = 0.25$. The atomic concentrations in the host alloy are then given by $c_i = y_i/(1 - \Delta c)$.

The atomic volumes in each of the 6 considered alloys can be obtained from the computed equilibrium lattice parameters a_i as $\Omega_i = a_i^3/4$. These volumes are linearly expanded (as a function of concentration) around the host composition in the domain defined by the 6 alloy compositions.

$$v_i = \sum_j \frac{\Omega_i - \Omega_j y_j}{\Delta c} \tag{1}$$

The average atomic volume in the 'host' alloy can then be expressed as $\Omega_0 = \sum_i v_i y_i/(1 - \Delta c)$. The volume misfit is given by:

$$\delta_i = \frac{1}{\Omega} \frac{\partial \Omega}{\partial c_i} = \frac{v_i - \Omega_0}{\Omega_0} \tag{2}$$

It can be related directly to the linear atomic-size misfit (the change in the lattice parameter),

$$\varepsilon_i = \frac{1}{a} \frac{\partial a}{\partial c_i} \tag{3}$$

since $\varepsilon_i = \delta_i / 3$. $\varepsilon_i = \delta_i/3$.

The results for the misfit parameters are given in Table 1. Our calculations take into account the electronic and magnetic contributions, but not the phonon contribution, to thermal expansion. Consequently, the thermal expansion coefficient that can be derived from the computations, $\alpha_L \cong 10 \cdot 10^{-6}$ K^{-1}, is smaller than the experimental value in the same temperature interval, $\alpha_L = 20 \cdot 10^{-6}$ K^{-1} [1]. However, the effect of phonons on the lattice misfit parameters is not expected to be significant.

Table 1 shows that the misfit parameters for the main alloying elements (Fe, Cr, Ni) are quite small. Cu has moderate value, whereas W and Nb show large values of atomic-size misfits. Since local relaxations around impurities are not fully taken into account, the misfit values of W and Nb can be expected to be exaggerated.

Table 1: Calculated volume and atomic-size misfit (%) of the alloying elements in the fcc Fe-Cr-Ni-based austenitic stainless steel 23Cr25NiWCuCo.

$i =$	Fe	Cr	Ni	Cu	Nb	W
$\delta_i(1000 \text{ K})$	−1.02	1.34	0.64	14.07	75.81	62.60
$\varepsilon_i(1000 \text{ K})$	−0.34	0.45	0.21	4.69	25.27	20.87

4. Solute atmospheres at dislocations

With a dislocation core radius equal to the Burgers vector, the maximum interaction energy between a solute atom and an edge dislocation is given by [23]

$$U_i^{\max} = \frac{1}{3\pi} \frac{(1+\nu)}{(1-\nu)} G\Omega_0 \delta_i \tag{4}$$

where G is the shear modulus, ν is the Poisson's ratio of the material, and b is the length of the Burgers vector. With a Poisson's ratio $\nu = 0.3$ and an elastic modulus $E = 145$ GPa, as well as the calculated values of Ω_0 and δ_i at 1000 K, one finds an interaction energy of: $U_i^{\max} \sim 0.78 \cdot \delta_i$ (eV). This gives 0.11 eV for Cu, 0.59 eV for Nb, and 0.49 eV for W.

Due to the lattice misfit, it is energetically favourably for the solutes to be located close to the dislocations. Therefore, atmospheres of solutes are created around the dislocations. If the dislocations are not moving (they are static), the concentration of solute atoms c_i^{stat} can be expressed as [4],[23]

$$c_i^{stat} = c_i^0 e^{-\frac{U_i(x,y)}{kT}} \tag{5}$$

where c_i^0 is the concentration of solute i in solid solution, k Boltzmann's constant and T the absolute temperature. U_i is the interaction energy between the solute and the dislocation. (x,y) are the Cartesian coordinates of the position of the solute relative to an edge dislocation that is climbing in the y-direction. The concentration of solutes around a moving dislocation is slightly more complicated. The concentration c_i^{dyn} of solutes around a dislocation moving in the y-direction can be expressed with the help of the following equation [4],[23]

$$c_i^{dyn} = \frac{vc_i^0}{D_i^{sol}} \left(e^{-\frac{U_i(x,y)}{kT} - \frac{vy}{D_i^{sol}}} \right) \int_{-\infty}^y e^{\frac{U_i(x,y')}{kT} + \frac{vy'}{D_i^{sol}}} dy' \tag{6}$$

where v is the velocity of the dislocation, and D_i^{sol} the diffusion coefficient for the solute i. The climb velocity v is given by

$$v = M_{\text{climb}} b \sigma_{appl} \tag{7}$$

M_{climb} is the climb mobility and σ_{appl} the applied stress. M_{climb} can be expressed in terms of the coefficient of self-diffusion D_S and the activation energy for the solutes Q_{sol}. The size of Q_{sol} will be considered below.

$$M_{\text{climb}} = \frac{D_s b}{kT} \exp(-\frac{Q_{sol}}{kT}) \tag{8}$$

Results from eqs. (5) and (6) are shown in *Fig. 1* for the steel 23Cr25NiWCuCo
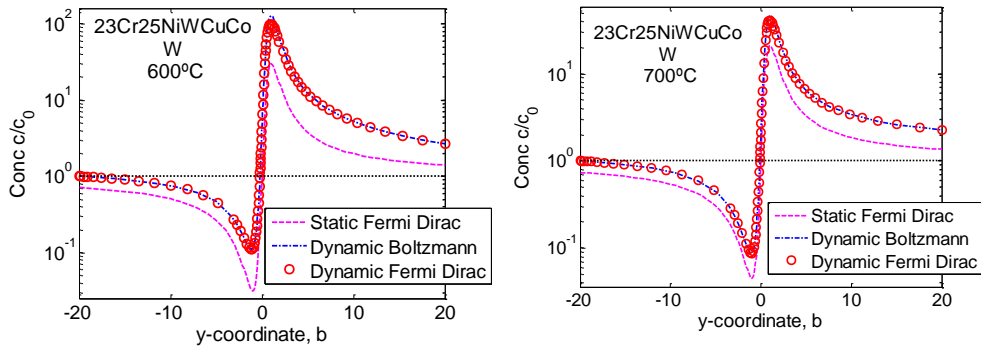
Fig. 1. Concentration of tungsten solutes around an edge dislocation at a) 600 ºC and b) 700 ºC. The dislocation is either non-moving (static, eq. (5)) or climbing in the y-direction, eq. (6).

As can be seen from *Fig. 1*, the concentration of W around a non-moving (static) or a climbing dislocation is up to 100 times larger than the average solute concentration. This high concentration is highly localised to the dislocation core. In fact, it appears about a Burgers vector away from the centre of the dislocation. On the log scale, the static solution gives a more symmetric distribution than the dynamic solution. The peak value is larger for the dynamic solution. The peak value decreases somewhat with inceasing temperature, *Fig. 1*b. In *Fig. 1*, Fermi-Dirac statistics should be used, since it allows only one solute at each atomic position although the effect is small in *Fig. 1*. This restriction is not enforced for the Boltzmann distribution.

In *Fig. 2* the predicted maximum solute concentration at the dislocations according to eq. (6) as a function of temperature is shown for the elements W, Nb and Cu.
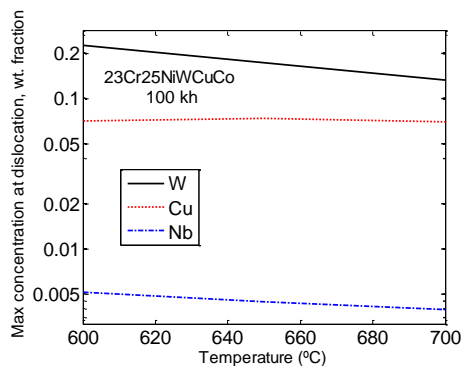
Fig. 2. Maximum concentration at dislocation of W, Nb and Cu according to eq. (6)

The highest concentration has W, followed by Cu and Nb. The temperature dependence of the maximum concentration is weak. For W and Nb the concentration is reduced with increasing temperature. Such a drop is not seen for Cu. The reason is that the maximum interaction U_i^{max} is much larger for W and Nb than for Cu.

5. Solid solution hardening

If solutes are present, it makes the dislocations slow down. This can be modelled with the help of a drag stress [23]

$$\sigma_i^{drag} = \frac{F}{bL} = \frac{kTv}{bD_i} \int_A \frac{(c_i - c_i^0)^2}{c_i} dA \tag{9}$$

where σ_i^{drag} is the drag stress from solute i, F the force per unit length L of the dislocation and A the area surrounding the dislocation. Hirth and Lothe [23] demonstrated that the integral in eq. (9) can be computed approximately with the static distribution of solutes, eq. (5). This simplifies the computation due to the complexity of the dynamic solution in eq. (6). The result is the following expression for the drag stress

$$\sigma_i^{drag} = \frac{vc_0\beta^2}{bD_ikT} I(z_0) \tag{10}$$

where $z_0 = \beta/r_0 kT$ and the integral $I(z_0)$ is

$$I(z_0) = \int_1^{z_0} \frac{2\sqrt{2\pi}}{3} z^{-5/2} e^z dz \tag{11}$$

$I(z_0)$ can be evaluated numerically directly.

Eq. (10) cannot be compared to experiments for 23Cr25NiWCuCo directly because the elements W, Nb, and Cu give contributions to both solid solution and precipitation hardening. Instead, a comparison has been made to the alloys Ni20Cr and Ni20Cr6W [24]. Creep data for these alloys are available at 1173 K [25]. For Ni20Cr6W all tungsten is present in solid solution. The results demonstrate that the model can fully account for the difference between Ni20Cr and Ni20Cr6W [24].

The contribution of W, Nb and Cu to solid solution hardening in 23Cr25NiWCuCo is shown in *Fig. 3*. The solution hardening of W is significantly higher than that of Cu and Nb. The amounts of solutes at the dislocations are much lower for Cu than for W, *Fig. 2*, since the interaction energy is lower than for W. The low solubility of Nb atoms gives a small contribution to the solid solution hardening. With increasing time and temperature, the solid solution hardening is reduced. The total solution hardening is obtained by simply adding the contribution from the individual elements. For 23Cr25NiWCuCo, the contribution from W dominates the solid solution hardening.
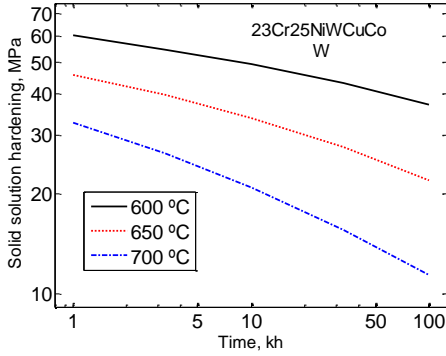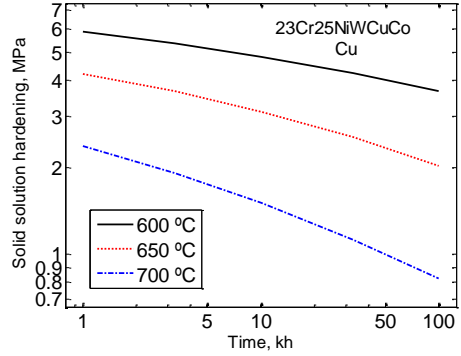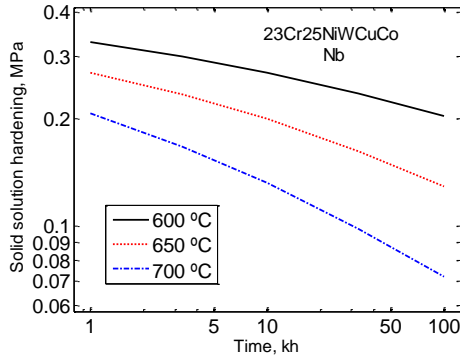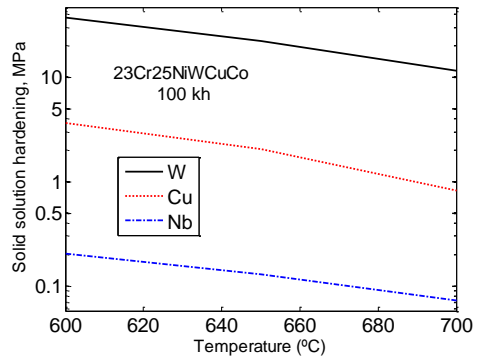
Fig. 3. Solid solution hardening for 23Cr25NiWCuCo according to eq. (10) as a function of temperature and time; a) W, b) Nb, c) Cu, d) comparison between W, Cu and Nb at long times

The distribution of solutes is sharply peaked around the dislocations. This was shown in *Fig. 1.* When the dislocations move, the solutes have to jump out and into this region. This requires thermal activation in addition to that for self-diffusion. Consequently, the creep rate is lowered by the factor [4]

$$f_{sol} = \exp(-Q_{sol} / kT) \tag{12}$$

Thus, the solid solution hardening raises the activation energy of creep, cf. eq. (8). This explains why the activation energy for creep for austenitic steels is much higher than that for self-diffusion. The activation energy Q_{sol} is taken as the maximum interaction energy U_i^{max} from eq. (4). The U_i^{max} value for the element W with the largest contribution to the solid solution hardening is selected.

6. Comparison of strengthening mechanisms

Solid solution hardening, dislocation hardening and precipitation hardening are the main strengthening mechanisms in 23Cr25NiWCuCo. The contributions from dislocation and precipitation hardening are analysed elsewhere [26]. To illustrate the relative importance of the different mechanisms, they are shown in *Fig. 4*.
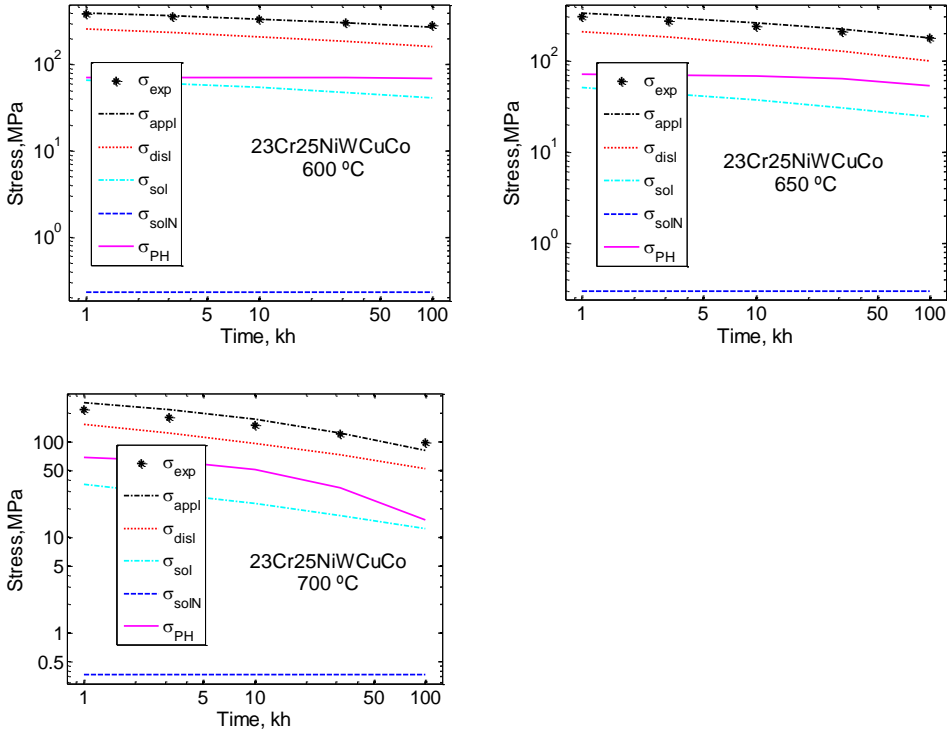
Fig. 4. Contribution to the creep strength of 23Cr25NiWCuCo from dislocations, precipitates and elements in solid solution; a) 600 ºC, b) 650 ºC, c) 700 ºC

The largest contribution to the creep strength comes from the dislocations, σ_{disl}. The second largest contribution is from the precipitation hardening, σ_{PH}. The effect of solid solution hardening σ_{sol} is also of utmost importance. A fourth contribution for nitrogen in solid solution is also shown, σ_{solN}. The expression in eq. (10) gives a negligible contribution for the fast diffusion of interstitial elements. Instead, it is the break stress σ_{break}, which is of importance [4]

$$\sigma_{break} = \frac{U_i^{max}}{b^3} \int_{y_L}^{y_R} c_i^{dyn} dy \qquad (13)$$

The integral in (13) is performed over a solute distribution such as the one in *Fig. 1*. The misfit parameter has been estimated from lattice expansion data for very large nitrogen contents [27]. The value for the volume lattice misfit becomes $\varepsilon_i = 0.075$. The resulting contribution to the solid solution hardening is very small, *Fig. 4*. It is believed that this lattice misfit parameter is significantly underestimated, because for lower concentration of N much higher values are obtained [28].

The total creep strength is obtained by adding the contributions from the different mechanisms.

$$\sigma_{appl} = \sigma_{disl} + \sigma_{PH} + \sigma_{sol} + \sigma_{solN} \tag{14}$$

The predicted creep strength is marked σ_{appl}. It should be directly comparable with the measured creep rupture strength σ_{exp} in *Fig. 4*. As can been seen, the predicted strength is in good agreement with the rupture strength that has been obtained from a rupture strength extrapolation [2].

7. Conclusions

Solid solution hardening in the austenitic stainless steel 23Cr25NiWCuCo (Sandvik Sanicro 25) has been analysed. The steel is intended for use in supercritical fossil fired plants with advanced data.

- Lattice misfit parameters for alloying elements in 23Cr25NiWCuCo have been derived using first-principles calculations based on density functional theory.

- A model for the effect of solid hardening on the creep strength has been further developed and used for the austenitic stainless steel. In the model, clouds of solutes are assumed to form around dislocation and slow down their motion and thereby increase the strength.

- The solid solution strengthening as a function of temperature and time has been computed for the elements W, Nb, and Cu. The magnitude of solution hardening can be explained in terms of the size of the lattice misfit parameters and its effect on the the accumulation of solutes around the dislocations.

Acknowledgments

References

[1]   *Sanicro 25 (Tube and pipe, seamless)*, Datasheet by Sandvik Materials Technology. http://www.smt.sandvik.com/en/materials-center/material-datasheets/tube-and-pipe-seamless/sanicro-25/

[2] Högberg, J., Chai, G.,Kjellström, P., Boström, M., Forsberg, U., Sandström, R. Creep behavior of the newly developed advanced heat resistant austenitic stainless steel grade UNS S31035. American Society of Mechanical Engineers, Pressure Vessels and Piping Division (Publication) PVP, 2010.

[3] H. Magnusson and R. Sandström, Modelling of the influence of laves phase on the creep properties in 9% Cr steels, ASME Pressure Vessels and piping Conference -8th International Conference on Creep and Fatigue at Elevated Temperatures-CREEP8, pp. 519-526, 2008

[4] Sandstrom R, Andersson HCM. The effect of phosphorus on creep in copper. J Nucl Mater. 2008;372:66-75.

[5] P. Hohenberg and W. Kohn, Phys. Rev. **136**, B864 (1964).

[6] L. Vitos, *Computational Quantum Mechanics for Materials Engineers* (Springer-Verlag, London, 2007).

[7] P. Soven, Phys. Rev. **156**, 809 (1967).

[8] B. L. Gyorffy, Phys. Rev. B **5** 2382 (1972).

[9] B. L. Gyorffy, A. J. Pindor, J. B. Staunton, G. M. Stocks, and H. Winter, J. Phys. F **15**, 1337 (1985).

[10] N. D. Mermin, Phys. Rev. **137**, A1441 (1965).

[11] L. Vitos, P. Korzhavyi, and B. Johansson, Nature Materials **2**, 25 (2003).

[12] V. I. Razumovskiy, A. V. Ruban, and P. A. Korzhavyi, Phys. Rev. B **84**, 024106 (2011).

[13] V. I. Razumovskiy, A. V. Ruban, and P. A. Korzhavyi, Phys. Rev. Lett. **107**, 205504 (2011).

[14] L. Vitos, P. A. Korzhavyi, and B. Johansson, Phys. Rev. Lett. **96**, 117210 (2006).

[15] P. A. Korzhavyi, B. Sundman, M. Selleby, and B. Johansson, in *Integrative and Interdisciplinary Aspects of Intermetallics*, MRS Symposium Proceedings **842,** edited by M.J. Mills, H. Clemens, C-L. Fu, and H. Inui (MRS, Warrendale, 2005), pp. S4.10.1-6.

[16] E. Kabliman, P. Blaha, K. Schwarz, A. V. Ruban, and B. Johansson, Phys. Rev. B **83**, 092201 (2011).

[17] J. P. Perdew, K. Burke, M. Ernzerhof, Phys. Rev. Lett. **77**, 3865 (1996).

[18] J. Kollár, L. Vitos, H. L. Skriver, in: H. Dreyssé (Ed.) *Electronic Structure and Physical Properties of solids: The uses of the LMTO method*, Lecture Notes in Physics (Springer-Verlag, Berlin, 2000), p. 85.

[19] A. V. Ruban and H. L. Skriver, Phys. Rev. B **66**, 024201 (2002).

[20] A. V. Ruban, S. I. Simak, P. A. Korzhavyi, H. L. Skriver, Phys. Rev. B **66**, 024202 (2002).

[21] I. A. Abrikosov, A. M. N. Niklasson, S. I. Simak, B. Johansson, A. V. Ruban, and H. L. Skriver, Phys. Rev. Lett., 76 (1996) 4203.

[22]   I. A. Abrikosov, S.I. Simak, B. Johansson, A. V. Ruban, H. L. Skriver, Phys. Rev. B **56**, 9319 (1997).

[23]   J.P. Hirth, J. Lothe, Theory of Dislocations, McGraw-Hill, New York, 1968.

[24]   P. A. Korzhavyi, R. Sandström, First-principles evaluation of the effect of alloying elements on the lattice parameter of a 23Cr25NiWCuCo austenitic stainless steel to model solid solution hardening, to be publ. (2014)

[25]   T. Matsuo, K. Nakajima, Y. Terada, M. Kikuchi, High temperature creep resistance of austenitic heat-resisting steels, Materials Science and Engineering, A 146 (1991) 261-272

[26]   M. Farooq, R. Sandström, O. Tassa, Precipitation hardening and other contributions to the creep strength of an 23Cr25NWCuCo austenitic stainless steel, to be publ. 2013

[27]   C. Templier, J.C. Stinville, P. Villechaise, P.O. Renault, G. Abrasonis, J.P. Rivière, A. Martinavičius, M. Drouet, On lattice plane rotation and crystallographic structure of the expanded austenite in plasma nitrided AISI 316L steel, Surface and Coatings Technology, 204 (2010) 2551-2558.

[28]   M. Kikuchi, T. Tanaka, K. Hamagami, Y. Ogura, R. Tanaka, Lattice dilation of 25cr-28ni and 25cr-28ni-2mo austenitic steels by dissolved nitrogen, Metallurgical Transactions A, 7 (1976) 906-908.

Heat-affected zone formation behaviour of 9Cr–1Mo weld metal

Yuta Tanaka, Keiji Kubushiro, Yasuko Masuda, Noriko Saito

IHI Corporation, 1, Shin-Nakahara-Cho, Isogo-ku, Yokohama, 235-8501, Japan
E-mail: yuta_tanaka@ihi.co.jp

Abstract

Heat-affected zones (HAZ) are formed in the weld metal as well as the base metal because the heat of the molten pool is conducted to the neighbouring metal in the process of multi-pass welding. However, the HAZ formation process in the weld metal of Mod. 9Cr-1Mo steel welded joints are not fully understood based on a detailed microstructural assessment. In this study, the grain refining temperature in the weld metal was investigated using simulated HAZ specimens. Optical microscope observation showed that the simulated HAZ specimen with a peak temperature of 875°C was the most fine-grained, well-recovered microstructure of all the specimens after the base metal had been tempered for a long time. On the other hand, the grain refining temperature in the weld metal was higher than that in the base metal despite a lower A_{c1} temperature. This means that the nucleation of globular austenite in the process of reverse transformation is delayed due to a large prior austenite grain size in the weld metal.

Keywords: 9Cr-1Mo, weld metal, heat-affected zone, reverse transformation, EBSD

1. Introduction

Modified 9Cr-1Mo steel, representative of high Cr ferritic heat-resistant steels, has been widely used for high temperature structural components of steam power plants because of its high creep strength, low thermal coefficient, and corrosion resistance. Many concerns have been reported on the poor performance of heat-affected zones (HAZ) in modified 9Cr-1Mo steel welded joints [1]. A HAZ is formed depending on the thermal history during welding both in the base metal and weld metal of the welded joint, and the microstructures become inhomogeneous owing to the difference in heating temperatures. Existing studies indicate that creep fracture occurs in fine grained HAZ close to the base metal among inhomogeneous microstructures and it is well known as Type IV cracking [2-5].

The microstructure of a HAZ close to the base metal is characterized by tempered martensite and precipitates of carbides/nitrides distributed along the intergranular or intragranular boundaries. The creep strength reduction mechanism of HAZ has been discussed in terms of the recovery resistance of the tempered martensite, such as dislocation strengthening, solid-solution strengthening, and precipitation strengthening. Aside from this, in order to explain why the fine grain is formed, the microstructural changes of the weld joint after welding and post-weld heat treating have been intensively investigated [6-10]. In this study, the α/γ reverse transformation behaviour is focused on to understand the HAZ formation process and to reveal the factors causing grain refinement.

HAZ are formed in the weld metal as well as close to the base metal because the heat of the molten pool is conducted to the neighbouring metal in the process of multipass welding.

However, the HAZ formation process in the weld metal is not fully understood based on a detailed microstructural assessment. Figure 1(a) shows the macro structure of a weld metal by submerged arc welding. A magnification of area (b) shows the HAZ in the weld metal, which is characterized by the initial untempered martensite with a columnar structure (P1), together with the coarse grained (P2) and fine grained (P3) microstructures formed by the thermal cycle of subsequent weld passes. Since the initial microstructure and its grain size in the weld metal differ from those in the base metal, the α/γ reverse transformation process in the weld metal is not necessarily the same as the base metal. The creep properties of HAZ are usually investigated using simulated HAZ specimens, which are

Figure 1 : Macro structure of weld metals (a) and optical micrograpgh image (b) which is divided into columnar structure (P1), coarsed grain (P2), and fined grain (P3).

produced by rapid heating to peak temperatures around A_{C1} to A_{C3}, A_{c1} being the temperature at which martensite to austenite transformation starts during heating, A_{c3} that at which it finishes. This paper discusses the differences in the HAZ formation process between the base metal and weld metal using simulated HAZ specimens, and experimentally observed orientations will be characterized using electron backscattering diffraction (EBSD) methods, which has been found to be a powerful technique for studying the local crystallographic properties of a number of microstructures.

2. Experimental procedure

Simulated HAZ heat treatment was conducted using modified 9Cr-1Mo steel specimens having a diameter of 10 mm and a gauge length of 40.5 mm. Normalized and tempered steel was employed as the base material of the simulated HAZ specimens, and shielded metal arc welding steel as the weld metal. The center of the gauge length was heated to peak temperatures of 800–1250°C at a rate of 50 °C s^{-1}, holding at the peak temperature for 5 s. In order to evaluate the recovery behaviours, the simulated HAZ specimens were tempered at 740°C for 50 hrs. Vickers hardness tests were carried out for the simulated and tempered specimens. Microstructural evolution was characterized using an optical microscope and SEM/EBSD. EBSD analysis was conducted in an FE-SEM with the specimen tilted by 70° after polishing with colloidal silica. In this study, the EBSD images are represented as inverse

pole figure (IPF) maps. The IPF maps show the crystallographic orientations using suitable color codes.

3. Results and Discussion

3.1. Effect of α to γ reverse transformation temperature on grain refinement

In the early stage of γ formation above A_{c1}, either globular γ or acicular γ preferentially forms and grows on the grain boundaries such as the prior γ boundaries, packet boundaries, and block boundaries. The nucleation of globular γ grains represents diffusion-controlled growth, which is well known as diffusion reverse transformation. In contrast, acicular γ grains follow a diffusionless shear mechanism and a Kurdjmov-Sachs (K-S) orientation relationship such as a martensitic transformation. With regard to the shear reverse transformation, it may be accompanied not only by diffusionless type but also by diffusion type. However, since it is difficult to distinguish them, both meanings are included in "*shear reverse transformation*" in this paper. The coalescence of acicular γ grains with the same orientation results in a reconstitution of the original prior γ grains. This is called the γ grain memory effect. It follows that the nucleation and growth of globular γ rather than acicular γ are the important processes in grain refinement.

Figure 2 shows optical microscope images of base metals which were tempered at 740°C for 50 hrs after the simulated HAZ heat treatment at each peak temperature. At a peak temperature of 875°C, fine grained microstructure was observed. This indicates that a microstructure heated to around 875°C recovers easily by aging treatment. The hardness after the simulated HAZ heat treatment increased with the increase of peak temperature, and the amount of hardening from 800°C to 900°C was very large as shown in **Fig. 3**; which means that 875°C is equivalent to two phase regions (α+γ). This rapid hardening corresponds to the quantity of fresh martensite transformed from two phase regions (α+γ).

In the case of the weld metal, its hardness increased like the base metal in the almost same temperature region. When heated to 800°C, while the base material was still a tempered martensite, the transformation from austenite to a fresh martensite was identified in the weld metal from displacement change. These results mean that A_{c1} of the weld metal is low compared with the base metal. The optical microscope images of the weld metal at each peak temperature are shown in **Fig. 4**. Around the grain refining temperature of the base metal (875°C), significant grain refinement was not observed in the weld metal, but it was at 950°C. Therefore, grain refinement by the nucleation of globular γ might be delayed to the high temperature side, and acicular γ may have been generated preferentially.
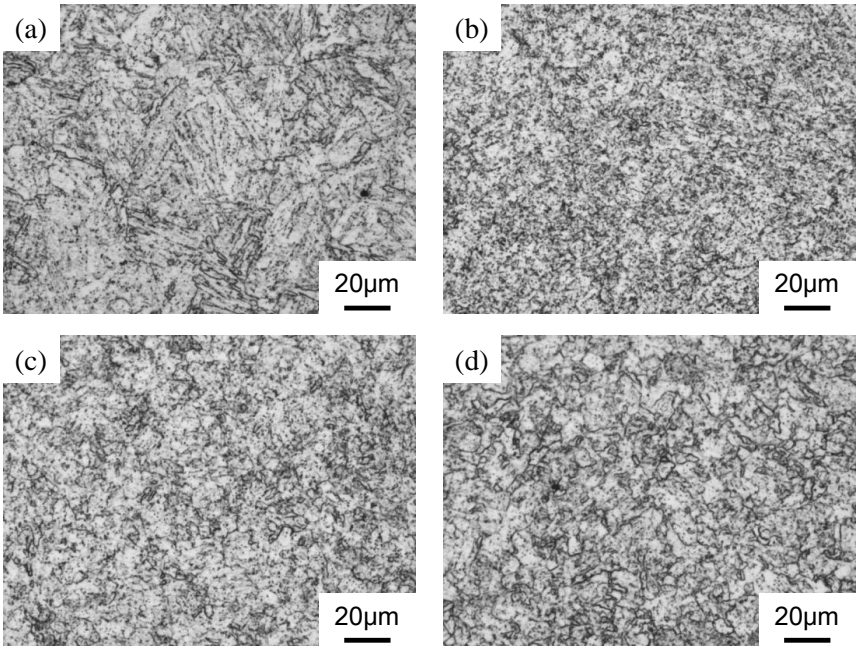
Figure 2 : Optical microscope images of base metals which were tempered at 740℃ for 50 hrs after the simulated HAZ heat treatment at each peak temperature: 800℃ (a), 875℃ (b), 950℃ (c), 1000℃ (d).

Figure 3 : Vickers hardness after the simulated HAZ heat treatment at each peak temperature and after tempering at 740℃ for 5hrs.

231
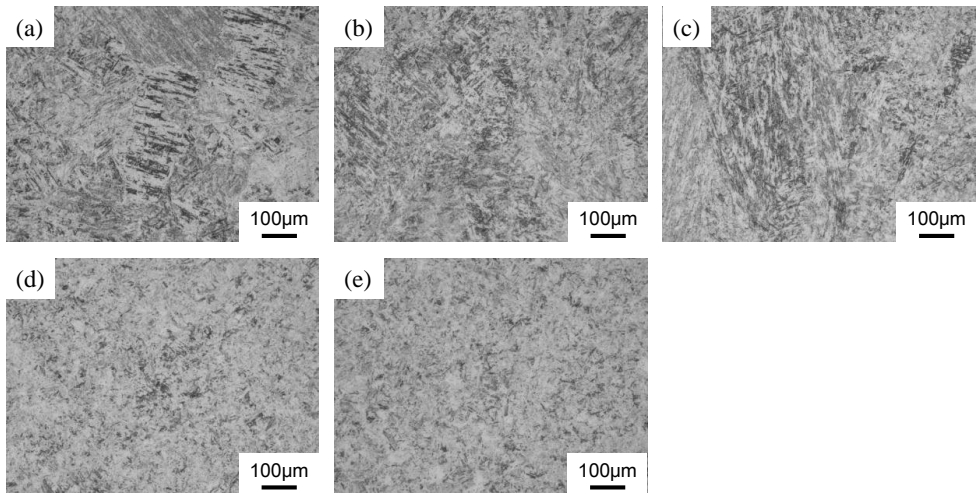
Figure 4 : Optical microscope images of base metals which were tempered at 740℃ for 50 hrs after the simulated HAZ heat treatment at each peak temperature: 800℃ (a), 850℃ (b), 900℃ (c), 950℃ (d), 1000℃ (e).

3.2. Characterization of reverse transformed austenite using EBSD

EBSD is an analysis technique for determining phase as well as crystal orientation. This technique is useful for characterizing the martensite [9]. The martensite transformed from one austenite grain displays a characteristic pole figure pattern as shown in **Fig. 5**. This pattern is characterized by 24 crystallographic variants of martensite according to the K-S orientation. The acicular γ grains and martensite have a K-S orientation relationship. Therefore, it can be confirmed from the pole figure after the simulated HAZ heat treatment whether the transformation is the shear type. **Figure 6** shows inverse pole figure images and pole figures at the peak temperatures of 900°C
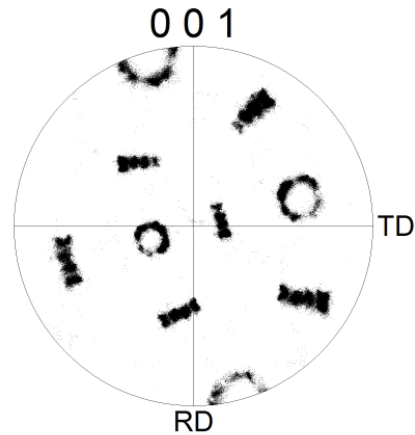
Figure 5 : Typical pole figure showing the {100} poles of martensite variantsfrom one austenite grain

and 950°C corresponding to the boundary temperatures of grain refinement. The columnar structure remained at 900°C, while changing to the fine grained microstructure at 950°C.

The pole figures indicated that reverse transformed austenite at 900°C was acicular γ, and random grains (globular γ) increased around 950°C. Grain refinement was promoted, and

random grains increased with recovery by tempering treatment at 740°C for 50 hrs, as shown in **Fig. 6 (e,f)**. This revealed that two kinds of austenite generation, acicular γ and globular γ, competed with each other in the α/γ reverse transformation, which determines the grain refinement temperature of a material. The following has been reported as factors in prioritizing the generation of acicular γ over globular γ: (i) the growth of retained γ nucleated in the lath boundary [11], (ii) a decrease in grain boundary energy by segregation, which is related to the heating rate [12], (iii) the restriction of crystal orientation by residual stress and so on [13], (iv) prior austenite grain size [14]. The prior austenite grain size of the weld metal is much larger than that of the base metal. In addition, the retained γ was not observed. Therefore, the generation of acicular γ is likely associated with the prior austenite grain size. As is the case for the above grain refinement mechanism, revealing the factors influencing the α/γ reverse transformation behaviour will be useful for designing alloys with improved creep properties.
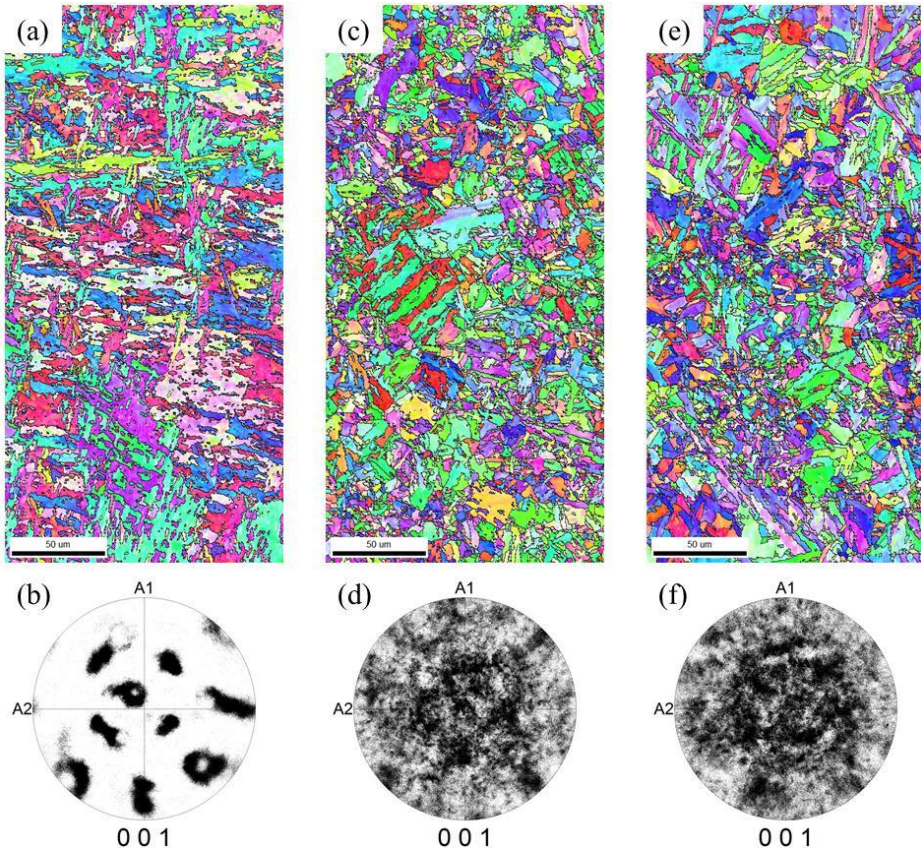
Figure 6 : Inverse pole figure images (a, c, e) and pole figures (b, d, f) in the boundary temperature of grain refinement: the simulated HAZ heat treatment at 900 °C (a, b), 950 °C, and the simulated HAZ heat treatment at 950 °C, followed by aging treatment (e, f).

233

4. Conclusions

The α/γ reverse transformation behaviour was investigated in order to understand the HAZ formation process and to reveal the factors influencing grain refinement. In this study, we focused on the grain refining mechanism of the weld metal. The conclusions are as follows.

(1) Modified 9Cr-1Mo steel base metal was fine-grained at 875°C due to the nucleation of globular γ grains. On the other hand, the microstructure of the weld metal was not changed at this temperature, and grain refining was observed at 950°C owing to the delay of the nucleation of globular γ grains despite the fact that A_{c1} of the weld metal is lower than that of the base metal.

(2) The α/γ reverse transformation with shear mechanism had priority over the nucleation. As a result, acicular γ was preferentially formed with the K-S orientation, followed by the formation and growth of globular γ.

(3) It is suggested that the generation of acicular γ in the weld metal was associated with the prior austenite grain size.

Reference

[1] F. Masuyama: "Creep degradation in welds of Mod.9Cr-1Mo steel," *International Journal of Pressure Vessels and Piping*, 83, 819-825 (2006).
[2] M. Matsui, M. Tabuchi, T. Watanabe, K. Kubo, J. Kinugawa, F. Abe: "Degradation of Creep Strength in Welded Joint of 9%Cr Steel," *ISIJ Int.*, 41, S126-S130 (2001).
[3] F. V. Ellis, S. O. Hilton, J. F. Henry, J. E. Bynum: "Influence of service exposure on base and weld metal of 1/2Cr-1/2Mo-1/4V high-pressure steam inlet piping," *Journal of Pressure Vessel Technology*, 104(2), 120-129 (1982).
[4] H. Tezuka, T. Sakurai: "A trigger of Type IV damage and a new heat treatment procedure to supress it. Microstructure investigations of long-term ex-service Cr-Mo steel pipe elbows," *International Journal of Pressure Vessels and Piping*, 82, 165-174 (2005).
[5] N. Komai, F. Masuyama: "Microstructural degradation of the HAZ in 11Cr-0.4Mo-2W-V-Nb-Cu steel (P122) during creep," 42, 1364-1370 (2002).
[6] K. Sawada, K. Kudo, F. Abe: "Creep behaviour and stability of MX precipitates as high temperature in 9Cr-0.5Mo-1.8W-VNb steel," *Materials Science and Engineering A*, 319-321, 784-787 (2001).
[7] T.C. Totemeier, H. Tian and J.A. Simpson: "Effect of normalising temperature on creep strength of modified 9Cr-1Mo steel," *Metallurgical and materials transactions*, 37A, 1519-1525 (2006).
[8] H. Morimoto, S. Ohkita, H. Sakurai: "Creep Rupture Properties of Welded Joints of W Containing 9Cr Ferritic Heat Resistant Steel," *Quarterly journal of the Japan Welding Society*, 15(4), 664-673 (1997).
[9] K. Kubushiro, S. Takahashi, K. Morishima: "Microstructure development of welding joints in high Cr Ferritic steels," *9th Liege Confernce: Materials for Advanced Power Engineering 2010*, 370-379.
[10] Y. Tanaka, K. Kubushiro, S. Takahashi, N. Saito, H. Nakagawa: "Creep-Induced Microstructural Changes in Large Welded Joints of High Cr Heat Resistant Steel," *6th International Conference on Creep, Fatigue and Creep-Fatigue Interaction*, 55, 41-44 (2013).
[11] S. T. Kimmins, D. J. Gooch: "Austenite memory effect in 1 Cr–1 Mo–0·75V(Ti, B) steel," Metal Science, 17(11), 519-532 (1983).
[12] S. Matsuda, Y. Okamura: "Reverse transformation of low-carbon low alloy steels," *Tetsu-To-Hagane*, 60, 60-72 (1974).
[13] S. Watanabe, T. Kunitake: "On the formation of austenite grains from prior martensitic structure," *Tetsu-To-Hagane*, 61, 96-106 (1975).
[14] C. R. Das, M. Divya, S. K. Albert, A. K. Bhaduri, B. S. Murty: "Microstructural evolution in the intercritical heat affected zone of a boron containing modified 9Cr-1Mo Steel," *Welding World*, 53, 511-515 (2009).

Part B

New Materials

DEVELOPMENT OF FERRITIC HEAT-RESISTANT STEELS BASED ON NEW MATERIALS DESIGN CONCEPT

Y. Toda, M. Auchi, M. Shibuya, K. Sawada, H. Kushima, K. Kimura

National Institute for Materials Science
(1-2-1, Sengen, Tsukuba, Ibaraki 305-0047, Japan – TODA.Yoshiaki@nims.go.jp)

Abstract

To save fossil fuel resources and to reduce CO_2 emission, considerable efforts have been directed toward the research and development of heat-resistant materials that can help in improving the energy efficiency of power plants by increasing their steam temperature and pressure. Instead of the conventional 9-12Cr ferritic heat-resistant steels with a tempered martensitic microstructure, the authors have proposed "Precipitation Strengthened 15Cr Ferritic Steel" based on the new material design concept that is a solid-solution treated ferrite matrix strengthened by intermetallic compounds. In this study, the creep strength of the developed 15Cr ferritic steels with various Ni contents was investigated. As a result of the creep tests for the 15Cr steels at 923, 973, 1023 K up to about 65 000 h, it was found that the creep strength of the 15Cr steels was two times higher than that of the conventional 9Cr ferric heat-resistant steels at every temperatures. The creep rupture lives of the steel were 10 to 100 times longer than that of the conventional versions. The creep rupture strength of the 15Cr steels after 100 000 h was estimated to be 100 to 130 MPa at 923 K and 45 to 70 MPa at 973 K from Larson-Miller parameter method. In addition, the thermal linear expansion coefficients of the 15Cr steels were lower than that of conventional steels and alloys at the temperature from 323 K to 1023 K. Then, the authors believe the precipitation strengthened 15Cr ferritic steel is a candidate material of the high-temperature structural components in high-efficient thermal power plants.

Keywords: Creep strength, Ferrite matrix, Intermetallic compounds, Precipitation strengthening, Thermal linear expansion coefficient

1. Introduction

To save fuel resources and reduce CO_2 emissions, there is a growing need to increase the energy efficiency of conventional fossil-fired power stations. One strategy is to develop high-strength, heat-resistant materials that permit operation at higher steam temperatures and pressures. Considerable efforts have thus been directed toward the research and development of heat-resistant materials [1-3], especially austenitic heat-resistant steels and nickel-based superalloys, due to their superior creep strength and oxidation resistance. However, the authors' view is that the development of ferritic heat-resistant steels with high creep strength is also advantageous for realizing high energy-efficiency power plants. Ferritic heat-resistant steels are ideal for large and thick high-temperature structural components, due to their useful properties of high thermal conductivity, low thermal expansion coefficient, low susceptibility to thermal fatigue, low requirement for rare metals, and lower cost than austenitic steels or Ni-based superalloys [4].

The authors have proposed 15Cr steels, which include a higher chromium content than that of conventional 9 or 12Cr ferritic heat-resistant steels with a tempered martensitic microstructure

[5]. It has also been discovered that higher long-term creep strength than that of the conventional ferritic heat-resistant steels can be conferred on these new-concept precipitation-strengthened 15Cr ferritic steels with a ferrite matrix by optimizing the alloy content and applying heat treatments [6-12]. In the present study, the long-term creep strength of the 15Cr ferritic steels with various Ni contents were investigated. We believe that the findings of this study will prove useful for the development of new ferritic heat-resistant steels for use in high-energy efficiency power plants operated at 973 K and above.

2. Materials design concept and experimental procedure

Table 1: The chemical compositions of the conventional 9Cr ferritic heat-resistant steel (T92) [13] and the 15Cr steels with three Ni contents used in this study (mass%).

Samples	Fe	C	Si	Mn	Ni	Cr	Mo
T/P92	Bal.	0.07~ 0.13	~0.50	0.30~ 0.60	~0.40	8.00~ 9.50	0.30~ 0.60
0.0Ni	Bal.	0.046	0.22	0.49	<0.01	15.00	1.00
1.2Ni	Bal.	0.049	0.20	0.51	1.21	15.02	1.00
2.0Ni	Bal.	0.048	0.23	0.51	2.00	14.96	0.99

Samples	V	Nb	W	Co	N	B
T/P92	0.15~ 0.25	0.04~ 0.09	1.50~ 2.00	—	0.030~ 0.070	0.001~ 0.006
0.0Ni	0.19	0.043	6.07	2.97	0.033	0.0030
1.2Ni	0.20	0.051	6.04	2.96	0.042	0.0028
2.0Ni	0.20	0.050	6.07	2.98	0.036	0.0029

Table 1 shows the chemical compositions of the conventional 9Cr ferritic heat-resistant steel (ASME SA-213/SA-213M Grade T92) [13] and the 15Cr steels with three Ni contents used in this study. The following mentioned contents were modified for making the developed 15Cr steels.

• The Cr content was increased up to 15 % in order to obtain a ferrite matrix [5], because the authors believe that ferrite phase is more suitable for the improvement in long-term creep strength than tempered martensitic microstructure [10]. In addition, the increase in Cr content is expected to improve in steam oxidation resistance.

• The W content was increased up to 6 % in order to promote the precipitation of Laves phase (Fe_2W), which is one kind of intermetallic compound, as a precipitation-strengthening factor [6]. The high-temperature and long-term stability of Fe_2W is expected to be high, because the melting point of W is high and the diffusion rate of W is low.

• It has already been found that 3 %Co addition decrease in the coarsening rate of Fe_2W and make the morphology of them very fine [6].

• The C and N contents were reduced in order to improve in the long-term stability of microstructure [7].

- It has been found that the 2.0 %Ni addition improve in the impact toughness of the 15Cr steels drastically [8]. However, Ni addition decreases in the creep strength at 923 K slightly [9]. The effect of Ni content on the creep strength at higher temperature was investigated in this study.

The steel was melted in a vacuum induction furnace. An ingot weighing 10 kg was hot-forged into a round bar 15 mm in diameter and solution-treated for 0.5 h at 1473 K, followed by water quenching. The creep test specimens were round-bar test piece with 6 mm in gauge diameter and 30 mm in gauge length. The creep tests were conducted at 923, 973, and 1023 K at stresses ranging from 30 to 240 MPa for up to about 65 000 h in air. Creep deformation was measured using an extensometer attached to the gauge portion of the specimens.

The temperature dependence of thermal linear expansion coefficients of the 15Cr steels was measured be means of a push-rod type dilatometer using specimens with 3 mm in diameter and 15 mm in length.

3. Result
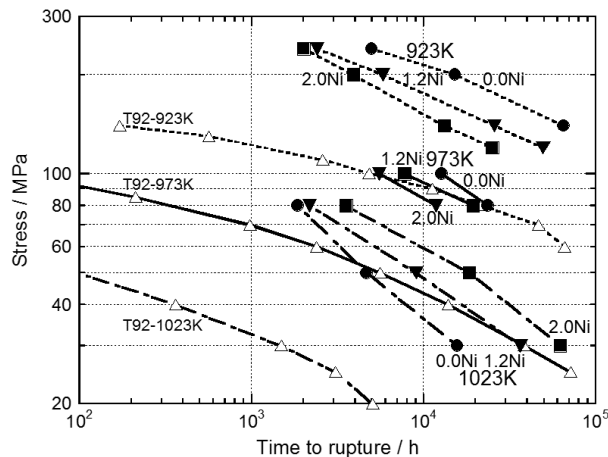
Figure 1: The creep stress vs. time to rupture curves for the 15Cr steels without Ni (solid circles), with 1.2 %Ni (solid triangles), 2.0 %Ni (solid squares), and the conventional T92 steel (open triangles) [14] at 923 K (dashed lines), 973 K (solid lines), and 1023 K (dash-dotted lines), respectively.

Figure 1 shows the creep stress versus time to rupture curves for the 15Cr steels without Ni (solid circles), with 1.2 %Ni (solid triangles), and 2.0 %Ni (solid squares) at 923 K (dashed lines), 973 K (solid lines), and 1023 K (dash-dotted lines), respectively. In the same Figure, the curves for a 9Cr-0.5Mo-1.8W-V-Nb steel tube (ASME SA-213/SA-213M Grade T92) [14] under the same temperatures are shown by open triangles. T92 steel is conventional ferritic

heat-resistant steel with a tempered martensitic microstructure; it possesses the highest creep strength of ferritic heat-resistant steels.

The creep strength of the 15Cr steels is about two times higher than that of T92 steel at every temperature. The creep rupture-lives of the steels are approximately 100 times longer than those of T92 steel at 923 and 973 K, and 10 ~ 100 times longer than those of T92 steel at 1023 K. Among the 15Cr steels, the addition of Ni decreases the creep strength at 923 K. However, the addition of Ni increases the creep strength at 1023 K.

In order to compare all data for creep-ruptured times in Figure 1 by compensating for differences in the creep test temperatures, the data in Figure 1 are arranged by Larson-Miller Parameters (LMP), which is expressed as $T_{(K)}(C + \log t_{R(h)})$, where $T_{(K)}$ is absolute temperature, C is a constant ($C = 20$ in this study), and $t_{R(h)}$ is time to rupture, in Figure 2. The creep rupture strength of the 15Cr steels without Ni, with 1.2 %Ni, 2.0 %Ni, and T92 steel [14] are plotted in Figure 2 by the same kinds of symbols and lines as Figure 1, respectively. The creep strength of the conventional 16Cr-12Ni-Mo austenitic stainless steels tube (JIS SUS 316H TB) [15] are also plotted in the same figure by open circles.
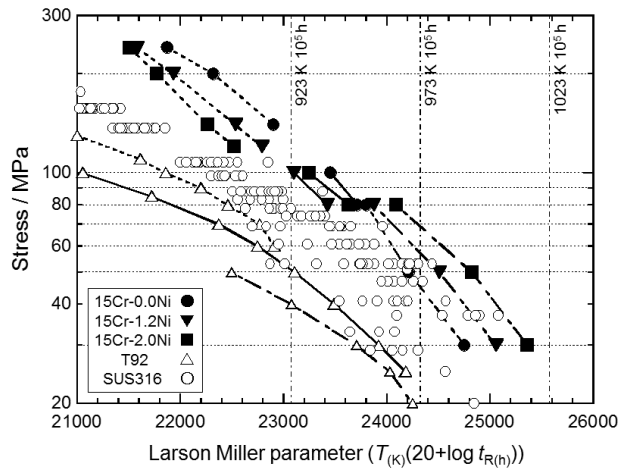
Figure 2: The creep stress vs. Larson-Miller Parameter curves for the 15Cr steels without Ni (solid circles), with 1.2 %Ni (solid triangles), 2.0 %Ni (solid squares), T92 steel (open triangles) [14], and the conventional SUS316 steels (open circles) [15]. These data were obtained from the creep tests at 923 K (dashed lines), 973 K (solid lines), and 1023 K (dash-dotted lines), respectively.

It can be seen from this Figure that the creep strength of the 15Cr steels is twice as those of T92 steel at every times and temperatures. Normally, the creep strength of ferritic steels is lower than those of austenitic types, due to the fast diffusion rates of elements in ferrite phase.

However, the creep strength of the 15Cr ferritic steels is higher than those of SUS 316H austenitic steels under low-temperature and short-term conditions, and is almost as high as that at high-temperature and long-term conditions.

The three vertical dash-dotted lines in Figure 2 correspond to LMP values of 100 000 h at 923, 973, and 1023 K, respectively. From Figure 2, the creep rupture strength after 100 000 h of the 15Cr steels can thus be estimated to be as 100 to 130 MPa at 923 K and 45 to 70 MPa at 973 K, which strength level that is double that of conventional ferritic heat-resistant steels, and also superior to that of conventional austenitic heat-resistant steels.

Figure 3 shows the (a) elongation and (b) reduction of area of the creep-ruptured specimens of the 15Cr steels and T92 [14] with time to rupture by the same symbols as Figure 1 and Figure 2. The elongation of almost of the 15Cr-0.0Ni steels and T92 steels is lower than 20 %. In contrast, the elongation of almost of the 15Cr with 1.2 %Ni and 2.0 %Ni steels is higher than 20 % even though the time to rupture of the specimens is longer than 10 000 h. In the same way, the reduction of area of almost of the 15Cr-0.0Ni steels and T92 steels is lower than 30 %. However, the reduction of area of all of the 15Cr with 1.2 %Ni and 2.0 %Ni steels is higher than 50 %. Then, 1.2 %Ni or 2.0 %Ni addition improve in the ductility of the creep ruptured 15Cr steels drastically.
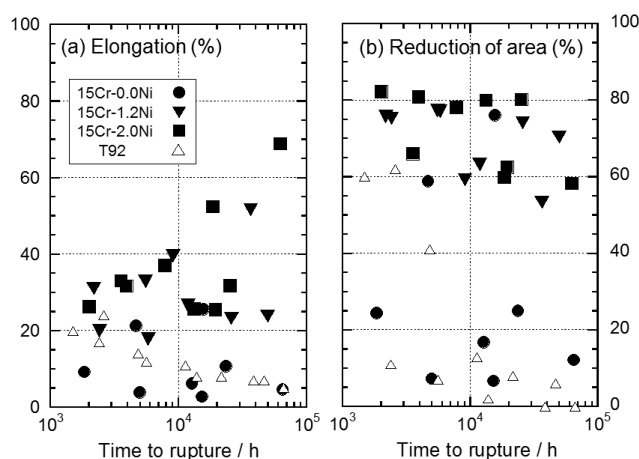
Figure 3: The (a) elongation and (b) reduction of are of the creep-ruptured specimens of the 15Cr steels without Ni (solid circles), with 1.2 %Ni (solid triangles), 2.0 %Ni (solid squares), and T92 steel (open triangles) [14].

Figure 4 shows the temperature dependence of thermal linear expansion coefficients of the 15Cr steels by same symbols as Figure 1 to 3. The coefficients of some kinds of the conventional ferritic (9Cr-1Mo and 12Cr, 13Cr) or austenitic (18Cr-8Ni, 25Cr-20Ni) steels, and the nickel-

base superalloys (NCF600, NCF800) [16] are also plotted in the same figure. The thermal expansion coefficients of the 15Cr steels are lower than that of any steels and alloys at the temperature range between 323 K and 1023 K. The significant difference between the coefficients of the 15Cr without Ni and that of 1.2 %Ni steels is not recognized. The coefficients of the 15Cr with 2.0% Ni steels are similar with those of the other two 15Cr steels at the higher temperatures than 823 K. Although 2.0 %Ni addition increase the coefficients slightly at 823 K and below, the coefficients of the 15Cr with 2.0 %Ni steels are lower than those of the conventional high Cr ferritic steels. It was found that Ni addition don't affected to the thermal linear expansion coefficient harmfully.
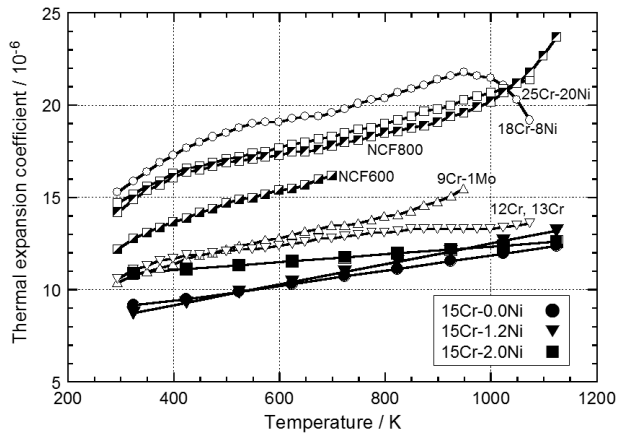
Figure 4: The temperature dependence of thermal linear expansion coefficients of the 15Cr steels without Ni (solid circles), with 1.2 %Ni (solid triangles), 2.0 %Ni (solid squares), and some kinds of the conventional ferritic, austenitic steels and the nickel-based superalloys [16].

4. Discussion

Figure 5 shows the temperature dependence of the calculated equilibrium mole fractions of austenite phase of the 15Cr steels with the various Ni contents by the solid curves. The solid symbols show the experimental volume fractions of martensite phase after the solid-solution treatment [8, 9]. Not only ferrite phase but also martensite phase were observed in the matrix of 15Cr steels with Ni after solid-solution treatment. The volume fractions of martensite phase were 16.7 % and 31.2 % in the steels with 1.2 %Ni and 2.0 % Ni, respectively [8, 9]. That is because also austenite phase is estimated to be stable at the solid-solution temperature in the 15Cr steels with Ni as shown in Figure 5, and austenite phase transform to martensite phase during water quenching at the solid-solution treatment. During creep exposure, only coarsened block-like particles were precipitated sparsely within martensite phase of the 15Cr steels with Ni, although a lot of fine precipitates were formed homogeneously within the ferrite matrix. As

a result of reduce of the precipitation-strengthening effect of the martensite phase, the creep strength of the 15Cr steels with Ni is decreased at 923 K [9].
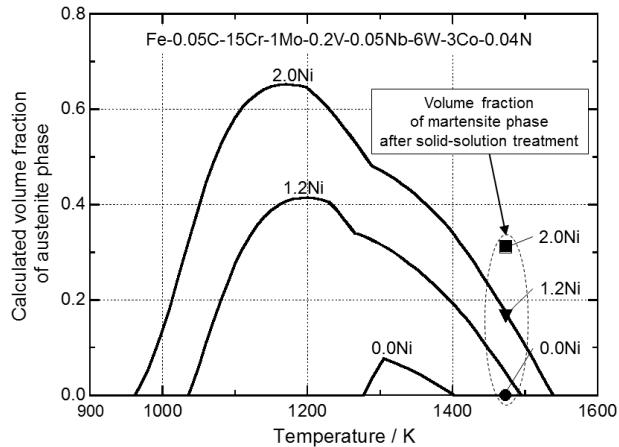
Figure 5: The temperature dependence of the calculated equilibrium mole fractions of austenite phase of the 15Cr steels with the various Ni contents. The solid symbols show the experimental volume fractions of martensite phase after the solid-solution treatment [8, 9].

In contrast, the addition of Ni improve in the creep strength of the 15Cr steels at 1023 K as shown in Figure 1, and the reason of which is unclear. The authors suppose that austenite phase was formed from the martensite phase at 1023 K in the 15Cr steels with Ni, because austenite phase is calculated to be stable at 1023 K in the steel as shown in Figure 5. Generally, the creep rate of FCC structure is lower than that of BCC structure, since the diffusion rate of elements in FCC phase is low. Then, the Ni addition is speculated to improve the creep strength of the 15Cr steels at 1023 K through the forming austenite phase.

The addition of Ni improve in not only the high-temperature creep strength and the impact toughness [8] but also the creep ductility of the 15Cr steels as shown in Figure 3. And the thermal linear expansion coefficient of them is not affected drastically by the addition of Ni. The 15Cr steels are expected to have excellent steam oxidation resistance because of higher Cr content than that of the conventional 9-12 Cr ferritic heat-resistant steels. And the 15Cr steels are expected to be lower cost materials that Ni-base superalloys, because of including not so much rare metals even though the 2.0 %Ni addition. Then, the authors believe that the precipitation-strengthened 15Cr ferritic steels are attractive candidate materials for high-temperature structural components in high-efficient thermal power stations.

5. Conclusions

245

The authors have proposed "Precipitation-Strengthened 15Cr Ferritic Steel", which has solution-treated ferrite matrix with low dislocation density, and is strengthened by precipitation of intermetallic compounds. And the long-term creep strength of the 15Cr steels with various Ni contents were investigated. The following results were obtained;

• The creep strength of the 15Cr steels was two times higher, and the creep rupture lives were 10 to 100 times longer than that of the conventional 9Cr ferritic heat-resistant steel at 923, 973, and 1023 K.

• Using the Larson-Miller parameter method, the creep rupture strength of the 15Cr steels after 100 000 h was estimated to be 100 to 130 MPa at 923 K and 45 to 70 MPa at 973 K. Their creep strength level was comparable to or higher than that of the conventional austenitic steels.

• The addition of Ni improve in the creep strength at 1023 K and the creep ductility of the 15Cr steels, and doesn't affect the thermal linear expansion coefficients of the 15Cr steels harmful, although the addition of Ni reduce the creep strength at 923 K slightly.

• The 15Cr steels are expected to have excellent steam oxidation resistance and to be lower cost materials that Ni-base superalloys. Then, the authors believe that the precipitation-strengthened 15Cr ferritic steels are attractive candidate materials for high-temperature structural components in high-efficient thermal power stations.

References

[1] M. Fukuda, Advanced USC technology development in Japan, *Proceedings of the 9th Liege Conference: Materials for Advanced Power Engineering*, 5-19, (2010).

[2] H. Tschaffon, 700 °C power plant technology -status and challenge, *Proceedings of the 9th Liege Conference: Materials for Advanced Power Engineering*, 20-28, (2010).

[3] P. M. Barnard, L. W. Buchanan, M. Barrie, Material development for supercritical boilers and pipework - bridging the gap?, *Proceedings of the 9th Liege Conference: Materials for Advanced Power Engineering*, 39-54, (2010).

[4] Y. F. Yin, R. G. Faulkner, Physical and elastic behavior of creep-resistant steel, *Creep-resistant steels*, 217-240, (2008).

[5] K. Kimura, K. Seki, Y. Toda, F. Abe, Development of high strength 15Cr ferritic creep resistant steel with addition of tungsten and cobalt, *ISIJ Int.,* **41**, S121-S125, (2001).

[6] Y. Toda, K. Seki, K. Kimura, F. Abe, Effects of W and Co on long-term creep strength of precipitation strengthened 15Cr ferritic heat resistant steels, *ISIJ Int.,* **43**, 112-118, (2003).

[7] Y. Toda, H. Tohyama, H. Kushima, K. Kimura, F. Abe, Improvement in creep strength of precipitation strengthened 15Cr ferritic steel by controlling carbon and nitrogen contents, *JSME Int. J. A,* **48**, 35-40, (2005).

[8] Y. Toda, H. Tohyama, H. Kushima, K. Kimura, F. Abe, Influence of chemical composition and heat treatment condition on impact toughness of 15Cr ferritic creep resistant steel, *JSME Int. J. A,* **48**, 125-131, (2005).

[9] Y. Toda, M. Iijima, H. Kushima, K. Kimura, F. Abe, Effects of Ni and heat treatment on long-term creep strength of precipitation strengthened 15Cr ferritic heat resistant steels, *ISIJ Int.,* **45**, 1747-1753, (2005).

[10] K. Kimura, Y. Toda, H. Kushima, K. Sawada, Creep strength of high chromium steel with ferrite matrix, *Int. J. Press. Vessels Pip.,* **87**, 282-288, (2010)

[11] M. Shibuya, Y. Toda, K. Sawada, H. Kushima, K. Kimura, Effect of nickel and cobalt addition on the precipitation-strength of 15Cr ferritic steels, *Mater. Sci. Eng. A,* **528**, 5387-

5393, (2011).

[12] M. Shibuya, Y. Toda, K. Sawada, H. Kushima, K. Kimura, Effect of precipitation behavior on creep strength of 15%Cr ferritic steels at high temperature between 923 and 1023 K, *Mater. Sci. Eng. A,* **592**, 1-5, (2014).

[13] Japan Society of Mechanical Engineers, Standards for Thermal Power Generation Facilities, (2000).

[14] National Institute for Materials Science, Data sheets on the elevated-temperature properties of 9Cr-0.5Mo-1.8W-V-Nb steel tube for power boilers (ASME SA-213/SA-213M Grade T92) and 9Cr-0.5Mo-1.8W-V-Nb steel pipe for high temperature service (ASME SA-335/SA-335M Grade P92), *NIMS creep data sheet No. 48*, (2002).

[15] National Research Institute of Metals (present address: National Institute for Materials Science), Data sheets on the elevated-temperature properties of 18Cr-12Ni-Mo stainless steel tubes for boilers and heat exchangers (SUS 316H TB), *NRIM creep data sheet No.6B*, (2000).

[16] Japanese Industrial Standards Committee, Constructuon of Pressure Vessel, *Japanese Industrial Standard B 8267*, (2008).

CURRENT STATUS OF THE DEVELOPMENT OF CREEP-RESISTANT, ALUMINA-FORMING AUSTENITIC STAINLESS STEEL ALLOYS

Yukinori Yamamoto*, Michael P. Brady, Govindarajan Muralidharan, Bruce A. Pint

Materials Science and Technology Division, Oak Ridge National Laboratory
Oak Ridge, TN 37831-6083, USA
e-mail: yamamotoy@ornl.gov (*corresponding author)

Abstract

This paper overviews the recent advances in the development of wrought and cast, creep-resistant, alumina-forming austenitic (AFA) stainless steel alloys at Oak Ridge National Laboratory. AFA alloys exhibit good high-temperature oxidation resistance through the formation of a protective Al_2O_3 scale together with good creep resistance achieved through the precipitation of multiple types of second-phases. The formation of an external, protective alumina-scale at elevated temperatures offers oxidation resistance superior to that of chromia-forming conventional stainless steels, especially in water-vapor containing environments. The microstructure of AFA alloys primarily consists of austenitic single-phase matrix together with MC (M: mainly Nb), $M_{23}C_6$ (M: mainly Cr), (Fe,Ni)Al-type B2, $Fe_2(Nb,Mo)$-type C14-Laves, and Ni_3Al-type $L1_2$ phases, depending upon the composition and temperature. The creep properties strongly depend on the types and amounts of such second-phase precipitates, which can be controlled by proper alloying additions. Recent work has focused on developing AFA alloys with improved creep properties. Wrought alloy compositions based on Fe-14Cr-3Al-32Ni-Nb-Ti with additional strengthening from coherent $Ni_3(X)$ dispersions have been developed with improved creep resistance in the range of 700-750 °C without losing alumina-scale formability. Cast versions of AFA alloys based on Fe-14Cr-3Al-25Ni-1Nb-C with protective alumina-scale formability along with creep resistance comparable to that of a traditional chromia-forming, cast austenitic stainless steel (HN, Fe-20Cr-25Ni base) at temperatures up to 750 °C have been developed successfully. Further improvement of the cast AFA alloys to increase the upper operating temperatures above 950 °C is being pursued.

Keywords: austenitic stainless steels, alumina-forming, creep, oxidation resistance, computational thermodynamics

Author's note: Part of this paper is based on the recent alloy development studies and new findings published in references 1-18.

1. Introduction

Over the decades, numerous world-wide efforts have been made in the area of heat resistant steel and alloy development to meet with the demands of higher temperature capabilities in various metal-base structural components for near-future advanced fossil-fired boiler/steam turbine power plants [19, 20]. The materials of interest range from bainitic/ferritic-martensitic steels and austenitic stainless steels to Ni base alloys, depending on the components or the service temperatures/pressures. The efforts mainly focus on further improvement of high

temperature strength, oxidation/corrosion resistance, fabricability, together with inexpensive material cost compared to the materials currently in services [21, 22].

Heat-resistant austenitic stainless steels are widely used in industrial applications ranging from energy production to chemical processing, and they rely on the external Cr_2O_3 (chromia)-based scale formation for the surface protection in various industrial environments and a wide temperature range. However, compromised oxidation resistance of the chromia-based scales in the presence of aggressive species such as water vapor, carbon, sulfur, etc. [23] prevents the higher temperature capability needed to achieve improved efficiencies. Al_2O_3 (alumina)-forming austenitic (AFA) stainless steel alloys, on the other hand, offer the potential for superior high-temperature oxidation and corrosion resistance compared to conventional stainless steels and Ni-base alloys which use chromia-based scales. This is due to almost two-orders of magnitude slower growth kinetics and greater stability of external alumina-scales at elevated temperatures, particularly in the presence of water vapor species encountered in many industrial process and energy production environments [24, 25]. Development efforts for AFA stainless steels can be found starting from the late 1970's in literatures [26-30]. However, none of them successfully achieved the balanced properties of oxidation resistance and creep strength at elevated temperatures, because of the detrimental effects of the Al addition on the high-temperature strength such as strong BCC stabilizing effect of Al or sacrificing carbo-nitride strengthening due to the formation of coarse AlN [31, 32].

The current authors have successfully developed creep-resistant AFA stainless steels which targeted the high temperature applications in the range of ~600-900 °C, through a guidance of computational thermodynamics [1-18]. The alloys possess a unique combination of excellent oxidation resistance through the alumina scale formation and good creep properties via nano-scale carbides or coherent intermetallic second-phase precipitates, as well as inexpensive material cost relative to the commercially available chromia-forming heat resistant steel alloys. The studies also focused on scientific understanding of how the key alloying elements play the roles of improvement or detriment on the stability of the protective alumina-scale and high temperature creep strength. To date, various AFA grades have been developed which include the alloys with higher temperature oxidation resistances up to 950 °C, low-Ni containing inexpensive materials, or high creep strength comparable or superior to advance austenitic stainless steels or Ni-base alloys.

In this paper, the recent advances in the development of creep-resistant AFA stainless steel alloys at Oak Ridge National Laboratory have been overviewed. Design strategies of initial alloy development, extended studies for improving higher temperature capability, commercialization efforts, and new developmental directions such as "intermetallic strengthened AFA alloys" and "cast version of AFA alloys", are presented.

2. Carbide-strengthened wrought AFA

2.1. Alloy design

In order to avoid the formation of BCC (δ-Fe) or sigma (σ-FeCr) formation in the austenite (γ-Fe) matrix which degrades the high-temperature strength significantly [3], computational thermodynamic tools were used to predict the range of Cr and Al contents of γ-Fe matrix free from δ-Fe/σ-FeCr formation. It should be noted that the Cr addition is known to reduce the Al additions needed for alumina-scale formation in the alumina-forming alloys, through the so-called "third element effect" [24], so that both elements are the key for the AFA alloy design. Figure 1 shows the upper limits of Cr and Al additions to avoid δ-Fe phase formation in a temperature range from 600 to 1200 °C (1a) and σ-FeCr phase formation at 650, 700, 750, and 800 °C (1b), based on thermodynamic calculations of Fe-Cr-Al-(20,25,30)Ni-1Nb-2Mo-0.1C (wt%) alloys [9, 14]. The Al addition decreases the Cr upper limit to avoid δ-Fe formation significantly, although the δ-Fe free region expands with increasing Ni additions because of strong FCC stabilizing effect of Ni. On the other hand, the Cr upper limits for σ-FeCr free region are insensitive to the Ni addition at the designated temperatures, especially below 750°C. These results suggest that the AFA alloy compositions have to be selected relative to the intended application temperature range to be used. For the higher temperature use, such as above 800 °C, ~14 wt% Cr combined with up to ~5 wt% Al can be used to avoid σ-FeCr formation, and more than 25 wt% Ni would be required to eliminate δ-Fe formation. At temperatures around 650 °C, the amount of the Cr addition would be limited to around 12 wt% or less for 3 – 5 wt% Al containing alloys to remain σ-FeCr free. Note that the composition ranges free from the δ-Fe and σ-FeCr formation can be expanded by using proper alloying additions; i.e. increasing C, Mn, or Cu and reducing Mo or W. High Ni and Nb contents would be preferred for better oxidation resistance [7, 10] but they also increase raw material costs. The AFA alloy compositions must be selected based on achieving a balance of these considerations.
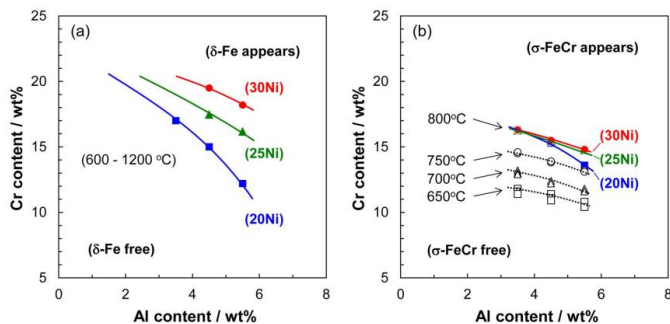
Figure 1:   Predicted phase diagram of Fe-Cr-Al-(20,25,30)Ni-1Nb-2Mo-0.1C showing limitations of Cr and Al additions to avoid the formation of (a) δ-Fe in a range from 600 to 1200 °C, and (b) σ-FeCr at 650, 700, 750, and 800 °C (after references 9 and 14).

Various alloying additions are utilized in the AFA alloys to realize the unique combination of oxidation resistance and high temperature creep strength. Table 1 summarizes the effects of alloying additions on properties of the AFA alloys developed to date [14]. It describes the advantages and disadvantages of various key alloying additions as a function of concentration (qualitatively low to high), based on insights obtained from the AFA alloy development effort as well as well-known trends from conventional austenitic stainless steel alloys [1-18, 33]. As with conventional stainless steel alloys, optimization of composition for AFA alloys reflects competing and often contradictory effects of the various alloying additions on oxidation resistance, high temperature mechanical properties, workability, and raw material cost.

Table 1: Effects of alloying additions on the properties of AFA alloys [14]

Key alloying elements	Effect of alloying addition		
		Relatively low amount	Relatively high amount
Al	Advantage:	• Less δ-Fe stabilizing effect	→ • **Protective alumina scale formation** • Strengthening by intermetallics (B2-NiAl, γ'-Ni$_3$Al)
	Disadvantage	• Internal oxidation of Al	→ • Stabilize δ-Fe, M$_{23}$C$_6$, and σ-FeCr • Interfere N additions for strengthening (by AlN formation)
Cr	Advantage:	• Less δ-Fe stabilizing effect	→ • **Protective alumina scale formation (third element effect)**
	Disadvantage	• Internal oxidation of Al	→ • Stabilize δ-Fe, M$_{23}$C$_6$, and σ-FeCr
Ni	Advantage:	• Less expensive raw material cost	→ • **Stabilize γ-Fe**, B2-NiAl, and γ'-Ni$_3$Al • Protective alumina scale formation
	Disadvantage	• Less γ-Fe stabilizing effect	→ • Higher cost
Nb	Advantage:	• Reduce coarse carbides	→ • **Protective alumina scale formation** • MC and Fe$_2$Nb for strengthening
	Disadvantage	• Internal oxidation of Al • Stabilize M$_{23}$C$_6$ relative to MC	→ • Un-dissolved MC appears at solutionized condition because of low solution limit of Nb in γ-Fe.
Mo, W	Advantage:	• Less expensive raw material cost	→ • Increase solution hardening effect
	Disadvantage	• Less solution hardening effect	→ • Stabilize σ-FeCr and δ-Fe • Higher cost
C	Advantage:	• Reduce coarse carbides	→ • Stabilize γ-Fe relative to δ-Fe
	Disadvantage	• Less γ-Fe stabilizing effect	→ • Stabilize M$_{23}$C$_6$ relative to MC
Y, Hf	Advantage:	• Good workability	→ • Stabilize protective alumina scale
	Disadvantage	• Less protective alumina scale	→ • Too much addition results in less workability.
Ti, V, N	Advantage:	• Protective alumina scale formation (Ti+V < 0.3 wt%, N < 200wppm)	→ • Increase high-temp. strengthening due to M(C ,N) formation • Nitrogen stabilizes γ-Fe matrix.
	Disadvantage	• Less high-temperature strength	→ • Internal oxidation of Al

Most of the AFA alloys rely on second-phase precipitation strengthening, so that the alloy compositions are controlled to maximize the strengthening from second-phases at the targeted service temperature (~600-900 °C). The second-phases also need to be mostly soluble into the γ-Fe matrix at elevated temperatures (~1100-1250 °C) in order to control fine dispersions of

the second-phase precipitates for strengthening. Figure 2 shows typical microstructures of the AFA alloys after solution heat-treatment at 1250 °C (2a, scanning electron microscope back-scattered electron image, SEM-BSE), after aging for 2000 h at 750 °C (2b, SEM-BSE), and after creep-rupture testing for around 2000 h at 750°C and 100 MPa (2c, transmission electron microscope bright field image, TEM-BFI). Note that the alloys in the images are Fe-12Cr-4Al-1Nb-0.1C base (2a, 2b) and Fe-14Cr-2.5Al-0.9Nb-0.08C base (2c), respectively [14]. The solution heat-treatment resulted in γ-Fe single matrix with a limited amount of coarse MC-type carbides (M: mainly Nb), consistent with the results of thermodynamic calculations [9, 14]. After aging at 750 °C dense and fine second-phase dispersions can be observed, consisting of mainly (Fe,Ni)Al-type B2 phase (rod-like particles with dark contrast, 300 nm - 1 μm size) and Laves phase (spherical particles with bright contrast in the matrix, less than 500 nm size), together with the coarse MC (brighter particles near the grain boundary, 1-2 μm size) that remained from solution heat-treatment. However, such B2 and Laves phase precipitates exhibit a limited effect for improving the high-temperature tensile strength [3, 9, 12, 28, 34]. The main source of the creep resistance was provided from nano-scale MC carbide formation with around 10 nm size, as shown in Fig. 2c, which were effective in pinning dislocations in the γ-Fe matrix to increase the creep resistance. Cold-work (e.g. cold-rolling) applied prior to the creep testing was also effective to improve creep properties because the introduced dislocations act as nucleation sites [35-37], which resulted in almost doubled creep-rupture lives of AFA alloys at 750 °C [3, 9].
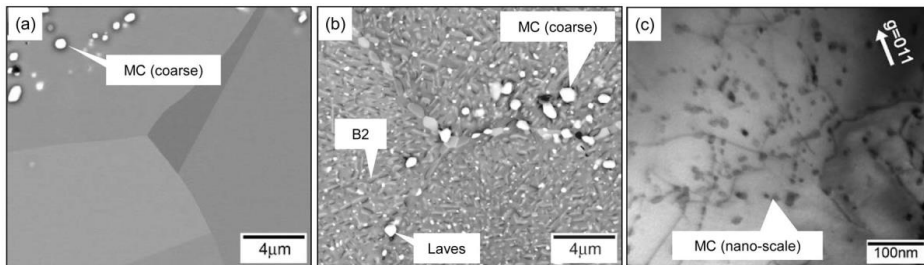
Figure 2: SEM BSE and a TEM BF images showing a typical microstructure of AFA alloys: (a) after solution heat-treatment at 1250°C, (b) aged at 750 °C for 2000 h, and (c) after creep testing at 750 °C and 100 MPa for 2000 h (after reference 14).

2.2. Oxidation resistance

An unexpected finding in AFA alloys is that oxidation resistance correlates not simply with the level of Al and Cr additions, but also with the level of Nb and Ni additions. Figure 3 shows plots of the Al and Nb contents in AFA alloys relative to alumina scale formation [8, 11, 14]. The alloys above the boundary lines exhibit high oxidation resistance due to the formation of external, protective alumina scale at designated conditions (based on 20-50 x 100 h cyclic oxidation testing, total 2000-5000 h exposure). Below the lines, the alloys show internal oxidation of Al with the formation of Fe- and Cr-rich oxide nodules after a certain

number of cycles of oxidation tests. The relative amounts of Al and Nb needed for the external alumina scale formation in air increase moderately from 800 to 900 °C (Fig. 3a). Increasing the Ni level from 20 to 25-26 wt% significantly decreases the amount of Nb needed for alumina scale formation at 900 °C in air, indicating that the Ni addition is also a key to improve oxidation resistance. In air with 10 volume % water vapor at 800 °C, on the other hand, much higher Nb (2.5-3 wt%) rather than high Al is needed for the protective alumina scale formation (Fig. 3b). Resistance in oxidizing environments containing high concentrations of water vapor is a key issue not only for fossil-fired steam plants, but also for applications ranging from combustion environments in gas turbines and engines to chemical/petrochemical processing to solid oxide fuel cell heat exchangers. It should be noted that virtually all the AFA alloys developed to date show good oxidation resistance at 650-700 °C in water vapor conditions, which is the temperature range of interest for near-future advanced fossil-fired steam plants [19-22].
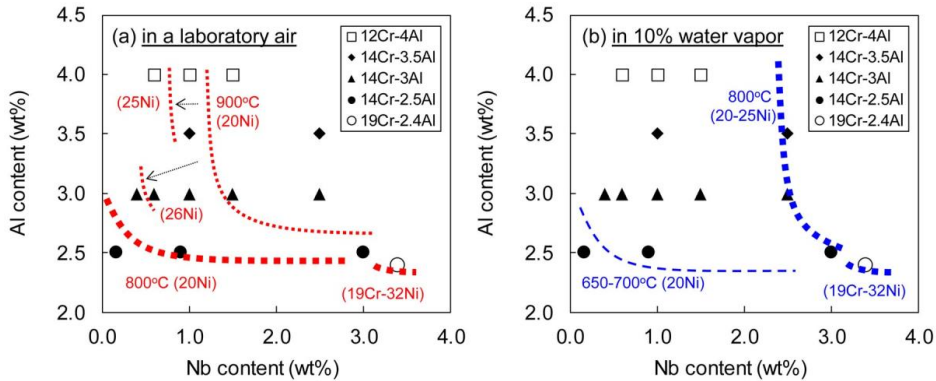
Figure 3: Composition maps of alumina scale formation as a function of Al and Nb level in (a) air and (b) air with 10% water vapour, showing the lower limit boundary lines exhibited high oxidation resistance after total 2000 – 5000 h exposure (after reference 14).

The solubility of Al in the γ-Fe matrix is on the order of ~2 to 2.5 wt% Al, so that the higher-Al containing alloys, such as the alloys with 3 or 4 wt% Al, exhibit dispersion of B2 phase precipitate during aging [7, 9]. These precipitates act as Al reservoirs for the alumina scale growth [7], resulting in a B2-denuded zone directly underneath the scale (Fig. 4). The Al profile within the B2-denuded zone for the 3 and 4 wt% Al alloys remained constant at the 2-2.5 wt% Al range of the solubility limit of Al in the γ-Fe matrix. The 2.5 Al containing alloy (Fe-14Cr-2.5Al-21Ni-3Nb-0.2V base [8]) showed significant subscale Al depletion when oxidized at 900 °C in air, which is considered the source of loss of alumina scale formation ability [7]. Therefore, a minimum of 3 wt% Al in the alloy appears sufficient to maintain alumina scale formation in the 800-900 °C range, assuming with sufficient Nb addition.
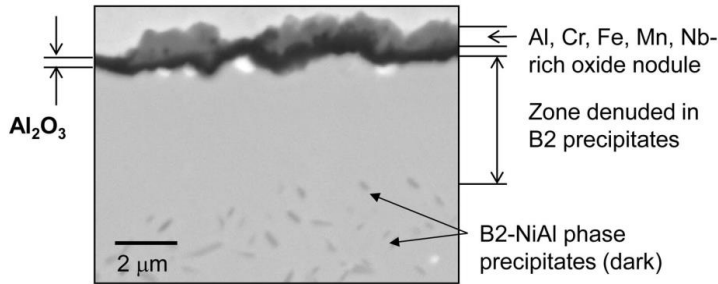
Figure 4: Cross-sectional SEM-BSE image of Fe-12Cr-4Al-20Ni-0.6Nb base alloy exposed at 900° C in air for 100 h (after references 7 and 8).

2.3. Creep and tensile properties

As described earlier, the temperature capability of AFA alloys depends on the alloy composition, which mainly relies on the Ni contents to maintain δ-Fe free γ-Fe matrix. Currently there are three different AFA grades, categorized by different Ni levels, as summarized in Table 2. The standard AFA grade utilizes nano-scale carbide strengthening such as MC or $M_{23}C_6$. A good oxidation resistance is expected up to 750-950 °C, depending upon the alloy composition (higher Ni and Nb would be required for higher temperature capability). The low Ni AFA[LN] grade targets inexpensive material cost by using lower Ni content, to a level comparable to type 347 austenitic stainless steel (18Cr-11Ni base), with an excellent oxidation resistance up to 650-700 °C range and better creep strength than type 347. High creep strength AFA grade uses relatively higher amount of Ni addition, 30 to 35 wt%, which results in stable, coherent γ'-Ni$_3$Al L1$_2$ phase precipitates in γ-Fe matrix for additional strengthening (the details are described in Section 3).

Table 2: Composition ranges and characteristics of three different AFA grades.

AFA grade	Composition range, wt%	Remarks
Standard AFA	Fe-(14-15)Cr-(2.5-4)Al -(20-25)Ni-(1-3)Nb	• ~750-950 °C temperature limit for Al$_2$O$_3$ formation • higher temperature ranges need higher Ni and Nb + rare earth additions • MC and M$_{23}$C$_6$ strengthening
Low Nickel AFA[LN]	Fe-14Cr-2.5Al-12Ni -0.6Nb-5Mn-3Cu	• ~ 650-700 °C temperature limit for Al$_2$O$_3$ formation • M$_{23}$C$_6$ strengthening
High Creep resistance AFA	Fe-(14-19)Cr-(2.5-3.5)Al -(30-35)Ni-3Nb	• ~750-850 °C temperature limit for Al$_2$O$_3$ formation • Coherent g'-Ni$_3$Al strengthening

Creep properties of two different standard AFA grades (20Ni-1Nb base and 25NI-2.5Nb base) and a AFA[LN] grade are shown in Figure 5, by using Larson-Miller Parameter (LMP) plotted as a function of stress. The AFA with 20Ni-1Nb is the best MC strengthened AFA to date which shows comparable creep properties to a chromia-forming, advanced austenitic stainless steel alloy 709 (Fe-20Ni-25Ni-Mo-Nb base). The AFA with 25Ni-2.5Nb is designed for high

temperature oxidation resistance at 800 °C, but exhibits relatively low creep resistance among the series of AFA. However, the creep strength is still ~20% higher than that of type 347. The AFA[LN] grade shows a good creep property close to the AFA 20Ni-1Nb or the alloy 709.
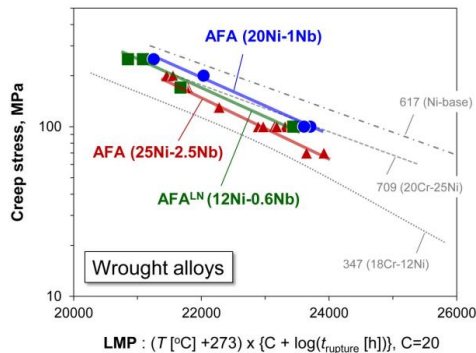
Figure 5: LMP plot showing the creep properties of three different AFA grades (two standards and one AFA[LN]), compared to those of commercial, chromia-forming heat resistant austenitic stainless steels (type 347 and alloy 709) and Ni base alloy (alloy 617) [1].

The raw material costs of the AFA alloys and commercial heat resistant steel alloys estimated from the prices of major elements [38], and then normalized by type 347 material cost, are plotted in Figure 6. The breakdown of each elemental cost reveals that Ni is dominant for the total raw material cost in the presented alloys. The costs of the AFA[LN] grade and the AFA with 20Ni-1Nb are equivalent to that of type 347 and alloy 709, respectively. The AFA with 25Ni-2.5Nb exhibited almost a half of the cost of Ni-base alloy 617. Since there is an advantage of oxidation resistances in the AFA alloys compared to the commercial chromia-forming alloys, the cost performances are significant.
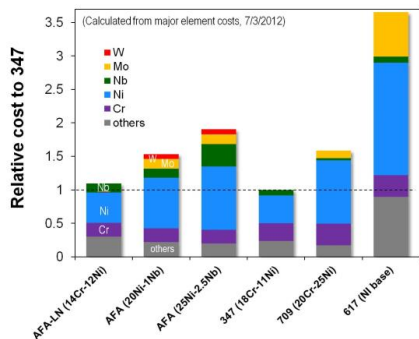
Figure 6: Comparison of relative raw material cost of AFA alloys and commercial heat resistant steel alloys, normalized by the cost of type 347 stainless steel calculated from the elemental prices based on July 2012 data [38].

2.4. Commercialization efforts

One of the strong candidate applications for AFA steel alloys is foil products which aim to be used as a recuperator in combined gas turbine systems with higher operation temperature or a better cost performance than that of the materials currently used [39]. The evaluation of oxidation and creep resistances of AFA foils have systematically been conducted in order to assess the feasibility of the AFA foils to be used as a commercial-base heat exchanger product [18]. Figure 7 summarizes the advantage of an AFA foil product (AFA-F4: 25Ni-2.5Nb base) compared to commercially available chromia-forming alloy 120 (Fe-25Cr-37Ni-base) exposed at 800 °C in a water-vapor containing environment, showing the soundness of the AFA foil as a structural material even after 10,000 h exposure.
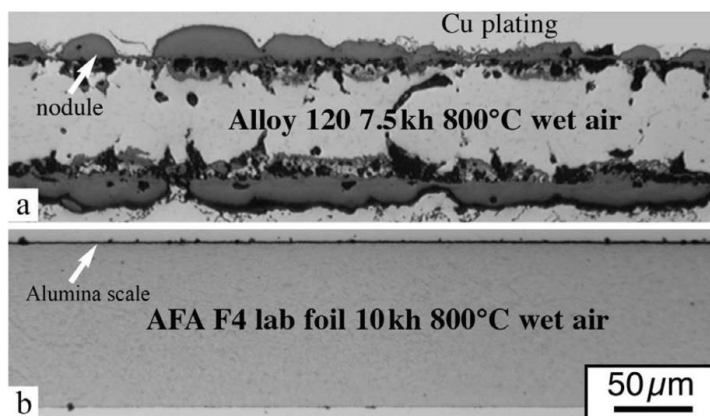
Figure 7: Cross-sectional microstructure of foils of (a) commercial alloy 120 after 7,500 h in wet (10%H₂O) air and (b) AFA F4 foil after 10,000 h at 800 °C in wet air (after reference 18).

Commercialization effort was conducted with several industrial partners to manufacture the AFA foil products by using commercially available fabrication processes, such as vacuum-induction-melting + vacuum arc re-melting (VIM-VAR), hot- and cold-rolling, annealing, etc., in the commercial-base factory equipment/lines. The standard AFA grade with 25Ni-2.5Nb was selected for the first trial foil fabrication. Figure 8 depicts the sequence of the AFA foil manufacturing trials starting from 22,000 kg VIM-VAR ingots (8a), foil with 380 mm width and 100 μm thickness (8b), and a final heat-exchanger product coil made of the folded AFA foil (8c). Various environmental tests of the AFA foils or sheet products are currently in progress, such as in a water-vapor, steam, fireside boiler, supercritical H_2O, supercritical CO_2, molten salts, molten metal, syngas, sulfidation, carburization, metal dusting, as well as an actual engine test of a combined gas turbine. Comprehensive evaluation of various mechanical/functional properties of the AFA alloy was performed systematically and reported elsewhere [40].
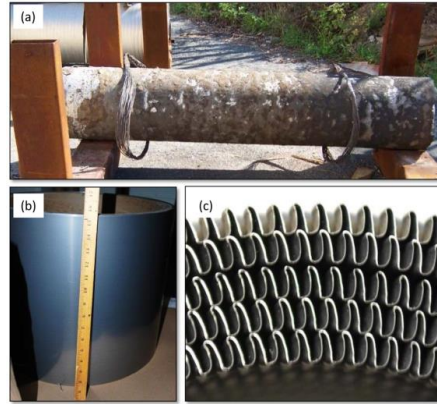
Figure 8: Appearance of Fe-14Cr-3.5Al-25Ni-2.5Nb base AFA alloy; (a) 10,000lb VIM-VAR ingots (courtesy from Carpenter Technology Corporation), (b) a rolled AFA foil with 100 μm thickness and 380 mm wide, and (c) edge of a coil of folded AFA [18].

3. Intermetallic-strengthened AFA

Coherent γ'-L1$_2$ Ni$_3$(Al, Ti) precipitates has successfully been introduced as a strengthening second-phase of AFA alloys which achieve the best creep properties to date among the series of AFA alloys at 700-750 °C, together with excellent oxidation resistance through alumina-scale formation [6, 14]. Alloys with base compositions of Fe-14Cr-32Ni-3Nb-(3-4)Al-(1-3)Ti with or without the Zr, C, and B additions have been used to investigate the stability of L1$_2$ relative to B2. The amount of L1$_2$ increased with increasing Ti additions, and a significant stabilization of the L1$_2$ was achieved by Zr addition. Further additions of C and B was found to successfully improve both creep and oxidation properties. Table 3 summarizes the analyzed compositions of the alloys used in this study.

Table 3: Analyzed compositions of intermetallic strengthened AFA alloys [16].

Name	Analyzed composition (wt%)										Remarks
	Fe	Cr	Ni	Al	Si	Nb	Ti	Zr	C	B	
41	45.73	14.03	32.26	3.96	0.14	2.88	0.98	-	-	-	4Al-1Ti
41Z	45.62	14.02	32.23	3.93	0.12	2.81	0.96	0.27	-	-	4Al-1Ti + Zr
41ZC	45.38	14.03	32.23	3.98	0.14	2.86	0.97	0.29	0.102	-	4Al-1Ti +Zr,C
42Z	44.32	13.97	32.45	3.91	0.13	2.95	1.95	0.30	-	-	4Al-2Ti + Zr
32Z	45.29	14.00	32.47	2.95	0.13	2.93	1.97	0.29	-	-	3Al-2Ti + Zr
33Z	44.23	14.02	32.46	2.98	0.14	2.96	2.88	0.29	-	-	3Al-3Ti + Zr
32ZCB	45.36	13.99	32.46	2.97	0.14	2.80	1.88	0.29	0.065	0.005	3Al-2Ti + Zr,C,B
A286	56.2	14.5	25	0.15	0.2	-	2.1	-	0.04	0.006	1.25Mo, 0.3V,0.2Mn, 0.015P

The effect of the Ti, Al, C, and B additions on the predicted amounts of L1$_2$, B2, and Laves phases is shown in Figs. 9a, 9b, and 9c, respectively. The amount of L1$_2$ phase increases with increasing the Ti addition, but it is insensitive to the Al addition. In contrast, the amount of B2 does not show strong Ti dependence, but decreases significantly with decreasing Al addition.

Laves phase shows an opposite tendency of Al dependence to that of the B2 phase, although the amount is much lower than the other phases. The C addition (*41ZC*) or the C and B additions (*32ZCB*) do not change the predicted amounts of $L1_2$ and B2 phase when compared with the alloys without C and B (*41Z* and *32Z*), but lower the calculated amount of Laves phase in the alloys *41ZC* (above 750 °C, not shown in the figure) and *32ZCB*. This is attributed to the formation of MC-type carbide (M: mainly Nb) lowering available Nb for Laves phase formation.
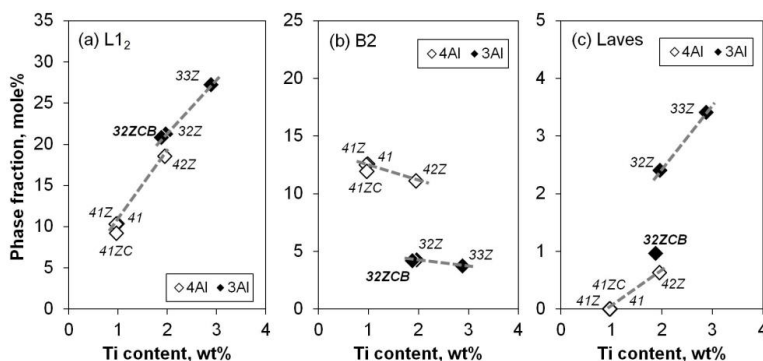
Figure 9: Effect of Ti, Al, C, and B additions on phase stability of $L1_2$, B2, and Laves at 750 °C (after reference 16).

The Zr addition is also the key to stabilize $L1_2$ phase relative to B2 drastically. Figure 10 illustrated microstructure of two AFA alloys without and with the Zr addition (alloy *41* and *41z*, respectively) after aging at 750 °C for 2,000 h. Alloy *41* (10a) showed macroscopically uniform distribution of multi second-phase dispersions of B2, Laves, and $L1_2$ precipitates. On the other hand, alloy *41Z* which contained 0.3 wt% Zr resulted in a large increase in the amount of spherical $L1_2$ dispersions, and decreases in B2 and Laves precipitates in the γ-Fe matrix (10b). Mechanism of $L1_2$ stabilization is still unknown, but the Zr addition resulted in increasing the creep-rupture life at 750 °C and 100MPa more than 4 times compared with the alloy without Zr [16].
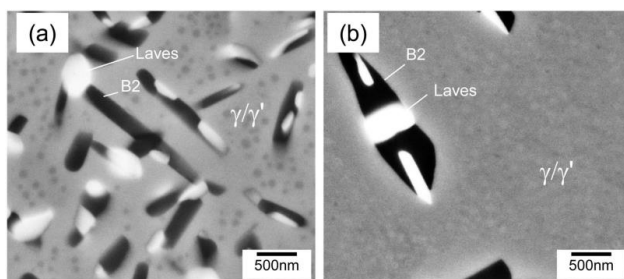
Figure 10: SEM BSE images of (a) alloy 41 and (b) alloy 41Z, aged at 750 °C for 2000 h.

Although the Ti addition increases the amount of $L1_2$ phase, it also degrades the oxidation resistance of AFA alloys by shifting the internal to external alumina formation behavior in the AFA Fe-Ni-Cr-Al composition range [1, 2, 5]. The C and B additions successfully mitigated the effect of Ti addition on the oxidation resistance, and also resulted in a significant improvement of the creep properties at 700-750 °C. Figure 11 shows the mass changes of the intermetallic strengthened AFA alloys at 800°C in air + 10% H_2O (11a), and the LMP plot of the alloy *32ZCB* compared with the other AFAs and commercial heat resistant steels and alloys (11b). The alloy *41Z* exhibited very slow mass gain kinetics for up to 2,000h, indicating good oxidation resistance. In comparison, the chromia-forming A286 showed abrupt mass loss only after 200h at the same test condition. However, the mass changes of AFA alloys at a given exposure time increased with increasing Ti additions. The combined additions of C and B in the alloy *32ZCB* showed a drastic improvement of the oxidation resistance compared to the alloy *32Z*. Such additions were previously reported to be beneficial to favoring alumina formation in the AFA composition range in water vapor environments, ostensibly by providing microstructural sites where hydrogen introduced into the alloy from the water vapor can segregate, minimizing detrimental effects on internal/external oxidation transition [13]. The alloy *32ZCB* also showed the best creep resistance among the series of AFA alloys to date (Fig. 11a). Although the improvement mechanism is still unclear, it is hypothetically due to the boron addition increasing the lattice misfit between γ-Fe and $L1_2$ to increase the resistance of creep deformation in the γ-Fe matrix [16]. Further optimization of both creep and oxidation resistance of the intermetallic strengthened AFA is currently in progress.
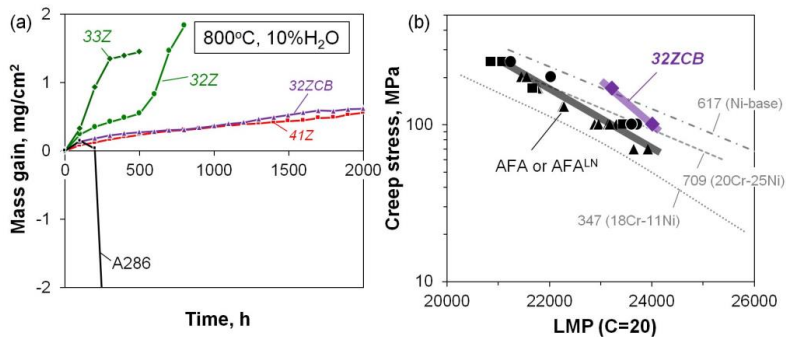
Figure 11: (a) Mass changes of the AFA alloys at 800°C in 10% water vapor, and (b) LMP plot of the alloy 32ZCB compared with the other AFAs and commercial heat resistant steels and alloys (after reference 16).

4. Cast AFA

A cast version of AFA steel alloys was also developed successfully which exhibits good advantages compared to commercially available chromia-forming cast austenitic stainless steel alloys [40]. Potential applications of cast AFA alloys include, but are not limited to,

components in combustion environments or industrial process environments, such as exhaust manifolds, hardware for operating in exhaust streams, nozzles in oxygen enriched streams, furnace rolls, reformer tubes, chemical/petrochemical plant tubes, and so on. The cast AFA alloy compositions were selected through a guidance of computational thermodynamic tools to optimize solidification microstructure with maximized strengthening carbide formation at service temperatures, as well as expected good oxidation resistance and castability. Table 4 summarizes the analyzed compositions of the optimized cast AFA alloys to date. The lab-scale heat (~500 g) was made through an arc-melting and drop-casting technique. The centrifugal cast tubes with a size of 90 mm OD x 16-19 mm WT x 1800 mm L, shown in Figure 12, were prepared by an industrial partner through a commercial manufacturing process. They did not show any damages such as cracks or void formation by visual inspection.

Table 4: Alloy compositions of cast AFA fabricated by arc-melting (lab heat) and centrifugal casting (tube) through a commercial manufacturing technique.

Name	Composition (wt%)														
	Fe	Cr	Mn	Ni	Cu	Al	Si	Nb	V	Ti	Mo	W	C	B	P
Lab heat	49.86	14.11	1.92	25.28	0.51	3.49	0.48	0.94	0.05	0.05	1.98	1.00	0.29	0.008	0.020
Centrifugal cast tube	48.38	14.64	1.98	25.19	0.62	3.49	0.91	1.01	-	0.14	1.93	1.26	0.36	0.012	0.012

Figure 12: Centrifugal cast AFA tubes with 90mm OD x 16-19 mm WT x 1800 mm L (courtesy from Duraloy Technologies, Inc.).

Figure 13 compares the high temperature properties of the developed cast AFA alloys with commercially available chromia-forming cast austenitic stainless steels. The best cast AFA alloys exhibited promising creep properties comparable to Grade HN (Fe-20Cr-25Ni base) [41] and superior oxidation resistance to that of Grade HP (Fe-25Cr-35Ni base) up to 750-800 °C. Microstructure characterization of the creep-rupture specimens revealed that nano-scale $M_{23}C_6$ carbides pinned the dislocations in γ-Fe matrix which presumably act as the dominant factor to increase the creep resistance, as expected through the phase prediction from thermodynamic calculations. Further optimization of alloy compositions capable of improved oxidation resistance at higher temperature (~950°C) is currently being pursued.
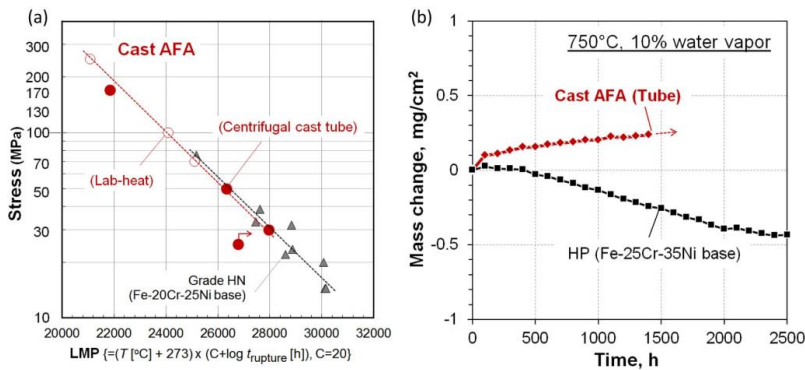
Figure 13: (a) LMP plot of Cast AFA alloy compared with Grade HN cast austenitic stainless steel [41], and (b) mass changes of Cast AFA and Grade HP exposed at 750 °C in air with 10% water vapor.

5. Summary

The current advances in the development of wrought and cast, creep-resistant, alumina-forming austenitic (AFA) steels at Oak Ridge National Laboratory have been overviewed. The AFA alloys possess a unique combination of excellent oxidation resistance through the alumina-scale formation and good creep properties via nano-scale carbides or coherent intermetallic second-phase precipitate formation, as well as inexpensive material cost relative to commercially available chromia-forming heat resistant steel alloys. The effect of alloying additions on the AFA alloy design was systematically studied, which allowed expanding the available alloy composition range with alumina-scale formability and applying various strengthening mechanisms. AFA alloys developed to date have demonstrated promising oxidation resistance from ~600-900 °C which is in the temperature range of interest for near-future advanced fossil-fired steam plants. Commercialization efforts of the AFA foil product are currently in progress with the support of various industrial partners.

6. Acknowledgements

References

[1] Y. Yamamoto, M.P. Brady, Z.P. Lu, P.J. Maziasz, C.T. Liu, B.A. Pint, K.L. More, H.M. Meyer, and E.A. Payzant, *Science* 316 (2007), pp. 433–436.

[2] M.P. Brady, Y. Yamamoto, M.L. Santella, B.A. Pint, Scripta Mater., 57 (2007) 1117-1120.

[3] Y. Yamamoto, M.P. Brady, Z. P. Lu, C. T. Liu, M. Takeyama, P. J. Maziasz, and B. A. Pint, Met. Mater. Trans. A, 2007, vol. 38A (11), pp. 2737-2746.

[4] M.P. Brady, Y. Yamamoto, Z.P. Lu, P.J. Maziasz, C.T. Liu, B.A. Pint, Bruce, M.L. Santella, Stainless steel World, (2008) 1-4.

[5] M.P. Brady, Y. Yamamoto, M.L. Santella, P.J. Maziasz, B.A. Pint, and C.T. Liu: JOM 60 (2008), pp.12–18.

[6] Y. Yamamoto, M. Takeyama, Z.P. Lu, C.T. Liu, N.D. Evans, P.J. Maziasz, M.P. Brady, Intermetallics 16 (2008), pp. 453-462.15.

[7] M.P. Brady, Y. Yamamoto, B.A. Pint, M.L. Santella, P.J. Maziasz, L.R. Walker: Mater Sci Forum, 2008, vol. 595-598, pp. 725-732.

[8] Y. Yamamoto, M.P. Brady, M.L. Santella, B.A. Pint, P.J. Maziasz: "Creep-Resistant, Alumina-Forming Austenitic Stainless Steels For Higher Temperature Use In Power Generation Systems," in proc. the 33rd International Technical Conference on Coal Utilization & Fuel Systems (June 1-5, 2008, Clearwater, FL), B. A. Sakkestad, ed., Coal Technology Association, Gaithersburg, MD (2008).

[9] Y. Yamamoto, M. Santella, M.P. Brady, H. Bei, P. Maziasz, Met. Mater. Trans. A, 40a (2009) 1868-1880.

[10] Y. Yamamoto, M. Santella, C. Liu, N. Evans, P. Maziasz, M.P. Brady, Mater Sci Eng A Struct Mater, 524 (2009) 176-185.

[11] M.P. Brady, Y. Yamamoto, M. Santella, L. Walker, Oxid Met, 72 (2009) 311-333.

[12] H. Bei, Y. Yamamoto, M.P. Brady, M. Santella, Mater Sci Eng A Struct Mater, 527 (2010) 2079-2086.

[13] M.P. Brady, K. Unocic, M. Lance, M. Santella, Y. Yamamoto, L. Walker, Oxid Met, 75 (2011) 337-357.

[14] Y. Yamamoto, M. Brady, M. Santella, H. Bei, P. Maziasz, B. Pint, Met. Mater. Trans. A, 42A (2011) 922-931.

[15] B.A. Pint, M.P. Brady, Y. Yamamoto, M.L. Santella, P.J. Maziasz, W. Mattews, Journal of Engineering for Gas Turbines & Power, 113 (2011) 102302-1.

[16] Y. Yamamoto, G. Muralidharan, and M.P. Brady, Scripta Mater., 69 (2013) 816-819.

[17] M.P. Brady, J.H. Magee, Y. Yamamoto, D Helmick, L Wang, Mater Sci Eng A Struct Mater, 590 (2014) 101-115.

[18] B.A. Pint, S. Dryepondt, M.P. Brady, Y. Yamamoto, # GT2013-94940 , in Proceedings of ASME Turbo Expo 2013: Turbine Technical Conference and Exposition, San Antonio, Texas, June 3-7, 2013.

[19] R. Viswanathan and W. Bakker: J. Mat. Eng. Perf., 2001, vol. 10, pp. 81-95.

[20] R. Viswanathan and W. Bakker: J. Mat. Eng. Perf., 2001, vol. 10, pp. 96-101.

[21] R. Viswanathan, R. Purgert, P. Rawls: "Coal-Fired Power Materials," Advanced Materials & Processes, August 2008, pp. 47-49.

[22] R. Viswanathan, R. Purgert, P. Rawls: "Coal-Fired Power Materials Part II," Advanced Materials & Processes, September 2008, pp. 41-45.

[23] P. Kofstad, High Temperature Corrosion (Elsevier, London, 1988)

[24] F. Stott, G.C.Wood, and J. Stringer: Oxid Met, 44 (1995) 113.

[25] E.J. Opila, N.S. Jacobson, D.L. Myers, E.H. Copland; JOM, 58 (2006) 22.

[26] T. Fujioka, M. Kinugasa, S. Iizumi, S. Teshima, I. Shimizu, "Heat-Resistant Austenitic Stainless Steel" (U.S. Pat. 3,989,514, Nov. 2, 1976).

[27] J. A. McGurty, "Austentitc iron Alloys" (U.S. Pat. 4,086,085, April 25, 1978).

[28] D. Satyanarayana, G. Malakondaiah, D. Sarma, Mater Sci Eng A Struct Mater, 323 (2002) 119.

[29] V. Ramakrishnan, J. A. McGurty, N. Jayaraman, Oxid Met, 60 (1988) 185.

[30] B. A. Pint, R. Peraldi, P. J. Maziasz, Mater Sci Forum, 461-464 (2004) 815.

[31] R.W.K. Honeycombe, Steels Microstructure and Properties, Edward Arnold Ltd., London, UK, 1981, 6–10.

[32] J.P. Shingledecker, P.J. Maziasz, N.D. Evans, M.J. Pollard, in: R.S. Mishra, J.C. Earthman, S.V. Raj, R. Viswanathan (Eds.), Proceedings of a Symposium Sponsored by Materials Science & Technology 2005, Pittsburg, Pennsylvania, 2005, pp. 129–138

[33] L. Colombier and J. Hochmann, Stainless and Heat Resisting Steels, St. Martin's Press, New York, 1968.

[34] D. Satyanarayana, G. Malakondaiah, D. Sarma, Materials. Characterizaiton, 2001, vol. 47, pp. 61-65.

[35] P. J. Maziasz: Journal of Metals, 1989, vol. 41, pp. 14-20.

[36] R. W. Swindeman, P. J. Maziasz, E. Bolling, and J. F. King: Oak Ridge Natl. Lab. Rep. ORNL-6629/P1, Oak Ridge, TN, 1990.

[37] R. W. Swindeman and P. J. Maziasz, in Proc. of the 1st Int. Conf. on Heat-Resistant Materials, K. Natesan and D. J. Tillack, eds., ASM International, Materials Park, OH, 1991, pp. 251-259.

[38] "MetalPrice.com (Jul. 2012)," http://www.metalprices.com/index.asp

[39] P.J. Maziasz, B.A. Pint, J.P. Shingledecker, N.D. Evans, Y. Yamamoto, K.L. More, E. Lara-Curzio, Int. J. of Hydrogen Energy 32 (2006) 3622– 3630

[40] M.P. Brady, Y. Yamamoto, G. Muralidharan, H. Roger, B.A. Pint, "Deployment of Alumina Forming Austenitic (AFA) Stainless Steel", ORNL/TM-2013/479 (2013).

[41] Steel Castings Handbook, Supplement 9, High Alloy Data Sheets: Heat Series, Steel Founders' Society of America (2004).

HIPERFER – HIGH PERFORMANCE FERRITIC STEELS

B. Kuhn*, M. Talik

Forschungszentrum Jülich GmbH, Institute for Energy and Climate Research
Microstructure and Properties of Materials (IEK-2)
*Contact e-mail: b.kuhn@fz-juelich.de

Abstract

The "Energiewende" will present strong new requirements for the German electricity generation and supply sector. Component manufacturers and utilities accept the challenge and plan for the design, operation and maintenance of a new generation of highly flexible regenerative (e.g. concentrated solar, biomass fired, gas to liquid) and conventional (fossil fired) future power plants. Information on the suitability of the materials, which are traditionally employed in thermal power generation, is scarce and ideas for the development of new, tailored materials are widely missing. To tackle this deficit novel High performance Ferritic (HiperFer) steels with supreme resistance to thermomechanical fatigue are presented and benchmarked to ferritic-martensitic T/P92 and austenitic AISI310 in terms of thermomechanical fatigue and creep strength. The alloy design philosophy is described; future alloy development and possible implications on production and heat-treatment are outlined.

Keywords: HiperFer steel, thermomechanical fatigue, creep, Laves phase, alloy design

1. Introduction

Resource preservation and maximization of economic success by improved plant efficiency was the driving force in past alloy development for advanced ultra-supercritical steam power plants. In Germany the "Energiewende" - the intended transition of electricity supply towards regenerative power sources - poses a great challenge in terms of load flexibility, thermal cycling capability and downtime corrosion resistance for the materials employed in new concentrated solar power, biomass fired or gas to liquid plants, but also in the safeguarding conventional fossil fired power plants. In order to balance erroneous availability forecasts of fluctuating regenerative power sources (wind, solar) and vice versa to bridge short periods of low conventional power demand, the minimum load capability of conventional steam power plants will have to be decreased, while on the other hand start-up times and load ramps (especially coming from minimum load) will have to be increased to ensure grid stability and to avoid economic loss [1]. Traditional empirical criteria in plant design were for example an expected life time of approximately 200.000 hours, including 200 hot starts (< 8 h of idle) per year, 50 warm starts (< 72 h of idle) per year and 2 cold starts per year. In contrast to this the future design criterion regarding lifetime is unknown and criteria regarding cyclic operation are considering up to 100 - 500 hot starts (< 8 h of idle), 50 – 120 warm starts (< 72 h of idle) and 2-20 cold starts per year [2].

Under these preconditions it seems to be doubtful if the past alloy development philosophy, with the ultimate goal of reaching a 100.000 hour creep rupture strength of 100 MPa at 650 °C, is still suitable. A paradigm shift towards improvement of thermomechanical fatigue resistance, cyclic steam oxidation and downtime corrosion resistance in combination with adequate creep strength seems to be indicated.

Design of tailored materials for future energy technology will play a key role not only in ensuring technical feasibility, but also in maintaining future economic wealth. The thermomechanical fatigue and creep properties of High performance Ferritic (HiperFer) 18 - 23 wt.-% chromium model steels, strengthened by dispersion of intermetallic Laves phase particles, demonstrate the potential of such alloys for application in highly efficient and highly flexible future supercritical steam power plants, no matter if these will be fired by fossil or biogenic fuels or solar powered.

2. Experimental

2.1. Materials

The chemical compositions of the trial steels in Tab. 1 (model-1/-2, 22Cr-1/-2, 18Cr-1) were measured by Inductively Coupled Plasma Optical Emission Spectroscopy (ICP-OES). The compositions of the commercial Crofer® 22 H [3-5] steels (H-1/-2) were measured by Glow Discharge Optical Emission Spectroscopy (GDOES).

Tab.1: Chemical compositions of the tested materials

Material:	Batch:	C	N	Cr	W	Nb	Si	Mn	La	Fe	Ti
Crofer® 22	model-1	0.002	0.007	22.23	2.02	0.48	0.27	0.43	0.093	R	0.065
	model-2	0.002	0.011	22.38	1.91	0.52	0.25	0.44	0.017	R	0.037
	H-1	0.007	0.015	22.93	1.94	0.51	0.21	0.43	0.082	R	0.07
	H-2	0.004	0.02	23.00	2.00	0.50	0.30	0.40	0.07	R	0.05
HiperFer	22Cr-1	0.001	0.006	23.79	2.25	0.49	0.25	0.45	0.131	R	0.003
	22Cr-2	0.002	0.007	22.72	2.45	0.58	0.22	0.47	0.036	R	0.004
	18Cr-1	0.001	0.005	18.17	1.95	0.51	0.25	0.45	0.132	R	0.057

Commercial Crofer® 22 H was applied in both hot-rolled and solution annealed condition. To study the influence of initial dislocation density solution annealed material was plastically pre-deformed at ambient temperature applying a strain rate of $10^{-3}s^{-1}$ and later on tested for hardness, thermomechanical fatigue and creep properties. The model steels were creep tested in the hot-rolled state only because of limited availability. All the materials were manufactured by Outokumpu VDM. The thermomechanical treatment parameters of the investigated steels are given in Tab. 2.

Tab.2: Thermomechanical treatment parameters

Material:	Hot rolling:	Solution annealing:	Cooling:	PD*:
H-1/-2 (SA)	unknown	1075 °C / 22 Min.	Air	none
H-1 (HR)	unknown	none	Air	none
H-1 (TMT)	unknown	1075 °C / 22 Min.	Air	$10^{-3}s^{-1}$ to 3 % plastic deformation, ambient
trial steels	1050 – 980 °C	none	Air	none

*PD: pre-deformation by cold-working to increase dislocation density

2.2. Mechanical testing

2.2.1 Hardness testing

Hardness testing (HV0.1; force level: 1000 mN) was accomplished applying an automated Fischerscope® H100 indenter. The given hardness values represent the average of 10 measurements per material batch.

2.2.2 Thermomechanical fatigue and creep testing

In thermo-mechanical fatigue and creep testing cylindrical specimens with gauge diameters of 6.4 / 7 mm and gauge lengths of 30 / 15 mm were utilized.

Single specimen, dead weight load, lever arm type creep machines with continuous elongation measurement at the gauge length of the specimens and multi-specimen string machines for interrupted creep tests (with 1000 hours interval strain measurement) were applied for constant load creep experiments. In the single / multi-specimen creep machines the specimen temperature was controlled with an accuracy of +/- 2 °C / +/- 3 °C. Type R (Pt/RhPt) thermocouples were attached to the specimens gauge length for temperature control in the single specimen experiments, while shielded temperature measuring rods (type R) in close vicinity to the specimens were used in the multi-specimen machines. In all tests the specimens were heated up within 1.5 h and kept for 1 h to establish equilibrium conditions before applying the load.

In thermomechanical fatigue experiments induction heating was applied. Temperature and strain control at the gauge length of the samples was accomplished by Type R sling thermocouples and directly attached extensometers. The tests were carried out in total strain control, with

$$\varepsilon_t = \varepsilon_m + \varepsilon_{th}.$$

ε_t: total strain, ε_{th}: thermal strain, ε_m: mechanical strain

Out-of-phase (OP) / in-phase (IP) experiments were carried out with $\varepsilon_m = -\varepsilon_{th}$ and $\varepsilon_m = \varepsilon_{th}$ in two temperature ranges (250 - 650 °C, 50 - 650 °C), heating/cooling the specimens within 40 s (dT/dt = 10 Ks^{-1}). In case of the lower minimum temperature experiments the cooling rate below 200 °C was constricted and thus the cooling cycle took 85 s. No holding times at maximum or minimum temperatures were applied. The lifetime was evaluated by intersection of linear approximations of the "upper shelf"- and the "downhill"-slope of the σ_{Range} line (cf. Fig. 1a).

3. Results and discussion

3.1. Initial hardness

Table 3 displays the initial hardness values. The cold-worked (H-1 (TMT)), the hot-rolled Crofer® 22 H (H-1 (HR)) and the hot-rolled Crofer 22 model steels (model-1/-2) present higher hardness than the solution annealed (H-1 (SA)) standard material. Because all the materials were free from hardening precipitates prior to mechanical testing [6, 7], this is caused by increased dislocation density only.

Table 3:   Hardness of the tested materials

Material:	Batch:	Hardness [$HV_{0.1}$]:
Crofer® 22	H-1 (SA)	197
	H-1 (HR)	223
	H-1 (TMT)	237
	model 1	217
	model 2	226
HiperFer	22Cr-1	218
	22Cr-2	223
	18Cr-1	216

3.2. Thermomechanical fatigue

In out-of-phase (OP) thermomechanical fatigue experiments from 250 – 650 °C T92 yielded 3150 cycles, while AISI310 failed around 2990 cycles. The ferritic-martensitic material presented supreme initial stress range because of strengthening by dislocations from the martensitic transformation, followed by a pronounced decrease of the stress range (from 840 MPa to 635 MPa within 30 cycles) because of recovery of excess dislocations. Softening continued until 750 cycles before the material entered a stable phase, which lasted up to approx. 1875 cycles, where damage was initiated. In contrast to this the austenitic AISI310 material presented comparatively low initial strength (465 MPa) with continuous cyclic hardening until rapid failure.

The solution annealed Crofer® 22 H batches H-1 and H-2 reach lifetimes ranging from 4125 (H-1) to 4600 (H-2) cycles. The cold-worked H-1 material (H-1 (TMT): ~ 4300 cycles) lies well in the range opened by the solution annealed materials (cf. shaded area in Fig. 1a). While the solution annealed Crofer® 22 H batches presented a comparatively low initial stress range of 445 MPa, followed by cyclic strain hardening (because of dislocation strengthening) up to 555 MPa within the first 20 cycles and softening (because of recovery) in the upcoming 40 cycles, the cold-worked material exhibited higher initial stress range of 635 MPa (because of initially increased dislocation density) followed by cyclic softening (because of recovery of excess dislocations) in the early cycles. After approximately 60-80 cycles all the three batches were in a state of comparatively moderate softening before they reached a stable phase. Depending on the material state (e. g. initial dislocation density) the initial behavior can thus more or less be adjusted to act like austenitic steel (low dislocation density state, e. g. after solution annealing) or like ferritic-martensitic steel (high dislocation density state, e. g. cold- or hot-rolled state). However pronounced the (intended) variations in the early stage may be,

267

the life span of the ferritic material was at least about 35 – 55 % longer in comparison to T92 and AISI310.
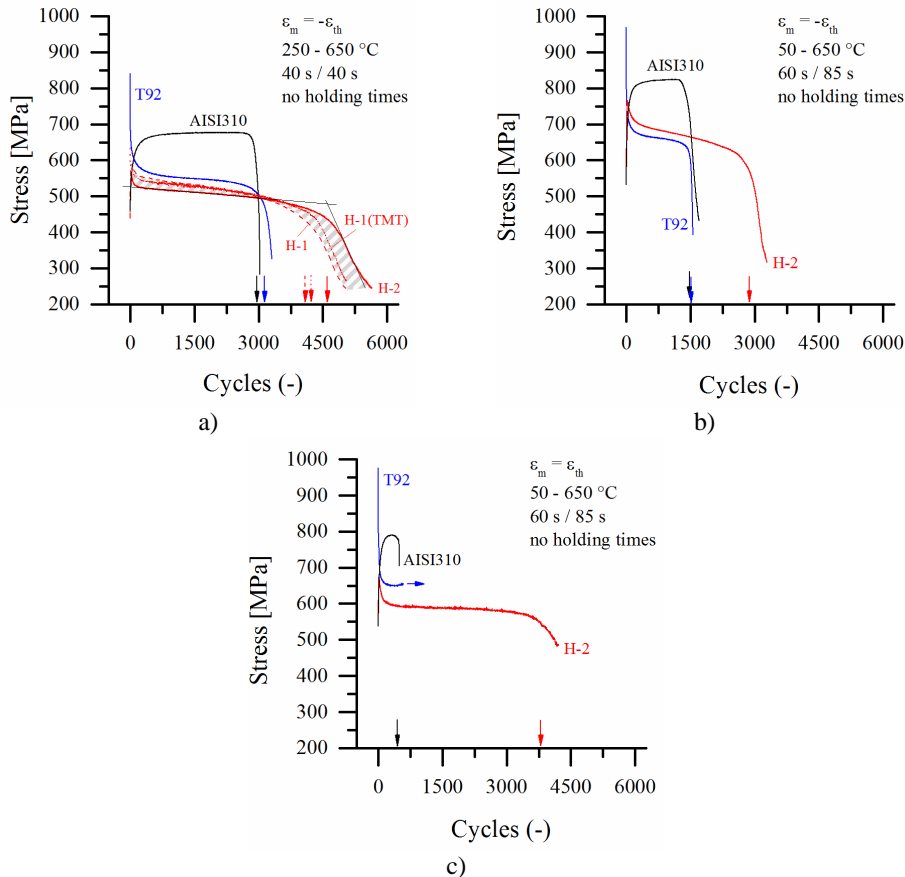
Figure 1: Thermomechanical fatigue life of Crofer® 22 H, T92 and AISI310:
a) Out of phase cycles from 250 – 650 °C
b) Out of phase cycles from 50 – 650 °C
c) In phase cycles from 50 – 650 °C (T92 experiment in progress)

The same qualitative material behavior was found in 50 – 650 °C out-of-phase (OP) experiments (Fig. 1b): T92 and AISI310 failed after 1500 cycles, while Crofer® 22 H (batch H-2) nearly reached double the lifetime. It yielded further extended life (cf. Fig. 1c: 3760 cycles) in in-phase (IP) experiments in the same temperature range, while AISI310 exhibited a dramatic drop in lifetime to 480 cycles. At the submission deadline the running T92 experiment had reached 584 cycles and thus already surpassed AISI310.

Summarizing it may be stated, that the fully ferritic materials perform the better the more severe the thermomechanical fatigue testing conditions become. State of the art materials performed worse under all conditions applied so far.

3.2. Creep

3.2.1 The significance of thermomechanical treatment state

Unlike in strain-controlled thermomechanical fatigue the thermomechanical treatment history of the ferritic material does play an important role in creep, like it is demonstrated by the creep rate vs. stress plots in Fig. 2.
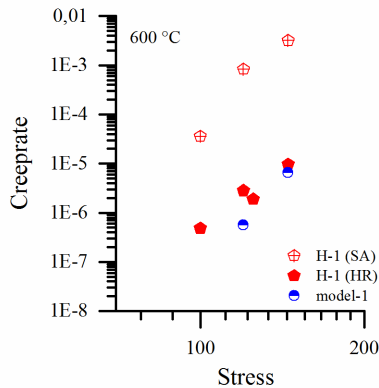
Figure 2: Impact of thermomechanical treatment history on the minimum creep rate: Solution annealed vs. the hot-rolled Crofer® 22 H (H-1(HR/SA), data replotted from [9]) and model-1 steels

The solution annealed H-1(SA) material shows relatively high minimum creep rates. The hot-rolled (H-1(HR) and model-1) batches exhibit values lowered by approximately 2.5 orders of magnitude. Because all the materials feature almost identical chemical compositions (Tab. 1) and are of similar initial hardness (Tab. 3) it can be concluded, that the creep strengthening effect stems from increased dislocation density. In [6] it was outlined that *"enhanced initial dislocation density can be considered to have a manifold impact on the microstructural properties and thus the mechanical strength of such materials: First, enhanced dislocation density gives a (short-term) strengthening effect itself. Second, it may boost precipitation kinetics. Third, it changes the morphology of the Laves phase particles."* Further proof for these findings are given in [7].

3.2.2 Stress rupture performance of the model alloys

Fig. 3 displays the creep rupture performance of the hot-rolled Crofer® 22 model-1/-2, the HiperFer 22Cr-1/-2 and 18Cr-1 model steels along with the solution annealed commercial Crofer® 22 H batch (H-1(SA)) and benchmarks it to T/P92 and AISI310. The solution annealed batch H-1(SA) exhibited weak performance at 600 °C, but all the hot-rolled steels outperformed AISI310 in creep performance up to medium testing durations of more than 10.000 hours. Formation of the (Fe,Cr) σ-phase to the grain boundaries was successfully reduced by a cutback in chromium content to 18 wt.-% in the 18Cr-1 steel [8], which like all the ~ 2 W, 0.5 Nb, 0.25 Si variants ruptured around 30.000 hours (120 MPa, 600 °C).
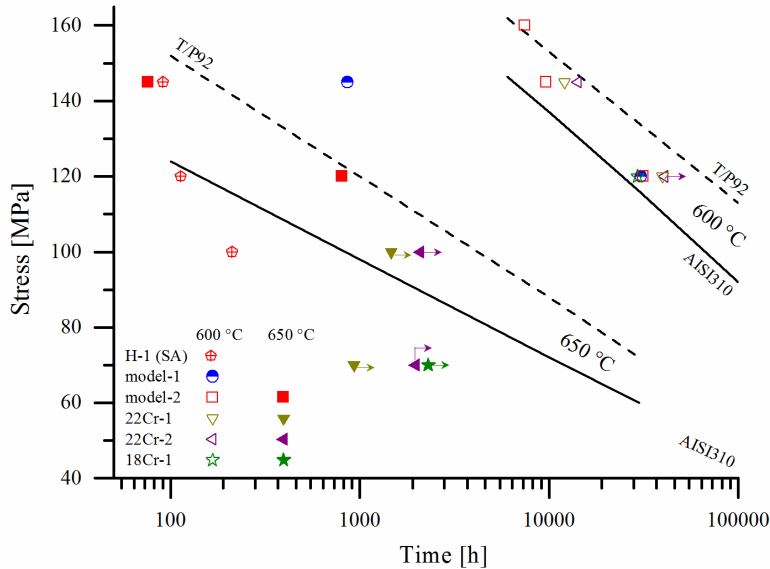
Figure 3: Stress rupture performance of ferritic steels in comparison to ferritic-martensitic T/P92 [10] and austenitic AISI310 [10] (open symbols: 600 °C, filled symbols: 650 °C, experiments marked with arrows: in progress)

The deviation in short-term performance between the two Crofer 22 model steels (model-1/-2) cannot be explained by different amounts of Laves phase formation, because of nearly similar chemical compositions (Tab. 1). The "high hardness" model-2 steel ($HV_{0.1}$: 226) even performs better than T/P92 at short time / high stress (160 MPa). In contrast to this the "low hardness" ($HV_{0.1}$: 217) model-1 steel showed comparatively weak rupture strength at intermediate stress (145 MPa). At low stress (120 MPa) / in intermediate term, where dislocation strengthening does play a minor role, both batches perform alike with rupture appearing after appr. 30.000 hours. The high stress (145, 120 MPa) / short-term rupture performance of the model-2 steel at 650 °C confirms this result.

Owing to increased tungsten and niobium contents the HiperFer 22Cr-1/-2 model alloys showed improved creep resistance in short- (≤ 15.000 h) and medium-term durations (~ 40.000 hours) at 600 °C. The 22Cr-2 alloy even approximates T/P92 in short-term testing at comparatively high stress (145 MPa). The 120 MPa experiment is still running and currently reached 43.970 hours. This boost in performance is caused by increased formation and stability of the strengthening $(Fe,Cr,Si)_2(Nb,W)$ Laves phase particles [11]. At 100 MPa / 650 °C both steels show better performance than AISI310 (experiments running). 70 MPa experiments were initiated for the three HiperFer model steels (18Cr-1, 22Cr-1/-2) and currently reached times up to 2.400 hours.

4. Further alloy development

The creep strength of the proposed alloys is determined by various factors like type, phase fractions, morphology and stability of the intermetallic $(Fe,Cr,Si)_2(Nb,W)$ Laves-phase precipitates. All of these influencing factors are not exclusively determined by alloy

composition. Furthermore they are affected by initial dislocation density and sub-grain structure and thus governed by the thermomechanical treatment history (hot-rolling parameters, cooling rate), too [6, 7]. For this reason boosting the phase fraction of strengthening particles is not the only matter of importance in further compositional optimization of the proposed alloys.
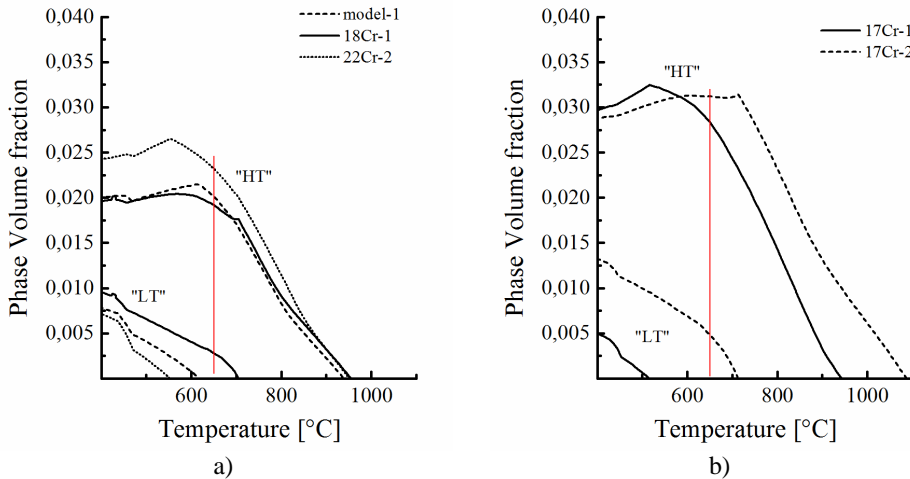
Figure 4: Thermocalc (TCFE6.2) modelling results of the partitioning of the Laves phase in (a) the Crofer® 22 model-1 and the HiperFer 18Cr-1 and 22Cr-2 trial alloys and (b) two HiperFer 17Cr variants for enhanced Laves phase volume fraction.

Partitioning of the Laves phase into an "LT-phase" (Fig. 4a: stable up to comparatively low temperatures from 550 – 700 °C), which is high in niobium and low in tungsten content and a high niobium / low tungsten "HT-phase" (stable up to temperatures exceeding 900 °C, Fig. 4a) is highly sensitive to compositional changes what influences the long-term stability of the particle size distribution in the 18Cr-1 alloy [11] (cf. Fig. 4a). The cutback in chromium content yielded reduction of the σ-phase, but also shifted the stability limit of the LT-phase to approx. 700 °C (from well below / slightly above 600 °C in the 22Cr-2 / model-1 steels, Fig. 4a). The presence of a fast growing, Laves-phase forming element consuming phase might deteriorate creep strength especially at 650 °C in this alloy. For this reason the results of 650 °C creep testing (Fig. 3) will yield valuable information for further development.

The dissolution temperature of the HT-phase determines the thermomechanical treatment temperature/time window. All changes in chemical composition in favor of mechanical strength (creep, impact, ductility and thermomechanical fatigue), weldability, high temperature oxidation or aqueous corrosion resistance thus pose possible implications for processing. Typical Laves phase forming elements like W, Nb and Si shift the dissolution temperature of the HT-phase upwards, what will necessitate adjustment of the hot-rolling parameters. Fig. 4b exemplarily displays Thermocalc (TCFE6.2) modelling results of the partitioning of the Laves phase in two HiperFer 17Cr variants for enhanced Laves phase volume fraction. These steels will form 22 / 33 % (17Cr-1 / 17Cr-2) more of the desired HT-phase at 650 °C than the currently strongest 22Cr-2 alloy. While the dissolution temperature of the HT-phase remains unchanged in case of the 17Cr-1 steel it shifts to about 100 °C

higher temperature in case of the 17Cr-2 alloy. The 17Cr-2 variant may be considered to be advantageous with respect to creep strength (because of the higher absolute amount of both phases), but regarding avoidance of the fast coarsening LT-phase and uncomplicated processing (the rolling parameters of the 22Cr-2 alloy can be applied) the 17Cr-1 alloy would be clearly favorable.

5. Conclusion and outlook

Unlike state of the art ferritic-martensitic and austenitic materials, the proposed HiperFer steels provide a favorable combination of steam oxidation, fireside and downtime corrosion resistance, low thermal expansion and good thermal conductivity. Therefore they offer excellent thermomechanical fatigue resistance, which surpasses state of the art ferritic-martensitic and austenitic materials by far. In terms of creep strength the currently available trial steels outplay conventional alloys like T/P91, VM-12 [6, 8] and AISI310 and approach the performance of the currently strongest available material T/P92. Thermodynamic equilibrium calculations suggest that further increase in the volume fraction of strengthening Laves phase precipitates is possible at even higher temperature.
The alloying system can thus be considered to pose plenty of potential for further optimization towards tailored microstructure materials for future, highly flexible thermal power plants.

Future work will be focused on the optimization of the chemical composition towards adequate creep strength, increased impact toughness and further reduced σ-phase formation, while maintaining the excellent steam oxidation and corrosion properties. Other main issues will be the evaluation of thermomechanical pre-treatment procedures with reference to production and application and the development of welding procedures including interactive base / weld metal optimization.

Acknowledgement

References

[1]   I. Pfaff: Energiewende und die Rolle des konventionellen Kraftwerksparks. VDI-Fachkonferenz „Dampfturbinen in Kraftwerken", Wiesbaden, Germany 26-27 March, (2014)
[2]   U. Tomschi: Aufgaben thermischer Kraftwerke im Zuge der Energiewende. VDI-Fachkonferenz „Dampfturbinen in Kraftwerken", Wiesbaden, Germany 26-27 March, (2014)
[3]   Crofer[®] 22 H – Material Data Sheet, http://www.thyssenkruppvdm.com/ downloads/ materialdatenblaetter.html?L=1
[4]   J. Froitzheim, G. H. Meier, L. Niewolak, P. J. Ennis, H. Hattendorf, L. Singheiser, W. J. Quadakkers: Development of high strength ferritic steel for interconnect application in SOFC. Journal of Power Sources, 178, 163–173, (2008)

[5]   B. Kuhn, C. Asensio Jimenez, L. Niewolak, T. Hüttel, T. Beck, H. Hattendorf, L. Singheiser, W.J. Quadakkers: Effect of Laves phase strengthening on the mechanical properties of high Cr ferritic steels for solid oxide fuel cell interconnect application. Materials Science and Engineering A, 528, 5888–5899, (2011)

[6]   B. Kuhn, M. Talik, J. Zurek, T. Beck, W. J. Quadakkers, L. S. Singheiser, H. Hattendorf: Development of high chromium ferritic steels strengthened by intermetallic phases. Proceedings from the 7th EPRI International Conference on Advances in Materials Technology for Fossil Power Plants, Hawaii, 22-25 October, 1081 -1092, (2013)

[7]   Z. W. Hsiao, B. Kuhn, S. M. Yang, L. C. Yang, S. Y. Huang, L. Singheiser, J. C. Kuo, D. Y. Lin: The influence of deformation on the precipitation behavior of a ferritic stainless steel. Proceedings of the 10th Liége conference on Materials for Advanced Power Engineering, Liége, Belgium, 14-17 September (2014)

[8]   B. Kuhn et al: Development of high chromium ferritic steels strengthened by intermetallic phases. Materials Science and Engineering A, 594, 372-380, (2014)

[9]   S. Brett, B. Kuhn, J. Rantala, C. Hyde: Impression Creep Testing for Material Characterization in Development and Application. Proceedings of the 10th Liége conference on Materials for Advanced Power Engineering, Liége, Belgium, 14-17 September (2014)

[10]   ECCC Datasheets 2005, ASTM Grade 92, Type310

[11]   B. Kuhn, M. Talik, J. Lopez Barrilao, W. Chen, J. Ning: Microstructure evolution and creep strength of High performance Ferritic (HiperFer) steels. Proceedings from the 3rd International ECCC- Creep & Fracture Conference, Barceló Aran Mantegna, Rome, Italy, 5-7 May (2014)

DEVELOPMENT OF CASTABLE PRECIPITATION HARDENED NI-BASE ALLOYS FOR 750°C TECHNOLOGY WITHIN NEXTGENPOWER PROJECT

R. Leese (1) S. Roberts (2)

Goodwin Steel Castings Limited, Ivy House Foundry, Ivy House Road, Hanley,
Stoke-on-Trent, Staffordshire, ST1 3NR, UK
(1) Metallurgist (2) Technical Director

Abstract

The increasing world wide demand for electricity and the political motivation to reduce carbon dioxide emissions is dictating the need to increase the net efficiency of the next generation of coal fired power plant. This has lead to the initiation of many research and development programmes throughout Europe.

In order to achieve a net efficiency of 45%, live steam temperatures of 750°C are required in A-USC plants operating CCS technology. [1] Currently, commercially availible steels have an upper temperature limit of around 620°C and it is unlikely they can be developed to operate above 660°C. On the otherhand, Ni-base alloys have the potential high temperature properties to meet the unforgiving parameters of A-USC technology. Therefore, material development has focused on nickel alloys. European programs such as AD700, COMTES, European 50+ and more recently, NextGen Power and Macplus, have investigated the use of nickel alloys in the steam turbine.

So far only solid solution strenghted alloys such as alloy 625 have been proven in full size demonstration castings, however these have an upper limit of around 700°C. Therefore it is precipitation hardended ni-base alloys, strengthened by the precipitation of gamma prime γ' and/or gamma double prime γ" when aged around 800°C, that are likely to have the required high temperature strength, that have been the focus of development within the workpackage of SP2 of the NextGenPower project.

Keywords: Casting, NextGenPower, A-USC, Ni-Alloy, Precipitation Hardened.

1. Introduction

The metallurgy of precipitation hardened alloys is more complex than that of solid solution strengthened alloys, and requires a much more demanding process control. The ability of the methods engineer to accurately predict liquid shrinkage in nickel alloys is also essential for the production of a high integrity component. This is an important issue as the solidification characteristics of nickel alloys are different than for conventional steels and the value of accurate material data sets and calibration of predictive tools is essential.
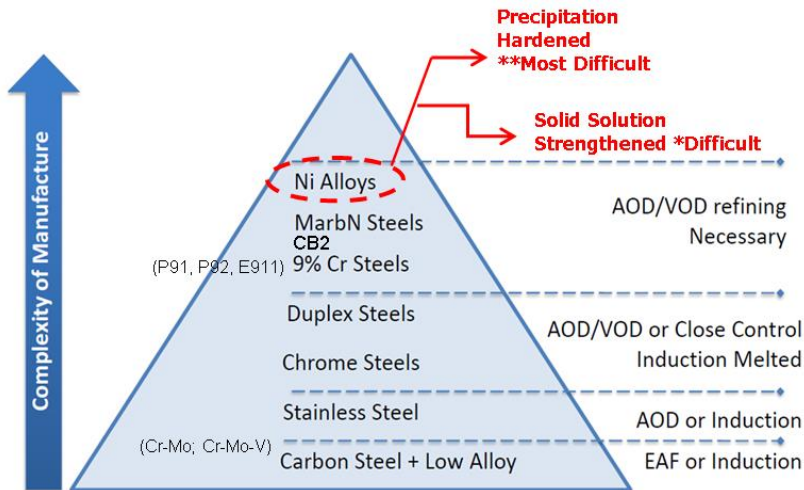
Figure 1 - A representation of casting material processing/manufacturing complexity

The successful production of heavy section nickel alloy castings requires a significant leap in technology, specialised processes and understanding than that required for similarly sized steel castings. Nickel alloys require specialised secondary refinement techniques such as AOD, VOD or VODC to obtain optimum quality and require much different approaches for method design because of the higher concentrations of aluminium and titanium.

In addition to the castability issues of these alloys there are challenges regarding microstructural integrity. Due to the inherent nature of the solidification of castings during their production, heavy sections can have

vastly different properties to that of thin. Within NextGenPower Goodwin have made significant progress and this paper summarises the breakthroughs on route to the ultimate aim of producing the worlds first full scale demonstration casting in a precipitation hardened alloy.

2. Candidate alloys

The initial task was to establish candidate precipitation hardened alloys that had the potential to be utilised in cast turbine applications. Knowledge and casting experience from previous R&D projects such as AD700 was drawn upon and the alloys selected were alloy 282, 263, 105, 230 and 740H. During the first SP2 work package technical meeting this selection was narrowed down to three alloys alloy 282, alloy 263 and 740H on the basis of creep strength, sufficient room temperature ductility, oxidation performance and perceived weldability. Special thanks go to Haynes International and Special Metals who allowed Goodwin to produce trial melts of cast alloy 740, 740H and 282 for R&D.

3. Casting of trial melts

Trial melts of the selected alloys have been cast in the form of a step block with section steps of 100mm, 200mm and 300mm respectively, the design of which can be seen in Figure 4. These sections closely represent the wall thicknesses that would be expected in a typical range of steam turbine cast components, and so are very representative of typical cooling rates during solidification. Goodwin's previous experience showed that small scale trial castings rarely qualify how a nickel alloy behaves when cast in heavy sections.

The chemical composition chosen for these trials were predominately the prescribed wrought chemistry and to our best knowledge had never been produced as heavy section cast components.

Alloy	C	Si	Mn	Ni	Cr	Mo	Nb	Co	Al	Ti	Fe
Alloy 740H	0.046	0.32	0.30	BAL	24.6	0.54	1.31	19.57	1.22	1.36	0.22
Alloy 282	0.034	0.36	0.03	BAL	19.3	8.01	0.03	10.0	1.40	2.10	0.21
Alloy 263	0.057	0.34	0.37	BAL	19.8	5.61	0.01	19.6	0.42	2.05	0.07

Table 1- Trial melt chemical compositions

4. Analysis of trial step blocks

All the step block castings, to varying degrees suffered from microstructural cracking during the heat treatment process, which in cast alloy 282 and 740H blocks resulted in volumetric cracks that were detected upon radiographic examination.

Figure 2 - Cracking detected by RT in a 180mm section thickness area of the cast alloy 282 step block. Similar defects were seen in the cast 740H step block. Cast alloy 263 passed RT examination but surface inspection showed deep surface crazing.

Material evaluation and characterisation of each alloy was conducted by Loughborough University who established that the volumetric cracking, although different in each alloy, was always associated with cracked carbides dispersed along the grain boundaries, and often worse in the heaviest sections of the material. The microstructural cracking resulted in premature mechanical failures as seen in table 2. Some cracking was also associated with grain boundary vacancies.
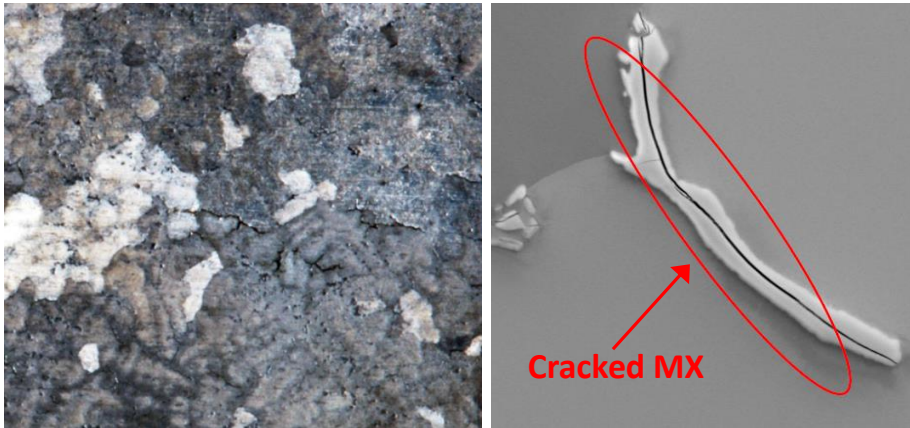
Figure 3 – Example of microstructural cracking associated with cracked MX precipitates after heat treatment

A major deliverable was to manufacture a full scale demonstration casting to evaluate the castability and mechanical performance of the most promising alloy investigated. Due to technical difficulties in producing material with good heavy section microstructural integrity it was decided that further development was required before proceeding to the full scale demonstration casting.

After a period of evaluation and development three additional blocks were manufactured with modified chemistries and optimised heat treatments. The idea being to evaluate these new materials before proceeding to select one of the materials for the full scale component.

5. Casting of modified alloy trial melts

Extensive R&D was conducted in collaboration with Loughborough University which included:
   1) Materials characterisation
   2) Thermodynamic simulation
   3) Stress analysis
   4) SEM, EDX and TEM analysis

Modified chemical composition step blocks were designed and cast in Alloy 282-Mod, Alloy 263-Mod and Goodwin proprietary alloy, Alloy G130 (Ni-24.5Cr-20Co-Ta). These alloys were selected because they showed predicted castability potential and microstructural stability in comparison to the previous castings produced to the wrought chemistry. Again, these step blocks had 100mm, 200mm and 300mm sections to represent those of a typical turbine component.

Figure 4 - Modified cast alloys after knock out of the mould

Each block was heat treated using an optimised cycle. These cycles were determined by laboratory testing after extensive modelling and characterisation performed by Loughborough University.

5.1 NDT of modified alloys step blocks

All the modified alloys showed improved volumetric integrity after heat treatment. However, cast alloy 282M still had evidence of volumetric cracking while cast alloy 263M and G130 passed RT assessment to ASTM E446/186/280 level 1.

Figure 5 – RT graph of G130 step block

5.2 Microstructural characterisation of modified alloys

The modified alloys exhibited vastly improved microstructures after heat treatment. Alloy G130 showed very few MX precipitates and those observed were not cracked therefore microstructural integrity was very good. However cast alloy 282M did still contain cracked Mo-rich carbide

precipitates although fewer were observed compared to the original castings produced to the wrought composition. Cast alloy 263M, also showed improvements with regards to the modifications made. However heavy section ductility (Table 3) was similar to that of cast alloy 282M which showed a marked reduction compared to G130. This may indicate potential microstructural deficiencies which are still being evaluated.
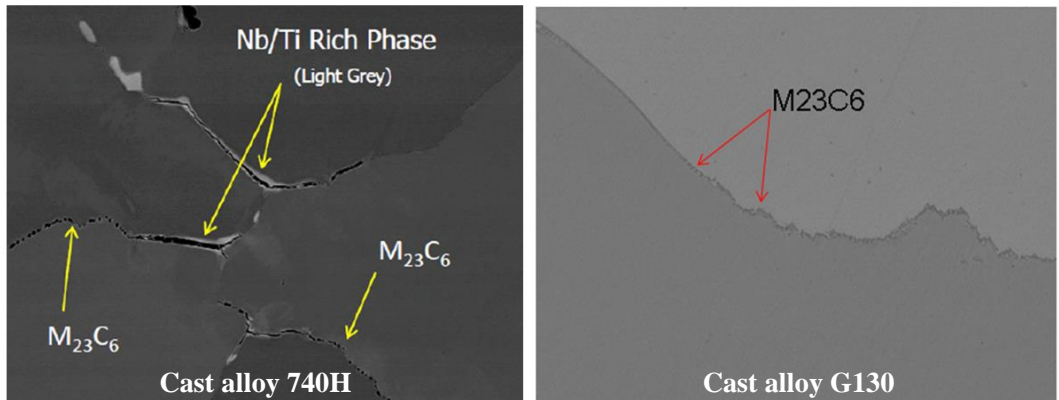
Figure 6 -Example of the improved microstructure in the cast G130 composition compared to the cast 740H composition after optimised heat treatment.

5.3 Mechanical properties

The mechanical properties of the cast alloys can be seen in Table 2. The original castings produced to the wrought compositions exhibited low ductility and early failures were experienced. This was a result of the microstructural cracking observed.

Alloy	Yield (N/mm^2)	UTS (N/mm^2)	Elongation (%)	R of A (%)	Impacts @ RT (J)
[1] Alloy 740H	545	560	5	11.5	22/43/37 Avg 34
[1] Alloy 263	444	496	9	-	-
[1] Alloy 282	No result – samples fractured prematurely				
[2] Alloy G130	410	691	30	42	128/136/110 Avg 125
[2] Alloy 282 MOD	588	751	15	18	52/50/50 Avg 51
[2] Alloy 263 MOD	506	718	29	28	150/184/205 Avg 180

Table 2 - Mechanical properties obtained from a 50mm section. All material in the solution treated and aged condition.
[1] Premature failures due to microstructural cracking, [2] No premature failures

The mechanical properties of alloy G130 are a little weaker at room temperature than the cast alloy 282M and 263M yet a marked increase in tensile strength and ductility over these alloys was observed, which was particularly apparent in heavy sections.

Test material from the modified cast alloys were tested by partners within the NextGenPower project which included room temperature mechanical testing and high temperature stress rupture testing.

6. Cast Alloy G130 development:

After a further evaluation period Goodwin successfully cast G130 modified variant compositions (G130A & G130B) which combined further chemistry changes with optimised heat treatments. The preliminary mechanical testing data can be seen in Table 3 where the mechanical properties of both 100mm and 200mm sections show a marked increase in UTS and ductility over cast alloy 282M and cast alloy 263M.

G130 series of alloys produced show good through section mechanical properties whilst other cast precipitation hardened alloys experience a dramatic reduction in mechanical strength in 200mm sections.

Alloy	Cast section thickness	Yield (N/mm^2)	UTS (N/mm^2)	Elongation (%)	R of A (%)	Impacts @ RT (J)
Alloy G-130B	200mm	456	708	39.4	36.7	124/128/134
Alloy 282 MOD		498	554	5	6	88/98/44
Alloy 263 MOD		451	487	9	7	228/228/230
Alloy G-130B	100mm	494	713	38	36.6	168/145/142
Alloy 282 MOD		545	671	14	23	74/85/44
Alloy 263 MOD		419	647	31	50	252/232/246

Table 3 - Mechanical properties obtained from 100mm and 200mm sections from 1500kg cast step blocks

Alloy G130B exhibits high ductility through section, an important factor when considering the difficulty of welding precipitation hardened cast alloys.
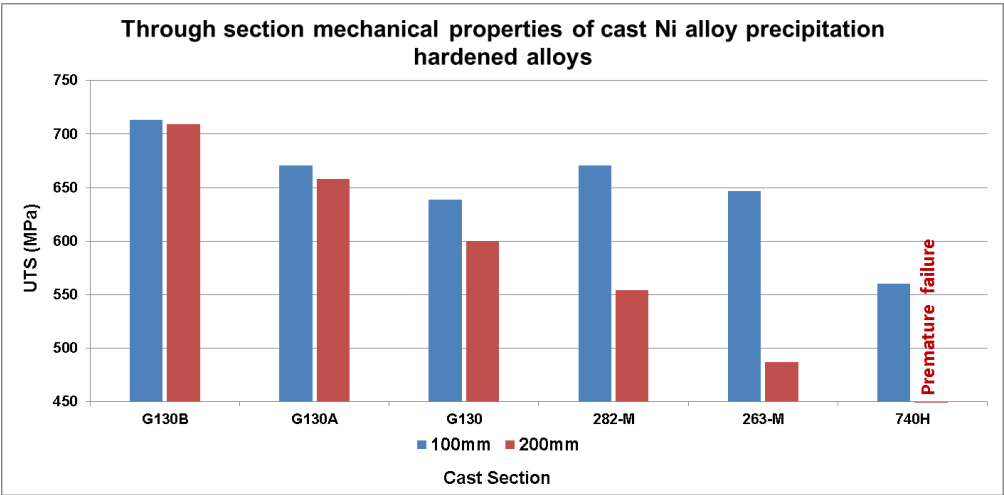
Figure 7 - Through section mechanical properties of modified cast Ni-alloy precipitation hardened alloys in relation to section thickness. Note: No UTS value obtained for cast Alloy 740H due to premature failure caused by microstructural cracking

7. Cast Alloy G130 Stress Rupture:

Short term stress ruptures of G130 alloys plotted against LMP are shown in Figure 8 . The graph shows that the materials meet the target of 80MPa for 100,000hrs at 700°C and likely to approach this criteria for 750°C.

283
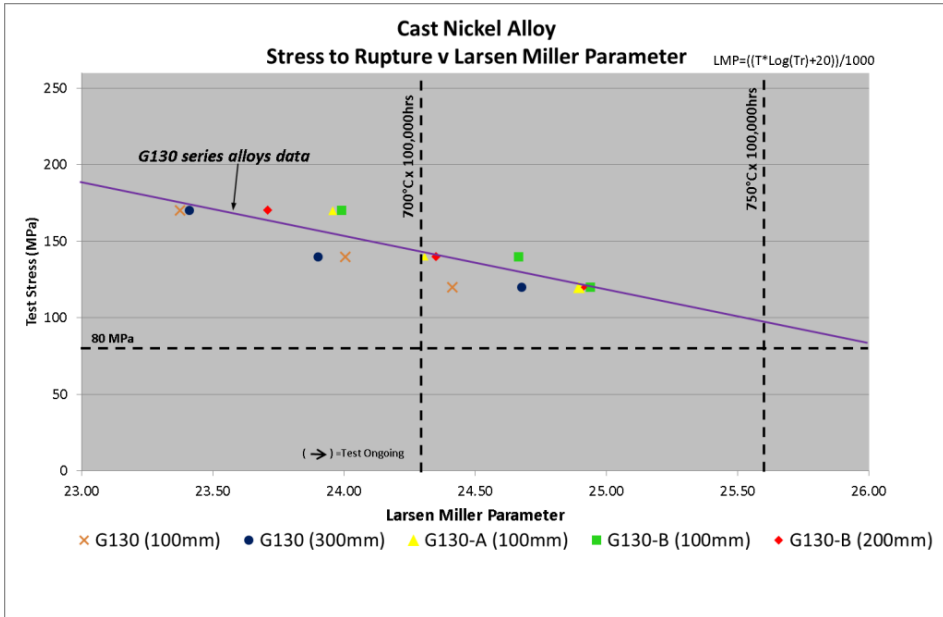
Figure 8 - Stress Rupture plotted against LMP for alloys G130, G130A and G130B

8. Conclusions

Over the last 15 years, Goodwin has been involved in the advancement in technology of cast nickel alloys for advanced ultra super critical applications (A-USC). Within NextGenPower and MacPlus projects, Goodwin have successfully overcome many challenges relating to the complexity of casting precipitation hardened Ni alloys and have developed a castable Ni-base superalloy that is looking very promising for suitability for manufacture of cast turbine components operating at 750°C.

9. Acknowledgments

We would like to acknowledge the work that Loughborough University has contributed in the characterisation and evaluation of the nickel base cast alloys discussed in this paper, and especially the help of Professor Rachel Thomson and her team.

10. Notes

The use of the word "Goodwin" with in this paper relates specifically to the company "Goodwin Steel Castings Ltd, Ivy House Road, Hanley, Stoke-on-Trent, UK".

11. Bibliography

[1] Project description. NEXTGENPOWER. [Online] 2010. [Cited: April 7, 2014.] http://www.nextgenpower.eu/index.php/about.

Z-PHASE NITRIDES IN MARTENSITIC CREEP RESISTANT STEELS

J. Hald,

DTU Mechanical Engineering, Technical University of Denmark
Produktionstorvet 425, 2800 Kgs. Lyngby, Denmark
jhald@mek.dtu.dk

Abstract

Precipitation of Z-phase nitrides (CrMN) explains a large number of observed instabilities in long-term creep strength of current martensitic 9-12%Cr creep resistant steels. These steels are strengthened by fine MN nitrides based on V and Nb, which are gradually replaced by coarse Z-phase particles during creep exposure.

Z-phase precipitation is strongly accelerated by increased contents of Cr, Co and Ni in the steels. MN strengthened 12Cr martensitic steels experience creep instability within 5,000-30,000 hours at 600-650^{0}C, whereas 9Cr steels are normally stable in long-term creep. However, Z-phase precipitation can also affect 9Cr steels like Grade 91, MARBN and BH within 100,000 hours at 600-650^{0}C, possibly caused by their contents of Ni or Co.

Z-phase forms only by transformation of pre-existing MN nitrides, which pick up Cr from the steel matrix. The accelerating effect of Cr on Z-phase formation is well explained by thermodynamic modelling, while the mechanism of acceleration by Co and Ni remain unclear.

The detrimental effects of Z-phase on creep performance could be overcome by 10Cr steels, which cannot form Z-phase due to very low N content; or by low C 11-12Cr steels, where fine Z-phases based on CrTaN on CrNbN are used as strengthening agents.

Keywords: Martensitic 9-12%Cr steels, Creep, Z-phase precipitation, Effect of Cr, Co and Ni.

1. Introduction

The martensitic creep resistant 9 Cr steels, Grades 91 and 92 for steam pipework and FB2 and CB2 for large forgings and castings, allow construction of steam power plants with advanced live steam parameters up to 300 bar and 600^{0}C. Improved creep strength of these alloys as compared to earlier martensitic grades such as 9CrMo and 12CrMoV is due to precipitation hardening by fine MN nitrides based on V and Nb, and to stabilization of the martensitic microstructure by additions of W and B [1].

Many attempts have been made to develop even stronger martensitic 9-12Cr creep resistant steels for higher steam parameters. These attempts have mainly been based on precipitation strengthening by MN nitrides similar to the mentioned 9Cr steels. However, it has been found that the fine MN nitrides may in many cases (slowly) be replaced by coarse CrMN Z-phase nitrides, and this causes a severe loss of long-term creep strength. [2-4]

The present paper reviews observations and understanding of Z-phase precipitation in martensitic creep resistant steels, and identifies possible pathways to overcome the detrimental effects of Z-phase precipitation. This could enable the development of stronger martensitic creep resistant steels.

2. Z-phase in martensitic creep resistant steels

2.1. Observations

The complex nitride Z-phase (Cr(V,Nb)N) was first found in martensitic creep resistant steels in 1987 by Schnabel et. al. in the steel X19CrMoVNbN 11 1 (X19), which is well-known for sigmoidal creep behaviour [5]. However, they did not make any conclusions about connections between the appearance of Z-phase in the steel and the loss of creep stability. In 1996 Vodarek and Strang investigated steels similar to the X19 steel, but with varying Ni contents between 0.5 wt% and 1.15 wt%. They discovered that Z-phase precipitation causes dissolution of fine MX carbonitrides and a loss of creep strength. Further, they concluded that increasing Ni content accelerates the Z-phase precipitation and MX dissolution, [2,3]. In the following years, Z-phase was found in a number of martensitic steels as summarised in 2006 [4].

In 2006 an investigation of Z-phase precipitation in several 9-12%Cr creep resistant martensitic steels concluded that the Cr content in the steels has a strong accelerating effect on the Z-phase precipitation. (Cr,V)N strengthened steels with around 12%Cr show Z-phase precipitation and loss of creep strength within 5,000-30,000 hours at 600-650^{0}C, whereas steels with around 9%Cr can show very limited Z-phase precipitation and good creep strength for more than 100,000 hours at 600^{0}C [4].

The observed correlation between Cr content and Z-phase precipitation rate explains the poor microstructure stability for MN strengthened 12Cr steels, which are under development for service at temperatures of 620-650^{0}C, where high Cr content is needed for resistance against steam oxidation. Furthermore, it explains the observed good microstructure stability of the 9Cr grades.

However, more recent observations have demonstrated that 9Cr steels can also experience comprehensive Z-phase precipitation before 100,000 hours.

In 2008 Helis et. al. [6] and Kaufmann et. al. [7] showed correlation between increased Co content and accelerated Z-phase formation in 9Cr steels with 1-5 wt% Co.

In 2011 Sawada et. al. [8] demonstrated that the 9Cr steel Grade 91 can show considerable formation of Z-phase before 100,000 hours at 600^{0}C, and that this can lead to a loss of creep strength. In 2013 and 2014 the same group of researchers indicated that increased Ni content up to 0.28 wt% in the steel plays a role in the observed accelerated loss of creep strength, although the mechanism remains unclear, fig. 1 [9,10].

In 2014 Kobayashi et. al. found a similar loss of creep strength in steel Grade 91 with only 0.09 wt% Ni [11], which indicate that other effects than Ni content can explain observed losses in creep strength. Other investigators found only limited Z-phase formation in Grade 91 after close to or more than 100,000 hours at 600^{0}C in steels containing 0.11wt%Ni [12]; 0.12 wt% Ni [13] and 0.13 wt% Ni [14].
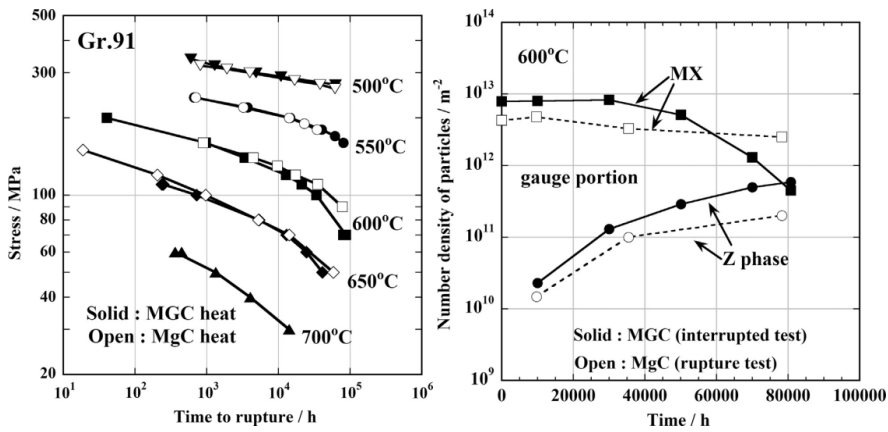
Fig. 1. Z-phase precipitation at 600 ⁰C in steel Grade 91 with 0.04 wt% Ni (MgC) and 0.28 wt% Ni (MGC) [10].

2.2. Thermodynamics, kinetics and formation mechanism

A thermodynamic model of the Z-phase was developed in 2007 based on experimental observations. It shows that Z-phase is a stable nitride in 9-12%Cr steels alloyed with conventional amounts of V, Nb and N [15]. This means that it is the kinetics of the Z-phase precipitation which controls the microstructure stability of the steels. Calculations of driving force for Z-phase formation with the thermodynamic model was used to estimate the influence of individual alloying elements on Z-phase precipitation rate. They indicated a strong accelerating effect of Cr on Z-phase formation similar to experimental observations. Furthermore, the calculations indicated that an increase of the C content would delay the Z-phase formation, since C ties up Cr in carbides and thus reduces the amount of Cr available for Z-phase formation.

However, the observations that increased contents of Co and Ni can lead to accelerated Z-phase formation, even in steels with low Cr content, is not well understood. None of the elements Co or Ni are included in the Z-phase itself in significant quantity, and the thermodynamic effect on Cr activity in the steel matrix seems small. [15,16].
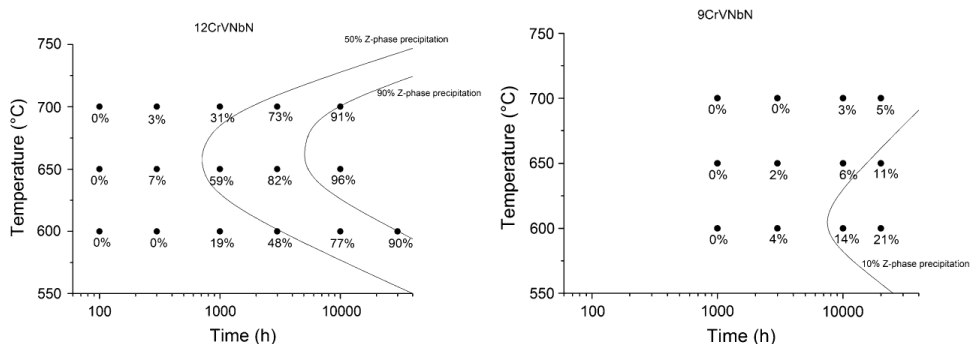
Fig. 2. Amount of MN transformed to Z-phase in 12CrNbVN and 9CrNbVN model alloys [14]

TTP diagrams for Z-phase formation in commercial 9-12%Cr steel grades were published by Sawada et. al. in 2007 [17]. They confirmed the accelerating effect of Cr on Z-phase formation and indicated that the nose of the TTP diagrams lies at 650^{0}C. More recent studies of TTP diagrams for 9Cr and 12Cr model alloys indicate that the nose moves to lower temperatures around 600^{0}C for reduced Cr contents, fig. 2 [18].

Microstructure studies of the formation mechanism of Z-phase have shown that the Z-phase does not nucleate on its own in martensitic steels. Instead it forms by diffusion of Cr from the steel matrix into the MN particles [19]. This slowly transforms the MN particles in to Z-phases, fig. 3 [20].
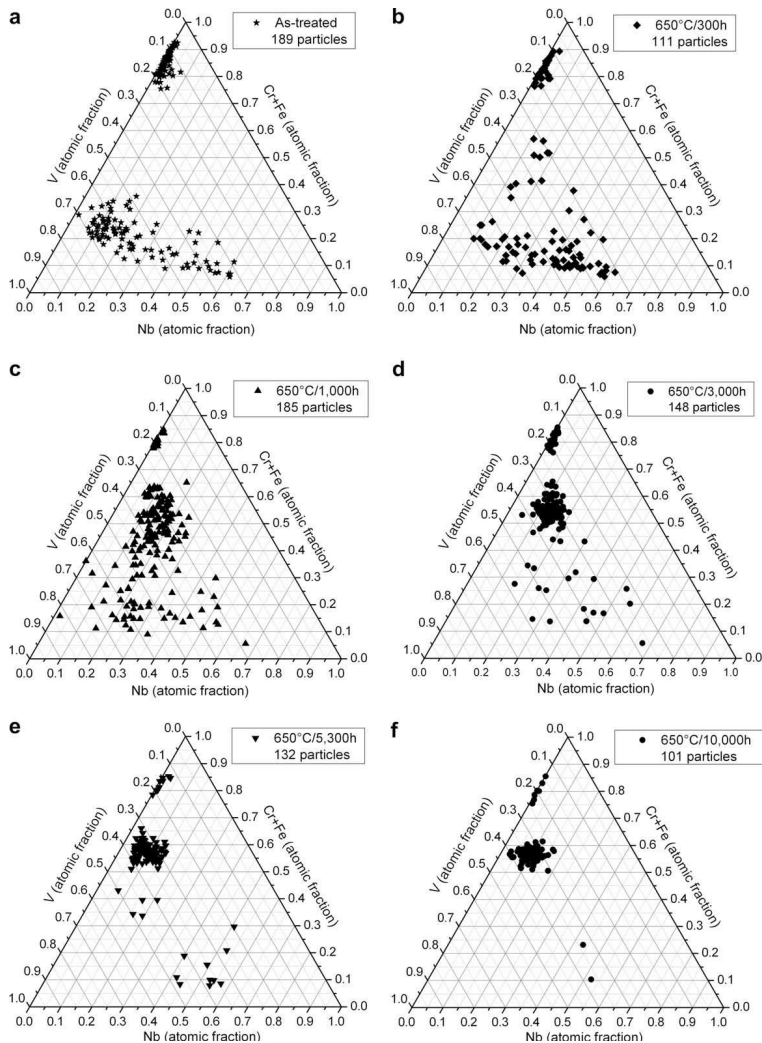
Fig. 3. Evolution of chemical composition of Nitrides in a 12CrMoVNbN alloy during ageing up to 10,000 hours at 650 ^{0}C [20].

On the atomic scale this transformation is seen as the formation of double atomic layers of Cr inside the MN cubic crystal. These Cr planes gradually transform the MN crystal into the tetragonal Z-phase crystal, fig. 4.
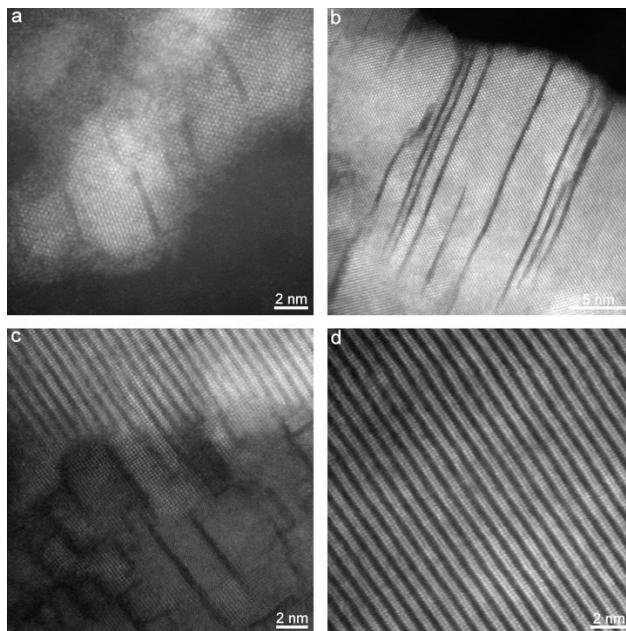
Fig 4. Atomic scale images of the transformation of a cubic TaN (a) into a tetragonal CrTaN Z-phase (d). Double atomic layers of Cr (dark) form in the MN crystal. [21].

The fact that Z-phase forms only from pre-existing MN particles explains the sluggish nature of Z-phase precipitation in 9-12CrVNbN steels. Furthermore it explains the observations that when applying low tempering temperatures to martensitic steels, which result in the formation of hexagonal M_2N precipitates (mainly Cr_2N) rather than the cubic MN in the as-tempered steel, then the Z-phase formation is significantly delayed during creep [22]. The M_2N needs to dissolve and MN needs to precipitate before Z-phase can form by transformation of the MN particles.

Once a (V,Nb)N particle has transformed into a Cr(V,Nb)N Z-phase it can grow relatively fast. Large Z-phase particles of 0.5 μm diameter were observed after 15,000 hours at 650^0C in 12%Cr steels [4] and after 30,000 hours at 650^0C in 9Cr steels [23]. During growth the Z-phase consumes the fine MN particles.

3. New steel developments

There is an ongoing interest to develop stronger creep resistant martensitic steels, since this could allow the construction of steam power plants with more advanced steam parameters and higher efficiency at only limited cost increases. The aim is to develop a steel with 100,000 hour creep rupture strength of 100 MPa at 650^0C. At the same time the steel should have high

Cr content of 11-12% to reduce steam oxidation rates. Due to Z-phase precipitation, all attempts to develop 11-12%Cr steels based on precipitation strengthening by fine (V,Nb)N nitrides have failed [1].

In recent years there has been good progress in the development of 9-10%Cr steels, which show good prospects to reach improved creep properties as compared to steel Grades 92, FB2 and CB2. Table 1 and fig. 5 shows recent results of these developments. However, for applications at steam temperatures above 620^{0}C the 9-10%Cr steels will need surface coatings for oxidation protection.

	P92	BH	TAF	MARBN			Belgorod
Mass %				NIMS	NPM1	NPM2	
C	0.11	0.03	0.18	0.078	0.074	0.090	0.10
Si	0.10	0.36	0.50	0.31	0.29	0.30	0.06
Mn	0.45	0.49	1.0	0.49	0.44	0.51	0.10
Cr	8.82	9.12	10.5	8.88	9.26	9.26	10.0
Mo	0.47	0.15	1.5	-	-	-	0.70
W	1.87	2.40	-	2.85	2.84	2.92	2.0
Ni	0.17	0.01	0.1	-	0.06	-	0.17
Co	-	1.8	-	3.00	2.95	2.88	3.0
V	0.19	0.20	0.2	0.20	0.21	0.20	0.20
Nb	0.06	0.05	0.15	0.051	0.056	0.050	0.05
Ti	-	-	-	-	-	-	0.01
N	0.047	0.050	0.02	0.0079	0.013	0.010	0.003
B	0.0020	0.0060	0.0400	0.0135	0.0120	0.0100	0.0080
Norm	1070ºC	1050ºC	1150ºC	1150ºC	1150ºC	1150ºC	1060ºC
Temp	780ºC	780ºC	700 C	770 C	770 C	770 C	770 C

Table 1. Chemical composition (Mass%, bal. Fe) and heat treatment of new 9-10%Cr steels.

The TAF steel developed by Fujita in the 1950s based on 10.5wt%Cr and high Boron of 400 ppm is still among the strongest martensitic creep resistant steels [24]. But due to its high Boron content it has limited practical applicability.

3.1. MARBN steels
Much attention is focused on the developments of the so-called MARBN steels, which are 9Cr3Co3WVNb steels alloyed with 100-140 ppm of Boron, and with reduced amount of N around 0.010 wt%. The first development results of MARBN were published by NIMS in 2004 [25], but no long-term creep data beyond 18,000 h/650^{0}C have been published by them since 2006 [26]. Recently, European researchers have taken up the development of the MARBN steel, and long-term creep data have been published in 2010 [27] and 2014 [28].

It has been found that the MARBN steels can also be sensitive to Z-phase formation. After 24,000 hours at 100MPa/650^{0}C, Z-phase formation and dissolution of MN nitrides was found in the NPM1 steel [27, 29]. As seen in fig. 5 this led to a loss of creep strength. The Z-phase formation is probably accelerated by the Co content around 3wt%. The loss of creep strength implies that a significant strengthening of the MARBN steels is due to precipitation hardening by MN nitrides. However, with adjustments of the composition as in the NPM2 steel, table 1, it seems possible to delay the Z-phase formation, and the MARBN steel could reach the strength level of TAF, fig. 5
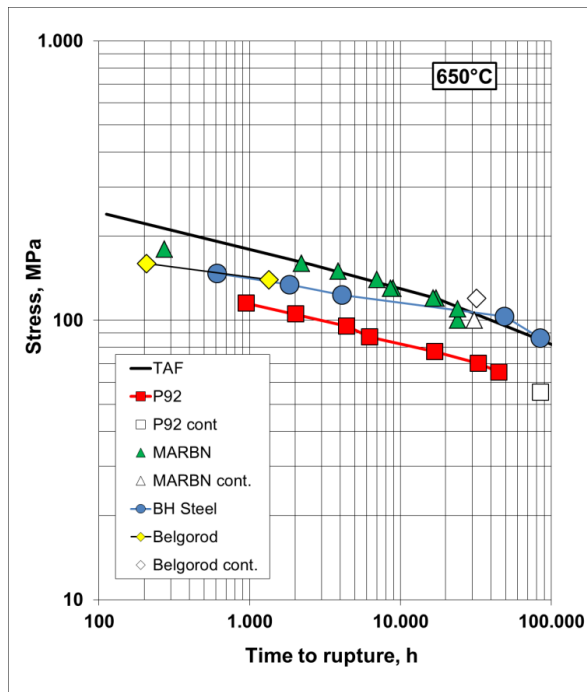
Fig. 5. Creep rupture strength of new 9-10%Cr steels.

3.2. Low C steel BH

The BH steel contains similar Nitrogen, but a reduced amount of C and increased Boron and Co as compared with steel Grade 92, table 1. This steel shows better creep performance than the TAF steel at 100MPa/650^{0}C, and excellent microstructure stability up to 50,000 hours at 650^{0}C, fig. 5 [30]. However, in the long term around 80,000 hours the strength drops to the level of TAF. The improved long-term performance compared to the MARBN steel could be caused by the reduced Co content of 1.8 wt% as compared to the 3 wt% in the MARBN steels. This will significantly delay the formation of Z-phase in the BH steel.

3.3. Z-phase in new 9%CrCo steels

In summary, the creep strength of the new 9CrCo steels MARBN and BH rely more or less on precipitation strengthening by fine MN nitrides. This is lost by Z-phase precipitation in the long-term range, whereby the creep strength is reduced. Z-phase precipitation seems to be accelerated by the Co content in the steels. However, both steels are still significantly stronger than the P92 up to more than 30,000 hours at 650^{0}C.

3.4. Low N 10Cr steel

A 10Cr steel under development at Belgorod State University shows excellent stability up to 35,000 hours at 650^{0}C and better long-term creep strength than the TAF steel, fig. 5. [31]. The steel is based on the TOS 110 steel earlier developed at Toshiba [32], but the composition has been altered with reduced Nitrogen and addition of Titanium [33,34], table 1. Since the Z-phase is a Nitride, which do not incorporate Carbon, Z-phase precipitation can be avoided by elimination of nitrides, which could transform in to Z-phase. Only V, Nb and Ta nitrides are

known to form Z-phase CrMN [35]. TiN will not transform into Z-phase. Elimination of the Z-phase transformation could be an explanation for the excellent microstructure stability of the Belgorod steel.

3.5.   Z-phase strengthened steel.

The idea to use fine Z-phase particles as strengthening agents in the martensitic steels was presented in 2008 [35]. By strong acceleration of the Z-phase transformation the growth phase for Z-phase could be suppressed, and a distribution of fine Z-phase particles could be achieved, which could provide stable long-term precipitation hardening. [16]. In order to accelerate the Z-phase transformation the Cr content should be high, C should be as low as possible, and Z-phase should be of the type CrNbN or CrTaN [36]. The need for high Cr indicated that it could be possible to produce a stable 12Cr martensitic creep resistant steel.

Low C 12Cr test alloys have been manufactured and tested, see table 2, and it has been confirmed that fine Z-phases based on CrTaN can be precipitated in the steel, and these remain fine up to 10,000 hours at 650^0C [16]. It was found that Ta-based Z-phases are more stable than Nb-based Z-phases. Furthermore, it was found that increasing content of C reduces the Z-phase transformation speed, since the MX carbonitrides need to get rid of carbon before the CrMN Z-phase nitride can form.

	wt%, bal. Fe											
	Cr	C	B	Ta	Nb	N	W	Ni	Co	Cu	Mn	Si
Z3	11,64	0,005	0,004	0	0,26	0,036	2,82	1,47	5,4	0	0,49	0,3
Z4	11,79	0,005	0,004	0,39	0	0,033	2,9	0,5	7,3	0	0,48	0,3
ZL3	12,1	0,06	0,0063	0,36	0	0,049	2,47	0,19	3,5	1,95	0,21	0,31

Table 2. Compositions of test alloys of Z-phase strengthened steels.
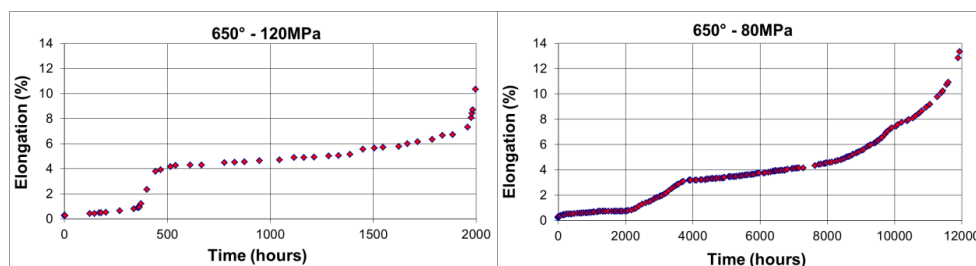
Fig. 6. Creep curves of steel Z4, revealing strain instabilities.

Creep strength close to steel P92 has been obtained, but creep tests revealed instabilities in the steels, where the strain "jumped" up to 3% over several 100 hours, fig. 6.

Because of their low C content, the Z-phase steels need high amount of austenite formers like Co, Ni, Mn or Cu in order to avoid the formation of δ-ferrite. It is currently suspected that this high content of austenite formers could lead to formation of isothermal austenite similar to observations in low C supermartensitic steels, and that this causes the creep instabilities [37].

Ongoing research aims to investigate the effect of reduced amounts of austenite formers on the creep stability of Z-phase strengthened steels [38].

4. Summary

The formation of Cr(V,Nb)N Z-phase particles in 9-12%Cr martensitic creep resistant steels strengthened by (V,Nb)N nitrides explains a large number of observations of poor microstructure stability and loss of long-term creep strength.

Z-phase precipitation is strongly accelerated by increased contents of Cr, Co and Ni in the steels. MN strengthened 12Cr martensitic steels experience creep instability within 5,000-30,000 hours at 600-650^{0}C, whereas 9Cr steels are normally stable in long-term creep. However, Z-phase precipitation can affect 9Cr steels like Grade 91, MARBN and BH within 100,000 hours at 600-650^{0}C, possibly caused by contents of Ni or Co.

The formation mechanism for Z-phases is well understood. Z-phase forms (slowly) by transformation of pre-existing MN nitrides, which pick-up Cr from the steel matrix. Once it has formed, the Z-phase grows (fast) by consumption of untransformed MN particles.

Thermodynamic modelling provides a good explanation of the acceleration of Z-phase formation by increased Cr content, whereas the mechanisms for acceleration by Ni and Co are not well understood.

In order to overcome the detrimental effects of Z-phase the development of stable high Cr martensitic steels should either be based on suppressing Z-phase formation (low N steel) or on strengthening by other precipitates than MN. This could include using the Z-phase itself as a strengthening agent.

5. References

[1] J. Hald, Proc. 9th Liége Conference. *Materials for Advanced Power Engineering 2010* (ed. J. Lecompte-Beckers et. al.), 55-66, Forschungszentrum Jülich (2010)

[2] A. Strang, V. Vodarek, *Mater. Sci. Tech* 12, 552 (1996)

[3] A. Strang, V. Vodarek, *Microstructural development and stability in high Chromium ferritic power plant steels* (ed. A. Strang et. al.), No 1, 31-52, The Institute of materials, London (1997)

[4] H. K. Danielsen, J. Hald, *Energy Mater.* 1, 49 (2006)

[5] E. Schnabel, P. Schwaab, H. Weber, *Stahl und Eisen* 107, 691-696 (1987)

[6] L- Helis, Y. Toda, T. Hara, H. Miyazaki, F. Abe, *34th MPA Seminar,* Stuttgart, Germany, 9.1-9.20 (2008)

[7] F. Kaufmann, G. Zies, K. Maile, S. Straub, K. H. Mayer *34th MPA Seminar,* Stuttgart, Germany, 4.1-4.14 (2008)

[8] K. Sawada, H. Kushima, M. Tabuchi, K. Kimura, *Materials Science and Engineering A,* 528, 5511-5518 (2011)

[9] K. Kimura, K. Sawada, H. Kushima, Y. Yoda, *Procedia Engineering*, 55, 2-9 (2013)

[10] K. Sawada, H. Kushima, T. Hara, M. Tabuchi, K. Kimura, *Materials Science and Engineering A,* 597, 164-170 (2014)

[11] S. Kobayashi, K. Sawada, T. Hara, H. Kushima, K. Kimura, *Materials Science and Engineering A,* 592, 241-248 (2014)

[12] C. G. Panait, W. Bendick, A. Fuchsmann, A. F. Gourgues_Lorenzon, J. Besson, *Int. J. Press. Vessel Pip.* 87, 326-335 (2010)

[13] L. Cipolla, S. Caminada, D. Venditti, H. K. Danielsen, A. Di Gianfrancesco, Proc. 9th Liége Conference. *Materials for Advanced Power Engineering 2010* (ed. J. Lecompte-Beckers et. al.), 272-285, Forschungszentrum Jülich (2010)

[14] H. G. Armaki, R. Chen, K. Maruyama, M. Igarashi, *Materials Science and Engineering A,* 527, 6581-6588 (2010)

[15] H. K. Danielsen, J. Hald, *Computer Coupling of Phase Diagrams and Thermochemistry*, 31, 505-514 (2007)

[16] H. K. Danielsen, J. Hald, Proc. 9th Liége Conference. *Materials for Advanced Power Engineering 2010* (ed. J. Lecompte-Beckers et. al.), 310-319, Forschungszentrum Jülich (2010)

[17] K. Sawada, H. Kushima, K. Kimura, M. Tabuchi, *ISIJ International,* 47, 5, 733-739, (2007)

[18] H. K. Danielsen, P. E. Di Nunzio, J. Hald, *Met. and Mater. Trans. A*, 44A, 2445-2452, (2013)

[19] H. K. Danielsen, J. Hald, *Materials Science and Engineering A,* 505, 169-177 (2009)

[20] L. Cipolla, H. K. Danielsen, D. Venditti, P. E. Di Nunzio, J. Hald, M. A. J. Somers, *Acta Mater.* 58, 669-679 (2010)

[21] H. K. Danielsen, J. Hald, M. A. J. Somers, *Scripta Mater.* 66, 261-264 (2012)

[22] K. Sawada, K. Suzuki, H. Kushima, M. Tabuchi, K. Kimura, *Materials Science and Engineering A,* 480, 588-563 (2008)

[23] K. Sawada, H. Kushima, K. Kimura, *ISIJ International,* 46, 5, 769-775, (2006)

[24] T. Fujita, N. Takahashi, *Trans. ISIJ*, 18, 702-711, (1978)

[25] K. Sakuraya, H. Odaka, F. Abe, in Proc. *4th International Conf. Advances in Materials Technology for Fossil Power Plants,* (ed. R. Viswanathan, et. al.), Hilton Head Island, USA, October 2004, 1270-1279, ASM International (2005)

[26] H. Semba, F. Abe, *Energy Mater.* 1, 4, 238-244, (2006)

[27] P. Mayr, I. Holzer, M. Albu, G. Kothleitner, H. Cerjak, S. M. Allen, in Proc. *6th International Conf. Advances in Materials Technology for Fossil Power Plants 2010*, 640-653, ASM International (2011)

[28] C. Schlacher, C. Béal, C. Sommitsch, S. Baumgartner, P. Mayr, *Proc. 3rd International ECCC Conference Creep & Fracture 2014,* Paper #11, Rome (2014)

[29] P. Mayr, F. Méndez Martin, M. Albu, H. Cerjak, *Materials at High Temperatures,* 27, 1, 67-72, (2010)

[30] T. Fujita, Personal communication

[31] R. Mishnev, N. Dudova, R. Kaibyshev, *Proc. 3rd International ECCC Conference Creep & Fracture 2014,* Paper #66, Rome (2014)

[32] Y. Tsuda, M. Yamada, R. Ishi, O. Wanatabe, M. Miyazaki, Proc. 6th Liége Conference. *Materials for Advanced Power Engineering 1998* (ed. J. Lecompte-Beckers et. al.), I, 331-340, Forschungszentrum Jülich (1998)

[33] N. Dudova, R. Kaibyshev, *ISIJ International,* 51, 5, 826-831 (2011)

[34] N. Dudova, R. Mishnev, R. Kaibyshev, *ISIJ International,* 51, 11, 1912-1918 (2011)

[35] H. K. Danielsen, J. Hald, *Scripta Materialia,* 60, 811-813 (2009)

[36] J. Hald, H. K. Danielsen, *34th MPA Seminar,* Stuttgart, Germany, 6.1-6.16 (2008)

[37] N. Nakada, T. Tsuchiyama, S. Takaki, N. Miyano, *ISIJ Internatonal,* 51, 2, 299-304 (2011)

[38] European Union FP7 Project Z-Ultra (GA Nr. 309916), (2013)

MODELLING AND MANUFACTURE OF A MOCK-UP ROTOR FORGING IN A HIGH STRENGTH PRECIPITATION HARDENED NI ALLOY

Parkin C.[1], Vanstone R. [1], Notargiacomo S. [2], Zanin E. [2], Massazza M. [3], Perolino M.M. [3]

[1]Alstom Power, Ferrous Alloy Development, Rugby
[2]Centro Sviluppo Materiali S.p.A, Rome
[3]Cogne Acciai Speciali S.p.A, Aosta

Abstract

Steam turbines operating with inlet steam temperatures of 760°C will require nickel-base alloys in the highest-temperature sections to provide necessary elevated-temperature yield and creep-rupture strength. These alloys will need to be precipitation strengthened by the gamma-prime phase to achieve the required strength of approximately 100,000 hours creep-rupture life at 750°C and 100MPa. As part of the Framework 7 project "MACPLUS" the nickel alloy HAYNES®282® was chosen for manufacture of a rotor forging mock-up. This alloy was selected as it offers an optimum combination of attributes essential to design including high-temperature strength, weldability, and formability. A forging sequence was designed to fulfil the requirements for production of a full-scale welded rotor forging in HAYNES®282® and modelled using finite element software QForm. This allowed the temperatures, strains, strain rates and press loads to be determined. This sequence was then adapted and remodelled for production of a reduced scale mock-up such that similar strains and therefore a representative microstructure of the full-scale forging could be achieved. A mock-up rotor forging in HAYNES®282® was completed using the 5000 ton press at Cogne Acciai Speciali.

Keywords: Haynes 282, modelling, forging, strain, recrystallization, heat treatment

1. Introduction

The development of improved martensitic 9-12%Cr steels for rotor applications with operating temperatures up to 620 °C was one of the main activities of the joint research projects COST (501, 522 and 536). Trial melt investigations during the COST 522 project determined the best candidate to be a 9%CrMoCoVNbNB steel (coded FB2 for forged steel). This steel grade has since shown high long-term high temperature creep strength along with reasonable ease of fabrication for large forgings. This material is now being established in new supercritical steam turbine projects in Europe and the U.S with operating temperatures up to 620 °C [1].

For further development of fossil power plants there is the requirement for increased thermal efficiency and lowering of CO_2 emissions. In order to achieve these objectives, advanced ultra-supercritical (A-USC) power plants operating with steam temperatures up to 760 °C are being researched. Research programs in both Europe and the U.S (such as the AD700 project and Advanced Materials for Ultra Supercritical Boiler Systems project) have already been carried out to improve thermal efficiency through utilisation of materials with higher temperature capabilities [2-4]. More recent European projects such as MACPLUS are further developing this research.

Higher operating temperatures mean a shift to materials of higher strength than the FB2 steel. Nickel base superalloys are required in A-USC conditions due to the high temperature creep strength requirements. The creep potential of the nickel base alloys must be at least 100 MPa

rupture strength at 750 °C for 100,000 hours. It is also desirable to have high yield strength, fracture toughness and thermal conductivity, but low coefficient of thermal expansion. Additionally, from a manufacturing perspective, the alloys need to be produced in forgings ~ Ø1000 mm and up to 12 tons. Alloys would also require welding in section thicknesses up to 200 mm.

2. Alloy Selection

From the previous research programs a number of nickel-base alloys have emerged as candidates for steam turbine applications. Figure 1 shows the average creep-rupture strength of various alloys [5]. Alloys such as Inconel 740 and Haynes 282 stand out as candidates for the hottest regions of the turbine. Inconel 740 offers a creep strength higher than the solid-solution strengthened alloys but the relatively recent development of Haynes 282 provides improved strength at higher temperatures [6, 7]. The solid solution strengthened alloys such as Inconel 617 and Haynes 230 are more suitable for use at intermediate temperatures up to about 720 °C

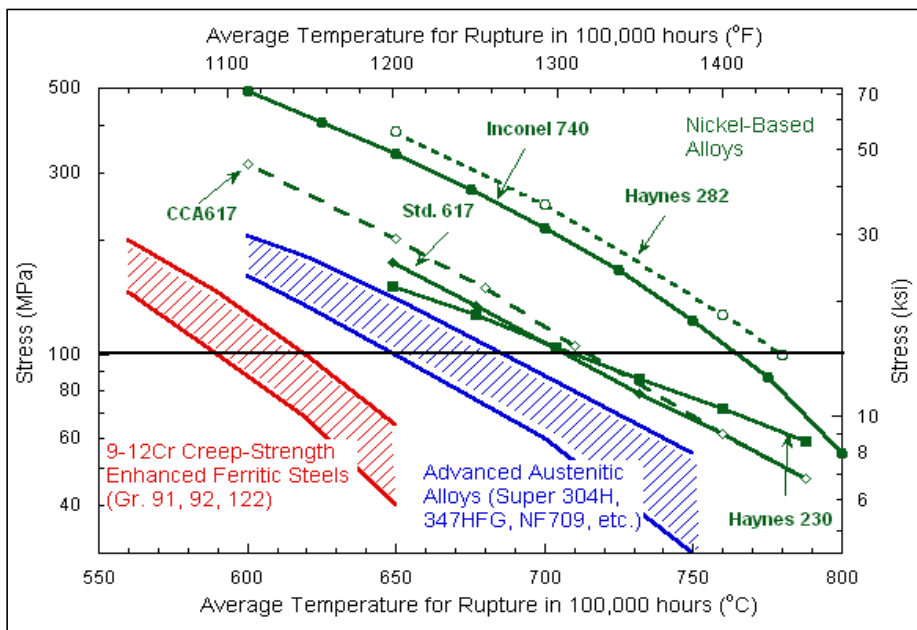*Figure 1: Average 100,000 hour stress rupture as a function of temperature for candidate alloys [5]*

For the European project MACPLUS, Haynes 282 was selected as the prime candidate for a precipitation-strengthened nickel-base alloy because it was judged to represent the best combination of high-temperature strength, weldability and formability.

3. Design of Full Scale Rotor Forging Sequence

To carry out forging modelling of the Haynes 282 alloy, firstly, the geometry of the full-scale rotor forging was identified by Alstom. A HP shaft with a ruling section of approximately 850 mm was chosen. From this geometry a forging sequence was developed to provide consolidation and closure of porosity of the material with adequate reduction in each sequence to provide sufficient strain to the core of the material to allow recrystallization.
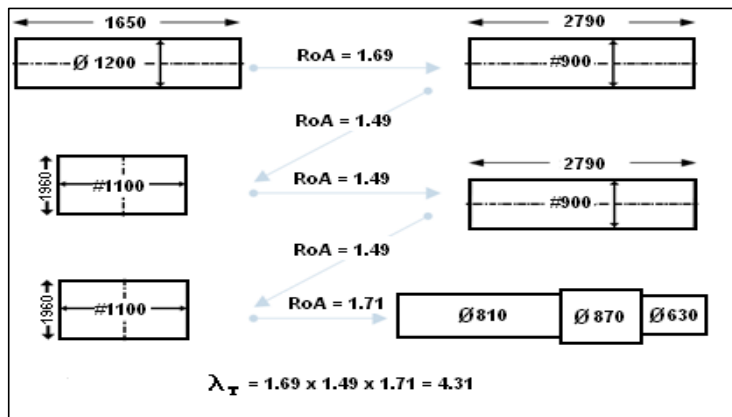
Figure 2: Forging procedure for full-scale HP rotor

The designed forging sequence is shown above in figure 2. The sequence is developed from standard forging practices for rotor forgings. The sequence starts with an electroslag remelted (ESR) ingot 1200 mm in diameter and drawn to an octagon of 900 mm width. The workpiece is reheated and upset forged to a diameter of 1100 mm followed by drawing back to an octagon of 900 mm width. The piece is finally reheated and upset forged to a diameter of 1100 mm followed by forging to its final shape with a maximum diameter of 900 mm. The application of reheats in this sequence assumes ideal conditions whereby the flow stress of the material is sufficient to allow reduction to be met in one heat. By modelling this sequence we are able to determine the true number of heats required for each reduction based on flow stress, heat loss during forging and the calculated load.

4. Modelling Forging of Full Scale Rotor

In order to accurately model the rotor forging process of the Haynes alloy, it was necessary to determine the stress required as a function of temperature, strain and strain rate. Isothermal hot compression tests using a Gleeble test machine were carried out by Centro Sviluppo Materiali (CSM) to characterize the thermo-mechanical behaviour of the candidate alloys. Tests were carried out at temperatures of 900 °C, 1050 °C and 1200 °C and at strain rates of 0.01 s^{-1}, 0.1 s^{-1} and 1.0 s^{-1}. Each test was performed up to strains of 0.9. Flow stress data were also provided by Haynes for temperatures 900 °C, 950 °C, 1000 °C 1050 °C, 1100 °C, 1150 °C and 1200 °C and at strain rates of 0.1s^{-1}, 1.0s^{-1} and 10s^{-1}. The data developed at CSM were found to be in good agreement with data provided by Haynes. The generated data were input into commercial software QForm for modelling of the proposed forging sequence.

Other important parameters required to model the sequence included heat transfer coefficient to tools, heat transfer to air, emissivity and friction. The heat loss from the workpiece to the die causes a decrease in the workpiece temperature and as such an increase in flow stress which in turn increases the press load required to perform the forging. The friction between the dies and the workpiece influences the flow of material within the deformation zone. The values for heat transfer to tools and friction were taken from literature [8]. The values for emissivity and heat transfer to air were taken from the QForm database.

Figure 3 shows the complete simulated forging sequence. It can be seen that as compared to the proposed sequence there are additional intermediate reductions with reheats required to meet the total deformation. The introduction of additional reheats was to account for surface temperatures dropping below the recommended value. The minimum forging temperature is defined by the formation of gamma prime. It was therefore considered necessary to perform a reheat when surface temperatures dropped below the γ'solvus. In all cases press loads did not exceed 90 MN.
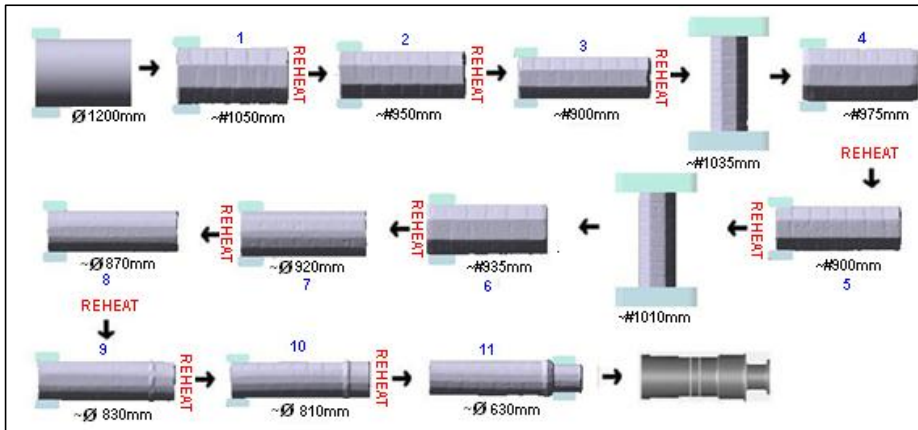
Figure 3: Complete modelled sequence for full-scale rotor forging

Figure 4 shows the accumulated strain after completion of each of the drawing operations in the forging sequence. It can be seen that the strain distribution varies in each operation due to the applied level of deformation. In the first operation the part is deformed from a cylinder to an octagon with a reduction ratio of approximately 1.22 and although the second drawing operation has a similar reduction ratio, the accumulated strain at the centre is greater in the second operation. This increase in achieved strain is due to the part being already formed into an octagon which allows for better penetration to the centre with flat tools than forging from a round section where most of the initial deformation is in forming flat surfaces. The second drawing operation shows the greatest amount of accumulated strain due to having the greatest amount of reduction in the process (1.24). The fifth and sixth drawing operations show a similar level of strain in the core but with lower deformation ratios (1.17), this is because the starting section size is smaller allowing improved penetration to the core in these cases. It can be seen in the operations where drawing has followed an upset that the end faces show low levels of strain due to a "barrelling" effect. During upsetting the material in the centre can deform more easily than at the interface with the tools as friction forces combined with faster cooling near the die surfaces cause material in this region to resist deformation. The

subsequent geometry for drawing therefore varies with a larger cross-section in the middle than at the end-faces and as such there is reduced deformation near the ends. Operations 7-10 show similar levels of achieved strain with the part now going from octagon to round (16 sided).
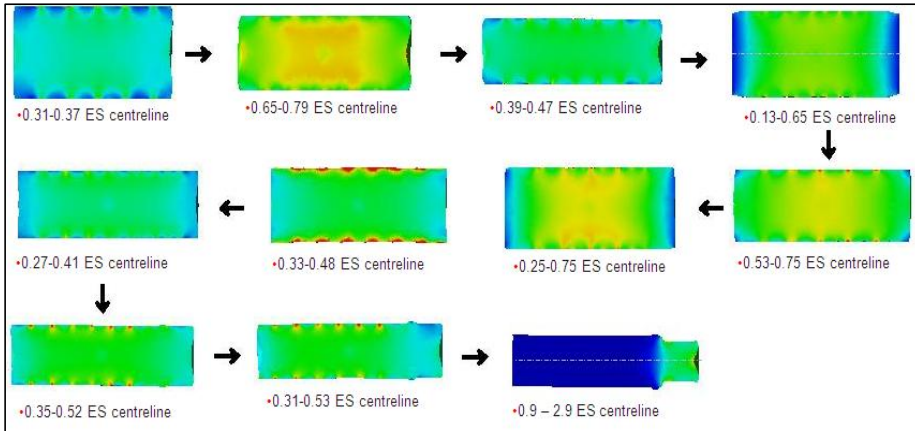
Figure 4: Accumulated strain for each drawing step of the modelled forging sequence

Analysis of this initial simulation of the forging sequence for the full-scale rotor showed that the procedure could be amended with modification of the geometries to be achieved and therefore the overall reduction ratio. Figure 5 shows the new forging sequence with fewer intermediate operations and as such fewer reheats. In this new procedure the maximum bite depth was increased to provide improved strain for recrystallization and heats were introduced after upsetting. Overall, it can be seen that the number of reheats can be reduced from 10 to 8 but the overall reduction ratio is decreased to 3.53. Operations seven and onwards were performed at a lower forging temperature to prevent grain growth.
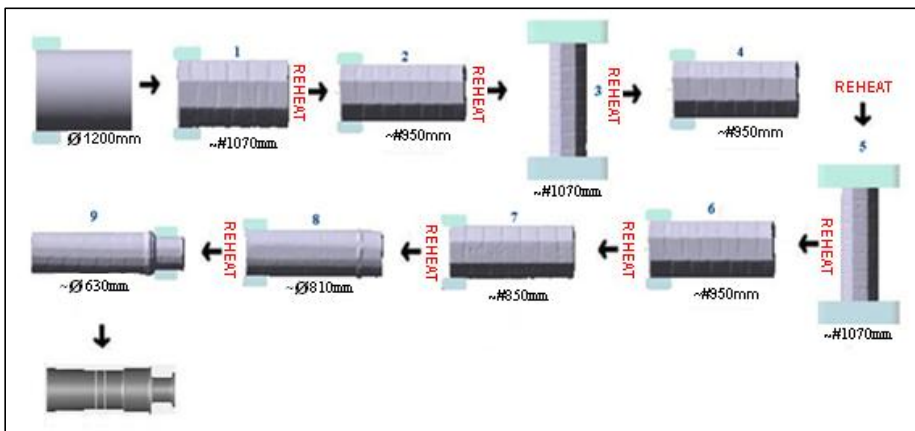
Figure 5: Adapted full scale forging procedure using larger bites and fewer reheats

Figure 6 shows the strains developed in drawing operations 1, 2, 4, 6 and 7 of the new process. It can be seen that the strain in the first operation is improved by going to larger bites. The strain achieved in operation 2 is similar to that achieved previously. The strain reached in operation 4 after upsetting is similar to that in operation 5 of the previous process but without the requirement of an additional heat after upsetting. Due to the increased reduction after upsetting the strain at the end faces is also improved. Operation 7 which was performed at the lower forging temperature shows an accumulated strain of 0.85 which is sufficient for recrystallization. This is much more improved than in the previous simulation due to the removal of intermediate reheats, applying larger bites and therefore having a greater amount of deformation in one heat. The grain size evolution was also calculated during this operation. Material parameters for the Johnson-Mehl-Avrami-Kolmogorov (JMAK) model [9] (provided by Haynes) were implemented in QForm. The grain size at the start of this operation was taken to be 300 μm (~ASTM 0) across the part and after running this operation the grain size at the core was predicted to be around 120-130 μm (ASTM 2.5 - 3) with a maximum of 300 μm in low strain areas of the surface.
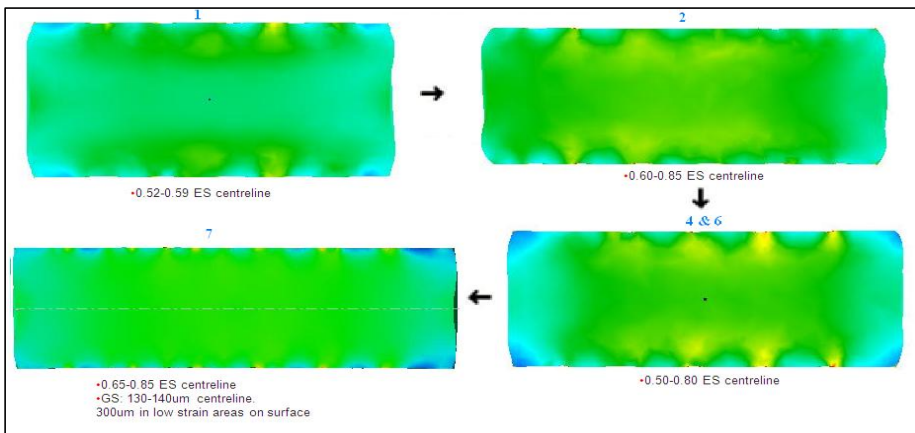
Figure 6: Accumulated strain for new forging procedure at drawing steps 1, 2, 4, 6 and 7

5. Design of Mock-up Rotor Forging Sequence

Haynes International provided an ESR ingot of 508 mm in diameter and 1000 mm in length to manufacture a reduced scale mock-up. The proposed forging sequence for the reduced scale mock-up is shown in figure 7 below. This procedure accounts for the deformation achieved in the full-scale simulation and therefore has reductions which aim to produce similar strain distributions as achieved for the full-scale part.
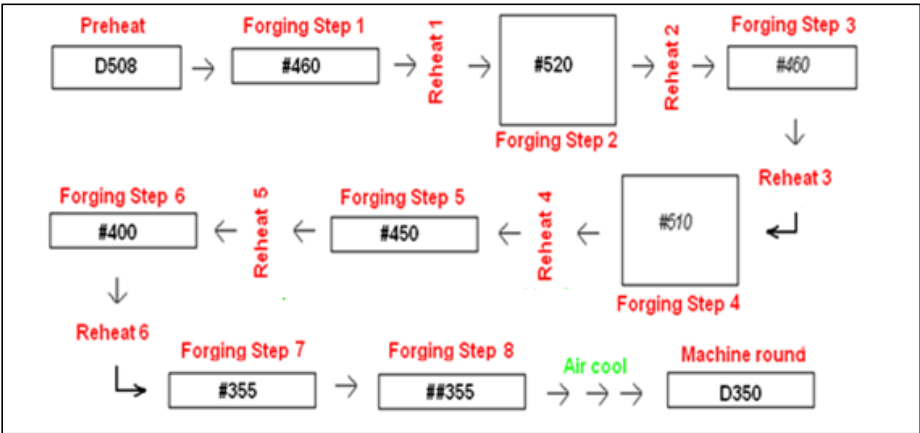
Figure 7: Mock-up forging sequence

6. Modelling Forging of Mock-up Rotor

Figure 8 shows the strains developed in the drawing operations of the mock-up forging. It can be seen that the strain in the first drawing operation is similar to that of operation 2 of the full size forging. The strain achieved in drawing operation 3 and 5 is higher than those achieved from drawing after upsetting of the full scale part (1.12 compare to 0.82). Although there is considerable difference in strain between these operations, above 0.8 of strain at the temperatures and strain rates achieved it is expected that the material will fully recrystallize. Steps 6 and 7 of the forging simulation show a good distribution of strain which is sufficient to give full recrystallization. The grain size was also calculated for these two operations and predict similar results to that of the full-scale forging with final grain sizes along the centre ranging from 120-130 μm (ASTM 2.5 -3) when assuming an initial grain size of 300 μm (~ASTM 0). Overall there was good correlation between the full-scale forging and the mock-up forging and as such manufacture of the mock-up to the developed procedure should produce a microstructure representative of the full-scale forging.
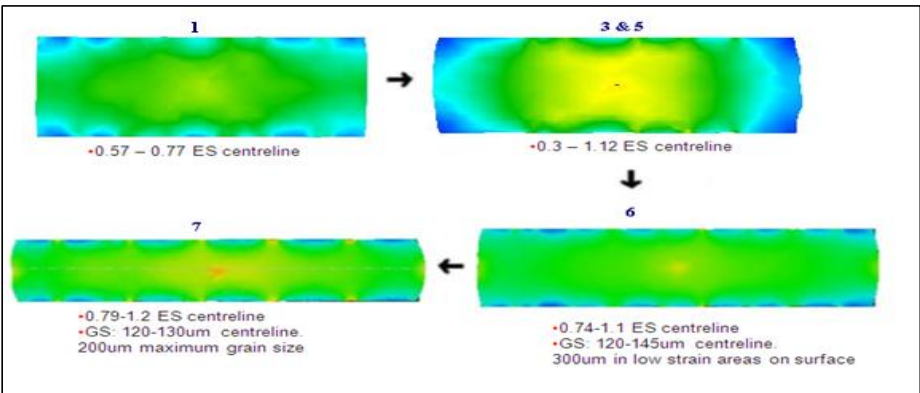
Figure 8: Accumulated strain for mock-up forging procedure at drawing steps 1, 2, 4, 6 and 7

7. Modelling of Heat Treatment

The cooling rates of the full-scale rotor and mock-up rotor were simulated with the larger rotor quenched in water and the smaller rotor cooled in air. It was found that the surface temperature of the larger rotor quenched in water reduces much more rapidly than the smaller rotor cooled in air as is expected. However, due to the smaller section size, the temperature at the centre of the smaller rotor cools at a similar rate to the centre of the water quenched full-scale rotor. Therefore it was decided - to obtain a microstructure at the centre of the mock-up representative for the full-scale rotor - that the part would be air cooled after solution treatment.

The full heat treatment cycle was modelled to calculate the times to reach temperature, soak and cool back to room temperature. Figure 6 shows the simulated surface and centre heating and cooling cycle of the mock-up for each heat treatment condition. The total heat treatment cycle takes approximately 115 hours.
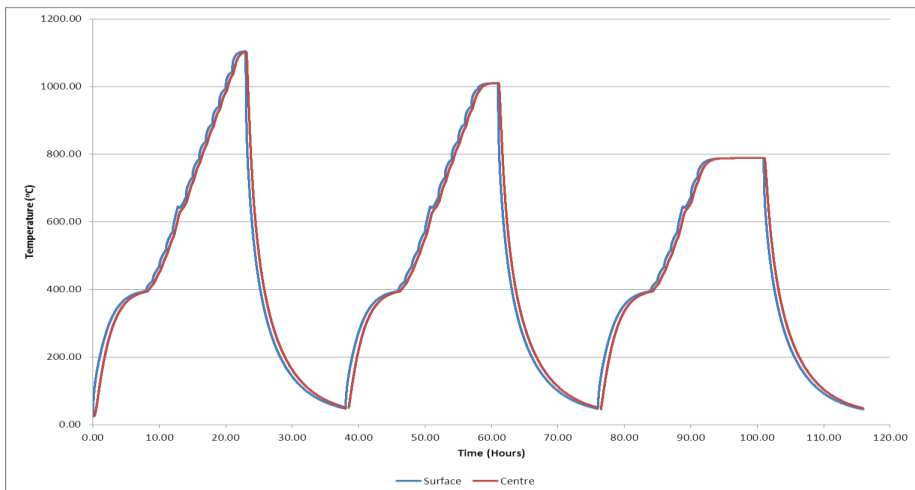
Figure 6: Modelled heat treatment cycle

8. Mock-up Manufacture

A 508 mm diameter ingot was supplied by Haynes and was forged by Cogne Acciai Speciali with guidance from Alstom, CSM and Haynes specialists. The part took 55 hours to preheat with a 16 hour forging/heating cycle. The mock- up was successfully forged but some surface cracking developed during steps of the forging sequence. Cracking was attributed to 3 possible causes:

• Reheat time after first upset was insufficient for complete soaking at temperature of the part. This was due to the time from forge back to furnace being longer than anticipated. Subsequent soak times were extended by a minimum of 30 minutes to compensate.
• Tool temperatures were lower than in previous steps. As a consequence, tool heating times were extended.

303

- Rotation of the part was changed. One end was forged to size and shape before passing to the other manipulator to forge the opposite end. Subsequent steps were performed with rotation at the end of each pass.

Although lateral cracks were formed on the surface during the drawing operations, it was deemed unnecessary to stop the forging as these cracks were evaluated to be shallow and therefore did not appear to extend deep under the surface. These cracks healed and closed up on subsequent forging operations. In addition to the cracking, a "burst" formed at one end face of the forging, this is likely to be due to hotter internal sections of the forging flowing around the cooler surfaces and the higher strain level achieved at the unconstrained end of the forging. In future it will be beneficial to heat the dies to a higher temperature to reduce heat loss at the surface and carefully monitor surface temperature to prevent surface cracking. Nevertheless, such surface defects should be outside the machining envelope of the final part.
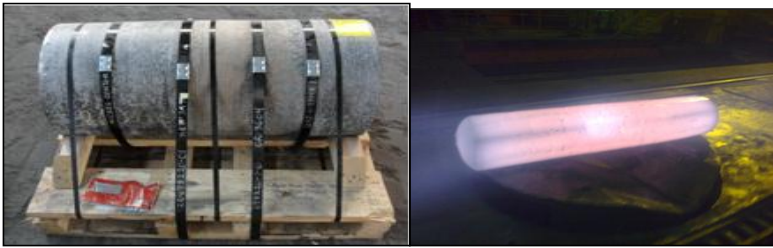
Figure 7: Starting ingot and finished forging

Completion of the forging will involve the following steps:

- Cropping the ends and performing microstructural analysis in the as-forged condition to determine grain size and microstructure.
- Performing heat treatment in line with model prediction (solution annealing and ageing treatments).
- Perform ultrasonic testing to determine attenuation (dB/m) and minimum detectable defect size (MDDS).
- Material from the forging will be taken to demonstrate mechanical properties and welding procedures.

9. Conclusions

In order to design a new generation of steam turbines with operating temperatures up to 760 °C, a mock-up rotor forging was manufactured in Haynes 282.

The mock-up forging procedure was developed by modelling the necessary forging steps. Modelling was performed using commercially available software QForm. The forging procedure was produced to be represenatrtive of that of the full scale forging by developing similar levels of strain for each step. Simulations for both full-scale and the reduced scale mock-up predict a grain size of ASTM 2.5-3 on completion.

The mock-up was succesfully manufactured in line with the proposed procedure with only minor surface defects emerging during forging. The part is now to be heat treated and a section cut to perform the necessary mechanical tests to demonstrate the suitability for use under 760 °C service conditions

10. Acknowledgements

11. References

[1] Vanstone, R., Chilton, I., and Jaworski, P., "Manufacturing Experience in an Advanced 9%CrMoCoVnbNB Alloy for Ultra-Supercritical Steam Turbine Rotor Forgings and Castings," Journal of Engineering for Gas Turbines and Power, Vol. 135 (6), pp. 062101, (2013).
[2] Rudolph, B., Kjær, S., and Bugge, J., "Development of a PF Fired High Efficiency Power Plant (AD700)," Proceedings of the Riso International Energy Conference, pp. 69-80, (2007).
[3] Viswanathan, R., Henry, J. F., Tanzosh, J., Stanko, G., Shingledecker, J., Vitalis, B., and Purgent, R., "US Program on Materials Technology for Ultra-Supercritical Coal Power Plants," Journal of Materials Engineering and Performance, Vo. 14 (3), pp. 281-292, (2005).
[4] Marion, J., Frappart, C., Kluger, F., Sell, M., Skea, A., ' Vanstone, R., "Advanced Ultra-Supercritical Steam Power Plants," Proceedings of the Orlando POWER-GEN International Conference, pp. 1-15, (2013)
[5] Shingledecker, J. P.,"Metallurgical Effects on Long-Term Creep-Rupture in a New Nickel-Based Alloy," Tennessee Research and Creative Exchange, Doctoral Dissertation, (2012).
[6] Pike, L. M., "Development of Fabricable Gamma-Prime Strengthened Superalloy," Proceedings of the 11th International Symposium on Superalloys, pp. 191-200, (2008).
[7] Klarstrom, D. L., Pike, L. M., and Ishwar, V. R., "Nickel-Base Alloy Solutions for Ultrasupercritical Steam Power Plants," Procedia Engineering 55, pp. 221-225, (2013)
[8] Boyko, C., Henein, H., and Dax, F. R., "Modelling of the Open-Die and Radial Forging Processes for Alloy 718," Superalloys 718, 625 and Various Derivatives, The Minerals, Metals and Materials Society, pp. 107-124, (1991).
[9] Wang, J., Chen, J., Zhao, Z., and Ruan, X. Y., "Modeling of Microstructural Evolution in Microalloyed Steel During Hot Forging Process." Acta Metallurgica Sinica,Vol. 19 (4), pp. 279-286, (2006).

STUDY ON PRECIPITATE STABILITY IN 9-12%CR STEELS

Hilmar K. Danielsen

Technical University of Denmark, Department of Wind Energy, Materials Science and Characterisation (Frederiksborgvej 399 228B, 4000 Roskilde, Denmark – hkda@dtu.dk)

Abstract

The long term creep strength of 9-12%Cr steels relies on precipitation strengthening. Especially the finely distributed MX precipitates, (V,Nb)N, are known for their high strengthening effect. However the MX precipitates are not thermodynamically stable, and will eventually be transformed into Z-phase, Cr(V,Nb)N, which will not be as finely distributed, and thus a loss in creep strength will occur. This transformation process can take longer than the lifetime of the power plant they are intended to be used in, but high Cr levels will accelerate the process significantly. A quantification of the replacement rate with varying temperature and Cr content is carried out in this paper.

By replacing the V content of the steels with Nb or Ta it was possible to get a very quick transformation rate of MX into Z-phase. This ensured a very fine distribution of Z-phase precipitates and thus high initial creep strength. However the coarsening rate of the Z-phase was found to be significantly higher than that of MX, and is thus not suitable for long term creep strength at high temperatures.

W is normally added to modern 9-12%Cr steel to increase creep strength. This causes the precipitation of relative large granular Fe_2W Laves phase precipitates. Experiments show that is possible to get much finer precipitation of elongated Laves phase by adding Cu to the steel. With time the elongated Laves phases become granular, but not as large as in steels without Cu. The addition of Cu has also been shown to increase initial impact energy significantly.

Keywords: 9-12%Cr steels, Z-phase, Laves phase

1. Background

9%Cr martensitic steels are extensively used in fossil fired steam power plants because of their high creep and fatigue strength, oxidation resistance and moderate cost. The long term creep strength of these steels is dependent upon precipitation strengthening. These precipitates have to be stable at operating temperatures up to 600°C for 20 to 30 years. In order to increase the efficiency of the power plants, it has been attempted to raise the operating temperature up to 650°C. This requires an increased Cr content to 11-12% for better oxidation resistance and more stable precipitates. However, the high Cr content has created microstructure instabilities, causing the creep strength to drop drastically during long term service. Thus studying the long term precipitate stability at high temperatures is of crucial importance.

2. Experimental

X-ray powder diffraction was applied using a Bruker D8 Advance powder diffractometer equipped with Cu-radiation. In order to avoid interference from matrix reflections, the precipitates were extracted from the bulk by electrolysis in an acidic solution of 5% HCl in 95% ethanol, dissolving the matrix while gathering the precipitates by sedimentation. Some of the very small MX precipitates may not have been fully recovered by the sedimentation process.

Transmission electron microscopy was applied on carbon extraction replica and thinfoils in bright field and in High Angle Annular Dark Field (HAADF) mode. A FEI Titan instrument equipped with a spherical aberration corrector on the probe forming lenses was used in addition to a JEOL 3000F FEGTEM.

	Cr	C	V	Nb	Ta	N	W	Mo	Co	Ni	Mn	Si	Cu	B
12CrVNbN	11.85	0.005	0.183	0.76	-	0.061	-	-	-	1.29	0.32	0.40	-	-
9CrVNbN	9.11	0.004	0.207	0.80	-	0.059	-	-	-	1.27	0.34	0.41	-	-
12CrTaN	11.79	0.005	-	-	0.39	0.033	2.90	-	7.30	0.50	0.48	0.30	-	0.004
12CrTaNCu	11.96	0.005	-	-	0.36	0.058	2.46	0.21	6.49	1.03	0.47	0.29	1.00	0.007
12CrTaNCuC	12.1	0.06	-	-	0.36	0.049	2.47	-	3.50	0.19	0.21	0.31	1.95	0.006
12CrNbN	11.6	0.003	-	0.26	-	0.04	2.42	0.20	4.82	0.46	0.47	0.29	0.92	0.003
12CrNbNCu	11.64	0.005	-	0.26	-	0.036	2.82	-	5.4	1.47	0.50	0.30	-	0.004

Table 1: Compositions of the alloys used in this work in wt%, balance Fe.

3. Results

3.1 Precipitation rate of Z-phase

The primary beneficial precipitates of the 9-12%Cr steels are the MX type (V,Nb)N particles, which precipitate as finely distributed small particles during tempering and are considered to have a low coarsening rate at high temperatures. However they are not thermodynamically stable, and they will slowly be replaced by a similar but more Cr rich nitride, the Z-phase, Cr(V,Nb)N. As the slow nucleation of the Z-phase causes them to grow to large sizes, consuming the finely distributed MX in the process, the creep strength will drop dramatically. This drop in strength is particularly common in 11-12%Cr steels compared to 9%Cr steels [1].

Two experimental alloys, 12CrVNbN and 9CrVNbN, were designed in order to follow the Z- phase precipitation in these steels [2], and they are identical except for the Cr content. They do not contain any C, W or Mo as not to precipitate non-nitride particles, such as carbides or Laves phase, which could interfere in XRD measurements. After short term annealing, both alloys contain only M_2X and MX nitrides, see figure 1. Two separate populations of MX nitrides could be identified, (V,Nb)N and (Nb,V)N, which have lattice parameters in between those of VN and NbN.

Figure 1 shows XRD powder diffraction patterns of thermal aging of the 12CrVNbN alloy at the left side and of the 9CrVNbN alloy at right side. Three different temperatures and several different times of exposure were used. For graphical representation, the spectra of 12CrVNbN use the {111} peak of Cr_2N as reference points (except for 600°C/30,000h), and spectra of 9CrVNbN use the {200} (V,Nb)N peak as reference points. These peaks were used as they were judged to have the least change throughout the time of exposure, although it must be remembered that all peak sizes are relative. The spectra from the two alloys show the 12CrVNbN alloy to have a much larger amount of Cr_2N. The lattice parameters of the MX are slightly higher for the 12CrVNbN alloy. This is most likely because the Cr_2N contains some V, making the MX more Nb rich relatively to those in the 9CrVNbN alloy.
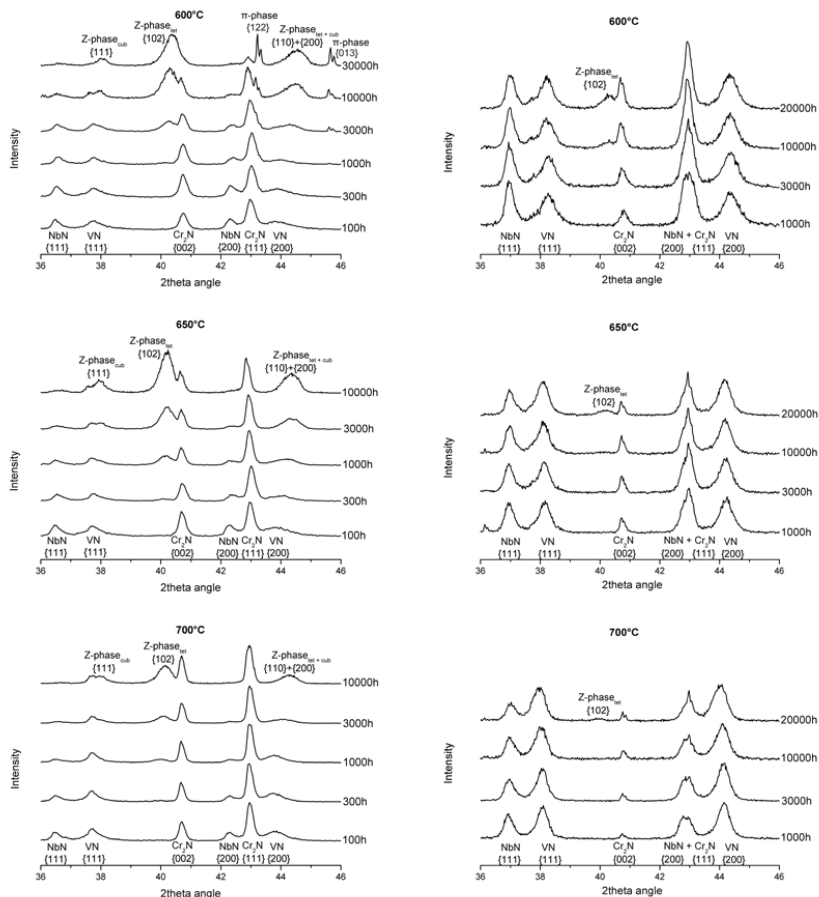
Figure 1: XRD spectra of nitride evolution in 12CrVNbN (left) and 9CrVNbN (right). [2]

The main feature of the spectra is that with time Z-phase peaks replace the MX peaks. The main Z-phase peak (tetragonal) at 2θ angle $= 40$ is visible at all temperatures at the longest exposure time. As the V-rich MX transform into Z-phase, a gradual shift in (V,Nb)N peak position towards a lower lattice parameter corresponding to the cubic Z-phase [3] takes place. This is especially visible in 12CrVNbN, as the Z-phase precipitation is progressing faster. At 600°C in the 12CrVNbN, the Cr_2N peaks are replaced with time by new peaks corresponding to an A13 crystal structure (same as β-manganese) which is believed to belong to the π-nitride, a chromium and iron rich nitride usually found in austenitic steels [4].

A rietveld refinement was done in order quantify how much of the MX was transformed into Z-phase. This data was plotted into TTP curves for both alloys in order to quantify the Z-phase precipitation speed. Comparing 12CrVNbN and 9CrVNbN shows the Z-phase to precipitate considerably faster in the 12%Cr alloy at all temperatures, see figure 2. The Z-phase precipitation is fastest at 650°C for the 12CrVNbN while in 9CrVNbN it is

fastest at 600°C. Using a thermodynamic model of the Z-phase [5], the Z-phase is predicted to be stable up to higher temperatures for higher Cr contents. Thus an increase in Cr is expected to raise the TTP curve to higher temperatures. As no data was available from temperatures lower than 600°C, the 9CrVNbN TTP curve in figure 2 is based on an estimate that the precipitation will be slower at 550°C. These results might indicate that the Z-phase content in 9%Cr steels could be underestimated if accelerated tests at 650°C are used. The Cr content in the matrix of the model alloys is higher compared to commercial alloys, as they do not form $Cr_{23}C_6$ because of the low C content. A commercial alloy containing 0.1%C will effectively have a 1% lower Cr content in the matrix. Thus the data in figure 2 would correspond to 13%Cr and 10%Cr commercial alloy containing 0.1%C.
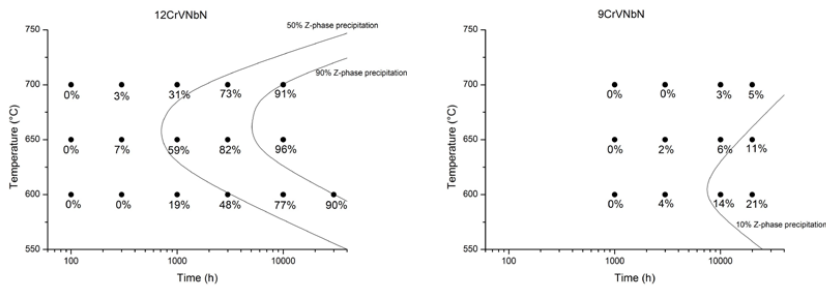
Figure 2: TTP curves of the amount of MX transformed into Z-phase. [2]

3.2. Z-phase strengthened steels

The obtained TTP curves in figure 2 show the Z-phase precipitation is impossible to avoid using standard MX strengthening, although it might be delayed sufficiently if a low Cr content is used. When using a Cr content of 11-12%, which is needed for oxidation resistance at 650°C, the Z-phase will precipitate and remove the crucial strengthening effect of the MX precipitates. Thus it has not been possible to produce martensitic steels with both long term creep strength based on MX and oxidation resistance based on Cr at 650°C.
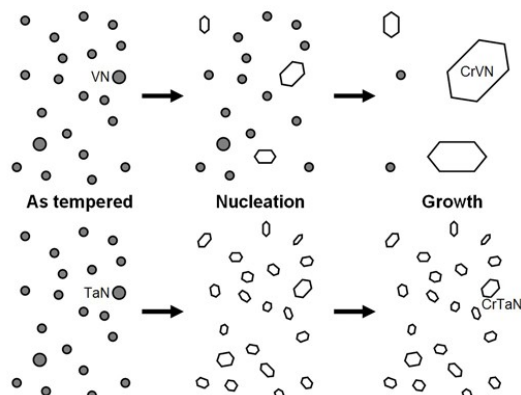
Figure 3: An illustration of a slow V-based Z-phase precipitation (top) and a fast Ta-based Z-phase precipitation (bottom). [6]

A new concept which aimed at using Z-phase as a strengthening agent instead of MX was tested in this work [6]. In normal V/Nb-containing steels the precipitation rate of Z-phase is relatively slow, usually taking years. Thus the few nucleated Z-phases have plenty of time to consume nearby MX precipitates during growth, leading to a coarse distribution of large Z-phases. If a very fast precipitation rate of Z-phase could be obtained, lots of Z-phase particles would nucleate, and the fine MX precipitates would quickly be replaced by fine Z-phase precipitates, avoiding the growth process altogether, see figure 3. The finely distributed Z-phase would act as a strengthening agent as seen in austenitic steels, where they are thermally stable with a low coarsening rate. This could be combined with a high Cr content for oxidation resistance, in fact a high Cr content would be necessary in order to obtain a fast Z-phase precipitation.
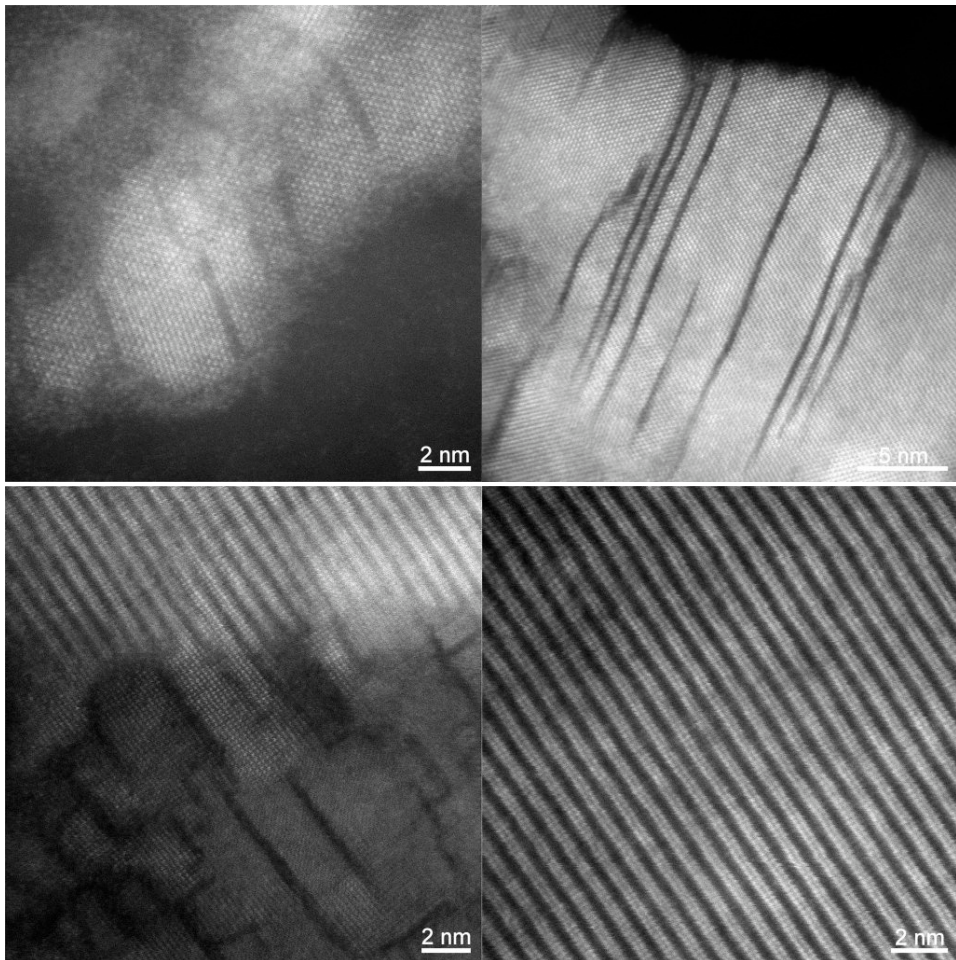
Figure 4: Different stages during transformation of TaN into CrTaN, from the beginning of formation of Cr layers inside the MX to a fully transformed Z-phase. [7]

In order to obtain a very fast Z-phase precipitation, Ta or Nb was used instead of V. The results below focus primarily on Ta-containing steels, as they precipitated Z-phase faster and had much better creep strength. The C content was kept very low, as C would stabilize the MX type Ta(N,C) carbonitrides; the Z-phase is believed to be a more pure nitride [8]. In these steels the TaN MX were quickly replaced by CrTaN Z-phases, in the very low C version this happened already during tempering. When investigating the nucleation of Z-phase in these steels using atomic resolution microscopy, it was seen that the TaN were transformed crystallographically and compositionally into CrTaN by Cr diffusion from the matrix into the MX. Figure 4 shows the transformation, where Ta atoms are bright and Cr atoms are dark, the N atoms are not visible. It can be seen how Cr atoms enter the TaN cubic crystal structure as double layers. Eventually the MX is transformed into a regular AABBAABB type tetragonal crystal structure with alternating TaN double layers and Cr double layers. EDS measurements confirm areas containing dark layers are Cr rich. These results show that a transformation from MX to Z-phase takes place, which has also been suspected in more conventional V/Nb steels [9-10].
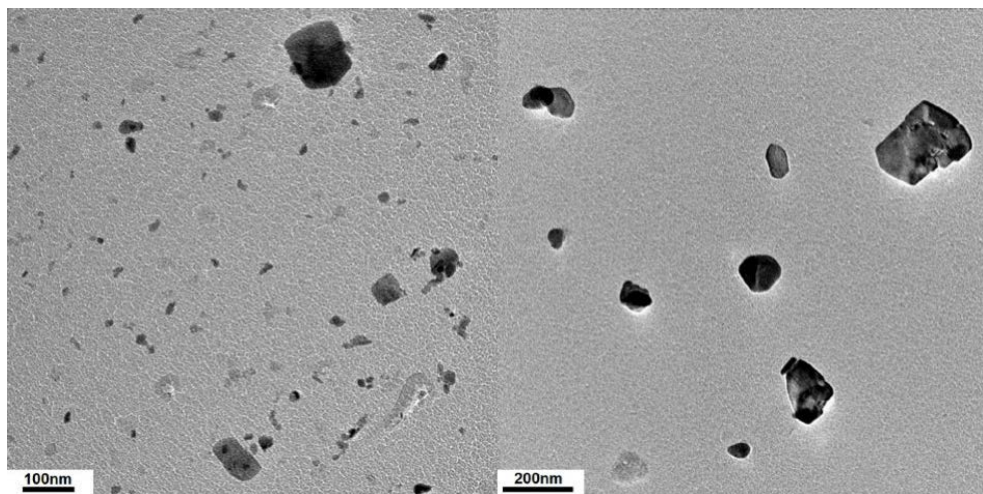
Figure 5: CrTaN precipitates from the 12CrTaN alloy, exposed at 650°C for 1000h (left) and 38000h (right). It shows the Z-phase to have a relative high coarsening rate compared to MX type precipitates in 9-12%Cr steels.

In the 12CrTaN and 12CrTaNCu alloys the Z-phases transform already during tempering and are present as very small finely distributed precipitates which provide a higher initial creep strength than commercial grades such as P92. In 12CrTaNCuC the transformation is slower, taking hundreds of hours at 650°C. Unfortunately the coarsening rate of both CrNbN and CrTaN type Z-phases were found to be higher than (V,Nb)N type MX at temperatures of 600-650°C, see figure 5. Thus the stability of Z-phase in austenitic steels could not be transferred to martensitic steels and the long term creep strength of the Z-phase strengthened steels cannot compare to that of P92 at these temperatures.

Investigating the CrTaN Z-phase in thinfoils, an interface layer a few nanometers thick between the Z-phase nitrides and the steel matrix could be observed [11]. Upon closer investigations this interface layer was shown to be amorphous, that is the crystalline nature of the nitride stopped shortly before reaching the steel matrix, see figure 6. Darkfield investigations of SAED and FFT of atomic resolution imaging confirmed that the interface between the nitride and matrix was amorphous. Since the precipitate particles were completely embedded inside the steel matrix, this was not an influence of sample preparation. The steel matrix in figure 6 is set not to be in focus on purpose, as the steel crystal structure is present below and above the nitride. Carbon extraction replicas showed the amorphous shell had the same chemical composition as the rest of the Z-phase. In carbon extraction replicas the amorphous shell crystallized during beam exposure in the TEM, see figure 6, adapting the same crystal structure as the interior crystalline nitride.
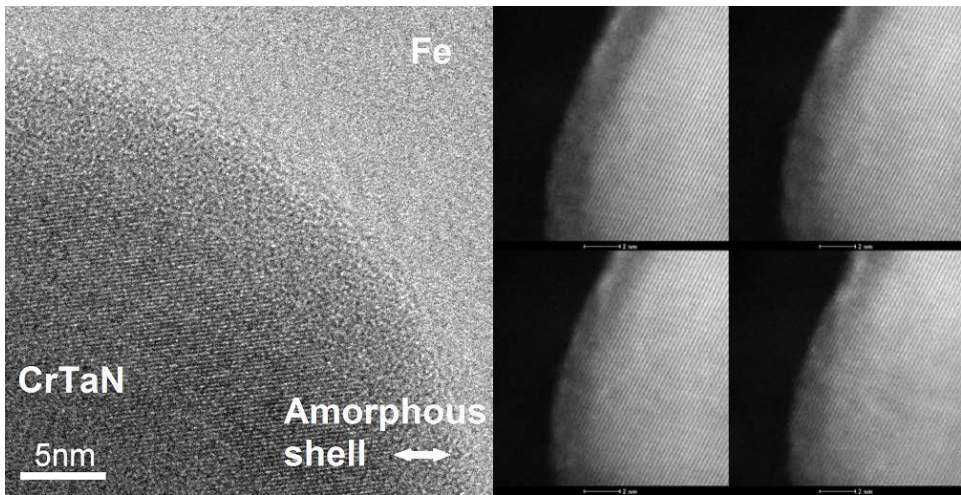
Figure 6: The amorphous interface between steel matrix (not in focus) and CrTaN Z-phase (in focus). Crystallisation of CrNbN interface in a carbon extraction replica. [11]

These amorphous shells are of similar thickness as the intergranular glassy films (IGF) often observed in sintered materials [12]. The crystallisation of the amorphous shell where the matrix has been removed indicates that the amorphous shell is purely an interface effect: It is only present to separate the crystalline nitride from the crystalline ferrite, indicating a very high interfacial energy. As the interfacial energy governs the coarsening rate, the appearance of the amorphous shell would explain why the Z-phase has such a high coarsening rate compared to the MX.

3.3 Morphology of Laves Phase

Different variations of the V-free steels where designed partly to investigate the morphology of Laves phase, $Fe_2(W,Mo)$. These intermetallic phases have previously been observed to appear with two different morphologies, most frequently with almost equiaxed granular shapes but sometimes with elongated needle shape [13]. The Laves phase is only observed in its elongated form in Cu-containing steels and is eventually replaced by granular Laves phase during exposure at 650°C [13]. These results were confirmed in this work when comparing alloys with and without Cu, primarily the 12CrNbN and 12CrNbNCu alloys.

In the Cu containing steels, the Laves phase precipitated primarily in its elongated morphology, although granular particles could also be observed, see figure 7. During exposure at 650°C of the Cu and containing alloys, the granular Laves phase was found to grow faster, the average particle becoming larger by volume compared to the elongated Laves phase. The elongated morphology should theoretically also be the optimal shape for increasing creep strength. After about 10.000h of exposure the elongated Laves phase had mostly been replaced by granular particles. Comparing alloys with and without Cu, the Laves phase size distribution was smaller in the Cu containing alloys, even after 10.000h/650°C where the Laves phase was granular. The alloys were not investigated at 600°C.
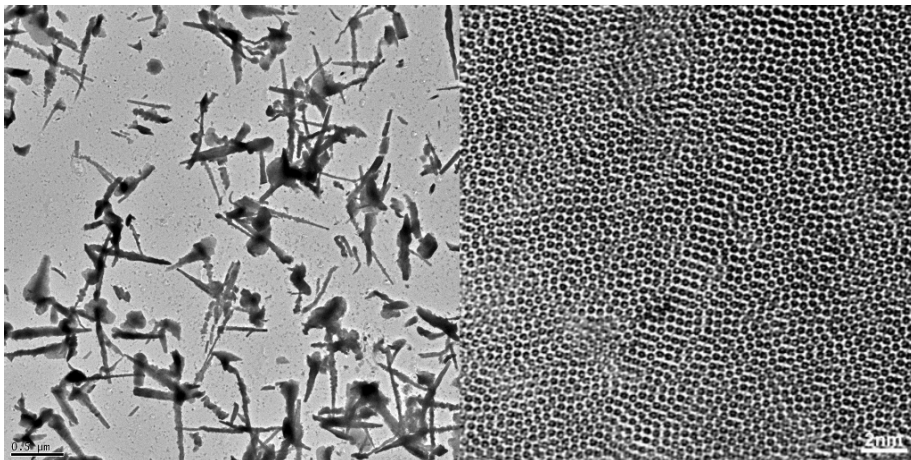
Figure 7: Elongated and granular Laves-phases in 12CrNbNCu after 24h at 650°C. The crystal structure of the Laves phase is highly disordered for both types.

Atomic resolution TEM investigations of the crystal structure of the Laves phase showed both morphologies to be very disordered after short term exposure, see figure 7. Using XRD measurements these results were confirmed. For short term exposure very broad peaks are present, but with time the peaks became sharper, indicating an ordering of the Laves phase crystal structure. The results for Cu and Cu-free alloys were almost identical, indicating granular and elongated Laves phases are crystallographically the same. The measured lattice parameter of the matrix for Cu and Cu-free alloys showed no difference. Thus the difference in morphology is not caused by a difference in crystal structure.

Specimens of 12CrTaN and 12CrTaNCu were sent to Chalmers University of Technology for atom probe investigations and t o Siemens Industrial Turbomachinery for mechanical testing. Mechanical testing showed a very marked difference in impact toughness, 3J for CrTaN and 46J for 12CrTaNCu. SEM investigations showed a high density of Laves phase at the prior austenite grain boundary after tempering in 12CrTaN, which is believed to be the cause of the low impact toughness [14]. The Laves phase distribution in 12CrTaNCu is much more homogenous. Atom probe investigations revealed that the Laves phase itself contained no Cu, nor had any Cu segregated at the Laves/matrix interface. The Cu precipitated as pure copper particles, 98%Cu, but participated in no other precipitates [14].

It is speculated that the Cu particles act as nucleation sites for Laves phase particles, and this causes the difference in morphology. In Cu-free alloys the Laves phase nucleates in the bcc ferrite matrix along grain boundaries or other defects. This nucleation will give the Laves phase its most stable orientation relationship with the matrix and a granular shape. In Cu-containing alloys the Laves phase nucleates at the fcc copper precipitates. This nucleation is easier for the Laves phase, and with small copper particles finely distributed in the microstructure it gives less nucleation along the grain boundaries. It is speculated that the good orientation between fcc copper precipitates and Laves phase does not translate well into the bcc ferrite matrix. Thus elongated Laves phases appear which try to minimize the high interface energy and misfit with the matrix. Ultimately the granular orientation relationship with the matrix is more stable, and the elongated Laves phases will re-orient themselves or be dissolved by coarsening.

4. Conclusions

Quantitative XRD measurements of model alloys show the precipitation speed of the Z-phase to be very dependent on the Cr content. It is not feasible to combine long term creep strength based upon MX nitrides and oxidation resistance based upon 11-12%Cr contents.

Z-phase was attempted to be used as a strengthening agent instead of MX. Atomic resolution imaging showed that MX can quickly transform itself into Z-phase already during tempering. The very fine distribution of Z-phase gave high initial creep strength. However the coarsening rate of Z-phase was higher than that of MX, and is thus not suitable for long term exposure at 600-650°C. A thin amorphous shell separated the Z-phase from the ferrite matrix, indication of a very high interfacial energy, which could explain the high coarsening rate.

Observation of Laves phase morphology showed elongated shapes dominated in alloys with Cu, instead of the normal granular shape. The elongated Laves phase was found to be smaller by volume and more homogenously distributed. With time the elongated Laves phase were replaced with granular ones at 650°C. It is speculated that the elongated Laves phase use copper precipitates as nucleation sites.

References

[1] Danielsen HK, Hald J, behaviour of Z-phase in 9-12%Cr steels *Energy Materials,* Vol. 1, pp. 49-57 (2006)

[2] Danielsen HK, Di Nunzio PE, Hald J, kinetics of Z-phase precipitation in 9 to 12 pct Cr steels, *Metallurgical Materials Transactions A,* Vol. 44A, pp. 2445-2452 (2013)

[3] Danielsen HK, Hald J, Grumsen FB, Somers MAJ, on the crystal structure of Z-phase Cr(V,Nb)N, *Metallurgical Materials Transactions A,* Vol. 37A, pp. 2633-2640 (2006)

[4] Kikuchi M, Sekita T, Wakita S, Tanaka R, formation and composition of pi-phase nitride in a high chromium-high nickel austenitic steel containing 0.4% nitrogen, *ISIJ* Vol. 67, pp. 1981-1989 (1981)

[5] Danielsen HK, Hald J, a thermodynamic model of the Z-phase Cr(V,Nb)N, *Computer Coupling of Phase Diagrams and Thermochemistry*, Vol. 31, pp. 505-514 (2007)

[6] Danielsen HK, Hald J, influence of the Z-phase on long-term creep stability of martensitic 9 to 12% Cr steels, *VGB PowerTech,* Vol. 5, pp. 68-73 (2009)

[7] Danielsen HK, Hald J, Somers MAJ, atomic resolution imaging of precipitate transformation from cubic TaN to tetragonal CrTaN, *Scripta Materialia,* Vol. 66, pp. 261-264 (2012)

[8] Karlsson L, Henjered A, Andren HO, Norden H, composition and crystallography of nitride precipitates in an austenitic stainless steel containing niobium and vanadium, *Materials Science and Technology,* Vol. 1, pp. 337-342 (1985)

[9] Danielsen HK, Hald J, on the nucleation and dissolution process of Z-phase Cr(V,Nb)N in martensitic 12%Cr steels, *Materials Science and Engineering A,* Vol. 505, pp.169-177 (2009)

[10] Cipolla L, Danielsen HK, Venditti D, Di Nunzio PE, Hald J, Somers MAJ, conversion of MX nitrides to Z-phase in a martensitic 12% Cr steel , *Acta Materialia,* Vol. 58, pp. 669-679 (2010)

[11] Danielsen HK, Kadkhodazadeh S, Grumsen FB, Somers MAJ, new amorphous interface for precipitate nitrides in steel, *Philosophical Magazine*, in press

[12] Luo J, stabilization of nano-scale quasi-liquid interfacial films in inorganic materials: a review and critical assessment, *Critical Reviews in Solid State and Materials Science,* Vol. 32, pp. 67-109 (2007)

[13] Ku BS, Yu J, effects of Cu addition on the creep rupture properties of a 12% Cr steel, *Scripta Materialia,* Vol. 45, pp. 205-211 (2001)

[14] Fang L, Andren HO, effect of copper addition on the toughness of new Z-phase strengthened 12% chromium steels, *Advances in Materials Technology for Fossil Power Plants, editors Gandy D, Shingledecker J,* pp. 1116-1126 (2014)

TURNING LAVES PHASE AND $M_{23}C_6$ INTO DESIRABLE PHASES IN NOVEL MARTENSITIC CREEP RESISTANT STEELS

Qi Lu[1], Wei Xu[2], Sybrand van der Zwaag[3]

Novel aerospace materials group, Delft University of Technology, Delft, The Netherlands
[1]q.lu@tudelft.nl; [2]w.xu@tudelft.nl; [3]SvanderZwaag@tudelft.nl

Abstract

Generally Laves phase and $M_{23}C_6$ are regarded as undesirable phases in corrosion resistant creep resistant steels due to their very high coarsening rates and the resulting depletion of beneficial alloying elements from the matrix. In this study a computational alloy design approach is presented to design martensitic steels strengthened by Laves phase and/or $M_{23}C_6$, for which the coarsening rates are tailored such that they are at least one order of magnitude lower than in existing alloys. Their volume fractions are optimized by tuning the chemical composition as well. The composition domain covering 10 alloying elements at realistic levels is searched by a genetic algorithm to explore the full potential of simultaneous maximization of the volume fraction and minimization of the coarsening rate of precipitates. The investigation of effects of alloying elements suggests that Co and W can dramatically reduce the coarsening rate of Laves and $M_{23}C_6$ and yield high volume fractions of precipitates, while Mo has no significant effect. The strengthening effects of Laves phase and $M_{23}C_6$ in the newly designed alloys are compared to existing counterparts, showing substantially higher precipitation strengthening contributions especially after a long service time.

Keywords: precipitation strengthening, Laves phase, $M_{23}C_6$, coarsening rate, genetic algorithm

1 Introduction

Martensitic creep resistant steels have been used widely in high temperature components in power plant applications. To increase the operation temperature so as to improve the efficiency, new high strength materials are necessary since existing martensitic steels are not stable enough at higher temperatures. Generally, alloy designers are inclined to add desirable features to the

alloy system and get rid of undesirable components. However, in practice some undesirable components cannot be eliminated fully. Laves phase and $M_{23}C_6$ phase are two such examples that commonly appear in creep resistant steels and generally are considered as detrimental phases due to their very high coarsening rates [1] and the resulting depletion of useful elements, such as Mo or Cr, from the matrix. One of the possible solutions is to remove these two phases by decreasing Mo and Cr levels. However, these two elements are crucial to the creep property, i.e., Mo increases the solid solution strengthening and stabilizes the microstructure, while a high amount of Cr is required to maintain good corrosion and oxidation resistances. A more attractive alternative is to tailor the stability of these two 'undesirable' phases to an acceptable level by adding specific alloying elements. The coarsening rate of $M_{23}C_6$ is known to be moderately decreased by adding B or Co [2-4]. Abe [5, 6] reported that the coarsening rate of Laves phase can be effectively reduced by replacing Mo with W. The morphology of Laves phases also changes from needle-shaped to spherical, which is more coherent and stable. In addition to the better stability of W-based Laves phase precipitates, increasing the W content also leads to a beneficial higher volume fraction of precipitates. As a result, some recent research now uses Laves phase as the main strengthening precipitate in the design of new creep resistant steels [7, 8]. A high W (6wt.%) ferritic creep resistant steel has been designed and displays an extraordinary creep strength [9, 10], attributed to the superior stability of Laves phase (Fe_2W) even after 10,000 hours of service.

Therefore, by adding alternative chemical elements, the properties of undesirable phase can be harnessed by turning them into desirable phases. However, the design of new alloys cannot be simply done by only changing the compositions of such elements, as it may change dramatically the thermodynamic and kinetic properties of the alloy, and may also yield other undesirable phases. Moreover, the full potential of the new design concept is almost impossible to be explored by the traditional trial and error method. To address these challenges, a computational design approach coupling thermodynamics and kinetics is developed in combination with genetic algorithm. The search space covering 10 alloying elements is explored to evaluate the full potential of Laves phase and $M_{23}C_6$ as strengthening precipitates.

2 Model description

As mentioned in the introduction, either Laves phase or $M_{23}C_6$ are selected to be optimised as the main strengthening particles in the new steels by tailoring their volume fractions and coarsening rates. Martensite is chosen as the (initial) microstructure of the matrix because of its good creep strength and its high resistance to thermal and creep fatigue during service in power plants [11]. Thus, the target microstructure is: 1) a fully martensitic matrix; 2) a high volume fraction of Laves phase or $M2_3C_6$ with a tuned low coarsening rate throughout its intended life time and 3) a limited volume fraction of undesirable phases. In order to achieve the above described microstructural features, a computational alloy design model coupling with a Genetic Algorithm (GA) has been developed. More computational details of the genetic algorithm can be found in a previous publication [12].

Firstly, random compositions and heat treatment parameters are generated by the GA from the predefined ranges which are listed in Table 1. 11 variables are taken into account (10 alloying elements and the austenisation temperature) and uniformly spaced at 32 levels between predefined minimal and maximal values. As mentioned in the introduction, W and Mo have similar functions but significant difference in stabilizing the precipitates. To illustrate this difference in the clearest manner, the search domains were specified for either Mo or W. The service temperature is fixed at 650°C.

Table 1 *Search ranges (in wt.%) for 10 chemical elements and the range for the austenisation temperature T_{aus} (in ^{o}C).*

	C	Cr	Ni	Ti	Mo/W	Al	Co	Nb	N	V	Fe	T_{aus}
Min.	0.001	8.00	0.001	0.001	0.001	0.001	0.001	0.001	0.001	0.001	Bal.	900
Max.	0,15	16.00	20.00	3.00	10.00	10.00	10.00	5.00	0,15	1.00		1250

Then, to check if the candidate composition and heat treatment can achieve the desirable microstructure, various go/no-go criteria are defined and applied in the sequence of the thermal treatments that the steels are subjected to. In precipitation-hardened martensitic creep-resistant

steels, the typical heat treatment includes an austenisation/solution treatment to dissolve undesirable primary precipitates and to achieve compositional homogeneity, followed by quenching and a tempering treatment to form desirable precipitates in the martensitic matrix. The present study deals with Laves phase or $M_{23}C_6$ strengthened steels for very long term applications and hence the final precipitate state after long term service will be close to the equilibrium condition at the service temperature rather that at the tempering temperature. Therefore, in the present study the tempering temperature is set at the service temperature (650 °C). Following the sequence, thermodynamic calculations are performed at austenisation temperature and three go/no-go criteria are defined: (1) the equilibrium volume fraction of austenite should be larger than 99%; (2) the amount of primary carbides should be less than 0.5% in volume. (3) liquid and delta phase should be absent. After austenisation, martensitic creep resistant steels are quenched to room temperature, and the austenite should completely transform to martensite. Therefore, a fourth go/no-go criterion is imposed: (4) the Martensite start (T_{Ms}) temperature should be higher than 250 °C. The T_{Ms} is obtained by calculating the chemical composition using the formula proposed by Ishida [13]. After quenching to room temperature, the alloy is used at its service/ageing temperature. Hence a second set of themodynamic calculations at the service temperature is performed. Two additional go/no-go criteria at this application temperature are enforced: (5) The amount of precipitates other than Laves phase/$M_{23}C_6$ should be less than 1 vol%. Here Laves phase and $M_{23}C_6$ are defined as the main strengthening precipitates in the Laves phase strengthened systems and $M_{23}C_6$ strengthened systems respectively. (6) The Cr concentration in the matrix upon completion of the precipitation reactions should at least be 11 wt.% to assure adequate corrosion and oxidation resistance.

Finally, the aim of this study is to tailor the undesirable Laves phase or $M_{23}C_6$ to desirable phase by tuning the chemical composition and heat treatments, so as to dramatically reduce their coarsening rates. Therefore, the precipitation hardening (PH) of Laves phase or $M_{23}C_6$ is considered to be the optimisation criteria to rank all qualified solutions fulfilling all above 6 go/no-go criteria. The PH is determined by the precipitate particle size, its density and distribution [14], and depends on their initial condition and evolution during service. Given the extremely long service time, Laves phase and $M_{23}C_6$ will grow and coarsen considerably during

the exposure at high temperatures, and hence change the inter-particle spacing. The precipitation hardening contribution σ_p is inverse proportional to inter-particle spacing, which is estimated by considering the coarsening kinetics only [15-17],

$$\sigma_p \propto 1/L = \sqrt{f_p}/r = \sqrt{f_p}/\sqrt[3]{r_0^3 + Kt} \tag{1}$$

in which

$$r_0 = 2\gamma/\Delta G_v \tag{2}$$

and

$$K = 8\gamma V_m^p / \sum_{i=1}^{n} \frac{9(x_i^p - x_i^{mp})^2}{x_i^{mp} D_i / RT} \tag{3}$$

where L is the average inter-particle spacing, f_p is the equilibrium volume fraction of the strengthening precipitate at the service temperature, r_0 is the critical precipitate nucleus size, γ is matrix-precipitate interfacial energy, ΔG_v is volume thermodynamic driving force for the precipitation. V_m^p is the molar volume of precipitate. K is the coarsening rate and t is the exposure time at the high temperature. x is equilibrium interfacial concentrations (in mole fraction) of Laves phase or $M_{23}C_6$ former elements on both matrix (m) and precipitate (p) sides. T is the service temperature and D is corresponding diffusion coefficient. All thermodynamic values including f_p, ΔG_v, x_i^p, x_i^{mp}, D_i and V_m^p required in the calculations are calculated via Thermo-Calc® using the TCFE6 and Mob2 databases.

In summary, the time and temperature dependent inter-particle spacing of Laves phase or $M_{23}C_6$ is taken as the PH optimisation parameter. In this study the service time is set at 10^5 h. The factor $1/L$ (**Eq. (2)**) is called the 'PH factor' and to be optimised by tuning the chemical composition and heat treatment parameters.

3 Model applications

The GA based search covering about 10^6 of unacceptable or less well performing variants, led to four alloys with highest long term precipitation strengthening. Their composition, austenisation temperatures, volume fraction, coarsening rate and PH factor of Laves phase or $M_{23}C_6$ are listed in Table 2. The alloys strengthened by Laves phase with either W or Mo as the modifying element, and those strengthened by $M_{23}C_6$ with either W or Mo as the modifying element are labelled as Alloy LavesW, Alloy LavesMo, Alloy $M_{23}C_6$W and Alloy $M_{23}C_6$Mo, respectively. These alloys generally have the composition with high Cr levels and a maximal Co level. The high Co level is required so as to keep a high Cr level in the matrix and hence obtain a fully austenitic matrix at the austenisation temperature. For the LavesW alloy the W level equals the imposed maximum level. In contrast, for the LavesMo alloy the Mo level is well below the maximum possible level. In both $M_{23}C_6$ alloys the C and Cr levels are equal to the maximal values, but the Mo and W levels are relatively low. In general the lower concentration levels are the results of strict go/no-go constraint boundaries being met in the optimisation cycles. Concentration of Ni in Laves phase strengthened alloys LavesW and LavesMo is much higher (3-5 wt.%) than that in $M_{23}C_6$ hardened steels to further stabilize austenite at austenisation temperature, since the content of ferrite stabilizer elements W in alloy LavesW or Mo, Al and Nb in alloy LavesMo are much higher than that in $M_{23}C_6$ hardened steels.

Table 2 Composition of four designed alloys(in wt.%), austenisation temperature T_{aus} (in °C), SSS factors (SSSF) and PH factors (PHF) at 650 °C.

	C	Cr	Ni	Ti	Mo	W	Al	Co	Nb	N	V	Taus/K	VP/% laves/$M_{23}C_6$	K / m^3/S Laves/$M_{23}C_6$	PH factor at 10^5 h
lavesW	0,001	10,84	3,23	0,11	0	10	0,001	10	0,324	0,030	0,001	1512	11.3	8.57E-31	4,98E6
$M_{23}C_6$W	0,15	16	0,01	0,01	0	1,61	0,001	10	0,001	0,0058	1	1342	3.05	7.39E-30	1,26E6
LavesMo	0,001	10,07	3,23	0,11	4,19	0	0,001	10	1,775	0,001	0,001	1523	9.5	6.1E-29	1,11E6
$M_{23}C_6$Mo	0,15	16	0,01	0,01	0,97	0	0,001	10	0,001	0,0058	0,39	1455	3.02	1.46E-29	1.0E6

It is interesting to note that the coarsening rate of Laves phase or $M_{23}C_6$ in W containing alloys is much slower than that in Mo containing alloys. Clearly W has a higher capacity to stabilize the precipitates. To further visualize its effect on coarsening rates, the PH factors evolution over time

for all alloys are shown in **Fig. 1**. The PH factors of all four alloys decrease with time but with different kinetics. In Laves phase strengthened alloy, the degradation kinetics of alloy LavesW is much slower, leading to a much higher PH factor at the long service time. The W effect is also observed in $M_{23}C_6$ strengthened alloy but the difference is less pronounced. Moreover, the coarsening rate of Lave phases in alloy LavesW is close to that of the well accepted very stable MX carbonitride, proving that undesirable Laves phase can be turned into desirable precipitates. Furthermore, the volume fraction of Laves phase (11.3 vol%) is much higher than the maximum allowed volume fraction of MX carbonitride (0.5 to 1 vol%) which increases the final strengthening contribution of precipitates.
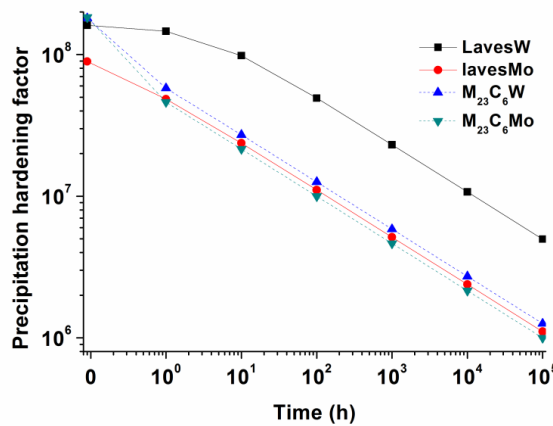
Figure 1: The degradation behaviour of PH factors with service time for the four designed alloys.

4 Discussion

4.1 Effects of alloying elements on the precipitate configuration

As demonstrated in the model application section, the type of alloying element can significantly influence the precipitate characteristics. To further explore this effect, the compositions of alloys LavesW and LavesMo are taken as baselines and the concentrations of Co, W in each alloy are

varied while keeping the levels of all other elements unchanged. As shown in **Fig. 2**, the two vertical dashed lines represent the predefined ranges of alloying elements (cf. Table 1). The green box defines the concentrations that meet all the go/nogo criteria. The black arrows indicate the original compositions of alloys LavesW or LavesMo, which, as expected, always show the highest PH factor in the predefined ranges, suggesting the robustness of the model. As observed in **Fig. 2a and 2c,** addition of Co in both alloys can significantly decrease the coarsening rate (by ~10 times in Alloy LavesW and by ~5 times in Alloy LavesMo) and increase the volume fraction of Laves phase, and hence together lead to a substantial increase in PH factors (Eq. (1)). The difference in **Fig. 2a and 2c** is that the volume fraction of Laves phase in Alloy LavesMo reaches a maximum value at 10wt.% Co and then decrease with further addition of Co. The effect of W is similar to that of Co, as shown in **Fig. 2b**. When the concentration of W is low (<0.3wt.%), there is no Laves phase since W is the main Laves forming element. At a further increase in W concentration, Laves phase begins to form and its concentration increases almost linearly and reaches maximum PH at the upper limit of 10wt%. At the same time, the coarsening rate of Laves phase is significantly decreased. On the contrary, addition of Mo in alloy LavesMo increases the coarsening rate when Mo content is lower than 5 wt.% as shown in **Fig. 2d**. Further increase of Mo will only decrease the coarsening rate slightly. This explains why Mo containing alloy LavesMo has much higher coarsening rate than that of W added alloy LavesW. The effects of both Co and W on coarsening rate of Laves phase agree very well with the existing experimental results [3, 5]. By analysing the coarsening rate as defined in Eq. (3), it is found that the coarsening rate mainly depends on the diffusion coefficients and concentration gradients of alloying elements at the interface. The diffusion coefficient of W at the set temperature of 650 °C is very low, 10^{-20} m^2/s, while those of other elements (including Mo) are higher than 10^{-19} m^2/s. As shown in **Fig. 2b**, the coarsening rate decreases rapidly with the addition of W when its content is lower than 2.5wt.%. This is the combined effect of concentration gradient at the interface and the low diffusion coefficient of W. Further addition of W only slightly decreases the coarsening rate, suggesting there is no significant change in interface concentration gradient. This phenomenon is not so pronounced in Co, since an increase the Co level also decreases the diffusion coefficients of other alloying elements [3].
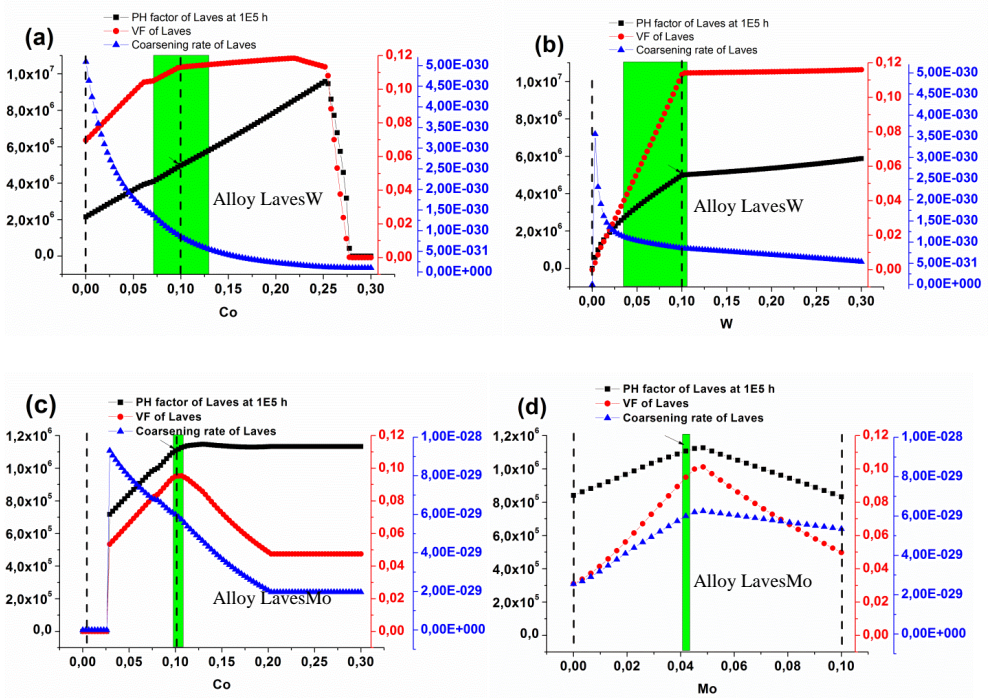
Figure 2: Effect of concentration variation of alloying element on the volume fraction (VF), coarsening rate and PH factor of Laves phase. (a) Co, (b) W in alloy LavesW and (c) Co and (d) Mo in alloy LavesMo. The two vertical dashed lines indicate the predefined range of alloying elements. The green box defines the concentration range that meets all the go/no-go criteria, and the concentration in other areas do not fulfil one or multiple go/no-go criteria. The black arrows indicate the original composition in alloy LavesW or LavesMo.

4.2 Combination of $M_{23}C_6$ and Laves phase in one alloy and comparison to existing alloys

Generally $M_{23}C_6$ precipitates are located at lath boundaries and have a positive effect by pinning the lath boundaries during creep, while the W-enriched Laves phase is generally found in the grain interior [6] and restricts the movement of dislocations. Both effects can decrease the creep

324

rate, especially if coarsening rates of both can be maintained at a low value during service. It will be very interesting to combine both precipitates in one alloy to further optimise the creep resistance. However, the optimisation procedure as sketched above can only deal with one PH factor. In order to optimise both PH factors simultaneously in one alloy, two optimisations are performed respectively: either only for Laves, or only for of $M_{23}C_6$ at 10^5 h, while the PH factors of both precipitates are recorded for all eligible solutions that fulfil all the go/no-go criteria in both optimisations. The analysis was only performed for the search space containing W. Putting all the qualified solutions together, the property map in **Fig. 3** was constructed. The best combination of two precipitates can be found as indicated by the circle on the upper right corner. The new alloy, which has only slightly lower PH factors than either maximum from dedicated single optimization, is labelled as Alloy LavM. Its composition, austenisation temperature and PH factor are listed in **Table 3**.

Table 3 Composition of four designed alloys(in wt.%), austenisation temperature T_{aus} (in °C), SSS factors (SSSF) and PH factors (PHF) at 650 °C.

	C	Cr	Ni	Ti	Mo	W	Al	Co	Nb	N	V	Taus/K	PH factor of Laves at 10^5 h	PH factor of $M_{23}C_6$ at 10^5 h
LavM	0,15	12,39	1,3	0,01	0	10	0,001	10	0,001	0,068	1	1489	4,59E6	1,32E6

To benchmark the newly designed alloy against existing alloys, the PH factor after 10^5 h of exposure to 650 °C for Laves phase and $M_{23}C_6$ were calculated for a number of commercial 9-12Cr% martensitic creep resistant steels (other precipitates than Laves phase and $M_{23}C_6$ were not considered in this part). The calculated existing alloys are 9Cr1Mo, 9Cr2Mo, 9Cr1Mo1WVNb, 9Cr1MoVNb, 9Cr2MoVNb, 11Cr2.6W2.5CoVNbBN, 9Cr0.5Mo2WVNb, 11Cr3W3CoVNbTaNbN, 12Cr1MoV, 12Cr0.4Mo2WCuVNb, 12Cr0.6Mo0.3V0.4NbN, 12Cr1MoWV and 12Cr1Mo1WVNb. Their results are shown in **Fig. 3**, as indicated by stars. The PH values for all existing alloys are located in the lower left corner, indicating that in existing alloys Laves phase and $M_{23}C_6$ indeed have no significant strengthening effects for long time exposure due to the high coarsening rate. By the simultaneous optimisation of volume fraction and coarsening rate, not only alloy LavM itself but also many other solutions with different combinations of PH factors of Laves phase and $M_{23}C_6$, as shown in **Fig. 3**, can significantly

outperform existing alloys. This clearly demonstrates that undesirable phases can be altered to desirable phases by tuning the composition and heat treatment parameters. In addition to the considerations presented in the current paper, other criteria such as cost, weldability, processibility etc, can also be taken into account to calculate optimal alloy compositions. Additional consideration will eliminate some solutions in the figure, but there is still a substantial potential to improve the long term creep strength of current martensitic creep resistant stainless steels by taking up this new alloy design concept.
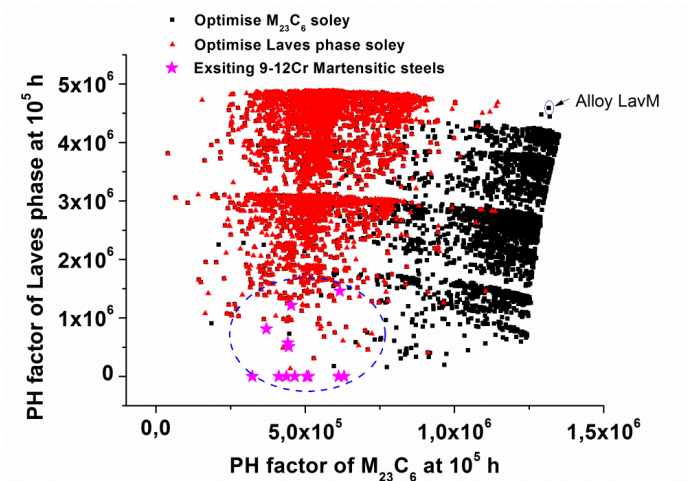
Figure 3 Simultaneous optimisation of PH factors of Laves phase and $M_{23}C_6$. The values of existing alloys, as indicated by star symbols, are also put on the plot to compare to the designed solutions.

5 Conclusions

A computational alloy design approach has been developed to design martensitic creep resistant steels strengthened by Laves phase and $M_{23}C_6$ by tailoring their coarsening rates to a minimum and simultaneously tailoring their volume fraction to a maximum level. The coarsening kinetics of both precipitates can be significantly lowered by changes in the overall alloy composition and

the precipitation hardening contributions are hence substantially increased by tuning the composition and heat treatments. The main Laves phase forming elements, i.e. W and Mo, have different effects on the coarsening rate of Laves phase. Addition of W significantly decreases the coarsening rate, while in some regimes a higher Mo level increases the coarsening rate. For W alloyed creep resistant steels, the combination of Laves phase and $M_{23}C_6$ shows great potential in designing new alloys outperforming existing martensitic creep resistant steel grades.

References:

[1] Taneike M, Abe F, Sawada K, Creep-strengthening of steel at high temperatures using nano-sized carbonitride dispersions, Nature, 424, 294-6, (2003).

[2] Abe F, Horiuchi T, Taneike M, Sawada K, Stabilization of martensitic microstructure in advanced 9Cr steel during creep at high temperature, Mater Sci Eng, A, 378, 299-303, (2004).

[3] Gustafson Å, Ågren J, Possible effect of Co on coarsening of $M_{23}C_6$ carbide and Orowan stress in a 9% Cr steel, ISIJ Int., 41, 356-60, (2001).

[4] Kipelova A, Odnobokova M, Belyakov A, Kaibyshev R, Effect of Co on creep behavior of a P911 steel, Metall Mater Trans A, 44, 577-83, (2013).

[5] Abe F, Creep rates and strengthening mechanisms in tungsten-strengthened 9Cr steels. Mater Sci Eng, A, 319-321, 770-3, (2001).

[6] Abe F, Effect of fine precipitation and subsequent coarsening of Fe2W laves phase on the creep deformation behavior of tempered martensitic 9Cr-W steels, Metall Mater Trans A, 36 A, 321-32, (2005).

[7] Kuhn B, Talik M, Niewolak L, Zurek J, Hattendorf H, Ennis PJ, et al, Development of high chromium ferritic steels strengthened by intermetallic phases, Mater Sci Eng A, 594, 372-80, (2014).

[8] Tarigan I, Kurata K, Takata N, Matsuo T, Takeyama M, Novel concept of creep strengthening mechanism using grain boundary Fe 2Nb Laves phase in austenitic heat resistant steel, Mater Res Soc Symp Proc., 1295, 317-22, (2011).

[9] Kimura K, Seki K, Toda Y, Abe F, Development of high strength 15Cr ferritic creep resistant steel with addition of tungsten and cobalt, ISIJ Int., 41, S121-S5, (2001).

[10] Toda Y, Tohyama H, Kushima H, Kimura K, Abe F, Influence of chemical composition and heat treatment condition on impact toughness of 15Cr ferritic creep resistant steel, JSME International Journal, Series A: Solid Mech Materl Eng, 48, 125-31, (2006).

[11] Masuyama F, History of power plants and progress in heat resistant steels, ISIJ Int.;41, 612-25, (2001).

[12] Xu W, Rivera-Díaz-del-Castillo PEJ, van der Zwaag S, Designing nanoprecipitation strengthened UHS stainless steels combining genetic algorithms and thermodynamics, Comput Mater Sci, 44, 678-89, (2008).

[13] Ishida K, Calculation of the effect of alloying elements on the Ms temperature in steels, J Alloys Compd, 220, 126-31, (1995).

[14] Orowan E, Theory of dislocation bowing, London: Institute of Metals Symposium on Internal Stresses in Metals and alloys, 451, (1948).

[15] Kelly A, The strength of aluminium silver alloys, Philos Mag, 3, 1472-4, (1958).

[16] Ågren J, Clavaguera-Mora MT, Golczewski J, Inden G, Kumar H, Sigli C, Applications of Computational Thermodynamics: Group 3: Application of computational thermodynamics to phase transformation nucleation and coarsening, Calphad-Computer Coupling of Phase Diagrams and Thermochemistry, 24, 41-54, (2000).

[17] Robert WC, Haasen P, Physical Metallurgy, Amsterdam, North-Holland, Elsevier, 3, 2044-46, (1996).

INFLUENCE OF HIGH TEMPERATURE EXPOSURE
ON THE MICROSTRUCTURE OF FILET WELD JOINTS OF "NEW"
CrMoNbV BAINITIC STEEL FOR MEMBRANE WALLS

Krzysztof Cieszyński [2]
Stanisław Fudali[1]
Grzegorz Cempura [2]
Grzegorz Michta [2]
Aleksandra Czyrska-Filemonowicz [2]

[1]RAFAKO S.A., Lakowa 33 , PL- 47400 Raciborz
[2] AGH University of Science and Technology, Al. A. Mickiewicza 30, PL - 30059 Krakow

Abstract

This article is focused on the influence of high temperature exposure on the microstructure and hardness of filet weld joints fabricated from "new" CrMoNbV bainitic steel. Results of these tests are very important for manufacturers of pressure elements and for users of the power plants. A possible application of "new" CrMoNbV steel for large scale membrane wall to be installed in the test loop in one of the commercial Power Plants is discussed in the paper.

Keywords: T24, Membrane walls, CrMoNbV, Fillet welded joints, Steam power plants.

1. Introduction

The 7CrMoVTiB10-10 (T24) steel is widely used for gas-tight membrane walls of furnace chambers in the majority of USC parameter boilers in Western Europe, Czech Republic and Slovenia [1]. The "new" CrMoNbV bainitic steel was manufactured in Japan by the Nippon Steel Sumitomo Metal Corporation. This steel was successfully implemented for production of tube elements ten years ago, however it was not recognized by producers of energy boilers at that time. CrMoNbV steel has very good welding properties and approx. 30% better creep resistance in the temperature range from 430 to 530 °C in comparison to traditional steels, like 13CrMo4-5 and 10CrMo9-10, containing 1% Cr content. Corrosion resistance of CrMoNbV steel on the steam side as well as on flu gas is similar to steels containing 1-2% Cr [2]. CrMoNbV has not been used for fabrication of pressure elements for energy industry in large scale by now. Some tubes were purchased by a Japanese company and installed, as a superheater of main steam outlet, in one of the power plants operating with conventional steam parameters [3]. The results of these trials are not known.

Figure 1 below presents the average of long-time (100 000 h) creep rupture strength of available materials which can be used for gas-tight membrane walls in furnace chambers for USC parameters boilers [4-6]. Nickel based alloys have a very good creep rupture strength, but are expensive. T92 steel shows the best properties, but requires heat treatment after welding, increasing thus the cost of installation and repair of gas-tight membrane walls. T24 and T23 steels require special treatment at each stage of production (production, installation and repair), therefore have hardly any perspective of application. RAFAKO proposes gas-

tight membrane walls production from the CrMoNbV steel. Membrane walls produced from this material guarantee achievement of presupposed parameters and a reliable performance of a boiler.
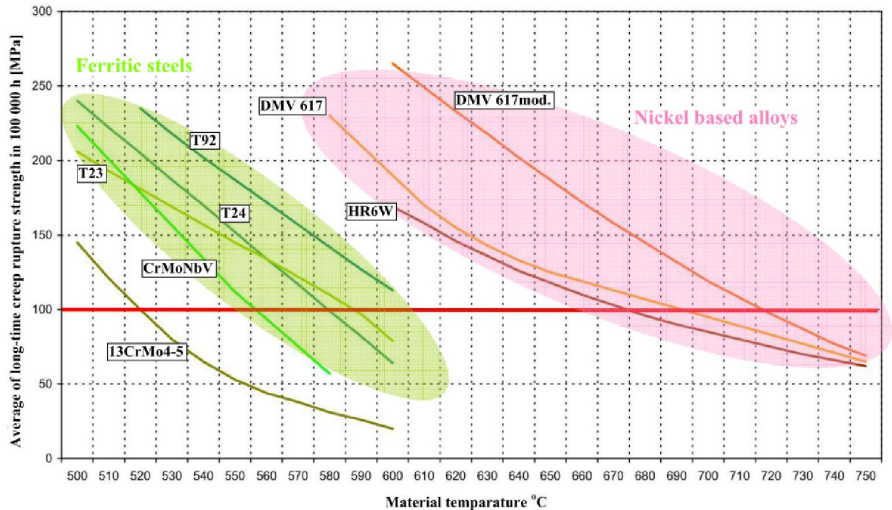

Figure 1. Average of long-time creep rupture strength in 100 000 h for materials designated for gas-tight membrane walls [4-6].

2. Experimental details

The chemical composition (in wt%) of CrMoNbV bainitic steel provided by Nippon Steel Sumitomo Metal Corporation (NSSMC) is given in the Table 1.

Material	Chemical composition [wt %]										
	C	Si	Mn	P	S	Cr	Mo	Nb	V	S.Al	B
CrMoNbV	0.04-0.12	≤ 0.5	0.1-0.9	≤0.025	≤0.001	1.05-1.45	0.3-0.5	0.02-0.08	0.05-0.2	≤0.03	0.001-0.006

Table1. Chemical composition of CrMoNbV steel [2].

The tube Ø42.4 x 7.1 mm and fin (bar) of 18.6 x 6(8) mm, were delivered after normalization at 975 ºC and tempering at 720 ºC [2]. According to the manufacturer data, mechanical properties of CrMoNbV steel after such treatment are as follows: R_m = 570 MPa, A = 20%. The limit of yield strength at temperature of 500 ºC is more than 390 MPa and creep rupture strength (550 ºC/100 000 h.) is 112 MPa [2].

The following investigation was performed by now [7]:
- fillet welded joints - automatic method 121 - PEMA 200/6,
- butt welded joints - manual method 141,

- mechanical tests of welds mentioned above – hardness and Charpy V notch impact tests,
- annealing of fillet welded joints samples,
- microstructural analyses of the welds and base materials (as received as well as aged samples).

All welds were performed under industrial conditions, however samples were only up to 2 m long. Mechanical tests of the as received CrMoNbV steel and welded joints comprised hardness test, impact test and tensile test measurements. Hardness tests of butt welded joints were performed along two lines across whole samples, namely near outer and inner part of the welded tube. Hardness tests of fillet welded joints were performed along three lines across whole samples, namely near outer and inner part of the welded tube. All mechanical tests were realized in Research Laboratory of RAFAKO S.A. recognized by Office of Technical Inspection (Certificate No LB-119/07).

Investigation of the weldments under the operational- and higher range of temperatures gives insight into the stability of the steel microstructure, therefore samples were isothermally heated at 550 and 600 ºC up to 500 hours in vacuum. Heat treated specimens were embedded in quartz pipes in vacuum. Temperature during aging was controlled and stable during whole duration of the tests.

Microstructural investigations were performed using light microscopy (LM) techniques utilising Axio Imager M1M of Zeiss and Scanning Electron Microscopy (SEM) techniques utilising Merlin Gemini II of Zeiss. LM and SEM investigations were conducted on polished and etched specimens. Specimens were etched using Vilella reagent for 30 seconds at room temperature.

Chemical composition analyses of tested welds were conducted by SEM- Energy Dispersive X-ray Spectroscopy (EDS), which allowed for obtaining chemical element maps of selected elements.

3. Results and discussion

a) Conditions of welding process (as received weld) butt welded joints

Welding process of butt joints was made at following conditions:
- welding procedure 141 (TIG - manual method)
- welded position - PC, PH
- dimensions of welded tube - Ø42,4 x 7,1 mm
- welded wire material: UNION IP23, diameter - Ø2 mm and Ø2,4 mm
- average amperage for grain layer of approx. 110A
- number of passes 3-4
- maximal temperature of inter-pass was not exceeding 280 ºC
- protective atmosphere gas - argon

Butt welded joints were performed without post weld heat treatment (PWHT).

b) As received weld, fillet welded joints.

Welding process of fillet joints was made at following conditions:
- welding procedure 121 (PEMA - automatic method)
- dimensions of welded tube - Ø42,4 x 7,1 mm + 6,0 mm (fin)
- welded wire material: UNION IP23
- number of passes 1
- preheat temperature - 100 ºC (dehydrogenation)
- number of tubes 3
- number of fins (bars) 4
- graduation between center of tube - 60 mm

The automatic welding process of fillet welded joints prepared on PEMA machine under industrial conditions is illustrated in Figs 2a-c given below.
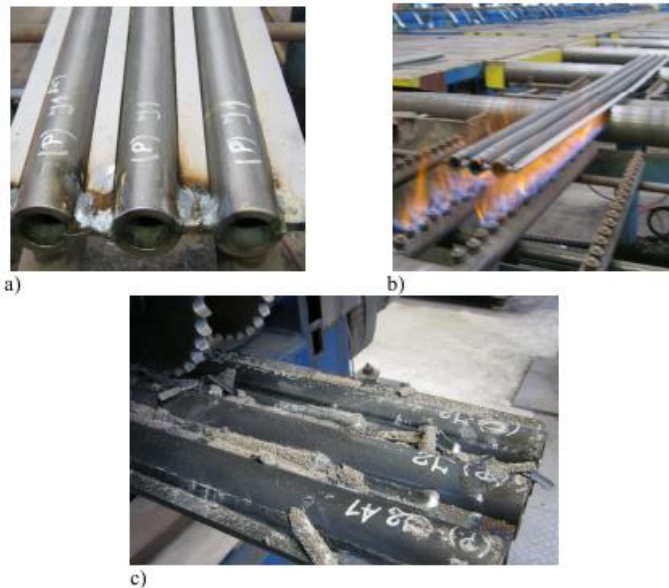
Figure 2. Fillet joints welding process: a) preassembling the tubes with the bending wall fins b) preheating of preassembled membrane wall elements c) membrane wall after completed joining process [7].

3.1 Mechanical tests of welded samples as received.

Experimental pieces of membrane walls constructed from CrMoNbV steel were made in RAFAKO S.A. Joints were made by an automatic submerged-arc welding method UP (121) and a manual method TIG (141). The flat bar steel for joining the tubes of the membrane wall were produced in 6 mm and 8 mm thickness. All joints were made without heat treatment after welding. For research purposes the following welding authorizations were obtained:

WPQR – Nr 4-30-VP 157/12 rev. 0 – this authorization allows production of butt weld joints by TIG (141) method without heat treatment [8]

WPQR – Nr 4-30-VP 125/12 rev. 0 and **WPQR – Nr 4-30-VP 126/12 rev. 0** – this authorization allows production of automative fillet weld joints (tube - flat) by UP (121) method without heat treatment [9].

As shown in Fig. 3, joints made from CrMoNbV bainitic steel characteristically have very high fracture work, in comparison to T23 and T24 steels. Practically, investigated samples of T23 and T24 steels did not exceed 27 J required by the EN 10216 norm. For CrMoNbV steel average fracture work equals 120 J.
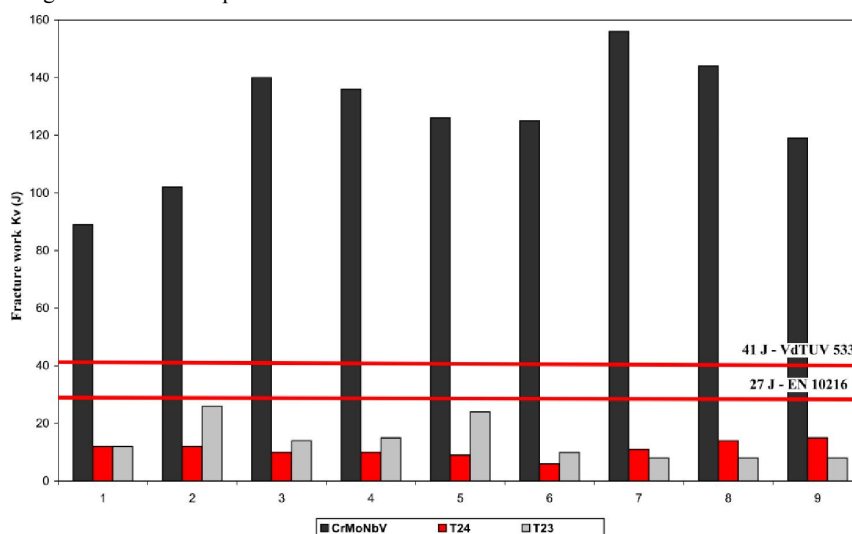

Figure 3. Fracture work of weld joints from CrMoNbV, T24, T23 steels without heat treatment after welding [7].

Results of hardness testing of fillet weld joints shown that the maximum average value occurs in the heat affected zone on the side of flat bar steel and equals 296 HV 10. In this area the maximum value of all the measurements equalled 320HV 10.

Samples after annealing were too small for impact test investigations. Results of hardness testing of annealed samples show that the maximum average value occurs in the weld near the flat bar and equals 266 HV10. Measurements were conducted on the sample after annealing at 600 ⁰C for 1000 h.

3.2 Microstructure of the as-received and heat treated specimens

Welded joints were visually investigated according to the PN EN 17637 norm. Visual investigations did not show any failures of the weld. Penetration test confirmed results of visual investigations of the weld.

3.2.1 Microstructure of the as received steel.
As received bar as well as pipes revealed homogeneous, fine-grained ferrite-perlite microstructure (grain size of about 10 μm). The microstructure of the pipe and the bar was similar. Typical microstructures observed using LM and SEM are presented in Fig. 4.
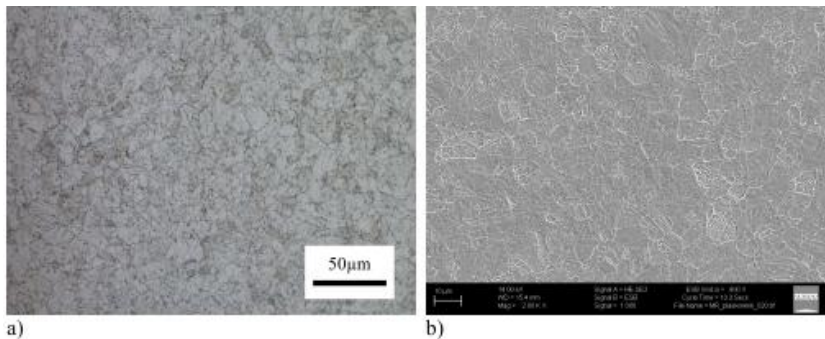

Figure 4. As-received microstructure of the pipe and bar used for construction of the membrame walls. Homogeneous ferrite-perlite microstructure with fine grains; a) LM and b) SEM images

3.2.2. Microstructure of the welded joints (without annealing)
The investigation of welded joints was made in accordance to standard procedure for filled welded joints, it means without post weld heat treatment (PWHT). A typical microstructure of the weld is presented in Figs 5-8. In the base material a fine grained ferritic-bainitic microstructure was observed (Fig. 5).
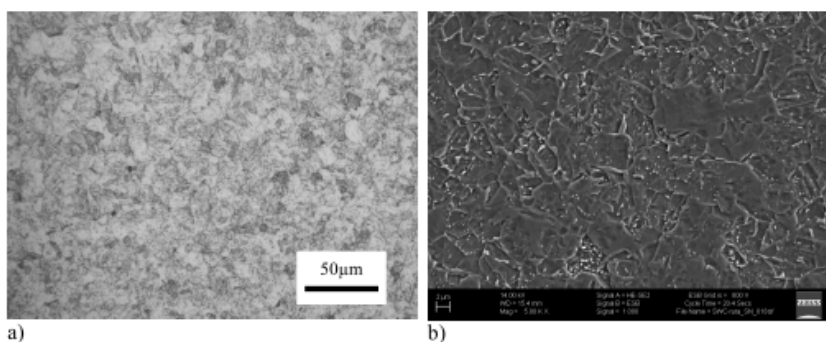
Figure 5. Microstructure of the base material, a) LM, b) SEM

In the heat affected zone (HAZ) a bainitic microstructure with coarse grained large prior-austenite grains was observed (Fig. 6).
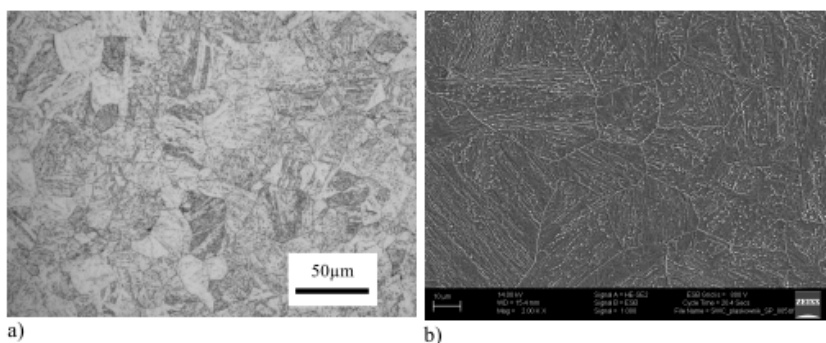

Figure 6. Microstructure of the heat affected zone (HAZ), a) LM, b) SEM

The microstructure of the fusion line, which separates the base material and the weld, is presented in Figs 7a and b.
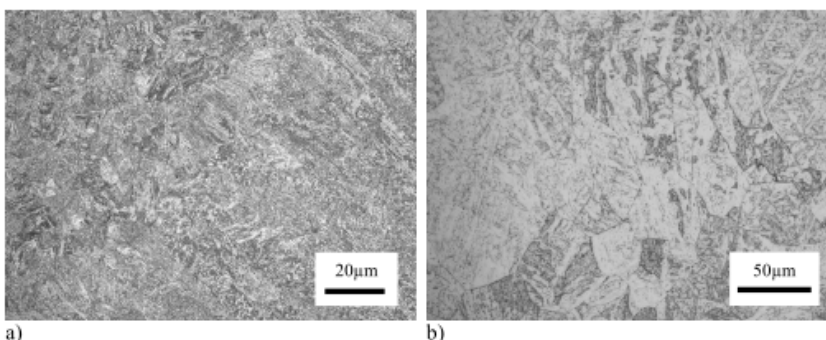

Figure 7. Microstructure of the fusion line shown at lower (a) and higher magnification (b), LM

Weld microstructure is presented in Fig. 8. The bar (a) and pipe (b) side has similar microstructure.
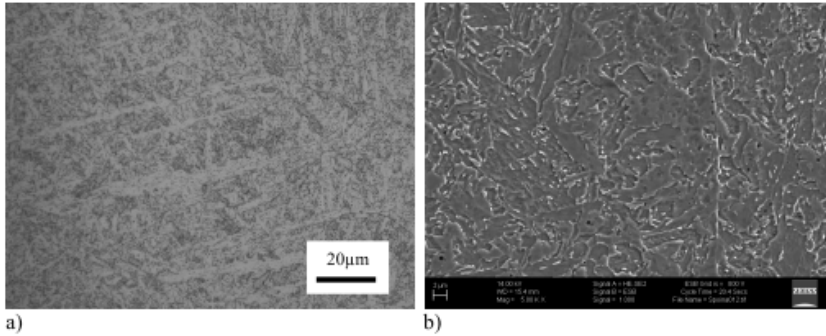
Figure 8. Microstructure of the weld: bar a) LM, pipe (b), SEM

3.2.3. Microstructure of the welded joints after annealing

The microstructure of the welds in the as-received and annealed samples was very similar. The same zones of the welds were identified (i.e. base material, HAZ and fusion line). In the weld microstructure after annealing, Cr- and Mo-rich particles, precipitated mainly at grain boundaries, were found. Figs 9 and 10 show the microstructure containing carbide precipitates and EDS chemical element maps (Cr and Mo) of the specimen annealed at 600 ˚C for 500 h.

Figure 9. Microstructure and EDS element maps of the specimen after 500h of annealing at 600 °C (a), Cr map (b), Mo map (c)

Figure 10. Microstructure of the specimen after 500 h of annealing at 600 °C, precipitates at the grain boundaries, a) LM, b) SEM

4. Conclusions.

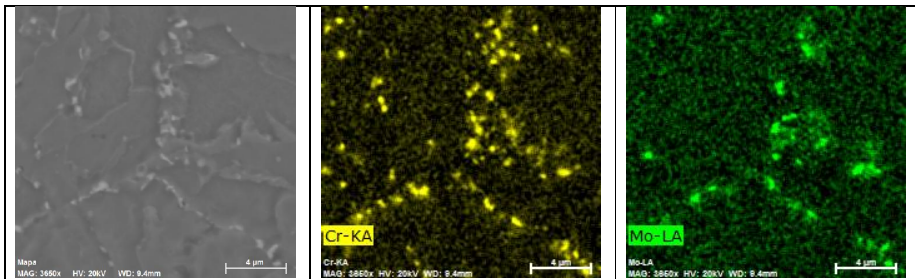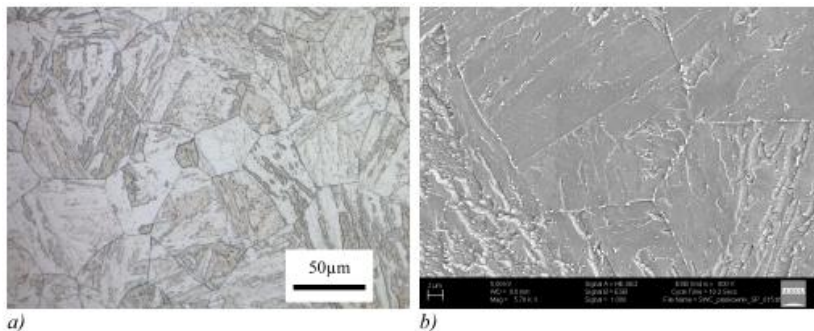- All experimental weld joints of membrane walls constructed from CrMoNbV steel were made under industrial conditions without any defect in RAFAKO S.A. company.
- The following welding authorizations by TUV were obtained: **WPQR – Nr 4-30-VP 157/12 rev. 0;** production of butt weld joints by TIG (141) and**WPQR – Nr 4-30-VP 125/12 rev. 0**,**WPQR – Nr 4-30-VP 126/12 rev. 0;** automative fillet weld joints (tube – flat bar) by UP (121) method without heat treatment after welding.
- In the microstructure of the specimen annealed at 600 ˚C for 500 h, a large number of Cr and Mo-rich particles, preferentially at the grain boundaries, were precipitated,
- Comparing to others steels dedicated to USC and A-USC power plant membrane walls, the CrMoNbV steel does not require the post weld heat treatment after welding, and is cost-saving in comparison to nickel based alloys.

Acknowledgements

References

[1] S. Fudali, J. Hajda, A. Kucybała *Assessment of base material, weld metal deposit and manufacturing process of gas-tight membrane walls made of 7CrMoVTiB10-10 steel grade*, Proceedings of Internal VGB Workshop, 7.07.2011, Stuttgart, unpublished
[2] T. Nakashima, K. Miyata, H. Hirata, M. Igarashi, A. Iseda Development of high strength 1.25Cr-0.4Mo-Nb-V steel tube; *Advances in Materials Technology for Fossil Power Plants: Proceedings from the Fifth International Conference 2007 (ASM International)*, 5th International conference on advances in materials technology for fossil power plants; March 01, 2008 – pages 129-139
[3] Unpublished information

[4] National Standard of the People's Republic of China - GB 5310 – 2008

[5] EN 10216-2 2009 and VdTUV data sheet

[6] Sumitomo Metal Industries, Ltd. Creep rupture properties of CrMoNbV steel, *Bulletin No. 12180W*, June 2012

[7] Internal RAFAKO S.A. process for investigation of new materials for membrane walls, unpublished

[8] TUV authorization for welding technology process by TIG (141) for CrMoNbV steel butt welded joints without heat treatment after welding

[9] TUV authorization for welding technology process by UP (121) for CrMoNbV steel automative fillet welded joints without heat treatment after welding.

TUBACEX TX310HCbN COMMERCIAL RELEASE

Alfredo Undabeitia[a], Alejandra Lopez[a], Raquel Rodriguez[a], Florent Decultieux[b], Thomas Rieger[c]

[a] Tubacex S.A, Llodio, Spain;
[b] Vallourec Research Center France (VRCF), 60, Rue de Leval, Aulnoye-Aymeries, France;
[c] Vallourec Research Center Germany (VRCG), Theodorstrasse 111, 40472 Düsseldorf, Germany

Abstract

TUBACEX S.A. is one of the world's leaders of seamless stainless tube manufacturers and has a strong experience in the Powergen market. Following its commitment as main actor in the supply of premium grades for the Ultra Super Critical Boiler industry, Tubacex cooperates closely with Vallourec in terms of research and development. Intensive efforts of the joined R&D team aimed a robust and efficient production process for tubes with optimized properties. As a result Tubacex S.A. is glad to announce the commercial release of TX310HCbN grade (commercial designation for TP310HCbN according to ASME SA 213 and standardized steel grade UNS S31042).

In order to meet the challenging process conditions required by USC technology, TX310HCbN presents excellent fireside corrosion and steam side oxidation properties thanks to the special content of Cr (25%), higher than in any other austenitic, and balance additions of Nb and N which enhance the material properties at high temperature and at creep condition via the solid solution strengthening and precipitation hardening mechanisms.

Currently supplied under ASME specification (ASME SA 213 UNS S31042) Tubacex is going through an exhaustive qualification program so as to be an approved vendor for this material by the highest European standard for premium grades that is to be VdTÜV. This thorough exercise complies both audited short term tests (already successfully ran) together with long term creep evaluation (for which ongoing tests have passed 3000 h).

Keywords: UNS S31042, TX310HCbN, powergeneration, boiler tube

1. Introduction

Coal fired power plants will ensure the electrical energy supply in the mid-term future. But an improved efficiency is needed to balance ecological and economical issues [1].

Therefore the sector of Ultra Super-Critical (USC) power plants is in continuous development. Materials are subject to severe service conditions (temperatures above 600 ºC, pressures above 300 bars) and environment (high chlorine and sulfur environments during the whole life cycle of the power plant). The necessity of increasing the efficiency of these units together with reducing CO_2, NO_x and SO_2 emissions is a challenge for both suppliers and design experts. The correct definition of the grade standard to be used in the USC design is mainly governed by the following factors: creep strength, steamside oxidation resistance, fireside corrosion resistance and fabricability.

The corresponding development activities for adequate tubing materials led to the qualification of the advanced austenitic boiler grades UNS S30432, TP347HFG and TP310HCbN. In addition to the introduction into the relevant regulations (e. g. ASME SA213 or VdTÜV data sheets), the grades have been proven under field conditions in industrial test loops and USC boilers [2, 3].

There is a direct impact of the molten sodium-potassium – iron sulfates present at the 600ºC-750ºC temperature range on the boiler in the corrosion behavior of the material. Resistance to fireside corrosion effect is achieved and consequently increased by a proportional relation to the chromium content in the steel [4].

The high Cr-content in the austenitic steel TP310HCbN was designed to especially fulfill these tight corrosive conditions. It is listed in the relevant standards, Table 1. The corrosion resistance of TX310HCbN is superior to the competing USC austenitic grades (UNS S30432, TP347HFG) due to its 25 % Cr content. Table 2 shows a comparison of the chemical compositions of the advanced austenitic boiler grades.

Specification	Country	Description
ASTM A 213 ASME SA 213	USA	Seamless Ferritic and Austenitic Alloy-Steel Boiler, Superheater and Heat-Exchanger Tubes (UNS: S31042)
ASME Code case 2115-3	USA	Austenitic Stainless Steel Tubes (25Cr-20Ni-Nb-N)
VdTÜV Material Data Sheet 546 03.2008	Europe	X6CrNiNbN25-20 (1.4952)

Table 1 : Specifications applicable for TX310HCbN.

Grades		C	Mn	P	S	Si	Cr	Ni	N	Nb (Cb)	Al	B	Cu
TX304HB *18Cr-9Ni-3Cu-Cb-N*	min	0.07	-	-	-	-	17.0	7.5	0.05	0.30	0.003	0.001	2.5
	max	0.13	1.00	0.040	0.010	0.30	19.0	10.5	0.12	0.60	0.030	0.010	3.5
TX347HFG *18Cr-10Ni-Cb*	min	0.06	-	-	-	-	17.0	9.0	n.s.	8xC	n.s.	n.s.	n.s.
	max	0.10	2.00	0.045	0.030	1.00	19.0	13.0		1.10			
TX310HCbN *25Cr-20Ni-Cb-N*	min	0.04	-	-	-	-	24.0	19.0	0.15	0.20	n.s.	n.s.	n.s.
	max	0.10	2.00	0.045	0.030	1.00	26.0	22.0	0.35	0.60			

Table 2: Chemical composition of advanced austenitic grades

The typical microstructure of TX310HCbN is shown in Figure 1. The homogeneous microstructure and the balanced alloying concept provide excellent mechanical properties in the short term (both at room and high temperature) together with high creep resistance in the long term.
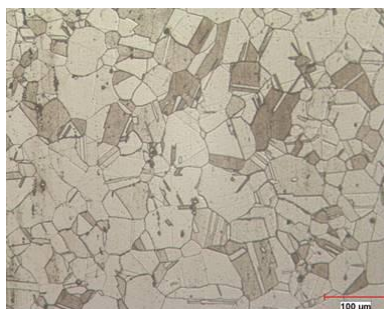
Figure 1 : Typical austenitic microstructure of TX310HCbN

2. Manufacturing process

Tubacex has established a full solid and stable manufacturing route for TX310HCbN grade. It covers the entire process chain from steel making via hot and cold deformation to the final heat treatment.

2.1 Melting

Scrap is classified and melted together with balanced additions of the required alloying elements so as to achieve the desired chemical composition in the arc furnace. Once the

chemistry checks are positive the melt is submitted to the Argon Oxygen Decarburization process, reducing the carbon content on the heat and reducing the presence of non desired elements such as sulfur. During this step the chemistry and temperature are checked again in order to have a positive control of each stage of the reaction. The heat is then casted into ingots, preheated on the pit furnace, forged and rolled to the final bar size required for the subsequent hot forming process.

2.2   Hot forming

Round bars are heated in induction furnaces and pierced with the consequent loss of temperature. Temperature is recovered with a second induction heating stage up to the optimum pre-extrusion value. Material is then hot formed via extrusion press to the final hollow dimension. The hollows are then transferred to the cold forming process.

2.3   Cold forming

Hot finished hollows are received and first submitted to cold worked plastic deformation throughout the available Pilger devices, from which the final tube outside diameter and wall thickness are defined in close tolerances.

Previously degreased, the cold worked tubes are then submitted to the final solution annealing heat treatment indicated by the applicable standards. In the particular case of TX310HCbN final solution annealing temperature range is specified on the ASME and TÜV standards by the values indicated in Table 3.

Heat Treatment	ASME SA213 TP310HCbN	VdTÜV 546 03.2008
Solution treatment	Min 1040°C Min 1900°F	1180°C to 1270°C 2156°F to 2318°F
Cooling media	Water or other rapid cooling	Cooled rapidly in water, air or protective gas

Table 3 : Specified heat treatment temperature ranges according to ASME SA213 and VdTÜV 546.

3. TX310HCbN mechanical characterization results

At room temperature (RT)

Standard	Grades	Rp0.2 MPa [ksi]	Rm MPa [ksi]	Min Long. Elongation %	Maximum Hardness	Impact Energy [J]	Grain size
A213	TP310HCbN	Min. 295 [43]	Min. 655 [95]	30	256HBW - 100 HRB	-	7 or coarser
SA213 CC2115-2	UNS: S31042	Min. 295 [43]	Min. 655 [95]	30	100 HRB	-	7 or coarser
VdTÜV 546	X6CrNiNbN25-20	Min. 295 [43]	655-900 [95-131]	30	-	Long: 85	-
TX310HCbN average		377	756	47	87HRB	212	5

Table 4 : Average mechanical test results for TX310HCbN grade at room temperature
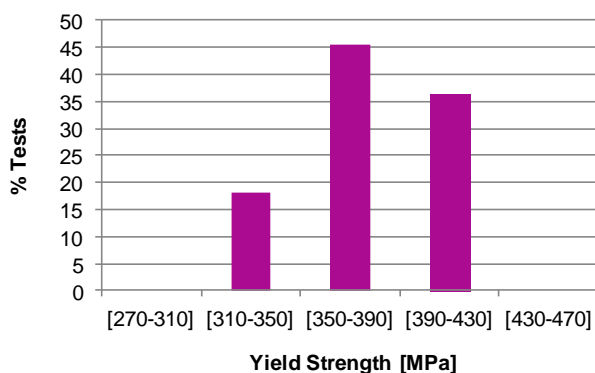

Figure 2 : Statistical yield strength test results for TX310HCbN grade at room temperature

Our average (Table 4) and statistical results (Figure 2) demonstrate that for all properties and for all tests our values are well above the limits established by European (VdTUV 546) and American standards (ASME SA213 TP310HCbN)

At high temperature (HT)

Mechanical properties at high temperature have been evaluated up to temperatures of 800 ºC.
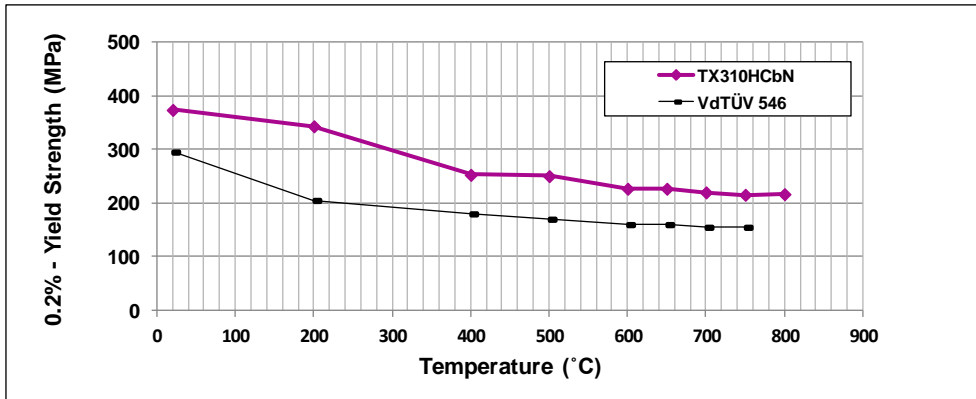
Figure 3 : Yield strength test results for TX310HCbN grade at high temperature
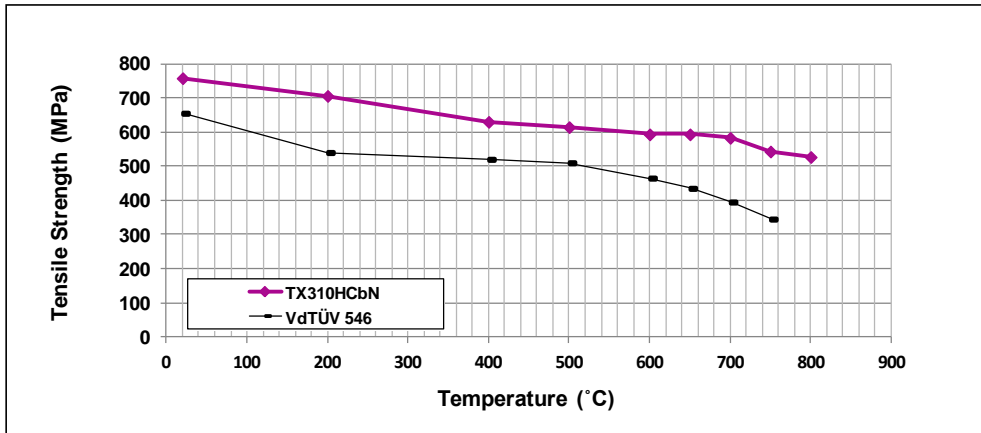

Figure 4 : Tensile strength test results for TX310HCbN grade at high temperature

The presented test results of yield and tensile strength , indicated by the purple solid line in Figure 3 and Figure 4 demonstrate the appropriate mechanical behavior at high temperatures of TX310HCbN exceeding the limits established by VdTÜV 546.

4. Creep evaluation

Prior to the TX310HCbN final industrialization process the Tubacex-Vallourec joint R&D team have performed an intensive study via short term creep tests in order to correctly adjust and define the main parameters that characterize this grade, that is to be:
- Solution annealing temperature
- Chemistry

On a second stage, so as to evaluate the long term behavior of TX310HCbN a thorough creep test analysis has been executed.
This analysis is carried out simultaneously via:

- VdTÜV audited qualification tests
  As already mentioned, aiming being listed as an approved vendor on the corresponding VdTÜV material datasheet (ref 546) an externally-audited creep test matrix has been launched covering the full Ultra Super Critical process range
  Temperature (ºC): 650-750

  Expected times (h):3000-30000
  All of our tests show a positive behavior towards European VdTÜV standards, with a longest running sample running for more than 7000h
- Internal R&D tests.
  Extrapolating Larson Miller Parameter (LMP) results for VdTÜV qualification and internal R&D creep tests versus VdTÜV 546 creep data
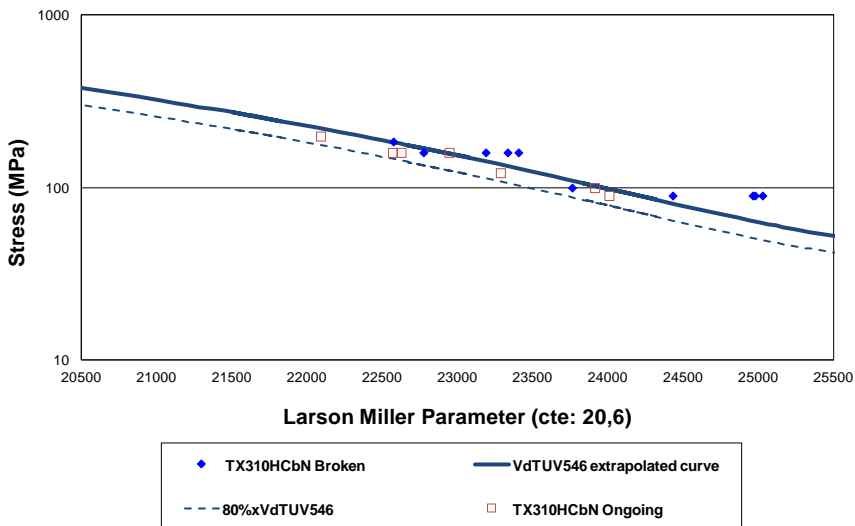
Figure 5 : TX310HCbN LMP creep test results vs. VdTÜV 546 extrapolated creep curve

As indicated on Figure 5 all our ongoing / ruptured tests are inside the LMP acceptance scatterband indicated by VdTUV 546 standard with a total cumulated creep time of more than 75500 h.

5. Oxidation performance

It is frequently found that the steam oxidation resistance of TP310HCbN steel is significantly higher than that of TP347HFG and UNS S30432 steels, basically because of the large difference in Cr content. In the literature it is sometimes referred to two alloy families, namely low Cr < 20 % (TP347HFG and UNS 30432) and high Cr > 20 % (TP310HCbN) [5].

To prove the performance of the TX310HCbN steel, a substantial oxidation test program is running at the laboratories of Vallourec Research Center Germany (VRCG) and in cooperation with external research partners. These tests are carried out in an Ar-50 % H_2O atmosphere at 650 °C and at 700 °C. The total exposure times shall sum up to more than 30 000 h. Results of the oxidation tests after 1 000 h exposure time at 650 °C and 700 °C are shown in Figure 6. Figure 6 a and b show the macropictures of the samples after 1 000 h exposure at 650 °C and the corresponding micrograph. Figure 6 c and d show the pictures after exposure at 700 °C. The samples were Ni-coated before the metallographic preparation. In the micrographs the resin appears as a dark layer on top of the pictures, followed by the fair appearing Ni-coating. After exposure at 700 °C for 1 000 h (Figure 6 d), two types of scale can be discerned between the Ni-coating and the bulk tube material at the bottom of the pictures. The micrographs reveal a continuous scale layer on the sample surfaces for both temperatures. Complementary data on mass gain during exposure does not show any spallation for both temperatures. The scale is thicker after exposure at 700 °C due to the faster oxidation kinetics at the higher temperature. The Cr-rich topotactic layer is very thin for both test conditions: after 1 000 h exposure at 650 °C the thickness is less than 1 µm. At 700 °C the maximum thickness of the inner scale is less than 20 µm, respectively. Figure 6 e and f display a comparison of the maximum thickness of the topotactic layer between the advanced austenitic grades for boiler applications UNS S30432, and TP310HCbN steels. The Tubacex's material is compared to commercial reference samples which were run in the same test series. Though minor differences are visible between Tubacex and competitors' materials: the performance is comparable within the usual scatter of the experimental setup. The two low Cr grades UNS S30432 (Tubacex and reference) exhibit a comparable oxidation resistance. The thickness of the inner oxide layer is significantly higher after the exposure at 700 °C compared to the exposure at 650 °C for 1 000 h due to the temperature influence. The high Cr grade TX310HCbN and the reference show a significantly better oxidation performance compared to the low Cr grade at both temperatures. These observations confirm the positive influence of the increased Chromium content on the oxidation performance reported e.g. in [5]. The oxidation performance of the Tubacex steel TX310HCbN is comparable to reference samples of the same grade.
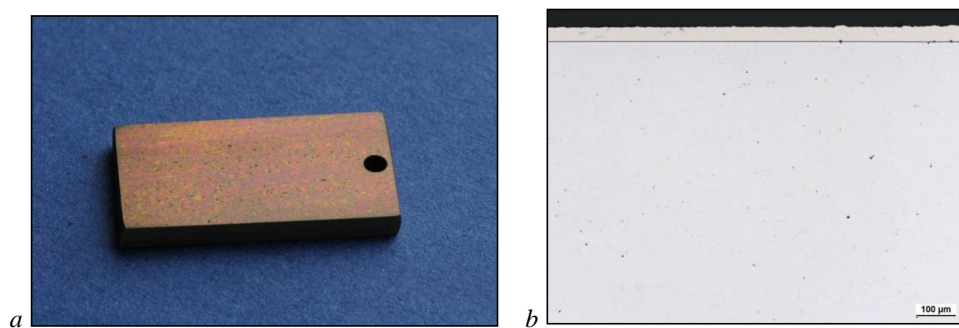
a) Macropicture of TX310HCbN steel and b) Metallographic cross section after 1000h exposure at 650 °C in Ar-50%H_2O.

c

d
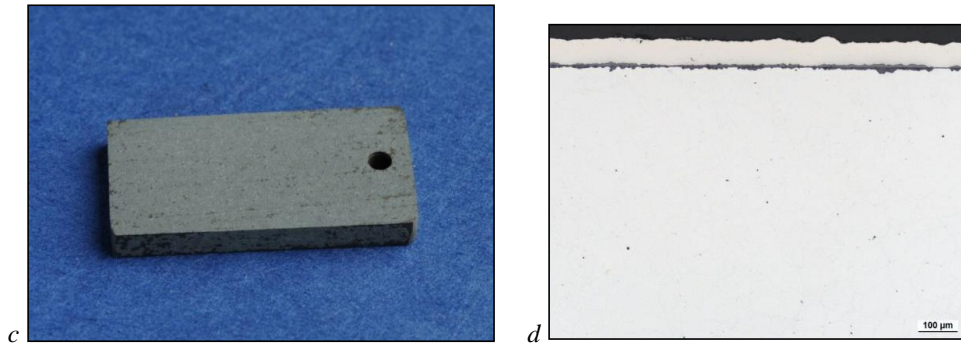
c) Macropicture of TX310HCbN steel and d) Metallographic cross section after 1 000 h exposure at 700 °C in Ar-50%H_2O.

e

f
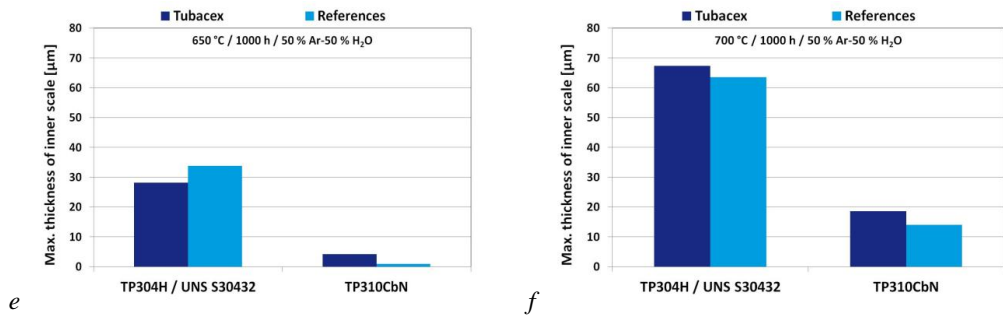
Maximum measured thickness of inner scale after 1 000 h exposure at e) 650 °C and f) 700 °C.

Figure 6 : Results of oxidation tests.

6. Bending

To characterize the bending behavior of TX310HCbN a test matrix was elaborated by the joint Tubacex-Vallourec R&D team.

Bending trials according to the requirements of EN 12952-5 were carried out on tubes of dimensions OD x WT [mm] 51.0 x 9.0. The bending was done with axial thrust to an angle of 180° at room temperature with radii from 51 mm to 200 mm, i.e. OD/R ratios from 1.0 to 3.9 representing soft to severe bending conditions. No lubricant or interior tooling was used. The characterization comprised visual inspection, liquid penetrant test, deviation from circularity and evaluation of the thickness.

As a conclusion the cold bent tubes of TX310HCbN fulfilled the requirements of EN 12952-5 for the studied bending conditions. Complementary R&D activities include the study of the resulting creep properties to evaluate the necessity of post bending heat treatments.

347

7. Welding

Technological tests were carried out to characterize the welding behavior of TX310HCbN. Therefore an audited qualification test program was successfully run at an external laboratory. As a result a welding procedure specification was established according to EN ISO 15609-1. All requirements were met to be listed in VdTÜV data sheet 546 for the grade X6CrNiNbN25-20.

Further weldability studies have been conducted at the Belgian Welding Institute (Zwijnarde, Belgium) in coordination with Vallourec. Representative thermal simulations were done of the heat affected zone in similar and dissimilar welds with post welding heat treatment (PWHT). The results proved that the performance of TX310HCbN is in line with the state of the art. Crack free welding of TX310HCbN and operation in the specified service conditions are possible. Furthermore similar and dissimilar welds to T92 were carried out by tungsten inert gas welding (TIG) with filler materials Thermanit 617 and Thermanit Nicro 82. All tests according to EN ISO 15614-1 were passed, complementary creep tests are ongoing.

8. Conclusion

The technology of Ultra Super Critical (USC) power plants implies severe conditions for boiler construction and service. It requires challenging performance of the used materials in terms of corrosion, oxidation and creep performance. In order to meet those challenging conditions TUBACEX S.A. announces the commercial release of the advanced austenitic boiler grade TX310HCbN which is the commercial designation for TP310HCbN (ASME SA 213 / UNS S31042). In cooperation with Vallourec, a robust production route was established to produce the high-Cr grade TX310HCbN with optimized properties. Additional qualification for VdTÜV datasheet 546 is ongoing. Therefore an exhaustive and audited qualification program was launched. All short term results fulfill the requirements, the ongoing creep tests have passed 3000h.

9. References

[1]   J.M. Sarver, J.M. Tanzosh, The steamside oxidation behaviour of candidate USC materials at temperatures between 650 °C and 800 °C, in: Proc. 5th Int. Conf. on Advances in Materials Technology for Fossil Power Plants, R. Viswanathan, D. Gandy, K. Coleman (Edts), pp. 471-487, 2008.
[2]   R. Uerlings, U. Bruch, H. Meyer, VGB Powertech, No. 3, pp. 43-49, 2008.
[3]   A. Iseda, H. Okada, H. Semba, M. Igarashi, in: Proc. 5th Int. Conf. on Advances in Materials Technology for Fossil Power Plants, R. Viswanathan, D. Gandy, K. Coleman (Edts.), pp. 185-196, 2008.
[4]   R. Viswanathan, W.T. Bakker, Materials for boilers in ultra supercritical power plants, Proc. 2000 Int. Joint Power Generation Conf., Miami Beach, Florida, US, July 23-26, 2000.
[5]   Y.Sawaragi, H.T., A.Iseda, K.Yoshikawa, The Development of New Stainless Steel Tubes with High Elevated Temperature Strength for Fossil Power Boilers and Chemical Plants. The Sumitomo Search, Vol. 44, pp. 146-158, 1990.

THE INFLUENCE OF DEFORMATION ON THE PRECIPITATION BEHAVIOR OF A FERRITIC STAINLESS STEEL

Z W Hsiao[1], B Kuhn[2], S M Yang[3], L C Yang[1], S Y Huang[1], L Singheiser[2], J C Kuo[1], D Y Lin[4*]

[1]Department of Materials Science and Engineering, National Cheng-Kung University, 701 Tainan, Taiwan, R.O.C.

[2]Forschungszentrum Jülich GmbH, Institute of Energy and Climate Research (IEK), Microstructure and Properties of Materials (IEK-2), 52425 Jülich, Germany

[3]Technical Department, Thintech Materials Technology Corporation, Kaohsiung 821, Taiwan (ROC)

[4]Department of Chemical and Materials Engineering, National University of Kaohsiung, 811 Kaohsiung, Taiwan, R.O.C.

Contact e-mail: dylin@nuk.edu.tw

Abstract

Uniform precipitation of intermetallic Laves phase particles is crucial for optimum performance of a new type of high performance ferritic stainless steels for high temperature application. The present paper is focused on the impact of thermomechanical pre-treatment on particle microstructure. Cold worked specimens with different deformation ratios of 0 %, 3 %, 6 % and 10 % were prepared, precipitation heat treated at 700 °C for 10 hours and subsequently observed for precipitate type and size distribution.

Microstructural analysis proved that there was no significant change in the size and number of MX type precipitates (TiN and NbC) after cold deformation and heat treatment, but indicated that the mean particle size of the strengthening Laves phase particles can be reduced from appr. 200 nm (without cold-working) down to 50 nm by cold-working. Ambient temperature pre-deformation homogenizes the dispersion and strongly increases particle number, which is obviously caused by the introduction of nucleation sites. Cold-worked specimens achieved strongly improved strength in first intermediate stress creep experiments.

Keywords: Ferritic stainless steels, thermomechanical treatment, Laves phase, strengthening, creep

1.   Introduction

Ferritic/martensitic steels are common materials for the application in thermal power plants [1]. High-strength ferritic 9-12% Cr martensitic-ferritic steels, usually with a tempered

martensitic structure, strengthened by precipitation of MX-type carbonitrides and carbides [2], are utilized in high-pressure steam pipes, headers, superheaters and reheaters (SH/RH). However, the tempered martensite microstructure is not stable, causing a decline in creep strength during long-term operation [3]. Furthermore the comparatively low content of chromium limits the steam oxidation resistance of $9 - 12$ Cr steels and for this reason their application temperature to currently appr. 610 °C [1]. For these reasons new materials with improved creep strength and enhanced resistance to steam oxidation and corrosion have to be developed.

According to dislocation theory [4], plastic deformation is caused by the movement of dislocations. Materials can be strengthened by solid solution and/or the "Orowan mechanism", i.e. by precipitation of secondary phase particles. Both solutions hinder dislocation movement. Obstructing dislocation movement thus is the major goal in the design of creep resistant steels. This can for example be reached by tuning the type, amount, size distribution and stability of precipitates [5, 6].

A new type of 22% (wt.%) Cr ferritic steel, named Crofer® 22 APU was developed by Forschungszentrum Jülich IEK-2 and Outokumpu VDM (formerly ThyssenKrupp VDM) for application as an interconnector material [7] in high temperature solid oxide fuel cells (SOFCs). In order to improve creep resistance in the temperature range from 700 °C to 800 °C and to reduce production costs, W, Nb and Si have been added to the original Crofer® 22 APU composition, resulting in the new steel grade Crofer® 22 H [8]. Both steels exhibit excellent resistance to oxidation at high temperature because of their comparatively high contents of chromium, but Crofer® 22H reveals increased creep strength on the basis of combined solid solution (mainly by W) and precipitation strengthening by intermetallic Laves phase $(Fe,Cr,Si)_2(Nb,W)$ particles [9-11].

Combined solid solution / particle strengthening are also the strengthening mechanisms in state of the art ferritic-martensitic 9-12 Cr steels. However in contrast to the novel high chromium materials discussed here, these materials are strengthened by MX-type particles (carbides, nitrides and carbonitrides) and the intermetallic Laves phase [12-16] is mostly regarded as a detrimental phase, because it drags W from the matrix and thus decreases solution strengthening.

The 9-12 Cr steels undergo martensitic transformation during cooling from austenitization temperature, which increases the materials dislocation density (responsible for short-term strengthening contribution) and creates a large number of preferred nucleation sites for subsequent precipitation during tempering. Fully ferritic steels like Crofer® 22 H do not undergo martensitic transformation during cooling from hot-rolling, but the impact of initial

350

dislocation density on particle microstructure and creep strength of Crofer 22 H like steels is a major one [10, 17]. For this reason, a smart combination of hot-rolling, cooling and precipitation heat-treatment parameters is mandatory to create an optimum mechanical property profile of the resulting material. Because such high performance ferritic steels are comparatively new, nothing is known about their thermomechanical treatment. The present paper outlines a first approach to tune particle microstructure and precipitation heat-treatment to give favorable creep strength.

2. Experimental

Commercial Crofer® 22 H manufactured by Outokumpu VDM by conventional arc melting was investigated in this study. The material was hot-rolled at 980 °C to a final sheet thickness of 12 mm, solution annealed at 1075 °C for 22 minutes and air cooled to ambient temperature resulting in an equi-axed grain structure with a mean grain size of appr. 110 μm. Tensile specimens with 6 mm in gauge diameter and 30 mm in gauge length were machined from the plate material. Cold deformation was accomplished by ambient temperature tensile deformation with a constant strain rate of $5 \times 10^{-3} s^{-1}$ up to plastic strains of 3, 6 and 10 %.
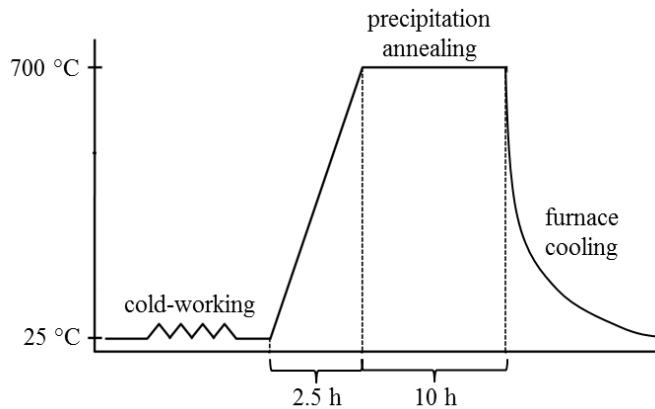

Fig. 1: Schematic of cold-working and precipitation treatment procedure

After cold-working, samples for heat treatment with / without cold-working were cut from the gauge sections / heads of the tensile specimens and then precipitation annealed at 700 °C for 10 h (Fig. 1; specimen identifiers summarized in Tab. 1). After annealing the samples were ground using SiC paper, polished in diamond suspension and electrolytically etched to enhance the particle / matrix contrast. Light optical micrographs (OM) were taken for the evaluation of average grain size. Particle size distribution and precipitate morphology were

characterized utilizing a Zeiss Merlin high resolution field emission scanning electron microscope (FESEM) equipped with energy dispersive X-ray spectroscopy (EDS) for chemical analysis.

Tab. 1: Specimen identifiers of annealing specimens with / without cold working

Amount of cold-work	0 %	3 %	6 %	10 %	0 %	3 %	6 %	10 %
Precipitation treatment	-	-	-	-	700 °C, 10 h	700 °C, 10 h	700 °C, 10 h	700 °C, 10 h
Specimen ID	0%	3%	6%	10%	0%PA	3%PA	6%PA	10%PA

3. Results and discussion

3.1 Initial microstructure

According to ASTM standard E112-10 the solution annealed material ('0%', without cold-working and heat treatment) presents an average grain size of 128 μm. A small variation of grain size was encountered in specimens '3%' to '10%' and '3%PA' to '10%PA' because of plastic pre-deformation (caused by the longitudinal elongation of grains, discussed in section 3.2). Few small primary (sizes from 2 to 10 μm) TiN, NbC and (Ti,Nb)(C,N) particles already form in the melt and disperse randomly at grain boundaries and grain interiors. Furthermore few, but very fine intermetallic $(Fe,Cr,Si)_2(Nb,W)$ Laves phase precipitates (Fig. 2) can be found in the grain interiors, which form during comparatively slow cooling after solution treatment (1075 °C, 22 Min.).
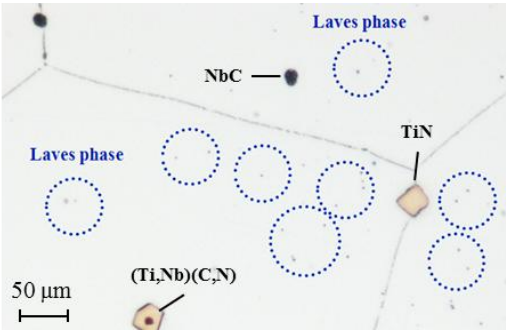

Fig.2: Typical initial microstructure of solution annealed commercial Crofer® 22 H (specimen '0%')

3.2 Microstructure after annealing

3.2.1 Primary precipitates and grain size

The primary precipitates did not undergo noteworthy changes during precipitation annealing. Fig. 3 shows a typical backscatter electron image and the chemical composition of such particles. EDX mappings taken before and after annealing confirmed the precipitates to be composed of Ti, Nb, C and N (cf. Fig. 3).
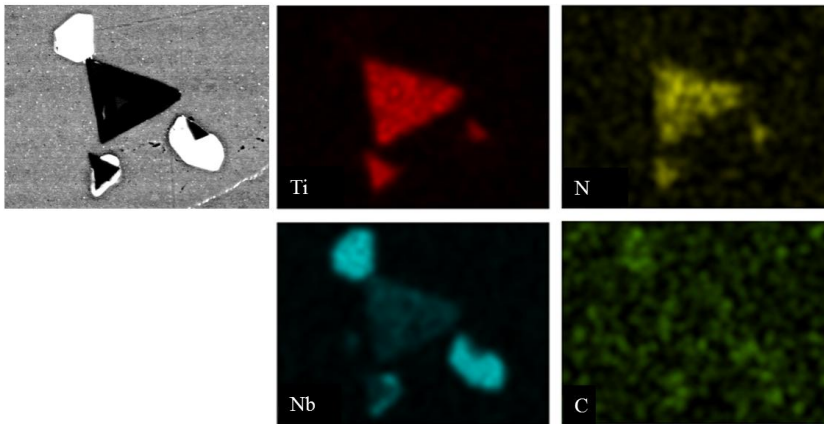

Fig. 3: Typical BSE micrograph and chemical composition of MX-type particles.

The grain size evolution with increasing degrees of ambient temperature pre-deformation is similar for the material before and after precipitation annealing (e. g. Fig. 4).
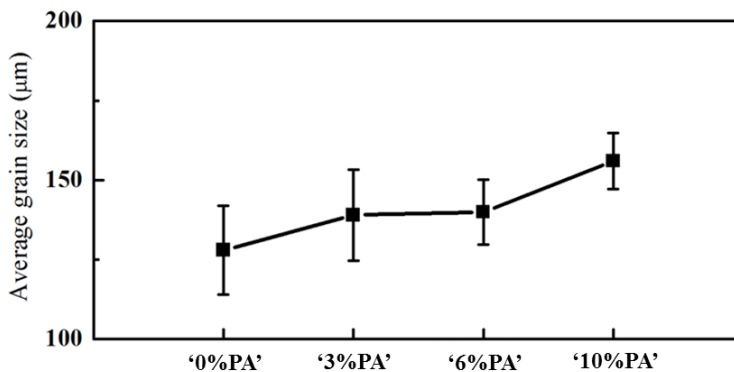

Fig.4: Variation of average grain size with pre-deformation (similar before and after precipitation annealing)

Precipitation treatment thus does not induce any changes in the grain structure. Within the range of scatter the slight upward trend in average grain size corresponds well with the elongation of grains by increasing amounts of cold-work. Both stored plastic deformation energy and precipitation treatment temperature are too low to induce recrystallization or grain growth. Furthermore, nucleating Laves phase particles block grain boundaries and dislocations, and effectively hinder them in movement.

3.2.2 Impact of cold-work on precipitation of the Laves phase and creep performance

a)   *b)*

c)   *d)*
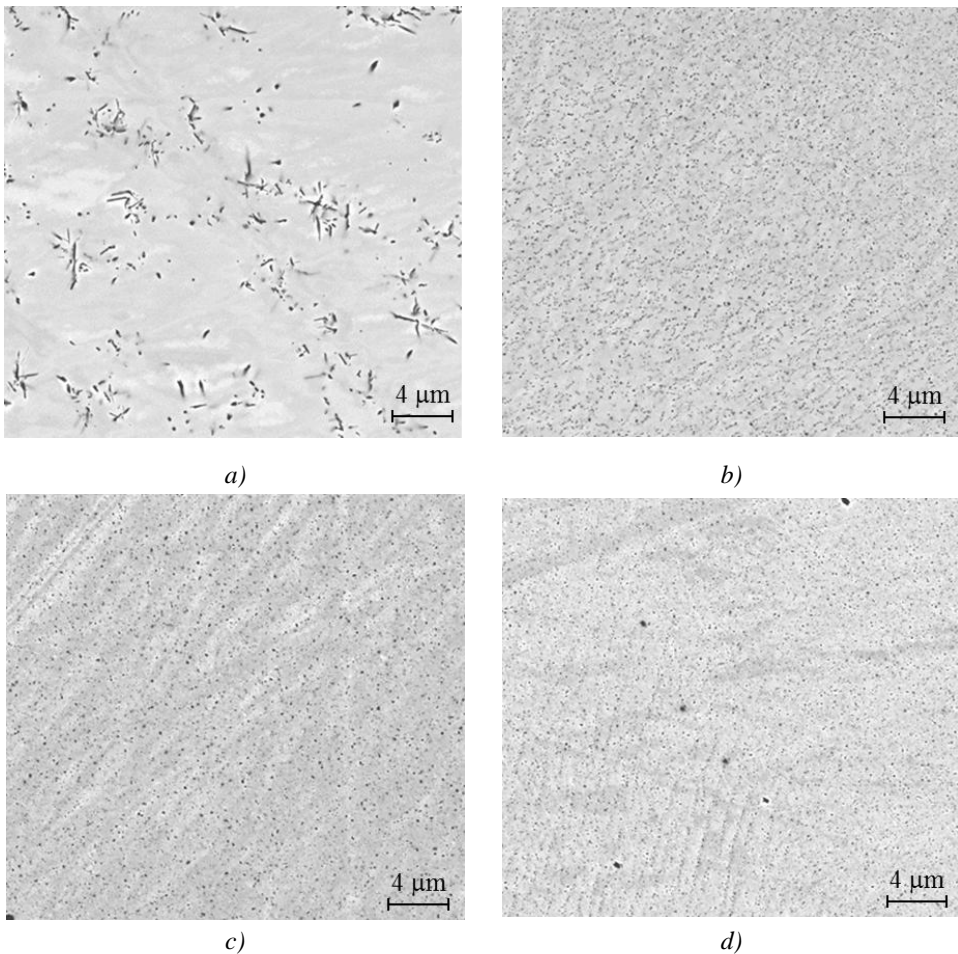
Fig. 5: Particle microstructure after precipitation annealing: Without cold-working (a: '0%PA'), with 3 % (b: '3%PA'), 6 % (c: '6%PA') and 10 % (d: '10%PA') of deformation (FESEM images, inverted for better contrast)

To outline the impact of cold-working on Laves phase precipitate morphology, number and size distribution, detailed high resolution SEM characterization was undertaken, which unveiled the grain boundaries to be decorated and the grain interiors to be occupied by large numbers of fine Laves phase particles (Fig. 5b-d). The as-received (undeformed) material shows a small number of comparatively coarse, needle shaped Laves phase particles (Fig. 5a). Cold working thus strongly decreases the size, increases the number and changes the morphology of the Laves phase precipitates, because it boosts dislocation density (and thus the number of possible nucleation sites) and the diffusion rates of the Laves phase forming elements. Fig. 6 displays the chemical composition of the intermetallic Laves phase precipitates at the grain boundaries of specimen '3%PA' (3 % of cold-work). The EDX measurement confirms the Laves phase to contain W and Nb. Cold-working did not change the chemical composition of the Laves phase. Further in-depth examination by high resolution transmission electron microscopy would be necessary to confirm the Laves phase to contain Si [11].
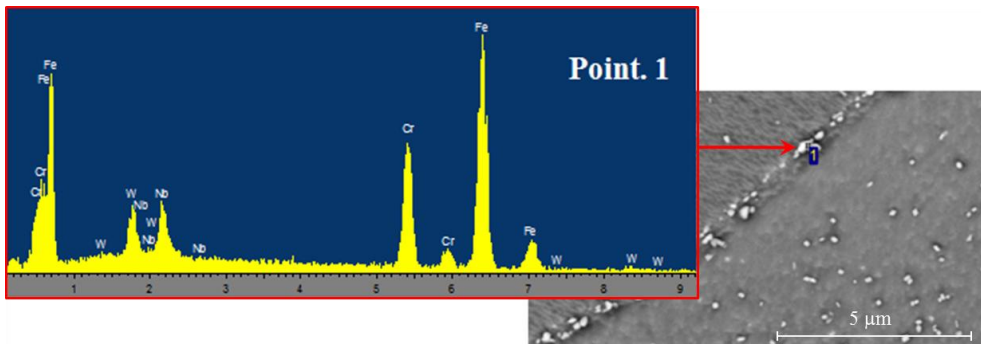

Fig. 6: Chemical composition of the Laves phase at a grain boundary

As outlined in the previous section, the particle morphology can be greatly influenced by cold-working, but increasing the degree of cold deformation beyond 3 % (Fig. 5b) only yields comparatively small further changes (Fig. 5c, d). Fig. 7 displays results from quantitative image analysis (calculated from at least 50000 particles per specimen) concerning the area fraction and the mean particle diameter after precipitation annealing at 700 °C for 10 h. The undeformed material (specimen '0%PA') exhibits the highest mean particle diameter (231 nm) and lowest particle area fraction (2,75 %). By cold-working the mean Laves phase particle diameter can be decreased from 74 nm (3 % of cold work, '3%PA') down to 52 nm (10 % of cold work, '10%PA'), coinciding with an increase in particle area fraction to values in the range of 5.2 – 5.5 %.
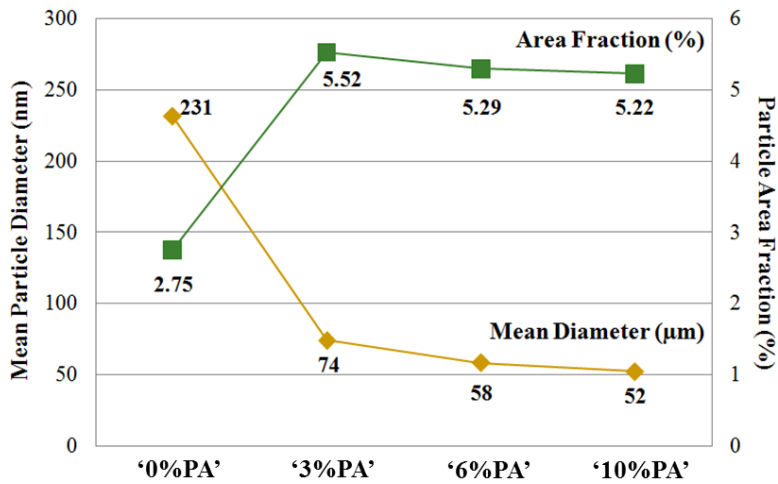
Fig. 7: Variation of mean particle size and area fraction with increasing amount of cold-work:
0 % ('0%PA'), 3 % ('3%PA'), 6 % ('6%PA') and 10 % ('10%PA')

To evaluate the influence of the changes in particle size, number and interparticle spacing on the creep properties, constant load creep experiments were conducted. Fig. 8 displays the response of commercial Crofer® 22 H in three different thermomechanical treatment states to an initial creep stress of 120 MPa at 600 °C. Apparently the pre-treatment state has a strong impact on creep resistance. Solution annealed material failed after only 106 hours of testing. Precipitation annealing prior to creep testing ('0%PA') leads to even shorter rupture time of 62 hours, while cold-working is very effective in enhancing creep strength ('3%' experiment in progress; '0%' and '3%' data partly replotted from [10]). The direct comparison to P92 at a lower stress of 100 MPa demonstrates the great potential of this kind of new steel. A variety of different thermomechanical

pre-treatment parameter sets is still under evaluation in running creep experiments.
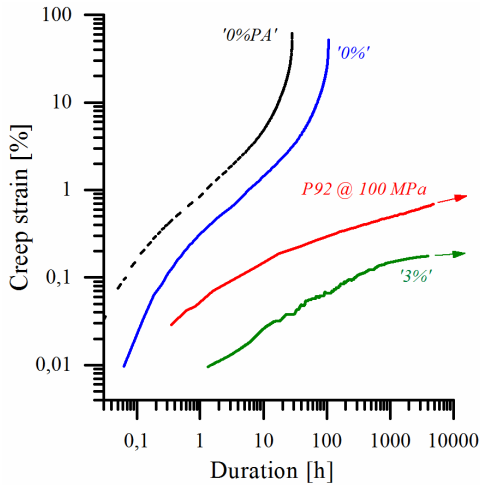

Fig. 8: Creep curves of Crofer® 22 H (600 °C, 120 MPa): Solution annealed ('0%'), precipitation annealed ('0%PA') and cold-work by 3% ('3%') in comparison to P92 at 100 MPa

4. Conclusion

Fully ferritic steels do not undergo martensitic transformation during cooling, but initial dislocation density has a strong influence on the precipitate microstructure and resulting mechanical properties (i. e. creep strength) of such steels. For this reason proper thermomechanical treatment (hot-rolling, cooling and precipitation heat-treatment parameters) is mandatory in order to obtain optimal technological and mechanical properties of the resulting material. Mean Laves phase precipitate size and area fraction in commercial Crofer® 22 H, a high chromium fully ferritic steel, were characterized in terms of sensitivity to thermomechanical treatment state. The results show that by ambient temperature pre-deformation, with / without precipitation annealing the mean size and area fraction of strengthening Laves phase particles can be effectively altered in order to enhance creep strength. In this way, varying the thermomechanical treatment parameters offers a high degree of freedom in matching the mechanical property profile of Laves phase strengthened, fully ferritic, high chromium steels to different future applications.

References

[1]   R. Viswanathan, W. Bakker, Materials for ultrasupercritical coal power plants-boiler materials: Part 1, *Journal of Materials engineering and performance*, Vol.10, pp.81-95, (2001)

[2]   H. Cerjak, P. Hofer, and B. Schaffernak, The influence of microstructural aspects on the service behavior of advanced power plant steels, *ISIJ International*, Vol.39, pp.874-888, (1999)

[3]   K. Kimura, H. Kushima, and F. Abe, Heterogeneous changes in microstructure and degradation behavior of 9Cr-1Mo-V-Nb steel during long term creep, *Key Engineering Materials*, Vol.171-174, pp.483-490, (2000)

[4]   R. E. Reed-Hill, R. Abbaschian, Physical Metallurgy Principles 3rd edition, *PWS Publishing Company, Boston,* (1991)

[5]   R.D.K. Misra, G.C. Weatherly, J.E. Hartmann, and A.J. Boucek, Ultrahigh strength hot rolled microalloyed steels: Microstructural aspects of development, *Materials Science and Technology*, Vol.17, pp.1119-1129, (2001)

[6]   A.J. Craven, K. He, L.A.J Garvie, and T.N. Baker, Complex heterogeneous precipitation in titanium-niobium microalloyed Al-killed HSLA steels - I. (Ti,Nb)(C,N) particles, *Acta materilia*, Vol.48 , pp.3857-3868, (2000)

[7]   Crofer® 22 APU, *Material Data Sheet No.4046*, (2010)

[8]   Crofer® 22 H, *Preliminary Material Data Sheet No.4050*, (2008)

[9]   B. Kuhn, C.A. Jimenez, L. Niewolak, T. Huettel, T. Beck, H. Hattendorf, L. Singheiser, and W.J. Quadakkers, Effect of Laves phase strengthening on the mechanical properties of high Cr ferritic steels for solid oxide fuel cell interconnect application, *Materials science and engineering A*, Vol.528, pp.5888-5899, (2011)

[10]   B. Kuhn, M. Talik, J. Zurek, T. Beck, W. J. Quadakkers, L. S. Singheiser, H. Hattendorf: Development of high chromium ferritic steels strengthened by intermetallic phases. *Proceedings from the 7th EPRI International Conference on Advances in Materials Technology for Fossil Power Plants, Hawaii, 22-25 October,* 1081 -1092, (2013)

[11]   B. Kuhn et al: Development of high chromium ferritic steels strengthened by intermetallic phases. *Materials Science and Engineering A*, 594, 372-380, (2014)

[12]   H.K.D.H. Bhadeshia, Design of ferritic creep-resistant steels, *ISIJ International*, Vol.41, pp.626-640, (2001)

[13]   PJ Ennis, A Czyrska-Filemonowicz, Recent advances in creep-resistant steels for power plant applications, *Sadhana*, Vol.28, pp.709-730, (2003)

[14]   K Maruyama, K Sawada, and J Koike, Strengthening mechanisms of creep resistant tempered martensitic steel, *ISIJ International*, Vol.41, pp.641-653, (2001)

[15]   O. Prat, J. Garcia, D. Rojas, C. Carrasco, and A.R. Kaysser-Pyzalla, Investigations on coarsening of MX and $M_{23}C_6$ precipitates in 12% Cr creep resistant steels assisted by computational thermodynamics, *Materials Science and Engineering A*, Vol.527, pp.5976-5983, (2010)

[16]   D. Rojas, J. Garcia, O. Prat, C. Carrasco, G. Sauthoff, and A.R. Kaysser-Pyzalla, Design and characterization of microstructure evolution during creep of 12% Cr heat resistant steels, *Materials Science and Engineering A*, Vol.527, pp.16-17, (2010)

[17]   S. Brett, B. Kuhn, J. Rantala, C. Hyde: Impression Creep Testing for Material Characterization in Development and Application. *Proceedings of the 10th Liége conference on Materials for Advanced Power Engineering, Liége, Belgium, 14-17 September (2014)*

Part C

Manufacturing, Processing and Examination

DEMONSTRATION OF HETEROGENEOUS WELDING OF NICKEL-BASED ALLOYS IN MANUFACTURE OF FULL-SCALE WELDED ROTOR FOR A−USC TURBINE

S. Hreben, P. Vitek, V. Polivka

Doosan Škoda Power, Ltd., Tylova 57, 31600 Plzen, Czech Republic
E-mail: stanislav.hreben@doosan.com

Abstract

Carbon Capture and Storage (CCS) has become promising technology to reduce CO_2 emissions. However, as a consequence of CCS installation, the electrical efficiency of coal fired power plant will drop down. This phenomenon requires increase in base efficiency of contemporary power plants. Efficiency of recent generation of power plants is limited mainly by maximum live steam temperature of 620°C. This limitation is driven by maximal allowed working temperatures of modern 9−12% Cr martensitic steels. Live steam temperatures of 750°C are needed to compensate the efficiency loss caused by CCS and achieve a net efficiency of 45%. Increase in the steam temperature up to 750°C (A-USC turbine) requires application of new advanced materials. Precipitation hardened nickel-based superalloys with high creep-rupture strength at elevated temperatures are promising candidates for new generation of steam turbines operating at temperatures up to 750°C. Manufacture of welded IP turbine rotor combining nickel-based A263 with 10% chromium martensitic steels is showed in this paper. Development of welding procedure for above mentioned material combination is presented. Structure, microstructure and mechanical properties of prepared heterogeneous weld joints are investigated. Full-scale rotor welding in material combination A263 + 10%Cr martensitic steel is demonstrated.

Keywords: A-USC turbine, nickel-based alloys, creep resistance, heterogeneous welding

1. Introduction

Reduction of CO_2 emissions is one of the main goals of EU in the next years. Particularly, 20% reduction will be required by EC in 2020. To reduce CO_2 emissions to mentioned level, implementation of Carbon Capture and Storage (CCS) in coal power plants is needed. However, application of CCS technology is related with decrease of power plant efficiency. To compensate this decrease in efficiency, higher temperatures of live steam flowing through turbine are needed. Of course, higher steam temperature has significant impact on material selection for boiler and turbine components. Live steam temperatures of 700 − 750°C call for application of nickel-based superalloys with sufficiently high creep rupture strength at $750°C/10^5h$ [1,2]. NEXTGENPOWER is unique international collaborative project demonstrating application of new alloys and coatings in boiler, turbine and interconnecting pipework and should show new directions in design of A-USC power plant. In this project, precipitation hardened gamma-prime nickel-based alloy Nimonic 263 (A263) was selected as a promising material for high pressure (HP) steam turbine rotor. In the case of intermediate pressure (IP) steam turbine rotors, it is really demanded to master dissimilar weld joint of nickel-based alloys with advanced 9-12% Cr martensitic steels in order to manufacture welded IP rotor. Based on the heat balance calculations of NEXTGENPOWER A-USC power plant, inlet steam temperature of IP turbine is 750°C. However, IP turbine outlet stem temperature is around 350°C. Thus, it is not necessary to manufacture whole IP turbine rotor from A263 as a single piece, but combine this material with less expensive

9-12% Cr martensitic steels that can be applied in less hot section of IP turbine, see Figure 1. This will significantly reduce the price of turbine set. Manufacture of welded rotors combining 10% Cr and low alloy martensitic steels has been developed and demonstrated [3-4].

With respect to A263, similar weld joint has been mastered in past [5]. Recommended approach is to weld this material in solution treated condition. As a filler metal, Nimonic 263 is typically used. Precipitation hardening 800°C/8hours should be applied after welding to achieve sufficiently high tensile and creep strength of both base material and filler metal. This approach cannot be used for dissimilar weld joint of A263 with 9-12% Cr martensitic steel because of too low tempering temperatures of 9-12% Cr steel (650 – 710°C). If temperature of post-weld heat treatment (PWHT) overcomes tempering temperature of 9-12% Cr steel strength and creep properties of this steel are then negatively affected. Particularly, COST F (X14CrMoVNbN10-1) martensitic steel with tempering temperatures around 700°C was chosen as a rotor material for less hot section of IP turbine in this project because of its very good creep properties up to 600°C.
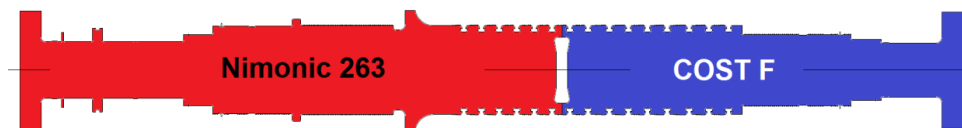

Figure 1: Dissimilar weld joint Nimonic 263 + COST F applicable for IP turbine of A-USC power plant.

With respect to above mentioned aspects, A263 has to be welded in precipitation hardened condition (800°C/8h) in the case of dissimilar weld joint A263 + COST F, because precipitation hardening cannot be carried out after welding due to tempering temperatures (approx. 700°C) of COST F steel on the other side of the weld joint. Heterogeneous welding of A263 + COST F was carried out by Doosan Skoda Power, Ltd. in this project. TIG hot wire narrow gap welding was used to demonstrate manufacture of welded rotor.

2. Experimental

All presented homogeneous and heterogeneous weld joints were manufactured by TIG hot wire narrow gap welding. Unique experimental welding stand allowing welding of rotor parts in vertical position was used. Welding head was kept in fixed position whereas the welded samples rotated on the table. Example of the welded samples in vertical configuration on the table of the experimental welding stand is shown on Figure 2. Weld joints with diameter ≤300 mm were welded on experimental welding stand. For higher diameters, production welding stand was used. Nickel-based welding consumable not requiring post-welding precipitation hardening was used. Two different welding torches V2 and WP27 were applied for root and filling passes, respectively. Development of welding procedure had two phases. Firstly, homogeneous weld joint A263 + A263 was investigated in order to explore weldability of A263 in precipitation hardened condition and to optimize PWHT of filler metal and HAZ between A263 and filler metal. Samples with diameter of 160 mm were used. In

second phase, welding of heterogeneous combination A263 + COST F was carried out for samples with diameter of 300 and 500 mm, respectively. Typical welding depth was 100 mm.

Figure 2: Configuration of welding samples Nimonic 263 + Nimonic 263 Ø160 mm on experimental welding stand with narrow gap torch.

In the case of similar weld joint A263 + A263, no pre-heating was applied on welded samples. The interpass temperature was kept below 100°C in order to avoid hot cracking. Welding parameters found for homogeneous combination A263 + A263 were used as a background for welding of heterogeneous combination A263 + COST F. In the case of heterogeneous combination A263 + COST F, two approaches, with and without cladding of COST F with nickel-based cladding metal, were applied. Pre-heating of COST F was used during welding process without cladded COST F. In the case of option with cladded COST F, pre-heating of COST F discs was used during cladding process. However, no pre-heating of cladded COST F was applied during heterogeneous welding A263 + COST F. For both variants with/without cladded COST F, interpass temperature was kept as low as possible during main weld operation. PWHT of welded samples was carried out in electric furnace at controlled temperatures and durations. Macrostructure and microstructure evaluation, tensile, hot tensile test and Charpy impact test and short-term creep tests were performed for manufactured weld joint.

Numerical analysis of plastic strains was done by SYSWELD 2013.0 tool. 2D rotationally symmetric model with diameter of welded discs of 500 mm was used.

3. Results and Discussion

3.1. *Homogeneous Weld Joint A263 + A263 Ø160 mm*

Properties of similar weld joint A263 + A263 has been investigated at first as a background for final heterogeneous weld joint A263 + COST F. A263 was welded in precipitation hardened condition. Three different PWHT were applied and compared with not heat treated weld joint. All three PWHTs were carried out with the same temperature but different duration, where time_1<time_2<time_3. Temperature of PWHT was chosen with respect to typical tempering temperatures of COST F steel used in heterogeneous combination of A263 + COST F. Results on tensile test at 20°C are shown in Fig. 3. Cap, filler and root of the weld joint were analyzed. All the samples were broken in the filler metal. As can be seen

in Fig. 3, longer PWHT leads to increase of tensile strength. This phenomenon is most likely attributed to carbide formation and precipitation of gamma prime phase in filler metal.
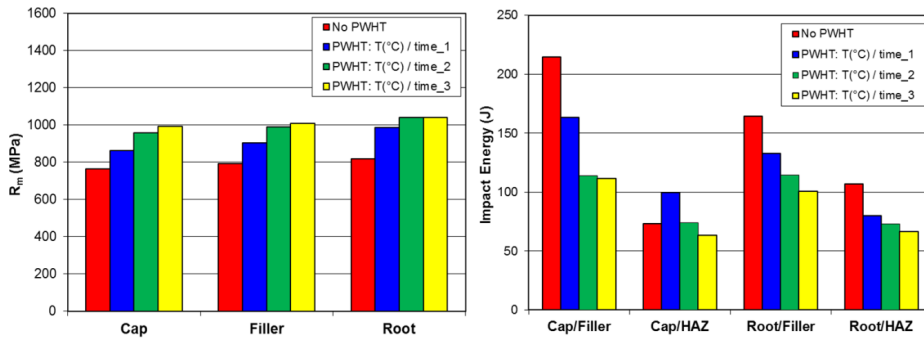

Figure 3: Room temperature tensile strength and impact energy of weld joint A263 + A263 measured for various PWHTs. Tensile properties were measured in cap, filler and root area of the weld joints. Impact energy was measured for filler metal and HAZ in root and cap area of the weld joint.

Results on Charpy impact tests are shown in Fig. 3 for various PWHTs. V-notch was placed in filler metal and heat affected zone (HAZ) for cap and root of the weld joint. As expected, decrease in impact energy is related with growing tensile strength of weld joint. Longer PWHT time leads to more strength but less ductile structure of filler metal and HAZ. From rotor design perspective, optimal combination of the strength and toughness is required. Thus, PWHT T(°C)/time_2 was chosen as the best option optimizing tensile and fracture toughness properties of filler metal and HAZ between A263 and filler metal. This PWHT was used also for heterogeneous weld joint A263 + COST F in further steps of development.
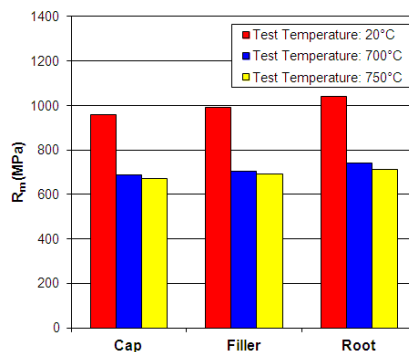

Figure 4: Tensile strength at elevated temperatures measured for homogeneous weld joint A263 + A263 treated with optimal PWHT T(°C)/time_2. Tensile properties were analyzed for cap, filler and root area of the weld joints.

For optimal PWHT T(°C)/time_2, hot tensile test at 700 and 750°C was carried out and compared to results measured at room temperature, see Fig. 4. Cap, filler and root of the weld joint were analyzed. Elevated temperatures of tensile test led to decrease of tensile strength from 1000 MPa to 700 MPa. All the samples were broken in filler metal.

3.2. Heterogeneous Weld Joint A263 + COST F Ø300 mm

To demonstrate heterogeneous welding of A263 + COST F with diameter of 300 mm, welding parameters found for homogeneous combination A263 + A263 were used. As has been indicated, two approaches were applied to master heterogeneous welding of A263 + COST F. In the first case, easier approach was chosen and COST F steel was welded without nickel-based cladding. Material A263 was used in precipitation hardened condition. In this case, it was necessary to pre-heat COST F prior and during welding process. Applied pre-heating caused difficulties in keeping of interpass temperatures below recommended 100°C, which increases risk of hot cracking.
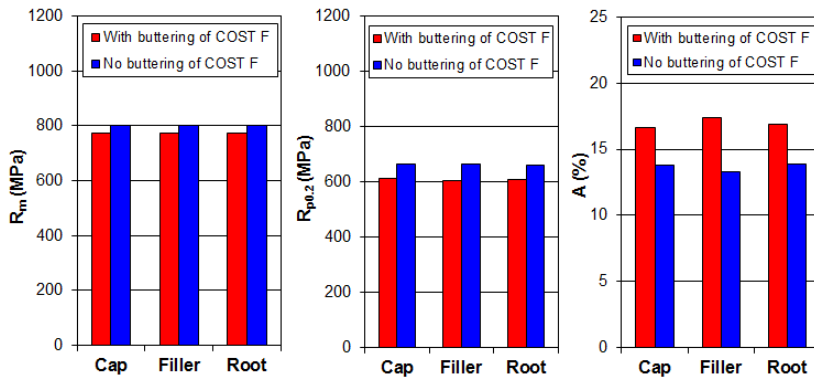

Figure 5: Tensile test results of dissimilar weld joint A263 + COST F carried out at room temperature for both variants with/without cladding of COST F.

In the second case, pre-heated COST F was cladded with nickel-based cladding metal at first. After cladding process, stress relief heat treatment was carried out. Then, the nickel-based cladding of COST F was machined down to required shape of the bevel. Welding of A263 and cladded COST F was performed without preheating of cladded COST F counter piece. This approach enables to keep interpass temperatures as low as possible. For both variants, with/without cladding of COST F, optimal PWHT found for homogeneous weld joint A263 + A263 was used to relief the internal stresses.

Results of room temperature tensile test are shown on Fig. 5 for both variants with/without cladding of COST F. All the samples were broken in COST F base material, which indicates that tensile strength of filler metal is higher than tensile strength of COST F base material. Thus, COST F is the weakest material in heterogeneous weld joint from the tensile strength point of view. Furthermore, tensile test of both variants of weld joints showed that tensile strength of COST F after welding operation and application of PWHT are lower than those of the same material prior welding, see $R_m = 750 - 800$ MPa after welding and

PWHT compared to original $R_m = 870$ MPa. This decrease of tensile and yield strength of COST F after welding is most likely related with PWHT of weld joint at temperatures very close to tempering temperature of COST F base material. Moreover, approach with cladding of COST F provides slightly lower tensile and yield strength then approach without cladding. This can be explained by longer exposition of COST F base material during PWHT to temperatures close to tempering temperature of COST F for variant with cladding of COST F. Particularly, two PWHTs, one for cladding and one for whole weld joint, were applied. On the other hand, only one PWHT was used for variant without cladding of COST F. From perspective of tensile properties and complexity of weld joint manufacture, variant without cladding of COST F is simpler and provides higher tensile strength at still sufficient elongation.
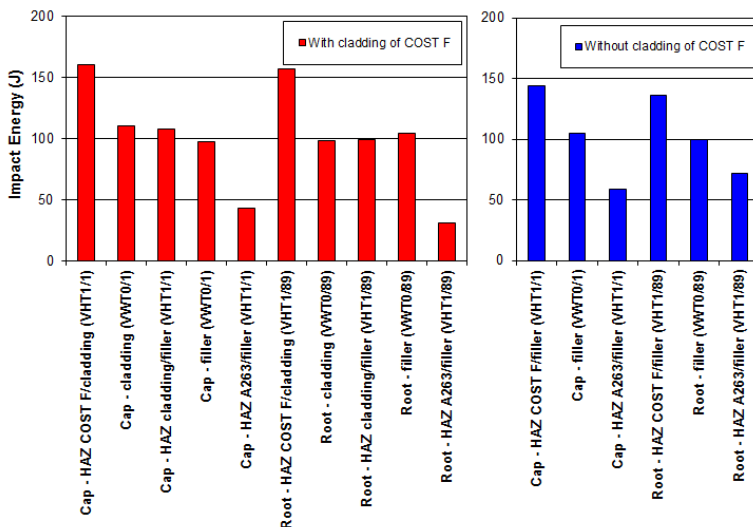

Figure 6: Charpy impact test of dissimilar weld joint A263 + COST F carried out at room temperature for both variants with/without cladding of COST.

Results on Charpy impact test are shown on Fig. 6. V-notch was placed in various areas of the weld joints, see x-axis in Fig. 6. As can be seen, most critical area of the weld joint is HAZ between filler metal and A263 (see the lowest impact energies measured in this location for both variants with/without cladding of COST F). However, from the perspective of rotor design and structural calculations, even the lowest measured impact energies are sufficiently high and acceptable.

Macrostructure of heterogeneous weld joint A263 + COST with/without cladding of COST F is shown on Fig. 7. Cross-sections taken from three different locations were analyzed for both variants. No defects and cracks were indicated on all analyzed cross-sections. Both weld joints meet requirements of quality degree B (the highest quality) given by EN ISO 5817. Short-term creep resistance was investigated at two different temperatures, 550 and 600°C. These test temperatures were chosen based on assumed operation temperature of weld

joint in future A-USC turbine, 580°C. Aimed time-to-rupture was 1000h. Results measured on samples taken from central zone of the weld joint are summarized in Table 1. If there was breakage of certain sample, rupture zone was always located in COST F base material. The same behaviour was observed also for samples acquired from root and cap zone of the weld joints.
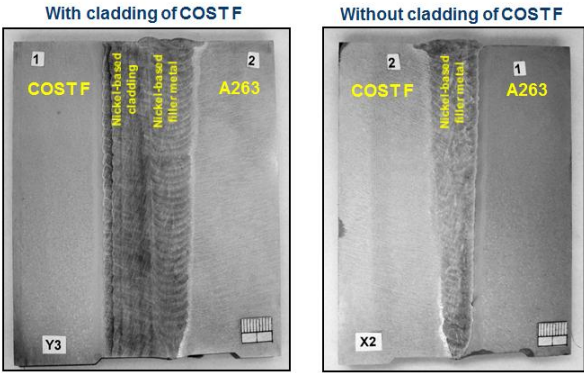

Figure 7: Macrostructure of dissimilar weld joint A263 + COST F taken for both variants with/without cladding of COST F.

	Temperature (°C)	Stress (MPa)	Without Cladding on COST F		With Cladding on COST F	
			Test Time (h)	Fracture	Test Time (h)	Fracture
	550	220	1223	No	1007	No
	550	220	1001	No	1007	No
	550	220	Ongoing	---	Ongoing	---
Central zone	600	160	116	COST F base material	1007	No
	600	160	1003	No	246	COST F base material
	600	160	Ongoing	---	Ongoing	---
	600	160	Ongoing	---	181	COST F base material

Table 1: Short-term creep properties of weld-joint A263 + COST F. Creep tests were carried out at temperatures 550 and 600°C with target time-to-rupture 1000h.

3.3. Heterogeneous Weld Joint A263 + COST F Ø500 mm

Experiences achieved during welding of A263 + A263 and A263 + COST F on experimental equipment were transferred to production welding stand which is typically used for manufacture of real welded rotors in Doosan Skoda Power, Ltd. Material combination A263 + COST F with diameter of 500 mm was welded. Both variants with/without cladding of COST F were examined again. Optimized A263 with increased creep rupture strength and improved structural stability was used in this case. Welding process is showed on Figure 8. Comprehensive mechanical testing of both weld joints is ongoing now.

Figure 8: Welding of A263 + COST F Ø500 mm. Two counterpieces before welding (a), welding process (b), finished weld joint (c).

Numerical simulation of distribution of plastic strains across the weld joint was carried out for both variants (with/without cladding of COST F) of A263 + COST F Ø500 mm weld joint. PWHT was also taken into account in the simulation. Weld joint processed without cladding exhibited lower values of plastic deformations, Figure 9. The highest values of plastic strains were found especially at transition between cladding of COST F and filler metal.
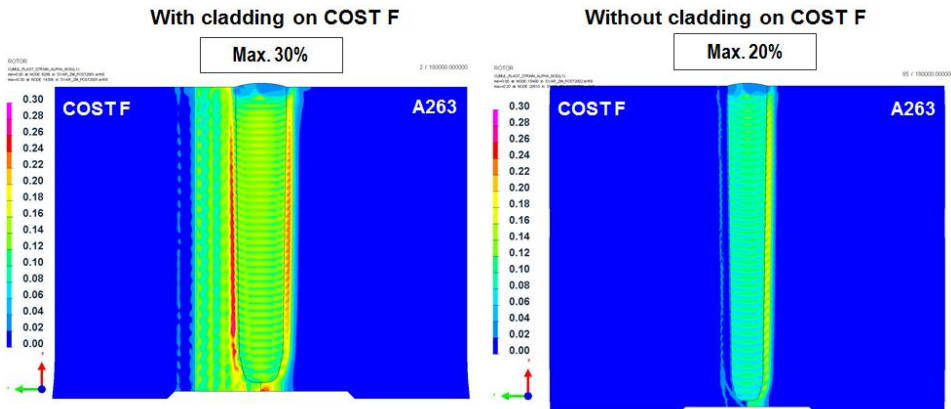

Figure 9: Numerical simulation of plastic strains after welding and PWHT of both variants with/without cladding on COST F.

3.4. Full-scale Rotor Weld Joint A263 + COST F Ø1000 mm

Next step in the NEXTGENPOWER project in term of heterogeneous rotor welding is demonstration of full-scale rotor welding on production welding stand in Doosan Skoda Power. Based on achieved experiences, heterogeneous full-scale weld joint A263 + COST F with diameter of 1000 mm will be welded and extensively tested. Base material A263 and COST F with diameter of 1000 mm has been delivered to Doosan Skoda Power and manufacture of counter-pieces has been finished. Welding process is planned for April 2014.

*Figure 10: Rings for demonstration of rotor welding taken from full-scale rotor from A263
with diameter of 1000 mm.*

4. Conclusions

It was demonstrated that Nimonic 263 can be successfully welded in precipitation hardened condition. Optimal PWHT was found for homogeneous weld joint A263 + A263 with respect to optimal combination of tensile strength and toughness. Heterogeneous welding of A263 + COST F has been mastered. Two approaches with/without cladding of COST F with nickel-based cladding metal were investigated. With respect to tensile strength, toughness, calculated plastic deformations across the weld joint and efficiency of welding process, variant without cladding of COST F seems to be more suitable approach. Macrostructure of both heterogeneous weld joints A263 + COST F with/without cladding of COST F met requirements on the highest quality degree given by EN ISO 5817. Demonstration of rotor welding in material combination A263 + COST F was mastered on production welding stand in Doosan Skoda Power, Ltd.

Acknowledgements

References

[1] N. Lückemeyer, H. Kirchner, H. Almstedt, "Challenges in advanced-USC steam turbine design for 1300°F/700°C", *Proceedings of ASME Turbo Expo 2012*, Copenhagen, Denmark, June 2012.

[2] M. Fukuda, E. Saito, Y. Tanaka, T. Takahashi, S. Nakamura, J. Iwasaki, S. Takano, S. Izumi, "Advanced USC technology development in Japan", *Proceedings of Advances in Materials Technology for Fossil Power Plants 2010*, Santa Fe, New Mexico, USA, August 2010.

[3] T. Shige, S. Itou, R. Magoshi, T. Ichimura, Y. Kondou, *"Development of Large-Capacity, Highly Efficient Welded Rotor for Steam Turbines"*, *Mitsubishi Heavy Industry Ltd. Technical review*, Vol. 38, No. 1 (2001).

[4] J. Hutchinson, R. Conroy, R. Stalker, "Fabricated Turbine Rotors for Advanced Steam Turbines", *Siemens Power Generation, Public Report*, August 2004.

[5] J. Minwoo, L. Jae-Hyun, W. T. Kwan, K. Sangshik, "Effect of Welding and Post-weld Heat Treatment on Tensile Properties of Nimonic 263 at Room and Elevated Temperatures", *Metallurgical and Materials Transactions A,* Vol. 42, No. 4 (2011), pp. 974-985.

STATE OF THE ART OF WELDING OF HIGH TEMPERATURE MATERIALS FOR MODERN POWER PLANTS

Martin Schmitz-Niederau, Olena Trunova

voestalpine Böhler Welding Germany GmbH, Unionstraße 1, 59067 Hamm, Germany

Abstract

Continuous increase in steam parameters (temperature and pressure) of fuel fired power plants requires application of improved high creep and corrosion resistant alloys for the components. Currently used steel grades could be divided in three classes depending on maximum working temperature: bainitic (T < 550 °C), martensitic (T < 620 °C) and austenitic (T < 670 °C) steels. For temperatures higher than 700 °C Ni-base alloys should be applied. For all new materials the matching filler metals must be developed and approved to fulfil the strength and corrosion requirements under service conditions together with good weldability. In the present paper an overview of welding materials and procedures developed by voestalpine Böhler Welding for application in modern power plants is presented and discussed.

Keywords: Welding consumables, High creep strength steels, Ni base alloys

1. Introduction

Improving output and efficiency of fuel fired power plants by increasing steam temperatures and pressures requires application of high creep and corrosion resistant alloys. In currently used steel grades an improvement of creep strength could be achieved by modification in chemical composition in combination with bainitic (grade 22, 23 and 24) or martensitic (grade 91, 92 and VM12-SCH) microstructure stabilized during tempering. However, the oxidation and corrosion behaviour of these alloys in steam limit their operation temperature to 620 °C [2-4].

In power plants with super critical parameters (T > 600°C) application of austenitic stainless steels is required for the high temperature regions of superheaters and reheaters. Higher steam temperature will cause the need for improved corrosion/oxidation resistance over increased creep strength. Therefore, the austenitic steels with higher Cr-content will enable higher operating temperatures. Recently developed steel grades DMV 304H Cu and DMV 310N with additions of copper, niobium and nitrogen for high temperature strength and creep resistance can be used up to 650 °C and 670 °C, respectively [5-7]. Even higher operating temperatures require application of Ni-base alloys like 617 or 263 [8, 9].

The development of new tube and pipes steels must be accompanied by the development of welding consumables matching these steels. It is important that the respective welding filler materials possess sufficient characteristics. It remains a challenge to warrant an optimum balance between high temperature creep characteristics as well as adequate strength and

toughness in the weld metal with sufficient scaling resistance for current and further demands. This paper gives an overview about the welding materials and procedures for the steel grades as well as Ni basis alloys currently used in the new power plant projects in Germany and Europe.

2. Welding materials and procedures

Table 1 gives an overview about welding consumables developed and approved by voestalpine Böhler Welding Germany for the common welding processes such as Gas Tungsten Arc Welding (GTAW), Shielded Metal Arc Welding (SMAW) and Submerged Arc Welding (SAW). The choice of welding process depends on the joint configuration and on material thickness. For thicker material filler metal must be added. In most cases the filler metal matches the base material according to its chemical and mechanical properties.

Base material		Filler metal		
		GTAW	SMAW	SAW
T/P22	10CrMo9-10	Union I CrMo 910	Phoenix SH Chromo 2 KS	Union S 1 CrMo 2 / UV 420 TTR(-W)
T/P23	7CrWVMoNb9-6	Union I P23	Thermanit P23	Union S P23 / UV P23
T/P24	7CrMoVTiB10-10	Union I P24	Thermanit P24	Union S P24 / UV P24
P91	X10CrMoVNb9-1	Thermanit MTS 3	Thermanit Chromo 9 V	Thermanit MTS 3 / Marathon 543
P92	X10CrWMoVNb9-2	Thermanit MTS 616	Thermanit MTS 616	Thermanit MTS 616 / Marathon 543
VM12-SCH	X12CrCoWVNb12-2-2	Thermanit MTS 5 Co T	Thermanit MTS 5 Co T	-
DMV 304 H Cu	X10CrNiCuNb18-9-3	Thermanit 304 H Cu	Thermanit 304 H Cu	-
DMV 310 N	X6CrNiNbN25-20	-	Thermanit 310 N	-
Inconel 617 mod.	NiCr23Co12Mo mod.	Thermanit 617	Thermanit 617 D	-
Alloy 263	NiCo20Cr20MoTi	Thermanit 263	Thermanit 263	-

Table1 : Welding consumables for high temperature alloys

To achieve optimal structure and properties in the weld metal special attention must be paid to heat control during the whole welding process including preheat and interpass temperature as well as to the proper post-weld heat treatment (PWHT). Furthermore, weld joints must be resistant to hot cracking what furthermore necessitates an optimization of welding parameters such as heat input, weld build-up, bead thickness, etc.

The most critical welding parameters depending on the material type will be discussed below in more detail for the SMAW process.

2.1. Welding of bainitic 2.25% Cr steels (T/P22, T/P23, T/P24)

Based on conventional steel grade 10CrMo9-10 (T22) two modern steel grades T/P23 and T/P24 were developed to enhance the creep properties. This was achieved by addition of precipitation hardening/strengthening elements such as V (W, Nb in case of T/P23) and Ti. The chemical compositions are given in Table2.

Grade		C	Si	Mn	Cr	Mo	V	W	Nb	Ti
T/P 22	min.	0.05	-	0.30	2.00	0.90				
	max	0.15	0.50	0.60	2.50	1.10				
T/P 23	min.	0.04	-	0.1	1.90	0.05	0.20	1.45	0.02	
	max	0.10	0.50	0.6	2.60	0.30	0.30	1.75	0.08	
T/P 24	min.	0.05	0.15	0.30	2.20	0.90	0.20			0.05
	max	0.10	0.45	0.70	2.60	1.10	0.30			0.10

Table 2: Compositions of bainitic steels

Matching welding consumables are available for GTAW, SMAW and SAW processes (see also Table1). In Table 3 the typical chemical compositions of matching filler metals (SMAW) for 10CrMo9-10 (T/P22), 7CrWVMoNb9-6 (T/P23) and 7CrMoVTiB10-10 (T/P24) base materials are shown. It can be seen that welding consumables for T/P23 and T/P24 base materials were alloyed with niobium instead of titanium, because in case of Ti it is very difficult to avoid its burn out during welding. Due to the similar strengthening mechanism for Nb and Ti, creep properties similar to the base material could be achieved.

Grade	Filler metal (SMAW)	C	Si	Mn	Cr	Mo	V	W	Nb
T/P 22	Phoenix SH Chromo 2 KS	0.07	0.25	0.7	2.2	0.9			
T/P 23	Thermanit P23	0.06	0.2	0.5	2.2		0.22	1.6	0.04
T/P 24	Thermanit P24	0.1	0.2	0.5	2.4	1.0	0.22		0.04

Table 3: Compositions of filler metals for T/P22, T/P23 and T/P24

For the GTAW-process of thin-walled tubes from T23/T24 no PWHT is required because the hardness values in weld are below 350 HV10. Furthermore, sufficiently high impact strength values in the as welded condition (>120J) could be reached. In that case, it is important to weld thin beads, especially in the top layer.

A PWHT which is necessary for SMAW and SAW processes at wall thicknesses > 10 mm must be carried out at the temperature of 740 °C for 2 hours. This leads to a reduction in hardness to 230 HV10 with simultaneous increase in toughness up to appr. 150 J. The PWHT can be carried out from the interpass temperature T < 250 °C, no additional cooling is needed prior to PWHT. During PWHT thick-walled components also undergo an intermediate stress

relief at 500 - 550 °C to prevent stress relief cracking of the components. The typical heat cycles for 10CrMo9-10 (T/P22), 7CrWVMoNb9-6 (T/P23) and 7CrMoVTiB10-10 (T/P24) base materials are shown in Table 4.

Base material	Filler metal	preheat T	interpass T	PWHT
T/P 22	Phoenix SH Chromo 2 KS	180 - 220°C	200 - 250°C	690 °C / 2 h
T/P 23	Thermanit P23	180 - 220°C	200 - 280°C	740 °C / 2 h
T/P 24	Thermanit P24	200 - 220°C	200 - 280°C	740 °C / 2 h

Table 4: Recommended temperature cycle during welding of bainitic steels

2.2. Filler metals for martensitic 9.0 % -12% Cr steels (91, 92, VM-12)

The high creep strength of advanced 9–12% Cr martensitic steels could be achieved by the variation of additions like V, Nb and W as precipitation hardening / strengthening elements in combination with C, B and N. The martensitic microstructure is stabilized during tempering by controlled carbides and/or carbo-nitrides precipitation. The higher Cr content in VM-12 steel is balanced by addition of Co to avoid ferrite formation.

The chemical compositions of base materials and matching filler metals are given in Table 5 and Table 6, respectively.

Grade		C	Si	Mn	Cr	Ni	Mo	V	W	Nb	Co
P91	min.	0.08	0.20	0.30	8.0	-	0.85	0.18		0.06	
	max	0.12	0.50	0.60	9.5	0.40	1.05	0.25		0.10	
P92	min.	0.07	-	0.3	8.5	-	0.30	0.15	1.5	0.04	
	max	0.13	0.50	0.6	9.5	0.40	0.60	0.25	2.0	0.09	
VM12-SHC	min.	0.10	0.40	0.15	11.0	0.10	0.20	0.20	1.3	0.03	1.4
	max	0.14	0.60	0.45	12.0	0.40	0.40	0.30	1.7	0.08	1.8

Table 5: Compositions of martensitic steels

Grade	Filler metal (SMAW)	C	Si	Mn	Cr	Ni	Mo	V	W	Nb	Co
P91	Thermanit MTS 3	0.09	0.2	0.6	9.0	0.33	1.0	0.2		0.05	
P92	Thermanit MTS 616	0.11	0.2	0.6	8.8	0.6	0.5	0.2	1.6	0.05	
VM12-SHC	Thermanit MTS 5 Co T	0.13	0.3	0.7	11.3	0.8	0.3	0.2	1.5	0.07	1.6

Table 6: Compositions of filler metals for P91, P92 and VM12-SHC

To assure sufficient toughness (Charpy V- notch (CVN)≥41J) in the weld metal the Ni-content in the filler metals was increased to 0.8% compared to the maximum 0.4% in the base materials. Furthermore a proper PWHT is required to reach such toughness values. The

recommended PWHT for P91/P92 steels is 2 hours at 760°C, whereas for VM12 material the temperature must be increased up to 770°, as shown in Table 7. Because the welding process is carried out in the martensitic temperature range (200-300°C), the heat control during welding as well as PWHT is a very important issue to achieve sufficient mechanical properties in the weld metal.

Base material	Filler metal	preheat T	interpass T	PWHT
P91	Thermanit MTS 3	200 - 250 °C	200 - 300 °C	760 °C / 2 h
P92	Thermanit MTS 616	200 - 250 °C	200 - 300 °C	760 °C / 2 h
VM12-SHC	Thermanit MTS 5 Co T	200°C	200 - 280 °C	770 °C / 2 h

Table 7: Recommended temperature cycles during welding of martensitic steels

2.3. Filler metals for austenitic steels (Super 304H, 310 N)

Due to higher Cr content the austenitic steels exhibit higher corrosion resistance than ferritic steels. Furthermore, the proper addition of Nb and N results in an increased elevated temperature strength and creep resistance. The effects of solid solution strengthening by nitrogen together with the precipitation hardening by fine and stable NbCN are used. An optimization of the amount of Ni, Nb and N increased the austenite stability compared to standard 18/8 CrNi and 18/8/2 CrNiMo steels. The chemical compositions of two steel grades developed by SMST are given in Table 8.

Grade		C	Si	Mn	Cr	Ni	Cu	Nb	N
DMV 304 H Cu	min	0.07	-	-	17.0	7.5	2.5	0.3	0.05
	max	0.13	0.30	1.0	19.0	10.5	3.5	0.6	0.12
DMV 310 N	min	0.04	-	-	24.0	17.0		0.2	0.15
	max	0.10	0.75	2.0	26.0	23.0		0.6	0.35

Table 8: Chemical compositions of austenitic steels

Both base materials are weldable using filler metals for Ni- based alloys, i.e. Thermanit 617 commonly used for alloy 617. The matching filler metals for these steel grades are currently under development. The chemical compositions of filler metals are given in Table 9. The compositional modifications for Thermanit 310 N are still in progress.

Grade	Filler metal (SMAW)	C	Si	Mn	Cr	Ni	Cu	Nb	Mo	N
DMV 304 H Cu	Thermanit 304 H Cu	0.09	0.32	3.34	17.7	16.3	2.91	0.38	0.9	0.21
DMV 310 N	Thermanit 310 N	0.06	0.65	3.25	24.0	20.5	-	0.40	0.3	0.35

Table 9: Chemical compositions of filler metals for DMV 304 H Cu and DMV 310 N

Because of high susceptibility of austenitic stainless steels to hot cracking, the weld metals are alloyed with higher Mn content than the base metal. Furthermore, intergranular reheat cracking is also a critical issue for the stabilised austenitic steels. After fast cooling from welding temperature, the finely precipitated niobium carbonitrides generate residual stresses in the heat affected zone.

Low heat input together with the interpass temperature below 150 °C is necessary to suppress hot cracking. Preheating and heat treatment after the welding process in the fabrication of these steel grades are not mandatory. However, if the material is sensitised after welding, a post welding treatment (solution treatment) can be done to restore the properties, mainly to increase the wet corrosion resistance.

3.4. Filler metals for Ni base alloys (Inconel 617 mod, Alloy 263)

In Ni-base alloys the high temperature strength is reached by two strengthening mechanisms: solid solution or/and precipitation hardening. Alloy 617 is a typical solid solution hardened Ni-base alloy. Standard Ni-base was modified to fullfill higher creep rupture properties at 700 °C. In Alloy 617 mod the content of C, Si, Mn and Fe is reduced, whereas the minimal contents of Cr, Co, Al and Ti are slightly increased compared to Alloy 617. The higher amount of Ti in combination with Co-addition in Alloy 263 results in the formation of γ' $Ni_3(Al, Ti)$-precipitates and thus in precipitation strengthening of the alloy. The chemical compositions of Inconel 617 mod and Alloy 263 are given in Table 10.

Alloy		C	Si	Mn	Cr	Co	Mo	Ti	Al	Fe
Inconel 617 mod.	min	0.05	-	-	21.0					-
	max	0.08	0.3	0.3	23.0	12.0	9.0	0.4	1.0	1.5
Alloy 263	-									
	nom	0.06	0.3	0.5	20.0	20.0	6.0	2.1	0.5	0.5

Table 10: Chemical compositions of Ni-base alloys 617mod. and 263

Alloy 617 mod. can be welded in the same way as alloy 617, but the risk of hot cracking remains very high. The welding parameters should be adjusted to low interpass temperature (max. 150°C) and low heat input to restrict formation of hot cracks. Moreover, it is difficult to set corresponding composition of the welds, especially for alloy 263 with higher Ti content, using existing filler metals.

Therefore, the so called "duplex electrode concept" was applied in case of these alloys. In this approach, critical alloying elements were transferred gradually into the arc to avoid burn out of Al and Ti as well as to limit transfer of Si. The determined chemical composition of welds corresponded to the respective base material analysis, as shown in Table 11. The Si content in the welds arose from additives used in electrodes cover, but no negative effect on joint

properties was observed. After welding a heat treatment of 3 h at 980 °C / 4 h at 810 °C should be carried out for alloy 617 mod. / alloy 263, which prevents relaxation cracking under service conditions.

Alloy	Filler metall	C	Si	Mn	Cr	Co	Mo	Ti	Al	Fe
Inconel 617mod.	Thermanit 617 D	0.06	0.6	<0.3	21.0	11.0	9.0	0.3	1.2	1.0
Alloy 263	Thermanit 263	0.06	0.7	<0.2	20.0	20.0	6.0	2.0	0.3	0.5

Table 11: Chemical compositions of weld metals for Inconel 617 mod. and Alloy 263

3. Summary

Continuous increase in operation conditions of modern fossil fired power plants (temperature and pressure) leads to perpetual modification of high temperatures materials with the aim to improve creep strength and corrosion resistance. Parallel to this process, the welding consumables must be developed or/and improved as well.

It is a big challenge to match the filler metals to advanced materials because the weld joints should have a high corrosion resistance and even better mechanical properties than the base material. Therefore, the number of welding parameters to be considered and controlled increases drastically. Producing reliable components can be achieved by using proper welding consumables together with recommended welding parameters.

References

[1] Advances in Materials Technology for Fossil Power Plants: Proceedings from the Sixth International Conference, Santa Fe, New Mexico, USA, 2010.
[2] R. Fuchs, H. Heuser, B. Hahn, Experiences regarding the processing of new power plant steels at the erection of high performance power plants, EPRI, 2010.
[3] M. Jarrar, G. Gevelmann, H. Heuser, K. G. Tak, T/P24 (7CrMoVTiB10-10) a bainitic-martensitic steel grade for super heater and water wall applications in modern ultra super critical power plants lessons learned, 10th Liège Conference on Materials for Advanced Power Engineering, 2014.
[4] V. Knezevic, M. Subanovic, Olivier Hamart, H. Heuser, K. G. Tak,Experiences in the production and welding of 9-12% Cr steels explained on grades 92 and VM12-SHC for USC power plants, 10th Liège Conference on Materials for Advanced Power Engineering, 2014.
[5] Datasheet Boiler Grade DMV 304 HCu, in Salzgitter Mannesmann Stainless Tubes, 2008.
[6] Datasheet Boiler Grade DMV 310 N, in Salzgitter Mannesmann Stainless Tubes, 2008.
[7] R. Fuchs, H. Heuser Welding of the austenitic alloys Super 304H, 347H FG and 310N, EPRI, 2009.

[8] Datasheet DMV 617 mod, in Salzgitter Mannesmann Stainless Tubes, 2010.

[9] F.Grimm, Entwicklung von Nickelbasis-Doppelmantel-Elektroden für das Lichtbogen-handschweißen von Kraftwerkskomponenten ausAlloy 617 mod. und Alloy 263, 5. FDBR-Werkstofftagung, 2012.

CREEP BEHAVIOUR OF WELDED JOINT OF A THICK-WALLED P92 STEEL PIPE

V. Sklenička[1,2] , K. Kuchařová[1], M. Kvapilová[1.2], M. Svobodová[3], L. Horváth[3],
P. Král[1] and M. Svoboda[1,2]

[1] Institute of Physics of Materials, Academy of Sciences of the Czech Republic, 616 62 Brno, Czech Republic (sklen@ipm.cz)
[2] CEITEC- IPM, Institute of Physics of Materials, Academy of Sciences of the Czech Republic, 616 62 Brno, Czech Republic (sklen@ipm.cz)
[3] UJP PRAHA, a.s., 156 10 Prague – Zbraslav, Czech Republic (svobodova@ujp.cz)

Abstract

As candidate materials for thick-walled components, up to now, most attention has been paid to improving tempered martensitic creep-resistant 9-12%Cr steels. Further requirements involve ease of fabrication processes, including welding. Welding in all its varieties is still the major joining and repair technology for power plant components. However, it is generally accepted, that the microstructure of the joined materials is strongly influenced by the welding process and thereby their creep behaviour and properties can be altered.

In this work, the creep behaviour of welded joint of a real thick-walled P92 steel pipe with the nominal dimensions of 524 mm OD and 90 mm wall thickness was investigated at 600 and 650°C using uniaxial tensile creep tests. Creep smooth cross-weld specimens were machined from different positions of the weld representing the welding sequence, namely at the root bead, the central (mid) layers and top layers close to final pass. Creep tests were followed by metallographic and fractographic analyses of crept specimens to explain the observed creep behaviour.

No substantial differences were found in the minimum creep rate, the time to fracture and creep ductility for creep specimens taken from different locations of the weld. Activation analysis of the creep data leads to conclusion, that creep tests were performed in the region of power-law (dislocation) creep and the rate controlling creep deformation mechanism is most probably climb of intragranular mobile dislocations.

Keywords: 9-12%Cr steels, thick-walled pipe, welding, high temperature creep, creep testing

1. Introduction

As candidate materials for thick-walled components exposed to high temperature service, up to now, most attention has been paid to improving tempered martensite creep resistant 9-12%Cr steels [1-8]. The steadily improved creep-resistant modified 9-12%Cr steels have been used to construct new coal-fired ultra-supercritical (USC) power plants with higher efficiency. The W-modified 9%Cr steel P92 was introduced in plants in 2001 [2]. Increasing use of newly developed high temperature creep-resistant steels requires great efforts into the

development of new fabrication processes, including the applied welding procedures. Welding in all its varieties is still the major joining and repair technology for power plant components.

It is of great importance that matching weld materials for creep-resistant 9-12%Cr steels are developed simultaneously to base materials [9]. However, it should be noted, that special deoxidation practices, additions of microalloying elements, improvement of weldability and handling remain the detailed knowledge of the individual filler material manufacturer. Nevertheless, both similar and dissimilar welded joints of creep - resistant 9-12%Cr steels exposed to high temperature creep show very similar behaviour in tendency [10]. Numerous creep tests of cross-weld specimens showed that at lower testing temperatures there is no substantial difference between the base metal and the cross-weld creep strength [11]. This difference becomes more important as the temperature increases and as the applied stress level is lowered. Thus, the ratio of the creep rupture strength of cross-welds to the base materials creep strength is dependent on creep loading conditions and welding procedure.

Special attention has to be aimed to the creep behaviour of multilayer welding joints. Multilayer welds are formed by subsequent deposition of weld bead on solidified formerly deposited runs [9]. Thus it can be expected that the heat affected zone (HAZ) of base material and regions with different microstructure may be formed within the weld metal. Therefore, it is necessary to study creep resistance, fracture mode and fracture locality of multilayer welding joints besides the parent materials.

In this work, the creep behaviour of multilayer similar welds of an actual thick-walled P92 steel pipe was investigated using uniaxial tensile creep tests at 600 and 650°C. Smooth cross-weld specimens were machined from different locations of the weld representing the weld sequences, namely at the root beads, the mid layers and layers close to final passes. Creep tests were followed by microstructural and fractographic analyses.

2. Experimental material and procedures

2.1. A thick-walled P92 steel pipe and welding procedure

The material of the pipe under investigation was the W-modified 9%Cr steel P92 (ASME Grade 92) for thick section boiler component and steam lines. The outer diameter and wall thickness of the pipe were 524 and 90 mm, respectively. A multipass circumferential welded similar joint using TIG welding process with U-groove preparation was made by an orbital welding head POLYCAR MP S with a rotation device POLYCAR HPMP-1900. Welding material was Thermanit MTS616 supplied by Böhler Welding Germany. The chemical composition (in wt.%) of the filler metal was 0.102C, 0.72Mn, 0.25Si, 0.008P, 0.003S, 1.75W, 0.49Ni, 8.70Cr, 0.207V, 0.46Mo, 0.065Nb, 0.052N and 0.06Cu. The electrode size 0.8 mm was used. The applied preheated temperature was ranging from 200 to 250°C, while

the interpass temperature was between 200 and 300°C. A post weld heat treatment (PWHT) was applied consisting of tempering at 760°C / 4 h then furnace cooling to 400°C (cooling rate of about 100 – 150°C /h) and final air cooling.

2.2. Creep testing

The creep smooth cross-weld flat specimens having gauge length of 50 mm and cross-sectional area of 5 mm x 3.2 mm were machined from following different positions in the weld: R - root, C – central and T - top. The creep testing was conducted at 600°C and 650°C with the testing temperature maintained to within ± 0.5°C of the desired value. The applied tensile stress ranged from 60 MPa to 250 MPa. All of the tests were run until final fracture of the specimen. The creep elongations were measured using a linear variable differential transducer (the strain was measured with a sensitivity of 5×10^{-6}) and they were continuously recorded digitally and computer processed.

2.3. Microstructural and fractographic investigations

The following creep testing specimen was prepared for microstructural and fractographic examination by means of both transmission and scanning electron microscopy. Transmission electron microscopy (TEM) studies were carried out on thin foils prepared from gauge parts of the crept specimens using a Philips CM12 TEM/SEM microscope equipped with EDAX Phoenix system. The metallographic longitudinal sections and the fracture surfaces were investigated using scanning electron microscope (SEM) Tescan Lyra 3 XMU equipped with electron backscatter diffraction (EBSD) facility.

3. Experimental results

3.1. Creep behaviour of the weld joint

Representative standard creep curves of the weld joint at different testing temperatures are shown in Fig.1. In this case the creep specimens were machined from the central position (mid-thickness) of the weld joints. The creep curves exhibit very short primary creep regime followed by an apparent steady deformation and an accelerating tertiary creep regime. Figure 2 illustrates creep behaviour of creep specimens machined from different positions of the weld. While a routing of the creep curves of the specimens crept at 600°C and 160 MPa indicates some tendency of position dependency (Fig. 2a), the creep curves corresponding to creep exposure at 650°C and 100 MPa provide no clear predication (Fig.2b). The results of all creep tests carried out on the welds at two different temperatures are summarized in Tab. I for both testing temperatures 600 and 650°C. In general, as can be seen from Tab. I, no systematic and substantial clear differences in creep behaviour of specimens machined from various positions of the weld were found.
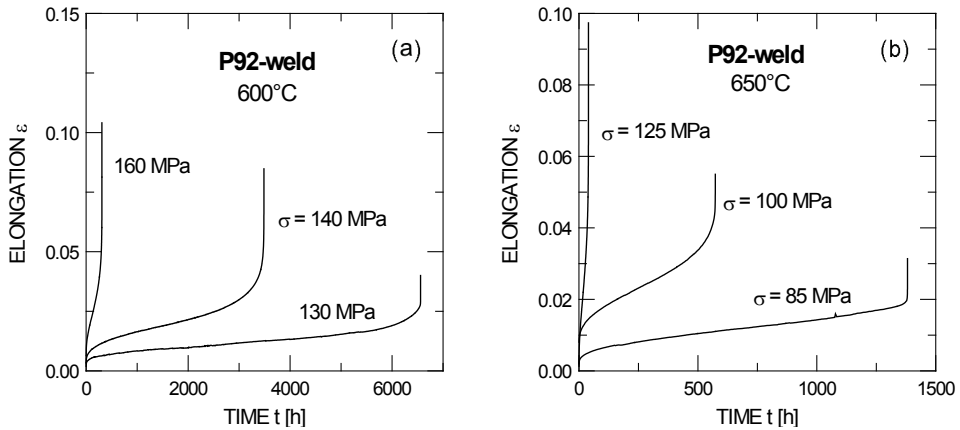
Figure 1: Standard creep curves for the weld joints (central position) at temperatures
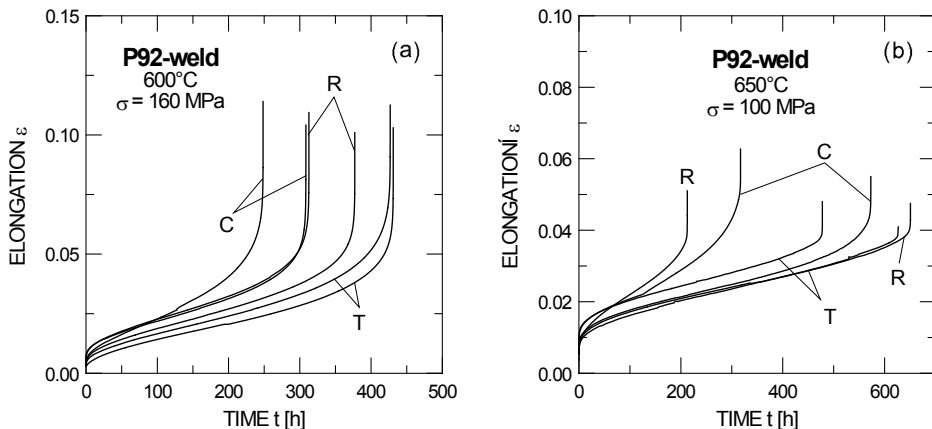(a) 600°C, (b) 650°C and different levels of stress.

Figure 2: Standard creep curves for creep specimens machined from R - root, C – central and
T – top positions of the weld joints: (a) 600°C, 160 MPa and (b) 650°C and 100 MPa.

3.2. Microstructure characterization and fractographic features

According to the thermodynamic calculations, ferrite, $M_{23}C_6$ carbides and MX carbonitrides,
Laves phase and Z-phase are equilibrium phases for P92 steel at creep test temperatures [12].
Based on the results of our experimental investigations on the same P92 steel which have
been already published [13] the following microstructure components were found. The prior
austenite grain boundaries are decorated by a network of $M_{23}C_6$ arbides. Particles of this
phase are also observed on sub-grain boundaries as well as inside of the sub-grains. There are

tiny precipitates of minor phase, present both on the grain boundaries and inside the former martensitic laths. Microstructural investigation of the crept specimens revealed significant precipitation and growth in the Laves phase during relatively longer creep exposures at low stresses. No noticeably change was observed in the number density of MX precipitates during creep exposure. The TEM investigation did not reliably reveal any amount of Z-phase in the crept specimens, apparently due to short-term creep exposures.

Table 1:Results of creep testing at 600°C and 650°C (Positions of the creep specimen in the weld joint:R-root, C-central, T-top)

Position in weld	600°C				650°C			
	Stress	Time to fracture	Fracture elongation	Minimum creep rate	Stress	Time to fracture	Fracture elongation	Minimum creep rate
	σ [MPa]	t_f [h]	ε_f [%]	$\dot{\varepsilon}_m$ [s⁻¹]	σ [MPa]	t_f [h]	ε_f [%]	$\dot{\varepsilon}_m$ [s⁻¹]
C	120	8707.1	3.7	3.7×10^{-10}	60	9313.2	2.5	1.7×10^{-10}
C	130	6558.7	4.0	4.4×10^{-10}	75	3758.4	2.8	5.4×10^{-10}
T					75	2068.6	2.3	1.2×10^{-9}
R	140	4619.6	6.6	8.2×10^{-10}	85	1259.3	3.4	2.3×10^{-9}
C	140	3485.5	8.4	1.4×10^{-9}	85	1381.2	3.1	2.1×10^{-9}
T	140	3414.7	8.3	1.4×10^{-9}	85	1343.2	2.9	2.0×10^{-9}
R	160	377.2	10.1	2.2×10^{-8}	100	212.5	5.1	2.6×10^{-8}
R	160	312.8	10.9	2.5×10^{-8}	100	650.7	4.7	9.2×10^{-9}
C	160	248.3	11.4	3.6×10^{-8}	100	317.1	6.2	1.5×10^{-8}
C	160	308.5	10.4	2.4×10^{-8}	100	572.9	5.5	9.6×10^{-9}
T	160	426.8	11.2	2.0×10^{-8}	100	477.8	4.8	1.0×10^{-8}
T	160	431.1	10.3	1.8×10^{-8}	100	626.8	4.1	8.3×10^{-9}
R	200	16.08	11.6	5.5×10^{-7}	125	38.7	9.6	2.3×10^{-7}
C	200	17.00	12.6	5.7×10^{-7}	125	39.6	9.7	2.2×10^{-7}
T	200	18.31	10.9	4.8×10^{-7}	125	38.2	10.7	2.4×10^{-7}
R					150	5.28	11.9	2.1×10^{-6}
C					150	5.79	12.5	2.0×10^{-6}
T					150	5.18	11.2	2.1×10^{-6}
C	250	0.64	11.9	1.5×10^{-5}	175	1.05	13.5	1.2×10^{-5}

In general, fusion similar welded joints of 9-12%Cr creep-resistant steels consist of three different zones; base metal (BM), weld metal (WM) and heat affected zone (HAZ). The HAZ is a transition region between weld metal and unaffected base metal. It could be subdivided into further microstructural areas depending on the peak thermal cycles experienced during welding and also on the transformation kinetics of the steel. The EBSD grain maps of the different constituents of the P92 steel weld joint are shown in Fig. 3. Indeed, three distinct regions of the joint namely base metal, HAZ and the weld metal were detected. In the weld fusion zone, grains were oriented more or less transverse to the welding direction towards the fusion boundary (Fig. 4). Similar grain orientation pattern in the fusion zone has been reported by Sakthivel et al. [14].
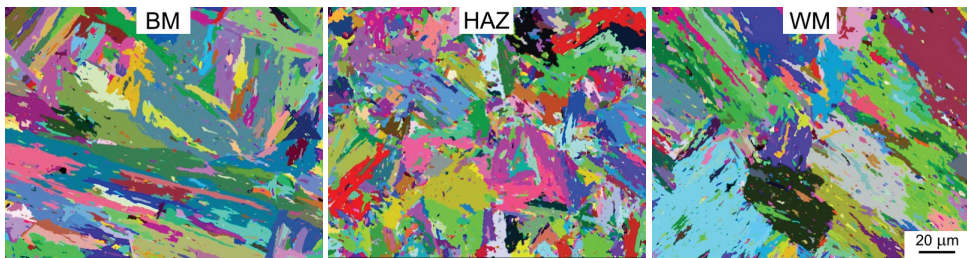
Figure 3: The EBSD grain maps showing three distinct regions of the weld: BM - base metal, HAZ – heat affected zone and WM - weld metal.
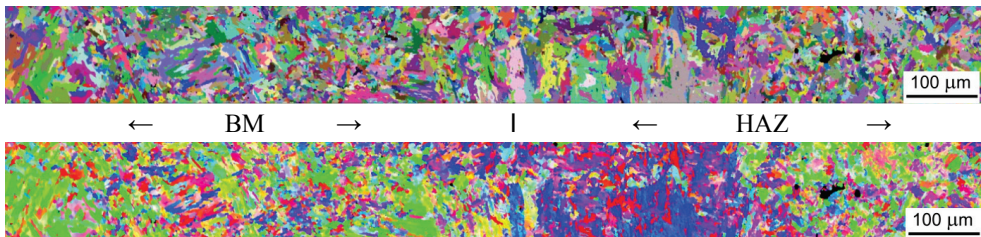
Figure 4: The EBSD grain and orientation maps of the longitudinal section of base metal and HAZ of the P92 steel weld joint (central position).

Creep cavitation has been investigated on the longitudinal metallographic sections of the creep fractured specimens across the weld joint under different loading conditions. Creep cavities were observed to a different amount in the crept specimens at both temperatures. However, their occurrence was limited to low stress regime (up to 140 MPa at 600°C and 100 MPa at 650°C). A higher number of cavities was found in the fine grained region of the HAZ which is adjacent to the base metal (Fig. 5a). The inhomogeneity of spatial distribution of

isolated cavities leads to inhomogeneity of more advanced forms of creep damage, such as the coalesced cavities and later grain boundary microcracks. The last stage of fracture process is characterized by the formation type IV creep crack due to long range coalescence of creep damage and its a relatively quick propagation through a cross-section of the creep specimen (Fig. 5b). The SEM investigation of creep fracture surface of the specimens machined from different locations of the weld joint did not revealed any substantial changes in microfractographic features of creep fracture surface. Comparison of fracture surfaces for both low stress and high stress regimes is given in Fig. 5c and d. Whereas in low stress regime type IV cracking fracture in the fine grained HAZ of P92 steel weld joint is mostly intergranular (Fig. 5c and a), a characteristic transgranular ductile dimple mode of fracture was observed in high stress regime (Fig. 5d). At high stress level, the fracture was frequently located in weld metal due to a local loss of a stability of plastic deformation of metal matrix.
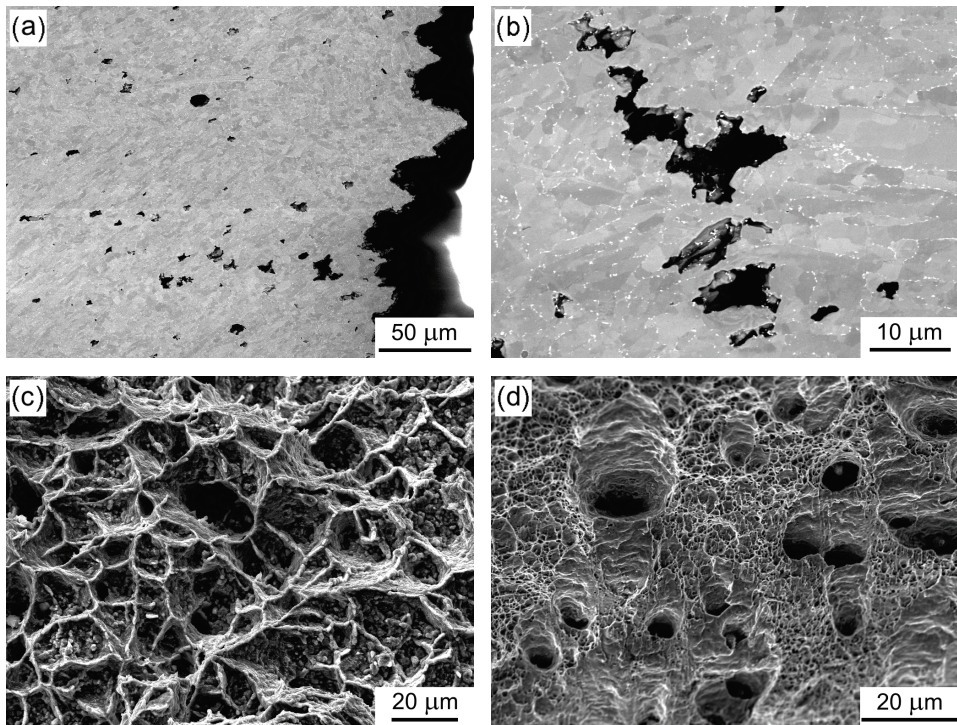
Figure 5: Creep damage and fracture of the weld joint at 600°C and 140 MPa: (a) cavitation and intergranular fracture profile, (b) formation of type IV creep crack, (c) intergranular fracture surface and (d) transgranular ductile fracture at 600°C and 200 MPa.

4. Discussion and conclusive remarks

A question naturally arises: in which creep regime were the creep tests performed? The stress dependences of the minimum creep rates and times to fracture are given in Fig. 6 using the data from Table I.
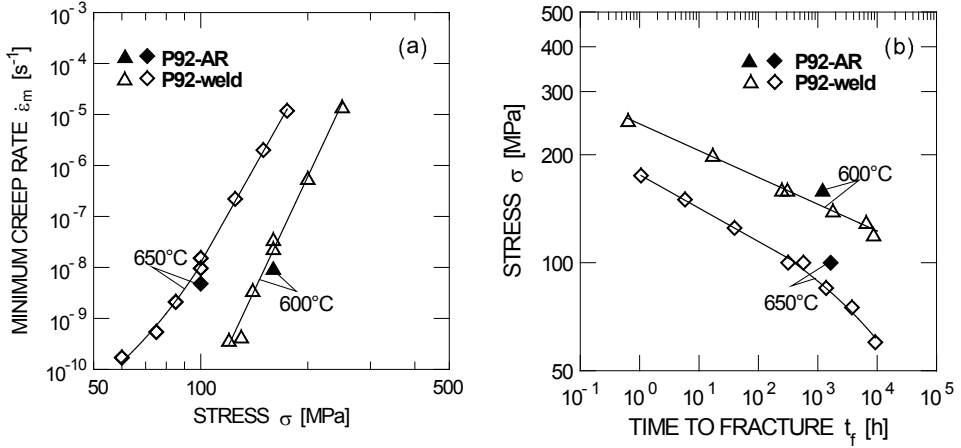
Figure 6: Stress dependences of (a) the minimum creep rates and (b) the time to fracture. Selected experimental points for as-received state, P92-AR were taken from [13].

The evaluated values of the stress exponent n of the creep rate $n = \left(\partial \ln \dot{\varepsilon}_m / \partial \ln \sigma \right)_T$ indicate that all creep tests were performed in the region of power-law or dislocation creep. The values of the stress exponent n (the slopes in Fig. 6a) were determined from 8 to 16 depending on the test temperature and the applied stress level. The evaluated values of the stress exponents m of creep life $m = -\left(\partial \ln t_f / \partial \ln \sigma \right)_T$ are similar to the values for stress exponent n. This can be explained by the fact, that both the creep deformation and fracture processes are controlled by the same mechanism(s) and the rate controlling creep deformation mechanism is most probably climb of intragranular mobile dislocations.

For industrial implications it is of great importance to consider a weld strength factor (WSF) during the design stage of new high temperature components. The European Creep Collaborative Committee (ECCC) defined WSF in its recommendations [15] as follows:

$$\text{WSF } (t,T) = R_{u\,(w)\,/\,t/\,T} \, / \, R_{u\,/t/T} \, , \qquad \qquad (1)$$

where $R_{u(w)\,/\,t\,/T}$ is the rupture strength of the weld at a specified time and temperature, and $R_{u\,/t\,/T}$ is the corresponding strength of the base metal at the same time and temperature. Very recently, we have published the relevant creep data for the same base metal (P92 steel) [13] as

examined in this report. The WSF values for $t = 10^3$ h calculated from (1) are 0.9 and 0.85 for temperature 600°C and 650°C, respectively. As an example, in the German AD2000-Merkblatt B0, a constant WSF of 0.8 is given for component designed using creep rupture strength values [10]. However, it cannot be excluded that this factor is not constant and depends on material type, stress level, temperature and time and can be either higher but also significantly lower [16].

Finally, no different fracture features on the creep fracture surfaces were found on individual fractured creep specimens at different positions across of the weld. Thus, it may be concluded that the fracture location (HAZ, base metal) and fracture type depend rather on the creep loading conditions than on the welding procedure and welding parameters used.

Acknowledgements

References

[1] Mayer K.-H., "The Development of creep-resistant steels", in *Creep resistant steels*, eds. F. Abe, T.-U. Kern and R. Viswanathan, Woodhead Publishing Limited, Albington, UK, pp.15-77 (2008).

[2] Hald J., "Microstructure and Long-Term Creep Properties of 9 – 12%Cr Steels", *Int. J. Press. Vessels and Piping*, vol. 85, pp. 30-37 (2008).

[3] Sklenička V., Kuchařová K., Svoboda M., Kloc L., Buršík J. and Kroupa A., "Long Term Creep Behaviour of 9 – 12%Cr Power Plant Steels", *Mater. Characterization*, vol. 51, pp. 35-48 (2003).

[4] Abe F., "'Strengthening mechanisms in steel for creep and creep rupture", in *Creep resistant steels*, eds. F. Abe, T.-U. Kern and R. Viswanathan, Woodhead Publishing Limited, Albington, UK, pp.279-304 (2008).

[5] Di Gianfrancesco A., Tiberi Vipraio S. and Vendini D., "Long Term Microstructural Evolution of 9-12%Cr Steel Grades for Steam Power Generation Plants", *Procedia Engineering,* vol. 55, pp. 27-35, (2013).

[6] Abe F., "Analysis of Creep Rates of Tempered Martensitic 9%Cr Steel Based on Microstructure Evolution", *Mater. Sci. Eng. A*, vol.510-511, pp.64-69, (2009).

[7] Giroux P.F., Dalle F., Sauzay M., Malaplate J., Fournier B. and Gourgues-Lorenzon A.F., "Mechanical and Microstructural Stability of P92 Steel under Uniaxial Tension at High Temperature, *Mater. Sci. Eng. A*, vol. 257, pp.3984-3993, (2010).

[8] Sklenička V. and Kloc L., "Creep in Boiler Materials: Mechanisms, Measurement and Modelling", in Power Plant Life Management and Performance Improvement , ed. E. Oakey, Woodhead Publishing Limited, Albington, UK, pp. 180-221, (2011).

[9] Baune E., Cerjak H., Caminada S., Jochum C., Mayr P., and Pasternak J: "Weldability and properties of new creep-resistant materials for use in ultra supercritical coal fired power plants", in the *8th International Conference on Materials for Advaced Power Engineering 2006*, eds. J. Lecomte-Beckers et al.,Forschungszentrum Juelich GmBH, Liege, pp. 871- 891, (2006).

[10] Cerjak H. and Mayer P., "Creep strength of welded joints of ferritic steels", in *Creep resistant steels*, eds. F. Abe, T.-U. Kern and R. Viswanathan, Woodhead Publishing Limited, Albington, UK, pp. 472-503, (2008).

[11] Masuyama F., Matsui M. and Komai N: "Creep rupture behaviour of advaced 9-12%Cr steel weldment", *Key Engineering Materials*, vol.171-174, pp. 99-108 (2000).

[12] Sklenička V., Kuchařová K., Svoboda M., Kroupa A. and Čmakal, J.: "Creep Behaviour and Microstructural Changes of Advaced Creep Resistant Steels after Long-term Isothermal Ageing", *Mater. Sci. Forum*, vol. 654-656, pp. 504-509 (2010).

[13] Sklenička V., Kuchařová K., Kvapilová M., Král P., Svoboda M., Svobodová M. and Čmakal J. :"The Effect of Hot Bending on Creep in a Thick-Walled P92 Steel Pipe", *Proceedings of the 3rd Inter. ECCC2014 Creep & Fracture Conference*, Centro Sviluppo Materiali, Rome, May 5-7, (2014).

[14] Sakthivel T., Vasudevan M., Laha K., Parameswaran P., Chandravathi K.S., Panneer Selvi S., Maduraimuthu V., Mathew M.D.: "Creep rupture behavior of 9Cr-1.8W-0.5Mo-VNb (ASME grade 92) ferritic steel weld joint", *Mater. Sci. Eng. A*, vol. 591, pp. 111-120 (2014).

[15] *ECCC Recommendations*. Vol. 2 Part 2b [Issue 2] "Terms and terminology for weld creep testing" (2003).

[16] Sandström R. and Tu S.T.: "The effect of multiaxiality on the evaluation of weldment strength reduction factors in high-temperature creep", *Trans ASME*, vol. 116, pp. 76 – 80 (1994).

MECHANICAL PROPERTIES AND MICROSTRUCTURE OF JOINTS IN X13CrMoCoVNbNB9-2-1 (PB2) STEEL PRODUCED WITH AND WITHOUT POST-WELD HEAT TREATMENT

Mirosław Łomozik[1], Krzysztof Kwieciński[1], Anna Zielińska-Lipiec[2],
Robert Jachym[1], Paola Mariani[3]

[1] Instytut Spawalnictwa, Testing of Materials Weldability and Welded Constructions
Department, 44-100 Gliwice, Bł. Czesława 16-18, Poland,
e-mail: miroslaw.lomozik@is.gliwice.pl
[2] AGH University of Science and Technology, Faculty of Metals Engineering and Industrial
Computer Science, 30-059 Krakow, al. A. Mickiewicza 30, Poland,
e-mail: alipiec@agh.edu.pl
[3] TENARIS Dalmine, Bergamo, Italy, e-mail: pmariani@tenaris.com

Abstract

The subject of the research included butt joints of X13CrMoCoVNbNB9-2-1 (PB2) steel pipes with an outer diameter of 219.1 mm and wall thicknesses amounting to 31 mm. The one joint was welded conventionally i.e. with a post-weld heat treatment and second joint - without a heat treatment, using temper beads technique. Root runs were welded using the TIG (Tungsten Inert Gas) method (welding method no. 141) with a Böhler-manufactured Thermanit MTS 616 wire, whereas filling and face runs were MMA (Manual Metal Arc) welded using Böhler-manufactured Thermanit MTS 5 Co1 covered electrodes (welding method no. 111). A conventionally made joint was subjected to post-weld stress relief annealing at $770^{\circ}C$ for 3 hours. The joints underwent NDT (Non-destructive Testing) (Visual Testing - VT and Radiographic Testing - RT), destructive testing (static tensile tests, impact strength tests, side bend tests and hardness measurements) as well as structural examination using light microscopy (LM) and transmission electron microscopy (TEM). The scope of structural tests included examining the microstructure of the coarse-grained areas of the heat-affected zone (HAZ) of joints, comparing the morphology of these areas and determining the types of carbide precipitates in the HAZ in a joint subjected and not subjected to a post-weld heat treatment (PWHT). On the basis of the tests carried out it was stated that:
- tensile strength of the joint welded with temper beads technique is slightly higher than the strength of the joint welded with a heat treatment;
- conventionally welded joint subjected to a heat treatment is characterised by good plastic properties, which was confirmed by meeting the criteria in the impact strength test, bend tests and hardness measurements;
- weld plastic properties in the joint welded with temper beads technique are poor and fail to meet the criteria in the impact strength tests and hardness measurements;
- weld absorbed energy of the joint welded without a heat treatment is determined by the structure of martensite, its tempering degree and by the presence of ferrite delta in the microstructure;
- coarse-grained HAZ area in the joint welded with temper beads technique is characterised by greater dislocation density and lower size of sub-grains in comparison with the analogous area of the joint welded using a heat treatment;
- coarse-grained HAZ areas of the joints welded with and without a heat treatment contain $M_{23}C_6$ and NbC carbides and as well as V(C,N) carbonitrides.

Keywords: martensitic steel for operation at higher temperature, welded joint, heat-affected zone, mechanical properties, heat treatment.

1. Introduction

In the nearest future neither nuclear nor alternative energy will be capable of satisfying 100% of the global demand for power. For this reason, starting new conventional power stations and revamping already existing ones continues to remain important. At the same time it is necessary to reduce the emission of pollutants and decrease power generation costs, which is directly related to increasing the efficiency of power units in power stations.

An increase in efficiency is obtained by increasing key operation parameters, i.e. steam pressure and temperature. Presently used martensitic steels, such as X10CrWMoVNbB9-2 (T/P92), enable designing power generation systems in which the temperature of superheated steam may reach 625°C. Obtaining better operation parameters is possible only by using new materials for the production of boiler and pipeline elements. For this reason, the recent dozen or so years have seen research undertaken to develop new grades of structural steels, whose mechanical properties, creep strength and heat resistance would enable using these steels at even higher temperatures [1]. The EU research project COST 536 [2] involved, among others, the development of experimental martensitic steel grade X13CrMoCoVNbNB9-2-1 temporarily designated as PB2.

Steels for operation at higher temperature are generally characterised by limited weldability. That is why after welding joints must often undergo a post-weld heat treatment (PWHT), which is primarily carried out for decreasing the values of welding stresses and improving the plastic properties of welds and heat-affected zones (HAZ) of joints [3, 4].

In industrial practice, particularly during repair welding, usually carried out in large objects, conducting the post-weld heat treatment of joints can create many difficulties. In situations, where due to technical reasons the possibility of performing conventional PWHT is limited or impossible it is advised that during welding the temper beads technique (TBT) should be carried out [5-7]. This method consists in a specific manner and appropriate sequence of making individual beads in a weld so that, as a result of a controlled thermal cycle, it should be possible to obtain the effect of tempering hardening structures both in the weld metal and in the HAZ of a welded joint [5-7].

2. Test materials and welded joints

The subject of tests was butt joints of pipes in X13CrMoCoVNbNB9-2-1 (PB2) steel grade having the external diameter of 219.1 mm and wall thickness of 31 mm. The chemical composition of PB2 steel is presented in Table 1, whereas its mechanical properties are listed in Table 2.

Table 1 Chemical composition of X13CrMoCoVNbNB9-2-1 steel (PB2) according to manufacturer's data [8]

Steel	Chemical element content, %							
	C	Mn	Si	P	S	Ni	Cr	Mo
PB2	0.135	0.31	0.076	0.0058	0.001	0.15	9.28	1.51
	V	N	Co	Nb	B	Al	Cu	Ti
	0.19	0.026	1.33	0.053	0.0091	0.007	0.031	0.001

Table 2 Mechanical properties of X13CrMoCoVNbNB9-2-1 steel (PB2) according to manufacturer's data [8]

Steel	R_e, MPa	R_m, MPa	$A_{min.}$, %	HV10
PB2	610	763	21.5	258

Joints were welded using the following filler metals manufactured by the Böhler company:

a) Thermanit MTS 616 grade wires having a diameter of 2.4 mm for TIG (Tungsten Inert Gas) welding (welding method no. 141),

b) Thermanit MTS 5 Co1 grade electrodes having a diameter of 3.25 mm with a basic coating for manual welding MMA (Manual Metal Arc) (welding method no. 111).

Joints were made in the following manner: a root run was TIG welded, whereas filling runs and the face were MMA welded. Gas from group I1As was used as backing gas. Welding was carried out in a flat position (PA). Two welded joints were made. One joint was welded conventionally, i.e. welding was followed by a heat treatment consisting in stress relief annealing at 770^oC for 3 hours (welding variant 1). The other joint was welded using the temper beads technique (TBT) without a post-weld heat treatment (welding variant 2).

The welding parameters were within the range:

a) joint welded with heat treatment: TIG - current intensity 150-170 A, arc voltage 12-13 V, MMA - current intensity 100-160 A, arc voltage 23-30 V;

b) joint welded with temper beads technique: TIG - current intensity 150-170 A, arc voltage 12-13 V, MMA - current intensity 100-130 A, arc voltage 23-30 V.

The diagrams preparation of joint edges for welding and sequence of passes laying in weld are presented in Figure 1.
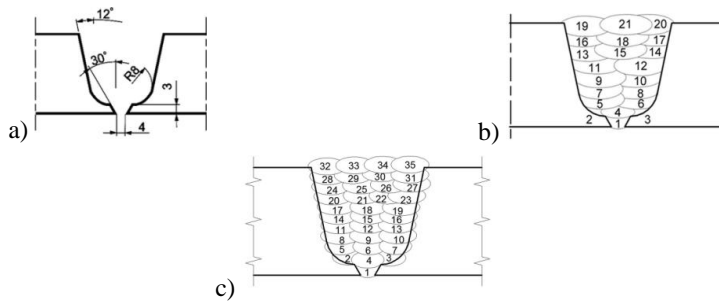
Fig. 1. Diagrams: a) Preparation of joint edges for welding, b) Sequence of passes laying during welding with heat treatment, c) Sequence of passes laying during welding with temper beads technique

3. Tests and results

The welded joints were subjected to non-destructive visual testing (VT) and radiographic testing (RT), as a result of which it was stated that the joints represented the quality level B according to the requirements of standard EN ISO 5817. Afterwards, following the requirements of standard EN ISO 15614-1 destructive tests were carried out. The tests included static tensile tests, impact tests (a notch incised in the weld, HAZ and in the parent metal), side bend tests and hardness measurements.

The tensile strength R_m of the welded joints was determined according to the requirements of standards EN 4136 and EN ISO 6892-1. The results of the tensile tests of the welded joints in variants 1 and 2 and of the parent metal of the PB2 steel are presented in Figure 2 in the form of the average values from the two test pieces tested.
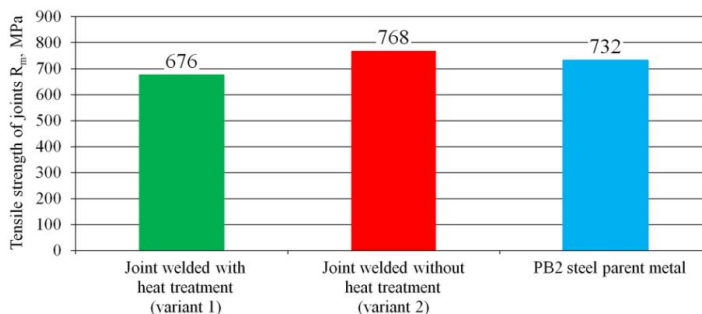
Fig. 2. Tensile strength R_m of joints welded in variants 1 and 2 in comparison with the tensile strength R_m of the PB2 steel parent metal

The absorbed energy of welded joints was measured at the ambient temperature in accordance with the requirements of standards EN 12952-6, EN ISO 148-1 and EN ISO 9016. The standard specifies that the minimum value of the HAZ absorbed energy at the ambient temperature on test pieces with a normal cross-section (10 x 10 mm) should amount to 24 J.

In turn, standard EN 10216-2 specifies that the minimum value of absorbed energy for the parent metal (PM) should be 27 J. Figure 3 presenting the results of testing the absorbed energy of welded joints contains both criterion values.

a)   b)

c)   d)
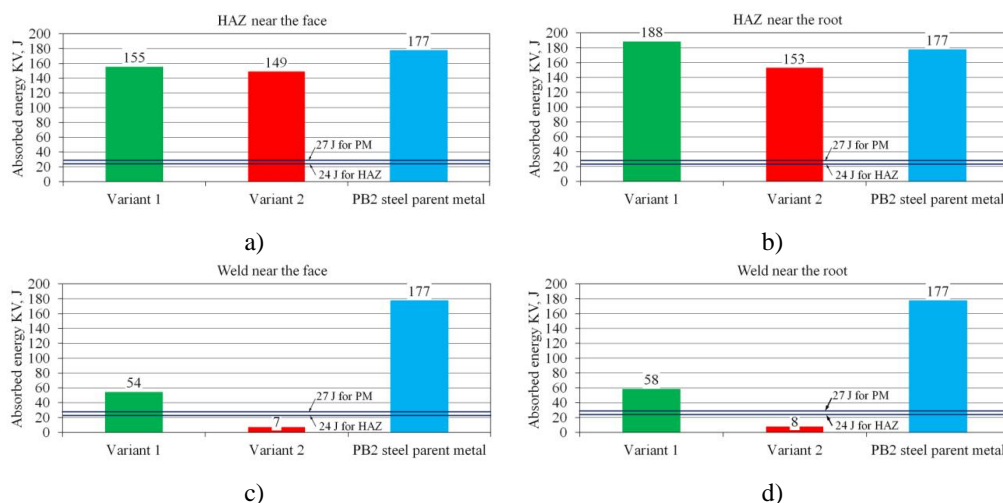
Fig. 3. Absorbed energy of various areas of joints welded in PB2 steel: a) HAZ near the face, b) HAZ near the root, c) Weld near the face, d) Weld near the root

Side bend tests of welds in welded joints were carried out in conformity with the requirements of standards EN ISO 15614-1 and EN ISO 5173 using a bending mandrel with a diameter of 60 mm. According to the requirements stated in standard EN ISO 15614-1 a positive test result requires obtaining a bend angle of 180° without the presence of scratches and cracks on a test piece surface during bending. The results of the bend test are presented in Table 3.

Table 3 Results of side bend tests of welded joints

Welding variant	Test piece no.	Bend angle, ^{o}	Remarks
1 (welding with PWHT)	1	180	no scratches and cracks
	2	180	no scratches and cracks
	3	180	no scratches and cracks
	4	180	no scratches and cracks
2 (welding without PWHT)	1	75	crack in HAZ
	2	85	crack in HAZ
	3	95	crack in HAZ
	4	75	crack in HAZ

Hardness measurements related to welded joins were carried out in accordance with the requirements of standard EN ISO 9015, using the Vickers hardness test with the force applied on the indenter being 98.1 N (HV10). Due to the fact that PB2 steel has not been classified in standards yet, the hardness criterion adopted was that for the 6th material group

after a heat treatment amounting to 350 HV. The arrangement of hardness measuring points is presented in Figure 4, whereas the results of these measurements are presented in Figure 5.
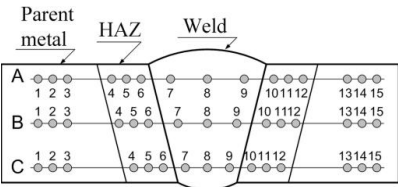
Fig. 4. Arrangement of hardness measuring points in welded joints

a)

b)
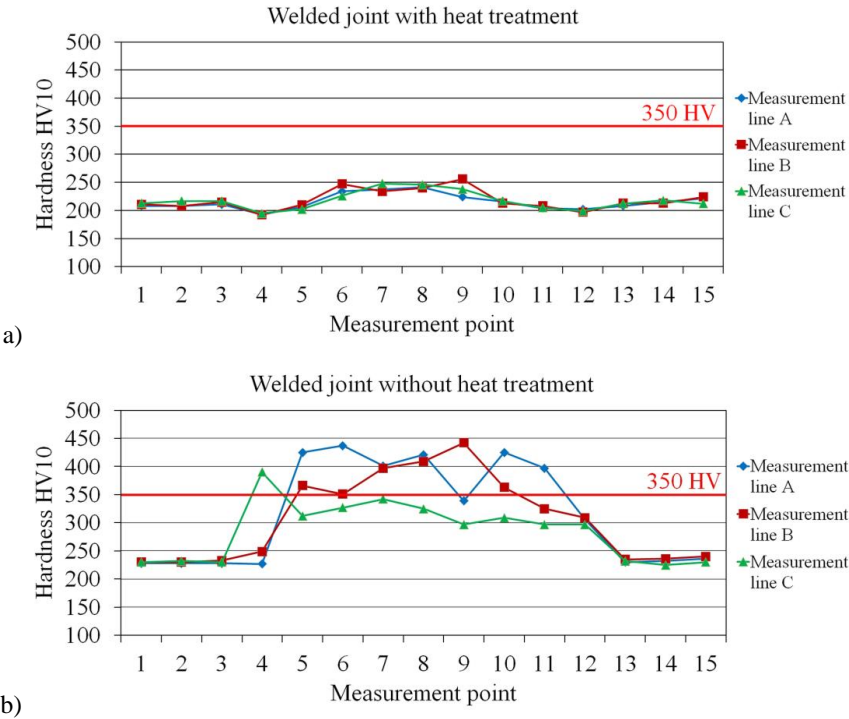
Fig. 5. Results of HV10 hardness measurements in welded joints: a) Joint with PWHT,
b) Joint without PWHT (using the temper beads technique)

Each welding variant was sampled for fragments for microscopic metallographic tests carried out in conformity with the requirements of standard EN ISO 17639. The microstructure of the welded joints was revealed using iron (III) chloride ($FeCl_3$). Exemplary results of the microscopic metallographic tests (LM) are presented in Figure 6. Detailed light microscopy observations revealed the presence of ferrite δ (ferrite delta) in the weld of the joint welded using the temper beads technique (welding variant 2) (Figure 6c).

a)   b)   c)
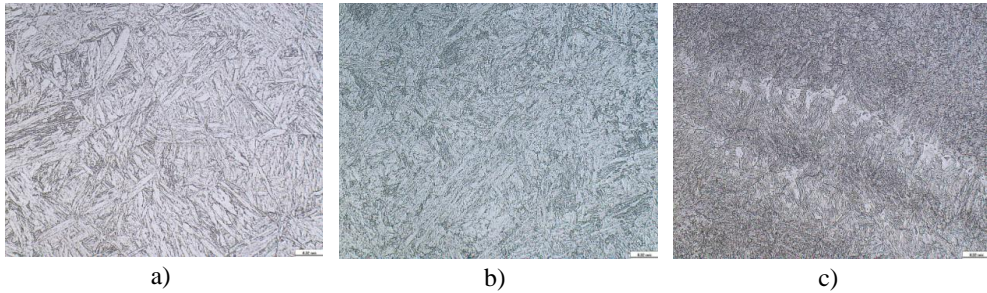
Fig. 6. Microstructure of welded joint without PWHT, i.e. using temper beads technique:
a) Parent metal of PB2 steel. Tempered martensite, b) HAZ. Martensite, c) Weld. Martensite
+ ferrite delta. Etchant: FeCl₃, mag. 500x

In order to thoroughly examine the microstructure in the welded joints subjected and not subjected to PWHT it was necessary to carry out structural examination using transmission electron microscopy (TEM). The carbide precipitates were identified by performing SAED (Selected Area Electron Diffraction). The example of a typical microstructure observed in the HAZ of the welded joint subjected to PWHT is presented in Figure 7, whereas the microstructure observed in the HAZ of the joint welded using the temper beads technique is presented in Figure 8.

a)   b)

c)
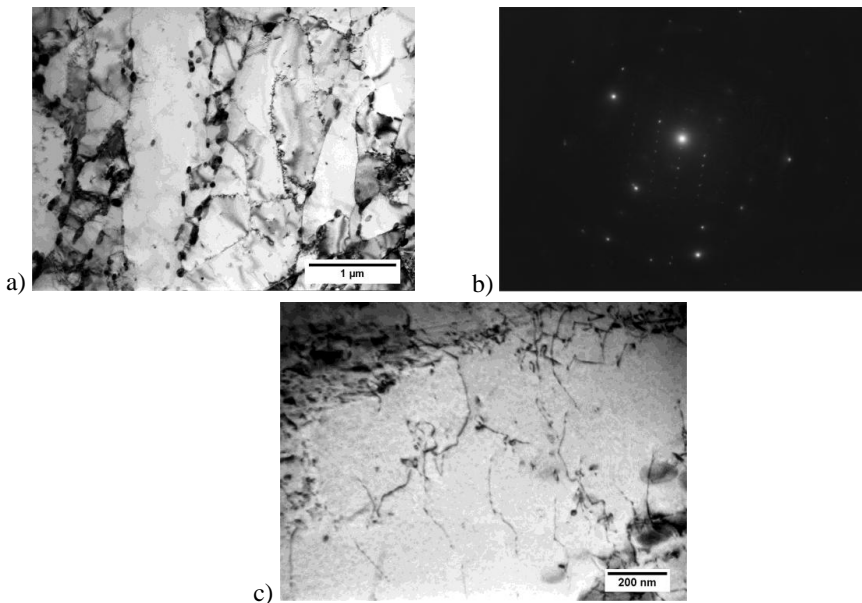
Fig. 7. HAZ area in the joint welded using PWHT (variant 1): a) Morphology of ferrite subgrains, visible carbides of $M_{23}C_6$ type, b) Diffraction pattern $[013]\alpha \, || \, [\,\overline{223}\,]M_{23}C_6$, c) Dislocation density in subgrains, visible precipitates of V(C,N) carbonitrides

395
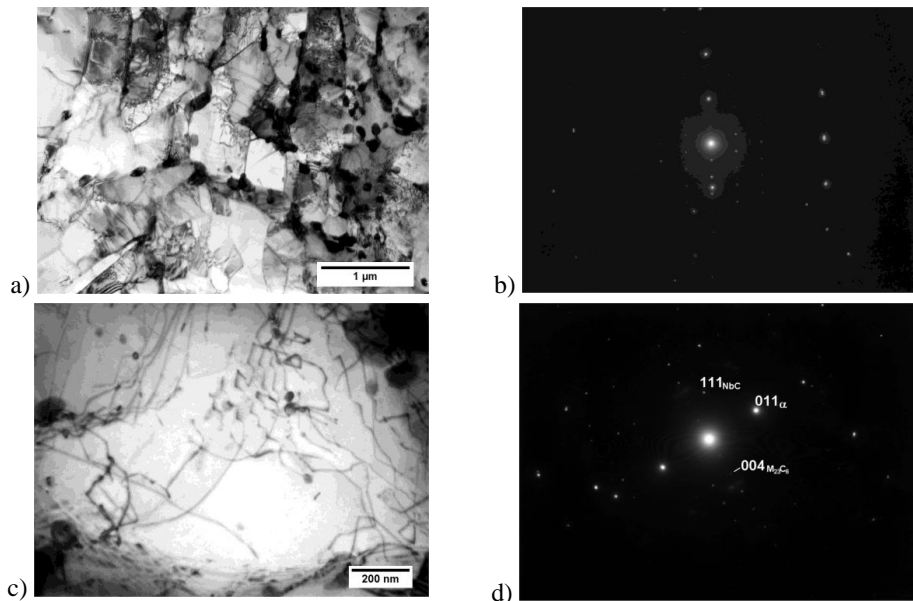
Fig. 8. HAZ area in the joint welded without PWHT, i.e. using the temper beads technique (variant 2): a) Morphology of ferrite subgrains, visible carbides of $M_{23}C_6$ type, b) Diffraction pattern [$\overline{112}$]α || [013]$M_{23}C_6$, c) Dislocation density in subgrains, visible NbC type carbides, d) Diffraction pattern for NbC type carbides

4. Analysis of test results

The static tensile test of the welded joints did not reveal any significant differences in the strength R_m of the joints as regards welding variants with and without a heat treatment, i.e. using the temper beads technique. The average tensile strength values were restricted within the range between 676 MPa (for welding variant 1) and 768 MPa (for welding variant 2). The tensile strength of the joint welded using the temper beads technique was slightly higher than the R_m of the PB2 steel parent metal amounting to 732 MPa (Fig. 2).

The impact test results revealed that in the HAZ of the welded joints in both welding variants the values of absorbed energy were high and significantly exceeded the criterion value of 27 J for the parent metal and 24 J for the HAZ area. In the case of the HAZ area absorbed energy, both near the face and near the root, it was possible to observe that the joint welded with PWHT revealed slightly higher values of absorbed energy in comparison with the joint welded using the temper beads technique. While analysing the impact test results for the weld area it was possible to observe that the criteria of 24 of 27 J were satisfied only by the joint welded with a post-weld heat treatment. The results of absorbed energy related to the weld in the joint which did not undergo PWHT failed meet the criteria of 24 and 27 J (7 and 8 J near the face and near the root respectively) (Fig. 3).

In the bend test positive results, i.e. a bend angle of 180° was obtained only for the welded joint subjected to a post-weld heat treatment. In turn, the welded joint subjected to the temper beads technique was characterised by bend angles restricted in the range between 75° and 95° and failed to meet the required criterion of a bend angle (Table 3).

The hardness measurements revealed that the joint welded with PWHT was, in all areas, characterised by uniform hardness values, significantly below the allowed criterion of 350 HV. In turn, the welded joint subjected to the temper beads technique revealed values exceeding 350 HV10, particularly in the HAZ areas, where the highest values reached approximately 450 HV10 (Fig. 5). From Figure 5b) shows that used in tests temper beads technique was not sufficient to obtain a corresponding reduction of microstructure hardness in the HAZ and weld. Therefore, more research is needed in order to optimize the welding techniques and to improve its effects.

The microscopic metallographic examination using light microscopy (LM) revealed the presence of ferrite delta in the microstructure of the weld of the joint not subjected to a heat treatment (Fig. 6c).

The microstructural examination in films (TEM) revealed that greater dislocation density was present in the coarse-grained HAZ area of the welded joint subjected to the temper beads technique if compared with the analogous area of the welded joint subjected to PWHT. In addition, the coarse-grained HAZ area of the welded joint not subjected to a heat treatment was characterised by the greater size of subgrains in comparison with the joint subjected to PWHT. The analysis of dispersive precipitates revealed the presence of complex carbides $M_{23}C_6$, NbC carbides and V(C,N) carbonitrides in the HAZ areas of the joints welded in both variants (Fig. 7 and 8).

5. Concluding remarks

On the basis of the tests conducted it was possible to formulate the following conclusions:

1. The tensile strength of the welded joint subjected to a heat treatment and that subjected to the temper beads technique equals the strength R_m of the parent metal of PB2 steel.

2. The tensile strength of the welded joint subjected to the temper beads technique is slightly higher than that of the joint welded conventionally and subjected to PWHT.

3. For both welding variants the absorbed energy of the HAZ area is high and several times exceeds the criteria of 27 and 24 J adopted for the parent metal and HAZ respectively.

4. The plastic properties of the weld of the welded joint subjected to the temper beads technique are poor and fail to meet the criteria in the impact test and hardness test.

5. The reason for the low plastic properties of the weld of the welded joint subjected to the temper beads technique is the presence of ferrite delta in the microstructure and high hardness of martensite (above 350 HV10).

6. The coarse-grained HAZ area in the welded joint subjected to the temper beads technique is characterised by greater dislocation density and smaller size of subgrains in comparison with the analogous area the welded joint subjected to PWHT.

7. The coarse-grained HAZ areas of the welded joint subjected to a heat treatment and that not subjected to PWHT contain $M_{23}C_6$ carbides, NbC carbides and V(C,N) carbonitrides.

References

[1] Hernas A., The steels and alloys high-temperature creep resistance, *Publishing house of Silesian University of Technology*, Gliwice, (1999).

[2] Alloy development for critical components of environmental friendly power plant. European research project, Instytut Spawalnictwa, 2005-2008.

[3] Brózda J., Constructional steels and their weldability, Instytut Spawalnictwa, Gliwice, (2009).

[4] Tasak E., Ziewiec A., Metallurgy of welding, *Publishing house JAK*, Kraków, (2008).

[5] Aloraier A.S., Ibrahim R.N., Ghojel J., Eliminating post-weld heat treatment in repair welding by temper bead technique: role bead sequence in metallurgical changes, *International Journal of Pressure Vessels and Piping*, no 153-154, pp. 392-400 (2004).

[6] Łomozik M., Morphology and Toughness of Heat Affected Zone Regions of Steel Welded Joints in the Aspect of Temper Bead Application, *Publishing house of AGH University of Science and Technology*, Kraków, p. 19 (2007).

[7] Łomozik M., Kwieciński K., Jachym R., Urzynicok M., Mariani P., Mechanical properties of butt welds in PB2 steel pipes welded using conventional and temper bead technique, *Energetyka*, pp. 725-729, November (2012).

[8] COST 536 PB2 steel. Size ODxWT 219.1x31 mm. Order no 1011211-002. Mechanical test certificate. Tenaris Dalmine, (2010).

INFLUENCE OF PROCESS PARAMETERS AND JOINT DESIGN ON MICROSTRUCTURE AND HIGH TEMPERATURE PROPERTIES OF DIFFUSION BRAZED JOINTS

Martin Frommherz[*], Alfred Scholz, Matthias Oechsner

Fachgebiet und Institut für Werkstoffkunde, Technische Universität Darmstadt

Grafenstraße 2, 64283 Darmstadt

*Corresponding author: frommherz@mpa-ifw.tu-darmstadt.de

Abstract

The influence of process parameters and geometric design on microstructure and mechanical properties of diffusion brazed joints for high temperature application e.g. hot gas turbine components was exemplarily investigated in a recent study based on the alloy Hastelloy X. Several brazing experiments were carried out with varying braze foil composition, brazing temperature and brazing time to evaluate the influence of process parameters. The joint microstructure was investigated with light microscopy, scanning electron microscopy and EDX. Concerning the joint design, uniaxial short-term (tensile) and long-term (creep) experiments were performed on diffusion brazed butt joints and scarf joints with varying joint angle and joint gap width. The process parameter study shows that the mechanisms of the diffusion process are mainly determined by the fine grained microstructure and the high molybdenum content of the base material. Highly stable Mo-B precipitations in the interdiffusion zone and Mo-Si precipitations using braze foils containing silicon inhibit a full homogenization of the joint microstructure, which clearly affects the mechanical properties. Furthermore, the heat treatment leads to a significant softening of base material properties due to over-aging and grain growth. The influence of joint design on the strength is dependent on the microstructure of the joint and the temperature dependent deformation behavior. Combining optimized process parameters and adjusting the joint angle, high strength joints were obtained even for high temperature application.

Keywords: diffusion brazing, Hastelloy X, joint design, process parameter, scarf joint

1. Introduction

Diffusion brazing, also referred to as transient liquid phase bonding (TLP), is one preferential joining method for gas turbine materials, especially for nickel-base alloys, which are prone to solidification or strain age cracking. Diffusion brazing is a bonding process which combines the benefits of high temperature brazing with the high efficiency of diffusion bonding. A thin layer of alloying metal containing a melting point depressant is placed between two pieces of substrate material, where a thin liquid layer is formed during heating up to the brazing temperature. The diffusion of melting point depressants into the parent material at bond temperature results in a complete isothermal solidified joint [1]. Under optimized process conditions, precipitation-free and homogeneous joints can be achieved, resulting in joint strength comparable to the parent metal [1]–[3].

For the application of diffusion brazing two fundamental objectives are relevant. First of all, a material specific optimization of process parameters must be carried out. Secondly, the

geometric boundary conditions of the joint must be considered, especially for the application of diffusion brazing to thin-walled components. Up to now, the influence of joint design and geometric boundary conditions on the mechanical properties of diffusion brazed joints was not investigated in detail.

In this publication, results of the investigation of the influence of (i) process parameters and (ii) geometric design on microstructure and mechanical properties of diffusion brazed joints are presented for the nickel-base alloy Hastelloy X. The primary objective of this research is to identify predominant factors affecting joint strength, leading to optimized process parameters and an optimized joint design. To investigate the influence of process parameters, brazing experiments were carried out with varying braze foil composition, brazing temperature, brazing time and gap width. Due to the correlation of joint microstructure and joint strength, the evaluation of the influence of process parameters is mainly based on metallographic investigations. Furthermore, the influence of the braze cycle on base material properties was investigated in detail. The influence of the joint design on short- and long-term properties was investigated using butt joints and scarfed joints with varying joint angle and gap width.

2. Experimental

The investigations were conducted on diffusion brazed joints of the nickel-base alloy Hastelloy X. The alloy is a polycrystalline wrought alloy with exceptional oxidation and corrosion resistance and is recommended for use in furnace components, e.g. combustion chambers. For the investigation, sheet metal with a thickness of about 3-5 mm for the base metal and amorphous brazing foils with a thickness of about 37 µm for the interlayer respectively, were used. Amorphous braze foils show substantial advantages in regard to braze properties (wetting of the substrate, flow characteristics) and application [4]. The nickel-base braze foils contain, besides chromium, differing proportions of the melting point depressants boron and silicon to allow investigation of the influence of the amount and type of melting point depressant on joint microstructure. The chemical composition of these materials is presented in Table 1.

Table 1: Nominal chemical composition of parent metal and brazing foils

(wt.-%)		Ni	Cr	Fe	Mo	Co	W	C	Mn	Si	B
Hastelloy X[1]	parent material	bal.	22	18	9	1,5	0,6	0,1	1	1	0,008
VZ2150[2]	braze foil (38 µm)	bal.	18,2	--	--	--	--	--	--	7,3	1,15
MBF50[3]	braze foil (38 µm)	bal.	19	--	--	--	--	0,08	--	7,3	1,5
MBF80[3]	braze foil (37 µm)	bal.	15,2	--	--	--	--	0,06	--	--	4,0

Brazing trials and heat treatments were performed by the project partner ALSTOM (Switzerland) Ltd. The preparation of the surface of the substrate material was conducted in

---

[1] technical data sheet: Haynes Corporation
[2] technical data sheet: Vitrobraze
[3] technical data sheet: Metglas

accordance with an internal standardized specification, which included grinding, cleaning of the substrate surface and the application of the braze foil. Gap width was varied using one (37/38 µm) or three (111/114 µm) braze foils. It is emphasized, that in general no distance holder was used. Braze tests were carried out in a vacuum furnace at brazing temperatures 1120°C and 1170°C under a constant load of about ~0,05 MPa with varying dwell times up to 15h at maximum brazing temperature. A schematic drawing of brazed metal sheet blanks for the extraction of the test specimens is presented in Figure 1.

Short- and long-term mechanical properties at a temperature range of room temperature to 900°C were investigated using flat test specimens with varying joint angle from 22,5° to 90° (see Figure 2).
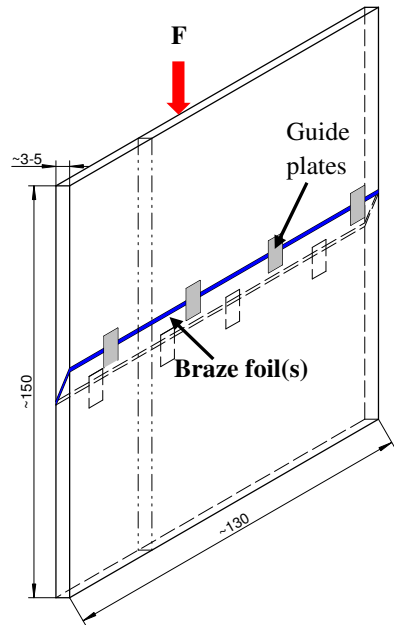
Figure 1: Diffusion brazed metal sheets.
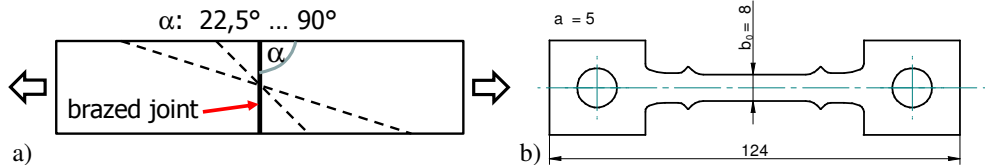
Figure 2: Variation of joint angle α (a) and flat test specimen for the determination of mechanical properties of diffusion brazed sheets (b).

3. Influence on joint microstructure

To achieve mechanical properties comparable to the parent material, the main objective is to produce sound joints with a homogenous composition and similar microstructure [1], [5]. Principally this can be achieved due to the full isothermal epitaxial solidification of the liquid layer at brazing temperature and a homogenization of the joint by a post diffusion heat treatment. However, insufficient process parameters can lead to the formation of eutectic solidified residual melt, intermetallic phases and solidification porosity.
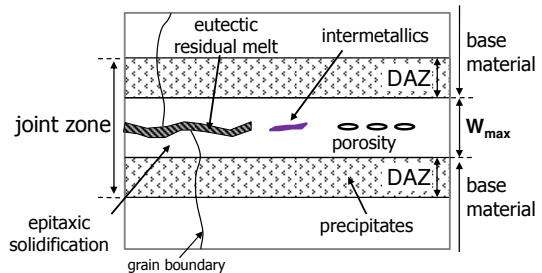
Figure 3: Diffusion brazed joint, schematic.

Furthermore, dependent on the combination of base material and braze foil composition, the diffusion of melting point depressant and the interdiffusion between braze melt and base material can lead to precipitation in the interdiffusion zone (DAZ: diffusion affected zone), see Figure 3 [6]–[8].

In the case of the alloy Hastelloy X, the precipitation in the DAZ and the homogenization of the fusion zone are two essential issues which are fundamental to properties of the diffusion brazed joints.

3.1. Precipitations in the diffusion affected zone (DAZ)

The complex mechanisms brazing Hastelloy X are mainly determined by the fine grained polycrystalline microstructure and the high molybdenum content of the wrought alloy. The results show that the diffusion of the melting point depressant into the base material leads to an extensive formation of precipitation in the substrate grains as well as grain boundary precipitates. When brazing foils containing pure boron are used, needle-like precipitates form in the substrate grains and at the grain boundaries. Due to the considerable faster diffusion along the grain boundaries, two distinct diffusion zones are formed (Figure 4, Figure 5). The precipitations were identified using EDX and WDX measurements as borides with high contents of molybdenum and chromium. Thermodynamic calculations suggest that the precipitations are borides of crystal structure type M_3B_2.
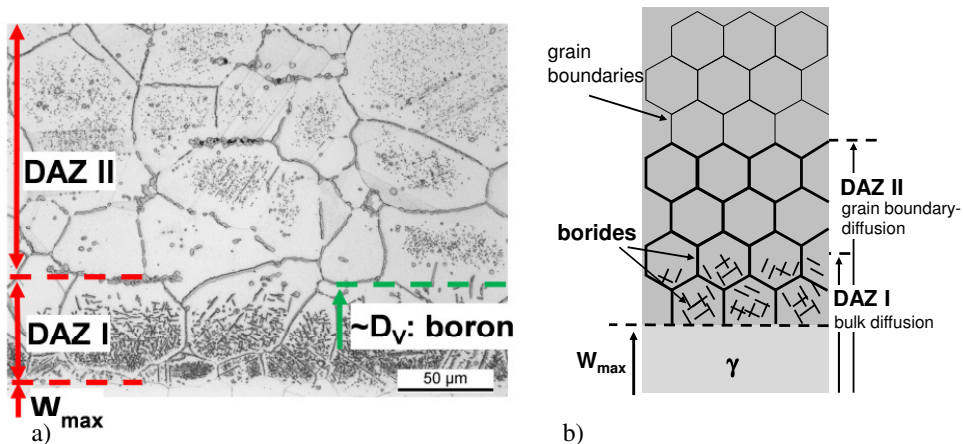
Figure 4: Diffusion affected zone (DAZ) when using brazes containing boron: formation of needle-like precipitations in substrate grains as well as grain boundary segregation (a) and schematic diagram of diffusion mechanisms (b).

Using silicon as a substitute for boron (MBF50, VZ2150) can significantly reduce the extensive formation of borides; however, in the interdiffusion zone of silicon, a formation of blocky precipitates occurs. These precipitates contain high contents of silicon and molybdenum and form an almost continuous line of blocky precipitates (Figure 5).
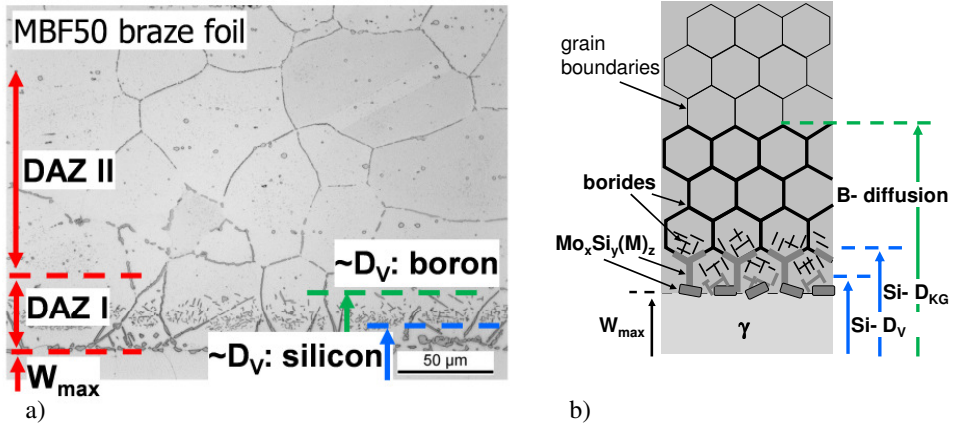
Figure 5: Diffusion affected zone (DAZ) using brazes containing silicon: formation of a quasi-continuous precipitation line (a) and schematic diagram of diffusion mechanisms (b).

3.2. Homogenization of the joint

Prolonging the dwell time was supposed to improve the homogenization of the joint. However, the results showed that the precipitations are very stable and do not dissolve in the nickel matrix. In contrast, in the case of the silicon containing braze foils, the precipitations coarsen significantly with increasing dwell time (Figure 6a). The quasi-continuous line of precipitations remain unaffected and prevents a homogenization of the joint microstructure by prohibiting an epitaxial growth of substrate grains into the joint. With the use of the braze foil with pure boron as melting point depressant, the homogenization heat treatment leads to a decreasing amount of precipitation in the substrate grains, yet the highly stable grain boundary precipitates even coarsen and prevent a full homogenization of the joint area, leading to a persisting discontinuity in microstructure (Figure 6b).

4. Influence of the brazing cycle on base material properties

The brazing cycle clearly influences the mechanical properties of the parent material. The brazing cycle leads to a degradation of the base material properties due to over-aging dependent on brazing temperature and hot dwell time. Coarsening of carbides will occur due to the high temperature loading. TTT diagrams in [9] show, that in the range of the brazing temperature, no carbides of the type $M_{23}C_6$ and no μ- or σ- phase will form. Only carbides of the type M_6C exist at this temperature. Long dwell times lead to a coarsening and to an over-aging of the microstructure (see [10]).

A massive grain growth at temperatures in the range of the solution annealing temperature (actual: 1170°C) is typically observed for Hastelloy X. Grain boundary precipitates, which prevent the grain growth at lower temperatures, will dissolve, leading to extensive grain growth. At lower temperatures (actual: 1120°C) no grain growth is observable; however, a significant coarsening of carbides occurs (Figure 7).
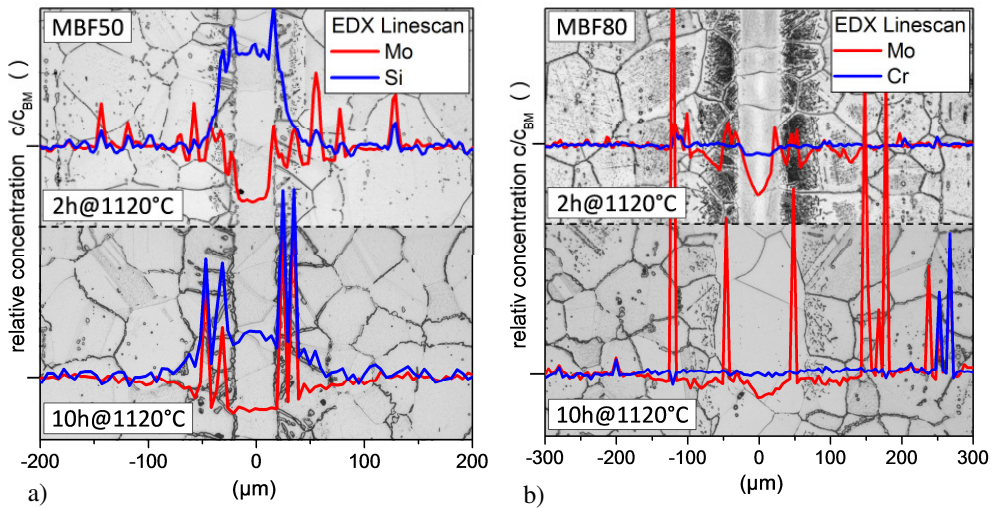
Figure 6: EDX line scans of braze joints at different dwell times. Precipitations containing silicon and molybdenum lead to a discontinuity in joint microstructure (a) and highly stable molybdenum precipitations prevent a full homogenization of the braze joint (b).
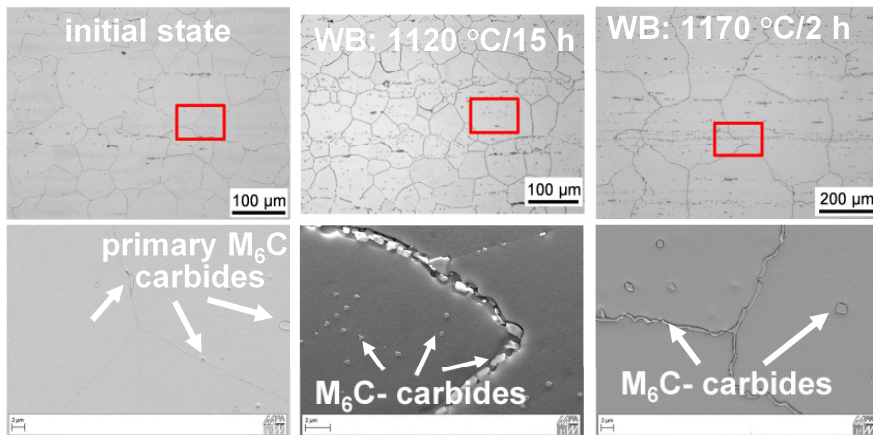
Figure 7: Development of base material microstructure as a function of the brazing cycle.

The over-aging and grain growth lead to a significant softening of base material properties at a brazing temperature of 1170°C (Figure 8). The drop in the yield strength in particular is pronounced due to the massive grain growth (Figure 8a). The creep rate is increased by a factor of 3-5 dependent on the annealing temperature (Figure 8b). In contrary, at very high temperatures (actual: 900°C), the influence of the brazing cycle on base material properties is negligible. Quasi-static mechanical properties and the creep behavior are more or less identical to those of the initial condition.
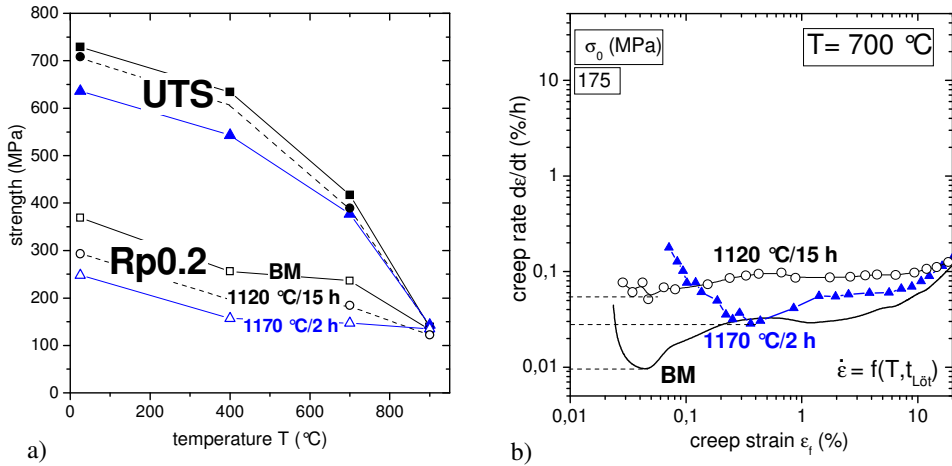
*Figure 8: Influence of the heat treatment of the brazing cycle on base material properties:
quasi-static short-term properties (a) and creep rates at 700°C (b).*

5. Variation of geometric boundary conditions

In the following chapter, selected results of the influence of geometric boundary conditions on short- and long-term properties are presented. In detail, results of tensile and creep tests as well as investigations of the deformation and damage behavior in correlation to the joint design, joint microstructure and mechanical properties are shown. The influence of joint design on the strength is dependent on the microstructure of the joint and the temperature dependent deformation behavior. Combining optimized process parameters and adjusting the joint angle allows high strength joints to be obtained even at high temperatures.

5.1. Influence of joint design at low application temperatures

At low temperatures, the ideal joint angle is a function of the braze alloy composition and process parameters and is not dependent on the geometric boundary conditions. The observed yield strength is only dependent on the brazing cycle, which leads to a degradation of base material properties (see Chapter 4.). The tensile strength is a function of the joint angle as well as of the process parameters (α, c_{braze}, T_{cycle}, t_{cycle}); see Figure 9a.

With optimized process parameters (MBF80 braze foil, 1120°C/15h), no improvement of the joint strength by a change of joint angle can be achieved. The maximum joint strength is currently observed at the butt joint ($\alpha = 90°$), approximately 95% of the base material. Thus by optimizing the process parameters, the potential of an improvement of joint strength by the joint design is irrelevant. In addition to the direct geometric influence (variation of normal and shear stresses), the variation of the joint angle has an influence on joint microstructure and thus on the mechanical properties. Logically, as transient liquid phase bonding is a diffusion controlled joining process, missing bulk volume at low joint angles leads to a higher precipitation density in the overlapping area and thus to an embrittlement. As a result, at low

405

joint angles, damage initiates in the overlapping area, leading to a premature failure of the base material (Figure 10a).
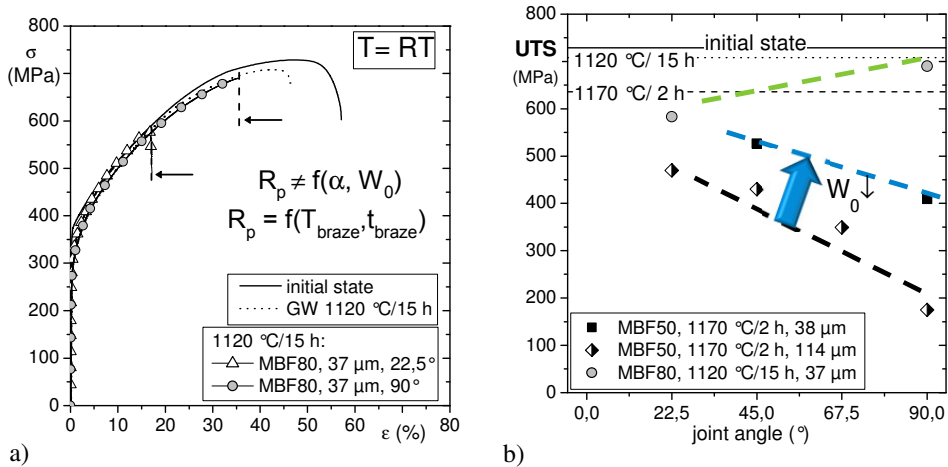
Figure 9: Influence of the joint angle α and the process parameters on joint strength at room temperatures.
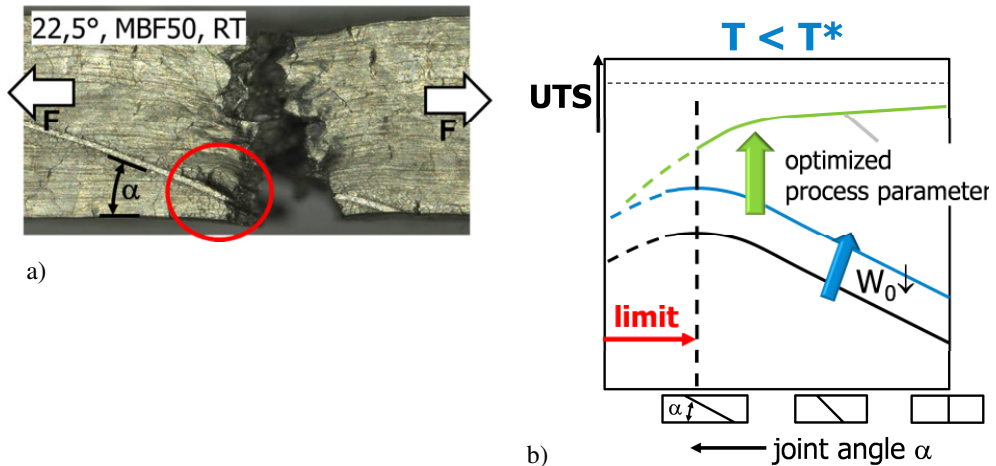
Figure 10: Premature failure at low joint angles: embrittlement of the base material as a result of missing diffusion bulk volume (a) and schematic diagram of joint strength dependent on joint angle, gap width and process parameters (b).

A further reduction of the joint angle will not result in a higher joint strength, but rather in a more pronounced degradation of the base material due to the embrittlement in the overlapping area. Thus, a suitable joint design must provide enough diffusion bulk volume. This is especially important in thin-walled turbine components. Figure 10b shows trend lines of joint strength dependent on geometric boundary conditions and process parameters based on the experimental results and the microstructural observations.

5.2. Influence of joint design at high application temperatures

The influence of the joint design on joint strength or a benefit in joint strength must be considered in relation to temperature. With increasing temperature, the interdiffusion zone respectively the diffusion affected zone on the joint properties has a decreasing influence on mechanical properties. The joint strength is mainly dependent on the high temperature properties of the joint microstructure, which is primarily determined by the homogenization of the joint.

At a temperature of about 700°C, the joint strength is high enough to achieve creep strength comparable to the base material (Figure 11a) even in case of the butt joint (α=90°). In contrast, at 900°C, no sufficient creep strength is observed. Thus, minimizing the joint angle α, respectively minimizing the shear and normal stresses, the creep strength can be significantly improved by a factor of 3-4 (Figure 11b). As shown in Chapter 5.1., a smaller gap width would lead to a higher creep strength as a result of a better homogenization of the joint and the increased geometric constraint. Regarding reduced braze joint properties, finite-element- calculation showed that joint angles causing high shear stresses in the joint should be avoided at all costs. High shear stress will lead to a localization of shear deformation in the braze joint; no supporting effect of the substrate material is observed. This leads to a macroscopic embrittlement and a drop in joint creep strength. Minimizing the joint angle ($\leq$ 22,5°) minimizes the shear and normal stresses in the joint plane. Together with the greater supporting effect of the base material, this results in a stress redistribution to the base material leading to a decrease in creep deformation in the joint and a higher joint creep strength. Combining optimized process parameters (longer hot dwell time) and minimizing the joint angle, creep strength comparable to the base material can be observed.
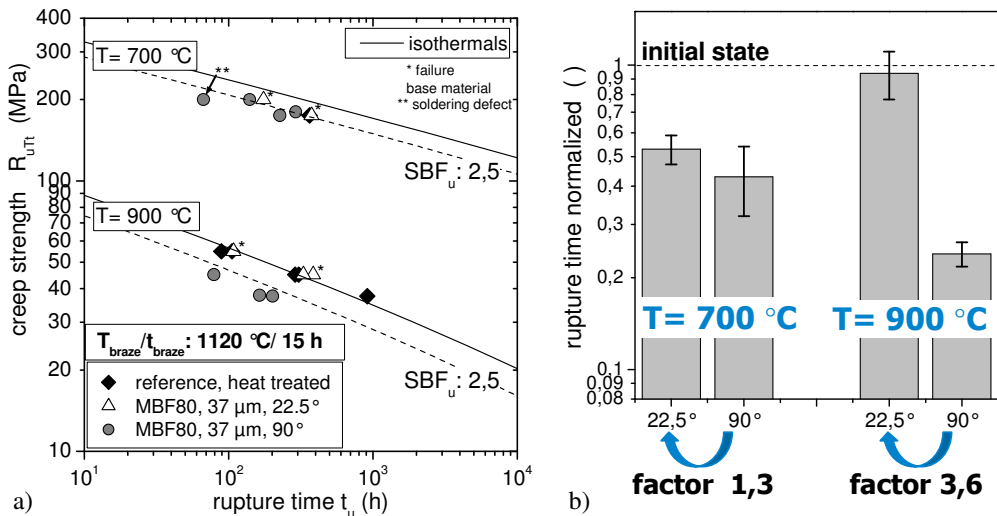
Figure 11: Improvement of creep strength by adjusting the joint design: creep rupture diagram at 700°C and 900°C (a) and temperature dependent benefit in joint strength (b).

For the investigated braze joints with small joint angles, a change of fracture position from the joint to the base material adjacent to the joint zone (Figure 12a) is a typical feature. It is assumed that the boride grain boundary precipitations in the diffusion affected zone hinder grain boundary sliding. This results in a higher creep strength of the DAZ supporting the original joint microstructure against a further creep deformation, leading to the observed change in fracture position. 100% of the base material creep strength is achieved. Figure 12b shows trend lines of the creep strength dependent on the joint angle and the process parameters based on the experimental results and the microstructural observations.
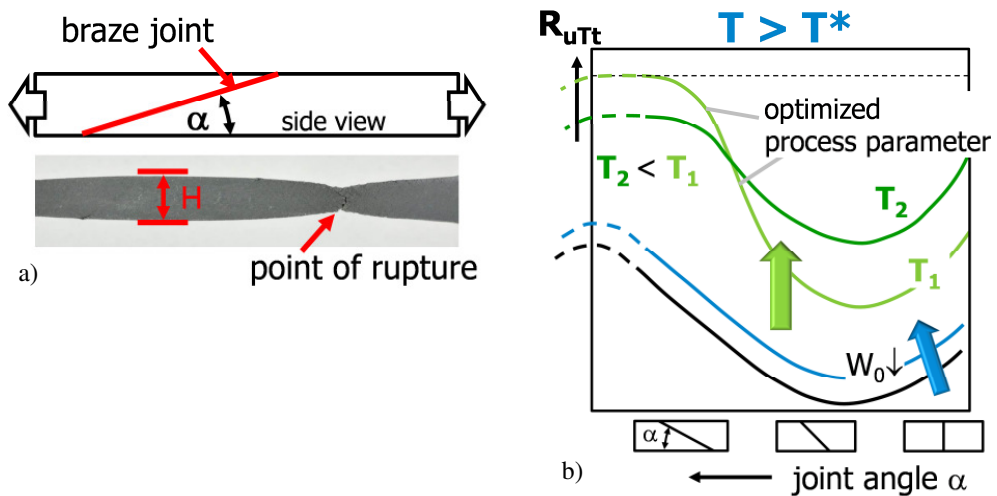
Figure 12: Change of fracture position adjacent to the joint zone in the case of the scarfed joint (α= 22.5°) (a) and trend lines of creep strength based on experimental and microstructural results (b).

The results show that, especially for high application temperatures, a sufficient homogenization of the braze joint is indispensable to achieve properties comparable to the base material. However, regarding not fully homogeneous joints, high creep strength can also be achieved by adjusting the joint angle.

Nevertheless, it is believed that the precipitations in the diffusion affected zone will have a pronounced impact on joint strength under dynamic loads, especially under thermo mechanical fatigue conditions due to the brittle behavior at low temperatures. This has to be investigated in detail in further experiments.

6. Conclusions

The influence of process parameters and geometric design on microstructure and mechanical properties of diffusion brazed joints was investigated. The results show that in the case of Hastelloy X, the mechanisms during the diffusion brazing process are mainly determined by the fine grained microstructure and the high molybdenum content of the alloy. Highly stable

precipitations in the diffusion affected zone prevent a full homogenization of the joint microstructure. Especially in the case of the silicon containing brazes, the precipitates form a quasi-continuous line leading to a pronounced discontinuity in the joint microstructure. Furthermore, the brazing cycle leads to a significant degradation of base material due to over-aging and grain growth. The influence of the joint design on joint strength is dependent on the temperature dependent deformation and damage behavior. Besides the direct input of joint design on joint strength by minimization of normal and shear stresses in the joint plane, the effect on bulk diffusion causing an embrittlement of the base material must be considered. Through combining optimized process parameters and adjusting the joint angle, high strength joints were obtained even for high temperature applications.

In principle, the results can be transferred to other wrought polycrystalline alloys, which contain high amounts of boride and silicide forming elements. These boundary conditions have to be kept in mind adapting the diffusion process to new materials.

7. References

[1] D. S. Duvall, W. A. Owczarski, and D. F. Paulonis, "TLP Bonding: A New Method for Joining Heat Resistant Alloys," *Welding Journal*, pp. 203–214, (1974).

[2] K. Nishimoto, K. Saida, D. Kim, S. Asai, Y. Furukawa, and Y. Nakao, "Bonding phenomena and joint properties of transient liquid phase bonding of Ni-base single chrystal superalloys," *Welding in the World*, vol. 41, pp. 121–131, (1998).

[3] D.-U. Kim and K. Nishimoto, "Creep rupture and fatigue properties of transient liquid phase bonded joints of Ni base single crystal superalloy," *Materials Science and Technology*, vol. 19, no. 4, pp. 456–460, (2003).

[4] A. Rabinkin, "Brazing with (NiCoCr)-B-Si amorphous brazing filler metals: alloys, processing, joint structure, properties, applications," *Science and Technology of Welding & Joining*, vol. 9, pp. 181–199, (2004).

[5] W. Li, T. Jin, X. F. Sun, Y. Guo, H. R. Guan, and Z. Q. Hu, "Study of Ni-Cr-Co-W-Mo-B interlayer alloy and its bonding behaviour for a Ni-base single crystal superalloy," *Scripta Materialia*, vol. 48, no. 9, pp. 1283–1288, (2003).

[6] X. Wu, R. S. Chandel, and H. Li, "Evaluation of transient liquid phase bonding between nickel-based superalloys," *Journal of Materials Science*, vol. 36, pp. 1539–1546, (2001).

[7] O. A. Ojo, N. L. Richards, and M. C. Chaturvedi, "Isothermal solidification during transient liquid phase bonding of Inconel 738 superalloy," *Science and Technology of Welding & Joining*, vol. 9, pp. 532–540, (2004).

[8] N. P. Wikstrom, O. A. Ojo, and M. C. Chaturvedi, "Influence of process parameters on microstructure of transient liquid phase bonded Inconel 738LC superalloy with Amdry DF-3 interlayer," *Materials Science and Engineering: A*, vol. 417, no. 1–2, pp. 299–306, (2006).

[9] J.-C. Zhao, M. Larsen, and V. Ravikumar, "Phase precipitation and time–temperature-transformation diagram of Hastelloy X," *Materials Science and Engineering: A*, vol. 293, no. 1–2, pp. 112–119, (2000).

[10] H. M. Tawancy, "Long-term ageing characteristics of Hastelloy alloy X," *Journal of Materials Science*, vol. 18, no. 10, pp. 2976–2986, (1983).

8. Acknowledgements

TECHNOLOGIES OF MANUFACTURING FINNED TUBES

Janusz Adamiec*, Michał Stopyra*, Michał Więcek**

* Silesian University of Technology, Faculty of Materials Science and Metallurgy
Institute of Material Science, 40-019 Katowice, Krasińskiego 8, Poland,
Janusz.adamiec@polsl.pl, Michal.stopyra@polsl.pl
** Energoinstal SA, 40-203 Katowice, Roździeńskiego 188d, Poland
mwiecek@energoinstal.pl

Abstract

Finned tube heat exchangers are characterized by higher thermal efficiency than plain tube heat exchangers, thus they are being introduced into the power generation industry. The present paper presents a brief review of methods of manufacturing finned tubes which might be applied in modern supercritical steam power plants. The innovative, highly efficient laser welding method is highly distinguishable among others. Laser welded finned tubes comply with the requirements of the highest quality level B according to PN-EN ISO 13919.

Keywords: Finned tubes, manufacturing methods, laser welding, materials for power industry

1. Introduction

An increase in demand for electric energy and European Union directives (2001/77/EC, 2001/80/EC, 97/23EC) require that the Polish power industry increase the efficiency of power plants and reduce CO_2 and NO_x emissions. The modernization of currently used boiler units and development in the areas of boiler design, manufacturing process, and operation are essential in order to meet these requirements [1-3]. Progress in the power industry is determined by the development of materials engineering and processing technologies.

Heat exchangers, especially steam superheaters, are crucial elements in modern boilers. One of the methods of increasing boiler efficiency is to improve the rate of heat transfer by increasing the surface area of the heat exchanger. This may be achieved by the use of finned tubes (fig. 1). They contribute to improved heat efficiency and a decreased cost of energy production.

There are many methods of manufacturing finned tubes. The simplest one is winding a tape about a tube. This method is relatively cheap, but the divided structure of a finned tube does not ensure sufficient conditions for efficient heat transfer. Moreover, thermal expansion of fin and tube materials and vibrations may lead to further deterioration of thermal efficiency over the operating time [4]. This is why technologies have been developed that allow the

manufacture of integral fin tubes, characterized by higher thermal efficiency (2.5 times higher compared to plain tubes and 1.5 times higher compared to tubes with separate fins) and stability. The technologies may be divided into two groups on the basis of whether they involve mechanical working or welding. The mechanical working technologies require the use of materials with excellent cold-workability. Another limiting factor is the maximum fin height, thus the methods are mostly used to manufacture low-finned tubes. The welding technologies allow the manufacture of tubes with a wide range of fin heights and various fin shapes (solid or serrated). However, in welded spiral fin tubes, the weld length may reach 20 meters per 1 running meter of the tube. This indicates an increased probability of welding defects. In addition, a characteristic state of stress occurs which may cause cracking during manufacturing and operation. In response to demand for an effective method allowing the manufacture of high quality finned tubes of heat resistant materials, the laser welding method was developed.

The aim of the present work is to review the available technologies of manufacturing finned tubes with regard to production of heat exchangers for the power generation industry.

Fig. 1. Welded finned tubes with solid (a)[5] and serrated (b) fin [5]

2. Plastic working technologies

The most common method of manufacturing plastic worked finned tubes is rolling. This method allows the production of both monometallic (integral) (fig 2a, 3) and bimetallic finned tubes (fig 2b). The latter consist of two tubes, one inside the other, which are rolled without the use of a mandrel. Rolled finned tubes are manufactured using three-roll helical rolling mills (fig. 2a). There are two variants of this method: deepening and thinning. The first method is based on plastic deformation by means of tool insertions of progressively increasing outer diameter, which gradually penetrate the outer tube walls, extruding the fin until its required height is reached (fig 3b). The width of the fin tip remains constant. This method is only used to produce low-finned tubes . The other variant consists in tool insertions of progressively increasing thickness (fig 3a). As a result, fin thickness is reduced while fin height is increased. The method involves the use of both radial and axial drafts and larger deformations. However, it allows the production of high-finned tubes [4].
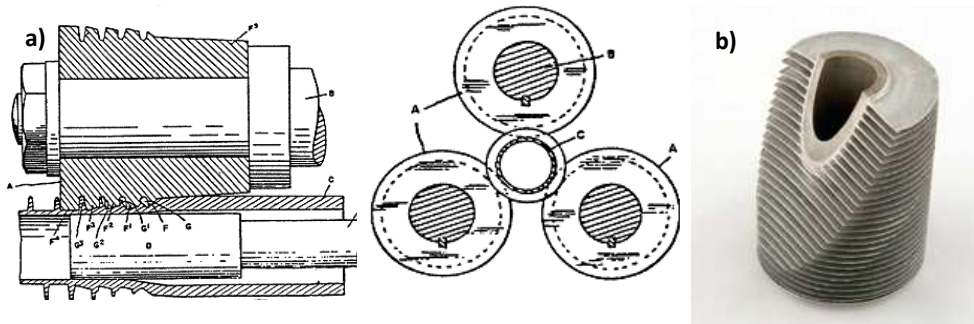
Fig. 2. Sketch of finned tube rolling process (a) [6], rolled bimetallic finned-tube (b) [7]

The materials used for producing integral finned tubes are mainly aluminum and its alloys and copper and its alloys. Low-alloyed steels may be used to manufacture low-finned tubes, as rolling finned tubes of high-alloyed austenitic steels involves serious technological difficulties. Pure aluminum (Al99.5) is particularly recommended for rolling high-finned tubes due to its excellent cold workability. Some Al and Cu alloys may also be used for rolling high-finned tubes, but the maximum fin height is limited in this case. In bimetallic tubes (fig. 2a), the outer tube is made of Al, Cu, and their alloys, and the inner tube may be made of any metallic material. However, heat efficiency of bimetallic tubes decreases at elevated temperature due to a difference between the thermal expansion coefficients of the outer and inner tube materials [4].

Recently, some new plastic working methods of fin tube production have been developed. They allow the manufacture of tubes with the so-called three-dimensional fin, which is formed in complex technological processes like RWE (Rolling – Wedging – Extruding – fig. 4) [8-12]. However, they are not used on an industrial scale yet.
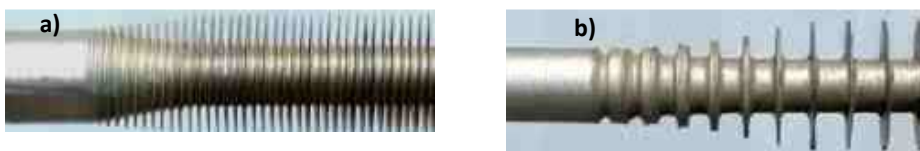
Fig. 3. Finned tubes with fin formed by deepening (a) [4] and thinning (b) methods [4]
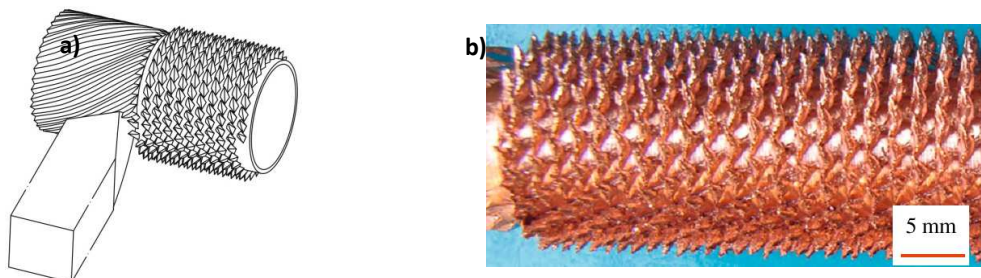
Fig. 4. Sketch of fin forming by RWE (a) [8]; finned tube manufactured by RWE (b) [8]

413

3. Welding methods

The development of the technology of brazing finned tubes was stimulated by the disadvantages of mechanically produced finned tubes, in particular their reduced heat efficiency caused by contact resistance [13]. Brazing allows the selection of different materials for tubes and fins and joining fins of different heights and shapes to the tube. The strip of which the fin is made may be bent or serrated in order to increase the heat transfer area.

Brazed finned tubes are commonly manufactured in a semi-automatic brazing process in furnaces with a protective gas atmosphere. The uniform temperature field inside the furnace provides low thermal stress. It is possible to use nickel brazing compounds, which melt over the entire surface of the tube and form a coating that increases corrosion resistance. It also forms a smooth fillet surface at the base of the tube, which prevents the accumulation of impurities and stress concentration to a higher degree than rough fillet [14]. Brazed finned tubes allow operation at temperatures up to 350°C and even up to 650°C if protective coatings are applied [15, 16].

One of most common methods of manufacturing finned tubes is gas metal arc welding (GMAW). There are two variants of this method. The first variant is based on forming a fillet weld between the tube and the fin (fig. 5). This variant is characterized by low efficiency [17]. The other variant involves but-welding of the tube and the fin [18] (fig. 6a), which enables lower consumption of filler wire and allows using U-shaped fin (fig. 6b). However, the quality of such joints is usually lower, as a number of welding defects (lack of joint penetration, undercuts, spatters) occur [17].
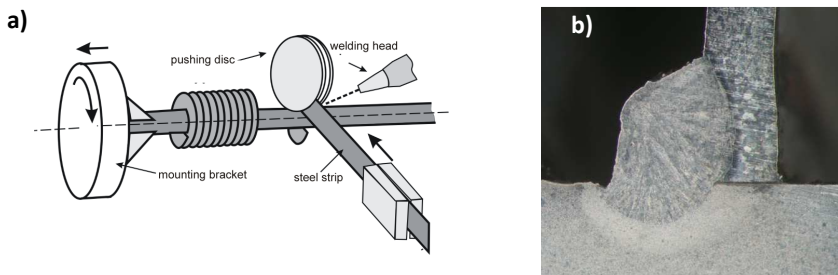
Fig. 5. GMAW welding of finned tubes with fillet weld (a); fin-tube fillet joint (b)
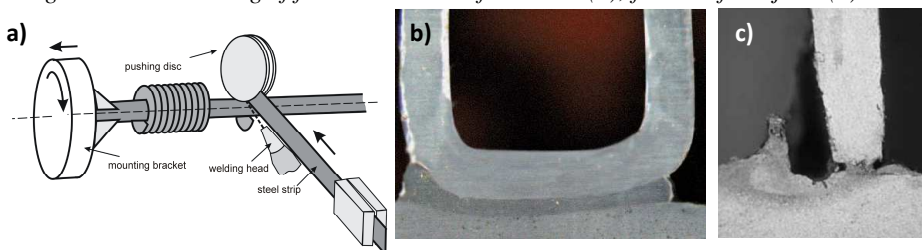
Fig. 6. GMA welding of finned tubes with butt-weld (a), U-shaped fin-tube joint [19] (b); defective fin-tube butt joint (c)

Another method of finned tube production is high frequency resistance welding (fig. 7a). It involves heat and pressure to obtain a bond between fin and tube. Forming the fin around the tube and welding heat cause deformation of the fin base, which provides a contact area wider than the fin itself. However, corrugation at the fin base may cause flow disturbance (pressure drop) resulting in poor performance. Problems associated with fin formation may be eliminated by using segmented fin. A typical welding defect in this method is liquid metal expulsion along the fin edges [20]. A variant of HF welding method has been developed that introduced the laser as an additional heat source (fig. 7b) [21].
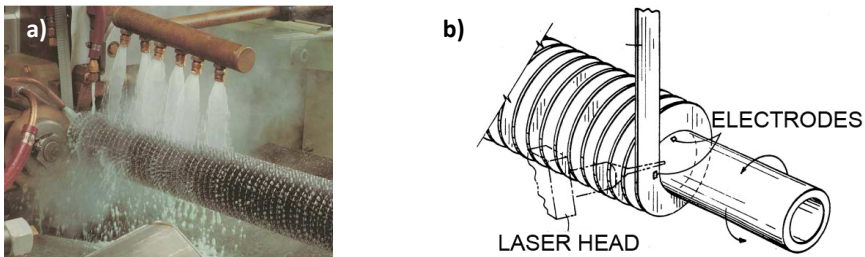
Fig. 7. High frequency welding of finned tubes [22] (a); laser assisted high frequency welding [21] (b)

The laser welding technology is an alternative for GMAW and HF welding. Currently, lasers are not used for welding boiler components for the energy industry due to the limited beam power, difficulties in forming a joint with precision, the possibility of hardening in both the narrow heat-affected zone and the weld zone, and hot cracking susceptibility. However, laser welding is highly efficient, which is why efforts were undertaken in Energoinstal S.A. to develop a method of laser welding of finned tubes using the Nd: YAG disk laser. As a result, a unique welding station was created (fig. 8). It consists of two production lines which allow maximizing the laser utilization rate (fig. 8a). While one tube is being welded using one line, another is being prepared using the other line. An induction heating system and a painting chamber are integrated with the welding station. The increase in performance due to applying the laser welding technology is up to 1000% in comparison with GMAW welding (fig 8b).

Fig. 8. Laser welding station [24] (a), Laser welding of finned tubes (b)

415

4. Results of laser welding of fin tubes

Welding tests were performed using steel grades P235GH, 13CrMo4-4 and 10CrMo9 for tubes and grade X2CrTi12 for fins, with a laser power within the range of 4÷6 kW, rotational speed within the range of 100÷250 rpm, and in a protective argon atmosphere. The joints performed were characterized by thorough penetration along the whole length of the weld (fig. 9a). The joints welded by 4 kW laser at 100 rpm complied with the highest requirements of PN-EN 13919 (quality level B). Increase in laser power to 5 kW resulted in occurrence of welding defects (incompletely filled groove and spatter caused by centrifugal force) acceptable in quality level C. However, the joints performed at 250 rpm did not meet the requirements of quality level D due to the scope of welding defects (incompletely filled groove and undercuts).
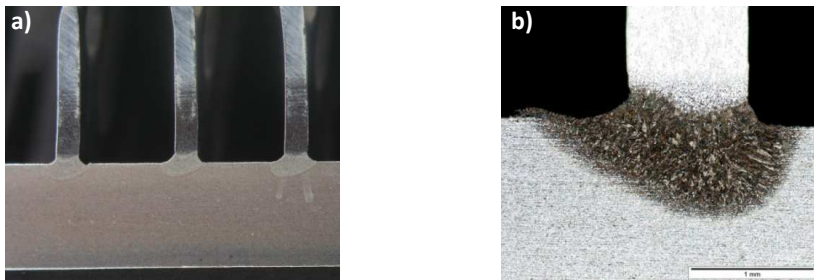
Rys. 9. Fin-tube weld joint, laser's power – 4 kW, rotational speed – 100 rpm (a);
microstructure of P235GH-X2CrTi12 joint (b) [17]

The analysis of the microstructure of the weld joints revealed the presence of ferrite-martensitic structure in a narrow (50÷100) heat affected zone (fig. 9b) and the presence of martensite in the weld zone. In the case of grade P235GH tube, weld joint hardness was lower than the limit value according to PN-EN 15614-11 (380 HV), thus there was no need to preheat the tubes. In the case of Cr-Mo grades, preheating is essential to avoid excessive hardening of the weld and HAZ.

5. Summary

The application of new materials is impossible without development of processing technology. The method of manufacturing finned tubes for heat exchangers operated in modern supercritical boilers must allow the use of heat resistant materials (with maximum operating temperatures above 600°C) and be highly efficient. Laser welded finned tubes manufactured by Energoinstal S.A. comply with the highest requirements of PN-EN ISO 13191. Moreover, productivity has increased by an order of magnitude in comparison with conventional methods. Despite the fact that the cost of implementation of the laser welding technology is high, the overall cost of manufacturing laser welded finned tubes is 3.5 lower than in the case of GMAW welded tubes.

Acknowledgements

References

[1]   Brózda J.: *Stale energetyczne nowej generacji stosowane na urządzenia energetyki o parametrach nadkrytycznych i ich spawanie*. Biuletyn Instytutu Spawalnictwa, Gliwice nr 5/2006

[2]   Najgebauer E. Patrycy A.: *Zobowiązania polskiej energetyki wobec UE*. http://www.cire.pl/publikacje/zobowiazaniawobecUE.pdf (28.07.2013)

[3]   Brózda J.: *Stale żarowytrzymałe nowej generacji, ich spawalność i właściwości złączy spawanych*, Biuletyn Instytutu Spawalnictwa, Gliwice nr 1/2004

[4]   Richert J.: *Innowacyjne metody przeróbki plastycznej metali*, Wydawnictwo AGH, Kraków 2010

[5]   Gawrysiuk W., Troszka A.: *Techniczno-ekonomiczne aspekty spawania wiązką laserową rur ożebrowanych w kotłach energetycznych*, Przegląd Spawalnictwa nr 5/2012, Sigma p. 8-11

[6]   US Patent No 2562782: Integral finned tube, 1951

[7]   http://www.cemal.com.pl/produkt/high_finned_bimetallic_tubes/ (28.07.2013)

[8]   Wan Z., Tang Y.: *Production of integral serrated outside finned tube using a combined method of rolling and wedging/extruding*, International Journal of Machine Tools & Manufacture 50 (2009), 487-490

[9]   Wan Z., Yan H., Tang Y.: *Forming mechanism of integral serrated high fins by plowing-extruding based on variational feed*, Transactions of Nonferrous Materials Society of China 20 (2010) 400-404

[10] Xiang J., Tang Yy., Ye B., Zhou W., Yan H., Hu Z.: *Compound forming technology of outside 3D integral fin of copper tubes*, Transactions of Nonferrous Materials Society of China 19 (2009) 335-340

[11] Xia W., Wu B., Tang Y., Ye B.: *On chopping–extrusion of integral-fin copper tubes*, Journal of Materials Processing Technology 138 (2003) 385–389

[12] Tang Y., Xia W., Liu S., Zeng Z., Ye B.: *Fin formation during pre-roll ploughing of copper 3D outside fin tube*, Transactions of Nonferrous Materials Society of China 11 (2001) 712-716

[13] Jannick P., Meurer C., Swidersky H.: *Potential of brazed finned tube heat exchangers in comparison to mechanically produced finned tube exchangers*, 9th International Refrigeration Conference at Purdue, 2002

[14] US Patent No 2807074: *Manufacturing of brazed fin tube and the like*, 1957

[15] http://www.boilerroom.com/econinfo.html (28.07.2013)

[16] http://www.tex-fin.com/custom.html (28.07.2013)

[17] Adamiec J. Gawrysiuk W. Więcek M.: *Spawanie rur ożebrowanych laserem światłowodowym*, Przegląd Spawalnictwa 11 Sigma (2009), p. 82-86

[18] European Patent No 0604439 B1: Finned tube

[19] http://www.rosink.bilfinger.com/en/products-and-services/fintube-division/helically-finned-tubes/noh-welded-u-fins/ (28.07.2013)

[20] http://www.lbltrading.com/suppliers/spirogills/spiro-gills-fin-tubing-brochure.pdf (28.07.2013)

[21] US Patent No 5343015 A: *Laser assisted high frequency welding* (1994)

[22] http://www.thermatool.com/information/brochure/Thermatool-spiral-fin-tube-welding-system.pdf (28.07.2013)

[23] Adamiec J. Gawrysiuk W. Więcek M.: *Zautomatyzowane stanowisko do spawania rur ożebrowanych laserem dyskowym*, Biuletyn Instytutu Spawalnictwa, Gliwice (5) 2010, p. 55-58

[24] http://citl.energoinstal.pl/pl-PL/hala_i_laser.html (28.07.2013)

THE PECULIARITIES OF CASTING AND MANUFACTURING OF TURBINE DETAILS FROM NICKEL SUPERALLOY

Sergey S.B. Belikov [1], Yevgeny E.L. Sanchugov [2], Valery V. P. Valuev[3]
Stanislav S.A. Lukin[4]

(1) National technical University, Zhukovskogo str.64, 69063 Zaporozhye, Ukraine
(2) University Hanover, FUH, section Institute of Mechanic Dynamic, Appelstr. 11, 30167 Hanover, Germany, sanchugov@aol.com
(3) State Polytechnic University, 195251 Saint Petersburg, Polytechnicheskaya 29, Russian Federation
(4) State Polytechnic University, 195251 Saint Petersburg, Polytechnicheskaya 29, Russian Federation

Abstract

Problems of the influence regimes of vacuum precision casting and crystallization on the structure and properties of nickel superalloy KhNi64WMoCoAlTiL are researched. Process of electrical erosion machining (EDM), the efficiency of use of cooling liquids cleared from mechanical pollution by EDM are studied.
Superalloy KhNi64WMoCoAlTiL is used for example instead of IN738 for hot part elements of gas turbine GTN 25 I at compressor stations (Pipeline Russia-EU).

Keywords: nickel superalloy, vacuum precision casting, electrical erosion (discharge) machining (EDM)

1. Introduction

The introduction of methods of vacuum precision casting, electrical erosion (discharge) machining (EDM), the efficiency of use of cooling lubricant liquids cleared from mechanical pollution by EDM - are the basic directions of rational use of materials.
In the present work we researched the influence regimes of casting and crystallization on the structure and properties of high-temperature nickel alloy KhNi64WMoCoAlTiL [1], which is used for example instead of IN738 for hot part elements of gas turbine GTN 25 I at compressor stations (Pipeline Russia-EU) and studied process of electrical erosion machining (EDM), the efficiency of use of cooling liquids cleared from mechanical pollution at EDM.

2. Methods of research

Alloys for the study were obtained by induction melting in VIAM-24, UPPF-1, UPPF-2M furnaces at a pressure of 5,3…1,4 Pa in crucibles with basis lining. The molten alloys were cast under vacuum into heated ceramic molds. The temperature and time regimes of melting and casting were chosen depending on the aims of the study and the shape number of performs for specimens and pars.
We used the methods of light and electron spectroscopy and performed standard mechanical tests.
The crystallization kinetics of the alloys was studied in the high-temperature VDTA-8M3 termoanalyzer for differential thermal analysis (DTA).

3. Results and their discussion

3.1. The influence regimes of vacuum precision casting and crystallization

A study of the crystallization kinetics of the alloy KhNi64WMoCoAlTiL showed that the liquidus temperature in crystallization from 1600°C was 1360°C and the solidus temperature was 1240°C.

We used the method of experimental design for the choice of temperature regimes of casting.

The optimization parameters were:
-   The time before failure (τ, h) at 900°C, $\sigma = 250$ MPa;
-   The elongation ($\delta\tau$, %) at 900°C, $\sigma = 250$ MPa and
-   The size of macro grains.

The independent variables were:
-   The temperature of overheating T1 (1500…1600°C),
-   The temperature of metal bath under casting into heated ceramic molds T2 (1460…1560°C) and
-   The temperature of molds T3 (700…850°C).

Analyzing the results of the study we obtained adequate regression equations describing the effect of the temperature regimes of casting on the optimization parameters (in the ranges of the study), namely:

$$\tau = -360,3 + 0,335T_1 \quad (1)$$
$$\delta_\tau = -16,35 + 0,009T_1 + 0,011T_3 \quad (2)$$

The temperature of metal bath under casting is influenced only slightly the parameter of high-temperature strength and the elongation (in the range of study). We also established that as the temperature of overheating T1 increased from 1500 to 1600°C, the time before failure grows from 130h to 170h (the temperature of molds – 850°C) and the macro grains in homogeneous in size decreased. At the temperature rise of molds T3 from 700 to 850°C, an elongation grows (by 30…40%). However, it does not influence much on the long-term strength. The obtained models are used to predict the relation between the time before failure, the elongation, the size of macro grains and melting and casting regimes of alloy KhNi64WMoCoAlTiL. The received results have shown, that the temperature of overheating and the temperature of metal bath under casting in temperature intervals from 1560 up to 1600°C and from 1500 up to 1560°C accordingly, allows to receive a required level of mechanical properties high-temperature nickel alloy KhNi64WMoCoAlTiL.

Fig. 1: The stationary turbine rotor blade (nickel alloy KhNi64WmoCoAlTiL, which is used for example instead of IN738 for hot part elements of gas turbine GTN 25 I at compressor stations (Pipeline Russia-EU))

3.2. Methods of electrical erosion machining (EDM)

Methods of electrical erosion machining (EDM) and the efficiency of use of cooling liquids cleared from mechanical pollution at EDM. Pockets on root of the blade, interconnect between the major cool hole and the root pocket, film cool holes are produced by electrical erosion machining (EDM).

The efficiency of use of cooling liquids cleared from mechanical pollution by **EDM**, confirmed by long practice of various engineering enterprises. Among the methods and devices that can be used to clear the cooling liquids, centrifuge occupies a special place. Precipitation is very complex hydraulic process.

If the flow regime of sediment particle size d is in the laminar region, the movement of the deposited particles is described by the equation [2].

$dr/d\tau = k_0 d^2 r$ (3) where: $k_0 = \Delta p \omega^2 / 18\mu$; Δp - difference between the densities of the dispersed phase and dispersion medium, kg/m3; r- radius; ω - rotor speed; μ - dynamic viscosity of the dispersion medium, Pa s.

After the transformation formula (3) can be obtained pattern changes in the relative concentration of polydispersed solid phase of the layer of sediment, depending on the radius r.

$C_f / C_{cs} = (r^2 / 2\sqrt{k_0 \tau_1}) \int [F(d) dr / r^3 \cdot \sqrt{\ln(r/r_0)}]$

where: Cf – concentration of the solid phase with a particle size from zero to d at the surface of radius r kg/m3; Ccs - concentration of the suspension kg/m3; τ_1 - the duration of centrifugation.

Duration of centrifugation τ_1 for cooling liquids of electro erosive Machine found experimentally.

It is possible to intensify significantly the process of cleaning of cooling liquids, if used for this purpose not only precipitation, but filtering centrifuge i.e. process is conducted in two stages:

The first stage- removal of sediment with particle sizes of more than 80 microns is performed on continuous-current filtering inertial centrifuges.

The second stage- removal of sediment with particle sizes less than 80 microns is performed on decanting centrifuge.

4. Conclusions

1. The liquidus temperature of nickel superalloy KhN64WMCYuTL in crystallization from 1600°C is 1360°C and the solidus temperature is 1240°C.
2. Recommended temperature regimes of casting for alloy KhN64WMCYuTL:
   - the temperature of overheating T1 (1560…1600°C),
   - the temperature of metal bath under casting into heated ceramic molds T2 (1500…1560°C) and
   - the temperature of molds T3 (750…850°C).
3. The centrifugal technique is the promising equipment for intensifying and improving the quality of clean cooling liquids.
4. The purified cooling liquids can intensify the process of abrasive machining and significantly increase the resistance of blade tools.

Reference
1. S. B. Belikov, … A. D. Koval, … E. L. Sanchugov, *High-temperature nickel alloy, Patent CA,* SU 80-2928707, C 22C 0019-05, 1980.
2. M.I. Iljin, S.A. Lukin, V.G. Kornienko, *Clearing of cooling lubricant liquids in centrifugal machines, Tool*, *17-18*, S-Petersburg, 75-78

MICROSTRUCTURE AND MECHANICAL PROPERTIES OF DISSIMILAR WELDED JOINTS MADE OF TEMPALOY A-3 AND T91 STEELS

Robert Jachym[1], Michał Urzynicok[2], Krzysztof Kwieciński[1], Mirosław Łomozik[1], Paola Mariani[3], Yusuke Minami[4]

[1] Instytut Spawalnictwa, 44-100 Gliwice, Poland, ul. Bł. Czesława 16-18,
e-mail: robert.jachym@is.gliwice.pl
[2] Boiler Elements Factory „ZELKOT", 42-286 Koszęcin, Poland, ul. Nowy Dwór 8,
e-mail: mu@zelkot.pl
[3] TenarisDalmine, Dalmine, Italy, e-mail: pmariani@tenaris.com
[4] TenarisNKKTubes, Kawasaki, Japan, e-mail: yminami@nkktubes.co.jp

Abstract

This article presents experience gained while welding dissimilar joints of steels TEMPALOY A-3 and T91, with the use of EPRI P87 and Inconel 82 filler metals. The destructive and non-destructive tests were carried out according to the EN ISO 15614-1/A1:2010 Standard. All joints are characterised by high quality, which is confirmed by the results of destructive and non-destructive tests. The tests involving the said steel grades belong to the very few carried out in the world.

Keywords: TEMPALOY A-3, EPRI P87 filler metal, Inconel 82 filler metal, pipe butt welds.

1. Introduction

The development of modern steels for power industry is stimulated primarily by European legal regulations connected with environmental protection dispositions. Setting more restrictive requirements related to the limitation of the pollutants emission in to the atmosphere (mainly CO_2 and NO_x) requires necessarily an increasing of the power units efficiency and a fuel consumption reduction, achievable by raising the steam parameters - temperature and pressure. Increasing steam parameters caused previously used Mo, Cr-Mo, Cr-Mo-V steels, as well as high-chromium X20CrMoV12-1, to stop meeting such restrictive requirements. This has led to the development and implementation of new steel grades characterised by properties superior to those of previously used materials. Components operating in a temperature range up to approximately 625°C are ferritic steels with a maximum chromium content of 12%, characterized by a martensitic microstructure and showing high mechanical properties and creep strength, enhanced steam oxidation and hot corrosion resistance [1-4]. Above this temperature it is necessary to use austenitic creep resistant steels and alloys based on Ni [5]. As austenitic steels are cheaper than Ni-based alloys, components operating at temperatures above the use of ferritic steels and below approximately 765°C are made of austenitic steels. Long-time research has led to the

development of two grades of austenitic steel by the Tenaris-NKK-Tubes company, namely TEMPALOY AA-1 and TEMPALOY A-3. The analysis of the weldability of the latter steel grade is the subject of this article.

2. General characteristics of TEMPALOY A-3 steel

TEMPALOY A-3 steel is registered as KA-SUS30904J4HTB according to Japanese Standards METI, in ASTM A-213 as UNS S30942 and in ASME Standards as Code Case No. 2598. This steel is austenitic and contains 22% Cr and 15% Ni. Its microstructure does not contain delta ferrite. Factors directly responsible for creep strength are niobium carbonitrides present inside the grains and at grain boundaries in the as-delivered state as well as chromium and niobium nitrides (CrNbN).

During operation in the 600÷750°C temperature range the microstructure undergoes further strengthening due to $M_{23}C_6$ carbides precipitation at grain boundaries. It is also possible to observe the formation of small amounts of sigma phase and networks of Z phase particles composed mainly of chromium nitrides rich in niobium.

The Z phase precipitates do not undergo growth even after long-time operation at very high temperatures, thus enabling an effective blocking of dislocation movement [6].

High corrosion resistance and steam oxidation resistance are promoted by a high chromium content. Corrosion test were performed in an environment simulating coal ash combustion: a synthetic ash composed by $34\%Na_2SO_4 + 41\%K_2SO_4 + 25\%Fe_2O_3$ was applied on the samples which were surrounded by a mixture of $1\%SO_2 + 5\%O_2$ and N_2 balance.

At 700ºC after 100 hours TEMPALOY A-3 corrosion resistance is approximately 20% higher than that of TP321H austenitic steel, whereas steam oxidation resistance at 700ºC is five times greater than for TP321H steel after 1000 h.

3. Subject of tests

The material which underwent tests was a welded joint with an outside diameter (OD) of 38 mm, wall thickness of around 7 mm, made of TEMPALOY A-3 (ASTM A213, UNS No. S30942) and T91 (ASTM A213) tubes. The chemical composition of both steels is presented in Table 1. The tubes were welded with TIG in PF position.

Table 1. Chemical composition of welded steels acc. to Material Test Report (MTR)

Contents of chemical elements, %										
Grade	C	Si	Mn	Ni	Cr	Mo	N ppm	V	Nb	B
A-3	0.05	0.28	1.38	15.61	21.9	n.d.	1596	n.d.	0.62	0.0021
T91	0.10	0.35	0.44	0.21	8.25	0.94	440	0.21	0.08	n.d.

n.d. = not determined

The mechanical properties of the tested material in the as-delivered condition are presented in Table 2.

Table 2. *Mechanical properties of tested steels acc. to MTR*

Mechanical properties			
Grade	Re, MPa	Rm, MPa	E., %	HV
A-3	537	780	41	188
T91	548	697	19.9	n.d.

n.d. = not determined

After welding, all the joints were subjected to stress relief annealing at a temperature of 760°C, for approx. 30 minutes.

3.1. Filler metals for dissimilar welding

The selection of a filler metal for welding depends on the chemical composition of the base metal and operational conditions of joints. Consumables used in welding processes should ensure that the chemical composition and properties of the weld metal match those of the used base metal.

A filler metal grade EPRI P87 was designed in view of the production of dissimilar joints between ferritic steels such as T91/T92 and austenitic steel e.g. S304H and TEMPALOY grade series.

Previously applied Ni-based consumables (e.g. Inconel 82) were responsible for the generation of a zone poor in carbon (the so-called white zone), whereas the use of, for instance, alloy Inconel 617 was economically unjustified and gave rise to post-weld micro-cracks.

Owing to the optimally selected chemical composition of EPRI P87 wire, dissimilar joints made with the latter practically have no decarburised zone. In order to limit the thermal expansion of the weld metal it was necessary to reduce the content of manganese below 2%, whereas to eliminate micro-cracks it was necessary to optimise the content of niobium and carbon acc. to the relation of Nb:C>10 [7]. Table 3 presents the chemical composition of Metrode-manufactured EPRI P87 solid wires and Inconel 82 wires.

Table 3. *Chemical composition of filler metal acc. to producer's data*

Grade	Contents of chemical elements, %										
	C	Mn	Si	Cr	Ni	Mo	Nb	Ti	Co	Al	Fe
EPRI P87	0.11	1.55	0.16	8.52	rest	2.02	1.09	n.d.	n.d.	n.d.	38.8
Inconel 82	0.035	2.99	0.08	20.0	rest	n.d.	2.42	0.35	n.d.	n.d.	1.27

4. Subject of tests

Tests involved the production of dissimilar joints of steel TEMPALOY A-3 with steel T91, welded with Metrode-manufactured solid wires EPRI P87 and Inconel 82 (ASME SFA 5.14 ERNiCr-3).

The production of the aforesaid welded joints was followed by non-destructive tests i.e. VT, PT and RT. The tests were carried out following the quality level B of the Standard ISO 5817. After carrying out NDT, the test pieces were sampled for destructive tests.
The scope of destructive tests included:
- static tensile test of welded joint,
- bend test,
- impact test,
- macro- and microscopic metallographic tests,
- hardness measurements.

4.1. Tensile test results

The objective of the tests was to determine the tensile strength (R_m) of a welded joint and the verification of test results compared to the required minimum R_m value for the base metal (BM) of 590 MPa for TEMPALOY A-3 steel (specified by the ASTM A213 Standard) and 630 MPa (value specified by the EN 10216-2 Standard for X10CrMoVNb9-1 and more restrictive than the R_m provided by ASTM A213 Standard) for T91 steel. The static tensile test was carried out in accordance with the requirements of the EN ISO 6892-1 Standard. The results for joints welded with the EPRI P87 and Inconel filler metals are shown in Figure 1.
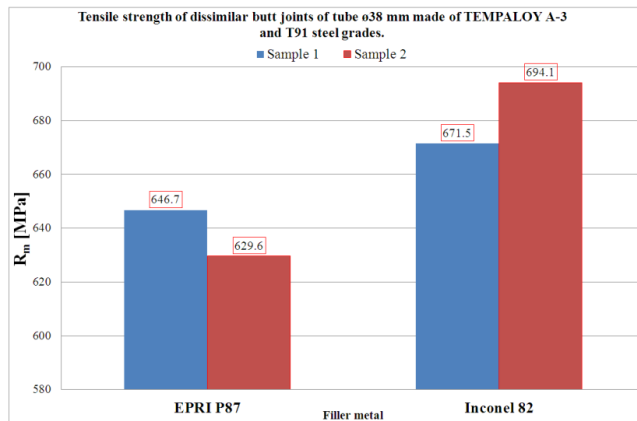
Figure 1. Results of tensile tests of butt joints of tube with OD=38 mm made of TEMPALOY A-3 and T91.

4.2. Impact test results for weld and HAZ

The impact tests were carried out at +20°C on Charpy V-notched specimens taken from the base metal (BM), the weld metal (WM) and the heat affected zone (HAZ) in accordance with the requirements of EN ISO 9016 and EN 148-1:2010.
The tests were carried out in order to determine the value of impact energy for the weld and HAZ. The criterion in the EN 12952-6 Standard specifies that the minimum value of impact energy for the HAZ of normal cross-section (10 x 10 mm) specimens should amount

to 24 J at the room temperature, whereas EN 10216-2 states that the minimum value of impact energy for the base metal should be 27 J. The value of 24 J is marked in the diagram as a dark line (Fig. 2).

The impact energy results obtained for the weld and HAZ are considerably higher than the values referred to in the aforesaid Standards, even though the test were performed on subsize specimens (5 x 10 mm). Figure 2 shows the average values from three measurements.
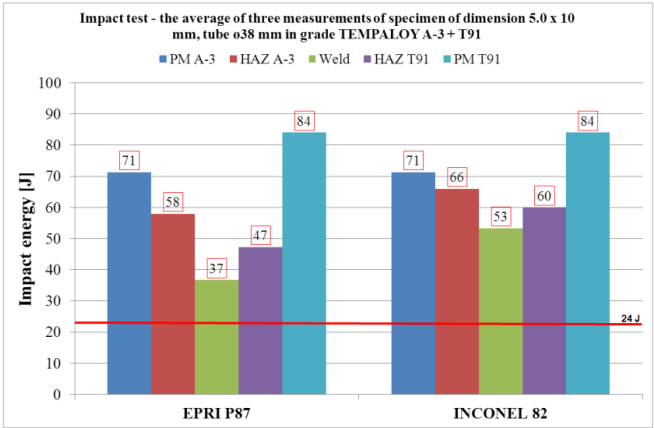
Figure 2. Impact energy of weld metal, HAZ and base metal in butt joints of tube with OD=38mm made of TEMPALOY A-3 and T91.

4.3. Bend test results

A bend test with extending the face and root of the weld was performed in accordance with the requirements of the EN 15614-1 and EN ISO 5173 Standards. As per EN 15614-1, the test criterion consists in obtaining a sample bend of 180° without scratches and cracks on the surface. The results obtained in the tests satisfy the requirements of the Standard.

4.4. Hardness measurement results

Hardness measurements were carried out in accordance with the Standard EN ISO 9015-1:2011 taking into consideration the Standards EN 15614-1 and EN 12952-6. Hardness measurements are not required for austenitic steel, yet they were performed for study purposes. The Standards listed above define that the maximum hardness for martensitic steels should amount to 350 HV$_{10}$. Figure 3 presents the schematic arrangement (lines and points) of hardness measurements, whereas the results of measurements are presented in Figures 4 and 5 accordingly.
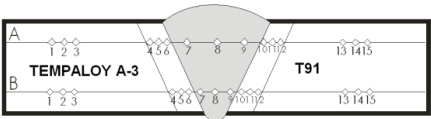
Figure 3. Arrangement of hardness measurement points in the welded tested joints
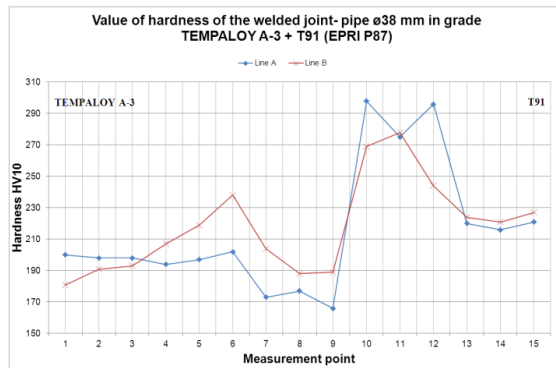
Figure 4. Results of hardness measurements of butt joint welded with EPRI P87
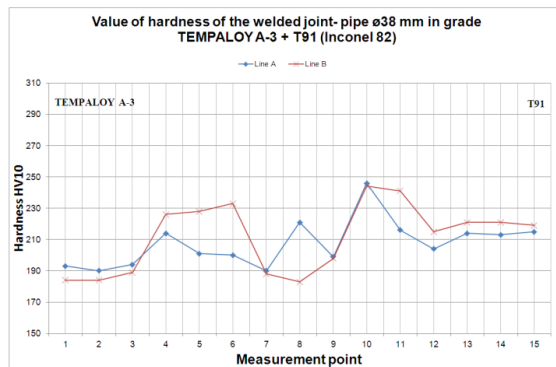
Figure 5. Results of hardness measurements of butt joint welded with Inconel 82

4.5. Results of macroscopic and microscopic metallographic tests

Micro- and macroscopic metallographic tests were carried out following the requirements of the Standard EN 1321. A criterion adopted for assessment was the quality level B according to the Standard ISO 5817, which was satisfied in the case of the test joints. The results of the microscopic tests did not reveal any welding imperfections in the micro-scale and confirmed the existence of proper microstructure in all the zones of the dissimilar joint made of TEMPALOY A-3 and T91 steel grades. Figure 6 and 7 present the results of the macro- and microscopic tests in the form of photographs and descriptions of the structures identified in the characteristic zones of the welded joint.

Grade TEMPALOY A-3 and T91 welded with EPRI P87; etchant: Adler; quality level: B.

base metal – T91; etchant: FeCl3; mag. 200x, tempered martensite

HAZ – EPRI P87- TEMPALOY A-3; electrolytic etching; mag. 200x, austenite

HAZ – EPRI P87-T91; etchant: FeCl3; mag. 200x, tempered martensite

base metal – TEMPALOY A-3; electrolytic etching; mag. 200x, austenite

weld metal
electrolytic etching; mag. 200x, austenite + delta ferrite

Figure 6. Results of macro- and microscopic metallographic tests of dissimilar butt joint made of TEMPALOY A-3 and T91 steels (EPRI P87).

The results of microscopic examination revealed that the use of an EPRI P87 filler metal enabled obtaining a very narrow decarburised zone in comparison with such filler metals as 309L or ERNiCrMo-3. A narrow decarburised zone makes it possible to reduce the "weakened zone" of the ferritic/martensitic material. The lower thermal expansion of the EPRI P87 filler metal in comparison with, for instance, IN617 eliminates stresses generated during operation between the weld and materials being welded, which also directly affects the life of a welded joint.

Grade TEMPALOY A-3 and T91 welded with Inconel 82; etchant: Adler; quality level: B.

base metal – T91; etchant: FeCl3; mag. 200x, tempered martensite

HAZ – EPRI P87- TEMPALOY A-3; electrolytic etching; mag. 200x, austenite

HAZ – EPRI P87-T91; etchant: FeCl3; mag. 200x, tempered martensite

base metal – TEMPALOY A-3; electrolytic etching; mag. 200x, austenite

weld metal electrolytic etching; mag. 200x, austenite

Figure 7. Results of macro- and microscopic metallographic tests of dissimilar butt joint made of TEMPALOY A-3 and T91 steels (Inconel 82).

5. Conclusions

On the basis of the aforesaid tests it was possible to come to the following conclusions:

1) Dissimilar joints made of TEMPALOY A-3 and T91 steel grades, TIG welded in PF position are characterised by high quality, which is confirmed by the results of destructive and non-destructive tests.

2) On joints made by INCONEL 82 filler metal, the mechanical and plastic properties achieved were higher than those obtained on material welded by EPRI P87.

3) The application of filler metal Metrode EPRI P87 and Inconel 82 made it possible to obtain very good results on a dissimilar welded joint and the LM investigations confirmed the absence of welding micro-imperfections.
4) The decarburised/carburised zone in the EPRI P87 welded joint is very narrow, which favourably affects the operational properties of the joint.
5) In order to determine the suitability of joints made with TEMPALOY A-3 and T91 for the application on an industrial scale it would be worthwhile to perform additional creep tests and deeper microstructural investigations.

EPRI P87 is not yet included in the EN code thus its use may be limited in European projects. The results shown in this work and further advanced microstructural investigations and creep tests will enable obtaining more detailed knowledge of the welded joint properties and their industrial usability.

Acknowledgements

References

[1] M. Urzynicok, K. Kwieciński, M. Szubryt, J. Słania, Application of new GMAW welding methods used in prefabrication of P92 (X10CrWMoVNb9-2) pipe butt welds. 9th Liege Conference on Materials for Advanced Power Engineering, September 27th - 29th, Liege, Belgium, (2010).

[2] M. Urzynicok, K. Kwiecinski, M. Szubryt, Testing butt joints in pipes made of VM12-SHC martensitic steel, Welding International, iFirst article, pp. 1-6, (2012).

[3] K. Kwieciński, M. Urzynicok, M. Łomozik, Practical experience with welding new generation steel PB2 grade assigned for power industry. Archives of metallurgy and materials, Vol. 56, Issue 1, pp. 37-45, (2011).

[4] R. Jachym, K. Kwieciński, M. Urzynicok, M. Łomozik, Properties of thickwelded similar and dissimilar joints made of TEMPALOY A-3 steel assigned for power industry. 9th International Conference on Trends in Welding Research, Chicago IL, USA, (2012).

[5] M. Urzynicok, R. Jachym, K. Kwieciński, P. Mariani, Y. Minami: Application of EPRI P87 in dissimilar austenitic-martensitic welded joints of TEMPALOY AA-1 and T92

steel grades. 7th International Conference on Advances in Materials Technology for Fossil Power Plants, Big Island of Hawai, USA, (2013).

[6] Caminada S., Cumino G., Cipolla L., Venditti D.,Di Gianfrancesco A., Minami Y., Ono T.: Creep properties and microstructural evolution of austenitic TEMPALOY steels. International Journal of Pressure Vessels and Piping 87, pp. 336-344, (2010).

[7] Schingledecker J.: Update on EPRI P87 Filler Metal. Boiler Reliability Interest Group, Baltimore 22.04.2010

Giant Castings for Power Generation Applications
Process Development and Experiences
with Materials C91, C911, CB2
for Heavy-Walled Cast Components

Reinhold Hanus

Voestalpine Giesserei Linz GmbH, (reinhold.hanus@voestalpine.com)

Abstract

The voestalpine Foundry Group, with Austrian locations in Linz and Traisen, manufactures heavy steel castings for steam and gas turbines, for compressors for oil and gas production, for the chemical industry, for heavy machinery and for offshore technologies. Castings with weights ranging from 50 kg to 200 tons can be manufactured in the two foundries. Each of the markets mentioned before has its specific challenges. This article deals with large components for steam turbines. Characteristics of material development, foundry processing (melting, moulding, heat treatment, NDT, fabrication welding and process welding) are explained, primarily focusing on newly developed high-alloyed 9–12% Cr steels and their properties in heavy-walled castings. Newest results and experiences with the newly developed COST material CB2 are an important part of the provided information, as well as heavy fabrication welds of C911 and C91 with different welding methods.

Keywords: High Cr Steel Castings, Foundry Technology, 9-12% Cr-Cast Steelgrades

1. Typical Procedure in the Steel Foundry

1.1 Standard Processes

Figure 1 shows the major steps in a manufacturing process for heavy steel castings (e.g. for power plant construction). After creation of the casting technology design, construction of the wooden pattern and moulding, casting starts with the melting and pouring process. The casting is removed from the mould (shake out) after a solidification period (2 to 6 weeks, depending on wall thickness, complexity and material). To be able to adjust the microstructure towards desired material parameters depending on the respective application (creep resistance, cryogenic toughness, magnetic properties, high strength, etc.), the most important steps to be taken are chemical composition and heat treatment. Following rough machining (mechanical processing with machining allowances), the casting is tested by means of a non-destructive methods (magnetic particle testing and ultrasonic testing). All deviations from the acceptance standard are excavated. The excavations are again checked by means of a magnetic particle testing, before they are welded (process welding), fabrication welding of weld-on components are performed in the same cycles. Both process and fabrication welds are stress-relieved. Between the production steps, the component is consistently dimensionally checked to determine whether certain necessary tolerances might become a problem during finishing and application. A final non-destructive test is carried out in the foundry, before the casting is passed for finish machining.

Figure 1: Typical production schedule for heavy steel castings

1.2 Melting Process

Figure 2: Production of molten steel at voestalpine Giesserei Linz GmbH
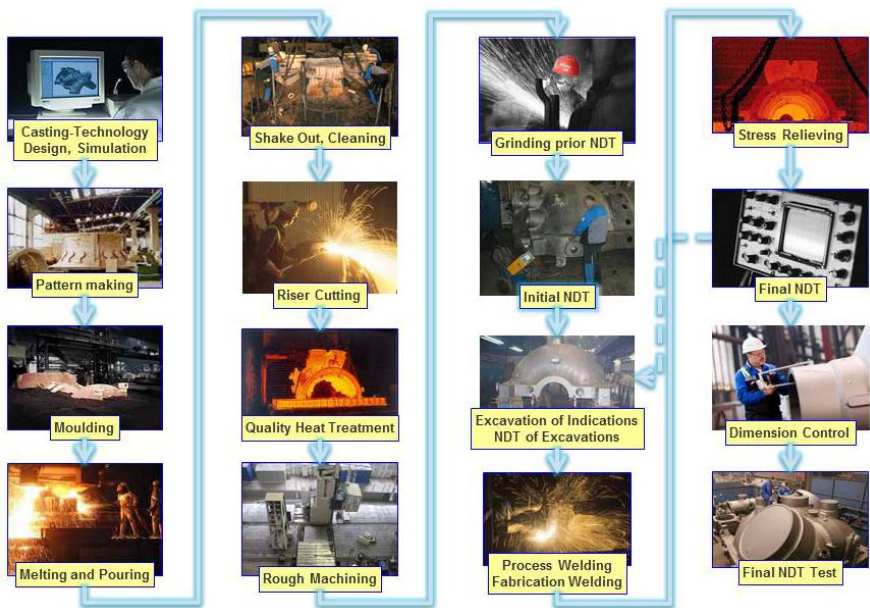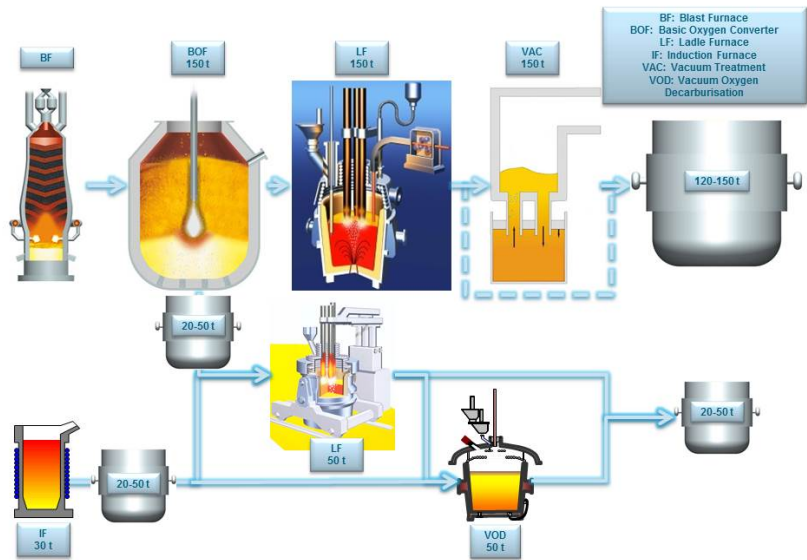
The standard process line of the melting process in the voestalpine foundry starts in the LD steelmaking plant of the parent company, in a basic oxygen furnace with a capacity of 150 tons. Here, non-alloy steel is produced and tapped into the ladles of the foundry, which have capacities between 20 and 50 tons. The ladles filled with non-alloy molten steel are transported into the foundry to the ladle furnace, where secondary metallurgical treatment takes place (alloying with ferro-alloys, heating with three graphite electrodes, purging with argon or nitrogen).

Figure 3 Casting at voestalpine Giesserei Linz GmbH, with a 50 ton ladle

2. Special Features in the Processes for Giant Components Using the Example of a Giant Steam Turbine

As a consequence of the exceptional size of the parts, almost all foundry processes require special measures and sophisticated logistics during transport, heat input, testing, welding, etc. Outer casings with weights of up to 100 tons, often in combination with high-alloy materials (12% Cr steel) and complex designs, pose a special challenge for engineers and skilled workers.

2.1 Engineering, Quality Planning

Since most of the parts are high-stressed components, technological planning and quality assurance are of major importance. Often, several parties (customer, end customer, 3rd party organisation) are involved in the processes from initial technical negotiations with the customer to final acceptance.

The manufacturing and test-sequence schedules for the respective parts contain the individual process steps including tasks and responsibilities, applicable specifications and the necessary testing, reporting, recording and acceptance steps.

In most instances, all tests must be accepted by a certified third party. Obviously, this requires a tremendous amount of quality work and engineering effort in the preparatory phases.

2.2   Patternmaking and Moulding of "Giants"

As a consequence of the large size of an outer casing half (e.g. 6.5 m x 6 m x 3 m for a 1700 MW plant), one of the challenges during patternmaking is to construct a sufficiently robust wooden pattern (see Figure 4). Another challenge is to support and stabilise the steam outlets, which have in mentioned part a diameter of 2 m and protrude from the upper half on both sides, at patternmaking as well as during fixing sand core in the mould cavity).

Figure 4 Wooden pattern for outer casing, upper half with steam outlet

2.3   Melting and Pouring Process

Giant parts with a weight of 100 t are cast in the special process line (200 tons of molten steel).

Following treatment in the basic oxygen furnace, 150 tons of molten steel are transported to the ladle furnace of the voestalpine steel plant. There it is alloyed to the required composition, treated in a vacuum unit and transported to the foundry with special vehicles. With special metallurgic logistics, 200 tons of liquid high alloyed steel can be provided for pouring into the giant mold of a component up to 100 tons rough casting weight.

The limit for low- and unalloyed steel is even twice as high.

*Figure 5 Casting with a heavy ladle (150 tons of molten metal),
fully alloyed in the LD steelmaking plant*

437

2.4 Heat Treatment, Shot Blasting, Finishing

Finishing operations (arc-air cutting, grinding, shot blasting) make up a significant part of the manufacturing process for steel castings. voestalpine Giesserei Linz GmbH has invested in large units for handling such parts.

Figure 6 heat-treating furnace and blasting shop - Super Size

2.5 Rough Machining

Following quality heat treatment, the cast parts are transported to a machining shop, where they are machined observing a machining allowance of 5–6 mm. Transporting these large parts is a big challenge and necessitates special measures concerning means of transport, transport with cranes in the buildings, and safety precautions for the entire logistics planning. Finish machining takes places after the entire casting process is completed. Only few machining plants have the machines suitable for such purposes. Effective coordination between foundry and machining shop is essential for preventing dimensional problems, which would have grave consequences in such large parts.

Figure 7 Outer casing half during rough machining

438

2.6   Welding

Welding is an essential processing step in the manufacture of steel castings.

Fabrication welds (welding of rolled, forged or cast pipes, connecting pieces, elbows, nipples, etc.) and surface-layer welds for special surface requirements (hardness, corrosion resistance) are carried out in the welding shop of the foundry. Giant components require special measures concerning welding parameters and welding positions.

Figure 8 Positioning for fabrication welding

2.7   Non-Destructive Testing and Final Inspection

Special emphasis is placed on non-destructive testing, both from a technical and a logistical perspective. All cast parts for the energy industry are tested by means of magnetic particle tests and ultrasonic tests (standard probes and angle-beam probes). Fusion faces are usually inspected by means of radiographic tests. This requires a lot of testing personnel and vast experience. Since the parts need to be turned over several times, and some areas can only be reached in certain positions, it is absolutely necessary to plan the test sequence very carefully. Considering the fact that, in addition to the in-house inspections (initial testing, testing after heat treatment cycles), final inspection is often carried out three times (internal, customer, representative of end customer), it becomes obvious that the testing department has to make a tremendous amount of effort. In some cases, the acceptance of a large-scale turbine (non-destructive testing, mechanical properties, documentation) takes several weeks.

Figure 9 Outer casing top part during acceptance by customer and third party (non-destructive ultrasonic testing)

3. Heavy Steel Castings for Thermal Energy Generation Plants

Components made of cast steel are an essential part of all thermal power plants. They are mostly static parts of turbines, such as outer and inner casings, vane carriers, valve casings, elbows (weights of the individual parts range from 1 to 100 tons). The components are exposed to internal pressure and high thermal stress. Because of their complex designs, they require the highest standards regarding casting process planning, material processing, process-planning and process execution. Heat treatment steps are particularly complex, and require a considerable amount of time because of the large wall thicknesses.

Since most orders are individual orders, serial production is impossible. Each cast part is unique.

3.1   Materials and Developments in the Manufacturing Process for Steam Turbines.

The casting materials most commonly used for turbine components of power plants are the G20Mo5, G17CrMo5-5, G17CrMo9-10, G17CrMoV5-10 steel grades (alloyed with Mo, CrMo and CrMoV) [1]. These low-alloy, creep-resistant materials are used in the creep range at temperatures of up to 550°C.

In order to reduce emissions of hazardous substances and CO_2, efforts are made to continually improve efficiency in power plant processes

In the case of thermal power plants, this can be achieved by continually improving the turbine design, combining the gas and steam processes, and by increasing the temperatures and pressures (live steam, superheated steam). Today, especially in the field of medium pressure turbines, temperatures of up to 625°C are possible. This was taken into account in the course of large-scale, international research projects.

Higher Cr contents and the use of elements such as V, Nb, W, Co, N, B could significantly increase creep strength. These grades are generally known as 9–10% Cr steels. In the course

of large-scale research projects, materials are continuously further developed to achieve even higher temperatures (up to 700°C) and higher efficiency in thermal power plants. Coal-fired pilot power plants with an efficiency of more than 50% are in plan to be erected, using nickel-based materials and complex alloyed 9–10% Cr steels. Figure 10 provides an overview of the limits of use for high-temperature turbine materials.
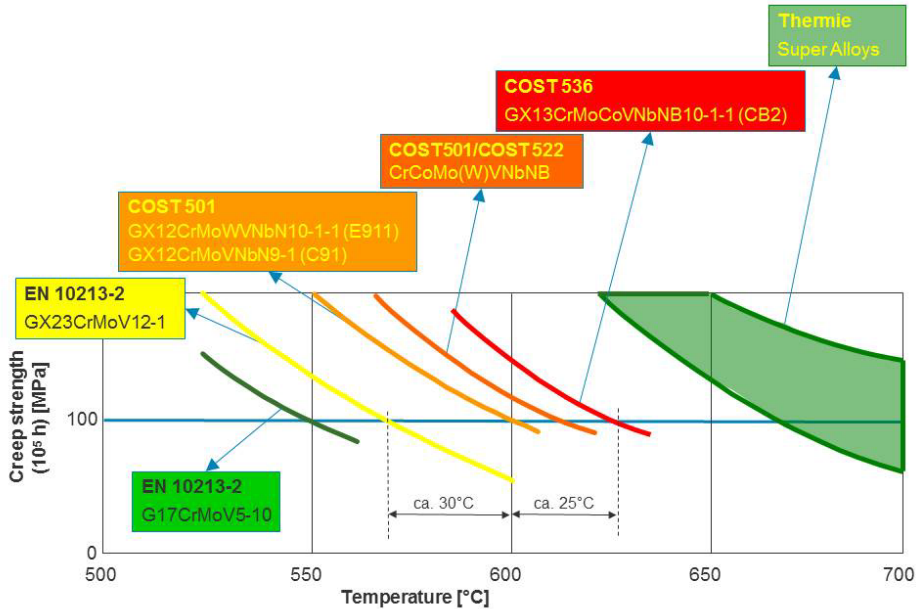
Figure 10 Limits of use for high-temperature turbine materials

State of technology for commercial production of heavy components is at this moment steel grade CB2 for use up to 630°C. After research & development within joint European COST-projects, this material grade is best candidate as a compromise of good creep resistance, castability, weldability and creep resistance of weld connections. This is based on lots of test melts and welding investigations with verified data on screening mechanical testing, creep-rupture tests, exposure tests and metallographic investigations.

Steel	Heat #	C	Mn	Cr	Ni	Mo	V	Nb	Co	W	B	N
CB5	171	,129	,21	10,15	,15	1,45	,20	,059	2,98		,0105	,0320
CB6	172	,13	,20	10,89	,15	1,44	,20	,061	2,95		,0109	,0232
CB8	173	,17	,20	10,86	,15	1,42	,21	,061	2,94		,0106	,0240
CB9	174	,17	,20	10,90	,16	1,47	,20	,060	5,91		,0105	,0206
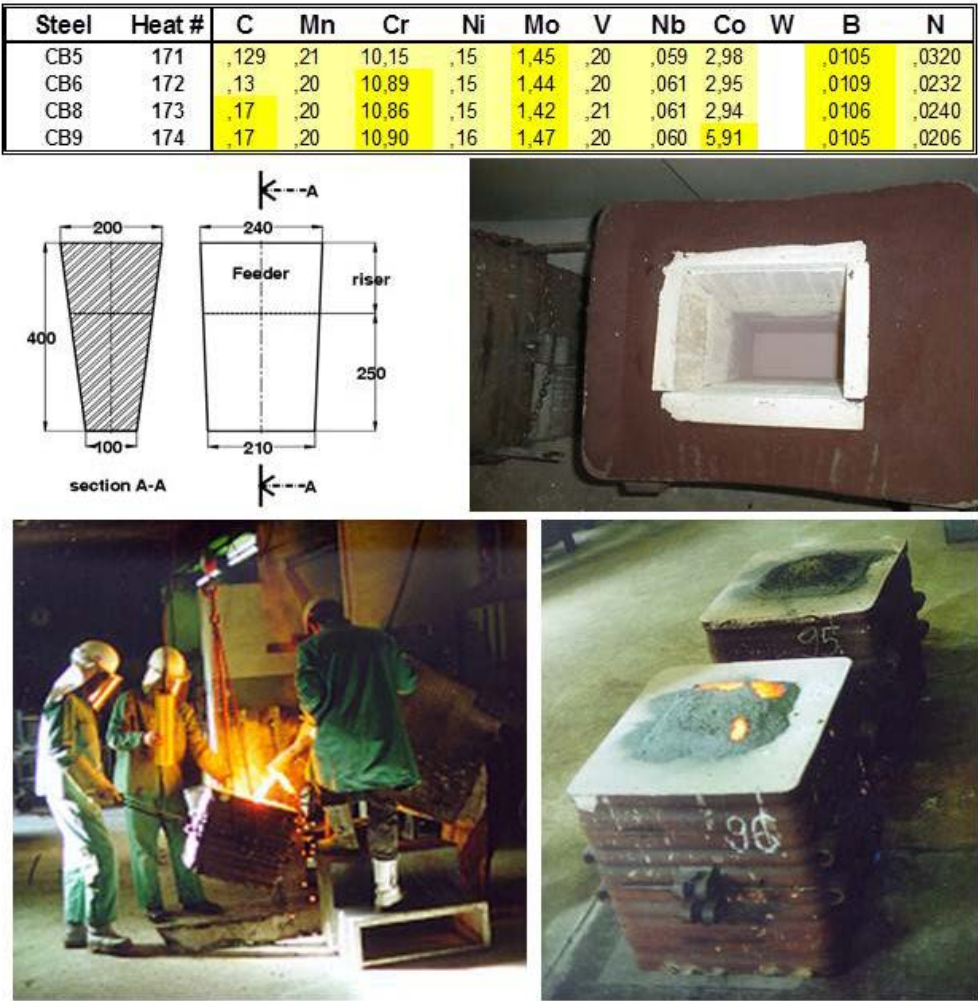
Figure 11 Examples of test melts made for the COST working packages

From some of the promising alloys pilot components were produced with extensive effort, to show up the behaviour of the alloys in heavy walls and component like size and processes.

Steel	Heat #	C	Mn	Cr	Ni	Mo	V	Nb	Ti	Co	B	N
CB2	Ladle 204253	,127	,85	9,33	,15	1,49	,20	,062	,003	,97	,0096	,0210

Figure 12 CB2 pilot components for investigations

Beside the base material, lots of weld connections were performed for investigations of their mechanical and creep behaviour and metallographic studies of weld consumables and Heat Affected Zones, but also Welding Procedure Qualifications have been established out of the cross welds.
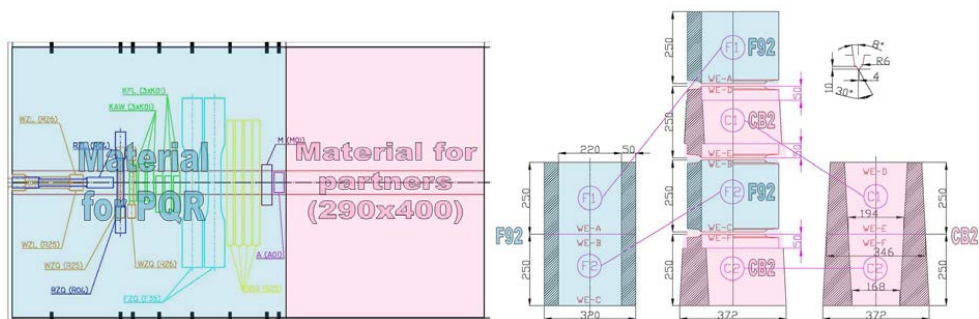
Figure 13 Welding Investigations and Procedure Qualifications: CB2-CB2 and CB2-P92

8 PQR's for base metal process- and fabrication-welding as well as fabrication welds for non-matching weld connections, like CB2-P92/P91 with flux cored arc and shielded metal arc welding are available meanwhile.

Lots of investigations for optimisation of weld consumables were performed in working-packages within KW50plus together with our project partners in Kapfenberg and Hamm, in order to get a good combination of creep strength, toughness and weldability (latest reference [3]).

443

Based on the well done transfer of C91 an C911 from research (COST 501) to commercial production and a process experience of more than 10.000 tons and 500 cast components up to 60 tons per piece, the newly developed CB2 could successfully be introduced in the same way. Figure 14 shows that the creep rupture data of the heavy components of production process are in line with the good results from the test melts of COST (details see [2]).
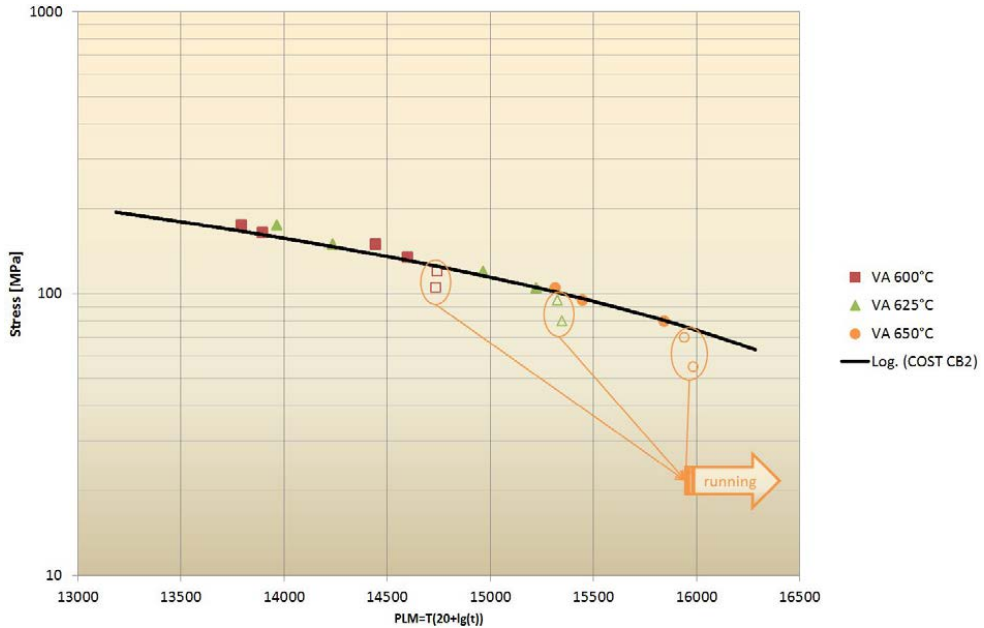
Figure 14 Creep strength of CB2 test melts and heavy pilot components

The base material shows more than 100.000 hours creep time for the original CB2-testblock from COST 501/COST 522 and apprx. 50.000 hours for the pilot-casting components from COST 536.

3.2   Examples of Cast Components for Thermal Power Plants made of C91, C911, CB2

Turbine manufacturers do not only improve materials, but also their processes in order to achieve even higher efficiencies. They develop new process routes (single/double superheating of steam after initial pressure stages). Furthermore, the designs of steam-carrying components are continuously improved. Steam power plants built to cover the base load not only increase their efficiency, but also their capacity. As a result, the key components of such a turbine casings are becoming bigger and bigger.

The processes in the foundry must be adapted to meet these challenges. Examples of different cast components with heavy FAB-welds are shown in Figures 15 to 17. Of course cost and cycle time of the newly developed material grades are increased, due to

- higher material costs
- excessive heat treatment and welding logistics to ensure process capability

- higher ratio of process (repair) welding, as the material- and solidification parameters are more complex

Figure 15 High-pressure outer casing with welded-on valves (31 t + 2 x 19 t = 69 t)

Figure 16 9 cast- and 8 forged components welded together for a main steam valve

Figure 17 Biggest CB2 casings: IP-inner casing upper half (34tons) and lower half (34 tons)

4. Summary

Meanwhile the interest for CB2 in Asia, especially China is high and we have more than 100 cast components, with a total tonnage of approx. 1.500 in order. Components like valves in different and complex designs and inner casings in a weight range from 10 to 40 tons, heavy walled with and heavy FAB-welds (matching and non-matching), up to 185 mm.

4. References

[1] EN 10213
[2] Staubli, Hanus, Weber, Mayer, Kern, The European Efforts in Development of New High Temperature Casing Materials – COST536, *Liege Conference 2006*
[3] Baumgartner, Schuler, Ramskogler, Schmidtne-Kelity, Sarić, Schnitzer, Enzinger, Lochbichler, Mikrostrukturentwicklung von CB2 Fülldraht-Schweißungen, FVW/FVHT 36. Vortragsveranstaltung, November 2013

ANALYSIS OF MICROSTRUCTURAL CHANGES DURING HIGH TEMPERATURE EXPOSURE BY MEANS OF NON-DESTRUCTIVE MICRO-MAGNETIC METHODS

M. Rabung[1], B. Kuhn[2]

[1]Fraunhofer Institute for Nondestructive Testing (IZFP)
Saarbrücken, Germany
Contact e-mail: Madalina.Rabung@izfp.fraunhofer.de

[2]Forschungszentrum Jülich GmbH, Institute for Energy and Climate Research
Microstructure and Properties of Materials (IEK-2)
Contact e-mail: b.kuhn@fz-juelich.de

Abstract

Microstructural changes during thermal ageing of ferromagnetic materials can be detected in a rapid and non-destructive way by means of micro-magnetic methods. The Fraunhofer Institute for Nondestructive Testing (IZFP, Saarbrücken, Germany) prove the suitability of the technique for the characterization of microstructural changes caused by both mechanical pre-treatment and thermal ageing (at different times and temperatures) of the ferritic steel Crofer 22® H. The testing scheme was based on four magnetic methods: Barkhausen noise, incremental permeability, upper harmonics and eddy current analysis.

Keywords: Non-destructive testing, microstructure, precipitation, nucleation, aging

1. Introduction

Development of candidate alloys for the application in future advanced ultra super critical (AUSC) steam power plants is a time consuming and thus expensive task. In case of novel high chromium fully ferritic "HiperFer" steels (based on the alloying philosophy of Crofer® 22 H, developed at Forschungszentrum Jülich, IEK-2 in cooperation with Outokumpu VDM [1-3]) the impact of for example thermomechanical pre-treatment on microstructure evolution and mechanical properties is vastly unknown. Differing alloy composition, initial dislocation density and subsequent thermal ageing produces populations of strengthening $(Fe,Cr,Si)_2(W,Nb)$ Laves phase precipitates, largely deviating from each other in terms of particle number, size distribution and inter-particle spacing (Fig. 1) and thus differing creep strength [4, 5]. Evaluating suitable processing parameters for thermomechanical material pre-treatment to ensure sufficient initial strength from conventional methods alone (correlation of mechanical and hardness testing results with high resolution microscopy) is an exhaustive task, which would have to be repeated for any new alloy or thermomechanical treatment parameter set. The results of micro-magnetic characterization indicate a significant influence of the microstructural state on the magnetic properties of the material: Due to the nucleation and growth of precipitates the thermally aged states show different magnetic permeability than the solution-annealed material. Because of a decrease of the compressive residual stresses during annealing the coercivity of the material simultaneously dropped with increasing time.
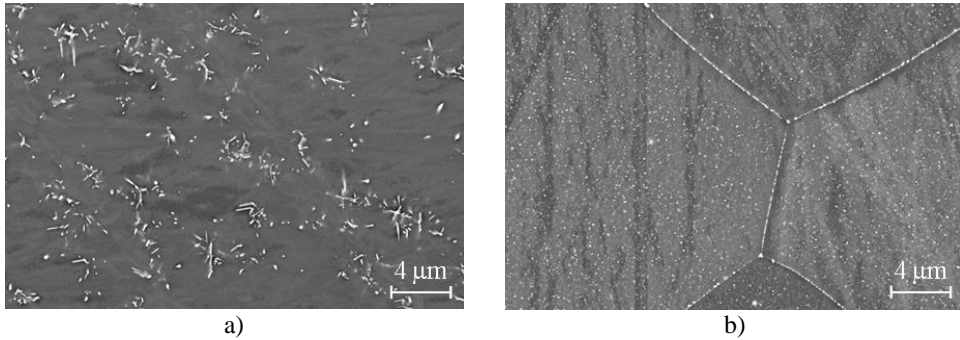
Figure 1: Laves phase population after precipitation treatment (700 °C / 10 h). Initial material state: (a) solution annealed and (b) cold worked.

Magnetic hysteresis loop measurements confirmed the results of the other micro-magnetic tests. Thus, based on this method future rapid pre-characterization of microstructural changes seems possible, which would speed up the process of evaluating initial dislocation density / annealing time / annealing temperature parameter sets beneficial for mechanical strength.

Examples of the practical application of this testing technique are given for solution annealed and cold-worked materials with and without precipitation treatment and first trial micro-magnetic / microstructure property correlations will be presented.

2. Experimental

2.1. Material

Commercial Crofer® 22 H sheet material (thickness: 2.5 mm) from Outokumpu VDM was applied in this study. The chemical composition was measured by glow discharge optical emission spectroscopy (GDOES) and is given in Tab. 1.

Tab.1: Chemical composition of Crofer® 22 H

Batch-ID:	C	N	Cr	W	Nb	Si	Mn	Al	Ti
Crofer® 22 H	0.009	0.018	22.56	1.97	0.49	0.24	0.43	0.019	0.06

2.2. Thermomechanical treatment

Tensile specimens of the geometry depicted in Fig. 2 were lasercut from the solution-annealed sheet material and deformed (except of specimen "17", cf. Tab. 2) at ambient temperature with a strain rate of $10^{-3}s^{-1}$ up to 3 % of plastic deformation to boost the formation of a large number of small precipitates during subsequent precipitation annealing by increasing the initial dislocation density. Table 2 summarizes the times and temperatures applied in the annealing experiments. After heat treatment the gauge portions were cut from the tensile specimens along the sections A-A and B-B (cf. Fig. 2), resulting in flat specimens (40 mm / 15 mm / 2.5 mm) for micro-magnetic characterization.

Specimen ID:	Deformation state:	Temperature [°C]:	Time [h]:
17	none	0	0
16	cold de-formed	0	0
15	cold de-formed	700	10
14	cold de-formed	650	10
13	cold de-formed	600	30
11	cold de-formed	700	500
12	cold de-formed	650	500
10	cold de-formed	600	1000
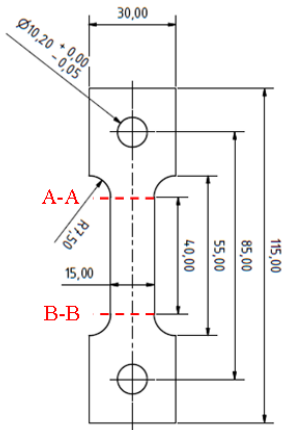
Figure 2: Flat tensile specimen geometry utilized for cold-deformation

Tab. 2: Annealing times and temperatures

2.3. Micro-magnetic measurements

Fraunhofer IZFP pursues the so-called 3MA-technique ("Micro-magnetic Multi-parameter Microstructure and Stress Analysis") in order to solve the inverse problem of target quantity prediction from a limited set of calibration data [6]. 3MA uses a large number of micro-magnetic parameters (currently 41) which are derived from four micro-magnetic methods (harmonics analysis of the magnetic tangential field strength H_t, analysis of the magnetic Barkhausen noise $M(H_t)$, incremental permeability $\mu\Delta(H_t)$ analysis and eddy current imped-ance measurements at different operating frequencies. These parameters, say X_i, (i = 1, 2, 3, …) are measured on well-defined calibration specimens. "Well defined" means that the cali-bration specimens are reliably described by reference values such as mechanical hardness (according to Vickers or Brinell, etc.) or strength values like yield and/or tensile strength, or residual stress values measured, for instance, by X-ray diffraction. A model of the target func-tion is assumed (for instance Vickers hardness HV(X), or strength value like $R_{p0.2}(X)$, or re-sidual stress $\sigma_{res}(X)$. This model is based on the development of the target function by using a (mathematically) complete basis function system, which is a set of polynomials in the micro-magnetic measurement parameters X_i. The unknowns in the model are the development coef-ficients. These coefficients are determined by a least-squares algorithm minimizing a norm of the residual function formed by the difference of the model function to the target reference values. In order to stochastically find a best approximation, only one part of the set of speci-mens is used for calibration of the model, the other independently selected part is applied to check the quality of the model (verification test). By using the least squares approach the un-known parameters are the solution of a system of linear equations. The 3MA method is par-ticularly sensitive in mechanical property determination, as the relevant microstructure gov-erns the material behavior under mechanical loads (strength and toughness) in a similar way to the magnetic behavior under magnetic loads, i.e., the magnetization in a hysteresis loop. Because of the complexity of microstructures and the superimposed stress sensitivity there is an absolute need to develop a multiple-parameter approach.

449

In order to find the best measurement parameters, which allow the best differentiallity between different samples, the micromagnetic measurements were performed at 21 magnetic field amplitudes (10 to 90 A/cm). The magnetization frequency was 40 Hz.

2.4. Microstructural examination

2.4.1 Metallographic preparation, high resolution FESEM examination and quantitative image analysis

After micro-magnetic characterization the samples were cut, embedded in epoxy resin, ground and vibration polished for 3.5 hours in a dilute KOH suspension and electrolytically (1.5 V, 3-5 s) etched in 5 % H_2SO_4 to increase the precipitate / matrix contrast. A Zeiss Merlin scanning electron microscope was utilized to produce high resolution images (2.5k-fold magnification, 6144 * 4608 pixels) for quantitative image analysis. The commercial software package AnalysisPro® was applied to evaluate precipitate evolution from FESEM images.

3. Results and Discussion

3.1. Particle size distribution evolution

600 °C

Fig. 3 displays FESEM micrographs from specimens "13" after 30 hours and "10" after 1000 hours of annealing at 600 °C (a, d: raw images; b, e: inverted for better contrast; c, f: particle size distributions). The inverted detail micrographs (b, e) give a qualitative impression of the quantitative particles size distribution evaluation results (c, f): With increasing time the absolute number of particles only dropped slightly (from 17165 to 13484), but the smallest particle fractions (c: ECD: 11, 14 nm) disappeared and a bi-modal distribution with two local maxima (f: 18, 90 nm) developed with time.

| a) FESEM micrograph (raw image) from specimen "13" after annealing 600°C/30 h | d) FESEM micrograph (raw image) from specimen "10" after annealing 600°C/1000h |

| b) FESEM (inverted image) from specimen "13" after annealing 600°C/30h | e) FESEM (inverted image) from specimen "10" after annealing 600°C/1000h |
| c) particle size distributions from specimen "13" after annealing 600°C/30h | f) particle size distributions from specimen "10" after annealing 600°C/1000h |

Figure 3: Laves phase particles and particle size distributions in specimens "13" after 30 h and "10" after 1000 h at 600 °C

650 °C

In comparison to the 600 °C / 30 h specimen (13484) a remarkably lower amount of particles was found after 10 hours of annealing at 650 °C (Fig. 4a: 6262, maximum at an ECD of 71 nm). Aging up to 500 hours causes a further decrease in all size fractions to a total number of particles of 2303 (Fig. 4b).
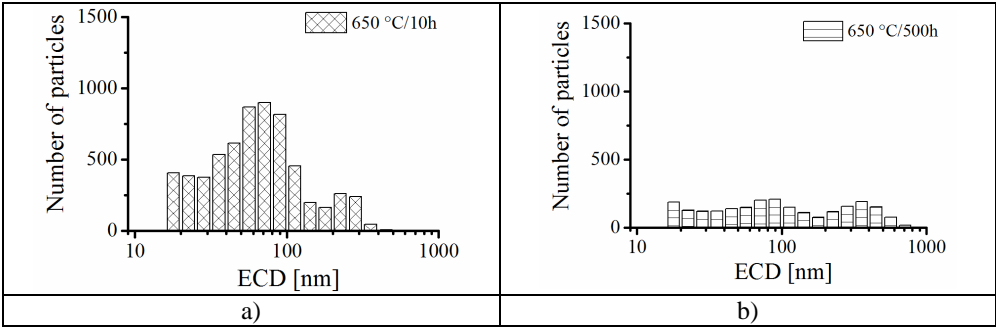
Figure 4: Laves phase particle size distributions in specimens "14" after 10 hours (a) and "12" after 500 hours (b) of annealing at 650 °C

At 700 °C it can be clearly seen that the small particle fractions (ECD < 100 nm) disappeared and grew into larger ones (ECD > 200 nm) in the long-term. The absolute number of particles (16426) after 10 h at 700 °C nearly equals the state after 30 hours at 600 °C (cf. Fig. 5c). Nevertheless the size distribution already presents a bi-modal shape after only 10 h at 700 °C. In the long-term the total number of particles dropped to 693 with the maximum at an ECD of 284 nm after 500 h.

700 °C
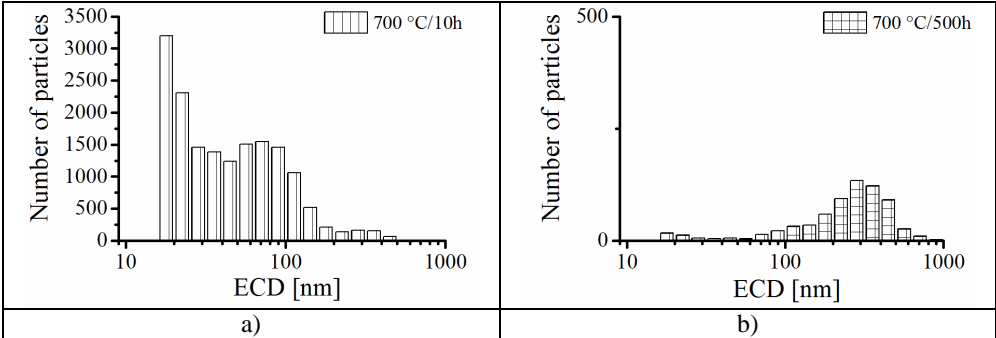
Figure 5: Laves phase particle size distributions in specimens "15" after 10 hours (a) and "11" after 500 hours (b) of annealing at 700 °C

3.2. Micro-magnetic measurement results

3MA measurements on the described Crofer® 22H samples were performed to characterize the ageing processes at different temperatures and durations (Table 2). Figure 6 exemplarily shows the coercivity of the samples (H_{co} – y-axis) derived from the upper harmonics analysis at different magnetic field amplitudes (MagAmp - x-axis).
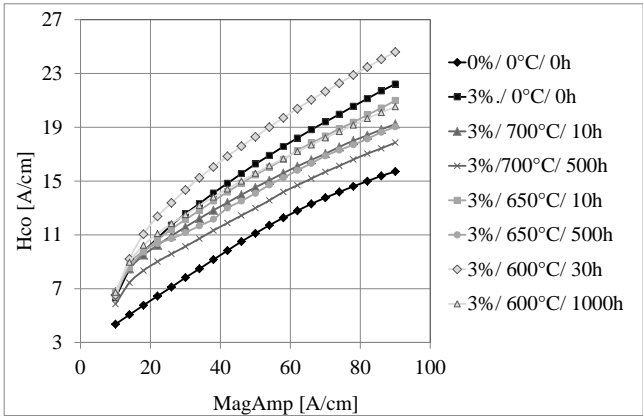
Figure 6: Coercivity derived from the upper harmonics analysis, (H_{co}), as function of magnetic field amplitude (MagAmp). The legend presents the thermal ageing temperatures (°C) and durations (h)

It can be observed that at all magnetic field amplitudes the coercivity of the undeformed sample (Fig. 6: 0%/0°C/0h) is smaller than the coercivity of the plastically deformed sample.

An explanation for this finding is the enhanced dislocation density of the cold-worked specimen, which impedes the Bloch-wall motion. As a consequence the Bloch-walls need more force for their motion, what causes higher coercivity force [6].

It was observed, that the magnetic field amplitude of 70 A/cm allows the best discrimination of heat treatment states.

The micro-magnetic investigations show that a clear differentiation between the non-thermally aged / non-deformed state (specimen "17"), non-thermally aged / deformed state (specimen "16" in Fig. 7) and the plastically deformed specimens with heat treatment at 700 °C, 650°C and 600 °C is possible. The micro-magnetic test statistics exemplified in Fig. 7 and 8 show that the thermally aged states (cf. Tab. 2) can be distinguished from each other, and also from the non-thermally aged state.
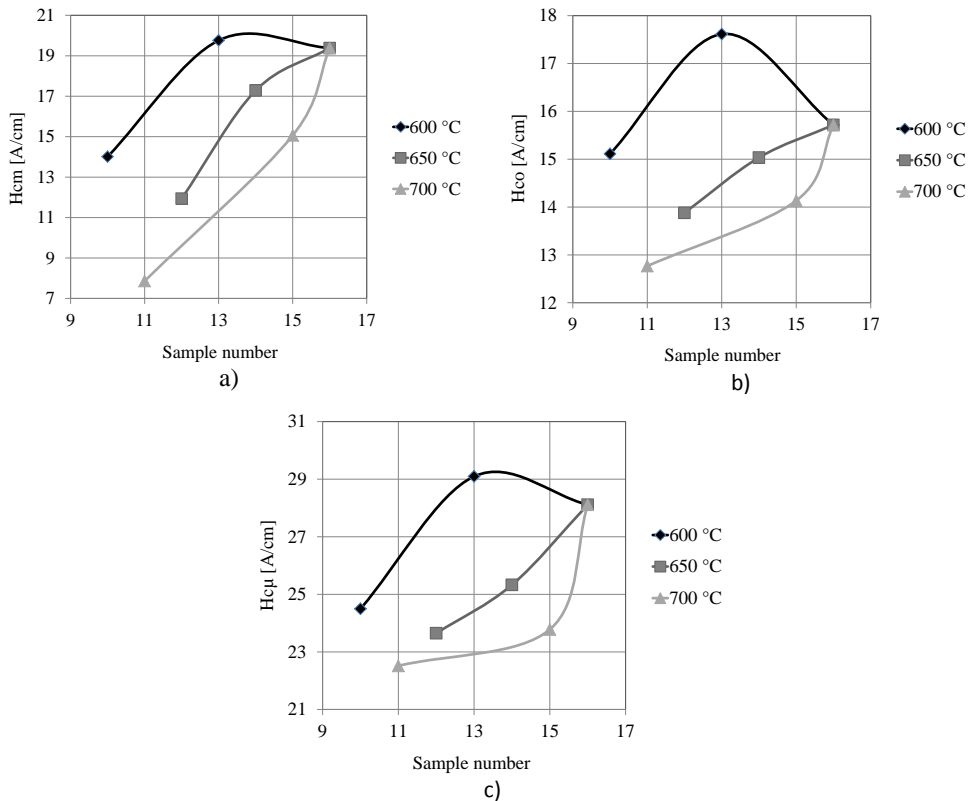
Figure 7: Coercivity, H_{cm} derived from the Barkhausen noise analysis (a), H_{co} derived from the upper harmonics analysis (b) and $H_{c\mu}$ derived from the incremental permeability (c) for different thermal ageing states (numbers on x-axis mark specimen nr. according to Tab. 2)

453

The micro-magnetic test statistics are influenced by the:

- compression residual stresses induced during cold working, which decrease during thermal ageing.
- precipitation of the Laves-phase particles during thermal ageing.

Measurements of the coercivity, H_{cm} derived from the Barkhausen noise analysis, H_{co} derived from the upper harmonics analysis and $H_{c\mu}$ derived from the incremental permeability show that the microstructure evolution induced by thermal ageing as well as the decrease of the compressive residual stresses influence the magnetic hardness of the material. The reason for analyzing the coercivity with different methods is to assess different surface layers of the material, depending on the penetration depth, which is highest for the harmonics analysis (up to 3 mm) and lowest for high-frequency incremental permeability (less than 100 µm, depending on the frequency). Generally a decrease of compressive residual stresses causes a decrease of coercivity [7]. An increase in the number of particles causes an increase in coercivity, because the Bloch-walls are more impeded to move [7].

In case of thermal ageing at 600 °C the increase of the number of Laves phase particles during the first stage (Fig. 7: sample 16 (0 h) → 13 (30 h)) predominantly influences the coercivity and leading to a rise. In case of thermal ageing at 650 °C (Fig. 7: sample 16 (0 h) → 14 (10 h)) and 700 °C (Fig. 7: sample 16 (0 h) → 15 (10 h)) the decrease of the compressive residual stresses predominantly influences the coercivity during the first stage of the thermal ageing leading to a decrease. At all temperatures the decrease of the compression residual stresses superimposed with the diminishment in the number density of Laves-phase particles causes a further decrease of coercivity during the second stage of thermal ageing (up to 500 / 1000 h @ 700, 650 / 600 °C).

The magnetic hardness of a material decreases by the increase in magnetic permeability. Measurement of the maximum incremental permeability, μ_{max} (Fig. 8) confirms the behavior of coercivity.
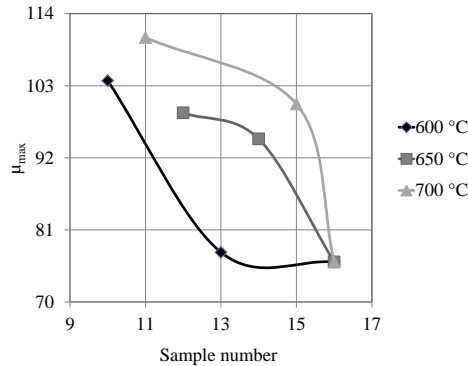
Figure 8: Maximum of the incremental permeability, μ_{max} for different thermal ageing states (numbers on x-axis mark specimen numbers according to Tab. 2)

4. Conclusion and Outlook

The presented results show that by means of micro-magnetic investigation a clear differential-lity between plastically deformed and non-deformed material is possible. This research proved that micro-magnetic measurements are suitable for characterization of microstructure evolution during thermal ageing especially at 600 °C. For a better understanding of these phenomena more thermal ageing experiments will be carried out to better characterize the initial (< 30 h) and ageing (30 to 1000 h) phases. Further micro-magnetic measurements will be carried out on all states of thermal aging.

In order to evaluate the influence of the compressive residual stresses (caused by increased dislocation density from thermomechanical processing) accompanying transmission electron microscopic characterization and X-ray measurements will be performed at differently cold-worked and heat-treated specimens. Evaluation of the impact of dislocation density on micro-magnetic measurement results by examination of cold-worked and heat-treated specimens is planned to be studied.

References

[1]   J. Froitzheim, G. H. Meier, L. Niewolak, P. J. Ennis, H. Hattendorf, L. Singheiser, W. J. Quadakkers: Development of high strength ferritic steel for interconnect application in SOFCs. Journal of Power Sources, 178, 163–173 (2008)
[2]   B. Kuhn, C. Asensio Jimenez, L. Niewolak, T. Hüttel, T. Beck, H. Hattendorf, L. Singheiser, W. J. Quadakkers: Effect of Laves phase strengthening on the mechanical properties of high Cr ferritic steels for solid oxide fuel cell interconnect application. Materials Science and Engineering A, 528, 15 July 2011, pp. 5888–5899
[3]   B. Kuhn, M. Talik, L. Niewolak, J. Zurek, H. Hattendorf, P.J. Ennis, W. J. Quadakkers, T. Beck, L. Singheiser: Development of high chromium ferritic steels strengthened by intermetallic phases. Materials Science and Engineering A, 594, 372–380 (2014)
[4]   B. Kuhn, M. Talik, J. Zurek, W. J. Quadakkers, T. Beck, L. Singheiser, H. Hattendorf: Development of high chromium ferritic steels strengthened by intermetallic phases. Advances in Materials Technology for Fossil Power Plants, Proceedings from the Seventh International Conference, Waikoloa, Hawaii, USA, 22-25 October, 1081- 1092 (2013)
[5]   B. Kuhn, M. Talik, J. Lopez Barrilao, W. Chen, J. Ning: Microstructure evolution and creep strength of High performance Ferritic (HiperFer) steels. Proceedings from the 3rd International ECCC- Creep & Fracture Conference, Barceló Aran Mantegna, Rome, Italy, 5-7 May (2014)
[6]   I. Altpeter, R. Becker, G. Dobmann, R. Kern, W. Theiner, A. Yashan: Robust Solutions of Inverse Problems in Electromagnetic Non-Destructive Evaluation. Inverse Problems 18, 1907-1921 (2002)
[7]   E. Kneller, Ferromagnetismus, Springer Verlag, Berlin, 364 (1962)

KNOW-HOW AND PROCESS DEVELOPMENT FOR COMPONENTS USED IN (A)USC POWER PLANTS

C. Lochbichler[1], F. Füreder-Kitzmüller[2], G. Zeiler[3], S. Paul[3], J. Klarner[4], T. Vogl[4],
S.°Baumgartner[5], R. Schnitzer[5], R. Hanus[6], M. Schmitz-Niederau[7], D. Kreuzer-Zagar[7],
S.°Schramhauser[8], U. Trenkmann[9], M. Schuler[10], N. Enzinger[10]

Affiliations: [1]voestalpine Edelstahl GmbH (formerly voestalpine Giesserei Traisen GmbH),
[2]voestalpine Stahl GmbH, [3]Böhler Edelstahl GmbH&CoKG, [4]voestalpine Tubulars GmbH,
[5]voestalpine Böhler Welding Austria GmbH, [6]voestalpine Giesserei Linz GmbH,
[7]voestalpine Böhler Welding Germany GmbH, [8]Buderus Edelstahl GmbH,
[9]ENPAR Sonderwerkstoffe GmbH, [10]Graz University of Technology

Abstract

The voestalpine group initiated a group-wide R&D project called "KW50plus – Kraftwerk50plus" which is focused on the know-how, material and process development for the production of highly advanced components and welding consumables used in the construction of USC and A-USC power plants. Participants in this interdisciplinary project are the voestalpine foundry group in Linz and Traisen, voestalpine Böhler Welding group in Kapfenberg and Hamm, voestalpine Tubulars in Kindberg, Böhler Edelstahl in Kapfenberg, Buderus Edelstahl in Wetzlar, ENPAR Sonderwerkstoffe in Gummersbach, and the Institute of Material Science and Welding Technology at the Graz University of Technology.

The main focus of the project is on the implementation of pilot and industrial scale production of castings and forgings, as well as tubes and welding consumables made of highly creep resistant materials to be used in the temperature range of 620 and beyond 700°C. Types of materials dealt with are mainly 9-12% Cr steels (e.g. CB2, and FB2 steel) and nickel based alloys (e.g. Alloy 625, and Alloy 617), which have been developed in the past but never have been processed in industrial scale until now.

This paper will give an overview of the state of the development in material and process know-how as well as in industrial component manufacturing practice (e.g. castings like turbine casings and valves made of CB2 steel, welding qualification procedures for CB2 and dissimilar welds of Nickel base alloy with 9-12% Cr steel, material testing of base materials and welding consumables) at voestalpine.

Keywords: CB2 castings, FB2 and heavy forgings, CB2 welding consumables, EB welding, creep resistant tubes

1. Introduction

1.1. State of the art in material processing and applications

In the COST 501 project new 9-12% Cr steels for steam temperatures of up to 600°C were designed, prototypes were manufactured and extensive material testing in the form of short- and long-term tests were carried out. At that time two of the new steels, W-alloyed Cr steel (COST E) and Mo-alloyed Cr steel (COST F), were already qualified and strongly supported the development of a new generation of coal-fired thermal power plants with steam temperatures of 600°C and supercritical steam pressures of up to 300 bar.

Additional COST-initiatives (COST 522, and COST 536) and other comprehensive projects (e.g. Thermie AD700) were implemented to further improve the materials to be used at 625°C and beyond. As a result, the materials FB2, CB2 and A625C were found to be potential candidates for forgings and castings respectively. Prototypes from different manufacturers using different production technologies were produced and the associated piping and welding consumables were developed as well. In the course of this testing some process related problems arose that have to be solved for large-scale production. The long-term properties of these parts are still in the test phase – until the end of 2009 creep data of just over 50.000 hours was known. However, 100.000 hours of long-term values are a prerequisite to get new high-temperature materials approved by the European legal regime.

The newly developed material grades are mainly creep resistant martensitic steels for the use of up to 625°C and steam pressures above 300 bar and Nickel based alloys for the use at 700°C and above to achieve steam turbine efficiencies above 50%. Figure 1 summarises the steps in material development in respect to increasing steam temperatures and pressures for the USC and A-USC technology.
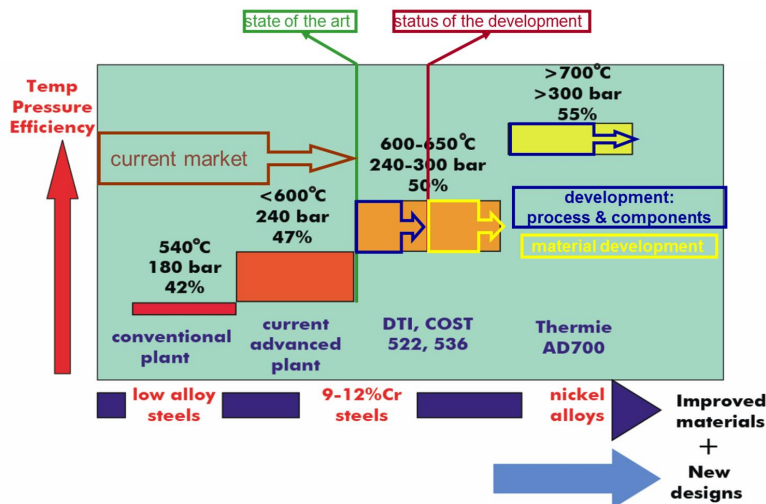
Figure 1: Steps in the development of the materials for (A)-USC power plants

For the 700°C technology, Ni-based alloys such as Alloy 625, Alloy 617, Alloy 263, and Alloy 740 were tested and the best candidates for each of the respective components were chosen. Pilot components were manufactured and thereby some unresolved issues in the processes (e.g. machining, non-destructive testing) appeared.

1.2. Goals, key aspects, and expected results of the KW50plus project

Components produced by voestalpine are used in the steam generator and in the turbine. Such key components are pipes/tubes, tubes leading the steam into the turbine, cast turbine and valve casings, forged turbine rotors and generator shafts, discs and blades, as well as welding consumables for all welding processes needed in the mentioned components. Figure 2 gives an overview of components in steam turbine construction which can be supplied by voestalpine.
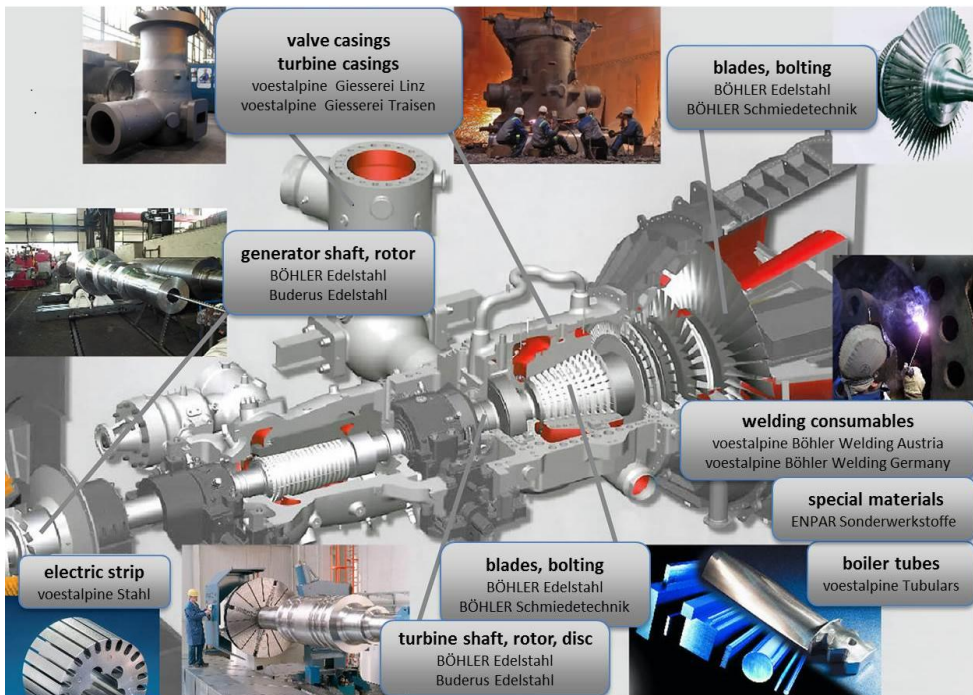
Figure 2: Typical applications of voestalpine products in steam turbine constructions

The main goals of the KW50plus project are the further material design and composition optimization in terms of producibility under conditions given in industrial scale production as well as the corresponding process development and optimizations to speed up the time-to-market of recently developed highly advanced materials like e.g. FB2 and CB2 and corresponding welding consumables.

Key aspects of the project are put on
- metallurgy of 9-12% Cr steels as well as engineering steels for heavy ingot casting in respect of melting processes and their limits, alloying concepts, solidification and segregation behaviour, and precipitation,

- heat treatment in respect of mechanical properties and microstructure, influence of component size, precipitates, time-temperature relationships, and residual stresses,
- development, welding trials and welding qualification procedures, approval of welding consumables for welding CB2, influence of micro chemistry and PWHT parameters,
- material characterization (chem. analysis, qualitative and quantitative metallography, creep testing) of base materials, welding consumables and welds, and
- determination of thermophysical data, modelling and simulation (solidification, segregation, precipitation, heat treatment, microstructure, stresses, hot tears, forging and pipe rolling processes) of industrial processes.

Expected project results are the industrial scale introduction of the martensitic 9-10% Cr steels CB2 and FB2 for the application at 625°C, cast Nickel base alloy 625 for the application at 700°C, and the development of new martensitic 9-10% Cr steels (MarBN steels) for the application at 650°C as this temperature is seen as the technical border of the martensitic steel family.

Finally, the voestalpine group wants to consolidate the position as a full package service, material and solution provider for the power generation industry.

2. Working packages and results

2.1. Castings

2.1.1. Heavy Steel Castings
Out of the European COST framework, where lots of 9-12% Cr-steel grades were investigated and evaluated for cast steel grades, the so called CB2 turned out to be the best candidate for 630°C so far. The material grade GX12CrMoCoVNbNB9-2-1 was introduced to commercial production for heavy steel casting components. Based on long-term experience with C91 and C911 steel grades, the process development could be done in a reliable way.
Meanwhile, we have results for the base materials showing more than 100.000 hours creep time for the original CB2-testblock from COST 522 and approximately 50.000 hours for the pilot-casting components from COST 536. The welding procedure qualification was also initiated within COST-working packages. Today we can show up PQR's for base metal process- and FAB-welding as well as FAB welds for non-matching weld connections, such as CB2-P92/P91 with FCAW and SMAW up to wall thicknesses of 180 mm per EN 15614-1 and 200 mm per ASME Sect. IX. [1]

Many investigations for optimisation of weld consumables were performed in working-packages within KW50plus together with our project partners in Kapfenberg and Hamm to ensure a good combination of creep strength, toughness and weldability.

Figure 3: SMAW with CB2 filler for Welding Qualification at voestalpine Foundry Linz

In the beginning, the market was cautious and limited to pilot inquiries, especially in Europe. Meanwhile, the demand for CB2 in Asia, especially China, is high and we have more than 100 cast components, with a total tonnage of approximately 1.500 in order. Components include valves in different and complex designs and inner casings with a weight range from 10 to 40 tons and with heavy walled and heavy FAB-welds (matching and non-matching) of up to 185 mm. Also, automatic and semi-automatic weld processes are being developed for heavy FAB-welds, together with our partner.

Figure 4: IP inner casing for advanced coal-fired steam turbines, material grade: CB2, made at voestalpine Foundry Linz in 2013

2.1.2. Castings made of Nickel base alloy

The voestalpine Foundry Traisen specializes in castings for advanced USC components made of the nickel based alloy A625. Several pilot components (e.g. nozzle box, valve bodies, tubes) have been delivered in the recent past. The focus is on the process development regarding moulding, melting, and pouring, as well as finishing operations like welding

including constructions welding of heavy wall similar and dissimilar joining of steel (i.e. 9-12% Cr, CB2) and cast nickel based components. [2][3]

As construction welding of different material combinations becomes more important, different welding procedures have been investigated [4]. Recent investigations deal with electron beam welding (EBW) for joining A625 cast material with A617 forged material. Advantages are less heat input, less weld preparation and no need for welding consumables. EBW also offers reduced total lead time. Figure 5 shows a comparison weld build up between SMAW and EBW dissimilar joints. [5]

Figure 5: Dissimilar welding of A625 cast and CB2, comparison between electron beam and stick welded joints, wall thickness 50 mm, voestalpine Foundry Traisen, 2013

Both procedures were successfully investigated and showed acceptable results according to given welding qualification standards. Figure 6 shows macrosections of EB welded joints of cast Alloy 625. Latest developments were dedicated to the weldability of A625 cast components to A617 forged parts. The producibility was proven by the successful manufacturing and witness inspection of a pilot valve made of A625 with EB welded connection tubes out of forged A617. A welding procedure qualification acc. EN15614-11 was successfully performed.
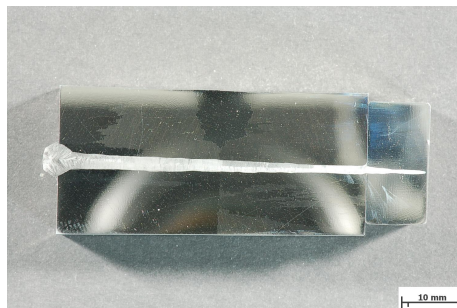
Figure 6: Electron beam joints of Alloy 625, weld thickness: 50mm, voestalpine Foundry Traisen, 2013

461

2.2. Forgings

2.2.1. Forgings made of COST FB2
Specifically, the 9-10% Cr grades steels have the highest potential to meet the required creep resistance level for critical components in steam power plants.

Under COST 501 (1983-1997), the 9-10% Cr steels E, F and B2 for the use of up to 600°C have been developed, trial rotor forgings with body diameters of up to 1200 mm have been manufactured and a lot of testing work has been performed. COST E and F have meanwhile become standard materials for ultra-supercritical (USC) power plants with 580-600°C steam temperatures. The trend for even higher steam conditions was the subject of the COST 522 programme (1998-2003) where the very promising properties of FB2 test material, produced by Böhler and based on B2 from COST 501 with the addition of Co (Table 1), led to the manufacture of a trial rotor forging.

Table 1: Chemical compositions of steels B2 and FB 2

Steel	C	Si	Mn	Cr	Mo	W	Ni	Co	V	Nb	N	B
B	0.17	0.07	0.06	9.3	1.55	-	0.12	-	0.27	0.064	0.015	0.010
FB2 test	0.13	0.05	0.82	9.32	1.47	-	0.16	0.96	0.20	0.05	0.019	0.0085
FB2 trial	0.13	0.09	0.33	9.08	1.43	-	0.16	1.26	0.22	0.054	0.022	0.0076

The first full size FB2 rotor forging with a final weight of 17 tons was manufactured by Böhler in 2000-2001 via the BEST (Böhler Electro Slag Tapping) melting route; afterwards, forgings from Societa delle Fucine Terni (conventional steel making method) and Saarschmiede (ESR process) followed. Manufacturing the test melts, trial rotor forgings and test results have already been reported in several papers [6][7][8][9].

The results of creep tests obtained so far show that all the data lies in one narrow scatter band confirming the trial melt behaviour of FB2. In Figure 7 [7] the values are all above the rotor B2 line.
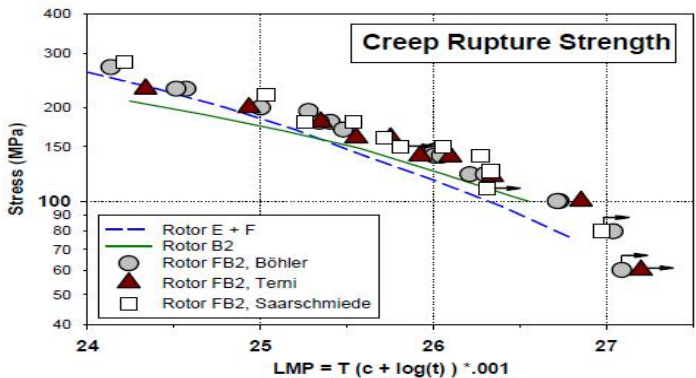
Figure 7: Creep rupture strength of COST FB2 test rotors in comparison to other COST rotor alloys (with arrow: running specimens) [7]
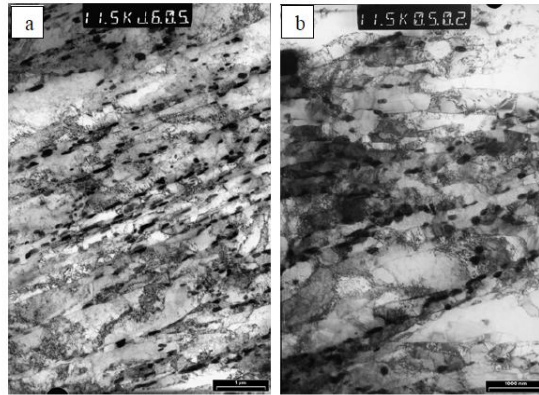
Figure 8: Microstructure of FB2: after QHT (a); gauge section (b) (600°C, 100 MPa) after 56.500 hours [10]

During creep, under the influence of temperature and stress, usually dislocation density decreases, sub-grains form and grow, M23C6 particles coarsen, the martensite laths become much wider and also new phases like the laves phase appear. This is not the case for FB2 because of its support for high temperature stability:

- a martensitic structure with narrow martensite laths, which are decorated with and therefore stabilised by M23C6 carbides, stabilised itself by Boron [11]
- a high dislocation density, which is preserved for longer times
- and Nb, V carbonitrides (up to about 1 µm); which avoid grain growth during austenitisation and are stable during creep

A representative TEM image of steel FB2 is shown in Figure 8 [10].

Under the influence of temperature, the Laves phase also appears in FB2 but is very small (0.6-0.8µm) and homogeneously distributed and, therefore, has no negative effect on creep.

The excellent creep resistance of FB2 and the successful transformation of trial melt behaviour for large components led to the start of industrial production and orders for new USC power plant projects in Germany, USA and Asia, which have been placed within the last years.

Based on the experience with the COST FB2 trial rotor forging, the manufacturing technology had to be fitted to the appropriate dimensions and the melting route has been changed from BEST to conventional casted ingots with total weights of 22 to 28 tons due to the smaller dimensions of the shafts. Until today, forgings have been manufactured with delivery weights from 7 to 9.2 metric tons.

The basic manufacturing steps for the forgings were set as follows:

- Melting the steel in an Electric Arc Furnace (EAF), followed by
- ladle furnace (LF) and Argon Oxygen Decarbonisation (AOD) or
- Ladle furnace with Vacuum Degasing (VD),

- casting the ingot by bottom pouring process,
- homogenising and hot-forming,
- preliminary heat treatment, pre-machining, ultrasonic testing,
- quality heat treatment (QHT), machining and final testing.

Forging was carried out on the 52 MN forging press, consisting of cogging, upset forging, followed by final forging (shaping) and preliminary heat treatment (PHT) by martensitic transformation and tempering.

After pre-machining the rotors to achieve a defect-free surface, ultrasonic tests were performed to confirm the internal quality of the forgings and then the quality heat treatment for adjusting the mechanical properties was carried out by austenitising at 1100°C / spray quenching and double tempering to the target 0.2 % yield strength of $\geq$ 650 N/mm². Double annealing was performed in order to ensure a totally annealed martensitic microstructure.

The rotors were then machined and checked (Figure 9) using ultrasonic testing to determine the minimum detectable defect size (MDDS). No defects were found; the measured MDD's ranged from 1.5 mm for a smaller part with $\varnothing$ 860 mm up to 2.2 mm for parts with a diameter of 1120 mm respectively. There was an improvement of 0.5-0.8 mm compared with the preliminary heat treated condition.

Figure 9: Quality heat-treated and machined FB2 Forging; delivery weight 9.2 tons

All turbine shaft parts are subject to mechanical technological testing to ensure their suitability for use. The properties are checked at different test positions; specimens in tangential direction from the outer segments on both ends of the forging (top and bottom) and in some cases specimens were taken from a near centre test ring of 350 mm in diameter and 300 mm from the face end. The results of the basic strength and toughness properties are summarised in Figure 10.
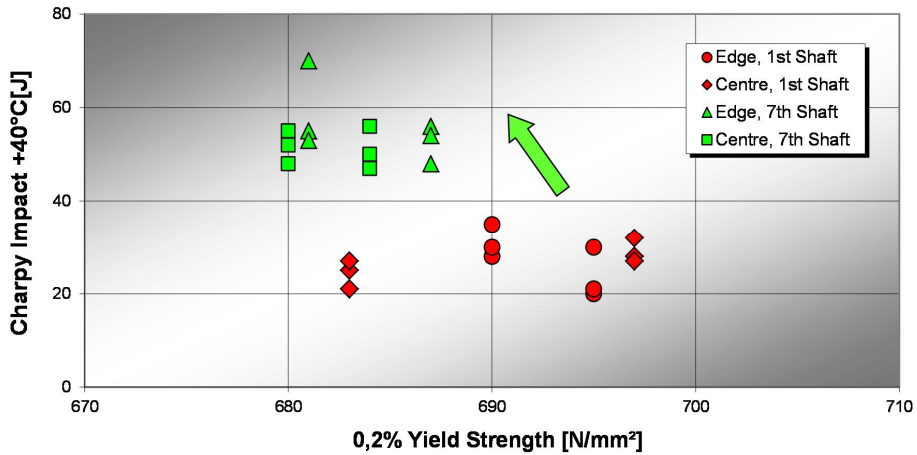
Figure 10: Yield strength and Charpy impact properties of FB2 rotors

In addition, short-term creep tests at 600°C and 160 MPa load were performed on one shaft part at t = 1300h in order to compare the creep behaviour with the results achieved on the FB2 trial melt and the FB2 trial rotor forging from the COST programme. Four test specimens in total, one from each test location, were taken in tangential direction: two from the edge and two further from the near centre position. The achieved results, plotted as a creep strain versus time curve, are shown in Figure 11.

After 1200 hours testing time, the creep strain is on average on the same level as the FB2 trial rotor.
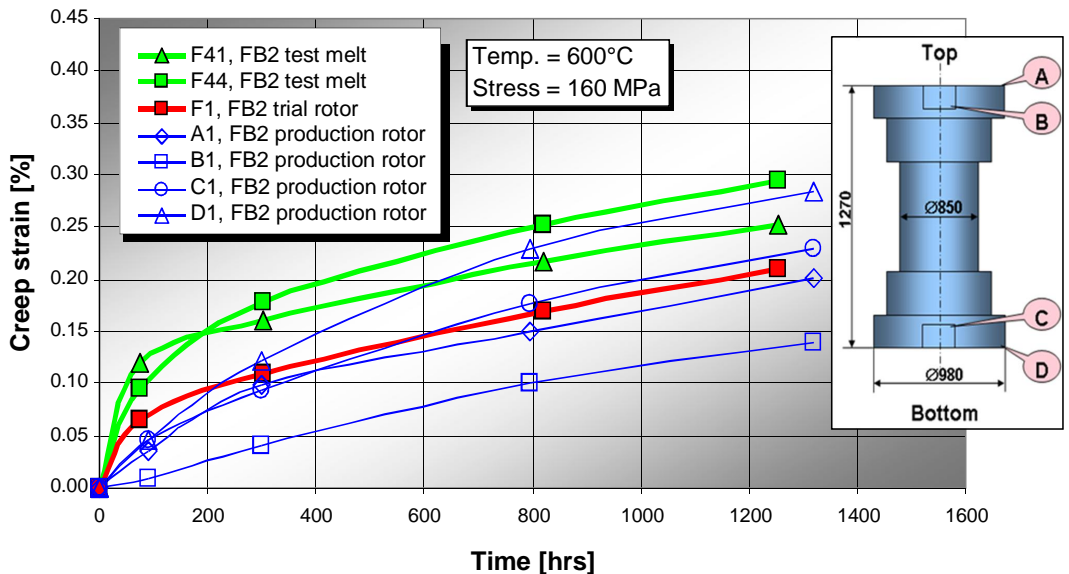
Figure 11: Results of the short term creep testing in comparison to FB2 trial melt as well as trial rotor forging

465

Metallographic examinations showed that the microstructure in the edge as well as the near centre position are tempered martensite with a grain size of 0-1 acc. to ASTM E112 in the edge and about 00 in the near centre area. Furthermore, in all examined sample locations the microstructure was free of δ-ferrite but contained some isolated Boron nitrides.

The content of Boron in the steel is essential. Boron has to be in solid solution in order to stabilise the M23C6 carbides for a high level of creep resistance. Also, Nitrogen is necessary for the formation of the MX precipitates which are basically Nb, V – carbonitrides. If there are too many Boron nitrides (BN) in the microstructure, the creep properties will not achieve the expected level due to a lack of B and N in the matrix. Therefore, B and N have to be balanced very carefully (Figure 12).
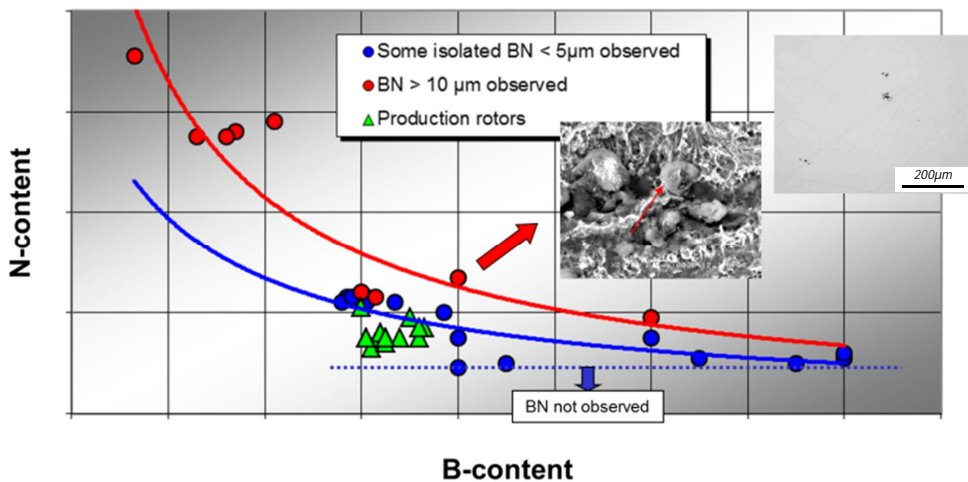
Figure 12: Influence of Boron and Nitrogen on Boron Nitrides generation

All of these results are achieved by industrial melts with at least 3.5 tons and based on 9-12% Cr steels. Larger Boron Nitrides (BN) were observed along and above the red line, with smaller isolated ones along the blue line. Having N contents below the blue dotted line, BNs could never be observed. Our production rotors were in the field of some isolated and small BN, which are unavoidable and in this size and content not detrimental to the creep properties.

In order to improve the quality of the forgings especially MDDS, development work is needed to further improve the grain size for a better ultrasonic detectability (Figure 13).
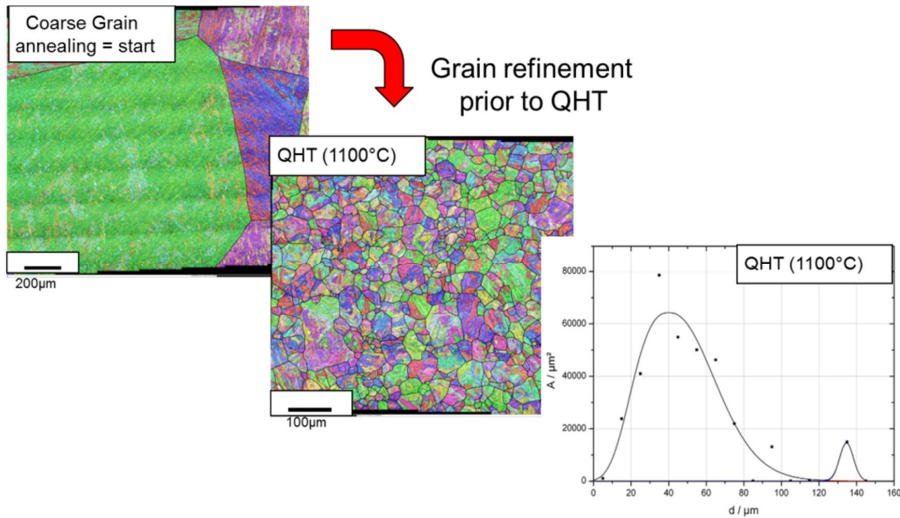
Figure 13: Results of grain refinement trial in laboratory

Furthermore, with respect to the fabrication of larger forgings, the intention of Böhler is increasingly more focussed on the use of re-melted (PESR) materials due to a better consolidation of the ingots, less segregations and better homogeneity of the product. Test material manufactured out of ingots with up to 540 mm in diameter has already been produced successfully and an up-scaling to a 32 tons ingot is currently in progress.

2.2.2. Heavy Forgings
In order to accompany the market development and meet future demands on heavy forgings, one sub-project realized by Buderus Edelstahl was the development of a new forging ingot as a basis for generator shaft forgings for 800 MW power plants. The main focus was, for example, on up-scaling an existing 160 ton ingot to 190 tons with consistent ingot quality.

The methodical approach consisted of three steps:

- designing the ingot, assisted by numerical simulation
- carrying out trial casts, and
- validating the ingot quality

The expected results of the numerical investigations were not quantitative predictions of absolute values of typical solidification phenomena such as porosity, segregation, non-metallic inclusions etc. and their exact position, shape and size. Instead, mould parameters such as H/D ratio, conicity or hot top design have been investigated on their qualitative impact on solidification.

Since the segregation behaviour as well as the degree of cavity and size of non-metallic inclusions are functions of solidification time and therefore ingot size, the ingot quality was proven based on these characteristic measured values by investigation of the trial cast. In order to examine the quality, the first cast was forged to a trial bar and dissected to investigate the internal ingot. The degree of segregation was evaluated by analysing mainly the carbon and sulphur content. The design goal, a solidification geometry and therefore behaviour with a minimum of segregation, was achieved as shown in Figure 14.
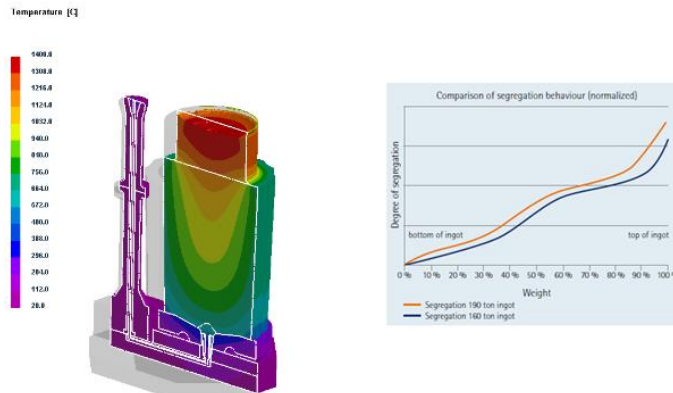
Figure 14: Numerical simulation 190 ton ingot and comparison of segregation behaviour between a 160 ton and the new 190 ton ingot

Size and amount of non-metallic inclusions were evaluated by metallographic investigations and did not show any deterioration. The evaluation of cavity was carried out indirectly by ultrasonic testing of the bar after forging and heat treatment with a validated forging program. The forging process was analysed by FEM-simulation as can be seen in Figure 15. The bar did not show retained porosity. After having proven the fulfilling of all requirements the ingot is approved and cleared for production. Meanwhile the first shafts have been successfully produced and delivered.
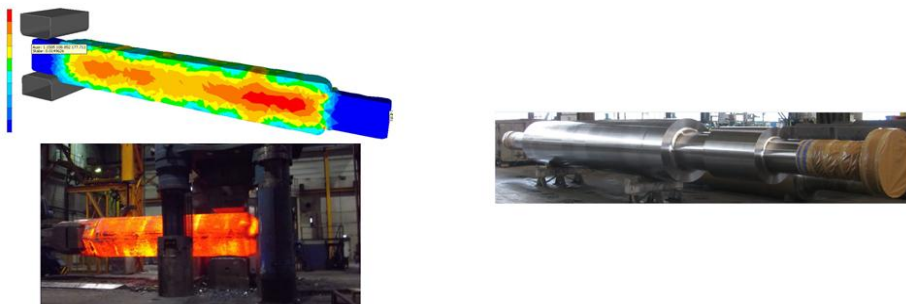
Figure 15: Numerical simulation based process control, forging process of 190 ton ingot and generator shaft, forging made of steel 27NiCrMo15-6

2.3. Heat resistant tubes

Currently, voestalpine Tubulars is producing alloyed boiler tubes up to grade 10 CrMo 9 10. In general, the trend in power plant construction is towards higher and higher application temperatures (630-650°C is currently standard, for new projects partially above 700°C). Furthermore, projects are usually tendered as packages. As a quality supplier, this also means having to offer higher alloyed grades to be considered for all-inclusive tenders. For voestalpine Tubulars, this involves being able to produce grades such as T91, T92 , T23, T/P5, and T/P9. The integration into the group project is essential because thereby sales and technical synergies with the project partners in the voestalpine can be used (for example, with the Böhler Welding).

The main goals of the KW50plus project are listed below:
- Investigation of the workability of the grades T91, T92, T23, and T/P5, T/P9 in accordance to ASTM A 213
- Investigation of the internal error / cups problem at higher alloy steels
- Simulation of the cross-rolling process with internal defects
- Production of high-quality pre-materials (rolled over / continuous casting)
- Determination of the "natural" rejection figures for these steel grades

First, simulations with the new materials, using a FEM model created to evaluate the workability of pre material quality, are performed. After positive finalization, production tests with parameter variations are conducted. The essential criterion is to examine the internal error problem when cross-rolling these steel grades. Finally, specimens for creep tests are to be produced out of the generated tubes and then be tested.

Methodology by
- Simulation calculations for the new materials
- Production experiments with recording of all production parameters and implementation of all mechanical- technological tests including creep tests

The results of these rolling trials showed that in this steel grade there is no slipping in the cross-rolling mill and no internal defects (Figure 16).

Figure 16: Interior view of a pipe after experimental rolling
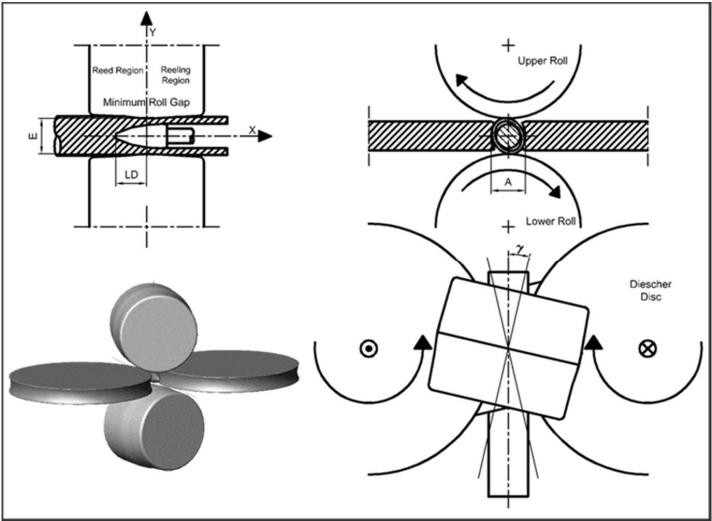
Figure 17: Process of tube rolling
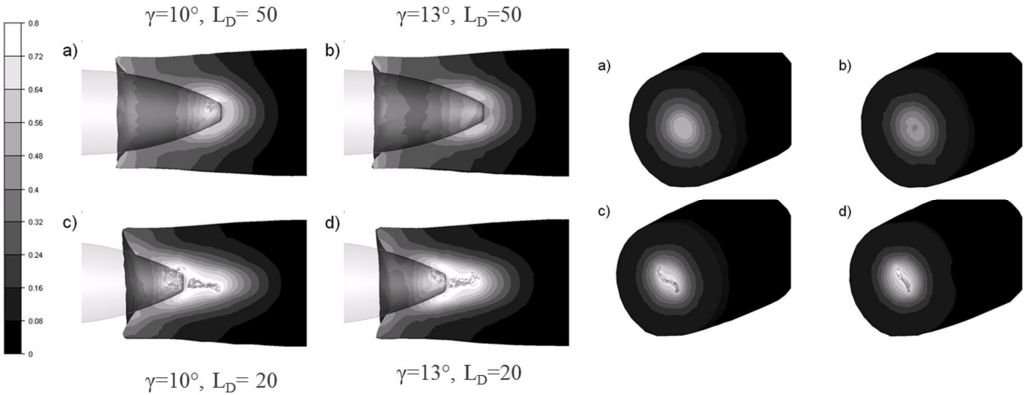
Figure 18: Numerical simulation of tube rolling, to investigate process parameter related mistakes

470

When carrying out the rolling trials, it was necessary to know the individual transition temperatures for this material throughout the rolling process, as well as for the subsequent heat treatment process. For that reason, the material simulation program JMAT Pro 6.2 was purchased, with which the necessary constitutional diagrams for the manufacturing process (Figure 19) were simulated.
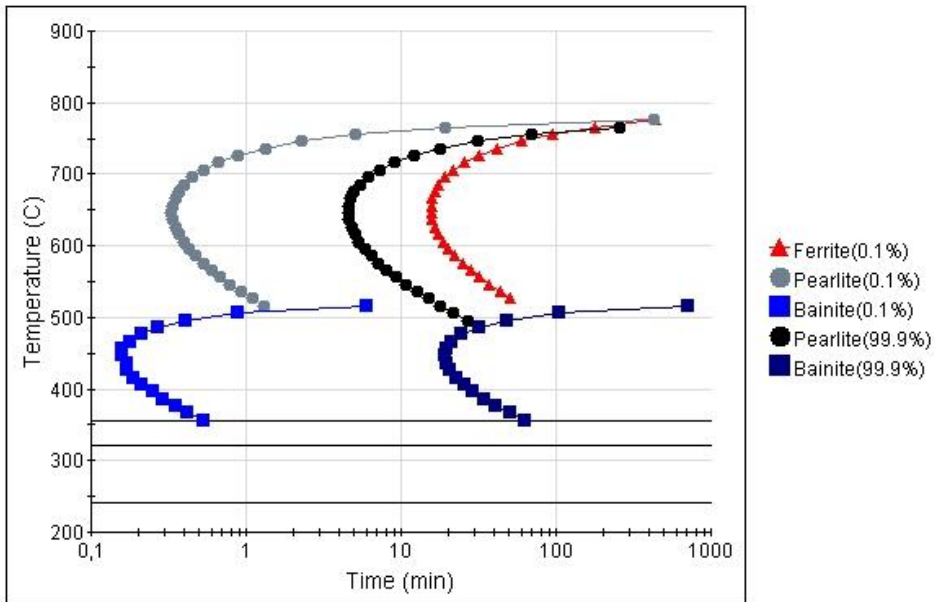
Figure 19: Time Temperature Transition plot of T/P5, simulated with JMat Pro 6.2

2.4. Welding consumables

With the development of the base material, the development of matching welding consumables was started as well [12].Originally, the chemical composition of all weld metal was kept close to the chemical composition of the base material. Due to the detrimental influence of high boron contents on hot cracking susceptibility and impact toughness, care was taken in an appropriate adjustment of the boron content [13].To fulfil the requirement of higher impact values at ambient temperature, the increase of Ni-content was discussed. As nickel has been shown to be detrimental for long term creep properties of P91 [14], the high Ni-content was highly controversial.

2.4.1. Development of a flux cored wire for CB2 welding
The flux cord wires used in the Flux Cored Arc Welding (FCAW) process provides several technical and economic advantages: a rutile slag system providing good out-of-position weldability, easy handling and high productivity [15]. To provide these advantages also for welding, the new developed cast steel CB2 a matching flux cored wire has been developed

471

based on the rutile/basic slag system of the already available 9% Cr flux cored wires for welding P91 and P92. The investigation of the influence of Ni on mechanical properties at ambient temperature and creep rupture strength at 625°C showed that Ni slightly increases yield without appreciable effect on tensile strength and enhances impact energy, especially in combination with higher annealing temperature and longer annealing time. However, a reduction in creep rupture strength was already observed after short testing times [16]. Therefore, the Ni content of the CB2 flux cored wire weld metal is kept in the range of the base metal. The actual chemical composition of the weld metal and the mechanical properties at ambient temperature with a PWHT of 730°C/24h are shown in Table 2 and Table 3, respectively.

Table 2: Chemical Composition of Böhler CB2 Ti-FD Flux Cored Wire Weld Metal [wt.%]

C	Si	Mn	Cr	Mo	Co	Ni	V	Nb	N	B
0.12	0.2	0.9	9.0	1.5	1.0	0.2	0.2	0.03	0.02	0.006

Table 3: Mechanical Properties of All Weld Metal at Ambient Temperature with PWHT 730°C/24h

Y.S. [MPa]	590
T.S. [MPa]	740
El. [%]	17
CVN@RT [J]	30

The welding procedure qualifications for FCAW of CB2 were conducted successfully at the voestalpine foundries in Linz and Traisen [1]. To get a better understanding of the material's behaviour, the influence of chemical composition and PWHT on mechanical properties was investigated at the Graz University of Technology [17]. Additionally, the microstructural precipitation development during welding, heat treatment and creep processes was simulated and the simulations were then compared to the investigated microstructure [18]. The main objective of this ongoing project is to find linking parameters between microstructure and mechanical properties. Some approaches and a literature survey were presented at the IIW intermediate meeting 2014 [19].

2.4.2. Development of a covered electrode for CB2 welding
Although flux cored wire is preferred in many cases for reasons of welding properties, this technique cannot scope with all welding tasks, namely welding of parts with difficult accessibility. Therefore, in the context of the project COST 536, a CB2 matching covered electrode was developed from a lower alloyed 9 % Cr core wire [12]. This electrode already passed the welding procedure qualification at voestalpine Giesserei Linz. Nevertheless, the welded joint and all of the weld metals showed lower creep resistance compared to the base material.

In order to improve the creep properties, the alloy concept of the electrode has been optimized by increasing the content of boron and, in a second step, decreasing the content of nickel.

The optimum for the boron content concerning impact properties, hot cracking resistance, and creep resistance turned out to be about 50 ppm.

The lowering of the nickel content to about 0.2 % drops the toughness to around 20 J after a post weld heat treatment of 12 hours at 730 °C. To get higher toughness values, a PWHT with higher temperature and / or longer holding time is mandatory.

One disadvantage of a semisynthetic electrode is the irregular distribution of some elements like carbon and boron in the weld metal, so a core wire alloyed electrode is being produced. As soon as the core wire is available, the electrode will be optimized regarding the impact properties and long term creep tests will be performed.

3. Summary and Outlook

In this paper the topics including castings, forgings, tubes and welding consumables were discussed and some results of the voestalpine project "KW50plus" were presented.

For the 9-10% Cr steels, cast components out of CB2 were as far developed to be introduced into production. Additionally, the development of the CB2 filler metal was effectively completed.

Furthermore, pilot components for the Ni-based components for 700°C steam power plants were successfully produced at foundry Traisen and promising welding procedures investigated.

This project is still in progress and is being followed with great determination by the voestalpine group. One reason for that is the future market situation for coal power stations. Coal remains the global dominant energy source for electricity production with even further potential growth in the future.

Acknowledgements

Reference list

[1] C. Lochbichler, E. Schmidtne Kelity, S. Baumgartner "Latest Developments of Cast Materials and Welding Consumables for Coal-fired Steam Turbines Components / Nickel-base Alloy A625 and CB2 Steel for the A-USC Technology", PowerGen 2013, Vienna

[2] C. Lochbichler, "Manufacturing of Cast Components made of Nickel-base Alloy 625 for 700°C Class A-USC Steam Turbine Applications", proceedings of *International Gas Turbine Conference*, Osaka, 2011

[3] C. Lochbichler, "Sand Castings made of Alloy 625 and Dissimilar Welding for Steam Turbine Applications", proceedings of *Advanced Fossil Gen Summit 2012*, Beijing, 2012

[4] Bernhard Berger, "Dissimilar Schweißen von Guss-Stücken (Konstruktionsschweißungen) NIBAS 625 mit warmfestem Cr-Stahl COST CB2", *Diploma Thesis*, University of Graz, 2012

[5] Christoph Wiednig, "Electron Beam Welding Alloy 625", *Diploma Thesis*, University of Graz 2013

[6] G. Zeiler, W. Meyer, K. Spiradek-Hahn, J. Wosik: "Experiences in Manufacturing and Long-Term Mechanical & Microstructural Testing on 9-12% Chromium Steel Forgings for Power Generation Plants"; *4th International Conference on Advances in Materials Technology for Fossil Power Plants (EPRI)*, Conference CD, Hilton Head Island, South Carolina, USA, pp. 222-236, (2004)

[7] T.U. Kern, B. Scarlin, B. Donth, G. Zeiler, A. DiGianfrancesco; "The European Cost 536 Project for the Development of New High Temperature Rotor Materials"; *17th International Forgemasters Meeting*, 03-07. November 2008, Santander

[8] A. Di Gianfrancesco, L. Cipolla, D. Venditti, S. Neri, M. Calderini; "High Temperature Properties and Creep Behaviour of a CrMoCoB (FB2) Steel Trial Rotor", *17th International Forgemasters Meeting*, 03-07. November 2008, Spain

[9] T.U. Kern, M. Staubli, K.H. Mayer, B. Donth, G. Zeiler, A. DiGianfrancesco; "The European Effort in Development of new High Temperature Rotor Materials – COST 536", *proceedings of 8th Liege COST Conference*, 18. -20. Sep. 2006, Liege, Belgium

[10] F. Kager, N. Boeck, K. Spiradek-Hahn, S. Hoefinger, M. Brabetz, G. Zeiler; "Superior Long-term Creep Behaviour and Microstructural Evolution of 9% Cr-Steels with Boron", *proceedings of 8th Liege COST Conference*, 18. -20. Sep. 2006, Liege

[11] L. Lundin; "High Resolution Microanalysis of Creep Resistant 9-12% Chromium Steels", 1995, Goeteborg, Chalmers University, *PhD Thesis*

[12] E. Bauné, H. Cerjak, St. Caminada, C. Jochum, P. Mayr, J. Pasternak, Weldability and Properties of new Creep Resistant Materials for use in Ultra Supercritical coal fired Power Plants, Materials for Advanced Power Engineering 2006, *Proceedings Part II*, pp. 871-891 (2006)

[13] S. Baumgartner, G. Posch, P. Mayr, Welding advanced martensitic creep resistant steels with Boron containing filler metal, *Welding in the World*, Vol. 56, No. 7/8, pp. 2-9 (2012)

[14] K. Kimura, K. Sawada, H. Kushima and Y. Toda, Microstructural Stability and Long-term Creep Strength of Grade 91 Steel, Energy Materials: Materials Science and Engineering for Energy Systems, Vol. 4, No. 4 , *8th Charles Parsons Turbine Conference 2011*, pp. 176-183 (2011)

[15] G. Posch, S. Baumgartner, M. Fiedler, GMA-Welding of creep resistant steels with flux cored wires (FCAW): perspectives and limitations, *Proceedings of the IIW International Conference on Advances in Welding and Allied Technologies*, pp.619-624 (2009)

[16] S. Baumgartner, M. Schuler, R. Schnitzer, N. Enzinger, Inluence of Nickel on the Mechanical Properties fo a CB2 Flux Cored Wire Weld Metal, *Proceedings of the 10th Liège Conference*, 2014

[17] M. Schuler, C. Ramskogler, S. Baumgartner, N. Enzinger, R. Schnitzer, Simulation of microstructure and modelling of mechanical properties of welding materials from CB2 flux cored wires, Proceedings of the 10th Liège Conference 2014

[18] S. Baumgartner, M. Schuler, C. Ramskogler, E. Schmidtne-Kelity, A. Sarić, R. Schnitzer, C. Lochbichler, N. Enzinger, Mikrostrukturentwicklung von CB2 Fülldraht-Schweißungen, 36. Vortragsveranstaltung der Arbeitsgemeinschaft für warmfeste Stähle und Hochtemperaturwerkstoffe, Düsseldorf, (2013)

[19] M. Schuler, S. Baumgartner, R. Schnitzer, N. Enzinger, Modelling mechanical properties of 9% chromium weld metals, IIW Doc. II-C-465-14

Part D

Gas Turbine Materials

GADOLINIUMZIRCONATE, A THERMAL BARRIER COATING OF NEWEST GENERATION

W. Stamm[1], E. Bakan[2], R. Vaßen[2], M. Frommherz[3], A. Scholz[3],
M. Oechsner[3], M. Rudolphi[4], M. Schütze[4]

[1]Siemens AG Energy Sector (werner.stamm@siemens.com)
[2] Forschungszentrum Jülich GmbH, Institut für Energie- und Klimaforschung IEK-1, 52425
Jülich, Germany (e.bakan@fz-juelich.de, r.vassen@fz-juelich.de)
[3]Institut für Werkstoffkunde, Technische Universität Darmstadt, Grafenstraße 2, 64283
Darmstadt (frommherz@mpa-ifw.tu-darmstadt.de, scholz@mpa-ifw.tu-darmstadt.de,
oechsner@mpa-ifw.tu-darmstadt.de)
[4]DECHEMA-Forschungsinstitut, Theodor-Heuss-Allee 25, 60486 Frankfurt am Main,
Germany (rudolphi@dechema.de, schuetze@dechema.de)

Abstract

In the last decade new TBC systems were investigated as protection for hot path components. One of the most promising materials is the system gadolinium zirconate (GZO), which is coated as a bi-layer system with partially stabilized zirconia as a carrier material and with GZO on top. Siemens has published in some announcement that this type of coating system is applied in their new SGT5-8000 H generation. Based on the limited stability range of GZO in the phase diagram it is important to increase knowledge about process features. In this paper, the requirements of powder will be discussed and details of the optimized deposition technique will be provided. This knowledge is a fundamental need for getting a sufficient TBC quality for service life. The DFG/FVV joint research project will provide structural differences of GZO related to physical properties and spallation behaviour of the coating. In addition, results of 4-point bending tests in accordance with acoustic emission measurements to determine the critical strain will be discussed. Finally the potential of the GZO coatings system as a design integrated thermal barrier coating in the future will be evaluated.

Keywords: gadolinium zirconate, thermal barrier coating systems, spallation, physical properties, deposition technique

1. Introduction

Yttrium-stabilized Zirconia is used as a standard material for thermal barrier coatings for over 30 years because of its remarkable properties [1]. However, one disadvantage of YSZ is the limitation of the maximum surface temperature to about 1200 °C for long-term applications. At higher temperatures phase transformations and sintering effects result in crack formation, a decrease in strain tolerance and a higher thermal conductivity, which lead to a degradation of the coating system. In the last decade new thermal barrier coating materials were investigated for hot path components. The selection of new TBC materials is restricted to a few fundamental properties, like high melting point, high sintering stability, no phase transformation between room temperature and application temperature, low thermal conductivity, a CTE close

to the substrate, chemical resistance and a good bonding (adhesion strength) to the metallic substrate [2]. Furthermore, no chemical reactions should take place between the ceramic material and the bond coat material or the thermally grown oxide layer.

One of the most promising candidates are pyrochlore structures ($A_2B_2O_7$), in this case especially $Gd_2Zr_2O_7$ (GZO), which are typically coated as double layer coatings on a bottom layer of partially stabilized zirconia (YSZ) [3]. The bottom layer of YSZ provides a higher fracture toughness to withstand the thermal stresses arising at the ceramic metallic interface, reduces the thermal mismatch of the ceramic layer with the metallic substrate (compared with single-layered GZO) and prevents a possible reaction of GZO with the thermally grown oxide (Al_2O_3), where perovskite-type phases can form at long term high temperature exposures. One main issue to provide reliable TBC coatings with a sufficient quality is the processability of the GZO layers via atmospheric plasma spraying (APS), providing coatings with a tailored microstructure, e.g. distinct levels of porosity. Gadolinia is prone to evaporate in the plasma plume which may result in non-stoichiometric GZO coatings, where metastable cubic zirconia can develop. Areas with not stabilized zirconia undergo phase transformation and specific volume changes during thermal cycling which result in a low thermocylic performance. Consequently, the high potential of the new TBC system is only applicable, if a reliable processing routine can be achieved as well as a quantitative description of the relevant degradation mechanisms is available.

In this paper, the requirements on the powder and the optimized deposition technique for GZO coatings will be discussed. Additionally, first results of the characterization of the mechanical properties related to microstructure and spallation behaviour are presented in comparison with the conventional APS-YSZ coatings. These properties act as input parameters for the lifetime modelling approach. In addition, results of 4-point bending tests with in-situ acoustic emission measurements to determine the critical strain will be discussed.

2. Process Development

2.1 Experimental

In this research project, three TBC systems (each with a variation of porosity (LP - low porosity / HP - high porosity) and a total thickness of approx. 500 µm) are investigated and are schematically presented in figure 1. Two bi-layer systems (S2 and S3) with a 400 µm GZO layer on top of a 100 µm YSZ layer are produced by Praxair, (S2, F4 spray gun) and Jülich, S3, TriplexPro spray gun). A conventional 500 µm APS-YSZ system produced by Praxair (S1, F4 spray gun) serves as a baseline system for comparison with state of art TBCs. Through two distinct levels of porosity (LP: 5-9 %; HP: 16-20 %) of the topcoat, the influence of microstructural parameters on the mechanical properties, damage mechanism and lifetime will be investigated. For the substrate material a single crystal superalloy (PWA1483)

was chosen. A standard CoNiCrAlY bond coat (LCO22, R_a= 8-14 µm, ~330 µm thick) was applied by a low pressure plasma spray (LPPS) process.
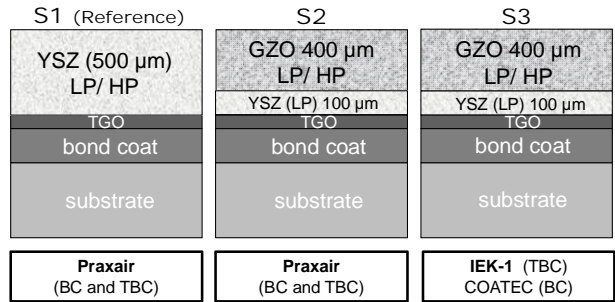
Figure 1: Overview over the investigated APS- TBCs: conventional YSZ coating S1, GZO/YSZ double layer coatings: S2 (Praxair) and S3 (IEK-1) with a variation in porosity (LP/HP) of the topcoat.

2.2 Coating Process

The samples used to study the industrial coating process (systems S1 and S2) were coated by Praxair with a Sulzer Metco F4^{TM} gun with proprietary spraying parameters, the samples for system S3 were coated by APS in a Multicoat facility (Sulzer Metco, Wohlen, Switzerland) with a TriplexPro^{TM} gun mounted on a six-axis robot. The 9 mm diameter nozzle was used with a 1.8 mm diameter feedstock injector. The plasma gas composition was 46 standard liters per minute (slpm) Ar and 4 slpm He.
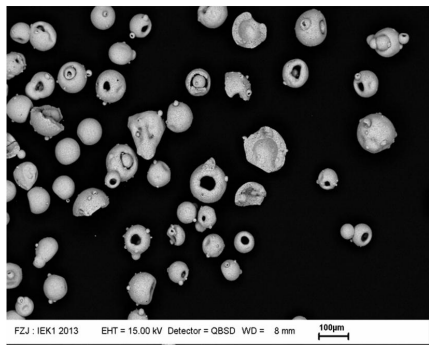
Figure 2: SEM image showing the morphology of GZO powder used for this investigation.

The feedstock powders for the ceramic top coats were a commercially available 7YSZ powder (Sulzer Metco 204NS, d_{10}=28 µm, d_{90}=85 µm) and spray-dried $Gd_2Zr_2O_7$ powder (H.C. Starck Amperit 835.090, d_{10}=60µm, d_{90}=117µm). Figure 2 shows the hollow spherical morphology of the GZO powder as observed with an SEM.

Double layer APS YSZ/GZO (100/400µm) topcoats were coated on LPPS bondcoated substrates for burner rig and 4-point bending tests. Table 1 shows the varied spray current and stand-off distances used for the GZO layer deposition leading to different porosities. Lower currents and longer distances provide lower GZO porosity as a result of lower particle temperatures and hence unmolten or re-solidified particles. On the other hand, high currents increase the particle temperatures resulting in dense coatings due to highly molten particles. A porous and dense GZO microstructures produced with low and high spray currents, respectively can be seen in figure 3.

Table 1: Spray currents and stand-off distances for spraying of GZO layers.

Current (A)	Stand-off Distance (mm)
300	75
325	95
325	75
325	65
450	95
525	95
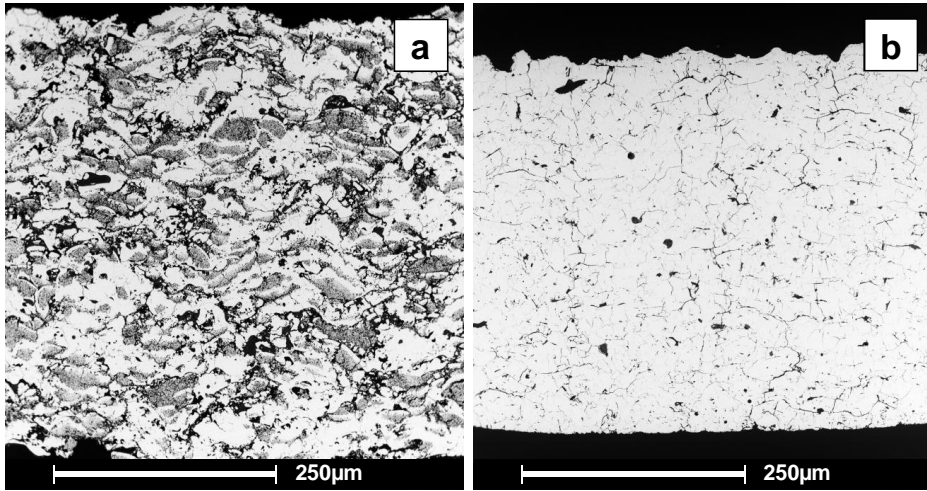
Figure 3: Cross-section scanning electron microscope images of GZO coatings; (a) 325A-95mm, (b) 450A-95mm.

3. Testing

3.1. Burner Rig Test

Gas burner test facilities operating with a natural gas/oxygen mixture were used to evaluate the thermal cycling behaviour of the systems. During the test, surface temperature was meas-

ured with an infrared pyrometer. Additionally, the substrate temperature was measured by a thermocouple located in the center of the substrate. The surface temperature was fixed at 1400±50 C, while the substrate temperature was adjusted to 1050±30°C.

Figure 4 shows a comparison of lifetime with a standard YSZ system, where the influence of GZO porosity on lifetime can also be seen. It is obvious that the double-layer concept is able to provide significant lifetime improvement at 1400°C surface temperature. This improvement seems to be rather pronounced for double layers with more porous GZO layers. On the other hand, double layers with low GZO porosity showed early failures.
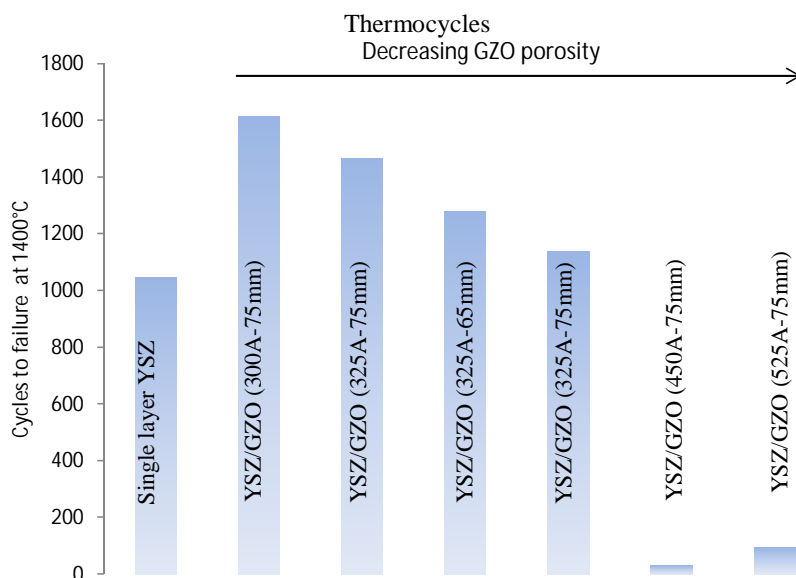
Figure 4: Burner rig test results of GZO/YSZ double-layer systems and standard YSZ tested at 1400°C surface temperature.

3.2. Data Assessment for Lifetime Modelling

The stiffness and the crack resistance are fundamental properties of the ceramic topcoat, which have a great influence on damage and lifetime of the thermal coating system. E.g. the stiffness represents the strain tolerance of the ceramic coating where a high strain tolerance is indispensable for a good thermo-cyclic performance. These properties can significantly change with time and temperature, leading to a degradation of the TBC system [1]. Moreover these properties act as input parameters for the used lifetime assessment model (see chapter 4). The stiffness of the ceramic topcoat was determined using impulse excitation. The critical energy release rate respectively the crack resistance or fracture toughness for a delamination

of the ceramic topcoat was determined using a modified 4- point bending setup. The samples used to generate the following data were coated by Praxair (system S1 and S2), the samples coated by FZ Jülich (system S3) are currently under investigation.

3.2.1. Stiffness (elastic modulus)

Freestanding ceramic layers were obtained by spraying the ceramic layer on graphite substrate plates and detaching the ceramic layer of the graphite substrates with a heat treatment of about 700 °C/12 h in air. Rectangular specimens with a thickness of approx. 650 µm were prepared by laser beam cutting at the DFI. Due to the small thickness and the high damping of the resonance frequency it was not possible to attain reliable resonance peaks for the freestanding layers. To get better results, the ceramic layers were applied to steel substrates with a 2-K epoxy adhesive (UHU endfest plus) (figure 5a). Impulse excitation measurements were conducted with a resonance frequency and damping analyser (RFDA System, IMCE) at the department of Nonmetallic-Inorganic Materials (NAW, TU Darmstadt). With the impulse excitation test method, the elastic modulus of a homologous beam specimen is related to the resonance frequency by

$$E = 0{,}946 \cdot \left(\frac{mf^2}{b}\right) \cdot \left(\frac{l}{h}\right)^3 \cdot \left[1 + 6{,}585 \cdot \left(\frac{h}{l}\right)^2\right] \tag{1}$$

where f is the measured resonance frequency, m is the mass, b, l and h are the dimensions (width, length, height) of the specimen. In composites, the modulus of the coating can be determined using the beam theory of composites. The stiffness of a k-layer composite beam is equal to the sum of the stiffness of the components:

$$\overline{E_C \cdot I_C} = \sum_k E_k \cdot I_k \tag{2}$$

where E_k is the Young's modulus and I_k is the moment of inertia of each layer. Therefore the stiffness E_{TBC} of the topcoat can be determined by a successive measurement of each layer.

In this publication, the stiffness results for the conventional YSZ coating for low and high porosity levels (S1, prepared by Praxair) are presented. The GZO coatings are currently under investigation. These results will be presented in a further publication. In the as-sprayed condition, the mean value for the low porosity layers is about 33-35 GPa, for the high porosity layers the stiffness is about 23-24 GPa (figure 5b). For the freestanding layers only a small sintering effect was observed during the first 100 h of exposure time. No significant influence of temperature was observed. The stiffness of the ceramic topcoat reaches a constant value of about 50 GPa for S1, LP and 37 GPa for S1, HP. The results are consistent with literature data. Large sintering effects are only observed at much higher annealing temperatures (>1250°C, see [4]).
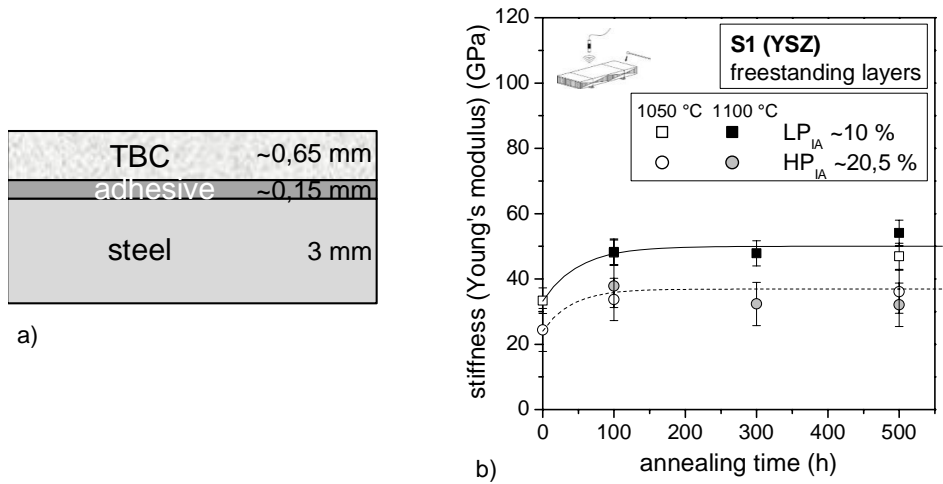
Figure 5: Freestanding ceramic layers prepared by Praxair with different levels porosity were obtained and applied to steel substrates, schematic (a) and stiffness of Layer system S1 (YSZ) determined with impulse excitation (b).

3.2.2. Crack Resistance

The critical energy release rate for delamination was evaluated using a modified four-point bending setup developed according to [5]–[8]. Additionally, the asymmetric 4-point bending devices, developed in [7], was used, see figure 6a. Delamination of the ceramic topcoat is thereby achieved by attaching a stiffening layer to the layer system. The stiffening layer suppresses the segmentation of the brittle ceramic topcoat and increases the stored elastic energy in the specimen as well as the driving force for delamination. The asymmetric setup enables stable crack propagation over a quite a long distance of about 30-40 mm.
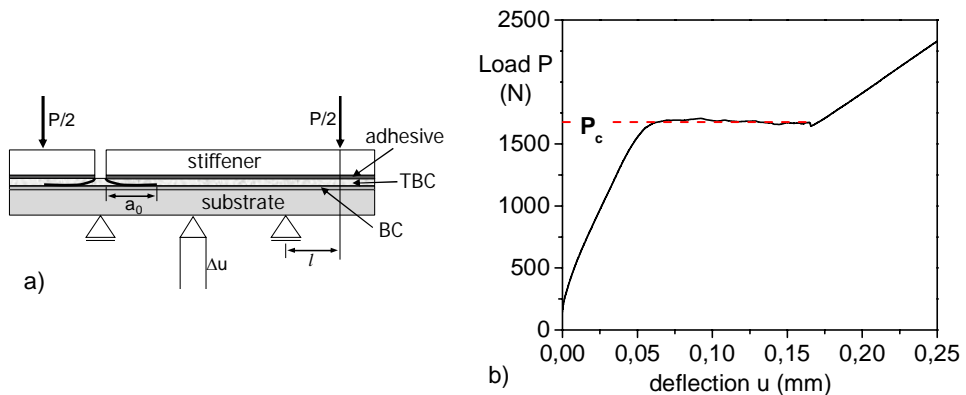
Figure 6: Asymmetric 4-point bending setup, for further details see [7] (a) and load deflection curve during four-point bending (b).

485

The stiffeners were applied using a thin layer of an epoxy adhesive. Interface pre-cracks ($a_0 \sim$ 10 mm) were generated by three-point bending. The pre-crack was introduced to serve as a crack-starter. Due to the decreasing bending moment during 3-point bending stable crack growth is achieved. To determine the critical energy release rate, the pre-cracked specimen is loaded in a four-point bending device with a constant crosshead speed of 0,1 mm/min. The deflection Δu of the bending specimen was measured with a linear variable differential transformer (LVDT). Deviation from the linear slope of the load- deflection curve (stiffness of the pre-cracked specimen) indicates further crack propagation. Stable crack growth occurs at the critical load P_c (figure 6b). When the crack reaches the inner loading line, crack propagation is prohibited due to the decreasing moment of inertia resulting in an increasing load.

As was shown in [9] the energy release rate for delamination reaches a steady-state value if the delamination cracks have a large crack length compared with the thickness of the delaminating layer (e.g. $a > t_C + t_{Stiffener}$). If the delamination occurs between the layer j and j+1 of a k-layer composite the energy release rate can be determined according to [8] by an analytical solution of the difference in the stored elastic energy before and after the delamination by:

$$G_C = \frac{M_b^2}{2b^2}\left(\frac{1}{E_{C,j}^* I_{C,j}^*} - \frac{1}{E_{C,k}^* I_{C,k}^*}\right) \qquad ; \qquad M_b = \frac{P_c l}{2b} \qquad (3)$$

with the corresponding elastic modulus $E_{C,j/k}^*$ and the moment of inertia $I_{C,j/k}^*$. M_b is the applied bending moment per unit width at the critical load P_c, where b is the specimen width and l the distance between the inner and outer spans of the four-point bending device.

First results show, that the critical energy release rate for delamination of the double layer coatings (S2: GZO/YSZ, industrial coating process) is significantly lower compared to conventional YSZ monolayers (S1: YSZ HP), see figure 7. Regarding the APS-YSZ coatings, the crack resistance is mainly determined of the damage evolution at the YSZ/BC interface. The decreasing interfacial strength at high oxidation times is correlated with an accelerated growth of interface TGO+TBC cracks after a critical aging time. It is supposed, that a critical time at temperature exists at which the onset of a substantial decrease in energy release rate occurs. Further, it is reported in literature [10], [11], that crack coalescence and accelerated crack growth correspond to a critical TGO thickness > 9 µm, which is consistent with these observations.
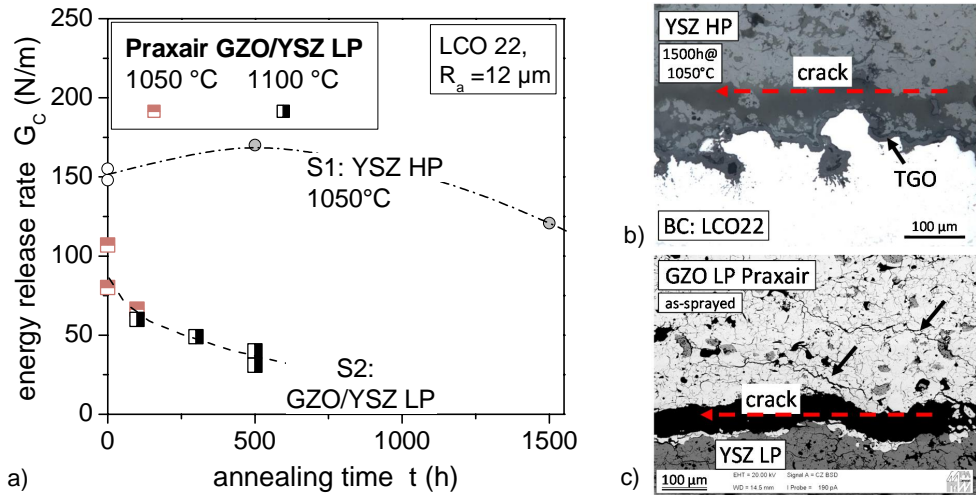
Figure 7: Critical energy release rate for delamination of the double-layer coating Praxair S2:GZO/YSZ-LP (a) and crack paths for S1: YSZ-HP (b) and S2:GZO/YSZ-LP (c).

Regarding the double layer coatings, delamination occurs adjacent to the interface between both ceramic layers. It is evident from the crack path, that the GZO layer has the lower fracture toughness of both layers. Some cracks branch out into the GZO layer as well as pieces of the GZO coating break off while the crack is propagating between the ceramic layers. Obviously isothermal oxidation leads to a significant decrease of the delamination resistance. It is believed, that non-stoichiometric gadolinium zirconate, respectively free zirconia due to improper process parameters can lead to a substantial degradation of layer properties. This is currently investigated in detail. The tests are presently continued on double layer coatings sprayed by FZ Jülich (S3: GZO/YSZ). Due to the fact, that these layers are optimized in regard to a stoichiometric composition, it is believed that these coatings will show no degradation due to phase changes.

3.2.3. Critical Strain Measurement by 4-Point Bend Testing

The critical strain to failure of the thermal barrier coating is an important input for the used lifetime assessment model. A schematic of the test setup used is shown in figure 8, together with a typical measurement result. The bending setup is equipped with an in-situ acoustic emission measurement system to record acoustic signals that are generated by cracking in the ceramic top layer. Two sensors are used to allow a linear location of the acoustic signals and by this an elimination of noise signals not originating from the sample. An example of a measurement result from a bi-layer sample (figure 8) shows two significant peaks in the acoustic emission signal (red bars) along with two kinks in the stress-strain curve (black line). The peaks correspond to the compressive shear failure of the top GZO layer and successive failure (compressive shear) of the underlying YSZ layer. Together with crack length meas-

urements after careful metallographic inspection this data will serve as a basis for the lifetime assessment approach.
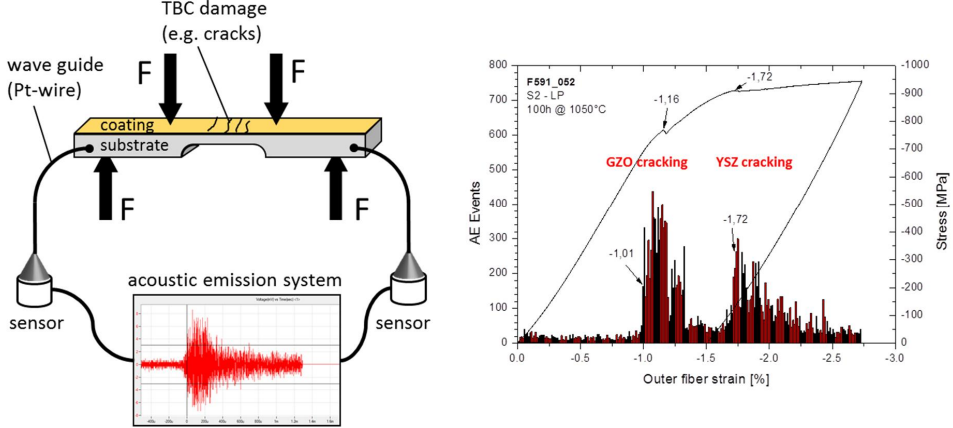
Figure 8: Test setup for 4-point bend testing used at DECHEMA-Forschungsinstitut with TBC sample (left) and typical measurement result (right).

4. Lifetime Assessment

A fracture mechanics approach is used for lifetime assessment of the thermal barrier system. It is based on the theory of brittle fracture by Griffith [12] and modifications by Irwin [13] and relates the critical strain to cause fracture of the ceramic coating to the defect structure within the coating. With the use of the acoustic emission technique it is possible to differentiate different failure modes and by this establishing mechanical stability diagrams as shown in figure 9 for the YSZ system S1. The basis for the calculated lines is the Griffith equation (4) and modifications thereof (see ref. [14]):

$$\varepsilon_c = \frac{K_{Ic}}{f \cdot E \sqrt{\pi c}} \tag{4}$$

The lines delineate areas of safe operation (with respect to thermal or mechanical loads) from areas where failure of the thermal barrier coating will occur. Together with the defect growth kinetics derived from metallographic inspection this data can be used for lifetime assessment of the thermal barrier coating system, with respect to the different failure modes.
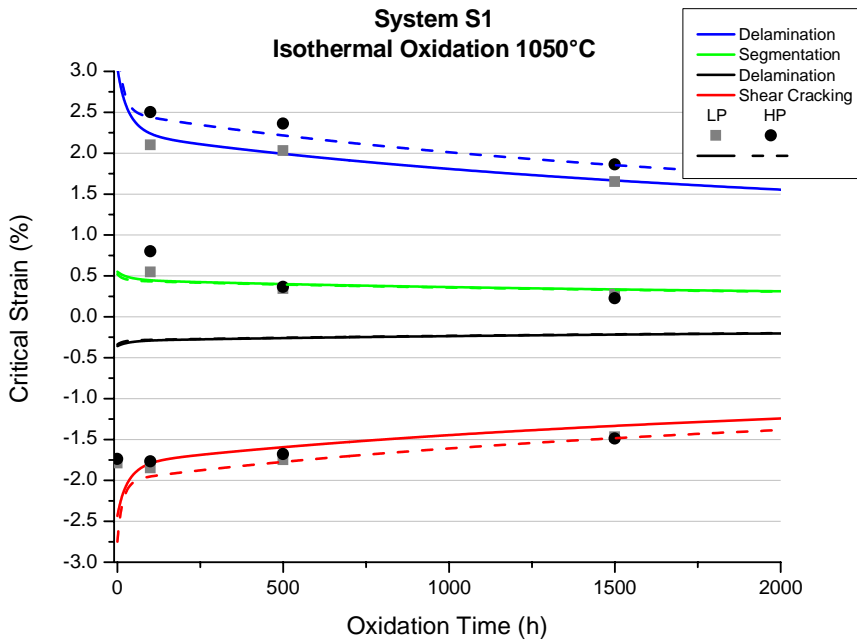
Figure 9: Modelled and experimental critical strain values of YSZ system S1 (low porosity, LP and high porosity, HP) as a function of oxidation time at 1050°C.

The first results from the bi-layer thermal barrier coating system S2 with low porosity indicate (compare right graph in figure 8), that the room temperature mechanical stability of the low porosity GZO layer is inferior to the stability of the standard YSZ system S1 shown in figure 9. After 100h of oxidation at 1050°C the GZO layer shows compressive shear failure at -1% strain, while the YSZ system S1 undergoes compressive shear failure at a significantly higher strain level of about -1.75%. This is probably due to the lower fracture toughness of the gadolinium zirconate and the low porosity of the GZO layer, which in turn results in a low compliance of the ceramic coating. It is therefore expected that the high porosity bi-layer systems which are currently being oxidized will show better performance in the mechanical tests.

5. Summary

In this work, a detailed study of the processing parameters was performed to allow production of GZO layers with tailored microstructure for next generation thermal barrier coatings. Especially the influence of APS spaying parameters on the coating porosity was investigated. Burner rig tests demonstrate a significantly better performance of high porosity GZO/YSZ bilayer coatings compared with YSZ coatings under thermocyclic loading conditions at high temperatures. As expected, the porosity of the coating strongly affects the mechanical properties and thus the mechanical stability of the coating system. Consequently, special care must

be taken to establish production routes that lead to reproducible results. Impulse excitation measurements in combination with stiffener-modified 4-point bending tests (Charalambides tests) and 4-point bending tests with in-situ acoustic emission measurement were employed to generate a comprehensive data set of Young's modulus, energy release rate and critical strain values for each ceramic layer component. The data was generated initially on standard YSZ coatings with comparable thickness (500µm, system S1) and is currently expanded to the bi-layer GZO/YSZ coatings. First results indicate a lower critical energy release rate for the bi-layer systems compared with the standard YSZ coating and lower critical strain values for mechanical failure of the GZO top layer in room temperature mechanical 4-point bending experiments. Despite these lower values the observed lifetime in burner rig experiments great-ly exceeds the lifetime of standard YSZ coatings. This indicates that the room temperature measurements may not sufficiently represent the situation with a thermal gradient across the coating thickness. Currently, in depth metallographic investigations of the GZO layers are performed to analyse the crack growth kinetics in the ceramic coatings for life estimation pur-poses.

6. Acknowledgement

References

[1]   D. R. Clarke, M. Oechsner, and N. P. Padture, "Thermal-barrier coatings for more efficient gas-turbine engines," *MRS BULLETIN*, vol. 37, pp. 891–898, (2012).
[2]   X. Q. Cao, R. Vassen, F. Tietz, and D. Stoever, "New double-ceramic-layer thermal barrier coatings based on zirconia–rare earth composite oxides," *Journal of the European Ceramic Society*, vol. 26, no. 3, pp. 247–251, (2006).
[3]   R. Vaßen, F. Traeger, and D. Stöver, "New Thermal Barrier Coatings Based on Pyro-chlore/YSZ Double-Layer Systems," *International Journal of Applied Ceramic Techno-logy*, vol. 1, no. 4, pp. 351–361, (2004).
[4]   S. R. Choi, D. Zhu, and R. A. Miller, "Effect of Sintering on Mechanical Properties of Plasma-Sprayed Zirconia-Based Thermal Barrier Coatings," *Journal of the American Ceramic Society*, vol. 88, no. 10, pp. 2859–2867, (2005).
[5]   P. G. Charalambides, J. Lund, A. G. Evans, and R. M. McMeeking, "A Test Specimen for Determining the Fracture Resistance of Bimaterial Interfaces," *Journal of Applied Mechanics*, vol. 56, no. 1, pp. 77–82, (1989).
[6]   I. Hofinger, M. Oechsner, H.-A. Bahr, and M. Swain, "Modified four-point bending specimen for determining the interface fracture energy for thin, brittle layers," *International Journal of Fracture*, vol. 92, no. 3, pp. 213–220, (1998).

[7]   M. Oechsner, "Ein Beitrag zur Lebensdauervorhersage von keramischen Wärmedämmschichten," Dissertation, (2001).

[8]   Y. Yamazaki, A. Schmidt, and A. Scholz, "The determination of the delamination resistance in thermal barrier coating system by four-point bending tests," *Surface and Coatings Technology*, vol. 201, no. 3–4, pp. 744–754, (2006).

[9]   A. G. Evans, M. D. Drory, and M. S. Hu, "The cracking and decohesion of thin films," *Journal of Materials Research*, vol. 3, no. 5, pp. 1043–1049, (1988).

[10]   O. Trunova, "Effect of Thermal and Mechanical Loadings on the Degradation and Failure Modes of APS TBCs," Rheinisch-Westfälische Technische Hochschule, Aachen, (2006).

[11]   O. Trunova, T. Beck, R. Herzog, R. W. Steinbrech, and L. Singheiser, "Damage mechanisms and lifetime behavior of plasma sprayed thermal barrier coating systems for gas turbines—Part I: Experiments," *Surface and Coatings Technology*, vol. 202, no. 20, pp. 5027–5032, (2008).

[12]   A. A. Griffith, "The phenomena of rupture and flow in solids," *Philosophical Transactions of the Royal Society of London A*, vol. 221, pp. 163–198, (1921).

[13]   G. R. Irwin, "Fracture," in *Encyclopedia of Physics*, New York, NY: Springer, (1958).

[14]   M. Schütze, *Protective Oxide Scales and Their Breakdown*. Chichester, UK: Wiley, (1997).

DAMAGE EVOLUTION AND TGO-GROWTH / FRACTURE MECHAN-ICS BASED LIFE PREDICTION OF APS TBC SYSTEMS UNDER THERMOCYCLIC LOADING

T. Beck[1]
O. Trunova[2]
R. Vaßen[3]
L. Singheiser[4]

[1] Technische Universität Kaiserslautern – WKK: beck@mv.uni-kl.de
[2] voestalpine Böhler Welding Germany GmbH: Olena.Trunova@voestalpine.com
[3] Forschungszentrum Jülich – IEK 1: r.vassen@fz-juelich.de
[4] Forschungszentrum Jülich – IEK 2: l.singheiser@fz-juelich.de

Abstract

The present contribution compares the damage evolution of conventional and segmented atmospherically plasma sprayed Y_2O_3-stabilized ZrO_2 thermal barrier coatings during thermal cycling with different dwell times at maximum temperature. In spite of its x 1.5 higher thickness, the segmented TBC reaches –due to its higher strain tolerance- the same lifetimes as the conventional one in case of thermal cycles with 120 min high temperature dwell time. In case of very short (2 min) dwell times, delamination occurs slightly earlier in the segmented TBC due to accelerated crack formation in the relatively dense zone of the TBC close to the interface to the bondcoat. For sufficiently long high temperature dwells, the oxidation and fracture mechanics based life assessment model proposed earlier is in excellent agreement with the experimental results, both of the segmented and conventional coating. In case of very short dwell times, the lifetime of the segmented coating is slightly overestimated due to the accelerated crack growth in the interface region of the TBC mentioned above, which is not yet taken into account in the model.

Keywords: APS TBC, Segmented TBC, thermal cycling, damage evolution, life assessment,

1. Introduction

Thermal barrier coatings (TBCs) serve for the thermal protection of hot section components in gas turbines to improve their lifetime and thermal efficiency [1,2]. With increasing operating temperature of advanced gas turbines, spallation failure of TBCs becomes more and more critical for engine integrity, since loss of the TBC causes exposure of the metallic blade material to hot gases at temperatures far beyond the operation limit of advanced Ni-superalloys. Thus, the understanding of spallation failure and underlying damage mechanisms is a key issue for further TBC development and a requirement for the full integration of TBCs into component design.

For further improvement in gas turbine power output and efficiency based on increasing turbine inlet temperature the development of prime reliant coatings is required. This must be accompanied with the development of lifetime prediction models, which allow a sufficiently accurate reflection of the main damage mechanisms as well as parameter identification and model validation with a limited number of experiments. One of the most important factors which influence TBC performance, especially under cyclic thermal loadings, is the strain tolerance of the ceramic coating which is strongly dependent on the coating composition, thickness and microstructure, i.e. microcracks as well as pore content, size, shape and distribution. The desired combination of microstructure and properties can be achieved by development of appropriate plasma spray coating processes [3,4].

The present paper addresses the effect of high temperature dwell time on the failure and lifetime of conventional and segmented APS TBCs under thermal cycling. Furthermore, the TBC life prediction model developed earlier at Forschungszentrum Jülich, IEK-2, for conventional coatings has been applied to the segmented coatings considering their higher thickness and lower Young's modulus. The comparison of predicted and experimentally determined lifetimes is discussed.

2. Experimental details

The investigated TBC system consisted of the single crystal Ni-base superalloy CMSX-4 as substrate, a vacuum plasma-sprayed NiCoCrAlY bond coat and an APS (atmospherically plasma sprayed) TBC of zirconia partially stabilized with about 8 wt.-% yttria (YSZ). The bond coat thickness was ~150 μm and the TBC thickness was ~300 μm for conventional (TBC I) and ~500 μm for segmented (TBC II) coating, respectively. The microstructure of both TBC variants in as coated condition is shown in Fig.1.

The spraying conditions for manufacturing of the conventional and the segmented coatings have been quite different. The conventional coatings were produced using a Sulzer Metco Triplex I torch operated with an A3000 control unit. The precursor material was a Sulzer Metco 204 NS YSZ powder with a mean particle size of about 50 μm. During deposition the hollow cylindrical substrates with a diameter of 10 mm were rotated at a high speed. The stand-off distance was 90 mm and the substrate was intensively cooled with compressed air to maintain a surface temperature of about 350°C. The gun power was 22 kW using 20 slpm Ar and 13 slpm He plasma gases. Due to these rather cold spraying conditions a porosity level of about 12 % measured by mercury porosimetry was achieved. Accordingly, many pores and micro-cracks can be found in the coating microstructure (see Fig. 1 a). These features are essential for the strain-tolerance of these coatings.

The segmented coatings are produced using much hotter spraying conditions, resulting in the formation of rather dense coatings with a reduced number of micro-cracks. The high tensile stress levels in these coatings as a result of the quenching of the deposited splats are reduced by the formation of segmentation cracks as described in [5]. Such segmented APS topcoats

have been produced in a Sulzer Metco Multicoat facility with a Triplex II torch. For the deposition of the segmented coatings the gun power was increased to about 57 kW and the stand-off distance was below 100 mm. In addition, only minor substrate cooling was applied which lead to a deposition temperature of about 600°C. A fine fused and crushed YSZ powder with a mean particle size below 30 μm guaranteed a complete melting of the feedstock during spraying. Furthermore also the feed rate was increased compared to the conventional coating which resulted in an improved intersplat bonding. As an additional measure the robot program and the substrate rotation was modified to establish optimised deposition conditions. Typically, these spraying conditions lead to the formation of segmentation cracks with a density of about 8 cracks/mm (Fig. 1b). The porosity level of the coatings is below 8%.

Thermal cycling tests were carried out in an infrared furnace from Xerion GmbH with a power of 6 kW. The temperature was controlled using a pyrometer calibrated with Pt/Pt-Rh-thermocouples. Cooling of the specimens was enhanced by compressed air flow directed to the specimen surface. Hollow cylindrical specimens with an internal diameter of 6 mm, an external diameter of 10 mm and a length of 25 mm, which were coated with conventional and segmented TBCs as described above, were used.

The thermal cycles consisted of heating with a rate of 2 °C/s followed by a dwell time at maximum temperature, cooling to minimum temperature with 2 °C/s and 1 min dwell time at minimum temperature. Thermal cycling experiments were carried out with temperature ranges of 60-1050°C and 60-1100°C, respectively. For both maximum temperatures tests with dwell times of 2 min and 120 min were performed. The microstructural investigations were carried out after metallographic preparation using optical (Leica-MEF4M) as well as scanning electron (LEO 1530-"Gemini") microscopy.
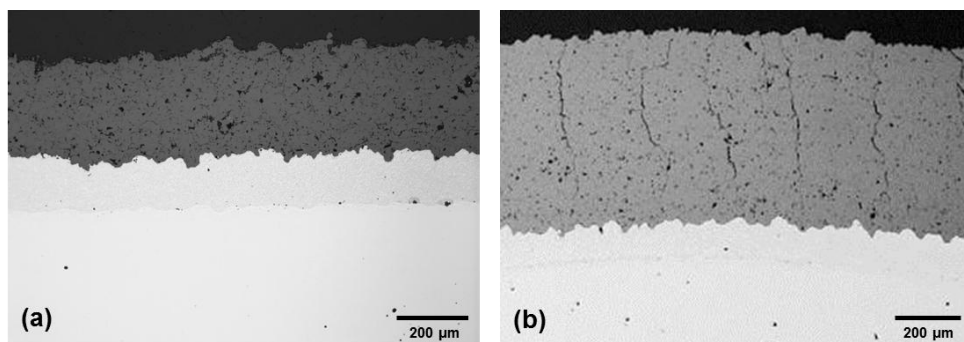
Figure 1: Microstructure of (a) conventional and (b) segmented TBC system in as received state.

3. Results and discussion

3.1. Thermal cycling

A series of thermal cycling tests in the temperature range 60–1050°C with 2 hours high temperature dwell time was carried out to investigate damage evolution, microstructure changes and failure of conventional APS TBCs, as reported and discussed in [6]. It was shown that during the first phase of delamination crack growth the crack length is strongly correlated with the thickness of the thermally grown oxide (TGO) formed between BC and TBC during high temperature exposure. As soon as certain crack length, which depends on the BC/TBC interface roughness, is reached, accelerated crack growth driven by TGO growth and thermal mismatch stresses was observed. Furthermore, TBC lifetime in terms of number of cycles to failure decreases with increasing high temperature dwell time as well as with increasing maximum temperature [6].

Additional thermal cycling tests with 2 and 120 min high temperature dwell time in both temperature ranges (60-1050°C and 60-1100°C) on segmented TBCs proved that the number of cycles to failure decreases with increasing maximum temperature. Delamination failure occurred after 4420, 534, 2400 and 200 cycles, respectively. The experimentally determined lifetimes for conventional and segmented TBCs are summarized in Fig 2. For 120 min high temperature dwell time, the segmented coating reaches in spite of its distinctly higher thickness nearly the same lifetime as the conventional TBC. For the very severe cycling conditions with 2 min high temperature dwell, the lifetime of the thicker segmented TBC is lower than that of the conventional one. However, it should be noted that the segmented TBCs exhibit serious lifetime advantages in case of thermal cycling with thermal gradients applied in burner rig tests, as reported in [7].
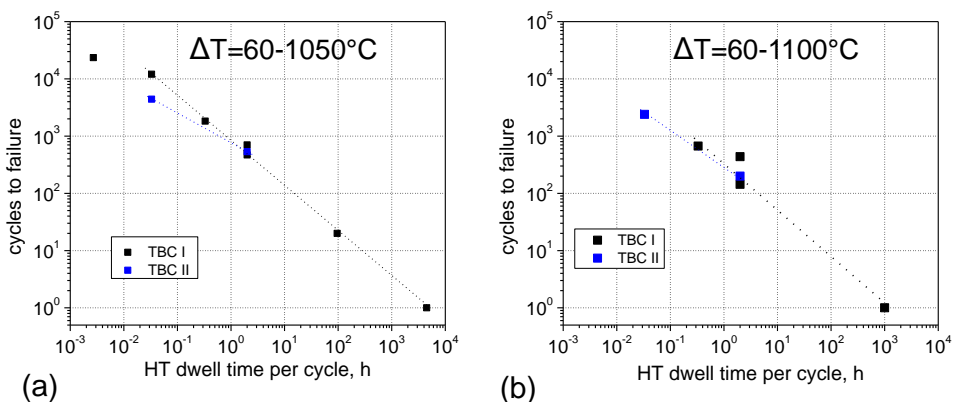
Figure 2: Cyclic lifetimes of conventional (TBC I) and segmented (TBC II) coatings as a function of high temperature dwell time in temperature range (a) 60-1050°C and (b) 60-1050°C.

495

Typical failure modes after thermal cycling with 120 and 2 minutes dwell time in temperature range 60-1050°C are shown in Fig.3. As expected on the background of similar lifetimes (Fig. 2), the thermally grown oxide (TGO) thickness is with about 9 µm and about 6 µm after cycling with 120 min and 2 min dwell time, respectively, similar for both TBC types. However, the delamination crack path of the segmented coating is shifted from the TGO into the TBC compared to the conventional TBC (Fig.3 b and d). This difference in failure behaviour is attributed to the relatively dense structure of the segmented TBC close to the interface to the TGO.
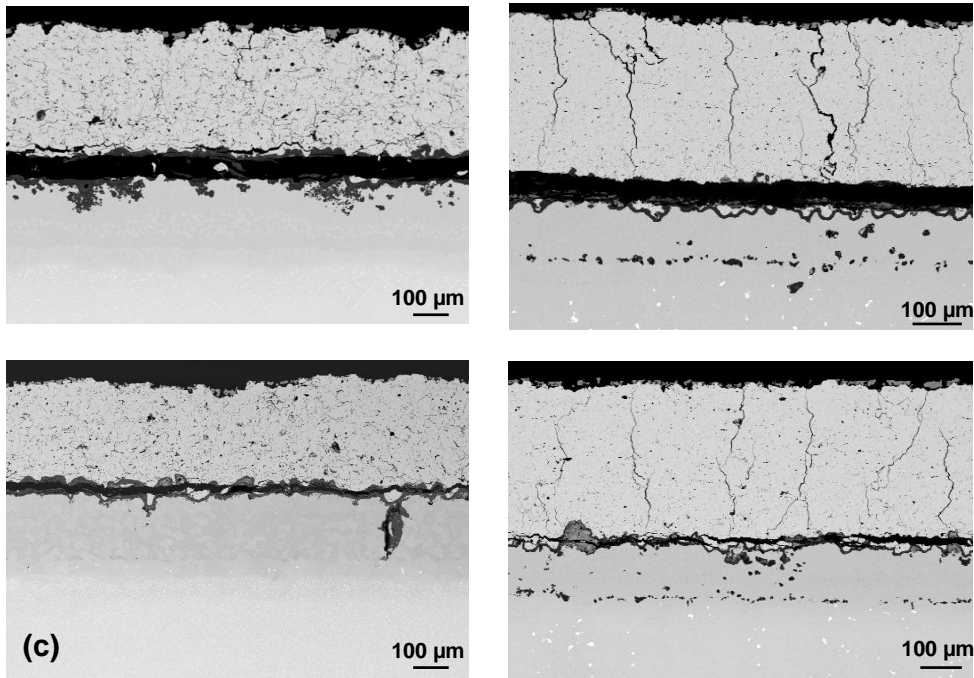
Figure 3 : Longitudinal sections of conventional and segmented TBCs after thermal cycling in temperature range ΔT=60-1050°C with: (a),(b) 120 min and (c),(d) 2 min high temperature dwell time.

3.2. Lifetime prediction

The experimental results were used for the validation of the life prediction model described in [8,9], and to prove its applicability for the novel TBC type with segmented structure. The following model approach was used for the TBC life prediction:

- Delamination crack growth is divided in two stages. The transition point between both stages corresponds to a critical TGO thickness which depends on the BC / TBC interface roughness.

- In first stage the crack length is assumed to increase proportionally to the TGO thickness.

- The crack growth in the second stage is calculated using a fracture mechanics approach, which takes into account stresses induced by thermal misfits between layers, lateral TGO growth and brittle-to-ductile transition of the BC.

More detailed information about the model approach, the applied equations and the numerical implementation is given in [9].

For stage I of damage evolution, the TGO thickness evolution is calculated using a cubic law typical for the oxidation kinetics of MCrAlY BCs, which was adjusted to the experimentally determined TGO growth. The temperature dependence of oxidation rate constant was assumed to follow an Arrhenius law. Because the same BC was used for the conventional and the segmented TBC, identical TGO growth laws were assumed in the present study
The fracture mechanics approach used to assess stage II of the damage evolution reflects the contribution of the crack energy induced by thermal misfits as well as by lateral TGO growth. Most of the model parameters are directly obtained from measurements, i.e. of thermal expansion coefficient and elastic properties of separate layers. With both parts of the energy release rate the crack propagation rate da/dN is calculated numerically cycle by cycle. Furthermore only the temperature range between ductile-to-brittle transition temperature of the bond coat and minimum cycle temperature was taken into account for the fracture mechanics calculation according to acoustic emission analysis which proves that crack growth only occurs in this temperature range [10].

To calculate cyclic life of the segmented TBCs only two input parameters were changed from the values used for the conventional TBC: (i) the higher thickness of the segmented TBC and (ii) its lower Young's modulus. The latter was, according to compressive tests at free standing TBCs set to a value of 25 GPa for the conventional TBC. Because no experimental values were available for the segmented TBC, the Young's modulus of this variant was assumed to 20 GPa, a similar value as reported for EB-PVD TBCs [11] which also exhibit a columnar microstructure. All other parameters, i.e. crack growth coefficient, crack growth exponent and the weighting factor for the influence of TGO growth on delamination crack growth, were fitted to experimental results of the conventional TBC and remained unchanged for the lifetime assessment of the segmented TBC.

In Fig. 4 the comparison between experimental thermal cycling life and the model predictions is shown. For the conventional TBC system the predicted lifetimes are in good agreement

with experimental data over the considered wide range of high temperature dwell times for both temperature ranges. For the segmented TBC a slight overestimation of the experimental values becomes obvious, especially for shorter dwell times. This is attributed to the fact that the higher Young's modulus of the dense sublayer of the TBC close to the TBC / BC interface (Fig. 1b) is not considered in the model so far.
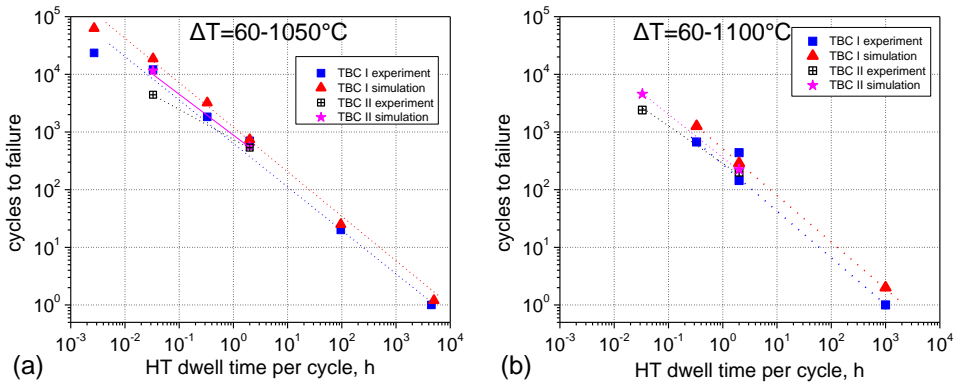
Figure 4: Experimentally determined and predicted TBC lifetimes for thermal cycling with different HT dwell times in temperature range (a) 60-1050°C and (b) 60-1100°C.

4. Summary and conclusion

For isothermal and thermocyclic ageing of conventional APS-YSZ TBC the following conclusions can be drawn:

- Lifetime in terms of accumulated time at maximum temperature decreases with increasing temperature range and decreasing dwell time

- Delamination cracks propagate mainly in the TGO and along the TGO / TBC interface

- The life prediction model based on TGO growth and fracture mechanics described in [8,9] predicts temperature and dwell-time influence with good accuracy

The key results for the segmented APS-YSZ TBC can be summarized as follows:

- For relatively long thermal cycles, i.e. 2 h high temperature dwell time, similar lifetime are reached as for the conventional TBC in spite of a x1,5 higher thickness

- For severe thermal cycling, i.e. 2 min high temperature dwell, slightly shorter lifetimes than for the conventional TBC are observed

- Compared to the conventional TBC, the delamination crack path is shifted to the relatively dense near-interface region of the TBC which may cause accelerated crack propagation, especially in case of short cycle times

- The fracture mechanics based model proposed in [8,9] is suitable for life prediction in case of relatively long dwell times. For shorter T-t cycles the influence of the dense near-interface region of the TBC need to be additionally considered

5. References

[1] R.A. Miller, Thermal barrier coatings for aircraft engines: history and directions, *J. Therm. Spray Technol.* 6 (1997) 35-42.

[2] N.P. Padture, M. Gell, E.H. Jordan, Thermal barrier coatings for gas-turbine engine applications, *Science* 296 (2002) 280-284.

[3] R. Vaßen, M.O. Jarligo, T. Steinke, D.E. Mack, D. Stöver, Overview on advanced thermal barrier coatings, *Surface and Coatings Technology* 205 (2010) 938–942.

[4] A. Vaidya, V. Srinivasan, T. Streibl, M. Friis, W. Chi, S. Sampath, Process maps for plasma spraying of yttria-stabilized zirconia: An integrated approach to design, optimization and reliability, *Materials Science and Engineering* A497 (2008) 239–253.

[5] H. Guo, R. Vaßen, D. Stöver, Atmospheric Plasma Sprayed Thick Thermal Barrier Coatings with High Segmentation Crack Density, *Surface and Coatings Technology* 186, 3 (2004) 353-363

[6] O. Trunova, T. Beck, R. Herzog, R.W. Steinbrech, L. Singheiser, Damage mechanisms and lifetime behaviour of plasma sprayed thermal barrier coating systems for gas turbines—Part I: Experiments, *Surface and Coatings Technology* 202 (2008) 5027-5032.

[7] R. Vaßen, H. Guo, D. Stöver, Manufacture and properties of segmented thermal barrier coatings, *Proceedings of the 29th International Conference on Advanced Ceramics and Composites*, Cocoa Beach, Florida, January 23-28, 2005 / eds. D. Zhu, K. Plucknett. - S. 37 - 45 (2005)

[8] T. Beck, O. Trunova, R. Herzog, R.W Steinbrech, L. Singheiser, Damage mechanisms and lifetime behaviour of plasma sprayed thermal barrier coating systems for gas turbines—Part II: Modeling, *Surface and Coatings Technology* 202 (2008) 5901-5908.

[9] O. Trunova, T. Beck, R.W. Steinbrech, R. Herzog, L. Singheiser, Damage evolution and lifetime prediction of thermal barrier coatings during cyclic oxidation, *Procs TSM 137th Annual Meeting & Exhibition*, New Orleans, 2008.

[10] O. Trunova, P. Bednarz, R. Herzog, T. Beck, L. Singheiser, Microstructural and acoustic damage analysis and finite element stress simulation of air plasma-sprayed thermal barrier coatings under thermal cycling, *Int. J. Materials Research* 10 (2008) 1129-1135.

[11] C.Pfeiffer, E.Affeldt, M.Göken, Miniaturized bend tests on partially stabilized EB-PVD ZrO_2 thermal barrier coatings, *Surface and Coatings Technology* 205, 10, (2011), 3245-3250

EVALUATION OF HIGH TEMPERATURE BEHAVIOUR OF A NEW LOW DENSITY NICKEL BASE SUPERALLOY FOR AERONAUTICAL GAS TURBINE BLADE APPLICATIONS

G. Angella[1], R. Donnini[1], J.S.Hou[2b], M. Maldini[1a], D. Ripamonti[1], T. Ranucci[1], L. Zhou[2]

[1]CNR – IENI, Via Cozzi 53, 20125 Milano, Italy
[2]CAS – IMR, 72 Wenhua Road, Shenyang, China

[a]maldini@ieni.cnr.it
[b]jshou@imr.ac.cn

Abstract

The aim of the following investigation is to evaluate the creep and low cycle fatigue (LCF) properties of DD417G, a new low density, Re free, nickel base superalloy for aeronautical gas turbine blades, developed by the Institute of Metals Research (IMR-CAS) Shenyang, PRC.
Constant load creep tests have been carried out from 750 up to 1000°C, at stresses between 90 and 750 MPa to produce time to rupture up to 6000 hours.
The creep behaviour of DD417G has been analysed in terms of times to rupture and shapes of the creep curves in function of the applied stress/temperature.
Time to rupture: the experimental results are compared with competing alloys taking into account the low density of the here presented alloy.
Creep curve shape: the experimental creep curves are characterised by a long predominant tertiary/accelerating creep, where the creep strain rate increases linearly with the accumulated strain, while the primary creep is small. The LCF tests, performed at 750°C and 850°C in longitudinal strain controlled conditions, have evidenced a fairly stable cyclic response. Basquin and Coffin-Manson relationships can adequately predict the fatigue life of the alloy.
Examination of fracture surfaces revealed that fracture, induced by creep damage, is internal and mainly starts from γ/γ' eutectic island and pore-initiated cracks. However, fatigue damage starts on the external surface and propagates inward in stage II mode

Keywords: DD417G, creep, low cycle fatigue, single crystal.

1. Introduction

The continual demand of increasing the operating efficiency and durability of gas turbine has been closely related to improvements in turbine blade materials and cooling system. The development of single crystal casting processes has led to the design of new superalloys with superior creep and fatigue properties over conventionally cast and directionally solidified materials and now they are widely utilized in gas turbine industry [1, 2]. For the blades in the first stage of turbines, Re containing superalloys are generally utilised; in other stages, were lower temperatures are achieved, first generation Re free superalloys can be used with a consistent reduction of the production costs compared with the more performing last generation superalloys.

In this investigation, the new Re free single crystal nickel base superalloy DD417G has been studied to evaluate its creep and fatigue properties.

2. Materials and experimental procedures

The DD417G is a first generation, Re free, nickel base superalloy to be used for single crystal components as gas turbine blades and vanes. The alloy, with a low density of 7.858 g/cm^3, has been developed by the Institute of Metal Research-CAS Shenyang (PRC).

The DD417G nominal chemical composition is compared, in Table 1, with RR2000, a low density nickel base superalloy, CM186LC SX, a relatively cheap nickel based Re-bearing superalloy, that can be used in service without solutioning treatment, but with only a two stage ageing treatment and CMSX4, a well know and studied second generation superalloy with about 3% wt. of Rhenium. The alloy was supplied by the Institute of Metal Research-CAS, Shenyang, PRC, in form of 12 mm diameter and 240 mm long bars, with the axis having 10° maximum deviation from the <001> crystalline orientation. The bars were heat treated at 1260°C/4h then air cooled (AC) to have a fully γ' solutionised structure, through the removal of most of the eutectic colonies. The solution treatment, without causing incipient melting, was able to sufficiently homogenize the alloy, in order to minimize unwanted TCP phase formation. Then the alloy was aged at 1100°C/1h/AC + 850°C/16h/AC to obtain well-aligned cubic γ' particles of about 330 nm in size. The volume fraction of γ' particles, coherently embedded in the γ matrix, was about 65% (Figure 1).

Creep and Low Cycle Fatigue tests have been carried out at IENI-CNR (I) on solid cylindrical specimens having 5.6 mm gauge diameter and 28 mm gauge length, machined off from the cast bars. Creep strain was continuously monitored using a pair of capacitive transducers connected to extensometers clamped to ridges delimiting the specimen gauge length. Over 200 strain/time readings were automatically recorded during each creep test. All creep strain in this paper are true strain, defined by $\varepsilon = ln(1+\Delta l/l_o)$ where l_o and Δl are the initial length and the elongation of the specimen gauge length. Three Pt/Pt13%Rh thermocouples were placed in the gauge length to control and monitor temperature gradients during creep.

Constant load and temperature creep tests were performed in the temperature range 750-1000°C and stresses between 90 to 750MPa, producing time to rupture up to 6000 hrs.

The LCF specimens were cylindrical with a diameter of 6 mm and a gauge length of 10 mm. Sample heating was achieved using an induction coil. The temperature was controlled by thermocouples spot welded outside the specimen gauge length. The tests were performed, at 850 and 750°C, under strain controlled conditions at a strain rate of $10^{-3}s^{-1}$ with a triangular wave form (R = −1). During the tests, the stress response and the hysteresis loop were recorded.

Fracture surfaces observations were performed on fatigued samples in a Hitachi S3400N scanning electron microscope.

Microstructural observations were carried out with a JEOL JSM-6301F field emission scanning electron microscope. Samples were conventionally polished and chemically etched with a solution of 4 g $CuSO_4$ + 20ml H_2O + 10ml HCl.

Table 1: Chemical composition of DD417G superalloy compared with other benchmark single crystal superalloys (wt%).

alloy	C	Cr	Co	Mo	Al	Ta	Ti	B	V	Re	Ni
DD417G	0.021	8.7	10.1	3.04	5.19	-	4.38	<0.005	0.98	-	Bal.
RR2000	0.015	10	15	3	5.6	-	4	-	1	-	Bal.
CM186LC	0.069	6.0	9.3	0.5	5.7	3.4	0.7	0.015	-	2.9	Bal.
CMSX4	0.0025	6.5	9.7	0.6	5.6	6.5	1.04	0.002	-	2.9	Bal
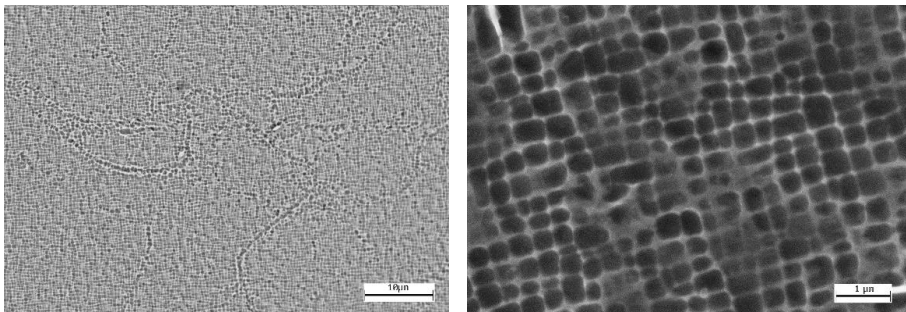
Figure 1 : SEM micrographs of DD417G alloy heat treated at 1260°C/4h/AC + 1100°C/1h/AC + 850°C/16h/AC

3. Experimental Results and Discussion

3.1. Creep Results

The results of the experimental creep tests are reported in Table 2. Nickel base superalloys, as many complex engineering alloys of interest for high temperature applications, often exhibit a dominant accelerating creep stage, whereas primary and secondary stages are less important and sometimes negligible, both in amplitude and duration. The here studied alloy has confirmed this behaviour as shown in Figure 2a, where typical creep curves obtained at different stresses and temperatures are plotted. The importance of the accelerating stage is better displayed in a strain rate vs. strain plot (Figure 2b) where it is shown that a large portion of the accelerating stage manifests a linear strain softening in agreement with the results obtained on other nickel base superlloys [3-7]. Only in the last 10-20% of the creep life, fracture mechanisms, as crack propagation and localized reduction of area, provide an extra contribution of strain rate. Figure 3 shows, in a Larson Miller plot, the equivalence of the creep resistance of DD417G, the competitor RR2000, with equivalent low density, and CM186LC SX.

Table 2 : Experimental tests and corresponding results on DD417G

Temp (°C)	Stress (MPa)	Time to ε = 10% (h)	Time to rupture (h)	Elongation (%)	Z_u (%)
750	700		106*	1.26*	
	650	1661	2041.3	28.7	31
800	560	621	737.2	26.7	34.7
	500	1410	1601.6	27.0	40.4
850	450	344	395.9	35.9	40.6
	360	874	971.6	37.3	52.3
	300	2625	2837.3	25.2	41.6
900	300	350	398.0	38.4	51.1
	220	1665	1780.0	28.6	49.8
	170	5565	5756.4	27.6	52.4
950	225	222	241.8	30.4	55.7
	170	890	940.3	30.5	55.6
	115	4864	5057.3	33.9	54.4
1000	145	347	361.9	46.5	59.0
	115	1280	1288.8	19.1	46.7
	90	5516	5516.4	12.9	46.4

*interrupted test
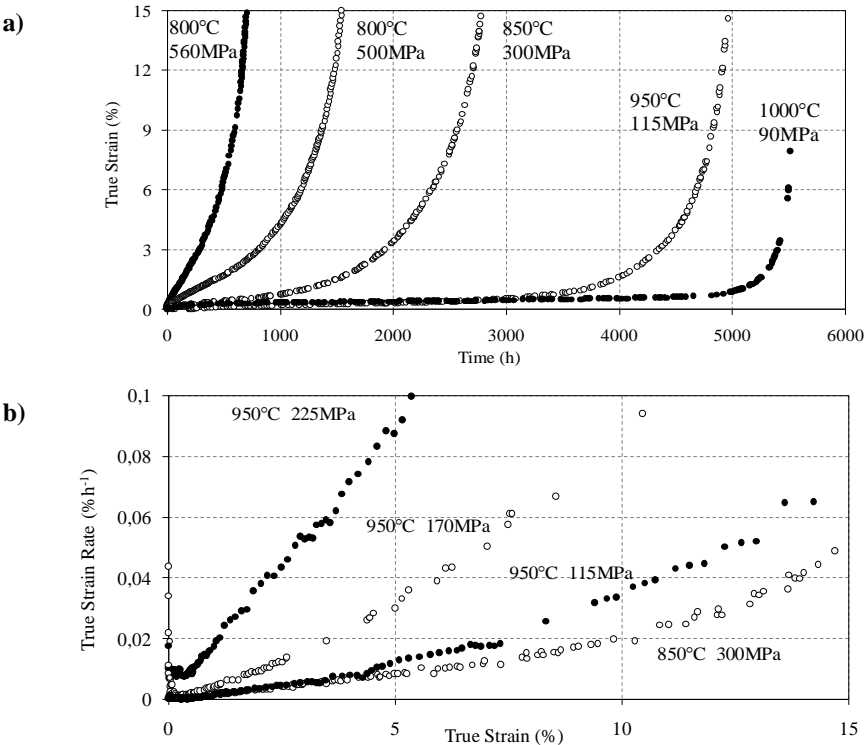
Figure 2 : Examples of creep curves: (a) true creep strain vs. time and (b) true creep rate vs. true creep strain. The accelerating stage exhibits a linear strain softening behaviour.
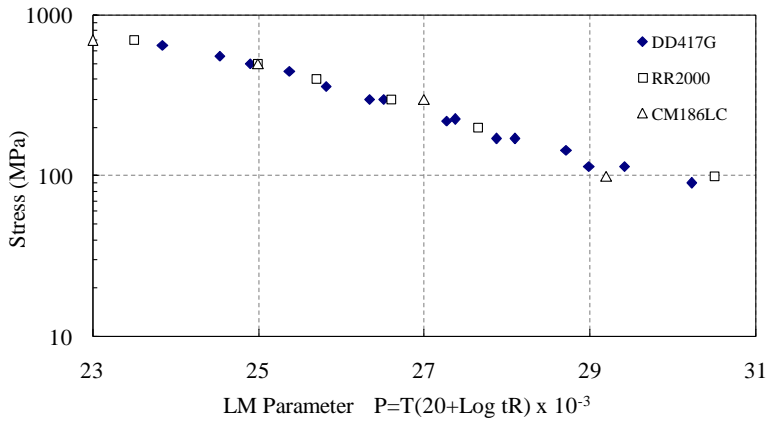
Figure 3 : Comparison of the creep stress rupture behaviour between DD417G, RR2000 and CM186LC.

3.2. LCF Results

Plots of elastic and plastic strain components versus number of cycle to failure at 750 and 850°C are reported in Figure 4. The fatigue life of the alloy can be described by the Basquin and Coffin-Manson empirical relationships as follows, respectively:

$$\frac{\Delta\varepsilon_{el}}{2} = \frac{\sigma_f}{E} \cdot (N)^{-b}$$

$$\frac{\Delta\varepsilon_{pl}}{2} = \varepsilon_f \cdot (N)^{-c}$$

(1)

with σ_f the fatigue strength coefficient and *b* fatigue strength exponent, while ε_f and *c* are the failure ductility coefficient and fatigue ductility exponent respectively. These parameters are determined by least square method as showed in Figure 4 and listed in Table 3.

Table 3 : Parameter values for the Basquin and Coffin -Manson relationships corresponding to the experimental data.

T(°C)	σ_f/E	*b*	ε_f	*c*
750	0.015	-0.09	0.001	-0.30
850	0.021	-0.15	4.54	-1.34
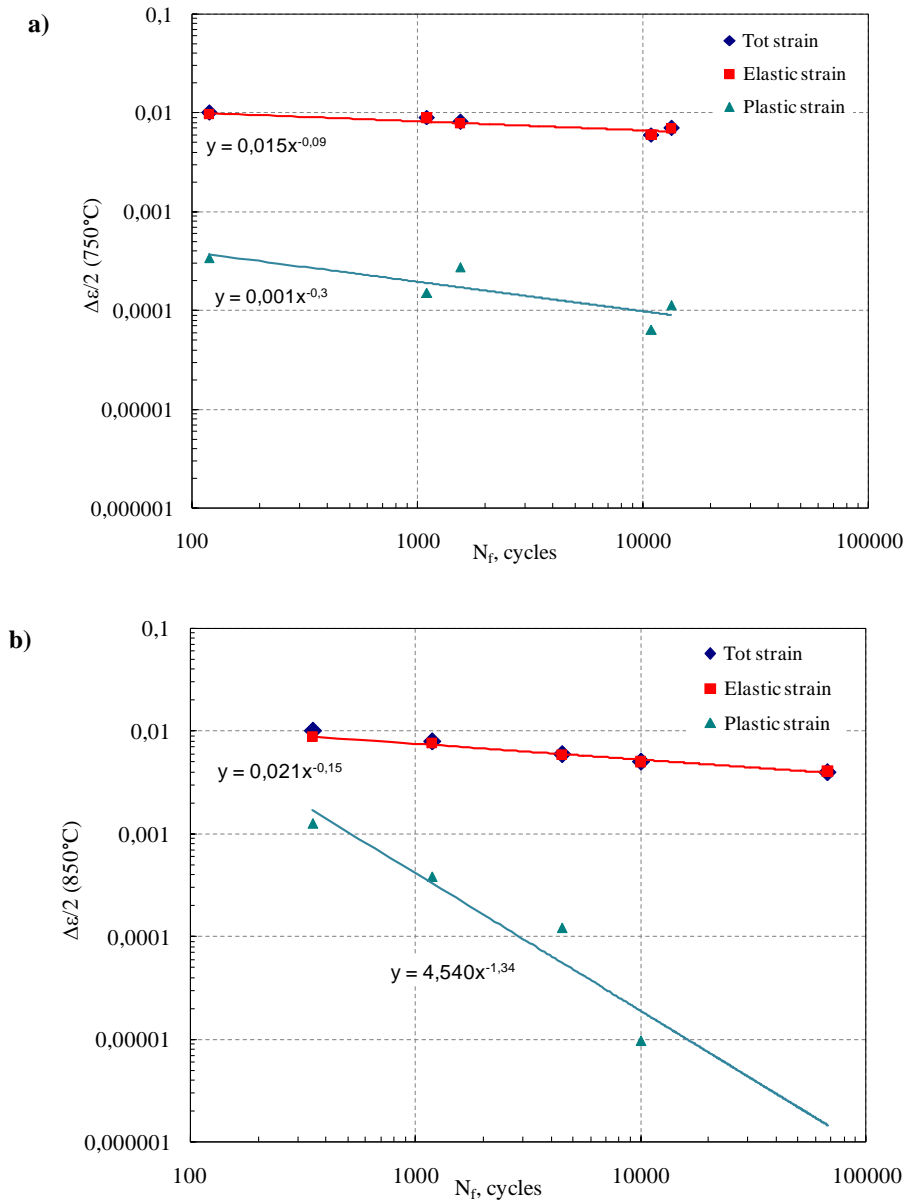
Figure 4: Coffin-Manson curves with related plastic and elastic components, for (a) 750°C and (b) 850°C.

The plastic strain component results significantly lower than the corresponding elastic one. This is due to the low Young modulus in the <001> direction, which significantly reduces the plastic zone in the hysteresis loop. This characteristic increases the fatigue life compared to

505

other polycrystalline nickel-base superalloys. Table 3 indicates that the parameters of the elastic component σ_f/E and b remain basically very similar, confirming a predominant elastic behaviour at the experimentally explored conditions. At 850°C, through Figure 4 and the different ε_f and c values in Table 3, an increasing of ductility is showed, affecting the fatigue behaviour. A transition life number of cycles N_T is indeed calculable, comparing the terms of elastic and plastic components, $\Delta\varepsilon_{el}/2 = \Delta\varepsilon_{pl}/2$:

$$N_T = \left(\frac{E \cdot \varepsilon_f}{\sigma_f} \right)^{\frac{1}{b-c}} \tag{2}$$

According to Eq. 2 with the parameters of Table 3, N_T is equal to about 90: below this limit, significant plastic strain occurs, as depicted in the Coffin-Manson plot in Figure 5.
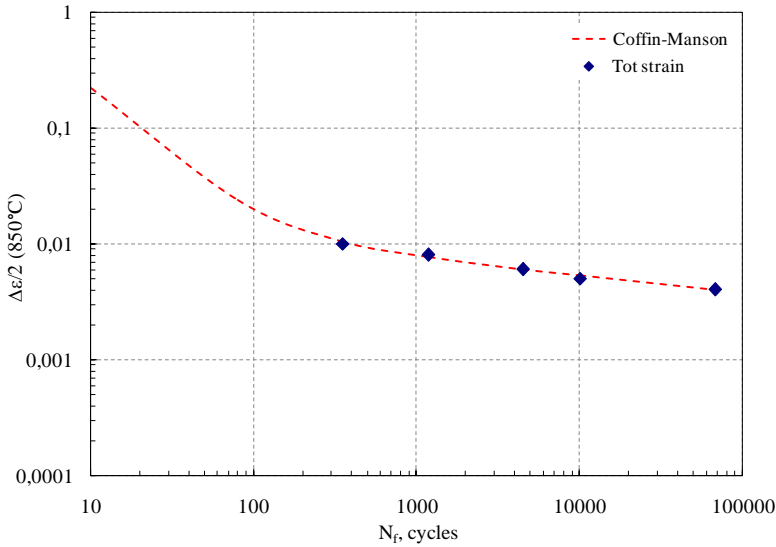
Figure 5 : Coffin-Manson curve (total strain vs. cycles to failure) at 850°C.

At 750°C the plastic component can be considered not significant for the fatigue resistance, even at ε=1%. These results are indeed explainable observing that $\Delta\varepsilon_{pl}/2$ value, at the aforesaid strain level, is one order of magnitude lower than the one at 850°C (see Figures 4), so the plastic component affects the total behaviour to a lesser extent.

4. Metallography

4.1 Creep fracture

As found in other single crystal nickel base superalloys [8,9], creep cracks can initiate at γ/γ′ eutectics, or at casting pores located between dendrite arms and they slowly propagate anisotropically along planes perpendicular to the applied stress (Figure 6).

Figure 7 shows a typical morphology of creep fracture surfaces. They mainly consist of square-like facets oriented on (001) planes associated with casting pores in the centre, where the cracks are nucleated. The creep crack behaviour of DD417G is consistent with the fractography of other SX nickel base superalloys [8,9].
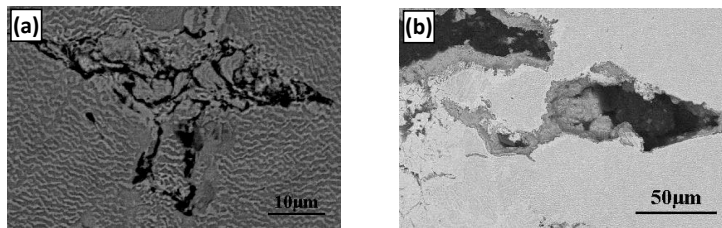
Figure 6: SEM micrographs showing cracks in DD417G alloy starting from (a) γ/γ′ eutectics and (b)cast porosity after creep at 900°C/220MPa.
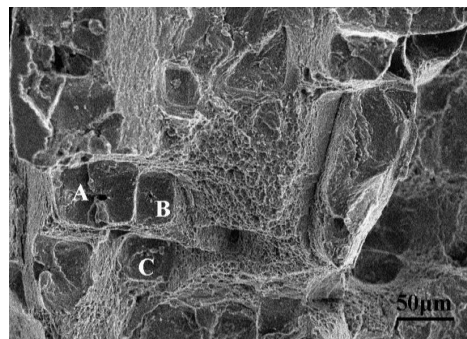
Figure 7: SEM observation of fracture surface after creep test at 850°C/300MPa. A, B, and C indicate square-like planes

4.2 Low cycle fatigue fracture

Fatigue failure mechanisms involve crack (or cracks) nucleation at the external surface of the specimen, and their propagation inward during stage II. At 850°C under total strain amplitude of 1.0%, the fracture surface is wavy and composed of different smooth facets (Figure 8a), confirming the beginning of a not negligible plastic component under these test conditions. Multiple crack initiation sites exist on all fracture surfaces, suggesting that cracks initiate

from both surface and internal microporosity and further propagate in stage II. Many fatigue striations are observed and parallel secondary cracks are presented in the region of fatigue striations (Figure 8b). As the total strain amplitude decreases (0.8%) the fatigue behavior is basically elastic and a smoother failure surface can be observed (Figure 8c). The feature is confirmed at lower applied strain (0.5% in Figure 8e), where crack still initiates at the specimen's surface.
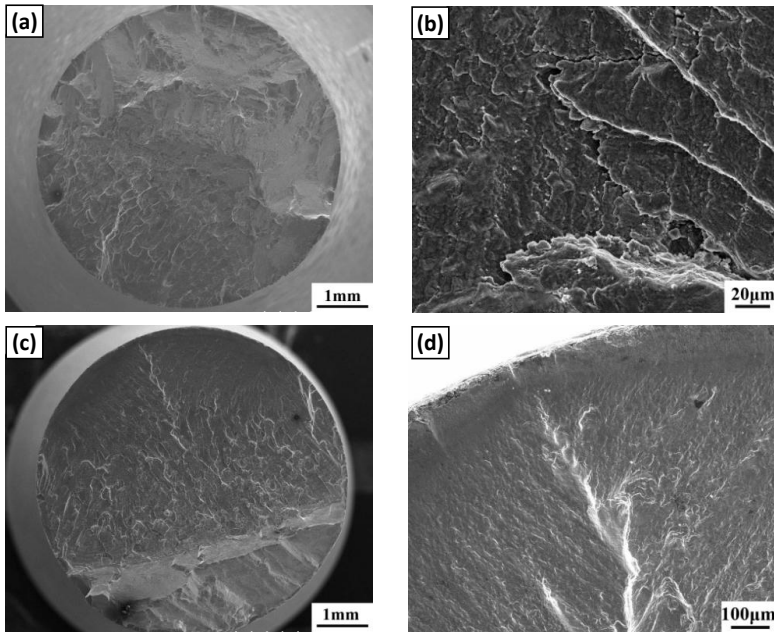
Figure 8: SEM Fractographs of DD417G alloy after LCF at 850 ^{o}C: (a and b) $\Delta\varepsilon_t/2= 1.0$ %,; (c) $\Delta\varepsilon_t/2= 0.8$ %, (e) $\Delta\varepsilon_t/2=0.5$ %.

5. Conclusions

The creep and LCF testing investigation on single crystal DD417G at different temperatures has shown that:

- The DD417G alloy exhibits creep behaviour comparable to RR2000 and CM186LC single crystal alloys, components of similar low density, and CM186 LC SX.
- The accelerating/tertiary creep stage, that dominates the creep curves for all the test conditions here explored, shows a linear relationship between creep rate and creep strain.
- Specimen failures were predominantly seen to initiate from microporosity and the eutectic colonies.

- In strain control LCF tests, the fatigue life of the alloy can be satisfactorily described by Coffin-Manson and Basquin empirical relationship. The plastic component does not affect the fatigue resistance up to 750°C, whilst it can be significant at 850°C.
- The LCF fractures start from the specimen surface and propagate inward during stage II, with the presence of fatigue striations.

Acknowledgements

References

[1] Erickson G.L. and K. Harris, DS and SX superalloys for industrial gas turbines, in Proc. of Conf. Materials for Advanced Power Engineering Part II, Liege (Belgium), 1994, pp.1055-1074.

[2] P. Caron and T. Khan, Third generation superalloys for single crystal blades, in Proc. of Conf. Materials for Advanced Power Engineering Part II, Liege (Belgium), 1998, pp. 897-912.

[3] B. F. Dyson and M. McLean, Particle-coarsening, σ_0 and tertiary creep, *Acta Metallurgica,* Vol. 31 (1983), pp.17-27.

[4] M. Maldini and V. Lupinc, A representation of tertiary creep behaviour in a single crystal nickel-based superalloy, *Scripta Metallurgica,* Vol.22 (1988), pp. 1737-1741.

[5] M. Maldini, H. Harada, Y. Koizumi and V. Lupinc, Tertiary creep behaviour of a new single crystal superalloy at 900°C, *Scripta Materialia,* Vol. 43 (2000), pp. 637-644.

[6] M. Maldini and V. Lupinc, Modelling creep of single crystal CM186LC alloy under constant and variable loading, *Materials Science and Engineering A*, Vol. 408 (2005), pp. 169-175.

[7] P.J. Henderson and J. Lindblom, High temperature creep in a <001> single crystal nickel-base superalloy,", *Scripta Materialia*, Vol. 37 (1997), pp. 491-496.

[8] S.H. Ai, V. Lupinc and M. Maldini, Creep fracture mechanisms in single crystal superalloys, *Scripta Metallurgica et Materialia*, Vol. 26 (1992), pp. 579-584.

[9] A.H. Sherry and R. Pilkington, The creep fracture of a single-crystal superalloy, *Materials Science and Engineering A*, Vol. 172 (1993), pp. 51-61.

Long term creep behaviour and microstructural evolution of IN718

A. Di Gianfrancesco, P. Lombardi, D. Venditti: Centro Sviluppo Materiali SpA, Rome, Italy

S. Neri, M. Calderini: Società delle Fucine: Terni Italy

R. Montani, L. Foroni: Foroni Metals: Gorla Minore, Italy

a.digianfrancesco@c-s-m.it

Abstract

The 718 is a very well know superalloy developed in the worldwide in the 1960s used for aircraft engine, petrochemical plants, oil and gas applications, with a very wide operating temperatures spectrum and an upper temperature limit close to 650°C.

The continuous trend in efficiency improving for the new fossil fuel fired plants for power generation needs an increasing in temperature and pressure of the critical components: boiler and turbine. Therefore the tubes, cast and forged components in the hottest part of the plant are hardly stressed and steel and alloys with improved creep performances are required.

The steam turbine inlet temperature for the new generation plants is scheduled in the range of 720°C with a pressure of 350MPa and the high and intermediate pressure rotor sections are going to be produced in superalloys. In the frame of the Thermie Advanced (700°C) Pulverised Fuel Power European Project a trial rotor disk has been forged by Società delle Fucine in Italy using a billet produced by AOD + double VAR remelting at Foroni Metals.

A new heat treatment was developed by Centro Sviluppo Materiali to increase the microstructural stability in the range of 650-750°C and to improve the creep behaviour. Now the longest creep tests are over than 100.000 hours and a creep data assessment show an increase of about 50°C respect to the standard UNS718 material.

This work summarize the 12 years of work done that could now open the possibility of use the 718 superalloy up to 700°C for forged components in the new steam turbine for the Advanced Ultra Supercritical Power Plants.

Key words: IN718, forging, rotor, creep resistance, mechanical properties, microstructural evolution, heat treatment.

1. Introduction

The driving forces improving the production of electric power have changed from growth of demand in the 60's to considerations concerning environment and efficiency in the 90's. In 1996 the European Commission approved in the frame of the THERMIE programme the demonstration project "*Advanced ("700°C") PF Power Plant*" proposed by a large group of material and components suppliers of the power industry, R&D centres and leading utilities. The aim of the project was to develop a new generation of coal fired power plant able to raise up to 375 bar/700°C steam conditions and to increase electrical efficiency up to 52-55% [1].

Consequently in the hottest part of the steam cycle it will be no longer possible to use steel components, but new nickel-based superalloys are required; then it is necessary to optimise, test and qualify these materials.

In parallel, studies on the design of the large critical components have been performed to optimise the size as function of production limits.

At the beginning of the program several existing superalloys have been taken into account for screening tests in order to evaluate the most promising candidates for the component manufacture.

The Italian contribute to the program has been focused on the INCONEL 718 super alloy. It is well known by literature [2] that the maximum operating temperature for IN718 treated in the standard conditions (UNS7718) is about 650°C. Therefore a new heat treatment was developed to increase the high temperature behaviours of the IN718 and his microstructural

stability to target the AD700 goal and a prototype disk was produced [3]. After the optimisation of the heat treatment, by mechanical and short term creep tests, a long term creep program was launched in order evaluate the creep resistance of the new modified heat treatment, as well as, microstructural analysis to investigate the alloy stability.

The aim of this paper is to present the results of this test programme that are discussed in relationship with the microstructure evolution in the service conditions.

2. Material production

One ton billet produced by Electric Arc Furnace, followed by Argon-Oxygen Degassing refining and double VAR (Vacuum Arc Remelting) remelted by Foroni Metals, has been forged by Società delle Fucine using a 12.600 ton press, following a procedure designed by model simulations in order to promote recrystallisation. Figure 1 shows the billet during the forging steps and the prototype forged disk having the following final dimensions: diameter 850mm and thickness 350mm [3]. Table 1 shows the chemical analysis of IN718 billet compared with that of the standard UNS7718; the trace elements are the following: Pb <0.2, Bi <0.1, Se<1.0, Sn<10, Ag < 1.0 (values in ppm).
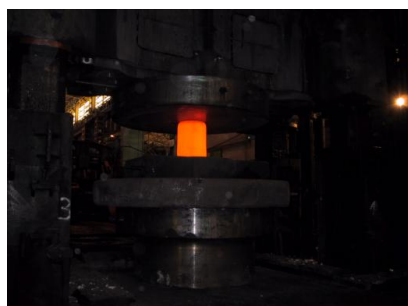
Figure 1: IN718 billet before forging and the prototype disk after forging

	C	Ni	Fe	Cr	Mo	W	Co	Nb	Ti	Al	B	Zr	Mn	Si	P	S
Standard UNS7718	<0.08	50-55	Bal	17-21	2.8-3.3	/	<1	4.8-5.5	0.7-1.2	0.2-0.8	<0.006	/	<0.35	<0.35	/	<0.015
Foroni Billet	0.03	54	17.5	18.5	3	<0.1	<0.1	5	0.9	0.5	0.004	<0.0005	0.15	0.15	0.008	0.001

Table 1: Chemical analysis of Foroni IN718 billet (WT%.)

3. Heat treatment and mechanical behaviour of prototype disk

During the Phase 1 of the Thermie AD700 project [4] a new heat treatment has been developed by CSM [3], in order to improve the high temperature properties of the IN718 and in particular the creep behaviour. After the promising results obtained respect to the conventional heat treatment, the new one was applied on the trial disk and the mechanical properties obtained have been compared with those obtained by the convention heat treatment.

The standard IN718 super alloy is characterised by the precipitation of cuboidal γ' phase (Ni₃Al,Ti) and γ'' phase (Ni₃Nb), acicular and fine, as consequence of the amount of Nb in the matrix. Also MC carbides are present. The γ'' phase, during exposure at high temperature, evolves into the δ phase, coarse and gets acicular, producing a reduction of properties and ductility.

Trials to modify the heat treatment have been done by Cao and Kennedy [5] improving the temperature of the first stage of precipitation treatment up to 760 or 850°C and of the second stage up to 650°C.The heat treatment developed by CSM had the aim to stabilise γ' e γ'' phases: the solubilisation temperature has been increased up to 1065°C, 55°C over the standard, followed by air cooling and two aging stages. Also relatively high aging temperatures have been employed, as summarised in table 2. The room temperature properties of the treated material, showed in table 2, were in agreement with the UNS standard requirements.

Figure 2 shows a comparison of the obtained microstructures. A largest amount of γ'' phase is present in the modified treated material. No traces of δ-phase have been found in the material after the modified heat treatment. It means that the higher temperature effect on austenitic grain and cooling rate are enough to avoid the cross of the d-phase nose formation (figure 3) [6].

	Solubilisation (°C/h/Cooling)	First aging (°C/h/Cooling)	Second aging (°C/h/Cooling)	YS (MPa)	UTS (MPa)	Elong. (%)	Impact energy (J)	Grain size (ASTM No.)
Standard	927-1010	720/8/FC	620/8/air	>1035	>1240	>10		
Foroni Stand.	1000/2/water	718/8/FC	621/8/air	1135	1403	20.4	74	5
Foroni Mod.	1065/1/air	760/8/FC	650/12/air	1120	1335	27.0	80	4

Table 2: Heat treatment conditions and mechanical properties (FC = Furnace cooling)

To evaluate the microstructural stability and the mechanical behaviour after standard and modified heat treatment (HT), aging tests were carried out at 700 and 750°C up to 10200 h: the tensile strength slightly decrease after aging (Figure 4). It is important to take into account that aging at 750°C for 3000 h, according with Larson Miller Parameter (LMP), is equivalent to 60.000 hours at 700°C [7].
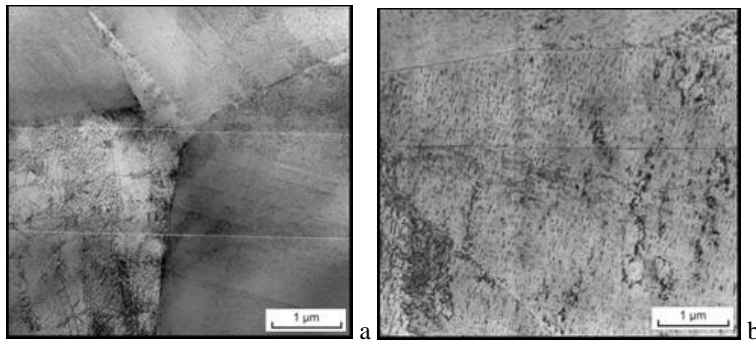
Figure 2: Microstructure after standard heat treatment: a) conventional HT; b) modified HT
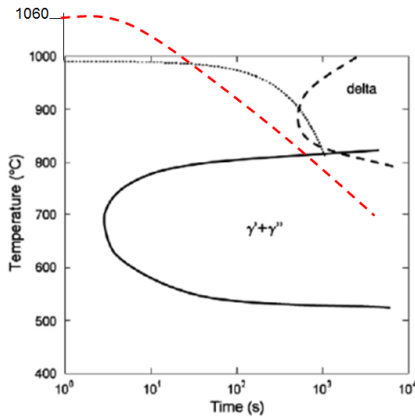
Figure 3: CCT curve (solid line) of alloy 718 according Slama and Cizeron [6], with possible
cooling curve (red dotted line) obtained without δ-phase formation.
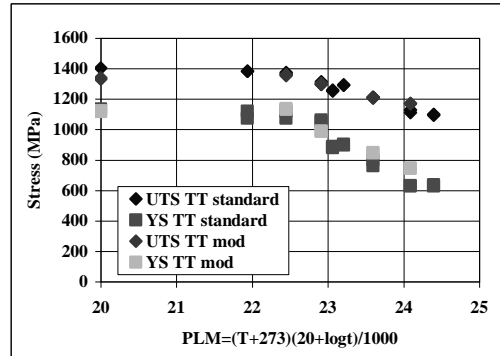
Figure 4: Effect of aging on to mechanical properties

4. IN718 Creep behaviour with new heat treatment

In order to evaluate the creep behaviour of the IN718 with modified heat treatment, a long term creep test program was defined in the temperature range 650-750°C with smooth and notched specimens [8].

At present two specimens are still running at 750°C over than 100.000 hours: figure 5 shows the isothermal curves of smooth and notched specimens. The Mod IN718 creep behaviour is not sensitive to notch.

Regarding the minimum creep rate vs applied stress at the different temperatures a variation of the Norton exponent (n) from 11,5 at 650°C up to 1,4 at 750°C as bee evaluated, showing a change in the creep mechanisms from dislocation to diffusive creep. Comparison with literature data was not possible because the only available data are at very high stress [9].

An assessment has been made by the ECCC (European Creep Collaborative Committee) procedures in 2009 [10]. In figure 6 the current creep results of the smooth broken specimens are plotted and compared with the data assessment. The value to obtain rupture at 700°C in 100.000 is predicted in the range of 120 MPa, because the 130MPa specimen broken in 78.000 hours. A new assessment will be carried out as soon as last rupture data will be available. In fact the current assessment seems quite good and has to be confirmed for the 750°C, because the last running specimen at 60MPa is over than 100.000 hours. The current status of this test is presented in figure 7, where it is possible to note that the strain curve is still in the secondary stage.

The material with new heat treatments is not affected by notch effect in fact in figure 8 it is possible to appreciate that the master curves are very similar.
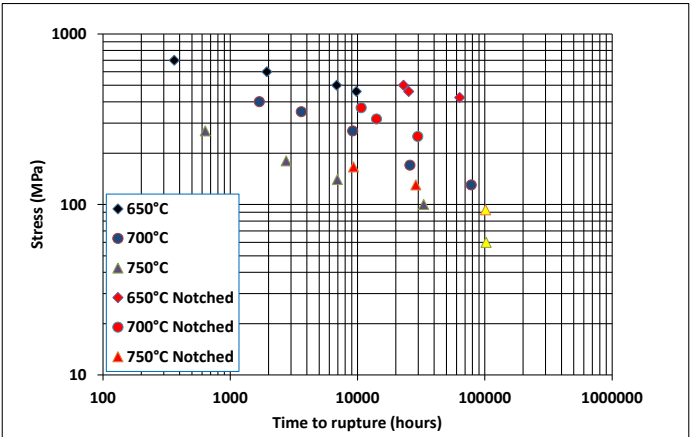
Figure 5: Isothermal curves of smooth and notched specimens (yellow point are test still running)

The creep behaviours of IN718 mod superalloys have been compared with ORNL data from literature on standard material [11]. The modified treated material shows the same creep resistance at 650°C, but a relevant increase of the rupture time at the highest temperatures, especially at 750°C. The modified treated material shows at 100MPa the same rupture time of the standard material, but with an increase of about 50°C in term of service temperature.

Furthermore the creep ductility showed by the IN718 with the modified heat treatment, appears interesting, in terms of elongation and reduction of area to rupture, that increase with the temperature and the test time. The figures 9 shown the elongation to rupture and the reduction of area versus time to rupture (t_r), giving evidence that the physiological evolution of γ'' in δ-phase doesn't reduce ductility of the material with the modified treatment. This behaviour was just observed in literature [12] and was related to the effect of δ particle to guide crack advance in a zigzag path resulted in absorbing strain energy and increasing plasticity. Further analyses in order to confirm this mechanism are still in progress.
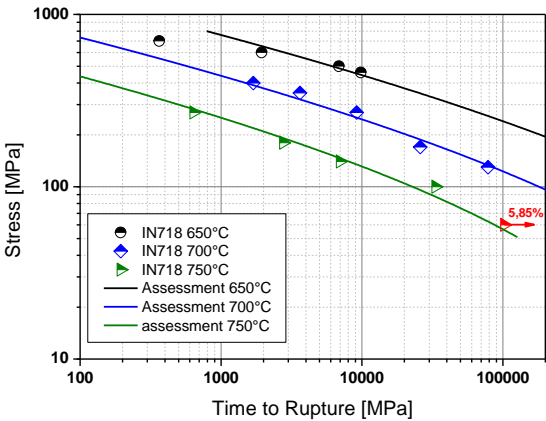
Figure 6: 2014 creep data assessment with current smooth test running (red symbol)
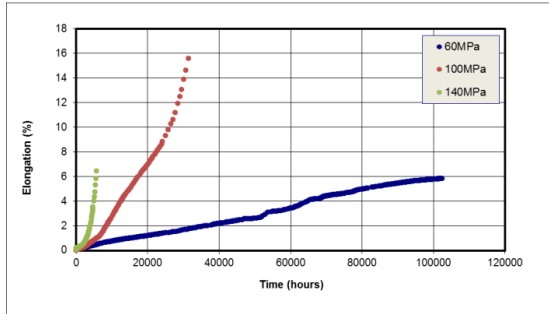
Figure 7: creep curves at 750°C
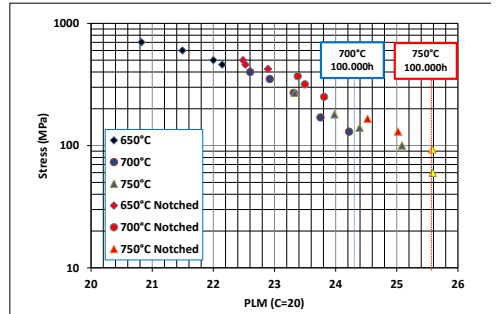
Figure 8: Comparison of master curves of IN718 Mod smooth and notched specimens (the yellow points on the right are the specimens still running over 100.000 hours)
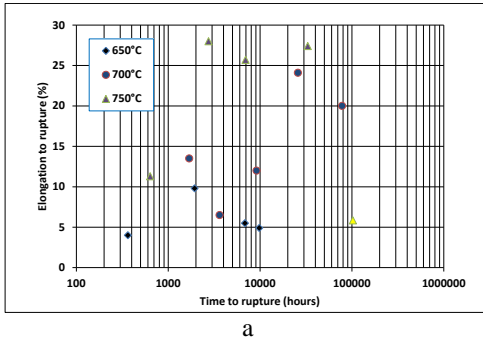
a
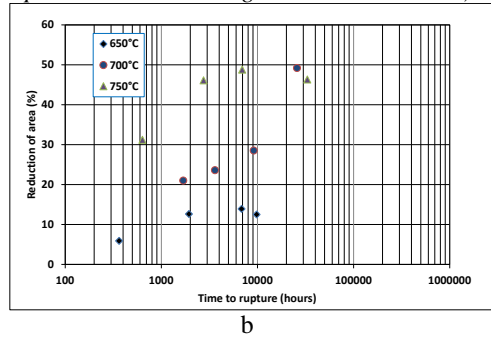
b

Figure 9: Creep Ductility of Mod IN718: a) elongation and b) reduction of area vs rupture time (yellow point is test still running)

5. Microstructural evolution

In order to understand the effect of the modified treatment on creep behaviour, TEM investigation have been performed on samples with the conventional and modified treatments, in as received and aged conditions. Figures 10 shown a comparison of the microstructure evolutions after 3000hours at 700°C and 750°C for the modified treated material: at this magnification, on the specimen aged at 700°C only γ'' can be recognised, being γ' too finer to be observed. At 750°C fast coarsening of both γ' and γ'' phases is well evident, as well as the formation of the large δ plates, due to γ'' transformation. Figures 11 the microstructure after 3000 hours at 750°C for the standard treated material shows a reduced amount of γ'' phase, if compared with the microstructure of material, in the same ageing conditions, when is treated with new heat treatment. (figures 10b and 11), giving evidence of the effect of the new heat treatment to reduce the transformation kinetics of γ'' into δ phase.

515
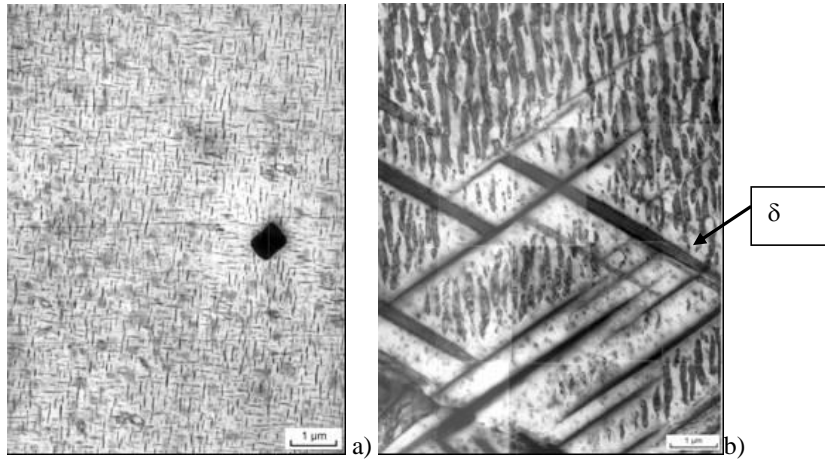
Figure 10: IN718 Mod treated material: TEM image on thin foil after 3.000 hours of aging:
at 700°C; b) at 750°C

Quantitative analyses on aged specimens have been carried out to define the evolution of the
main phases [13]. The measured of γ', γ'' and δ sizes are respectively reported in the figures
12, 13 and 14, where the 750°C temperature and aging time have been transformed in 700°C
and the equivalent time defined using Larson-Miller parameter (i.e. 750°/6000h it is
equivalent to 700°C/60.000h). The results gives evidence that all the phases in the standard
treated material show faster growing compared with the modified treatment. After 3,000 h at
750°C, the measured precipitate size distribution shows that γ' particles coarsening is rather
similar both heat treatments, growing up to 80 nm; γ'' particles grow up close to micrometric
dimension after 5,000-10,000 h and then they decrease. This phenomenon can be related to
the formation of δ phase which precipitates at the expense of γ''. By means of the modified
heat treatment, the nucleation and growth rates of δ phase are delayed.
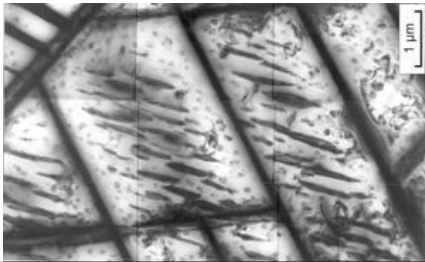
Figure 11: IN718 standard treated material:
TEM image on thin foil after 3.000 hours of aging
at 750°C

516
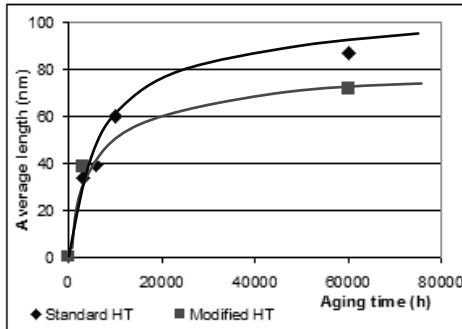
Figure 12: γ' phase coarsening in aging tests
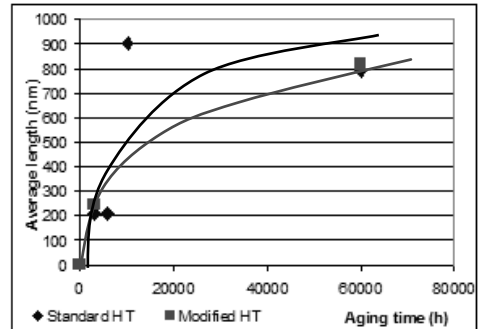
Figure 13: γ'' phase coarsening in aging tests
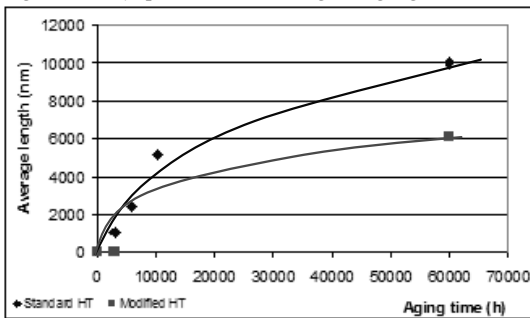
Figure 14: δ phase coarsening in aging tests

Additional microstructural analyses on IN718 mod have been carried out on crept specimens: the heads of these specimens have been analysed by light microscopy, SEM + EDS and by STEM + EDS analysis. The figures 15 and 16 show clearly the stages of evolution of the microstructure with the transformation of the γ'' in to δ phase starting from the grain boundary. The δ phase nucleates at the grain boundary and grows into the grain (figure 15-16a) and a relevant amount is present in the specimens aged at 700 and 750°C (figure 15-16 b and c).

With investigations at higher magnification the phases in the specimens aged at 700°C for 25.860 hours were identified, as shown in figure 17: Niobium reach round shape carbides and acicular δ−phase were observed, as well as some small γ'' particles between the δ-phase particles still the presence of, meaning that the transformation γ'' to δ it is not jet completed in these ageing conditions.

a) b) c)
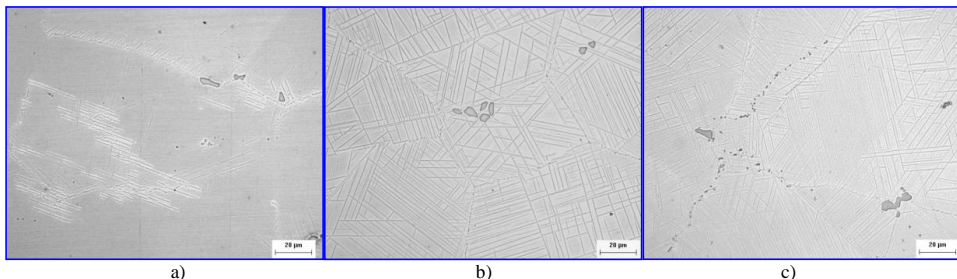
Figure 15: IN718 mod microstructures of aged specimens by light microscopy: a) 650°C – 25355h; b) 700°C – 25860h; c) 750°C – 33206h

517
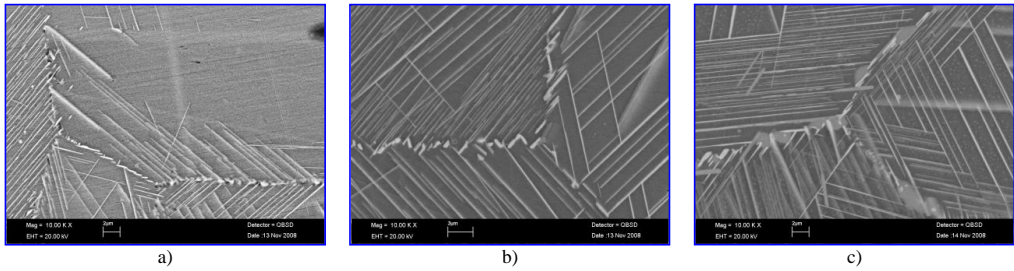
Figure 16: IN718 mod microstructures of aged specimens by SEM: a) 650°C – 25355h; b) 700°C – 25860h; c) 750°C – 33206h
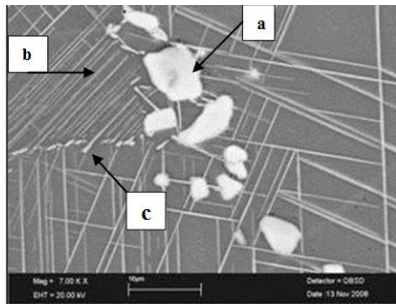
Figure 17: SEM images of the crept specimen at 700°C after 25.860 hours: a) MC Nb rich particles; b) δ phase; c) γ'' phase

At 750°C the transformation of γ'' into δ-phase appears completed, as can be observed by figure 18, showing that γ' it is still present [14] and practically no more γ'' is observable. The other small dark particles, mainly observable at the grain boundaries, are Ti reach carbides (Figure 19).

The TEM analysis on thin foil on the specimen at 750°C after 33.206 hours (figure 20) confirm that γ'' transformation has been completed, but there is still present a relevant amount of small γ' particles. This evidence is in agreement with the TTP diagram (figure 21), proposed by Thomas and co-workers [16]. Figure 22 shows a typical example of Orowan climb of a dislocation on a γ' particle confirming that γ' continues to supply a strengthening effect.

The microstructural investigations by SEM and TEM will continue as soon as the creep specimens still running will be broken in order to consolidate the knowledge in the evolution of the phases on the IN718 with this modified treatment.
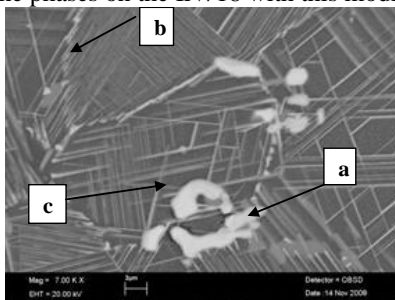
Figure 18: SEM images of the crept specimen at 750°C after 33206 hours: a) MC Nb rich particles; b) δ phase; c) γ' phase
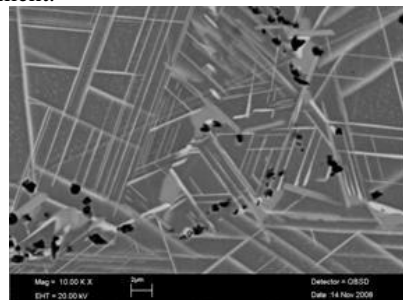
Figure 19: SEM images of the crept specimen at 750°C for 33.206hours: Ti reaches carbides (black particles)

518
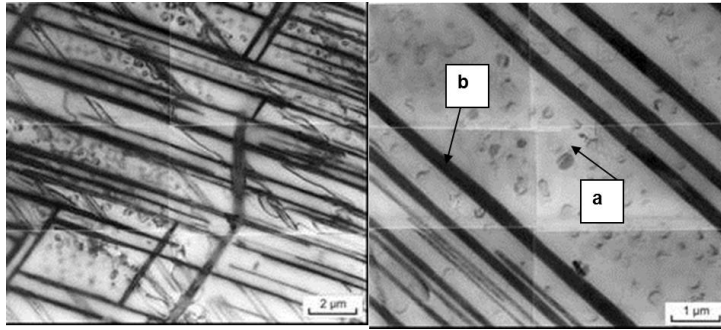
Figure 20: TEM images of the crept specimen after 33.206 hours at 750°C: a) δ-phase; b) γ'-phase
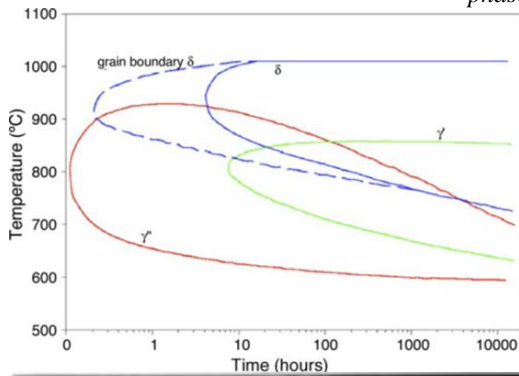
Figure 21: TTP diagram for IN718 proposed by Thomas and Co [15]: red star indicates the position of the experimental specimen aged 33.206 hours at 750°C.
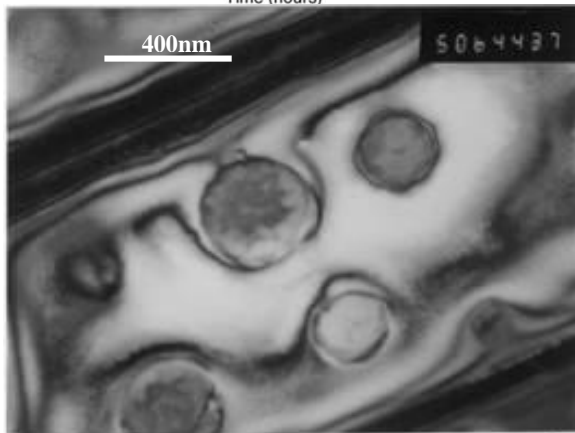
Figure 22: Orowan climb of a dislocation on a γ' particle in the specimen after 33.206 hours at 750°C

6. Discussion and Conclusions

The manufacture of a trial rotor disk for possible application at 700°C in steam turbine has been provided. The trial disk has been successful forged at Società delle Fucine using an AOD double VAR billet produced by Foroni Metals.

A new heat treatment to improve the creep resistance has been developed. The capability of the new heat treatment to increase the creep behaviours of IN718 at temperature over then 650°C has been confirmed from the results of the long term creep tests. The assessment of the

creep data could be able to guarantee 120 +/- 15 MPa at 700°C, but in the next future a new one will be realised after the rupture of the specimens still running.

Comparing the behaviour of the standard IN718 at 704°C, the new treatment at the same stress (100MPa), but at T = 750°C, it is able to guarantee the same time to rupture: that means that an improvement of about 50°C in the service temperature has been obtained. Two specimens are still running at 750°C over 100.000 hours.

Other relevant results are that the new heat treatment it is able to guarantee a very good ductility of creep specimens after high temperature and long-time tests, without embrittlement phenomena.

The reasons of these improved behaviours for the new heat treatment have been explained, on the base of metallographic investigations, as follow:

- The new heat treatment promote the γ' and γ'' precipitation, without presence of δ-phase after heat treatment,
- The presence of γ'' after heat treatment delay the nucleation of δ-phase, as well as, the transformation of γ'' in to δ-phase,
- The γ' is more stable and it is still present, without relevant growing phenomena, after long term at 750°C.

Further microstructural investigation has been planned and will carry out on the two creep specimens still running, when broken.

On the basis of results obtained the Inconel 718 with modified heat treatment can be included in the list of candidate materials for the manufacture of forged components, such as rotor disks or bolts, for the new generation of advanced Ultra Super Critical power plant that will be operate with 700°C steam temperature.

Acknowledgements

References

1. R.Kehlhofer, "*Power Engineering, status and trends", Materials for power advanced engineering*", 1998
2. Guo, Han, You, "*Creep Crack Growth behaviour of alloy 718", Superalloy 718, 625, 706 and Various Derivates*", Ed. Loria, 1998
3. A. Di Gianfrancesco & others: *Mechanical and microstructural qualification of a prototype IN718 forged disk*; IFM2003, Kobe October 2003
4. *www.ad700.dk/ -*
5. W. D. Cao and R. L. Kennedy: improving stress rupture stress rupture life of alloy 718 by optimizing Al, Ti, P and B contents: Superalloys 718, 625, 706 and various derivatives: TMS 2001, edited by F.A. Loria
6. C. Slama, G. Cizeron, Etude du comportement structural de l'alliage NC 19 Fe Nb (Inconel 718), Les ´editions de Physique, 1997.
7. M. Sundararaman, P. Mukhopadhyay, S. Banerjee: Precipitation and Room Temperature deformation of Inconel 718 Superalloy 718, 625, 706 and Various Derivates, Ed. Loria, 1994
8. A. Di Gianfrancesco and Others: Mechanical and microstructural qualification of a prototype IN718 forged disk IFM2003 Kobe Japan 2003, pag. 471
9. A. Di Gianfrancesco & others: Mechanical and microstructural qualification of a prototype IN718 forged disk: ECCC Conference, Zurich CH 22-24 April 2009
10. R.W. Hayes, "Creep deformation of Inconel 718 in the 650°C to 760°C temperature regime", Superalloy 718, 625, 706 and Various Derivates, Ed. Loria, 1991
11. Creep data validation and assessment procedures: ECCC Recommendations Volumes 2005
12. C. R. Brinkman, M. K. Booker, and J. L. DingCreep and Creep-Rupture Behavior of Alloy 718"; Superalloy 718, 625, 706 and Various Derivates, Ed. Loria, 2001

13. Z. Yun et al., Superalloys 718, 625, 706 and various derivatives; TMS, ed. Loria, 1997, p. 229.
14. J. Dong, X. Xie, Z. Xu, S. Zhang, M. Chen, J. Radavich: TEM study on microstructure behaviour of Alloy 718 after long term exposure at high temperature: Superalloys 718, 625, 706 and various derivatives; TMS, ed. Loria, 1994, p. 649.
15. A. Thomas, M. El-Wahabi, J.M. Cabrera, J.M. Prado: High temperature deformation of Inconel 718; Journal of Materials Processing Technology 177 (2006) 469–472

STRUCTURE AND PROPERTIES OF HYBRID LASER+MAG JOINT OF NICKEL ALLOY DMV 617 MOD.

Adamiec Janusz, Adam Hernas

Silesian University of Technology, Faculty of Materials Science and Metallurgy Institute of Material Science, 40-019 Katowice, Krasińskiego 8, Poland, janusz.adamiec@polsl.pl, adam.hernas@polsl.pl

Abstract

The purpose of this work was to perform experimental butt tubular joints, welded with the laser method and with the hybrid method (laser and MAG) from the DMV 617 mod alloy. One-run welding with the hybrid method (laser + MAG) allows one to make a welded joint that meets the requirements of the "C" level quality according to PN EN ISO 13919. The joint is characterized by a correct shape index amounting to 1. Results of the structural tests and microanalysis of the chemical composition of the experimental hybrid joint constitute a basis for the development of an approved technology of manufacturing of joints in the B class according to PN EN ISO 13919.

Keywords: nickel alloys, alloy 617, hybrid welding, laser welding

1. Introduction

Growing demand for electricity and the requirements of EU directives, e.g. 2001/77/EC, 2001/80/EC and 1997/97/23/EC result in the necessity to modernize the European power industry and to undertake activities in the scope of design, manufacture and operation of power energy equipment [1-3].

In the boiler part of modern power units an important role is played by tubular elements of heat exchangers, mainly of superheaters, thick-walled live steam pipes, finned tubes and tight membrane walls [4]. In the construction of power industry equipment one uses on an increasingly more frequent basis, apart from new materials, such as nickel alloys (DMV 617 mod), new technological solutions, such as laser and hybrid welding [5,6].

The application of high power lasers for welding both by large companies and small businesses is on the increase [5,6]. One observes an annual 7-8% increase in the number of laser equipment sold in the last decade [5,7,8].

The application of laser equipment for welding purposes has many advantages. It also contributes to a drop of prices of the lasers, with a simultaneous increase in their reliability, as well as an increased power and better quality of the emitted beam.

Currently, lasers are not used for the welding of boilers intended for the power industry, because of the limited power of the beam, difficulty in the precise preparation of the joint, possible occurrence of a cure both in the narrow heat affected zone and in the fusion weld, and a tendency for hot cracking displayed by the fusion welds. There are however many advantages of lasers, and in particular of the laser + MAG hybrid systems, i.e. stability of the welding process, less rigid requirements regarding the joint preparation, low welding energy, significantly increased welding performance and the ability to perform a one-side welding.

Hybrid laser arc welding is a combination of MAG arc welding and laser welding (Fig. 1) or a combination of other methods of arc welding (TIG, plasma) with the laser.

The application of laser equipment for welding purposes has many advantages. It also contributes to a drop of prices of the lasers, with a simultaneous increase in their reliability, as well as an increased power and better quality of the emitted beam.

Currently, lasers are not used for the welding of boilers intended for the power industry, because of the limited power of the beam, difficulty in the precise preparation of the joint, possible occurrence of a cure both in the narrow heat affected zone and in the fusion weld, and a tendency for hot cracking displayed by the fusion welds. There are however many advantages of lasers, and in particular of the laser + MAG hybrid systems, i.e. stability of the welding process, less rigid requirements regarding the joint preparation, low welding energy, significantly increased welding performance and the ability to perform a one-side welding. Hybrid laser arc welding is a combination of MAG arc welding and laser welding (Fig. 1) or a combination of other methods of arc welding (TIG, plasma) with the laser. A combination of these methods in one single HLAW process removes the limitations imposed on welding with the laser only, where it is difficult to adjust the elements to be joined. Welding with the laser only requires a very careful preparation of the edges of the elements to be joined and their accurate adjustment. Also the gap between the elements to be joined should not exceed 0.2 mm.

Due to the high speeds of welding, reaching, depending on the thickness and the type of the welded material, to a few, and in the case of thin metal sheets, up to 8-10 m / min, one encounters a problem with the hardening and brittleness of the welded joints. One can also see imperfections in the form of concave faces, melt-through, incomplete fusion, cracks, blowholes and blisters. Besides, during the welding process the fusion weld loses part of its alloy components, which burn and evaporate. Figure 2 shows the geometrical shape of the fusion weld made with the MAG method, with the laser and with the hybrid method (laser + MAG). Combination of the laser welding process with the conventional MAG welding process allows one to eliminate the weakest points of the laser welding, i.e.: less rigid requirements regarding the preparation of the edges of the elements to be joined and their adjustment, concave face - incomplete cross-section of the fusion weld, high hardness and brittleness due to the additional increased linear energy of the arc. This last feature is particularly useful when connecting not only low-alloy steels, such as P235, P355, but also 16Mo3, 13CrMo4-5, 10CrMo9-10 alloy steels.

It is also advisable to undertake research into the application of the laser welding and hybrid welding technologies to the most modern materials with a high potential for being used in the power industry, namely the nickel alloys and, in particular, the DMV 617 mod alloy.

2. The purpose and scope of the research

The purpose of this work was to perform experimental butt tubular joints, welded with the laser method and with the hybrid method (laser and MAG) from the DMV 617 mod alloy.

The scope of the work included: preparation of the test material, performance of technological tests of the remelting and welding processes, assessment of the macrostructure and hardness of the joint. Additionally one performed microanalysis of the chemical composition to reveal possible heterogeneity of the chemical composition.
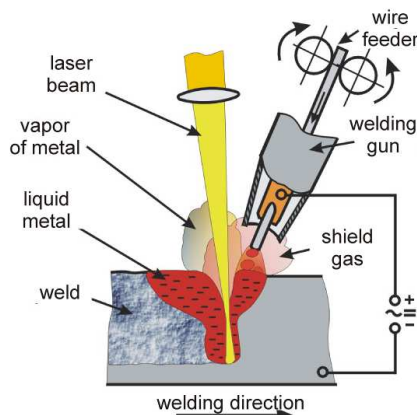
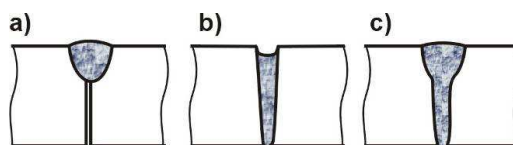Fig. 1. The hybrid (laser + MAG) welding process [10]

Figure 2. Geometry of the welded joint made with a) the MAG method, b) with the laser, c) with the hybrid method (laser + MAG) [10]

3. Technological tests of the welding process

Technological tests of the remelting process and laser welding, as well as of the hybrid welding with the HLAW method were performed at a robotized welding station equipped with a disc laser of the power of 8 kW (Disklaser 8002, manufactured by the Trumpf company) and with a Cloos Romat 400/30 robot (Fig. 3).
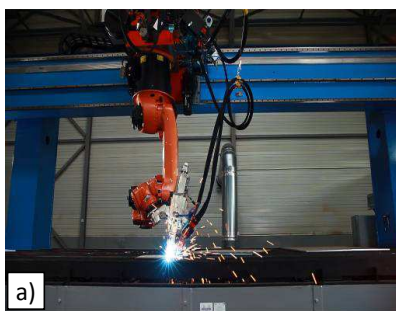
Fig. 3. Station for technological tests of laser and hybrid welding of the DMV 617 mod alloy, Energoinstal SA

Technological tests of the remelting process

Technological tests of the remelting process were performed in the downhand position (PA) on a welding positioner. The power of the laser beam ranged from 1500 W to 3000 W. The beam was focused on the surface of the tube. Technical argon was used as the shielding gas. Sample faces of the joint penetration are shown in Figure 4.

The visual tests showed that a full remelting of the wall on the entire circumference of the tube was achieved with the application of a laser beam of the power of 3000 W (Fig. 5d). Remelting with a beam of the power of 2500 W allows one to make a full joint penetration on the ¾ circumference, due to the heating of the material in the initial stage of the process (Fig. 4c).

524

	1500 W	2000W	2500 W	3000 W
Face	a) 5 mm	b) 5 mm	c) 5 mm	d) 5 mm
Root	5 mm	5 mm	5 mm	5 mm
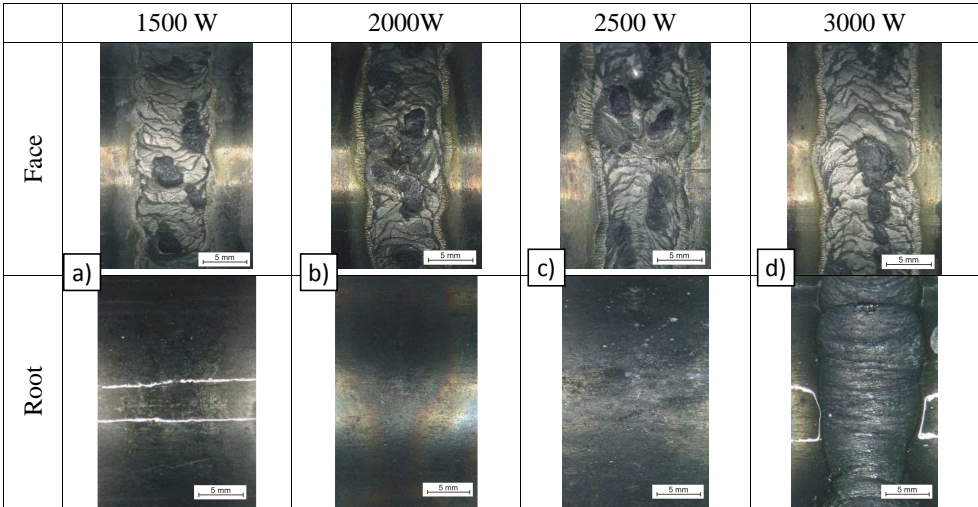
Fig. 4. Faces and root of the joint penetration of the tube of DMV 617 mod alloy, made with a disc laser, beam power: a) 1500 W, b) 2000 W, c) 2500 W, d) 3000 W

For this reason, it is necessary to use a variable power of the laser beam during the welding process. Smaller beam power (less than 2000 W) does not fully remelt the wall of the tube (Fig. 4a, b).

Laser welding tests

To perform a butt joint with the laser, the edges of the tube were prepared in accordance with Figure 5. To obtain an even joint penetration on the entire circumference of the tube, one applied a pulsed beam with a decreasing power, according to a diagram shown in Figure 6. Additionally argon 4.8 was used as the forming gas, at the flow of 11 l / min. Sample face and root of the joint are shown in Figure 7. Analysis of the visual test results shows that the laser welding of a tubular joint made of 617 DMV mod alloy is only possible with the application of an additional material.
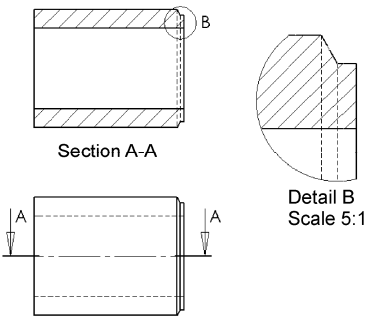
Fig. 5. Preparation of the edges for laser welding (butt joint) of a tube made of DMV 617 mod alloy
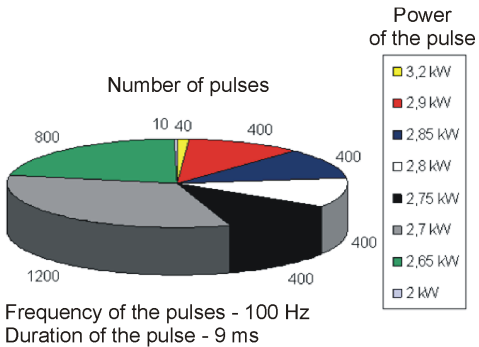
Fig. 6 Diagram showing the applied parameters of the laser beam for welding of the DMV 617 mod alloy

525
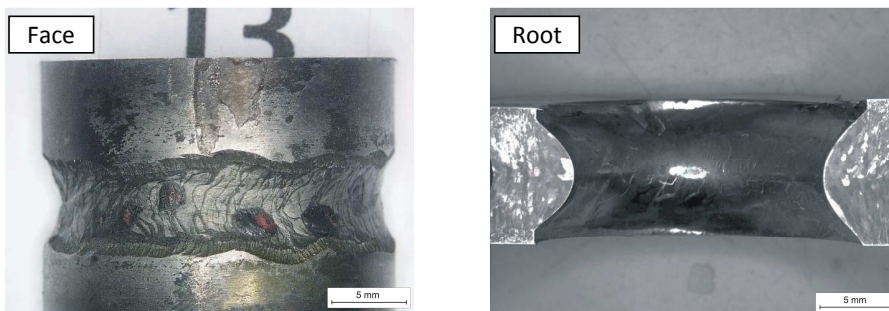
*Fig. 7. Face and root of the fusion weld of a tube of DMV 617 mod alloy,
made with a disc laser*

It was found that the face of the fusion weld was concave and needed to be filled in the welding process, i.e. hybrid welding or another form of arc welding (TIG) (Fig. 7a). Application of a variable power beam during the welding process allowed one to achieve a correct fusion penetration on the entire circumference of the joint (Fig. 7b).

On this basis one developed a new welding technology, in which the remelting is performed with a disc laser, which ensures a correct, uniform root, while the TIG method is used for filling and arranging the face (141). Laser remelting was performed with a laser beam, which was modeled according to a diagram shown in Figure 6. An additional material (Thermanit 617) was used for the welding (filling and face) with the TIG method. The welding current amounted to 80A. The view of the face and root is shown in Figure 8. The visual examinations revealed no welding imperfections.
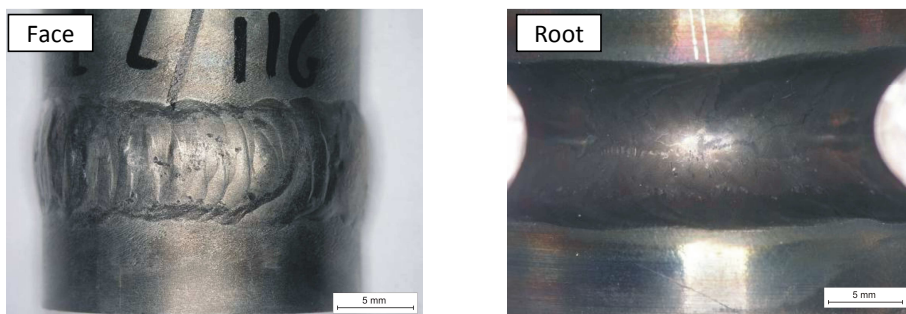
*Fig. 8. Face and root of a fusion weld made with a combined method: remelting - disc laser
and filling and face - TIG method, of a tube made of DMV 617 mod alloy*

The technological tests of laser welding were supplemented with attempts to weld the joint penetration with a disc laser according to the parameters shown in Figure 3 and with the performance of the filling layer with the hybrid method. The following process parameters were applied for MAG welding (135): wire feed - 12m/min, dynamics of the arc - 40, -50 arc length, welding current - 95 A, arc voltage - 20.9 V, shielding gas - Argon 5.0. The face and the root are shown in Figure 9. The visual examinations revealed too big reinforcement and undercut. Such imperfections are not allowed in class B according to PN EN 13919 (Fig. 9).

HLAW (laser + MAG)

For the hybrid welding (laser + MAG), the edges of tube were prepared in accordance with Figure 10. Such a preparation of the joint allows one to make the face without a too high reinforcement and does not require an additional laser remelting.

The joint to be welded was made with one wall, which allows one to significantly increase the efficiency of the joining process. Parameters of the laser beam were applied in accordance with Figure 11, while the MAG welding parameters were the same as those applied in the performance of the filling and the face (Fig. 9). A sample joint is shown in Figure 12. The performed visual examinations did not reveal welding imperfections according to EN 13919. The joint was approved for the B quality class.
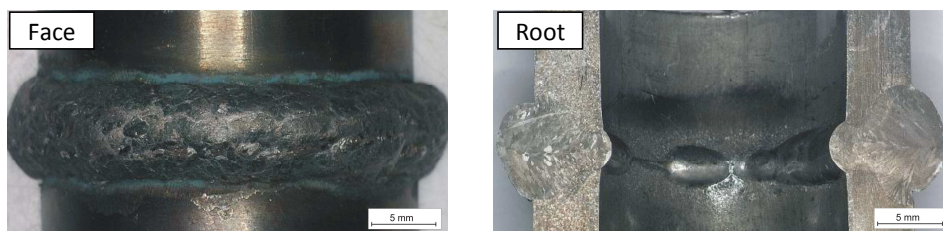
Fig. 9. Face and root of a fusion weld made with the combined method: remelting - disc laser and filling and face - laser + MAG hybrid, of a tube made of DMV 617 mod alloy
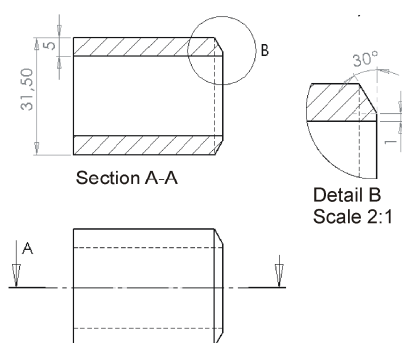
Figure 10 Diagram showing preparation of the joint for hybrid welding
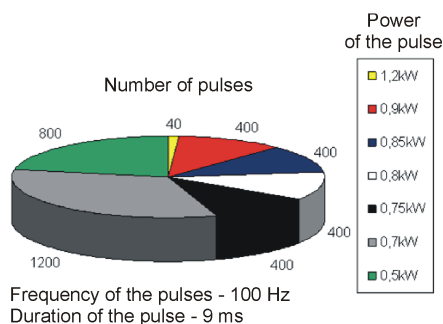
Fig. 11 Diagram showing the applied parameters of the laser beam for hybrid welding (laser + MAG) of a tube made of DWV 617 mod alloy
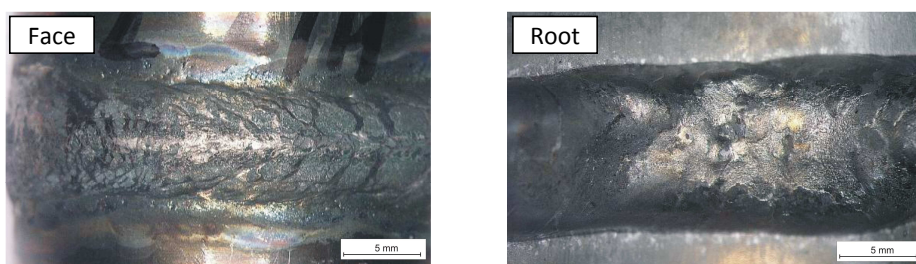
Fig. 12. Face and root of a fusion weld made with the hybrid technique, of a tube made of DMV 617 mod alloy.

527

4. Macrographic examinations

The macrographic examinations were performed on samples cut perpendicular to the welding direction. The prepared metallographic microsections were etched in the Cr12361 (Adler A5) reagent. Sample macrostructures observed with a stereoscopic microscope SZX 9 in the dark field are shown in Figures 13-14. Records from the visual assessment were enclosed as attachments (No. 327/MA/13).

The performed analysis of the structure of the joint penetrations confirms the results of the visual examinations. It was found that remelting with a laser beam with a power of up to 2000 W was not sufficient to achieve the joint penetration (Fig. 13a,b). Increasing the beam power to above 2500 W allows one to achieve a full joint penetration (Fig. 13c,d). Increased power results in an increased width of the joint penetration. Remelting with a beam power of 3000 W causes leakage of the material and may result in leakage from the side of the root. A similar leakage was also observed from the side of the root in the joint made with a laser (Fig. 14a).

This joint also showed a significant imperfection in the form of a lack of filling of the face. This requires the application of additional welding methods, which provide additional material to the welding puddle.

Supplementation of the fusion weld with the TIG method ensures obtainment of a correct face with a correct angle of the transition of the fusion weld into the material (Fig. 14b). A welded joint made with the combined method (laser + TIG) is characterized by the typical structure, i.e. the native material, a narrow, poorly marked heat-affected zone and the fusion weld area.
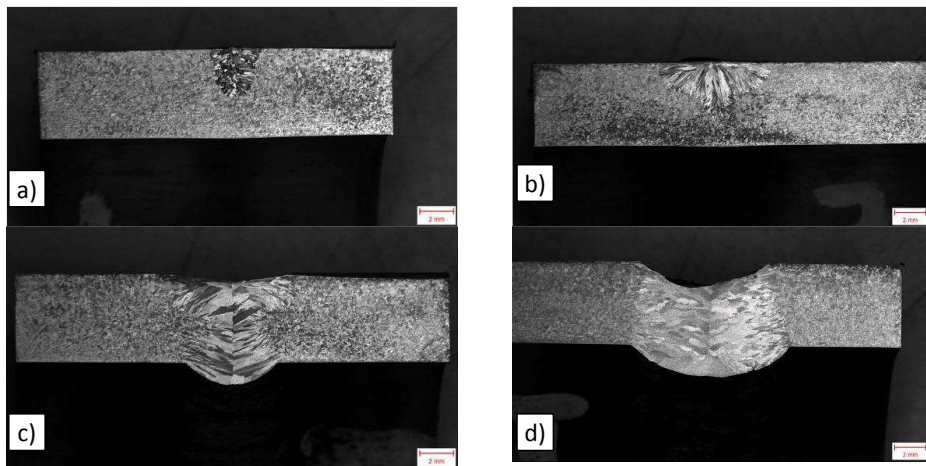
Fig. 13. Macrostructure of a joint penetration of a tube made of DMV 617 mod alloy, made with a disc laser, beam power: a) 1500 W b) 2000 W c) 2500 W d) 3000 W

Filling of a joint, in which the remelting was performed with a laser, the hybrid method (laser + MAG) results in the occurrence of a reinforcement and undercut, inconsistent with the requirements of the PN EN 13919 standard (Fig. 14c). Also, the shape of the fusion weld is disadvantageous, because of its considerable contraction.
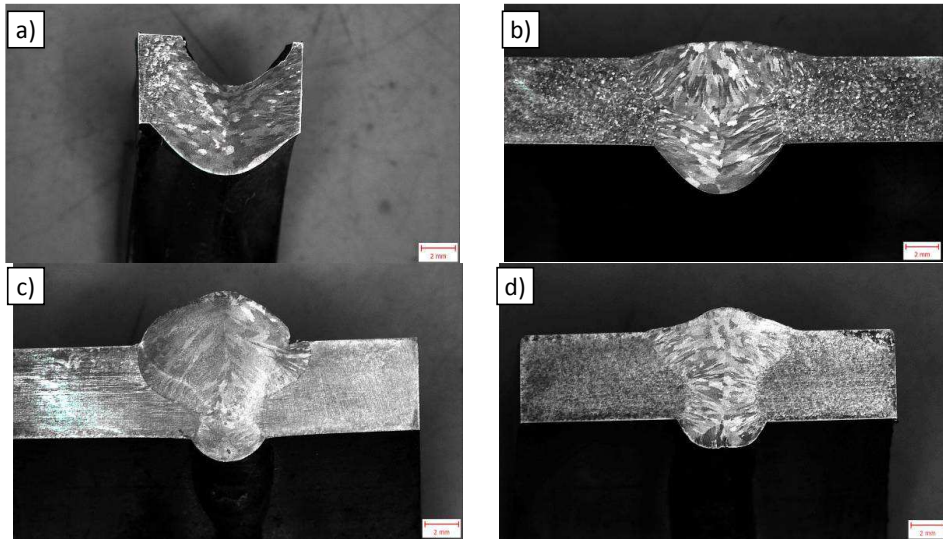
Fig. 14. Macrostructure of the joints of a tube made of DMV 617 mod ally, made with: a) disc laser, beam power according to Fig. 7, b) joint penetration - disc laser, filling and face - TIG, c) joint penetration - disc laser, filling and face - hybrid (laser + MAG), d) with one run with the hybrid method (laser + MAG)

A joint made with the hybrid method possesses a correct structure (Fig. 14d). Analysis of the shape revealed a slight leakage, which is however acceptable for Class C (below 1.2 mm). The joint shape index, calculated as a ratio of the joint width to the height is 1, which also proves the correctness of the developed hybrid welding technology.

5. Measurement of the joint hardness

The hardness was measured in accordance with the PN-EN ISO 9015-1 with the Vickers method with a load of 98N (HV10) with Innovatest Nexus 4300 hardness tester. Distribution of the measurement points and the measurement results is shown in Figure 15
Analysis of the hardness distribution did not reveal any significant differences between particular zones of the joint (Fig. 17). The joint hardness ranged from 166 HV to 198 HV (a difference of 32HV) (Fig. 1), which confirms absence of a hardened or softened zone in the joint.

7. Conclusions

Experimental technological tests of laser welding and hybrid welding of butt joints of tubes with 31.5 mm in diameter and with 5.0 mm thick walls, made of DMV 617 mod alloy were performed. Based on the remelting test results, one proved that it was possible to achieve a correct joint penetration with a disc laser. The applied beam power should range from 2500 W to 3000 W. It was also found that because of a possible leakage in the area of the root, it was necessary to use a combined welding method or hybrid method. Application of such a technology allows one to add additional material that will supplement the missing material in the fusion weld.
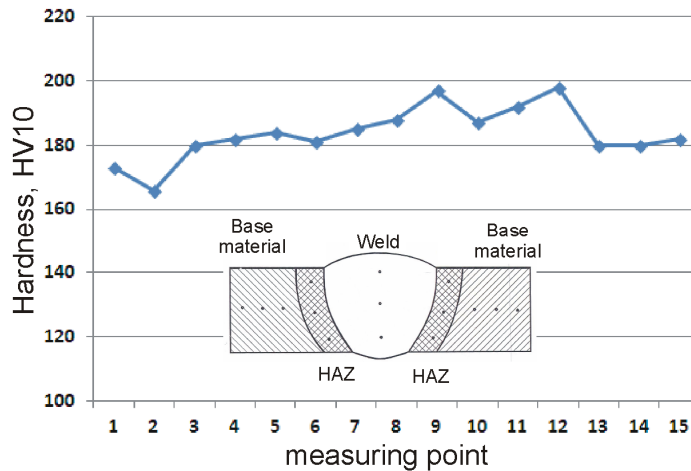
Figure 15: Distribution of the hardness measurement points in a joint made with the combined method (laser + TIG) and Distribution of hardness in a tubular joint of DVM 617 mod alloy, made with the combined method (laser + TIG)

The performed technological tests of welding with combined methods, i.e. laser remelting, filling with the TIG method or with the hybrid (laser + MAG) method showed that the filling of a fusion weld with the TIG method gave good results. Analysis of the structure and hardness distribution shows that the developed technological guidelines can constitute a basis for the qualification of the welding procedures according to PN EN ISO 15614-11. Application of hybrid welding for the filling of the joint and formation of the face did not give positive results, because of the revealed considerable reinforcement and undercut.

One-run welding with the hybrid method (laser + MAG) allows one to make a welded joint that meets the requirements of the "C" level quality according to PN EN ISO 13919. The joint is characterized by a correct shape index amounting to 1. Results of the structural tests and microanalysis of the chemical composition of the experimental hybrid joint constitute a basis for the development of an approved technology of manufacturing of joints in the B class according to PN EN ISO 13919.

References

[1] Brózda J.: *Stale energetyczne nowej generacji stosowane na urządzenia energetyki o parametrach nadkrytycznych i ich spawanie*. Biuletyn Instytutu Spawalnictwa, nr 5/2006 [Steels for power engineering applied inn the power industry equipment with supercritical parameters and their welding. Bulletin of the Institute of Welding], no. 5/2006]

[2] Najgebauer E., Patrycy A., *Zobowiązania polskiej energetyki wobec EU* [Obligations of the Polish power industry towards the EU], www.geoland.pl

[3] Brózda J., *Stale żarowytrzymałe nowej generacji, ich spawalność i właściwości złączy spawanych*, Biuletyn Instytutu Spawalnictwa [New generation high-temperature creep resistant steels, their weldability and properties of the welded joints, Bulletin of the Institute of Welding] no. 1/2004.

[4] Huseman R.: *Advanced (700 ^{o}C) PF Power Plant*: A Clean Coal European Technology. Advanced Material for AD700 Boilers, Cesi Auditorium, Milano, 2005.

[5] Gawrysiuk W., Adamiec J., Więcek M.: *Możliwości spawania laserowego i hybrydowego ścian szczelnych oraz rur ożebrowanych*, Konferencja Spawanie w Energetyce, Opole – Jarmołtówek 2008 [Possibilities of laser and hybrid welding of tight walls and finned tubes, "Welding in the power industry" conference, Opole - Jarmołówek 2008]

[6] Stano S.: *Lasery YAG w zrobotyzowanych stanowiskach spawalniczych*, Materiał Seminarium „Rozwój spawania i cięcia laserem CO_2 i YAG oraz możliwości wykorzystania" Instytut Spawalnictwa 2005 [YAG lasers in robotic welding stations, Materials from the Seminar "Development and possible applications of CO_2 i YAG laser welding and cutting" the Institute of Welding 2005]

[7] Adamiec J. Adamiec P., Wiecek M.: *Spawanie laserowe ścian szczelnych* „XII naukowo-techniczna Konferencja Spawalnicza, Materiały Konferencyjne Międzyzrdoje 2007 [Laser welding of tight walls. 12th Scientific and Technical Welding Conference. Conference Materials. Międzyzdroje 2007]

[8] Laser Focus World/ *Industrial Laser Solution -annual economic review*, PennWell's Laser & Photonics Marketplace (2006). (http://ils.pennnet.com).

[9] Thieme J.: Fiber Laser – new challenges for the Materials Processing, Lassertechnik Jurnal, No. 3. 2007

[10] Adamiec J., Gawrysiuk W., Więcek M.: *Nowe możliwości spawania hybrydowego laser + MAG paneli ścian szczelnych*, Konferencja Power Welding 2013 „Materiały i technologie stosowane w budowie kotłów o parametrach nadkrytycznych o temperaturze pary do 700 ^{o}C, Ostaniec 2013 [new possibilities of hybrid welding laser + mag of tight wall panels. Power Welding 2013 Conference" Materials and technologies applied in the construction of boilers with supercritical parameters and steam temperature of up to 700 ^{o}C, Ostaniec 2013]

DEVELOPMENT OF LOW RHENIUM 2ND GENERATION SINGLE CRYSTAL SUPERALLOYS WITH OPTIMUM ENVIRONMENTAL AND MECHANICAL PROPERTIES

K. Kawagishi, R. Zhu, T. Yokokawa, T. Kobayashi, Y. Koizumi, M. Yuyama and H. Harada

National Institute for Materials Science, 1-2-1 Sengen, Tsukuba, Ibaraki, Japan 305-0047

KAWAGISHI.Kyoko@nims.go.jp

Abstract

The Si modified 2nd generation superalloys have been developed and their applicability for high temperature uses has been evaluated. The thermal cyclic oxidation has demonstrated that the alloys had less mass loss than the CMSX-4® and meanwhile the oxidation resistance increased with the increase of Si content. Microstructural observations suggested that the addition of Si enhanced spallation resistance of the scales during environmental attack and therefore the ability of oxide scale to protect from degradation has been improved. Excess of Si addition showed much worse creep properties especially at high temperature regions due to the formation of a considerable amount of the TCP precipitations, while it achieved the superior resistance against oxidation and corrosion. The alloy containing optimum amount of Si showed balanced environmental and creep performances, and it presented high resistance against oxidation and corrosion and meanwhile it retained sufficient mechanical strengths comparing favourably with the CMSX-4 especially in the low and high temperature range. This alloy containing less Re can be a good replacement alloy of the expensive CMSX-4 for gas turbine uses.

CMSX-4 is a registered trademark of Cannon-Muskegon Corporation.

Keywords: Ni-base superalloy, single crystal, rhenium, oxidation, creep.

1. Introduction

Based on many decades of efforts, nickel-base single crystal superalloys used for hot section turbine engines retain significant mechanical strengths at high temperatures. For instance, the 1st generation superalloy TMS-6 that was developed by National Institute for Materials Science (NIMS) in 1984 has shown superior creep rupture strengths at test conditions of 1040°C /137MPa and 900°C /392MPa [1]. Later, considering the contribution of Re addition to the solid solution strengthening of γ phase, 1.20 wt% Re containing 2nd generation superalloys have been developed to maximize the strengthening and high temperature capability. Furthermore, to reduce the density, Nb has substituted Ta in the γ' precipitates and the superalloy has been upgraded. These alloys have demonstrated excellent creep strengths in comparison with most commercially superalloys. However, due to the presence alloying elements such as W, Mo, Ta, and Re that provide the high temperature strengths, the alloys tend to be susceptible to environmental attack especially oxidation and corrosion. Thus the most demanding requirement is now the improvement of oxidation and corrosion resistances but without largely sacrifices the mechanical strengths. Besides structure and homogeneity, chemical composition can affect the oxidation and corrosion resistance. Minor additions of reactive elements such as Hf, Si, Y, or Pt etc. have been found contribute greatly to the

improved oxidation behaviour [2-8]. On the other hand, these elements may have a deleterious effect on the mechanical properties [8]. Despite the reorganization that Si plays an effective but critical role in improving oxidation resistance, Si addition was usually in a very small amount and it is very difficult to study the Si addition effect in detail. Hereby this present work develops Si modified superalloys and evaluates how it is involved in the oxidation and corrosion resistance enhancement.

2. Experimental Procedure

1.20 wt% Re containing 2nd generation superalloy A, upgraded alloy B by Nb substituting Ta, and two new superalloys C and D, in which 0.15 wt% and 0.25 wt% respectively of Si have substituted Ni in the Alloy B, have been cast using standard directional solidification in NIMS. The nominal compositions of alloys with a few representative nickel-based single crystal superalloys including a GE patented alloy E [9], SRR99, and CMSX-4 are listed in Table 1.

Table 1:   Nominal compositions of a few superalloys. (wt%, Ni bal.)

Alloy	Weight percent											Density (g/cm^3)
	Co	Cr	Mo	W	Al	Ti	Nb	Ta	Hf	Re	Si	
TMS-6	-	9.20	-	8.70	5.30	-	-	10.40	-	-	-	8.90
Alloy A	-	9.00	-	8.00	5.40	-	-	10.00	-	1.20	-	8.92
Alloy B	-	9.00	-	8.00	5.40	-	2.30	5.80	-	1.20		8.74
Alloy C	-	9.00	-	8.00	5.40	-	2.30	5.80	-	1.20	0.15	8.73
Alloy D	-	9.00	-	8.00	5.40	-	2.30	5.80	-	1.20	0.25	8.73
Alloy E	7.50	13.00	-	3.80	6.60	-	-	5.00	0.15	1.60	0.05	8.30
SRR99	5.00	8.50	-	9.00	5.50	2.20	-	2.80	-	-	-	8.49
CMSX-4	9.60	6.50	0.60	6.40	5.60	1.00	-	6.50	0.10	3.00	-	8.75

The oxidation resistance was measured by cyclic oxidation in air, in which specimen was kept cyclically at 1100°C for 1h and then 1h cooling outside the furnace. Mass-change measurement has been used to characterise the cyclic oxidation kinetics of the superalloys.

In the hot corrosion crucible test, specimens were soaked in a mixture salt consisted of 75 wt% NaSO$_4$ and 25 wt% NaCl in crucibles. They were kept at 900°C for 20 h in air atmosphere and then all scales were removed from the specimens. The metal loss was measured by the shrinkage in specimen height.

The creep tests were carried out at four different temperature/strain conditions - 800°C /735MPa, 900°C/392MPa, 1000°C/245MPa, and 1100°C/137MPa. Time to 1 % creep strain

and rupture life were recorded. The creep properties including the time to 1 % strain and rupture life were measured by elongation.

3. Results and Discussion

The oxidation resistance was measured by cyclic oxidation in air and the result is shown in Figure 1. When the oxidation starts, all alloys gain weight however the weight may gradually decrease due to the successive delamination of oxides upon cooling. With extended cycles, the silicon modified alloy C and D displayed slow degradation rate in comparison with the alloy B or CMSX-4, which demonstrated their excellent long-term resistances against spallation. The alloy A shows comparable property with Si modified alloys because it does not contain Nb and the oxidation resistance is not degraded. From this result, it is clear that the addition of Si significantly improved the oxidation resistance compared to alloy B without Si. The cross sectional microstructure images after cyclic oxidation shown in Figure 2 further confirmed that good adherences of the alumina scales of alloy C and D to the base materials. It is considered that Si in Ni-base superalloy increases Al activity, and alumina formation is promoted for these alloys.
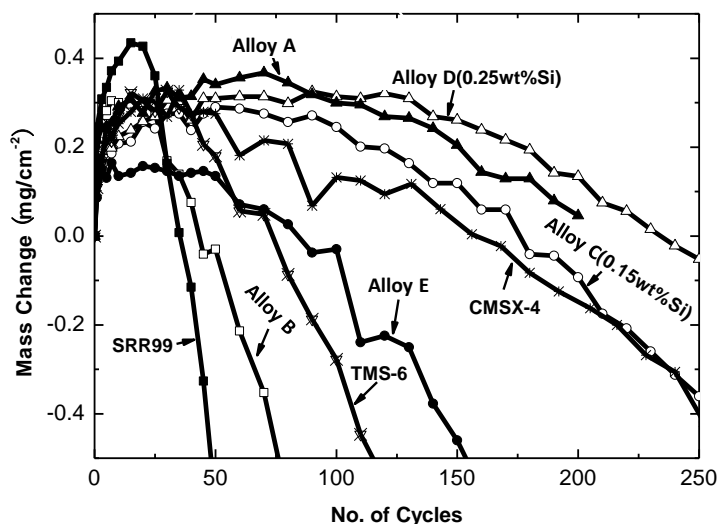
Figure 1 :   Mass change for superalloys during 1h cycles oxidation at 1100°C in air.

In the hot corrosion crucible test, as shown in Figure 3, small metal losses have been seen in alloy A, B and the Si modified alloy C, D while other alloys experienced much higher metal

loss by orders of magnitude. It is clear that the addition of Si does not give disadvantage to the hot corrosion resistance.
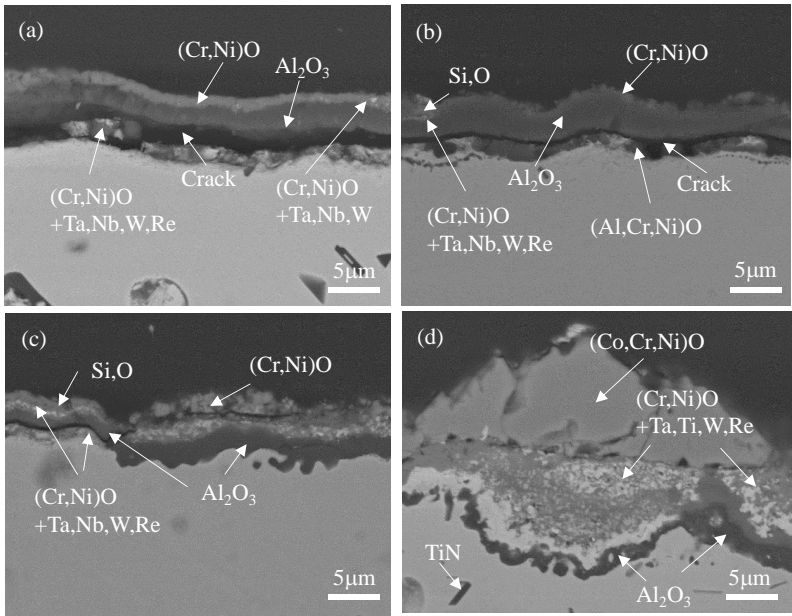
Figure 2 :   Cross sectional SEM images of superalloys (a)alloy B, (b)alloy C, (c)alloy D and (d)CMSX-4 after 1100°C for 250 cycles.
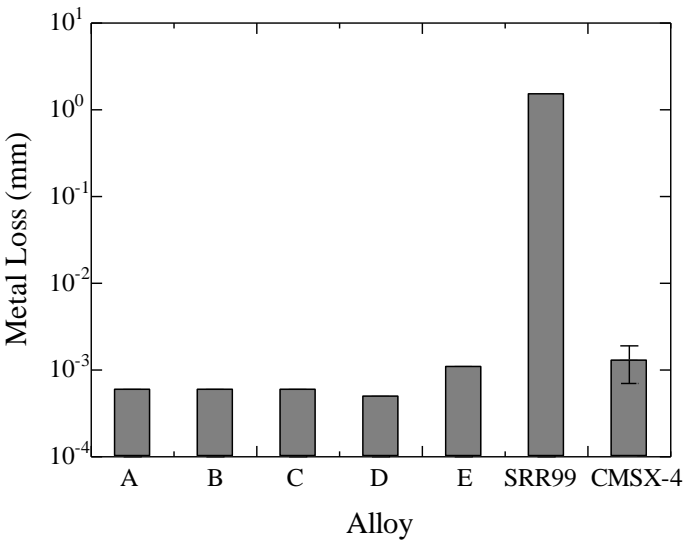
Figure 3 :   Metal losses in hot corrosion test at 900°C.

Figure 4 shows the Larson-Miller plots of the times to 1 % strain and creep lives. Maximum times to 1 % strain and rupture life occurred at alloy C at 800°C/735MPa. However in the intermediate temperature region, such as 900°C/392MPa and1000°C/245MPa, their performances have become even worse than the Alloy B while the CMSX-4 has shown the longest times to either 1% creep strain or rupture. In high temperature region such as 1100°C /137MPa, the times drop significantly with the increase of silicon addition. Fractured specimens were sliced perpendicular to the <001> direction and observed using SEM (scanning electron microscope). The failure of alloy C and D were interpreted by the formation of topologically closed packed (TCP) phase precipitation during high temperature creep. Excess addition of Si seems to enhance TCP formation during high temperature creep, thus it is necessary to find optimal amount of Si addition for obtaining both of excellent oxidation and mechanical property.
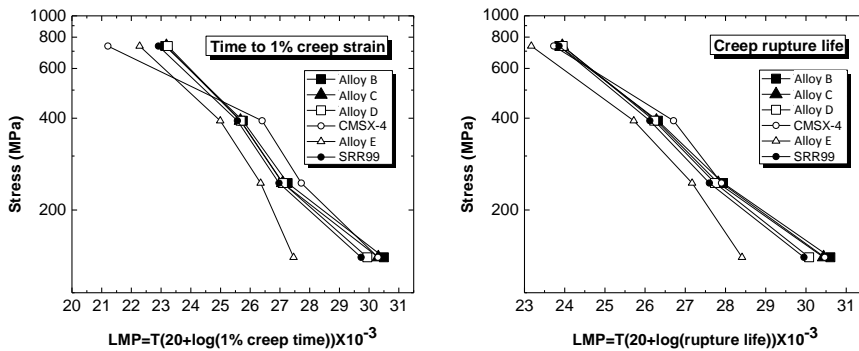
Figure 4 :   Larson-Miller plots of time to 1% creep strain and creep rupture lives.

4. Conclusions

The Si modified alloys, alloy C and alloy D, have been developed and their applicability for high temperature uses has been evaluated. The thermal cyclic oxidation has demonstrated that both the alloy C and D had less mass loss than the alloy B and CMSX-4 and meanwhile the oxidation resistance increased with the increase of Si content. In addition, the alloy C showed the higher hot corrosion resistance than both alloy B and CMSX-4. Microstructural observations suggested that the addition of Si enhanced spallation resistance of the scales during environmental attack and therefore the ability of oxide scale to protect from degradation has been improved. Unfortunately, though the alloy D presented the superior resistance against oxidation and corrosion, its creep properties were much worse than the alloy B especially at high temperature regions due to the formation of considerably amount of the TCP precipitations. While the Si may accelerate the nucleation rate of the TCP phases, the

mechanical strength decreases with the increase of Si content. In contrast, alloy C showed balanced environmental and creep performance. It presented high resistance against oxidation and corrosion whilst the creep strength compared favourably with alloy B and the 3 % rhenium alloy CMSX-4 in the low and high temperature region. However, there was a creep deficiency compared to CMSX-4 under some creep conditions. Alloy C, which has been named TMS-286 is a potential low cost candidate for application in parts that are not limited by creep in the intermediate temperature region.

Acknowledgements

References

[1]   T. Yamagata, H. Harada, S. Nakazawa and M. Yamazaki, "Alloy Design for High Strength Ni-base Single Crystal Alloys", *Superalloys 1984*, TMS, Warrendale, PA, pp.157-166 (1984).
[2]   K. Kawagishi, A. Sato, T. Kobayashi and H. Harada, "Effect of Alloying Elements on the Oxidation Resistance of 4th Generation Ni-base Single-crystal Superalloys", *Journal of the Japan Institute of Metals*, Vol. 69, No. 2, pp. 249-252 (2005).
[3]   A. Sato, K. Kawagishi, H. Harada and H. Imai, "Oxidation Resistances of Silicon-Containing 5th Generation Ni-Base Single Crystal Superalloys", *J. Japan Inst. Metals,* Vol. 70, No. 2, pp. 180-183 (2006).
[4]   A. C. Yeh, K. Kawagishi, H. Harada, T. Yokokawa, T. Kobayashi, Y. Koizumi, D. H. Ping and J. Fujioka, "Development of Si-Bearing 4th Generation Ni-Base Single Crystal Superalloys", *Superalloys 2008*, TMS, Warrendale, PA, pp.619-682 (2008).
[5]   D. E. Jones and J. Stringer, "The Effect of Small Amounts of Silicon on the Oxidation of High-Purity Co-25 wt.% Cr at Elevated Temperatures", *Oxidation of Metals*, Vol. 9, No. 5, pp. 409-413 (1975).
[6]   B. Haflan and P. Kofstad, "Corrosion of Nickel with Small Alloy Additions of Si, Fe, and Mn in SO_2+O_2/SO_3 at 700 °C", *Oxidation of Metals*, Vol. 25, No. 3-4, pp. 217-234 (1986).
[7]   J. A. Haynes, B. A. Pint, Y. Zhang and I. G. Wright, "Comparison of the Cyclic Oxidation Behavior of β-NiAl, β-NiPtAl and γ-γ' NiPtAl coatings on Various Superalloys", *Surface & Coatings Technology*, Vol. 202, No. 4-7, pp. 730-734 (2007).
[8]   F. H. Scott, B. Glesson and P. Castello, "The Effect of Platinum Additions on the Oxidation of Directionally-Solidified Ni-Cr-Al-Y-Cr_3C_2 Alloys at 1,100 and 1,200°C", *Materials at High Temperatures*, Vol. 16, No. 1, pp. 15-26 (1999).
[9]   K. S. O'Hara, W. S. Walston, C. G. Mukira and M. R. Jackson, US patent 6,905,559 B2, issued 2005-06-14.

EFFECTS OF SULPHUR ON HIGH TEMPERATURE PROPERTIES OF A Ni-BASE SINGLE CRYSTAL SUPERALLOY, TMS-1700

Yuichiro JOH[1,2], Toshiharu KOBAYASHI[2], Tadaharu YOKOKAWA[2],
Kyoko KAWAGISHI[2], Makoto OSAWA[2], Shinsuke SUZUKI[1], Hiroshi HARADA[1,2]

[1]Waseda University
3-4-1 Okubo, Shinjuku, Tokyo 169-8555, Japan
[2]National Institute for Materials Science (NIMS)
1-2-1 Sengen, Tsukuba Science City, Ibaraki 305-0047, Japan
OSAWA.Makoto@nims.go.jp

ABSTRACT

Effects of sulphur on high temperature properties of a Ni-base single crystal superalloy were examined in this study. Up to 100ppm sulphur was intentionally added to a 1st generation Ni-base single crystal superalloy, TMS-1700. Oxidation and creep tests were performed on the single crystal specimens. The specimens were evaluated using SEM and EPMA. It has become clear that all the specimens indicated similar behavior until about 20 cycles in the cyclic oxidation tests. When the sulphur concentration increased, the onset of separation of the oxide scale became earlier and thus the oxidation resistance decreased. The oxidation resistance decreased with increasing sulphur concentration. Specimens with higher sulphur contents tended to rupture earlier in the creep tests; sulphur decreases the creep strength in the Ni-base single crystal superalloy. Sulphur reduces the high temperature properties of Ni-base single crystal superalloys.

Key words: Ni-base single crystal superalloy, sulphur, cyclic oxidation, creep strength

1. Introduction

Ni-base single crystal superalloys have excellent high temperature properties and have been used for components of gas turbines and jet engines. Turbine blades made of advanced single crystal superalloys enable to improve the thermal efficiency of the turbine system, and consequently reduce the fuel consumption and CO_2 emission. The number of elements constituted in these superalloys increases and kind of rare metals are added in order to improve the high temperature properties as new generation superalloys were developed [1]. Adding these metals rises life time costs of advanced single crystal turbine blades, and accordingly inhibits spreading of them in the gas turbines and jet engines. Hence, reduction of life time cost of the advanced single crystal turbine blades is the most important issue.

Recycle of scrapped turbine blades is an effective method in order to reduce life time cost. However, not all of the constituent elements are recycled by the current methods. Only some part of elements are chemically extracted from them and reused as alloying metals for new productions. The authors expect that a direct recycling process in which the materials of scrapped turbine blades are melted and used for cast into new products is the most effective methods to reduce the life time cost of turbine blades made of Ni-base single crystal superalloys. The direct recycling process enables to reproduce turbine blades without large

consumption of new rare metals whose costs are much influenced by the world economic conditions.

When recycling this kind of advanced single crystal turbine blades, a contamination of impurity and slight change of alloy composition are inevitable due to an environment or repair history and contamination of coating materials. Hence, it is difficult to obtain the original alloy composition identical to regular materials from recycled scrapped turbine blades. Though these kinds of impurities might hardly affect the Ni-base single crystal superalloys with slight small amount, it is supposed easily that the amount of impurity included in the superalloy increases after repeated recycling.

This study focused on the sulphur, which is confirmed as a contamination to scrapped turbine blades and generally reduces high temperature properties. J.X.Dong intentionally added sulphur to Ni-base polycrystalline superalloy, INCONEL 718, and analysed the influences of creep characteristic [2]. As a result, it was clarified that the creep characteristic decreased as sulphur content increased. In addition, it is generally known that sulphur segregates to oxide/metal interface. The segregation layer of sulphur causes the separation of the oxide scale and reduces oxidation resistance [3]. Whereas most of the studies about the oxidation resistance and creep characteristic were performed for polycrystals, there are few studies on the single crystal in the Ni-base superalloy. Therefore, the purpose of this study is to clarify the effects of sulphur on high temperature properties of Ni-base single crystal superalloy.

2. Experimental procedures

The investigation was carried out on a Ni-base superalloy, TMS-1700[4]. Its chemical composition is given in Table 1. Single crystal specimens were obtained by lost wax casting using the directional solidification vacuum furnace. Up to 100 ppm by weight sulphur was added as NiS prior to the casting. After this process, sulphur content in these specimens was measured by carbon-sulphur analyser on infrared absorption method (LECO, CS444LS). The measurement points were 5 mm from the top and bottom of the specimen (the single crystal specimens were 10 mm diameter and 135 mm length). On all the specimens, quantity of sulphur was analysed after the heat treatment (1320 °C for 5 h, 1150°C for 4 h and 870 °C for 20 h). Up to three times, at least twice the analyses were performed at each measurement point. The creep tests were performed under the condition of 1100°C / 137MPa. Cyclic oxidation tests were performed at 1100°C up to 100 cycles in air; heating (1h) and cooling (1h) were repeated in each cycle. The shape of the specimens was cylinder with 9 mm diameter, and 5 mm height. Weight of the specimen was measured by electronic balance after each cycle. Surface area of the specimen was defined as its surface area derived from a diameter and height before the test. After these tests, the specimens were evaluated using SEM and EPMA.

Table 1 Nominal composition of TMS-1700 (wt%)

Ni	Cr	Mo	W	Al	Ta	Hf	Si
Bal.	9.0	0.6	7.6	5.4	10.0	0.1	0.04

3. Results and discussion

3.1. Sulphur concentration in specimens

Fig. 1 shows the results of chemical analysis of all prepared specimens by using the infrared absorption method. The target sulphur concetration well represents the analysed value, though some errors exist between them. In this paper, concentration of specimens represents the added amount of the sulphur instead of the analysed value.
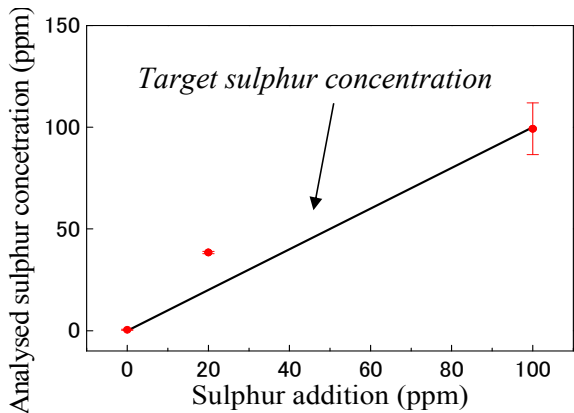
Fig. 1 Results of chemical analysis of sulphur after heat treatment. Error bar around plots indicates the maximum and minimum value.

3.2. Cyclic oxidation test

Fig. 2 shows the results of cyclic oxidation test. In Fig. 2, the weight increases during initial about 20 cycles and decreases at higher cycles in all specimens. The weight loss was caused by separation of the oxide scale, because the oxide scale was found in the crucible used. In addition, the weight change tends to become larger with increasing sulphur addition, and the degree of the weight loss becomes larger as the sulphur concentration is increased. It is confirmed that sulphur reduced the oxidation resistance of the single crystal superalloy.
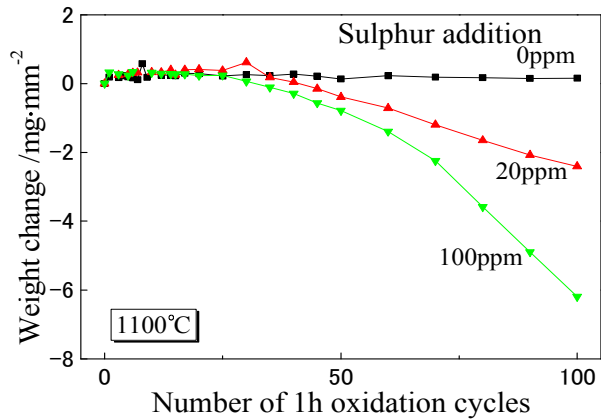
*Fig. 2 Weight changes of specimens with various sulphur addition obtained by
cyclic oxidation test until 100 cycles. Vertical axis means the number of
cycles and the cross axis means a weight change per surface area.*

3.3. Creep test

The creep tests were performed under a condition of 1100°C / 137MPa. Fig. 3 shows the results of creep tests performed in this study. In this figure, it is clearly shown that the rupture time becomes shorter with increasing quantity of sulphur addition. The rupture time in the specimen with 100 ppm sulphur addition decreased by about 50 % from the rupture time in the one with no sulphur addition. In this study, here we found that the creep strength decreased by sulphur addition even in Ni-base single crystal superalloys. It is assumed that the decrease of creep strength is caused by two factors; oxidation and structure factor. Following section discusses the reason why creep strength decreased.
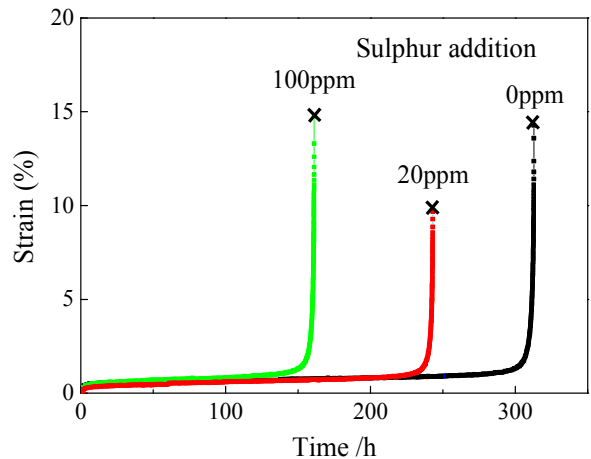
*Fig. 3 Results of creep test at
1100°C / 137MP.*

First, we will discuss the oxidation factor which causes the decrease of creep strength. It was clearly shown in section 3.2 that the oxidation resistance decreased by sulphur addition in Ni-base single crystal superalloys. Here, we analysed the effect of the oxidation resistance on the creep strength. The decrease of effective cross section area negatively influences the creep rupture time. We estimated to what extent the oxidation effects to shorter creep rupture time.
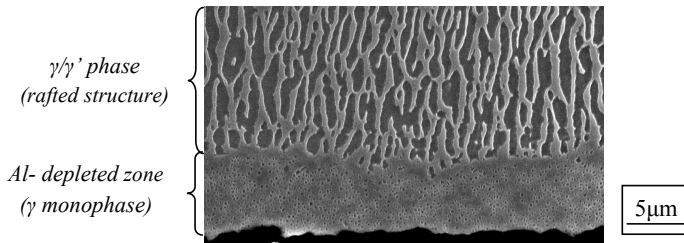
Fig. 4 An SEM image of Al-depleted zone at surface of ruptured creep specimen.

A γ phase area was observed on the vicinity of the whole surface of the ruptured specimen by using SEM (Fig. 4). This structure was also observed in a cross section of cyclic oxidation specimen after the test, identified as an Al-depleted zone by EPMA analysis. A previous study showed that the creep rupture time of γ monophase is less than about 1/600 of that of γ/γ' phase under the same condition [5]. Then, the effective cross section area that contributes to the creep strength is smaller than the area calculated by specimen shape in these creep tests. Hence, we measured the thickness of Al-depleted zone and calculated the effective cross section area for each specimen by observing the surface of specimen after creep tests. The measuring point of the Al-depleted zone was 3 mm from a gauge mark of the creep specimen and mean value is derived from ten measurement values. Fig. 5 shows the result of the measurements. The thickness of Al-depleted zone stays in the narrow range from 0 to 20 ppm sulphur specimens. The thickness tends to increase in the 100 ppm sulphur specimen (Fig. 5). The value of the thickness in 100 ppm sulphur specimen was approximately twice as large as the other specimens. The results showed that thickness of Al-depleted zone increases with increasing sulphur addition.
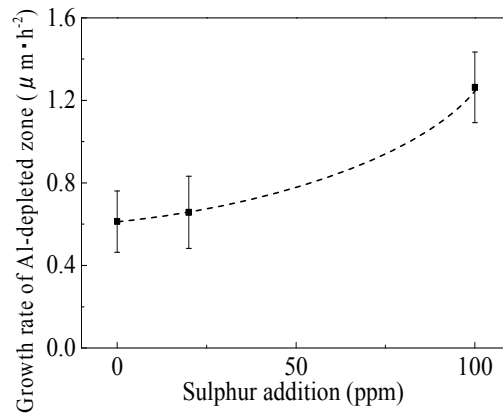
Fig. 5 Growth rate of Al -depleted zone obtained by division of the thickness by square root of rupture time to correct the influence of oxidation time. The line is just guide line to clarify the tendency of the data.
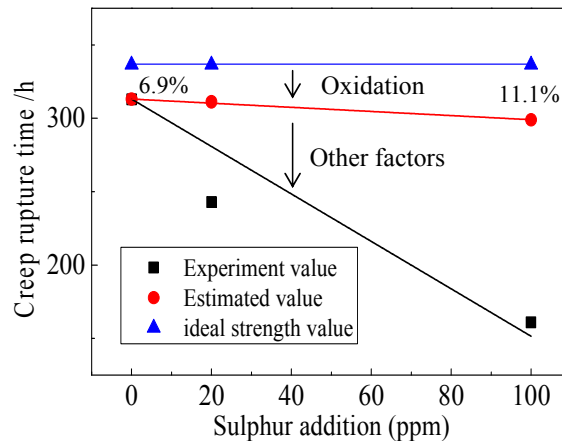
Fig. 6 Influence of oxidation to creep rupture time.

The effective cross section area was derived by subtracting thickness of the Al-depleted zones from the diameter of the creep specimen. The effective stress was calculated by using the value of the effective cross section area and load. Expected rupture time considering the influence of the oxidation alone was calculated from the experimental creep rupture time of specimens without sulphur addition by the effective cross section and a Larson-Miller plot of specimens. The result is shown in Fig. 6. The reduction of the creep rupture time was calculated to be 11.1 % by addition of 100 ppm sulphur under assumption of constant influence of oxidation. However, 11.1 % reduction was much smaller than the experimental results. Hence, not only the oxidation factor but also other factors must effect the reduction of creep rupture time. The oxidation factor, increase of effective stress, has apparent effect, but

cannot fully explain the observed reduction of creep rupture time. It is supposed that sulphur influences the microstructure and deformation mechanism of Ni-base single crystal superalloys and decreases the creep strength. Further investigation on such factors will be required.

4. Conclusions

We intentionally added sulphur to Ni-base single crystal superalloy, TMS-1700, and performed cyclic oxidation and creep tests to clarify the effects of sulphur on high temperature properties in Ni-base single crystal superalloys. The following results were obtained,
1) The oxidation resistance decreases with increasing sulphur content in case of single crystal superalloys.
2) The creep strength also decreases with increasing sulphur content. One of the factors is the increase of effective stress caused by increasing Al-depleted zone. It is suggested, however, that creep strength reduction is caused mostly by some other factors. Further work is needed to clarify these factors.

Acknowledgements

References

[1] H.Harada, High temperature materials for gas turbines: the present and future, In *International Gas Turbine Congress*, Tokyo,(2003)
[2] J.X. Dong, X.S. Xie, R.G. Thompson, Influence of sulphur on stress-rupture fracture in INCONEL 718 superalloys, *Metall. Mater. Trans. A*, Vol.31A, pp.2000-2135(2000)
[3] P. Marcus, J. Oudar, Studies of the influence of sulphur on the passivation of nickel by Auger electron spectroscopy and electron spectroscopy for chemical analysis, *Mater. Sci. Eng.,* Vol.42, pp.191-197(1980)
[4] K.Kawagishi et al , Japan Patent Pending, application number 2014-034720(2014,2,24)
[5] T.Murakumo, Y.Koizumi, K.Kobayashi, H.Harada, Creep strength of Ni-base single crystal superalloys on the γ/γ' tie - line, Superalloys 2004, ed. T.E.Howson *et al*, *TMS*, pp.155-162(2004)

Influence of alloying elements on microstructure and creep strength of a 6th generation Ni-base single crystal superalloy, TMS-238

Yuki Takebe[1, 2], Tadaharu Yokokawa[2], Toshiharu Kobayashi[2],
Kyoko Kawagishi[2], Hiroshi Harada[1, 2], Chitoshi Masuda[1, 2]

[1]Waseda University

2-8-26 Nishiwaseda, Shinjuku-ku, Tokyo, 169-0051, Japan
[2]National Institute for Materials Science (NIMS)
1-2-1 Sengen, Tsukuba Science City, Ibaraki, 305-0047, Japan
yokokawa.tadaharu@nims.go.jp

Abstract

Alloy development for turbine blade materials with higher temperature capabilities is crucial in order to improve the thermal efficiency in jet engine and gas turbine systems for mitigating CO_2 emission. The 6th generation Ni-base single crystal (SC) superalloy, TMS-238, developed by NIMS has a stable microstructure and 1120 °C temperature capability (1000 hours creep rupture life under stress of 137 MPa). In this study, we investigated the influence of alloying elements on microstructure and creep strength of TMS-238, and examined the possibility of further improvement of temperature capability of this alloy. TMS-238 was selected as a baseline alloy and we designed five derivative alloys (A : +1 wt% Mo, B : + 1wt% W, C : + 1 wt% Re, D : + 0.5 wt% Mo / +1 wt% W, and E : + 0.5 wt% Mo / + 1 wt% Re). Alloys labeled as A to E have longer creep rupture lives than TMS-238 when tested under the condition of 1150 °C / 137 MPa. On the other hand, rupture lives of alloys A to E when tested under the condition at 1000 °C and 900 °C and at higher steresses were shorter than TMS-238. It was clarified that fine TCP precipitates caused the shortening of the rupture life of these alloys. So far, TMS-238 is the best alloy with excellent phase stability and creep strength compared with the five derivative alloys investigated. Development of alloys beyond TMS-238 might be possible, if the TCP phase precipitation is suppressed under lower temperature and higher stress conditions but further investigation is needed to achieve this goal.

Keywords: Superalloys, Single Crystal, The 6th generation, TMS-238, Creep.

1. Introduction

Alloy development for turbine blade materials with higher temperature capabilities is crucial in order to improve the thermal efficiency in jet engine and gas turbine systems for mitigating CO_2 emission and saving fossil fuels [1]. In particular, higher temperature creep strengths are demanded because turbine blades are exposed to high temperature and high stress environments. The addition of rhenium (Re) to single crystal (SC) superalloys has received attention because of its contribution toward improvement of creep strength, however, the excessive addition of Re can also cause formation of topologically close packed (TCP) phases, which are detrimental to mechanical properties, when the alloy is exposed to elevated temperature environments [2]. The 4th generation SC alloys contain 2 – 3 wt% Ru to suppress TCP phases. The 5th generation SC alloy contains 5 – 6 wt% Ru and Re, and strengthened by

545

making dislocation network on the γ/γ' interface finer than those in 4th generation SC alloys. The 6th generation SC alloy contains decreased Mo and W, and increased Ta contents for improving oxidation and hot-corrosion resistances [3]. The 6th generation SC superalloy, TMS-238, developed by the National Institute for Materials Science (NIMS) has a stable microstructure and the best creep strength in the world (1120 °C temperature capability, under stress of 137 MPa and rupture life 1000 h) [4]. However, it is necessary to improve the temperature capability of TMS-238 for further improvement of thermal efficiency in jet engine and gas turbine systems. In this paper, we report the possibility of further improvement in temperature capability of TMS-238 by increased alloying additions.

2. Experimental

TMS-238 was selected as a baseline alloy and we made five derivative alloys. To improve the creep strength, we examined the addition of Mo, W and Re. Mo, W and Re contents were simply increase by 1 wt% in alloy A, B and C, respectively. On the other hand, in alloy D and E, Mo and W, and Mo and Re contents were increased, respectively. Here, Ru content of all the alloys were increased by 2 wt% to suppress TCP phases formation during high temperature exposure. The nominal compositions of alloys investigated in this study are listed in Table 1.

The alloys were vacuum-induction melted and cast to 10 mm diameter / 130 mm length bars using a directional solidification casting furnace. All samples were solution treated at 1345 °C for 20 h and aged at 1150 °C for 2 h and 870 °C for 20 h. Crystallographic orientation of the cast bars were examined by X-ray Laue method, and cast bars having longitudinal direction within 4° of <100> orientation were selected for creep test specimens. The creep tests specimens were 4mm in diameter and 22 mm in gauge length. Creep tests were conducted under following conditions: 900 °C / 392 MPa, 1000 °C / 245 MPa, 1150 °C / 137 MPa. The microstructure of all the crept specimens were investigated by scanning electron microscope (SEM), transmission electron microscope (TEM) and electron microprobe analyzer (EPMA). For TEM observation, discs were cut perpendicular to stress axis and ground to 90 μm thick and polished in a twin-jet electron-polisher at 45 V / 15 mA and at – 37 °C. The electrolyte consisted of 13 % perchloric acid, 80 % ethanol and 7 % glycerol. Furthermore, the phase stability of the alloys was investigated by quantitative measurements of amount of TCP precipitates.

Table 1: Nominal compositions of alloys investigated in this study (wt%, Ni bal.).

Alloys	Co	Cr	Mo	W	Al	Ta	Hf	Re	Ru	Increased elements
TMS-238	6.5	4.6	1.1	4.0	5.9	7.6	0.1	6.4	5.0	(Baseline)
A	6.5	4.6	**2.1**	4.0	5.9	7.6	0.1	6.4	**7.0**	+1Mo, 2Ru
B	6.5	4.6	1.1	**5.0**	5.9	7.6	0.1	6.4	**7.0**	+1W, 2Ru
C	6.5	4.6	1.1	4.0	5.9	7.6	0.1	**7.4**	**7.0**	+1Re, 2Ru
D	6.5	4.6	**1.6**	**5.0**	5.9	7.6	0.1	6.4	**7.0**	+0.5Mo, 1W, 2Ru
E	6.5	4.6	**1.6**	4.0	5.9	7.6	0.1	**7.4**	**7.0**	+0.5Mo, 1Re, 2Ru

3. Results and Discussions

Microstructures of alloy TMS-238 and alloys A to E before creep tests are shown in Figure 1. In this figure, fine and coherent γ/ γ' microstructures are observed in all specimens but no TCP precipitates at all.

Creep curves of TMS-238 and alloys A to E tested under the 1150 °C / 137 MPa condition are shown in Figure 2. It is found that the creep rupture lives of all the alloys A to E are longer than that of TMS-238. Particularly, the creep rupture life of alloy B and C are approximately three times as long as that of TMS-238.

The micrographs of TMS-238 and alloys A to E tested under the 1150 °C / 137 MPa condition are shown in Figure 3. There are no TCP precipitates in TMS-238 and alloy C. Figure 4 is the low magnification SEM image of alloy B, and the fraction of TCP precipitates are extremely low. Therefore, creep rupture lives of alloys B and C became longer than that of TMS-238 due to the effective strengthening by the W and Re additions, respectively. The creep rupture lives of alloy E, A and D are also longer than TMS-238 but due to the significant amount of TCP precipitates the improvements are limited.

In contrast, as shown in Figure 5, alloys A to E have obviously shorter creep rupture life than TMS-238 when tested under the 1000 °C / 245 MPa condition. To clarify the reason why creep rupture lives of alloys A to E were shorter than that of TMS-238, the microstructure of crept specimens were investigated by SEM observation, in Figure 6. There are no TCP precipitates in TMS-238. On the other hand, large amounts of fine TCP precipitates are observed in all the other specimens.

Figure 7 shows the relationship between area fraction of fine TCP precipitates and creep rupture life for TMS-238, alloy B and alloy C. Creep rupture lives of alloys under various conditions are plotted against the area fractions of TCP precipitates. It is shown that creep property is degraded with increase in the area fractions of TCP precipitates.

Finally, the TCP phase was investigated by transmission electron microscope (TEM). Figure 8 shows TEM bright field image of the crept specimen of alloy B tested under the 1000 °C / 245 MPa condition. The morphologies of precipitates are plate-like. The composition of the precipitate was examined by elemental mapping analysis with EMPA. The elemental mapping showed that the precipitate contained large amount of Ru and Re. Therefore, the TCP phase in alloy B might be δ phase [5]. However, we need further experiments to determine it as δ phase.
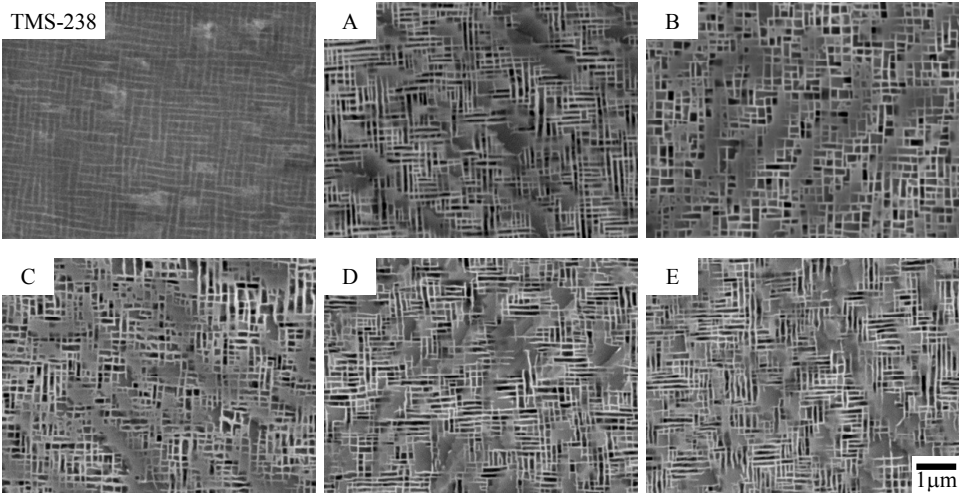
Figure 1: SEM micrographs of TMS-238 and alloys A to E before creep tests.
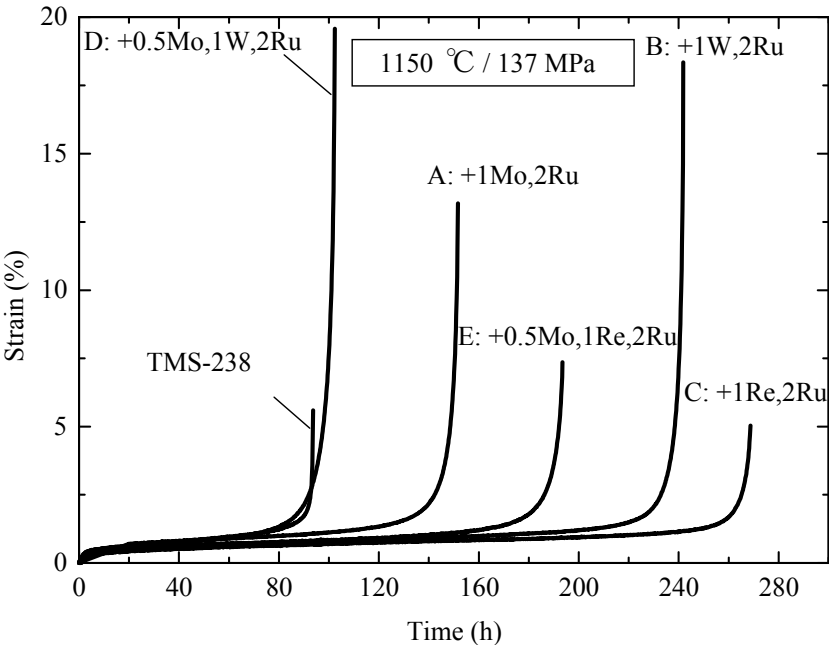
Figure 2: Creep curves of TMS-238 and alloys A to E tested under the 1150 °C /137 MPa condition.
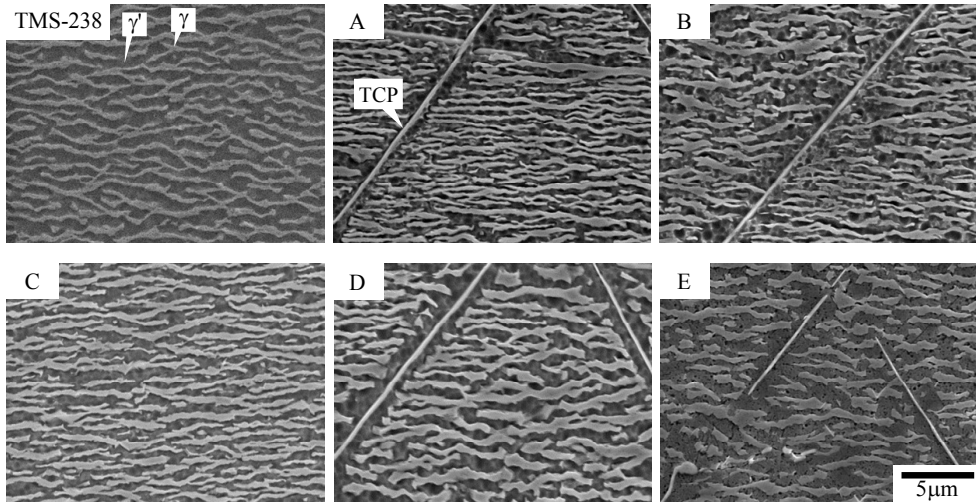
Figure 3: SEM micrographs of TMS-238 and alloys A to E tested under the 1150 °C / 137 MPa condition.
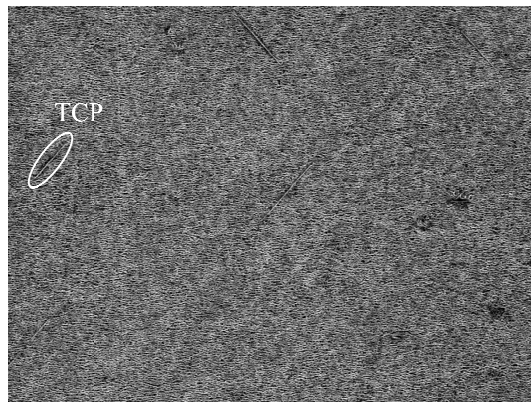

Figure 4: The low magnification SEM micrograph of alloy B tested under the 1150 °C / 137 MPa condition.
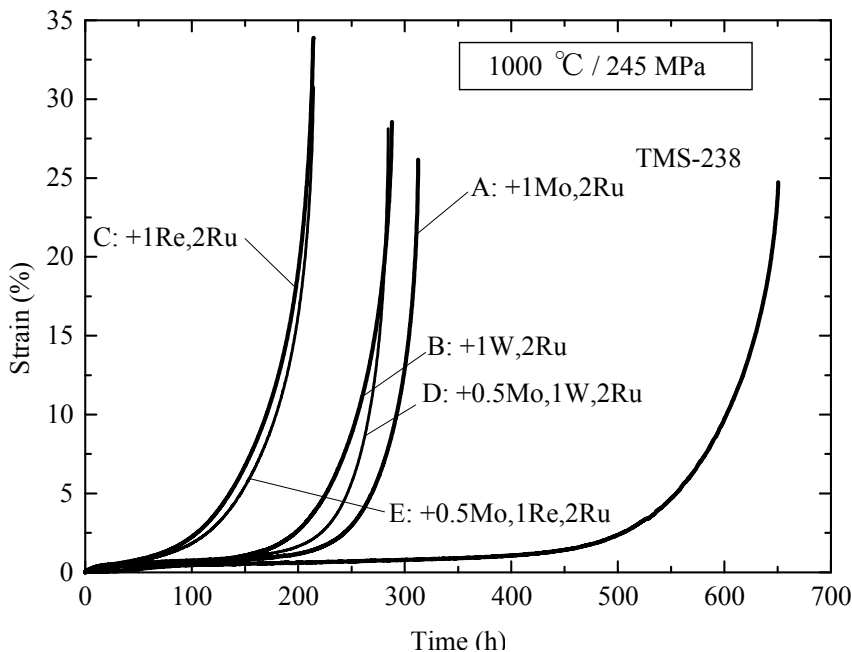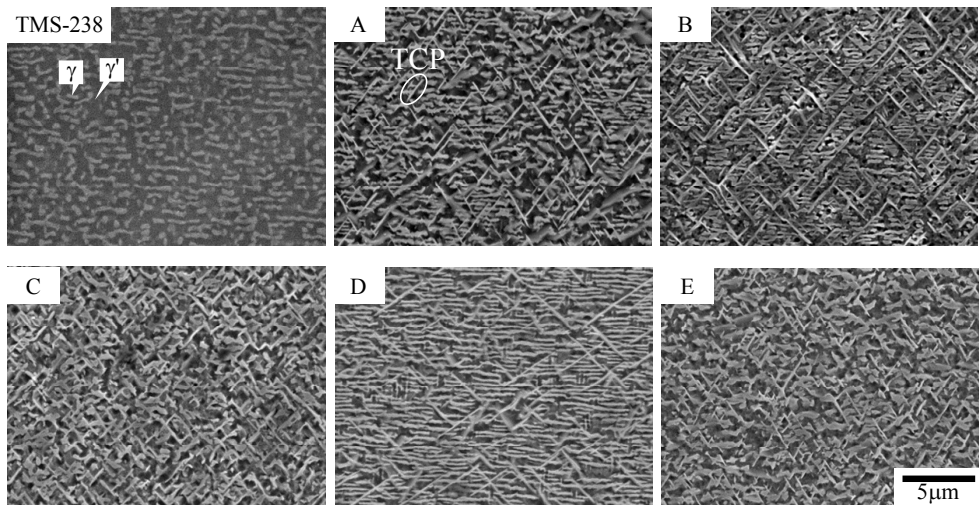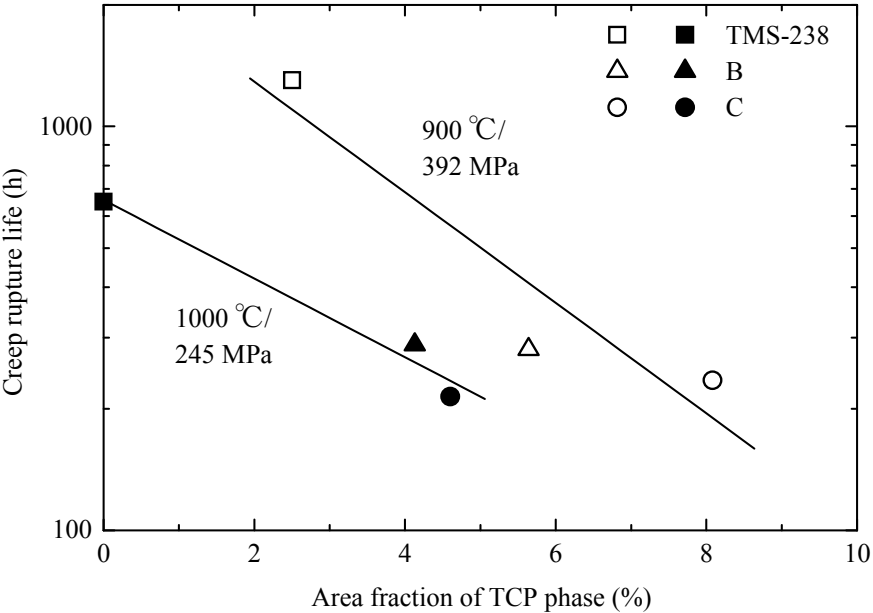
Figure 5: Creep curves of TMS-238 and alloys A to E tested under the 1000 °C /245 MPa condition.

Figure 6: SEM micrographs of TMS-238 and alloys A to E tested under the 1000 °C / 245 MPa condition.

Figure 7: Relationship between area fraction of TCP precipitates and creep rupture life for TMS-238, alloys B and C.
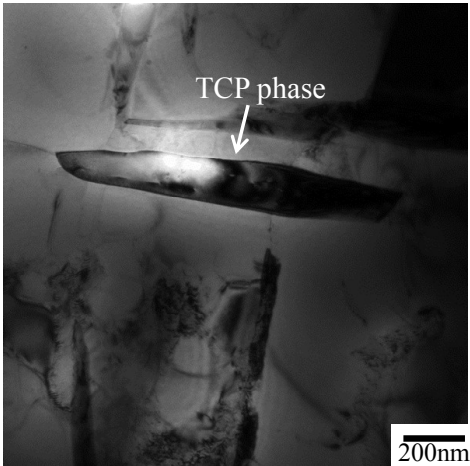
Figure 8: TEM bright field image of alloy B tested under the 1000 °C / 245 MPa condition.

4. Conclusions

The improvement of the temperature capability was attempted by the addition of strengthening elements such as Mo, W and Re with a phase stabilisation element, Ru, to the 6th generation single crystal superalloy, TMS-238. The five TMS-238 derivative alloys, alloys A to E were investigated and their microstructure and creep properties were compared with TMS-238. It was found that almost all the derivative alloys, especially alloy C strengthened by Re addition and phase stabilised by Ru, have longer creep rupture life compared with TMS-238 when tested under the 1150 °C / 137MPa condition. However, when tested under lower temperature and higher stress conditions, all the derivative alloys had shorter creep rupture life than TMS-238. It was clarified that fine TCP precipitates were formed in crept specimens, which caused the shortening of creep rupture life. Consequently, TMS-238 is the best alloy with excellent phase stability and creep strength in all the creep test conditons compared with the five derivative alloys. Development of alloys beyond TMS-238 might be possible, if the TCP phase precipitation is suppressed under lower temperature and higher stress conditions but further investigation is needed to achieve this goal.

References
[1] A. Sato, H. Harada, A. C. Yeh, K. Kawagishi, T. Kobayashi, Y. Koizumi, T. Yokokawa and J. X. Zhang; *Superalloys 2008*, Seven-Springs, Pennsylvania, TMS (2008) pp. 131-138.
[2] T. Hino, Y. Yoshioka, K Nagata, H. Kashiwaya, T. Kobayashi, Y. Koizumi, H. Harada and T. Yamagata; *Materials of Advanced Power Engineering* (1998) pp. 1129-1137.
[3] T. Kobayashi, Y. Koizumi, T. Yokokawa and H. Harada; *Journal of the Japan Institute of Metals*, (2002). 66 (9) pp. 897-900.
[4] K. Kawagishi, A. C. Yeh, T. Yokokawa, T. Kobayashi, Y. Koizumi and H. Harada; *Superalloys 2012*, Seven-Springs, Pennsylvania, TMS (2012) pp. 189-195.
[5] Q. Feng, T. K. Nandy and T. M. Pollock; *Mater. Sci. Eng. A 373*, 2004, pp. 239-249.

Morphology of the γ' phase in a nickel-based single crystal superalloy NKH71 with several heat treatments

Takaoki TAKESHITA[1], Yoshinori MURATA[1], Nobuhiro MIURA[2], Yoshihiro KONDO[2], Yuhki TSUKADA[3] and Toshiyuki KOYAMA[3], Akira YOSHINARI[4]

1) Department of Physics, Materials, and Energy Engineering, Graduate School of Engineering, Nagoya University, Furo-cho, Chikusa, Nagoya 464-8603, Japan
   e-mail: murata@numse.nagoya-u.ac.jp
2) Mechanical and Machining System, Mechanical Engineering, National Defense Academy, Hashirimizu 1-10-20 Yokosuka, Kanagawa 239-8686, Japan
3) Department of Materials Science and Engineering, Graduate School of Engineering, Nagoya Institute of Technology, Gokiso-cho, Showa, Nagoya 466-8555, Japan
4) MITSUBISHI HITACHI POWER SYSTEMS, LTD.
   1-1, Saiwai-cho, 3-chome, Hitachi-shi, Ibaraki-ken, 317-0073, Japan

Abstract

NKH71 is a Re free nickel-based single crystal superalloy. The long-term creep strength of this alloy is superior to that of the practical used 2nd generation superalloy, CMSX-4, containing Re but the short-term creep strength is inferior to that of CMSX-4. This may be caused by high dislocation density in the initial microstructure of NKH71 before creep. In order to arrange the initial morphology of the γ' phase in NKH71, eight kinds of processes in heat treatment are carried out. After a series of heat treatments, the microstructure in each specimen is examined with scanning electron microscopy (SEM) and transmission electron microscopy (TEM). From SEM, it is found that the initial morphology of the γ' phase depends on both the cooling rate after solution heat treatment and temperatures of the 1st step aging. It is also found by TEM that this morphological change of the γ' phase affects directly dislocation density at the interface between the γ and γ' phases.

Keywords: nickel-based superalloy, heat treatment, morphology of gamma-prime, dislocation density, free energy

1. Introduction

In advanced fossil power plants, the combined system consisting of both a gas turbine and a steam turbine is adopted, and the thermal efficiency of this system depends considerably on the temperature capability of the heat-resistant alloys used for the gas turbine. Single crystal (SC) nickel-based superalloys are used in the turbine blades in gas turbines because of their high strength and outstanding oxidation resistance at elevated temperature.

The SC nickel-based superalloys are known to be strengthened by the precipitation of the γ' phase (Ni_3Al type $L1_2$ structure) in the γ phase of nickel solid solution. This γ' phase shows fine cubic shape and lines up tidily in the <001> direction in the γ phase by suitable heat treatments. However, it changes to a tabular shape so-called the raft structure under creep stress.

In nickel-based superalloys, a complicated heat treatment is employed, i.e, a combination of a solution heat treatment, 1st step aging and 2nd step aging. In the 1st step aging, the γ' phase is arranged in a proper shape and size, and then both the composition and the volume fraction of the γ' phase are arranged in the 2nd step aging. The conditions of these heat treatments depend on the alloy composition, and one of the most important points is to find the suitable heat treatment for the alloy [1,2].

In this research, the single crystal nickel-based superalloy, NKH71, developed as a Re free alloy is used. This alloy shows creep strength equivalent to the 2nd generation SC alloy which contains 3%Re and is used practically. However, the creep strength of NKH71 in a short-term shows low compared with that of the 2nd generation SC alloy [3]. This is probably because NKH71 alloy has higher dislocation density before creep than the 2nd generation SC alloy, and hence the morphology of the γ' phase changes in the early stage of creep, resulting in low creep strength in a short-term [4].

The purpose of this study is to investigate a suitable heat treatment condition, in order to decrease the dislocation density before creep.

2. Experimental procedures

Table 1 Chemical composition of NKH71(wt%).

Cr	W	Mo	Ta	Ti	Al	Ni
12.19	7.75	0.49	5.78	1.21	4.98	Bal

Chemical composition of NKH71 is shown in Table 1. A single crystal of this alloy was grown to the direction of [001] and the size is $\phi 15$ in diameter and 160mm in length. Samples of about 3mm thickness were cut from the SC at perpendicular to [001], and they were heat treated systematically in the conditions, as shown in Table 2 and Fig.1.

In order to arrange the morphology of the γ' phase in NKH71, two kinds of processes in heat treatment are carried out. The one is the process that the sample is aged directly from the solution temperature to the 1st step aging temperature (sample A,B,C and D), and the other is the process that the sample is air-cooled from the solution temperature to the room temperature before the 1st step aging (sample E,F,G and H). Except for these different procedures, the other heat treatment conditions are the same in the two kinds of processes. In both processes, temperature of 1st step aging varies 1125ºC, 1100ºC, 1075ºC or 1050ºC, although the temperature of the 2nd step aging is constant at 871ºC.

After a series of heat treatments, each specimen sectioned parallel to the (001) is examined with scanning electron microscopy (SEM) and transmission electron microscopy (TEM). Specimens for the SEM observation were etched electrolytically with a supersaturated oxalic

acid aqueous solution. Foils suitable for TEM observation were prepared by electropolishing with a 10% perchloric acid-alcohol solution using a twin jet polisher.

The TEM observations were carried out with two different **g**-vectors on the same region in oder to observe all dislocation [5].

Table2 Heat treatment conditions employed in this study.

Sample	Solution	1st Step aging	2nd Step aging
A	1300°C/28.8ks, cooling(0.12°C/s)	1125°C/14.4ks, cooling(0.06°C/s)	871°C/72ks,A.C
B	1300°C/28.8ks, cooling(0.12°C/s)	1100°C/14.4ks, cooling(0.06°C/s)	871°C/72ks,A.C
C	1300°C/28.8ks, cooling(0.12°C/s)	1075°C/14.4ks, cooling(0.06°C/s)	871°C/72ks,A.C
D	1300°C/28.8ks, cooling(0.12°C/s)	1050°C/14.4ks, cooling(0.06°C/s)	871°C/72ks,A.C
E	1300°C/28.8ks,A.C.	1125°C/14.4ks, cooling(0.06°C/s)	871°C/72ks,A.C
F	1300°C/28.8ks,A.C	1100°C/14.4ks, cooling(0.06°C/s)	871°C/72ks,A.C
G	1300°C/28.8ks,A.C	1075°C/14.4ks, cooling(0.06°C/s)	871°C/72ks,A.C
H	1300°C/28.8ks,A.C	1050°C/14.4ks, cooling(0.06°C/s)	871°C/72ks,A.C
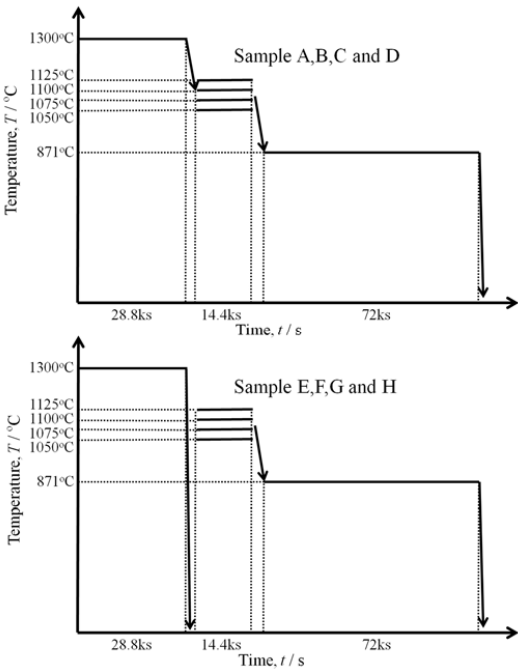
Fig.1 Schematic illustrations showing the heat treatment conditions employed in this study.

3. Experimental results and discussion

3.1. Microstructure observation by SEM

Figure 2 shows SEM images of samples A,B,C and D aged directly from the temperature of solution heat treatment to the 1st step aging temperature. In the figure, the γ' phase does not form cubic shape irrespective of the aging temperature, indicating that the coherency of the interface of γ/γ' phase is broken. The average grain sizes of the γ' phase in Fig.2 are (a)1.09μm,(b)0.86μm,(c)1.01μm and (d)0.98μm, respectively, and no difference in the γ' morphology is observed in spite of the 1st step aging temperature.

Figure 3 shows SEM images of samples E,F,G and H which are air-cooled from the temperature of solution heat treatment to room temperature before the 1st step aging. In this case, the γ' phase shows cubic shape and arranges in order along <001>. The average grain sizes of the γ' phase in Fig.3 are (a)0.59μm,(b)0.47μm,(c)0.42μm and (d)0.36μm, respectively. It is found that the size of the γ' phase increases with increasing temperature of the 1st step aging.
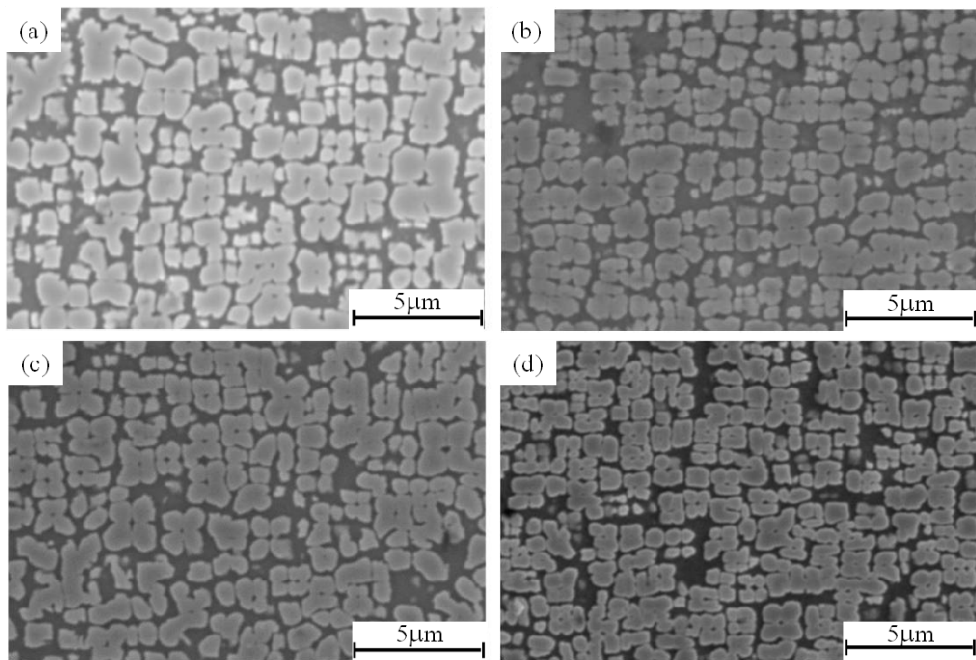
Fig.2 SEM images showing the γ' morphology in NKH71 alloy,(a) sample A,(b) sample B,(c) sample C and (d) sample D. Temperatures of the 1st step aging are (a) 1125ºC,(b) 1100ºC,(c) 1075ºC and (d) 1050ºC.
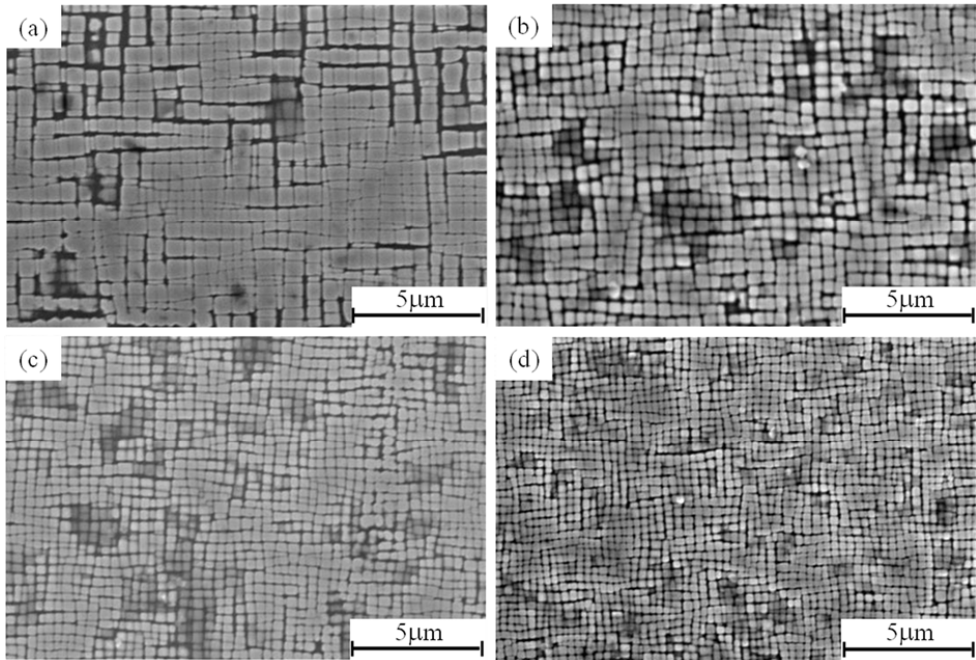
Fig.3 SEM images showing the γ' morphology in NKH71 alloy,(a) sample E,(b) sample F,(c) sample G and (d) sample H. Temperatures of the 1st step aging are (a) 1125ºC,(b) 1100ºC,(c) 1075ºC and (d) 1050ºC.

Comparing the results of Fig.2 to Fig.3, it is found that the morphology of the γ' phase depends on the process of solution heat treatment before the 1st step aging and that air cooling after solution heat treatment is needed to form the cubic γ' phase. Furthermore, it is implied that fine γ' phase is formed during air-cooling from the solution temperature and grows during the 1st step aging.

The cubic shape of the γ' phase is a result that elastic strain energy becomes a comparable order of magnitude to the chemical interfacial energy. Therefore, the result observed in Fig.2 shows that the γ' phase has no effect of the elastic strain energy because of the break in the lattice coherency between the γ and γ' phases.

3.2. Microstructure observation by TEM

Figure 4 shows TEM micrographs of sample A, sample E and sample H. As shown in Fig.1, sample A is prepared by the 1st step aging directly from the solution temperature, and samples E and H are prepared by air-cooling from the solution temperature before 1st step aging. As is found in Fig.2, the γ' phase grows considerably, and hence coherency between the γ and γ' phases is broken. As a result, many dislocations are introduced into the γ/γ' interface. In fact, dislocation density of sample A is $\rho=1.0\times10^{14}$m^{-2}. On the other hand, as shown in Figs.4(b)

557

and (c), the γ' phase keeps cubic shape in samples E and H, although a few dislocation is introduced in sample E. Dislocation density of sample E and sample H is $\rho=8.4\times10^{13}m^{-2}$ and $\rho=6.9\times10^{12}m^{-2}$, respectively.
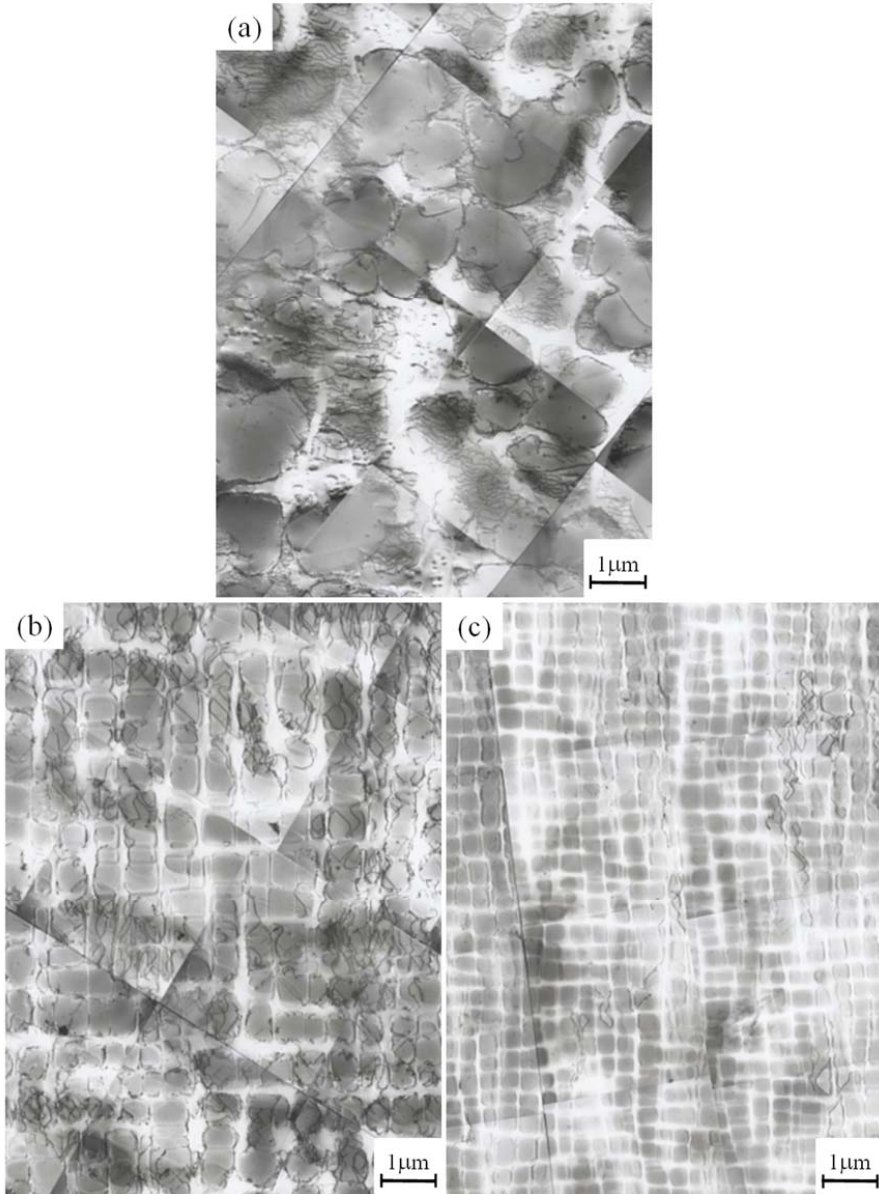
Fig.4 TEM images showing the γ' morphology and dislocations in NKH71 alloy,(a) sample A,(b) sample E and (c) sample H.
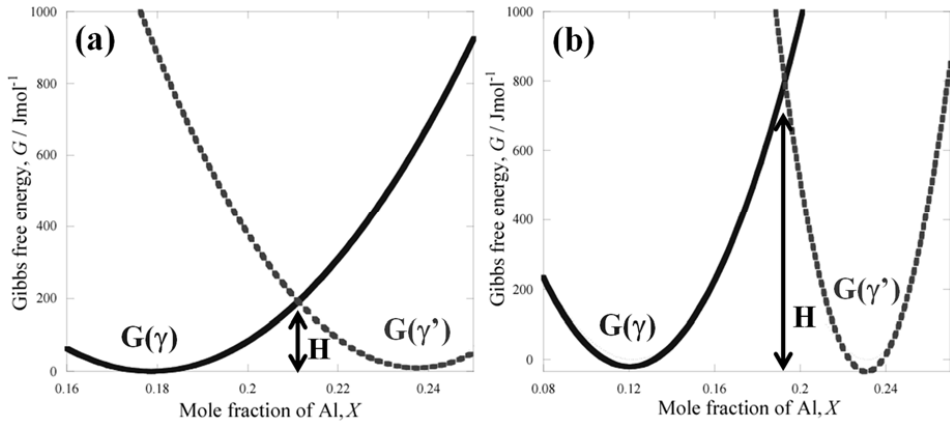
Fig.5 Gibbs free energy curves of Ni-Al binary system at (a)1200ºC, (b)750ºC.

3.3. Origin of the morphological change depending on the process

As shown in Fig.2 and Fig.3, the size of the γ' phase depends on heat treatment processes. This can be explained using the Gibbs free energy of the γ and γ' phases, which forms a double well curve [6], as shown in Fig.5. This can be drawn using thermodynamic data base of Thermo-Calc. Figure 5(a) corresponds to sample A, in which the nucleation of the γ' phase occurs at high temperature. When temperature is high, the height of the potential (H) becomes low. In such a case, driving force for the nucleation becomes small, and hence the number of nucleus of the γ' phase decreases, resulting in the formation of a large γ' phase, as shown in Fig.4(a). On the other hand, in samples E and H, which are air-cooled from solution treatment temperature to room temperature before the 1st step aging, the γ' phase becomes fine, because nucleation of the γ' phase occurs at lower temperature. In this case, the potential height of Gibbs free energy becomes high as shown in Fig5(b), and driving force for the nucleation becomes large. As a result, the γ' phase becomes small, as shown in Fig.4(c).

4. Conclusion

In order to reduce the dislocation density in NKH71 after the solution heat tratment, various heat treatments were performed. After the heat treatments, SEM and TEM observation were carried out. The obtained conclusion is as follows.

The process that air-cooling from solution temperature to room temperature is needed to obtain fine and cubic γ' phase which forms as orderly line along <001> direction. In such a case, there is few dislocation between the γ and γ' phases. When the process that the direct aging from solution temperature to 1st step aging temperature is employed, the γ' phase becomes large and granular shape. In this case, coherency between the γ and γ' phases is broken, resulting in a large number of dislocations in the interface of the two phases.

559

Reference

[1] G.E. Fuchs, Solution heat treatment response of a third generation single crystal Ni-base superalloy, *Materials Science and Engineering A* 300 52-60 (2001).

[2] Y. Jinjiang, S.Xiaofeng, Z.Nairen, J.Tao, G.Hengrong, H.Zhuangqi, Effect of heat treatment on microstructure and stress rupture life of DD32 single crystal Ni-base superalloy, *Materials Science and Engineering A*, 460-461, 420-427, (2007).

[3] Y. Murata, R. Hashizume and A. Yoshinari, N. Aoki, M. Morinaga and Y. Fukui, Alloying Effects on Surface Stability and Creep Strength of Nickel Based Single Crystal Superalloys containing 12mass%Cr, *Superalloys2000*, 285-294, (2000).

[4] Y. Kubo, *Collected Abstracts of the 2011 Autumn Meeting of the Iron and Steel Institute of Japan*, pp.1002, (2011).

[5] N. Miura, F. Tanaka, K. Kurita, Y. Kondo and T. Matsuo, DISLOCATION SUBSTRUCTURE AT γ/γ' INTERFACE OF SINGLE CRYSTAL NICKEL-BASED SUPERAOLLY, CMSX-4, CREPT AT 1273K, 250Mpa, *Materials for Advanced Power Engineering 2006*, 465-474, (2006).

[6] Y. Tsukada, Y. Murata, T. Koyama and M. Morinaga, Phase-Field Simulation on the Formation and Collapse Processes of the Rafted Structure in Ni-Based Superalloys, *Materials Transactions*, 49, 484-488, (2008).

APPLICATION OF EQ COATING TO EB-PVD TBC

K. Matsumoto, K. Kawagishi and H. Harada

National Institute for Materials Science, 1-2-1 Sengen, Tsukuba-shi, Ibaraki 305-0047, Japan
email: matsumoto.kazuhide@nims.go.jp

Abstract

To prevent the formation of Secondary Reaction Zone (SRZ) in the log-time high-temperature exposure of the turbine blades, thermodynamically equilibrium phase such as gamma-prime phase of the substrate is use as an oxidation-resistant bond coat. The previous study clarified that this equilibrium (EQ) coating showed excellent interface stability and it didn't degrade mechanical strength due to the SRZ formation.

In this study, Thermal Barrier Coating (TBC) life test of Electron Beam-Physical Vapour Deposition (EB-PVD) ceramics coated EQ coating was investigated with other conventional MCrAlY coatings. The 4th and 5th generation superalloys were used for substrates. About 150 μm thick of EQ coating, conventional NiCoCrAlY and CoNiCrAlY coating were formed by Low Pressure Plasma Spray (LPPS) and High Velocity Oxygen Fuel (HVOF) on the substrates. After polishing the surface of deposited bond coat, specimens were pre-oxidized in the EB-PVD chamber in 0.2 Pa of oxygen partial pressure. 150 μm thick of YSZ was deposited by EB-PVD on the pre-oxidized bond coat, following the pre-oxidation. Samples were heat treated cyclically in an electric furnace at 1135 °C with 1 h cycles. Fast cooling rate was obtained by air blow with each cooling cycle. Interrupted and failed samples were observed by SEM and EPMA.

The results are as follows. Spraying process and conditions are important for EQ bond coating in TBC formation. LPPS EQ bond coat in TBC system has much better thermal cycle spallation life than HVOF EQ bond coat. LPPS EQ bond coat meeting Ni-base SC superalloy of 4th generation TMS-138A had excellent performance of TBC spallation life, achieved 4 times longer than conventional MCrAlYs and diffusion bond coats. And recycling of TBC with EQ bond coat will be discussed.

Keywords: EQ bond coat, equilibrium, thermal barrier coating, EB-PVD, thermal cycle characteristics.

1. Introduction

Applying the conventional coatings such as Pt-Al or MCrAlY to advanced generation single-crystal superalloys, a harmful layer so called SRZ is formed at the interface of coating and substrate [1-3] due to the interdiffusion during the high temperature exposure and the oxidation resistance of the coating layer and the mechanical properties of the substrates result in degradation [4]. Various techniques such as "diffusion barrier" [2, 5-7] and "carburization" [3] have been employed to minimize interdiffusion between the bond coat and the substrate, but these techniques still have some problems in complicated manufacturing process and long-time exposure in high-temperature.

In our previous research [8-12], a new coating system, "EQ coating" has been developed. In this system, stable phases in equilibrium thermodynamically with substrate such as γ' phase are used as coating materials, and SRZ formation between the coating and the substrate is suppressed. Interdiffusion is minimized because chemical potentials of alloying elements in the substrate and coating in equilibrium state are equal. Based on Rene-N5 superalloy, EQ coating, named TMBC-1, was developed.

In this study, TMBC-1 was applied to bond coat material of EB-PVD TBC with YSZ top coat material. The LPPS and HVOF were used as bond coat processes and thermal cycle characteristics were investigated. And also, EB-PVD TBC with LPPS TMBC-1 was compared with conventional MCrAlY bond coats in thermal cycle characteristics

2. Experimental Procedure

The substrate material was 4th generation single crystal superalloy TMS-138A developed by NIMS. The top coat material was 8YSZ (8wt% Y_2O_3-ZrO_2) and bond coat materials were TMBC-1 (EQ coating), NiCoCrAlY and CoNiCrAlY. Table 1 shows compositions of substrate and bond coat materials.

Table 1 Compositions (wt. %) of the superalloy substrate and the bond coats

	Co	Cr	Al	Mo	W	Ta	Re	Ru	Hf	Y	Ni
TMS-138A	5.8	3.2	5.7	2.8	5.6	5.6	5.8	3.6	0.1	—	balance
TMBC-1	6.2	4.0	8.1	1.0	4.5	9.9	—	—	0.4	0.1	balance
NiCoCrAlY	21.5	17.0	12.4	—	—	—	—	—	—	0.7	balance
CoNiCrAlY	38.5	21.0	8.0	—	—	—	—	—	—	0.5	balance

TMBC-1, γ' EQ coating, was designed for 2nd generation superalloy Rene'N5. Rene'N5 is practically used and has better oxidation resistance than 4th and 5th generation superalloy. Regarding the cost and its low diffusion rate, Re was removed from γ' phase composition in the designed coating. And then, 0.1wt% of yttrium was added to improve the oxidation resistance.

Table 2 shows bond coating process and 6 kinds of specimens prepared. Bond coating was carried out on one side of 10mm diameter plate specimen using LPPS and HVOF with process conditions with alumina blasting, arc cleaning in LPPS, substrate pre-heating and so on. Spraying powders of NiCoCrAlY and CoNiCrAlY were used and EQ spraying powders were prepared for LPPS and HVOF respectively. Then we got 6 kinds of specimens.

Table 2   Bond coating process and 6 kinds of specimen

LPPS	HVOF
1. Alumina blasting 　 #60 particle (200μm) 2. Arc cleaning 3. Substrate pre-heating：600℃ 4. Plasma gas：Ar　45 NLPM 　　　　　　　H2　8 NLPM 　 Carrier gas：　Ar　2 NLPM 5. Pass: 4 pass Spraying powders 　NiCoCrAlY: NI191(PRAXAIR) 　CoNiCrAlY: AMDRY9951(SULZER) 　EQ: Prepared for LPPS	1. Alumina blasting 　 #60 particle (200μm) 2. Substrate pre-heating：130℃ under 3. Fuel：20.8 L/h　O2：898 NLPM 4. Pressure：8 bar 5. Carrier gas: N2　2 NLPM 6. Pass: 16 pass Spraying powders 　NiCoCrAlY: NI191(PRAXAIR) 　CoNiCrAlY: AMDRY9954(SULZER) 　EQ: Prepared for HVOF

YSZ top coat was formed using EB-PVD equipment developed by NIMS [13].
After polishing of bond coat surface, pre-oxidation and YSZ top coating were carried out.
Thermal cycle testing was carried out using electric furnace with conditions of 1 hour exposure to 1135 ℃ and 1 hour cooling. Specimens automatically move in and out of the electric furnace. The spallation life was defined that spallation occurred more than 50% of top coat area.
The bond coat microstructure and TGO (Thermal Grown Oxide) observation of interrupted specimens during thermal cycle testing were analysed by Scanning Electron Microscope (SEM). The concentration mapping was analysed by Electron Probe Micro Analyzer (EPMA).

3. Results and Discussion

Fig.1 shows the result of thermal cycle testing about TBCs with EQ bond coat and MCrAlY bond coat formed by LPPS and HVOF respectively. Spallation lives of MCrAlY bond coat of both LPPS and HVOF were shorter than that of EQ bond coat. The TBC with TMBC-1 (EQ) bond coat formed by LPPS had the longest spallation life.
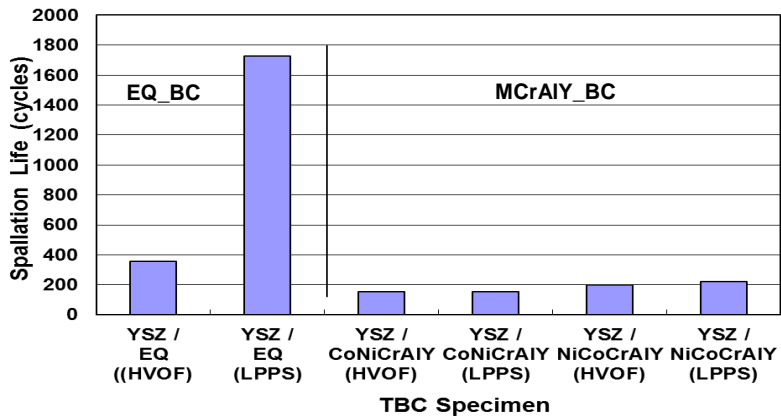
Fig.1   Result of Thermal Cycle Testing

As TBC spallation occurs by bond coat oxidation, as-sprayed EQ bond coat microstructure was investigated shown in Fig.2. LPPS EQ bond coat has less pores and oxygen was not detected. On the other hand, HVOF EQ bond coat has a lot of pores and oxygen was detected.
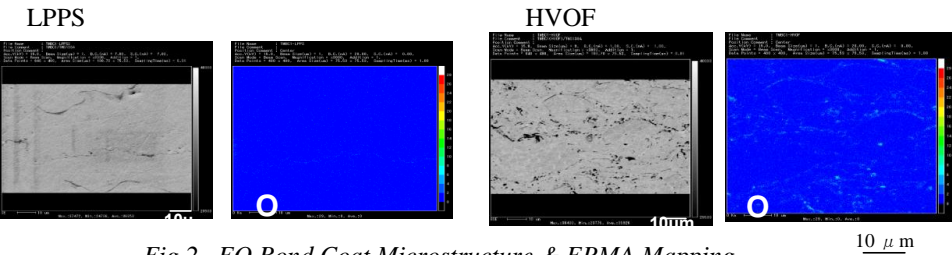
Fig.2   EQ Bond Coat Microstructure & EPMA Mapping

Then, pore areas of EQ bond coat was measured. Fig.3 shows the image processing result of pore area enlarged 3000amplitude using optical microscope.
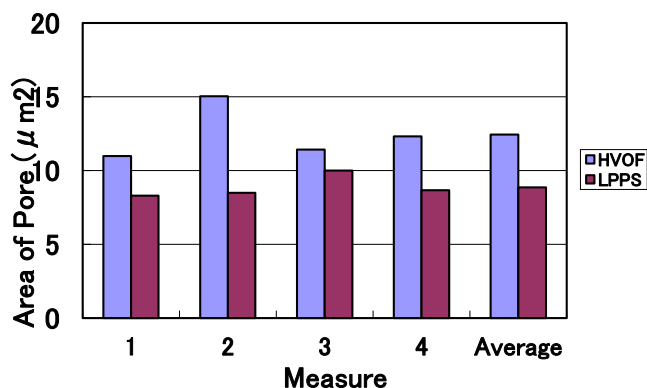
Fig.3   Image Processing Result of EQ Bond Coat Pore Area

The average pore area of LPPS bond coat is less than that of HVOF. This suggests that HVOF EQ bond coat has more oxidizing tendency during thermal cycle testing.

The particle size distribution of EQ spray powder for LPPS and HVOF were measured by laser diffraction technology shown in Fig.4. The average powder size of LPPS is 20 μm and that of HVOF is 40 μm. And also, the particle size of conventional MCrAlYs of both LPPS and HVOF is 40 μm. This suggests that there is the relationship between particle size and pore existence of bond coat.
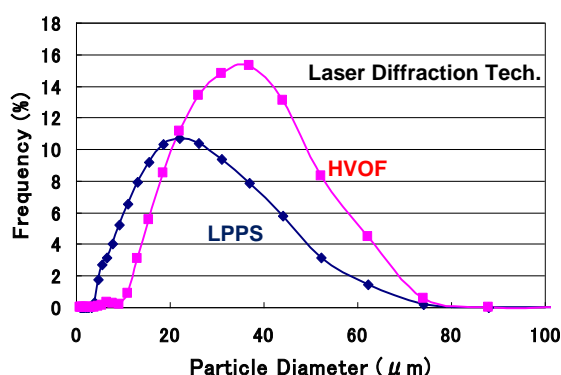
Fi.4   Particle Size Distribution of EQ Spray Powder

Fig.5 shows spallation lives of TBCs with various bond coats and interrupted specimens shown as dotted line. In order to clarify TMBC-1 performance, TGO growth was investigated. Fig.6 shows the near TGO microstructure of interrupted TBC specimen with NiCoCrAlY bond coat interrupted at 50, 200 and 300 cycles. The TGO thickness increased with thermal

cycle increasing. At 300 cycles, cracks initiate and propagate along the TGO and bond coat interface. The microstructure of CoNiCrAlY bond coat is the same as NiCoCrAlY.
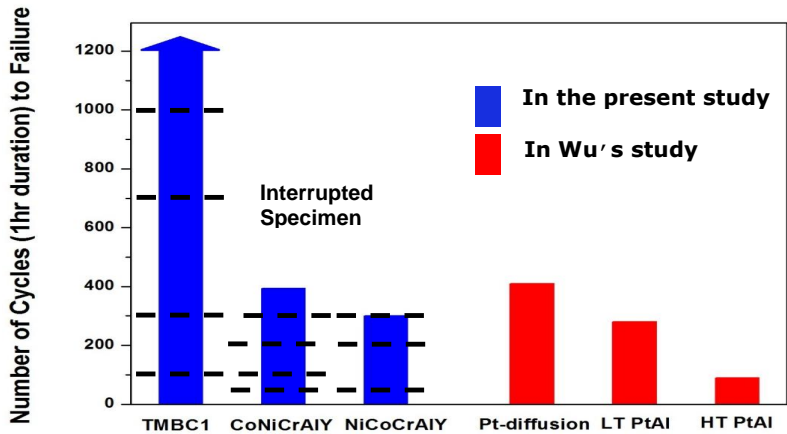
Fig.5   Spallation Lives of TBCs with Various Bond Coats
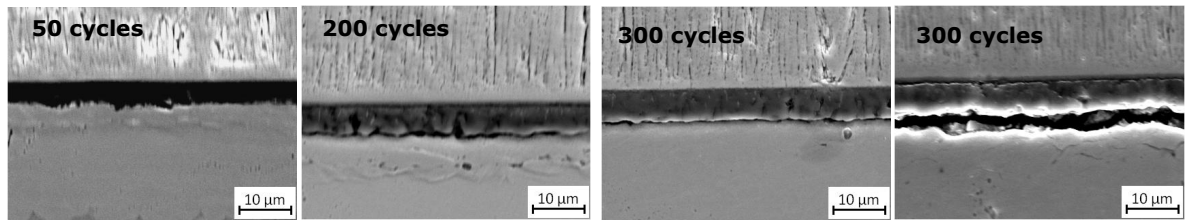
Fig.6   Interrupted TBC Specimen with NiCoCrAlY Bond Coat

Fig.7 shows the microstructure of TBC specimen with TMBC-1(EQ) bond coat interrupted at 100, 300, 700 and 1000 cycles. Cracks initiate and propagate along YSZ top coat and TGO interface. Then, there are some TGO protrusions into the bond coat.
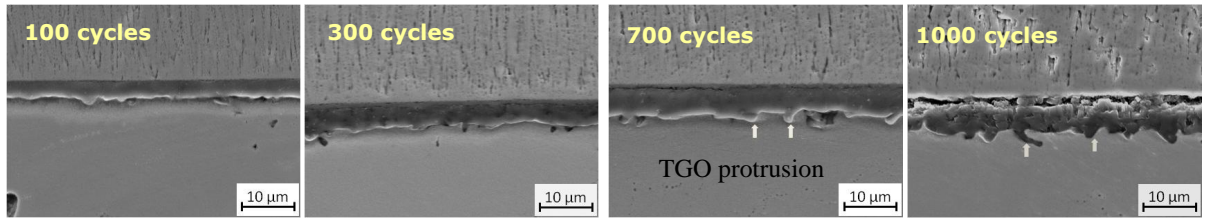
Fig.7   Interrupted TBC Specimen with TMBC-1 (EQ) Bond Coat

Fig.8 shows TGO thickness change with thermal cycles about 3 kinds of bond coat and spallation life cycles shown as dotted lines.

TGO growth rate of TMBC-1 is smaller than that of MCrAlYs. This is the reason why TBC with EQ bond coat on TMS-138A has longer spallation life than conventional MCrAlY bond coat.

Spallation life of TBC with EQ bond coat was around 1700 cycles. That is 4 times longer than conventional MCrAlYs.
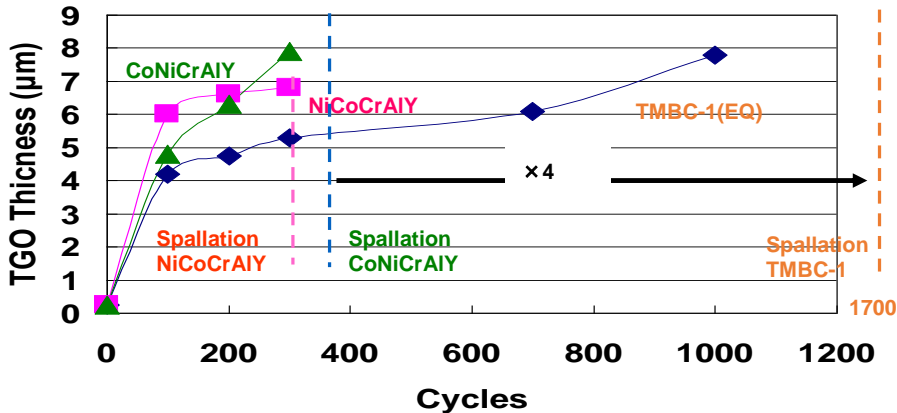
Fig.8   TGO Thickness Change and Spallation Life of 3 kinds of TBC

4. Conclusion

Spraying process and conditions are important for EQ bond coating in TBC formation.

LPPS EQ bond coat in TBC system has much better thermal cycle spallation life than HVOF EQ bond coat.

LPPS EQ bond coat meeting Ni-base SC superalloy (4th gen. TMS-138A) has excellent performance of TBC spallation life, achieved 4 times longer than conventional MCrAlYs and diffusion bond coat.

5. References

[1]   W. S. Walston, J. C. Schaeffer and W. H. Murphy: Superalloy 1996, (TMS, 1996) pp.9-18.
[2]   Y. Matsuoka, Y. Aoki, K. Matsumoto, A. Sato, T. Suzuki, K. Chikugo and K. Murakami, "The Formation of SRZ on a Fourth Generation Single Crystal Superalloy Applied with Aluminide Coating", Superalloy 2004 (2004), pp. 637-642.
[3]   I. E. Locci, R. A. Mackay, A. Grag and F. J. Ritzert, "Successful Surface Treatments for Reducing Instabilities in Advanced Nickel-Base Superalloys for Turbine Blades", NASA/TM-2004-212920, March (2004).

[4]   O. Lavigne, C. Ramusat, S. Drawin, P. Caron, D. Boivin and J. –L. Pouchou, "Relationships Between Microstructural Instabilities and Mechanical Behavior in New Generation Nickel-Based Single Crystal Superalloys", Superalloy 2004 (2004), pp.667-675.
[5]   T. Narita, S. Hayashi, H. Yukawa, M. Noguchi and M. Miyasaka, "Alloy Coating, Method for Forming the Same, and Member for High Temperature Apparatuses", U. S. Patent 6830827 (2004).
[6]   I. T. Spitzberg, R. Darolia, M. R. Jackson, J. C. Zhao and J. C. Schaeffer, "Diffusion Barrier Layer", U. S. Patent 6306524 (2001).
[7]   R. G. Wing, "Method of Aluminising a Superalloy", U. S. Patent 6080246 (2000).
[8]   H. Harada, A. Sato and K. Kawagishi, Japanese Patent Pending, Tokugan 2005-092542 (2005).
[9]   A. Sato, H. Harada and K. Kawagishi, "Development of New Bond Coat 'EQ Coating' System", Metall. Mater. Trans. A, Vol. 37, No. 2 (2006).
[10] K.Kawagishi, JOM (2008, 7), pp. 31-35
[11] K.Kawagishi, A.Sato and H.Harada: J. Japan Inst. Metals, Vol.70, No2 (2006), pp. 188 – 191
[12] K.Kawagishi, A.Sato, K.Matsumoto, T.Kobayashi, H.Harada, A.Aoki and M.Arai: J. Japan Inst. Metals, Vol.71, No2 (2007), pp. 226 – 232
[13] K.Matsumoto and H.Harada: Japanese Patent 4735813 (2011)

MICROSTRUCTURE OF γ' PRECIPITATES IN THE MIDDLE PART OF A FIRST STAGE HIGH PRESSURE TURBINE BLADE OF A Ni-BASED SUPERALLOY AFTER SERVICE AND FOLLOWING AGING

Nobuhiro Miura*, Shiho Yamamoto**, Yoshihiro Kondo***

*National Defense Academy, 1-10-20 Hashirimizu Yokosuka, Kanagawa 239-8686, Japan
nmiura@nda.ac.jp
**Tohoku University, Aoba-yama 02, Aoba-ku Sendai, Miyagi 980-8579, Japan
b4tm5341@s.tohoku.ac.jp
***National Defense Academy, 1-10-20 Hashirimizu Yokosuka, Kanagawa 239-8686, Japan
kondo@nda.ac.jp

Abstract

To estimate the temperature distribution, stress distribution, and stress direction in a blade in service, the morphology of γ' precipitates in Ni-based superalloy serviced in the middle part of a first stage high pressure turbine blade of a jet engine was investigated before and after aging. Microstructure observations of the blade were performed with a FE-SEM on both sides of (001) and (010) planes, from the interface between the coating layer and the matrix to near the internal cooling channel on the pressure and suction sides of the middle part. The blade was aged at 1273 K up to 2.52×10^6 s and the morphology of γ' precipitates was investigated on the aged specimens at the same portions as before aging. After serviced blade, most of the γ' precipitates remained cuboidal in shape at the internal cooling channel side. However, rafted γ/γ' structures formed as the parallel to (010) at the vicinity of coating layer of the pressure side. At the trailing edge, well aligned rafted γ/γ' structures formed as the parallel to (001) were appeared at all portions of the pressure and suction sides. After simple aging, the rafted γ/γ' structures appeared in the direction parallel to the blade surface at the vicinity of coating layer of the suction side, while at the leading and trailing edge of the pressure side, coarsening of the γ' precipitates were observed. At the internal cooling channel side of the all portions, the γ' precipitates were coarsened. From these results, the microstructural evidence indicates that the extremely complicated high stresses were loaded at the internal region of the middle part of the blade. Contrast to this, the uni-axial tensile stress perpendicular to the blade surface and/or multi-axial compressive stresses parallel to the blade surface is expected to act on the blade in service. And at the trailing edge, the tensile stress is subjected to the [100] direction.
Keywords: Turbine blade, Superalloy, Microstructure, γ' precipitates, Rafted γ/γ' structures

1. Introduction

Single crystal Ni-based superalloys have been used in jet engine 1st stage high pressure turbine (1st HPT) blades because of their excellent high-temperature creep rupture strength, ductility and the thermal fatigue properties [1–6]. It is well known that cuboidal γ' precipitates of single crystal Ni-based superalloys with a stress axis in the [001] orientation transform into plate-like precipitates perpendicular to the stress axis during high-temperature creep deformation [1,7–9]. It is currently impossible to measure the temperatures and stresses in blades in service because they rotate at high speeds and in high temperatures. Therefore, the attention has focused upon the evaluation of serviced blades based on the morphology of γ' precipitates [10,11].

In our previous work, the morphology of γ' precipitates in a single crystal of Ni-based superalloy serviced in the 1st HPT blade of a jet engine was examined to estimate the temperature and stress distributions in the blade in service. It was possible to estimate the in-service blade environment that the leading and trailing edges of the pressure side of the middle part and the leading edge of the suction side of the middle part were exposed to the highest temperature and stress conditions based upon a qualitative assessment of the γ' precipitate morphology. This microstructure evidence showed that the main stress of the in-service blade was not the centrifugal force by the rotation but the thermal stress

568

with cooling [10]. However, most of the suction side of the blade, γ' precipitates remained cuboidal in shape. This microstructural evidence suggests that the estimation of stress distribution was difficult, although the temperature was presumed to have been low. Moreover, these results and the estimations were only at the vicinity of blade surface regions.

To shelter the high temperature combustion gas up to the melting point of Ni, latest 1st HPT blades were covered with the Thermal Barrier Coating (TBC), and cooled the inside and the surface by air [4]. In this case, it was supposed that the differences between the coefficient of thermal expansion of the TBC and the metal matrix, and the temperature difference between the matrix of the blade surface and the vicinity of the internal cooling channels was generated the thermal stress which was caused by the large thermal gradient. However, the detail of the temperature and the stress distribution of internal portions of a blade in service had not been reported yet.

In our previous work, the cuboidal γ' precipitates in an as-heat treated single crystal Ni-based superalloy, CMSX-4, connected to three <100> directions and coarsened with simple aging at 1273 K. In contrast, by aging the CMSX-4 without stress after the interrupted creep test at the stages when the γ' precipitates were still cuboidal, the γ/γ' structure became rafted perpendicular to the creep-interrupted stress axis. And the extent of the rafted γ/γ' structure depends on the creep-interrupted strain [12, 13]. Based on these experimental results, the simple aging of serviced blade was expected to cause the formation of rafted γ/γ' structures corresponding to the stress history in service.

In this study, the morphological of γ' precipitates in a single crystal Ni-based superalloy serviced in the middle part of a 1st stage HPT blade of a jet engine was investigated before and after aging to estimate the temperature distribution, stress distribution, and stress direction in a blade in service.

2. Experimental procedure

A single crystal Ni-based superalloy was prepared in the form of a cooled 1st HPT blade by precision casting. The crystal growth direction of [001] in a blade was attained to the directional precision casting. After employing the defined solution treating and aging, coating was applied to the surface of the airfoil. The blade was in service for several thousand hours as the 1st HPT blade of an aircraft jet engine. The exact crystal orientation of the blade was determined by the X-ray Laue back-reflection technique.

The orientation between the [100] direction and the line from the leading edge to the trailing edge was 23 deg. The blade was cut parallel to the (001) plane at 22 mm from the tip by an electron discharge machine. The part was then cut parallel to the (100) plane (from the leading edge to the trailing edge) at 14mm intervals into four portions. Microstructure observations of the part of five partitions from the interface between the coating layer and the matrix to near the internal cooling channel were performed by field emission scanning electron microscope (SEM) on both sides of the (001) and (100) planes, and on both the suction and pressure sides. These specimens were then aged at 1273 K for 2.52 × 10^6 s, and SEM observations were performed again at the same locations. The specimens for SEM observation were prepared metallographically and electro-etched with a supersaturated oxalic acid aqueous solution.
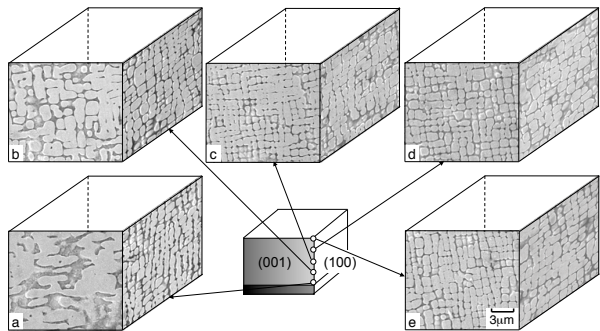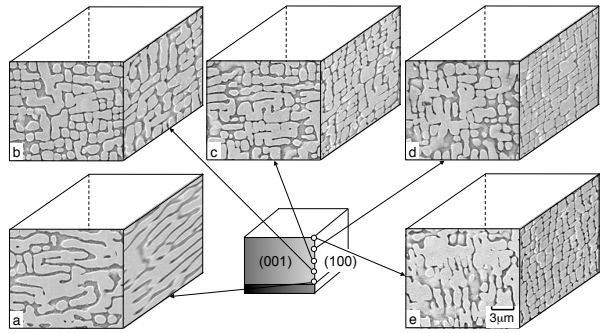

Fig.1. SEM micrographs of the pressure side of the leading edge: (a) the surface, (b) 0.1, (c) 0.2, (d) 0.4 mm and (e) the vicinity of internal cooling channel portion.

3. Discussion

3.1 Morphology of γ' precipitates in different portions of the serviced blade

3.1.1 Pressure side

SEM observation are performed on the middle part of the serviced blade cut parallel to the (001) and (100) planes.

SEM micrographs of the pressure side of the leading edge are shown in Fig.1.

In the portion of the interface between the coating layer and the matrix, that is the surface portion, coarsening of γ' precipitates is observed at the (001) plane, while in the (010) plane, some of the cuboidal γ' precipitates contact each other toward the [010] direction (Fig.1-(a)). In the portion 0.1 mm from the interface between the coating layer and the matrix (that is, the 0.1mm portion), the cuboidal γ' precipitates contact with each other toward the [100] and [001] directions in (001) and (100) planes respectively (Fig.1-(b)). The cuboidal γ' precipitates become rounded in other portions (Fig.1-(c)-(e)).

SEM micrographs of the pressure side of the 15mm part from the leading edge are shown in Fig.2.

In the surface portion, well-aligned rafted γ/γ' structures perpendicular to [010] direction are observed (Fig.2-(a)). In the 0.2, 0.3 and 0.5 mm portions, the adjacent γ' precipitates are in contact with each other toward the [100] and [001] directions (Fig.2-(b)-(d)). In the vicinity of internal cooling channel, that is the

Fig.2. SEM micrographs of the pressure side of the 15 mm part from the leading edge: (a) the surface, (b) 0.2, (c) 0.3, (d) 0.5 mm and (e) the vicinity of internal cooling channel portion.
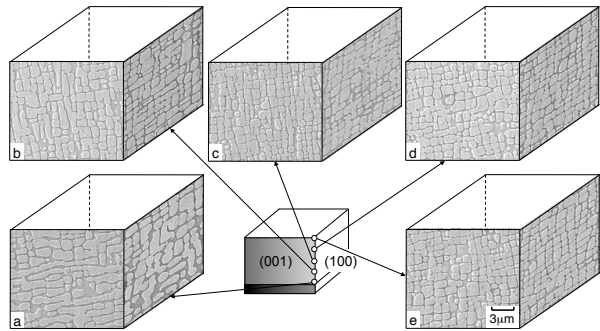

Fig.3. SEM micrographs of the pressure side of the 28 mm part from the leading edge: (a) the surface, (b) 0.2, (c) 0.4, (d) 0.6 mm and (e) the vicinity of internal cooling channel portion.
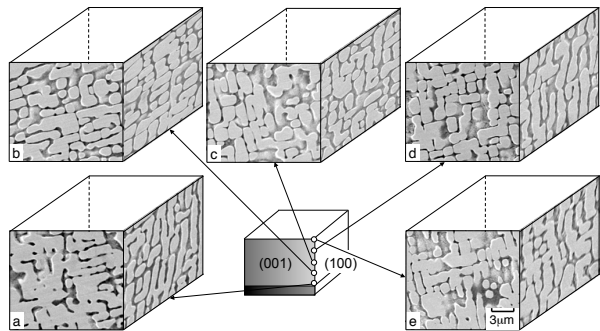

Fig.4. SEM micrographs of the pressure side of the trailing edge: (a) the surface, (b) 0.1, (c) 0.2, (d) 0.4 mm and (e) the vicinity of internal cooling channel portion.

cooling channel portion, the rafted γ/γ' structures start to collapse in the (001) plane (Fig.2-(e)).

SEM micrographs of the pressure side of the 28mm part from the leading edge are shown in Fig.3.

In the surface portion, some of the cuboidal γ' precipitates contact with each other along the (010) plane (Fig.3-(a) and (b)), while other portions, most of the cuboidal γ' precipitates still remain (Fig.3-(c)-(e)).

SEM micrographs of the pressure side of the trailing edge are shown in Fig.4.

In the surface, 0.4 mm and cooling channel portion, the rafted γ/γ' structures perpendicular to longitudinal direction, that is parallel to the (001) plane are observed (Fig.4-(a), (d) and (e)). On the contrary, the low completion rafted γ/γ' structures parallel to the (010) plane are observed in the 0.1mm portion (Fig.4-(b)). In the 0.2mm portion, coarsened γ' precipitates are observed (Fig.4-(c)).

3.1.2 Suction side

SEM micrographs of the suction side of the leading edge are shown in Fig.5.

In the surface side, a few γ' precipitates connected to parallel to the (010) plane in both planes (Fig.5-(a) and (b)). The other portions, the cuboidal γ' precipitates become rounded (Fig.5-(c)-(e)).

SEM micrographs of the suction side of the 15 mm part from the leading edge are shown in Fig.6.

The cuboidal γ' precipitates remain the same shape in all portions.

SEM micrographs of the suction side of the 28 mm part from the leading edge are shown in Fig.7.

In the surface side, the cuboidal γ' precipitates become rounded (Fig.7-(a) and (b)), while most of the cuboidal γ' precipitates still remain as well as the 15 mm part.

SEM micrographs of the suction side of the trailing edge are shown in Fig.8.

Morphology of γ' precipitates are drastically changed to the other parts. In the surface portion, the collapsed rafted γ/γ' structures can be observed at the (100) plane (Fig.8-(a)). At the (001) plane, the γ' precipitates are agglomerated coarse, the turning of the matrix obviously from the γ phase to the γ' precipitates occurs. In other portions, the rafted γ/γ' structures parallel to the (010) plane are observed. Particularly, completeness of the rafted γ/γ' structures is obtained in the vicinity of internal cooling channel (Fig.8-(b)-(e)).
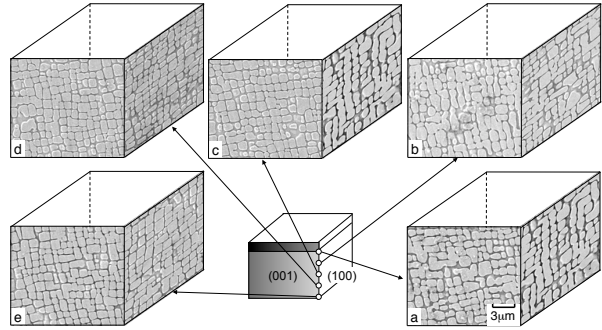

Fig.5. SEM micrographs of the suction side of the leading edge: (a) the surface, (b) 0.4, (c) 0.8, (d) 1.2 mm and (e) the vicinity of internal cooling channel portion.
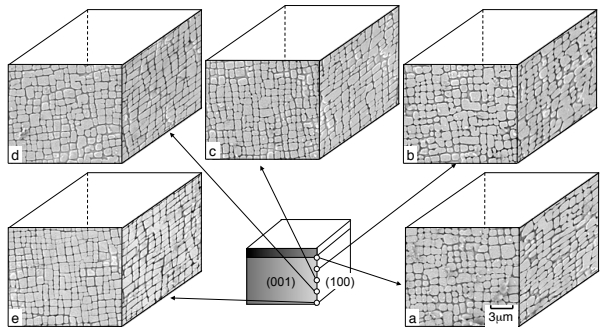

Fig.6. SEM micrographs of the suction side of the 15 mm part from the leading edge: (a) the surface, (b) 0.4, (c) 0.7, (d) 1.1 mm and (e) the vicinity of internal cooling channel portion.
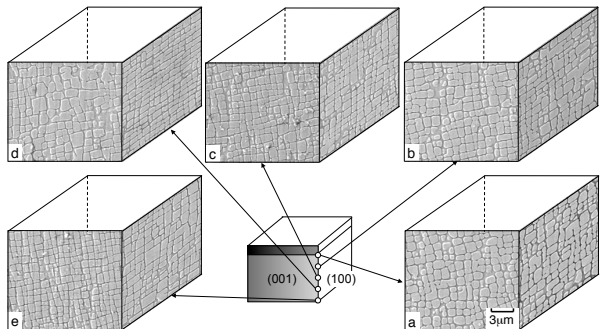

Fig.7. SEM micrographs of the suction side of the 28 mm part from the leading edge: (a) the surface, (b) 0.4, (c) 0.8, (d) 1.2 mm and (e) the vicinity of internal cooling channel portion.

571

In this way, the marked morphological changes in the γ' precipitates are observed at the each portions of the middle part of the blade. The morphological change of cuboidal γ' precipitates will be thought to result from the differences in the temperature and stress distributions and the stress directions in service.

3.2 Morphology of γ' precipitates in different portions of the serviced blade after simple aging

As mentioned above, the cuboidal γ' precipitates in an as-heat treated single crystal Ni-based superalloy, connected to three <100> directions and coarsened with simple aging at 1273 K. In contrast, by aging a single crystal Ni-based superalloy without stress after the interrupted creep test at the stages when the γ' precipitates were still cuboidal, the γ/γ' structure became rafted perpendicular to the creep-interrupted stress axis. And the extent of the rafted γ/γ' structure depends on the creep-interrupted strain [12,13]. Therefore, by subjecting the serviced blade to simple aging, the morphological change of γ' precipitates is expected due to the stress revel, distribution and directions. To estimate the stress distribution and the stress directions in a blade in service, the microstructure observed blade is aged at 1273 K, which is the estimated operating temperature in service for 2.52×10^6 s and the morphology of γ' precipitates is investigated on the blade at the same portions as before aging.

3.2.1 Pressure side
SEM micrographs of the aged blade on the pressure side of the leading edge are shown in Fig.9.
Remarkable coarsening of γ' precipitates are observed in all portions. Width of γ channels is expanded, compared with the same
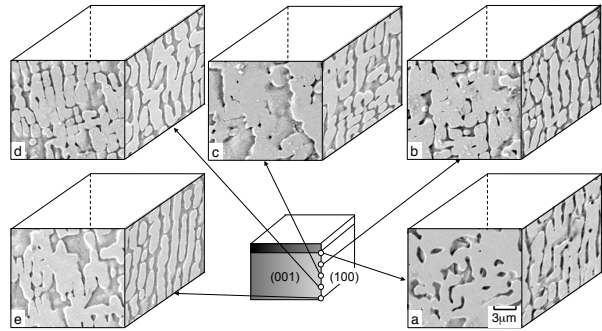

Fig.8. SEM micrographs of the suction side of the trailing edge: (a) the surface, (b) 0.1, (c) 0.2, (d) 0.4 mm and (e) the vicinity of internal cooling channel portion.
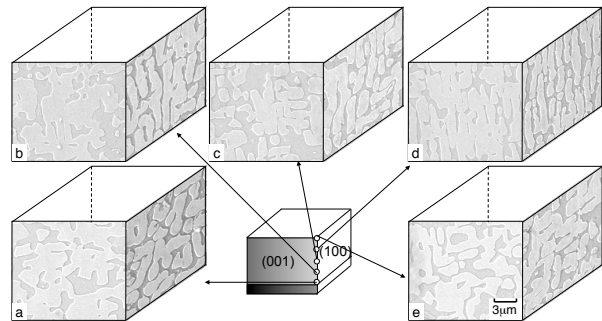

Fig.9. SEM micrographs of the aged blade on the pressure side of the leading edge: (a) the surface, (b) 0.1, (c) 0.2, (d) 0.4 mm and (e) the vicinity of internal cooling channel portion.
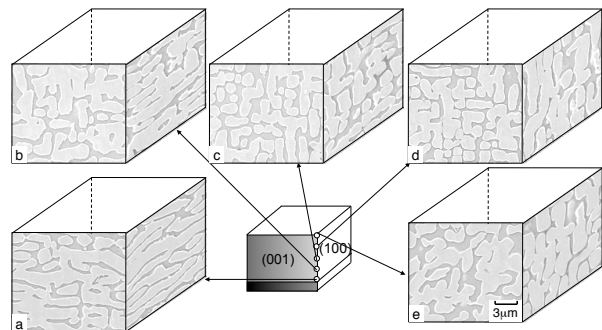

Fig.10. SEM micrographs of the aged blade on the pressure side of the 15 mm part from the leading edge: (a) the surface, (b) 0.2, (c) 0.3, (d) 0.5 mm and (e) the vicinity of internal cooling channel portion.

572

portion of the serviced blade (Fig.1). In the 0.1, 0.2 and 0.4mm portions, low completely rafted γ/γ' structures parallel to the (001) plane at the (100) plane are obtained.

SEM micrographs of the aged blade on the pressure side of the 15 mm part from the leading edge are shown in Fig.10.

Even after the aging, the surface portion hold in the well-aligned rafted γ/γ' structures as in the serviced (Fig.10-(a)). In the 0.2 mm portion, the rafted γ/γ' structures parallel to the (010) plane are observed, and the interface between the γ/γ' phase is straight (Fig.10-(b)). The other portions, the γ' precipitates are coarsened (Fig.10-(c)-(e)).

SEM micrographs of the aged blade on the pressure side of the 28 mm part from the leading edge are shown in Fig.11.

Coarsening of γ' precipitates are observed in all portions as well as the leading edge.

SEM micrographs of the aged blade on the pressure side of the trailing edge are shown in Fig.12.
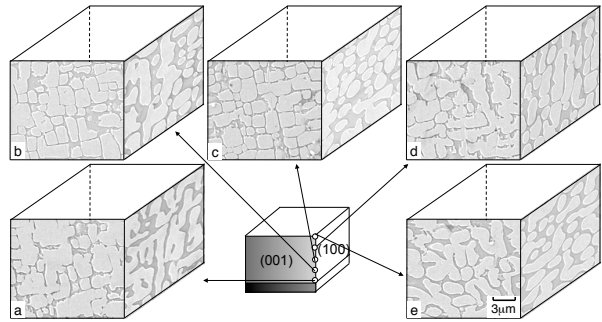

Fig.11. SEM micrographs of the aged blade on the pressure side of the 28 mm part from the leading edge: (a) the surface, (b) 0.2, (c) 0.4, (d) 0.6 mm and (e) the vicinity of internal cooling channel portion.
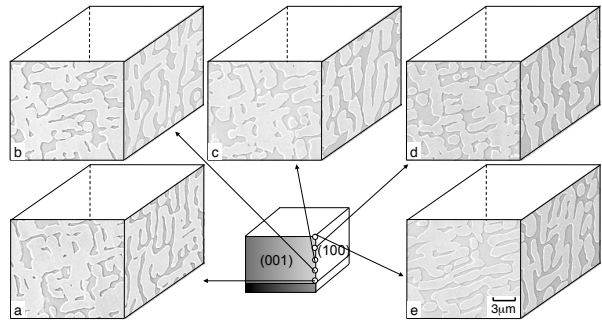

Fig.12. SEM micrographs of the aged blade on the pressure side of the trailing edge: (a) the surface, (b) 0.1, (c) 0.2, (d) 0.4 mm and (e) the vicinity of internal cooling channel portion.

In the (100) plane of the all portions, the completely rafted γ/γ' structures which are parallel to the (010) plane are observed. On the contrary, coarsening of the γ' precipitates are obtained in the (001) plane. In this part, morphology of γ' precipitates are obviously changed in the serviced blade (Fig.4).

3.2.2 Suction side

SEM micrographs of the aged blade on the suction side of the leading edge are shown in Fig.13.

The γ' precipitates contact with each other toward three <100> directions are observed in the (001) and (100) planes respectively.

SEM micrographs of the aged blade on the suction side of the 15 mm part from the leading edge are shown in Fig.14.

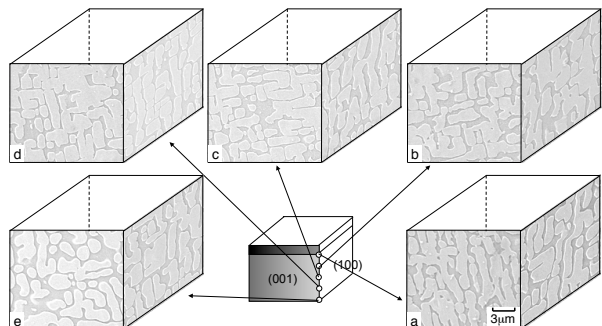In the surface portion, well-aligned rafted γ/γ' structures parallel to the

Fig.13. SEM micrographs of the aged blade on the suction side of the leading edge: (a) the surface, (b) 0.4, (c) 0.8, (d) 1.2 mm and (e) the vicinity of internal cooling channel portion.

(010) plane are observed, and the interface between the γ/γ' phase is straight (Fig.14-(a)). In the 0.4, 0.7 and 1.1 mm portions, the adjacent γ' precipitates are connected in the two specific directions, that is, the [001] and [100] directions (Fig.14-(b)-(d)). However, in the cooling channel portion, coarsening of the γ' precipitates are obtained (Fig.14-(e)). Whereas the same morphology of γ' precipitates regardless of the portion in the serviced blade (Fig.7), microstructure is significantly different by the portion in the aged blade.

SEM micrographs of the aged blade on the suction side of the 28 mm part from the leading edge are shown in Fig.15.

Further coarsening of γ' precipitates are observed in all portions.

SEM micrographs of the aged blade on the suction side of the trailing edge are shown in Fig.16.

In the (100) plane, high, completely rafted γ/γ' structures parallel to the (001) plane are observed, while at the (001) plane, the rafted γ/γ' structures start to collapse. The volume fraction of γ' precipitates are reduced in comparison with the other parts. The direction of rafted γ/γ' plates in the trailing edge is different from that of the 15 mm part from the leading edge.

In this way, the marked morphological changes in the γ' precipitates are observed at the each portions of the aged blade.

4. Discussion

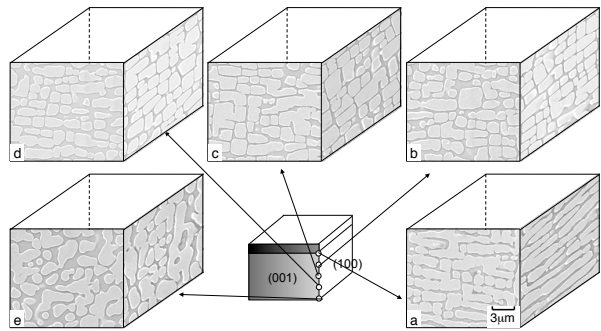### 4.1 Temperature distribution of blade in service

Fig.14. SEM micrographs of the aged blade on the suction side of the 15 mm part from the leading edge: (a) the surface, (b) 0.4, (c) 0.7, (d) 1.1 mm and (e) the vicinity of internal cooling channel portion.
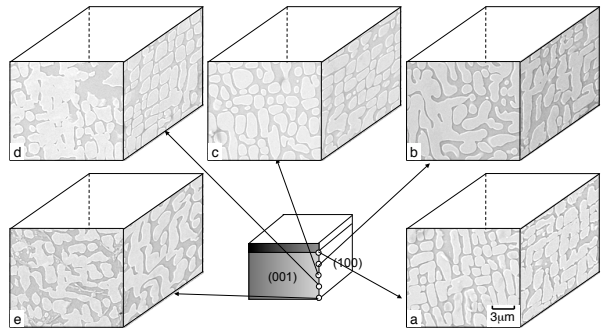

Fig.15. SEM micrographs of the aged blade on the suction side of the 28 mm part from the leading edge: (a) the surface, (b) 0.4, (c) 0.8, (d) 1.2 mm and (e) the vicinity of internal cooling channel portion.
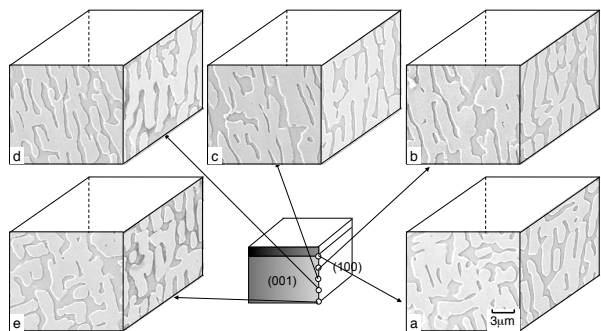

Fig.16. SEM micrographs of the aged blade on the suction side of the trailing edge: (a) the surface, (b) 0.1, (c) 0.2, (d) 0.4 mm and (e) the vicinity of internal cooling channel portion.

Fig.17 shows the schematic illustration of the microstructure distribution in the middle part of the

serviced 1st HPT blade.

The distribution from the cuboidal γ' precipitates sides to collapsed rafted γ/γ'structures sides is shown in five colors from brown to white.

Morphological changes of γ' phase is promoted to the pressure side than the suction side.

At the suction side, the γ' precipitates kept cuboidal in shape in the cooling channel portion from leading edge to trailing edge side. The pressure side of the 15 mm part from the leading edge, morphological

Fig.17. Schematic illustration of the microstructure distribution in the middle part of the serviced 1st HPT blade.

change is occurring from the surface to the cooling channel portion. In the trailing edge portion, rafted γ/γ'structures is observed in all areas of both the pressure and suction side, in particular, rafted γ/γ'structures starts to collapse at the vicinity of the interface between the coating layer and the matrix.

In this way, the temperature is comparatively high at the vicinity of the interface between the coating layer and the matrix where the rafted γ/γ' structures are observed. It is assumed that at the vicinity of cooling channels in the 15 mm part is exposed to high temperature because of the microstructure changes are occurred to the inside from the surface. Rafted γ/γ'structure and one start to collapse are observed in trailing edge at all regions.   This microstructure evidence indicated that the trailing edge is exposed to the highest temperature condition in the middle part of the 1st HPT blade in service.
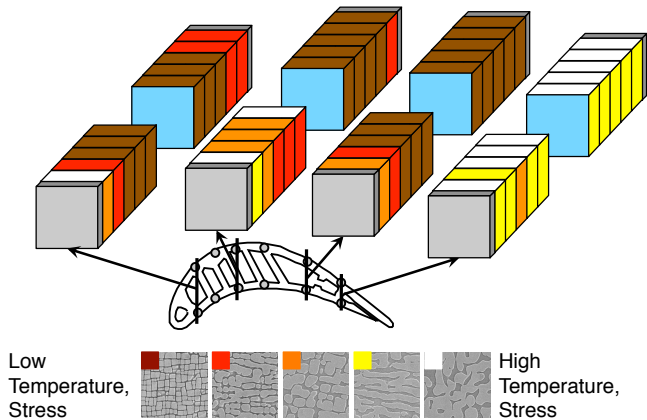
4.2 Stress distribution of blade in service

It is well understood that the cuboidal γ' precipitates turn to rafted γ/γ' structures perpendicular to the tensile stress axis [1,7-9,14], and that the cuboidal γ' precipitates turn its shape to the rod-shaped structure parallel to the compressive stress axis [15-17]. The stress distribution and directions in a blade in service will be discussed based on the above evidences and the results of the microstructure observations of the serviced and aged blade.

Fig.18 shows the schematic illustration of the microstructure distribution in the middle part of the aged 1st HPT blade.
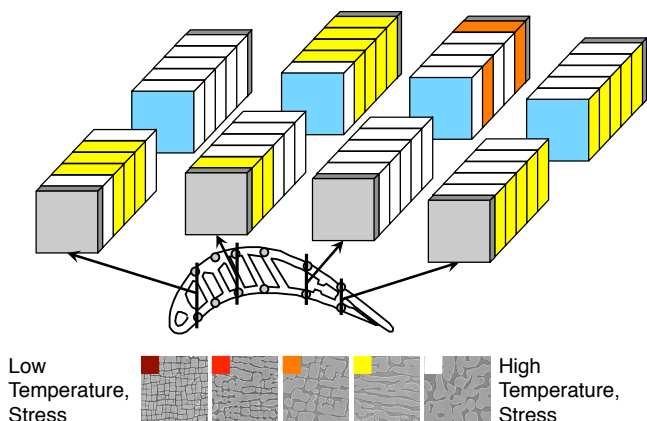
Coarsening of the γ' precipitates

Fig.18. Schematic illustration of the microstructure distribution in the middle part of the aged 1 st HPT blade.

are observed in most portions of the blade.

At the trailing edge in all regions, rafted γ/γ' structures parallel to the (001) plane appear on the (100) plane. This microstructure evidence indicated that the amount of deformation is extremely high and the high tensile stress is loaded to the [001] direction, that is, the longitudinal direction at the vicinity of the blade surface to the internal cooling channel in the 1st HPT blade in service. Tensile stress is considered to result from the centrifugal stress in rotation.

Contrast to this, at the 15 mm part from the leading edge, rafted γ/γ' structures parallel to the (010) plane are observed at the pressure and suction side of the vicinity of the blade surface. This microstructure evidence indicates that the uniaxial tensile stress perpendicular to the blade surface and/or multi-axial compressive stress parallel to the blade surface are expected to act on the blade in service. However, rafted γ/γ' structures are not observed in internal regions. It is supposed that very complicated stresses are load or there is almost stress influence on the interrnal portions.

Consequently, very complicated stresss is load on the blade in service, and the stress direction and stress distribution are different by the part and portions.

5. Conclusions

The morphology of γ' precipitates of a nickel-based superalloy serviced in the middle part of a 1st HPT blade of a jet engine was investigated before and after aging to estimate the temperature and the stress distribution, and the stress directions in service. The following conclusions were obtained.

1) After serviced blade, most of the γ' precipitates remained cuboidal in shape at the internal cooling channel side. However, rafted γ/γ' structures formed as the parallel to (010) at the vicinity of coating layer of the pressure side. At the trailing edge, well aligned rafted γ/γ' structures formed as the parallel to (001) were appeared at all portions of the suction sides.

2) After simple aging, rafted γ/γ' structures parallel to (010) plane were appeared at the vicinity of the blade surface side at the 15mm portion from the leading edge, while at the trailing edge in all portions, that were formed parallel to the (001) plane.

3) Tensile stress from the longitudinal direction of a blade was loaded at the trailing edge in all portions. On the contrary, the uni-axial tensile stress perpendicular to the blade surface and/or multi-axial compressive stresses parallel to the blade surface was expected to act on the blade in service.

4) Consequently, very complicated stresss is load on the blade in service, and the stress direction and stress distribution are different by the part and portions.

Acknowledgement

6. References

[1] T. M. Pollock and A. S. Argon, Creep Resistance of CMSX-3 Nickel Base Superalloy Single Crystals, Acta Metall. Mater., 40(1992)1, p.1.

[2] M. Matsuoka , Aeronautics course 7, Jet Engine, Japan Aeronautical Engineers' Association, (Tokyo, 2003), p.62.

[3] H. Harada, Superalloys: Present and Future, JSPS Rep. of the 123rd Committee on Heat Resisting Metals and Alloys, 48(2007), p.357.

[4] Y. Yoshioka, Evolution of Superalloys as Gas Turbine Materials and Perspective on the Future, JSPS Rep. of the 123rd Committee on Heat Resisting Metals and Alloys, 48(2007), p.365.

[5] S. Walston, A. Cetel, R. MacKay, K. O'Hara D. Duhl and R. Dreshfield, Joint Development of a Fourth Generation Single Crystal Superalloy, Proc. of 10th Int. Symp. on Superalloys2004, (2004), p.15.

[6] T. Fujimura, Materials Technology on Aircraft Gas Turbine Engines, Journal of the Gas Turbine Society of Japan, 32(2004), p.174.

[7] M. Fahrmann, E. Fahrmann, O. Paris, P. Fratzl and T. M. Pollock, An Experimental Study of the Role of Plasticity in the Rafting Kinetics of a Single Crystal Ni-base Superalloy, Proc. of the 8th Int. Symp. on Superalloysl996, (1996), p.191.

[8] D. Mukhherji, H. Gabrisch, W. Chen, H. J. Fecht and R. P. Wahi, Mechanical Behavior and Microstructure Evolution in the Single Crystal Superalloy SC16, Acta Mater., 44 (1997), p.3143.

[9] N. Miura, Y. Kondo and T. Matsuo, Stress Dependence of Strain Attained to Rafting of γ' phase in Single Crystal Nickel-based Superalloy, CMSX-4, Proc. of 9th Int. Conf. on Creep and Fracture Engineering Materials and Structures, (2001), p. 437.

[10] N. Miura, N. Harada, Y. Kondo and T. Matsuo, Morphological Change in γ' Phase in Different Portions of First Stage High Pressure Turbine Blade of PWA1480, Proc. of the 7th Liege Conf. on Mater. for Adv. Power Eng. 2002, (2002), p.245.

[11] N. Miura, K. Nakata, M. Miyazaki, Y. Hayashi and Y. Kondo, Morphology of γ' Precipitates in Second Stage High Pressure Turbine Blade of Single Crystal Nickel-based Superalloy After Serviced, Mat. Sci. Forum, Vols. 638-642 (2010), p.2291

[12] N. Miura, K. Kurita, Y. Kondo and T. Matsuo, Change in Morphology of γ' of Prior-crept Single Crystal Ni-based Superalloy, CMSX-4, With Simple Aging, Mat. Sci. Forum, Vols. 539-543 (2007), p.3024.

[13] N. Miura, Y. Kondo and Y. Murata, Formation Mechanisms of rafted structure of Single Crystal Ni-based Superalloys, JSPS Rep. of the 123rd Committee on Heat Resisting Metals and Alloys, 54 (2013), p.33.

[14] Y. Hayashi, N. Miura and Y. Kondo, Creep Resistance of Single Crystal Nickel-based Superalloy, CMSX-4, at 1073K, Current Advances in Materials and Processes, 20 (2007), p.1229.

[15] U. Tetzlatt and H. Mughrabi, Enhancement of the High-temperature Tensile Creep Strength of Monocrystalline Nickel-based Superalloys by Pre-rafting in Compression, Proc. of the 9th Int. Conf. on Superalloys 2000, (2000), p.273.

[16] L. Shui, S. Tian, T. Jin. and Z. Hu, Influence of Pre-compression on Microstructure and Creep Characteristic of a Single Crystal Nickle-base Superalloy, Mater. Sci. and Eng. A, 418 (2006), p.229.

[17] K. Nakada, N. Miura and Y. Kondo, Change in Morphology of γ' Precipitates and Dislocation Substructure of a Single Crystal Nickel-based Superalloy, CMSX-4, with Compressive Creep Deformation, JSPS Rep. of the 123rd Committee on Heat Resisting Metals and Alloys, 50(2009), p.219.

DEVELOPMENT OF NI-CO-BASE SUPERALLOYS BASED ON NEW CONCEPT FOR HIGH TEMPERATURE TURBINE DISK APPLICATIONS

*Junzo Fujioka, *Yuefeng Gu, *Chuanyong Cui, *Tadaharu Yokokawa, *Toshiharu Kobayashi, *Hiroshi Harada, **Tadashi Fukuda, ***Akira Mitsuhashi

*National Institute for Materials Science (NIMS)
1-2-1 Sengen, Tsukuba Science City, Ibaraki 305-0047, Japan
**MMC Superalloy Corporation
**476 Shimoishido-shimo, Kitamoto City, Saitama, 364-0023, Japan
***Mitsubishi Materials Corporation
1975-2 Shimoishito-kami, Kitamoto City, Saitama, 364-0022, Japan
Fujioka.junzo@nims.go.jp

ABSTRACT

Recently, we developed a new kind of cast-and-wrought (C&W) Ni-Co base superalloys (TMW alloys) for the applications to turbine disk and high-pressure compressor of jet engines. TMW alloys were designed by mixing two kinds of γ/γ' two-phase superalloys, Ni-base superalloy and Co-Ti alloy. The temperature capability of TMW alloy aimed up 50°C compared to U720Li, the best alloy of current C&W disk superalloys. In the subscale study, the forgeability of 50 kg ingot was identified by the processes of extrusion, hot rolling and manufacturing pancakes. The property assessments of the rolled plates indicated the temperature advantage of TMW alloys. The successful manufacturing of full-scale pancakes of some TMW alloys proved that fine grain structures of 10 to 20 μm could be obtained and good processability could be expected. Results of tensile and creep tests of the pancakes showed that the temperature capability of TMW alloys increased at least 50 °C compared to U720Li.

Key words: Turbine disk superalloys, C&W, Ni-Co-base alloys, TMW alloys, U720Li

1. Introduction

Turbine disk is the important part which accounts for 20% of weight and 10% of price in the turbofan engine [1], and the most critical part because its destruction leads to serious trouble.

Improvement of Specific Fuel Consumption (SFC) is the important issue for commercial airplanes. For this purpose, increase of temperature capability of turbine disk alloys is required in order to increase the turbine inlet temperature (TIT) and decrease the cooling air in the engine.

National Institute for Materials Science (NIMS) has developed cast-and- wrought Ni-Co-base superalloys (TMW alloys) based on new concept for high temperature turbine disk applications. In this paper, trend of developing superalloys for disk, developing of TMW alloys in NIMS and trial production of disk in the NEDO project are described.

2. Trend of development of materials for high pressure turbine disk applications

Figure 1 shows a photograph [2] and the temperature-stress distribution in the high pressure turbine disk of jet engine for airplane. TIT of modern engine reaches over 1600°C and the temperature of the outer periphery of turbine disk reaches 700°C, therefore the creep strength

is required. In addition, the tensile strength and the low-cycle fatigue strength are required because the rotating speed of engine reaches 10,500 rpm and internal stress reaches about 1000MPa. Moreover, the crack propagation properties are important because there is a need for the application of damage-tolerant design.

Table 1 shows chemical composition of representative disk alloys. Disk is produced by Cast-and wrought (C&W) method or Powder metallurgy (P/M) method. Chemical composition is based on Ni and contains 10-20% Cr, up to 20% Co, up to 10% Mo, up to 6% Al, up to 5% Ti, and small amount of B, Zr, C. Some alloys contain W, Ta, Hf and Nb.
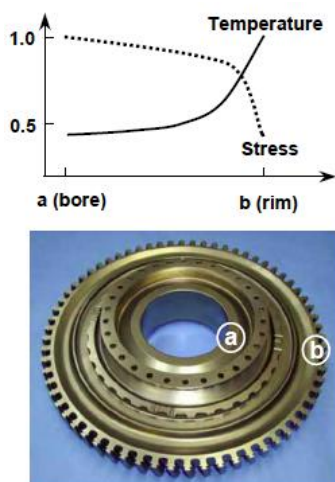
Figure 1 Temperature and stress in the HP turbine disk. Latest aero engines : 1000MPa at bore and 700℃ at rim.

Table 1 Chemical composition of disk alloys.   (wt%, Bal:Ni)

Cast-and-Wrought (C&W) alloys

Alloy	Cr	Co	Mo	W	Nb	Ti	Al	C	B	Zr	Other
Rene41	19	11	10	-	-	3.1	1.5	0.09	0.01	-	
Astroloy	15	15	5.25	-	-	3.5	4.4	0.06	0.03	0.06	
Inconel718	19	-	3	-	5.1	0.5	0.5	0.08	-	-	18.5Fe, 0.15Cu
Waspaloy	19.5	13.5	4.3	-	-	3	1.4	0.07	0.006	0.09	
U720Li	16	15	3	1.25	-	5	2.5	0.025	0.018	0.03	

Powder Metallurgy (P/M) alloys

Alloy	Cr	Co	Mo	W	Nb	Ti	Al	C	B	Zr	Other
Rene95	14	8	3.5	3.5	3.5	2.5	3.5	0.16	0.01	0.05	
IN100	10	15	3	-	-	4.7	5.5	0.15	0.015	0.06	1.0V
Rene88DT	16	13	4	4	0.7	3.7	2.1	0.03	0.015	0.03	
N18	11.5	15.7	6.5	-	-	4.35	4.35	0.015	0.015	0.03	0.45Hf
RR1000	15	18.5	5	-	1.1	3.6	3	0.027	0.015	0.06	0.5Hf, 2Ta
ME3	13.1	18.2	3.8	1.9	1.4	3.5	3.5	0.03	0.03	0.05	2.7Ta

Figure 2 shows the history of developing turbine disk alloys and the targets of TMW alloys in NIMS. There was an increase of 70°C in temperature capability of C&W alloys since 1950s, but there was no improvement since U720Li in 1980s. Alloys with higher temperature capability than U720Li have been developed by the P/M method, and latest P/M alloys have temperature capability of 50°C higher than U720Li. In Japan, alloy development and trial manufacturing of pancake by P/M method was done in the national project in 1980s [3], but the research results have not been put to practical use, and there is no production facility and technology now. On the other hand, abroad, Rolls-Royce Ltd
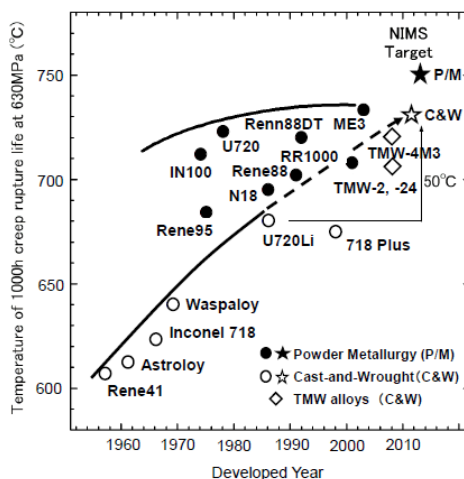

Figure 2 History of developing turbine disk alloys and target of new TMW alloys at NIMS.

has used P/M alloys since Trent 800 and has plans to use their original RR1000 alloy in Trent 1000 engine [4]. General Electric

579

Company put P/M ME3 alloy to practical use in GP7282 engine of Airbus A380 [5]. In Fig.2 newly developed TMW alloys are shown and TMW-4M3 has the temperature capability comparable to P/M alloys and close to the NIMS target.

3. Development of TMW alloys at NIMS

3.1 Alloy design based on new concept

As shown in Figure 2, the target of NIMS is development of alloys with temperature capability of 50°C higher than U720Li by C&W process which is capable of producing domestically and has the cost half the P/M alloys'.

Effort of increasing γ' volume fraction in Ni-base superalloys has been paid in order to increase high temperature strength and U720Li has the γ' volume fraction of 45%. However alloys with γ' volume fraction higher than U720Li are not able to be forged, so it has been thought in the world that as far as produced by the C&W method U720Li is all they can produce and it is impossible to develop alloys better than U720Li.

On the other hand, Co-base superalloys are used for turbine vane and combustion chamber of jet engines. Until now, Ni-base superalloys and Co-base superalloys have been developed and used as separate alloys. However, NIMS has developed new superalloys focusing attention that there exist widely unexplored and promising compositional range of so-called Ni-Co-base superalloys between Ni-base alloys and Co-base alloys, especially Co-Ti alloys which precipitate γ' phase. And, NIMS has developed new Ni-Co-base superalloys and has broken through the limits of C&W alloys.

Figure 3 shows the new concept of NIMS. This concept is the integration of two kinds of two phase superalloys, that is, Ni-base and Co-base superalloys [6]. γ-γ' phases of fcc/L1$_2$ structure from Ni-base superalloys to Co-base superalloys exist continuously [7] [8], and γ'-precipitated Co-base superalloys exist at the point where Co and Ti content increases with constant ratio. If the Co content of Ni-base superalloys increases solely, forgeability and phase stability increase but miss the strength. On the other hand, if the Ti content increases solely, the strength increases but miss the phase stability. Therefore, new alloys with high strength, high phase stability and forgeability are born by increasing Co and Ti contents at the same time. These new alloys are the TMW alloys.
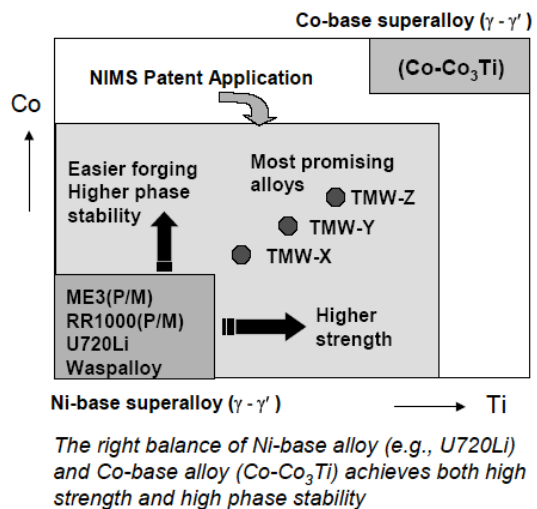

Figure 3 New concept for designing disk superalloys.

3.2 Trial production of sub-scale material

TMW alloys have been designed by the new concept shown in figure 3. Table 2 shows chemical composition and γ' volume fraction of designed TMW alloys. Comparing to U720Li,

TMW alloys contain higher Co of 21.8 to 26.2 wt% in order to increase forgeability and phase stability and higher Ti content of 5.1 to 6.2 wt% in order to increase strength and temperature capability by increasing γ' volume fraction. Alloy design and verification test were conducted in order to suppress the harmful phase of η phase [9] [10].

Table 2 Chemical composition and γ' volume fraction of U720Li and TMW alloys. (wt%, Bal:Ni)

Alloy	Cr	Co	Mo	W	Ti	Al	C	B	Zr	γ' vf
U720Li	16.0	15.0	3.0	1.25	5.0	2.5	0.025	0.018	0.03	45
TMW-2	14.4	21.8	2.7	1.10	6.2	2.25	0.023	0.015	0.033	48.7
TMW-24	13.8	25.0	2.6	1.1	5.6	2.2	0.015	0.015	0.03	45
TMW-3	16.5	23.3	3.1	1.2	5.1	1.9	0.026	0.018	0.022	40
TMW-4	14.9	26.2	2.8	1.1	6.1	1.9	0.014	0.017	0.019	45
TMW-4M3	13.5	25.0	2.8	1.2	6.2	2.3	0.015	0.015	0.03	49.5

γ' vf : Volume fraction of γ' at 760℃

Subscale trial production of designed TMW alloys by C&W process was done at Special Metals Ltd. The result are shown in Figure 4. U720Li was produced at the same time in order to compare it within the same product condition. High pressure compressor blade was precision-forged at Sumiju Precision Forging Co., Ltd. and cut and polished at Taguchi Pattern Works Co., Ltd.

Table 3 shows the evaluation result. Heat treatment test was done [11] and TMW alloys were heat treated under the same condition as U720Li. TMW-2 and TMW-4 have the same formability and phase stability as U720Li and higher strength than U720Li. These two alloys, comparing with U720Li, have 70°C higher temperature capability of 0.2% prof stress and higher creep strength [6] [12] [13] [14]. High strength and good formability of TMW alloys were demonstrated by these results.

Extrusion (50Kg VIM)

12:1

Rolling (50Kg VIM)

12x90x500 mm

Pancake (100Kg VIM+VAR)

TMW-2

HP compressor blade

Table 3 Formability, phase stability and 0.2% proof stress at 750℃ of TMW alloys

Alloy	Fomability	Rolling	
		Phase stability	0.2% PS at 750℃
U720Li	Good	Acceptable	888MPa
TMW-2	Good	Acceptable	977MPa
TMW-3	Good	η phase	951MPa
TMW-4	Good	Acceptable	993MPa

Heat treatment condition after rolling :
1100℃x4h、OQ+650℃x24h、AC+760℃x16h、AC

Figure 4 TMW alloy products by C&W process

4. Trial production and evaluation of full-scale disk in the NEDO project

4.1 Outline

The trial production and evaluation were conducted in the project titled " Research and development of production technology of high temperature turbine disk" sponsored by New Energy Development Organization (NEDO) in 2007 to 2008 aimed at the early domestic production of high-performance turbine disk by using domestic facilities for C&W process. Trial production of real scale pancake was done at MMC Superalloy Corporation and evaluation of pancake was performed.

4.2 Alloys for trial production and technologies of melting, forging and heat treatment

Alloys for trial production are TMW-2, TMW-24 and TMW-4M3 whose chemical compositions are shown in Table 2. Pancake of U720Li was also produced in order to compare TMW alloys with U720Li precisely. TMW-24 and TMW-4M3 are alloys which improve phase stability of TMW-2 and TMW-4, respectively, and real scale pancakes of TMW-24 were produced before [2] [15].

Figure 5 shows production process and products. Triple melt which combines three kinds of melting process was adopted in the melting step. The ingot with controlled chemical composition is produced in the first melting of Vacuum Induction Melting (VIM). Large inclusions are eliminated by the removing of sulfur in the second melting of Electroslag Remelting (ESR) where the ingot produced by VIM is used as the consuming electrode. Moreover, elimination of small inclusions and degas are done in the third melting of Vacuum Arc Remelting (VAR). In the VAR, the ingot with suppressed segregation and fine structure is produced by the high cooling capacity of water cooled cupper mold. Triple melt is very useful for reducing inclusions [16], so this is adopted as the melting method in the production of rotating parts such as turbine disk where high quality is required. In the basic test and trial melting of 2 tons class ingot by the triple melt, it is confirmed that all TMW alloys are melted successfully and obtained ingots have the quality which could be supplied to forging.

In the forging of 2 ton class VAR ingot, billets of 200 mm diameter were manufactured without cracking. Pancakes of all TMW alloys with 440 mm diameter were successfully manufactured by forging from billet. Sub-solvus heat treatment which is used for U720Li was done for manufactured pancakes : solution treatment (1100°C x 4h 、 Oil quenching) + aging 1 (650°C x 24h、
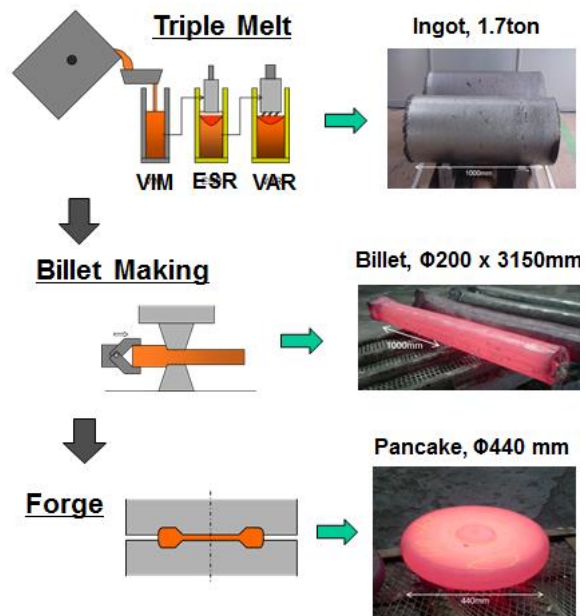

Figure 5 C&W process of manufacturing real-scale pancakes

582

Air cooling) + aging 2 (760°C x 16h、 Air cooling). Some TMW-4M3 was solution treated at higher temperature of 1120°C in order to precipitate much more γ' phase. As shown in Figure 6, pancakes have sound microstructure even at macro and micro scale level, have homogeneously distributed grains of 10 to 20 μm diameter and have the quality suited for turbine disk.

4.3 Properties of disk-shaped products

Figure 6 Macro- and micro-structures in the cross section of the machined pancake (TMW-2, φ400mm)

4.3.1 Targets

The target of this project was to realize the disk forging that has 50°C higher temperature capability comparing to U720Li which has the highest temperature capability among current forged disk alloys. Evaluation standards of temperature capability were determined as follows according to the questionnaire survey of domestic and international engine makers [2] : ① Temperature for 100h life of 0.2% creep strain at the stress of 630MPa, ② Temperature corresponding to 0.2% proof stress of U720Li at 650°C.

4.3.2 Test methods

Tensile test, creep test, low-cycle fatigue test, fatigue crack growth test and tests of physical properties were conducted. Test specimens were removed through-thickness center of pancakes of φ 440×65 mm. Tensile, creep and low-cycle fatigue specimens were removed tangentially through-thickness center. Specimens of fatigue crack growth test were removed in such a way that the notch bottom was in the thickness direction and the crack growth direction was in the radius direction. All mechanical tests were conducted according to ASTM standards.

4.3.3 Test results

Figure 7 shows the results of tensile tests. All TMW alloys have tensile strength higher than U720Li at any temperature and TMW-4M3 has the highest tensile strength above 500°C. TMW-4M3 has also the highest 0.2% proof stress. TMW-2 and TMW-4M3 maintain the 0.2% proof stress of U720Li at 650°C even above 700°C, so the target of 50°C higher temperature capability was achieved.

Figure 8 shows Larson-Miller Parameter (LMP) plots for time to 0.2% creep strain. Temperatures in the figure show the difference of temperature capability between TMW alloys and U720Li. This temperature capability is the temperature for 100h life of 0.2% creep strain at the stress of 630MPa. LMP values of TMW alloys are higher than those of U720Li at any stress level and TMW-2 and TMW-4M3 have advantages of 58°C and 76°C, respectively comparing to U720Li. This result, combined with the result of tensile tests, shows the achievement of the target, that is, 50°C higher temperature capability comparing to U720Li.

Figure 9 shows Larson-Miller Parameter (LMP) plots for creep rupture life. TMW alloys show larger LMP values and higher creep rupture strength than U720Li. TMW-2 and TMW-4 have the advantage of 26°C and TMW-4M3 has the advantages of 40°C for the temperature capability (the temperature for 100h creep rupture life at the stress of 630MPa) comparing to U720Li.

Figure 10 shows the relationship between total strain range and failure life of strain-controlled low-cycle fatigue tests. TMW alloys have longer life than U720Li.
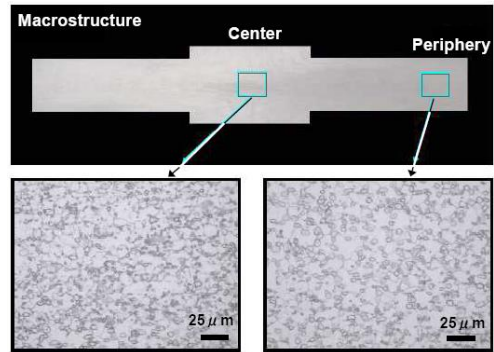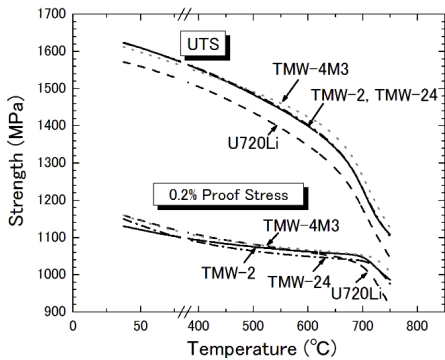
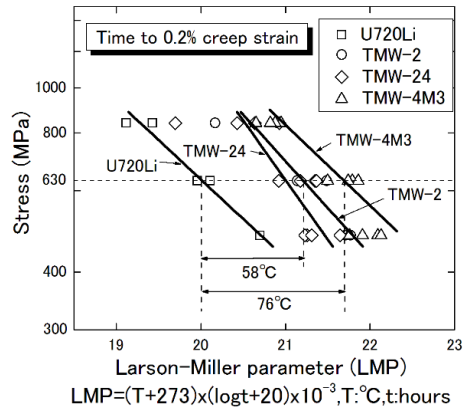Figure 7 Tensile strength of U720Li and TMW alloys.

Figure 8 Larson-Miller plot of 0.2% creep life of U720Li and TMW alloys.
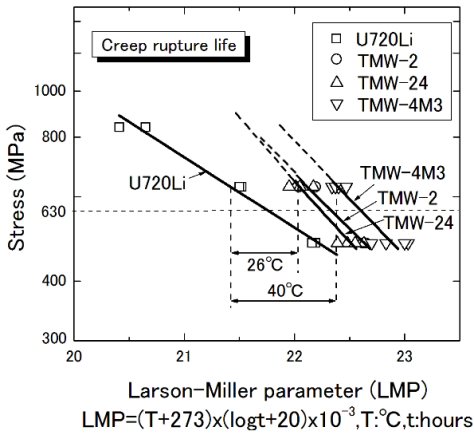

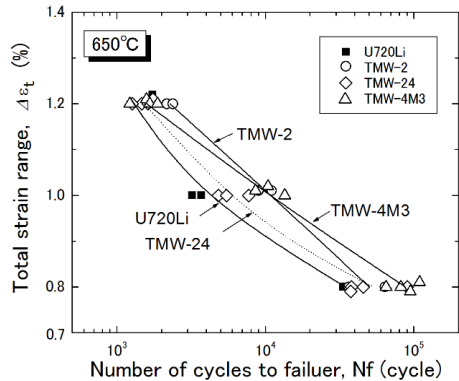Figure 9 Larson-Miller plot of creep rupture life of U720Li and TMW alloys.

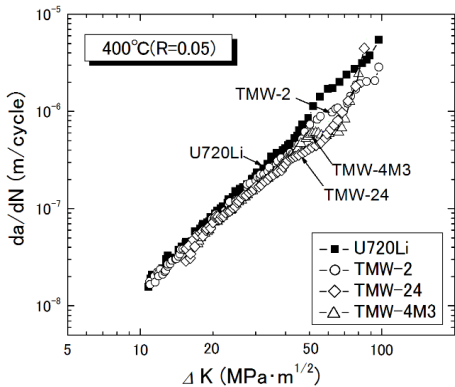Figure 10 Strain-controlled low cycle fatigue life at 650°C.
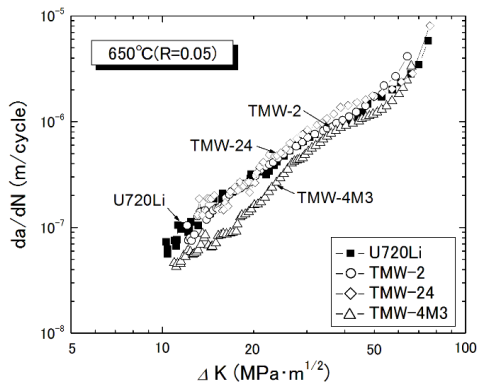

Figure 11 Fatigue crack growth rate at 400°C.

Figure 12 Fatigue crack growth rate at 650°C.

584

Figure 11 and figure 12 show relation between crack growth rate (da/dN) and stress intensity factor ($\triangle$K) at 400°C and 650°C at the stress ratio (R=Pmin/Pmax) of 0.05. These results show that crack growth properties of TMW alloys are the same or higher than U720Li.

Above-mentioned good mechanical properties of TMW alloy are considered not only by the higher γ' volume fraction because the γ' volume fraction of TMW-24 is equivalent to U720Li as shown in Table 2. Contribution of other strengthening mechanisms is being investigated. One of mechanisms is considered that deformation cutting γ' is inhibited because chemical composition of γ' phase of TMW alloys with higher Co and Ti content, that is (Ni, Co, others)$_3$(Al, Ti, others), is different from U720Li. Another mechanism is considered that deformation resistance is increased by the interaction between dislocation and twin crystal [17]. Twin crystal is easily formed by decrease of stacking fault energy, that is, formation energy of twin crystal, because twin crystal was observed after mechanical tests in TMW alloys [17].

5. Summery

A new kind of cast-and-wrought (C&W) Ni-Co base superalloys (TMW alloys) were developed for the applications of turbine disk and high-pressure compressor. Trial production of forgings from 50Kg melt by cast-and wrought (C&W) process was done, and it was demonstrated that TMW alloys had higher temperature capability than U720Li, the highest current disk alloys and had good phase stability and forgeability.

Next, utility-scale pancakes of turbine disk were successfully manufactured by the C&W process starting from 2 tons class triple melt and it was identified that forged pancakes had uniform and fine grains of 10 to 20 μm required for turbine disk. These results demonstrated that TMW had the compatibility for commercial production by the commercial process.

Results of mechanical tests showed that TMW alloys had temperature capabilities 58 to 76 °C higher for the creep strength and more than 50 °C higher for the 0.2% proof stress compared to U720Li. Low-cycle fatigue strength and crack growth properties were the same or superior to than U720Li.

NIMS has a patent on TMW alloys [18] . In the future, we would like to go forward the practical use of TMW alloys as the first domestic C&W superalloys for high temperature turbine disk by enhancing cooperation among research institutes, material companies, and engine makers. And we would like to contribute to the progress of airplane industries in the world.

This paper has been written by translating and updating a Japanese paper [19].

Reference
[1] R.C.Reed:The Superalloys - Fundamentals and Applications, Cambridge University Press, Cambridge UK (2006)
[2] Report of leading investigation on development of manufacturing high temperature turbine disk, NEDO (September 2006)
 [3] Michio Yamazaki : Handbook of controlling technology of high performance crystals, Japanese Standards Association (1991).
[4] I.Molyneux : "Rolls-Royce Ti Supply Chain", CBM Global Trends Conference 2005 (Oct. 2005).
[5] UEET(Ultra-Efficient Engine Technology Program) : Fiscal Year 2002 Performance Report.
[6] Y. Gu, H. Harada, C. Cui, D. Ping, A. Sato, J. Fujioka : Scripta Materialia, 55 (2006), pp.815-818.
[7] C.Y. Cui, Y.F. Gu, D.H. Ping, T. Fukuda, H. Harada : Materials Transactions, Vol.49, No.3, pp.424-427 (2008).

[8] C.Y. Cui, Y.F. Gu, D.H. Ping, H. Harada : Intermetallics, 16(2008), pp.910-916.

[9] C.Y. Cui, Y.F. Gu, D.H. Ping, T. Fukuda, H. Harada : Materials Science and Engineering A, 485, pp.651-656 (2008).

[10] C.Y. Cui, Y.F. Gu, D.H. Ping, T. Fukuda, H. Harada : Metallurgical and Materials Transactions A, Vol.40A, pp.282-291 (Feb. 2009).

[11] T. Fukuda, Y.F. Gu, C. Cui, H. Harada : J. Japan Institute of Metals, Vol.71, No.9, pp.424-427 (2008).

[12] C.Y. Cui, Y.F. Gu, H. Harada, A. Sato : Metallurgical and Materials Transactions A, Vol.36A, pp.2921 -2927 (Nov.2005).

[13] Y.F. Gu, C. Cui, H. Harada, T. Fukuda, D. Ping, A. Mitsuhashi, K. Kato, T. Kobayashi, J. Fujioka : Superalloys 2008, Eds. R.C. Reed et al., pp.53-61 (Seven Springs, PA, USA:TMS, Sept. 2008).

[14] Y.F. Gu, C. Cui, D. Ping, H. Harada, T. Fukuda, J. Fujioka : Materials Science and Engineering A, 510-511, pp. 250 -255 (2009).

[15] T. Fukuda, A. Mitsuhashi, K. Kato, H. Harada, Y.F. Gu : J. Japan Gas turbine Society, Vol.35, No.4, pp.275-279 (2009).

[16] J.M. Moyer, L.A. Jackman, C.B. Dasczik, R.M. Davis, R.F. Jones : Superalloys 718, 625, 706 and Various Derivatives, Eds. E.A. Loria, pp. 39-48 (TMS, 1994).

[17] Y. Yuan, Y.F. Gu, C. Cui, T. Osada, T. Yokokawa, H. Harada : Advanced Engineering Materials, 13, pp. 296 -300 (2011).

[18] European patent No. 1842934 (2011)

[19] J.Fujioka, Y.F. Gu, C. Cui, T. Yokokawa, T. Kobayashi, Hiroshi H. Harada, T. Fukuda, A. Mitsuhashi : J. Japan Gas turbine Society, Vol.40, No.2, pp.107-112 (2012).

Part E

Corrosion, Thermomechanical Fatigue and Modelling

THE EUROPEAN CREEP COLLABORATIVE COMMITTEE (ECCC) – REBIRTH AND REVIVAL

Dr David J. Allen

IMPACT PowerTech Ltd, Nottingham, UK
allens@greenbank57.freeserve.co.uk

Abstract

The European Creep Collaborative Committee (ECCC), established in 1991, operated successfully until 2005 as a European Thematic Network. Its achievements included the creation of a series of Post-Assessment Tests to improve reliability in creep data assessment and the production of a series of high temperature materials Data Sheets supported by technical Recommendations. However, EC funding ceased in 2005, and whilst ECCC continued on a voluntary basis, some momentum was lost.

Since 2011, ECCC has seen a rebirth and revival, with the creation of a "Joint Industrial Programme" (JIP) to support a central administrative Secretariat operated by CSM, Rome, alongside technical management of testing, assessment and data collation by manufacturers, end users and materials institutions throughout Europe. The JIP has brought ECCC back to full operating strength and is now delivering new insights into high temperature materials performance.

This paper describes the ECCC revival and outlines some of the main new developments taking place. It explains how members contribute expertise, data, testing and analysis, while a nationally based system governs the equitable input of resources. The paper also highlights recent advances in assessment technology, ECCC activities on ferritic, austenitic and nickel-base materials, and novel modelling and testing methodologies.

Keywords: creep, testing, assessment, high temperature design strength

1. Introduction

The European Creep Collaborative Committee (ECCC) is a unique European institution. Its members participate both on a national basis and as individual organisations. They contribute through creep testing at national level, technical input at organisation level, and financial input to a central Secretariat. New members often find ECCC rules complex and confusing. The older members who developed the rules can offer only one justification - it works. It provides an equitable balance between

potentially conflicting interests, and meets industrial needs in supporting the safe design and operation of high temperature plant.

The clearest proof that it works is that ECCC survived the withdrawal of EU financial support in 2005 and is now an autonomous collaborative entity. ECCC is governed on the basis of a "Joint Industrial Programme" (JIP), funded by its members, in parallel with a central Secretariat, established for 3 years from September 2011 at CSM, Rome [1]. Recently, ECCC agreed to renew the JIP for a second 3-year period, September 2014 to August 2017, and keep the Secretariat at CSM. A highly successful Conference, attended by over 150 delegates in May 2014, also attests to the effective revival of ECCC [2].

Whereas ECCC primarily addresses the high temperature materials engineering issues of today, the Liège Conferences – previously known colloquially as COST Conferences – primarily address high temperature materials development for the future. This Conference thus provides living witness to the survival of this vital collaborative development programme, despite the EU decision that "European Collaboration in Science and Technology" for high temperature power plant no longer merits continuity of government support. The ongoing KMM-VIN WG2 programme on Materials for Energy, which follows on from COST 536, therefore has much in common with the ECCC JIP. It may be useful to share our experiences and views on how best to cope without consistent support from Europe – and, on whether Europe has the right policies for our future industrial development.

2. A Brief History

The primary aims of ECCC, as set out on its foundation in 1991, are [3]:

(i) to co-ordinate the generation of creep data collation and analysis of creep data for metals commonly used for high temperature plant throughout Europe

(ii) to interact with, and supply information to the formal European Standards organisations and their technical committees

iii) to mutually exchange technical information relating to current and future activities on material developments

iv) to develop rules for data generation, collation/exchange and assessment.

ECCC's founders recognised that creep testing is expensive, that creep data grow enormously in value when pooled and analysed, and that effective collaborative Creep Groups had already been established in several major European nations. Hence, the imperative for ECCC was to establish an overarching collaborative mechanism which could command confidence, bring the National Creep Groups together, and establish an equitable framework for pooling their resources. The explicit national basis of the collaboration would nowadays be viewed with disfavour by the EU collaborative research programmes, but to ECCC it is fundamental to successful long-term collaboration.

An important if paradoxical principle is that confidentiality promotes openness. Each Nation contributes valuable confidential data in exchange for the opportunity to receive data from others. This is controlled on a defined but flexible basis through a Memorandum of Understanding signed by technical participants. Data are confidential, but data assessment should be an open process, to enable vigorous technical debate and to reach consensus. ECCC therefore set up two types of Working Group: the "open" Group WG1 on data generation and assessment, which all ECCC members can join, and the "closed" WG3.x Groups on specific high temperature material classes, where membership is restricted to active contributors in each area. The role of WG1 was critical in creating a sufficient consensus to ensure that ECCC assessments would command respect throughout Europe. This was eventually achieved by allowing any model, but then applying Post-Assessment Tests (PATs) to determine whether its predictions meet objective acceptance criteria [4].

2.2. Creep Data Generation and Assessment

The traditional core function of ECCC has been to collate, generate and assess creep rupture data on the leading high temperature materials in current use, and to publish Data Sheets providing strength values

available for use in European Standards. An outline description of this process illustrates the structure and operation of ECCC.

The WG3.x Groups collate creep data, commission creep testing programmes provided by member nations, and act as technical forums. They select materials for rupture strength assessment, obtain specialist technical assistance from WG1, and take charge of the assessment process which culminates in production of a Data Sheet.

Data exchange is governed at the macro level by ECCC's Management Committee involving representatives of each member Nation, and at the micro level by the Convenor of the appropriate WG3.x Group. The Convenor's role is to balance the potentially conflicting interests of various stakeholders - manufacturers, end users, institutes, etc. – and decide on what data should be circulated within ECCC to whom and for what purpose. A data set is assessed by at least two different assessors from different countries using different methodologies, the results are compared, and a preferred assessment is chosen by the Working Group. Crucially, the Post-Assessment Tests [4] should be applied to verify that an assessment result is physically realistic, that its predictions match the trend of the observed data across the spectrum from the short to the long term, and that whilst deviance between observation and prediction should be reasonably low, the prediction must also be sufficiently robust to provide adequate confidence in its extrapolation beyond the range of the data. The selected assessment is then used to draw up a table of recommended mean rupture strength values which forms the basis of an openly published ECCC Data Sheet. The creep test data are kept confidential, but a digest of the assessment reports is commonly published. The broad technical issues hence become public knowledge, and independent observers can make their own evaluations.

The ECCC materials assessment process route thus brings a high level of openness and objectivity into what can inevitably be a contentious and difficult arena, for both commercial and technical reasons. Neither ECCC nor any other organisation has an unblemished record of successful creep rupture strength prediction. ECCC has not been immune from the general tendency, over the past two decades and more, toward over-optimism. Nevertheless, there are good grounds for believing that this problem is

being gradually conquered, and that ECCC Data Sheets and Recommendations in general have commanded worldwide respect as a force for realism and rationality in establishing the baseline for high temperature plant design, operation and life assessment. This achievement, and the organisational structure which had made it possible, were what was placed at risk when EU funding was withdrawn in 2005.

2.3. Public Funding – Boon or Obstacle?

At the outset, it was EU Thematic Network funding which established ECCC as an effective working organisation. Industrial members who joined ECCC received financial support from Europe, while the project Coordinators, ERA and later ETD, gained substantial support to provide an administrative Secretariat. Wisely, ECCC also set up a parallel management structure led by volunteer technical experts to establish the working principles. An initial four-year programme in 1993-97 was successfully renewed in 1997-2001 and again in 2001-2005.

Then the merry-go-round stopped turning. The proposal for 2005-2009 was rejected. An organisation raised on public funding faced the need to wean itself off. Over the six leaner years which followed, reduced efforts were put into ongoing testing and technical exchange, while unsuccessful attempts were made to find new sources of external support. The funding philosophy had turned against long term commitments. EU research programme management nowadays prefers to support ad-hoc collaborations between individual companies and organisations from across Europe, who form temporary alliances to spend public funds on limited-term one-off projects. It is questionable whether this philosophy truly delivers best value for the taxpayer.

Even in the 1990s, EU R&D funding had strongly favoured blue-skies speculative research over practical development, which was commonly considered too unimaginative, too intellectually second-rate, and/or too close to market to justify public funding. To indicate novelty, ECCC's first four-year project "Creep", had to be followed by successive "Weld-Creep" and "Advanced Creep" projects, each promising a new start, each promising to address new challenges. The real needs for continuity, long term data generation and the gradual construction of reliable technical

593

Recommendations and Data Sheets, had to be downplayed in the interests of winning competitive funding. ECCC's fourth project proposal may well have failed largely because we had run out of good new words to use.

2.4. Rebirth and Revival

By 2010, the needs were becoming clearer. ECCC could – in many ways – cope quite well without large injections of cash. We could manage without the free travel which Europe had provided. What we really needed was organisation and discipline. The EU Network structures had established clear membership rules, reporting requirements, deadlines, and a central administrative Secretariat. These were the necessities which had to be replicated without European funding. Crucially, CSM of Italy stepped forward with an offer to carry out the Secretariat function, to be supported by a "Joint Industrial Project" (JIP), with a membership subscription set at 2500 euros per organisation per year.

The agreed structure [1] is very simple. ECCC, an independent voluntary organisation with no direct financial responsibilities or funds, continues largely on an unchanged basis. The JIP is a private non-profit programme currently undertaken by CSM, and it operates separately and in parallel. The JIP is tasked with the basic organisation of ECCC including financial contract management, six-monthly meetings, documentation, administrative support, and records management via controlled website access. CSM draws a fixed fee to cover this operational budget. Surplus funds generated from subscriptions are held within the JIP to be spent at ECCC's discretion on technical work or on improved JIP operation. Crucially, continuing membership of ECCC is now subject to a requirement to join the JIP.

Costs were driven down to a minimal level in a largely successful attempt to avoid losing valuable members in cost-conscious times. Remote managers across Europe faced new applications for a subscription to an organisation which had previously allowed free entry. In 2005, the last year of the EU funded programme, Merckling [4] records an ECCC membership of 48 organisations. Today, the JIP has a membership of 32 organisations, and the list is growing. In the context of the economic downturn and political pressures against high temperature technology

arising from its role in climate change, this – and the strength and depth of the recent ECCC Conference [2] – represents a considerable success.

3. The Joint Industrial Programme – JIP 1

As we approach the end of the first JIP period, it is appropriate to review what it has achieved. We no longer need to give impressive names to specific periods of time. We describe 2011-2014 as JIP 1, and in 2014-2017 we will proceed with JIP 2.

Not everything is perfect - yet. Some European nations, which have considerable facilities and expertise in high temperature technology but do not have active National Creep Groups, have found participation difficult. ECCC will explore mutually acceptable solutions. We used to gain significant input from the petrochemical industry, which we would like to restore, alongside other high temperature industries such as solar thermal, energy from waste, and advanced nuclear generation. Creep testing is a time-consuming activity, and delays while machines run can sometimes provide cover for delays before they start to run. Nevertheless, ECCC "JIP 1" has developed and agreed a new series of creep testing programmes on its conventional four-yearly cycle within each of the WG3.x Working Groups, many of which are now well under way. There has also been a very encouraging level of interest in new technical work programmes, both to re-evaluate previous assessments of well-known materials in the light of new data and insights, and to develop and extend assessment technologies into new and innovative areas. Finally, the nine-volume ECCC Recommendations on Creep Data Validation and Assessment Procedures have been substantially revised and updated.

3.1. WG3A – Ferritic Steels

WG3A has long been ECCC's most active WG3.x Group, no doubt encouraged by the relatively open commercial environment in high temperature boiler technology and the overriding importance of creep in thick section component design and performance. Past highlights have included the compilation and assessment of very large creep rupture databases on the leading steels P91, E911 and P92, which have done much to put early performance claims into proper perspective, and will

shortly be updated to include the most recent long term test results. In JIP 1, new test programmes include a systematic exploration of performance in P92 materials and welds. In the context of adverse plant experience with welds in P91 and P122, this will help clarify whether P92 welds might be at similar risk. Parallel programmes include for example a Belgian programme on dissimilar welding austenitic steel to P92 which is giving interesting pointers as to the optimum filler metal choice.

Turning to technical work, there has recently been an upsurge of interest in using large ECCC datasets to analyse the influence on creep behaviour of secondary experimental variables such as chemical composition and heat treatment, and to look at relationships between creep strength and ductility. Nardone [5] and Spindler [6] have each developed modified rupture strength predictions for P91 which take account of individual cast chemical composition. A parallel analysis of the ECCC data set, concentrating specifically on the deleterious influence of nickel, has shown that this varies with time and temperature in a complex way, and becomes much more significant in the long term [7]. This analysis confirms Japanese results on a different data set [8], and aligns with microstructural evidence that nickel promotes the long term precipitation of Z phase and dissolution of the strengthening MX precipitates [9].

These developments clearly offer opportunities for exploitation in life assessment and design with current materials. Further, a better understanding of how compositional factors affect the performance of well-tested materials such as P91 and P92 could also play a role in the development of improved materials. Thus, for example, long term test data and modelling on P91 and P92 could offer vital pointers toward minimising long term Z phase formation in future martensitic steels.

ECCC is not a materials development organisation. The expensive long term testing and assessment which ECCC undertakes is intended to support proven materials in practical operation, and should not be wasted on experimental variants most of which will be discarded. However, the potential for learning from older materials data how best to develop newer materials should not be overlooked. Additionally, it may sometimes be judged that a novel material, albeit not yet in commercial operation, is sufficiently well established in preferred composition and/or promising in

properties to merit inclusion in ECCC's programme. Hence, MARBN steel is now the subject of a new WG3A test programme. Further, collaborative interchange between ECCC and materials development programmes such as KMM-VIN is to be welcomed and promoted. As ECCC overcomes the remaining difficulties in assessing today's leading materials, the case for tackling tomorrow's materials may strengthen.

3.2. WG3B – Austenitic Steels

WG3B has historically been a smaller Working Group, dealing as it must with a plethora of competing candidate materials for boiler thin section applications where creep is only one of the important materials selection criteria. Nevertheless, an extensive range of alloys has been assessed. There is considerable interest in testing and data collation on the leading material Sanicro 25, which we expect to commence shortly under JIP 2. Work is also ongoing in a number of areas including HR120, 316H modelling and 347H weld metals.

3.3. WG3C – Nickel-Base Alloys

WG3C probably has the most diverse remit of the WG3.x Groups. Activities in steam plant materials overlap with WG3B, while activities on gas turbine alloys tend to involve different organisations and operate in a more commercially restrictive environment. How ECCC should react to that is a matter of debate. Whereas WG3A test programmes are typically designed to feed into and fill gaps in large pooled data sets which can be well handled by sophisticated assessment techniques, WG3C has had to consider the value of generating a small data set, largely on its own, and then attempting to undertake a reasonably reliable assessment. The major ten-year WG3C programme on GTD111, reported at the ECCC Conference [10], shows both the merits and the difficulties of such an endeavour. After iterated assessments on a sparse but valuable data set, significant advances in understanding were eventually achieved, including insights into the differing behaviour of directionally solidified and equiaxed materials which are of general relevance to a wider class of blading alloys.

A more conventional assessment has also been carried out on the larger data set available on Alloy 617B, a variant of Alloy 617 designed for enhanced creep properties [11]. WG3C is also supporting a parallel materials modelling project, in partnership with the German Creep Group, to clarify the differences in precipitation sequence between 617B and 617 which may correspond to differences in creep behaviour. A collaborative testing programme is also being initiated on Alloy 718+, a newly introduced gas turbine material variant offering potentially improved creep strength. As is often the case, ECCC sees its "USP" (unique selling point) as the capability to provide an independent and objective evaluation

3.4. WG1 – Creep Data Generation and Assessment Procedures

WG1 is nowadays the busiest Working Group, with active subgroups also pushing the boundaries of assessment technology into new fields. The core interest continues to be in creep rupture data and the extent to which ECCC's Recommendations and PATs ensure a high quality assessment. Spindler [12] led an illuminating exercise in which he generated an artificial "ideal data set" IDS1, based on a simple mean rupture strength equation, combined with a randomisation procedure to generate pseudo "data points" with a typical range of scatter. Round-robin trial volunteers from WG1 were invited to carry out their own assessments on IDS1 and to apply the PATs. A wide range of models was produced, some but not all in close conformity with the original generating equation. In some cases, "predictions" in long term extrapolation showed substantial over-optimism, including predictions based on rigorous mathematical data fitting procedures which passed the conventional PATs.

There may be a number of causes for these difficulties. Attention has however been concentrated on PAT2, the post-assessment test which compares observed and predicted life data over the range from short to long term. Clearly, the appropriate assessment should not show bias, for example a tendency to under-predict rupture life in the short term while over-predicting life in longer term tests. If the predicted and the observed life data are plotted against each other and the correlation evaluated on a purely visual basis, it does not matter which series is plotted on which axis. However, when a mean equation is fitted to the "predicted vs observed" data points using a mathematical procedure such as least-

squares fitting, then the result depends on which variable is plotted on the x and which on the y axis. The reason is that by mathematical convention, the least-squares fitting procedure minimises the sum of the squares of the residuals (distances between each individual data point and the best-fit line) in the y direction. This therefore produces a best-fit line which depends on which variable (in our case, predicted or observed life) is plotted on the y axis. For any set of data, creep-related or otherwise, reversing which variable is plotted on which axis will result in a change, sometimes a considerable change, to the resulting best-fit equation. The traditional PAT2 tests have been based on one specific option, with observed life plotted on the x axis. WG1 has sought to determine, by a second series of round-robin trials on real datasets [13], whether a "reversed PAT" with observed life plotted on the y axis would be more appropriate.

The four model data sets varied considerably in their response to assessment, and again, there were substantial differences between models produced by experienced assessors. The PATs did act to eliminate unsuitable models, but in the case of PAT2, the traditional and reversed PATs had different consequences. The traditional PAT tended to accept fewer models, but these often included the most optimistic outliers. The reversed PAT was less discriminating, but generally rejected the most optimistic models. The recommendation which ECCC will implement is therefore that the reversed PAT2 tests should now become the primary criteria addressing comparison of observed with predicted life data.

3.5. WG1 Subgroups

The subgroup on stress relaxation, led by Holmström, has recently reported its first project results [14]. In outline, a model data set was used in a round-robin assessment trial, the main focus of which was to test whether predictions based on a culled data set out to 10 hours could successfully be extrapolated to describe behaviour of the full data set extending to 3,000 hours. The results were sobering.

This has implications for stress relaxation and creep-fatigue testing, where common practice is to employ dwell periods of an hour or less, whereas the periods between transients on operating plant are often in thousands of

hours. Flexible plant operation, alongside the growing use of intermittent renewable energy sources, is of course a major current concern in our industries. The view presently taken within ECCC is that we will develop our expertise in creep behaviour as our remit to engage with these issues. Thus, topics such as relaxation process modelling and creep ductility exhaustion fall within our technical scope, whereas the parallel analysis of fatigue phenomena and plant transient modelling should be addressed outside ECCC.

The subgroup on small-scale testing seeks to produce ECCC guidelines on this type of testing, and to maximise comparability between these semi-nondestructive tests for plant condition monitoring and conventional uniaxial testing [15].

The newest WG1 subgroup addresses materials modelling, with the ultimate aim of supplanting empirically based creep assessment techniques with microstructurally based mechanistic models. ECCC Conference papers such as reference [16] illustrate both the promise and the difficulties encountered in this approach. If the ultimate goal still seems distant, there is no doubt that qualitative identification of key microstructural factors, and quantitative modelling of phase transformations and precipitation behaviour, are rapidly advancing to the benefit of high temperature technology. Quantitative modelling of the resulting mechanical behaviour, and its integration into practically viable assessment methodologies, remain as challenges for the future.

4. Future Prospects

We should not pretend that climate change can be ignored. Nor should we argue that changing the way we generate energy is just too difficult to do. Yet we would equally be wrong to ignore the major role which fossil fuel combustion will inevitably retain for many years into the future, or the carbon savings we could achieve by doing it better. Governments like clean renewable energy technologies which make good publicity. However, it may be the fossil power industry who – if they act responsibly – can actually do more to reduce the harm we are doing to our planet.

The implications are that we must not abandon the search for newer, better materials which can improve plant efficiencies and save carbon emissions. For ECCC, the fact that provision of long term design data takes time is all the more reason for getting it started quickly, once next generation materials can be identified with reasonable confidence. We should promote ECCC assessment as an objective evaluation, without which a critical high temperature material should not command confidence in the marketplace. We must work continuously to improve our assessment technology so that we continue to deserve that confidence. We should also accept our role in minimising the problems caused by fossil power generation. Industry, supported by ECCC, will need to concentrate on long term life assessment to maintain spare capacity at minimal cost, and on damage – resistant component replacements to cope with flexible plant operation.

4.1. European Future

ECCC, in common with the European high temperature plant development community, is learning how to cope with less continuity of support from governmental institutions. However, this cannot truly be described as a positive development. Nor can the retreat of government simply be explained as a response to the threat of climate change. The decisions to stop funding ECCC and a continuing COST 501/522/536 programme pre-dated the Horizon 2020 resourcing shift towards renewables. Further, ad-hoc fossil power R&D projects such as MACPLUS and NextGenPower have continued to attract EU support.

Considering global comparisons, the US has its "military-industrial complex" which brings together the aggressive commercial drive of private industry and the powerful support of national government. Similarly, the close links between government, industry and academia in Japan are legendary. Many successful emerging nations such as South Korea also have comparable partnerships between a strong state and strong private industry. All these nations demonstrate their commitment to achieving industrial and technical strength through the long term development of powerful, capable institutions and companies, in partnership between the private and public sectors.

Only in Europe are private enterprise and state enterprise so often seen as conflicting political ideals. Only in Europe are there overlapping levels of national and supranational government which support research and industrial development. Only in Europe is R&D treated as a primarily short-term endeavour, in which competitive funding is valued above long term collaboration and construction. Only in Europe is the role of the R&D funding agency so dominated by the need to balance national interests and promote geographic integration. Only in Europe is the development agenda so clearly determined by an internal political agenda.

Does it work? It would be wrong to give a one-sided answer. The EU has led the global response to climate change. Political governance deserves credit for that. Europe also led at the outset in promoting the concept of superalloy-based steam power plant through its AD700 programme, which answered the EU call for blue-skies innovation in R&D. Does Europe still lead in that field? Recently, the IEA carried out a comparative review [17], pointing out the need for a consistent, coordinated programme of research, development, demonstration and validation over a timescale of the order of two decades. The IEA concluded that, although significant programmes in Japan and China had begun at least a decade later than in Europe, there is every prospect that both will catch up or overtake.

ECCC, and KMM-VIN WG2, can survive and thrive as independent long-term collaborative institutions. In this author's personal view, Europe also needs a stronger, more joined-up national and supranational European programme to coordinate long term collaborative industrial research and development.

REFERENCES

[1] Merckling, G., Di Gianfrancesco, A., Holdsworth, S. R., Allen, D. J., Zanin, E., Kern, T-U., and Steller, I., "Joint Industrial Program Proposal for ECCC", February 2011. See "JIP Description" at:

http://www.c-s-m.it/en/business_sectors/energy_and_environment/eccc_joint_industrial_project.html

[2] 3rd International ECCC Creep & Fracture Conference, Rome, Italy, (5-7 May 2014).

[3] Thornton, D.V., 'The Activities of the European Creep Collaborative Committee", *Proc. Conf. "Life Assessment of Industrial Components and Structures"*, ERA/VALUE, Churchill College, Cambridge, (October 1993).

[4] Merckling, G., "Long Term Creep Rupture Strength Assessment: The Development of the European Collaborative Creep Committee Post Assessment Tests", *Proc. ECCC Conf. on Creep and Fracture*, London, pp. 3-11, (12-14 September 2005).

[5] Nardone, S., 2013, "Prediction of T/P91 (X10CrMoVNb9-1) Creep Strength Based on Materials Test Certificate Data", Presentation to ECCC WG3A, Rome, (5-7 September 2013).

[6] Spindler, M. W., "Summary of Results for Models Describing Meta Data Factors Affecting Creep Failure in Grade 91", Presentation prepared for ECCC WG3A, Rome, (5-7 September 2013).

[7] Allen, D. J., "Analysis of ECCC Creep Rupture Data on Grade 91 Steel – The Influence of Nickel", 3rd International ECCC Creep & Fracture Conference, Rome, Italy, Paper 16, (5-7 May 2014).

[8] Kimura, K, Sawada, K and Kushima, H, "Long-Term Creep Strength Property of Advanced Ferritic Creep Resistant Steels", Proc. Sixth International Conference on Advances in Materials Technology for Fossil Power Plants, EPRI, Santa Fe, New Mexico, Paper S3A 02_59, (August-September 2010).

[9] Sawada, K, Kushima, H, Hara, T, Tabuchi, M and Kimura, K), "Heat-to-heat variation of creep strength and long-term stability of microstructure in Grade 91 steels" Mater. Sci. Eng. A, 597, pp. 164-170, (2014).

[10] Allen, D. J., de Bruycker, E., Keustermans, J. P., Holmström, S., Gomes, M., Kolkman, H., Messelier-Gouze, C., and Vacchieri, E.,

"ECCC Test Programme and Data Assessment on GTD111 Creep Rupture, Strain And Ductility", 3rd International ECCC Creep & Fracture Conference, Rome, Italy, Paper 14, (5-7 May 2014).

[11] Krein, R., Di Gianfrancesco, A., Gotti, A., Lombardi, P., Gamble, W., and Barnard, P., "ECCC Assessment of Creep Rupture Strength for the New Nickel Alloy 617B", 3rd International ECCC Creep & Fracture Conference, Rome, Italy, Paper 69, (5-7 May 2014).

[12] Spindler, M. W., "Summary of Results for 11 CRDAs for Idealised Creep Rupture Dataset Number 1", Presentation to ECCC WG1, Rome, (29 October 2012).

[13] Spindler, M. W., et al, "ECCC Guidance for Creep Rupture Data Assessment", 3rd International ECCC Creep & Fracture Conference, Rome, Italy, Paper 145, (5-7 May 2014).

[14] Holmström, S., Friedmann, V., Klenk, A., Merckling, G., Norman, M., Pohja, R., Riva, A., Sandström, R., and Spindler, M. W., "Long Term Stress Relaxation Modelling", 3rd International ECCC Creep & Fracture Conference, Rome, Italy, Paper 72, (5-7 May 2014).

[15] Brett, S. J., "The Application of Small Scale Sampling and Impression Creep Testing to Power Plant", 3rd International ECCC Creep & Fracture Conference, Rome, Italy, Paper 70, (5-7 May 2014).

[16] Sandström, R., "Creep Strength in Austenitic Stainless Steels", 3rd International ECCC Creep & Fracture Conference, Rome, Italy, Paper 142, (5-7 May 2014).

[17] Nicol, K., "Status of Advanced Ultra-Supercritical Pulverised Coal Technology, IEA Clean Coal Centre Report CCC/229", (December 2013).

STEAM OXIDATION OF STEELS AND ALLOYS:
A NEW METHOD FOR COMPARISON OF LAB TESTS WITH OPERATING POWER PLANTS

S. Straub, R. Knödler

Alstom Power GmbH, Mannheim
Stefan.straub@power.alstom.com

Abstract

The oxidation stability of materials for high-temperature power plants is usually tested in the lab with equipments at constant temperatures. These test devices are valuable for a quick assessment of different steels and alloys. In realitiy, steam power plants operate at varying temperatures due to changing demands (day/night, summer/winter, outages...). This implies that testing of materials in operating power plants is necessary in order to come near the real operating conditions. In the past, this was done for a large variety of materials. However, the results obtained by these testings are not easily comparable to the lab tests, because of the continually changing temperatures.

Therefore, in the present publication a method was developed, which allows to obtain rate constants for the growth of oxide scales when temperatures are changing continuously. It turned out, that for martensitic steels lab tests and plant tests yield similar results, i.e. steam pressure and steam velocity do not influence scale growth. In contrast, Ni-base alloys show considerable higher oxidation rates in plant tests than in lab tests.

A comparison with literature data was conducted, which confirmed our approach.

Key words: Steam oxidation, power plants, martensitics, Ni-base alloys

1. Objective

Because of the higher temperatures in modern power plants it is necessary to get a precise knowledge of the oxidation rates of the steels and alloys that are used [1]. To date there is no standardised test method to determine oxidation rates in hot steam in the laboratory. The available data was generally obtained from tests in steam with different compositions at atmospheric pressure [2 -7]. Besides, in these laboratory tests exposure times of more than around 3,000 h are rarely exceeded.

While in these tests isothermal conditions prevailed, tests were also performed under cyclic loads, which produced some different results, as the thermal stresses can lead to premature spalling of the oxide layers [8]. However, the spalling behaviour of the steels, which is important for practical operation, cannot be simulated satisfactorily in the laboratory even with such thermal cycles.

More reliable data were obtained from tests in power plants, in which the samples were exposed to realistic conditions (pressures, temperatures, load cycles). Tests such as this were performed within the scope of a Brite-EURAM project in Vestkraft power plant in Denmark

[9 – 10]. Similar investigations were carried out in a power plant in Westfalen (Germany) [11-13].

However, in contrast to lab tests, a basic problem with tests in power plants is the variation of temperatures due to load cycles (e.g. day /night). This implies, that results from lab tests cannot be compared directly with power plant tests, because no single common temperature can be identified. Therefore, the aim of the present study is to provide a method by which data from cyclic tests can be compared reliably to tests at constant temperature. This can be achieved by calculating temperature-independent rate constants for both lab and plant tests. The detailed basis of this method is described in [16].

2. Method for analysing data from plant tests

An example for the raw data of our temperature distribution during tests in power plants is shown in fig. 1.
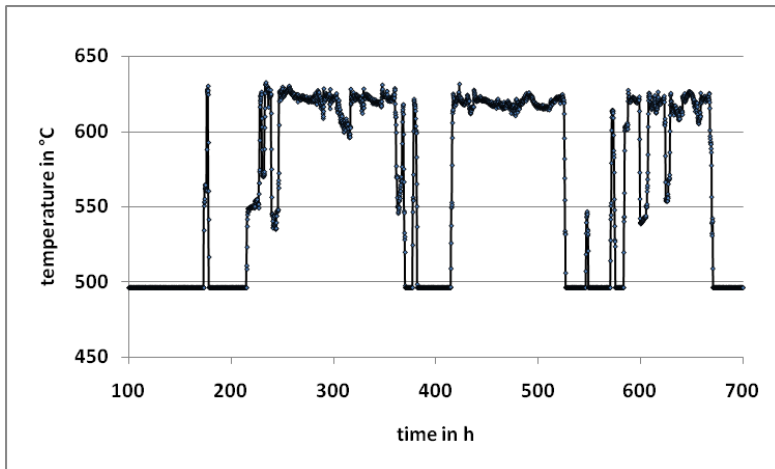
Fig. 1: Example for temperature variations of steel samples in an operating power plant boiler

For our purposes these data were transfered into histograms: for each temperature interval the respective operation time is given. For each of such periods the basic equation for the scale thickness x can be applied:

$$x^2 = kt, \quad where \quad k = k_0 \exp(-\frac{Q}{RT}) \quad ....(1)$$

where k is the rate constant in mm^2/h, Q the activation energy and T the absolute temperature. K_0 is the temperature-independent rate constant. Q is approximately 170 kJ/mol for martensitics[14] and 100 kJ/mol for Ni-base alloys [15]. However, the results are rather insensitive to variations of these values.

When the temperature changes during operation, the differential diffusion law must be applied:

$$\frac{dx}{dt} = k' * \frac{1}{x} \quad \ldots\ldots\ldots\ldots\ldots.(2)$$

$$\Longrightarrow \quad \int_{x0}^{x1} x\, dx = \int_{t0}^{t1} k'\, dt$$

Integration yields a temperature independent rate constant k_0 . For 3 (i.e. the 3 highest) different temperatures/times this becomes (where x_3 is the overall scale thickness):

$$k_0 = \frac{x_3^2}{\left(e^{-\frac{Q}{RT1}} * t_1 + e^{-\frac{Q}{RT2}} * (t_2 - t_1) + e^{-\frac{Q}{RT3}} * (t_3 - t_2) \right)} \quad \ldots\ldots\ldots (3)$$

By measuring the total scale thickness x_3 after a certain time/temperature regime, k_0 can be calculated by using eq. (3). Then, with this k_0, scale thicknesses for all sets of time/temperature profiles can be calculated , using eq.(1). However, it must be stressed, that this procedure is only applicable, if growth of the scale is (nearly) parabolic with no or negligible spallation.

3. Results

Table 1 shows the composition of the steels and alloys used in the present study:

%	Cr	Co	W	Mo	Fe	Ni
P92	8,9		1,9	0,5	bal	
FB2	9,3	1		1,5	bal	0,2
Waspalloy	19	13		4	< 2	bal
IN625	22			9	< 5	bal

Table 1: Main constituents of the investigated steels (nominal values).

The cylindrical samples had a diameter of 25 mm and were 20 mm high. They were mounted in 2 modules on carrier plates which were operated in bypass lines of a power plant boiler at 630°C and 725°C (maximum temperature). Therefore, the samples endured real boiler components during operation.

After being exposed, the samples were removed and their weight loss detected. Selected samples were subjected to metallographic analysis.

For the evaluation, the following profiles have been recorded:

Temp in °C	time	Temperature Profile #1 (630 °C – module)	Temperature Profile #2 (725 °C – module)
720	t1		6050 h
700	t2-t1		1750 h
680	t3-t2		750 h
635	t1	1950 h	
620	t2-t1	4000 h	
600	t3-t2	400 h	

Table 2: Temperature / time profiles for samples in the plant

Lab tests were carried out in a furnace at constant 650 °C for the martensitics and 750 °C for the Ni-base alloys. 100 % steam was used with a flow velocity of 5 cm/sec.

We used the data for weight gain, because they are more sensitive than scale thickness data – especially for the very small values for the Ni base alloys. There is a good correlation between scale thickness and weight gain, provided that no substantial spallation occurred.

As example for weight gain curves the following graphs shows lab tests of martensitic steels and of the Nickel base alloys:
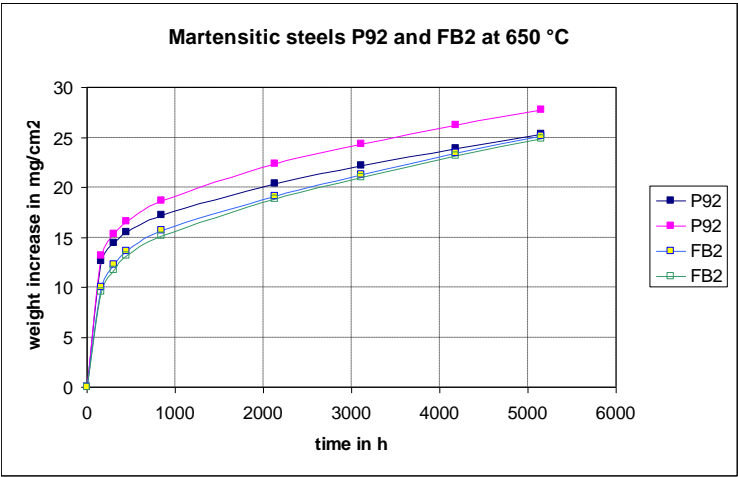
Fig. 2: Weight gain for P92 and FB2 in lab tests at 650 °C
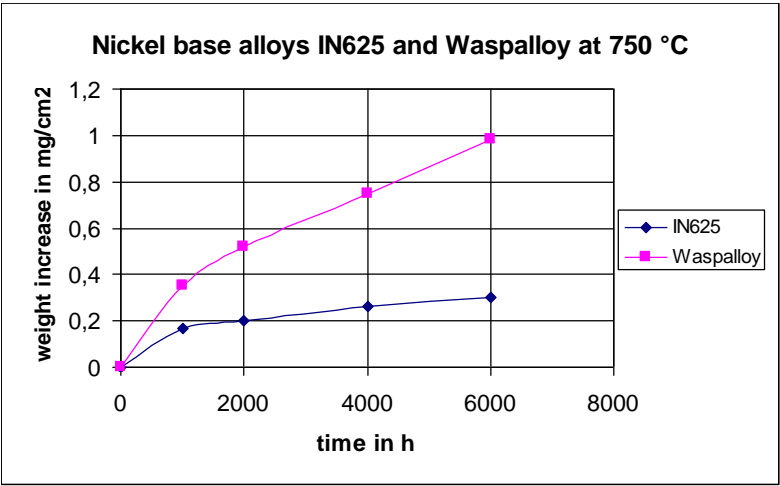
Fig. 3: Weight gain for IN625 and Waspalloy in lab tests at 750 °C

Data for the plant operation cannot be given in such a straightforward manner, because temperatures are changing continuously. Therefore, the oxidation rate is given in fig. 4 for the respective temperature/time profile of table 2:
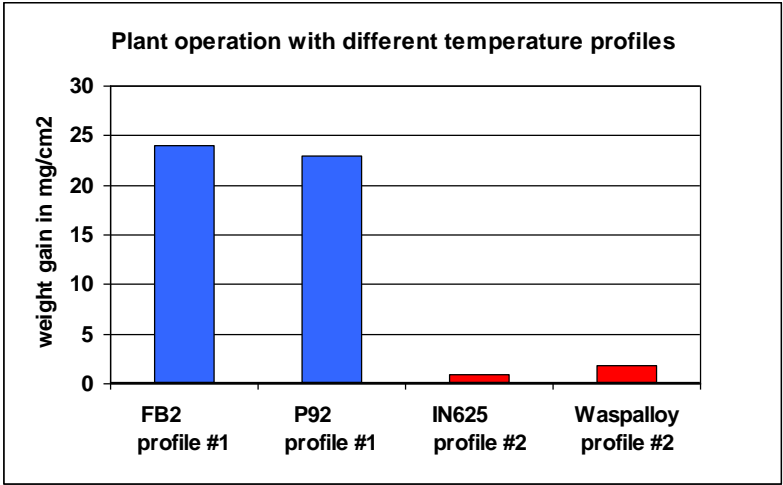
Fig. 4: Weight gain for samples, operated in the plant

A compilation of the oxidation data in the lab and in the power plant shows table 3:

	Lab tests				Plant tests			
	P92 650 °C 5000 h	FB2 650 °C 5000 h	Wasp 750 °C 5000 h	IN625 750 °C 5000 h	P92 profile #1	FB2 profile #1	Wasp profile #2	IN625 profile #2
Weight gain in mg/cm^2	27	25	0,9	0,28	23	24	1,85	0,95

Table 3: Compilation of lab and plant data

We found a good correlation between weight gain and oxide scale thickness: 10 µm scale corresponds to about 1,2 mg/cm^2. This value is confirmed by comparing our fig. 2 with fig. 18 of reference [17]. A micrograph of an FB2 sample after exposure in the plant is shown in fig. 5, exhibiting a dense inner Cr-Fe spinel layer and an outer porous magnetite layer with a tendency of spallation.
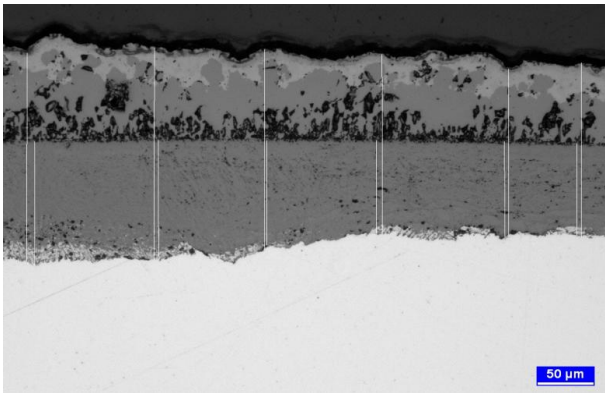
Fig. 5: FB2 in plant test after temperature profile #1: about 200 µm scale thickness

4. Calculation of rate constants

With the data in table 3, the rate constant k_0 was calculated from the weight gain data, using eq.(3). This was done for the plant tests and for the lab tests. Table 4 and fig. 6 shows the results:

K_o in mg^2/cm^4 h	P92	FB2	Waspalloy	IN625
Plant tests	1.6 10^9	1.75 10^9	129	34
Lab tests	1.45 10^9	1.25 10^9	32.8	3.2

Table 4: Oxidation rate constants for lab and plant operation, calculated from the experimental data
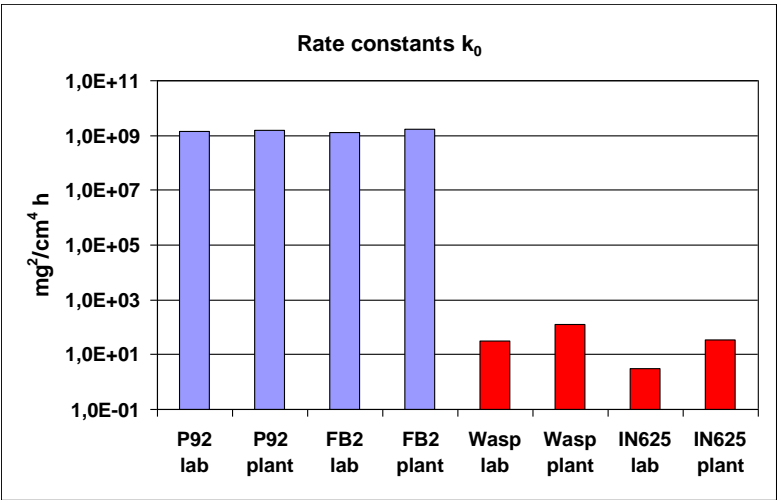
Fig. 6: Rate constants for martensitic steels and Ni-base alloys in lab test compared to plant tests

It can be seen, that for the martensitic steels there is almost no difference between lab and plant tests. In contrast, with both Ni-base alloys the plant test rate constants were considerably higher than the data from the lab tests. The difference in k_0 is a factor of 4 to 10, which means that the thickness of the oxide scales differ by a factor of 2 to 3. The reasons for the higher oxidation rates in the plant might be the higher pressure and/or the frequent thermal cycling. In addition, the different steam compositions (pH, oxygen, ….) might play a role.

5. Comparison with data from reference [17]

With our data from table 4 we were able to calculate rate constants for P92 (plant operation) for different temperatures. This is shown in fig. 7.
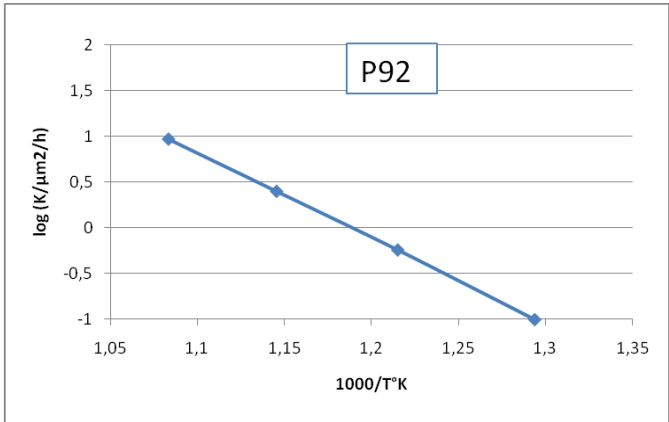
Fig. 7: Rate constants for P92,calculated from the values of table 4, as function of inverse temperature

If this curve is compared with the respective figure 19 in ref [17], a very good agreement can be observed – see figure below from this reference.
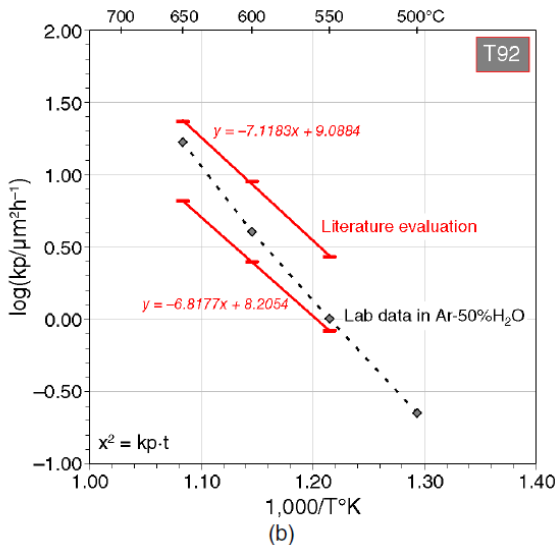
FIGURE 19. *Summary of scale growth kinetics (total scale thickness) for Grade 91 (a) and Grade 92 (b) solid lines show upper and lower limits of oxidation derived from literature evaluation (compare e.g., Figure 18). Data points relate to own laboratory experiments in Ar-50%H_2O obtained for a single batch of P/T91 and P/T92, respectively. Compositions of the used batches are given in Table 2.*

6. Conclusions

The method described in this publication allows the calculation of rate constants of oxide growth when a steel is exposed to more than one single temperature (fluctuating temperatures). This can be used to compare the results of lab tests with those of operating power plant tests.

The comparison with data from the literature confirmed the suitability of this approach.

7. References

1. Q. Chen, G. Scheffknecht, New boiler and piping materials – design considerations for advanced cycle conditions, VGB PowerTech 11 (2003), 91.
2. H. Meyer, D. Erdmann, P. Moser, S. Polenz, KOMET 650 – Kohlebefeuerte Kraftwerke mit Dampftemperaturen bis zu 650 °C, VGB PowerTech 88/3 (2008), 36.
3. K. Segerdahl, J.E. Svensson, L.G. Johansson: High temperature oxidation of 11 % Cr steel, Materials and Corrosion 53 (2002), 247.
4. R. Viswanathan, W. T. Bakker, Materials for boilers in ultra supercritical power plants, Proc. of Int. Power Gen. Conf., Miami Beach, Fl., USA, July 23 - 26, 2003.
5. I. G. Wright, B. A. Pint, Assessment of high-temperature oxidation behaviour of Fe-Cr steels in water vapour and steam, NACE CORROSION, Denver, CO, USA, April 8 - 1, 2002, paper No. 02377.
6. J. Zurek, M. Michalik, T. U. Kern, L. Singheiser, W. J. Quadakkers, The effect of water vapor content and gas flow rate on the oxidation mechanism of a 10 % -Cr ferritic steel in Ar-H_2O mixtures, Oxidation of metals 63 (2005), 401 – 422.
7. R. Knödler, S. Straub, Entwicklung von fortgeschrittenen Turbinenwerkstoffen mit hoher Kriechfestigkeit und hoher Oxidationsbeständigket, 39. Kraftwerkstechnisches Kolloquium, Dresden, 11.-12.10.2007, pp.302-310
8. D. Laverde, T. Gomez-Acebo, F. Castro, Continuous and cyclic oxidation of T91 ferritic steel under steam, Corrosion Science 46 (2004), 613.
9. R. Blum, Q. Chen, C. Coussement, J. Gabrel, C. Testani, L. V, Operational tests of superheater materials at high steam temperatures in a hard-coal fired steam generator, VGB PowerTech 10/86 (2001).
10. J. Gabrel, C. Coussement, R. Blum, Q. Chen, C. Testani, Superheater materials testing for USC boilers : Steam oxidation rate of 9 advanced materials in industrial conditions, Conference on high temperature corrosion and protection of materials, Les Embiez, 22 - 26 May 2000.
11. R. Knödler, S. Straub, B. Scarlin, KOMET650 – Erprobung von Materialien für den Einsatz in Dampfturbinen bei Temperaturen bis 650 °C , VGB PowerTech 88/3 (2008), 59.
12. R. Knödler, S. Straub, B. Scarlin, Oxidation von Stählen und Beschichtungen. Morphologie der Schichten, VGB Power Tech 88/9 (2008), 112
13. R. Knödler, S. Straub, Growth of oxide scales during steam oxidation at 650 °C, VGB PowerTech, 88/10 (2008), 66
14. H. Naoi, H. Mimura, Sumitomo Data package for NF616 ferritic steel, 2nd edition, March 1994
15. N. Hussain, A.H. Qureshi, K.A. Shahid, N.A. Chugtai, Oxid. of metals 61 (2004), 355
16. R. Knödler, S. Straub, Steam oxidation of martensitic steels and of Ni-base alloys, Oxid. of Met. , July 2014 (in print)
17. J. Zurek, E. de Bruycker, S. Huysmans, W.J. Quadakkers, Steam oxidation of 9% to 12% Cr steels: critical evaluation and implications for practical applications, Corrosion 70/2, 112

OPTIMIZATION OF OXIDATION RESISTANT COATINGS FOR AUSTENITIC AND MARTENSITIC STEELS IN POWER PLANTS

S. Straub, S. Jäger, R. Knödler,

Alstom Power GmbH, Mannheim
Stefan.straub@power.alstom.com

Abstract

In order to achieve higher efficiencies and lower CO_2 emissions, future power plants have to operate at higher temperatures of up to 650 °C. At this temperature, steels must be protected in order to reduce oxide scale growth and spallation of scales to a tolerable rate. Our approach was to achieve this goal by applying coatings on the basis of aluminium compounds in a slurry. In addition to low oxidation rates, such coatings are expected to be also beneficial for erosion protection. The basics of this procedure are well known, however, optimization for long-term operation of several ten thousand hours of operation is necessary. Therefore, we investigated the effect of parameters like coating thickness, surface treatment, diffusion temperature and time, number of coating steps and other process parameters.

It turned out, that coatings of this type reduces the thickness of the oxide scale considerably and that even in operating plants the coated samples showed a very stable long-time performance. The most important parameters for achieving good results were the surface conditions of the substrate and the diffusion temperature/time profile during preparation of the coatings.

Keywords: Steam oxidation, coatings, austenitic steels, martensitic steels

1. Objective

In order to achieve higher efficiencies and lower CO_2 emissions, future power plants have to operate at higher temperatures of up to 650 °C. As consequence, materials will be subjected to attack by steam oxidation. Therefore, steels must be protected in order to reduce oxide scale growth and spallation of scales to a tolerable rate. Because of the increasing temperatures in modern power plants it is necessary to obtain precise knowledge of the oxidation rates of the steels and alloys that are used [1]. To date there is no standardised test method to determine oxidation rates in hot steam in the laboratory. The available data were generally obtained from lab tests in steam with different compositions at atmospheric pressure [2]. Besides, in these laboratory tests exposure times of more than around 3,000 h were rarely exceeded.

Several studies report about tests to reduce oxidation rates by applying coatings on 9 wt. % Cr steels [3 – 6]. For the coating process, different oxidation-resistant materials were used, e.g. Al-slurry, HVOF, CVD or pack aluminizing. It should be noted, that up to now almost all of the substrate materials, used by different authors, were martensitic 9-11% Cr-steels. In contrast, we have tested also austenitic and Ni-base alloys. In order to improve coating stability, surface pretreatment methods were applied [7]. Although no extensive practical experience exists, the results obtained to date are very promising.

2. Methods

As substrate materials, a martensitic 9% Cr steel, a Ni-base alloy and an austenitic steel with about 17% Cr were used:
- Austenitic steel 1.4962: main constituents: 17% Cr, 13% Ni, 3% W
- Martensitic steel 1.4901 ("FB2"): main constituents: 9% Cr,1.5% Mo
- Ni-base alloy 2.4633 ("IN602"): main constituents: 24% Cr, 10% Fe, 2% Al, bal: Ni

The coating itself was an Al-based slurry, delivered by Indestructible Paints Ltd., Birmingham. Spraying was performed using a commercial spraying gun with a nozzle of 0.5 mm and 1 bar pressure. The coating was applied in a series of spraying steps. After each step, the layer was dried at 70 °C for 0.5 h. After the final step, diffusion heating was carried out at 700 °C for 5 h.

The test samples (20*10*5 mm) were grinded to an average roughness of 0.4 µm (corresponding to 600 SiC). Several samples were sandblasted with alumina until a roughness of 2.4 µm was achieved.

3. Results

As an example for the evaluation of the diffusion process, fig. 1 shows the element distribution, as determined by scanning electron microscopy:
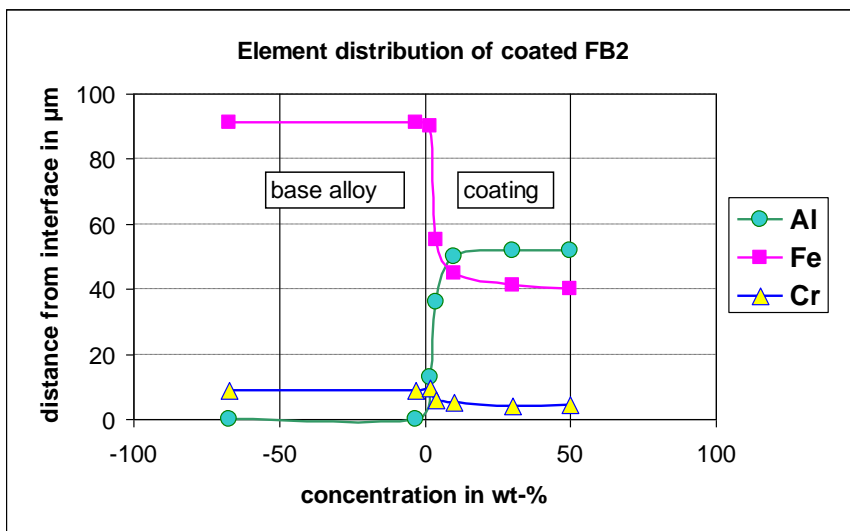
Fig. 1: Element distribution for the coated martensitic steel FB2

It can be seen, that Al and Fe diffuse into the layer, forming an FeAl intermetallic phase. Also, a small amount of Cr could be found in the layer.

Fig. 2 shows a micrograph of the sample characterized in fig.1:

Fig. 2: Micrograph of a coating on FB2, sand blasted substrate

As can be seen from fig. 2, the coating shows considerable inhomogeneities. This might be connected to the different expansion coefficients of coating and martensitic substrate. In contrast, the austenitic alloy and the Ni-base alloy yield more coherent coatings, as can be seen in fig. 3:
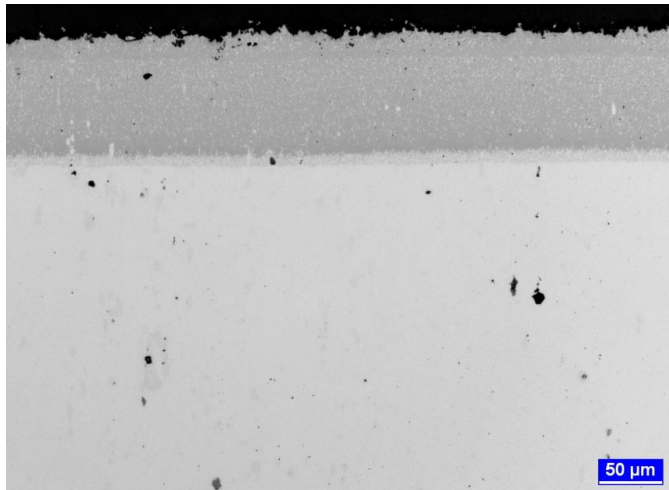
Fig. 3: Micrograph of a coating on IN602

4. Tests in steam atmosphere

The samples were exposed to superheated steam using a re-circulating arrangement. It works at ambient pressure at 650 °C. The steam has a flow velocity between 150 and 300 ml/h, which corresponds to about 4-8 cm/s (0.01 kg/m^2 s). De-ionized water with no additives was used. By continuous bubbling nitrogen through the reservoir, the oxygen content of the steam was kept below 20 ppb. The arrangement is shown in fig. 4.
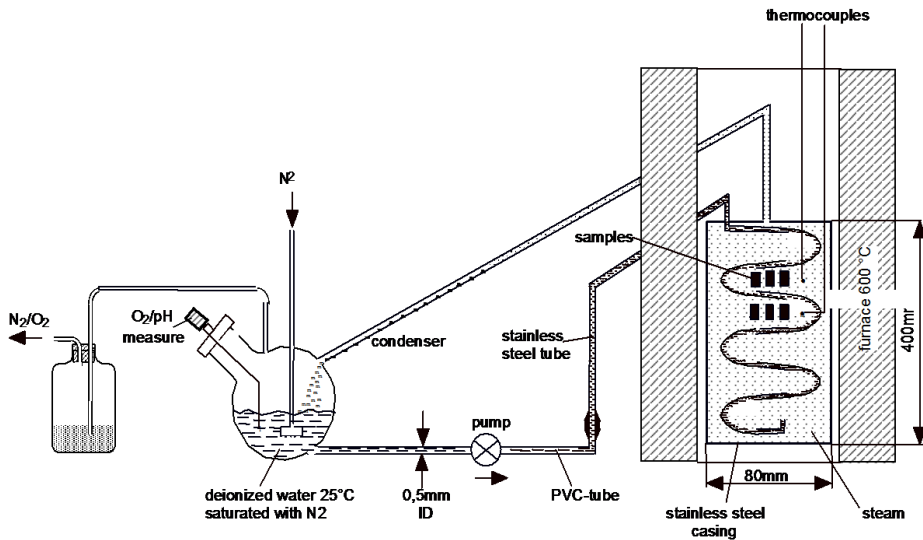
Fig. 4: Experimental arrangement for testing in circulating steam.

First test results after about 2000 h are shown in fig. 5 and 6. It is planned to continue testing up to at least 20.000 h to show the long-term stability of the coatings.

617
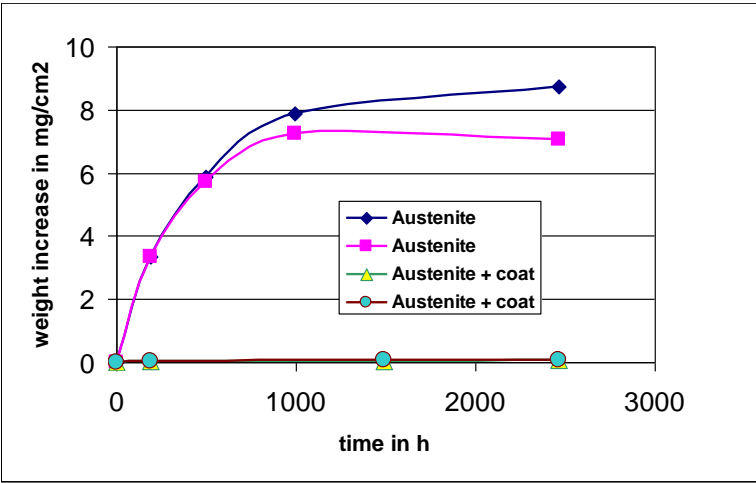
Fig. 5: Steam oxidation of coated austenite steel, compared to two uncoated samples
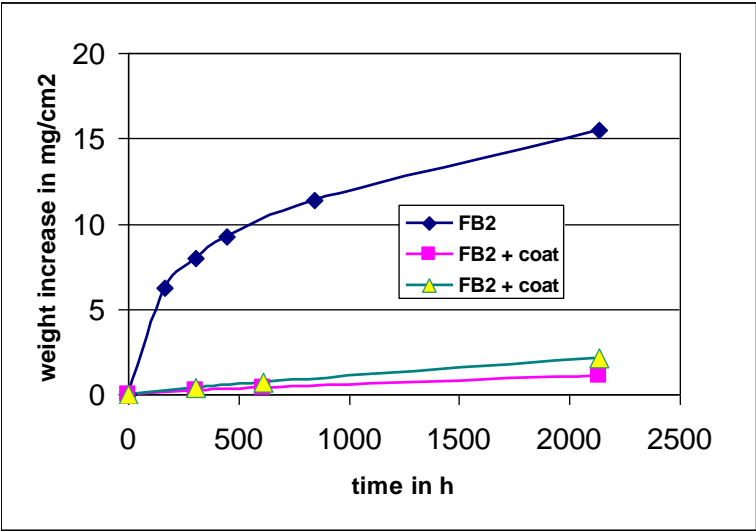
Fig. 6: Steam oxidation of coated martensitic steel, compared to an uncoated sample

A direct comparison of the different steels with and without coating shows fig. 7. These figures show, that in both steel types a considerable decrease in the oxidation rate is observed. In the case of the Ni-base alloys the effect is not so pronounced because the oxidation rates of the uncoated material are already very low.
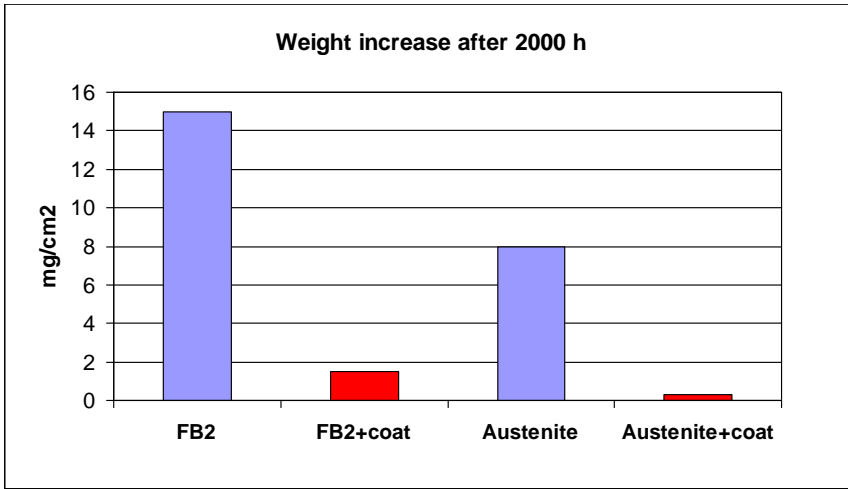
Fig. 7: Comparison of oxidation rates of different steels and coatings after 2000 h

After exposure in steam for as long as 31.200 h the coating is still in good shape, as fig. 8 shows. This was a steel with the same coating system as described above, but with a slightly different (not optimized) heat treatment.
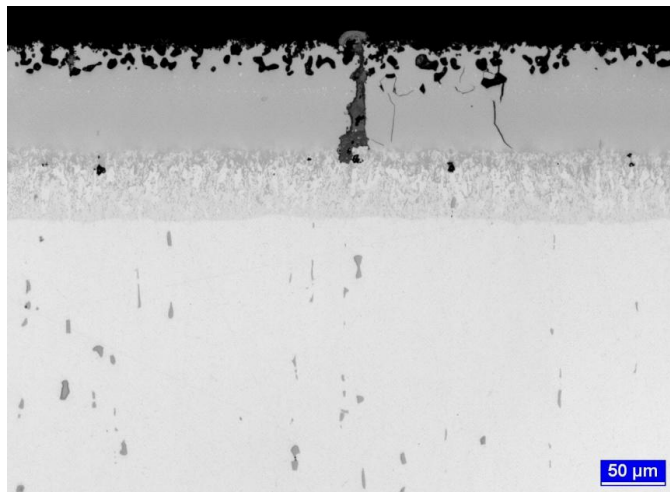
Fig. 8: Micrograph of a coating on the austenitic steel after 31.200 h at 650 °C in steam

619

5. Conclusion

The oxidation rates of coated steels (martensitic, austenitic and Ni-base alloys) could be lowered considerably by coatings, based on Al-slurries, which form a stable FeAl intermetallic phase. The present work showed that optimized coatings could contribute to the application of oxidation resistant steels in power plants for higher temperatures of up to 650 °C. Especially, it turned out that:

- During diffusion heating the slurry Al-coating is transformed yielding a compact FeAl intermetallic phase.
- With 3 consecutive slurry layers optimal adhesion and stability is obtained.
- Ni-base and austenitic steels show the best quality. Coatings on martensitic alloys must be further improved.
- Coating quality is better with grinded substrate surfaces than with rough surfaces.

References

[1] Q. Chen, G. Scheffknecht, New boiler and piping materials – design considerations for advanced cycle conditions, *VGB PowerTech* 11, 91 (2003).
[2] J. Zurek, M. Michalik, T. U. Kern, L. Singheiser, W. J. Quadakkers, The effect of water vapor content and gas flow rate on the oxidation mechanism of a 10 % -Cr ferritic steel in Ar-H_2O mixtures, *Oxidation of metals* 63, 401 – 422 (2005).
[3] M. Scheefer, R. Knödler, B. Scarlin, A. A. Bruna, D. N. Tsipas, New oxidation resistant coatings for steam power plants at 650 °C, *Materials and Corrosion* 56, 907 (2005)
[4] A. Aguero, U. Gonzales, M. Gutierrez, R. Knödler, R. Muelas, S. Straub, Comparison between field and laboratory steam oxidation testing on aluminide coatings on P92, *Mater. and Corros.* 62, 561 (2011)
[5] F.J. Perez, S.I. Castaneda, M.P. Hierro, Comparative study of micro- and nanostructural coatings for high-temperature oxidation in steam atmospheres: *Oxid. of metals* 80, 363 (2013
[6] R. Knödler, S. Straub, B. Scarlin: Oxidation of steels and coatings during exposion in an bypass of a steam power plant at 605 to 637 °C: *VGB Power Tech* 9, 112 (2008)
[7] X.D. Xiang, P.K. Datta: Shot peening effect on aluminide diffusion coating formation on alloy steels at low temperatures: *Scripta Mat.* 55, 1151 (2006)

MICRO AND NANO-STRUCTURE OF M152 STEEL AND ITS EVOLUTION DURING CREEP

A.Ramar[1], R. Oruganti[1], T.Vishwanath [1], S.Nalawade[1], V.K.Sivakumar[1], S. Swaminathan[1]
B.K. Prasanna[1], F. Mastromatteo[2], I. Giovannetti[2]

[1]GE Global Research , GE India Technology Center, EPIP, Whitefield, Bangalore 560066, India
[2]GE O&G, Nuovo Pignone, via F. Matteucci 2, Florence 50127, Italy

Abstract

The microstructural changes seen in service exposed M152 steel operating in the low temperature/high stress regime (~400°C/~650MPa) are detailed. These are compared with changes seen in creep samples whose tests have been interrupted at various strains. It is shown that the main creep controlling features are similar to those found in other ferritic/martensitic steels, namely, nano-scale MX carbonitrides and laths. Due to the low temperature of operation, the primary microstructural change observed is the growth of nano-scale laths (subgrains) and no discernible change is seen in any of the other features. It is proposed that creep strain and remaining life of M152 rotor steel can be determined from current lath size.

Key Text: Ferritic, Martensitic, laths, subgrains, M152, creep

1. Introduction

M152 steel belongs to the class of Fe-12Cr (12 wt.% Cr) martensitic stainless steels. It has a good combination of properties which include good ductility, high strength, uniform properties through thick sections and favorable strength at temperatures up to about 480°C [1]. Martensitic stainless steels possess a body-centered tetragonal (bct) crystal structure after quenching from an austenite phase (face-centered cubic structure) at high temperature. The chromium content is generally in the range of 10.5 to 18.0 wt.%, and carbon content may exceed 1.2 wt.%. The actual chemical composition of the investigated alloy is presented in Table.1. The M152 alloys finds application in steam turbine and gas turbine parts where their outstanding fracture toughness and good oxidation resistance up to approximately 425°C come into play[1,2].

C	Cr	Ni	Mo	Mn	V	Si	N	Fe
0.12	11.4	2.72	1.64	0.58	0.31	0.23	0.024	Balance

Table.1: Alloy composition of M152 steel

The microstructure of the M152 steels is quite complex having a hierarchy of structures going from prior austenite grains at the largest length scale to the laths at the nano-scale. In addition various types of precipitates are observed in this steel. The important precipitates may be broadly

classified into two types, namely Cr rich precipitates, MC (M=W, Mo, V) and M_2C (M=Cr). This aim of the current study was to evaluate the microstructural changes occurring in M152 steel that had seen significant service in a power generation turbine. The final goal was development of a method to assess consumed creep life and estimate remaining life.

2. Experimental details

Retired discs of M152 steels (>100,000h service) were taken for the microstructural investigation along with some interrupted crept samples that had been strained to a known value. Discs of 3 mm diameter were extracted from the high and low stress locations on these discs. Foils for TEM examination were prepared by electro-polishing at 253 K using a solution of 11% perchloric acid in ethanol with addition of 2% glycerol. Detailed microstructural analyses were performed using the JEOL 2011 high resolution TEM equipped with a LaB6 gun and a high resolution pole piece. Conventional weak beam (WB) dark field and bright field (BF) imaging modes were used for TEM observations directly. X-ray energy dispersive spectrometry (EDS) was used to identify the chemical composition of the observed oxide particles and the carbides, with an Oxford Instruments Si (Li) detector. The SEM analyses of the microstructure are performed from the etched samples in a field emission high resolution NOVA FEI SEM. Only those regions in the TEM foil that had a thickness in the range of 50–180 nm were investigated. Regions thinner than 50 nm were not examined since all dislocations would have escaped due to surface forces [3].

3. Results

The material in the low stress and high stress areas showed microstructure typical of tempered martensitic steel with body centered cubic structure as shown in Figure.1.
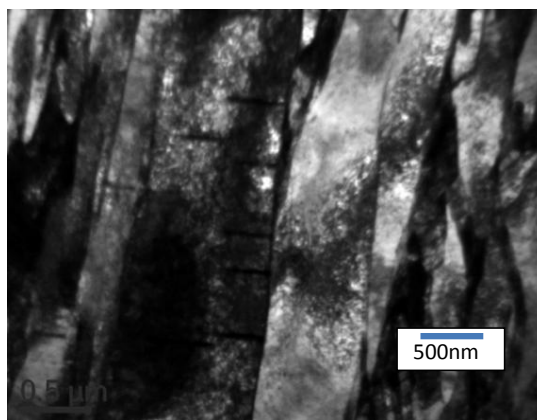
Figure.1: Structure typical of martensitic steel with laths boundaries

Ni was observed to form a thin austenitic film in between two neighboring laths which has been proposed as a mechanism to increase the fracture toughness of the alloy [2]. Other than Ni rich austenite films, approximately cube shaped Ni rich precipitates in the size range of about 10 nm were found to be sparsely distributed in the matrix. Cr rich oxides were homogenously distributed in the matrix with sizes in the range 200 – 600nm. The density of these oxides was higher in the laths with size greater than 500 nm. They had a needle type morphology and disposed perpendicular to each other. In addition a high density of MC (M=W, Mo, V) and M_2C (M=Cr) precipitates were also observed.
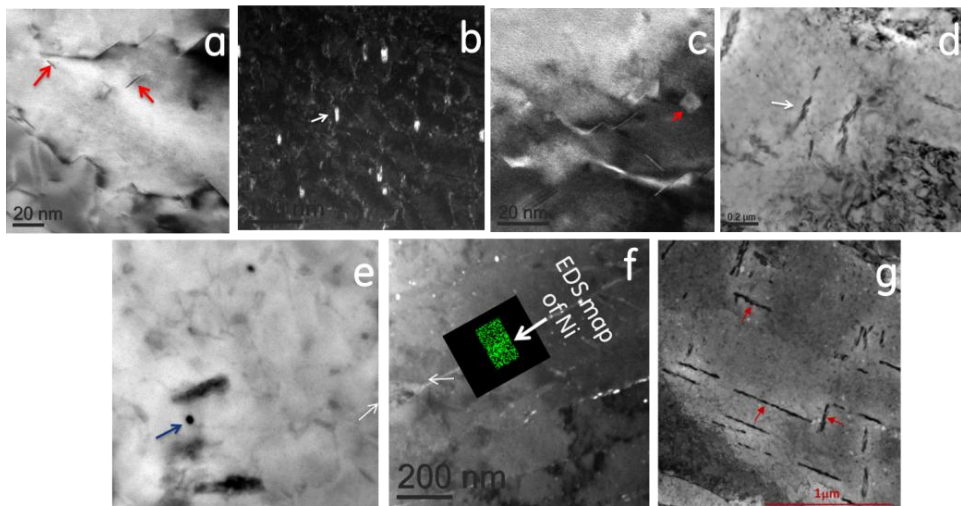
Figure.2: Types of precipitate observed (a) MX; (b) M_2X; (c) Ni rich; (d) Cr-O; (e) SiO_2; (f) Ni rich austenite film (g) Cr rich precipitates.

Both the MX and M_2X were oriented either parallel or perpendicular to g {200} in the [001] zone axis of the matrix as shown in Figure.3a. The arrows marked in Fig.3a fall either parallel or perpendicular to the g {200} reflection marked with the lines in the diffraction pattern (insert in the figure in M_2X) of the matrix taken in the zone axis [001] orientation. The orientation relationship of MX and M_2X holds true not only to the matrix but to each other. Fig.3b shows that both the MX and M_2X are found pinned to dislocations. These precipitates act as obstacles for the dislocation.

A detailed quantitative characterization of the various microstructural features was carried out to determine which feature can be used to relate to creep damage. The results of this analysis are tabulated in Table 2. It is seen that the only change is in the lath width with changes in all other features falling within the statistical bounds of the mean.
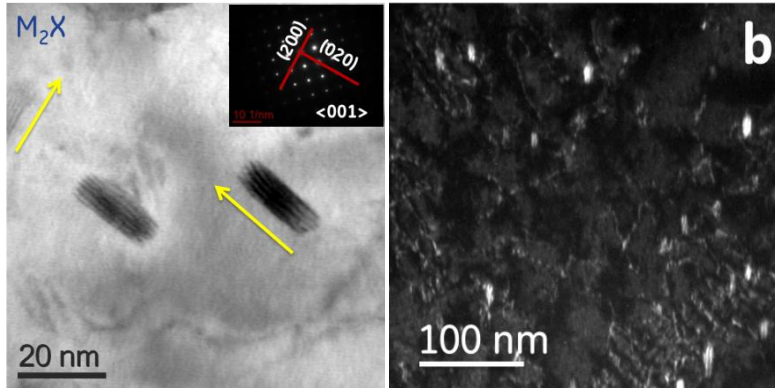
Figure.3: (a) MX and M₂X orientation relationship to the matrix and to each other, (b) M₂X precipitates found pinned to the dislocation

Feature	Size in nm	
	High stress region	**Low stress region**
Lath	**170±15**	**139±16**
MX	8.4±0.4	7.2 ± 0.4
M₂X	26±1.0	30 ± 1.0
Ni Rich film	26±1.6	28 ± 1.6
Cr-O	450±41	456± 38
Ni Rich precipitate	~10	~10
SiO₂	~42	~42

Table.2: Microstructural feature size distribution

3.1. Results on interrupted creep samples

Creep curves from tests that were interrupted at different strains are shown in Fig. 4. All these tests were carried out at the same stress and temperature (740MPa/380°C) and the different curves are from samples supplied by different vendors. It is seen that there is a large variability in the creep curves pointing to differences in starting microstructure and/or chemistry. Initial and final lath widths from these samples are shown in Table 3. It is seen that the lath width shows a consistent increase in all cases. No other microstructural changes were observed as is expected from the low test temperature.

From the results presented above, it is clear that lath width can be used as a marker for creep damage. Such an idea has been proposed earlier by Blum et al [4]. Since the temperature of operation was low, there is no possibility of confounding with evolution of other microstructural features.

624
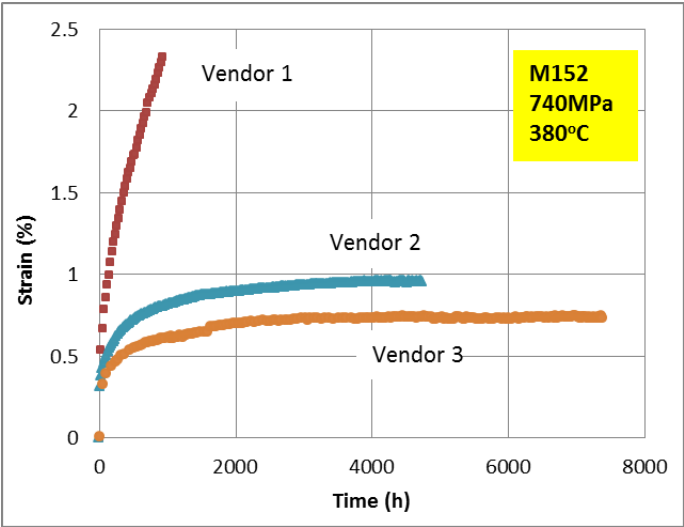
Fig. 4: Creep strain vs. time curves for M152 steel tested at 740MPa/380°C. Different curves correspond to material supplied by different vendors.

	Initial lath width (nm)*	Final lath width (nm)*
Vendor 1	132.0	291.0
Vendor 2	126.0	211.0
Vendor 3	122.0	170.0

*An average error of ±15nm exists for each measurement

Table 3: Initial and final lath width in crept M152 steel samples supplied by different vendors.

The equation proposed by Blum and co-workers relating lath width to creep strain is as follows:

$$\varepsilon = \varepsilon_w \ln\left[\log\left(w_o/w_\infty\right)/\log\left(w/w_\infty\right)\right] \tag{1}$$

where ε is the current strain, w_o, w and w_∞ are the initial, current and steady state subgrain widths respectively and ε_w is a numerical constant. Current studies are focused on determining the accuracy of this equation by characterizing a large number of samples crept to different strains under a wide stress/temperature range. Additional work is also being carried out to develop suitable methods to measure nano-scale laths on in-service rotors so that the ultimate goal of microstructure based remaining life estimation can be realized.

625

Summary and conclusions

M152 steel samples extracted from the high and low stress regions of a rotor used in a power generation turbine have been thoroughly analyzed for microstructural changes. The only change observed is the growth of nano-scale laths. The same change is observed in samples crept in the laboratory under nominally similar conditions. It is proposed therefore that lath width could be used as a measure of creep damage and possibly as a means to estimate remaining life of components made from this material.

References

[1] Davies JR (Ed). Stainless steels, *ASM Specialty Handbook, ASM International*, Ohio, 1994.
[2] J.W. Schinkel, P.L.F. Rademakers, B.R. Drenth, and C.P. Scheepens, "Ferritic Steels for High-Temperature Applications", *ASM*, Metals Park, OH, pp. 131-49 (1982).
[3] M. Hernandez-Mayoral, Z. Yao, M.L. Jenkins, M.A. Kirk, *Philos Mag*, 88, p. 2881 (2008).
[4] Wolfgang Blum and Gernot Gotz, "Evolution of dislocation structure in martensitic steels: the subgrain size as a sensor for creep strain and residual creep life", *Steel research international*, Vol. 70, pp. 274-278 (1999).

SMALL PUNCH CREEP TESTING FOR MATERIAL CHARACTERIZATION AND LIFE TIME PREDICTION

Stefan Holmström[1], Peter Hähner[1], Roger Hurst [2], Matthias Bruchhausen[1], Burkhard Fischer[1], Jean-Marc Lapetite[1], Mohita Gupta[1]

[1]European Commission, Joint Research Centre, Institute for Energy and Transport, Westerduinweg 3 NL-1755 ZG Petten, The Netherlands
Stefan.holmstrom@ec.europa.eu

[2] Institute of Structural Materials, College of Engineering, Swansea University, Singleton Park, Swansea, SA2 8PP, United Kingdom

Abstract

The Small Punch (SP) test is a miniature technique that can provide information on materials performance for a range of situations where standard testing is not applicable or considered too material consuming. The SP test is especially suited for determining material properties for heat affected zones in welds (local) and for nearly non-destructive testing of service exposed materials. Also, the SP test is a powerful tool for ranking novel materials produced in small quantities and for testing irradiated materials. The SP test is multi-axial in nature and the deformation and stress response is complex. The interpretation of SP test results is challenging and the validity of simplified transformation assumptions can be argued. In this paper SP test data generated following the SP testing Code of Practice are analysed for the determination of creep properties of P91 steel. The results are assessed and compared to corresponding uniaxial data and public domain results. Special attention is given to test set-up details, initial specimen deformation (creep), test repeatability and post-test examination procedures. The measured data scatter is used for determining expected life time prediction accuracy in creep.

Keywords: Small Punch, miniature testing, modelling, creep

1. Introduction

The small punch (SP) test is a miniature technique [1] where a hemispherical ended puncher (or a ceramic ball) deforms a thin metal disc until rupture. A SP creep test is performed with constant load ([1] part A) and a SP "tensile" test ([1] Part B) with a defined displacement rate, generally in the range of 0.2 to 2 mm / min. The SP specimens are commonly discs with a thickness of 0.25 – 0.5 mm and a diameter of 8 – 10 mm. There is a European Code of Practice (CoP) as a CEN Workshop Agreement, CWA 15627 [1] from 2006 and in Japan there is a recent standard for SP creep testing [2]-[3]. The SP test has become a tool of interest for characterizing materials in situations where standard testing is not applicable or considered too material consuming. The SP is especially suited for characterizing heat affected zones in welds, virtually non-invasive testing of service exposed materials and also testing novel materials produced in small quantities. In special material development projects the technique has shown excellent ranking capabilities [4]. The method is of course also still interesting for the original purpose of the technique, namely testing irradiated materials [5].

The SP test is multi-axial in nature and the deformation and stress response is complex [6]-[12]. The interpretation of SP test results is challenging and the validity of some simplified

transformation assumptions can be argued. In this paper SP test data generated following the SP testing CoP are analysed for the determination of creep properties of P91 steel. The results are assessed and compared to uniaxial creep data from NIMS [13] and public domain test results [9]. Special attention is given to test set-up details, initial specimen deformation (creep), test repeatability and post-test examination procedures. The measured P91 data scatter is compared to the results of Nonaka [2] for P22 steel.

2. Materials, test methods and results

The material used for the testing in this work is a P91 (X10CrMoVNb9-1) steel in thick plate product form and in "as received" product state (annealing at 1060 °C for 4 h and water quenching followed by tempering at 760 °C for 3 h and 20 min and air cooling) from ArcelorMittal. The material and testing is a part of the ongoing MATTER project. Small Punch test data from the European Union projects MATTER, INTEGRITY and LICON are used here for modelling purposes with other public domain SP creep data found for P91.

The main challenge of using SP as a testing technique to describe the uniaxial creep properties of materials is the conversion ratio of the load in a SP test and the corresponding stress in a uniaxial creep test. In the COP the following relationship is indicated for the ratio F/σ to relate the force F in a SP test to the stress σ in a uniaxial creep test with the same time to rupture;

$$F_{SP} / \sigma = 3.33 \cdot k_{SP} \cdot R^{-0.2} \cdot r^{1.2} \cdot h \qquad (1)$$

where R is the radius of the receiving hole, r the radius of the puncher or ceramic ball, h the specimen thickness and k_{SP} is the non-dimensional SP ductility parameter. The k_{SP}, the default value of which is $k_{SP}=1$, is considered to be material ductility dependent, and therefore deviates from unity [11] which increases the complexity of determining the uniaxial creep properties from SP test results.

In this work the determination of k_{SP} is done through a new approach utilising the Wilshire approach.

The uniaxial Wilshire model for time to rupture [14];

$$\frac{\sigma}{\sigma_{UTS}} = \exp(-k(t_r \cdot \exp(\frac{-Q}{R \cdot T}))^u) \qquad (2)$$

where σ is the applied stress, σ_{UTS} the ultimate tensile strength as a function of temperature, Q the apparent activation energy (here with an optimized value for the uniaxial data of 310 000 J/mol) and k and u are fitting parameters.

Correspondingly the Wilshire model can be fitted to normalized SP load data F/F_{max}. Here the maximum force at the test temperature is needed as F_{max} is also temperature dependent.

$$\frac{F}{F_{max}} = \exp(-k'(t_r \cdot \exp(\frac{-Q}{R \cdot T}))^{u'})$$
(3)

where F is the applied load, F_{max} the maximum (punch-through) load equivalent to the maximum load from a tensile SP test, Q the activation energy for uniaxial creep and k' and u' are SP fitting parameters.

Two different types of SP machines are used at the JRC, the older ones using direct top loading and the newer ones with electrical motor loading of the weights with pulley load transfer; these newer machines are equipped with load cells. The test machines are shown in Fig. 1 and a detail of an SP specimen insert with improved axiality is shown in Fig. 2.

Figure 1. The two different types of SP creep test machines
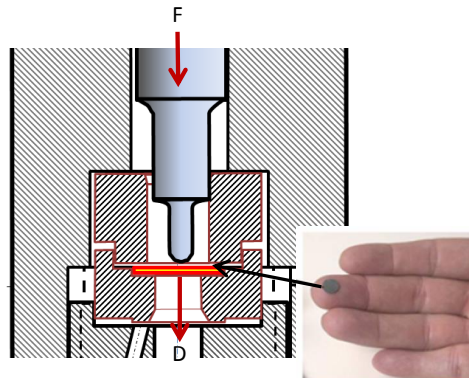
Figure 2. Detail of an improved test set-up for modular sample handling; F=force, D=displacement.

629

The machines with load cells can record the loading procedure at the start of the tests. This allows for accurately determining the initial deflection and the effective start of the tests which is difficult with machines without load cells. For determining F_{max} with the newer SP test machines a clear "overload" of 1.3 kN is lowered at an initial deflection rate of about 0.44 mm/s. After contact between puncher and specimen neither the deflection rate nor the load rate are constant because of the bending and strain hardening of the SP specimen. This "punch-through" test lasts about 3 seconds. At room temperature the punch-through deflection curve is almost identical to a SP "tensile" test performed in compliance with the COP. Manually increasing the weights until fracture occurs was also done at room temperature giving a fracture force similar to the ones measured by the "tensile" SP test and the creep machine punch-through. Punch-trough load curves at 450-600 °C are shown in Fig. 3. In Fig. 4 the relationship between the ultimate tensile strength and the SP maximum load is given.
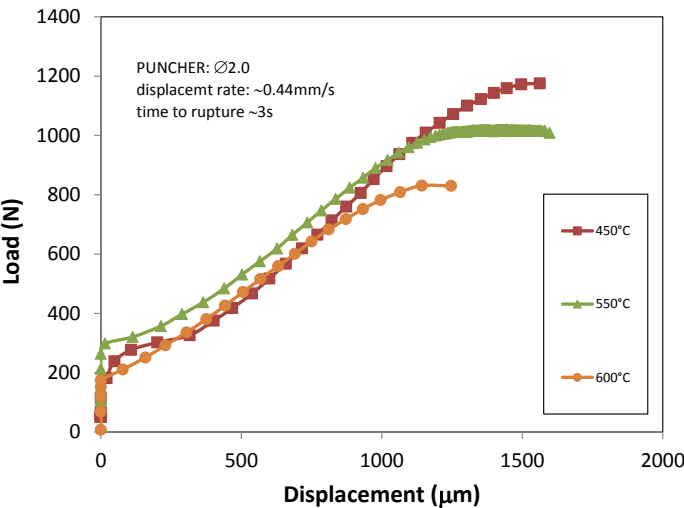
Figure 3. Deflection curves from punch through F_{max} determination tests.
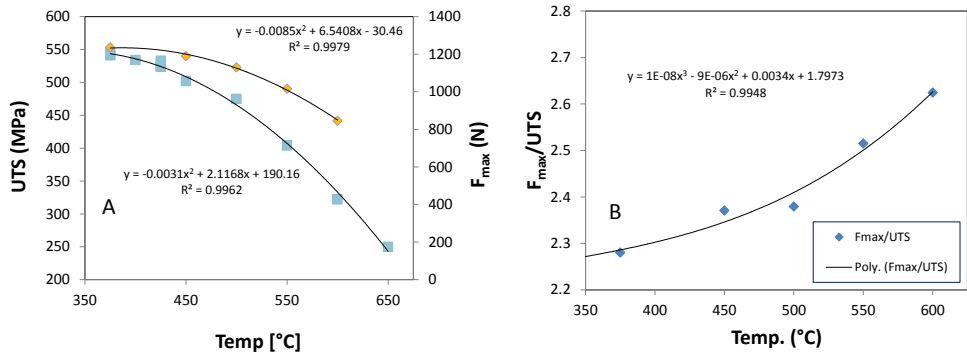
Figure 4. A) Ultimate tensile strength (squares) and maximum force (diamonds) as a function of temperature and B) the ratio of F_{max} over UTS as a function of temperature.

The creep models of Eqns 2 and 3 can now be plotted and compared. The Wilshire plots for uniaxial creep and SP creep are given in Figure 5.
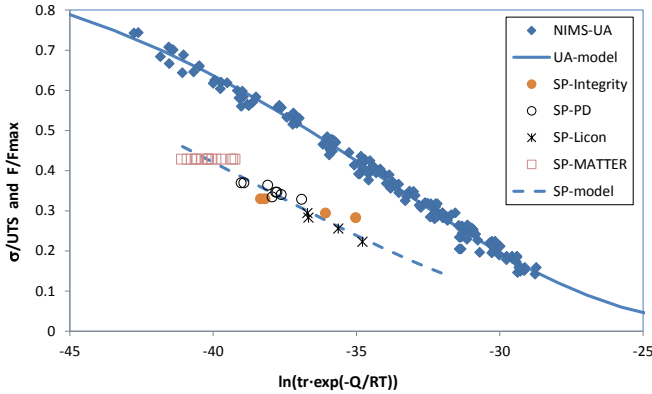
Figure 5. Wilshire models for uniaxial creep data (UA-model) and SP data (SP-model).

With these two models in place it is now possible to extract the ratio F/σ by dividing eq. 2 by Eq. 3. and solving for equal time to rupture ($t_{r-UA}=t_{r-SP}$). The resulting near linear relation between σ/σ_{UTS} and F/F_{max} is shown in Fig 6. together with k_{SP} as a function of load. It can be seen that the k_{SP} is clearly load dependent for P91.
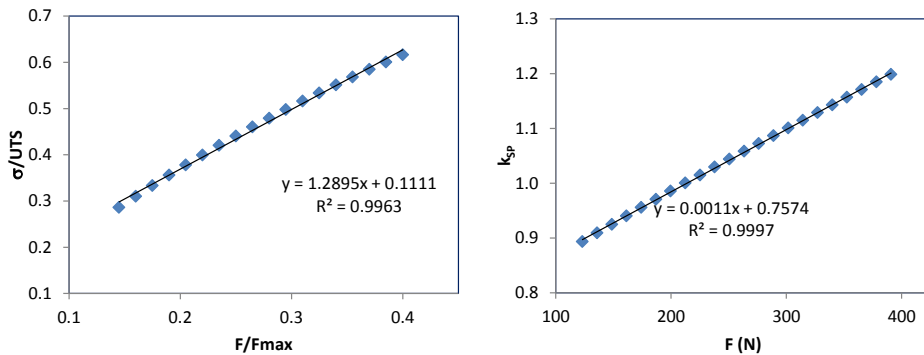
Figure 6. A) Near linear relationship between σ/σ_{UTS} and F/F_{max} and B) solved k_{sp} as a function of load using the relationship of A).

A methodology is now in place for determining the k_{SP} when uniaxial creep data is available. Finding a corresponding methodology that does not require actual uniaxial creep data is still a challenge that has not satisfactorily been solved.

To relate uniaxial strain response and the SP deflection response there is still a lot more to be done [15]. The large initial deflection (and plastic deformation) of the SP test clearly differs

from the standard uniaxial creep test as can be seen in Figs. 7-8. It can be seen that the "steady state" creep region in a SP test and the corresponding uniaxial test time spent in secondary creep are similar in duration, i.e. 50% of the testing time, the relative deflection and the relative strain increase during this period are also about the same (9-15%). The "primary" and the "tertiary" stages of the tests are however clearly different in terms of biaxial stress state, bending, true stress development, necking and "effective" rupture strain. Studying how these influence the overall (time to rupture) data scatter is a necessary step for further improvement of the models for a more comprehensive use of SP in creep life assessment.
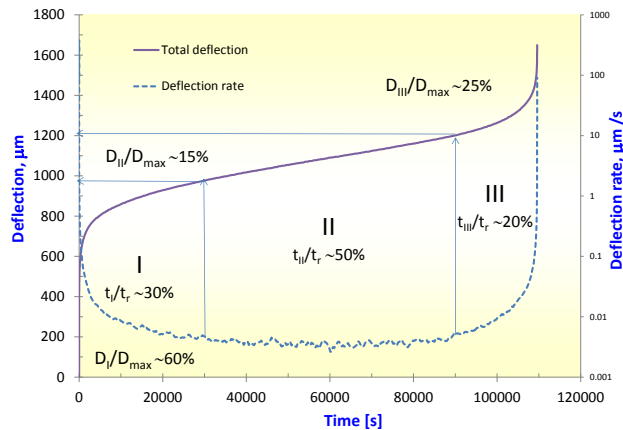
Figure 7. SP creep deflection and deflection rate as a function of time for a 600 °C / 364 N test.
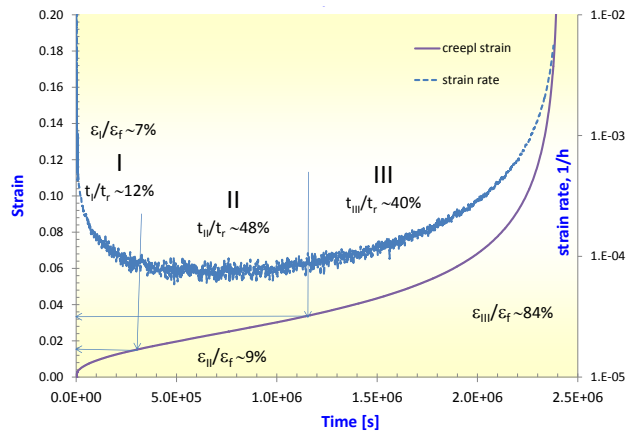
Figure 8. Uniaxial creep strain and strain rate as a function of time for a 600 °C / 155 MPa test.

The similarities in the "steady state" creep range of a uniaxial creep test and a SP tests can be used directly in the same manner as the Monkman-Grant relationship used in uniaxial testing as a more robust material parameter to correlate SP results to uniaxial minimum strain rate [4]. In future work it would be of interest to test the applicability of this with a larger data set

of SP and correlate directly SP deflection rates to uniaxial rupture times and determine if the predictions are improved and showing less scatter than correlating rupture times. It is also of importance to map the influence of clamping (drawing tests / bulge test / partly clamped) and to confirm the recommendations on clamping and post-test examination procedures given in the Code of Practice to ensure a minimum amount of tests result scatter.

3. SP data scatter analysis

To find out more about the expected scatter in SP testing a series of short duration tests were conducted on the direct loading machines at 600°C and a load of 364 N. Altogether 17 tests were conducted at the same load and temperature, 13 specimens extracted in the transverse direction (coded with AFD) and 4 in the longitudinal direction (coded as AFL). Both machines were used and it was shown that the machines gave statistically significantly differing results. The time to rupture for the AFD specimen in machine #10 (7 tests) gave rupture times of 10.2 h ± 24% (simple standard deviation). The corresponding result for machine #9 (5 tests) was 21.8 h ± 28%. The four AFL tests on machine #9 gave a mean rupture time of 9.3 h ± 26%. Combining all tests gives a rupture time of 13.6 h ± 52%
The tests are shown in Fig. 5 as SP-MATTER and in Fig. 9 categorised according to testing machine and specimen orientation.

It is to be noted that the AFD and the AFL tests were not randomly conducted and small improvements on the specimen holder and gripping of the SP specimen were introduced for both machines and an Argon leak was repaired in machine #10 over the period of testing. Therefore it is possible that the differences shown between the specimen testing directions and/or between machines have been affected by the changes.

Figure 9. SP test results, minimum deflection rate (μm/s) and time to rupture (h) for the tests at 600°C with a load of 364N

Post-test examinations were done to investigate whether the scatter in the data was related to punching off-centre. The distance between the centre of the sample and the centre of the puncher hole was measured as shown in Fig. 10. There was no evidence of a correlation between centering and measured rupture time.

Figure 10. SP off-centre measurement and its potential impact on rupture time.

Comparing the data scatter of this work to the Japanese round-robin results on P22 steel [2] the results seem rather satisfactory. The relative error of prediction for P22 was -45 to +89% for a load of 300N at 600°C. It should be noted that the punch diameter may not have been constant in these results.

5. Conclusions

In this work it has been shown for P91 steel that:

- SP testing machines equipped with load cells can be used for determining maximum force F_{max} as a function of temperature
- The ratio of F_{max} over ultimate tensile strength σ_{UTS} as a function of temperature can be described by a third degree polynomial
- This ratio used together with Wilshire equation fits both SP creep and uniaxial creep time to rupture as a function of F/F_{max} and σ/σ_{UTS} correspondingly can be used to define the SP ductility parameter k_{SP}.
- The SP test is very sensitive to small differences in testing machine configuration and subtle differences between nominally identical testing machines can cause data scatter of time to rupture of about a factor of 2, which can be considered comparable to the scatter expected from standard uniaxial creep tests (single and multiple specimen machines) of a single heat material.

Acknowledgements

References

[1]   CEN Workshop Agreement, CWA 15627:2006 E, "Small Punch Test Method for Metallic Materials," CEN, Brussels Belgium, December 2006.

[2]   Nonaka I. et al. Standardization of Test Method for Small Punch Creep in Japan, Proc. 12th Int. Conf. on Creep and Fracture of Engineering Materials and Structures, JIMIS-11, Kyoto, Japan 2012.

[3]   Standard for Small Punch Creep Test, Edited by The Micro Sample Creep Test Working Group, The Committee on High Temperature Strength of Materials, The Society of Materials Science, Japan, September, 2012.

[4]   Hurst R., Lancaster R., Norton G., Banik R., Bache R., A renaissance in small punch testing at Swansea University, Baltica IX. International Conference on Life Management and Maintenance for Power Plants. VTT Technology 106. VTT. Espoo (2013), 553 - 566

[5]   T. Misawa, T. Adachi, M. Saito, Y. Hamaguchi, Small Punch test for evaluating ductile-brittle behaviour of irradiated ferritic steels, Journal of Nuclear materials 150 (1987), pp. 194-202.

[6]   Blagoeva, D. T. & Hurst, R. C. Application of the CEN (European Committee for Standardization) small punch creep testing code of practice to a representative repair welded P91 pipe. Materials Science and Engineering A, 510-511 (2009) 219-223.

[7]   Yang, Z., Wang, Z. relationship between strain and central deflection in small punch creep specimens. International Journal of Pressure Vessels and Piping 80 (2003) 397-404.

[8]   Byun, T.S, Lee, E.H, Hunn, J.D, Farell, K., Mansur, L.K. Characterization of plastic deformation in a disk bend test. Journal of Nuclear Materials 294 (2001) 256-266.

[9]   Milicka, K., Dobes, F. Small punch testing of P91 steel. International Journal of Pressure Vessels and Piping 83 (2006) 625-634.

[10]   Ule, B. Sustar, T. Dobes, F. Milicka, K. Bicego, V., Tettamanti, S. Maile, K, Schwarzkopf, C., Whelan, M.P., Kozlowski, R.H, Klaput. J. Small punch test method assessment for the determination of the residual creep life of service exposed components: outcomes from a interlaboratory exercise. Nuclear Engineering and Design 192 (1999) 1-11.

[11]   Blagoeva, D. PhD Thesis: Development of a Residual Lifetime Prediction Methodology for Creep and Fracture Behaviour of Ferritic-Martensitic Steels using Small-Punch Testing Technique. (2009), VDM Verlag Dr. Müller e.K. ISBN 978-3-639-19118-9, p. 188

[12]   Rouse, J.P., Cortellino, F., Sun, W., Hyde, T.H., Shingledecker, J., Small punch creep testing: Review on modelling and data interpretation (2013) Materials Science and Technology (United Kingdom), 29 (11), pp. 1328-1345.

[13]   NIMS Atlas of creep deformation property No. D-1, Creep deformation properties of 9Cr1MoVNb steel tubes for boiler and heat exchangers, 2007.

[14]   Wilshire, B. Scharning, P.J, Hurst, R., A new methodology for long term creep data generation for power plant components. Baltica VII Conf. on Life Management and Maintenance for Power Plants, vol. 1, 2007, p. 196–207.

[15]   Holmström S., Auerkari P,. Hurst R., Blagoeva D., Using small punch test data to determine creep strain and strength reduction properties for heat affected zones, Materials Science and Technology. Institute of Materials, Minerals and Mining. Vol. 30 (2014) No: 1, pp. 63 – 66.

JRC INNOVATIONS IN MATERIALS DATA MANAGEMENT—DATA CITATION AND STANDARDS FOR ENGINEERING MATERIALS DATA

TSP Austin

European Commission Joint Research Centre Institute for Energy and Transport
(Postbus 2, 1755 ZG, Petten, The Netherlands – timothy.austin[at]ec.europa.eu)

Abstract

With ever increasing demands for improved transparency, traceability, and availability of data, the engineering materials community faces new challenges in its efforts to manage collections of data of differing inherent worth and levels of confidentiality. At https://odin.jrc.ec.europa.eu the European Commission JRC Institute for Energy and Transport (JRC IET) hosts the Online Data and Information Network (ODIN) Portal in support of energy and transport research. It consists of a collection of online databases organized into three categories, namely documents, engineering, and product information. In the engineering category, MatDB is an online database application that contains over 20.000 engineering alloys test results coming mainly from European R&D projects and provides a web-interface for data content, data entry, data retrieval and analysis routines. The database covers thermo-mechanical and thermo-physical properties data of engineering alloys at low, elevated and high temperatures for base materials and joints, including irradiated materials for nuclear fission and fusion applications, thermal barrier coated materials for gas turbines and properties of corroded materials.

As well as hosting scientific data, the ODIN Portal showcases the use of emerging technologies in support of improved data management. Enabling MatDB for data citation is one such initiative. In much the same way as digital object identifiers (DOIs) are routinely assigned to scientific publications, DataCite DOIs can now be assigned to individual data sets and thereby allow their citation. In all cases, DataCite DOIs resolve to an abstract that provides some basic information about the actual data set. As with conventional publications, access levels vary, so that data sets from publicly funded research could be expected to be openly available, while confidential data sets or data sets of high inherent worth would only be made available at the discretion of the owner. In the circumstance that such data are made available, then a means to exchange the data efficiently is required. In this respect, the JRC is actively involved in CEN Workshops concerned with development of harmonized ICT Standards for engineering materials data. As well as leading the development of these Standards, the JRC has enabled MatDB to demonstrate their use for innovative services in support of collecting, exchanging, and publishing engineering materials data.

Keywords: data, formats, citation, standards, datacite

1. Introduction

1.1. Data Management Infrastructures

In recent years, research funding agencies have begun to recognize the importance of incorporating data management into mainstream research practices. For example, all eight of

the UK Research Councils have adopted data management policies [1]. Consequently, in combination with support from agencies providing the necessary technical support, such as the Digital Curation Centre (DCC) and the Joint Information Systems Committee (JISC), many higher education institutes in the UK now stipulate data management policies [2]. Similarly at the European level, in the context of its legal obligation to share its own data the European Commission is committed to the more effective use of data generated through publicly funded activities [3]. In the domain of scientific research this is manifest in the Horizon 2020 Open Data policy. In the context of this widespread recognition of the inherent worth of research data and the potential for reuse, the Research Data Alliance (RDA) was established in March 2013 with the support of the European Commission, the U.S. Government and Australian Government. The purpose of the RDA is to accelerate international data-driven innovation and discovery by facilitating research data sharing and exchange, use and re-use, standards harmonization, and discoverability. To achieve these objectives, the RDA is focussed on the development and adoption of infrastructure, policy, practice, standards, and other deliverables. In the domain of engineering materials, these objectives are being pursued by the recently established RDA/CODATA Materials Data, Infrastructure & Interoperability interest group.

1.2. Data Citation and Publication

By making data available for reuse, data citation and publication have the potential to transform the scientific process. Global consortia, such as DataCite, and established players in the scientific publishing sector, such as Thomson Reuters, are delivering services that allow data sets to be published and cited in much the same way as conventional scientific publications.

DataCite is a consortium of leading technical libraries and information science institutes, including German National Library of Science and Technology, the British Library, and the California Digital Library. Its objectives are to establish easier access to research data on the Internet, increase acceptance of research data as legitimate, citable contributions to the scholarly record, and support data archiving that will permit results to be verified and re-purposed for future study. To achieve these objectives, the DataCite consortium operates an infrastructure that allows data sets to be referenced in much the same way as conventional scientific publications. At its foundation, this infrastructure relies on digital object identifiers (DOIs) in combination with bibliographic metadata [4]. The result is that once a data set has been assigned a DataCite DOI, it can be referenced in much the same way as a conventional publication. Further, given the co-operation between DataCite and Thomson Reuters, it is also possible to track data citation metrics, meaning that data sets published using DataCite DOIs have the potential to contribute to the career development of researchers in the same way as conventional scientific publications.

1.3. Engineering Materials Data

Since the early work of ASTM E49 and ISO TC 184/SC 4 in the 1980s, the engineering materials community has strived to develop technologies for engineering materials data. Amongst its various guidelines and recommendations, ASTM E49 guidelines on engineering materials databases [5] provided the foundation for a number of technologies, including MatML [6], NMC:MatDB [7], and JRC:MatDB [8]. Similarly, the work of ISO TC 184/SC 4 has yielded two standards specific to engineering materials data, namely ISO 10303 Part 45 [9] and ISO 10303 Part 235 [10]. To date however, the materials community, especially the industrial sector, has in large part failed to be engaged in the development and adoption of the mentioned technologies. Consequently there is still a requirement to deliver technologies for engineering materials data and demonstrate their added value.

1.4. JRC MatDB Materials Database

At https://odin.jrc.ec.europa.eu the European Commission JRC Institute for Energy and Transport (JRC IET) hosts the Online Data and Information Network (ODIN) Portal in support of energy and transport research. It consists of a collection of online databases organized into three categories, namely documents, engineering, and product information. In the engineering category, MatDB is an online database application that contains over 20.000 engineering alloy test results coming mainly from European R&D projects. The database covers thermo-mechanical and thermo-physical properties data of engineering alloys at low, elevated and high temperatures for base materials and joints, including irradiated materials for nuclear fission and fusion applications, thermal barrier coated materials for gas turbines, and properties of corroded materials. As shown in the table, MatDB supports data entry for an extensive range of thermo-mechanical test types. For each test type the database structure reflects international test standards and recommendations.

MECHANICAL PROPERTIES	IRRADIATION
CRACK GROWTH & FRACTURE	Irradiation creep
Creep crack growth	Swelling
Cyclic creep crack growth	In-pile relaxation
Fatigue crack growth	TENSILE
Fracture toughness	Compression
Impact	Multiaxial tensile
CREEP	Uniaxial tensile
Cyclic creep	Small punch tensile
Multiaxial creep	THERMO-PHYSICAL PROPERTIES
Torsional creep	Density
Uniaxial creep	Electrical resistivity
Small punch creep	Emissivity
RELAXATION	Linear thermal expansion
Multiaxial relaxation	Poisson's ratio
Uniaxial relaxation	Specific heat
FATIGUE	Shear modulus
High cycle fatigue	Thermal conductivity
Low cycle fatigue (load control)	Thermal diffusivity
Low cycle fatigue (strain control)	Young's modulus
Thermal fatigue	CORROSION
Thermo-mechanical fatigue	High temperature corrosion
Creep-fatigue interaction	Complex test

Figure 1 : MatDB test type support.

2. Methodology

The JRC is actively involved in various initiatives to promote the development of an infrastructure for engineering materials data.

2.1. Standard Data Formats for Engineering Materials Data

Framing new initiatives to develop data formats for engineering materials in an ICT Standards setting environment offers the possibility to engage a broad and representative group of stakeholders in the development of domain-specific technologies. CEN Workshops on electronic business are designed to support exactly this type of activity.

2.1.1. CEN Workshops on Engineering Materials Data

In a CEN Workshop, prenormative research in a specific domain is undertaken by a small team of technical experts. Their role is to perform the work that is necessary to achieve the objectives of the CEN Workshop. The work of the technical experts is in turn overseen by CEN Workshop registered participants (typically organizations with a vested interested in the domain of the CEN Workshop). In this respect, the role of the registered participants is to monitor the work of the technical experts and advise in case of departure from the objectives of the CEN Workshop. As a registered participant in a CEN Workshop, an organization can determine its level of commitment, ranging from simply reviewing the interim report and CWA, to participation at Workshop plenaries, to contributing knowledge/experience to the work of the project team.

Since 2009, two CEN Workshops on engineering materials data have taken place. The first was CEN/WS ELSSI-EMD, a 15-month project that focussed on test data and demonstrated the viability of deriving data formats from procedural testing standards. The second was CEN/WS SERES, a recently completed 24-month project on standards for electronic reporting in the engineering sector. The JRC has been closely involved in both Workshops, acting in the role of technical lead for CEN/WS SERES. Both projects delivered CEN Workshop Agreements [11,12] with corresponding technical specifications posted at http://uri.cen.eu/cwas.

The JRC MatDB materials database at https://odin.jrc.ec.europa.eu/alcor/Main.jsp has recently been enabled to use the technologies delivered by CEN/WS ELSSI-EMD, with the result that data can be imported and exported in a standard format.

2.2. Data Citation and Publication

To use DataCite DOIs for data citation and publication, a mandatory set of bibliographic data is required that provides some basic information about the data set. This mandatory data is defined by the DataCite metadata schema [4]. Typically, the DOI for a given data set will

resolve to a splash page that describes the data set and provides access to the data set. The combination of the DOI and the metadata thus allows data sets to be referenced and accessed.

The JRC MatDB materials database has recently been enabled to use DOIs for data publication. In its role as a data centre that hosts data collections on behalf of third parties involved in European research projects, the MatDB data publication service is free-of-charge to any organization with data entry rights. This means that for any organization planning to report their engineering materials in a scientific publication or technical report, there is the possibility to assign DOIs to data sets and list them in the bibliography in exactly the same way as references to conventional scientific publications.

3. Discussion

3.1. Data Management Challenges

In any domain, data management services need to address three key issues, namely acquisition, sharing, and reuse:

- **Data acquisition and transfer**—delays in data storage lead to a dissociation of test data and supplementary information. This leads to a loss of data quality, which eventually renders the data set unusable. Standard data formats provide a solution whereby data can pass between systems irrespective of local data formats.

- **Data sharing**—in the absence of any reward mechanism, there is the risk of loss of ownership and competitive advantage, meaning that in the circumstance data are placed in the public domain without there being any mechanism to insure acknowledgement in derivative works, ownership of the data has effectively been lost. Data citation offers a potential solution, whereby owners of data can be acknowledged in derivative works and hence gain credit for their contribution.

- **Data reuse**—data sets often remain hidden inside data silos. By exposing a limited amount of information about a data set data citation offers a means to discover data sets that would otherwise remain hidden.

3.2. Promoting Reuse of Engineering Materials Data

Although sharing and reuse of research data offer many potential benefits, the scientific community is inherently reluctant to share data. The reasons for this reluctance can be traced to a combination of cultural and technical issues. For example, while data generation is a necessary component of achieving research objectives, generating data is not the primary goal of a project, and so data preservation and reuse is often neglected. Furthermore, it is only natural that there is a reluctance to share data when the only beneficiary will be a third party that has invested no effort in its generation. To resolve the former, funding agencies need to

ensure that data management plans are a mandatory part of research proposals and that data sets are recognized project deliverables. For the latter, a mechanism is needed whereby efforts to share data are acknowledged and rewarded. DataCite DOIs offer just such a mechanism, enabling data sets to be published and cited in the same way as conventional publications.

As depicted in the following figure, in consequence of the JRC MatDB materials database now supporting DOIs for data publication, engineering materials data sets can now be cited in exactly the same way as conventional publication.

[23] ASTM standards 2009, Section 3, E 606 – 04, Standard Test Methods for Strain-Controlled Fatigue Testing, volume 03.01 Metals Test Methods and Analytical Procedures, ASTM International, West Conshohocken, PA, USA, 2009.

[24] R. Hurst, K. Turba, D. Blagoeva, P. Hähner, in: Creep and Fracture of Engineering Materials and Structures (Creep 2012 conference proc.), Japan Inst. of Metals, Sendai.

[25] J. Malaplate, F. Mompiou, J. Béchade, T. Van Den Berghe, M. Ratti, J. Nucl. Mater. 417 (2011) 205–208.

[26] K. Turba, Test data for small punch creep on material 14Cr 1W ODS at 650 °C, JRC Petten, 2013. http://dx.doi.org/10.5290/1000001 to http://dx.doi.org/10.5290/1000012 and http://dx.doi.org/10.5290/1000018 to http://dx.doi.org/10.5290/1000020 inclusive, v1.0, [data set].

[27] K. Turba, B. Fischer, F. de Haan, P. Hähner, C. Pantry, Test data for uniaxial creep on material 14Cr 1W ODS at 650 °C, JRC Petten, 2013. http://dx.doi.org/10.5290/1000013 to http://dx.doi.org/10.5290/1000017 inclusive, v1.0, [data set].

[28] F. Larson, J. Miller, Transactions of the ASME 74 (1952) 765–775.

[29] R. Klueh, J. Shingledecker, R. Swindeman, D. Hoelzer, J. Nucl. Mater. 314 (2005) 103–114.

[30] F. Monkman, N. Grant, Proc. ASTM 56 (1956) 593–620.

[31] ASTM standards 2009, Section 3,E 111 – 04, Standard Test Method for Young's Modulus, Tangent Modulus, and Chord Modulus, volume 03.01 Metals Test Methods and Analytical Procedures, ASTM International, West Conshohocken, PA, USA, 2009.

[32] M. Bruchhausen, F. de Haan, Test data for low cycle fatigue on material 14Cr 1W ODS at 650 °C and 750 °C, JRC Petten, 2013. http://dx.doi.org/10.5290/1000021 to http://dx.doi.org/0.5290/1000033 inclusive, v1.0, [data set].

[33] O. Basquin, Proc. ASTM 10 (1910) 625–630.

[34] S. Manson, Behavior of Materials under conditions of thermal stress, Technical Report, NACA Report 1170, 1954.

[35] L. Coffin, Jr., Applied Materials Research 3 (1962) 129–141.

[36] S. Ukai, S. Ohtsuka, J. Nucl. Mater. 367–370 (2007) 234–238.

Figure 2 : Data citations in a recent publication in the Journal of Nuclear Materials [13]

In the figure, references 26, 27, and 32 cite collections of data sets. As shown in Figure 3, selecting one of the data set links resolves to a MatDB splash page that describes the data set and provides access to the data set.

Figure 3 : MatDB data set splash page

Assigning DOIs to data sets and publishing them in the same way as conventional scientific papers provides the opportunity to promote data preservation, sharing, and reuse. The benefit to researchers is that their data can be cited in derivative works. While promoting the work of researchers, data publication does not imply that data is freely accessible. Instead, if a data set is restricted or confidential, then only some limited information will be visible. In the case that someone is interested to access such data, they would need to contact the owner of the data to request permission, at which stage the owner could either allow access according to specific conditions (such as citation in any derivative works, inclusion as a named author of any derivative works, etc) or simply deny the request.

The work to assign DOIs to data sets hosted at MatDB continues. Where data sets are open or freely available to registered users, the owners of the data are contacted with an offer to make their data sets citable. Typically, owners of such data sets recognise the value in data citation, and to date, DataCite DOIs have been assigned to 384 of the approximately 10.000 open data sets. Details of these and future DOI assignments are available from http://stats.datacite.org/?fq=allocator_facet%3A%22DELFT+-+TU+Delft+Library%22&#tab-datacentres.

3.3. Standard Formats for Engineering Materials Data

In an effort to engage the engineering materials community, CEN/WS ELSSI-EMD and CEN/WS SERES followed three common strands of activity, as follows:

- **Business**—examine the business case for Standards for engineering materials data by undertaking case studies on the implications of a transition to electronic data exchange.

- **Standardization and governance**— address ownership and publication issues in anticipation of a promotion of the prenormative technologies to informative/normative status.

- **Technologies**—develop the data formats.

The outcome of the work undertaken in the business and standardization strands has been to promote the longer term prospects for the technologies that have been developed. For CEN/WS ELSSI-EMD this is manifest in the fact that the ISO 6892-1 tensile testing Standard from which technical specifications were derived has been updated to make reference to the CEN/WS ELSSI-EMD technical specifications.

As the natural language analogy shown in the following figure is intended to depict, the standard formats for engineering materials data are intended to provide a *lingua franca* that enable systems with different local to data formats to communicate with one another.
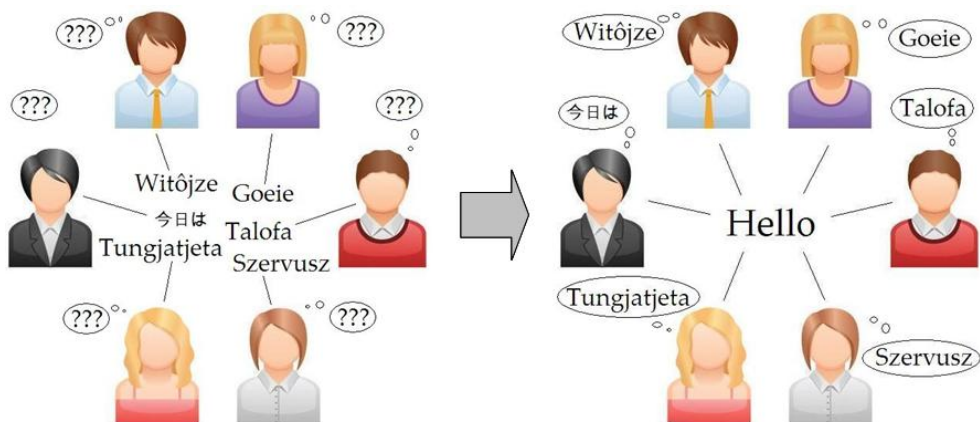
Figure 4 : Enabling communication

At the JRC, the use of standard data formats for systems integration has been demonstrated by enabling MatDB to use the CEN/WS ELSSI-EMD XML schema definition posted at http://uri.cen.eu/cwas/16200/2010/ed-01/technology/schema/xsd. As shown in the following figure, the result is that data can be transferred directly from a test facility to the database.
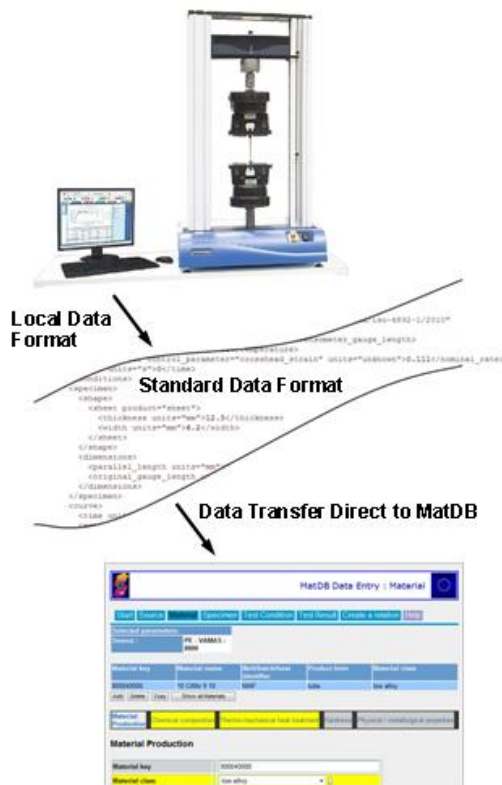
Figure 4 : Standard data formats for systems integration

4. Conclusions

In an effort to establish an infrastructure to promote the acquisition, sharing, and reuse of engineering materials data the JRC MatDB materials database has been enabled for both data citation and standard data formats.

The services that MatDB offers are freely available to the European research community and so help to support the development of engineering materials for energy applications.

5. References

[1] S Jones. Curation policies and support services of the main UK research funders, Digital Curation Centre, Version 2.1, 2012. Retrieved 9th May, 2014 from http://www.dcc.ac.uk/resources/policy-and-legal/overview-funders-data-policies.

[2] UK Institutional Data Policies, Digital Curation Centre. Retrieved 9th May, 2014 http://www.dcc.ac.uk/resources/policy-and-legal/institutional-data-policies.

[3] Commission decision of 12 December 2011 on the reuse of Commission documents (2011/833/EU).

[4] DataCite Metadata Schema 3.0 XML Schema. Retrieved 9th May, 2014 from http://schema.datacite.org/meta/kernel-3/metadata.xsd.

[5] ASTM Manual on the Building of Materials Databases, Crystal H. Newton, editor. ASTM Manual Series: MNL 19 (Philadelphia PA 1993).

[6] Materials Markup Language Public Review Draft 01, 06 June 2006. Retrieved 9th May, 2010 from http://docs.oasis-open.org/materials/materials-matml-spec-pr-01.htm.

[7] M Fujihara, Y Monma, H Yoshizu, and K Halada. Implementation of XML Database and TTP Analysis for Creep-Rupture Data of Heat Resisting Alloys, 21st International CODATA Conference, Kiev, 2008.

[8] TSP Austin and HH Over. MatDB Online - A Standards-Based System for Preserving, Managing, and Exchanging Engineering Materials Test Data, Data Science Journal, Vol. 11 (2012).

[9] ISO 10303-45: 2008 Industrial automation systems and integration -- Product data representation and exchange - Part 45: Integrated generic resource: Material and other engineering properties (2008).

[10] ISO 10303-235:2009 Industrial automation systems and integration — Product data representation and exchange — Part 235: Application protocol: Engineering properties for product design and verification (2009).

[11] CWA 16200:2010. A Guide to the Development and Use of Standards compliant Data Formats for Engineering Materials Test Data (2010). Retrieved 9th May, 2014 from ftp://ftp.cen.eu/CEN/Sectors/List/ICT/CWAs/CWA16200_2010_ELSSI.pdf.

[12] CWA 16762:2014. ICT Standards in Support of an eReporting Framework for the Engineering Materials Sector (2014). *In print*.

 [13] M Bruchhausen, K Turba, F de Haan, P Hähner, T Austin, Y de Carlan. Characterization of a 14Cr ODS steel by means of small punch and uniaxial testing with regard to creep and fatigue at elevated temperatures, Journal of Nuclear Materials, Volume 444, Issues 1–3, Pages 283–291 (2014).

THE EFFECT OF STEAM ON THE ELEVATED TEMPERATURE HIGH CYCLE FATIGUE LIFE OF ALLOY 282

Amit Shyam*, Shane Hawkins, Shibayan Roy, Sebastien Dryepondt, Donald Erdman, and Phil Maziasz

Materials Science and Technology Division
Oak Ridge National Laboratory
Oak Ridge, TN – 37831, USA
*Email – shyama@ornl.gov

Abstract

Nickel-base superalloys are candidate materials for the extreme temperature and pressure applications in advanced ultra-supercritical (A-USC) steam turbines. Quantification of the effect of steam on the fatigue life of components operating at elevated temperature remains a challenge. An elevated temperature experimental setup to measure the effect of 100% steam environment (1 atm) on the fatigue and creep-fatigue life of materials was developed and is described in this paper. This setup was utilized to investigate the effect of the steam environment on the high cycle fatigue response of wrought HR 282 at 800°C. Under the experimental conditions considered in this investigation, it was observed that the fatigue lifetime was not influenced by the testing environment. The fatigue lifetime was, however, influenced by the extreme values of the grain-size/grain-cluster distributions since these extreme size values were consistent with the size of the regions in the fracture surface that initiated the fatigue crack.

Keywords: steam effects; high cycle fatigue; nickel-base superalloys; microstructure; fatigue lifetime variability

1. Introduction

The next generation of steam turbines, called advanced ultrasupercritical or A-USC steam turbines, have an inlet steam temperature up to 760°C [1] and require the use of nickel-based superalloys. The desired superalloys need to possess adequate creep and fatigue resistance at elevated temperature in steam conditions [2]. The rotor and thick section materials require low cycle, hold-time and thermal fatigue resistance, whereas, for turbine airfoil materials, a prime requirement is high cycle fatigue resistance [2]. The effect of steam on the fatigue life of superalloys under extreme A-USC turbine conditions has not been quantified since elevated temperature fatigue data under 100% steam conditions is sparsely available.

In the present manuscript, we describe an experimental setup for performing fatigue testing at temperatures up to 800°C in 100% steam environment. The inlet steam chemistry was carefully controlled prior to introduction in the elevated temperature furnace environment. The present design is an improvement over previously reported designs (e.g. [3]) for steam fatigue testing where a ceramic susceptor was used around the gage-section of the specimen.

The elevated temperature high cycle fatigue (HCF) life of wrought HR 282 alloy in air and 100% steam environments is reported. HR 282 [4] is a relatively new alloy that displays excellent fabricability, high temperature creep and fatigue resistance and as such this alloy is a candidate for application in A-USC steam turbine conditions. It is shown that the microstructural variability determines the fatigue life variability in alloy 282 in both air and 100% steam conditions. Key features of the microstructure that determine the total fatigue life are identified by application of fractography and electron back scattered diffraction (EBSD) techniques.

2. Experimental Procedure

Alloy 282 rods were received in solutionized form and uniaxial fatigue testing specimens were machined according to specifications for surface finish in ASTM standard E466-96. Figure 1(a) shows the dimensions of the machined specimen. The grip sections of the uniaxial fatigue test specimens were threaded and 45 degree cuts were made on its ends to obtain reproducible alignment in tests. The specimen was threaded into N155 pull-rods and tightened with the aid of grooves in specimens and alloy 282 jamnuts. The specimen pull-rod assembly is shown schematically in Figure 1(b).
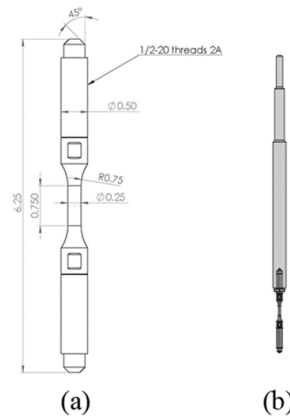
Figure 1 : (a) Geometry and dimensions (in inches) of the fatigue specimen. (b) Schematic of the specimen pull-rod assembly.

Prior to fatigue testing, the load train was aligned with an instrumented strain gaged specimen (3 rows of 4 strain-gages each) so that the bending strain was less than 5% of the uniaxial strain in the entire gage section. The experimental setup devised for elevated temperature steam fatigue testing is shown in Figure 2. The specimen pull-rod assembly was placed in an Inconel retort and a high temperature three zone clamshell furnace heated the retort and the specimen to the testing temperature. Three thermocouples were placed on the gage section of the specimen with the central thermocouple serving as the control thermocouple. The

temperature in the gage section varied within $\pm$ 5°C of the test temperature. The specimens were soaked at 800°C for 1 h prior to initiating the fatigue tests. This soak period ensured that the starting specimen hardness was >90% of the peak hardness of the material at the test temperature as shown in Figure 3 (see Section 3.1). The furnace had an extensometer port that was closed for the present experiments. The Inconel retort had air cooled bellows on both ends that allowed the pull-rod to be gripped by collet type grips. Air flow rate through the outer surface of the bellow was optimized to ensure no condensation at the ends of the retort and at the same time the temperature of the two bellows was continuously monitored to ensure that O-rings remained in their operational temperature range (<270°C). Steam condensation inside the retort led to a thermal imbalance (between three thermocouples that control the three zones of the furnace) in the specimen during testing. Five thermocouple (three from gage section and two from bellows) readings were continuously recoded during the fatigue testing. The entire assembly was placed in a mechanical testing frame and uniaxial load controlled fatigue tests were performed in an MTS servohydraulic machine at 800°C and a load-ratio of -1 and frequency of 10 Hz. For 800°C fatigue tests in air, the same setup was used without the sealing of bellows and introduction of steam in the system. No air flow was applied for the air tests.
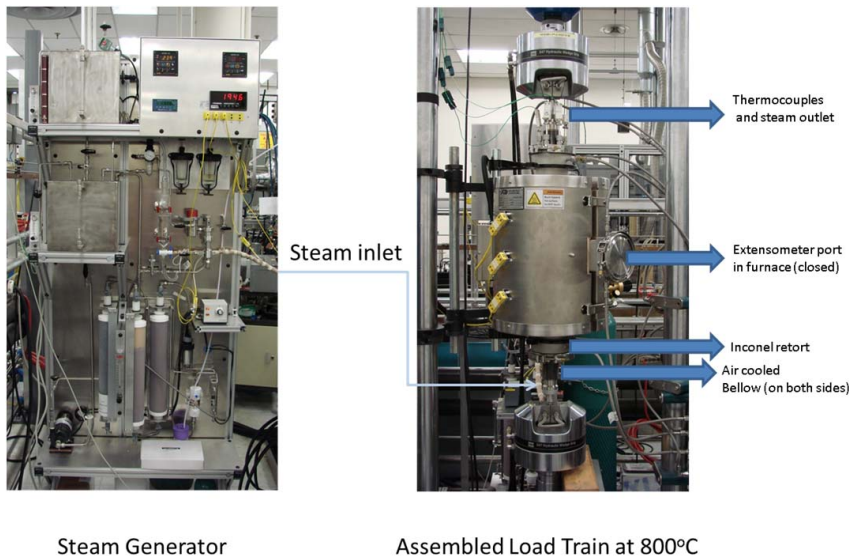
Figure 2 : The steam fatigue testing setup.

The steam generator (also pictured in Figure 2) allowed careful control of water chemistry prior to gasification and introduction of the steam in the retort from below. A closed loop including four different filters and Ar flowing in the main tank was used to deoxygenate and deionize the water. The steam inlet tube was wrapped in heating tape and maintained at

~150°C to ensure transmission of 100% steam into the retort and the steam outlet port was alongside the thermocouple outlet ports as shown in Figure 2. The steam outlet port had a pressure valve that allowed positive steam pressure to build before the valve opened. The steam exhaust was condensed and measured in a graduated cylinder and steam input and output rates were compared during testing. The input and output steam rates were found to be within the error of the measurement indicating good intermixing and no condensation or leaks of the steam in/through the retort environment.

Fatigue tests were performed to failure in both air and 100% steam environments. Fatigue fracture surfaces and crack initiation regions were characterized by scanning electron microscopy (Hitachi model S4800 Field Emission Gun SEM). Metallographically prepared HR 282 specimens were examined by light microscopy and electron backscattered diffraction (EBSD). The EBSD scans were performed in a JEOL model JSM 6500 ® field emission gun scanning electron microscope (FEG-SEM) equipped with EDAX HIKAR ® EBSD detector. The scans were recorded from the horizontal surface of the original stock material i.e. the scan normal remained parallel to the loading direction of fatigue specimens. For EBSD scans, the specimen surface was metallographically polished up to 2500 grit SiC paper and finished with 1 µm diamond paste. Since the EBSD technique requires a nearly strain free surface, the final surface preparation involved polishing with colloidal silica suspension in aqueous media. The EBSD scans covered a total area of 2 mm^2 with a step-size of 0.55 µm and confidence index of 0.7. The EBSD scans were carried out at an accelerating voltage of 20 kV and probe current of 20 nA with a working distance of 17 mm. The data were recorded along a hexagonal grid of pixel points and an effective binning of 4x4 at each pixel. The Kikuchi patterns so obtained were indexed using the standard generic face centered cubic Ni phase as per the composition of the matrix γ-phase.

The collected EBSD data were analyzed using TSL OIM ® (version 7.1, AMTEC Inc.) assuming a minimum boundary misorientation of 2°. For the purpose of the present work, the grain identification criterion, chiefly the minimum misorientation between individual entities in the EBSD generated microstructure, was altered. Four different values of 5°, 10°, 15° and 20° were considered for minimum misorientation between any pair of grains. Corresponding grain size distributions were calculated based on number fraction occurrence using 50 non-equal binning intervals. It is noted that, while defining the grains, the twins present within were not counted as separate entities. Two different types of twins boundaries were considered and excluded from grain defining algorithm which are typical for FCC metals, (a) 60° around <111> (Σ3) and (b) 38.9^o around <110> (Σ9).

3. Results and Discussion

3.1. Hardness measurements

The Vickers hardness (load = 200 gf) of the as-solutionized material was characterized as a function of exposure time at 800°C. The 800°C exposure simulates a one-step ageing treatment in alloy 282 where otherwise two step ageing treatments are performed to reach the peak material hardness by increasing the size of the γ' precipitates. The effect of ageing time (at 800°C) on the average hardness of alloy 282 material is shown in Figure 3. The material rapidly increases hardness and has a peak hardness of ~ 330 HV and the material reaches ~90% of peak hardness in 1 h of exposure. This is the soak time that was applied to the specimen before fatigue cycling in air or 100% steam environments.
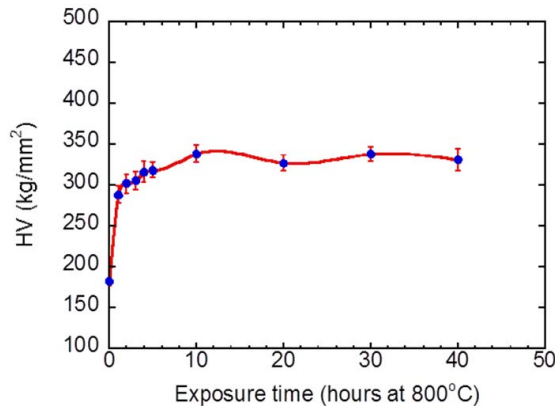
Figure 3 : The effect of 800°C exposure time in air on the Vickers hardness of HR 282. Error bars correspond to standard deviations about the average value from 10 measurements.

3.2. Microstructure

An orientation image micrograph for the alloy 282 is shown in Figure 4. Several observations can be made about the microstructure of alloy 282:

- The grain structure is equiaxed. Several grains are, however, several times larger than the average grain size. If twins are included as boundaries, the average grain size is around 13 µm, however, excluding the twins as boundaries, the average grain-size is around 29 µm.
- Annealing twins are ubiquitous in the microstructure of wrought superalloys. A large fraction of grains contain annealing twins and many contain multiple twins. Annealing twins are known to create elastic incompatibility around them and locally concentrate the stress to cause fatigue crack initiation.
- A qualitative assessment of the orientation distribution suggests a random texture in the material.
- Extremes in the microstructure are related to the fatigue behavior and these features are characterized and discussed separately in Section 3.5.
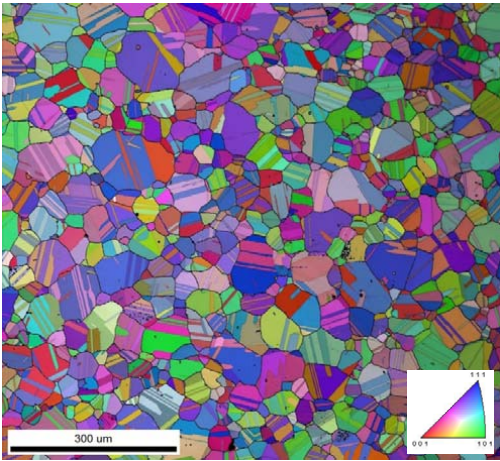
Figure 4 : EBSD characterization of the alloy 282 microstructure. The normal to the specimen plane coincides with the fatigue loading direction.

3.3. Fatigue behaviour at 800°C in air and 100% steam
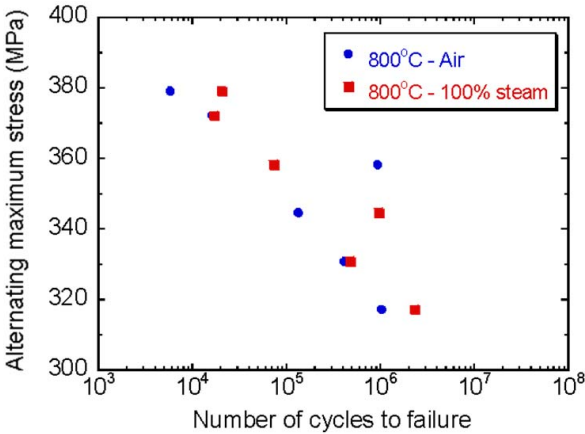
Figure 5 : The S-N behaviour of alloy 282 in air and 100% steam at 800°C. Frequency = 10 Hz and Load-ratio = -1 for testing.

The 800°C high cycle fatigue behavior of alloy 282 in air and 100% steam is shown as a stress life (S-N) diagram in Figure 5. It is stated that, under the experimental conditions considered (i.e. frequency = 10 Hz, load-ratio = -1, temperature = 800°C), there are no clear trends observed in terms of the effect of a 100% steam environment on the fatigue lifetime of this material. Some stress level testing results indicate that the 100% steam environment has a longer lifetime compared to the air environment, whereas, in other stress conditions the two lifetimes are the same and in still other stress conditions, the air environment test had a longer lifetime. The above results support the hypothesis that the variation in fatigue lifetime is due to the microstructural variability in the alloy and latter variation may overshadow the environmental effect on the high cycle fatigue life of the superalloy at elevated temperature. A high test frequency and completely reversed loading conditions also contribute in diminishing the effect of testing environment on the fatigue life.

3.4. Fracture surface characterization

The fracture surface of fatigue failed specimens was characterized. At higher stresses, the crack initiation was at the surface and at lower stresses, the crack initiation was sub-surface. For intermediate stresses, it was observed that regardless of the testing environment, the longer lifetimes (>>100,000 cycles) at the same stress level were associated with sub-surface crack initiation, whereas shorter lifetimes (<~100,000 cycles) were associated with surface crack initiation. Figure 6 illustrates an example of two different maximum stress levels where the longer lifetime is associated with sub-surface crack initiation; at 345 MPa the longer lifetime is associated with the 100% steam environment, whereas at 359 MPa with the air environment.
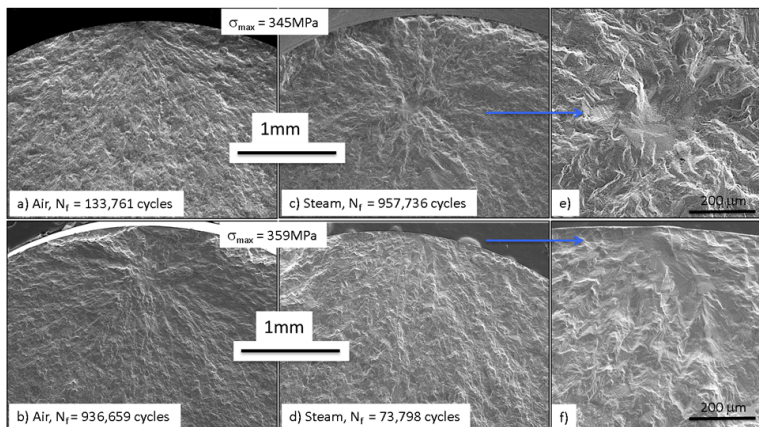
Figure 6 : Crack initiation site comparison at two stress levels in air and 100% steam.

The crack initiation sites had common features:

- Crystallographic crack initiation was observed. Subsequent transgranular propagation was observed from the crack initiation region. The crack initiation region and the morphology of the fracture surface around this region can provide information about the active deformation mechanisms [5,6].
- The size of the crack initiation region was in the range of 200-300 μm and this is nearly an order of magnitude larger than the average grain-size in the material (Figure 6e and 6f).
- Large single grains or multiple grains with low misorientation between them appeared to initiate fatigue cracks consistent with previous observations [7,8].
- The size of the flat transgranular surface crack initiation region was larger than the sub-surface crack initiation region.
- The above observations are related to the region corresponding to the tails of the microstructure distribution that is described in the next section.

3.5. Relationship between fatigue lifetime and extreme features in the microstructure

Previous research on disk superalloys (e.g. René′ 88 DT) [7-9] has indicated that the following features are common to the crack initiation regions:

- Presence of at least one annealing twin in the grain. The slip in the grain concentrates near the annealing twin.
- Large grains with high Schmid factor. Large grains are softer and allow for larger slip decohesion distance and, therefore, energetically favorable conditions for crack formation.
- Instead of large grains, clusters of smaller grains with low misorientation ($<20^{o}$) between them can, in effect, become the most favorable site for crack initiation.

As shown in the 282 microstructure in Figure 4, several grains contain annealing twins. A Schmid factor analysis of the EBSD data also indicated that a good fraction of grains had a high Schmid factor (>0.4). The above criteria for favorable crack initiation conditions can, therefore, be simplified to the probability of finding a large grain or grain-cluster (since a majority of grains have at least one annealing twin and at least one slip system with high Schmid factor).

Following an approach suggested by Miao et al. [7,8], Figure 7 shows the procedure employed to find the microstructural features that are likely to become fatigue crack initiation sites. The misorientation between neighboring grains to qualify the boundary between them as a grain boundary was successively changed from 5, 10, 15 to 20°. This procedure allows the identification of size and frequency of grain clusters with low misorientation that can serve as fatigue crack initiation sites. It can be seen in Figure 7 that when the grain definition is confined to lower misorientation (5 and 10°), the largest grain clusters are in the 150-200

μm range. When the grain definition misorientation value is increased (15 and 20°), even larger grain clusters of size 200-350 μm can be found in the microstructure. The fracture surface analysis indicates that the crack initiation regions are in the size range of 200-300 μm thus suggesting that large grain clusters with less than 20° misorientation collectively form microstructural neighborhoods that could nucleate fatigue cracks. Analysis of the tests performed to date suggests that the environment has little to no bearing on the fatigue crack initiation region distributions *in the conditions investigated*.
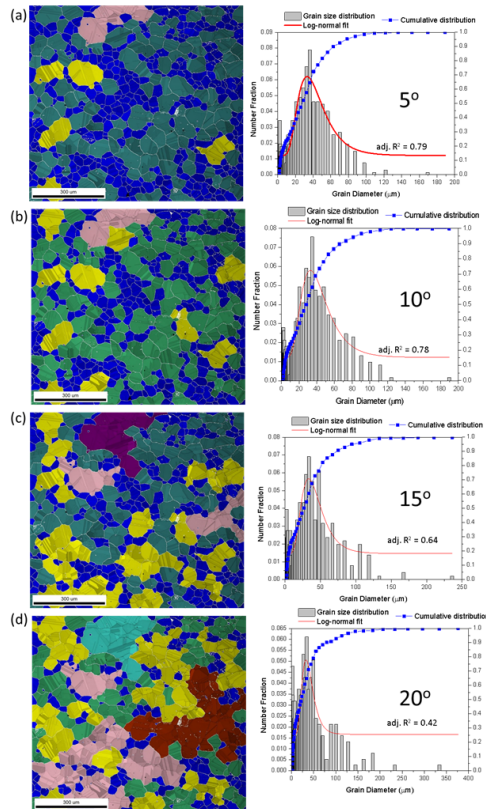
Figure 7 : Procedure for identification of tails of the grain size/grain cluster distribution that are responsible for fatigue crack initiation with a grain definition misorientation value of a)5º, b)10º, c)15º and d) 20º. Grain clusters are color-coded for various size ranges.

It is noted that Miao et al. [7,8] found surface crack initiation at room temperature and subsurface crack initiation at 593°C. Switching of the crack initiation site between surface and sub-surface regions at the same stress level is unique to this material and the employed temperature conditions and is related to unique microstructural configurations. A material

model for this behaviour utilizing extreme value distributions is being developed and will be reported in the future. The model will be capable of predicting the probability of surface/sub-surface fatigue crack initiation depending on the specimen/part geometry.

4. Conclusions

A setup to measure the fatigue response of materials in 100% steam environment at 800°C was developed and described in this paper. The effect of 100% steam environment on the elevated temperature high cycle fatigue lifetime of wrought superalloy 282 was investigated. It was concluded that the under the conditions investigated, fatigue lifetime was not influenced by the loading environment but was strongly related to the probability of finding large grain clusters with less than 20° misorientation. The findings will inform a probabilistic model for fatigue crack initiation.

Acknowledgements

References

1. R. Schwant, C. Shen and M. Soare, New Materials Enable Unprecedented Improvement in Turbine Performance, *Advanced Materials & Processes*, 171,pp. 18-22 (2013).
2. P. Jablonski, J. Hawk, C. Cowen and P. Maziasz, Processing of Advanced Cast Alloys for A-USC Steam Turbine Applications, *JOM*, 64, pp. 271-279 (2012).
3. M. B. Ruggles-Wrenn and T. P. Jones, Tension–compression fatigue of a SiC/SiC ceramic matrix composite at 1200°C in air and in steam, *International Journal of Fatigue*, 47, pp. 154-160 (2013).
4. L. Pike, Development of a Fabricable Gamma-Prime (γ') Strengthened Superalloy, *Superalloys 2008*, pp. 191-200 (2008).
5. A. Shyam and W. W. Milligan, Effects of deformation behavior on fatigue fracture surface morphology in a nickel-base superalloy, *Acta Materialia*, 52, pp. 1503-1513 (2004).
6. A. Shyam, S. A. Padula, S. I. Marras and W. W. Milligan, Fatigue crack propagation thresholds in a nickel-base superalloy at high frequencies and temperatures, *Metallurgical and Materials Transactions A,* 33, pp. 1949-1962 (2002).
7. J. Miao, T. M. Pollock and J. W. Jones, Crystallographic fatigue crack initiation in nickel-based superalloy René 88DT at elevated temperature, *Acta Materialia*, 57, pp. 5964-5974 (2009).
8. J. Miao, T. M. Pollock and J. W. Jones, Microstructural extremes and the transition from fatigue crack initiation to small crack growth in a polycrystalline nickel-base superalloy, *Acta Materialia*, 60, pp. 2840-2854 (2012).
9. M. D. Sangid, T. Ezaz, H. Sehitoglu and I. M. Robertson, Energy of slip transmission and nucleation at grain boundaries, *Acta Materialia*, 59, pp. 283-296 (2011).

Creep Damage Evaluation of Heat Resistant Ferritic Steels for Fuel Processing System by Hydrogen Thermal Desorption Analysis

Hayato Yamashita[1], Shin-ichi Komazaki[1]
Takahiro Ide[2], Harukuni Kameda[2] and Kazuhiro Kimura[3]

[1] Kagoshima University (Korimoto1-21-40, Kagoshima 890-0065, Japan)
[2] Tokyo Gas Co., Ltd (Tsurumi-ku Suehiro-cho1-7-7, Yokohama 230-0045, Japan)
[3] National Institute for Materials Science (Sengen1-2-1, Tsukuba 305-0047, Japan)

Abstract

The hydrogen desorption characteristic of three kinds of ferritic heat resistant stainless steels (18Cr-2.5Si steel, SUS444, SUH21) which were representative structural materials for the fuel processing system was investigated to examine the applicability of hydrogen as tracer for materials degradation and creep damage evaluation. Hydrogen charging into the creep specimens was conducted by means of cathodic electrolysis. Next, the hydrogen-charged samples were subjected to the thermal desorption analysis for measuring the hydrogen evolution curve. The experimental results revealed that the hydrogen evolution curve and its change with creep were different depending on the kinds of steel. The increase in the amount of desorbed hydrogen, C_H, was most significant in 18Cr-2.5Si steel. The lower the stress level was, more pronounced this increase in C_H was. However, the change in hydrogen desorption characteristic reflected not only the damage but also the microstructural changes.

Keywords: Ferritic Heat Resistant Stainless Steel, Fuel Processing System, Creep, Hydrogen, Thermal Desorption Analysis

1. Introduction

The residential cogeneration system using a polymer electrolyte fuel cell (PEFC) has been recently diffused in Japan, because of its exceedingly high energy efficiency and its ease of start/stop. In this system, hydrogen is produced by reforming natural gas. This gas reforming is carried out in the fuel processing system (FPS), and some sections of the FPS are exposed to high temperature of a maximum of 650°C and above during the reforming reaction. Since no such high temperature chemical reactor has been installed in houses, the several safety measures such as the application of high-class structural materials, the design with large safety factor and the integration of safety mechanisms are provided for operating the system for a prolonged period of time without accident. However, the present safety measures, which seem to be somewhat excess, cause the increase in cost, leading to the impediment to the more widely diffused system. These excess measures are attributable to the fact that there is no sufficient data and/or knowledge on the aging materials degradation, the high temperature damage, the deformation and fracture behavior of the relevant structural materials. The clarification of those things, particularly, the resistance to creep damage and deformation in

high temperatures enables the design to be more rational while maintaining high level of security, resulting in the contribution to the lower cost. Needless to say, it is essential to establish a procedure for detecting and evaluating the degree of materials degradation and/or creep damage of those materials in order to implement it.
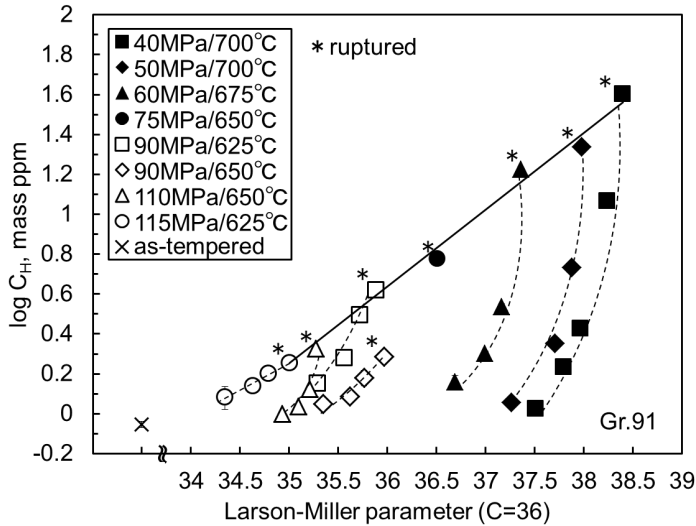

Figure 1 : Change in C_H measured on interrupted creep specimens of Gr.91 [8].

On the other hand, it has been well known that hydrogen is trapped by a variety of defects in steels such as vacancy, vacancy cluster, dislocation, grain boundary, precipitate and cavity, and it is easily released from those trap sites by heating. However, the desorption temperature range varies according to the kinds of trap sites, because of different binding energy between hydrogen and each trap site [1-6]. This interesting nature of hydrogen is likely to be available for taking hold of the materials degradation and creep damage of the structural materials for the FPS. With this point as background, preliminary to the present study, the authors [7,8] measured the hydrogen evolution curve for the creep ruptured specimens of 9%Cr ferritic steel (Gr.91) by the thermal desorption analysis (TDA). The experimental result revealed that the hydrogen desorption characteristic was significantly changed by the creep exposure. There was a strong likelihood that this change was attributable to the formation of geometric damage (defects), which was not annihilated by the re-normalizing, rather than the microstructural changes. As shown in Fig. 1, the amount of desorbed hydrogen, "C_H", increased monotonously with increasing Larson-Miller parameter (LMP), that is, consuming creep life, depending on the stress level. There was an almost linear correlation between the $\log C_H$ measured on the creep ruptured and the LMP, which was approximated by "$\log C_H = 0.39 \, \text{LMP} - 13.4$". This was a kind of criterion for creep rupture or fracture, and this equation meant that as far as the C_H did not reach this line, the fracture never occurred.

657

In this study, the change in hydrogen desorption characteristic of the structural materials for the FPS was investigated to examine the applicability of hydrogen as tracer for detecting and evaluating the materials degradation and creep damage. The TDA was applied to the interrupted creep specimens with various degrees of damage in addition to the ruptured specimens and the thermally aged specimens.

2. Materials and Experimental Procedures

2.1. Materials and Specimen Preparation

The materials used in this study were three kinds of ferritic heat resistant stainless steels, 18Cr-2.5Si steel, SUS444 and SUH21, which are representative structural materials for the FPS. The creep tests were carried out at a wide variety of temperatures (650-800°C) and applied stresses (10-30 MPa). The tests were stopped at several life fractions to prepare the interrupted creep specimens with various degrees of damage as well as the creep ruptured specimens. The thin plate-type specimen (6×9×0.6 mm) parallel to the loading direction was taken from the gauge and grip portions of the creep specimens. Finally, the specimen thickness was carefully adjusted to be 0.5±0.005 mm using emery paper of #2400, because the thickness has a significant influence on the below-mentioned hydrogen desorption characteristics.

2.2. Hydrogen Thermal Desorption Analysis

The hydrogen charging into the plate-type specimen was conducted by means of cathodic electrolysis in 0.1 mol/l NaOH aqueous solution containing 0.5 mass% NH_4SCN under a current density of 5 mA/cm^2. The charging time was 24 h and the solution temperature was kept to be 30°C during the charging. The thermal desorption analysis (TDA) was carried out at a temperature range from room temperature to 270°C. The heating rate was 100°C/h. The desorbed hydrogen carried with high purity argon gas was quantified by a gas chromatograph at intervals of 5 minutes. The flow rate of the argon carrier gas was fixed to be 1.2×10^{-5} m^3/min throughout the analysis. The hydrogen evolution rate was calculated as the amount of hydrogen desorbed in one minute per one gram of specimen.

3. Results and Discussion

3.1. Change in Hydrogen Evolution Curve with Creep

The hydrogen evolution curves measured on the creep specimens tested at 10 MPa as well as the as-received of the three steels are given in Fig. 2. It can be clearly seen that the change in curve is most significant in 18Cr-2.5Si steel (Fig. 2(a)), although precise comparison may not be advisable because of the difference in test temperature. A peak of hydrogen evolution rate appears at around 100°C for the as-tempered of 18Cr-2.5Si steel, whereas it is shifted to

higher temperature side for its creep specimens. The shift of peak temperature is more pronounced with increasing creep time, and it reaches as high as 140°C for the creep ruptured. It is worthy of note that the peak height significantly increases with increasing creep time. For the ruptured specimen, the peak height is raised up to 0.3 mass ppm/min, which is almost 10 times higher than that of the as-tempered.

In comparison with 18Cr-2.5Si steel, the changes in hydrogen evolution curve with creep are definitely not drastic for two other steels, namely, SUS444 (Fig. 2(b)) and SUH21 (Fig. 2(c)). However, it is very important to mention that a new peak of hydrogen evolution emerges at higher temperature side, *i.e.*, 150-220°C, in the creep specimens of SUH21, which is by no means seen in the as-received (Fig. 2(c)). Its height tended to increase with increasing creep time. To the contrary, the height of the peak located at lower temperature region decreased due to the creep exposure. This emergence of new hydrogen evolution peak seems to be closely associated with the defects (creep damage) and/or the deformation (creep strain), since it never appears in the hydrogen evolution curve of the grip portion, *i.e.*, the thermally aged steel.
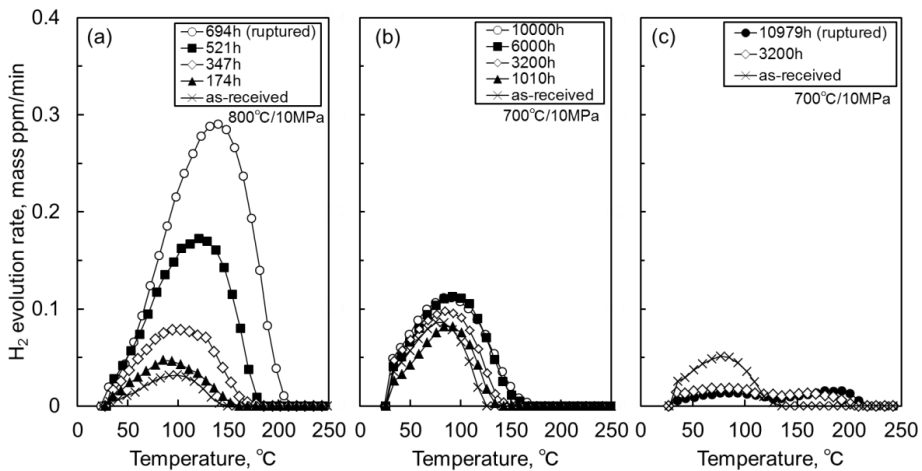
Figure 2 : Effect of creep time on hydrogen evolution curves of (a)18Cr-2.5Si steel, (b)SUS444 and (c)SUH21.

3.2. Change in Amount of Desorbed Hydrogen C_H with Creep

The amount of hydrogen desorbed during the analysis was determined by calculating the area below each hydrogen evolution curve, and it was denoted by C_H. Figure 3 shows the C_H obtained from the creep specimens of 18Cr-2.5Si steel, where the C_H is plotted as a function of Larson-Miller parameter (LMP). The C_H is relatively well arranged by the LMP for each stress level, and it increases with increasing LMP when the applied stress is fixed. The lower the stress level is, more pronounced this increase in C_H is. The C_H measured on the creep

ruptured, which is indicated with asterisk in this figure, is roughly placed on a single curve, and this correlation between the log C_H and the LMP is approximated as follows.

$$\log C_H = 0.12 LMP^2 - 5.1 LMP + 55 \quad (1)$$

This is a kind of criterion for creep rupture or fracture. The C_H rises with accumulating the creep damage and consuming its life, and then the creep rupture eventually occurs when the C_H crosses the curve (Eq. (1)). Conversely, as far as the C_H does not get to this line, the fracture never occurs.
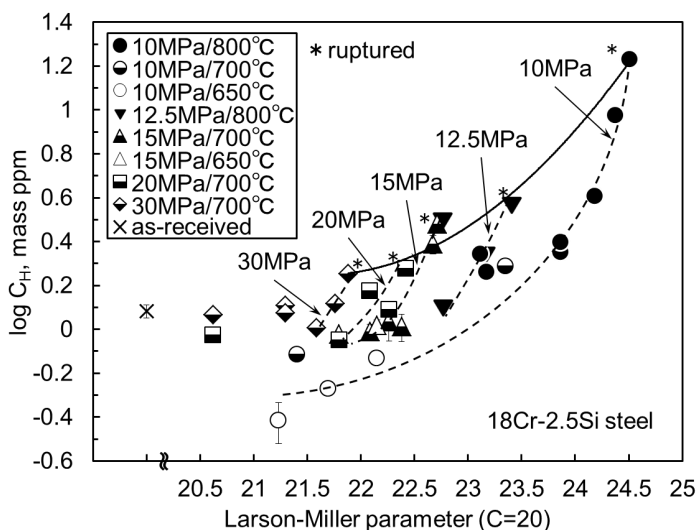
Figure 3 : Change in C_H measured on interrupted creep specimens of 18Cr-2.5Si steel.

The effect of re-solid-solution treatment (RSST) on the hydrogen evolution curve was investigated in order to discuss a possible source of the change in hydrogen desorption characteristic due to creep. Figure 4(a) shows the hydrogen evolution curves of the as-received and the creep specimen ruptured at 700°C/15 MPa, which were subjected to the RSST (1100°C, 1 h) before the analyses. The peak heights decrease by the RSST not only in the creep specimen but also in the as-received. This reduction in C_H in the as-received appears to be caused by the decrease in dislocation density, because the steel is supposed to be submitted to the cold-work before the service. The grain growth also may affect the change in desorption characteristic, because the grain boundary is one of the dominant sites of hydrogen trapping. In the case of the creep specimen, the reduction must result from the recovery of microstructural changes such as the solid-solution of precipitates in addition to the decrease in dislocation density and the grain growth.

It can be clearly seen from Fig. 4(a) that the C_H of the creep specimen is much larger than that of the as-received even after the RSST. This difference corresponds to the hydrogen associated with the creep damage, because the RSST makes the microstructures of both the

steels quite same. The hydrogen evolution curves of the as-received and the creep specimen were approximated by Gaussian distribution and then the difference between them was calculated. The result obtained is shown in Fig. 4(b) along with the SEM micrograph of cavity (damage) left in the creep specimen after the RSST. The result of Fig. 4(b) means that the hydrogen released from the damage (defects) makes an evolution curve with a peak temperature of 135°C.

	As-received	Creep ruptured (700°C/15MPa)
Before RSST	△	○
After RSST	▲	●
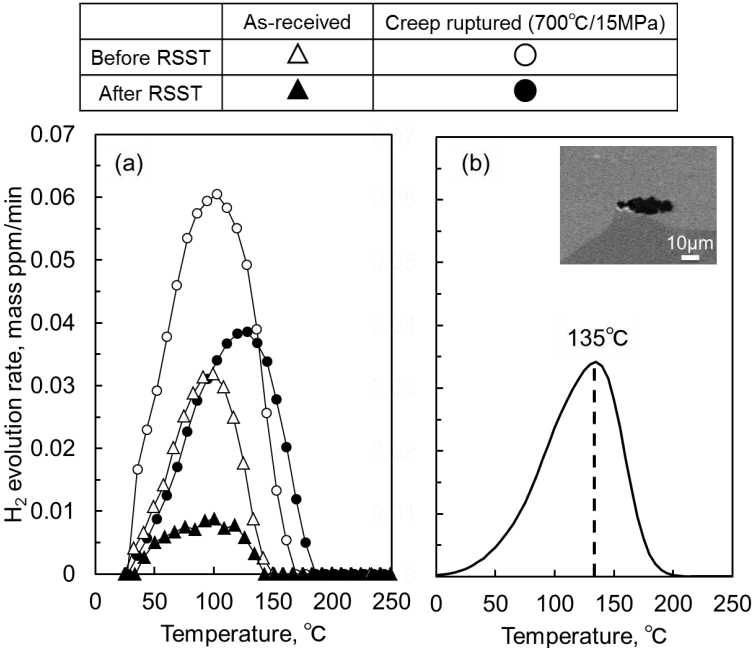
Figure 4 : (a) Effect of RSST on hydrogen evolution curve, (b) Difference between hydrogen evolution curves of as-received and creep ruptured subjected to RSST

3.3. Change in Amount of Desorbed Hydrogen C_H with Thermal Aging

The C_H seems to be also dependent on the test temperature (Fig. 3). Overall, the C_H measured on the specimens tested at 600°C is distinctly smaller than that on the as-received. Furthermore, in the low LMP region, the C_H of some specimens tested at 700°C are slightly smaller than the as-received too. This temperature dependence of C_H was not observed in the previous study using Gr.91 steel at all, and it is likely to be responsible for the change in microstructure rather than the above-mentioned damage. Figure 5 shows the C_H measured on the specimens, which were thermally aged at 650, 700, 750 and 800°C up to 10000 h. As mention above, the C_H decreases and becomes slightly smaller as compared with the as-received by the thermal aging at 650°C and 700°C, respectively. On the other hand, the thermal aging at 750 and 800°C causes a slight increase in C_H to the contrary.
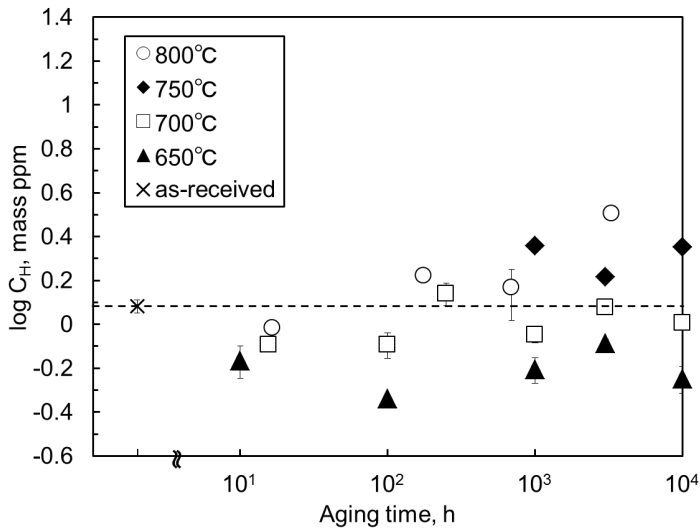
Figure 5 : Change in C_H measured on 18Cr-2.5Si steel with thermal aging.

The SEM microstructural examination revealed that σ phase, an intermetallic compound of Fe and Cr, precipitated in the specimens aged at 650°C (Fig. 6(a)), and its amount and size increased with increasing aging time. This σ phase formation was not in the least observed in the specimens aged at 800°C, because it exceeded the solid-solution temperature of σ phase. Since the aging temperature of 700°C is close to this solid-solution temperature, only a small amount of σ phase may be precipitated in the specimens aged at 700°C. Moreover, the aging above 750°C accelerated the precipitation and growth of niobium carbide (NbC), and a number of coarsened NbC were observed along grain boundaries in the specimens aged at 800°C (Fig. 6(b)). It has been known that the precipitates like carbide act as a strong trapping site of hydrogen and the solid-solution of alloying elements such as Cr, Nb and Si has an influence on the diffusion of hydrogen in steels [3,9,10]. Therefore, there is a strong likelihood that the above-mentioned changes in C_H with thermal aging are attributable to the precipitation of σ phase and NbC and/or the resultant change in solid-solution elements such as Cr and Nb.

In this way, it was revealed from the present study that, unlike the previous steel, *i.e.*, Gr.91, the change in hydrogen desorption characteristic reflected not only the damage (defects) but also the microstructural changes. In order to apply this technique to the procedure for detecting and evaluating the damage alone, it is required to separate the effects of defects and microstructural changes on the hydrogen evolution curve and extract the former alone.
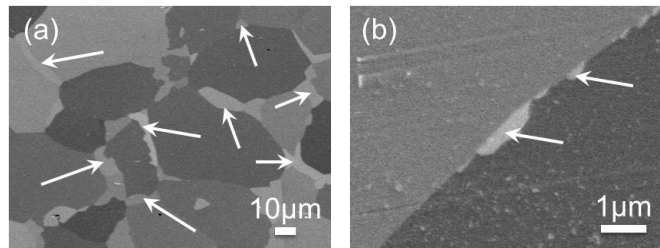
Figure 6 : SEM micrographs of specimens aged at (a) 650°C/10000h (an arrow indicates σ phase) and (b) 800°C/694h (an arrow indicates NbC)

4. Summary

The change in hydrogen desorption characteristic of three kinds of ferritic heat resistant stainless steels (18Cr-2.5Si steel, SUS444, SUH21), which are representative structural materials for the FPS, was investigated to examine the applicability of hydrogen as tracer for detecting and evaluating the materials degradation and creep damage. The hydrogen thermal desorption analysis was applied to the creep specimens and the thermally aged ones after the hydrogen charging. The experimental results revealed that the hydrogen evolution curve and its change with creep were different depending on the kind of steel. The increase in the amount of desorbed hydrogen, C_H, due to creep was more significant in 18Cr-2.5Si steel than two other steels. The lower the stress level was, more pronounced this increase in C_H was. It is very important to mention that the change in hydrogen desorption characteristic reflects not only the damage (defects) but also the microstructural changes like the precipitation of σ phase and NbC and/or the resultant change in solid-solution elements such as Cr and Nb. It is necessary to separate the effects of defects and microstructural changes and extract the former alone for applying this technique to the damage evaluation of the FPS.

References

[1] S. M. Myers, S. T. Picraux, and R. E. Stoltz, Defect trapping of ion-implanted deuterium in Fe, *J. Appl. Phys.*,50, 5710 (1979).

[2] S. M. Myers, D. M. Follstaedt, F. Besenbacher and J. Bottiger, Trapping and surface permeation of deuterium in He-implanted Fe, *J. Appl. Phys.*, 53, 8734 (1982).

[3] H. G. Lee and J. Y. Lee, HYDROGEN TRAPPING BY TiC PARTICLES IN IRON, *Acta Metall.*, 32, 131 (1984).

[4] K. Ono and M. Meshii, HYDROGEN DETRAPPING FROM GRAIN BOUNDARIES AND DISLOCATIONS IN HIGH PURITY IRON, *Acta Metall. Mater.*, 40, 1357 (1992).

[5] M. Nagumo, K. Takai, N. Okuda, Nature of hydrogen trapping sites in steels induced by plastic deformation, *J. Alloys Compd.*, 293–295, 310(1999).

[6] K. Takai, H. Shoda, H. Suzuki, M. Nagumo, Lattice defects dominating hydrogen-related failure of metals, *Acta Mater.*, 56, 5158(2008).

[7] S. Komazaki, T. Honda, T. Sakamura, K. Sawada, K. Kimura and Y. Kohno, Change in Hydrogen Desorption Characteristics of Mod.9Cr–1Mo Steel due to Creep, *Tetsu-to-Hagané*, 96, 614(2010).

[8] S. Komazaki, H. Yamashita, M. Yonemura and M. Igarashi, Creep Damage Evaluation of High Cr Ferritic Steel Based on Change in Hydrogen Desorption Characteristics, *Proceedings of the Seventh International Conference on Advances in Materials Technology for Fossil Power Plants, EPRI, Editors: D. Gandy and J. Shingledecker*, 744(2013).

[9] F. G. Wei, T. Hara, T. Tsuchida and K. Tsuzaki, Hydrogen Trapping in Quenched and Tempered 0.42C–0.30Ti Steel Containing Bimodally Dispersed TiC Particles, *ISIJ Int.*, 43, 539 (2003).

[10]J. O'M. Bockris, M. A. Genshaw and M. Fullenwider, THE ELECTRO-PERMEATION OF HYDROGEN INTO METALS, *Electrochimica Acta*, 15, 47(1970).

A PROPOSAL FOR A STRAIGHTFORWARD WAY TO ESTIMATE THERMO-MECHANICAL FATIGUE CRACK GROWTH

Falk Mueller*, Alfred Scholz, Matthias Oechsner
Fachgebiet und Institut für Werkstoffkunde, Technische Universitaet Darmstadt
Grafenstraße 2, 64283 Darmstadt, Germany

*Corresponding author: fmueller@mpa-ifw.tu-darmstadt.de

Abstract

The determination and estimation of thermo-mechanical fatigue crack growth (TMFCG) in cast nickel based super alloys is a complex subject. From one perspective, the TMFCG test technique is expensive and complicated. From the other, there are many active mechanisms in the TMFCG process. Based on isothermal and thermo-mechanical test results, an approximate procedure to obtain estimates of the TMFCG rates was developed and is described in this paper. In this proposed procedure a temperature-independent fatigue crack growth part and two temperature-dependent crack growth parts are considered. Temperature-dependent crack growth becomes significant above material-dependent critical temperature and is brought about by creep crack and oxidation damage. The activation energies for both damage mechanisms were determined. In respect to oxidation damage, γ'-depletion was found to play a dominant role.

The isothermal data presented in this paper allows for an estimation of isothermal and thermo-mechanical crack growth. Furthermore, it is possible to assess the fraction of the crack growth caused by the different sources: fatigue crack growth, creep crack growth and crack growth due to oxidation damage.

Keywords: nickel base cast alloy, crack growth, isothermal, thermo-mechanical, accumulation

1. Introduction

The combination of thermal and mechanical stress leads to damage in the material, which can be relevant to the service life of the component. Usually thermal and mechanical stresses lie relative to one another within a certain phase shift. A situation with maximum mechanical tensile stress at maximum temperature is referred to as an in-phase (IP) load. An out-of-phase (OP) load arises when the material undergoes compressive stress at maximum temperature and tensile stress at minimum temperature. Prediction of crack growth behavior is relevant to service life. The subject of crack behavior under thermo-mechanical stress conditions has remained practically uninvestigated as of today. Formerly developed approaches for the description of component applications are usually only valid for wrought nickel based alloys [1, 2].

The determination of crack growth under thermo-mechanical fatigue loading and its mechanism-based description impose high demands on the testing technology and the development of computational models. The test engineering must be able to simulate effects in the component such as those resulting, for example, from heating and cooling processes or approaches and retractions. In the evaluation, a substantial over- or underestimation of the service life must be avoided. In a series of research projects [3, 4, 5], the isothermal and thermo-mechanical crack growth behavior of cast nickel base alloy M-247 was investigated under a wide range of temperatures and loads. In this process, the named alloy type was investigated as both a randomly solidified (CC) and directionally solidified (DS) polycrystalline as well as a single crystal (SX). These alloys are catalogued under the following classifications: MAR-M 247 CC HIP, M-247 LC DS and M-247 LC SX.

The following describes the challenges involved in the test engineering as well as the developmental steps for the crack growth model up to its validation.

2. Experimental procedure

Studies on isothermal fatigue crack behavior shall be performed in accordance with [6] and/or [7]. There is no standard currently in effect regarding investigation of crack growth under thermo-mechanical fatigue damage loading. Relevant endeavors, however, have been initiated across Europe. Therefore, the investigations are initially conducted in accordance with [8], at least concerning the experimental procedure. A number of requirements must be met to achieve a suitable crack growth test method under thermo-mechanical fatigue loading conditions (permissible temperature gradients in axial and radial direction, among others). To meet the requirements specified in [8], an appropriate test bench was developed at the IfW Darmstadt (Figure 1a). The heating of the specimen is carried out using an induction heater (Figure 1b). Balanced heating and cooling rates up to 10 °C/s are possible using an ancillary compressed air cooling system. The tests can be performed under load-controlled as well as strain-controlled parameters. The measurement of displacement is carried out using an extensometer (Figure 1b). An alternating current potential drop (ACPD) system is used to monitor crack initiation and crack growth. With the test bench, crack growth measurements can be carried out under isothermal and thermo-mechanical load conditions on the specimen types shown in Figure 2. The maximum currently validated test temperature is 1050 °C.
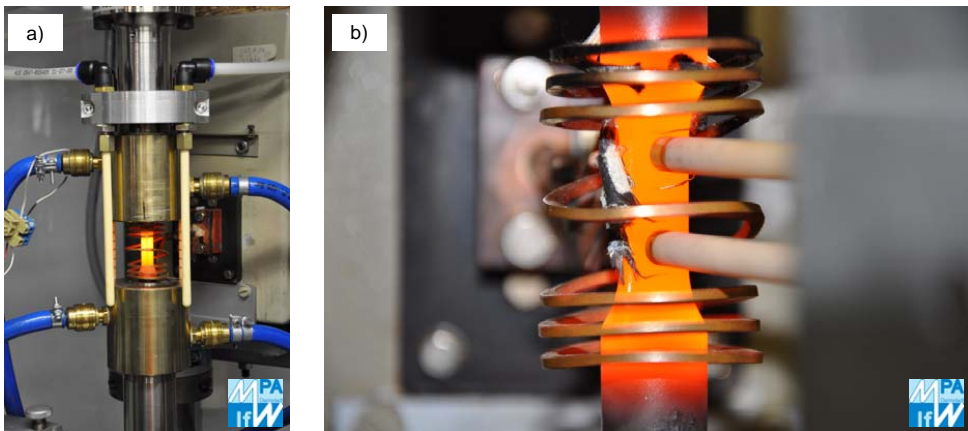
Figure 1. *Test bench at the IfW Darmstadt for crack growth measurements under isothermal and thermo-mechanical load conditions: a) Wide shot with specimen, clamping parts, induction coil, cooling system; b) Close-up with specimen, induction coil, extensometer, potential drop system wires*

3. Data Assessment

The crack growth rate da/dN is generated as a result of the load or strain-controlled fatigue crack tests under isothermal or thermo-mechanical strain conditions. The objective is to apply this crack growth rate versus appropriate fracture mechanics

parameters. To this end, parameters such as the linear elastic stress intensity factor ΔK_I, the elastic-plastic parameter ΔJ, and the crack tip parameter $\Delta CTOD$ are commonly used. For the calculation of the named parameters, reference is made to [9, 10, 11, 12].
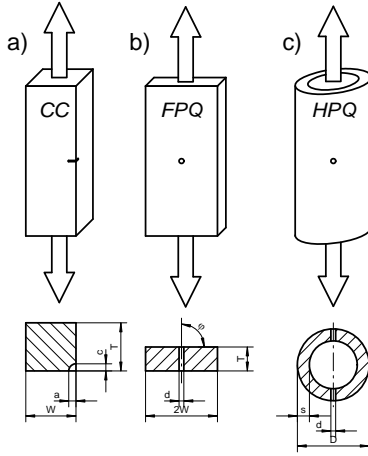
Figure 2. Specimen types for determination of the fatigue crack growth behavior under isothermal and thermo-mechanical load conditions, schematic: a) CC - corner crack specimen; b) FPQ – flat specimen with cross hole; c) HPQ – hollow specimen with cross hole

Demonstrably, time- and temperature-dependent phenomena which can lead to an increase of the crack growth rate arise during high-temperature crack testing. In Figure 3 this can be recognized for a number of load-controlled isothermal fatigue crack tests ($R_\sigma = -1$) on corner crack specimens made from the material MAR-M 247 CC HIP. In the use of the linear-elastic stress intensity factor ΔK_I (Figure 3a), the elastic-plastic parameter ΔJ (Figure 3b) as well as the crack tip parameter $\Delta CTOD$ (Figure 3c), an almost identical crack growth behavior results in the tested material up to a temperature of approx. 850 °C. At temperatures above 850 °C, higher crack growth rates are observed. This indicates that the parameters used can reproduce the time- and temperature-independent crack growth accurately and uniformly but cannot determine the time- and temperature-dependent acceleration effects.

Thus, at this time there exists no fracture mechanics-based parameter which can take into account "all" effects simultaneously. For this reason attempts must be made to determine at least the most important damage increments affecting crack growth and describe them in a sensible manner. In Figure 4, therefore, microstructure-specific properties of cast nickel alloys are schematically illustrated. In the example of the M-247 alloys it became obvious that the grain boundaries and grain orientations exert only minor influences on the crack growth. Crack growth, however, is influenced very substantially by oxidative processes in the area of the crack tip (Figure 5). In this regard, a γ'-depleted zone was observed which had a much lower resistance to crack propagation than that ascribed to the original microstructure [13]. This process represents a time- and temperature-dependent damage increment. As a second time- and temperature-dependent damage increment, a creep crack load was taken into account. As a time- and temperature-independent load, a fatigue damage increment was defined. In the following, an accumulation model is now proposed which takes into account in parallel the time-/temperature-independent and time- /temperature-dependent effects.

667
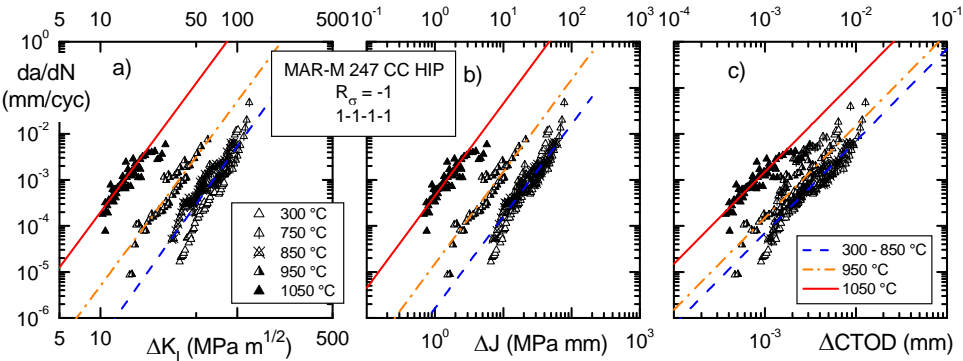
Figure 3. Crack growth rate da/dN under isothermal loading conditions as a function of a) ΔK_I; b) ΔJ; c) ΔCTOD, corner crack specimens
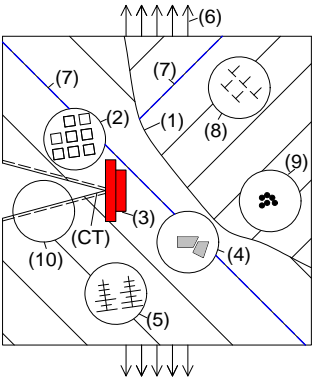
(CT) crack tip
(1) grain boundary
(2) γ/γ' structure
(3) deformation behavior/-capability
(4) precipitation / carbides
(5) dendrite structure
(6) external load
(7) grain orientation
(8) dislocation structure
(9) pores / discontinuities
(10) oxidation

Figure 4. Microstructure-specific properties of cast nickel alloys, schematic
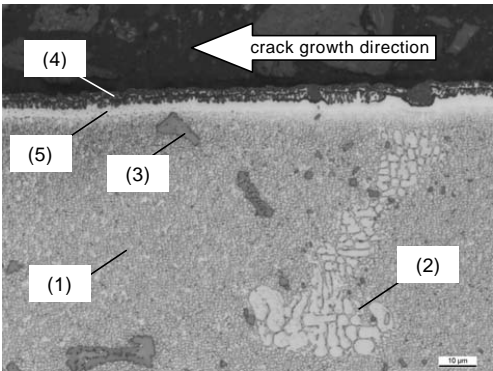
(1) γ/γ' structure
(2) eutectic
(3) carbides
(4) oxide layer
(5) loss of γ/γ' structure

Figure 5. Crack path from a fatigue crack test at 950 °C

4. Accumulation model O.C.F.

Accumulation models represent a relatively simple modus operandi for the purpose of describing even very complicated situations. Using such a model, damage increments are observed separately from one another [1, 2]. Possible interactions were not taken into account.

On the basis of the above-mentioned experimental results, three damage increments (oxidation, creep and fatigue) were used as a basis for the modeling of the crack growth behavior of M-247 alloys. As a net result, the total crack growth rate da/dN_{tot} is comprised of the following:

$$da/dN_{tot} = da/dN_o + da/dN_c + da/dN_f \,. \tag{1}$$

For every load cycle (Figure 6a), this results in a damage zone ahead of the crack tip, which, when the crack is opened, causes a corresponding increase in crack growth. (Figure 6b). Note that the fatigue increment da/dN_f is characterized by time/temperature independence. Only above a material-dependent temperature T_{crit} are the time/temperature dependent increments da/dN_o and da/dN_c added.
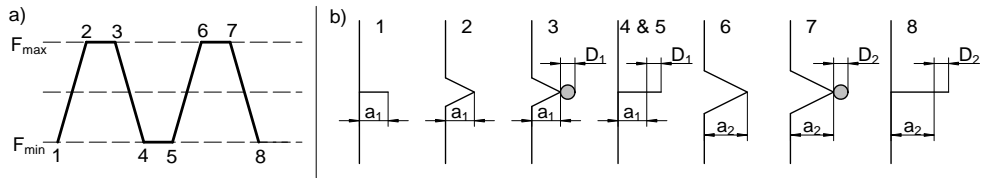
Figure 6. Load cycle (a) and damage evolution at the crack tip (b), schematic

Based on the above observations, the time/temperature independent **fatigue crack increment** is initially described by

$$da/dN_f = A_f \cdot \Delta K_{I\,eff}{}^{m_f} \tag{2}$$

(Figure 7a). With this relationship, the crack growth rate up to and including 850 °C for various R_σ-ratios and tensile dwell times up to 300 s are reproduced successfully. Crack closure effects are taken into consideration via the effective stress range of the cyclic stress intensity factor. The effective value is calculated using

$$\Delta K_{I\,eff} = U \cdot \Delta K_I = 0.35 + (2.2 - R_\sigma)^{-2} \cdot \Delta K_I \tag{3}$$

To clarify the time/temperature independence for the defined fatigue crack increment, the crack path from a fatigue test at 650 °C is documented in Figure 7b. The changes observed in the area of the crack tip at temperatures above 850 °C (see Figure 5) are not recognizable here.

The stress intensity factor K_I was also employed to describe the **creep crack increment**. The authors are aware that this parameter was thus being applied beyond its validity

limits. Nonetheless, the results show that the stress intensity factor was justified in this context.

The creep crack growth rate da/dt can be specified for each temperature (Figure 8a) using the determination of the activation energy. In Figure 8b a typical damage profile in the area of the crack tip with creep damage (T = 850 °C) is shown. To be taken into account here is that, particularly in the case of coarse-grained polycrystalline nickel cast alloys, the creep crack can feature unsteady gradients. For the recording of such behavior, a nominal stress based concept was introduced in [14] which is not, however, taken into account hereinafter. It is important to further investigate the creep crack behavior of DS- and SX-M-247 alloys.
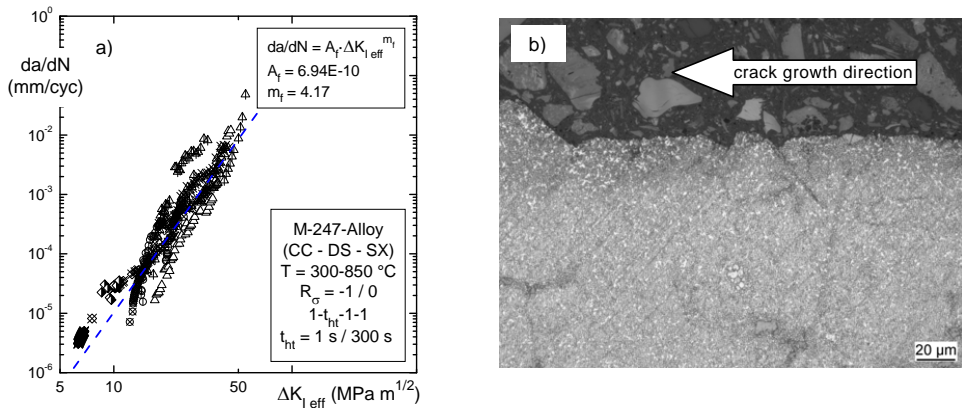
Figure 7.   Time and temperature independent crack growth, M-247 alloy: a) Crack growth rate da/dN as a function of $\Delta K_{I\,eff}$; b) Fatigue crack path at 650 °C
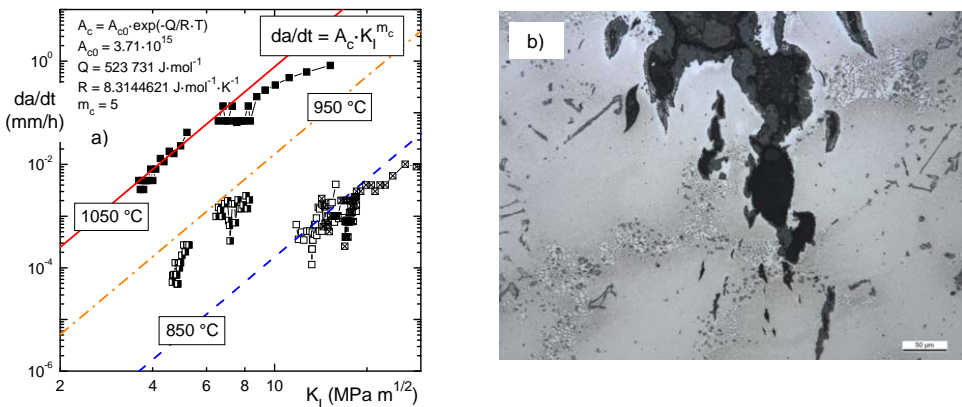
Figure 8. Time and temperature dependent creep crack behavior, M-247 alloy: a) Creep crack growth rate da/dt as a function of K_I, b) Creep damage in the area of the crack tip, MAR-M 247 CC HIP, T = 850 °C

As the next time/temperature dependent crack increment, an **oxidation increment** was defined, using the observations in the experimental investigations, which has as its basis the epitaxial growth of the γ'-depleted zone (Figure 9). To this end, parameters from [15] were drawn upon. The resulting growth laws at 850, 950 and 1050 °C are shown in Figure 9a. For purposes of comparison, the γ'-depleted zone was determined in our own investigations using random sampling on specimens from fatigue crack tests and annealing experiments (Figure 9b). The result is that, with the parameters from [15], the epitaxial growth of the γ'-depleted zone on the materials in the current investigation are described rather more conservatively. The improvement of the production route of M-247 alloys during the past 20 years probably plays a definitive role in this context. The parameters from [15] were used in the model. A validation would certainly be useful and necessary.
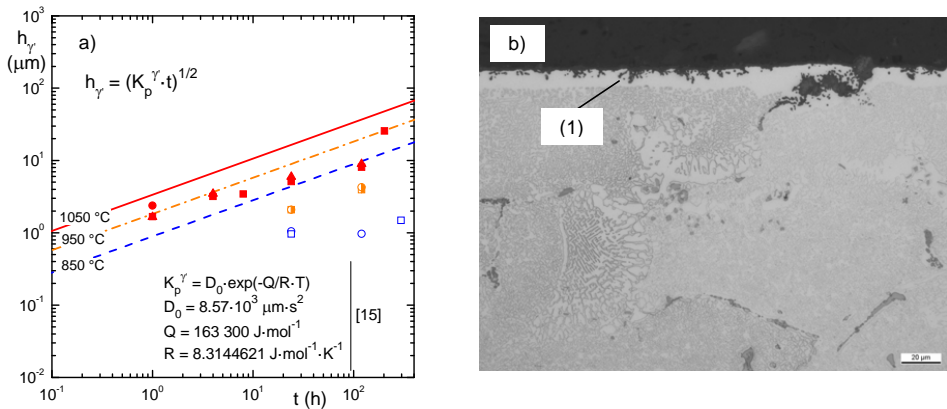
Figure 9. *Time and temperature dependent growth of the γ'-depleted zone at temperatures between 850 and 1050 °C, M-247 alloy: a) Growth law of the γ'-depleted zone, parameter from [15], data points from our own investigations of MAR-M 247 CC HIP and M-247 LC SX; b) γ'-depleted zone (1) from an annealing test at 950 °C*

5. Comparison to the experiments

With the above, the components of the accumulation model O.C.F. (**O**xidation - **C**reep - **F**atigue) have been introduced. Now it is necessary to monitor how well the experimental results can be duplicated. To this end, the measured crack growth rate will be compared with the calculated crack growth rate from load controlled isothermal tests on corner crack specimens. Figure 10 depicts the corresponding crack growth diagrams. On one side the experimental results on the DS and SX alloys at 950 °C (Figure 10a) and on the other, experimental results of the SX alloy at 1050 °C (Figure 10b) are considered. As can easily be recognized, the calculated crack growth rates are predicted somewhat conservatively but certainly within an acceptable range. The influence of temperature and dwell time is registered quite satisfactorily by the accumulation model O.C.F.

In the next step the measured crack lengths are compared to calculated crack lengths. Figure 11 depicts results for this from strain controlled (R_ε = -1) fatigue crack tests at

671

950 and 1050 °C. The tests were conducted on a hollow specimen with cross hole (Figure 11a, material: M-247 LC SX) and/or on a flat test piece with cross hole (Figure 11b, material: MAR-M 247 CC HIP). The conformity between the measured and calculated crack length is more than adequate.
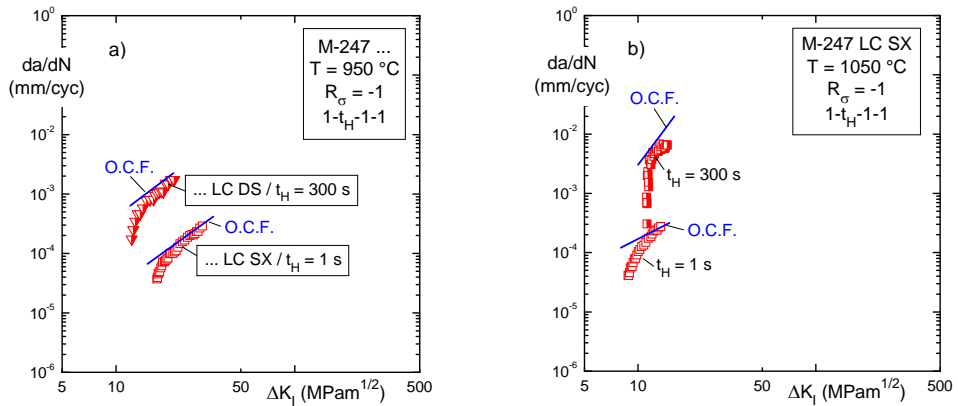

Figure 10. Measured and calculated crack growth rate da/dN from isothermal fatigue crack tests without and with tensile dwell time, corner crack specimens: a) T = 950 °C; b) T = 1050 °C
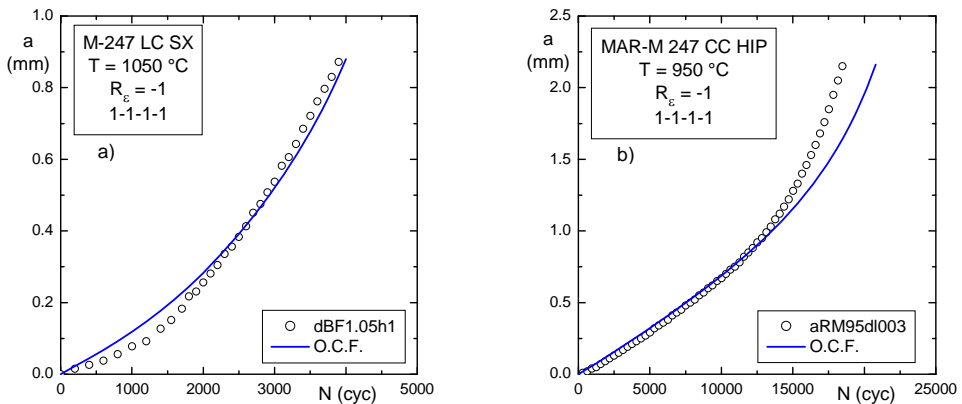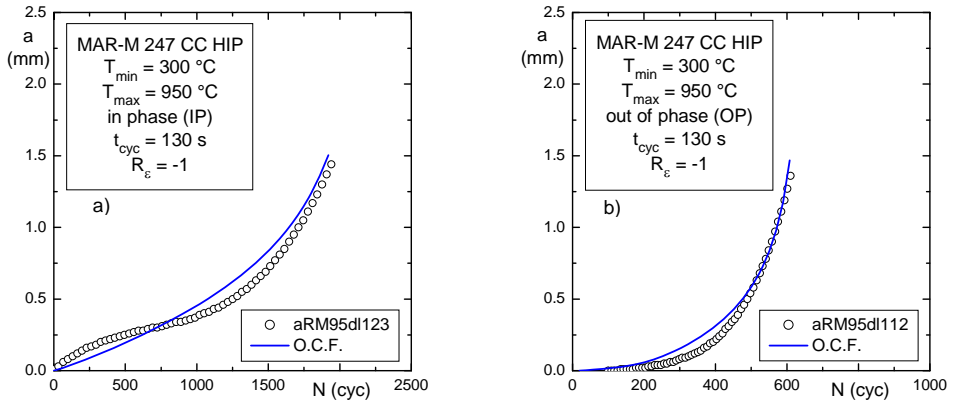

Figure 11. Measured and calculated crack length a from isothermal strain-controlled fatigue tests: a) Hollow specimen with cross hole, M-247 LC SX, T = 1050 °C; b) Flat specimen with cross hole, MAR-M 247 CC HIP, T = 950 °C

In Figure 12 a comparison is carried out between measured and calculated crack length from thermo-mechanical strain controlled ($R_\varepsilon = -1$) fatigue crack tests on flat specimens with cross hole. To make allowance for temperature cycles an internal equivalent temperature T_{eq} was defined. For this several suggestions were made (e.g. in [16]). In the

current setting, the internal equivalent temperature T_{eq} is calculated for the IP case (Figure 12a) to

$$T_{eq\ IP} = 0.9 \cdot T_{max} + 0.1 \cdot T_{crit} \ . \tag{4}$$

The Internal equivalent temperature T_{eq} for the OP case (Figure 12b) is calculated as

$$T_{eq\ OP} = 0.9 \cdot T_{krit} + 0.1 \cdot T_{max} \ . \tag{5}$$

The critical temperature T_{crit} named in the equations (4) and (5) corresponds to the temperature starting from which the time/temperature dependent effects must be taken into account. In the current case, for the examined M-247 alloys T_{crit} is equal to 850 °C. The conformity between measurement and calculation (Figure 12) is good.

As a practical corollary, the damage increments can be specified separately using the accumulation model O.C.F. For the two previously mentioned thermo-mechanical fatigue crack tests, the respective increments arising from oxidation / creep / fatigue are plotted in Figure 13. As indicated there, the time/temperature dependent increments have the greatest influence on the determined crack growth. The degree to which this calculation result corresponds to the actual fracture structure is the subject of current research.

All of the fatigue crack experiments carried out on the materials MAR-M 247 CC HIP, M-247 LC DS and M-247 LC SX (Table 1) in the context of this investigation were recomputed with the accumulation model O.C.F.. To permit a review of the quality of the recalculation, the cycle counts from the test and calculation were determined for selected crack lengths (Δa = 0.5, 1.0 and 1.5 mm) and graphically displayed in Figure 14a.

In general, the calculation results are on the conservative side. Test results which are described very conservatively by the model show a pronounced crack initiation phase, which is currently not reflected by the model. Further, two test results do not lie on the conservative side. In this case it must be taken into account that these data pertain to test results on the randomly solidified polycrystalline variation (MAR-M 247 CC HIP). Because of the extant coarse grained structure, effects can arise which are not captured by the model. These results were not taken into consideration in Figure 14b. A relatively narrow scatter band results.

For the further validation of the accumulation model O.C.F., fatigue crack tests under thermo-mechanical loading with dwell times should be considered. In addition the predictive quality of the model should be evaluated using probabilistic precepts.

Figure 12. Measured and calculated crack length a from thermo-mechanical strain-controlled fatigue tests on flat specimen with cross hole, MAR-M 247 CC HIP, T_{min} = 300 °C, T_{max} = 950 °C; a) IP loading; b) OP loading
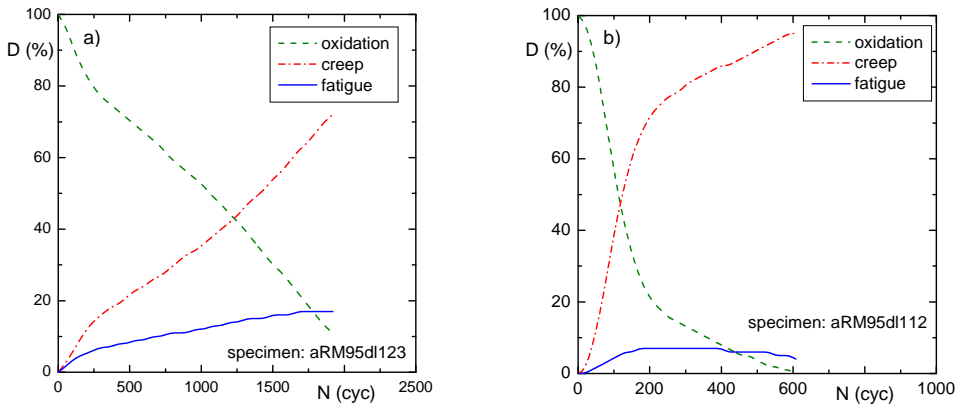

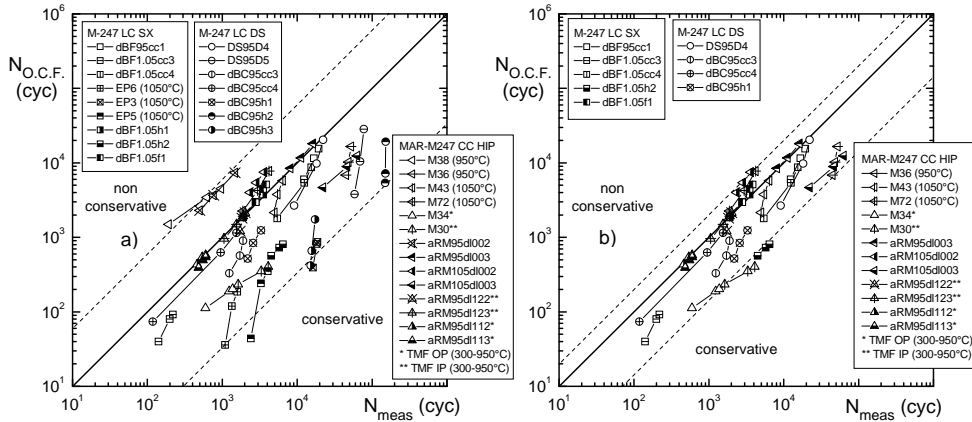*Figure 13. Damage increments D at crack growth from from thermo-mechanical strain-controlled fatigue tests on flat specimen with cross hole, MAR-M 247 CC HIP, T_{min} = 300 °C, T_{max} = 950 °C; a) IP loading; b) OP loading*

Figure 14. Comparison of measured and calculated number of load cycles to reach certain crack lengths: a) all tests in accordance with Table 1; b) tests within the constraints of O.C.F.

Material	Specimen type	T (°C)	Cycle (s)	Temp. control	OP / IP	R_σ (-)	R_ε (-)	Specimen no.
M-247 LC SX	Corner crack	950	1-1-1-1	isothermal	-	-1	-	dBF95cc1
	Corner crack	1050	1-300-1-1	isothermal	-	-1	-	dBF105cc3
	Corner crack	1050	1-1-1-1	isothermal	-	-1	-	dBF105cc4
	Corner crack	1050	1-1-1-300	isothermal	-	-1	-	EP6*
	Corner crack	1050	1-1-1-1	isothermal	-	0	-	EP3*, EP5*
	Hollow spec.	1050	1-1-1-1	isothermal	-	-	-1	dBF105h1
	Hollow spec.	1050	1-300-1-1	isothermal	-	-	-1	dBF105h2
	Flat specimen	1050	1-1-1-1	isothermal	-	-	-1	dBF105f1
M-247 LC DS	Corner crack	950	1-300-1-1	isothermal	-	-1	-	dBC95cc3, cc4
	Hollow spec.	950	1-300-1-1	isothermal	-	-1	-	dBC95h1, h3
	Hollow spec.	950	1-1-1-1	isothermal	-	-1	-	dBC95h2
	Corner crack	950	1-1-1-1	isothermal	-	-1	-	DS95D4*, D5*
MAR-M 247 CC HIP	Corner crack	950	1-1-1-1	isothermal	-	-1	-	M38**, M36**
	Corner crack	1050	1-1-1-1	isothermal	-	-1	-	M43**, M72**
	Corner crack	300 - 950	65-65	thermo-mech.	OP	-1	-	M34**
	Corner crack	300 - 950	65-65	thermo-mech.	IP	-1	-	M30**
	Flat specimen	950	1-1-1-1	isothermal	-	-	-1	aRM95dl002, dl003
	Flat specimen	1050	1-1-1-1	isothermal	-	-	-1	aRM105dl002, dl003
	Flat specimen	300 - 950	65-65	thermo-mech.	IP	-	-1	aRM95dl122, dl123
	Flat specimen	300 - 950	65-65	thermo-mech.	OP	-	-1	aRM95dl112, dl113
* Tests performed at the MPA Stuttgart / ** Tests performed at the IWM Freiburg								

Table 1. Overview of the fatigue tests performed, both isothermal (T = 950, 1050 °C) and thermo-mechanical (T = 300 - 950 °C), on corner crack specimens, hollow specimen with cross hole, and flat specimen with cross hole for the validation of the O.C.F. model; not shown are the isothermal tests on the set-up of the O.C.F. model.

675

6. Application to component

For the practical application of the accumulation model O.C.F. the following procedure is recommended (see also <u>Figure 15</u>):
1. Elastic-plastic analysis of the component without crack to determine the service life leading place (if applicable also the consideration of creep effects)
2. Calculation of the stress intensities on the basis of relevant substitute models of linear-elastic fracture mechanics or using FEM.
3. Crack growth using O.C.F.
4. Statements regarding component service life and/or allowable crack length.
Initial test calculations for effecting the described approach are pending.

| Elastic-plastic calculation of component without crack | Calculation of the stress intensities on the component with crack | Crack growth calculation | Service life and/or permissible crack length |
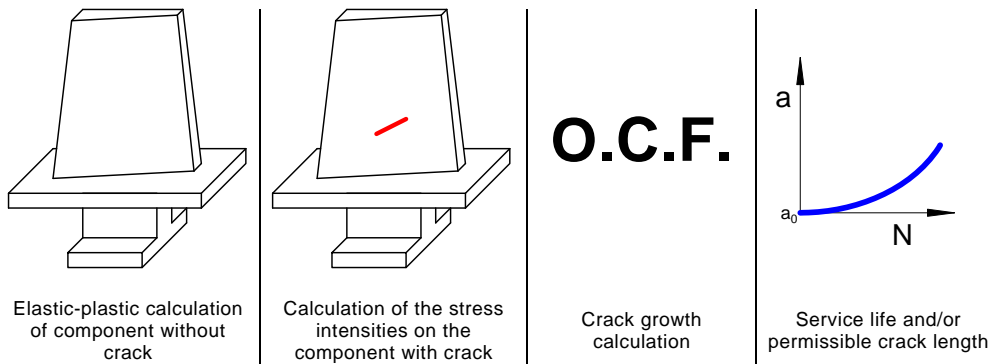
Figure 15. Methodology in the practical application of the accumulation model O.C.F., schematic

7. Concluding remarks

Using the example of the cast nickel alloy M-247, the accumulation model O.C.F. (**O**xidation - **C**reep - **F**atigue) was developed and validated on the basis of isothermal and thermo-mechanical fatigue crack growth tests. The accumulation model O.C.F. allows for separate damage increments to crack growth from fatigue, creep and oxidation. With the introduced model, crack growth can be successfully recalculated, whether from load controlled, strain controlled, isothermal or thermo-mechanical fatigue tests on fracture mechanics specimens, or on specimens with cross holes, respectively. In the model, temperature and dwell time effects are accounted for. The conformity between measured and calculated crack growth is more than adequate. A transfer to components is feasible. Emphasis is placed on the fact that the determined parameters for the accumulation model O.C.F. can be used for randomly solidified, directionally solidified as well as single crystal solidified M-247 cast nickel structures. After a further validation, the model will be available for practical application due to its ease of handling.

8. References

[1] Nicholas, T., M. Heil, G. Haritos: Predicting crack growth under thermo-mechanical cycling, International Journal of Fracture 41, 157-176, 1989.

[2] Affeldt, E., C. de la Cruz Lorena: Thermo-mechanical fatigue of a wrought nickel based alloy, Materials at High Temperatures, Vol. 30, 69-76, 2013.

[3] Rudnig, J.-M., M. Speicher, C. Berger, A. Scholz, F. Mueller, E. Roos, A. Klenk: Rissverhalten von Nickelbasis-Gusslegierungen mit unterschiedlicher Kornstruktur, Abschlussbericht zum AiF-Forschungsvorhaben Nr. 15 626 N, IfW Darmstadt, MPA Stuttgart, 2010.

[4] Serrano, L., C. Schweizer, M. Oechsner, C. Berger, A. Scholz, F. Mueller, M. Gumbsch, M. Schlesinger, S. Eckmann: Rissverhalten unter anisothermen Beanspruchungsbedingungen – Berechnungsverfahren für Nickelbasislegierungen, Abschlussbericht zum AiF-Forschungsvorhaben Nr. 15 525 N, IfW Darmstadt, Fraunhofer IWM Freiburg, 2011.

[5] Baumann, C., M. Speicher, M. Oechsner, A. Scholz, F. Mueller, K. Maile, A. Klenk, C. Kohler: Bewertung des Rissverhaltens von Fehlstellen hochtemperaturbeanspruchter Schaufeln aus Nickelbasisgusslegierungen, Abschlussbericht zum AiF-Forschungsvorhaben Nr. 17 195 N, IfW Darmstadt, MPA Stuttgart, 2013.

[6] EN 3873: Aerospace series - Test methods for metallic materials - Determination of fatigue crack growth rates using Corner - Cracked (CC) test pieces, European standard, 2010.

[7] ASTM E647-11: Standard Test Method for Measurement of Fatigue Crack Growth Rates, ASTM International, 100 Barr Harbor Drive, PO Box C700, West Conshohocken, PA 19428-2959, United States, 2011.

[8] ISO 12111: Metallic materials - Fatigue testing - Strain-controlled thermo-mechanical fatigue testing method, 2011.

[9] Rice, J. R.: A Path Independent Integral and the Approximate Analysis of Strain Concentration by Notches and Cracks, J. App. Mech. 35, pp. 379-86, 1968.

[10] Dai, Y., N. J. Marchand, M. Hongoh: Thermal Mechanical Fatigue Crack Growth in Ti64 and Ti6246, Fatigue 93, Proceedings of the 5th International Conference on Fatigue and Fatigue Thresholds in the International Fatigue Series (IFS), Montreal, Quebec, Canada, May 3-7, Editors: J.-P. Bailon and J. I. Dickson, 1993.

[11] Schweizer, C., T. Seifert, B. Nieweg, P. von Hartrott, H. Riedel: Mechanisms and modelling of fatigue crack growth under combined low and high cycle fatigue loading, International Journal of Fatigue, Volume 33, Issue 2, February 2011, pp. 194–202, 2011.

[12] Richard, H. A.; M. Sander: Ermüdungsrisse, Vieweg+Teubner, Wiesbaden, Germany, 2009.

[13] Sengupta, A., S. K. Putatunda: Kinetics of γ' precipitation and its influence on fatigue crack growth behavior of a new single-crystal nickel-based superalloy (CMSX-4G) at room temperature, Journal of Materials Engineering and Performance, February 1993, Volume 2, Issue 1, pp 57-68, 1993.

[14] Mueller, F., A. Scholz, C. Berger: Creep crack behaviour of a coarse grain nickel-base super alloy, Materials at High Temperatures, Vol. 28, 103–108, 2011.

[15] Sehitoglu, H., D. A. Boismier: Thermo-mechanical fatigue of MAR-M247: Part 2-Life Prediction, Journal of Engineering Materials and Technology, Vol. 112, 1990.

[16] TRD: Technische Regeln für Dampfkessel, Carl Heymanns Verlag, Taschenbuch-Ausgabe, 2007.

A STUDY OF CREEP-FATIGUE INTERACTION IN THE NICKEL-BASE SUPERALLOY 263

Pohja R.[1], Holmström S. [2], Nurmela A. [1], Moilanen P. [1]

[1]VTT Technical Research Centre of Finland, ESPOO (rami.pohja@vtt.fi)
[2]Joint Research Centre - IET, PETTEN

Abstract

Ni-based superalloys, such as alloy 263, have excellent creep strength at high temperatures due to precipitation of gamma prime (γ′). Therefore they are candidate materials for thick section components as well as tubing in advanced ultra-supercritical (A-USC) power plants where temperatures exceed 700 °C. Because of the lower thermal expansion coefficient the Ni-based superalloys are less prone to thermal fatigue damage than the austenitic stainless steels. A series of creep-fatigue (CF) and low cycle fatigue (LCF) tests have been performed in order to study the effect of the test temperature, hold time, total strain range and a pre-creep exposure of 178MPa / 3000h / 750ºC on the creep-fatigue life of alloy 263. All LCF and CF tests were performed using the high precision pneumatic loading system (HIPS) at temperatures in the range of 700-750ºC, the total strain range between 0.5-1.0% and with hold periods up to 10h in both tension and compression. In this paper stress relaxation time plots, σ-N plots and Δε-N plots are presented for alloy 263. The creep-fatigue test results are analysed using time fraction approach utilized in the nuclear material assessment and design codes, such as RCC-MRx and ASME III NH. The results are compared against public domain data and fitted to the recently developed Φ-model. The Φ-model utilizes the creep rupture strength and tensile strength for predicting CF life with a minimum amount of fitting parameters. It is shown that the number of cycles to failure for CF data for alloy 263 can be accurately predicted by the Φ-model. Furthermore, the practicality in using the time fraction approach for presenting the combined CF damage is discussed and recommendations for alternative approaches are made.

Keywords: Nickel-base superalloy 263, creep-fatigue, stress relaxation, modelling

1. Introduction

Power plant components working at high temperatures are subjected to load cycles that gradually accumulate life-limiting damage under more or less variable operating environments. Thermal and mechanical stresses, which promote fatigue type damage mechanisms, result from temperature and pressure changes during operation and start-ups/shut-downs. Even under steady operation, creep deformation will proceed at high temperatures. The evaluation and assessment of the combination of these mechanisms, the creep-fatigue interaction, is an important issue for the design, maintenance and life assessment purposes for power plant components.

Ni-based superalloys, such as alloy 263, have excellent creep strength at temperatures above 700°C due to precipitation of γ′. Because of the lower thermal expansion coefficient they are less prone to thermal fatigue damage than the austenitic stainless steels. The nickel-base superalloys are candidate materials for thick section components as well as tubing in advanced ultra super critical power plants.

This paper describes a study for the creep-fatigue (CF) interaction of nickel-base superalloy 263. Low cycle fatigue (LCF) tests with and without hold periods were carried out for alloy 263 parent material and cross-weld specimens. A creep exposure of 178MPa at 750°C for

3000h was conducted for a set of specimens before CF testing. The test results and data found from open literature were assessed using selected CF assessment and modelling methods.

2. Materials and experimental methods

The NIMONIC alloy 263 was provided by Special Metals Wiggin Limited for the experiments. The alloy 263 billet was solution heat treated for 2 hours at 1150°C with a water quench. An ageing heat treatment of 4 hours at 800°C was conducted for the billet. The chemical composition of the alloy is shown in table 1.

Table 1. The chemical composition of NIMONIC alloy 263.

Position	Chemical Composition (Weight % except where stated ppm)															
	C	Si	Mn	S	Ag (ppm)	Al	B (ppm)	Bi (ppm)	Co	Cr	Cu	Fe	Mo	Ni	Pb (ppm)	Ti	Ti+Al
Max	0.08	0.40	0.60	0.007	5	0.60	50	1	21.0	21.0	0.2	0.7	6.1	Bal	20	2.4	2.8
Min	0.04					0.30			19.0	19.0			5.6			1.9	2.4

The welding procedure for alloy 263 was carried out using a matching NIMONIC 263 filler metal. The cross-weld specimens were manufactured so that the fusion line between parent material and weld metal as well as the heat affected zone (HAZ) were located inside the gauge length of the CF test specimen. The hardness values measured from the weld metal and HAZ were slightly higher than those measured from parent material as shown in figure 1.
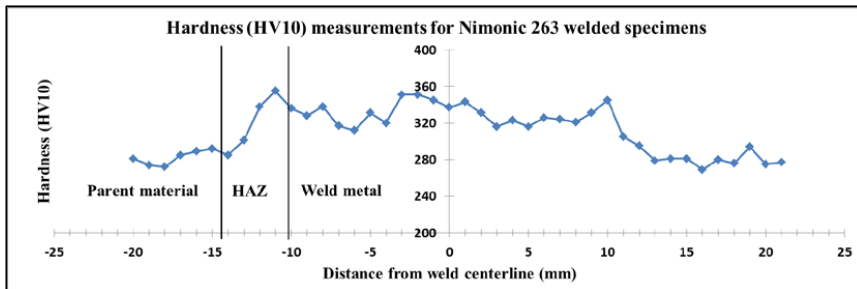
Figure 1. The hardness values measured from cross-weld specimen.

The CF testing was conducted using high precision pneumatic loading system (HIPS). Although the tests were conducted at air atmosphere, the pneumatic servo-controlled loading system is capable of operating in a range of extreme conditions such as at high temperature, pressurized water or steam, supercritical water (SCW) and irradiation environments. More detailed description of high precision pneumatic loading system and its capabilities is given in references 1 and 2.

Low cycle fatigue (LCF) tests with fully-reversed total axial strain control with and without hold periods were conducted for parent material and cross-weld specimens in air atmosphere. The temperature range for testing was between 700°C and 750°C. The strain rate was 0.1% / sec and the total strain range was between 0.5% and 1.0% of the gauge length. A hold period of 0.1-10.0h both in tension and in compression was introduced for a set of specimens. The tests were performed on material in both virgin state and in pre-crept condition. The pre-crept test specimens had been creep tested at 178MPa / 750°C for 3000h hours before CF testing.

The accumulated strain for all pre-crept parent material specimens was near 0.7%, but for cross-weld specimens the accumulated strain caused by pre-creep exposure ranged from 0.4% to 2.0%.

3. Test results

3.1. Peak stresses and number of cycles to failure

The number of cycles to failure used for the assessment in this study is defined as the number of cycles to 5% load drop. Peak stresses divided by the ultimate tensile strength of alloy 263 base material as a function of cycles for specimens tested at 750ºC are shown in figure 2. The number of cycles is normalized by the number of cycles to failure of the longest test. The tested specimens exhibited slight cyclic hardening during first few cycles followed by slight cyclic softening before failure. As expected, the peak stress increased when the total strain range was increased and the number of cycles to failure decreased when the total strain range and the length of the hold periods were increased. The cross-weld specimens exhibited higher peak stress levels than parent material specimens with equal total strain range. However, no significant difference in peak stress levels was discovered between pre-crept and virgin material specimens. The largest number of cycles to failure was achieved with a test having the total strain range of 0.6% without hold periods. The smallest number of cycles to failure was achieved with a pre-crept specimen. The total strain range for this specimen was 1.0% and the hold period was 10 hours both in tension and compression.
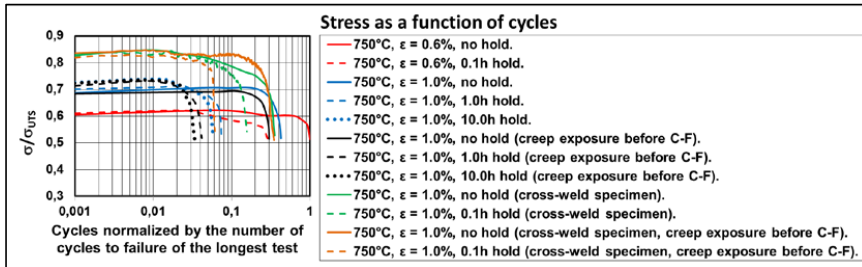
Figure 2. Peak stresses divided by UTS as a function of cycles for CF specimens tested at 750ºC.

3.2. Creep-fatigue life reduction

The Manson-Coffin model for LCF tests without hold periods at 750°C was fitted for alloy 263 using the test results and public domain data. [3, 4, 5, 6, 7 and 8] The Manson-Coffin model is presented in Equation 1:

$$N_f = (\frac{\Delta\varepsilon - C_1}{C_2})^{\frac{1}{C_3}}$$

(1)

where $\Delta\varepsilon$ is total strain range and C_1, C_2 and C_3 are fitting constants. The VTT test results for virgin state parent material specimens resided near the modelled curve, whereas the pre-crept parent material, cross-weld and pre-crept cross-weld specimens exhibited decreased number of cycles to failure compared to the modelled curve as shown in figure 3.
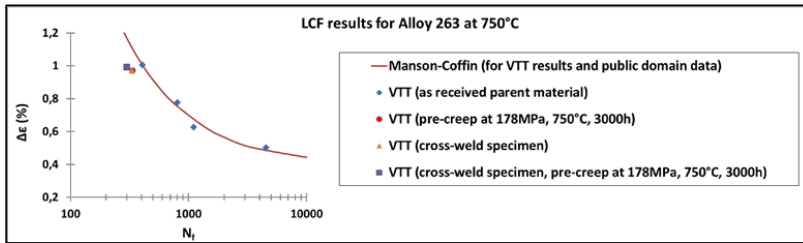
Figure 3. The Manson-Coffin model fit for alloy 263 LCF tests without hold periods and VTT test results at 750°C. [3, 4, 5, 6, 7 and 8]

As expected, a hold period of 0.1-10.0h decreased significantly the number of cycles to failure. For tests at 750°C with 1.0% total strain range a hold period of 10h decreased the number of cycles to failure with one order of magnitude as shown in figure 4.
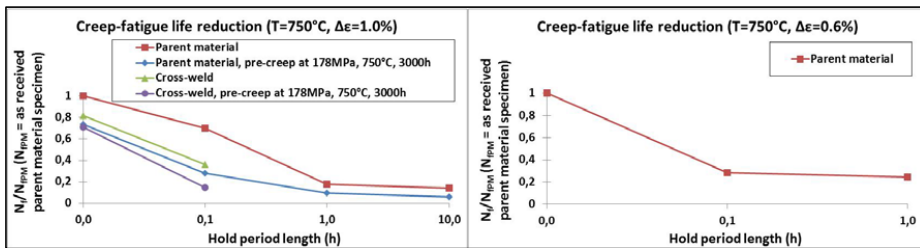
Figure 4. Creep-fatigue life reduction as a function of the hold period length for alloy 263 at 750°C with total strain range of 0.6-1.0%.

3.3. Stress relaxation behaviour during the hold period

The stress relaxation behaviour during the hold period was found to be similar for the cross-weld and parent material specimens. However, the pre-crept specimens exhibited slightly accelerated stress relaxation, both for parent material and cross-weld specimens as shown in figures 5 and 6. Based on the alloy 263 available creep test data, specimens pre-crept at 178MPa / 750°C for 3000h are expected to include a fair amount of accumulated creep damage. Furthermore, exposure at 750ºC for 3000h may cause the dissolution of the $M_{23}C_6$ carbides which also increases the creep and relaxation rates.
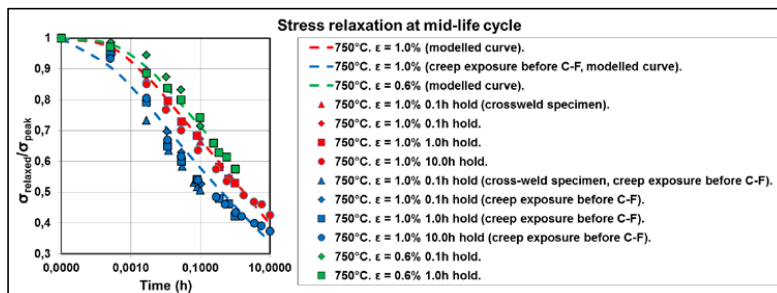
Figure 5. Observed and predicted relaxation behaviour during the hold period of the mid-life cycle for specimens tested at 750°C.

681

4. Creep-fatigue modelling

4.1. Stress relaxation model

The stress relaxation behaviour during the hold period was also modelled using modified Feltham equations. According to Feltham equations, the relaxed stress σ as a function of time can be expressed:

$$\sigma = \sigma_0 - s \cdot \log(1 + \upsilon t) \tag{2}$$

where σ_0 is the peak stress at the beginning of the hold period, t is time, s and v are fitting parameters. The parameter s can be determined as follows:

$$s = kT/V_a \tag{3}$$

where T is temperature and V_a is the apparent activation volume [9]. A dependency on the temperature, total strain range and stress was sought for parameters $k(T,\Delta\varepsilon,\sigma)$ and $v(T,\Delta\varepsilon,\sigma)$ for this study. Furthermore, a creep reduction factor was implemented in the modified Feltham model for this study in order to predict the stress relaxation behaviour for pre-crept parent material and pre-crept cross-weld specimens.

The relaxation behaviour of a test result found in literature [4] with 0.7% total strain range with 1h hold periods at 700°C was predicted along with the VTT test results to validate the model as shown in figure 6.
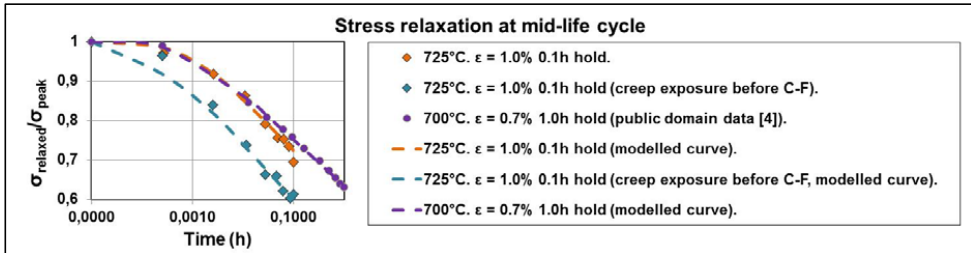
Figure 6. Observed and predicted relaxation behaviour during the hold period of the mid-life cycle for specimens tested at 700-725°C. [4]

4.2. Linear damage rule

The parent material test results with hold periods were assessed using linear damage rule with time fraction approach. This method is based on the simple assumption that fatigue damage can be expressed as summed cycle fractions and that creep damage can be expressed as summed time fractions. It is also assumed that these quantities can be added linearly to represent damage accumulation. Failure should occur when this summation reaches a certain value, so that:

$$\sum_j \left(\frac{t}{t_r}\right)_j + \sum_k \left(\frac{n}{N_f}\right)_k \leq D \tag{4}$$

where n is the number of cycles of exposure at a given strain range, N_f is the cycles to failure at the same strain range, t is the time of exposure at the same stress-temperature combination and t_r is the time to rupture at the same stress-temperature combination.

Most of the test results resided near the (0.3, 0.3) interaction locus in the linear damage rule plot as shown in figure 7.
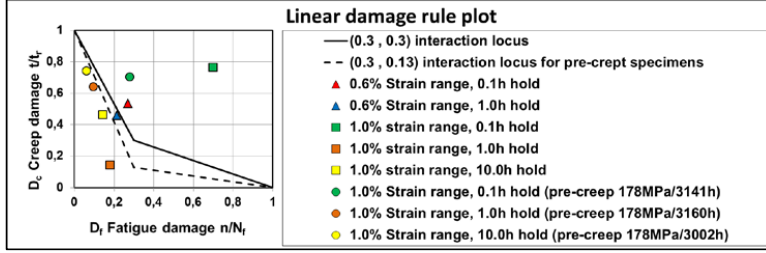
Figure 7. The linear damage rule plot for test results with the total strain range of 0.6-1.0% at 750°C.

In the linear damage rule the fatigue damage per cycle d_f is simply defined as:

$$d_f = 1/N_{f0} \tag{5}$$

where N_{f0} is the number of cycles to failure without creep damage (LCF) or design fatigue curve value. Now rewriting the Equation (4) to allow for predicting the number of cycles (N_{CF}) to failure using the locus point (F,C) (i.e. the coordination of the knee in the bi-linear interaction diagram) and the "known" fatigue damage d_f:

$$N_{CF} = \frac{C}{(1-F)d_c + Cd_f} \;\; if \;\; \frac{d_f}{d_c} \geq \frac{F}{C} \tag{6}$$

$$N_{CF} = \frac{F}{(1-C)d_f + Fd_c} \;\; if \;\; \frac{d_f}{d_c} < \frac{F}{C} \tag{7}$$

The above indicates that the prediction of the N_{CF} is also dependent of the defined interaction locus points. As most of the test results resided near the (0.3, 0.3) interaction locus in the linear damage rule plot, the interaction locus of (0.3, 0.3) was used for predicting the number of cycles to failure with linear damage rule later in this study. For pre-crept specimens, a corrected interaction locus was defined for the linear damage rule predictions, so that:

$$D_{c-corr} = D_c \cdot (1 - \frac{t_{exp}}{t_r}) \tag{8}$$

where t_{exp} is time at pre-creep exposure and t_r is time to rupture at equal stress and temperature. The linear damage rule was able to produce more accurate predictions with redefined interaction locus of (0.3, 0.13) for pre-crept specimens.

4.3. The Φ-model

The CF test results and results obtained from literature for alloy 263 were also assessed with recently developed Φ-model. The model predicts the expected life under tensile-compressive loading cycles with or without hold periods. The effective CF lifetime (t_{CF}) and corresponding number of cycles to failure (N_{CF}) are predicted utilizing the creep rupture properties and the ultimate tensile strength of the material. More detailed description of the Φ-model is presented in references 10 and 11. A creep reduction factor and a weld reduction factor were implemented in the Φ-model for this study in order to predict the results for pre-crept parent material, cross-weld and pre-crept cross-weld specimens. A comparison of the logarithmic

values of predicted versus measured number of cycles to failure for the test specimens and public domain data with 52 tests is shown in Figure 8. [3, 4, 5, 6, 7 and 8] Temperature range for the data set is 700-800°C, total strain range is from 0.45% to 1.20% and hold period length is from 0 to 10 hours. For tests without hold periods an effective hold period of 0.5 seconds was used for the Φ-model assessment for this study.
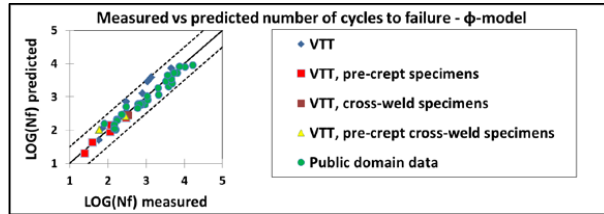
Figure 8. A comparison of the logarithmic values of predicted versus measured number of cycles to failure for the VTT test specimens and public domain data using the Φ-model. [3, 4, 5, 6, 7 and 8]

For the data assessed the Φ-model was able to predict the number of cycles to failure within a scatter factor of 2.70 with 99% confidence. The scatter factor Z [12] is defined as:

$$Z = 10^{2.5 \cdot \sqrt{\sum(LOG(N_{pred}) - LOG(N_{meas}))^2 / n-1}} \qquad (9)$$

where N_{pred} is the model prediction, N_{meas} the measured number of cycles and n the number of assessed data points.

4.4. Creep-fatigue model comparison

The Φ-model predictions were compared against the predictions of the linear damage rule for parent material tests at 750°C with the strain range from 0.6% to 1.0% and hold period length from 0.1h to 10h. The CF test parameters for these tests are shown in the legend of the figure 7. For this data set, the linear damage rule approach predicted the number of cycles to failure with the scatter factor of 4.11, whereas the Φ-model gave a closer fit to unity line with the scatter factor of 2.73, as shown in figure 8.
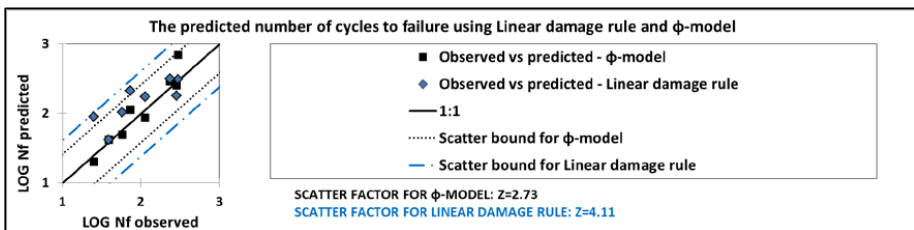
Figure 8. A comparison of the logarithmic values of predicted versus measured number of cycles to failure using the Φ-model and linear damage rule.

Furthermore, the Φ-model predictions were compared against the predictions of the Manson-Coffin model for parent material tests without hold periods at 750°C with the strain range from 0.5% to 1.0% and for parent material tests at 750°C with hold periods of 0.1-10.0h with the strain range from 0.6% to 1.0%. The pre-crept or cross-weld specimen test results were

not predicted in this comparison. The scatter factor for this data set with Φ-model was 4.85, whereas using the Manson-Coffin model the scatter factor Z reached an unsatisfactory value of 26.02, as shown in figure 9. The most inaccurate predictions produced by the Manson-Coffin model were naturally those for tests with hold periods. The cross-weld and pre-crept specimens were not included in this assessment, because the scatter factor for the Manson-Coffin model would reach even higher values than 26.02 with the cross-weld and pre-crept specimens.
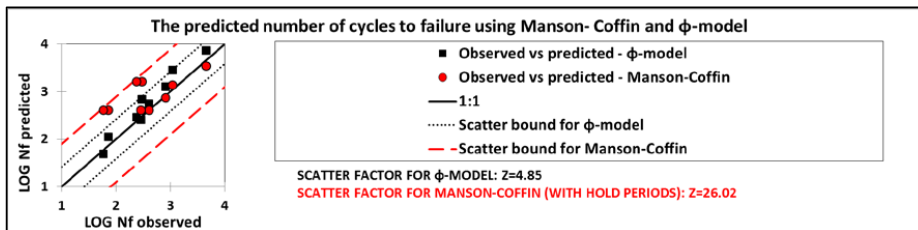
Figure 9. A comparison of the logarithmic values of predicted versus measured number of cycles to failure using the Φ-model and Manson-Coffin model.

5. Discussion

As expected, the test results indicated that a hold period at the maximum strain both in tension and compression reduces the number of cycles to failure and a pre-creep exposure of 178MPa at 750°C for 3000h additionally reduces cyclic life of the nickel-base superalloy 263 specimens. The cyclic life of the cross-weld specimens was slightly reduced compared to parent material specimens. The pre-creep exposure and hold periods had similar effect on the cyclic life of the cross-weld specimens than for parent material specimens. The stress relaxation behaviour during the hold periods was found to be slightly accelerated for the pre-crept specimens, both for the parent material and cross-weld specimens.

From modelling point of view, the linear damage rule approach was considered to be inaccurate for predicting the number of cycles to failure. Furthermore, the method was considered to be complicated because it requires peak stress and stress relaxation data (observed or modelled) for the calculation of the creep component of a single cycle (d_c), and the predictions are heavily dependent on how the total creep (D_c) and fatigue (D_f) fractions are defined.

The Manson-Coffin model as such produced considerably inaccurate predictions for CF data with and without hold periods with the scatter factor of 26.02. It might be possible to extend the Manson-Coffin model to additionally predict cyclic lives of cross-weld specimens, pre-crept specimens and tests with hold periods. Manson developed a method for predicting the tests with hold periods in the 60s [13] but further work has to be done to verify the applicability of the model for the alloy 263.

The Φ-model predicted the number of cycles to failure with scatter factor of 2.70 for the complete data set with 52 LCF and CF test results. The data set consisted of all tested specimens with or without hold periods, including the parent material, pre-crept parent material, cross-weld and pre-crept cross-weld specimens combined with the public domain

LCF and CF data. The Φ-model has been shown in earlier work to predict well the observed CF life of austenitic stainless steel 316FR and nickel alloy A230 subjected to isothermal strain controlled cycles with tensile hold periods [10, 11].

A significant advantage of the Φ-model to predict CF life is that at least for a given isothermal test type, it is not necessary to consider further details of individual CF cycles, such as features of relaxation, peak stress, softening or hardening behaviour. Furthermore, the method requires less fitting parameters than the most of the common CF assessment and modelling methods. The extrapolation in hold time may be possible in a similar way as for creep (longest time x 3), but this has still to be validated with culled data sets or by data with longer hold times. Furthermore, the Φ-model procedure allows a simple definition of CF damage $D_{CF} = N/N_{CF} = \Sigma t_h/t_{CF}$ where N is the consumed amount of cycles and Σt_h is the corresponding time in hold. For this damage parameter there is no need to separate creep and fatigue damage or life fractions. The Φ-method hence allows for more straightforward damage assessment for both design and later life assessment than the common methods using summed life (or strain) fractions. The approach may be applicable for many CF cases in power generation, where strain rates and cycling frequencies are low and even lower (more creep dominated) than in CF testing in the laboratory.

6. Conclusions

Creep-fatigue test results and selected models were evaluated and compared using the VTT CF test results and public domain data for nickel-base superalloy 263. The following conclusions were drawn from the evaluation:

(1) The cross-weld nickel-base superalloy 263 specimens exhibited decreased number of cycles to failure compared to the base material specimens.
(2) Introducing a pre-creep exposure of 178MPa at 750°C for 3000h decreased the number of cycles to failure for both parent material and cross weld specimens.
(3) Introducing a hold period of 0.1-10.0h decreased significantly the number of cycles to failure.
(4) The stress relaxation during the hold period of CF test was slightly accelerated for the pre-crept specimens.
(5) From the selected models, the Φ-model exhibited best overall performance for predicting creep-fatigue life of alloy 263. The Φ-model was able to predict the CF life for the whole data set of 52 data points, including cross-weld specimens in pre-crept and as welded condition as well as the public domain data, with a satisfactory scatter factor of 2.70. The linear damage rule and Manson-Coffin model produced more inaccurate predictions, and the assessment had to be done for culled data sets using these methods.

References

[1] Moilanen, P., *Pneumatic servo-controlled material testing device capable of operating at high temperature water and irradiation conditions*. A doctoral dissertation, VTT Publications: 532, pp. 70-130 (Espoo 2004).

[2] Pohja, R. *et al, Multifunctional High Precision Pneumatic Loading System (HIPS) for Creep Fatigue Testing*. Procedia Engineering, Vol. 55, No. 1, pp. 573-577 (2013).

[3] Zhang, S.-C *et al, Investigation on low cycle fatigue properties of superalloy GH3044 at elevated temperature*. Journal of Aeronautical Materials, ISSN 1005-5053, 02/2013, Volume 33, Issue 1, pp. 100 – 104 (2013).

[4] Kubushiro, K. *et al, Creep-fatigue properties of the candidate materials of 700°C-USC boiler*. Proceedings of CREEP8, 8th International Conference on Creep and Fatigue at Elevated Temperatures. July 22-26, San Antonio, Texas, USA (2007).

[5] Zhang, Y. and Knowles D., *Isothermal and thermomechanical fatigue of superalloy C263*. Superalloys 2000. Edited by Pollock, T., Kissinger, R., Bowman, R., Green, K., McLean, M., Olson, S. and Schirra, J. TMS (The Minerals, Metals & Materials Society) (2000).

[6] Semba, H. *et al, Creep strength and microstructure in 23Cr–45Ni–7W alloy (HR6W) and Ni-base superalloys for advanced USC boilers*. In: Proc.34th MPA-seminar, (2008).

[7] Wang, W. *et al, Influence of γ´ and grain boundary carbide on tensile fracture behaviors of Nimonic 263*. Materials Science and Engineering A, 523, pp. 242-245 (2009).

[8] Kusumoto, J. *et al, Life Prediction Method Under Creep-Fatigue Loading for Gas Turbine Combustion Transition Piece of Ni-Based Superalloy N263*. International Gas Turbine and Aeroengine Congress and Exhibition, American Society of Mechanical Engineers, ASME, (1997).

[9] Feltham, P., *Stress Relaxation in Copper and Alpha-Brasses at Low Temperatures*. Journal of the Japan Institute of Metals, Vol. 89, No. 1, pp. 210–214 (1961).

[10] Holmström, S. and Auerkari, P., *A robust model for creep-fatigue life assessment*. Materials Science & Engineering A, Vol. 559, No. 1, pp. 333-335 (2013).

[11] Holmström, S. *et al, Creep and Creep-fatigue Behaviour of 316 Stainless Steel*. Procedia Engineering, Vol. 55, No. 1, pp. 160-164 (2013).

[12] Holdsworth, S. *et al, Creep data validation and assessment procedures - ECCC Recommendations*. Vol. 5, ECCC publications, pp. 5-10 (2005).

[13] Manson, S., *A simple procedure for estimating high-temperature low cycle fatigue*. Experimenthal Mechanics, Vol. 8 (8), pp. 349-35 (1968).

COMPARISON OF ONCE THROUGH AND CLOSED LOOP APPARATUS FOR STEAM OXIDATION MEASUREMENTS AT AMBIENT AND ELEVATED PRESSURE

A T Fry, M Seraffon, J Banks, D Laing

National Physical Laboratory, Materials Division, Teddington, Middlesex, UK
(tony.fry@npl.co.uk)

Abstract

The effect of pressure on the oxidation rate and oxide scale morphology is the subject of continued research. Recent results from a closed loop high pressure system has raised concerns regarding data obtained previously from once through atmospheric steam furnaces. The results presented here show that the absolute values of mass change and oxide thickness for nominally the same test conditions (temperature and pressure) are influenced by the apparatus used. This became evident as tests at elevated pressure were conducted and the results from these tests compared to theoretical and modelled values. By comparing the extent of oxidation, in terms of mass change and oxide thickness, for Grade 92 material exposed to flowing and static ambient and elevated pressure steam, the influence of the different experimental approaches will be highlighted and these data used to reconcile experimental results from a previous intercomparison exercise conducted as part of a UK-US collaboration [1].

Keywords: Grade 92, Steam Oxidation, Recirculating, Kinetics, Once Through

1. Introduction

The corrosion rate of high temperature materials in aggressive environments is a critical parameter which governs material performance, component lifetime and process efficiency. Steam plants remain significant to the energy security of the UK whether that is via fossil, biomass or nuclear steam generation. With renewable energy coming online there is an increased requirement for flexible fossil power plants, placing structural components under more demanding thermal workloads. The exfoliation of steam grown scales is likely to be accelerated due to higher frequency of thermal transients and metal wastage rates will rise, especially as more austenitic materials are used as the requirement for higher temperatures increases [2]. With the cost of an unplanned outage in excess of £500K per day (£1-2m to repair a tube failure [2]) there is a greater requirement for accurate models of oxide growth, void formation and the effect this has on heat transfer, strain distribution and exfoliation. These in turn require more accurate simulation within the laboratory of plant conditions, to improve the comparability of laboratory scale to service grown scales [2]. Recent work has demonstrated that laboratory testing is still not replicating the morphology of plant grown scales, and that significant differences still occur in the measurement of oxidation kinetics between different laboratories [3].

Laboratory-scale tests are frequently used to generate understanding of high-temperature oxidation phenomena and to characterise and rank the performance of existing and future materials and coatings. Tests within the laboratory have the advantage of being well controlled, monitored and offer the opportunity of simplification which enables the parametric study of individual factors, such as temperature and pressure transients. Whilst it is agreed that laboratory testing provides an invaluable tool to characterise the performance of materials and to develop greater understanding of the mechanisms governing the oxidation processes,

they do have their limitations. The most obvious relates to reproducing plant conditions, since the precise conditions encountered in service are difficult if not impossible to reproduce in the laboratory and some degree of simplification is necessary, if only to reduce the cost of laboratory testing. Experimental parameters such as water chemistry, the presence of a heat-flux, and excursions in temperature, pressure, and heat-flux all influence, individually and in combination, the oxidation performance. Consequently there is a conflict between performing laboratory exposures in as inexpensive a manner as possible, and maintaining relevance to the industrial situation.

The importance of controlling laboratory procedures has been illustrated by the results of a 'round robin' exercise carried out under the auspices of the COST522 collaborative program in Europe [4]. Within this work specimens from the same batch of P92 alloy were exposed at 600 and 650 °C for a total time of 1,000 h, by nine different institutes each using their own particular procedures. The results of this inter-comparison produced a variation in the scale thickness values reported by the different laboratories, from 60 to 100 μm at 600 °C, and 40 to 240 μm at 650 °C, as shown in Figure 1.
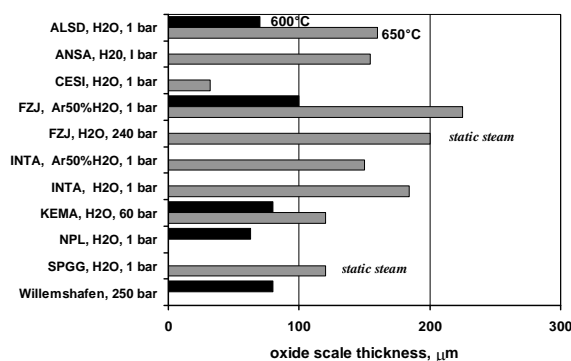
Figure 1 Intercomparison of scale thickness measurements on P92 martensitic steel after exposure to steam for 1000 h at 600 and 650 °C (after [6]).

The laboratory testing procedures used by the participants included the use of both once-through and recirculating exposure systems, and the use of water vapour in a carrier gas, usually argon, in varying concentrations, and 100% pure steam. Many of the tests were conducted at ambient pressure, with only three of the participants opting to use elevated pressure.

More recently there has been increasing amounts of activity whereby steam oxidation tests have been conducted at elevated pressures to produce more realistic operating conditions [1],[5]. Studies focused on understanding the effects of different experimental variables have been performed [3],[6] to enable such future standardisation of steam oxidation testing, but as yet no recognized standards are applied. One problem is that including more features in the laboratory exposures, such as heat flux, pressure, cycling etc. will increase the complexity of the test work, making it more expensive and difficult to control.

The influence of pressure on the oxidation of power plant materials has always been considered to be less significant than the effects of temperature and Cr content, but it still remains a subject of differing opinions. From the literature there is little consensus or clear indication as the effect pressure has on the steam oxidation of materials. For example Otoguro et al. [7] measured the maximum scale thickness on 4 austenitic alloys (SUS347HTB, 17/14CuMo, 20Cr/25Ni and 22Cr/35Ni) after exposure to steam for 500 h at 650 and 700 °C and pressures up to 35 MPa. The results showed that, by increasing the pressure at 650 °C, two of the alloys investigated exhibited a decrease in scale growth rate of approximately 20%, one of the alloys showed no influence of pressure on the scale thickness and one alloy exhibited an increase in scale thickness by a factor of 4. The same trend in results was observed at 700 °C. In a survey of plant exposed materials Montgomery and Karlsson [8] summarised data for the scale growth kinetics of martensitic steels (HCM12 and P92) to steam environments. The high pressure data for HCM12 implied a decrease in scale growth rate with increasing pressure whereas the high pressure data for P92 implied either no effect of pressure or a change in the pressure effect with temperature depending on interpretation. These data from plant exposures may also have been influenced by deviations in the operating conditions during the day to day operation. Laboratory measurements under more controlled conditions suggest that the pressure effect maybe dependant on the exposure temperature [9]. Work on 9Cr-1Mo steel over a range of pressures (2.7 – 166 bar) and temperatures (500, 550, 600 and 650 °C) for times up to 10,000 h [10], showed an effect of steam pressure for temperatures of 600 and 650 °C but not at the lower, more realistic, operating temperatures for AGRs. Metallography of the specimen revealed the development of porosity (Figure 2) in the scale at the higher temperatures which may explain the increase of the growth rate. Montgomery and Karlsson [8] also commented on the development of a porous scale suggesting that the increased porosity decreased the thermal conductivity of the scale leading to localised temperature increases and hence an increase in the oxidation rate.

Whilst the influence of pressure remains unclear from the literature, from a first principles approach, the effect of steam pressure on the rate of oxidation can be derived by considering the dependence of the diffusion process with respect to the oxygen partial pressure. Wright and Dooley [11] discuss this derivation and have tabulated the expected effect of steam pressure on the parabolic rate constant, kp, and oxide thickness, as shown in Table 1.

The purpose of the work detailed here was to investigate the pressure effect further for a selected range of materials, only Grade 92 data is considered here; as a consequence of this an interesting difference in the oxidation kinetics and scale morphology has been observed.
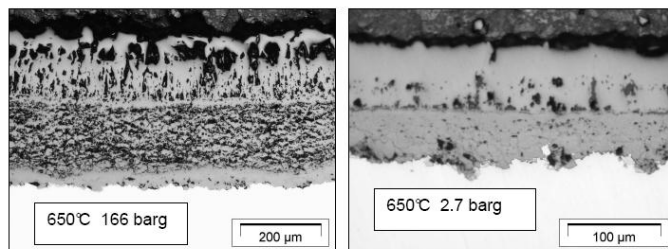
Figure 2 Scale morphology of 9Cr-1Mo samples exposed to steam at 166 and 2.7 bar at 650 °C [10].

Table 1 Expected effect of increasing steam pressure on oxidation kinetics (after [11]).

ΔP_{steam}, bar	k_p factor increase (magnetite)	Scale thickness increase (magnetite), %
1-17	1.4-1.5	17-23
1-34	1.5-1.7	22-30
34-241	1.2-1.3	12-16

2. Experimental Procedure

Steam oxidation exposures have been conducted under atmospheric pressure and at elevated pressure. For the atmospheric pressure tests, exposures were performed using a horizontal tube furnace consisting of three IN625 work tubes, into which alumina boats were placed holding the specimens. The feed water of the steam furnaces was deionised and deoxygenated by bubbling $N_{2(g)}$ through the water reservoir. Dissolved oxygen levels in the range of 5-13 and 200 ppb were recorded, depending on the purpose of the test. The liquid water was then passed into the furnace at a rate of ~3 ml min^{-1}, the water was heated and formed into steam which then flowed naturally through the furnace, exiting through a water trap on the far side of the furnace. In the case of the tests conducted with high levels of dissolved O_2, the specimens were loaded into the hot furnace tube under the flowing steam atmosphere. At the end of the exposure the specimens were carefully withdrawn under steam and allowed to cool in laboratory air. For the tests with low levels of dissolved O2 in the feed water the samples were heated under Ar, once at temperature the steam was introduced. At the end of the exposure the steam was switched off and the samples cooled under Ar. Exposures in both cases were conducted at 650 °C for times up to 3000 h.

Exposures at elevated pressure were performed using a high pressure recirculating steam loop and a static autoclave. The steam loop consists of a water treatment section which deionises and deoxygenates the feed water achieving levels of dissolved oxygen and conductivity of 2-5 ppb and ~5 μs/cm^2 respectively. The feed water was pumped into an evaporator vessel at a rate of ~10 ml min^{-1} which heats the water to produce steam at ~300 °C, this then passes through a superheater section which raises the temperature to ~450 °C. The specimens were suspended on a frame in the main pressure vessel which was heated to attain the desired exposure temperature on the specimens. The specimens were loaded into the pressure vessel which was then sealed. Once installed the rig was heated with the outlet of the pressure vessel left open. Through this orifice was fed a thermocouple which was used to set the controls of the heater bands such that the desired test temperature was achieved. Tests were performed at 650 °C at various pressures (25, 50 and 60 bar) for 1000 h. On completion of the exposure the vessel is vented and allowed to cool naturally.

In the case of the static autoclave the samples were loaded into alumina boats and placed into the autoclave with a volume of deionised but not deoxygenated water. The autoclave was heated and the steam atmosphere generated from the water in the vessel. A pressure relief valve ensured the correct pressure was maintained during the tests. Exposures were conducted at 650 °C f at 25 and 50 bar for times up to 2000 h. On completion of the exposure the samples were allowed to cool under pressure. As the vessel cools so the pressure reduces as the liquid condenses. Schematics of the atmospheric steam furnace and the high pressure loop are shown in Figure 3.
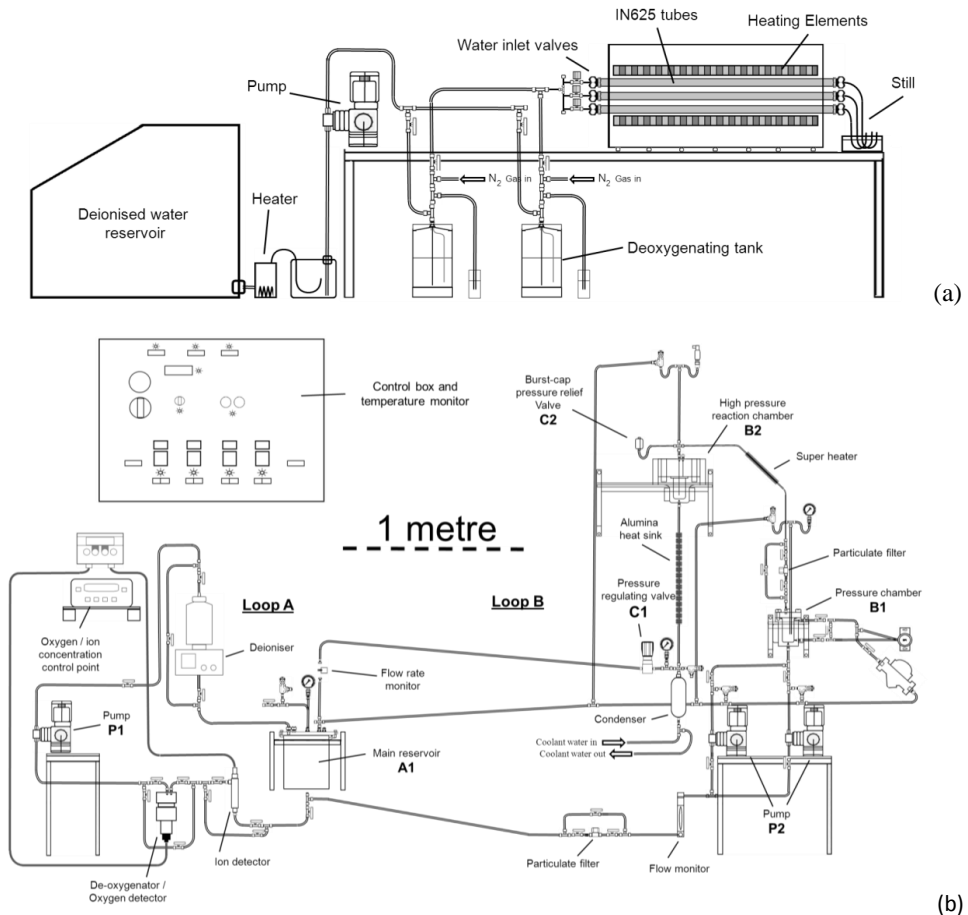
Figure 3 Schematics of the (a) atmospheric pressure rig and (b) the high pressure steam loop.

3. Results and Discussion

For clarity, only results from the tests performed on the Grade 92 material will be presented. These come from two different batches of material exposed over a number of years in a variety of NPL projects. The results from exposures at elevated pressure in the steam loop and the static autoclave are summarised in Figure 4. In the case of the static autoclave there is a progressive increase in the mass gain as a function of the exposure time and with increasing pressure. For the flowing high pressure steam loop there is an increase in the mass gain with increasing pressure, with a little overlap of data points for 50 and 60 bar. Exposures at 1 bar were also conducted in this apparatus and show lower mass gain than the higher pressure data. Oxide thickness measurements on the samples follow a consistent trend, as shown in Table 2.
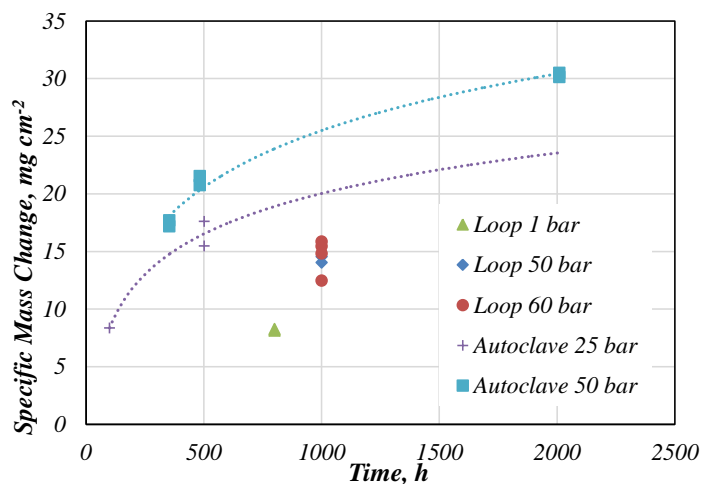
Figure 4 Specific mass change as a function of time and exposure method for P/T 92 at 650 °C.

Exposures conducted at ambient pressure in the once through flowing steam furnaces show as expected the mass change increases with exposure time up to times of 3000 h, (Figure 5). Two sets of data are presented for the tube furnaces, because the earlier data was conducted with a higher level of dissolved oxygen in the feed water, of approximately 200 ppb, whilst the later data had a lower level of dissolved oxygen of approximately 15 ppb (designated as tube furnace (low O2) in Figure 5). The data sets are self-consistent within themselves and in both cases for tube furnace data, the mass gain is significantly greater than that found in the recirculating steam loop. Comparison of the cross sectional microstructures of the samples reveal differences in the defect structure and porosity content in the scales. In the once through tube furnace samples, shown in Figure 6(a), a uniformly dispersed number of voids formed in the magnetite layer of the scale. There is generally little difference between the size and concentration of voids for the two levels of dissolved oxygen used in these exposures. The large void in Figure 6(b) is likely to be due to coalescence of voids at the magnetite/spinel interface. Figure 6(c) illustrates the cross section of the sample exposed to static steam in the autoclave, where the water was not deoxygenated. Voids are once again present, fewer in number but greater in size. From the micrograph the distribution appears less uniform, and the voids are not restricted to just the magnetite layer but are also present in the Fe-Cr spinel. Figure 6(d) presents the microstructural features of the sample exposed to 1 bar pressure within the recirculating steam loop. In this apparatus the water chemistry is controlled and maintained below 5 ppb of dissolved O_2. The micrograph shows the scale to be much thinner than in the previous exposures with voids non-uniformly distributed. These voids are much fewer in number, but those present are fairly large, relative to the oxide thickness. As the pressure increases (Figure 6(e) to (g)) the oxide scale thickens while remaining dense with a few large voids present in the scale. There is also evidence of detachment at the spinel/metal interface, this may be due to localised coalescence of pores or voids forming at the spinel/metal interface, or may simply be an artefact of the mounting and polishing. Comparing the morphology of Figure 6 with the images reported by Angell *et al.* [10] (Figure 2), similarities with the 2.7 barg micrograph are apparent with the morphology of the scales formed in the static autoclave (Figure 6(c)).

It is interesting to note that the oxide thickness values obtained from the static autoclave exposures (Table 2) are higher than the ones reported in the COST round robin (Figure 1). However, the steam loop data however agrees well with the reported data at 60 bar. The tube furnace data with high levels of dissolve O_2 whilst slightly lower, is close to the COST data.
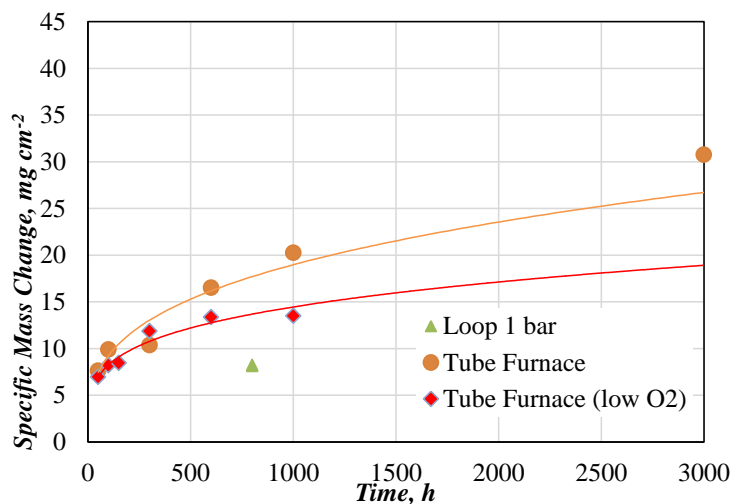
Figure 5 Specific mass change as a function of time and exposure method for P/T 92 at 650 °C exposed in the flowing steam tube furnace.

Table 2 Average values for specific mass change and total oxide thickness for P/T 92 samples exposed using different methods in static and flowing steam at ambient and elevated pressure at 650 °C.

Exposure Method	Pressure, bar	Time, h	Ave. Spec. Mass Change, mgcm^{-2}	Total oxide thickness, um
Flowing Steam Loop	1	800	8.2	60
	50	1000	14.29	88
	60	1000	15.64	117
Static Autoclave	25	100	8.36	58
		500	16.54	69
	50	100	-	78
		353	17.43	136
		483	21.14	159
		1000	-	201
		2000	30.31	239
Tube Furnace (low O_2 in brackets)	1	50	7.62 (6.96)	62
		100	9.91 (8.21)	129
		300	10.38 (11.88)	100
		1000	20.24 (13.49)	134
		3000	30.76	232

Reports in the literature [5] have commented that porosity may be responsible for the increase in the oxidation rate at higher pressure, however the results presented here in Figure 6 do not support this hypothesis, at least for pressures up to 60 bar and exposure times up to 1000 h.

Viewed in isolation the results of the elevated pressure exposures support the theoretical calculations that increasing pressure causes an increase in the oxidation rate, at least for the alloys exposed in this test programme. This has been also predicted by neural network modelling [12]. An unexpected observation from this work is the influence the exposure rigs have on the oxidation rate. In comparing the ambient and 1 bar data from the once through and recirculating steam loop a clear difference in the mass change and oxide thickness is observed between the two apparatus. For tests conducted with dissolved O_2 levels of ~200 ppb there is two fold decrease in the mass change compared with that of the recirculating loop using dissolved O_2 levels of ~5 ppb. Improved control of the dissolved O_2 levels in the tube furnaces shows a decrease in mass gain of 25% (Figure 5). Previous investigations into the effect of water chemistry on the oxidation rate did not show such a marked effect for Grade 92 material, suggesting that the control offered by closed loop systems is highly advantageous. These recent results can be used to explain the results of the COST round robin and an intercomparison exercise conducted in 2009 [3], [13]. Within this small intercomparison three laboratories exposed grade 92 material to flowing steam in tube furnaces, where two were at ambient pressure (labs A and B) whilst the third was at 17 bar (lab C) (Figure 7). In this intercomparison NPL was lab B and was using water with dissolved O_2 levels of 10-15 ppb. Taking into account the 25% drop in mass gain, with better control of O_2 this would essentially drop the lab B curve onto that of lab C. The water chemistry of lab C is not known. Modelling work not reported here supports these findings [12]
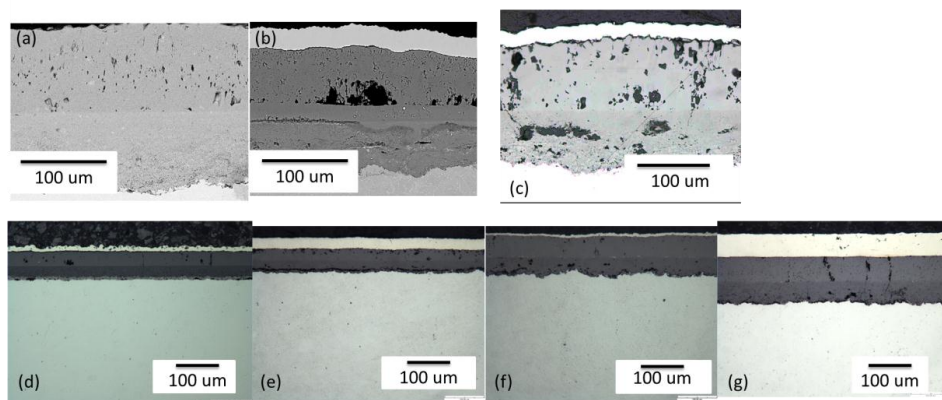
Figure 6 Micrographs of P/T92 exposed for 1000 h, 650°C to (a) flowing steam (once through tube furnace), (b) flowing steam (once through tube furnace (low O_2)), (c) static steam at 50 bar, (d) flowing steam a 1 bar (recirculating steam loop), (e) flowing steam at 25 bar (steam loop), (f) flowing steam at 50 bar (steam loop) and (g) flowing steam at 60 bar(steam loop).

The results presented here would support the hypothesis that differences seen in the oxidation data from the three apparatus is caused by differences in the control of water chemistry of the feed water used, and the added control of closed loop systems in preventing the O_2 leaching into the test environment. There is an additional concern that pre-oxidation of the specimen may be influencing the oxidation rates. In its current configuration this will certainly occur in the recirculating steam loop in the initial 5 to 6 hours of the exposure. This hypothesis is currently being investigated using pre-oxidised samples in the once through tube furnace.
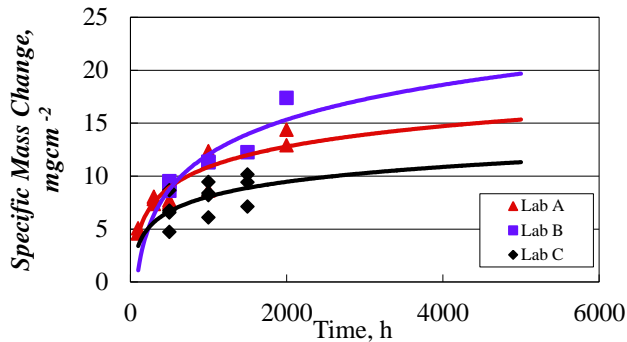
Figure 7 Intercomparison of specific mass change measurements on T92 martensitic steel after exposure to steam for up to 2000 h at 600 °C (after Ref [13])

4. Conclusions

The oxidation rate, in terms of specific mass change and oxide thickness, has been compared for steam oxidation exposures conducted on Grade 92 material using different exposure methods at a temperature of 650 °C for a range of pressures. Exposures conducted in the recirculation steam loop at 25, 50 and 60 bar pressure show increasing rates of oxidation for both mass change and oxide thickness measurements, as do tests conducted in a static autoclave at 25 and 50 bar pressure. The magnitude of the mass gain and oxide thickness are different to those exposed in the static autoclave. These measurements at elevated pressure have been compared to atmospheric tests conducted in a once through tube furnace and tests conducted at 1 bar in the recirculating steam loop. The results from the tube furnace were found to be higher, in terms of mass gain and oxide thickness, than in the recirculating loop data. The 1 bar data from the loop fitted the trend for the higher pressure data from the same apparatus agreeing with the theoretical predictions and neural network predictions [12] (not reported here). Whilst these differences do not greatly influence the oxidation kinetics they do have implications for life time predictions, heat transfer and spallation modelling with the tube furnace data producing over conservative values.

It is believed that the different water chemistries present in the different rigs is the root cause for these differences, and that once this is taken in to account, differences in data from a previous intercomparison exercise can be reconciled and better agreement between laboratories proposed. Further work is needed to support this hypothesis through measurement of the oxygen content in the steam more locally to the test samples and/or on exit from the system.

5. Acknowledgements

6. References

[1] A. T. Fry, I. G. Wright, N. J. Simms, B. McGhee and G. R. Holcomb, "Steam oxidation of fossil power plant materials: collaborative research to enable advanced steam power cycles," *Materials at High Temperatures,* vol. 30, no. 4, pp. 261-270, (2013).

[2] A. T. Fry, I. G. Wright and J. Shingledecker, "2nd EPRI-NPL Workshop on scale exfoliation from steam-touched surfaces," NPL, Teddington, (2012).

[3] A. T. Fry and E. M. Piedra, "Review of factors affecting steam oxidation testing," *Materials At High Temperatures,* vol. 28, no. 4, pp. 290-296, (2011).

[4] S. J. Osgerby and W. J. Quadakkers, "The influence of laboratory test procedure on scale growth kinetics and microstructure during steam oxidation testing," *Materials at High Temperatures,* vol. 22, pp. 27-33, (2005).

[5] J. P. Shingledecker, A. T. Fry and I. G. Wright, "Managing Steam-Side Oxidation and Exfoliation in USC Boiler Tubes," *Advanced Materials and Processes,* vol. 171, no. 1, (2013).

[6] P. J. Ennis and W. J. Quadakkers, "The steam oxidation resistance of 9-12% chromium steel," in *Materials for Advanced Power Engineering 2002*, (2002).

[7] Y. Otoguro, M. Sakakibara, T. Saito, H. Ito and Y. Inoue, "Oxidation Behavior of Austenitic Heat-resisting Steels in a High Temperature and High Pressure Steam Environment," *Transactions of the Iron and Steel Institute of Japan ,* vol. 28, no. 9, pp. 761-768, (1998).

[8] M. Montgomery and A. Karlsson, "Survey of oxidation in steamside conditions," *VGB Kraftwerkstechnik,* vol. 75, pp. 235-240, (1995).

[9] Y. Watanabe, Y. S. Yi, T. Kondo, K. Inui, T. Kishinami, H. Kimura and M. Sato, "Oxidation rate of advanced heat-resistant steels for ultra-supercritical boilers in pressurised steam," *Journal of Pressure Vessel Technology,* vol. 123, pp. 391-397, (2001).

[10] M. G. Angell, S. K. Lister and A. Rudge, "The effect of steam pressure on the oxidation behaviour of annealed 9Cr1Mo bolier tubing materials," in *Properties of water and steam ,* Dusseldorf, (2008).

[11] I. G. Wright and R. B. Dooley, "A review of the oxidation behaviour of structural alloys in steam," *International Materials Review,* vol. 55, pp. 129-167, (2010).

[12] A. T. Fry, M. Seraffon and J. Banks, "High pressure steam oxidation: Extents and influences," in *Advances in Materials Technology for Fossil Power Plants*, Waikoloa, Hawaii, (2013).

[13] A. T. Fry, "Standardisation in High Temperature Corrosion Testing," in *23rd Annual Conference on Fossil Energy Materials*, Pittsburgh, (2009).

INFLUENCE OF AMMONIUM SULPHATE ADDITIVE ON SUPERHEATER CORROSION AT INCREASED STEAM TEMPERATURE DURING COMBUSTION OF RECYCLED WOOD

A. Talus[1,*], R. Norling[1], P. Henderson[2]

[1] Swerea KIMAB, Isafjordsgatan 28A, SE-164 40 Kista, Sweden
[2] Vattenfall Research and Development AB, SE-169 92 Stockholm, Sweden
[*] Corresponding author, annika.talus@swerea.se

Abstract

One way to meet the target of reduced CO_2 emissions from fossil fuels in order to prevent global warming is to increase the use of biomass and recycled wood as fuels in energy production. The major drawback with these fuels, however, is that they contain corrosive compounds. Lower steam temperatures, compared to coal-firing, are required particularly for recycled wood because of increased corrosion problems with the superheaters and this limits the electrical efficiency. A major target for several research programmes in Sweden is to reach a steam temperature of 600 °C, when using 100% biofuel. A possible way to decrease the corrosion problems is to use additives or co-fire with fuels rich in sulphur. In this work the effect of ammonium sulphate as an additive is studied, when firing 100% recycled wood at simulated steam temperature of up to 610 °C, corresponding to a metal temperature of 640 °C. Ring specimens of stainless steel (304L) have been exposed on a probe with controlled cooling in a commercial bubbling fluidised bed (BFB) boiler of 63 MW thermal capacity for combined heat and power (CHP). Exposures were made for 3 hours with ring temperatures of 560, 600, and 640 °C. The experiments were performed with two different injection rates of ammonium sulphate, as well as without. A proprietary in-situ Alkali Chloride Monitor (IACM) was utilized to study the effect on flue gas composition during the exposures. The measurements showed a decreased KCl content in the flue gas with increased injection rate of ammonium sulphate. Deposit analysis using Scanning Electron Microscopy with Energy-Dispersive Spectroscopy (SEM-EDS) showed that the chloride content in the deposits decreased to very low levels when using ammonium sulphate addition, independently of injection rate. The initial corrosion attack has been studied by investigating cross-sections of the ring samples with SEM-EDS showing a major decrease in oxide growth and grain boundary corrosion attack when using ammonium sulphate addition. This is mainly attributed to the conversion of corrosive potassium chloride to less corrosive potassium sulphate. Concluding remarks from the study are that by using a sulphate addition in combination with stainless steel superheater tubes a substantial increase in steam temperatures could be achievable when firing 100% recycled wood.

Keywords: initial corrosion, alkali chloride, high steam temperature, deposit analysis, sulphate addition

1. Introduction

As the needs to slow down global warming are growing, so also does the challenge to find suitable alternatives for fossil fuels. Biomass and recycled wood are fuels that are increasing in the energy production industry. However, compared with fossil fuels, these fuel sources are much more corrosive. This drawback leads to the need for limiting the steam temperature to control the corrosion and thus limits the electrical efficiency of the plant. Typical steam temperatures for boilers fired with biomass or recycled wood are in the range 470-530°C, whereas 600°C is a common steam temperature for coal-fired plant. Therefore steam temperatures in biomass-fired plant need to be increased in order to achieve comparable energy efficiency as when using coal as fuel. A major target for several research programmes in Sweden is to reach a steam temperature of 600 °C, when using 100% biofuel. A major difficulty with biofuels, and particularly with recycled wood, is that corrosion problems are increasingly severe for the materials used in the superheaters. One way to decrease these corrosion problems is to use additives or co-fire with fuels rich in sulphur.

The use of ammonium sulphate as an additive has previously been shown to decrease the amount of alkali chlorides in the flue gas as well as the resulting corrosion on superheater materials operating with steam temperatures up to 570 °C in wood and waste wood mixtures [1-6]. The basic underlying mechanism can be described by the following reactions (1) - (2) where ammonium sulphate in aqueous solution is added to the flue gas and decomposes into ammonia, SO_3 and water. In the next step, water and SO_3 react with the potassium chloride in the gas phase forming potassium sulphate and hydrochloric acid [7]. Laboratory studies have shown that potassium sulphate is not as harmful for stainless steels in oxidising environments as potassium chloride [8]. Thus the corrosion is expected to decrease when K_2SO_4 deposits are present at the metal surface.

$(NH_4)_2SO_4(aq) \rightarrow 2\ NH_3(g) + SO_3(g) + H_2O(g)$ (1)

$2\ KCl(g) + SO_3(g) + H_2O(g) \rightarrow\ K_2SO_4(s) + 2\ HCl(g)$ (2)
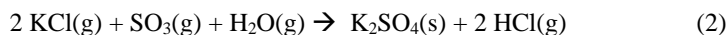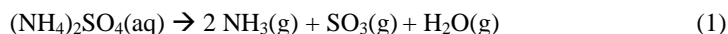
The use of many sulphate-containing compounds, including ammonium sulphate, for the reduction of corrosion in biomass-fired boilers has been patented by Vattenfall AB and the technology is described in more detail elsewhere [9, 10].

Most studies have been performed at metal temperatures up to 600 °C corresponding to a steam temperature of approximately 570 °C. By increasing the temperature at which the superheaters can perform well it is possible to increase the steam temperature in the boilers which leads to higher electrical efficiency. The present study is evaluating the effect of ammonium sulphate addition when firing 100% recycled wood at metal temperatures up to 640 °C corresponding to steam temperatures up to about 610 °C where the effect of sulphur additives is little known. Within each firing case in the study the only varying parameter is the

metal temperature, while the boiler environment is unchanged. As a result, the difference in corrosion behaviour is primarily caused by changes in reaction rate and deposit composition when adding ammonium sulphate.

2. Experimental

The exposures were performed in a commercial bubbling fluidised bed (BFB) boiler of 63 MW thermal capacity for combined heat and power (CHP). The boiler was fired using 100% recycled wood. Ammonium sulphate was injected at the exit of the furnace, directly before the empty pass of the boiler where the flue gas temperature is about 825 °C, at low (ASL) and high (ASH) rates. The amount of added sulphate is doubled in the ASH case. In addition, exposure without injection was performed as a reference (REF). During exposure the flue gas composition was monitored using a proprietary in-situ Alkali Chloride Monitor (IACM) which measures the sum of gaseous NaCl and KCl, giving instantaneous feedback regarding sulphation of the flue gas [11], as described by equation (2).

Ring specimens of stainless steel 304L (18Cr-8Ni, wt%) were exposed during three hours in the boiler in the different environments and the samples were in each exposure controlled to metal temperatures of 560, 600 and 640 °C (corresponding to steam temperatures of about 530, 570 and 610 °C, respectively) by the use of an internally cooled probe. Each ring was weighed before exposure and shortly after to obtain information on deposit growth rates. The probe with steel samples and the IACM were located after the empty pass directly before the first superheater where the flue gas temperature is about 725 °C.

After exposure, the ring specimens were analysed in order to study deposit chemistry and initial corrosion using Scanning Electron Microscopy with Energy-Dispersive Spectroscopy (SEM-EDS) and X-ray diffraction (XRD).

3. Results and discussion

3.1. Flue gas analysis

In Figure 1 the alkali chloride content in the flue gas measured using the IACM-technique is presented. The concentrations of alkali chlorides are decreased when injecting ammonium sulphate and the decrease is slightly improved at the higher injection rate.

3.2. Deposit analysis

The visual appearance of the investigated samples (Figure 2) shows cracks in the deposit for the samples exposed at 560 °C while the deposits for the higher temperatures appear intact. The weight increases of the exposed ring specimens show that addition of ammonium sulphate decreases the weight gain compared to the reference cases for all temperatures

(Figure 3a). By doubling the injection rate from ASL to ASH no further improvement is observed regarding the deposit growth rate.

Three areas (2 x 2.5 mm) at the surfaces were analysed using SEM-EDS for each sample. It was observed that the Cl content in the deposits on the reference samples decreased somewhat at the highest temperature (Figure 3b). This is probably a result of the metal temperature approaching the dew point of KCl leading to less deposition on the surface since also the amount of K is decreasing. Further, the analyses showed that ammonium sulphate addition is highly effective in decreasing the Cl content in the deposits at all tested temperatures independently of injection rate. This finding suggests a significant decrease in both initial and long term corrosion attack. Furthermore, this effect is expected to be enhanced by the distinct decrease in deposit growth rate, which further limits the amount of corrosive species present at the sample surfaces.

In the work by Viklund [12] the influence of KCl content in the gas phase on deposit chemistry was studied for the interval 5-35 ppm and metal temperatures of 500-600 °C. It was shown that for most conditions using ammonium sulphate additive to achieve a specific KCl content in the flue gas, lower Cl contents were detected in the deposits compared to when the same KCl content was achieved in the flue gas by lowering the KCl content in the fuel or by using a phosphate based additive. This was explained by a heterogeneous sulphation reaction
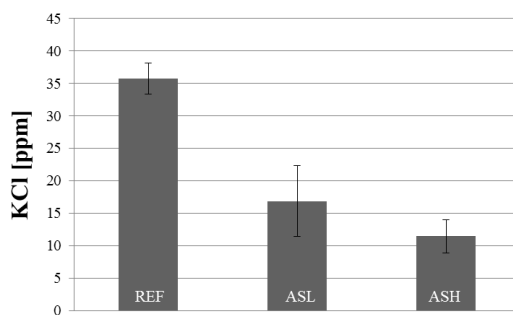
Figure 1. The alkali chloride content in the flue gas during exposure. The indicated standard deviations describe the fluctuation of alkali chloride, as recorded, during the exposure.

Figure 2. The windward side of the REF samples showing the deposit for all temperatures.

701

occurring in the solid deposit in addition to the homogeneous sulphation reaction occurring in the gas phase when adding ammonium sulphate. It is most probable that such a heterogeneous sulphation reaction is an important factor behind the very low Cl contents in the deposits at the two lower metal temperatures in this study. The reaction is believed to be analogous to reaction (2) except that it relates to solid KCl. At the highest temperature there could be an additional influence of getting close to the KCl dew point. The K and S contents being almost unchanged compared to the lower metal temperatures suggest that this effect is minor.
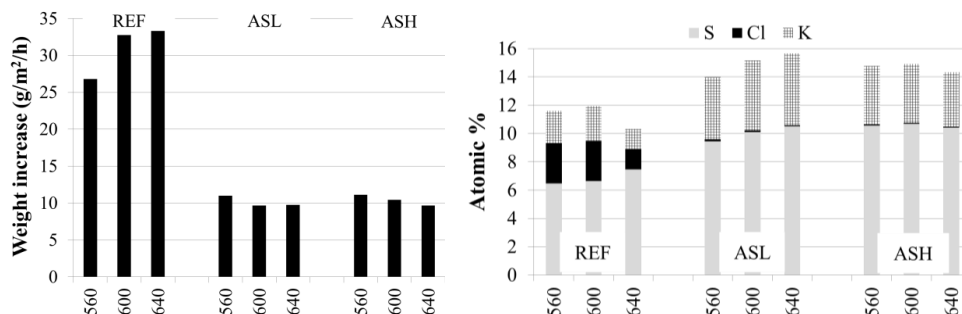
Figure 3. (a) left, deposit growth rate and (b) right, S, Cl and K levels in the deposits for the three injection rates (zero, low and high) after exposure at 560, 600 and 640 °C.

3.3. Initial corrosion of ring samples

Cross sections of the windward position (Figure 4) of samples exposed at 560 °C and 640 °C without (REF) and with ammonium sulphate injection (ASL) show that the deposits for the reference specimens are the thickest, which is well in accordance with the measured weight gains. However, spalling of the deposit and oxide in some places is seen at 560 °C, but not at 640 °C, indicating differences in oxide adhesion. For all reference samples, internal corrosion is observed in grain boundaries and also traces of alkali and metal chlorides in the deposit. The presence of internal corrosion is increasing with temperature indicating a significant diffusion dependency. No internal corrosion, alkali chlorides or metal chlorides are observed for the specimens exposed with ammonium sulphate injection and similar behaviour was observed for both ASL and ASH. The specimens exposed in 600 °C showed results corresponding to an intermediate state between those of 560 °C and 640 °C for all environments.

Further away from the windward position at the reference samples the deposit was still adherent for all temperatures. By comparing the deposits at these positions (Figure 5), the appearances of the deposit are observed to differ for 560 °C and 640 °C. At 560 °C, alkali chlorides are found in the deposit and close to the metal interface while for 640 °C mainly oxide islands and internal corrosion are observed but no alkali chlorides. These differences are probably the reason to the difference in adhesion and spalling behaviour.

By studying the metal interface at higher magnification for REF at 640 °C (Figure 6) it can be seen that the oxide islands present for the reference case consist of two different oxides, one enriched in chromium and one enriched in iron. In connection to these oxide islands the substrate below is depleted in chromium and iron resulting in an enrichment of nickel. This type of enrichment does not exist in the bulk metal. Visually it appears to be located close to a grain boundary. Thus, it is suggested to be a result of initial corrosion causing depletion of Cr and Fe by rapid diffusion through the grain boundary to the metal surface driven by the corrosion process.

Similar behaviour was observed by Karlsson et al. [13] at 600 °C during co-combustion of waste with and without the addition of a substantial amount of digested sewage sludge being rich in sulphur. The corrosion attack was attributed to chromate formation due to reaction with alkali chlorides. The chromate was concluded to subsequently decompose into relatively pure, but non-protective, chromium oxide nodules leading to further corrosion problems like internal oxidation. A similar mechanism may be active here for the reference case at the highest temperature, but is not clearly evident because the chromium oxide nodule is not as pure.
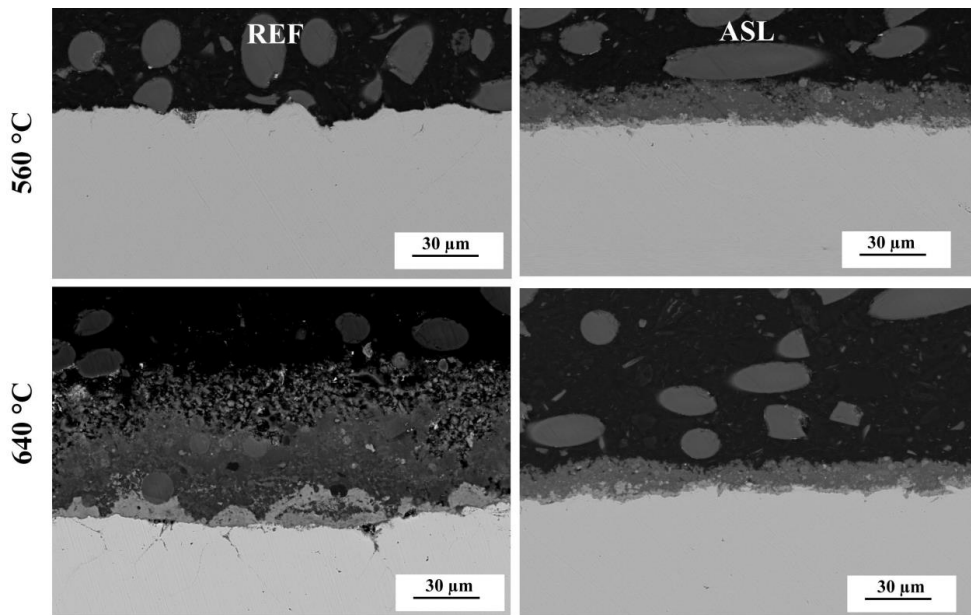
Figure 4. Cross sections of REF and ASL samples after exposure at metal temperatures of 560 °C (upper row) and 640 °C (lower row). Spalling has occurred in this area of 560°C REF, but the uneven alloy surface caused by corrosion attack can be clearly seen.
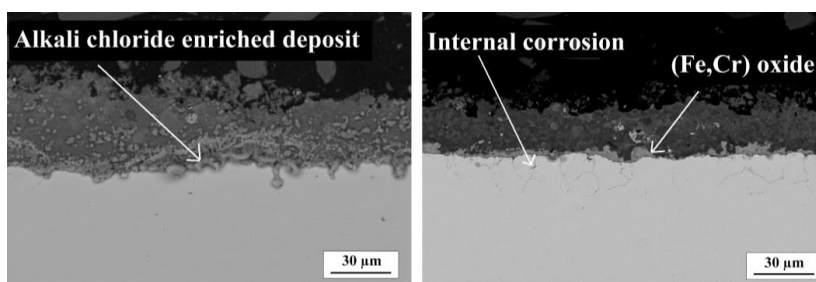
Figure 5. Cross sections of REF samples after exposure at 560 °C (left) and 640 °C (right).
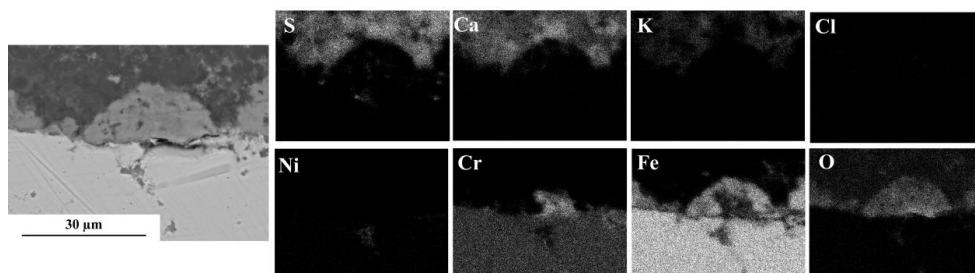
Figure 6. SEM images and EDS-maps of REF sample after exposure at 640 °C.

For the ASL sample (Figure 7), no oxide island like the ones for the REF-samples are observed, but a thin chromium rich oxide is seen close to the metal surface at some places. Although not continuous along the surface, which could be due to the short exposure time, this chromium rich oxide is suggested to be protective.
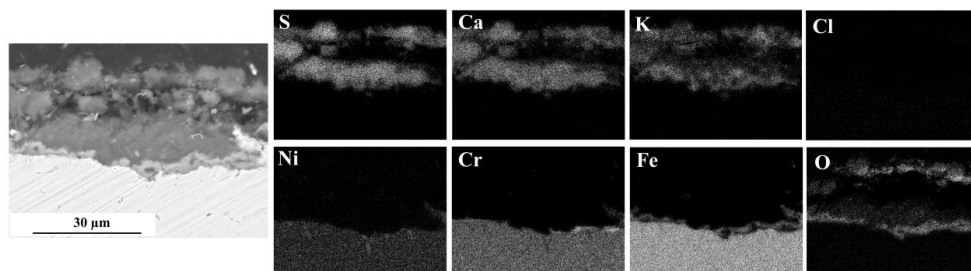
Figure 7. SEM images and EDS-maps of ASL sample after exposure at 640 °C.

For the reference samples where spalling of the deposit and oxide occurred, the areas of enrichment of nickel were more distinct and were analysed in more detail, (Figure 8). Some amounts of Cl, Ca, and S are also present in the corrosion pits which probably originate from the deposit. From elemental mapping (Figure 9) oxygen is shown not to be directly connected to nickel. The oxygen affinity for nickel is relatively low and the oxygen present in these areas is most likely present as an (Fe,Cr) oxide and nickel is present in its metallic form.

However, some amount of sulphur is detected in the pit which indicates that parts of the nickel also could be present as nickel sulphide.

	O	Si	S	Cl	Ca	Cr	Fe	Ni
Position 1	29.3	3.6	2.9	4.7	1.2	2.8	27.1	28.4

20 μm
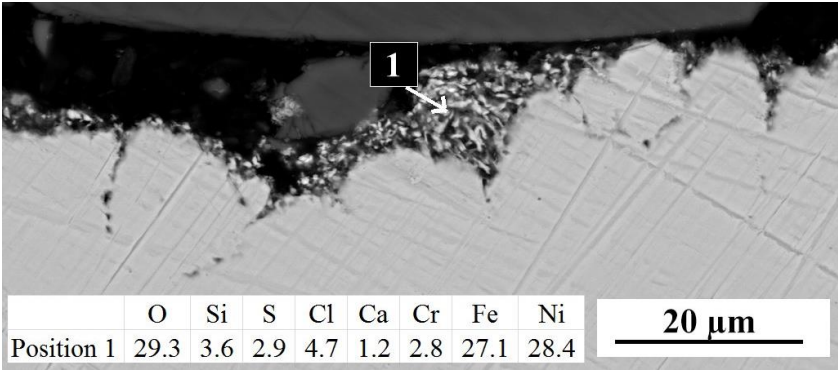
Figure 8. Typical corrosion pit in the reference sample exposed at 600 °C.
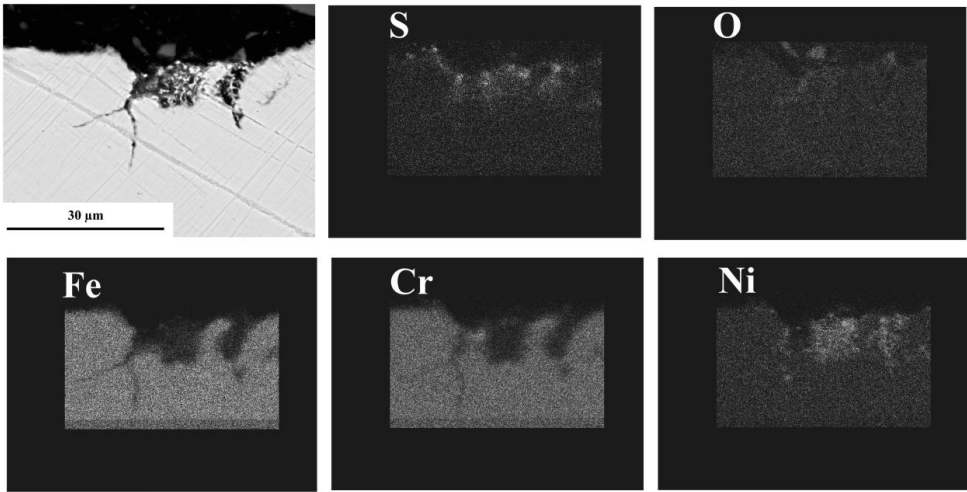
Figure 9. Elemental mapping of corrosion pit in reference sample at metal temperature 600 °C showing nickel enrichment in the corrosion attacks.

Analysis by XRD of REF and ASL samples exposed at 560 °C and 640 °C showed that KCl was present in the deposit for the REF samples, but was not detected for the ASL samples. A higher amount of Ca_2SO_4 was observed for the REF samples than for ASL; instead the amount of $K_2Ca_2(SO_4)_3$ was higher in ASL. Pure K_2SO_4 was not found in the deposits. These results verify the results obtained from the SEM-EDS measurements with a decrease of chlorides and a relative increase of potassium in the deposits for the ASL/ASH samples. This further argues for a positive effect of injecting ammonium sulphate even at higher metal temperatures.

4. Final remarks and conclusions

The beneficial effect of using ammonium sulphate additive at high temperatures, in this case a metal temperature of 640 °C, in order to decrease the risk for corrosion of superheater tubes has been shown through analysis of the alkali chloride content of the flue gas in the boiler, chemical and crystallographic analyses of deposits on exposed metal specimens as well as metallographic examination of the specimens. The most important finding in the study is that internal corrosion attack occurs after only a short time of exposure for the reference case at 640 °C and that it is prevented or delayed when ammonium sulphate is added. This further strengthens the viewpoint that a decrease in corrosion can be expected when using ammonium sulphate addition at these temperatures, at least from a perspective of initial corrosion. The decrease in initial corrosion is mainly considered to be a result of that less potassium chloride reaches the oxide-metal interface due to a successful sulphation reaction. It is believed that heterogeneous sulphation of the solid deposits is an important factor to achieve the very low Cl contents recorded. The influence of dew point of potassium chloride has been discussed, but is believed to be a significant factor only for the reference case.

The results from this commercial-scale boiler exposure indicate that the steam temperature target of 600 °C may be achievable for firing with 100% recycled wood by the use of an ammonium sulphate additive, but this needs further verification using long term exposure tests in order to exclude other influencing corrosion mechanisms controlled by other factors than alkali chlorides.

From the study the following conclusions are drawn:
- With injection of ammonium sulphate additive initial corrosion of stainless steel 304L is significantly lowered at a metal temperature of 640 °C.
- Internal corrosion is prevented for 304L during short term exposure when using ammonium sulphate as an additive.
- Alkali chloride content in the flue gas is decreased by the use of ammonium sulphate.
- Chlorine content in the deposit decreases significantly when using ammonium sulphate addition at metal temperatures in the vicinity of 560-640 °C.
- By using sulphate addition in combination with stainless steel superheater tubes a substantial increase in steam temperatures appears achievable when firing 100% recycled wood.

6. Acknowledgement

7. References

[1]   H. Kassman, J. Pettersson, B.-M. Steenari, and L.-E. Åmand, Two strategies to reduce gaseous KCl and chlorine in deposits during biomass combustion — injection of ammonium sulphate and co-combustion with peat, *Fuel Processing Technology*, vol. 105, pp. 170-180, (2013).

[2]   P. Viklund, R. Petterson, A. Hjörnhede, P. Henderson, and P. Sjövall, Effect of sulphur containing additive on initial corrosion of superheater tubes in waste fired boiler, *Corrosion Engineering, Science and Technology*, vol. 44, pp. 234-240, (2009).

[3]   H. Kassman, L. Bäfver, and L.-E. Åmand, The importance of SO_2 and SO_3 for sulphation of gaseous KCl – An experimental investigation in a biomass fired CFB boiler, *Combustion and Flame*, vol. 157, pp. 1649-1657, (2010).

[4]   M. Broström, H. Kassman, A. Helgesson, M. Berg, C. Andersson, R. Backman, et al., Sulfation of corrosive alkali chlorides by ammonium sulfate in a biomass fired CFB boiler, *Fuel Processing Technology*, vol. 88, pp. 1171-1177, (2007).

[5]   H. Kassman, M. Broström, M. Berg, and L.-E. Åmand, Measures to reduce chlorine in deposits: Application in a large-scale circulating fluidised bed boiler firing biomass, *Fuel*, vol. 90, pp. 1325-1334, (2011).

[6]   P. Henderson, P. Szakalos, R. Pettersson, C. Andersson and J. Högberg., Reducing superheater corrosion in wood-fired boilers, *Materials and Corrosion*, vol. 57 , pp. 128-134, (2006)

[7]   M. Almark, E. Edvardsson, and M. Berg, Reduction of alkali chlorides in flue gas and chlorine in deposits by phosphate addition, Proceedings of the *Impacts of fuel quality on power production and the environment*, Finland, (2012).

[8]   J. Pettersson, J-E. Svensson and L.-G. Johansson, Alkali induced corrosion of 304-type austenitic stainless steel at 600 °C; comparision between KCl, K_2CO_3 and K_2SO_4, *Materials Science Forum*, vol.595-598, pp.367-375, (2008)

[9]   *http://chlorout.vattenfall.com*, ChlorOut AB website, (2014-04-10).

[10]   C. Andersson, A method for operating a heat-producing plant for burning chlorine-containing fuels, *European patent EP1354167*, (2002).

[11]   C. Andersson, A method and a device for measuring, by photo-spectrometry, the concentration of harmful gases in the fumes through a heat-producing plant, *European patent EP 1221036*, (2002).

[12]   P.Viklund, *Super heater corrosion in biomass and waste fired boilers; Characterisation, causes and prevention of chlorine-induced corrosion*, Doctoral Thesis in Corrosion Science, pp.48 and paper V, Stockholm, Sweden, (2013).

[13]   S. Karlsson, J. Pettersson, L.E. Åmand., Reducing high temperature corrosion when burning waste by adding digested sewage slude, Proceedings of *The Swedish-Finnish Flame Days*, Sweden, (2011).

BOILER MATERIAL OPTIMISATION WITH CORROSION PROBE MEASUREMENTS

Satu Tuurna[1], Sanni Yli-Olli[1], Pekka Pohjanne[1], Jukka Meskanen[2], Jari Heikkilä[3]

[1]VTT Technical Research Centre of Finland, Espoo Finland, firstname.surname@vtt.fi
[2] Fortum Oyj, Espoo Finland
[3] Adven Oy, Kauttua Finland

Abstract

Combustion of different biofuels and waste generates highly corrosive gases and heavy metals chlorides as well as ashes containing alkaline chlorides and sulphates. Using such fuels in power and CHP boilers can pose a challenge for materials performance, and the pressure to maintain high efficiency increases the challenge further. Heat exchanger tubes may experience substantial thinning leading to premature failure as a result of fireside corrosion during the operation. Such failures cause unpredicted overhauls and availability losses. The change of material grade in the most critical components is one option to extend the lifetime of components. This paper summarises the results of exposure tests carried out in a CFB boiler using various wood, paper and plastic-based recycled trade and industry fuels suitable for energy use together with peat. The aim of the study was to find an alternative tube material for superheaters, in a location where the current type 347 austenitic stainless steel tube has experienced fireside corrosion up to 2 mm/a. The exposure test was carried out with an air cooled probe exposed in the boiler for a time up to 1400 hours with a nominal material temperature of 550 °C. Materials selected for the study were austenitic stainless steels types TP347H (UNS 34709), HR3C (TP310HCbN) and Sanicro 28 (UNS N08028). Following exposure, a section was taken from each specimen and examined using light microscopy and scanning electron microscopy. The results showed chlorine and sulphur species penetrating through grain boundaries into alloy structures. The higher alloying provides better corrosion performance, however all alloys suffered from corrosion attack.

Keywords: Corrosion monitoring, austenitic superheater steel

1. Introduction

Corrosion of metals exposed to high temperature gaseous environments in the presence of deposits has long been a challenge in boilers, furnaces and industrial process plants. The needed repair actions due to corrosion failures are highly expensive. Superheaters in waste to energy (WtE) plants normally operate at steam temperatures between 350 and 500°C, and the maximum achievable operation temperature and pressure are usually limited by the deposit induced corrosion. WtE plants are usually facing more serious corrosion problems than coal fired boilers. The higher corrosion rate is related to significantly higher chlorine and water vapour concentrations, lower sulphur concentration and increased amounts of alkali compounds [1-4]. Many material options used in conventional power plants have failed in the waste to energy plants, even with the decreased steam temperatures and pressures component failures occur. Alloy modification, the use of higher alloyed materials, is one way to mitigate corrosion and improve the energy generating efficiency.

Corrosion probes either with an air or water cooling system are used for monitoring corrosion in boilers. Probe testing enables long term material testing in real boiler conditions. Probes provide valuable information on the nature of the corrosion attack and forming corrosion products, and the behaviour of alloys in real boiler conditions [5-7]. The benefits of corrosion probe compared to coupon samples or clamps anchored on component surfaces are an accurate temperature control of probe and a shorter testing time; the probe can be removed when sufficient exposure time is reached without a maintenance shutdown. In this study, a corrosion probe without on-line properties was used to compare corrosion behaviour of alternative superheater materials in the operation conditions.

2. Experimental

The measurement campaign was carried out at Kauttua plant with three different materials TP347H (UNS 34709), HR3C (TP310HCbN) and Sanicro 28 (UNS N08028), Table 1. The plant is a pyroflow boiler with a nominal steam power of 60 MW. The steam mass flow is 24 kg/s at 80 bar pressure and 480°C temperature. The cross-section of the boiler and the sample probe location are shown in Figure 1. The probe was located in the superheater area where unexpected service failures typically occur. The plants overhaul records indicate several service failures annually in the superheater tubes due to corrosion. The average time for service overhaul in tube replacements has been 5 to 6 days. The current superheater tube material is a type 347 austenitic stainless steel.

Table 1: *Nominal composition of exposed materials*

	C	Si	Mn	Cr	Ni	Mo	Cu	Nb
TP347H	0.04-0.1	≤1.0	≤2.0	17.0-19.0	9.0-13.0			8*C~1.0
HR3C	0.04-0.1	≤1.0	≤2.0	24.0-26.0	19.0-22.0	---	---	0.2 - 0.6
Sanicro 28	≤0.02	≤0.6	≤2.0	27	31	3.5	1.0	

Typical fuel mixture is the recycled and waste wood from construction sites, forest residues and recovered fuel (REF) mainly from the packing industry. Table 2 shows the fuel mixture of the boiler during the measurement campaign.
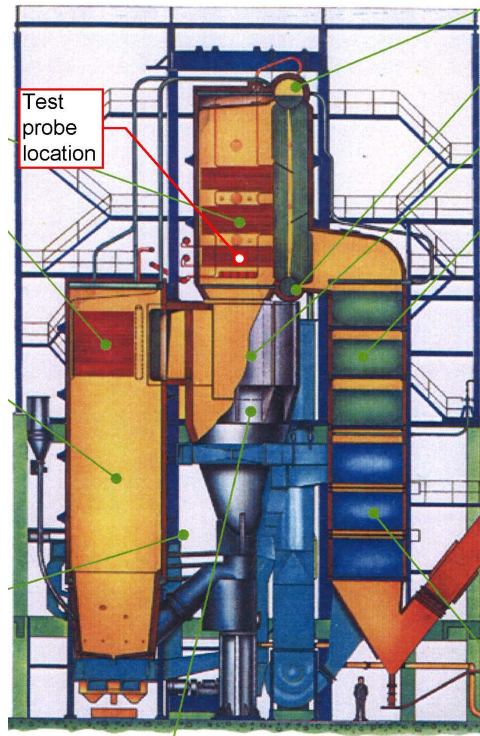
Figure 1. Boiler cross section.

Table 2: Fuel components during the measurement campaign

Fuel type	March	April
Coal	12%	5%
Peat	30%	2%
Recycled wood	27%	49%
Waste (REF)	31%	44%
Oil	0%	0%
Total	100%	100%

A temperature controlled, air cooled probe was placed in the superheater area in the second pass where the mean gas temperature was about 850°C. The probe was cooled to a surface temperature of 550°C. The probe working principle is shown in Figure 2. The temperature of the test probe was adjusted by pressurized air. PID-controller, connected to one of the thermocouples, adjusted the cooling air flow with a pneumatic control valve. The temperatures of the other thermocouples were monitored and logged by an online datalogger during testing.

After exposure a section was taken from each specimen and moulded in plastic after which the prepared and polished sample cross-sections and alloy microstructures were characterized with LOM, SEM and EDX. Assessment of material performance was based on the estimation of the depth of the material degradation. Oxide thickness measurements were not carried out due to spallation of the formed deposits and oxides after the probe removal.
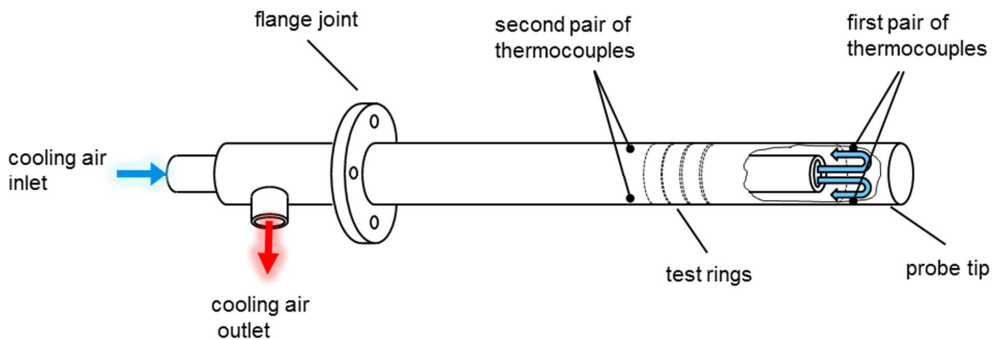
Figure 2: Outline of corrosion probe

3. Results

The test was started in March 2013, when the boiler was in normal operation. The test was ended in May 2013, when the boiler was in normal operation resulting in a total test duration of 1400 hours.

Figure 2 shows an overview of the probe after the testing campaign. A continuous deposit was formed on probe surface during the test. The base material did not seem to affect the deposit formation tendency and the deposit was visually similar on all test rings. The deposits formed were thicker on the windward side of the probe than on the leeward side. Spallation of deposits occurred during the transfer of probe from the plant to the laboratory.

Figure 3: Overview of corrosion probe after testing campaign

711

Metallographic cross sections were made from the samples to verify the type of the corrosion and the maximum corrosion depths as well as the composition of the remaining oxide layers. Table 3 summarises the depth of internal degradation of test materials below oxide scales, remaining oxide thickness values and estimated corrosion rate. The results are the average of ten measurements. The corrosion rate is based on the depth of internal degradation zone and the thickness of inner (Cr containing) scale. In the case of TP347H, the estimate is only very indicative due to heavy spallation of the oxide scales. However, the corrosion rate of TP347H is much higher than more alloyed HR3C and Sanicro 28.

Table 3: Measured depth of internal degradation below oxide scales, oxide thickness and estimated corrosion rate

	TP347H	HR3C	Sanicro 28
Internal degradation, windward [μm]	80 ± 5	25 ± 7	32 ± 3
Internal degradation, leeward [μm]	75 ± 3	16 ± 4	30 ± 10
Remaining oxide thickness [μm]	40	15	24
Estimated corrosion rate [μm/a]	>700	~200	~280

Figure 4 shows typical cross sectional view for TP347H material. The depth of the internal attack through grain boundaries was around 80 μm, slightly more in the windward side. Alloy TP347H was most heavily suffered during the measurement campaign. The oxide remains on the surface composed of two layers, the outer Fe rich layer and denser inner Cr rich layer. Corrosion proceeded first through grain boundaries and gradually degraded material. The depth of internal oxidation area was around 80 μm. The traces of sulphur and chlorine were detected on the oxidised grain boundaries inside the alloy. In the more detailed studies of grain boundaries no chlorine was detected but sulphur accumulations were observed at the grain boundaries, Figure 5.
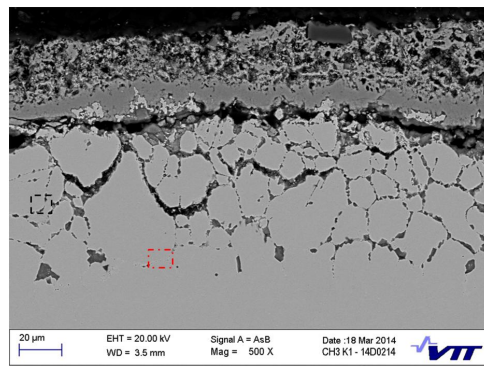
Figure 4: SEM image of TP347H sample. Dash line showing the placement of Figure 5.

	pt1	pt2	pt3	pt4	pt5
Fe	65.7	58.1	60.4	56.5	62.5
Cr	17.3	18.5	10.0	8.2	17.9
Ni	8.7	11.2	21.8	27.0	9.6
Si	0.4	0.3	0.3	0.5	0.4
Nb	0.5				
Mn	1.5	1.3	0.9	0.8	1.3
S		7.1	1.3	0.7	4.3
C	5.3	3.4	4.5	4.6	3.9
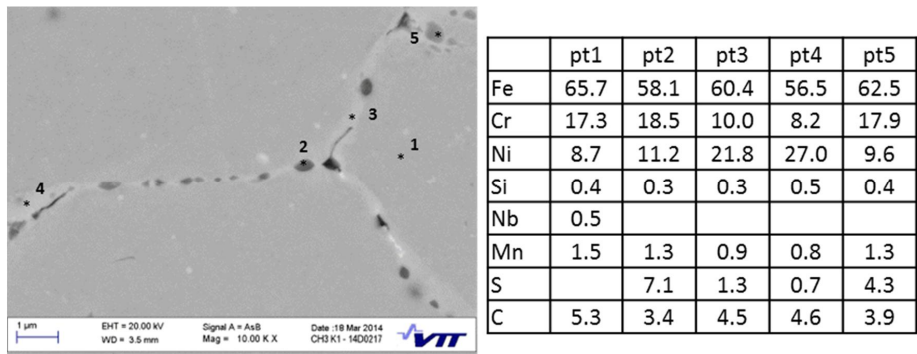
Figure 5: Detailed view and EDX point analyses of grain boundaries inside the TP347H alloy

Typical cross-sectional views of the HR3C and Sanicro 28 alloys are presented in Figure 6. The depths of internal degradation areas with chromium depletion were around 25 and 30 µm, respectively, below the oxide scales. The grain boundaries of HR3C alloy had suffered more severe corrosion compared to Sanicro 28, although the degradation area was somewhat thinner. Similar sulphur accumulations as in the case of TP347H were found in this chromium depleted area of alloy HR3C. Chromium rich precipitates had formed at the grain boundaries resulting in the chromium depletion of the surrounding areas (Figure 7), which facilitates the further progress of corrosion. The oxide scale formed on the HR3C alloy composed of three layers; the outer Fe rich layer, middle layer with spinel type Fr-Cr oxide and inner Cr oxide layer, Figure 7. The oxide formed on Sanicro 28 alloy composed of two layers; the outer Fe rich and inner Cr rich layer, Figure 8. Sulphur enrichment was observed at the alloy surface. Sulphur traces were also found in the internal degradation area, as well as some traces of chlorine.
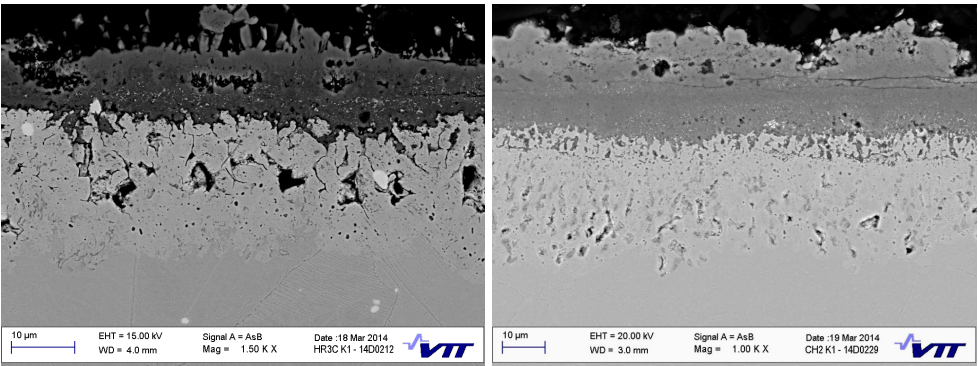
Figure 6: Cross sectional views of HR3C (left) and Sanicro 28 (right) samples

713

	pt1	pt2	pt3	pt4
Fe	51.4	42.7	51.8	51.4
Cr	25.2	31.6	9.8	8.8
Ni	18.0	14.6	19.8	24.9
Si	0.5	0.5	0.5	0.3
Mn			7.7	
S			5.2	0.2
C	4.9	10.5	5.5	4.9
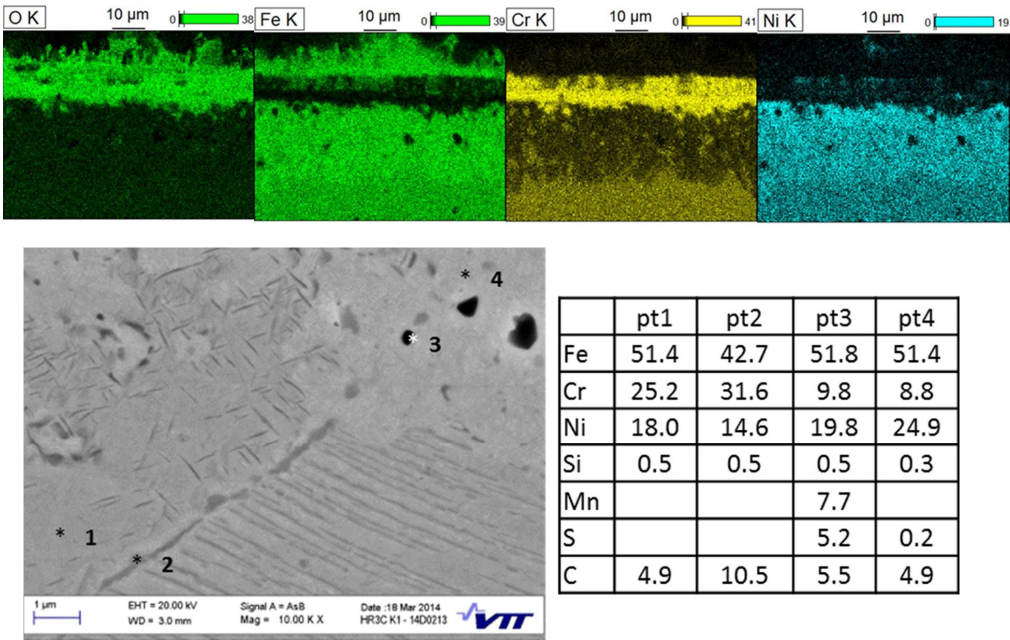
Figure 7: EDX analyses of HR3C sample after measurement campaign
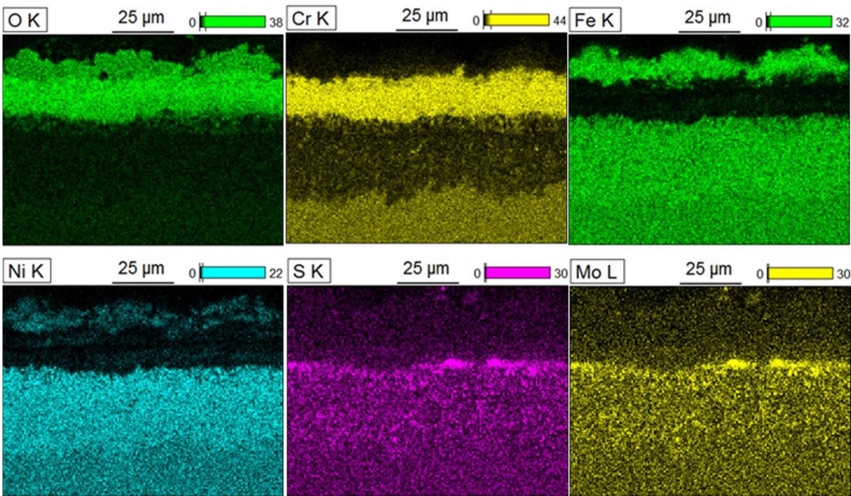
Figure 8: EDX mapping of Sanicro 28 alloy

714

4. Discussion and Conclusions

In this work corrosion behaviour of three austenitic alloys, TP347H, HR3C and Sanicro 28 was studied in a measurement campaign in a boiler burning waste wood, forest residues and REF mainly from the packing industry. Sample rings were installed in an air cooled probe at the superheater section. The duration of the measurement campaign was approximately 1400 h. Performance characterisation was based on the depth of the internal degradation area and oxide scale thickness. The major disadvantage of the current test set-up was that no information of the instantaneous corrosion rate was achieved. The influence of temporary process fluctuations due to variations e.g. in fuel composition, temperature and loads on the corrosion rate is difficult or even impossible to detect afterwards. The effective corrosion rate in a power plant is always fluctuating during combustion [8,9]. The used test set-up gives only average corrosion rate and is usable comparing different materials performance in the certain system or process. For more detailed information on temporary corrosion phenomena on-line probes currently developed [e.g. 9,10] are more useful.

The alloy TP347H suffered most during the test. Corrosion proceeded through grain boundaries very aggressively, and the depth of the internal degradation zone was over 80 µm. The thickness of the oxide scale could not be measured due to the heavy spallation of oxides after the removal of the probe from the boiler. Compared to the TP347H alloy the samples of HR3C and Sanicro 28 performed significantly better, although both materials also suffered from corrosion. The internal degradation area of HR3C alloy was somewhat thinner. However, the grain boundaries of HR3C alloy had suffered more severe corrosion compared to Sanicro 28, and corrosion will probably proceed quite rapidly through this area. However, at this state the difference between these two alloys is small and the testing period relatively short for reliable long term conclusions.

The results showed chlorine and sulphur species penetrating through grain boundaries into the alloys. Higher alloying provides better corrosion performance, although it did not restrain corrosion, only decreased it. The sufficient chromium and nickel content suppresses the corrosion tendency [1]. All oxides had a layered structure containing an outer iron rich layer gradually changing to chromium rich oxide layer near the substrate surface, although the parts of the outer scale layers were exfoliated with deposits. The spallation and regeneration of deposits and oxides are repeating due to e.g. flue gas temperature fluctuation and sooth blowing [11]. This phenomenon exposes the weakened material surfaces to direct contact with molten salts resulting in accelerated corrosion, and also slows down the regeneration of protective scales. It is proposed that a similar mechanism has also affected the corrosion in this case.

Based on the results a type 310 austenitic stainless steel could be a durable and cost effective material solution for the superheaters of the WtE boiler in question. If the operating conditions change to more aggressive, e.g. steam values are increased or lower quality fuels are used, alternative materials must be looked from nickel base super alloys.

Acknowledgements

References

[1] Viklund, P., Hjörnhede A., Henderson, P., Stålenheim, A., Pettersson, R., Corrosion of superheater materials in a waste-to-energy plant, *Fuel Processing Technology*, Vol 105, pp. 106–112 (2013).

[2] Pettersson, R., Flyg, J., Viklund, P., High temperature corrosion under simulated biomass deposit conditions, Corrosion Engineering Science and Technology, Vol 43, pp. 123-128, (2008).

[3] Ma, W., Rotter, S., Overview on the chlorine origin of MSW and Cl-originated corrosion during MSW & RDF combustion process. Bioinformatics and Biomedical Engineering, The 2nd International Environment and Public Health Track, ICBBE 2008, Shanghai, China (2008).

[4] Otsuka, N., Chemistry and melting characteristics of fireside deposits taken from boiler tubes in waste incinerators, Corrosion Science, 53, p 2269-2276 (2011).

[5] Kawahara, Y. Applications of high temperature corrosion-resistant materials and coatings under severe corrosive environment in waste-to-energy boilers, Journal of Thermal Spray Technology, Vol 16, p. 202-213 (2007).

[6] Farrell, D., On-line monitoring of fireside corrosion in power plant, 12th International Corrosion Congress, Corrosion Control for Low-Cost Reliability, (1993)

[7] Linjewile, T., Valentine, J., Davis, K. Harding N, Cox W. "Prediction and real-time monitoring techniques for corrosion characterisation in furnaces" In Life Cycle Issues in Advanced Energy Systems, Science Reviews, pp. 175-184, (2003).

[8] Henry, J.F, Nava, J.C, The Changing face of corrosion in coal-fired boilers. Conference on Unburned Carbon on Utility Fly Ash, (2005).

[9] Leino,T., Aho, M., Gynther, J., Ruuskanen, T., Häkkinen, M. Experiences from a Novel sensor for fireside corrosion monitoring during grate combustion of corn stover/wood chip blends. Energy Fuels, Vol 27, pp. 5653−5662 (2013).

[10] Matthes, S., Covino, B, Jr, Bullard, S., Williamson, K. Field test of high-temperature corrosion sensors in a waste-to-energy plant, Corrosion, Vol 66, pp. 025001-025001-12 (2010).

[11] Kawahara, Y. Evaluation of high-temperature corrosion life using temperature gradient corrosion test with thermal cycle component in waste combustion environments. Materials and Corrosion, Vol 57, pp. 60-72 (2006).

DEGRADATION ASSESSMENT OF SINGLE-CRYSTAL GAS TURBINE BLADES

Sanni Yli-Olli[1], Juhani Rantala[1], Jorma Salonen[1], Pertti Auerkari[1], Stefan Holmström[2]

[1]VTT Technical Research Centre of Finland
P. O. Box 1000, FI-02044 VTT, Finland
(sanni.yli-olli@vtt.fi)
[2]Joint Research Centre - IET
Petten, The Netherlands

Abstract

This paper describes a method for determining the effective in-service material temperatures at specified locations of coated single crystal gas turbine blades. For this purpose, the microstructural changes of diffusion coated new and aged blades have been evaluated for the characteristic features and kinetics of degradation. After comparing alternative approaches, two indicators appear to be particularly useful: a) the extent of gamma prime coarsening and degradation in the blade interior and b) the combined layer thickness of the intermediate diffusion zone (IDZ) and the zone with topologically close-packed (TCP) precipitates below the coating. The applicability of the indicators was demonstrated for selected ex-service blades. With both indicators the relevant service temperatures can be inferred, although not to the same level of uncertainty. The thickness of IDZ+TPC layers can provide the temperature estimates to a relatively good accuracy as long as the layers remain sufficiently intact for the assessment.

Keywords: Gas turbine blades, degradation assessment, single-crystal

1. Introduction

The service life of gas turbine blades in aircraft engines relies highly upon the durability of the blade material. For good high-temperature strength, the strongest blades are single crystal nickel superalloys, which does not have structure weakening grain boundaries, and at the same time contains a high volume fraction of strengthening small cubic gamma prime (γ') or $Ni(Al,Ti)_3$ particles that are initially coherent with the gamma (γ) matrix. The blades are protected against high temperature oxidation and corrosion with platinum aluminide (PtAl) diffusion coatings. During service both the substrate alloy and the coating show gradual time- and temperature-dependent changes. These changes may in turn reflect and indicate the effective operating temperature, when the service time and the kinetics of the observed change are known to a sufficient accuracy correlated with the associated exposure.

PtAl coatings are produced by depositing a thin layer of platinum on the superalloy substrate, with a vacuum diffusion heat treatment for improved adhesion, followed by aluminizing and final heat treatment. The PtAl coatings are typically (Ni,Pt)Al or beta (β) type aluminides, either inward- or outward-grown. The inward-grown coatings generally show three layers: a platinum rich layer on top, an intermediate beta layer, and a precipitate-rich interdiffusion zone (IDZ) on the inside. An outward-grown coating has typically two layers, the outer layer made of single-phase beta and/or ζ-PtAl$_2$, and the inner layer of IDZ. Platinum improves the oxidation resistance of aluminide coatings primarily by enhancing the protective alumina scale adhesion [1-4]. The blade material contains refractory alloying additions to improve creep strength, which also promotes the formation of topologically close-packed (TCP)

717

phases with the coating material at the coating substrate interface. The TCP phases can intrude into the substrate to a considerable distance and destroy the γ/γ' microstructure. These often plate-like or needle-like brittle phases can be detrimental to the mechanical properties of the blade [4-11].

In the initial state the small (coherent with γ matrix) cubic γ' particles are surrounded by an elastic stress field which has developed by negative misfit between γ matrix and γ' precipitates. Depending on stress, exposure time and temperature, the microstructure will degrade by gradual coarsening of the γ', precipitation of secondary phases and finally rafting or transformation of the γ'/γ structure towards platelet-like morphology [12-17]. Exposure at elevated temperatures accelerates any diffusion-controlled mechanism and thus also the degradation of the γ' precipitates. The misfit at the γ/γ' interface withstands the degradation of the γ' precipitates at the early stages but when the coherency is lost the γ' begins to coarsen.

This paper describes a method for determining the effective in-service material temperatures at specified locations of coated single crystal gas turbine blades, based on the time- and temperature dependent degradation of the substrate microstructure and the coating-substrate interface. For this purpose, the microstructural changes of diffusion coated new and aged blades have been evaluated for the characteristic features and kinetics of degradation.

2. Materials and methods

The base material of the blade was single crystal Ni-based superalloy Rene N4 (Table 1) [18]. The blade was coated with platinum aluminide coating.

Table 1: Nominal composition of the blade material N4 [18]

Element	C	Ni	Cr	Co	Mo	Al	Ti	Ta	W	B	Nb	Hf
wt.%	0.06	62	9.8	7.5	1.5	4.2	3.5	4.8	6.0	0.004	0.5	0.15

Small blade samples were subjected to an isothermal ageing treatment in laboratory conditions to simulate the degradation of the base material and coating. The aging was done at five different temperatures (950°C, 1000°C, 1050°C, 1100°C and 1150°C) for different durations varying from 7h to 2000h. The longest exposure time corresponds to the allowable effective operating time (EOT) of the actual turbine blades in service.

The samples for the ageing tests were cut from the blades and cleaned with ethanol before the ageing treatment. For ageing, the samples were heated up with the furnace, and air cooled to room temperature by taking them out of the furnace after the designated time of exposure. In few exceptional cases the samples were cooled down more slowly with the furnace.
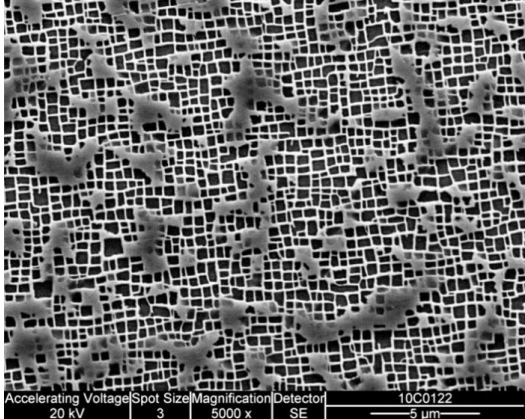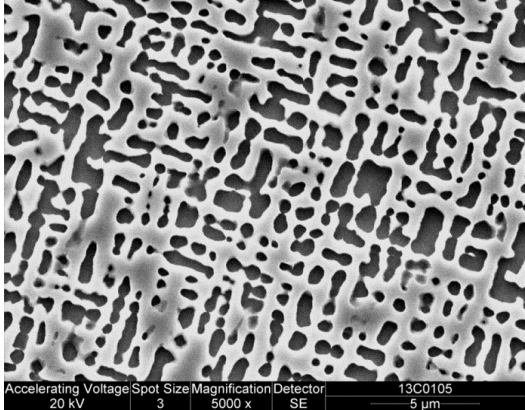
After the ageing treatment, polished and etched metallographic cross sections were prepared of all samples to visualise the microstructure the substrate alloy and coating interface. Samples were examined by light optical microscopy (LOM) and scanning electron microscopy (SEM).

3. Results

3.1 Assessment of service temperature from blade microstructure

During the isothermal ageing treatment the microstructure of the blade material exhibited time and temperature dependent degradation. The grade of degradation was visually evaluated, using classification to five main grades (1 to 5), and allowing for one intermediate level between each main grade. Starting from grade 1, which describes the initial microstructure up to grade 5 where rafting is predominant. Example microstructures of selected grades are shown in Table 2. The degradation of the gamma prime and gamma structure was mainly evaluated from inside the dendrites, from regions with the initial microstructures (grade 1) as shown in Table 2.

Table 2: Classification of microstructural degradation

Grade 1	
	Gamma prime precipitates are clearly cubic in form, and uniform in size. This grade corresponds mostly to as-new or fully rejuvenated microstructures.
Grade 4	
	Small amounts of separate gamma prime precipitates can still be seen (about 10-30 %). The gamma prime precipitates have often coalesced also in transverse direction. The gamma matrix still appears as a grid, without extensive coalescence.

The microstructural classification grade from each ageing treatment was fitted to a Larson-Miller type expression (1) [19] to describe the kinetics of the degradation of the gamma prime, so that for temperature T (K) after exposure time t (h)

$$x = A + k \cdot PLM \qquad (1)$$

where x is the gamma prime grade number and PLM=(logt+C)·T(K)/1000, with C=10 [1]. Hence the predicted temperature (K) as a function of gamma prime grade is

$$T(K) = 1000 \cdot \frac{x - A}{k \cdot [\log(t) + 10]} \qquad (2)$$

When the gamma prime grade number is <2 the slope parameter k is 0.374 and the intercept A is -3.604, for a grade number >2, k is 0.968 and A is -12.50. The fitting results are shown in Figure 1.
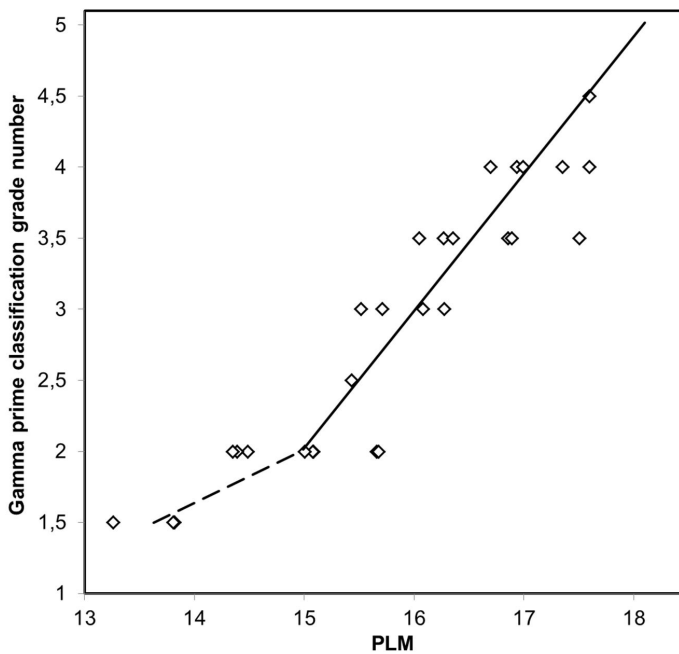
Figure 1: Bi-linear fit of gamma prime classification grade as function of PLM.

3.2 Assessment of service temperature from blade coating degradation

The coating consists of a beta (β) layer on top and an interdiffusion zone (IDZ). During aging a topologically closed packed (TCP) layer is formed. The initial thickness of the β-layer was 75 µm and that of the IDZ 24 µm. Practically no change was observed in the outer beta layer after 7 h exposure at 950°C, and the TCP zone of needle- or plate-like phases was very small

in the substrate under IDZ (Figure 2a). With increasing temperature and time the TCP zone comes more prominent and eventually becomes similar in thickness with IDZ (Figure 2b). After this the IDZ layer coarsens with an increasing amount of TCP, until after 2000 h exposure in 1050°C a continuous uniform TCP zone under IDZ zone no longer exists, instead individual needle-like TCP-phases are observed in the substrate (Figure 3a).

The beta layer remains almost unchanged after 2000 h at 950°C, without significant microstructural change in the beta phase, but some fragments of the β-phase had altered to γ' after 2000 h exposure at 1000°C. As the temperature increases the changing of the β –phase to the γ'-phase begins earlier and after 2000 h exposure in 1100°C the β-phase had totally disappeared (Figure 3b).
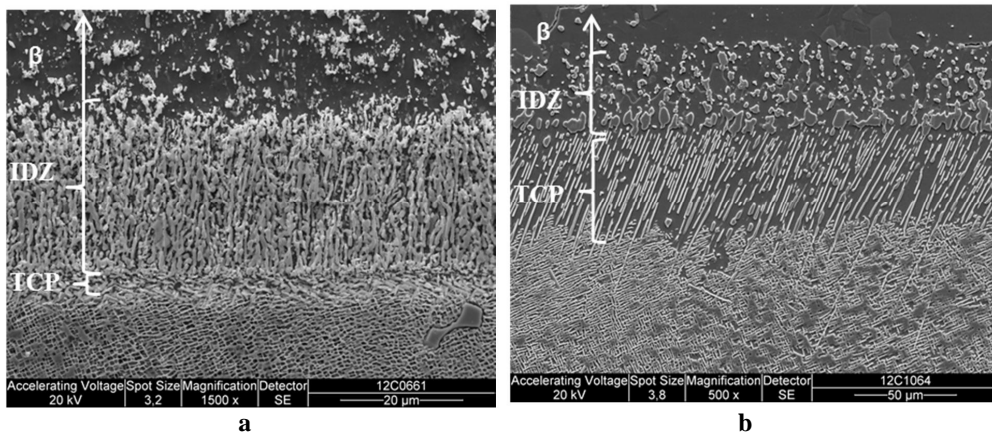
Figure 2: IDZ and TCP layers of the coating after a) 7 h at 950°C and b) 2000 h at 1000°C. Note different scales
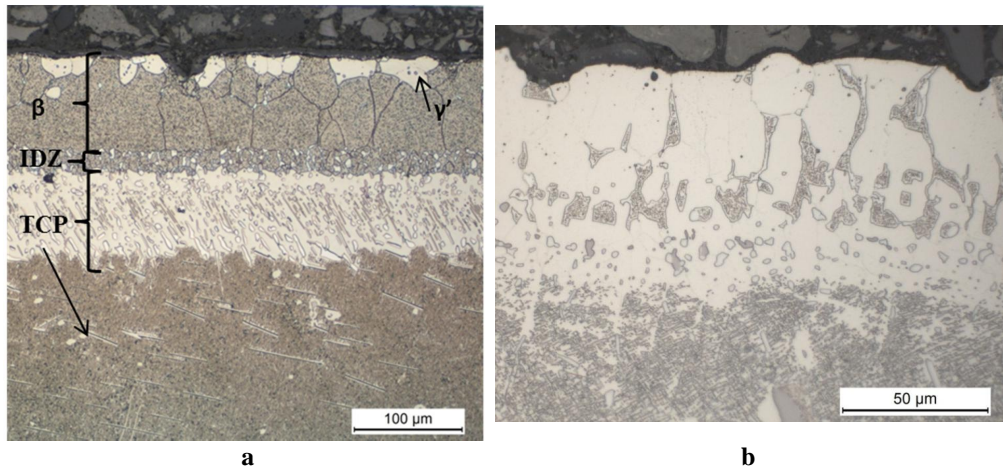
Figure 3: The outer layers of the coating after a) 2000 h at 1050°C and b) 2000 h at 1100°C. Note different scales

721

From the aged samples all the identified layers were measured. The combined thickness x (µm) of the IDZ+TCP layers (Figure 2) were fitted by a Larson-Miller type (PLM) of expression (3) [19] to describe the kinetics of the layer formation, so that for a temperature T (K) after an exposure time t (h)

$$\log(x) = 1.615 \cdot 10^{-4} \cdot T(\log(t) + 10) - 0.7759 = 1.615 \cdot 10^{-4} \cdot PLM - 0.7759 \qquad (3)$$

The correlation is fairly good for temperatures from 950°C to 1050°C, but at higher temperatures the kinetics apparently change and therefore the expression (3) does not work for temperatures above 1050°C, as can be seen from Figure 4.
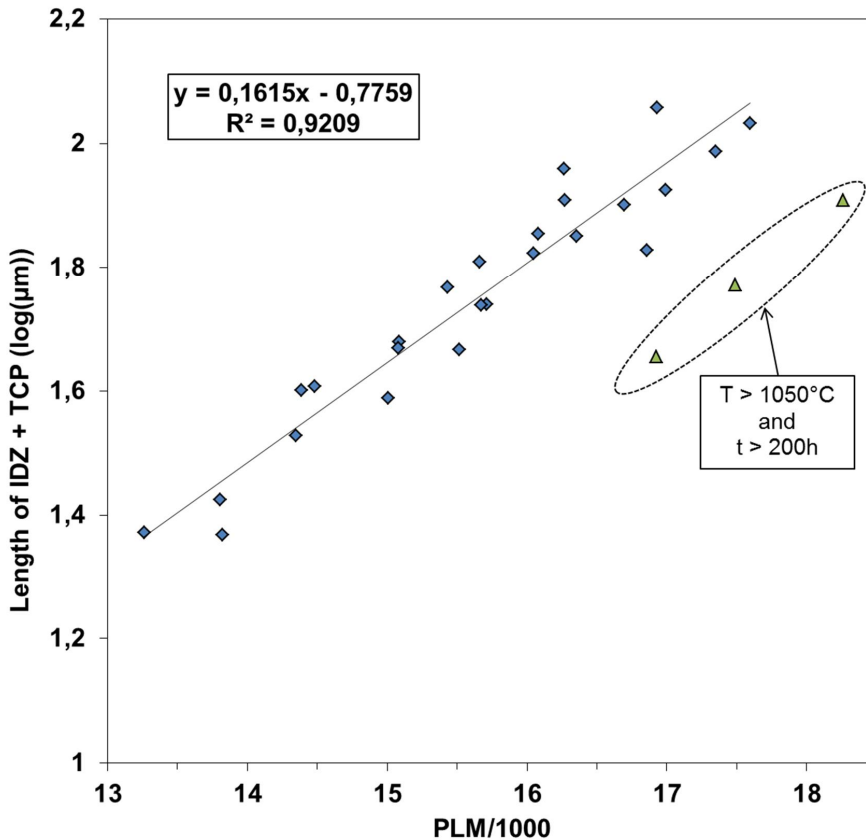
Figure 4: Combined thickness of IDZ and TCP layers as a function of PLM.

3.3 Application of the methodology

The described methodology was applied to an overheated turbine blade that had a locally oxidised region on the pressure side airfoil after 2417 h of effective operating time (EOT). With the new methods temperature was estimated using Eqs. 1 and 2 (microstructure) through the blade (Figure 5), and using the TCP+IDZ thickness at the cooling channel (Figure 6).

The results of the temperature evaluation are presented in Figure 7. The microstructure near the surface extended beyond the grading scale, and therefore the surface temperatures were linearly extrapolated from the temperatures obtained from inner structure, Figure 7. The results suggest a surface temperature exceeding locally 1200°C.
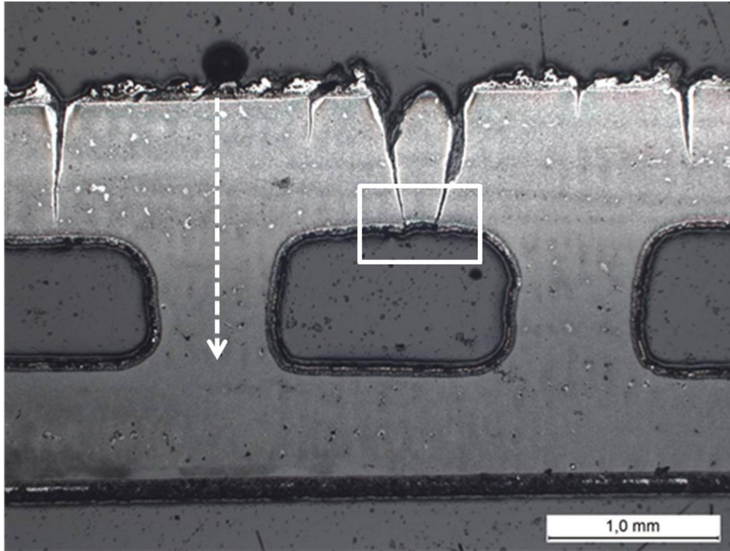
Figure 5: Overheated HTP blade, position of the microstructural temperature evaluation marked with a dotted line
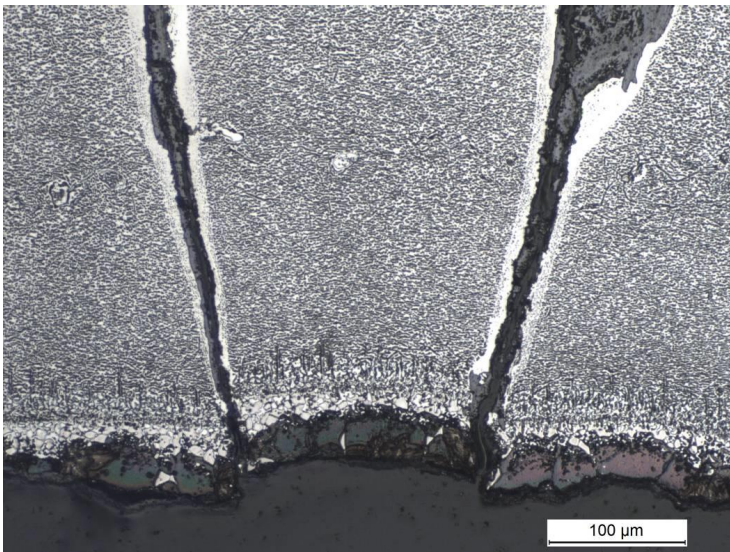
Figure 6: Cracks on the overheated blade (enlargement of Figure 5), location of the TCP+IDZ temperature evaluation.

723
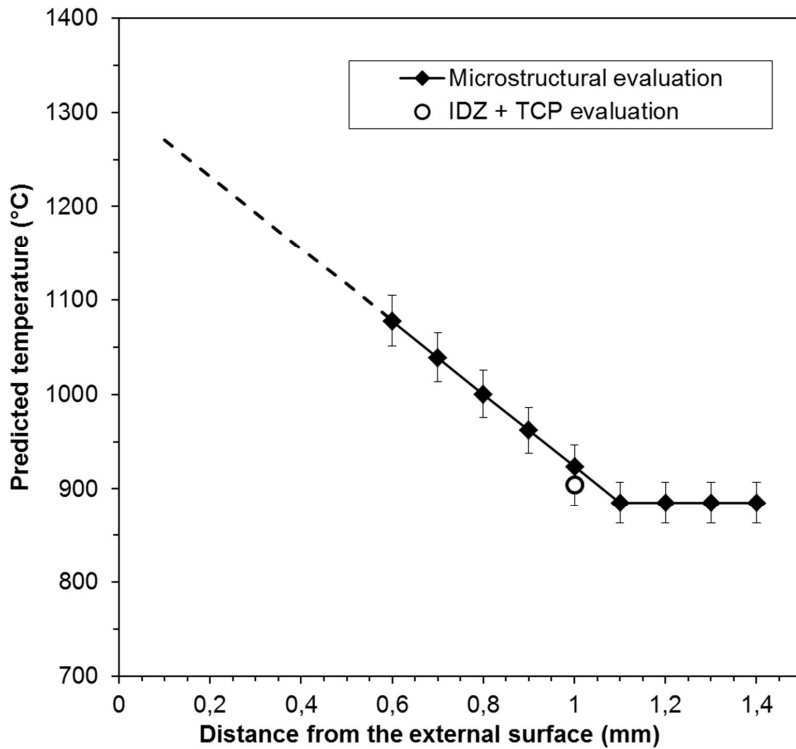
Figure 7: Predicted temperature distribution of the overheated blade.

4. Discussion

In comparison to many other comparable applications, the evaluation of the kinetics of thermal damage in the gas turbine materials of aircraft engines is unusually amenable to testing in the laboratory. Partly this is because testing and treatments can be often done in air, as the real service environment - with some important exceptions - is also largely oxidising due to the air excess provided by the compressor. Perhaps even more importantly, the expected service life of few thousand hours is not beyond the range accessible for experiments within a time frame of few months to a year. Consequently, the resulting conclusions do not need to rely on extrapolation in time, and one can avoid the associated uncertainty.

The composition and fabrication of the blade alloy (substrate) and the details of the diffusion coating process including the heat treatments will influence the initial microstructures and their evolution by thermal exposure during service. Therefore, the ex-service appearance of the substrate alloy (single crystal N4) and its PtAl diffusion coating are specific to the applied alloy, coating and their combination. The temperature gradient by internal cooling will result in a range of alloy microstructures in the through-thickness direction, particularly towards the specified blade life and at local hot spots of the blade surface.

Note that while exposure to elevated temperature will accelerate any diffusion-controlled mechanisms, diffusion can also be promoted by mechanical stress. Therefore when the microstructural grading is based on unstressed thermal exposure, applying it on real stressed blades will result in somewhat conservative temperature assessment. The coarsening and degradation of gamma prime in the microstructure of alloy N4 appears to include some nonlinearity. In particular, the appearance from grade 1 to 2 is resilient to change before much more substantial gamma prime coarsening and coalescence at the later stages.

At temperatures below 1050°C a clear dependence was observed between thermal exposure and the growth of the IDZ and TCP phases. Above 1050°C the TCP phase is thermodynamically less stable, and therefore no longer follows the same dependence. The combined thickness of IDZ and TCP layers seems to reflect the thermal exposure at the external surface with reasonable accuracy, suggesting that this measure and the corresponding fitted expression are useful for temperature estimates as long as the layers remain sufficiently intact. The natural disadvantage is the same as with the substrate microstructure, i.e. the need for destructive sampling. Another observed change was the emergence of gamma prime on the surface of the aluminide coating (beta layer). This layer was not showing as consistent trend in thickness as the selected IDZ and TCP layers.

The described methodology was applied to an example case of a locally overheated turbine blade. The case example suggests that the two temperature estimation methods are well correlated and that the methods can be used to evaluate the local metal temperature with fair confidence.

5. Conclusions

This work aimed to evaluate and classify the microstructural degradation of diffusion coated single-crystal gas turbine blades, so that the characterised features of degradation could be used for assessing the effective in-service material temperatures at the corresponding blade locations.

Two potentially useful indicative measures were evaluated for this purpose: a) gamma prime coarsening and degradation in the microstructure of the blade material (N4) to indicate the condition and temperature in the blade interior, b) combined thickness of the intermediate diffusion zone (IDZ) and topologically close-packed (TCP) precipitate layer of the PtAl diffusion coating to indicate the condition and temperature at the blade surface, as long as these layers remain sufficiently intact for the assessment.

The described methodology was applied to an example case of a locally overheated turbine blade. The case example suggests that the two temperature estimation methods are well correlated and that the methods can be used to evaluate the local metal temperature with fair confidence.

References

[1] D.K. Das, Microstructure and high temperature oxidation behaviour of Pt-modified aluminide bond coats on Ni-base superalloys, *Progress in Materials Science*, 58, 151-182, (2013).

[2]   N. Vialas, D. Monceau, Effect of Pt and Al content on the long-term, high temperature oxidation behaviour and interdiffusion of a Pt-modified aluminide coating deposited on Ni-base superalloys, *Surface & Coatings Technology*, 201, 3846-3851, (2006).

[3]   H. Svensson, J. Angenete, K. Stiller, Microstructure of oxide scales on aluminide diffusion coatings after short time oxidation at 1050°C, *Surface & Coatings Technology*, 177-178, 152-157, (2004).

[4]   J. Angenete, K. Stiller, E. Bakchinova, Microstructural and microchemical development of simple and Pt-modified aluminide diffusion coating during long term oxidation at 1050°C, *Surface & Coatings Technology*, 176, 272-283, (2004).

[5]   R.C. Reed, *The Superalloys: Fundamentals and Applications*. Cambridge University Press, Cambridge, (2006).

[6]   J.H. Chen, J.A. Little, Degradation of the platinum aluminide coating on CMSX4 at 1100°C, *Surface & Coatings Technology*, 92, 69-77, (1997).

[7]   C.M.F Rae, R.C. Reed. The precipitation of topologically close-packed phases in rhenium-containing superalloys, *Acta Materialia*, 49, 4113-4125, (2001).

[8]   C.M.F Rae, M.S. Hook, R.C. Reed. The effect of TCP morphology on the development of aluminide coated superalloys, *Materials Science and Engineering A,* 396, 231-239, (2005).

[9]   Dipak K. Das, Kenneth S. Murphy, Shuwei Ma, Tresa M. Pollock, Formation of secondary re-action zones in diffusion aluminide-coated Ni-base single-crystal superalloys containing ruthenium, *Metallurgical and Materials Transactions A*, Volume 39A, 1647-1657, (2008).

[10]   J.Y. Chen, Q. Feng, Z.Q. Sun, Topologically close-packed phase promotion in a Ru-containing single crystal superalloy, *Scripta Materialia*, 63, 795-798, (2010).

[11]   R.C. Reed, T. Tao, N. Warnken, Alloys-By-Design: Application to nickel-based single crystal super¬alloys, *Acta Materialia*, 57, 5898-5913, (2009).

[12]   T.M. Pollock, A.S. Argon, Directional coarsening in nickel-base single crystals with high volume fractions of coherent precipitates, *Acta Metallurgica et Materialia,* 42, 1859-1874, (1994).

[13]   N. Matan, D.C. Cox, C.M.F. Rae, R.C. Reed, On the kinetics of rafting in CMSX-4 superalloy single crystals, *Acta Materialia*, 47, 2031-2045, (1999).

[14]   T. Murakumo, Y. Koizumi, K. Kobayashi, H. Harada, Creep strength of Ni-base single-crystal superalloys on the γ/γ' tie-line, *Superalloys 2004*, TMS, (2004).

[15]   Yu Jinjiang, Sun Xiaofeng, Jin Tao, Zhao Nairen, Guan Hengrong, Hu Zhuangqi, Effect of Re on deformation and slip systems of a Ni base single-crystal superalloy, *Material Science and Engineering A*, 458, 39-43, (2007).

[16]   N. Ratel, B. Demé, P. Bastie, P. Caron, In situ SANS investigation of the kinetics of rafting of γ' precipitates in a fourth-generation single-crystal nickel-based superalloy, *Scripta Materialia*, 59, 1167-1170, (2008).

[17]   T. Tinga, W.A.M. Brekelmans, M.G.D. Geers, Directional coarsening in nickel-base superalloys and its effect on the mechanical properties, *Computational Materials Science*, 47, 471-481, (2009).

[18]   *Metals Handbook Desk Edition*, ASM International, Materials Park, OH, (1999).

[19]   R. Viswanathan, *Damage mechanisms and life assessment of high-temperature components*, ISBN: 0-87170-358-0, ASM International, p. 497, (1989).

THERMAL SPRAY COATINGS FOR HIGH TEMPERATURE CORROSION PROTECTION OF ADVANCED POWER PLANTS - PERFORMANCE AND FEASIBILITY STUDIES IN A BIOMASS-FIRED BOILER

M. Oksa[1], J. Kärki[2], J. Metsäjoki[1]

[1] VTT Technical Research Centre of Finland

Metallimiehenkuja 8, Espoo, Finland

[2] VTT Technical Research Centre of Finland

Koivurannantie 1, Jyväskylä, Finland

Abstract

The goal of carbon dioxide (CO_2) reduction in energy production has lead power plant operators to increase the efficiency by higher process parameters and to use alternative fuels instead of fossil fuels. Maintenance of power plant boilers experience great challenges due to use of difficult biomass and recycled fuels, which can cause severe corrosion damage to different boiler components and decrease lifetime of the metallic components. Investigation on suitable material solution to encounter the corrosion problems in even higher process temperatures is thus needed.

Thermal spray coatings to be applied up to 750 °C in biomass boiler conditions were sprayed and their high temperature corrosion resistance was validated in a 550 MWth circulating fluidized bed (CFB) burning mainly biomass. Three test campaigns were performed with controlled probe measurements, their duration varying from 1300 hours to 5900 hours. Two material test temperatures were set by the water and air controlled probe: 550 °C and 750 °C. The coatings were high velocity oxy-fuel (HVOF) sprayed nickel- and iron-based NiCr, Ni-21Cr, IN625, NiCrAlY, FeCr and arc sprayed NiCrTi. Two spray guns were applied to spray the metallic HVOF coatings in order to compare the effect of coating structure and oxygen content on the corrosion resistance. Applicability and performance of one ceramic coating Al_2O_3 with bond coat NiCrAlY was also tested. Reference tube materials were ferritic steel T92 and nickel super alloys A263 and A740. Most of the coatings showed excellent corrosion performance both at lower and higher test temperature. However, Ni-21Cr and IN625 corroded strongly at higher temperature and cannot be applied with high chlorine containing fuels such as biomass at temperatures as high as 750 °C. According to this study, corrosion performance validation of materials suitable for advanced power plants with higher steam and material temperatures is possible with temperature controlled probe exposure in real boiler conditions.

Keywords: Biomass, boiler, co-firing, thermal spray, coating, high temperature corrosion

1. Introduction

Higher efficiency demands, environmental requirements, in particular CO_2 emission reduction, and implementation of CO_2 capture technologies will require higher temperatures of steam and hence higher material temperatures in future power plants [1]. The goal of CO_2

reduction in energy production has lead power plant boiler operators to use alternative fuels instead of fossil fuels as well. Maintenance of power plant boilers experience great challenges due to use of difficult biomass and recycled fuels, which can cause e.g. severe corrosion damage to different boiler components [2]. The attempt to increase the efficiency by higher process parameters has led to decreased lifetime of metallic components of power plant boilers, because the corrosion damage may be even several millimetres per year. Investigation on suitable materials to encounter the corrosion problems in even higher process temperatures is needed [3]. Harsh conditions due to carbon neutral fuels, such as biomass, consist of high temperature flue gases, fly ash, gaseous species, vapour species and deposit formation on heat transfer surfaces. The corrosive species include e.g. SO_2, HCl, CO_2, H_2O, NO_x, Na, K, Zn and Pb [4, 5]. Severe corrosion mechanisms in the boilers burning difficult fuels include Cl gas corrosion and hot corrosion by molten phases (e.g. Zn-K-Cl) [2, 6].

As steam temperatures and pressures are increased, both the fireside and the steam-side aspects of the superheater and reheater tubes and the internal surfaces of the steam pipework will be progressively subjected to more aggressive conditions, which may lead to significantly increased wastage rates and other materials-related problems. In the EU FP7 project - Efficiency increases in existing and new build pulverised coal power plants with a view to CCS - "NextGenPower", research work has been performed on targeting to assist in the identification of appropriate solutions to these problems, mitigating the risks to the performance and integrity of the high temperature boiler components, through either materials and coating development or surface engineering [7]. This paper presents the results of high temperature corrosion testing and validation of thermal spray coatings in a co-fired boiler.

2. Materials and methods

Thermal spray coatings and their high temperature corrosion resistance was validated in a 550 MW_{th} circulating fluidized bed (CFB) burning mainly biomass. Three test campaigns were performed with controlled probe measurements, their duration varying from 1300 hours to 5900 hours. Two material test temperatures were set by the water and air controlled probe: 550 °C and 750 °C. The tested coating materials included several high velocity oxy-fuel (HVOF) sprayed Ni- and Fe-based high-Cr alloys, an arc sprayed NiCrTi coating and one aluminium oxide coating with a bond coat. Applied reference materials were ferritic steel T92 and nickel super alloys A263 and A740. The third test campaign was just concluded and hence the results presented in the following encompass the first two test periods.

2.1. The power plant boiler

The probe exposure trials were conducted at Alholmens Kraft power plant located in the western coast region of Finland, in the town of Pietarsaari. This facility is one of the largest biomass fuelled power plants in the world producing electricity, district heating and process steam and heat. The plant is combined condensing and CHP (combined heat and power) plant.

The probe exposure campaigns were conducted in a 550 MW_{th} circulating fluidised bed boiler which has live steam parameters of 194 kg/s, 165 bar, 545 °C, Figure 1. During the measurements the boiler was fired with varying shares of peat, coal, biomass (forest residues, industrial wood and bark etc.) and SRF (solid recovered fuel). Daily fluctuations in the fuel shares can be wide as well as the fluctuations in the whole process parameters due to changes in production rates.
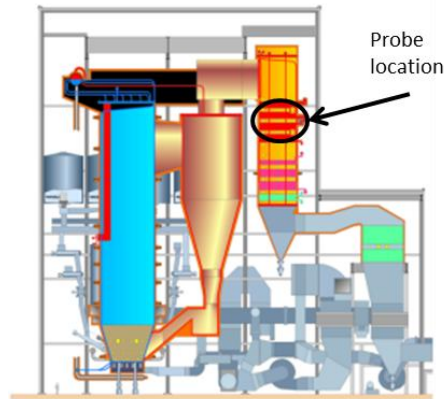
Figure 1 : Alholmens Kraft CFB boiler with installed probe location identified.

The overall corrosion probe test programme includes three exposure tests, with a total of 36 test specimens in a single corrosion probe exposed for periods between 1000 and 5900 hours. The probe was inserted into superheater area after the cyclones, as shown in Figure 1.

2.2. The measurement probe

VTT has extensive experience in the application of special probes for corrosion monitoring and deposit analysis in high temperature combustion plants. The latest development is an advanced water/air cooled probe which is approximately two meters in length and can accommodate two sections with six test rings in each. One section is water and air cooled and is exposed at metal temperatures of approximately 550 ºC and the second is air-cooled at metal temperatures around 750 ºC. A photograph of the probe with the two separate sample regions is presented in Figure 2.

There are several temperature measurements in different sides of the probe for both temperature areas. The primary head consists of stationary part in which there are four thermo-couples and area for detachable material rings. The length of a detachable material ring in the primary head is 12.5 mm/each and the outer diameter 48 mm. In the secondary head the detachable material rings are connected to the system through a separate extension ring. The length of a detachable material ring in the secondary head is 15 mm/each and the outer diameter 34 mm. There are two thermo-couples in the extension ring and material

Temperature set point 550 °C (windward)   Temperature set point 750 °C (windward)

Figure 2 : VTT's high temperature probe for two measurement temperatures.

temperatures of the detachable material rings are measured at three rings. The flue gas temperature is measured in the tip of the probe with one covered thermo-couple. The thermal expansion in primary and secondary heads as well as in the casing is eliminated with a special spring system consisting of four separate springs. The probe is air- and water-cooled with separate controllable cooling unit. During the tests the two metre casing remains cool by water cooling whereas the temperatures of the sample exposure heads are adjusted as desired by additional air cooling.

2.3. Plant and probe data analysis

Probe measurement was monitored on-line during the measurements and data gathered for further analyses. Process data was collected from the plant's reporting systems after each exposure campaign as well as monthly fuel data. A summary regarding probe behaviour, fuel usage and plant process parameters were made with spreadsheet calculation and analyses.

2.4. Coating materials

The tested coating materials were four Ni-based powders: NiCr (Ni-980-1/1260F, Praxair), Ni-21Cr (Diamalloy 4006, Sulzer Metco), IN625 (Diamalloy 1005, Sulzer Metco), and NiCrAlY (Amperit 413, H.C.Starck); one Fe-based powder (SHS9172HV1, Nanosteel); one Al_2O_3 powder (A1-1110-HP, Praxair); and a NiCrTi wire (TAFA Ni Cr 45 CT, Praxair). The chemical compositions of the Ni- and Fe-based coating materials are presented in Table 1. The coatings were sprayed on T92 (550 °C), A263 and A740 (750 °C) substrates. These materials were applied as reference materials in the trials.

Table 1 : Chemical composition of the Ni- and Fe based coating materials.

Material	Ni	Fe	Cr	Mo	Nb	W	C	B	Mn	Si	Cu	Ti	Y
NiCr	Bal.	1.1	46	...	...	...	0.1	...	...	2.1	...	...	...
Ni-21Cr	Bal.	0.9	21.2	9.0	...	9.3	0.8	0.7	...	...	4.2	...	...
IN625	Bal.	0.1	20.6	8.8	3.5	...	...	...	0.1	0.2	...	...	...
NiCrAlY	Bal.	...	22	...	...	...	...	...	...	...	...	...	1.0
FeCr	...	Bal.	18.6	3.6	7.1	8.6	2.1	< 5.0	1.1	1.6	...	...	...
NiCrTi	Bal.	...	42-46	...	...	...	...	...	...	...	...	0.3-1	...

2.5. Reference materials

A ferritic steel T92 was selected for lower test temperature 550 °C, and nickel super alloys Nimonic® 263 and Inconel® 740 for higher test temperature 750 °C. The chemical compositions of the reference materials are presented in Table 2.

Table 2 : Chemical composition of the reference materials.

	Ni	Fe	Cr	Mo	Co	Nb	W	Ti	V	Mn	Si	Al
T92	0.3	Bal.	9	0.3	...	...	2	...	0.2	0.5	0.2	0.2
A263	Bal.	0.5	20	5.7	20	...	...	2.1	...	0.4	0.2	0.7
A740	Bal.	0.7	25	0.5	20	2.0	...	1.8	...	0.3	0.5	0.9

2.6. Thermal spraying

HVOF (high velocity oxy-fuel) torches DJ Hybrid and CJS were used for most of the coatings. Al_2O_3 was sprayed on NiCrAlY bond coat with a HV2000 HVOF torch. NiCrTi coating was arc sprayed. Table 3 shows the process parameters of the sprayings.

Table 3 : Process parameters for HVOF [l/min] and arc spraying in different test campaigns (1-3). Spraying distance: 250 mm for CJS and DJ; 150 mm for HV2000 and arc.

Camp	Material	Method	Feed rate [g]	H$_2$	Kerosene	Propane	O$_2$	N$_2$	Air
1	FeCr	CJS 140 mm	50	100	16		850	12	
	NiCr, IN625, Ni-21Cr	CJS 140 mm	50	100	16		1000	12	
2	FeCr	CJS 140 mm	50	100	16		850	12	
	NiCr	CJS 140 mm	50	100	19		900	12	
	NiCr, IN625	DJ 2701	40			62	290	12.5	400
3	FeCr	CJS 140 mm	50	100	20		1000	12	
	FeCr, NiCr, Ni-21Cr, NiCrAlY	DJ 2701	40			62	290	12.5	400
	NiCrAlY+ Al$_2$O$_3$	HV2000 22 mm	10	750			300	20	

Camp	Material	Method	p [bar]	U [V]	I [A]
1-2	NiCrTi	Arc	3.5 / 2.5	30	220

2.7. Specimen characterization

After exposure the specimens were removed from the probe and embedded in resin on-site. Then the specimens were cross-sectioned by grinding and polishing. Ethanol was used in grinding instead of water to preserve water soluble compounds. The cross-sections were first studied with an optical microscope and subsequently with a scanning electron microscope (SEM) equipped with an energy-dispersive X-ray spectroscope (EDS).

3. Results

3.1. Process parameters and probe data

Plant electricity output varied a lot in short intervals depending on the electricity markets, Figure 3. This variation had an effect on the flue gas temperatures inside the boiler and further on the temperatures at the probe surfaces. Due to high variations in the plant load and process temperatures the probe temperature profiles were also fluctuating which had an effect on the stability of the controlled temperature on the windward surface.
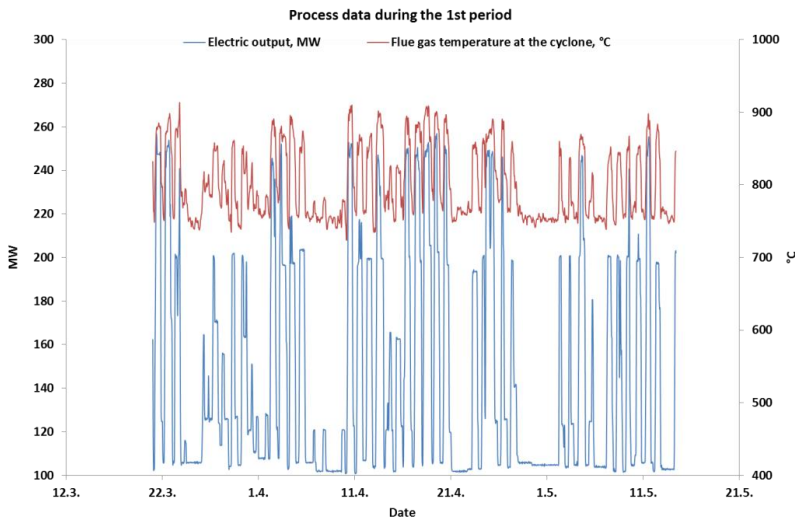
Figure 3 : Plant electricity output and flue gas temperature at the cyclone during the 1ˢᵗ period measurements.

During the measurements the boiler was fired with varying shares of peat, coal, biomass (forest residues, industrial wood and bark etc.) and SRF (solid recovered fuel). The average fuel energy shares during the monitoring periods as well as the monthly minimum and maximum values are presented in the table 4.

Table 4 : The average fuel energy shares and monthly minimum & maximum values during the monitoring periods I and II.

	Period I			Period II		
	average	min	max	average	min	max
Peat	31 %	20 %	46 %	15 %	8 %	19 %
Coal	10 %	9 %	10 %	31 %	20 %	45 %
Biomass	52 %	36 %	63 %	46 %	31 %	60 %
SRF	8 %	7 %	8 %	9 %	5 %	10 %

3.2. Corrosion resistance

3.2.1. Ferritic steel T92 at 550 °C

T92 ferritic steel had corroded in the boiler trials strongly. After the 1300 h test period, up to 200 µm thick porous corrosion product layer both at flue gas and leeward side had formed on the uncoated base material T92. The multilayered iron-chromium oxide was porous and detached from the metal surface. After the 5900 h exposure, the specimen was covered with over a 600 µm thick partly loose oxide scale consisting of several iron and chromium oxide layers, Figure 4. The layers contained e.g. K, S, Na, Cu and small amount of Cl.
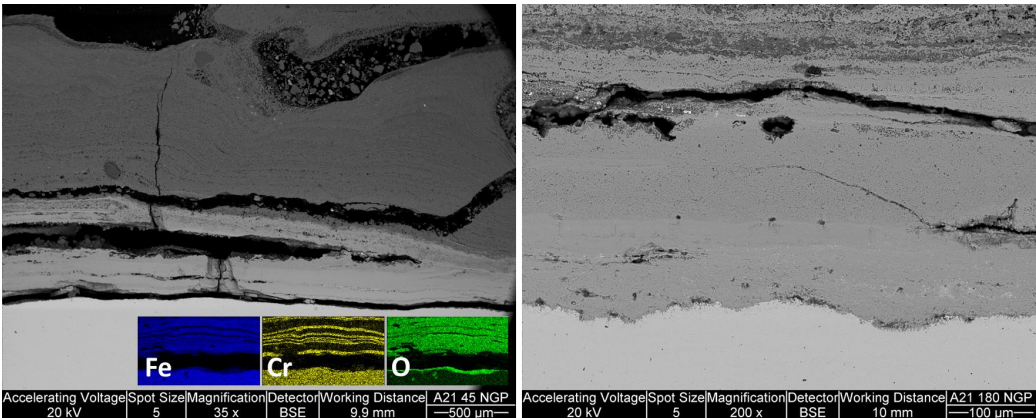
Figure 4 : SEM images (back scatter BSE) of the ferritic steel T92 after the 1300 hour exposure at 550 °C. Elemental maps showing layered structure of iron and chromium oxides.

3.2.2. Coatings at 550 °C

All the coated specimens endured the exposure at 550 °C without significant changes in the 1300 h exposure. IN625 had minor corrosion within the top 20 µm of the coating at flue gas side. FeCr was found to be corroded from the side with strongest corrosion at the leeward side, with a 30 µm thick corrosion product layer and internal coating degradation up to 20-40 µm depth. Chlorine was detected at the outer surface of the FeCr coating. A 1-2 µm thin Cr rich oxide layer was formed on Ni-21Cr, IN625, NiCr and NiCrTi coatings. Similar high corrosion performance was detected in the 5900 h trial.

3.2.3. Nickel super alloy A263 at 750 °C

In the 1300 h test trial, the uncoated nickel superalloy A263 had high corrosion resistance. A 1-10 µm thin Cr-rich oxide scale was formed on the material, where 10 µm represented slight pitting and internal attack. On average the scale was around 3 µm thin. The scale was observed to be thickest at the leeward orientation. S, Ti and Al were also found in the Cr-rich oxide scale. However, near the flue gas side the scale was lost during removal of the specimen from the probe and therefore the thickness in that region could not be measured. Deepest penetration into the material through grain boundaries was 10 µm. The A263 material showed high corrosion resistance in the boiler conditions in the longer exposure (5900 h) as well.

3.2.4. Coatings at 750 °C

The coatings exposed at 750° C showed clear differences between the coatings and also between locations within the specimens. Generally the flue gas direction had the most severe corrosion and the leeward direction the least. In the 1300 h exposure, IN625 (CJS) exhibited pit corrosion not only at flue gas direction but also at side areas of the test ring. In many cases the corrosion had propagated to the substrate and continued deeper into it and also widened the pit, Figure 5. At flue gas side the coating had been completely lost at a wide area. In the longer test trial, IN625 was consumed totally in the windward side. The strong corrosion had progressed down to substrate material A263.
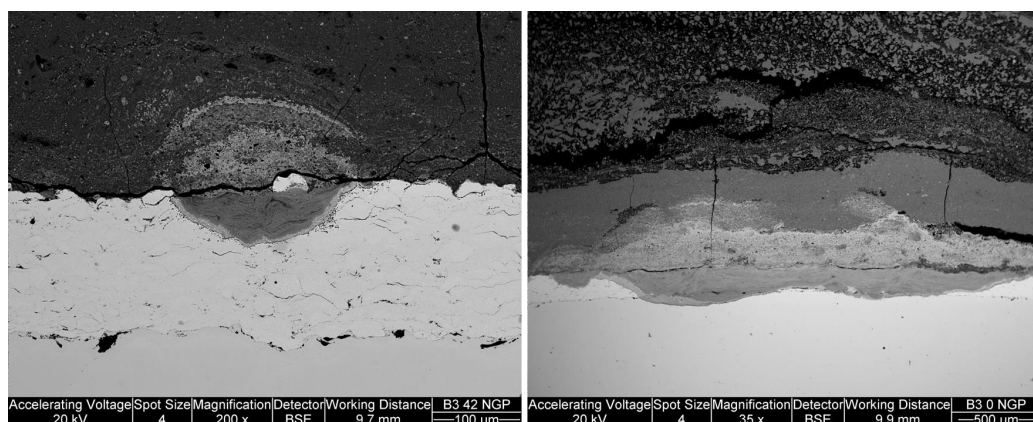
Figure 5 : SEM images (BSE) of IN625 (CJS) coating after the 1300 h exposure at 750 °C.

FeCr coating (CJS) was corroded rather uniformly in the 1300 h exposure. The highest corrosion rate was at flue gas side with a 25-55 μm thick corrosion product that consisted of two irregular layers. The outer layer was a porous Fe and O rich scale, which was partially mixed with the deposit. Under the topmost layer was a porous Cr and Nb rich layer. In the 5900 h exposure, FeCr coating was covered with an iron, chromium and niobium containing oxide layer with thickness of 50-100 μm. S, K, Na and Ca were present in the oxide layer.

A thin, 2 μm Cr_2O_3 layer was formed on the NiCr coatings in both exposures. A distinct precipitation of chromium from the nickel matrix was detected at 750 °C in particular with the NiCr (CJS) coating, Figure 6.

Ni-21Cr (CJS) coating was completely consumed on the flue gas orientation in the 1300 h trial. After the test, it was observed that the deposits around the specimen were massively bulging unlike on the other specimens.
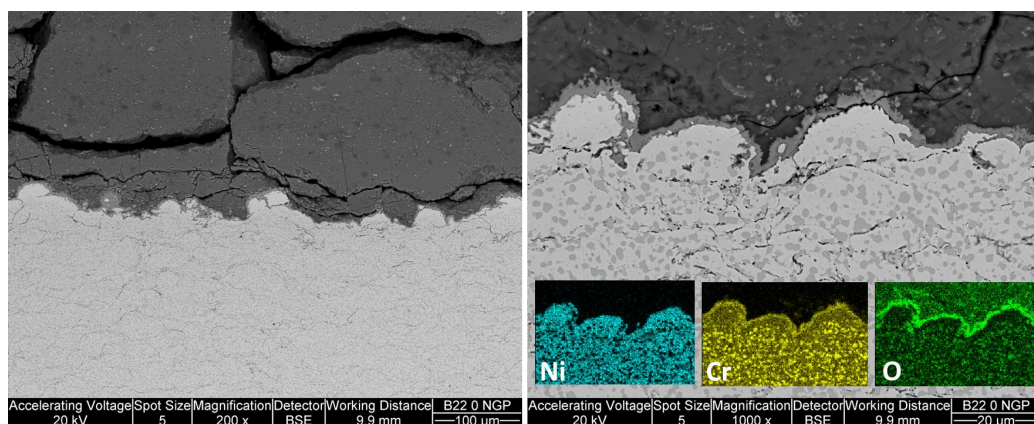
Figure 6 : SEM images (BSE) of NiCr (CJS) coating after the 5900 h exposure at 750 ℃.
Elemental maps of nickel, chromium and oxygen in small images.

The arc sprayed NiCrTi coating showed uniform corrosion throughout the coating surface in the 1300 h trial. The coating forming elements were protected by a Cr-rich layer on top of the coating, and e.g. sulphur was unable to penetrate the coating The thickness of the Cr and O-rich layer was at times up to 20 μm, but generally around 2-4 μm. In the longer test, a 20-30 μm chromium oxide layer covered the NiCrTi (Arc) coating.

4. Conclusions

The corrosion performance of the coatings at 550 °C was excellent compared to the ferritic steel tube material T92, which corroded strongly at 550 °C. Ni-based coatings NiCr (CJS), NiCr (DJ) and NiCrTi (Arc) showed excellent corrosion performance at both temperatures together with nickel super alloy A263. Ni-based Ni-21Cr (CJS) and IN625 (DJ) coatings endured in the exposure at 550 °C in excellent way as well, but at 750 °C the coatings failed completely. FeCr (CJS) coating gave sufficient protection to the substrate material at both test temperatures, but presented higher corrosion rate compared to the Ni-based coatings.

- The corrosion layer thicknesses were about 1/4 of the Fe-based coating and 1/10 or less of Ni-based coatings compared to the corrosion layer thickness of T92 at 550 °C.
- At the higher temperature 750 °C clear differences between the coatings emerged: NiCr (CJS) and NiCr (DJ) coatings showed highest corrosion performance.
- Nickel super alloy A263 showed sufficient corrosion resistance at 750 °C with a 10 μm thin protective Cr_2O_3 layer and some internal grain boundary attack.
- IN625 coating failed totally in the exposure at 750 °C. The corrosion had proceeded into to the A263 alloy, which had experienced grain boundary attack to about 30 μm deep.

5. Acknowledgements

6. References

[1] A.U. Syed, N.J. Simms, J.E. Oakey, Fireside corrosion of superheaters: Effects of air and oxy-firing of coal and biomass, *Fuel*, 101, 62-73, (2012).

[2] K. Natesan, J.H. Park, Fireside and steamside corrosion of alloys for USC plants, *International Journal of Hydrogen Energy*, 32, 3689 – 3697, (2007).

[3] R. Viswanathan, W.T. Bakker, Materials for boilers in ultra supercritical power plants, *Proceedings of IJPGC*, July, 1-22, (2000).

[4] S. Enestam, C. Boman, J. Niemi, D. Boström, R. Backman, K. Mäkelä, M. Hupa, Occurrence of zinc and lead in aerosols and deposits in the fluidized-bed combustion of recovered waste wood. Part 1: Samples from boilers, *Energy & Fuels*, 25, 1396-1404, (2011).

[5] J. Sandberg, C. Karlsson, R. Bel Fdhila, A 7 year long measurement period investigating the correlation of corrosion, deposit and fuel in a biomass fired circulated fluidized bed boiler, *Applied Energy*, 88, 99-110, (2011).

[6] M. Montgomery, et al., In situ corrosion testing of various nickel alloys at Måbjerg waste incineration plant, *Materials and Corrosion*, 64, 14-25, (2013).

[7] M. Oksa, S. Tuurna, T. Varis, Increased lifetime for biomass and waste to energy power plant boilers with HVOF coatings: high temperature corrosion testing under chlorine-containing molten salt, *Journal of Thermal Spray Technology*, 22, 783-796, (2013).

THE FIRESIDE CORROSION OF HR6W AND SANICRO 25 AUSTENITIC ALLOYS

Marta Lipińska-Chwałek[1], Małgorzata (Gosia) Stein-Brzozowska[2], Bogdan Rutkowski[1],
Aleksander Gil[1], Jörg Maier[2], Aleksandra Czyrska-Filemonowicz[1]
[1]AGH University of Science and Technology
[2]University of Stuttgart
(Marta.Lipinska-Chwalek@agh.edu.pl)

Abstract

HR6W (23Cr40Ni30Fe7WTiNb) and Sanicro 25 (22Cr25NiWCoCu) austenitic alloys are candidates for USC and A-USC boiler pressure elements: Sanicro 25 steel - for the operating temperature up to 680 ℃, while the Ni-based HR6W alloy – for the temperature range up to above 700 ℃.
The aim of the study was to compare the high temperature corrosion resistance of both austenitic tube materials subjected to the combustion atmosphere in real and laboratory conditions: (i) 30 h in a real combustion environment of 0.5 MWth test rig (pulverised fuel combustion rig) and subsequently (ii) 970 h in the laboratory corrosion test set-up, at the metal temperature of approximately 650 °C. This temperature corresponds to the operation temperature of the superheater in the USC boiler. The microstructural changes were investigated in detail by advanced electron microscopy methods. Both materials exhibited a formation of approximately 250 nm thick Cr-rich oxide scales on the outer tube surface, exposed directly to the combustion environment.

Keywords: austenitic alloys, Sanicro 25, HR6W, fireside corrosion, microstructure, TEM, USC, A-USC

1. Introduction

Due to plentiful and still relatively easy availability at low costs, fossil fuels remain most widely utilized primary energy source in much of the today world. Continuously increasing energy demand and tendency to cover these requirements with conventional, fossil - based power generation result in increasing environmental issues, caused by unavoidable greenhouse gases emissions. One of the solutions to reduce these emissions while maintaining fossils as a viable energy source option is to improve the efficiency of the related conventional steam power plants (SPPs), which is a direct function of the operating conditions (steam temperature and pressure). An expected efficiency increase of about 10 % HHV (high heating value), which can be nowadays achieved by moving from currently operating supercritical (580 °C, min. 25 MPa) to ultra-supercritical (USC) or advanced ultra-supercritical (A-USC) technologies (700 °C, min. 35 MPa, efficiency >45 % HHV) may bring overall, fuel-related emissions reduction of nearly 22%, but also a significant economic profit, due to reduced fuel consumption [1]. Implementation of the USC or A-USC SPPs requires however development of new materials, which can withstand these demanding operation conditions. Steam temperatures exceeding 600 °C, which are reached at the certain stages of the USC/ A-USC boiler superheater, are too demanding for conventional steels. Two recently developed materials, austenitic steel Sanicro 25 and Ni-base austenitic alloy HR6W, are suggested as potential candidates for application at USC and A-USC conditions. Sanicro 25 steel extends the range of steels application up to metal temperature of 680 °C. For the temperature range up to above 700 °C, where nickel-base materials with higher strength are necessary (e.g. Alloy 617 mod.), the Japanese Ni-base alloy HR6W is suggested. Sanicro25 and HR6W should enable reduction of the investment costs, due to their economical

compositional balance (costs preferential to that of modified Alloy 617 [1]) and satisfactory creep and corrosion resistance reported [2-4]).

The aim of this work is to compare corrosion behaviour of both materials by exposing them to real fireside corrosion environment. Applied testing methodology (combination of the exposure in combustion test rig during real coal firing conditions and laboratory test set-up) offers an advantage comparing to conventional laboratory tests, such as real combustion atmosphere, temperature gradient corresponding to the one faced by real superheater tube, real initial deposit (including the condensates, which settle during the tests), real tube geometry of tested materials etc. In comparison to very expensive field studies using test loops mounted in boilers, such methodology offers an interesting alternative in terms of costs, complexity and outcome.

2. Experimental details

2.1. Materials

The Sanicro25 (SANDVIK) and HR6W (Sumitomo Metals Industries, SMI) superheater tubes were delivered to the Institute of Combustion and Power Plant Technology (IFK), University of Stuttgart by RAFAKO S.A. in a form of head-on welded tubes, as presented in Fig. 1. Chemical compositions of the Sanicro25 and HR6W base materials, as-specified in the VdTÜV data sheets (0 and 00, respectively) are given in Table 1.

Table 1: Chemical composition of Sanicro25 and HR6W materials as-specified in the respective data sheets (VdTÜV).

wt%	C	Si	Mn	P	S	Cr	Fe	Ni	W	Co	Cu	Nb	N	B	Ti
Sanicro 25 0															
min.	0.03	nd	nd	nd	nd	21.25	rest	23.3	1.93	0.9	1.9	0.25	0.14	nd	nd
max.	0.11	0.45	0.63	0.028	0.018	23.75	rest	26.7	4.07	2.1	3.6	0.65	0.31	0.0083	nd
HR6W 0															
min.	nd	nd	nd	nd	nd	21.25	19.65	rest	5.9	nd	nd	nd	nd	nd	nd
max.	0.105	1.05	1.54	0.033	0.018	24.75	30.35	rest	8.1	nd	nd	0.4	nd	nd	0.25

Length of the tubes was adjusted to 7 cm long segments with the weld localised in the middle. The inner diameter was adjusted using the turning process whereas the outer diameter was left unchanged thus without affecting the original tube surface.

Figure 1: The welded tubes as delivered from RAFAKO S.A: Sanicro 25 OD 38 x 8,8 by SANDVIK, HR6W OD 38 x 8,8 by SMI.

2.2. Fireside corrosion exposures

2.2.1. Exposures in combustion chamber of 0.5 MW test rig KSVA

The 7 cm long segments of welded Sanicro 25 and HR6W superheater tubes, including the weld in the middle, were mounted at the corrosion probe and exposed to real combustion environment in 0.5 MW test rig KSVA (ger. *Kohlenstaub Verbrennungsanlage*) – pulverised fuel combustion test rig at the University of Stuttgart (IFK). To monitor the metal temperature, thermocouples were mounted at each metal ring at two positions respectively. The corrosion probe was positioned at the exit of the radiative and entrance of the convective zone of the combustion chamber, as showed in Fig. 2, at the gas temperature exceeding 1050 °C. The samples were cooled to approximately 650 °C, corresponding to the metal temperature of the respective superheater in an USC boiler.
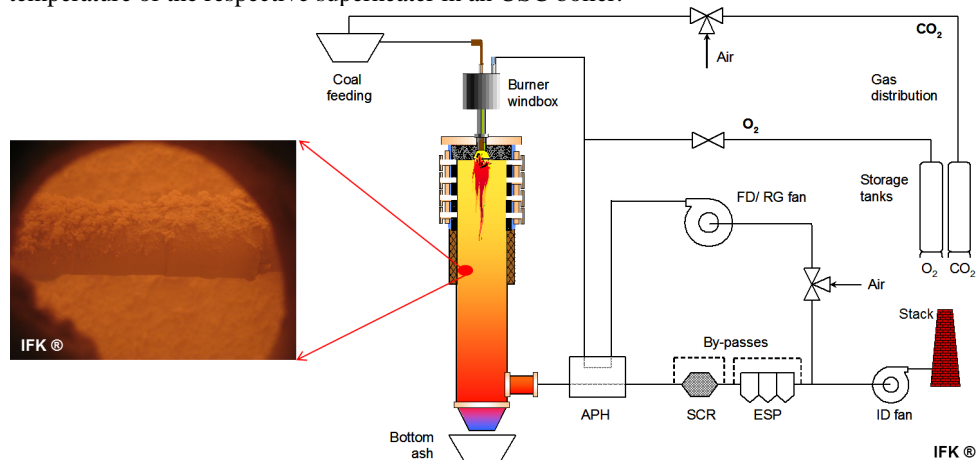
Figure 2: KSVA 0.5 MW combustion test rig at the University of Stuttgart with indication of the location of field corrosion tests.

The combustion tests were performed using a South-African hard coal (see Table 2). The average gas temperature at the section where the corrosion probe was positioned was approximately 1063 °C. Details of the respective combustion atmosphere are given in Table 3.

Table 2: Composition of the South-African hard coal used in the combustion test in KSVA

Ultimate analysis	raw	an (< 0.1 mm)	Main elements	
Total moisture, %	8.94	--	Silicium oxide (SiO_2)	47.43
Analytical moisture, %	--	2.05	Aluminium oxide (Al_2O_3)	26.9
Volatile matter, %	25.2	27.1	Calcium oxide (CaO)	9.91
Ash (O_2+815°C), %	13.3	14.3	Iron oxide (Fe_2O_3)	4.21
Fixed C (diff.), %	52.6	56.6	Sulphur oxide (SO_3)	3.08
Ultimate analysis	**raw**	**an (< 0.1 mm)**	Phosphor oxide (P_2O_5)	1.72
Carbon (C),%	62.8	67.5	Titanium oxide (TiO_2)	1.66
Hydrogen, total ($H_{tot.}$), %	5.25	4.26	Magnesium oxide (MgO)	1.57
Hydrogen ($H_{org.}$), %	3.74	4.03	Potasiumoxide (K_2O)	0.72

739

Nitrogen (N), %	1.64	1.76	Sodium oxide (Na_2O)	0.202
Sulfur (S), mg/kg	4120	4430	Some minor elements	
Sulfur (S), %	0.41	0.44	Strontium oxide (SrO_2)	0.33
Chlor (Cl), mg/kg	< 100	< 100	Barium oxide (BaO)	0.211
Fluor (F), mg/kg	180	194	Manganese oxide (MnO_2)	0.052

After exposure time of 30 h, crucial to obtain the initial oxidation and significant in terms of fireside corrosion original primary (and secondary) deposition layer, the samples were removed from the combustion chamber of KSVA (see Fig. 3) and exposed subsequently in the laboratory corrosion test set-up at IFK for further 970 h.

Figure 3: Metal rings covered with thick deposit layer after the 30 h exposure in the combustion chamber of the KSVA test rig.

2.2.2. Long-term laboratory exposures

The laboratory corrosion test set-up at IFK consists of electrically heated furnaces connected to a gas mixing station as described in detail by Stein-Brzozowska et al. [00. The gas atmosphere for the long-term laboratory tests was defined based on the gas composition as-measured at KSVA. Composition details of both atmospheres are compared in Table 3.

Table 3: Composition of gas atmospheres used in the combustion tests in KSVA 0.5 MW test rig and in laboratory set-up.

Constituent	KSVA combustion atmosphere	IFK laboratory gas atmosphere
SO_2	0.03 %-vol., dry (300 - 370 ppm)	0.1%-vol.
O_2	2.5 %-vol., dry	4.5 %-vol.
CO_2	15.5 - 16 %-vol., dry	16 %-vol.
H_2O	7-8 %-vol.	7 %-vol.
N_2	approx. rest	73.4 %-vol. (balanced)
CO	50 - 100 - 250 ppm dry	none

It was decided to increase slightly content of certain gas constituents, compared to the gas composition from the combustion tests, in order to be able to compare the results with other on-going fireside corrosion tests. Moreover, to simulate real boiler conditions, a fresh fly ash deposit layer was spread over the samples every 250 h, however, without removal of previous deposit layers. Once per week a pure CO_2 atmosphere was set for couple of hours in order to simulate alternating reducing conditions. Chemical composition of the ash deposit after completed exposure of 1000 h (30 h in KSVA and, 970 h in laboratory test set-up) is given in Table 4.

Table 4: Composition of the fly ash deposit after completed 1000 h exposure.

Constituent	Water-free content [mass %]	Constituent	Water-free content [mass %]
Total carbon (TC)	0.093	MgO	1.44
Total organiccarbon	0.032	MnO_2	0.060
Total inorganiccarbon	0.061	Na_2O	0.232
Al_2O_3	27.1	P_2O_5	1.426
BaO	0.200	SO_3	5.38
CaO	9.47	SiO_2	48.5
Fe_2O_3	2.87	SrO_2	0.292
K_2O	0.828	TiO_2	1.64

2.3. Microstructural investigation

Completed exposure tests were followed by microstructural investigation performed at the AGH University of Science and Technology in Kraków. Light microscopy (LM, Axio Imager M1m), scanning- (SEM, Merlin Gemini II) and transmission (TEM, probe Cs corrected TITAN CubedG2 60-300 with ChemiSTEM system, Tecnai G2 20 TWIN) electron microscopy were utilized for this purpose.

The samples of the tested tubes were prepared from the approximately 30 mm long and 7 mm wide pieces, cut out of the exposed segments along their length (see Fig. 4), with the weld material and at least 15 mm of the base (tube) material incorporated. Before cutting, the deposit was carefully removed from the tube surface and stored for further analysis. Fig. 4 shows photographs of the corrosion tested specimens after removal of the loose deposit. I and O abbreviations in Fig. 4 indicate inner (I) and outer (O) tube surface, respectively. Thin, electron-transparent samples (lamellae) for TEM investigation of the scales were cut by Focused Ion Beam (FIB) NEON CrossBeam 40EsB from the O surfaces at the positions located minimum 10 mm away from the weld and at least 5 mm away from the boundary of heat affected zone (HAZ), to assure that only corrosion products of the original base material were considered in current investigation.
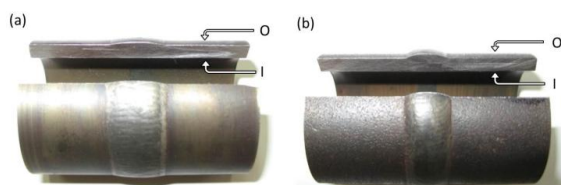
Figure 4: Photographs of the welded tubes of Sanicro 25 (a) and HR6W (b) after removal of the loose deposit and first cuts for the subsequent metallographic samples preparation.

STEM (Scanning Transmission Electron Microscopy) investigation was performed in order to characterize the scale morphology of both materials. HAADF (High-Angle Annular Dark Field) detector was used in order to obtain Z-contrast image of the materials. Chemical composition analyses of tested scales were conducted by EDS (Energy-dispersive X-ray Spectroscopy) which enabled determination of the chemical element maps of every sub-layer of the scales.

3. Results and discussion

The images of the scale-microstructure, as well as the respective chemical element maps for selected elements for Sanicro 25 and HR6W, collected using STEM-EDS are shown in Fig. 5 and Fig. 6, respectively. Oxide layers observed at the outer and the inner surface were irregular. Their thickness, measured from such images was found to vary between 200 and 300 nm. The analysis of EDS maps showed that chromium was the main element in corrosion products. So, it can be assumed that both scales consist mainly of Cr_2O_3. The Fe maps show that the scales formed at the outer tube surfaces are remarkably enriched in this element at the most outer layer of the scale. It is considered that the Fe-enrichment is associated with the initial stage of oxidation process, because at its beginning a large amount of iron oxide nuclei is formed on the alloy surfaces.
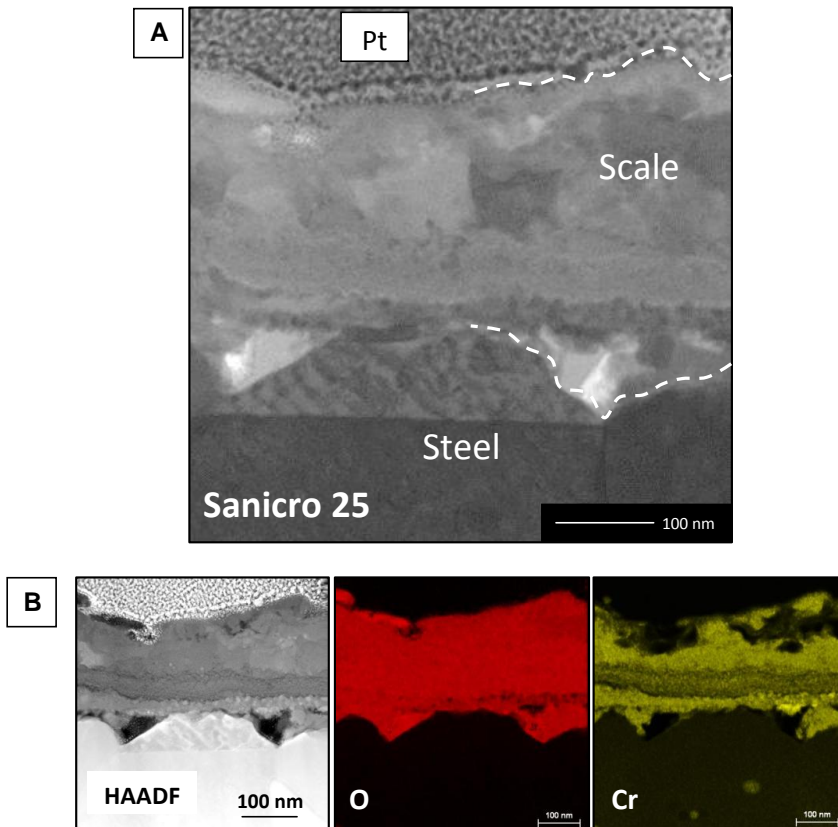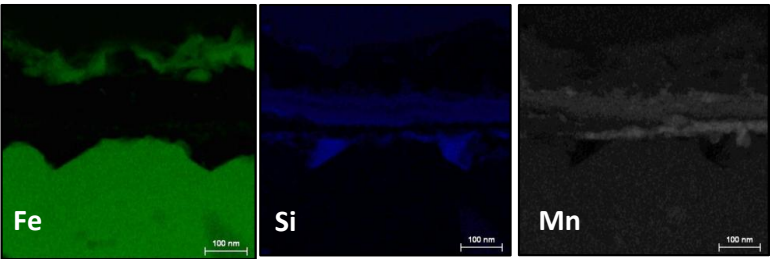
Figure 5: (A) STEM bright-field (BF) image of the scale formedat the outer surface of the Sanicro 25 tube after corrosion tests; (B) STEM-HAADF image andEDS maps for selected chemical elements.
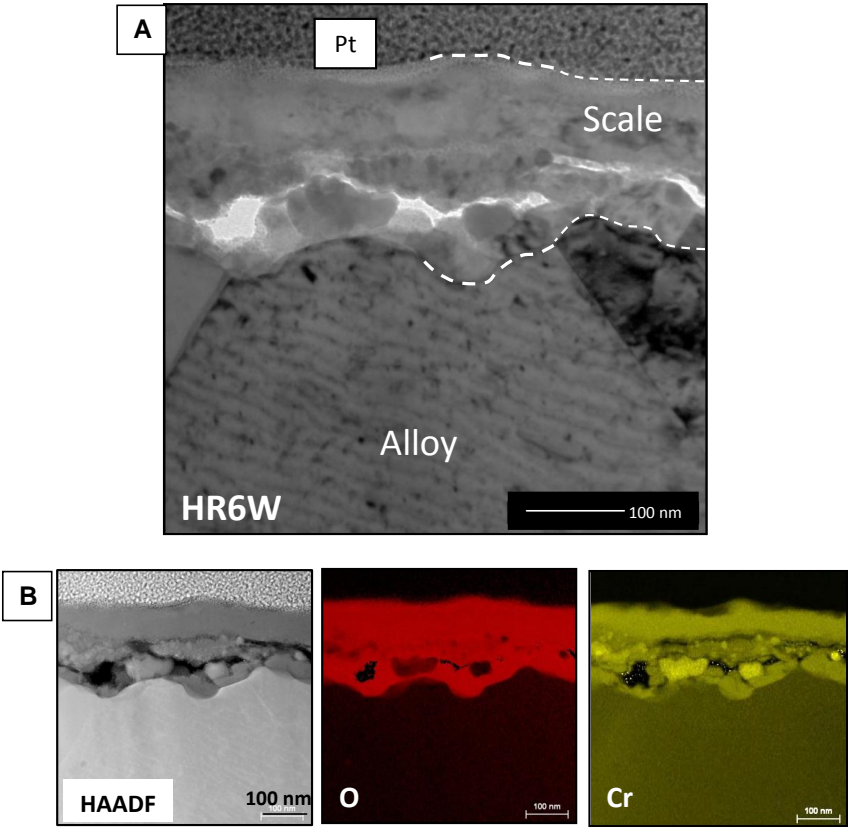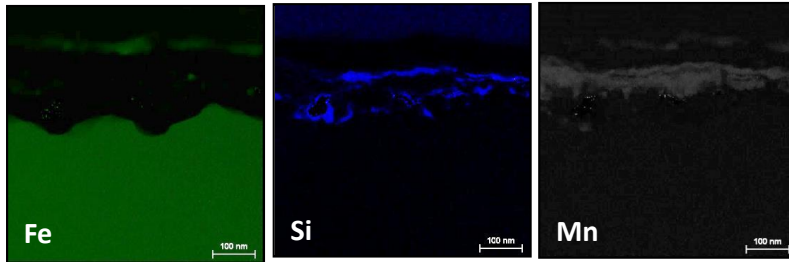
Figure 6: (A) TEM bright-field (BF) image of the scale formed at the outer surface of the HR6W tube after corrosion tests; (B) STEM-HAADF image and EDS maps for selected chemical elements.

Both alloys contain alloying elements (Si, Mn) which form the thermodynamically more stable oxides than Cr_2O_3. It was observed that these oxides precipitated mainly underneath the chromia outermost layer, forming separate sub-layers.

The result of EDS analyses did not reveal any presence of sulfur, neither within the oxide products nor in the base materials. It indicates that the scales formed on both materials in the atmosphere of aggressive exhaust gases containing SO_2 and H_2O and the ash deposit in the power plant boiler possess very good protective properties and provides an effective barrier to diffusion of sulfur.

4. Summary

Long-term real fireside corrosion testing of two candidate materials for USC/ A-USC boilers, Sanicro 25 austenitic steel and HR6W Ni-base alloy, was performed with the aid of two-step corrosion experiment combining 30 h exposure in a real combustion environment in 0.5 MW KSVA combustion test rig and 970 h in the laboratory corrosion test set-up. Selected testing temperature (650 °C) corresponds to the operation temperature of the respective superheater in the USC boiler. The microstructure of the scales was investigated in detail by advanced electron microscopy methods.

The most important results are summarized below:

- Both materials exhibited formation of very thin Cr-rich oxide scales on the outer tube surface, exposed directly to the combustion environment.
- Oxide layer grown on both materialshad a similar thickness and contained Fe-enrichment at its outer surface.
- Silicon and manganese oxides precipitated under chromia layer, forming separate sub-layers.
- The ash deposit particles, enriched in Al, Si and/or Ca, were found attached to the scale at the outer tube surface. Neither visible reaction with the scale nor their influence on the scale spallation was observed.

5. Acknowledgments

References

[1] Viswananthan R., Henry J. F., Tanzosh J., Stanko G., Shingledecker J., Vitalis B. and Purgert R., U.S. program on materials technology for ultra-supercritical coal power plants, *Journal of Materials Engineering and Performance* 14, 281-292, (2005)

[2] Ha V. T. and Jung W. S., Creep behaviour and microstructure evolution at 750 °C in a new precipitation-strengthened heat-resistant austenitic steel, *Materials Science and Engineering* A558, 103–111, (2012)

[3] Intiso L., Johansson L.-G., Canovic S., Bellini S., Svensson J.-E., Halvarsson M., Oxidation Behaviour of Sanicro 25 (42Fe22Cr25NiWCuNbN) in O_2/H_2O Mixture at 600 °C, *Oxidation of Metals* 77, 209–235, (2012)

[4] Rautio R. and Bruce S., Alloy for ultrasupercritical coal fired boilers, *Advanced Materials & Processes* 166, April, 35-37, (2008)

[5] WB 555, Warmfester austenitischer Stahl, Sanicro ® 25, *VdTÜV Merkblätter,* (2008)

[6] WB559/2, Hochwarmfeste Nickelbasislegierung HR6W Nahtloses Rohr, *VdTÜV Merkblätter* (2012)

[7] Stein-Brzozowska M., Zepf E., Maier J., Einfluss von Aschedepositionen auf die Korrosionsmechanismen an ausgewählten Überhitzerwerkstoffen unter Oxyfuel-Bedingungen, *41. KRAFTWERKSTECHNISCHES KOLLOQUIUM 2009*, Dresden, 13-14.10.2009, unpublished

Effect of Cold Work on Creep Strength of Nickel Base Alloys

Keiji Kubushiro, Kyohei Nomura, Hirokatsu Nakagawa

IHI Corporation, 1, Shin-Nakahara-Cho, Isogo-ku, Yokohama, 235-8501, Japan
(keiji_kubushiro@ihi.co.jp)

Abstract

Advanced USC (A-USC) plants, in which the steam temperature is over 700°C, have been developed. To achieve a steam temperature of over 700°C in an A-USC plant, the tubes made of Ni base alloys are necessary in addition to that made of ferritic steels and stainless steels. Materials applied to boiler tube at higher temperatures are selected by creep rupture strength, and the creep rupture strength at 100,000 hours is particularly important. Ni base alloys (HR6W, HR35, Alloy 617, Alloy 263 and Alloy 740H) are required. Because most Ni base alloys have never been applied to boiler tube, fabrication processes have to be developed. For example, the cold bent samples need to be heat treated (PBHT) after the bending process due to induced strain. In this case, the relationship between creep strength and plastic strain by bending has to be clarified. The creep strength of the candidates with plastic strain was investigated about HR6W, HR35, Alloy 617, Alloy 263 and Alloy 740H. When the pre-strain is less than 5%, Alloy 740H shows the same lifetime as one of the samples without pre-strain, but the ratio decreases to around 0.5 when the pre-strain is more than 7.5%. The test result shows the same tendency reported by some researchers and it is believed that the amount of precipitation at grain boundary changes. The lifetime ratio of Alloy 263 does not change due to pre-strain. The ratio of Alloy 617 increases with pre-strain and reaches double at 15% pre-strain. This is thought to be due to an increase of precipitation including Mo carbide at the grain boundary instead of δ phase (Ni3Mo) decreasing. The ratio of HR6W and HR35 is more than 10 when pre-strain is 5%. Increase of creep strength by pre-strain corresponds to the previous test results of austenitic stainless steels.

Keywords: A-USC, Pre-strain, Creep strength, Ni-base alloy, boiler tube

1. Introduction

In order to achieve higher thermal efficiency in thermal power systems, the steam temperature and pressure of boilers have been increased. In Japan, 600°C class USC power plants were developed in 1993, and 620°C class power plants have recently started operation. The thermal efficiency of USC power plants achieved a 2–3% improvement relative to SC power plants. 9Cr ferritic steels were first applied to thick walled pipes in Japan to realize 600°C class USC power plants [1]. Currently, 600°C class USC power plants supply half of the total energy produced by coal-fired power generation in Japan. Recently, Advanced USC (A-USC) plants, in which the steam temperature is over 700°C, have been developed [2], [3]. The steam condition of 700°C will achieve an improvement of more than 8% in thermal efficiency. To achieve a steam temperature of over 700°C in an A-USC plant, piping made of Ni base alloys is necessary in addition to that made of ferritic steels and stainless steels, which

is already in use. Materials applied to boiler piping at higher temperatures are selected by creep rupture strength, and the creep rupture strength at 100,000 hours is particularly important. Figure 1 shows the creep rupture strength at 100,000 hours of candidate materials for USC and A-USC boilers [4]–[9]. Above 650°C, materials with the higher strengths such as austenitic stainless steels, Ni base alloys (HR6W, HR35, Alloy 617, Alloy 263 and Alloy 740H) are required. Because most Ni base alloys have never been applied to boiler piping and tubes, welding and other fabrication processes have to be developed. In particular, it is very important to have an understanding of the relationship between creep strength and pre-strain when using materials, because plastic strain may be introduced in commercial manufacturing processes. Many studies have been conducted to investigate the relationship between the degree of working and creep strength for stainless steels and other materials [10] – [12]. However, few studies have been conducted to investigate the effects of pre-strain on creep strength of Ni-base alloys, so it is essential that the relationship between the pre-strain and creep strength of Ni-base alloys be studied. In this paper, it was studied the relationship between pre-strain and creep rupture strength of Ni-base alloys
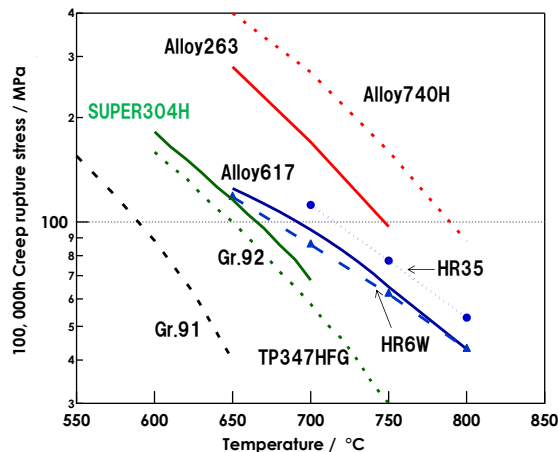
Figure 1 100,000 h creep rupture strength of boiler materials[3]

2. Experimental procedure

The chemical compositions of Alloy740, Alloy263, Alloy617, HR6W and HR35 are shown in Table1. The materials were subjected to a pre-strain of 5-15% in a room-temperature tensile test for simulating the cold work. Hereinafter, the material that was subjected to pre-strain is referred to as the pre-strained material, while the material that was not subjected to pre-strain is referred to as the non-pre-strained material. The creep rupture tests were conducted at a temperature of 750°C, the following stress (Alloy740, Alloy263 : 225MPa, Alloy617 : 180MPa, HR6W : 100MPa, HR35 : 160MPa). Microstructure of the ruptured specimens was observed by scanning electron microscope (SEM).

Table1 Chemical compositions (wt.%) of Ni-base alloys

Alloy	C	Ni	Cr	Mo	Co	Al	Ti	Nb	Si	W	Fe
Alloy740	0.03	Bal.	25	0.5	20	0.9	1.8	2	0.5	-	0.7
Alloy 263	0.06	Bal.	20	6	20	0.4	2.2	R	0.1	-	0.7
Alloy 617	0.06	Bal.	22	9	12.5	1	0.4	-	0.1	-	0.5
HR6W	0.07	45	23	-	-	-	-	-	-	7.0	Bal.
HR35	0.06	50	30	-	-	-	1.0	-	0.16	4.0	Bal.

3. Results and Discussion

3.1 Initial microstructure

Initial optical microstructures of Ni-base alloys are shown in figure 2. Alloy263, Alloy617 and Alloy740H had equiaxial grains of approximately 50μm, HR35 and HR6W had equiaxial grains of over 100μm. Vickers hardness of all alloys were under 200HV. There were no γ', laves phase in all alloys by SEM observation.
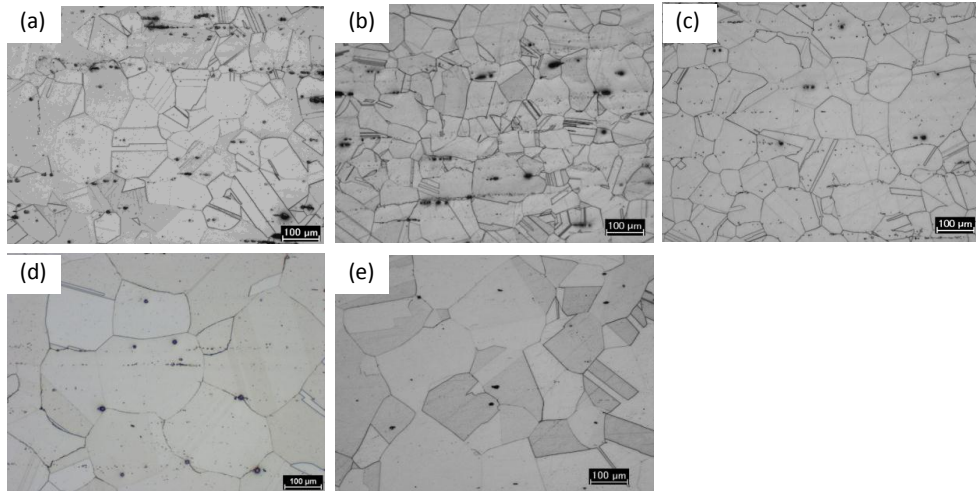
Figure 2 Initial optical microstructures of Ni-base alloy; (a) Alloy 740 (b) Alloy263 (c) Alloy617 (d) HR6W, (e) HR35

3.2 Creep rupture strength

Figure 3 shows the ratios between the life time to failure of pre-strained samples and the time to failure of samples without pre-strain. When the pre-strain is less than 5%, Alloy 740H shows the same lifetime as one of the samples without pre-strain, but the ratio decreases to around 0.5 when the pre-strain is more than 7.5%. The test result shows the same tendency reported by some researchers [8], [13] .The lifetime ratio of Alloy 263 does not change due to

748

pre-strain. The lifetime ratio of Alloy 617 increases with pre-strain and reaches double at 15% pre-strain. The life time ratio of HR6W is more than 10 when pre-strain is 5%, which corresponds to the results reported by Okada [14]. Increase of creep strength by pre-strain corresponds to the previous test results of austenitic stainless steels. The lifetime ratio of HR35 increases with an increase in the pre-strain up to 10%, above which it have almost same. Next, the discussion will focus on the difference of creep rupture strength for these alloys.
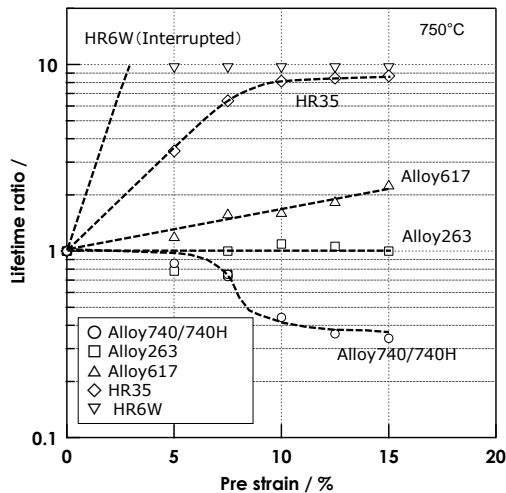
Figure 3 The effect of pre-strain on the creep rupture strength of Ni-base alloys

3.3 Alloy 740H

Figure 4 shows the results of observations conducted to examine the structure of the grain boundaries for Alloy740. The grain boundaries of the non-pre-strained alloy were almost entirely covered with precipitates. The grain boundaries of the pre-strained alloy, however, had many areas where no precipitates were found. Energy dispersive x-ray (EDX) analysis revealed that the precipitates at the grain boundaries were composed of Cr carbides and Nb carbides. Figure 5 shows the EDX analysis of intragranular precipitates for the non-pre-strained alloy. There were fine Cr carbides in the grain. The reason why precipitates on the grain boundary of the pre-strained alloy are lower than that of the non-pre-strained alloy is that the precipitation on dislocations in the pre-strained alloy only was occurred.

749
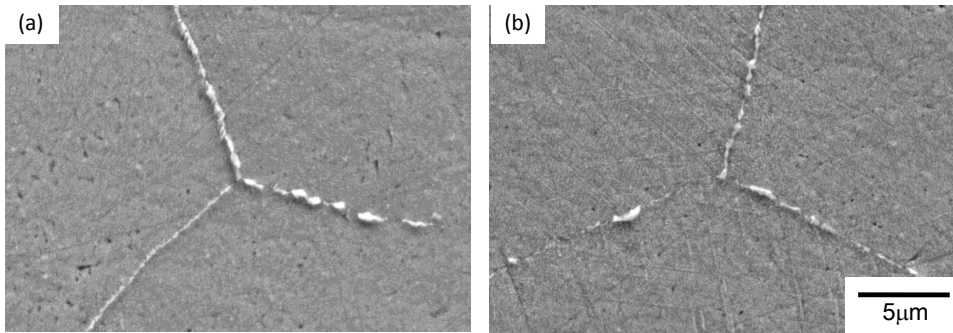
Figure 4 SEM images on the grain boundaries
(a) Non-pre-strained alloy, (b) pre-strained alloy
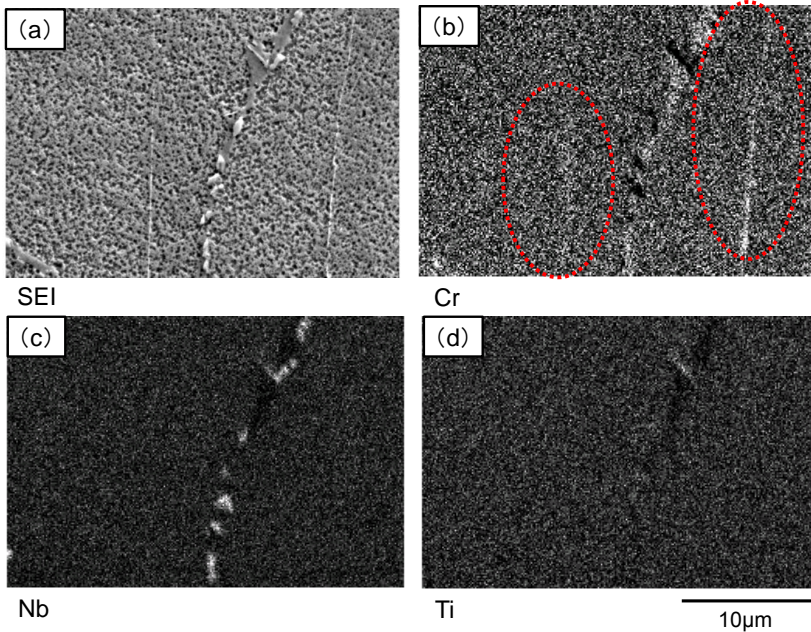
Figure 5 Results of EDX analysis for pre-strained alloy
(a) SEI, (b)Cr mapping (c) Nb mapping (d) Ti mapping

3.4 Allo263

 SEM results of ruptured specimens in Alloy263 are shown in figure 6. (a), (b) and (c) show the microstructure in the grain, (d), (e) and (f) show the microstructure around the grain boundary. There were many γ' in the grain, the volume fractions of γ' were almost constant with pre-strain. The precipitates on the grain boundary were almost constant with pre-strain too.
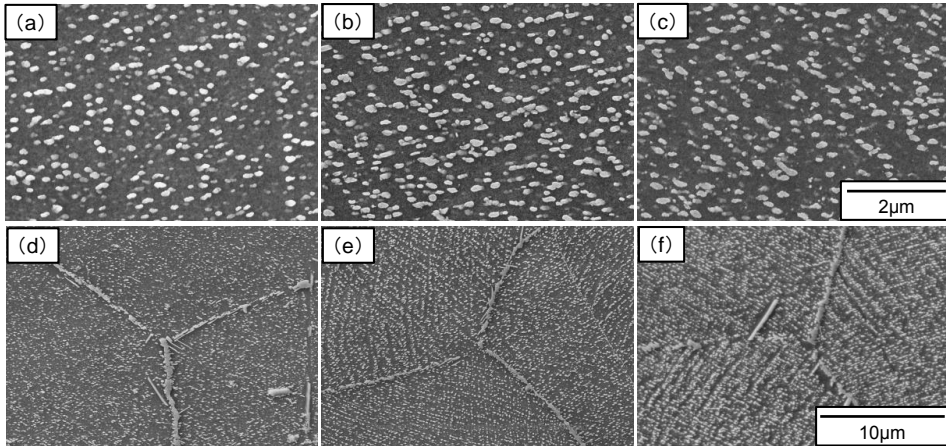
Figure 6 SEM images of ruptured specimens for Alloy 263
(a), (d) Non-pre-strained alloy, (b),(e)7.5% pre-strained alloy, (c), (f)15% pre-strained alloy

3.5 Alloy617

BEI of ruptured specimens in Alloy 617 with various pre-strain are shown in figure 7. The white precipitates seem to be Mo Carbides and δ phases, the gray precipitates are Cr carbides, the black precipitates are γ'. There were δ phases near the grain boundary in the only non-pre-strained alloy, Mo Carbides on the grain boundary increased with an increase in the pre-strain. γ' phases in the grain were almost constant with pre-strain. The grain boundary shielding ratio by precipitates increased with an increase in the pre-strain because of Mo carbides.
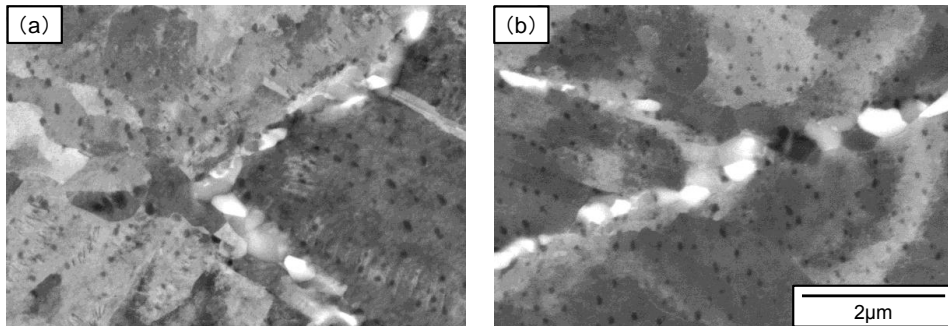
Figure 7 BEI of ruptured specimens for Alloy617
(a) Non-pre-strained alloy, (b)7.5% pre-strained alloy

751

3.6 The relationship between creep rupture strength and precipitates on the grain boundary for Ni-base alloy

The difference of precipitates on the grain boundary with pre-strain had been investigated. Next the relationship between creep rupture strength and precipitates on the grain boundary for Ni-base alloy are discussed. Figure 8 summarizes the result of the grain boundary shielding ratio by precipitates for three alloys and figure 9 illustrates the view showing a frame format of precipitates without γ'. The grain boundary shielding ratio by precipitates for Alloy740H decreased with an increase of the pre-strain. However, the grain boundary shielding ratio by precipitates for Alloy263 was constant with pre-strain. the grain boundary shielding ratio by precipitates for Alloy617 increased with an increase of the pre-strain. These results are consistent with the changing of creep rupture strength. The reason why the grain boundary shielding ratio by precipitates for Alloy740H decreased with an increase of the pre-strain is that C contents of Alloy740 H is lower than that of other alloys.
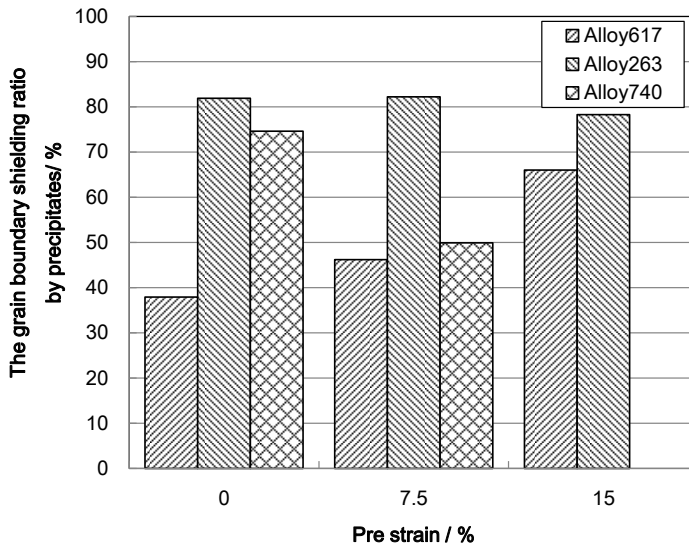
Figure 8 The result of the grain boundary shielding ratio by precipitates for three alloys

	Alloy617	Alloy263	Alloy740H
Non-pre-strained alloy			
Pre-strained alloy			
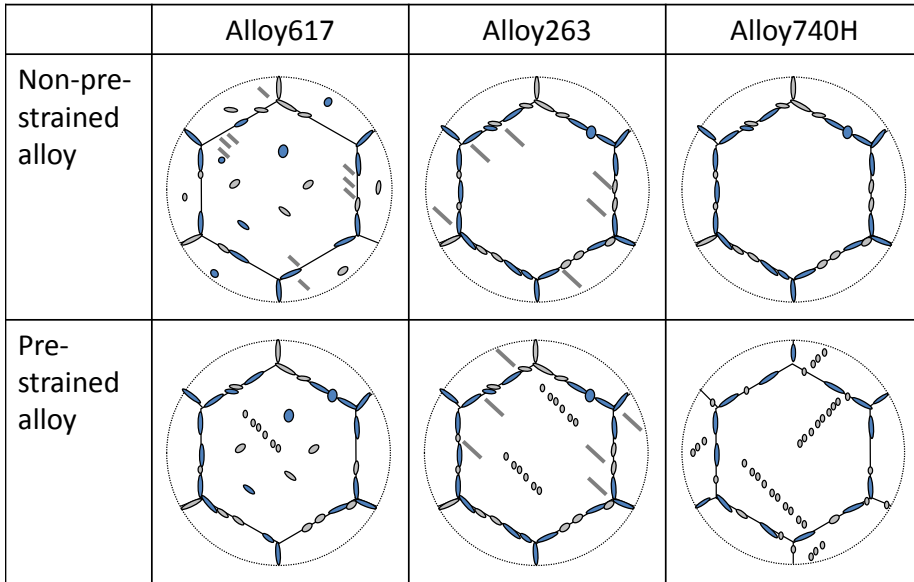
Figure 9 The view showing a frame format of precipitates without γ' for three alloys

4. Conclusion

The relationship between pre-strain and creep rupture strength of Ni-base alloy have been investigated. Our conclusions are as follows.

1. When the pre-strain is less than 5%, Alloy 740H shows the same lifetime as one of the samples without pre-strain, but the ratio decreases to around 0.5 when the pre-strain is more than 7.5%.
2. The lifetime ratio of Alloy 263 does not change due to pre-strain.
3. The lifetime ratio of Alloy 617 increases with pre-strain and reaches double at 15% pre-strain.
4. The life time ratio of HR6W is more than 10 when pre-strain is 5%.
5. The lifetime ratio of HR35 increases with an increase in the pre-strain up to 10%, above which it have almost same.
6. The changing of grain boundary shielding ratio by precipitates for Alloy617, Alloy263 and Alloy740H are consistent with the changing of creep rupture strength.

Reference

[1] H. Umaki, I. Kajigaya, T. Kunihiro, T. Totsuka, M. Nakashiro and R. Kume "Application of Large Diameter Steam Welded and Header of Super 9Cr Steel for 700MW Coal-Fired Boiler with 593C Reheat Steam Temperature"Ishikawajima-Harima Engineering Review, Vol. 31, No. 5, pp. 339 (1991)
[2] http://www.enecho.meti.go.jp/policy/coolearth_energy/coolearth-hontai.pdf

[3] K.Kubushiro, T. Matsuoka, Y. Ohkuma, H. Nakagawa, H. Aoki., "DEVELOPMENT OF WELDING AND FABRICATION TECHNOLOGIES IN ADVANCED USC BOILER" Advances in Materials Technology for Fossil Power Plants: Proceedings from the Seventh International Conference(2013)

[4] H. Semba, H. Okada, M. Igarashi and M. Yoshizawa., "Development of Fe-Ni and Ni-base alloys without γ' strengthening for advanced USC boilers" Proceedings of the 9th Liege Conference (2010)

[5] http://www.meti.go.jp/meti_lib/report/2012fy/E002041.pdf

[6] http://www.smst-tubes.com/en/products-services/downloads/technical-datasheets/

[7] http://www.specialmetals.com/documents/Nimonic%20alloy%20263.pdf

[8] http://www.specialmetals.com/documents/Inconel%20alloy%20740.pdf

[9] J.P. Shingledecker and G.M. Pharr., "Testing and Analysis of Full-Scale Creep-Rupture Experiments on Inconel Alloy 740 Cold-Formed Tubing" Journal of Materials Engineering and Performance, Vol.22, pp.454, (2012)

[10] T. Furuta, Y. Ogawa, R. Nagasaki, "The Effect of Cold Working on Creep Properties of 316 Stainless Steel Used as a Fuel Cladding in Fast Breeder Reactors " Tetsu- to- Hagane Vol.59, p.949 (1973)

[11] K. Ogawa, M. Ishii, H. Yoshizawa, S. Dote, T. Wada., "Pre-Strain Effect on the Elevated Temperature Mechanical Properties of Type 304 Stainless Steel " Journal of the Society of Materials Science, Japan Vol.35, pp.1284, (1986)

[12] F.Masuyama., "Cold Work Effect on Creep Rupture Strength of Austenitic Boiler steels" Proceedings of CREEP8, CREEP2007-26469, San Antonio, Texas (2007)

[13] K. Kubushiro, K. Nomura, S. Takahashi, M. Takahashi and H. Nakagawa., "Effect of Pre-strain on Creep Properties of Alloy 740" Advances in Materials Technology for Fossil Power Plants Proceedings from the Sixth International Conference (2010)

[14] H. Okada, H. Semba, S. Ishikawa, M. Yoshizawa., "Effect of Cold Working on Creep Properties of a 23Cr-45Ni-7W Alloy" CAMP-ISIJ, Vol. 25, pp.405 (2012)

HIGH TEMPERATURE CORROSION RESISTANCE OF METALLIC MATERIALS IN HARSH CONDITIONS

Novello F.[1], Dedry O.[2], De Noose V.[1], Lecomte-Beckers J.[2]

[1] CRM Centre for Research in Metallurgy (frederic.novello@crmgroup.be)
[2] ULg University of Liege (Jacqueline.Lecomte@ulg.ac.be)

Abstract

Highly efficient energy recovery from renewable sources and from waste incineration causes new problems of corrosion at high temperature. A similar situation exists for new recycling processes and new energy storage units. These corrosions are generally considered to be caused by ashes or molten salts, the composition of which differs considerably from one plant to another. Therefore, for the assessment of corrosion-resistance of advanced materials, it is essential to precisely evaluate the corrosion rate under conditions close to industrial conditions. To be able to advise their customers in selecting the right material or the right protective coating, the present authors are developing testing equipment and related procedures to assess the high temperature corrosion rate of metallic materials. This paper describes the testing equipment developed so far and presents the first results obtained in two corrosive environments: the aggressive condensates that affect waste incinerators (mixture of liquid/solid salts in oxidising conditions) and heat transfer fluids of electric power generating plants based on solar towers (mixture of liquid salts). Temperatures range from 400 to 650°C. Tested materials include 16Mo3 (0.3% molybdenum steel alloy), Inconel 625 (austenitic nickel-chromium-based superalloys), Nickel 200, Ni-57CrMoSiB (nickel-base coating with high chromium content and boron as additional element) and Grade 91 (9% chrome- 1% molybdenum steel alloy).

Keywords: High temperature corrosion testing, Waste incinerator, Solar salt, 16Mo3, Inconel 625, Nickel 200, Ni-57CrMoSiB, Grade 91

1. Introduction

Highly efficient energy recovery from renewable sources and from waste incineration causes new problems of corrosion at high temperature. A similar situation exists for new recycling processes and new energy storage units. These corrosions are generally considered to be caused by ashes or molten salts, the composition of which differs considerably from one plant to another.

High-temperature corrosion in waste incinerators has been widely studied [1-4] as a lot of plants suffered from wall thinning due to corrosion. In these waste to energy plants, the temperature is generally kept low (around 450°C) to avoid corrosion problems [2, 3]. Persson et al. studied high temperature corrosion in a 65 MW waste to energy plant [2]. They observed that the corrosion rate increased when extra chlorine was added to the fuel mix and extensive corrosion losses were found, even at low temperature materials (320 to 460°C). Phongphiphat et al. studied the high-temperature corrosion in a large scale municipal waste-to-energy plant [3]. They found that both temperature and deposits greatly influenced

corrosion rates. Ni-based alloy had lower corrosion rates than Fe-based alloy but they were more prone to localised corrosion.

Molten salts are already used in concentrated solar power (CSP) plants and studies have been conducted on the corrosion of metals in these salts [5-9]. For example, Fernandez et al. studied the corrosion of stainless steels and low-Cr steel at 390 and 550°C in solar salt [5]. They discuss the changes that occur in steels and solar salt after test. McConohy et al. evaluated thermophysical property changes and corrosion of nickel alloys at 600 and 680°C [6]. The authors conducted experiments on the metals and salt mixtures and found that the high operating temperatures of CSP plants result in physical and chemical changes. Gill et al presented the design of their molten salt corrosion test vessel [8]. Their vessel can work at temperatures up to 700°C.

Corrosion and the accompanying diffusion of impurities induce measurable changes in the properties of the material and the deterioration of the function of the technical systems [10-11]. Therefore, for the assessment of corrosion-resistance of advanced materials, it is essential to evaluate precisely the corrosion rate under conditions close to industrial conditions. To be able to advise their customers in selecting the right material or the right protective coating, the present authors are developing testing equipment and related procedures to assess the high temperature corrosion rate of metallic materials.

Two versatile equipment were designed to simulate environments mainly encountered in practice at high temperature.

The first one makes it possible to test samples in specific gaseous atmosphere or to combine the action of molten salt with the interaction of gaseous chemical elements.

The second type consist in a set of small reactors that enable to carry out a great number of tests under a large variety of testing conditions simultaneously, provided temperature is the same.

This paper describes the testing equipment developed so far and presents the first results obtained in two corrosive environments: the aggressive condensates that affect waste incinerators (mixture of liquid/solid salts in oxidising conditions) and heat transfer fluids of electric power generating plants based on solar towers (mixture of liquid salts).

2. Horizontal tubular furnace with controlled atmosphere

2.1 High temperature testing equipment

The testing equipment makes it possible to test samples in specific gaseous atmosphere or to combine the action of molten salt with the interaction of gaseous chemical elements. It

consists in a commercial tubular furnace through which a gas mixture with a controlled chemical composition flows (Figure 1). The design and the construction of the gas blending installation were achieved by the Industrial Solutions Unit of CRM.

The furnace can operate up to 1500°C. It has a heated length of 300 mm divided into three zones each with its own temperature controller to improve uniformity. The worktube has an inner diameter of 50 mm and a length of 1500 mm, which reduces the temperature of both ends of the tube and makes it possible to attach gas tight end seals. The temperature of the tube is monitored throughout its length by 10 thermocouples protected by an Inconel liner. In this way, the temperature of the samples can be determined accurately.

Figure 1: Tubular furnace and instrumentation

The gas blending installation is made of 4 mass flow controllers that enable to fine tune the composition and the flow rate of the mixtures to be injected into the furnace (Figure 2). If necessary, atmosphere can be humidified by a direct injection of water into the hot area of the furnace. Corrosion of the gas supply line is thus prevented by this separate injection.
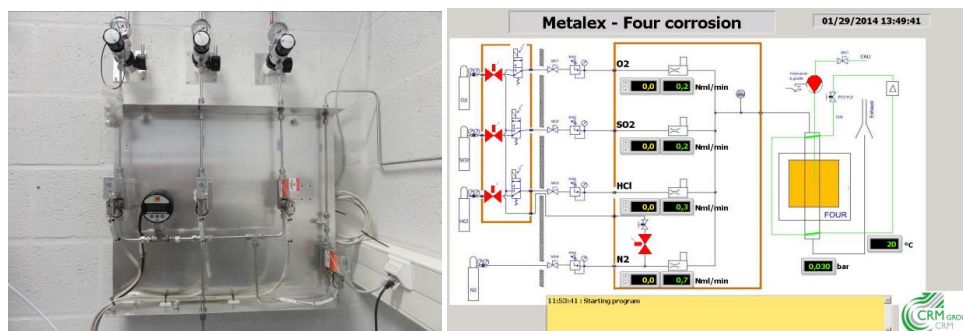
Figure 2: Gas blending installation

The complete installation is computer controlled through a graphic interface. It provides an automatic management of the temperature profile inside the furnace, the blending of gas and of security systems.

2.2 Trials in waste incinerator conditions

The tubular furnace was used to simulate the environment of the second path of the system that recovers the heat contained in the flue gases of a waste incinerator.

Table 1 summarizes the flue gas composition which is mainly made of nitrogen, water, carbon dioxide, oxygen and non-negligible amounts of hydrochloric acid and sulphur dioxide. The flow rate was adjusted so that the gas speed in the hottest area of the furnace was of 0.5 cm/s.

H_2O	18 %vol
O_2	8 %vol
HCl	1000 or 1500 mg/Nm³
SO_2	150 or 300 mg/Nm³
N_2	Balance

Table 1: Gas composition

To test the samples under conditions that are most similar to real operating conditions, some of them were covered with ashes (Figure 3) taken from a municipal waste incinerator. A simplified chemical composition of ashes is given in Table 2.

Step 1 : Establishing of a salt bath	Step 2 : Installation of the samples	Step 3 : Covering of the samples
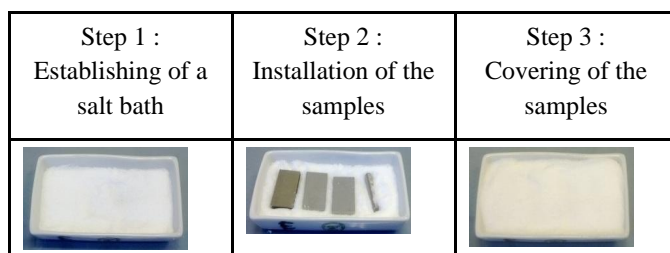
Figure 3: Establishment of the corrosion environment

	Al	Si	S	Cl	K	Ca	Zn	Pb
% wt.	1.1	2.9	8.2	3.6	4.1	27.9	2.6	0.5

Table 2: Ash composition

Three metallic alloys (Table 3) were subjected to the tests: 16Mo3, which is a carbon steel with improved creep resistance, Inconel 625, which is a nickel-based alloy increasingly used in waste incinerators and Nickel 200, which is an almost pure nickel grade.

	Fe	Ni	Cr	Mo	Autres
16Mo3	>98%	/	<0.3	0.25-0.35	Si, Mn, Cu, C
Inconel 625	<5	>58	20-23	8-10	Nb+Ta : 3.8-4.15
Nickel		≈99%			

Table 3: Metallic grade composition

The test plan described in Table 4 was undertaken to determine the influence of the amount of hydrochloric acid, of the amount of sulphur dioxide and of the presence of ashes on metallic wall corrosion.

	Trial nr. 1	Trial nr. 2	Trial nr. 3
[HCl] (mg/Nm³)	1000	1500	1500
[SO$_2$] (mg/Nm³)	150	300	300
Ashes	No	No	Yes
Temperature	450°C	450°C	450°C
Duration	200h	200h	200h

Table 4: Experimental plan

The results (Figure 4 and Table 5) indicate that Inconel 625 is not corroded whatever testing conditions.

Nickel 200 is slightly corroded (< 6µm/y).
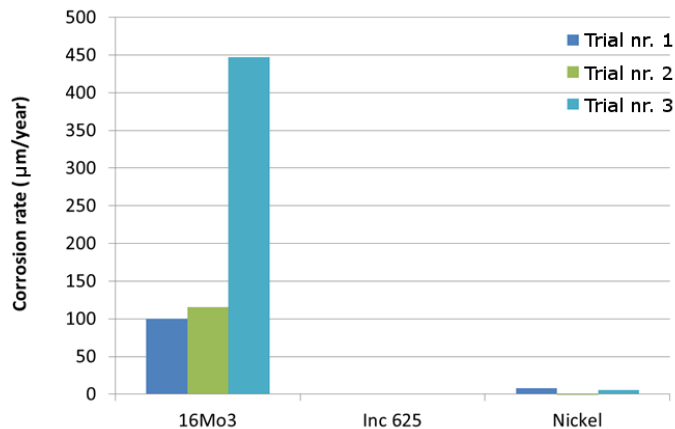
Figure 4: Corrosion rate (µm/y) based on the average mass loss of 3 samples

However, 16Mo3 is more corroded. For low levels of hydrochloric acid and sulphur dioxide, the corrosion rate is about 100 µm/y. For higher levels, a corrosion rate increase of 10% is

recorded. The presence of ashes considerably increases the corrosion rate to a value of 450 µm/y. This is confirmed by photographs of the sample after testing (Figure 5).

	Trial nr. 1	Trial nr. 2	Trial nr. 3
16Mo3	100 ± 14	115 ± 6	447 ± 195
Inc 625	0.3 ± 0.1	1 ± 1	1 ± 1
Nickel	8 ± 1	3 ± 1	5 ± 1

Table 5: Corrosion rate (µm/y) based on the average mass loss of 3 samples

Metallographic examinations of cross sections through 16Mo3 samples (Figure 6) reveal that the thicknesses of oxidation products are in a good accordance with the corrosion rate determined from mass loss measurements: Trial nr. 1 (~4 µm) < Trial nr. 2 (~7 µm) < Trial nr. 3 (~20 µm). Evidences of chloridation are clearly visible in the oxide layer of the sample covered with ashes (Trial nr.3). Indeed, it is made of several layers that have teeth oriented towards the metallic interface.
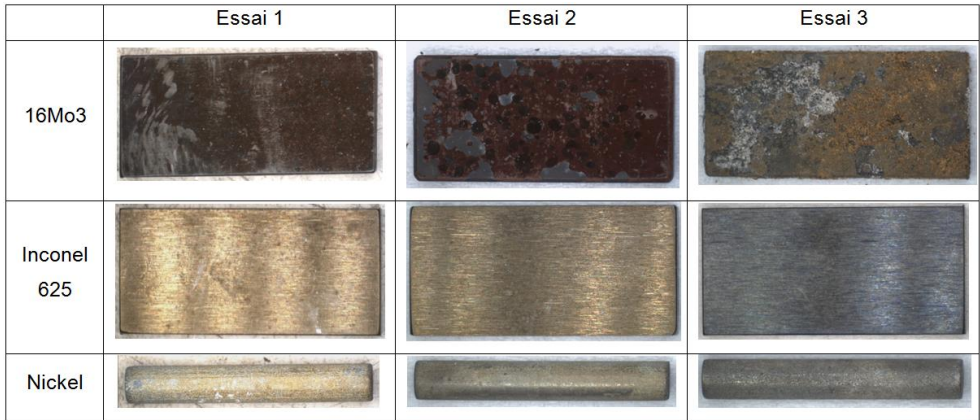
Figure 5 : Samples after trials
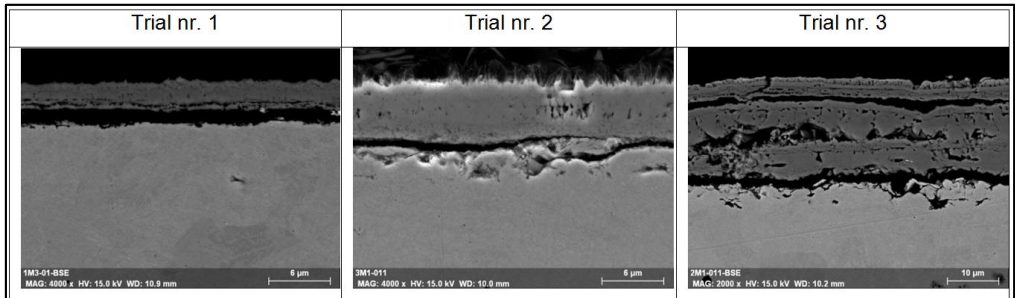
Figure 6: Metallographic cross sections of 16Mo3 samples

3. Tight reactors

2.1 High temperature testing equipment

Equipment described hereunder is devoted to corrosion tests in molten salt when gaseous chemical elements in the atmosphere do not interfere with the corrosion of immerged samples. It can also be used to test samples in the vapour phase due to salt volatilization. Two types of tight reactors are being developed in CRM. The first ones, which allow testing a large number of samples at the same time in a reduced volume of space, are made of quartz ampoules (Figure 7). They can withstand high temperatures (up to 1000°C) and a pressure of 5 bar.
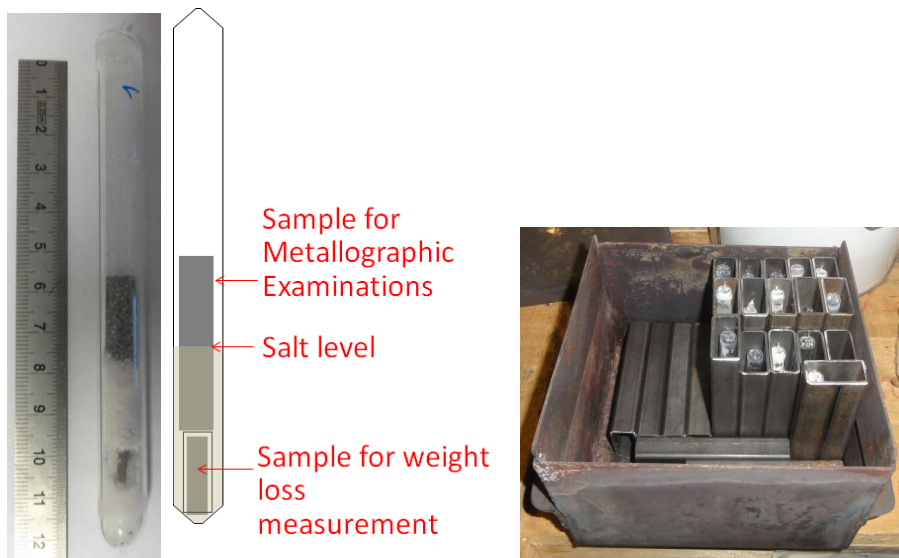
Figure 7: Quartz ampoules

For higher pressures or when quartz is not corrosion resistant, a tight metallic reactor, inside which a ceramic crucible is inserted to hold samples to test and salts (Figure 8), was designed. The pressure can rise up to 40 bar at 700°C.
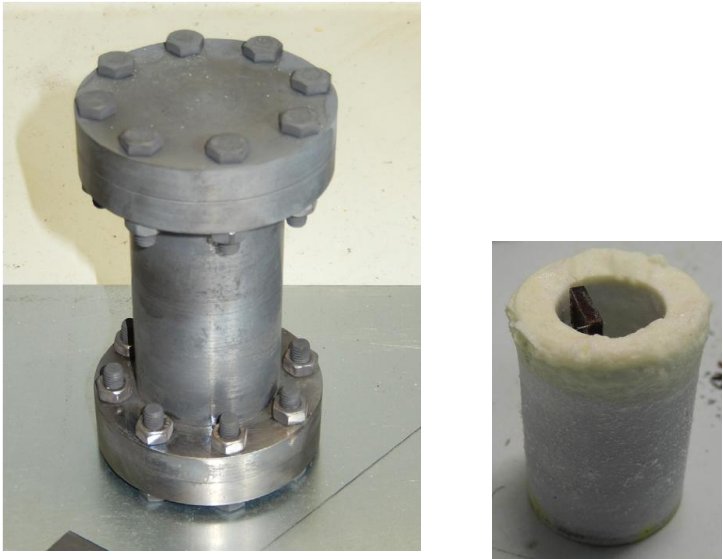
Figure 8: Tight metallic reactor and ceramic crucible

3.2 Trials in molten salt heat storage conditions

Tight reactors were used to determine the corrosion of ASTM P91 grade (Table 6) when subjected to nitrate and nitrite molten salts at 400°C. Molten salts are used as heat transfer fluids and for thermal energy storage in solar power plants.

	C	Cr	Mo	V	Nb
ASTM A335 Grade P91	0.1%	9%	1%	0.2	0.08

Table 6: Chemical composition of grade P91

Tests concern two commercially available salts. Binary mixture of sodium and potassium nitrate (Solar salt) and ternary mixture of potassium nitrate, sodium nitrate and sodium nitrite (Hitec). The influence of humidity and chlorides, which are unavoidable in industrial salt grades, was also observed. Testing conditions are summarised in Table 7.

Steel	Grade 91	
Temperature	400°C	
Salts	Salt 1 – Solar salt	NaNO3 60% wt., KNO3 40%
	Salt 2 – Hitec	NaNO3 7% wt., KNO3 53%, NaNO2 40%
Impurities	Water	0% wt., 0.5% and 1.5 %
	Chlorides	0% wt., 1.65 %
Durations	100, 500 and 1000 h	

Tableau 7: Testing conditions

At 400°C, results show that uniform corrosion rates, obtained by mass loss measurements, are less than 25 μm/y. Moreover, corrosion rates decrease during the first thousand hours to

stabilise at a low value of about 15 µm/y. Chlorides content and water do not seem to have an influence on uniform corrosion. However, some pits have been detected on samples exposed to 1.65% wt. of chlorides. Further tests should be made to confirm that pitting really occurs.
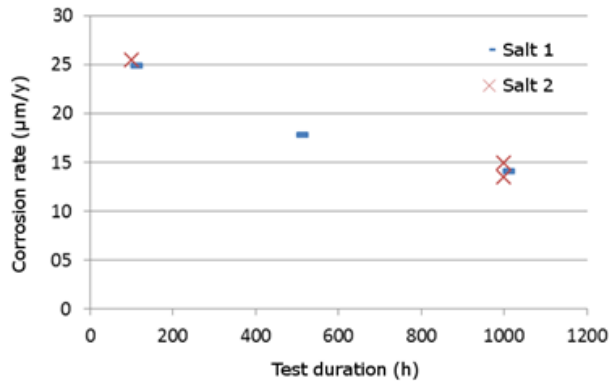
Figure 9: Corrosion rate versus test duration at 400°C

Furthermore, it seems that corrosion is more active in the vapour phase than in the liquid phase. Even if this needs to be confirmed, it would mean that special care should be given to the upper part of the storage tank which is in contact with the salt vapours.

Figure 10: Sample partially immerged in the salt

4. Synthesis

Two versatile equipment were designed to simulate environments mainly encountered in practice at high temperature:

- A tubular furnace through which a gas with a controlled chemical composition flows. It makes it possible to test samples in specific gaseous atmosphere or to combine the action of molten salt with the interaction of gaseous chemical elements.

- A set of tight reactors able to work at high temperature and pressure. They enable to carry out a great number of tests under a large variety of testing conditions simultaneously provided temperature is the same.

They were used to simulate two corrosive environments: aggressive condensates which affect waste incinerators (mixture of liquid/solid salts in oxidising conditions) and heat transfer fluids of electric power generating plants based on solar towers (mixture of liquid salts).

5. Acknowledgment

6. References

[1]   Flemming Jappe Frandsen, *Utilizing biomass and waste for power production – a decade of contributing to the understanding, interpretation and analysis of deposits and corrosion products*, Fuel 84 (2005) 1277-1294

[2]   K. Persson, M. Broström, J. Carlsson, A. Nordin, R. Backman, *High temperature corrosion in a 65 MW waste to energy plant*, Fuel Processing Technology 88 (2007) 1178-1182

[3]   A. Phongphiphat, C. Ryu, Y.B. Yang, K.N. Finney, A. Leyland, V.N. Sharifi, J. Swithenbank, *Investigation into high-temperature corrosion in a large-scale municipal waste-to-energy plant*, Corrosion Science 52 (2010) 3861-3874

[4]   Nobuo Otsuka, *A thermodynamic approach on vapor-condensation of corrosive salts from flue gas on boiler tubes in waste incinerators*, Corrosion Science 50 (2008) 1627-1636

[5]   A. G. Fernandez, M. I. Lasanta, F. J. Perez, *Molten Salt Corrosion of Stainless Steels and Low-Cr Steel in CSP Plants*, Oxidation of Metals, **78** (2012), 329-348

[6]   Geoff McConohy, Alan Kruizenga, *Molten nitrate salts at 600 and 680°C: Thermophysical property changes and corrosion of high-temperature nickel alloys*, Solar Energy, **103** (2014), 242-252.

[7]   A. M. Kruizenga, D. D. Gill, M. LaFord, *Materials Corrosion of High Temperature Alloys Immersed in 600°C Binary Nitrate Salt*, Sandia Report, March 2013

[8]   D. D. Gill, N. P. Siegel, R. W. Bradshaw, C. K. Ho, *Design, fabrication and testing of an apparatus for material compatibility testing in nitrate salts at temperatures up to 700°C*, ES2011, 2011

[9]   S.H. Goods and R.W. Bradshaw, *Corrosion of Stainless Steels and Carbon Steel by Molten Mixtures of Commercial Nitrate Salts*, Journal of Materials Engineering and Performance, 13 (1), 78-87, 2004

[10] Roger Abang, Alexander Findeisen, Hans Joachim Krautz, *Corrosion behaviour of selected power plant materials under oxyfuel power plant materials under oxyfuel combustion conditions*, Górnictwo i Geoinżynieria, **35** (2011), 23-42.

[11] Normenausschuss Materialprüfung (NMP) im Deutschen Institut für Normung e.V.: DIN EN ISO 8044 Korrosion von Metallen und Legierungen - Grundbegriffe und Definition Beuth Verlag Berlin 1999

[12]   Thomas Bauer, Nicole Pfleger, Doerte Laing, Wolf-Dieter Steinmann, Markus Eck, Stefanie Kaesche, *20 High-Temperature Molten Salts for Solar Power Application*, in "Molten Salts Chemistry", F. Lantelme and H. Groult eds, Elsevier, 2013.

Part F

Materials for Advanced Nuclear Power Plants

MATERIALS FOR ADVANCED NUCLEAR POWER PLANTS

Scibetta M., Konstantinovic M., Malerba L., Gavrilov S.
SCK-CEN, NMS, Mol (mscibett@sckcen.be)

Abstract

Advanced nuclear power plants are a sustainable option for the growing energy needs in a low carbon economy perspective. The move from a conceptual design to an actual nuclear power plant, heavily rely on materials which can be subjected to high neutron flux that can enhance material degradation in a way that is unique to nuclear systems. The methodology used to address nuclear materials issues for innovative reactors is illustrated with practical examples. In particular, the fitness for purpose of the T91 ferritic/martensitic alloy for the MYRRHA accelerator driven system research reactor is investigated. Examples of microstructure examinations used in support to modelling and phenomena understanding are given. The success of atomistic scale models to support the understanding of irradiation effect on Fe-Cr alloys is also illustrated in this paper.

Keywords: Nuclear material, GEN IV, MYRRHA, fusion

1   Introduction

Advanced nuclear power plants are a sustainable option for the growing energy needs in a low carbon economy perspective. Generation IV fission reactor concepts were selected to fulfill sustainability, economics, safety, reliability, waste reduction, proliferation resistance and physical protection requirements [1]. On the other hand, fusion power plants are envisaged after ITER as a long term sustainable option that does not produce transuranic and fission product wastes [2].

In contrast with the early nuclear era, the development of new nuclear concepts is a presently slow process, due to very stringent licensing requirements, the limited applicability of current nuclear codes, the demanding operating conditions and the lack of return of experience from operating Generation IV reactors. In this perspective, the qualification of structural material is a cornerstone to advanced nuclear development. This is acknowledged within the European Energy Research Alliance (EERA) by dedicating a Joint Program to Nuclear Material (JPNM) [3].

Nuclear materials can be subjected to high neutron flux that can enhance material degradation in a way that is unique to nuclear power plants. In particular, neutron irradiation can substantially affect ageing, and induce hardening, embrittlement, swelling and creep, as well as exacerbate the consequences of fatigue and material interaction with the chemical environment (e.g. corrosion, erosion…).

Materials need to be well characterized by specific experiments that are demonstrated to be representative of in service conditions. This is extremely challenging as advanced nuclear power plants are not yet in operation. Therefore, the physical understanding of the above mentioned effects, based on both modelling and advanced experimental characterization, is of prime importance to design test programs that will be useful in a licensing perspective and to justify the transferability from laboratory conditions to service conditions.

The activities within the EERA JPNM are divided in six subprograms [3]: prototypes (SP1), advanced steels (SP2), refractory materials (SP3), modeling of structural material (SP4), advance fuel (SP5) and modelling of fuel (SP6). Among those subprograms, this paper will concentrates on SP1, SP2 and SP4. SP1 focuses on demonstrators and prototypes supported by the European Sustainable Nuclear Industrial Initiative (ESNII). ESNII is in fact one of the three pillar supporting the Sustainable Nuclear Energy Technology Platform (SNETP) [4]. Although early (advanced nuclear power plant) demonstrators will be based on commercially available materials, their qualification in demanding conditions remains an important challenge. In this paper, the particular aspect of the MYRRHA reactor will be analysed. Amongst the materials included in SP1 are ferritic/martensitic steels with high-chromium content, that are candidate structural materials for Gen IV and fusion reactors, because of their potential to be used at high temperature, with better thermal properties and less radiation-induced swelling than austenitic steels. SP2 deals with improving the high temperature resistance of this class of otherwise already existing steels. SP4 is a cross cutting activity with the focus on modelling and experimental validation for structural materials, mainly steels.

2   Myrrha

MYRRHA, a flexible fast spectrum research reactor (50-100 MWth) is conceived as an accelerator driven system (ADS), able to operate in sub-critical and critical modes [5]. It contains a proton accelerator of 600 MeV, a spallation target and a multiplying core with MOX fuel, cooled by liquid lead-bismuth (Pb-Bi).

The deployment of innovative nuclear systems including MYRRHA ADS system relies primarily upon the availability of structural materials able to withstand their harsh operation conditions, in particular with respect to the material compatibility with the coolant under intense irradiation. The materials selection and qualification are critical issues for successful development of such nuclear systems.

The selection of structural materials is partly driven by their intrinsic properties. In particular the response of the material to the thermo-mechanical loading conditions, the coolant-material interactions, the irradiation and the synergetic effects of all previously mentioned degradation mechanisms. Therefore, it is important to be able to appropriately characterize these materials. However, the behavior of materials under operation conditions of innovative nuclear systems is not appropriately covered by the available testing and evaluation standards requiring updates of existing standard procedures and sometimes development of new ones. Today, individual laboratories rely on their own experience and on experimental and irradiation facilities available to them. Although it is possible to extract helpful qualitative information, it is difficult to interpret the various data quantitatively.

The three major material degradation effects that have been identified so far for nuclear systems with lead-bismuth coolant and for MYRRHA in particular are liquid metal corrosion, liquid metal embrittlement and irradiation effects.

2.1   *Liquid Metal Corrosion (LMC)*

Liquid Metal Corrosion (LMC) of steels in Lead-Bismuth Eutectic (LBE) might result in formation of protective oxide layers on the steel surface and retarding further corrosion due to slowing down the mass transport between material and environment. High enough dissolved oxygen concentration in LBE and moderate temperatures are necessary but not

sufficient conditions. Low oxygen concentration or high temperatures might result in the dissolution corrosion due to imperfect oxide layer. High flow rate and inhomogeneity of flow might lead to erosion corrosion and significant material losses.

The parameters influencing LMC have been identified as the following:

- Material: Chemical composition and homogeneity; special attention to elements that either help to create thin and dense oxide protective layer (Cr, Si, Al, etc.) or those which might cause severe dissolution due to high solubility in LBE (Ni, Mn); Microstructure (grain size, impurities, etc.);
- Environment: Temperature; Concentration of dissolved oxygen; Other impurities; Flow conditions (flow velocity, flow pattern);
- Time of exposure;
- Stresses in material.

This list of parameters might be still incomplete or not detailed enough since significant differences in corrosion behaviour of the same material in similar conditions have been observed.

Liquid Metal Corrosion of various steels in the liquid lead environment has been investigated quite extensively during the last decade. The total number of publications dedicated to this issue is approaching one hundred. Despite numerous investigations, the prediction of LMC and the explanation of the underlying mechanisms still remain challenging. A summary of data even for a single material like 316L steel, which was extensively investigated by many researchers, shows quite significant scatter in corrosion layer thickness, structure of the corrosion layers, and even type of corrosion reported for similar conditions. Moreover, sometimes the experimental conditions might be not properly reported since important parameters are not included in the description of the conducted experiments or in the worst case are reported incorrectly. It might concern the material specifications, test conditions like temperature, flow velocity and the dissolved oxygen concentration in the vicinity of the corrosion specimens particularly.

The Liquid Metal Corrosion can affect reactor operations in different ways:

- Material loss due to dissolution or erosion-corrosion might compromise integrity of components, especially thin wall components like fuel cladding and heat-exchanger tubes.
- The oxide layer which forms on the steel surface will hinder the heat transfer from fuel to primary coolant and from primary to the secondary coolants.
- The corrosion products might deposit in low temperature regions and to obstruct flow.

In order to address these effects in the design of MYRRHA, the following issues should be investigated:

- The assessment of the maximum corrosion depth should be done at the boundary operating conditions and little bit beyond of the corresponding components, e.g. dissolution corrosion should be investigated at the minimum allowable dissolved oxygen concentration, highest possible temperature, and at maximum flow velocity. Actually the minimum dissolved oxygen concentration should be verified by means of corrosion tests. This information will be quite important for the evaluation of the cladding performance.
- In order to assess the heat transfer processes in the fuel and in the heat exchanger the variation of the oxide layer thickness along the component surfaces is important. Therefore, assessment of the corrosion layer thickness as function of local conditions might be quite valuable. The thermal conductivity

of the oxide layers grown on steels in contact with LBE should also be measured.

- In order to develop components of the coolant conditioning system, which includes the oxygen supply, the cold trapping, and coolant filtering data concerning rates of oxygen consumption on steel surfaces and corrosion products release should be obtained.

The strategy to mitigate LMC for the MYRRHA reactor is based on three pillars. The first one is maximum temperature and lifetime constrains. The highest temperature of the material in contact with LBE (the hottest fuel pins) will be kept below 500 °C and according to preliminary assessments the lifetime of fuel pins will be limited to 2 Effective Full Power Years (EFPY). However, the latter limitation is not due to LMC only. The maximum temperature of the reactor vessel, which is the only non-replaceable component of the MYRRHA reactor with the anticipated minimum lifetime of 40 years will vary between 200 °C during shutdown and 270 °C at full power. The second pillar is the active oxygen control for the coolant. Here the dissolved oxygen concentration should be sufficient to form protective oxide layer on the surface of all components at all operating time. The avoidance of stagnant zones in the reactor design is also part of this strategy. The third pillar is the investigation of the LMC mechanisms, which will help to improve the material performance for the most susceptible components such as the fuel cladding and heat exchanger. It will also help to identify potentially susceptible zones and might also contribute to the inspection program.

The LMC effects, especially various types of localized corrosion might affect the mechanical properties and serve as the precursor of the material degradation effects like Liquid Metal Embrittlement or Stress Corrosion Cracking. This issue will be addressed in various screening tests, where pre-exposed mechanical specimens will be tested and exposure of pre-stressed specimens to LBE during long time is foreseen.

2.2   Liquid Metal Embrittlement

The effect of Liquid Metal Embrittlement (LME) is a reduction of ductility and fracture toughness of metals when simultaneously subjected to stresses and wetting by liquid metals [6]. This effect was observed for T91 steel in LBE environment as illustrated in Figure 1. In Slow Strain Rate tensile Tests (SSRT) LME appeared as a reduction of total elongation for specimens tested in LBE compared to specimens tested in an argon hydrogen gas mixture. Fractography and surface analysis of the broken specimens revealed the formation of multiple surface cracks and quasi-cleavage fracture surfaces as shown in Figure 2. Multiple tests performed under similar conditions on the same material show quite some scatter. This is probably because the initiation of the surface cracks is a stochastic process. However, the rupture of T91 specimens always happened after reaching the Ultimate Tensile Strength and the surface cracks were found in the necking region only. It was found that appearance of LME in SSRT tests depends on many parameters including the dissolved oxygen concentration in LBE, pre-exposure in LBE prior to the mechanical test, strain rate, and test temperature. However, parametric investigation of the LME by means of SSRT tests is a labour- and time-consuming effort since it requires a statistically representative amount of tests at each single condition due to high scatter of the data. Moreover, the results of SSRT tests reflect the combination of crack initiation and the crack propagation events.

Fracture toughness tests of pre-cracked T91 specimens also revealed accelerated rupture in LBE environment in comparison with tests performed in air as shown in Figure 3.

A quasi-cleavage fracture surface is clearly observed by fractography of specimens tested in LBE (Figure 4c). However, the pattern of the fracture surface allows one to suggest that cracks during the test start to grow from small spots at the intersection of the side groves and the fatigue pre-crack (Figure 4a). Furthermore, clearly distinguishable surface cracks were found in the side grooves (Figure 4b). This is probably because LBE did not reach the tip of the fatigue crack at the beginning of the experiment so that the crack starts to grow from spots where the contact between LBE and material has been provided by the geometry of the specimen. Penetration of LBE towards the crack tip is probably hindered by thin iron-chromium-oxide layers which are not wetted by LBE and formed in air on the crack surface. As one can see in Figure 4a the surface of the fatigue crack grown in air is not covered by LBE, whereas the surfaces of the crack grown in LBE are completely covered. Since the concentration of oxygen in LBE was quite low the oxide layer on the fresh fractured surfaces did not form and the surfaces were wetted by LBE (Figure 4a). It is important to notice that hindering of LBE penetration towards the crack tip is rather an experimental artefact than a real protective mechanism. The cracks which might form in operational conditions should be filled with LBE from the moment of its initiation. Due to limited mass exchange with the bulk the LBE inside the crack might be depleted in oxygen leading to a direct interaction of liquid metal with the fresh metal surface created by the crack.

The mechanism of LME of T91 steel in LBE environment is still not completely clear. Observations of the enhanced susceptibility of T91 steel to LME in low oxygen LBE after pre-exposure at higher temperature prior to mechanical testing might indicate that the direct contact between LBE and the bare material surface is one of the necessary conditions for the appearance of LME. In all the tests LME appears after significant plastic deformation of the region where cracks initiated or pre-existing cracks start to propagate. The important issue which should be clarified is why this plastic deformation is necessary. Is it to modify the microstructure of the material in order to make it more susceptible to LME or is it just to destroy the barriers like oxide films on the material surface promoting direct contact with LBE. This issue should be resolved in order to assess applicability of T91 steel as structural material for components, which will work under significant stresses in contact with LBE.

There are also some indications that contact with lead or LBE might reduce the fatigue lifetime [7-10] and enhance creep of T91 steel [10-12]. The enhanced creep of T91 steel was observed in lead alloys at temperatures which were higher than temperatures of SSRT tests where LME was observed. Also the strain rate in creep tests, which is normally volumetric parameter is affected by LBE [11]. Therefore the mechanism of enhanced creep might be different from the mechanisms of LME observed in SSRT tests and requires special investigation.
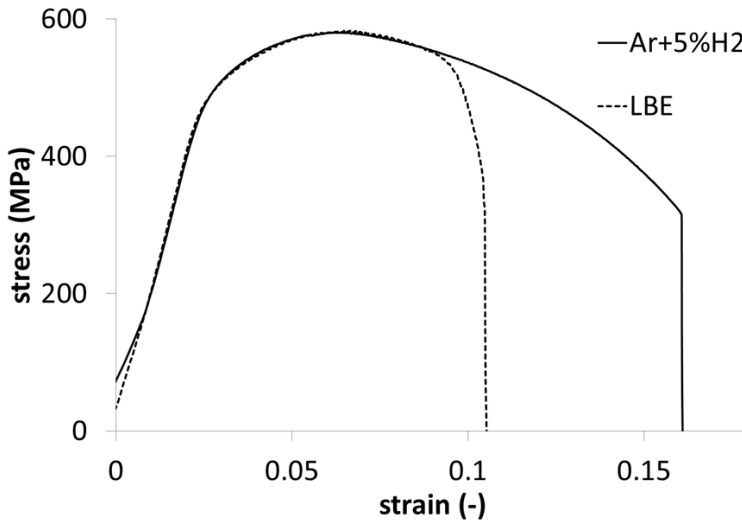
*Figure 1 : Stress-strain curves for slow strain rate tests, at $5 \cdot 10^{-5} s^{-1}$, of T91 steel in Ar+5%H$_2$
and in LBE containing $10^{-9} \div 10^{-10}$ wt.% of dissolve oxygen, at 350 °C.*
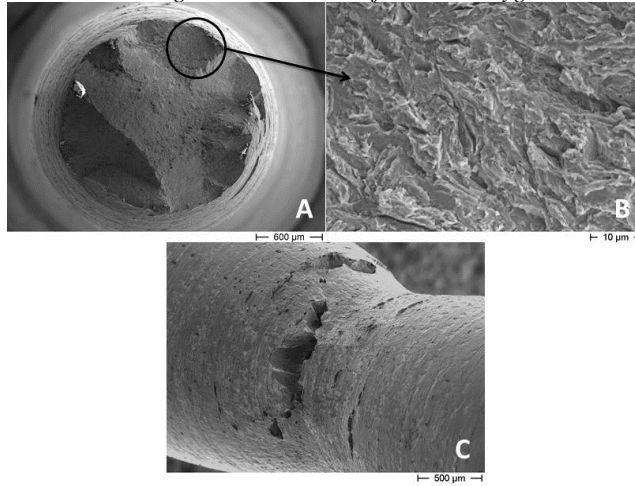
Figure 2 : SEM of fracture surface (a,b) and necking region (c) of T91 steel tested at $5 \cdot 10^{-5} s^{-1}$ in LBE containing $10^{-9} \div 10^{-10}$ wt.% of dissolve oxygen, at 350 °C.
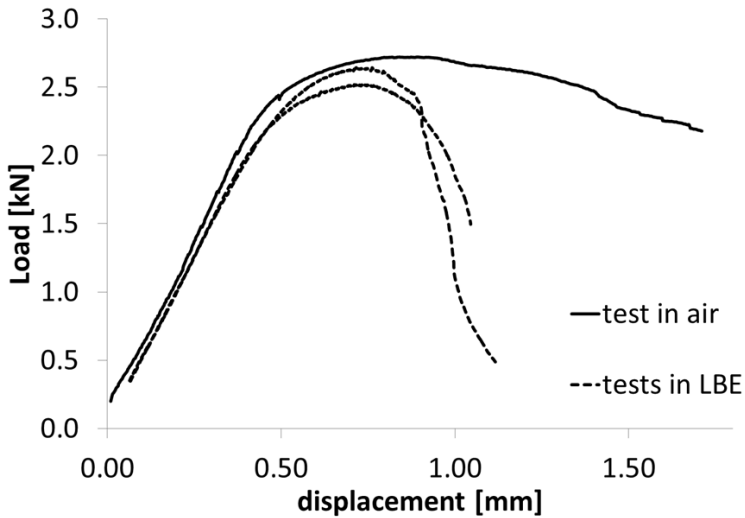
Figure 3 : Stress-strain curves for slow strain rate tests, at $5 \cdot 10^{-5} s^{-1}$, of T91 steel in Ar+5%H$_2$ and in LBE containing $10^{-9} \div 10^{-10}$ wt.% of dissolve oxygen, at 350 °C.

(a)   (b)

(c)
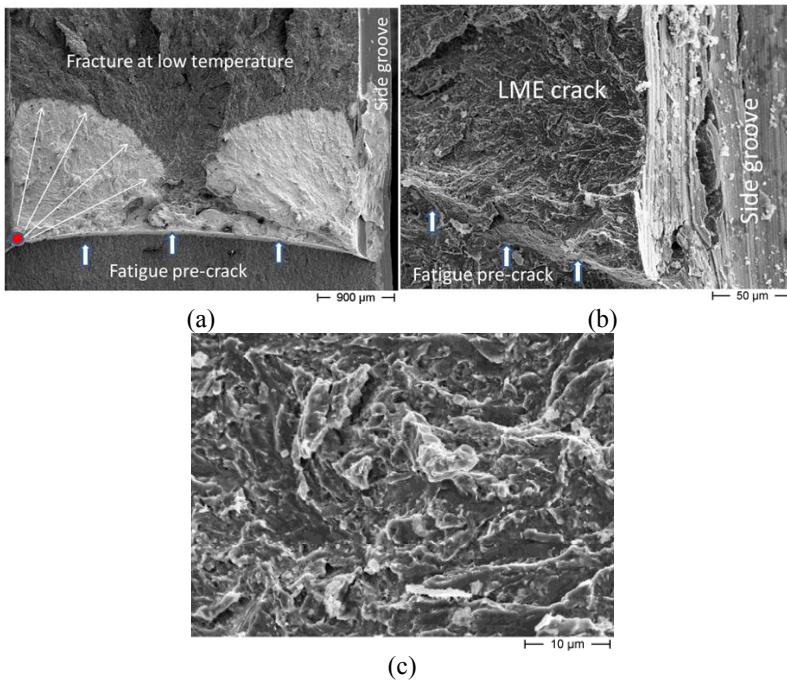
Figure 4 : SEM of fracture surface of T91 DCT specimens tested in LBE containing $10^{-9} \div 10^{-10}$ wt.% of dissolve oxygen, at 350 °C.

2.3 Irradiation effects

Since MYRRHA is the research reactor and the pilot plant for heavy liquid metal coolant technology the very high fuel burn-up is not the ultimate goal especially for the first core. The effects of swelling and irradiation creep will be accommodated by the design of the fuel assembly. It will therefore rely on an existing database of experimental results and design correlations describing these effects for the steel DIN 1.4970, which is selected as the candidate material for the cladding of the first core.

Irradiation embrittlement has been identified as the major concern for the candidate materials. The temperature range in MYRRHA is lower in comparison with sodium fast reactors. The experimental data concerning embrittlement of steels used in the core of fast reactors for irradiation temperatures below 350 °C are quite limited. Some of the data for irradiation embrittlement of austenitic stainless steels for temperatures around 300 °C were obtained in LWR programs. Therefore, assessing the irradiation induced degradation of mechanical properties of MYRRHA candidate materials in this temperature range is one of the important issues for selected. Work aimed at understanding and quantitatively predict irradiation embrittlement based on physical considerations is summarily reported in the next section.

3 Understanding irradiation embrittlement in ferritic/martensitic alloys

3.1 Approach

Ferritic/martensitic (F/M) steels with high-chromium content are candidate structural materials for Gen IV and fusion reactors, because of their higher swelling resistance, higher thermal conductivity and lower thermal expansion than austenitic steels [13-15]. They also exhibit reduced creep rate. However, differently from austenitic steels they undergo ductile-brittle transition below a certain temperature (DBTT). The DBTT is generally lower than room temperature, however it shifts to higher temperature as a consequence of neutron irradiation at <350°C. The applicability of these materials as structural materials in nuclear systems that operate in this range of temperature depends, therefore, on whether this shift keeps the DBTT acceptable or not.

The description and prediction of material mechanical behaviour after irradiation beyond empirical approaches is not an easy task, as it requires full understanding of the physical processes which are responsible for material degradation. These processes start with the collision of a high-energy neutron with an atom of the material, triggering a sequence of atomic collisions that lead to the production of large amounts of defects, namely vacancies and self-interstitials, both isolated and in clusters. These defects are mobile and, by diffusion inside the material, they lead over times varying from seconds to years to the formation of larger defects, potentially visible in the electron microscope (dislocation loops, cavities, …), as well as to the redistribution of chemical species. Both these processes determine significant changes in the macroscopic properties of the material. Our approach combines theoretical and experimental studies aimed at quantitatively understanding the physical origin of, e.g., irradiation hardening and embrittlement, starting from the defects which are formed in the material when irradiated and looking for the correlation between nano (micro)-structural properties and and changes with the macroscopic mechanical behaviour.

3.2 Fe-Cr binary alloys and steels - MIRE irradiation

F/M steels for future nuclear systems are typically chosen to contain Cr in the range 9-12%. To support this choice it is important to understand how the concentration of Cr affects the response of the material to irradiation. Fe-Cr alloys of different Cr content have thus been employed as model materials in irradiation experiments and subsequent characterization, namely Fe-2.5 wt.% Cr, Fe-5 wt.% Cr, Fe-9 wt.% Cr, Fe-12 wt.% Cr (nominal compositions), together with two 9 wt.% Cr steels, namely T91 and Eurofer 97. The material processing is described elsewhere [16]. The material composition is given in Table 1.

Table 1: The chemical composition of FeCr alloys and steels in wt.%.

Material	Composition in wt % (balance is Fe + a very low content of a few impurities not reported here)										
	Cr	Mo	W	Ta	V	Ni	Si	P	Mn	C	N
Fe-2.5% Cr	2.4	--	--	--	0.001	0.04	0.02	0.01	0.01	0.01	0.012
Fe-5% Cr	4.6	--	--	--	0.001	0.06	0.04	0.01	0.02	0.02	0.013
Fe-9% Cr	8.4	--	--	--	0.002	0.07	0.09	0.01	0.03	0.02	0.015
Fe-12% Cr	11.6	--	--	--	0.002	0.09	0.11	0.05	0.03	0.03	0.024
T91	8.3	0.96	< 0.01	--	0.24	0.24	0.32	0.02	0.43	0.10	0.030
Eurofer 97	9.0	< 0.001	1.1	0.13	0.19	0.07	0.07	< 0.005	0.43	0.12	0.016

The neutron irradiation was performed in the Belgian materials test reactor BR2. All materials were irradiated in the CALLISTO loop which is adapted to mimic as much as possible the environmental conditions of a commercial generation II pressurized water reactor (~ 300 °C, 150 bar). Three different irradiation doses were reached, namely 0.06, 0.6 and 1.5 dpa, at a neutron flux of about 7.5×10^{13} n cm^{-2} s^{-1}. The irradiation conditions are described with ample detail in [16]

3.3 Experimental characterization techniques

The characterization was performed at SCK•CEN using some of the microstructural techniques available in the controlled area, namely positron annihilaton spectroscopy (PAS)and two relaxation techniques, namely internal friction (IF) and magnetic after effect (MAE), as well as carrying out tensile tests for the mechanical properties.
PAS is particularly sensitive to vacancy-type defects, of size well below transmission electron microscopy resolution. It is thus the only technique that can provide information about vacancy clusters produced under irradiation and, to a certain extent, about their chemical environment. PAS experiments are performed with the Coincidence Doppler broadening (CDB) and positron annihilation lifetime spectrometers (PALS). The CDB spectra are measured using two Ge detectors. Details of the setup are described elsewhere [17]. The CDB spectrum provides the momentum distribution of core electrons, which can be used to determine the chemical environment of positron-electron annihilation site [18]. The results are typically shown as the CDB ratio spectra, which correspond to the momentum distributions normalized to that of non-irradiated (defect-free) pure iron. The PALS measurements, which provide the size and density of vacancy type defects, are performed with a spectrometer working in a triple coincidence mode with a time resolution of about 175 ps. The triple coincidence mode is used for irradiated materials in order to reduce the background originating from gamma-rays of the radioactive samples.

IF is based on the interaction between an applied mechanical stress field and anisotropic lattice distortions caused by either interstitial impurities or self-interstitial atoms, or by spatially extended defects, such as dislocations; thus, it provides information mainly about interstitial impurities and dislocations. The internal friction measurements were performed in an inverted torsion pendulum operating in free vibration at about 2 Hz (with a typical sample size of 1.3 x 1.3 x 30 mm^3), in the temperature range between 100 K and 600 K [19]. From the free decay signal, the resonance frequency (modulus), and the internal friction coefficient , Q^{-1}, are determined. Q^{-1} is proportional to the ratio of the energy dissipated during one cycle to the maximum elastic energy stored in the sample. The measurements have been performed at a strain amplitude of about 10^{-4}, in a He atmosphere with a heating rate of about 1.5 K/min, and no magnetic field is applied.

The magnetic affter effect (MAE) measurements are performed using an open magnetic circuit, working at 275 Hz and measuring the time dependence of the initial reluctivity [20]. Once the measurements are performed for all temperatures, typically in the temperature range from 100 to 500 K, the isothermal data are processed into isochronal curves, which show the relative change of initial reluctivity as a function of temperature.

Tensile specimens with a gage length of 12 mm and a diameter of 2.4 mm, with a fine mechanically polished surface were prepared and tensile tests were performed according to ASTM E8M-01 and E21-92 (1998) standards with an electro-mechanical test frame (INSTRON 8500, model 1362), and a crosshead speed of 0.2 mm/min corresponding to a strain rate of approximately 2.8 x 10^{-4} s^{-1}. The range of test temperatures was from -150°C to 300 °C. For the full set of results and details see [16].

3.4   Modelling techniques

Radiation damage in solids represents an extreme case in materials science, because atomic- or even nuclear-level processes are at the origin of changes in the performance of whole reactor components. Namely the almost instantaneous displacement of atoms localised in a region of a few nanometers by an energetic impinging neutron, with subsequent production of lattice defects (vacancies and self-interstitials, isolated and in clusters), repeated several times in different points of the material over time, is the seed of the degradation produced in the material by irradiation. In order to be able to describe the physical behaviour of materials under irradiation beyond empiricism, therefore, it is necessary that one develops models for nuclear reactions (activation, transmutation, …), atomic-level processes (cascades of atomic displacements, diffusion of chemical species and of defects, …), nano- and microscale processes (development of nanostructural features such as dislocation loops, segregation of chemical species that change locally the property of the material leading to e.g. localized corrosion, …), mesoscale processes (movement of dislocations that govern plastic deformation, or changes in grain boundary behaviour, …), and finally macroscale processes (crystal plasticity applied to aggregates of grains, or continuum mechanical calculations of stress and strain distributions in a component, …). The physical description of the behaviour of a material requires the use of models that address the correct scale for the phenomenon at hand. It also requires that the information about the behaviour of the material at a certain scale is somehow transferred to the higher scale, so that the model at this higher level can be more accurate. This is the principle of the multiscale modelling approach [21]. At SCK•CEN, we are specialized in developing and applying models that deal with atomic-level processes, bringing the information they provide to the level of nano/microstructural evolution and its effect on dislocation movement, which have been extensively applied to Fe-Cr alloys [22].

Atomistic models are based either on the use of quantum mechanical approximations for the calculation of electronic structures, so as to evaluate in a reliable way the energy state of relatively small groups of atoms, or on the use of empirical interatomic potentials that allow much larger systems to be studied, at the price of less reliability in the energy evaluation. The way to integrated models that allow macroscopic properties such as hardening and embrittlement to be fully predicted starting from more fundamental models is still long: several gaps still need to be filled, in particular to be able to translate the effects of radiation damage on dislocations mobility and properties into suitable constitutive laws for continuum mechanics calculations. However, the insight provided by existing modelling tools and approaches into the physical origin of macroscopic effects is valuable in itself because it allows a more correct interpretation of experimental results, guiding also the application of semi-empirical approaches of more direct use for the engineer. In particular, current models are more and more reliably capable of reproducing and predicting the nanostructural evolution undergone by the materials when irradiated, as observed in experiments, thereby providing physical bases for a semi-empirical deduction of the corresponding macroscopic properties, with a potential for safer interpolation and extrapolation.

3.5   *Microstructural experimental results*

The material properties are analyzed by positron annihilation and relaxation techniques (internal friction and magnetic after effect). Positron annihilation experiment is known to be sensitive to the presence of vacancies and vacancy-solute clusters, while the relaxation techniques provide information about the carbon distribution and dislocation dynamics.

The IF and MAE spectra of the tempered samples are shown in Figure 5. The IF and MAE spectra of tempered Fe2.5Cr sample exhibit the Snoek peak (the peak P1 in Figure 5), which is centered at about 306 K and at about 265 K, respectively. The difference in the temperature positions of the Snoek-peak observed in the MAE and IF experiments is a consequence of the difference between the relaxation times. Interestingly, Fe-5, -9 and -12%Cr alloys do not show the presence of the Snoek-peak. For the sake of simplicity, only the 12%Cr alloy result is shown in Figure 5. Moreover, no dislocation-relaxation processes are observed which indicates that dislocations are well annealed after tempering. These results show that there is essential difference in the carbon distribution between, on the one side, Fe2.5%Cr and, on the other, Fe-5, -9 and -12%Cr alloys. In the former, carbon is found to be present in the iron lattice, while in the latter case, due to large number of the grain boundaries, carbon atoms are mainly segregated there. Large number of grain boundaries is the characteristic of F/M steels, so the Fe-2.5%Cr alloy is expected to show dominantly ferrite properties. Due to large clustering affinity between carbon and vacancy, the difference in carbon distribution might have large consequence for the vacancy related defect formation in irradiated alloys. In turn, this will have an influence on the dislocation loop population, as is discussed in more detail below.
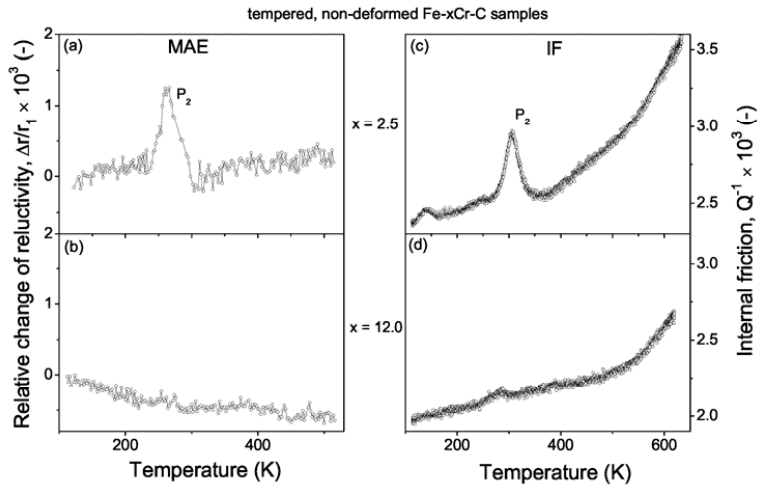
Figure 5 : The internal friction and magnetic after effect spectra of Fe2.5Cr and Fe12Cr alloys.

The positron lifetime components (PALS) in irradiated Fe-Cr alloys and steels, up to 0.06 dpa and 0.6 dpa, are presented in Figure 6. Due to high activity of the samples irradiated to 0.6 dpa the background signal was strongly reduced by setting discrimination level in the experimental setup. However, this also caused the strong reduction of useful signal, and consequently an increase in time required to collect the data. Because of that, the Fe-2.5%Cr and Fe9%Cr alloys irradiated to 0.6 dpa were possible to fit with only mean lifetime component.
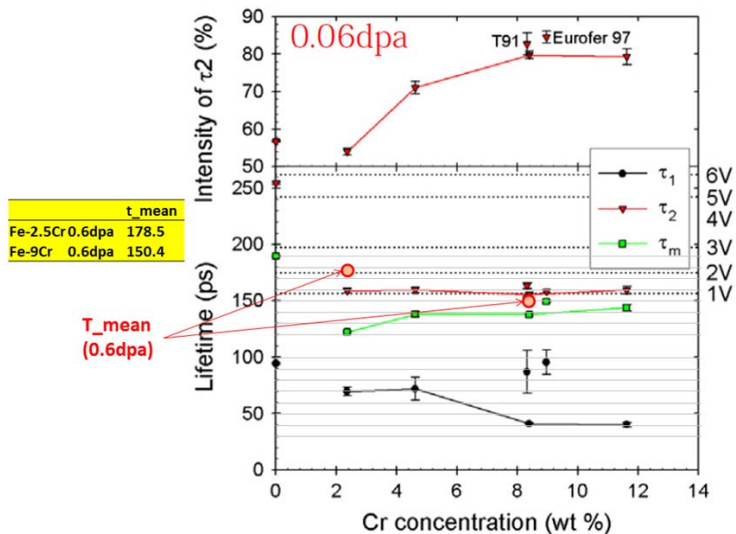
Figure 6 : The positron lifetime measurements in FeCr alloys and steel nutron irradiated up to 0.06 dpa and 0.6 dpa.

In the case of alloys irradiated up to 0.06 dpa, the mean positron lifetime slightly increases with increasing chromium content, as a result of the intensity increase of the second lifetime component. In pure iron irradiated to a comparable dose (see the points at 0 %Cr in Figure 6), the positron lifetime was observed to be much longer, i.e. vacancies were in clusters. It thus appears that in the Cr-rich alloys vacancy cluster formation is either delayed in dose or inhibited, as compared to pure iron.

The results for the two steels (T91 and Eurofer 97) are comparable to those of the model alloys for the second component, i.e. only single vacancies are detected, differently from the case of pure Fe. The positron lifetime first component is found to be somewhat longer than in the model alloys. This is most probably due to the presence of other alloying elements, which may attract positrons and annihilate them with a slightly higher positron lifetime than in pure iron (but still much lower than in the vacancy-type defects).

Interestingly, in the case of alloys irradiated up to 0.6 dpa, the lifetime component is observed to be different in Fe-2.5%Cr and Fe-9%Cr alloys. The value of about 180 ps is found in Fe-2.5%Cr while the value of about 150 ps in Fe-9%Cr, which is contrary to the behaviour of the mean lifetime component observed for 0.06 dpa irradiation, see Figure 6. This indicates the formation of larger clusters in Fe-2.5%Cr with respect to Fe-9%Cr.

The different behaviour of the Fe-2.5%Cr alloys at 0.06 dpa and 0.6 dpa can be explained on the basis of the carbon distribution. Namely, at low dose production most vacancies are coupled with carbon atoms which prevent their growth to large clusters. At higher dose, 0.6dpa, vacancies outnumber carbon atoms, which increases the probability for vacancy clustering.

3.6   Mechanical experimental results

Tensile tests on irradiated materials have been performed in the temperature range from 160°C to 300°C. The stress–strain curves, not shown here, clearly show irradiation hardening and loss of ductility when compared to the non-irradiated curves, with increase of yield strength and ultimate tensile strength, as well as reduction of uniform and total elongation. The presence of Cr influences radiation-induced hardening. This is clearly seen in Figure 7, where the yield strength increase as a function of Cr content is shown (test temperature RT). It is interesting to note the shallow minimum in radiation-hardening at 9%Cr: this minimum correlates with similar findings in F/M steels. In all Fe–Cr alloys hardening continues to increase with dose, up to the highest one, in contrast to the saturation observed in pure Fe (not shown), but similarly to what has been found in F/M steels irradiated under the same conditions, suggesting that the model alloys mimic the behaviour of steels in this respect. For more details, see [16].
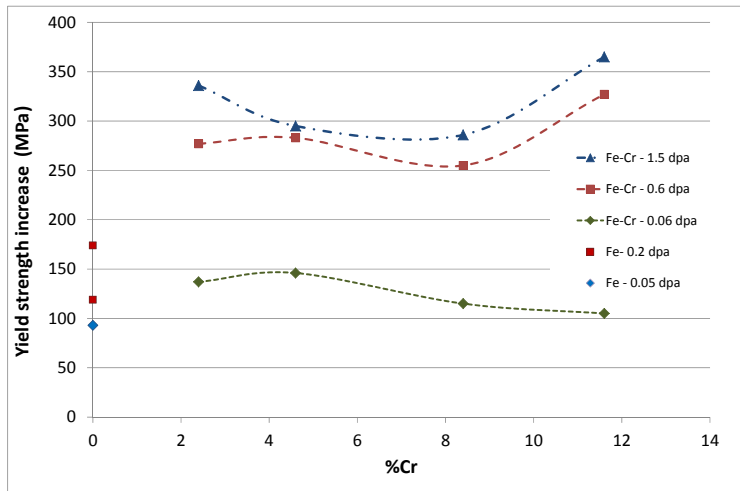
Figure 7 : Yield strength increase versus Cr content after irradiation to the three doses investigated. For comparison, data on pure Fe are shown as well (All tests at RT).

4 Interpretation of experiments with the support of models

Already the very first atomistic studies on Fe-Cr alloys revealed that Fe self-interstitials interact attractively with Cr atoms [23-26]. The consequence of this fact is that clusters of Self-Interstitial Atoms (SIA), which are known to diffuse fairly fast in one-dimension in Fe [25], are slowed-down in Fe-Cr alloys, as was soon predicted by atomistic models [26-28], following a non-monotonic dependence on Cr content that tends to disappear for large loop sizes (moreof SIA clusters (larger than 100 SIA96 atoms), as shown in Figure 8. The experimental confirmation of this prediction came *after* the model results were published [29].
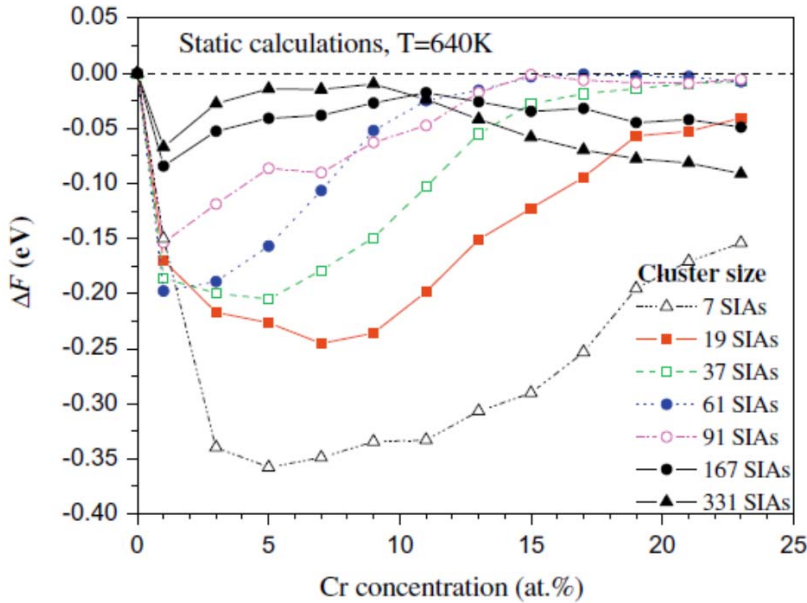
Figure 8 : Change in the Self-Interstitial Atom (SIA) clusters free energy for different sizes versus Cr content, estimated at T=640 K. The free energy change can be shown to be proportional to the ratio D_{FeCr}/D_{Fe}, between the diffusion coefficient of SIA clusters in Fe-Cr and in Fe [26].

Another expected consequence of the affinity between self-interstitials and Cr atoms, recently clearly shown by atomistic models [30, 31], is that Cr atoms will accumulate around self-interstitial clusters: several papers, directly or indirectly, suggest the latter prediction to be indeed correct [32-35], corroborated also by recent atom probe studies [36].

When the slowing down of self-interstitial clusters is introduced as a mobility rule in models that describe the nanostructural evolution under irradiation of materials, e.g. of kinetic Monte Carlo type [37], thereby simulating the behaviour of Fe-Cr alloys, spontaneously one obtains that the vacancy population decreases as compared to Fe, because slower self-interstitial clusters recombine more easily with vacancies. This is shown in Figure 9 [38] and agrees also quantitatively with the findings of PAS experiments [39]. The same simulations show that the density of visible dislocation loops decreases slightly with increasing Cr content.
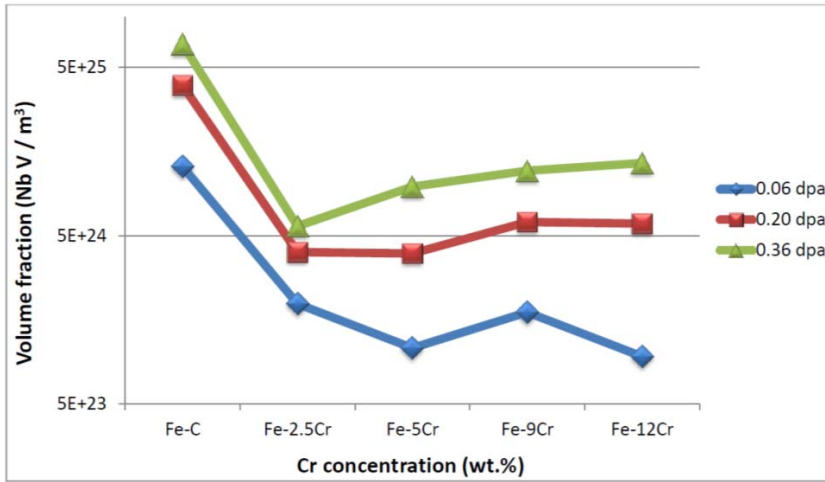
Figure 9 : Reduction of the volume fraction of vacancies after irradiation to the same dose in Fe and Fer-Cr alloys: the presence of Cr enhances recombination and decreases the amount of surviving vacancies. This model explains quantitatively the experimental results reported in [39].

Atomistic simulations allow the strength with which a defect produced by irradiation acts as obstacle to dislocation glide to be assessed, thereby allowing also an estimate of the corresponding hardening at grain level [40]. Studies of this type have been conducted, comparing the effect on dislocations of bare dislocation loops (clusters of self-interstitials) as opposed to loops decorated by Cr atoms [41, 42]. This study revealed that decorated loops are significantly stronger obstacles to dislocation motion than bare loops, as shown in Figure 10, where the mechanism of dislocation/defect interaction and the effect of Cr decoration are shown. This provides a reasonable explanation of the fact that, as can be seen in Figure 8, radiation hardening in Fe-Cr is higher than in Fe.
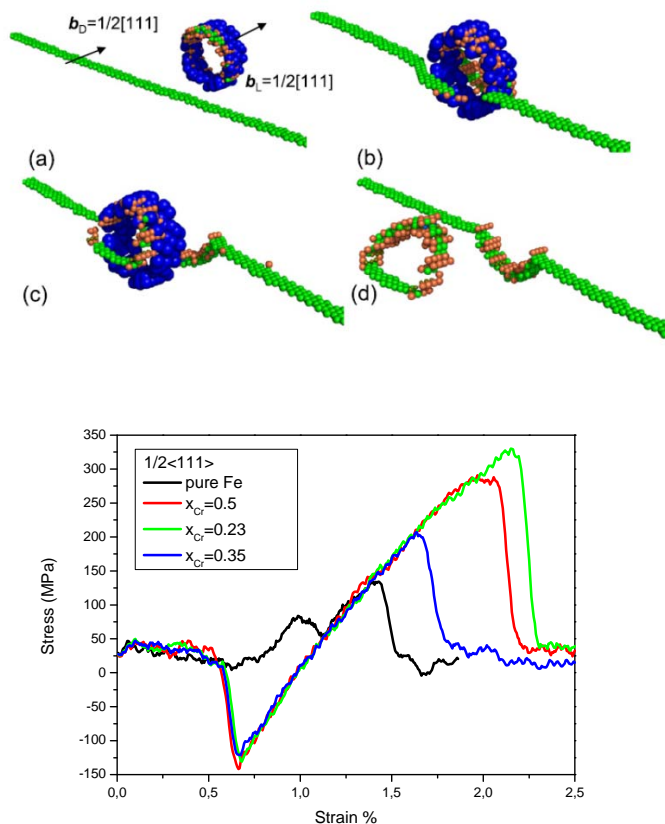
Figure 10 : (Above) Simulation of the interaction of a Cr-enriched $^1/_2\langle 111\rangle$ loop with an edge dislocation. Blue balls show Cr atoms which are located in the loop core. (a) The model before load is applied; (b) the dislocation approaches the immobilized loop; (c) segment substitution has occurred; (d) view of the dislocation-core atoms, showing the half absorbed loop [40, 41]. (Below) Stress-strain curves during the above interaction with varying levels of Cr-enrichment: the addition of Cr leads to significantly higher critical resolved shear stress.

In addition to the microstructural studies performed at SCK•CEN and described in the previous section, the neutron irradiated alloys were also analysed in other laboratories using atom probe tomography (APT) [43], small angle neutron scattering (SANS) [44] and transmission electron microscopy (TEM) [45]. APT and SANS identified the formation of two types of nanofeatures under irradiation: (i) high density (~10^{23} m^{-3}) of clusters rich in Cr, but containing also other impurities, namely Ni, Si and P, formed in all alloys; (ii) in the 12%Cr alloy also a high density of Cr-rich precipitates, clearly identifiable with the α' Cr-rich phase from the Fe-Cr phase diagram. In all cases the radius of these features did not exceed ~2 nm. TEM allowed dislocation loops to be seen, in decreasing density from 2.5 to 12%Cr (as obtained in the above-mentioned simulations), but overall similar to the density observed in Fe (~10^{21} m^{-3}). These loops, with diameters of ~10 nm, were uniformly distributed only in

the 2.5%Cr alloys, while in the others they accumulated at grain boundaries and dislocations. The uniform distribution of loops in the latter alloy can be ascribed to the fact that, as shown by IF and MAE, only in this one C atoms are uniformly distributed in the matrix. As a matter of fact, atomistic models clearly reveal that C-vacancy complexes act as traps for one-dimensionally migrating dislocation loops [46]: the absence of C atoms in the matrix and their accumulation at grain boundaries in the alloys with more than 2.5%Cr let loops free of migrating until they reach sinks, i.e. grain boundaries and dislocations, where they accumulate.

The combination of microstructural examination and models allows then the origin of hardening in irradiated Fe-Cr alloys to be rationalized and quantified:

- Vacancy clusters are very small in Fe-Cr alloys as compared to Fe, as shown by PAS, thus their effect on hardening can be neglected: vacancy type defects are certainly not the explanation for the increased radiation hardening in Fe-Cr as compared to Fe, visible in Fig. 7;
- Dislocation loops must contribute significantly to radiation-hardening especially in the 2.5%Cr alloy, where they are uniformly distributed and trapped by C-vacancy complexes [47]; however, if only loops were responsible for it, then the yield increase should be similar to the one in Fe, whereas it is larger in Fe-Cr [16].
- Quite clearly, the defects mainly responsible for hardening, those that add the contribution that is missing in Fe, must be the Cr-rich clusters that are present in all alloys, containing also other impurities: these are indeed likely to be small SIA loops decorated by Cr (and other impurities), because small loops are those that are more strongly slowed down by Cr atoms (Fig. 8) and on which, therefore, impurities may easily segregate (larger loops are less affected and migrate untrapped to the sinks). These are also significantly stronger obstacles than undecorated loops (Fig. 10).
- Finally, the further increase in radiation-hardening visible in Fig. 7 for 12%Cr must be ascribed to the presence of α'.

These considerations are supported by a quantitative assessment of the measured radiation-hardening, in a dispersed-barrier model framework [48]. Table 2 summarizes the situation and the correlation between observed nano- and micro-structure and radiation hardening.

Table 2. Summary of defect properties and mechanical properties of neutron irradiated Fe-xCr alloys.

		Fe	Fe-2.5Cr	Fe-5Cr	Fe-9Cr	Fe-12Cr
Carbon distribution (IF, MAE)		<0.0005	dissolved	segregated	segregated	segregated
Size of vacancy clusters (PAS)	0.06 dpa	~3-4 V (0.2dpa)	1 V	1 V	1 V	1 V
	0.6 dpa		2.5 V		1V	
Vacancy number density (model)	0.06 dpa	$9 \cdot 10^{24} m^{-3}$ (0.025 dpa)	$\sim 8 \cdot 10^{23} m^{-3}$	$\sim 7 \cdot 10^{23} m^{-3}$	$\sim 8 \cdot 10^{23} m^{-3}$	$\sim 6.5 \cdot 10^{23} m^{-3}$
Density and distribution of loops (TEM)	0.6 dpa	$\sim 4 \cdot 10^{21} m^{-3}$ (0.2 dpa)	$\sim 4 \cdot 10^{21} m^{-3}$	$\sim 3 \cdot 10^{21} m^{-3}$	$\sim 2 \cdot 10^{21} m^{-3}$	$\sim 10^{21} m^{-3}$
		uniform	uniform	non uniform	non uniform	non uniform
Density of Cr-rich clusters	0.6 dpa	//	$10^{23} m^{-3}$	$10^{23} m^{-3}$	$10^{23} m^{-3}$	$10^{23} m^{-3}$
Density of α'		//	//	//	$10^{23} m^{-3}$	$10^{24} m^{-3}$

precipitates						
ΔYield strength(MPa)	0.06 dpa	168	137	146	115	105
	0.6 dpa	(0.2dpa)	277	283	255	327

5 Summary and conclusions

Materials are acknowledged to play a crucial role in the development of advanced nuclear reactors. Materials will be subjected to unique conditions in future nuclear environments, in conjunction with stringent licensing requirements. The development of materials is therefore a challenging process. Early demonstrators such as MYRRHA will use commercially available materials such as T91 or DIN 1.4970 steels. However, large scale research programs is needed to verify their fitness for purposes under all operating conditions (temperature, liquid metal interaction, irradiation…). The development of ferritic/martensitic alloys should allow operating advanced reactors at higher temperature. The development of such steels is still in its early stage and rely on the combination of advanced microstructural characterization, mechanical testing and modelling. Engineering modelling of irradiation damage is nowadays more and more consolidated through atomistic and multiscale models, that allowing access to information that can hardly be obtained from experiments.

6 References

[1]   The Generation IV International Forum https://www.gen-4.org.
[2]   Demonstration Power Plants (DEMO) http://fusionforenergy.europa.eu/understandingfusion/demo.aspx.
[3]   Joint Programme on Materials for Nuclear http://www.eera-set.eu/index.php?index=25.
[4]   Sustainable Nuclear Energy Technology Platform http://www.snetp.eu/.
[5]   H. Aït Abderrahim, P. Baeten, D. De Bruyn, J. Heyse, P. Schuurmans and J. Wagemans, *Nuclear Physics News* **20(1)**, 24-28 (2010).
[6]   E. Glickman, "Mechanism of Liquid Metal Embrittlement by Simple Experiments: From Atomistics to Life-time", in *Multiscale Phenomena in Plasticity*, edited by J. Lepinoux, et al., The Netherlands: Kluwer Academic Publishers, 2000, pp. 383-401.
[7]   A. Weisenburger, et al., *J. Nucl. Mat.* **377(1)**, 261-267 (2008).
[8]   J.-B. Vogt, et al., "Coupling effects between corrosion and fatigue in liquid Pb-Bi of T91 martensitic steel" in *European Corrosion Congress EUROCORR 2005*, Proceedings, European Federation of Corrosion, Lisbon, 2005.
[9]   D. Gorse, et al., *J. Nucl. Mat.* **415(3)**, 284-292 (2011).
[10]   A. Jianu, et al., *J. Nucl. Mat.* **394(1)**, 102-108 (2009).
[11]   M. Yurechko, C. Schroer, O. Wedemeyer, A. Skrypnik, J. Konys, *J. Nucl. Mat.* **419**, 320-328 (2011).
[12]   B. Tomkins, "Structural Integrity Issues in the Nuclear Industry", in *Comprehensive Structural Integrity*, edited by I. Milne, et al., Elsevier, 2003, pp. 173-192.
[13]   LK. Mansur, AF. Rowcliffe, RK. Nanstad, SJ. Zinkle, WR. Corwin, RE. Stoller, J. Nucl. Mater. 329-333 (2004) 166-172.
[14]   RL. Klueh, AT. Nelson, J Nucl Mater 2007; 371: 37.
[15]   M. Klueh, A. Nelson, J. Nucl. Mater. 371 (2007) 37-52.
[16]   M. Matijasevic, A. Almazouzi, J. Nucl. Mater. 377 (2008) 147.
[17]   K Verheyen, M. Jardin, A. Almazouzi, J Nucl Mater. (2006);351:209.

[18]   P. Hautojärvi, Positrons in Solids, Topics in Current Physics, Springer, Berlin, vol 12; 1979.
[19]   M. J. Konstantinović, Phys. Rev. B 78, 052104 (2008).
[20]   B. Minov, LP. Vandenbossche, MJ. Konstantinović, L. Dupré, IEEE Trans Magn 2010;46:521.
[21]   L. Malerba, "Multi-scale modelling of irradiation effects in nuclear power plant materials", in Understanding and mitigating ageing in nuclear power plants: Materials and operational aspects of plant life management (PLiM), P.G. Tipping Ed., Woodhead Publishing Ltd. (2010) 456 (chapter 15).
[22]   D. Terentyev, G. Bonny, N. Castin, C. Domain, L. Malerba, P. Olsson, V. Moloddtsov, R.C. Pasianot, Journal of Nuclear Materials 409 (2011) 167.
[23]   D. Terentyev, L. Malerba, Journal of Nuclear Materials 329-333 (2004) 1161.
[24]   D. Terentyev, L. Malerba, M. Hou, Nuclear Instruments and Methods in Physics Research B 228 (2005) 156.
[25]   D. Terentyev, L. Malerba, M. Hou, Physical Review B 75 (2007) 104-108.
[26]   D. Terentyev, L. Malerba, A. Barashev, Philosophical Magazine Letters 85 (2005) 587.
[27]   D. Terentyev, P. Olsson, L. Malerba, A. Barashev, Journal of Nuclear Materials 362(2007) 167.
[28]   D. Terentyev, L. Malerba, A. Barashev, Philosophical Magazine 88 (2008) 21.
[29]   M.L. Jenkins, Z. Yao, M. Hernandez-Mayoral, M.A. Kirk, Journal of Nuclear Materials 389 (2009) 197.
[30]   E.E. Zhurkin, D. Terentyev, M. Hou, L. Malerba, G. Bonny, Journal of Nuclear Materials 417 (2011) 1082.
[31]   L. Malerba, G. Bonny, D. Terentyev, E.E. Zhurkin, M. Hou, K. Vortler, K. Nordlund, Journal of Nuclear Materials 442 (2013) 486.
[32]   E. Wakai, A. Hishinuma, Y. Kato, H. Yano, S. Takaki, K. Abiko, Journal de Physique IV 5 (1995) 277.
[33]   S. Ohnuki, H. Takahashi, T. Takeyama, Journal of Nuclear Materials 122-123 (1984) 317.
[34]   N. Yoshida, A. Yamaguchi, T. Muroga, Y. Miyamoto, K. Kitajia, Journal of Nuclear Materials 155-157 (1988) 1232.
[35]   I.M. Neklyudov, V.N. Voyevodin, Journal of Nuclear Materials 212-215 (1994) 39.
[36]   V. Kuksenko, C. Pareige, P. Pareige, Journal of Nuclear Materials 432 (2013) 160.
[37]   C. Domain, C. Becquart, L. Malerba, Journal of Nuclear Materials 335 (2004) 121.
[38]   M. Chiapetto and L. Malerba, to be published.
[39]   M. Lambrecht, L. Malerba, Acta Materialia 59 (2011) 6547.
[40]   D. Terentyev, G. Bonny, C. Domain, G. Monnet, L. Malerba, Journal of Nuclear Materials 442 (2013) 470.
[41]   D. Terentyev, A. Bakaev, Journal of Physics-Condensed Matter 25 (2013) 265702.
[42]   D. Terentyev, F. Bergner, Y. Osetsky, Acta Materialia 61 (2013) 1444.
[43]   V. Kuksenko, C. Pareige, P. Pareige, Journal of Nuclear Materials 432 (2013) 160.
[44]   C. Heintze, A. Ulbricht, F. Bergner, H. Eckerlebe, Journal of Physics: Conference Series **247** (2010) 012035.
[45]   M. Hernández Mayoral, private communication.
[46]   N. Anento, A. Serra, Journal of Nuclear Materials 440 (2013) 236.
[47]   D. Terentyev, N. Anento, A. Serra, Journal of Physics-Condensed Matter 24 (2012) 455402.

[48]   F. Bergner, C. Pareige, M. Hernández-Mayoral, L. Malerba, C. Heintze, J. Nucl. Mater. 448 (2014) 96.

DEVELOPMENT OF IMPROVED AUSTENITIC STAINLESS STEELS FOR INDIAN SODIUM-COOLED FAST REACTOR PROGRAMME

A.K. Bhaduri and T. Jayakumar

Metallurgy and Materials Group, Indira Gandhi Centre for Atomic Research,
Kalpakkam 603102, India
Email: bhaduri@igcar.gov.in; tjk@igcar.gov.in

Abstract

Austenitic stainless steels (SS) with appropriate mechanical and irradiation-resistant properties are crucial for realizing sodium-cooled fast reactors (SFRs). As core structural materials are subjected to intense neutron irradiation and high-temperature creep, selection of materials for wrapper and fuel cladding tubes is governed by its resistance to void swelling and creep. In the Indian 40 MWth Fast Breeder Test Reactor, the 316 SS, used as cladding and wrapper material, is imparted with 20% cold work to enhance void swelling resistance. For improved void swelling resistance, Alloy D9 (15Cr-15Ni-2.3Mo-Ti austenitic SS and Ti/C of 6) with 20% cold-work is chosen as cladding and wrapper material for the Indian 500 MWe Prototype Fast Breeder Reactor (PFBR) for achieving target fuel burnup of 100 GWd/t. In Alloy D9, Ti improves resistance to void swelling and creep, while Ni, P and Si significantly improve void swelling resistance. To further improve resistance to void swelling and creep, laboratory-scale heats with varying Ti, P and Si contents were produced. Based on detailed investigations on these heats, an improved Alloy D9 with 0.75%Si and 0.048%P (designated as Indian Fast Reactor Advanced Cladding-1, IFAC-1) has been developed. IFAC-1, a fully austenitic SS with higher P and Si content, has higher solidification-cracking susceptibility during welding. Extensive trials led to establishing optimum pulsed-TIG welding parameters for solidification-crack free welding of IFAC-1 cladding tubes with 316LN SS end plugs. Use of IFAC-1 cladding tubes would enable achieving fuel burnup beyond 130 GWd/t. In PFBR, with 40-years design life, 316LN SS with 0.02–0.03%C and 0.06–0.08% N, is used for structural components operating above 700K. For further improving high-temperature mechanical properties of 316LN SS, various heats with different N contents (of 0.07, 0.14 and 0.22%) were produced and investigated. Detailed evaluation of tensile, creep, low cycle fatigue, creep-fatigue interaction and weldability, led to development of nitrogen-enhanced 316LN SS with 0.12–0.14%N having better combination of mechanical properties. Matching composition electrodes with 0.14%N have also been developed for its welding. This paper describes R&D work carried out for developing advanced austenitic SS and their welding consumables for application in Indian SFRs.

Keywords: Core structural material; Reactor structural material; Welding; Mechanical properties; Void swelling

1. Introduction

Sodium-cooled fast reactor (SFR) technology represents the second of the three stage nuclear programme envisioned for India, to make use of the large thorium reserves available [1]. The difficulties in setting up of fossil-fuel powered plants due to limited coal reserves and the need for clean sources of electricity add to the importance of nuclear technology for India's development. In India, the Fast Breeder Test Reactor (FBTR) of 40 MWth has been operating successfully for over 25 years at the Indira Gandhi Centre for Atomic Research, Kalpakkam [1]. Based on this experience, a 500 MWe Prototype Fast Breeder Reactor (PFBR) has been designed indigenously and is at an advanced stage of construction, even as the design is being further optimised for enhanced economy with respect to cost of electricity production, for use in future reactors. Austenitic stainless steels (SS) with appropriate mechanical and irradiation-resistant properties are crucial for the realization of SFRs. Different varieties of stainless steels are used for the core structural (fuel cladding and wrapper) and reactor structural components.

As core structural materials are subjected to intense neutron irradiation coupled with high-temperature creep, the selection of material for the wrapper is mainly governed by its resistance to void swelling while that for the fuel cladding tubes is governed by its resistance to both void swelling and creep. In the FBTR, the 316 SS used for the fuel cladding tubes and hexagonal wrappers, is imparted with 20% cold-work (CW) to enhance its void swelling resistance. However, void swelling and irradiation-induced loss in mechanical properties render this 316 SS inadequate for fuel cladding and wrapper applications with higher fuel burnup. Hence, Alloy D9, a 15Cr-15Ni-2.3Mo Ti-modified austenitic SS with Ti/C ratio of 6, which has been designed around the standard 316 SS to improve its void swelling resistance, in the 20% cold-worked condition is chosen as the material for the fuel cladding and wrapper for the PFBR with a target fuel burnup of 100 GWd/t. To further improve the resistance to void swelling and creep-deformation of the fuel cladding material, a series of laboratory-scale heats, with varying titanium, phosphorus and silicon contents, have been investigated in detail to develop an improved Alloy D9 for use as fuel cladding tube material to ensure achieving fuel burnup of more than 130 GWd/t. Extensive trials have also been carried out for welding of 316LN SS end plugs to the cladding tubes made of the improved material for establishing optimum welding parameters for obtaining solidification crack-free end plug welds.

For the reactor structural components, 316 SS is the preferred material for SFRs due to its adequate creep strength, compatibility with liquid sodium and fabricability. For PFBR, with design life of 40 years, a 316LN SS, with 0.02–0.03 wt% carbon and 0.06–0.08 wt% nitrogen, is used for reactor structural components with operating temperature above 700K. In this 316LN SS, compared to the standard 316 SS, the carbon content has been reduced to avoid sensitization in the heat-affected zone during welding, and the nitrogen content has been increased to compensate for the loss in mechanical strength due to reduction in the carbon content. For further improving the high-temperature mechanical properties of 316LN SS, laboratory-scale heats with different enhanced nitrogen contents have been produced and detailed evaluation of their tensile, creep, low cycle fatigue, creep-fatigue interaction and weldability have been carried out to develop an optimised nitrogen-enhanced 316LN SS with better combination of mechanical properties to enable achieving longer design life of 60 years or more. Matching composition welding consumables have also been developed for welding of the optimised composition nitrogen-enhanced 316LN SS.

This paper presents the challenges and the progress made in the development of improved core and reactor structural materials and the associated welding technologies for higher fuel burn-up, with higher linear power, as also enhanced reactor design life required for improved economy of future commercial Indian SFR programme.

2. Improved Alloy D9 for Core Structural Material

The performance of core structural materials, which are subjected to intense neutron irradiation at high temperature during service, material problems such as void swelling, irradiation creep and helium embrittlement are of significance. The 20% CW 316 SS used in FBTR has shown a residual ductility of ~1% and extensive formation of voids leading to swelling at damage levels of ~80 dpa [2]. The 20% CW Alloy D9 (15Cr-15Ni-Mo-Ti-C) austenitic SS, with composition specifically tailored w.r.t. to carbon and titanium content for improved void swelling resistance and chosen for the PFBR, exhibits lower swelling and retains residual ductility >3% at damage level of up to 62 dpa [3]. The improved performance

of Alloy D9 is attributed to preferential fine-scale precipitation of TiC at intragranular dislocations in the austenitic matrix contributing to higher rupture strength and lower creep rate compared to 316 SS. Minor elements such as silicon, titanium and phosphorous are known to have a major influence on the void swelling behaviour of alloy D9 [4]. To further optimize the alloy composition for higher void swelling and creep resistances, laboratory-scale heats were produced with 0.025 and 0.04% P, 0.75 and 0.95% Si, and 0.16–0.30% Ti, while maintaining and the other alloying elements at the same nominal level as in Alloy D9, viz. 0.04C-14.2Cr-15.4Ni-1.6Mn-2.4Mo [5,6]. The void swelling resistance, creep and tensile properties, weldability and microstructural stability of these heats were systematically investigated to optimise the composition that enabled development of an improved Alloy D9, called Indian Fast Reactor Advanced Cladding-1 (IFAC-1) [7,8].

2.1. Creep properties

Creep properties of the heats with 0.025%P and 0.75%Si evaluated at 973K at different stress levels (Fig. 1) show that, at all the stress levels, the heat with Ti/C=6 exhibits the highest rupture life while the heat containing Ti/C=8.6 shows the lowest rupture life (Fig. 1a). Figure 1(b) clearly shows a peak in creep rupture life at Ti/C=~6, with the peak in rupture life being more pronounced at lower applied stresses. The variation of minimum creep rate with Ti/C ratio shows a similar trend (Fig. 1c) with a trough in the trend curve at Ti/C=6 that is more pronounced at lower applied stresses. The creep rupture ductility generally decreases with increase in Ti/C ratio. These results are broadly consistent with those reported in literature [9] in which creep rupture strength of 15Cr-15Ni SS is maximum for Ti/C=~5. While from our results, it appears that creep rupture life decreases with increase in phosphorus content, reports in literature indicate that in the range of 0.01–0.10%, phosphorus increases rupture life [10], and that there is a linear increase in creep rupture strength with increase in phosphorus content from 0.004% to 0.088% [9]. In austenitic SS, phosphorous is reported to delay the onset of tertiary creep and decrease the steady-state creep rate. This is because precipitation of M_2P, in which titanium is a major constituent, suppresses formation of primary MC-type carbides due to depletion of titanium, which in turn promotes precipitation of $M_{23}C_6$-type carbides [11].
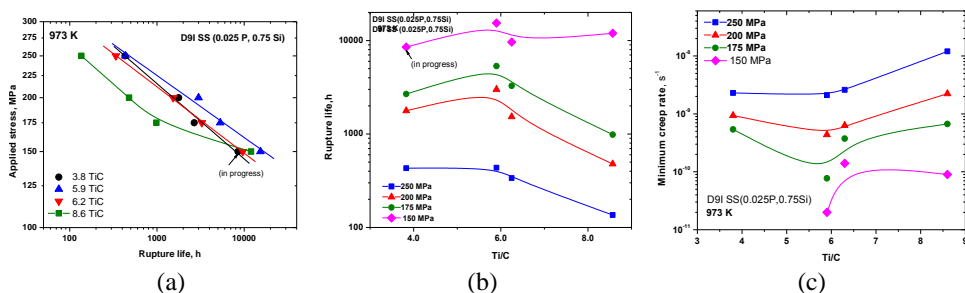
Figure 1: Variation of creep rupture life with (a) applied stress, and (b) Ti/C ratio and of (c) minimum creep rate with Ti/C ratio, for heats with 0.025%P, 0.75%Si and different Ti/C ratios tested at 973K

2.2. Void swelling

Intense neutron bombardment of cladding and wrapper in SFRs results in displacement of atoms leading to creation of point defects and clusters. Vacancies and interstitials produced during the displacement process either recombine or migrate to sinks to accumulate into voids or dislocation loops. As addition of Ti, P, Si, etc. in small concentrations has profound influence on swelling behavior of stainless steels [12], optimization of the concentration of these elements is essential for improving the void swelling resistance. The role of ion irradiation as a surrogate for neutron irradiation for deciphering basic processes and evaluating effects of minor element additions on radiation-induced phenomena is well established [13]. Accelerated heavy ions possess an inherent advantage of producing high displacement rates by virtue of their high displacement cross-sections compared to neutrons, thereby enabling studies pertaining to irradiation induced property changes at much shorter time than through in-pile neutron irradiation. The samples are first implanted with helium in order to simulate the effects of helium generated by neutron-induced transmutation reactions in reactor conditions. Helium plays a crucial role in void nucleation. The specimens which were pre-injected with ~0.3 appm.dpa^{-1} helium are subsequently implanted with 5 MeV Ni^{2+} ions, in the temperature range of 725–925K, to a fluence of ~9×10^{16} ions.cm^{-2} using a 1.7 MV Tandetron accelerator to obtain an irradiation level of ~100 dpa.

Four heats with different Ti, Si and P contents (in wt%), viz. Sample A (0.25Ti-0.024P-0.70Si, PFBR grade Alloy D9), Sample B (0.29Ti-0.022P-0.91Si), Sample C (0.25Ti-0.034P-0.74Si) and Sample D (0.29Ti-0.047P-0.77Si), were subjected to detailed investigations. For all the samples, void swelling initially increases as a function of irradiation temperature, reaches a peak value and then decreases with further increase in temperature. At lower temperatures, swelling is low because defect migration is low resulting in high steady-state concentration of interstitials and vacancies. This leads to enhanced recombination and only a few defects migrate to biased sinks such as dislocations to cause swelling. As temperature is increased, recombination is no more the dominant process as vacancies become mobile and defects migrate to sinks. At such temperatures, in presence of a dislocation bias (i.e., the dislocations absorb more interstitials compared to vacancies), void growth takes place. The drop in swelling at temperatures beyond the peak swelling temperature is due to thermal emission of vacancies from voids. The variation of void swelling with temperature for all the samples is in agreement with this physical understanding of void formation mechanism.

As seen from Fig. 2, peak swelling temperatures and magnitude of swelling at peak swelling temperature for samples A and C are similar although sample C contains 0.034%P. This behaviour can be ascribed either to formation of phosphide precipitates in lower number densities or to their near absence. Therefore, in these two alloys, only TiC precipitates play a dominant role in suppressing swelling. It is reported that, in alloys containing <0.03%P, irradiation-induced phosphide is a minor phase [14]. However, when Si content increases to 0.91% as in sample B, swelling at low temperature decreases. Hence, there can be no effect of phosphorus on swelling because the phosphorus content is less than that in sample C where no effect of phosphorus on swelling is observed. The increased concentration of silicon results in formation of γ′ precipitates (Ni$_3$Si), which act as recombination centres for point defects, thereby reducing swelling. Higher silicon content does not increase vacancy diffusion coefficient as there is no shift in peak swelling temperature. When phosphorous content is increased from 0.034 to 0.047%, drastic reduction in swelling is observed apart from shift in

793

peak swelling temperature towards lower temperatures. This suggests that, higher phosphorous content decreases peak swelling temperature by increasing diffusion of vacancies in the alloy. This is applicable for lower temperatures where phosphorus is in solution and affects vacancy diffusivity. It should be noted that the difference in swelling of Sample D in comparison to Sample C is less below the peak swelling temperature, whereas above the peak swelling temperature, the difference is drastic. This implies that below the peak swelling temperature, the effect of phosphorus in solution is at play, whereas above the peak swelling temperatures, M_2P precipitates should have formed. At phosphorus content of 0.04% or more, M_2P is the dominant phase in Ti-modified steels. These M_2P precipitates, which act as recombination centres for point defects and act as traps for gaseous helium atoms help in inhibiting void nucleation. The above results suggest that the effect of increasing phosphorus to enhance swelling resistance is dominant at higher temperatures. The peak swelling temperature and swelling at peak swelling temperature are significantly altered by varying titanium content. Differences in diffusion behavior and number density of TiC precipitates formed due to the variation in titanium content cause significant changes in the swelling behavior.
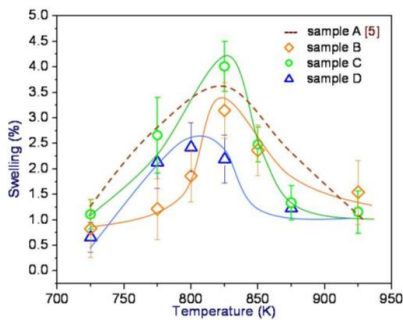
Figure 2: Temperature dependence of void swelling

Based on the results from swelling and creep studies, the nominal composition of the improved Alloy D9 has been optimized at 0.25%Ti, 0.75%Si and 0.04%P. The alloy has been designated as IFAC-1. A comparison of the creep properties of IFAC-1 and Alloy D9 is shown in Fig. 3 in the form of a Larson-Miller parameter plot, which shows that the creep properties of IFAC-1SS are comparable to that of Alloy D9.
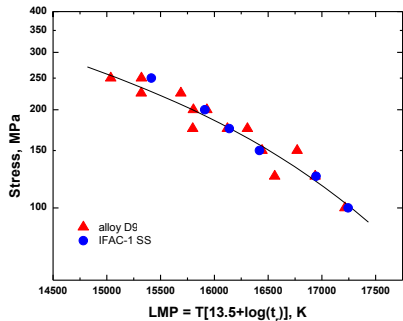
Figure 3: Comparison of creep properties of IFAC-1 and Alloy D9

2.3. Weldability

IFAC-1 is a fully austenitic SS, containing high levels of low-melting eutectic-phase forming elements, such as phosphorus, which makes it particularly susceptible to solidification cracking. Extensive pulsed gas tungsten arc welding (GTAW) trials, with varied weld parameters, have been carried out for welding of 316LN SS end plugs to IFAC-1 cladding tubes to establish the procedure for obtaining solidification-crack free welds. The solidification-cracking susceptibility of austenitic SS can be estimated based on the Cr_{eq}/Ni_{eq} ratio. When Cr_{eq}/Ni_{eq} is <1.5, the weld is highly susceptible to cracking [15]. IFAC-1 has Cr_{eq}/Ni_{eq}=1.1 and so is highly susceptible to weld cracking; 316LN SS with Cr_{eq}/Ni_{eq}=1.5 is on the borderline between cracking and no-cracking zones. The end plug geometry is suitably designed to ensure that during welding, sufficient amount of 316LN SS melts to add to the molten pool so that the molten zone consists of both IFAC-1 and 316 LN SS. Weld cracks of varied lengths and widths were observed during the initial trials (Fig. 4a). By systematically varying the welding parameters, such as peak current, background current, pulse width, pulse rate, welding speed, arc gap, electrode tilt, gas flow rate and total time of welding, the number of cracks and their dimensions were gradually brought down and finally completely eliminated [16]. A photograph of defect-free weld obtained is shown in Fig. 4(b). The cross-section of the weld joints showed that the end-plug weld bead penetration is more than 100% of the cladding tube wall thickness. Also, the weld joints of 316LN SS end plugs to the IFAC-1 cladding tubes made with optimised welding parameters were qualified in helium leak testing as they were found to withstand a leak rate of better than 10^{-7} standard-cm^3.s^{-1}, and by X-radiography tests that indicated absence of defects.

| | |
| (a) | (b) |
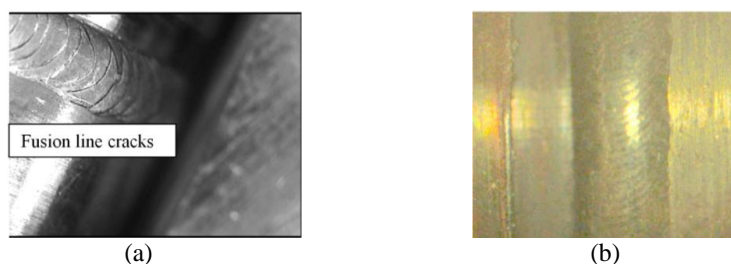
Figure 4: Photographs of IFAC-1-to-316LN SS end plug weld: (a) with defects and (b) defect free weld

3. Nitrogen-enhanced 316 LN SS for Reactor Structural Material

Currently, 316LN SS containing 0.02-0.03% C and 0.06-0.08% N has been used for all major high-temperature structural components of PFBR. While carbon content in 316LN SS is kept low to minimize its susceptibility to sensitization in the heat affected zone of welded components, alloying with 0.06-0.08%N enables maintaining its high-temperature strength to levels comparable to that of 316 SS with 0.06-0.08%C. As the design life of future SFRs is envisaged to be enhanced to 60 years from the present 40 years, nitrogen-enhanced 316LN SS with improved high-temperature mechanical properties is being developed. To optimize the enhanced nitrogen content, the effect of nitrogen content on its tensile, creep, low cycle fatigue and weldability behavior has been investigated in four heats of 316LN SS with varying nitrogen content of 0.07-0.22 wt%.

3.1. Tensile properties

In the temperature range 300-1123K, the yield strength and ultimate tensile strength increase linearly with increase in nitrogen content (Fig. 5) with the total elongation varying, as a function of nitrogen content, in the range of 41-57% at 300K and 33-69% at 1123K [17].
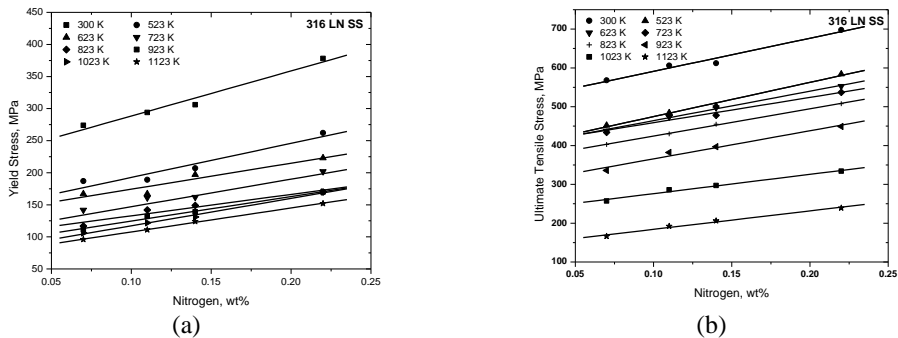
Figure 5: Variation of (a) yield strength and (b) ultimate tensile strength with nitrogen content for nitrogen-enhanced 316LN SS

3.2. Creep properties

There is significant increase in creep rupture life with increase in nitrogen content at all stress levels in the range 140-225 MPa (Fig. 6), with the rupture life increasing by almost ten times with increasing nitrogen content from 0.07 to 0.22 wt%. The beneficial effects of nitrogen arise due to higher solubility of nitrogen in the matrix than the carbon, reduction in stacking fault energy of the matrix and introduction of strong elastic distortions into the crystal lattice, giving rise to strong solid solution hardening [18]. Nitrogen also affects the diffusivity of chromium in austenitic stainless steels leading to retardation in coarsening of $M_{23}C_6$ thereby retaining the beneficial effects of carbide precipitation to longer times [19,20]. The increase in creep rupture strength with increasing nitrogen content could be correlated to decreasing tendency for sub-grain formation leading to uniform distribution of dislocations. However, creep rupture ductility decreases with increase in nitrogen content, with the variation of rupture ductility with rupture life showing a minimum in ductility at short durations and a continuous increase in ductility at longer rupture times, a trend characteristic of austenitic SS.
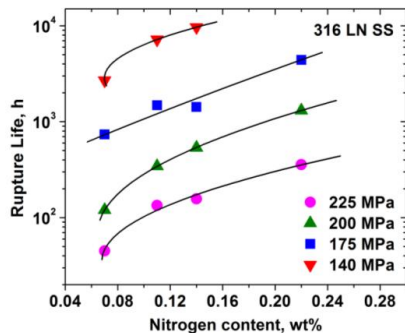
Figure 6: Influence of nitrogen on creep properties of 316LN SS at 923K

3.3 Low cycle fatigue properties

Studies on the influence of nitrogen content on low cycle fatigue (LCF) properties at various strain amplitudes between 300 and 873K [21] showed that the cyclic stress response curve is generally characterised by initial hardening, followed by saturation and then cyclic softening. The LCF life increases with increasing nitrogen content upto 0.14 wt%, beyond which the fatigue life saturates/decreases (Fig. 7). The increase in fatigue life with increase in nitrogen content has been attributed to increasing planar glide of dislocations and better slip reversibility (i.e., less slip localisation), whereas reduction in fatigue life at nitrogen contents above 0.14 wt% has been attributed to high matrix hardening and consequent decrease in residual ductility. Fatigue crack initiation and propagation is transgranular, with the crack initiation taking place along slip bands on the specimen surface. The initial crack propagation occurs over only one or two grain diameters along slip planes oriented at 45° to the applied stress axis (stage I), followed by transition to stage II cracking that shows up as striations on the fracture surface. With respect to the LCF properties, 0.14 wt% nitrogen is the optimum nitrogen content for the nitrogen-enhanced 316LN SS.
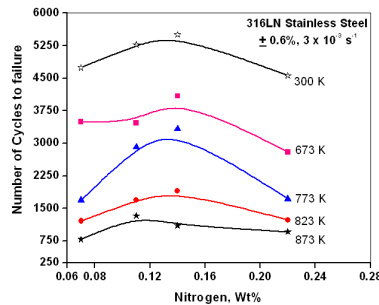
Figure7: Influence of nitrogen content on LCF life of 316LN SS at various temperatures

3.4 Weldability and welding consumable

Evaluation of the hot cracking susceptibility of the different heats of 316LN SS with varying nitrogen content was carried out [22]. Gleeble-based hot ductility tests revealed the on-cooling hot ductility behaviour of nitrogen-enhanced 316LN SS. The effect of nitrogen content on nil strength, nil ductility and ductility recovery temperatures, NST, NDT and DRT, showed that, with increasing nitrogen content, NST decreases upto 0.14%N beyond which it increases again, while its effect on DRT is the reverse. However, NDT decreases linearly with increasing nitrogen content. In hot ductility tests, nil ductility range (NDR = NST – DRT), which measures how fast ductility recovers during on-cooling test, is 40K and 50K for 0.07%N and 0.22%N steels, respectively, with the minimum being 30K for the 0.14%N steel. The Varestraint tests confirmed that the 0.22%N steel has the highest hot cracking susceptibility. Based on the weldability considerations, 0.14%N is found to be the optimum for the nitrogen-enhanced 316LN SS.

The 0.14% nitrogen in this optimised 316LN SS composition shifts the solidification mode of the weld metal to fully austenitic region, including that due to dilution of nitrogen from the base metal, thereby increasing its hot cracking susceptibility. This necessitated development and qualification of shielded metal arc welding electrodes, with chemical composition of weld

metal specified to contain 0.14%N based on evaluation using the WRC-1992 diagram [23]. To ensure ferritic mode of solidification and sufficient delta-ferrite for ensuring adequate resistance to hot-cracking, the chemical composition of the weld metal for nitrogen-enhanced E316-15N electrodes was suitably tailored. Using the E316-15M welding electrodes developed for PFBR as the basis [24], for the E316-15N specification, the content of three elements C, N and Cr were adjusted within the ASME specification window (Table 1). Also, to ensure adequate resistance to both hot cracking and elevated-temperature formation of sigma-phase, delta-ferrite content of 3-7 FN is specified for the E316-15N weld metal. Further, care has to be exercised during welding to avoid formation of nitrogen porosity. These modified E316-15N electrodes have been successfully developed, during which the most challenging was achieving the specified minimum toughness of 3.0 $daJ.cm^{-2}$ after 1023K/100h ageing heat treatment. This requirement assesses the susceptibility of the weld metal to embrittlement by sigma-phase by transformation of delta-ferrite during high-temperature exposure, and for which the Mo content has to be carefully controlled to the lower limit. Another challenge has been improving the slag detachability of the deposited weld metal, as poor slag detachability often necessitates extensive grinding and rework. All these necessitated evaluation of a large number of trial batches for optimizing both the composition of the weld metal and the flux.

Table 1: Chemical composition (in wt%) and delta-ferrite content (in FN) of E316-15 weld metal as per ASME and for welding 316LN SS with 0.07% and 0.14% nitrogen

Consumable	C	Cr	Ni	Mo	N	Mn	Si	P	S	Ti+Nb+Ta	Cu	Co	B	FN
E316-15 (ASME)	0.08 max	17-20	11-14	2-3	–	0.5-2.5	0.9 max	0.04 max	0.03 max	–	0.75 max	–	–	–
E316-15M (PFBR)	0.045-0.055	18-19	11-12	1.9-2.2	0.06-0.10	1.2-1.8	0.4-0.7	0.025 max	0.020 max	0.1 max	0.5 max	0.2 max	0.002 max	3-7
E316-15N (New)	0.040-0.050	19-20	11-12	1.9-2.2	0.12-0.16	1.2-1.8	0.4-0.7	0.025 max	0.020 max	0.1 max	0.5 max	0.2 max	0.002 max	3-7

4. Concluding Remarks

Extensive studies on the effects of Ti, Si and P on tensile, creep, void swelling resistance and weldability of modified Alloy D9 heats, resulted in the development of IFAC-1, containing 0.25%Ti, 0.75%Si and 0.04%P, for use as core structural material in future SFRs. IFAC-1 has higher void swelling resistance, comparable thermal creep properties, and capability for enhancing fuel burnup beyond 130 GWd/t. The optimum procedure for welding 316LN SS end plug to cladding tubes of this steel has also been established. Detailed studies on the effect of nitrogen content of 0.07-0.22% on tensile, creep and low cycle fatigue properties and also weldability resulted in optimizing the nitrogen content to 0.14% for the enhanced-nitrogen 316LN for use as reactor structural material in SFRs. Special-purpose E316-15N weld consumables have also been developed and qualified for welding of the optimised nitrogen-enhanced 316LN SS.

References

[1]   G.Srinivasan et al., Nucl Engg Design, **236** (2006) 796.
[2]   C.N.Venkiteswaran et al., J ASTM Intnl, **6** (2009).
[3]   Jojo Joseph et al., Proceedings FR-13 (2012)
[4]   G.S.Was, Fundamentals of Radiation Materials Science: Metals and Alloys, Springer-Verlag Berlin Heidelberg, 2007.
[5]   S.Latha et al*.,* Intnl J Pressure Vessels and Piping **85** (2008) 866.
[6]   S.Latha et al., J Nucl Mater, **409** (2011) 214.
[7]   S.Latha, M.D.Mathew, P.Parameswaran, K.Laha, S.Panneer Selvi, S.L.Mannan, Procedia Engineering, **55** (2013) 58.
[8]   S.Latha, M.D.Mathew, P.Parameswaran, M.Nandagopal, S.L.Mannan, J Nucl Mater, **409** (2011) 214.
[9]   M.Fujiwara, H.Uchida, S.Ohta, J Mater Sci, **13** (1994) 908.
[10]   M.I.Hamilton, G.D.Johnson, R.J.Puigh, F.A.Garner, P.J.Maziaz, W.J.S.Yang, N.Abraham, ASTM STP 1042 (1989) 124.
[11]   E.H.Lee, L.K.Mansur, J Nucl Mater, **278** (2000) 11.
[12]   P.J.Maziasz, J Nucl Mater, **200** (1993) 90.
[13]   D.J.Mazey, J Nucl Mater, **174** (1990) 196.
[14]   P.J.Maziasz, J Nucl Mater, **205** (1993) 118.
[15]   T.Takalo, N.Suutala, T.Moisio, Metall Trans A, **10** (1979) 1173.
[16]   M.D.Mathew, K.A.Gopal, S.Murugan, B.K.Panigrahi, A.K.Bhaduri, T.Jayakumar, Advanced Materials Research, **794** (2013) 749
[17]   V.Ganesan, M.D.Mathew, K.Bhanu Sankara Rao, Mater Sci Technol, **25** (2009) 614.
[18]   G.Shastry et al., Trans Ind Inst Metals, **58** (2005) 275.
[19]   G.Sasikala G. et al., Trans Ind Inst Metals, **53** (2000) 223.
[20]   G.Sasikala et al., J Nucl Mater, **273** (1999) 257.
[21]   M.D.Mathew, Procedia Engineering, **55** (2013) 17
[22]   G.Srinivasan, M.Divya, S.K.Albert, A.K. Bhaduri, A.Klenk, D.R.G.Achar, Welding in the World , **54** (2010) R322-R332
[23]   T.Jayakumar, A.K.Bhaduri, M.D.Mathew, S.K.Albert, U.Kamachi Mudali, Advanced Materials Research, **794** (2013) 670.
[24]   G.Srinivasan, A.K.Bhaduri, Trans Indian Inst Metals **60** (2007) 399-406

Part G

New Power Plant Cycles and Flexible Operation

Component Performance-driven Solutions for Long-Term Efficiency Increase in Ultra Supercritical Power Plants Macplus Project

Egidio Zanin (CSM), Edgardo Coda (Foster Wheeler), Paul Kilgallon (Doosan Babcock), Scott Lockyer (E.ON Technologies), Peter Mayr (TU Chemnitz), Christian Schlacher (TU Graz), Oriana Tassa (CSM), Rod.Vanstone (Alstom Power)

Egidio Zanin: Centro Sviluppo Materiali SpA (via di Castel Romano 100, 00128 Rome Italy, email: e.zanin@c-s-m.it)

Abstract

Since 1882 when Edison launched the first modern Power Station, the power generation system has been subjected to several transformations. Today, the wide use of renewables fonts has become a reality and new paradigms for designing energy infrastructures are required. The requirements in power generation are depending on region-specific conditions but needs as efficiency, flexibility and affordability can be considered as basic conditions.

An original feature of the future power plants is their integration in a network of diversified energy generation systems, imposing the capability of the power plants to vary the power output, flat out during the peak time, saving mode during quite periods, in order to mitigate the unavoidable oscillation of non-steady renewable power generation systems (e.g. solar, wind power plants). Macplus is a project funded by EU Commission aiming to improve critical components performances in A-USC Power Plants.

Keywords: components, A-USC, Efficiency, refractory, heat exchanger, steel, nickel alloy, advanced design

1   Introduction

The future prospects for coal-fired power plants in Europe will be critically dependent on our ability to make advanced, more efficient plant reliable and readily maintainable. The prospects for successful implementation of Carbon Capture and Storage (CCS) are also strongly dependent on plant efficiency. CCS itself involves an efficiency penalty, and becomes economically very questionable if considered for application to plant with only moderate starting efficiency. In the view of a sustainable development and implementation of CCS technologies also oxy-fuel combustion (with possible biomass co-firing) can be a promising enabling technology for CCS in pulverised coal fired boilers.

These requirements constitute a big challenge for the all components and materials inside the plants that need to counteract new extreme working conditions, namely: higher working temperatures, more corrosive environments, more severe thermo-mechanical loads.The increase in net efficiency is the sum of many, complex and prolonged improvement actions on materials, components and thermodynamic design optimisation of power plants for the given steam parameters. For this reason, only an integrated design and engineering approach to the problem may result in a cost-effective, affordable and long lasting solution, deserving industrial scaling-up.

2   Project Aims and structure

MACPLUS project aims to increase the net efficiency of coal fired plants by increasing the performance and reliability of some critical components identified as follow:
- Refractory materials of the combustion chamber (especially for oxy-combustion application),
- Headers and pipeworks (avoidance of weld Type IV cracking phenomena, working temperature increase),
- Super heaters (optimised creep performance in high temperature oxidation/hot corrosion environments),
- Coated pipes and boiler components able to withstand co-combustion conditions (high temperature oxidation/hot corrosion, erosion-adhesion and wear),
- HP and IP steam turbine rotor components and turbine casing operating at VHT.

The project started on January 1st 2011, will last 54 months and it is carried out by a Consortium of 24 partners, carefully selected to meet the needs of the project in terms of skills, competencies and understanding of the problem and possible solutions, each of them bringing specific knowledge of at least one aspect of the supply chain.

Research institutes:	CSM, TU Graz, VUZ, NPL, KTH, Loughborough University, VTT, IWM, TUV, Research Centre Juelich, DTU, Imperial College, CIUDEN, MPA Stuttgart
Material/Component Suppliers	Tubacex, CAS Cogne accia Speciali, Flame Spray, Goodwin Steel Castings
Engineering Companies	Alstom, Doosan Babcock, Foster Wheeler
Utilities	Endesa, RWE, E.ON

Table 1: Macplus participants

Other project targets are:
Relevant new scientific and technological know-how in terms of:
- microstructure stability up to 650-660°C and reduced susceptibility to Type IV cracking mechanisms of advanced martensitic steels, like MARBN (and their welds)
- microstructure stability of austenitic steels (and their welds)
- microstructure stability of Ni-based alloys up to 750-780°C (and their welds)degradation mechanisms and duration of Fe-base and Ni-base alloys in aggressive high temperature environments (high concentration of CO, CO_2, N_2, SO_2, SO_3, Cl- and F-base compounds deriving from the co-firing of biomass and industrial/urban waste)
- alloy design criteria and stability in highly demanding environments (e.g. temperature, oxidation and corrosion, abrasion, TMF) of metallic coatings and ceramic refractory materials
- creep and creep-fatigue behaviour of metallic materials (and their welded components) at higher temperature than available in the literature, under real environmental conditions (e.g. atmospheres) as awaited in existing and new build pulverised coal-fired USC power plants (in view of CCS)
- steam oxidation mechanisms in austenitic steels and Ni-based alloys up to 800°C.

Innovative solutions in material science (e.g. Fe-base and Ni-base materials, ceramics, coatings):

- advanced martensitic steels with judicious addition of Boron and Nitrogen (MARBN steels) for standard application up to 650-660°C
- austenitic steels (up to 30% Cr) for standard application up to 700-720°C
- Precipitation Hardened (PH) Ni-based alloys for standard application up to 750-780°C (in steam turbines and turbine casing, connection pipes and tubes)
- Surface-modified ceramic materials for application in oxy-combustion (pressurized) reactors, characterised by increasing addition of biomass co-firing (up to 20% within 2020), for operation at high temperature and variable thermo-mechanical load conditions.

Improvement of manufacturing techniques (melting, forging/casting, rolling/extruding, welding, etc.):
- melting, hot forging and casting procedures
- hot Rolling / Extruding procedures for MARBN and high alloy austenitic steels
- welding procedures and technologies (including hybrid laser) for homogeneous and inhomogeneous welds using MARBN, austenitic steels and Ni-based (forged/cast) alloys
- surface finishing effect in austenitic steels and Ni-based alloys for increased oxidation resistance at highest operation temperature.

Improvements in design criteria of materials and components for application in very demanding environments through the integration and development of engineering + metallurgy evolution models and new experimental test procedures and configurations:
- comparison of experimental test findings against design code requirements and practical component design methodologies
- reliability engineering analysis of the costs and risks of design with differing additional margins of safety, in particular to make better allowance for welds
- development of "condition monitoring techniques" – strain measurement is one candidate
- assessment of defect tolerance in parent and welds.
- metallurgically-based models for creep and creep-fatigue prediction in steels and Ni-based alloys:
- numerical issues of creep crack modelling in view of code and practice integration. Development of guidelines
- assessment of full scale high temperature components with stress/temperature gradients (pipe elbow, joints, etc.)
- extension of the model formulation to welded material and type IV fracture. Formulation of guidelines of the above into a "Design Advisory Tool"

In the first three years the main activities performed have been related to:
- definition of process conditions
- identification of critical components and related requirements
- identification of most interesting materials to be used
- characterisation of previously exposed samples
- preliminary test, investigations
- pilot plant tests
- innovative components/materials design
- prototypes production

805

2.1 Refractories

As regard refractory materials performance and lifetime in combustion reactors and main target is to create innovative refractory materials in high temperature oxy-fuel reactors. Macplus considers flexi burn reactors where operation can switch between air and oxy-fuel combustion repeatedly, thus allowing boiler operation depending on needs.

Figure 1: samples exposed in Ciuden Plant

From a refractory point of view, the peculiarity of this type of plants is that, during the oxy-combustion process, the flue gas recirculation provides an enrichment of minor species in the boiler which potentially can increase corrosion rates of the refractory lining the combustion chamber. Furthermore, certain oxy-fuel combustion processes can be designed to attain higher temperature in respect to air combustion with consequent increasing in the possible formation of liquid phases at the refractory surface.

Of recent critical concern, and serving as the focus of this discussion, are fuel composition and its effect on fouling and corrosion of the material lining of the boiler. In fact co-combustion of biomass with coal has become a very popular option to reduce the use of non-renewable fossil fuels. However the presence of alkalis in bio-fuel can degrade the refractory lining of the combustion chamber more rapidly, thus leading to a premature failure. Moreover the oft start-up/shut down operation of the plant, the switch between air and oxy combustion and load changes are severely challenging thermal shock resistance of the refractory materials.

To combine the thermal stress resistance of the bulk material and the corrosion resistance of the exposed surface, CSM proposes to employ Compositionally Graded Refractory materials (CGR). Such materials are characterized by a non-linear distribution of composition and properties over the volume which distinguishes them from the traditional isotropic materials. The chemical composition of CGR brick can be tuned for the special application in oxy-firing co-combustion process.

These newly realized CGR bricks were tested for the first time in an oxy-firing plant under co-combustion conditions. In particular they were tested at CIUDEN demo plant under real operating conditions and compared with other 14 different refractory test samples.

For the Macplus project, two subsequent test campaigns were realized in 2013. During the first session 100% pure anthracite was burnt and in the second session a blend (anthracite/olive cake pellets 70/30%en) was fired, 16 different refractory samples were exposed during both campaigns. The CGR materials are effective in reducing the cost/benefit

ration by minimizing the amount of precious corrosion/erosion resistant material and maximizing the amount of cheap thermal shock resistant material.

2.2 Headers and pipeworks

Weld "Type IV" cracking is a key life-limiting phenomenon which restricts the application temperature of current martensitic steels to no more than about 600-620°C. The new "MARBN" steel concept, combining nitrogen with boron strengthening, has been shown by laboratory testing to be potentially capable of eliminating the Type IV cracking mechanism and thereby enabling safe operation at higher temperatures. This will make advanced power plant of 45% efficiency with CCS economically viable by enabling a high fraction of the boiler headers and ancillary piping systems to be constructed from steel, so that the high costs of nickel super alloys are incurred only where steam temperatures in excess of 700°C are required.

Material of interest is high chromium steel with a composition incorporating high boron and low nitrogen, termed "MARBN". It has been shown in Japanese and European laboratories that interstitial micro alloying can apparently control recrystallisation during the welding thermal cycle in 9-12%Cr steels [1-14]. However, the fundamental mechanisms are not yet properly understood. This micro alloying approach provides, potentially, an innovative method of minimizing or eliminating the Type IV cracking problem in these steels. This will hence establish whether and for what compositional ranges the basic approach is truly viable. The more robust improvement of the new steel is in relation to compositional and processing parameters, the more viable it will be as a practical solution to Type IV cracking.

MACPLUS investigates claims of resistance to Type IV cracking in a new type of power plant steel with novel compositions, the use of advanced welding techniques to suppress Type IV cracking, and non conventional structural integrity assessment of components.
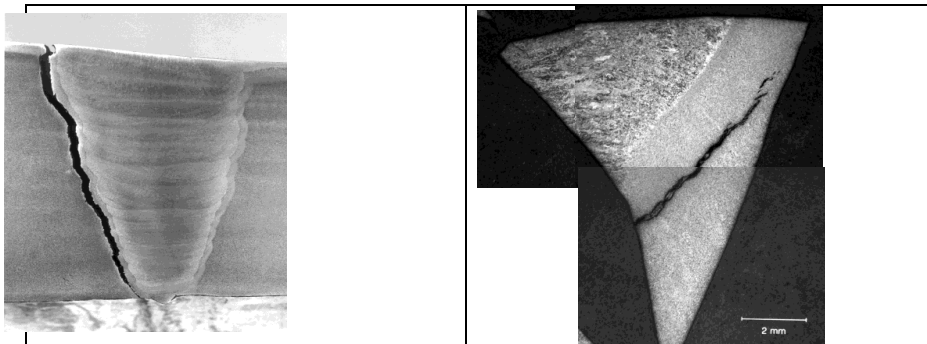
Figure 2: example of type IV Cracks in CRMoV and Grade 91 steels

Whilst it is Japanese work which points the way to successful micro alloying, the originators of the MARBN concept do not yet understand exactly why their selected steel variant appears to avoid weld heat-affected zone weakness, what ranges of alternative material compositions would show similar or better performance, and what might be the pitfalls in taking development beyond the laboratory and pursuing large-scale ingot casting and wrought product manufacture. This research will attempt to overcome these deficiencies by means of a

combination of empirical trials and controlled materials testing.

An alternative strategy is to suppress Type IV cracking by the means of novel welding processes such as, for example, Laser Beam Hybrid Welding (LBHW), Friction Stir Welding (FLAMEW) or Narrow Gap Welding (NGW). The goal here is to modify the Type IV strength level by modifying heat input during welding and the resulting stress state in the Type IV location.

The project aims to:
− to demonstrate MARBN steels applicability on the plant application scale;
− to identify alternative steel compositions to reduce costs and improve processability;
− to develop large scale manufacturing techniques and their demonstration in pilot component production;
− to develop and validate advanced automated welding processes to ensure that the weld itself does not become the "weak link";
to validate the design concept through long-term testing of weldments in MARBN steels.

Based on the chemical composition defined within the project, Cogne Acciai Speciali has produced 500 kg ingots that have been rolled at CSM.
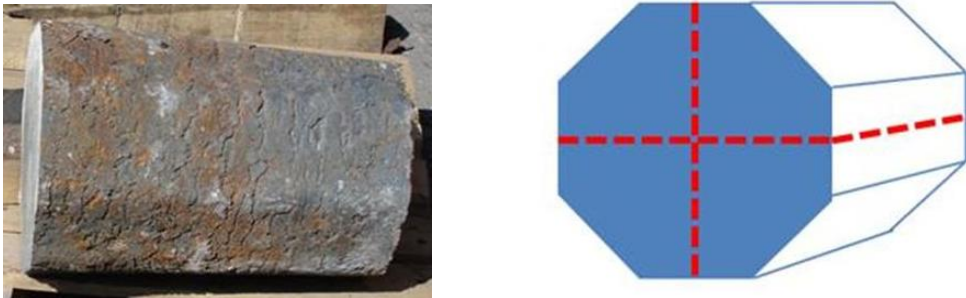
Figure 3: MARBN pilot full-scale pilot ingot obtained at Cogne steelwork (left) and preliminary cutting plan (right).

Figure 4: MARBN full-scale sub-ingot during hot rolling at the CSM mill.

The obtained material is now under study to determine its properties.

2.3 Superheaters

During operation the high-temperature materials suffer time dependant degradation by processes such as creep, fatigue, oxidation and corrosion. The materials performance is determined by the microstructure stability over prolonged time of operation up to 30 years. Our ability to understand and control the microstructure evolution by optimization of chemical composition, heat treatment and manufacturing processes is thus a vital element in the improvement of efficiency of the USC power plants. Experience has demonstrated that strong acceleration of the time dependent degradation processes in the laboratory by increase of load (mainly temperature or stress) on the materials can introduce critical changes in the microstructure evolution, which effectively prevents prolonged extrapolation of the time dependant materials performance to service like conditions. It is thus essential that the understanding and control of the microstructure evolution is based on investigations and characterization of materials after long-term exposure for several years under near operating conditions.

The use of new steel alloys opens several question marks:

1) Long-term microstructural stability. Actually there is no solid understanding of strengthening mechanisms governing long-term behaviour of new advanced austenitic in high temperature and aggressive environments.
    Available long-term exposed samples were exercised at maximum temperature of 650°C and limited times and showed rapid and extensive precipitation of several coarse phases (e.g. sigma phase, Laves phase, $M_{23}C_6$...). There is no available experimental and modelled knowledge about microstructure evolution of austenitic steels at 700°C within 100,000h.
2) Long-term oxidation/corrosion resistance. Austenitic steels show satisfactory strength and corrosion/oxidation resistance, further improved by surface treatment as shot-peening or blasting. However there are no evidence that the improvement obtained by shot-peening can be maintained in the long-term service.
3) Long-term creep resistance. Long-term creep tests are very limited and the predicted creep-rupture stresses within 100,000h at 700°C are not very reliable.
4) Optimisation of strength and alloy cost. Limited service experience with austenitic steels does not allow optimisation of chemical composition in order to reduce alloy cost: e.g. reduction of Cr and Ni content without negatively affecting the oxidation/corrosion/creep resistance in the long-term service.
5) Understanding and avoidance of reheat cracking in thick section Ni-base super alloys. The first experiences from rest rigs with thick section Ni based super alloys under simulated loads reproducing service like conditions in a 700°C power plant indicate that reheat cracking of new weldments could be a serious problem. This part of the project aims at understanding the phenomenon for selected Ni based materials based on microstructure investigations and at the development of heat treatment procedures to eliminate the problem.

One way to obtain the microstructure control is via physically based models of the microstructure evolution and the coupling between microstructure and performance of the materials. Such models need to be validated against results obtained by investigations on long-term exposed materials.

The same challenges will be faced by the use of Ni-based super alloys in power plants at 750°C, with even more difficulties requiring new stronger alloys has to be developed. The microstructure knowledge obtained inside the present project is highly useful for the alloy design of new stronger Ni base alloys.

An extensive test matrix of aged and exposed samples has been investigated to understand the main mechanisms of degradation of stainless steels and Ni alloys candidates for AUSC, operating at temperatures >700°C. Corrosion/steam oxidation tests have been performed to well understand the surface degradation phenomena. To evaluate the corrosion behaviour in highly aggressive environments commercial materials have been tested in laboratory and at pilot stage at Ciuden plant. Three stainless steels and three Ni-based alloys have been selected for investigations:

1) Stainless steels:	2) Ni-based alloys:
- 22% Cr Sanicro25	- IN617
- 25%Cr HR3C	- C263
- 25%Cr DMV310N	- IN740

The guidelines for the definition of the chemical composition modifications have been obtained by this previous work, both for stainless steels and Ni alloy.
Set up and validation of models have been performed by comparing the experimental and calculated results. On the base of the combined thermodynamic (Themocalc, JMatPro) and thermo-kinetic (MatCalc) modelling results, the optimized chemical compositions have been selected for the production of industrial tubes.

Figure 5: Fouling probe: a) samples before exposure; b) after campaign 1; c) after campaign 2.

MACPLUS is going to develop for EU Boiler-making and End-Users super heater prototypes (tubes) of modified improved commercial austenitic steels and Ni-based super alloy to be used in the hottest parts of PF power plant up to 700°C and 350bar, in order to raise global plant efficiency and guarantee improved net efficiency with use of CCS technologies. Prototypes will be installed in RWE and E.ON power plants for their validation.

Figure 6: Bar production of modified austenitic stainless steel [CAS]

The test rig consists of the soot blower unit (water or steam can be applied) on the top and the so-called corrosion probe (material to be tested) at the bottom. The corrosion probe consists of two parts: the boiler tube material which is to be tested and the supporting which is made of aluminium. The tube sample (weldments possible) itself is max. 500 mm long, has common superheater tube dimensions (e.g. 44.5 mm x 5.0 mm) and is equipped with three thermocouples. The inside is flushed with ambient air to cool down the metal surface. By measuring the metal temperatures using the thermocouples and varying the air flux, the metal temperature can be controlled.
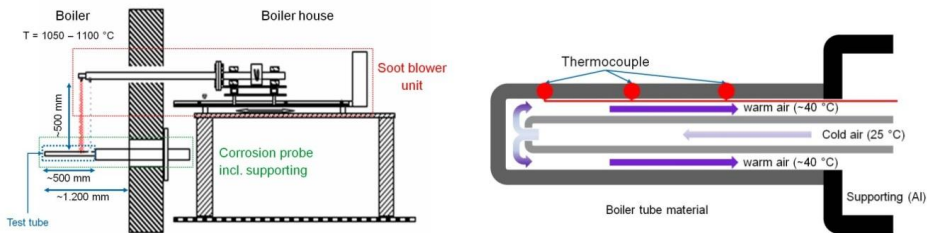
Figure 7: Schematic drawing of test rig (left) and the corrosion probe (right)
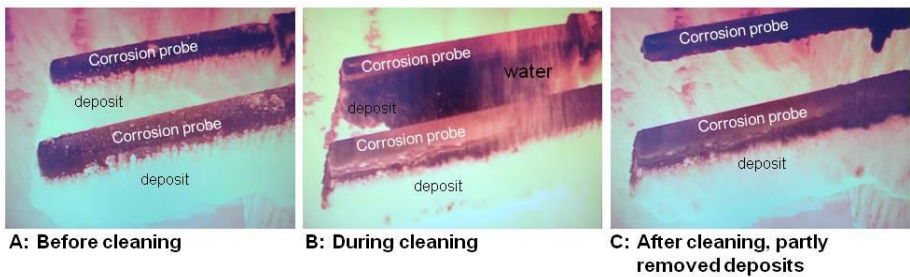
Figure 8: test rig at RWE Power AG

811

2.4 Heat exchangers protection

The oxy-fuel combustion of coal and the co-firing of biomass are relatively attractive options for the reduction of the CO_2 emission levels in advanced ultra-supercritical coal-fired plants. It is clear, however, that the high temperature boiler components will encounter ever more aggressive fireside corrosion and increasing rates of steam side oxidation at the operating temperatures that are required to improve plant efficiencies to levels that help to make the implementation of the CO_2 capture systems more viable. These issues represent a significant technical challenge to the industry. The resistance to fireside corrosion and steam-side oxidation of the principal alloys of interest for these applications is not well understood, and it is becoming increasingly clear that novel materials solutions will be required.

Fireside corrosion
Looking in the first instance at the fireside corrosion issues, it is well known within the industry that the service life of boiler tubes and other key high temperature components of coal-fired steam generators are increasingly affected by fireside corrosion, principally within the boiler furnace and in the final super heater and reheater banks. The rate of metal wastage is dependent on the flue gas and metal temperatures as well as that local ash deposit and flue gas chemistries. It is also recognised that these high temperature corrosion phenomena are extremely complex and difficult to study. Hot corrosion is the result of accelerated oxidation when metals/alloys are covered with contaminant salt films. The temperature range within which hot corrosion occurs strongly depends on the salt chemistry and gas constituents as well as the alloy composition. These phenomena have been observed in coal gasifiers, petrochemical process equipment, internal combustion engine exhaust systems, boilers, gas turbine engines on aircraft and in waste incinerators. Although oxygen and sulfur by themselves do not have significant corrosive effects, the overall environment in these processes leads to the formation of solid and molten salts that take part in corrosion.

Steam oxidation
At elevated steam temperatures, the rate of steam side oxidation of the internal surfaces of boiler tubes and steam pipework can become appreciable. It is generally agreed from the knowledge gained from cumulative plant experience, and from the results of laboratory and test loop experiments, that the key parameters that control the rate of steam side oxidation and the tendency of oxide layers to exfoliate and spall are as follows:
The rate of oxidation of any given material increases exponentially with increasing metal temperature. The rate of steam oxidation of boiler steels decreases with increasing chromium content.
For boiler tubes, the presence of a heat flux across the metal/oxide layer is considered to have significant effects both on the metal temperatures under the oxide, and on the growth rate and the physical nature of the oxide layer. For steam pipeworks, the heat flux effects are obviously of much less importance
Any significant temperature variations or cycling will also have a significant impact on the physical properties of the growing oxide layer, and therefore on the oxide growth rates
Oxide layers that grow to significant thicknesses will have a tendency to exfoliate, and to blister and spall. These are important and fairly complex phenomena, but they are not well understood. The impacts of exfoliation on heat transfer and on the integrity of the system

can be quite dramatic. It is clear that the geometry of the component, and the thickness and structure of the oxide layer will influence the risks of exfoliation, as will any significant temperature variations or temperature cycling experienced by the component.

MACPLUS is developing advanced surface engineering of the internal and external tube/pipe surfaces of high temperature boiler components. In general, the achievement of the optimum performance of a coating/base alloy system, in terms of cost, operating life and maintainability, is dependent on employing the best coating composition to resist the corrosion/oxidation attack, and ensuring that this is compatible with structural and fabrication requirements of the base alloy.

For the fireside, the emphasis is on the development of sprayable, particulate-based coating compositions and application technologies that can be used in-situ in either new build or retrofit applications, as well as for repair purposes.
Steam-side coatings must be applied during the fabrication of the tube/pipe components, ensuring compatibility with the base alloys, heat treatments, etc. It is proposed that these will be based on vapour phase, diffusion coatings, or on slurry-based systems.

Within Macplus, the main objectives are as follows:
- To collect and collate information about the utilisation of coated materials for the protection of high temperature components within the power industry
- To define the conditions on the steam side and fireside of the relevant boiler components and the technical and other requirements for the coatings
- To select/develop the appropriate coating compositions and the application technologies for the specific application in advanced coal-fired boiler plants
- To prepare suitable lab-scale test specimens of coated materials for examination and testing by other partners
- To perform and report the detailed lab characterisation of the coated specimens
- To identify the preferred coatings and other surface treatments for further examination at larger scale
- To perform the demonstration scale tests of the preferred protective coating technologies and to characterise the condition of the test components after exposure
- To perform and report the detailed cost-benefit analyses of the preferred coating technologies

Different type of coatings have been produced and tested in laboratory and at pilot stage at Ciuden plant.

Figure 9: Evaporator inlet clamp and INTREX clamps

The solutions explored have been:

For fireside:
- CSM specimens:
    - Fe16Cr (HVOF)
    - overaluminized (VPA) Fe16Cr
    - Fe26Cr (HVOF)
    - overaluminized (VPA) Fe26Cr
    - aluminized (VPA)
- ENDESA specimens:
    - high hardness steel + Al
- FLAME SPRAY specimens:
    - CoCrAlY
    - aluminized (slurry)

For Steamside
- Ni-50Cr (HVOF)
- Co based (electroplated)
- MCrAlY (electroplated)

The results of the experimental campaign are now under evaluation.

2.5 Turbine

As regards the turbine Macplus aims to increase the working temperature in next generation advanced ultra-supercritical power generation using latest generation high alloy steels (620°C – 670°C) and Ni based alloys (670°C -720°C). This is to be reached by understanding the full processing route (casting solidification, forging and heat treatments).

This is to be achieved by:
- using process models to predict best processing route in high alloys steels and Ni based alloys (solidification, forging and heat treatment modelling).
- manufacture of a full-scale casting and a forged rotor mock-up based on optimized process routes to validate the process models.
- applying the same approach to welded joints.

The following table highlights the candidate alloy systems chosen to be investigated:

Candidate alloy systems

	Forgings	Castings
600-620C +	B-modified martensitic steel FB2	B-modified martensitic steel CB2
700-720C	Solid solution strengthened Ni alloys 617	Solid solution strengthened Ni alloys 625
750C	Pptn hardened Ni alloys, 282	Pptn hardened Ni alloys e.g 282, 740H

- Green – process modelling
- Yellow – process modelling and validation through manufacture

Boron modified martensitic steel FB2 was chosen as a candidate due to extensive experience with this material through the COST European research projects (501, 522 and 536) and as such a broad property database exists.Alstom has numerous experiences in the manufacture of large diameter rotor forgings (up to 1.2 meters in diameter) in this material, (ref: MANUFACTURING EXPERIENCE IN AN ADVANCED 9%CrMoCoVNbNB ALLOY FOR USC STEAM TURBINE ROTOR FORGINGS AND CASTINGS; Rod Vanstone, Ian Chilton, Pawel Jaworski: Journal of Engineering for Gas Turbines and Power, June 2013)
Solid solution strengthened alloys 617 and 625 were chosen as candidate alloys again due to positive experience with these grades through a number of European joint research projects where significant data has been produced as well as the manufacture of large diameter trial rotor forgings and castings.

Finally, Macplus identified, candidate alloys needed to withstand the operating conditions of a steam turbine operating at a steam temperature of 760°C. Alloy 282 was seen to have a good combination of high temperature strength, weldability and formability of the Ni alloys investigated. Alloy 282 successfully met the 100,000 hour rupture strength of 100MPa at operating temperature and was shown to have the potential to be welded in large section thicknesses.
The following results have been achieved:
- The temperature constraints for the selected alloys have been established by thermodynamic modelling at CSM with JMatPro software.
- The physical properties required for the forging model have been calculated at CSM using JMatPro software. The properties are calculated as a function of the temperature and compared with existing data: good agreement is found. The data can be used in the forging model

- The rheology has been determined for by CSM. The stress-strain curves are measured as a function of temperature, strain and strain rate.
- Solidification simulations have been carried out by Goodwins to characterize the behaviour of alloy 625.
- Forging modelling simulations have been carried out at Altom using commercial software Qform
- A full scale casting has been successfully manufactured in steel CB2 by Goodwins.
- A mock-up forging has been successfully manufactured by Cogne following forging procedures designed by Alstom to simulate the forging conditions in a full sized forging.

Figure 10: Mock-up of Alloy 282 Forging Manufacture

2.6 Advanced Design and Testing Criteria for High Temperature Components

The work within this part of the MACPLUS project has the following key objectives and strategy.

- To support the design and in-service operation & maintenance of high efficiency USC plant.
- To develop guidelines/tools that help the plant designer and operator to minimise the occurrence of unplanned outages, thereby ensuring safety and maximising plant availability.
- To develop advanced computational models that can be referenced to experimental tests (laboratory and full scale) and design/assessment codes where appropriate.
- Review the design, assessment and computational methods developed as part of the research to identify simplified approaches that could be used in the field to assess plant condition.
- To develop innovative condition monitoring tools/strategies that have some link to the detailed testing and modelling, thereby providing confidence in component condition assessments based on the use of plant monitor data.
- To utilise wherever possible experience from current plant operation to identify and exploit the key technical opportunities. Define the key methods and techniques that can be applied to assess plant condition and qualify how they are applied.

- Many of the work package deliverables are in the form of guidelines, every effort should be made to ensure that they that can be used in the field and that future technical development and research needs are clearly identified.
- Above all, seek pragmatic solutions and guidelines that can be implemented by the Utilities.
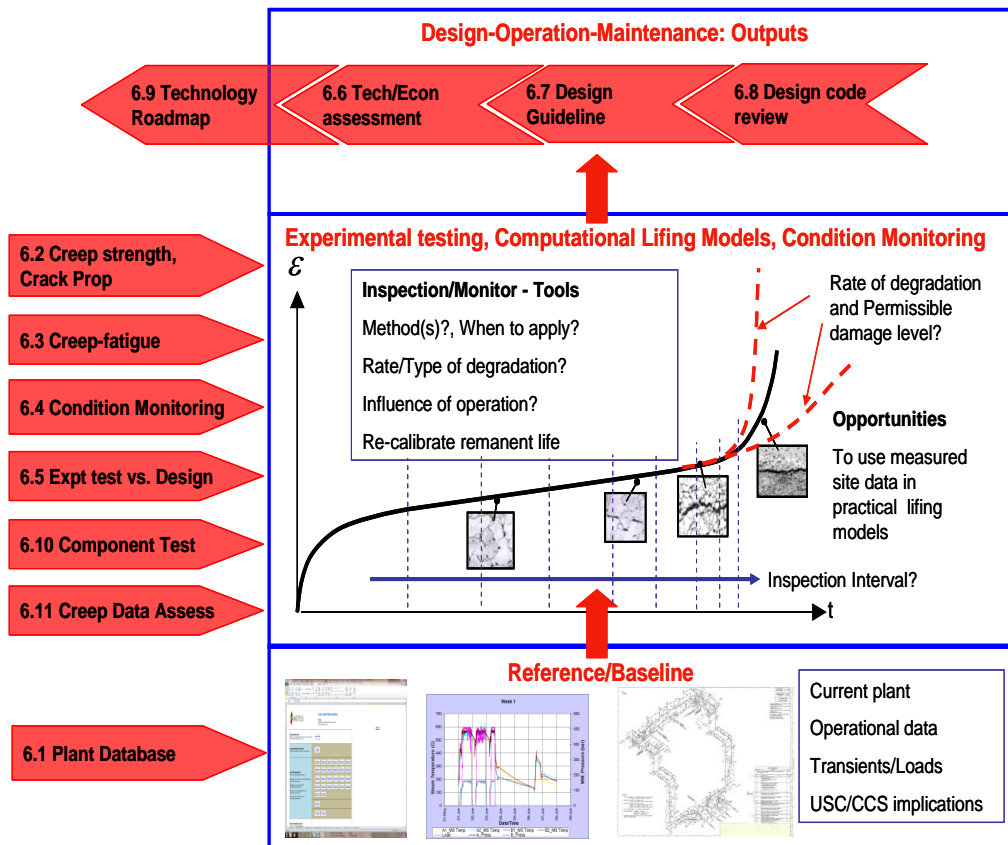
Figure 11: advanced design activity structure

Significant progress has been made in delivering the key objectives. A plant database has been populated and made available to partners via the MACPLUS website. The database contains a significant amount of historical plant operational data (anonymously provided) and samples of both normal and fault event thermal transients. Different approaches to the creep modelling and creep-fatigue modelling of both martensitic steels P91/P92 and Nickel base alloy materials and welds are being developed. These approaches will be further developed in 2014 and importantly will utilise data from proposed experimental tests based on stock P91 material from the component test and Nickel base alloys obtained from the COMTES700 project. Research to compile creep data for targeted project materials is ongoing and the information will be compiled into a database. This data is supporting the planning of

experimental tests and provides valuable information to support a review the different approaches that can be used for practical plant integrity assessments, using either simplified or complex methodologies, which is a key project output.

The key activity of this work is the testing, in a dedicated test rig, of a thick section component designed by RWE/TUV that will be subjected to daily load cycles indicative of plant operation, and in particular creep-fatigue damage mechanisms. The test component has been manufactured from P91 and the design has been developed using a finite element simulation undertaken by IWM that replicates the proposed cyclic loading conditions. The test specimen is comprehensively instrumented with a range of sensors covering; strain (electrical, optical, capacitive), crack detection, creep damage, acoustic, pressure and temperature. This provides comprehensive scope for online condition monitoring and more traditional outage type assessments when the test specimen is brought off load at periodic intervals. The component has been comprehensively assessed to determine its life and the results will be compared to the actual life. This along with the other experimental and assessment work will be used to review current assessment procedures for creep-fatigue and potentially offer new procedures for cycling power plant.

References

[1] F. Abe: Effect on Boron on creep deformation behaviour and microstructure evolution in 9%Cr steel at 650°C; Int. Journal of Material Research: 2008, vol. 99, pp.387-394
[2] F. Abe and others: Stabilization of martensitic structure in advanced 9Cr steel during creep at high temperature: Material Science and Engineering A 378 (2004), pp. 299-303
[3] D. J. Abson and others: Advances in welded creep resistant 9-12%Cr steels; 5th Int. Conf. on Advanced Materials Technology for Fossil Power Plants, 2-5 October 2007
[4] F. Abe: New development on Boron metallurgy of creep-resistant 9%Cr steel for USC power plant at 650°C; Int. Conf. High Strength Steels, Buenos Aires, 26-28 May 2008
[5] F.Abe: Precipitate design for creep strengthening of 9%Cr tempered martensitic steel for USC power plants: Science & Technology of Advanced Materials 9 (2008)
[6] B. Sonderegger, E. Kozeschnik, H. Leitner, H. Clemens, J. Svoboda and F.D. Fischer, Computational analysis of the precipitation kinetics in a complex tool steel", Int. J. Mat. Res. 99 (4), 2008, 410-415
[7] I. Holzer and E. Kozeschnik, „Predicted precipitate back-stress and creep rupture strength of the advanced 9-12 % Cr steel COST E2", Int. J. Mat. Res. 99 (4), 2008, 416-421
[8] Abe F, "Metallurgy for long-term stabilization of ferritic steels for thick section boiler components in USC power plant at 650°C", in 8th International Conference of Materials for Advanced Power Engineering 2006, Liege, Forschungszentrum Jülich, 2006
[9] P. Mayr, H. Cerjak, "The heat affected zone of Boron alloyed creep resistant 9% Chromium steels and their susceptibility to Type IV cracking", Advances in Materials Technology for Fossil Power Plants: Proceedings from the 5th International Conference; Marco Island, FL, USA, ASM International, pp. 914-926, 2008
[10] B. Wilshire: Long-term creep life prediction for a high chromium steel, Scripta Materialia, Volume 56, Issue 8, Pages 701-704
[11] K. Maruyama, K. Yoshimi: Influence of Data Analysis Method and Allowable Stress Criterion on Allowable Stress of Gr.122 Heat Resistant Steel; J. Pressure Vessel

[12] Fujita T: 'Future ferritic steels for high temperature service.' Proc EPRI/National Power Conf on New steels for advanced power plant up to 620°C, London, 11 May 1995 190-200

[13] Y. Takahashi: Study on creep-fatigue evaluation procedures for high chromium steels-Part II: Sensitivity to calculated deformation: International journal of pressure vessels and piping: 2008, vol. 85, n°6, pp. 423-440

[14] R. Wiswanathan & others: Materials technology for advanced coal power plants: www.msm.cam.ac.uk/phasetrans/2005/LINK/188.pdf

HIGH TEMPERATURE CORROSION ISSUES IN OXYFUEL PLANTS

W.J. Quadakkers, P. Huczkowski, A. Gerhardt [a)], U. Burchhardt [b)],
A. Chyrkin, T. Hüttel

Forschungszentrum Jülich, Institute of Energy and Climate Research (IEK-2),
52425 Jülich, FRG (j.quadakkers@fz-juelich.de)

[a)] Vattenfall Research & Development AB, D-13599 Berlin, Germany
[b)] Vattenfall Europe Generation AG, D-03050 Cottbus, Germany

Abstract

The oxidation behaviour of a number of candidate alloys for heat exchanging components in oxyfuel plants was investigated at temperatures between 550-700°C up to exposure times of 1000h in model gas mixtures containing high amounts of CO_2 and/or water vapour with and without addition of SO_2. The effect of deposits on the corrosion behaviour was in the present paper not addressed.

During exposure in CO_2 and H_2O/CO_2 rich gas mixtures at 550-650°C the oxidation rates and scale compositions of the low alloy steel 13CrMo 4 4 were similar to those observed in steam environments. In the mentioned gases the martensitic steels P92 and VM12 did not form the very slowly growing oxide scales which are commonly found during air oxidation. The steels formed double layered scales whereby the inner layer consisted of magnetite and FeCr-spinel whereas the outer layer was composed of magnetite with or without hematite. Addition of 1 or 3% oxygen was able to suppress the adverse effect of CO_2 on protective chromia scale formation but not that of water vapour. Addition of SO_2 to a simulated oxyfuel gas $Ar/CO_2/H_2O/O_2$ tended to suppress the internal oxidation commonly seen in case of martensitic steels.

At 550°C the studied austenitic steels exhibited very slow scale growth rates in all SO_2-free test gases. However, at and above 600°C the 17 – 18%Cr steels 1.4910 and TP347H FG started to form two-layered iron rich surface oxide scales whereby the outer oxide was prone to spallation upon thermal cycling. The austenitic steel 310N and the nickel base alloy 617 can, in first approximation, be considered as chromia forming materials in the used temperature range up to 700°C. Presence of water vapour in combination with intentionally added oxygen resulted in formation of volatile chromium oxyhydroxide leading at 700°C to a net weight loss for alloy 617 and in a change from pure chromia scale growth into a mixed, Fe rich oxide scale in case of the austenitic steel 310. At the mentioned temperature addition of SO_2 suppressed formation of the volatile Cr species resulting in improved oxidation resistance. However, at lower temperatures formation of Ni- and Co-base sulphates resulted in case of 617 in increased oxidation rates which were actually much higher than those found at 700°C.

Keywords: Oxidation, martensitic steels, austenitic steels, nickel base alloy, sulphur dioxide

1. Introduction

Increasing efficiency of fossil fuel fired power plants obviously results in a decrease in the CO_2 emissions [1-3], however, more stringent ecological requirements led to the demand for a further lowering of CO_2 emissions. The so-called oxyfuel process [4, 5] is frequently considered as a most promising technology for CO_2 capture from the exhaust gas in coal fired power plants. In an oxyfuel plant heat exchanging metallic components will be exposed to a flue gas that contains much higher CO_2 and water vapour contents than conventional flue gases [6]. Depending on the actually prevailing process, also the SO_2 partial pressure may be higher in the oxyfuel environment.

In literature many studies concerning the behaviour of low alloy steels, martensitic 9-12% chromium steels as well austenitic steels in water vapour rich gases, i.e. pure steam (see e.g. [7-11]) or combustion type gases [12, 13], in the temperature range 500-650°C are available. Also the behaviour of nickel and cobalt base alloys in such environments has been studied [11, 14, 15] although the information is far less extensive than that for the mentioned steels. Only few papers exist which relate to the oxidation behaviour of metallic materials in CO_2-rich test gases. A number of early studies [16-18] mainly deal with the behaviour of selected model alloys in CO_2 and few publications describe the oxidation behaviour of various materials exposed to CO_2-CO [19, 20] and CO_2-O_2 [21] environments. However, far less publications treat the oxidation resistance of metallic components exposed in the CO_2-H_2O-rich gases prevailing under oxyfuel conditions. Only recently a substantial number of publications [22 -30] on this subject became available, whereby the studies mainly related to low alloy and martensitic steels.

In the present study, the oxidation behaviour of selected candidate construction materials for heat exchanging components in oxyfuel plants in CO_2- and/or H_2O-rich gas mixtures with and without addition of oxygen and/or SO_2 will be presented. The test temperatures were correlated with the actual envisaged temperatures of the respective materials in real application [1-8, 31, 32], although in some cases the materials were tested in a wider temperature range. The main aim of the study was to elucidate the effect of the individual gas species (CO_2, H_2O, O_2 and SO_2) on the overall oxidation performance in a complex oxyfuel relevant environment. In the prevailing study, the effect of deposits was not addressed.

2. Experimental

The compositions of the materials selected for the present study are given in table 1. Specimens with dimensions of 20x10x2 mm^3 were machined from the prevailing thick walled tubes and ground to 1200 grit surface finish prior to oxidation testing. The specimens were oxidised at temperatures between 550 and 700°C in various gas mixtures, the compositions of which are given in table 2. In a few cases additional tests were carried out in laboratory air. Values for equilibrium activities of oxygen, carbon and sulphur as function of temperature in the various environments were presented in previous papers [22, 23, 27, 33].

The exposures were carried out in horizontal furnaces equipped with alumina reaction tubes and specimen holders. The mass changes of the specimens were measured after interrupting the oxidation tests in regular time intervals, mostly every 250h. Additionally, isothermal short term experiments were performed with exposure times ranging from 100 to 500h for obtaining more detailed information on the mechanisms of scale growth. The steel microstructure and the oxide scales formed on the specimen surfaces were examined using optical microscopy, Laser Raman spectroscopy (LRS) and scanning electron microscopy (SEM) equipped with an energy dispersive x-ray (EDX) detector. Selected specimens were examined by x-ray diffraction (XRD). Metallographic cross sections of the oxidised specimens were obtained by sputtering a nm thick gold layer, then electroplating with Ni, mounting in an epoxy resin and subsequently using conventional grinding and fine polishing.

3. Results and Discussion

3.1. Low alloy steel

The mass change data for the low alloy steel during discontinuous exposure in the five SO_2-free test atmospheres (Table 1) at 550°C indicated that the oxidation rates were not substantially affected by the variation in gas composition [27]. In all cases the metallographic cross sections revealed the oxide scales to consist of an outer magnetite/hematite layer and an inner layer mainly consisting of magnetite and minor amounts of chromium rich phase, likely Fe/Cr spinel [27]. The gas variations only resulted in slight differences in scale morphology, void formation and relative amounts of hematite in the outer oxide scale.

Table 1: Compositions of studied alloys in mass.-% as analysed using ICP-OES

	Cr	Ni	Mo	C	Nb	Al	W	N	V	Si	Mn	Ti	Co	Fe
13CrMo44	0.92	0.13	0.46	0.11	-	0.03	-	0.01	-	0.17	0.49	-	-	Bal.
P92	8.9	0.23	0.38	0.07	0.05	0.03	1.20	0.04	0.20	0.30	0.43	-	-	Bal.
VM12	11.4	0.20	0.27	0.11	0.05	0.02	1.50	0.04	0.22	0.44	0.17	-	1.50	Bal.
1.4910	16.5	12.3	2.23	0.02	-	-	-	0.12	-	0.38	1.28	-	-	Bal.
TP347H FG	18.1	11.7	-	0.08	0.50	-	-	-	-	0.39	1.60	-	-	Bal.
310N	24.6	20.8	-	0.07	0.43	-	-	0.02	-	0.33	1.20	-	-	Bal.
IN617	21.9	Bal.	8.70	0.06	-	1.17	-	0.02	-	0.08	0.07	0.5	11.3	1.14

Table 2: Compositions (in vol-%) of used test gases. Tests were carried out in the listed gases with and without 0.5% SO_2. The $Ar/CO_2/H_2O/O_2$ mixture listed in the table is in the following text termed as "Oxyfuel Gas"

	Ar	CO_2	H_2O	O_2
Ar/CO_2	50	50	-	-
$Ar /CO_2/O_2$	49	50	-	1
Ar/H_2O	50	-	50	-
CO_2/H_2O	-	70	30	-
$Ar/CO_2/H_2O/O_2$	12	60	25	3

3.2. Behaviour of Martensitic Steels in SO_2-free Gas

The martensitic steels P92 and VM12 showed during discontinuous air exposure at 550°C – 650°C very low oxidation rates due to formation of very protective chromium rich surface oxide scales, in agreement with previous findings [12]. Substantially higher weight changes and corresponding thicker, iron-base oxide scales were found in the other test gases. Thereby, the weight changes observed in Ar/CO_2 and Ar/CO_2/H_2O were slightly higher than those in Ar-H_2O. EDX analyses indicated that the thin oxide formed in air contained a substantial amount of chromium, whereas Laser Raman spectroscopy showed the thicker scales formed in the CO_2- and H_2O-containing gases to consist of an outer Fe_2O_3 layer on top of a faster growing layer consisting mainly of Fe_3O_4. Alloy VM12 frequently showed on one specimen, areas with this type of oxide morphology whereas other areas exhibited formation of very thin chromia base oxide scales (Fig. 1). This was especially the case in Ar-CO_2-O_2. For both martensitic steels the thick scales formed in Ar-CO_2, Ar-H_2O and Ar/CO_2/H_2O respectively exhibited similar morphologies with an inner layer consisting of Fe_3O_4 and Fe,Cr-rich spinel and an internal oxidation zone was found beneath this layer. This type of scale morphology has frequently been described by various authors for 9%Cr steels exposed to steam (see e.g. references [8, 10, 11]) or simulated combustion gases [12]
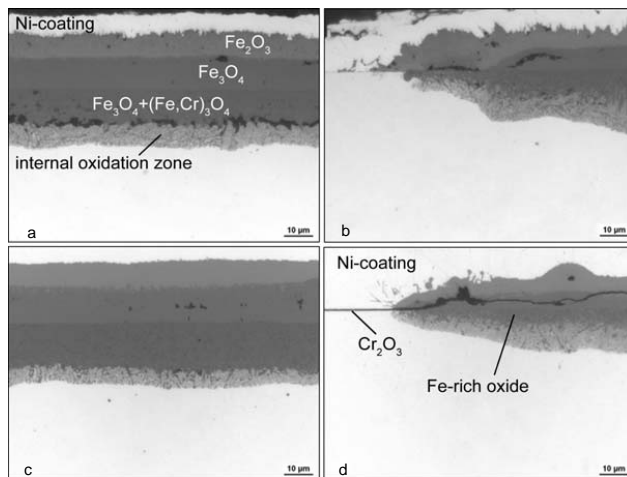
Figure 1: Metallographic cross sections of P92 (a,c) and VM12 (b,d) after 1000h oxidation in CO_2/H_2O (a,b) and Ar/CO_2/H_2O/O_2 (c,d) at 550°C

The low alloy steel showed in all used test gases the well known strongly increasing oxidation rate with increasing temperature. At 550°C P92 and VM12 showed scale growth rates which did not dramatically differ from that of the low alloy steel. Only upon temperature increase the beneficial effect of the higher chromium content for the oxidation resistance of the martensitic steels became apparent. Increasing the temperature to the practically irrelevant value of 700°C even resulted for VM12, especially in Ar-CO_2, in a decrease of the oxidation rate, the effect being less apparent in H_2O-rich gases [26, 27].

...

This type of temperature dependence can be correlated with the chromium distribution in the oxide scales as illustrated in Fig. 2, using the scales formed in Ar/CO_2 as an example. At all temperatures, chromium was found to be only present in the inner region of the oxide scale. Chromium enrichment compared to the bulk alloy chromium content only occurred at temperatures above 550°C, which is accompanied by a vanishing of the internal oxidation zone (Fig. 6). These findings concerning temperature dependent microstructural changes of the oxides are similar to those found for martensitic steels during long term steam oxidation [7, 11, 34].

Several authors [22-24, 28, 35] found that in CO_2 rich gases the martensitic steels may exhibit carburization. Mechanisms to explain why in CO_2 rich gases carburisation may occur, in spite of the fact that the equilibrium carbon activity is extremely small, were discussed in [22,26, 35]. The question, whether carburisation indeed occurs in mixed, CO_2 containing gases will depend on the gas permeability of the surface oxide scales and the competitive adsorption of the various gas molecules on the reaction surfaces. In mixed gases the presence of water vapour results in blocking of the adsorption sites for the other gas species (CO_2, O_2) with the result that additions of water vapour tend to suppress the carburization reaction [35]. Also, minor additions of SO_2 were found to decrease the tendency to carbon uptake.
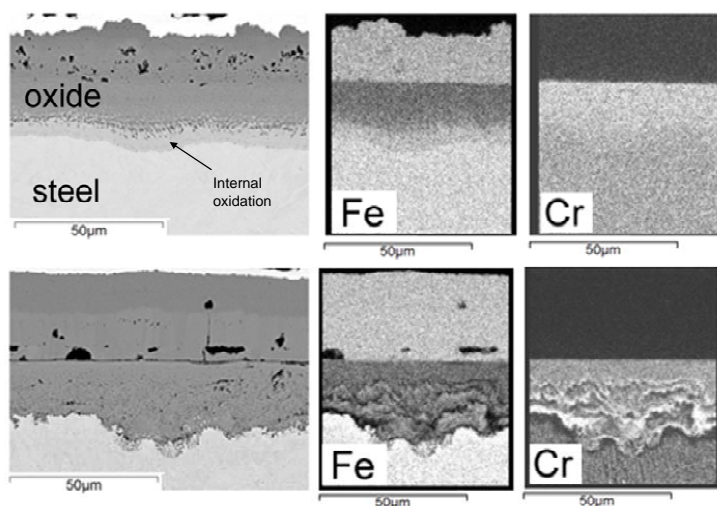
Figure 2: Typical example for temperature dependence of oxide morphology on VM12 during exposure in H_2O- and/or CO_2-rich gases. Shown are SEM images (left) and x-ray mappings of Fe and Cr (right) after 1000h exposure in Ar/CO_2 at 550°C (upper) and 650°C (lower).

3.3. Effect of SO_2 Additions on Behaviour of Martensitic Steels

The experimental results revealed that the effect of SO_2 addition on the scale formation mechanisms for martensitic steels substantially differed, depending on the prevailing base gas atmosphere [33]. The various types of corrosion attack affected by SO_2 cannot be explained by solely comparing equilibrium activities of the gas atmospheres with thermodynamic

stabilities of possible corrosion products. The results were found to be governed by relative rates of reactions of the various gas species occurring at the scale/gas- and scale/alloy interfaces as well as within the frequently porous corrosion scales [33, 36].

GDOES analyses of specimens exposed in SO_2 containing oxyfuel gas and in $Ar-H_2O-SO_2$ revealed presence of sulphur in the inner scale, especially near the interface between inner and outer oxide layer (Fig. 3). Additionally sulphur, tied up as Cr-sulphide was seen in the alloy near the interface with the oxide. The presence of sulphur near the interface between inner and outer layer was shown to originate from the early stages of oxidation whereas the sulphide formation in the alloy near the interface with the oxide was related to molecular transport of SO_2 through the surface scale [33]. The sulphur uptake did not dramatically affect the scale growth rates. An important morphological feature was that in the SO_2 containing gas the tendency to form an internal oxidation zone, commonly seen e.g. after exposure at 550°C, was suppressed (Fig. 4). This had as result that the inner scale tended to contain larger amounts of Cr-rich oxides, mainly Fe,Cr-spinel.
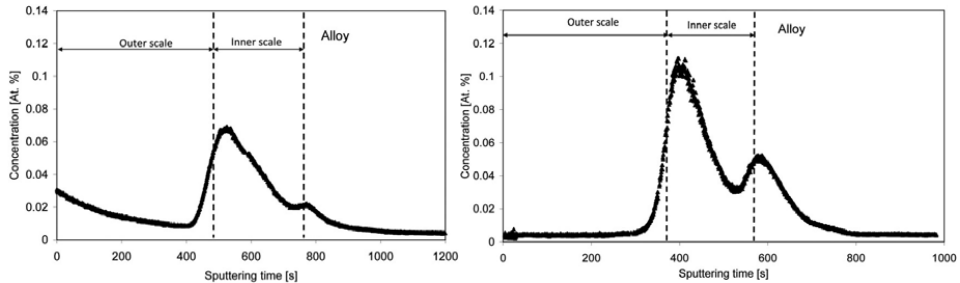
Figure3:Sulphur distributions (measured by GDOES depth profiling) in oxide scales formed during 250 h exposure at 550°C in SO_2-containing oxyfuel gas (left) and in $Ar–H_2O–SO_2$ (right).
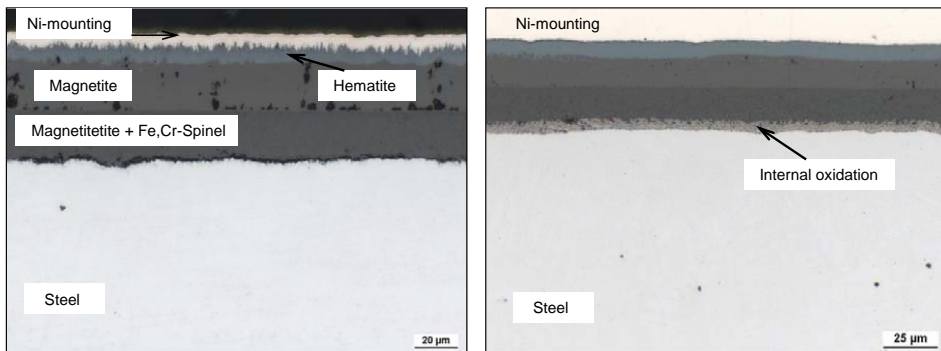
Fig. 4: Microstructures of P92 after 1000 hours exposure a 550°C in oxyfuel gas with (left) and without SO_2 (right).

3.4. Austenitic Steels and Nickel Base Alloy in SO₂-free Gases

Figure 5 shows weight change data of the three studied austenitic steels after 1000h exposure in different test gases. At 550°C all three materials exhibited, different from the low alloy steel as well as P92 and VM12, very low weight changes due to formation of protective chromia rich surface scales. Upon temperature increase the steels 1.4910 and TP347H FG started to gradually form specimen surface areas exhibiting double-layered surface scales (Fig. 6). A well known feature [10, 14, 34] is that this type of surface oxides on austenitic materials exhibits a large tendency to spallation upon temperature changes, confirmed by the measured weight losses for the two low-Cr austenitics after 1000h at and above 600°C (Fig. 5). The spallation mainly occurs at the interface between outer and inner oxide layer, i.e. near the initial alloy surface as shown by the cross sections in figure 6. It will be illustrated in a later section that the inner scale does in many cases not merely consist of oxides but is rather a zone characterized by a metallic matrix with finely dispersed internal oxides [10, 34].
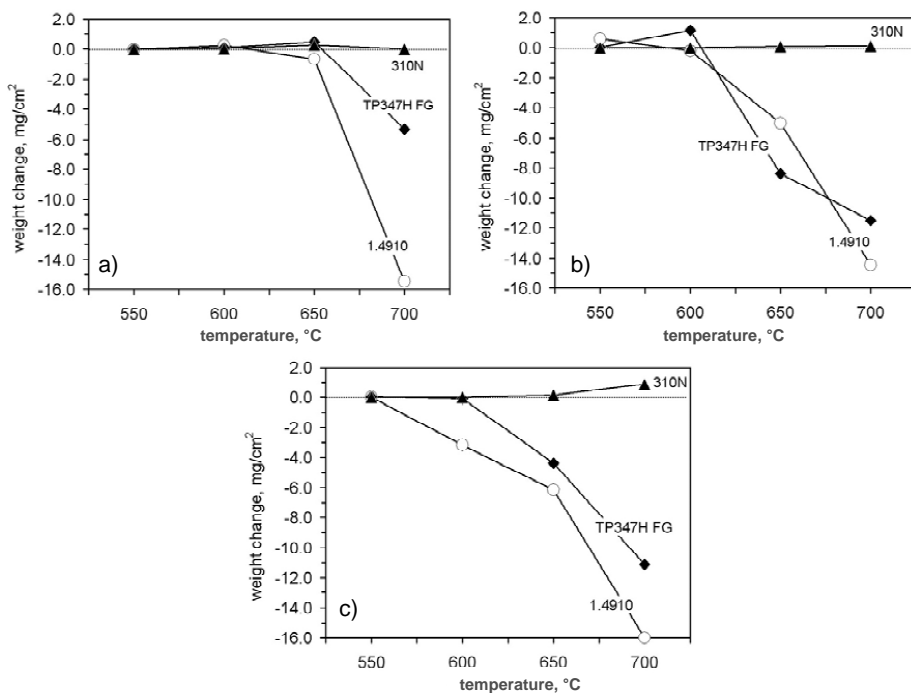
Figure 5: Temperature dependence of weight changes for the three tested austenitic steels after 1000h exposure in three different test gases. a) Ar/CO₂, b) CO₂/H₂O, c) Ar/CO₂/H₂O/O₂

The tendency for a change from chromia base scales to formation of double layered, iron rich oxide scales was more affected by the presence of water vapour than of CO₂. Apparently, the adverse effect of water vapour in hampering protective chromia scale formation is more pronounced for water vapour than for CO₂ [26]. This explains e.g. why after 1000h at 650°C the steel 1.4910 showed a substantial weight loss in CO₂/H₂O but not in Ar/CO₂ (Fig. 5). The

addition of 3% oxygen to the CO_2/H_2O mixture did, up to the maximum exposure time of 1000h, not have a substantial effect on the scale growth rate and the spallation kinetics. Only the relative amount of hematite in the outer scale tended to be increased by presence of intentionally added oxygen and a slightly larger tendency for suppression of protective chromia scale formation was found.

In all used test gases the oxidation rates of the high chromium austenitic steel 310N were very low, even up to 700°C (Fig. 5). In the gases without intentionally added oxygen the material formed extremely thin, well adhering chromia base oxide scales at all temperatures. At 550 and 600°C this was also the case in the simulated oxyfuel gas. However, at 650°C and especially 700°C the alloy started to exhibit local areas of iron rich surface scales on the specimen surfaces (Fig. 7), explaining the finding that the weight increases were in the oxyfuel gas $Ar/CO_2/H_2O/O_2$ higher than in $Ar/CO_2(O_2)$, $Ar-H_2O$ and in CO_2/H_2O (Fig. 8). Although the oxidation rates were even at the highest test temperature quite low, the addition of oxygen apparently had a detrimental effect on the oxidation resistance of this alloy in water vapour containing gases.
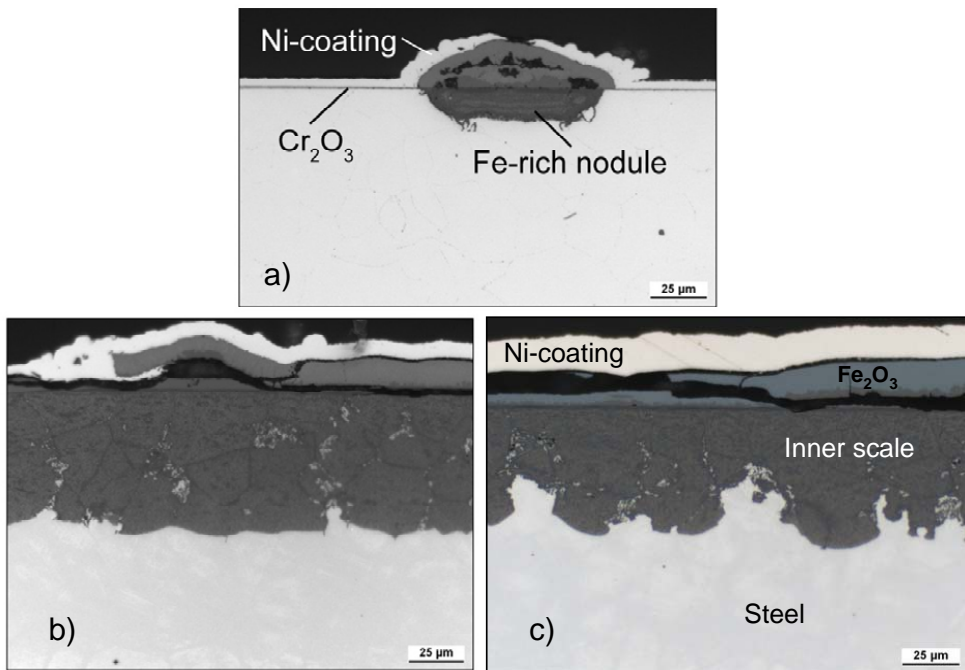
Figure 6: Metallographic cross sections of oxide scales formed on 1.4910 after 1000h exposure at 650°C in Ar/CO_2 (a), CO_2/H_2O (b) and oxyfuel gas $Ar/CO_2/H_2O/O_2$ (c). Fig.(a) shows a local nodule formation of iron-rich oxide whereby outer and inner oxide scale are still present. In figures b) and c) the outer oxide scales have virtually completely spalled during specimen cooling to room temperature.

827
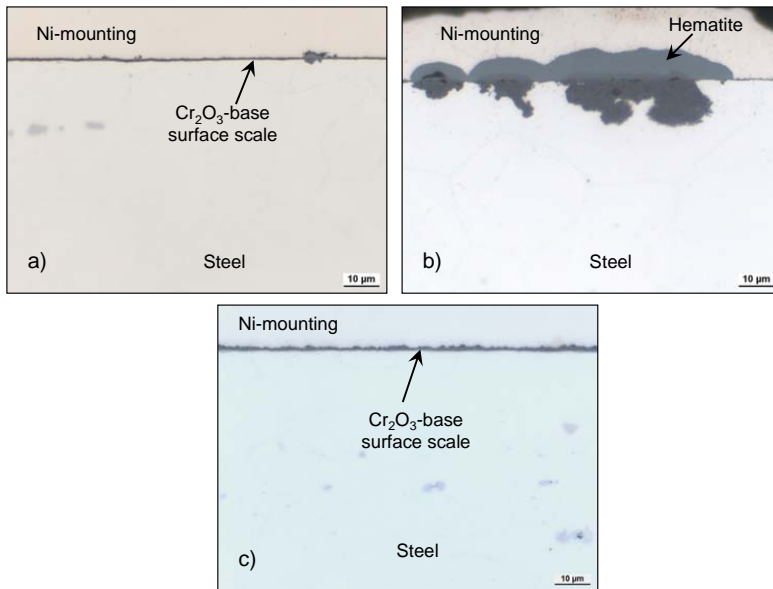
Figure 7: Metallographic cross sections of oxide scales formed on alloy 310N after 1000h exposure at 650 in CO_2/H_2O (a), oxyfuel gas (b) and SO_2 containing oxyfuel gas (c)
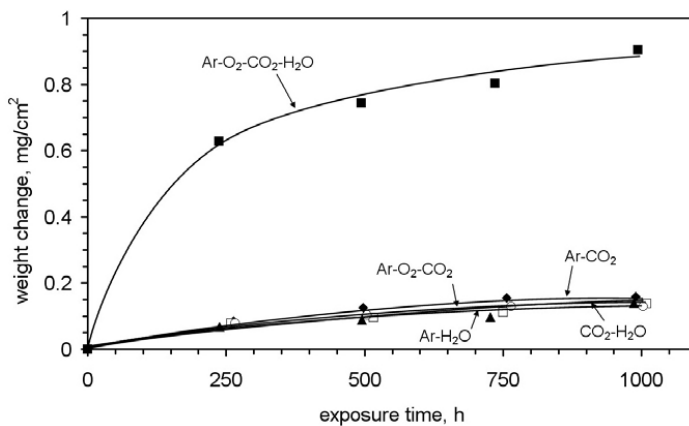
Figure 8: Weight changes of alloy 310N during exposure at 700°C in different environments

The nickel base alloy 617 showed in the whole considered temperature range in all used test gases formation of very protective chromia base oxide scales which was accompanied by very small weight gains. An exception was the oxyfuel gas $Ar/CO_2/H_2O/O_2$; in this gas the alloy showed a minor weight loss. This effect was found at 700 (Fig. 9) as well as 650°C [27]. The observation that this effect occurred in gases containing water vapour plus oxygen strongly

indicates that it is correlated with the formation of volatile Cr-oxyhydroxide $CrO_2(OH)_2$ [13, 37, 38]

$$1/2\ Cr_2O_3 + H_2O^{(g)} + 3/4\ O_2^{(g)} = CrO_2(OH)_2^{(g)} \qquad\qquad (1)$$
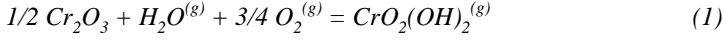
The vapour pressure of the volatile species is given by

$$p[CrO_2(OH)_2^{(g)}] = k.\ p[O_2^{(g)}]^{3/4}.\ p[H_2O^{(g)}] \qquad\qquad (2)$$

in which k is the equilibrium constant of reaction 1.

In wet, oxygen rich gases the evaporation of the oxyhydroxide at the scale/gas interface has as result that the oxidation process exhibits a para-linear behaviour [36] whereby the oxide initially thickens up to a given value after which a time independent oxide thickness prevails. In terms of weight change measurements, a weight increase is initially found which gradually changes into a weight loss during prolonged exposure. The volatilisation has as consequence that the chromium depletion in the alloy beneath the scale is more pronounced than in case of ideal parabolic oxidation without interference of volatilisation. In case of alloy 617 this does during exposure in the oxyfuel gas $Ar/CO_2/H_2O/O_2$ up to the maximum exposure time of 1000h not lead to a change from chromia formation into formation of e.g. poorly protective Ni-rich oxide scales. However, for the austenitic steel 310 the additional chromium loss due to volatilisation apparently depletes the chromium content in the subsurface zone in the alloy to such a low level that the growth of the virtually pure chromia scale can no longer be sustained and a change to formation of a less protective oxide occurs (Fig. 7 a, b). Consequently, the overall effect of the volatile oxyhydroxide formation in case of alloy 310 is that the overall weight gain, is higher in $Ar/CO_2/H_2O/O_2$ than in CO_2/H_2O and the other test gases (Fig. 8).
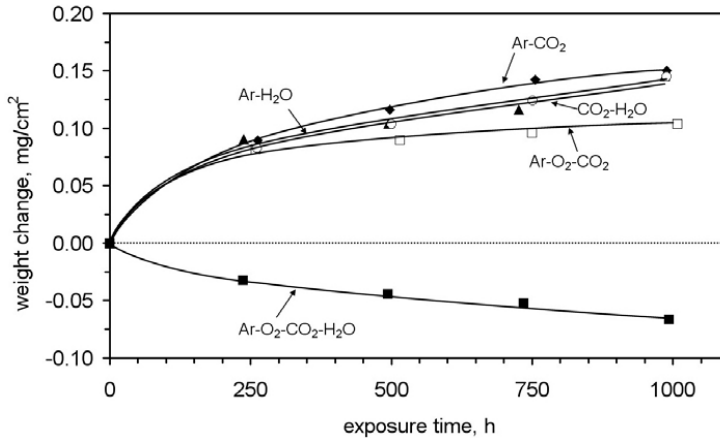
Figure 9: Weight changes of alloy 617 during exposure at 700°C in different environments

3.5 Effect of SO₂ Addition on Behaviour of Austenitic Steels and Nickel base alloy

Figure 10 shows metallographic cross sections of the austenitic 17%Cr steel 1.4910 after 1000h exposure at 650°C in simulated oxyfuel gas Ar/O$_2$/CO$_2$/H$_2$O with and without SO$_2$ addition. In the SO$_2$ free gas the so-called inner scale is in fact an internal oxidation zone in which Cr rich oxides are present as very fine precipitates within the initial alloy grains and in form of continuous bands along alloy grain boundaries. This inner scale morphology has been previously been described for this type of austenitic steel after steam exposure [10, 34]. Addition of SO$_2$ to the oxyfuel gas Ar/O$_2$/CO$_2$/H$_2$O results in a virtually complete suppression of the internal oxide morphology (Fig. 10). Instead, the inner scale consists of Cr-rich oxide which has as result that the growth rate of the outer scale is substantially decreased. Therefore, no indication of outer scale spalling is visible after the 1000h exposure. Although further studies related to the exact mechanism of the SO$_2$ effect are certainly necessary, the present results indicate that the effect imparted by the SO$_2$ addition is similar to that described in section 3.3 for the martensitic steels, i.e. SO$_2$ suppresses the tendency for Cr to become internally oxidized [33].
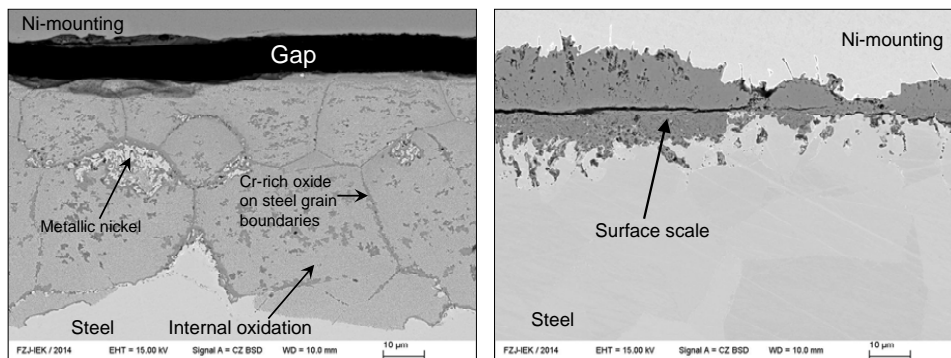
Fig. 10: Cross sections of austenitic steel 1.4910 after 1000h exposure at 650°C in oxyfuel gas with (right) and without (left) addition of SO₂.

A completely different effect of SO$_2$ addition was found for the "real chromia formers", i.e. steel 310 and alloy 617. For the latter material presence of SO$_2$ in the simulated oxyfuel gas appeared to suppress the weight loss during 700°C exposure (Fig. 9) to undetectably low values. This resulted in formation of a very protective chromia scale which only differed from that in the SO$_2$-free gas by minor differences in morphology and thickness. Apparently, the presence of 0.5% SO$_2$ in the gas virtually completely suppresses the formation of the volatile Cr species, described by reaction 1. Järdnäs et al [39] obtained a similar result when studying the effect of very low SO$_2$ additions on the oxidation behaviour of the austenitic steel 304 at 600°C in a O$_2$/H$_2$O model gas containing a much higher O$_2$ content than used in the present studies. The authors proposed that the formation of an outer sulphate was responsible for the suppression of Cr-oxy-hydroxide formation. Because in the used SO$_2$ containing oxyfuel gas, Fe- and Cr- sulphate are thermodynamically not stable at 700°C (Fig. 11) the prevailing observations may be related to competitive adsorption of the various gas molecules on the reaction surfaces [33, 36] whereby SO$_2$ blocks the adsorption sites for the other gas species, here especially oxygen and/or water vapour.

If presence of SO_2 hampers formation of volatile Cr species, it should, based on the considerations in section 3.4 have a positive effect on the protective chromia scale formation of the austenitic steel 310. Fig. 7c shows that this is indeed the case; whereas mixed, Fe-rich oxides are formed during exposure at 700°C in the SO_2-free oxyfuel gas (Figs. 7a,b), a very thin chromia base scale is formed if SO_2 is present in the test atmosphere.
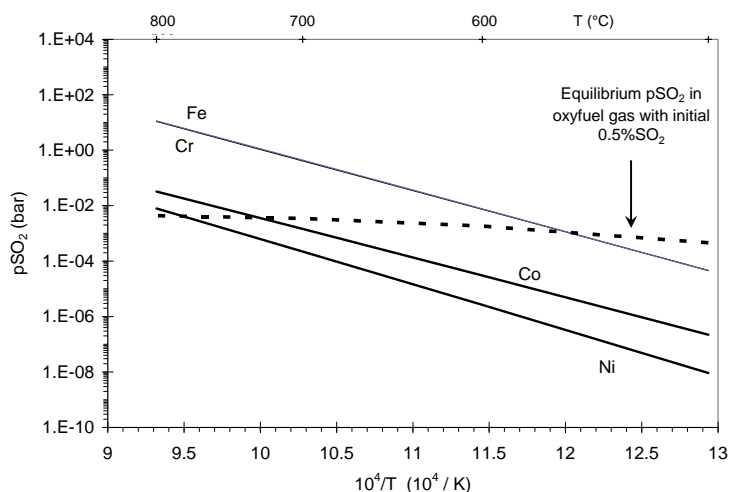
Fig. 11: *Equilibrium SO_2 partial pressures for transformation of oxides of Fe, Cr, Co and Ni into respective sulphates as function of reciprocal temperature at an oxygen partial pressure of 0.03 bar. Data are compared with equlibrium SO_2 partial pressures in oxyfuel gas with initial SO_2 content of 0.5%. Calculations carried out using software package FACTSAGE*

A completely different effect of SO_2 addition on the behaviour of the "real chromia formers" 310 and 617 was observed at lower temperatures, i.e. 550 and 650°C. Whereas hardly any influence of SO_2 addition on the corrosion rate of the austenitic steel 310 in oxyfuel gas was found at these temperatures, the nickel base alloy showed substantially enhanced oxidation when SO_2 was added. Thereby the corrosion rates of alloy 617 in the SO_2 containing gas at 550 and 650°C were substantially higher than at 700°C. Microstructural analyses revealed that the relatively high rates at 550 and 650°C were related to local formation of an outer layer containing Ni/Co base sulphate on top of a mixture of Cr base oxide and Ni-rich sulphide (Fig. 12). At 550°C the outer layer on the local nodules consisted of Ni-oxide and – sulphate beneath which Ni-rich sulphide was present. The latter likely originates from the transient stages of oxidation according to a mechanism described in reference [33, 36]. The formation of outer Ni- and Co-rich sulphates can qualitatively be explained by thermodynamic equilibrium considerations showing that the mentioned sulphates are the phases in equilibrium with the SO_2 containing oxyfuel gas whereby the stability of the sulphates relative to that of the respective oxides, decreases with increasing temperature (Fig. 11). At 650°C, the oxides of Fe and Cr rather than the respective sulphates would be the thermodynamically stable phases. This at least qualitatively explains why the adverse effect

of SO_2 on scale formation at 550 and 650°C became apparent for the nickel base alloy 617 but not for the austenitic steel 310.
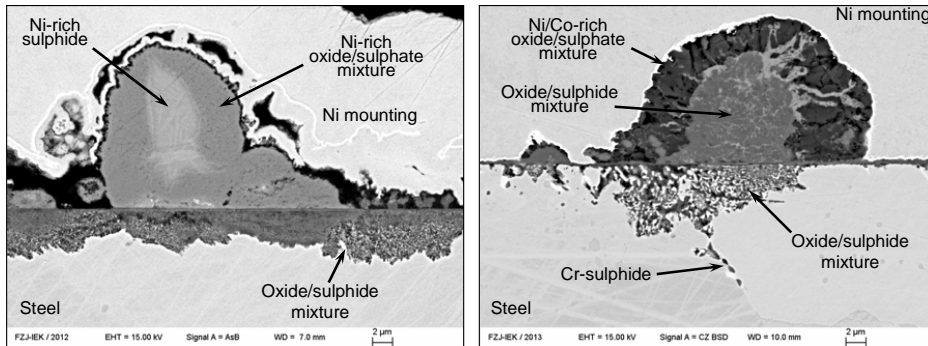
Fig. 12: Surface scales on alloy 617 after 1000h exposure in SO_2 containing oxyfuel gas at 550°C (left) and 650°C(right)

3 Summary and Conclusions

During exposure in CO_2- and $H_2O(/CO_2)$-rich gas mixtures (and absence of deposits) at 550-650°C the oxidation rate and scale compositions of the low alloy steel 13CrMo 44 are similar to those observed in steam environments. In these test gases the martensitic steels P92 and VM12 did, at temperatures between 550 and 650°C, not form the very slowly growing oxide scales which are commonly found during air oxidation. The adverse effect of water vapour on protective chromia scale formation was more pronounced than that of CO_2. The non-protective scale formation in Ar-CO_2 can be suppressed by oxygen additions of 1 or 3%, however, this positive effect of oxygen does not occur in water vapour rich gases

The behaviour of the three studied austenitic steels strongly depends on the prevailing alloy composition. At 550°C all studied austenitic steels exhibited very slow scale growth rates, however, at and above 600°C the 16 – 18% Cr steels 1.4910 and TP347H FG started to form two-layered iron rich surface oxide scales whereby the outer oxide was prone to spallation upon thermal cycling. Also for these alloys, the adverse effect of water vapour on protective chromia scale formation was more pronounced than that of CO_2. Addition of 0.5% SO_2 to a simulated oxyfuel gas Ar/O_2/CO_2/H_2O resulted at 600 – 700°C to lower scaling rates for these steels, the reason being the decreased tendency for Cr to become internally oxidized.

The high chromium austenitic steel 310N and the nickel base alloy 617 can, in first approximation, be considered as "real chromia formers" in the used temperature range up to 700°C. Presence of water vapour in combination with intentionally added oxygen led to formation of volatile chromium oxyhydroxide. In case of alloy 617 this resulted in a loss of chromium which may at 650 and 700°C become larger than the oxygen uptake by scale growth resulting in a net weight loss after prolonged exposure. For the austenitic steel 310N the formation of volatile Cr oxyhydroxide resulted in a critical chromium depletion in the

subscale depletion layer such that the pure chromia scale growth could no longer be sustained, leading to formation of more rapidly growing, Fe-rich oxide nodules.

Addition of SO_2 to the simulated oxyfuel gas suppressed the formation of volatile Cr oxyhydroxide in case of alloys 310 and 617, resulting in an improvement of oxidation resistance, especially for steel 310. For the latter material the SO_2 addition only marginally affected the oxidation rates at lower temperatures, i.e. 550 and 650°C. However, for alloy 617 the SO_2 addition had these temperatures an adverse effect on oxidation resistance due to the local formation of Ni- and Co-rich sulphates on top of transient Ni-sulphide.

4 Acknowledgements

5 References

[1]   D. Allen, J. Oakey and B. Scarlin: 'The New COST Action 522-power generation in the 21st century: ultra efficient, low emission plant', in Materials for Advanced Power Engineering, 1998, 1825-1839.
[2]   K. Weinzierl: VGB Kraftwerkstechnik (1994), 74(2), 109-114.
[3]   B.J.P. Buhre, L.K. Ellitot, C.D. Sheng, R.P. Gupta and T.F. Wall: Progress in Energy and Combustion Science, (2005), 31, 283-307.
[4]   K. Jordal, M. Anheden, J. Yan and L. Strömberg: Proceedings of 7th International Conference on Greenhouse Gas Control Technologies (GHGT-7), Vancouver, Canada, September 5-9, 2004.
[5]   T. Pikkarainen, A. Tourunen and J. Hämäläinen: Energy Materials, (2007), 2(2), 78-83.
[6]   B. Bordenet, F. Kluger, Materials Science Forum, (2008), 595-598, 261-269
[7]   J. Zurek, E. Wessel, L. Niewolak, F. Schmitz, T-U. Kern, L. Singheiser and W.J. Quadakkers: Corrosion Science, (2004), 46, 2301-2317.
[8]   R.J. Ehlers, P.J. Ennis, L. Singheiser, W.J. Quadakkers and T. Link, (2001), 'Life Time Modelling of High Temperature Corrosion Processes', European Federation of Corrosion Monograph, Nr. 34, Eds. M. Schütze, W.J. Quadakkers, J. Nicholls, The Institute of Materials, London, ISSN 1354-5116, 178 - 193
[9]   R.U. Husemann, VGB Kraftwerkstechnik, (1999), 10, 146-149.
[10]   A. N. Hansson, M. Montgomery, Materials Science Forum, (2005), 522-523, 181
[11]   J. Zurek, E. De Bruycker, S. Huysmans, and W.J. Quadakkers, (2014) Corrosion: 70 (2), 112-129.
[12]   M. Thiele, H. Teichmann, W. Schwarz, W.J. Quadakkers and H. Nickel: VGB Kraftwerkstechnik, (1997), 77(2), 135-140.
[13]   L. F. Tang, H. Asteman, J. E. Svensson, L.G. Johansson, M. Halvarsson, Oxidation of Metals, (2009), 77(1/2), 77 -105
[14]   I. Wright, R.B. Dooley, International Materials review, (2010), 55(3), 129-167

[15] L. García Fresnillo, A. Chyrkin, T. Hüttel, C. Böhme, J. Barnikel, D. Grüner, F. Schmitz, W.J. Quadakkers, Materials and Corrosion (2012), 63(10), 878–888

[16] G.B. Gibbs: Oxidation of Metals, (1973), 73, 173-183.

[17] J.E. Antill, K.A. Peakall and J.B. Warburton, Corrosion Science, (1968), 8, 689-701.

[18] C. T. Fujii and R. A. Meussner, J. Electrochem. Soc., (1967), 114(5), 435-442

[19] A. Rahmel: Werkstoffe und Korrosion, (1965), 16, 837-843.

[20] J.A. Colwell and R.A. Rapp: Metallurgical Transactions A, (1986), 17A, 1065-1074.

[21] A. Rahmel and J. Tobolski: Werkstoffe und Korrosion, (1965), 16, 662-676.

[22] J. Piron Abellan, T.Olszewski, H.J. Penkalla, G. H. Meier, L. Singheiser, W.J. Quadakkers, Materials at High Temperatures, (2009), 26(1), 63-72

[23] J. Pirón Abellán, T.Olszewski, G. H. Meier, L. Singheiser, W.J. Quadakkers, Intern. Journal of Materials Research, (2010), 101, 287- 299

[24] D. Huenert, A. Kranzmann, Corrosion Science, (2011) 53, 2306–2317

[25] R.J. Ehlers, D.J. Young, E.J. Smaardijk, A.K. Tyagi, H.J. Penkalla, L. Singheiser and W.J. Quadakkers, Corrosion Science, (2006), 48, 3428-3454.

[26] G.H. Meier, K. Jung, N. Mu, N.M. Yanar, F.S. Pettit, J. Pirón Abellán, T. Olszewski, L. Nieto Hierro, W.J. Quadakkers, G.R. Holcomb, Oxidation of Metals (2010) 74, 319–340

[27] W.J. Quadakkers, T. Olszewski, J. Piron-Abellan, L. Singheiser, VDI-Berichte (2102), VDI-Verlag Düsseldorf, (2010), ISBN, 978-3-18-092102-0, p. 81-103

[28] P. Becker and D.J. Young: Oxidation of Metals, (2007), 67, 267-277.

[29] B. A. Pint, J. K. Thomson, Materials and Corrosion, (2014), 65(2), 132–140

[30] B.A. Pint, CORROSION 2012, 11-15 March, Salt Lake City, Utah, Publication NACE International, NACE-2012-1635

[31] P.J. Ennis, A. Zielinska-Lipiec, O. Wachter and A. Czyrska-Filemonowicz, Acta Materialia, (1997), 45, 4901-4907.

[32] P.J. Ennis: Materials at High Temperatures, (2006), 23, 187-193.

[33] P. Huczkowski, T. Olszewski, B. Lutz, G.R. Holcomb, V. Shemet, G.H. Meier, L. Singheiser, W.J. Quadakkers, Materials and Corrosion, (2014), 65(2), 178–187

[34] W.J. Quadakkers, J. Zurek J, (2010), Shreir's Corrosion, Edts. Richardson J. A. et al., Amsterdam, Elsevier, vol. I, pp. 407-456

[35] T. Gheno, D. Monceau, D. J. Young , Corrosion Science, (2012), 64, 222–233

[36] D. Young, High Temperature Oxidation and Corrosion of Metals, Elsevier Corrosion Series, Amsterdam, (2008)

[37] M. Stanislowski, E. Wessel, K. Hilpert, T. Markus, L. Singheiser, J. of the Electrochem. Society, (2007), 154(4), A295-A306

[38] D.J. Young, B.A. Pint, Oxidation of Metals, (2006), 66 (3/4) 137-153.

[39] A. Järdnäs, J.E. Svensson, L.G. Johansson, Oxid. Metals (2008) 69, 249–263

CURRENT MATERIALS CHALLENGES FOR A TRANSITIONING U.S. POWER FLEET

J.P. Shingledecker

Electric Power Research Institute
1300 West W.T. Harris Blvd., Charlotte, NC 28262 USA
jshingledecker@epri.com

Abstract

The fossil power plant fleet in the U.S. is in a state of transition. Flat load growth, increasing environmental regulations, an abundance of low-cost natural gas, increased usage of renewables, and high construction costs are all driving significant changes in the operational mode of current fossil plants, the construction of new plants, and the needs for future materials research. Older pulverized coal-fired power plants are being shut down or retrofitted with enhanced environmental controls. Many older units are also being cycled. Natural gas combined cycle plants, once operated for peak load demand, are transitioning to base load generation. New plants, mainly combined cycle, are being designed for fast starts and variable demand. Materials challenges include thermal fatigue and creep-fatigue in older units, the implementation of newer high-strength materials for enhanced cyclic capability, and cost-effective life management of major assets. Future materials challenges include the use of stainless steels in higher efficiency heat-recovery steam generators and advanced materials for innovative supercritical CO_2 power cycles.

Keywords: natural gas, coal generation, advanced ultrasupercritical (A-USC), supercritical CO_2

1. Introduction

The fossil power plant fleet in the United States (U.S.) is in a state of transition. Flat load growth, increasing environmental regulations, the emergence of low-cost natural gas, increased usage of renewables, and high construction costs are all driving significant changes in the operational mode of current fossil plants, the construction of new plants, and the needs for future materials research. Figure 1 shows the electricity production in the U.S. from 2007 to 2012. While nuclear and hydro power generation has remained relatively constant, the biggest change is the increased use of natural gas replacing coal for power generation.

In 2012, record natural gas production leading to low fuel prices in the U.S. resulted in natural gas accounting for 31% of all net electricity generation while coal fell to less than 40% of the total net generation [1]. In the past, natural gas combined cycle plants (NGCC) had relatively low capacity factors and were used to meet peak demand which required cyclic operation. However, in 2012 18% of NGCC plants had capacity factors greater than 70% which was a significant increase from prior years indicating more NGCC plants became 'base load operation.' This fundamentally shifted the cyclic operation to traditionally baseload coal-fired power plants. At the same time, various environmental regulations have accelerated the retirement of older coal-fired power plants as shown in figure 2 by the dramatic increase in coal capacity retirements in 2012 compared to the previous 5 years. Predictions of capacity additions for coal show almost no new coal-fired power going forward with only ~11GW of coal-fired capacity added from

2005-2012. This has resulted in more coal capacity being retired in two years (2012-2013) than was added for the previous 8 years.
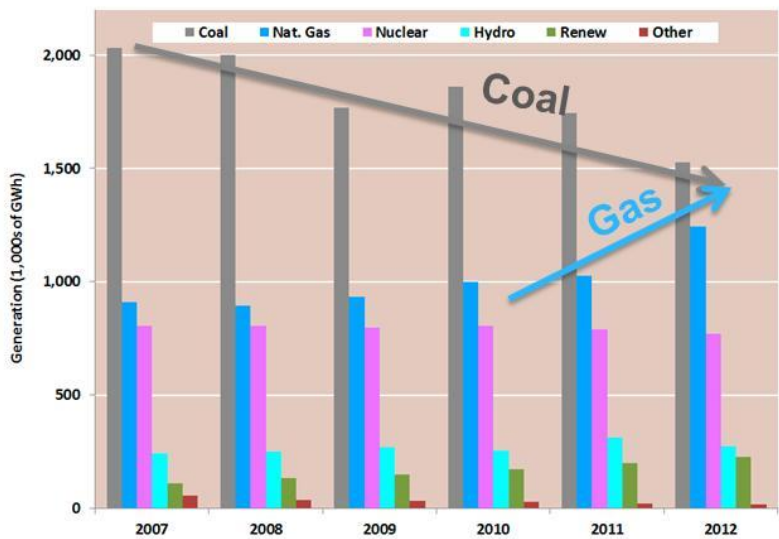
Figure 1. U.S. electricity generation by source and year adapted from [1]

Figure 2. U.S. Electric Capacity Retirements – arrow indicates increase in coal-fired retirements in 2012, adapted from [1]

The current coal-fired power plants in the U.S., which are generally older than 30 years, are being asked to operate in more flexible modes to meet market demands. As renewable energy continues to increase (see figure 1) and assuming natural gas prices stay relatively stable, these coal assets will need to operate in load following and/or low load conditions. At the same time, to maintain coal as a viable assets in a balanced portfolio of power generation technologies, new technologies will be needed to meet both the operational challenges of today and the environmental requirements of the future. Figure 3 shows the Coal Utilization Research Council (CURC)-EPRI roadmap for coal combustion technologies. The timeline indicates the key technology needs which include higher efficiency through Advanced Ultrasupercritcial (A-USC) power plants and new innovative cycles such as oxycombustion, chemical looping, and supercritical CO_2.
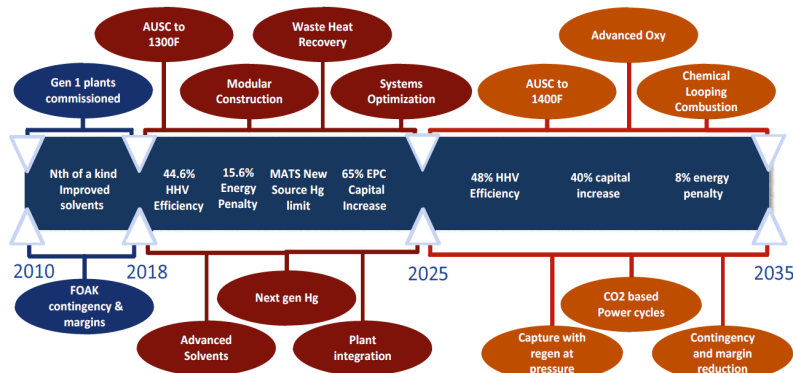
Figure 3. CURC-EPRI Combustion Roadmap [2]

As natural gas displaces base load coal-fired generation, improved overall cycle efficiency is possible not only from improved combustion turbine technology, but maximizing the performance of the heat recovery steam generator (HRSG) in the NGCC plant. Table 1 shows the trends for temperature and pressure increases in HRSGs resulting in higher efficiency NGCC plants. From the perspective of materials, the newest proposed designs have temperatures in excess of 600°C which will require stainless steel materials or more oxidation resistant ferritic steels. Higher-strength materials will be required for HRSGs in the future because not only will pressure and temperature increase but in order to accommodate load-following and renewable generation integration, thinner wall thickness are needed to minimizing thermal stresses from fast-start capability turbines.

2. Materials Issues

The new requirements for flexible operation of the current fleet combined with the desire to improve the next generation of NGCC plants and the need to develop new and innovative cycles provide a myriad of materials challenges. Four key areas which EPRI is engaged in is: creep-fatigue for materials in existing plants, the need to improve the damage tolerance and weld repair

Table 1. Heat Recovery Steam Generator (HRSG) Steam Condition Trends & Materials [Adapted from 3]

Vintage	Maximum Main Steam		Maximum Hot Reheat		Materials	
	Temp (°C)	Pressure (MPa)	Temp (°C)	Pressure (MPa)	Headers/Pipes	High Pressure Tube
1990's	568	12.4	568	3.1	P22, P91	T22, T91
2000's	585	16.5	596	4.8	P91/92, P23	T91, T23
Proposed (beyond 2012)	602	16.5	623	4.8	Stainless steels will be required, materials selection/evaluation ongoing	

of advanced steels (such as P91) in modern plants, the need to understand damage and propose improved materials/material combinations for dissimilar metal welds (DMWs) in HRSGs, and research and development of new nickel-based alloys to enable A-USC and supercritical CO_2 cycles.

2.1. Creep-Fatigue

To address the combined mechanism of creep and fatigue, EPRI initiated an international working group in 2006 to collaboratively address the challenges associated with creep-fatigue. A detailed roadmap and a series of critical reports have been produced through this program and reported on during these annual workshops which are reported on in [5]. Additional, EPRI has undertaken specific actions to advance the standardization of creep-fatigue including the creation and approval of two ASTM standards on creep-fatgiue testing [6], a code of practice [7], and facilitating an international round-robin test program [8]. A number of notable advancements have been drawn from this collaborative effort including: standardization of testing to ensure more data consistency, an assessment of which approaches are best for life management and component assessment in current plants (an example is shown in figure 4), and work with simplified approaches to help design codes such as ASME address creep-fatigue interaction and move from design-by-rule to design-by-analysis [10]. Using this knowledge and fundamental materials data and consensus, EPRI is currently working on putting these approaches into practice in practical life assessment strategies.

2.2. Damage Tolerance in Current Plants and Repair of Advanced Steels

In order to maintain reliability of the current fossil generation fleet operating in an increasingly flexible mode, weld repair is a critical activity. In the past 15 years, EPRI has documented over 46 failures of 'new' grade 91 steel alone [11, 12]. Long-term creep life of Grade 91 weldments is inferior to the parent or base material life due to failure in the "Type IV" heat-affected zone (HAZ) [13]. Based on the current service experience both documented and undocumented, in order to maintain reliability of the current fleet of supercritical fossil fired boilers and HRSGs, utitlies will need damage tolerant repair procedures to ensure both life and safety.
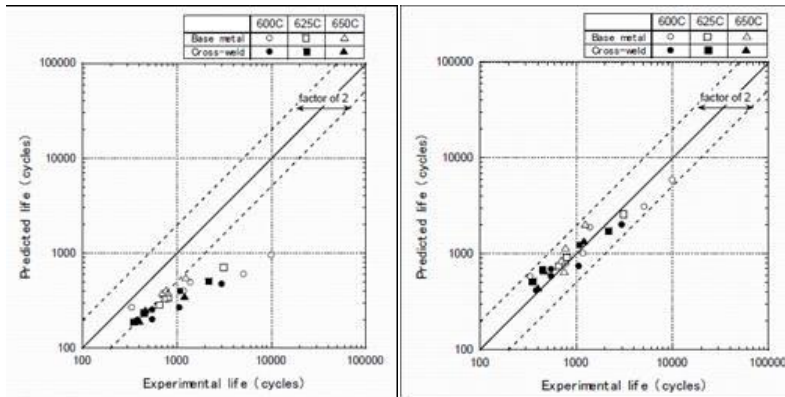
Figure 4. Comparison of experimental and predicted creep-fatigue lives for Grade 92 steel. Analysis was performed using strain fraction rule (left) and a more complex modified strain fracture rule (right) [9]
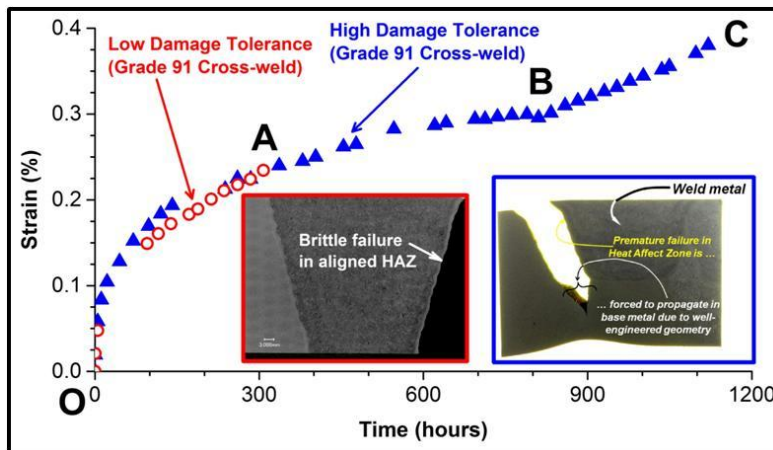
Figure 5. Strain to Failure for a Low Damage Tolerant Weld Design (highlighted in red) and a High Damage Tolerant Weld Design (highlighted in blue) for Simulated Repair Welds in an Ex-service Grade 91 Header tested at 625°C (1157°F) and 80 MPa (11.6 ksi)

An EPRI program on Grade 91 weld repair has been focused on this issue. Figure 5 shows a comparison of strain to failure curves for a low damage tolerance weldment (red curve) and for a high damage tolerance weldment (blue curve) [14, 15]. As shown in comparison to the post-test failures imbedded in the figure, the curve "OA" represents a brittle failure, typical of Grade 91 failures in the HAZ. The unique attribute of the damage tolerant curve is the section denoted "BC", where a period of stable crack growth is forced in the base material prior to stopping the test. This period of stable crack growth in the base metal is more likely to induce a leak-before-

break failure, and offers the potential for detection using traditional non-destructive evaluation methods such as acoustic emission or ultrasonic testing. It is proposed that any weld repair be constructed with a "well-engineered" philosophy that takes advantage of this behavior by including a step in the prep. Additional advantages to the "step weld design", as proposed in a schematic in Figure 6 are actively being researched for new welds, dissimilar metal welds between ferritic to ferritic components and dissimilar metal welds between ferritic to austenitic components. Regardless of the material combination, these different types of weldments suffer from common engineering challenges such as inspectability, aligned weak regions that can result in rapid crack propagation and the potential for catastrophic failure. A step weld design may induce a level of safety and integrity in fabrication that is not currently awarded using conventionally designed weldments.
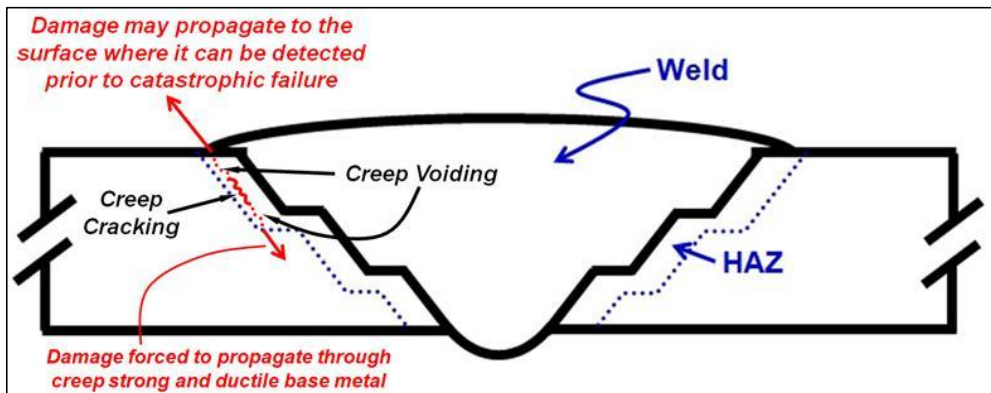
Figure 6. Design Philosophy for a Well-Engineered Step Weld for New Construction, Full Section Repair Welds, and Ferritic to Ferritic or Austenitic Dissimilar Metal Welds

2.3. Thick-Section Dissimilar Metal Welds for Future Heat Recovery Steam Generators

As temperatures and start-up rates in HRSGs increase (Table 1), new materials beyond grade 91 will be required for the high pressure and high temperature components including headers and tubing. Stainless steel, due to its improved oxidation resistance and high-temperature creep strength, is being proposed for these components. However, the current experience with high-temperature dissimilar metal welds (DMWs) in HRSG systems has been very poor. Specifically, the utility industry has seen numerous failures in thick section austenitic to ferritic DMWs in flow nozzles and intercoolers in times between 20,000 and 40,000 hours [16]. Figure 7 shows two examples of current industry experience with stainless steel flow nozzles welded into P91 (ferritic steel) piping systems. In both cases, the pipes failed with in the first 8 years of service in a catastrophic manner. The general approach to fabrication of these components is to apply nickel-based filler metals to the P91 in the shop (so-called 'buttering') and conduct a PWHT and then weld the stainless steel to the buttered P91 in the field without further PWHT.

Examinations of the damage show typical DMW failure modes, figure 8, with the formation of carbides along the weld fusion line leading to brittle failure. Due to the potential for catastrophic failure, the lack of good non-destructive evaluation techniques, and the availability of ferritic flow nozzles, EPRI recommends removal and replacement of all stainless steel flow nozzles. However, this experience is highly concerning for new HRSG designs, because thick-section stainless steels may be required and the experience to date has not shown desired lifetimes at lower/current operational temperatures. One solution to DMW failures is optimized weld metals which eliminate some damage mechanisms. American Electric Power's new ultrasupercritical (USC) power plant utilizes and EPRI developed filler metal (EPRI P87) to eliminate DMW failure modes in their highest temperature tube to tube welds between T91 and Super 304H [17]. Such material solutions combined with innovative designs (such as the step weld in figure 6) may provide the technology needed to address future DMWs and is an area of current research.
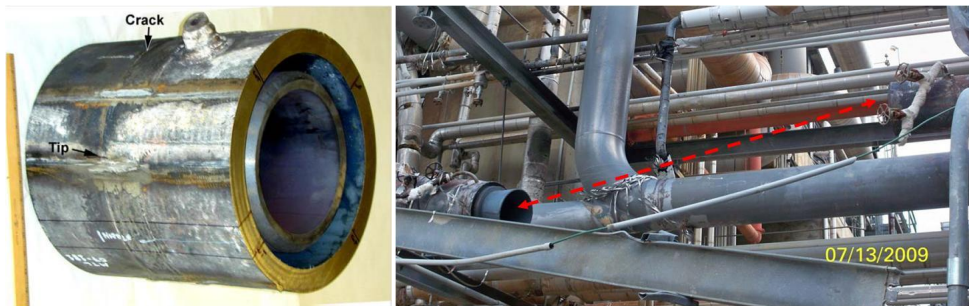
Figure 7. Two examples of cracked austenitic stainless steel flow nozzles in P91 HRSG piping systems after service for 6 to 8 years. In one case, catastrophic failure occurred resulting in complete separation of the pipe [16]
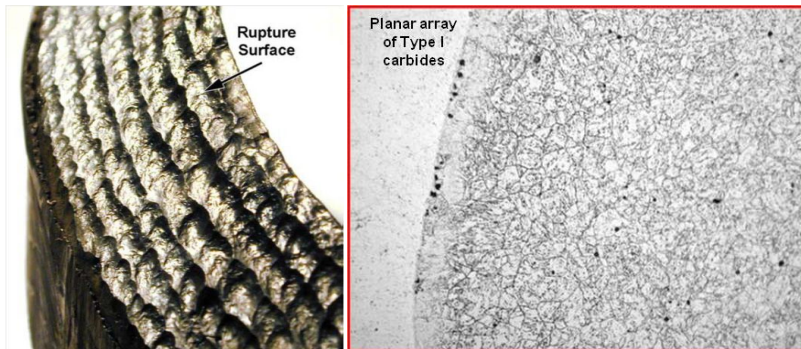
Figure 8. Observed damage in HRSG DMW failures

2.4 Advanced Alloys for A-USC and Innovative Cycles

To maintain coal as a viable option for future electricity production in the U.S., materials improvements are needed. Higher efficiency advanced ultrasupercritical (A-USC) cycles are attractive because an A-USC power plant with steam conditions up to 760°C (1400°F) and 35 MPa (5000 psi) can reduce all emissions, including CO_2, by 20% or greater compared to today's U.S. fleet [18, 19]. This is important because new U.S. regulations will limit the amount of CO_2 a new coal-plant can emit and if carbon capture and storage is needed, the most cost effective way to capture and store CO_2 is to not produce it or minimize the amount which needs to be captured.

The primary barrier to achieving these A-USC conditions is the high-temperature materials. The United States Department of Energy (U.S. DOE) Office of Fossil Energy and the Ohio Coal Development Office (OCDO) have been the primary supporters of a U.S. effort to develop the materials technology necessary to build and operate an advanced-ultrasupercritical (A-USC) steam boiler and turbine with steam temperatures up to 760°C (1400°F). The program is made-up of two consortia representing the U.S. boiler and steam turbine manufacturers (Alstom, Babcock & Wilcox, Foster Wheeler, Riley Power, and GE Energy) and national laboratories (Oak Ridge National Laboratory and the National Energy Technology Laboratory) led by the Energy Industries of Ohio with the Electric Power Research Institute (EPRI) serving as the program technical lead. Over 10 years, the program has conducted extensive laboratory testing, shop fabrication studies, field corrosion tests, and design studies [20]. The program successes are numerous [21] and some recent key results include ASME Boiler and Pressure Vessel Code acceptance of Inconel 740/740H (CC2702), the operation of the world's first 760°C (1400°F) steam corrosion test loop [22], and significant strides in turbine casting and forging activities [20]. The program has also showed that the materials designed for 760°C (1400°F) can have significant economic advantages at 700°C (1300°F) [23]. Based on the program successes, a follow-on effort to test components is under development. Unique to this program is the planned testing of the world's first A-USC steam turbine, figure 9.

New innovative cycles are also being considered for future fossil power generation. Unlike conventional pulverized coal plants which will require carbon capture and storage (CCS), these technologies fundamentally change the combustion process with the goal of producing pure or nearly pure streams of CO_2 to reduce the cost penalty with CCS. Some of the technologies which are being actively researched are based on supercritical CO_2 (S-CO_2) as the working fluid in a Brayton cycle. In the open loop configuration shown in Figure 10, theoretical calculations show efficiencies greater than 50% with an essentially pure stream of CO_2. For this cycle and many of the other S-CO_2 cycles being proposed, there are a number of materials challenges [24]. These challenges include high-temperature materials conditions (temperatures and pressures) similar to proposed A-USC conditions. Thus the materials technology being developed for A-USC appears transferable to future S-CO_2 cycles. However, some significant differences exist in the materials needs. First, no systematic study exists on material compatibility in S-CO_2 and the limited data shows effects of impurities, water vapor, and pressure are all important in oxidation and corrosion rates. Second, for some cycles scaling up to large scale (greater than 100MW) will require large volumetric flows. Thus, pipe and tube sizes will need to be maximized to ensure

economic advantages and there are material processing limitations when using high-temperature high-strength alloys. Finally, turbine technologies at these larger scales are largely unproven.
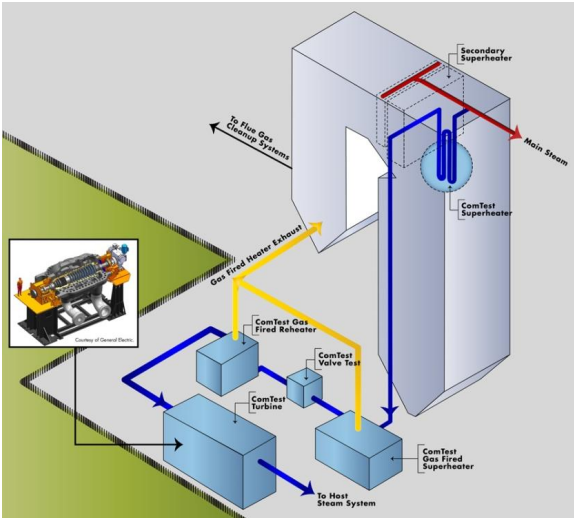
Figure 9. Schematic of proposed U.S. A-USC Component Test including an A-USC Turbine Operating at 760°C steam
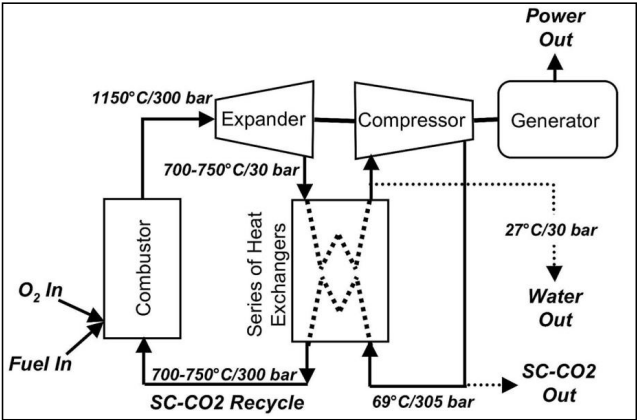
Figure 10. Example of an open-loop S-CO$_2$ Brayton cycle for power generation [24]

3.0 Conclusions

The U.S. power generation system is in a state of transition. Materials technologies are needed in this period to ensure the fossil fleet continues to provide reliable, safe, affordable, and

environmentally responsible electricity. Improved understanding of creep-fatigue will allow utilities to manage component life in aging assets while improving future design for faster start capability. Innovative welding repair techniques will enable safe operation of creep strength enhanced ferritic steels which are the backbone of the current generation of technologies. Research and solutions to thick section dissimilar metal weld damage is required to ensure future gas technologies will operate with maximum efficiency in a safe manner. Advanced materials and processes are an active area of research as they are the enabling technology for realizing higher efficiencies and dramatic reductions in CO_2 through advanced ultrasupercritical power plants and future innovative cycles. EPRI is actively and collaboratively engaged as leaders in all these materials research areas to help shape the future of electricity in the U.S. and abroad.

References

[1] "2012 State of the Markets Report." Federal Energy Regulatory Commission. Available at www.ferc.gov/oversight
[2] "The CURC-EPRI Coal Technology Roadmap. August 2012: Update." Available at: www.coal.org
[3] S. Hennessey, "Fast Startup Including the NFPA Purge Credit," *Presentation at the 2012 EPRI Fossil Life Assessment Conference, October 2012, Hilton Head, SC USA.*
[4] Ian Perrin. "Next Generation HRSGs." *Australian HRSG User Group,* December 4-6, 2012, Brisbane, Australia.
[5] Jonathan Parker, John Shingledecker. "EPRI Initiatives related to Flexible Operation of High Temperature Power Plant," *Proceedings to the 13th International Conference on Fracture (ICF13)*, June 16-21, 2013, Beijing, China.
[6] A. Saxena et al. "Harmonizing of Creep-Fatigue Test Methods Through the Development of ASTM Standards." *Advances in Materials Technology for Fossil Power Plants. Proceedings from the Seventh International Conference.* Oct. 22-25, 2013, Waikoloa, Hawaii USA. Published by ASM International © 2014. EPRI Report Number 3002002375. 1190-1205.
[7] S.R. Holdsworth, R.P. Skelton, B. Dogan. "Code of practice for the measurement and analysis of high strain creep-fatigue short crack growth." *Materials at High Temperature* 27(4), 2010. 265-283.
[8] *Final Report on Round-Robin Conducted in Support of Standard Test Method for Creep-Fatigue.* EPRI, Palo Alto, CA: 2013. 3002001719.
[9] *Program on Technology Innovation: Evaluation of the Creep-Fatigue Behavior of Grade 92 Steel and Its Predictability.* EPRI, Palo Alto, CA: 2011. 1024588.
[10] I. Perrin, D. Peters, N. Cofie, J. Parker, J. Shingledecker. "Recommended Design Guidelines for the Effects of Creep-Fatigue Interaction and Flaw Acceptance Criteria." RFP-ASMEST-12-02. *In publication, ASME S&T, LLC New York, New York, 2014.*
[11] *Service Experience with Grade 91 Components*. EPRI, Palo Alto, CA: 2009. 1018151.
[12] *Performance Review of T/P91 Steels*. EPRI, Palo Alto, CA: 2002. 1004516
[13] S.A. David, J.A. Siefert, Z. Feng. "Welding and weldability of candidate ferritc alloys for future advanced ultrasupercritical fossil power plants." Science and Technology of Welding and Joining, 2013. DOI 10.1179/1362171813Y.0000000152
[14] J. A. Siefert and J. D. Parker. "Well-Engineered Weld Repair of Grade 91 Steel." *11th International EPRI Conference on Welding and Repair Technology for Power Plants*. Naples, FL, 2014.
[15] J. D. Parker. "Damage Tolerance Considerations for High Energy Components Manufactured from Creep Strength Enhanced Ferritic Steels." *11th International EPRI Conference on Welding and Repair Technology for Power Plants*. Naples, FL, 2014.
[16] S. Paterson et al. "Early Service Life Cracking of Steam Piping Welds in Combined Cycle Power Plants.

[17] "AEP Uses New Filler Metal for Dissimilar Metal Welds in Ultra-Supercritical Plant." EPRI, Palo Alto, CA: 2010. 1020760. Publically available at:
http://www.epri.com/abstracts/Pages/ProductAbstract.aspx?ProductId=000000000001020760
[18] R. Viswananthan, J.F. Henry, J. Tanzosh, G. Stanko, J. Shingledecker, B. Vitalis, R. Purgert. "U.S. Program on Materials Technology for Ultra-Supercritical Coal Power Plants." *Journal of Materials Engineering and Performance.* Vol. 14 (3) June 2005. 281-292.
[19] J.P. Shingledecker, I.G. Wright. "Evaluation of the Materials Technology Required for a 760ºC Power Steam Boiler." *Proceedings to the 8th Liege Conference on Materials for Advanced Power Engineering 2006.* Forschungszentrum Jülich GmbH (2006) pp. 107-120.
[20] J. Shingledecker, R. Purgert, P. Rawls. "Current Status of the U.S. DOE/OCDO A-USC Materials Technology Research and Development Program." *Advances in Materials Technology for Fossil Power Plants. Proceedings from the Seventh International Conference.* Oct. 22-25, 2013, Waikoloa, Hawaii USA. Published by ASM International © 2014. EPRI Report Number 3002002375. 41-52.
[21] U.S Department of Energy and Ohio Coal Development Office Advanced Ultra-Supercritical Materials Project for Boiler and Steam Turbines. EPRI, Palo Alto, CA: March 2011. 1022770. Available:
http://my.epri.com/portal/server.pt?Abstract_id=000000000001022770
[22]R. Ganta et. al. "Steam Loop Testing of A-USC Materiasl for Oxidation and Fireside Corrosion – Alstom's Experience to Date." *Advances in Materials Technology for Fossil Power Plants. Proceedings from the Seventh International Conference.* Oct. 22-25, 2013, Waikoloa, Hawaii USA. Published by ASM International © 2014. EPRI Report Number 3002002375. 832-846.
[23] J. Shingledecker et al. "U.S. Program on Advanced Ultrasupercritical Power Plant Materials – The Economy of Using Advanced Alloys." *Proceedings to the IEA Clean Coal Centre Workshop: Advanced ultrasupercritical coal-fired power plants.* Vienna, Austria, 19-20 Sept. 2012.
[24] I.G. Wright et al. "Materials Considerations for Supercritical CO2 Turbine Cycles." *Proceedings of ASME Turbo Expo 2013: Turbine Technical Conference and Exposition.* GT2013, June 3-7, 2013, San Antonio, TX USA: GT2013-94941. © 2013 ASME

CHALLENGES OF FLUCTUATING LOADS FOR CONVENTIONAL POWER PLANTS

Ralf Mohrmann

RWE Technology GmbH, Huyssenallee 12-14, D-45128 Essen, ralf.mohrmann@rwe.com

Abstract

The application of high performance materials for high-temperature pressure parts in conventional power plants is controlled by the pressure equipment directive (PED). EN standards like the EN 12952 are widely used in Europe to fulfill the PED. More restrictive VGB standards like the materials specification VGB-R109 are applied especially for critical components.

Within the last ten years, renewable energy production in Germany increased by a factor of approximately 3 and this progression is predicted to continue. The priority of this renewable energy supply leads to a high demand on flexible energy production from conventional power plants.

The flexible service conditions of conventional power plants may differ from initial design criteria and may produce different damage characteristics compared to the established practice such as non-destructive investigation procedures. Therefore a VGB working group was founded to analyze and develop calculation methods especially for thick walled components, for weldments, for start-up and shut-down procedures and for the interaction of static and cyclic loading of critical components. The current status of these activities is presented and demands for future work are addressed.

1   Introduction

In Europe, the application of high performance materials for high-temperature pressure parts in conventional power plants is controlled by the PED [1]. The presumption of conformity with the PED is given if applicable EN standards are used for the calculation of component loading history due to power plant service loads (i.e. internal pressure, temperature) and if these component loads do not exceed material properties which are defined within the EN standards, respectively. The EN standards EN 12952, EN 13445 and EN 13480 are mainly used for the design of high-temperature pressure parts. More restrictive VGB standards like the materials specification VGB-R109, the specification for fabrication and installation of pipe works in conventional power plants VGB-R508L, or the specification for repeated inspections VGB-R509L are applied especially for critical components.
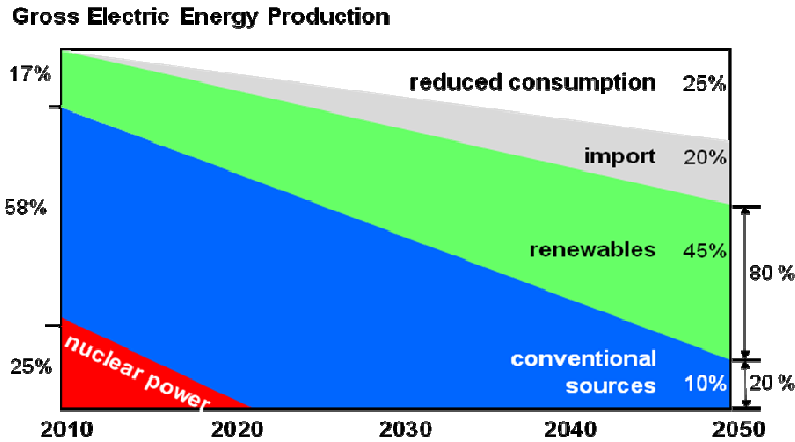
Figure 1: Gross Electric Energy Production in Germany [2]

Within the last ten years, renewable energy production in Germany increased by a factor of approximately 3 and this progression is predicted to continue. Figure 1 summarises the plans of the federal government of Germany for the gross electrical energy production until 2050.

The priority of this renewable energy supply leads to a high demand on flexible energy production from conventional power plants. Figure 2 compares the residual load characteristics, which is the current difference of electric energy consumption and the supply by renewable sources, for week 6 to 9 in 2008 with a prediction for the same period in 2050.
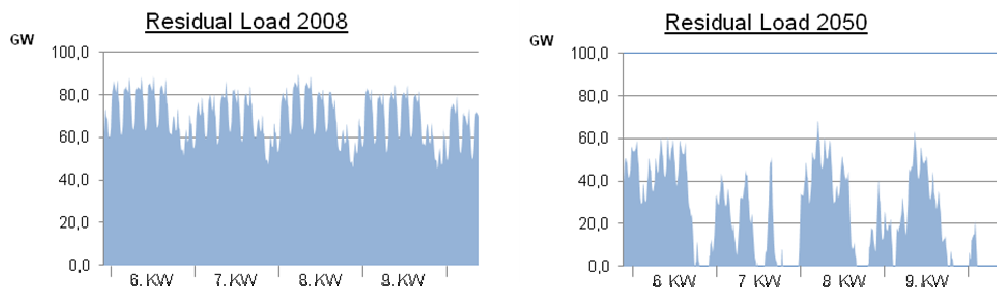
Figure 2: Residual Load characteristic for week 6 to 9 in 2008 (left) and in 2050 (right).

For the residual load in 2008, a power plant fleet with base load, mid-load and peak-load power plants was needed the ensure the electric power supply. In 2050 a power plant fleet designed for many load changes, high load gradients and low minimum load needs to be available.

847

2   Demands on Materials and Components

In the future, the flexible service conditions of conventional power plants may differ from initial design criteria and may produce different damage characteristics compared to the established practice such as non-destructive investigation procedures. Therefore a VGB working group was founded to analyze and develop calculation methods especially for thick walled components, for weldments, for start-up and shut-down procedures and for the interaction of static and cyclic loading of critical components.

2.1   Thick Walled Components

The analytical stress calculation methods implemented in the EN standards assume linear elastic materials behaviour in the whole temperature range and were developed mainly for thin walled components. Therefore alternative analytical stress calculation methods which are more appropriate for thick walled components and which allow stress redistribution due to the materials' creep behaviour are in the focus of the VGB working group. These methods will allow calculating more realistic (lower) stress values and as a consequence will reduce the minimum required wall thickness for thick walled components and will allow more flexible power plant service.

2.2   Weldments

Welded pipe to pipe connections and other weldments undergo a complex loading history due to the gradients of material properties of base metal, heat effected zone material states and the weld metal, respectively. In addition, geometric and process details like the orientation of the weldments with respect to the orientation of maximum principle stresses, pre- and post-weld heat treatment and the resolution of non-destructive testing should be considered consistently. Here, the VGB working group aims for a concept with separate weld reduction factors, one for material degradation and another for geometrical details including details of non-destructive testing.

2.3   Start-up and Shut-down Procedures

During start-up and shut-down procedures of conventional power plants, thermally loaded (thick walled) components undergo a superimposed fatigue load due to the constrained of components' thermal expansion. The resulting stress ranges are calculated and limit the number of allowable start-up and shut-down procedures. This allowable number differs in case of thick walled components comparing the (old) TRD standard, which is the current one for older power plants, with the EN standard up to a factor larger than ten, although they refer

848

to the same data base. The VGB working group addresses the underlying calculation methods and the data base, respectively.

2.4 Interaction of Static and Cyclic Loading

For quantitative lifetime assessment of critical power plant components, the component loading is split in static (creep) and cyclic loading parts. If both parts of this lifetime consumption are relevant, the interaction has to be taken into account. The (old) TRD standard and the EN standard EN 12952-4 proposes a linear superposition of the results for static and cyclic loading, respectively. This superposition method differs substantially from the method implemented in the ASME code [3]. The ASME code proposes a strong non-linear interaction of creep and fatigue lifetime consumption, where the interaction is reported as material dependent [3]. The strongest interaction is found for low alloyed ferritic material, where a cyclic lifetime portion of 15% will reduce the allowable creep lifetime portion down to 15%. The comparison given is valid only for the superposition methods implemented and not for the material properties implemented. The VGB working group addresses a strong need for a verified calculation method applicable for the interaction of static and cyclic loading and for specific test results for materials used in existing power plants at relevant load levels.

3 Summary

The future service of conventional power plants is controlled by the growing demand on flexible production of electric power. The power plant fleet should allow more load changes, high load gradients and low minimum loads. Specific attention should be given to the calculation methods for thick walled components, weldments, start-up and shut-down procedures and the interaction of static and cyclic loading portions. Therefore a VGB working group was founded to analyze and to develop further these calculation methods.

References
[1]   Pressure Equipment Directive: 97/23/EG

[2]   EWI/Prognos/GWS Studies

[3]   ASME Section 8 Devision 2 (API FFS 1)

EVALUATION OF WELDED JOINTS PROPERTIES AND MICROSTRUCTURE OF NEW AUSTENITIC STEELS SANICRO 25 AND HR6W

Adam Hernas[1], Marek Staszewski[1], Jerzy Pasternak [2], Stanisław Fudali[2]

[1] The Silesian University of Technology, 40-019 Katowice, Poland (a.hernas@polsl.pl)
[2] RAFAKO S.A., 47-400, Racibórz, Poland (j.pasternak@vp.pl)

Abstract

This article presents in brief the characteristics of materials used in fabrication of supercritical and ultra-supercritical boilers. Special attention has been paid to two material types, i.e. Sanicro 25 austenitic steel and Ni HR6W alloy in form of superheater tubes Ø 38.8 x 8.8 mm. The manufacturing technology of experimental, qualification welded joints has been described, as well as the results obtained from macro and microstructure examinations. Furthermore, the examination results of the basic mechanical and technological properties have also been presented. The tests and examinations performed are pioneering ones in Poland and allow to get valuable experience and own "know-how" in the domain of the welding and bending technologies for tubes to be applied in superheaters operated at the temperature of approx. 650°C.

Keywords: welding, bending process, technological and mechanical properties, steel structure stability

1. Introduction

The legal and environmental conditions, the requirement to improve the technical parameters of the power units, as well as the increase of the national energy security necessitate the construction of modern supercritical power units of high efficiency. However, the development of the power engineering technologies depends on the development of the materials technology, which ensures higher and higher required performance characteristics of the structural components [1]. In Poland we can observe three main directions with regard to the development of the coal power engineering, i.e.:

- Modernisation and construction of boilers having increased steam parameters in the range of 570°C and the efficiency of at least 36%,
- Designing and construction of boilers with efficiencies above 40% and their parameters being t = 600°C and pressure approx. 28MPa,
- Research works of anticipated character, carried out within the framework of the Strategic Project NCB&R, with the objective to develop the technology for highly efficient "zero emission" coal units with CO_2 capture for ultra-supercritical parameters (USC).

High-temperature creep resistant materials for application in the advanced power engineering have to possess very good temporary creep resistance, resistance to oxidation in water vapour and to high temperature corrosion in the flue gas environment. Another very crucial group of the requirements are technological properties, such as weldability, bendability and heat treatment parameters.

In the construction of supercritical and ultra-supercritical boilers, the following material groups have been used, with varying degrees of success, for pressure components [1-6]:low-

alloy steels, martensitic (9-12 %C) steels, austenitic Super304H, HR3C, Sanicro 25 and nickel based alloys (HR6W, Alloy 617, DMV617*mod.* and Inconel 740).

Temperature ranges of some selected materials and their temporary creep resistance are shown in Figure 1.
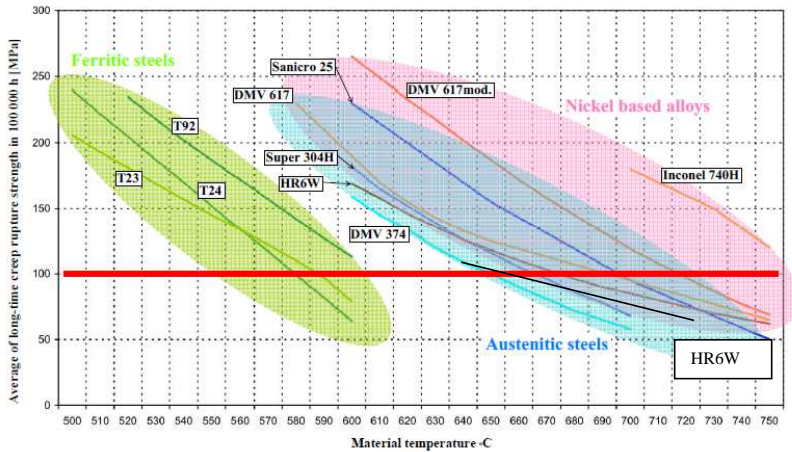
Fig. 1. The applied temperature ranges and average temporary creep resistance at 100,000 h for materials selected for fabrication of supercritical and ultra-supercritical power units [prepared on the base of VdTÜV, GB5310;2008 and PN-EN 10216-2;2009 data].

In the framework of the Strategic Research Project NCB&R, which has been run by the Silesian University of Technology and RAFAKO S.A. since 2010, the assumptions and preliminary boiler design for ultra-supercritical parameters and efficiency above 45% have been presented [7, 8]. The basic steam parameters – the live steam an reheat steam pressure and temperature are: 30MPa / 653°C / 674°C. The selected high-temperature creep resistant materials for application in critical pressure components of the boilers are provided in Table 1.

2. Characteristics of Sanicro 25 steel and HR6W alloy.

Sanicro 25 (i.e. 22Cr25NiWCoCu) is an austenitic steel dedicated steam superheater components of the designed, newly-built and highly efficient ultra-supercritical parameter boilers. The inventor and main producer of the steel is the company of SANDVIK from Sweden [3, 10, 12]. The steel possesses excellent high-temperature creep resisting and heat-resisting properties. The high creep resistance in combination with good corrosion resistance make Sanicro 25 steel an excellent applicant in steam superheater components, both for live and reheat steam. The material in question is capable of being used up to the temperature of 700 °C. [10, 12].

Table 1: List of some boiler components, their dimensions and high-temperature creep resistant material grades for application in boiler pressure components [7].

Materials provided for primary steam superheater components (SH3), with the following inlet steam parameters: $t_{medium} = 653$ °C; $p_{medium} = 30.3$ [MPa]				
Type of component	Material	Required calculated diameter x wall thickness [mm]	Design parameters T_{design} [°C], p_{design}	
Coils	X6CrNiNbN 25-20 (HR3C)	ϕ42.4 x 8	645	[MPa] 32
	NF709		660	32
	HR6W	ϕ42.4 x 8.8	674	32
	Sanicro 25		689	32
	NiCr23Co12Mo DMV 617 mod.		703	32
Outlet header	HR6W	ϕ220$_w$ x 75	668	31.5
Pipelines to turbine	HR6W	ϕ280$_w$ x 75	658	31.5

The alloy of Ni HR6W (23Cr – 45Ni – 7W) was developed in Japan in the late 1980s as the material for fabrication of highly-resistant tubes used in construction of ultra-supercritical boilers with live steam temperature above 650ºC. The Ni- HR6W alloy's creep resistance and microstructure stability at elevated temperatures is slightly lower in comparison with those of Alloy 617 [11]. Nevertheless, the high chromium content assures considerable resistance to oxidation in the water vapour atmosphere, as well as the resistance to high-temperature corrosion on the flue gas side. The material, taking into account the technological viewpoint and long-term operation at high temperature is not yet fully recognised in our country [4-6]. Table 2 provides the chemical composition of the materials tested. The making-up to 100% includes: Si, Mn, S and P.

Table 2. Chemical composition of Sanicro 25 steel and HR6W alloy. [10, 11]

Material	Chemical composition of tested materials [% mass]										
	C	Si	Cr	Ni	W	Co	Cu	Nb	B	N	Ti
Sanicro 25	0.064	0.18	**22.35**	**25.36**	3.37	1.44	2.98	0.49	0.0035	0.23	-
HR6W	0.08	0.20	**22.81**	**45.69**	8.00	-	-	0.19	-	-	0.11

3. Qualification of welding technology process for welded joints made of Sanicro 25 steel and HR6W alloy.

Taking into consideration the requirements of the pressure directive PED 97/23/UE, a series of similar and dissimilar welded joints was made from Sanicro 25 steel tubes, delivered acc. to VdTÜV WB 555, WG 8.2/ CEN ISO/ TR and tubes made of Ni- HR6W alloy, delivered in accordance with VdTÜV WB 559/2, WG 43/ CEN ISO/ TR, having the diameters of Ø 38.8 mm and wall thickness 8.8 mm. Qualification similar and dissimilar butt welded joints were produced at RAFAKO S.A. – without post-weld heat treatment, in the following combinations:

a) HR6W + Sanicro 25
b) HR6W + In 617
c) Sanicro 25 + In 617
d) HR3C + HR6W
e) Super304H + HR6W

This presentation includes the description of the technology and test results of Sanicro 25 and HR6W alloy tube welded joints. Owing to the tube dimensions, two basic welding methods were selected for the butt welded joints [8,9]:

a. manual 141 method (GTAW),
b. automatic 141Aut method.

Qualification test pieces of butt welded joints were made manually by 141 method (GTAW) in PC and PF welding positions (with no welded joint rotation), using welding rod Thermanit 617 (Ni-21Cr-9Mo-11Co-Al.,Ti), φ 2 mm, with the number of passes (filling beads) being 3-4.

Due to the requirement of the parameter repeatability and those of the Customer's, the 141Aut method was chosen as the recommended welding technology for manufacture of the boiler fabrication welded joints. This document also includes a description of qualification test pieces welding process by 141Aut method, as fabricated on the Polysoude automatic welding machine, type PS406. Here are the basic welding parameters for the 141Aut method:

- Tube diameter; φ38 x 8.8mm,
- Welding position PA (with rotation of the tube being welded), Shielding gas;"argon/ 1",
- Welding rod; Thermanit 617, (Ni-21Cr-9Mo-11Co-Al.,Ti), φ 0.8 mm,
- Welding current intensity; approx. 110A, for the filling beads approx. 130A,
- Number of passes; filling beads 7-8, Maximum inter-pass temperature $<140^0$C.

The selected details of preparation for welding of the butt welded joint, made by the 141Aut method and the welding process sequence are included in the WPS, Figure 2.
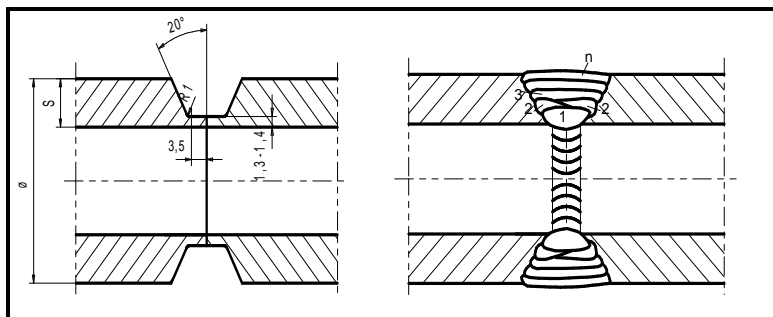
Figure. 2. Preparation details for welding of butt welded joints using the 141Aut method and the sequence of the welding process [8].

The welding technology qualification process was carried out in accordance with the requirements of standard PN-EN 15614 – 1. The scope of the welding technology qualification tests and examinations covered both non-destructive and destructive ones, including:

- Geometrical measurements and visual inspection of the welded joints after welding – according to EN 970, EN ISO 17637 and EN ISO 5817-B. The examination range was 100% of the welded joint surface;
- Dye-penetrant examinations of the welded joints in order to detect surface cracks were executed in compliance with standard EN 571. The examination range covered 100% of the welded joints' surface, for the acceptance level according to standard EN 23277;
- Radiographic examinations of the welded joints were performed in accordance with standard EN 1435, class B, the examination range was 100% of the welded joint's volume and the evaluation criteria were in compliance with standard EN 12517-1;
- Mechanical tests of the welded joints resistance to tension;
- Hardness measurements and evaluation of the welded joints' rupture labour;
- Macroscopic and microscopic examinations of the welded joints.

4. The examination results of mechanical properties, macro- and microstructure tests on welded joints tubes of Sanicro 25 steel and HR6W alloy.

4.1. Macro- and microstructure examinations of welded joints tubes made of Sanicro 25 steel and HR6W alloy.

The macrostructure tests and examinations had been prepared and then executed in accordance with standard EN 1321. Figure 3a presents some exemplary macrostructure of the manually welded butt welded joint.

In the original period of the HR6W alloy welded joint fabrication, the grain growth was ascertained, accompanied by the occurrence of precipitation processes on the grain boundaries (Fig. 3b). That decreased the welded joints' toughness and ductility, which were ruptured in the heat affected zone (HAZ) area during the tensile test. The rupture labour was approx. 40 J.
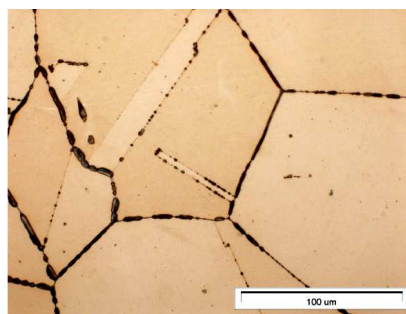
a)   b)

Fig. 3a) Macrostructure of welded joint made of HR6W alloy.
b) Unfavourable network of intermetallic phases in the HAZ, LM 200x)

In the second period the welding technological parameters were corrected. A fully satisfactory welded joint quality was achieved, confirmed by the microstructure and test results of the mechanical properties, as presented in the following part of this article (Figures 4 and 5).

The qualification test results of homogeneous and non-homogeneous welded joints made of Sanicro 25 and HR6W alloy showed the correct macro and microstructure of the welded joints. In the welded joint there is a homogeneous, fine dendritic microstructure with a small amount of primary releases (Fig. 4).

a)   b)
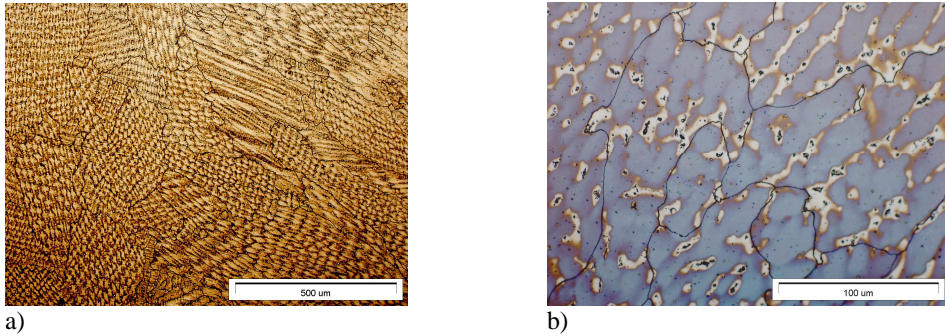
Fig.4   Typical microstructure of welded joint Sanicro 25 and HR6W, made with Thermanit 617 welding wire. Magnification 100 and 500x.

The fusion zone in the HAZ, both for Sanicro 25 and HR6W is characterised by good mixture of materials with fluent microstructure transition from the welded joint to the base material (Fig. 5).
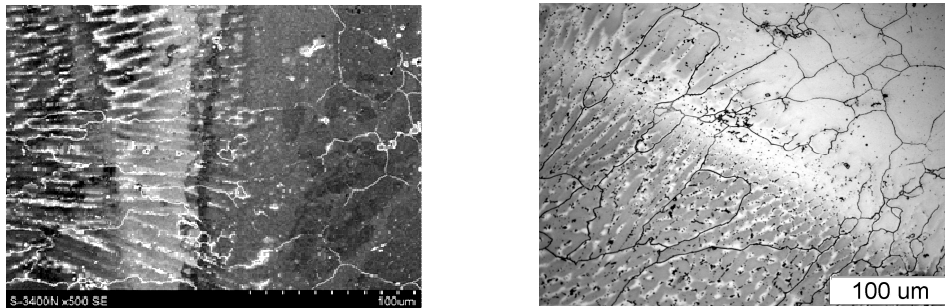
Fig.5 Examples of smooth microstructure transition from welded joint to the parent metal, a) HR6W welded joint, SEM, b) Sanicro 25 welded joint, LM.

4.2. Evaluation of qualification welded joints' process including assessment of mechanical and technological properties.

The scope of the examinations performed included identification of the characteristic properties of the base materials and welded joints, comprising, among other things, the evaluation of:

- Mechanical and technologies properties of base materials, HAZ and weld deposit after the welding process at ambient temperature and at the anticipated working temperature,

- Hardness of the welded joint components,

- Structure, including the analysis of welding processes' influence on the structure change process.

The summary of the base material mechanical test results – in the "as delivered" condition – made of Sanicro 2 steel and HR6W alloy, as well as those of the non-homogeneous Sanicro 25 + HR6W welded joints are presented in Figure 6.
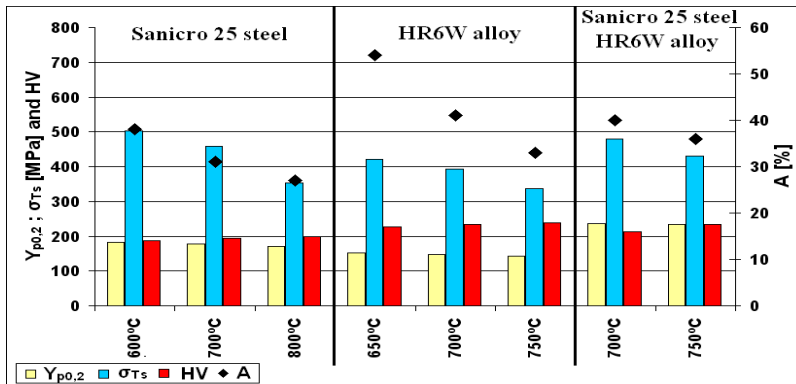
Fig. 6. Summary of key results from mechanical tests on base materials made of Sanicro 25 steel and HR6W alloy (in "as delivered" condition) and dissimilar Sanicro 25 + HR6W welded joints.

The examinations of the welded joint technological properties were performed at ambient temperature according to standard EN 895 and standard EN PN 15614-1 and included the evaluation of:

1- Bent test pieces, made in accordance with standard EN 910, The bending mandrel diameter, the internal roller, was 20 mm and the required bending angle was 180 degrees.
2- Impact strength according to standard EN 875 were made with Charpy V-notch with the examination of the weld area (VWT) and the HAZ area (VHT).

The examinations of the mechanical properties at room temperature, i.e. in the static tensile test, proved the expected welded joint quality, with the detected rupture zone in the parent material, and the bending radius in the bending test did not show cracks for angle 180° [8].

The results of the executed tests and examinations were verified in relation to the following standards, such as: EN-ISO 12952-5, EN-ISO 12952-6, VGB R 501H, VdTÜV - Werkstoffblat 555 and VdTÜV-Werkstoffblat 559/2.
The obtained results of the mechanical and technological properties of the welded joints are in compliance with the requirements included in the aforementioned standards and technical documents.

4.3 Hardness measurement results of selected welded joints.

The examinations of the hardness penetration pattern of HR6W welded joint along PM – HAZ – WELD – HAZ – PM lines are shown in Fig. 7. The welded joint and HAZ hardness

depends on the welding method, structure conditions and parent material hardness and amounts to approx. 205HV and approx. 165HV or the HAZ.
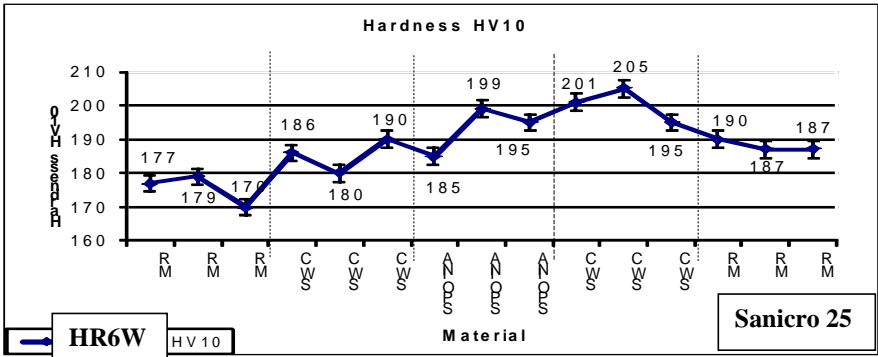
Fig. 7. Measurement results of qualification welded joint hardness along PM -HAZ - Weld - HAZ – PM lines.

5. Examinations of Sanicro 25 steel and HR6W substructure welded joints after long-term annealing (ageing process).

In the test programme of the research project, long-term ageing of the joints welded at the temperature of 750°C was also scheduled with the objective to analyse the release processes and the strengthening mechanisms in creep conditions. The examinations were carried out by means of LM, SEM and TEM. Some exemplary influence of ageing at the temperature of 750°C and after 2,000 hours is shown in Figures 8 and 9. In the welded joint structure one can observe numerous clusters of intermetallic phase releases on dendrite boundaries.
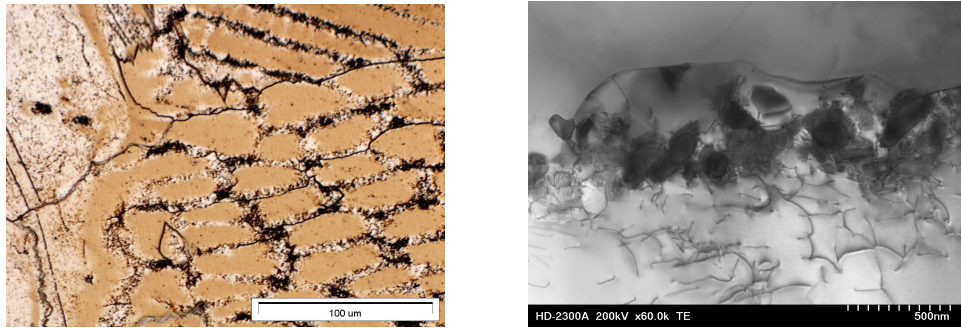
Fig. 8. Carbide release process in Thermanit 617 welded joint after 2,000 hours of ageing.
a) LM, magnification 500x, b) TEM thin foil.

a)   b)
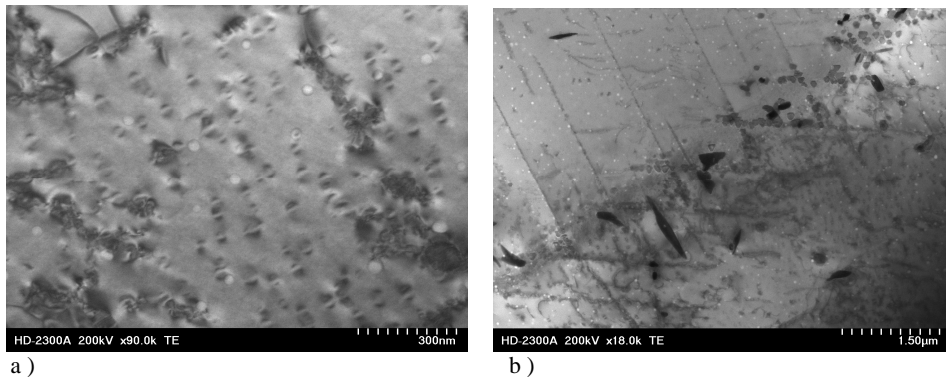
Fig. 9. Exemplary effects of ageing process at temperature 750°C after 2,000 hours:
a) Coherent copper precipitations in Sanicro 25 parent material and b) precipitations of
carbides and carbonitrides in HAZ transition area, TEM, thin foil.

9. Summary

- Complex evaluation of the welded joint quality was performed with the use of non-destructive examinations (NDT), destructive examinations, including elaboration of the similar and dissimilar welded joint structure and mechanical properties' characteristics.
- The homogeneous and non-homogeneous welded joints are compliant with the quality requirements of "B" class, according to PN EN 5817.
- The obtained test and examination results confirm that the base materials applied in welding, as well as the welding technology have been correctly selected and qualified in accordance with the referenced technical standards and harmonised standards, in relation to Directive 97/23/EC, as provided for the manufacturing conditions of a large boiler maker.
- The qualification of the welding technology was achieved for welded joints made of Sanicro 25 steel and HR6W alloy. It was conducted in accordance with standard PN EN 15614, with regard to mechanical properties and structure, by the Notifying Body TÜV NORD.
- Tensile strength of the welded joints Rm was: 690 – 742 MPa (depending on the welding technique), whereas their hardness (i.e. for the welded joint and HAZ) was < 260 HV10.
- The obtained results of the rupture labour in HAZ and deposited metal were from 64 to 143 J (depending on the parameters and welding technique).

Acknowledgments

References

1. Collective publication edited by A. Hernas: *Materiały i technologie do budowy kotłów nadkrytycznych i spalarni odpadów.* Wyd. SITPH, Katowice, 2009.
2. Smith D.: Doosan Babcock Energy – *Advanced Supercritical Boiler Technologies. Technical Semin.,* July 2009.
3. Rautio R., Bruce S.: *Sandvik Sanicro25, a new material for ultrasupercritical coal fired boilers. Sandvik Material Technology,* Database, 2010.
4. Semba H., Okada H., Yonemura M., Igrashaki M.; *Creep Properties and Microstructure of HR6W and Ni-base Superalloys for Advanced USC Boilers for 700ºC A-USCBoilers.* 5th Int. Conf. EPRI Florida, US, 2007.
5. Chi Sh., Zhan Z., Xu Y., Li L., Xiao X., Zhu Ch.; *Improvement of Stress-rupture Life for Modifed-HR6W Austenitic Stainless Steel. 6th Int.* Conf. EPRI Florida, US, 2008.
6. Huseman R.U.- *Babcock EU: Materials for AD700 Boilers. Ed.PF Power Plant CESI Audytorium.* Milano, 2005.
7. Sutowicz A., Cieszyński K.: *Nowoczesne technologie i materiały w kotłach nadkrytycznych -założenia projektowe referencyjnego kotła na parametry supernadkrytyczne.* Konf. PIRE, 2011 (in the Polish language only).
8. Hernas A., Tasak E., Sozańska M., Pasternak J., Szczucka-Lasota B., Fudali S., Krupa R.: Zgrzendek M.: Sprawozdanie z Projektu NCBiR: *Zaawansowane technologie pozyskiwania energii, Zadanie 1 Opracowanie charakterystyk własności technologicznych i użytkowych, Etap nr 17.IV.2.2* Badania materiałowe, Politechnika Śląska, 2012 (unpublished).
9. Hernas A.,Fudali S., Pasternak J., Sutowicz A*.: Dobór materiałów na elementy referencyjnego kotła o supernadkrytycznych parametrach pary.* Energetyka, z. nr XXII, November, 2011.
10. VdTUV – Werkstoffblatt, WB 555 – Grade Sanicro 25.
11. VdTUV – Werkstoffblatt, WB 559/2 – Grade HR6W.
12. Materials from the company of SANDVIK - *http://www.smt.sandvik.com/en/materials-center/material-datasheets/tube-and-pipe-seamless/sanicro-25/*

859

OXYGEN CARRIER RESEARCH FOR
CHEMICAL LOOPING COMBUSTION

[1]Frans Snijkers, [1]Marijke Jacobs, [1]Jasper Van Noyen,
[2]Tobias Mattisson, [2]Anders Lyngfelt,

[1]VITO, Sustainable Materials Technology, Boeretang 200, B-2400 Mol, Belgium;
frans.snijkers@vito.be
[2]Chalmers University of Technology, Energy and Environment, S-41296 Göteborg, Sweden;

Abstract

Chemical looping combustion (CLC) is a promising technology for energy production with inherent capture of carbon dioxide at minimal energy penalty. In CLC, oxygen is transferred from an air reactor to a fuel reactor by means of a solid oxygen carrier. Direct contact between air and fuel is avoided resulting in an undiluted CO_2 exhaust stream. A critical aspect of the technology is the oxygen carrier performance which has a very strong impact on the economic viability. Parameters such as particle size, density, porosity, strength, attrition resistance, reactivity, environmental aspects and cost, define the performance of the oxygen carrier. In this contribution it is shown that spray-drying is a versatile and scalable technique for the preparation of new and promising oxygen carriers with varying compositions. Different categories of materials have been produced and tested, such as perovskite type materials based on calcium-manganate, magnesium manganates, copper based materials, and iron manganates.

Keywords: chemical looping combustion, oxygen carrier, perovskite, calcium manganite, CO_2 capture

1. Introduction

1.1 Carbon Capture, Transport, Use and Storage

Carbon Capture, Transport, Use and Storage (CCTUS) is an important aspect in many national, international and global strategies to combat climate change. The European Academies Science Advisory Council (EASAC) published in 2013 a detailed report on the status of CCTUS technologies and challenges that need addressing to secure it as a viable component of strategies to mitigate climate change. While initial focus was mainly on underground or undersea storage projects, CO_2 is more and more regarded as a valuable chemical substance for enhanced oil or gas recovery and for the production of chemicals, plastics or building materials.

The dilution of CO_2 with other gasses is a problem for many use and storage applications. Hence, a main challenge regarding capture of CO_2, especially for high volumes, is separating it from other gasses. For example, a natural gas-fired power station with an electricity generating capacity of 500 megawatts produces around 180 tons of CO_2 per hour. The concentration of CO_2 in the flue gas of a natural-gas-fired combined cycle is around 4% by volume. A coal-fired power station with a similar electrical capacity produces about 400 tons of CO_2 per hour with around 14% CO_2 in the flue gas. Other large point sources of CO_2 emission are found in steel, refinery

and cement industries. The flue gas of cement kilns may contain up to 33% CO_2. Separation of large amounts of dilute CO_2 entails the addition of major items of equipment to a power station or industrial process, which require significant quantities of energy for their operation.

Three main approaches are considered technologically feasible for CO_2 capture at large point sources: post-combustion capture, pre-combustion capture and oxy-fuel combustion. For each approach, various technological solutions have been developed and small and medium scale evaluations have successfully proven their feasibility. However, integrated operation on a commercial scale remains to be demonstrated. Post-combustion capture tackles the problem by installing a separation process to treat flue gasses. While only minor modifications are needed to the existing production processes, the additional installations for flue gas separation are significant and require quite some floor space. The most developed concepts are based on amine scrubbing. A big demo installation has been build for instance at Technology Centre Mongstad in Norway. Oxy-combustion strongly increases the concentration of CO_2 in the flue gas by replacing air with oxygen for burning the fuel. Generally, oxygen is separated from nitrogen by cryogenic processing which has a relatively high energy penalty. Also membrane based gas separation processes have been developed but these have only been demonstrated so far on a limited scale. Pre-combustion capture avoids production of CO_2 in combustion by transforming the carbon based component of the fuel to hydrogen which only produces water when burned. CO_2 is separated before combustion when it is much more concentrated. An initial gasification step is needed when coal or biomass are used as fuel [1].

1.2 Chemical Looping Combustion

Chemical Looping Combustion (CLC) is a relatively new combustion technology that can be applied as a power production technique with inherent separation of CO_2. According to a report issued by the International Panel on Climate Change (IPCC), Chemical Looping Combustion (CLC) is among the cheapest technological options to capture CO_2. The technological concept was first developed in the 1980's to produce CO_2 and only recently picked up as a high potential capture technology. The term Chemical-Looping (CL) is commonly used for cycling processes in which oxygen is transported by a solid material, referred to as oxygen-carrier. For combustion processes, the oxygen depleted carrier can be regenerated by reaction with air or water. Such processes are known under the general term Chemical Looping Combustion (CLC). An example of a possible CLC reactor concept is provided in Figure 1. Several variations of CL processing are possible for combustion of gaseous or solid fuels. Two specific process modifications worth mentioning are SR-CLC in which steam reforming is integrated in the CLC process and Chemical Looping Reforming (CLR) for which the primary products are H_2 and CO.

The CLC process can be configured as two coupled fluidized bed boilers (CFB), but also a packed bed configurations are being considered. In order to transfer oxygen from the combustion air to the fuel, oxygen carriers are used. This avoids direct contact between air and fuel and after condensation of water, relatively pure CO_2 is obtained in a separate exhaust stream from the fuel reactor, making energy consuming flue gas separation unnecessary. Chemical looping technology is investigated for a variety of fuels: natural gas, but also solid fuels like coal and biomass, the latter resulting in a negative CO_2 footprint.

Chemical looping technology is gradually maturing, with both the number as well as the size of research and demonstration plants growing from kW to MW, with 100 MW on the drawing board. In the heart of CL technology is the oxygen carrier, which is indispensable for transferring the oxygen to the fuel. Over the past years a wide variety of materials have been proposed for this role, ranging from bulk mineral powders to oxygen carrier particles engineered for shape, size and composition. Several routes for the fabrication of oxygen carriers are being investigated: from simple size reduction and classification of bulk minerals to more elaborate processes comprising industrial process steps like spray drying or incipient wetness impregnation of porous substrates. A major part of the research effort is being devoted to critical issues for up-scaling of the oxygen carrier fabrication technology. For fluidized bed application, the spray drying technique appears to be very well suited. Spray dried oxygen carrier particles are characterized by a high sphericity, good free-flowing and fluidization properties and homogeneity on the micro-scale. Promising materials are Ni-, Cu-, Fe- or Mn-based, each with their pros and cons. Some of these materials release oxygen at the typical combustion temperatures. This property is highly desirable since it contributes to full conversion of fuel.
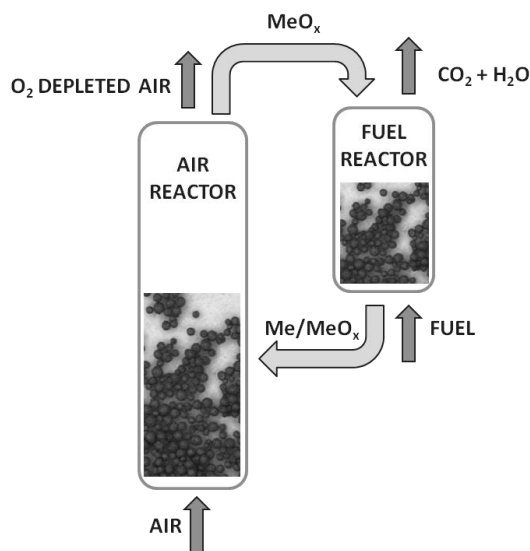
Fig. 1: CLC concept based on two interconnected fluidized-bed reactors

The first generation oxygen carriers was Ni-based, and up-scaling of these oxygen carriers was successfully demonstrated using the spray drying technique in European 6th framework project CLC Gas Power. However, due to cost of nickel and toxicity which requires special environmental/safety precautions, a search for Ni-free oxygen carriers was initiated with similar or superior performance in CLC. This was for instance the focus of the INNOCUOUS project, carried out under the European 7th Framework Program. A large variety of material compositions

was screened in order to develop a Ni-free oxygen carrier. Manganese, iron or copper oxide or combined oxides were used as main active component, alumina and zirconia were used as inert supports for increased strength and reactivity. Different categories of materials have been produced and tested, such as i) perovskite type materials based on calcium-manganate, ii) magnesium manganates, iii) copper based materials, and iv) iron manganates. This paper reports on the influence of the different steps in the manufacturing process on the CLC performance of oxygen carriers for a selection of calcium manganate materials with perovskite crystal structure [2].

2. Experimental

Oxygen carrier particles were produced at VITO with good free-flowing properties, high sphericity and homogeneity using commercial raw materials by spray-drying. Organic additives were used to disperse the powder mixture of inorganic materials in de-mineralized water. Planetary ball mills (Fritsch, Germany) or a horizontal attrition mill (Netzsch, Germany) were used to homogenize suspensions for small quantities or for larger amounts, respectively.

Water-based suspension were continuously stirred with a propeller blade mixer while being pumped to the 2-fluid spray-dry nozzle, positioned in the lower cone part of the spray-drier (type 6.3-SD, Niro, Denmark). Air in temperature was 220°C, air out temperature was 210°C. An air flow of 210kg/h was maintained.

Fig. 2: Niro 6.3-SD Spray dry plant and 2-fluid nozzle configuration at VITO

After spray-drying, the fraction within the required particle size range was separated from the spray-dried product by sieving. In order to obtain oxygen carrier particles with sufficient mechanical strength, sintering was performed in air at top temperatures in the range of 1100°C to 1350°C for 4 to 16 hours, using high temperature furnaces (Entech, Sweden; Bouvier, Belgium).

The chemical composition and possible phase formations in the Oxygen Carriers were investigated after the sintering process using X-ray powder diffraction. The X-ray analysis was performed on oxidized fresh samples and reduced samples after the reactivity tests. The shape and morphologyof the oxygen carriers, were studied using a optical microscopy and scanning electron microscopy (Jeol, FEGSEM). The force needed to fracture the particles, i.e., the crushing strength, was measured using a Shimpo FGN-5 device. The value presented is an average of the values obtained for fractured particles. The crushing strength test gives an indication of how resistant the oxygen carrier will be toward fragmentation and attrition in a real fluidised bed chemical-looping combustion application. Evaluation of the CLC performance of oxygen carrier materials was carried out at Chalmers University. All materials were characterized and tested either in a small scale batch reactor or by thermogravimetric analysis. Interesting materials were selected for tests in small continuously operating CLC units (300-500W) and most promising materials were further tested in 10 kW and/or 120 kW CLC units under continuous operating conditions.

3. Results and discussion

A critical aspect of CLC processes is the oxygen carrier performance which has a very strong impact on the economic viability of the technology. Parameters such as particle size, density, porosity, strength, attrition resistance, reactivity, conversion efficiency, environmental aspects and cost, define the performance of the oxygen carrier. Besides the conversion efficiency, the mechanical (crushing) strength of the particles is extremely important because the latter determines the resistance to attrition and hence operational use hours (lifetime) of the particles. In general, 10.000 hours is a minimum targeted lifetime. The relationship between attrition resistance and the crushing strength is not a straightforward one, yet a crushing strength above 1 N is considered to be a good indication for acceptable attrition resistance. Attrition leads to fines which are filtered off and the as such lost material needs to be replaced by addition of new particles.

Spray drying is a suitable technique for the preparation of oxygen carrier particles with high sphericity, high attrition resistance, good free-flowing properties and homogeneity on micro-scale. The mechanical strength of the final product can be tuned by different parameters such as sintering atmosphere, heating rate, temperature and different dwell time. All sintering treatments are done in air, and the two main parameters explored for selected compositions are time and temperature. After sintering, the particle size distribution was found to be within the specification of 100-200 μm, as verified using laser diffraction (Fig. 2).
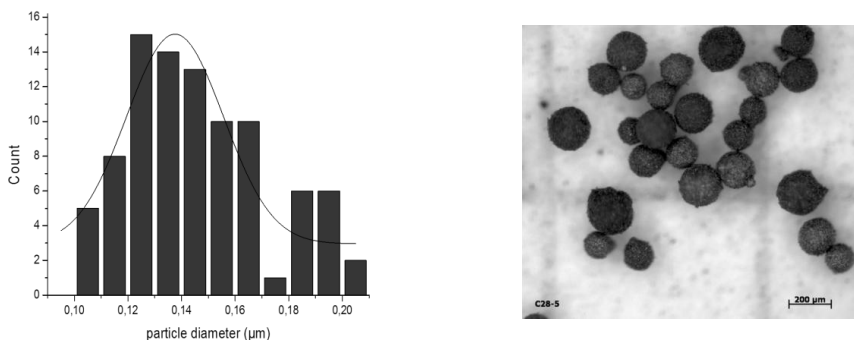
Fig. 3: left: particle size distribution for oxygen carriers after sintering,
right: optical microscopy picture of Mn-based oxygen carrier particles

Table 1 gives an overview of the effect of sintering temperature on crushing strength for selected compositions, measured using a Shimpo FGN-5 measurement device. Measurements using the Instron test bench (data not shown) verify the observed trends. The selected system of oxygen carriers shown in table 1 is designed to yield a perovskite structure, in this case with Ca and Mn as constituting elements ($ABO_{3-\delta}$, A=Ca, B=Mn). Some Fe was added to the composition for creating deficiencies by substitution in the structure. Such perovskite structures are known to show good performance for chemical looping combustion [2].

The results are presented in Table 1. Note that C=$Ca(OH)_2$, M=Mn_3O_4, F=Fe_2O_3. The number after an element is the weight percentage of the raw material in the synthesis recipe. The trend of increasing strength with sintering temperature is not linear, and dependent upon composition.

As shown in table 1, the increase in sintering temperature and sintering time can be used to increase the mechanical strength of oxygen carrier materials. There is however a trade-off with the particle reactivity (γ). The materials show a high methane conversion at 950°C as can been seen from table 1. The average methane yield is basically the extent to which the particles can convert the methane to CO_2 and H_2O. For the investigated materials the yield is between 87-98%, which is at least as good or better than Ni-based O-carriers [3]. Activity data could not be obtained for particles that showed to a low crushing strength to be tested in fluidized bed conditions. These experiments, which were carried out in a batch fluidized bed reactor, utilized an oxygen to fuel ratio of 57kg/MW. With respect to this bed inventory, the rates of reaction are very high, and are comparable to the baseline Ni-based oxygen carrier.

No problems related to defluidization and agglomeration were found during the reactivity testing. In summary, the calcium manganate based perovskite type material shows very promising results in terms of mechanical properties and performance for chemical looping [4,5].

865

Table 1. Crushing strength and activity data obtained on selected compositions

Sample	Sintering temperature (°C)	Crushing strength (N)	$\gamma(CH_4)$ at T=950°C
C49MF11	1100	0.40	-
	1200	0.97	0.98
	1300	1.38	0.92
C49MF5	1100	0.39	-
	1200	1.11	0.93
	1300	1.43	0.87

4. Conclusions

The fabrication of porous granules by spray-drying is a well established manufacture method for a wide range of products and industries, among others FCC catalysts. In this paper, it is shown that this manufacturing method is also highly suitable for the production of spherical oxygen carrier particles for chemical looping combustion, operated in coupled fluidized bed reactors.

Specifications such as bulk and particle density, mechanical strength, attrition resistance, particle size distribution and activity are defined by the overall manufacturing process of the oxygen carriers. By tuning specific process parameters, a wide range of different oxygen carriers were manufactured successfully. Adaptation of the sintering and sieving process led to the properties of the final product for application in coupled fluidized beds chemical looping combustion. This makes spray-drying a very well suited and flexible process for the production of oxygen carriers at the industrial scale.

5. Acknowledgements

6. References

[1] Nicolas Perrin, Richard Dubettier, Frederick Lockwood, Philippe Court, Jean-Pierre Tranier, Claire Bourhy-Weber, Michel Devaux, Energy Procedia, 37, (2013) 1389-1404;
[2] Magnus Rydén, Henrik Leion, Tobias Mattisson, Anders Lyngfelt, Applied Energy, 113, (2014) 1924-1932
[3] Erik Jerndal, Tobias Mattisson, Ivo Thijs, Frans Snijkers, Anders Lyngfelt, International Journal of Greenhouse Gas Control, 4, 1, (2010) 23-35.
[4] D. Jing, T. Mattisson, M. Ryden, P. Hallberg, A. Hedayati, J. Van Noyen, F. Snijkers, A. Lyngfelt, Ener. Proc. 37 (2013) 645-653.
[5] P. Hallberg, D. Jing, M. Ryden, T. Mattisson, A. Lyngfelt, Energy & Fuels 27 (2013) 1473-1481.

CHARACTERISATION OF MICROSTRUCTURE AND FORECASTING OF CREEP PROPERTIES OF ALLOYS IN740 AND IN617 FOR ULTRA-SUPERCRITICAL POWER PLANTS

S.F. Di Martino*, R.G. Faulkner*, S.C. Hogg*

[†] Corresponding author, Ph.D.; Tel. +44 01509 263171, Ext.: 4361; e-mail
S.F.Di-Martino@lboro.ac.uk
* Department of Materials, Loughborough University, LE11 3TU, UK

Abstract

Ni-base superalloys are prime candidate materials for long-term high temperature applications such as boilers in ultra-supercritical (USC) power plants, operating at temperatures and pressures as high as 750°C and 35 MPa. There is a transition required from their current application in aero engines, where there are shorter exposure times and higher operating temperatures. The investigation of their microstructural evolution as a function of thermal treatment and simulated service conditions out to longer times at forecasted service temperatures, coupled with modelling activities able to predict the microstructural evolution under these new conditions are undertaken to allow their development for long term exposures in power plants. The lack of widespread microstructural data for most commercial nickel base alloys makes this type of investigation even more important. In this study, the microstructural evolution of IN740 and IN617, two Ni-base candidate materials for USC applications, are thoroughly characterised by means of optical microscopy, hardness, field emission gun electron microscopy (FEGSEM), transmission electron microscopy (TEM), energy dispersive X-ray analysis (EDX) and electron back-scatter diffraction (EBSD) as a function of thermo-mechanical conditions. A method for phase identification can be confidently used to gather relevant information for modelling activity, such as: phase identity, volume fraction, size distribution, inter-particle spacing. The complete microstructural evolution of both alloys at temperatures ranging between of 650 and 750°C is investigated with a discussion of the phases encountered and their evolution, as well as their quantitative analysis. The data obtained are used both as input for and validation of a continuum damage mechanics (CDM) model for forecasting creep properties which has successfully been applied to 9 wt.%Cr ferritic steels.

Keywords: Ni-base alloys, ultra-supercritical power plants, microstructural evolution, creep, continuum damage mechanics

1. Introduction

New efficient advanced ultra-supercritical (USC) power plants are being developed in conjunction with carbon-capture technology. Ni base alloys are prime candidate materials for long-term, high temperature applications such as boilers, operating at temperatures and pressures as high as 750$^\mathrm{o}$C and 35 MPa. Such high temperature applications require research centered on high creep resistance. Forecasted requirements have set the targets to minimum creep strength of 100 MPa at 100000 h of service [1-3]. Since the microstructure of most of the candidate materials has not been investigated at such exposure periods of time, modelling activity is a useful aid in predicting the material response under simulated service conditions. The present investigation concentrates on two possible candidate materials, the high chromium Ni-base superalloys IN617 and IN740 [4-9], linking their microstructural evolution as a function of different thermo-mechanical treatment ranging between 650 and 750ºC, to the modelling activity which forecasts their creep behavior, comparing it to experimental data. The microstructural analysis, carried out by means of optical microscopy, field emission gun scanning electron microscopy (FEGSEM), field emission gun transmission electron microscopy (TEM), energy dispersive X-ray analysis (EDX) and electron backscatter diffraction (EBSD) , provides the characterisation of the microstructural constituents and the quantification of phase fractions, mean particle size and inter-particle spacing (IPS). The quantitative data obtained through the microstructural analyses serve as input and validation for the model's predictions. The model uses a continuum damage mechanics (CDM) approach which has been successfully used for the prediction of creep rupture properties of 9 wt.%-Cr ferritic steel [10] and which is now being adapted to the case of Ni-base superalloys systems.

2. Experimental procedure

2.1 Materials

The chemical compositions of the two alloys studied in this investigation are listed in table 1.

Table 1: Composition of IN617 and IN740 alloy investigated

Alloy	Chemical composition weight %												
	C	*Mn*	*Si*	*Al*	*Cr*	*Cu*	*Co*	*Mo*	*Fe*	*Ti*	*Nb+Ta*	*B*	*Ni*
IN740	0.03	0.3	0.5	0.9	25.0	--	20.0	0.5	0.7	1.8	2.0	--	*Bal*
IN617	0.05	--	--	0.08	20.0	--	10.0	8.0	--	--	--	--	*Bal*
	0.15	1.0	1.0	1.5	24.0	0.05	15.0	10.0	3.0	0.6	--	0.06	*Bal*

Table 2 summarises the thermal and thermo-mechanical treatments that the specimens underwent before investigation. The creep tests performed on alloy IN617 were not conducted to rupture. For phase quantification and modelling purposes, a fifth IN617 aged specimen was also investigated.

Table 2: Sample specifications

Specimen	Temperature (°C)	Load (MPa)	Time (h)
IN740			
AR	-	-	-
1	700	-	10000
2	750	-	3000
IN617			
AR	-	-	-
1	650	130	19299
2	700	110	20764
3	700	94	20168
4	750	68	16075
5	750	-	100

2.2 Investigation Procedure

Glyceregia (a mixture of glycerine, HCl and HNO$_3$) was used as reagent for etching IN740 samples and acetic glyceregia (a mixture of acetic acid, glycerine, HCl and HNO$_3$) was used for etching IN617 samples. A LEO 1530VP FEGSEM was used to image the sample surfaces. EDX was performed within the FEGSEM system using an Oxford Instruments X-Max 80mm^2 detector. EBSD analysis provided grain size and morphology. The system uses HKLNordlys F high speed Camera and Oxford Instrument Aztec EDX/EBSD microanalysis software for data collection. The grain size was also confirmed by using the mean linear intercept method. TEM thin foils of IN740 alloy were prepared by means of field ion beam (FIB) machine. A Nova 600 Nanolab Dual Beam

system was used for this task. The final thickness of the foil was in the 150-180nm range. A TEM JEOL 2000FX model was used to examine the microstructure and compare it with the findings obtained by means of FEGSEM. Bright field and dark field imaging, electron diffraction and EDX analysis were conducted for characterisation and the images were recorded by an integrated Gatan Erlangshen ES500W digital camera. Phase quantification, particle size and IPS analyses were carried out on all the samples investigated. The procedure has been explained in detail elsewhere [11].

3. Discussion

3.1 Microstructural analysis of alloy IN617 crept specimens and alloy IN740 aged specimens

The EBSD analysis showed a uniform grain structure which remained stable throughout the ageing treatments and creep tests. The calculated average grain sizes for each specimen are summarised in Table 3. The $\Sigma 3$ twin boundaries have not been included in the grain size analysis.

Table 3: Average grain size for the IN617 and IN740 specimens

Average grain size (µm)				
IN617				
sample AR	sample 1	sample 2	sample 3	sample 4
156 ± 36	137 ± 38	123 ± 31	176 ± 29	148 ± 28
IN740				
sample AR		sample 1		sample 2
69 ± 30		66 ± 28		72 ± 34

The phases precipitated in all the crept IN617 samples were: randomly distributed globular and blocky MX, $M_{23}C_6$ mainly decorating grain boundaries, M_6C mainly mixed with MX and $M_{23}C_6$; γ' (spheroidal) [6, 7, 13-18]. Furthermore, µ phase was identified in the samples exposed at temperatures equal or higher than 700ºC. As a representative result, Figure 1a shows the chemical analysis of a region of sample 3 which contains all the phases of interest. The γ' particles are too fine to be easily distinguished at this magnification, whilst all the other phases can be identified through both chemical and contrast information.

The investigation of microstructural evolution of IN740 as a function of ageing conditions has shown the following phases precipitated during exposure: a dispersion of γ' particles (cuboidal); large globular primary

MX; a population of $M_{23}C_6$ nucleated at GBs, twin boundaries, on MX particles and intra-granularly; a relatively small fraction of η precipitates, whose morphology becomes acicular only at 750°C, mainly nucleated on GBs and on MX particles; Si-rich G phase, partially mixed with $M_{23}C_6$ precipitates, nucleating on MX, GBs and, to a less extent, intragranularly [4,5, 18-23].

The EDX analysis performed on sample 2 (see Figure 1b) shows representatively all the phases encountered in both aged samples. The main difference between the microstructure of sample 2 and sample 1 is the absence of acicular η phase in the latter.
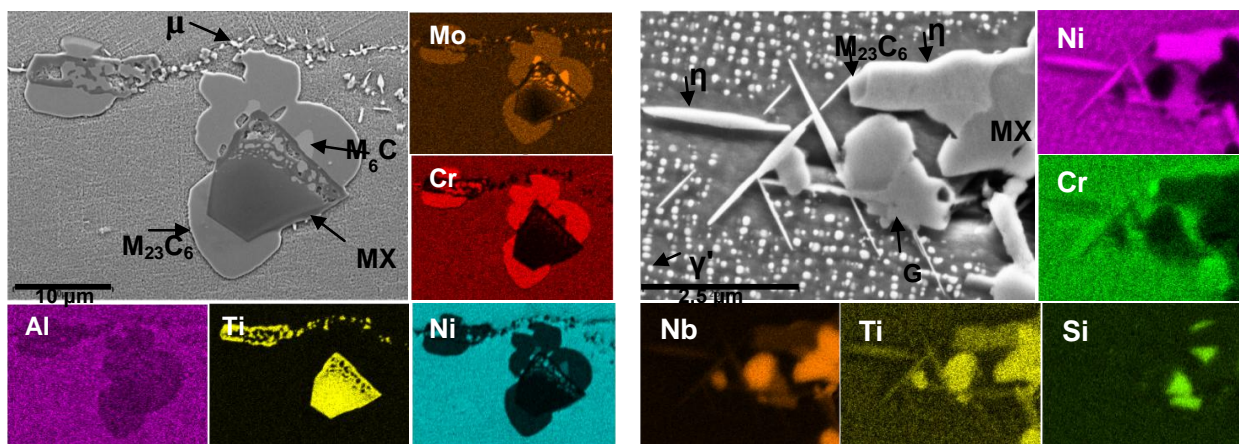
Figure 1a (left): EDX mapping analysis carried out on sample 3 where µ phase (bright contrast) is mixed with M_6C (Mo-rich with intermediate contrast), Cr-rich $M_{23}C_6$ and Ti-rich MX

Figure 1b (right): SE2 image and EDX mapping analysis carried out in IN740 sample 2 showing MX (Ti- and Nb-rich) precipitate evolving into η, G and $M_{23}C_6$, blocky and acicular η (Ni-rich), γ' (Ni-rich), G phase (Si- and Nb-rich), $M_{23}C_6$ (Cr-rich)

The microstructure of all the crept IN617 and aged IN740 specimens has also been quantified. For the purpose of this article, the IPS data for γ' and GB particles only will be listed. The complete set of results, including particle average size and phase fraction are shown elsewhere [11].

Table 4: IPS data for the IN617 and IN740 specimens;

IPS (µm)	IN740			IN617				
	AR	2	3	1	2	3	4	5
γ'	-	0.042 ± 0.005	0.7 ± 0.03	0.081 ± 0.01	0.2 ± 0.002	0.2 ± 0.002	0.43 ± 0.005	0.15 ± 0.01
GB Particles	-	0.101 ± 0.008	0.3 ± 0.02	0.19 ± 0.01	0.089 ± 0.007	0.03 ± 0.002	0.094 ± 0.007	0.29 ± 0.02

3.2 Continuum damage mechanics approach

3.2.1 Model Details

The modelling approach follows the reasoning of Dyson [12], adapted more specifically for high alloy ferritic steels by Yin and Faulkner [10]. The model, which has been adapted for the case of Ni-base alloys, is explained in detail elsewhere [11].

The general equation used to describe instantaneous creep rate, $\dot{\varepsilon}$, given as follows:

$$\dot{\varepsilon} = \frac{\dot{\varepsilon}_0}{(1-D_d)(1-D_s)} \sinh\left[\frac{\sigma(1-H)}{\sigma_0(1-D_P)(1-D_N)}\right]$$

Where $\dot{\varepsilon}_0$ is a temperature dependent constant defining the base level strain rate and σ_0 is a "composite" parameter containing several microstructural parameters [14]. σ is the applied stress. The four microstructural damage parameters are as follows: 1) D_d, a dislocation damage parameter; 2) D_s, a solute hardening parameter; 3) D_p, a precipitation hardening parameter, which is essentially related to the inter-particle spacing; 4) D_n, a cavity density term.

3.2.2 Application of the CDM model to alloy IN617

We have applied the CDM approach to both alloy IN740 and IN617. The results obtained for IN617 are presented here to representatively show how the model works. The solution hardening which is much more prevalent in the ferritic steels, like P92, has been neglected for the case of the nickel alloys. This has led us to using a minimal solute hardening damage parameter, Ds. D_n applies to the tertiary creep stage. Secondary creep is primarily controlled by slow evolution of the carbides and γ' phases through the process of coarsening, so that the mean inter-particle spacing increases with time. This parameter is inversely proportional to the strengthening effect of the particles, and so the precipitate evolution damage parameter, D_p, increases with time. We assume that primary

creep damage is almost instantaneous, and the hardening produced by the initial dislocation distribution leads to a maximum hardening parameter, D_d, from the beginning of the creep process. In summary D_d (at a maximum) and D_s (at a minimum) are constant throughout the creep life simulation for alloy IN617. The damage is primarily controlled by a particle coarsening based ramped D_p in secondary creep, and substantial increases in D_n in the later, tertiary stages of creep at 3% and 10% strain, caused by cavitation.

The strain at any instant in time, t, is therefore dependent on the particular combination of damage parameters for that time and strain, $t_{Dp,Dn,Dd,Ds}$. It is calculated from the following equation.

$$\varepsilon_{t\,Dp,Dn,DdDs} = \int_0^{t_{DpDnDdDs}} \dot\varepsilon\, dt = \dot\varepsilon\, t_{DpDnDdDs}$$

This method yields a slight over-estimate of the predicted strain, because it assumes that the damage parameters used have applied over the whole time involved. In fact, at shorter times, smaller damage parameters would have been in operation.

3.2.3 Results for alloy IN617

It is assumed that in this material at three temperatures, 750ºC, 850ºC, and 950ºC at stresses of 59, 54, and 46 MPa respectively there is zero solute hardening. 1-H is assumed to be 5 x 10^{-16}. D_n is assumed to be 0.95 at strains above 3%, and 0.99 above 10% strain.

At 750ºC D_p= 0.05 because at this low temperature and short time, precipitate coarsening will not have taken place. D_n and D_s =0.05 because there is no solute hardening as discussed above, and there is no tertiary stage for the times involved. For the relatively short times and low temperatures here, the primary damage accumulation will not have fully occurred, so D_d=0.95.

At 850ºC, D_p is ramped from 0.05 to 0.5 from 100 h to 1000 h, reflecting substantial coarsening gradually occurring over this time at the temperature concerned. D_n and Ds= 0.05 for the same reasons as discussed for 750ºC. Primary creep is complete after these times at higher temperatures than 750ºC and so D_d=0.99. At 950ºC the coarsening is complete after a few hours and so D_p is at a maximum of 0.5. D_s=0.05 and D_d=0.99 for the same reasons as are discussed for 850ºC. The curve is in tertiary creep after 100 hours and so D_n=0.05 for 100 h and, since the strain is between 3 and 10%, D_n is 0.9 for 200 h. The results are given in

Figure 3a and b. Fig. 3b shows results using real experimental data for Dp, taken from table 4. The gamma' IPS at 750C at sort times (100 h) is of 0.15 um (sample 5). After 16000 h the gamma' IPS is of 0.43 um (sample 4). This leads to a Dp value of approximately 0.67 after 16000 h. This in turn, gives an epsilon value of 6.5% at 16000 h as shown in Fig. 3b. Since the material was close to rupture after this time, we would expect the strain to be high at this point.
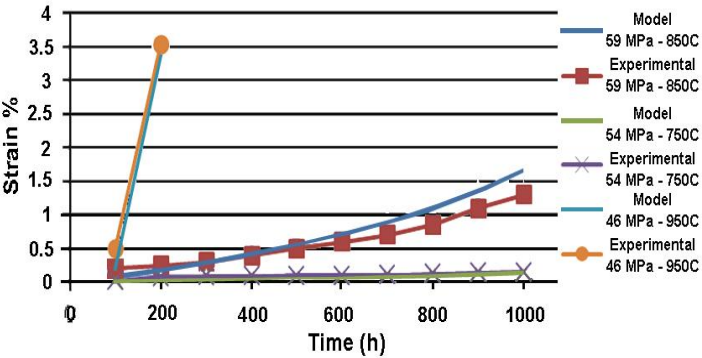
Figure 3a: Experimental (VTT data) and predicted creep curves for alloy 617 at 750, 850, and 950ºC, at 54, 59, and 46 MPa respectively
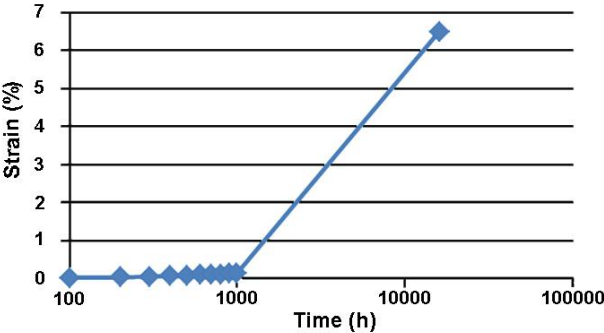
Figure 3b: Predicted creep curve for alloy 617 after 16000h at 750ºC using $D_p = 0.67$, based on experimental IPS data for γ' phase

4. Conclusions

The microstructures of Inconel 740 in the as-received and aged conditions and of Inconel 617 in the as-received and crept conditions have been characterised. The phases present have been identified and related to the

microstructural evolution of the two alloys. Inter-particle spacing analysis been carried out in all specimens, therefore providing data which have been used as input in a model forecasting the creep life of the alloys. The measured creep curves for alloy 617 agree well with predictions using a microstructural damage parameter based continuum damage mechanics approach.

Acknowledgements

REFERENCES

[1] Gibbons, T. B., "Superalloys in modern power generation applications", *Materials Science and Technology,* Vol. 25 (2009), pp. 129–135

[2] Viswanathan, R. *et al, "*U.S. Program on Materials Technology for Ultra-Supercritical Coal Power Plants", *Journal of Materials Engineering and Performance* Vol. 14 (2005), pp. 281–292

[3] Shingledecker, J. P., Swindeman, R. W., Wu, Q. & Vasudevan, V. K., "Creep Strength of High Temperature Alloys For Ultra-supercritical Steam Boilers", *4th EPRI Conference on Advances in Materials Technology for Fossil Power Plants,* 2007

[4] Evans, N. D., Maziasz, P. J., Swindeman, R. W. & Smith, G. D., "Microstructure and phase stability in INCONEL alloy 740 during creep", *Scripta* Materialia Vol. 51 (2004), pp. 503–507

[5] Shuangqun Zhao, Xishan Xie, Gaylord D. Smith, Shailesh J. Patel , "Research and Improvement on structure stability and corrosion resistance of nickel-base superalloy INCONEL alloy 740", *Materials & Design*, Vol. 27, Issue 10 (2006), pp. 1120-1127

[6] Gariboldi E., Cabibbo, M., Spigarelli, S. & Ripamonti, D., "Investigation on precipitation phenomena of Ni–22Cr–12Co–9Mo alloy aged and crept at high temperature", *International Journal of Pressure Vessels and Piping,* Vol. 85 (2008), 63–71

[7] Wu, Q., Song, H., Swindeman, R. W., Shingledecker, J. P. & Vasudevan, V. K., "Microstructure of Long-Term Aged IN617 Ni-Base Superalloy", *Metallurgical and Materials Transactions A,* Vol. 39 (2008), pp. 2569–2585

[8]   ZhaoS., Xie, X., Smith, G. D. & Patel, S. J. Research and Improvement on structure stability and corrosion resistance of nickel-base superalloy INCONEL alloy 740. *Materials & Design* **27**, 1120–1127 (2006)

[9]   Clark, D. E., Simpson, J. A., Totemeier, T. C. & Tian, H., *Microstructure And Strength Characteristics Of Alloy 617 Welds,* INL (2005)

[10] Yin Y.F., Faulkner R.G., "Continuum damage mechanics modelling based on simulation of microstructural evolution kinetics", *Materials Science and Technology,* Vol. 22, n. 8 (2006), pp.929-936

[11] Di Martino S.F., Faulkner R.G., Hogg S.C., "Characterisation of Microstructure and Creep Properties of Alloy IN740 for Ultra-Supercritical Power Plants", *Materials Science and Technology* (2014)

[12] Dyson B., "Use of CDM in marerials modelling and component creep life prediction", *Journal of Pressure Vessel Technology,* Vol. 122 (2000), pp. 281-296

[13] Ajit K. Roy, Muhammad H. Hasan, Joydeep Pal, "Creep deformation of Alloys 617 and 276 at 750-950^{0}C", *Materials Science and Engineering A",* Vol. 520 (2009), pp. 184-188

[14] Shah Hosseini H., Shamanian M., Kermanupar A., "Characterization of microstructures and mechanical properties of Inconel 617/310 stainless steel dissimilar welds", *Materials Characterization,*Vol. 62 (2011), pp. 425-431

[15] Rahman Md. S., Priyadarshan G., Raja K. S., Nesbitt C., Misra M., "Characterization of high temperature deformation behaviour of INCONEL 617", Mechanics of Materials, Vol. 41 (2009), pp. 261-270

[16] Chomette S., Gentzbittel J.-M., Viguier B., "Creep behaviour of as received, aged and cold worked INCONEL 617 at 850^{0}C and 950^{0}C", *Journal of Nuclear Materials,* Vol. 339 (2010), pp. 266-274

[17] Mankins W. L., Hosier J. C., Bassford T. H., "Microstructure and phase staibility of INCONEL alloy 617", *Metallurgical Transactions,* Vol. 5 (1974), pp. 2579-2590

[18] Mohammad A.-G., Mehdizadeh M., "Effect of long-term service exposure on microstructure and mechanical properties of alloy 617", *Materials and Design,* Vol. 32 (2011), pp. 2695-2700

[19] Evans N. D., Maziasz P.J., Swindeman R.W., Smith G.D., "Microstructure and phase stability in INCONEL alloy 740 during creep", *Scripta Materalia,* Vol. 51 (2004), pp. 503-507

[20] Shingledecker J.P., Evans N. D., Pharr G. M., "Influences of composition and grain size on creep-rupture behaviour of Inconel alloy 740", *Materials Science and Engineering A,* Vol. 578 (2013), pp. 277-286

[21] Zhao S., Xie X., Smith D.G., Patel S. J., "Research and improvement on structure stability and corrosion resistance of nickel-base superalloy

INCONEL alloy 740", *Materials and Design,* Vol. 27 (2006), pp. 1120-1127

[22] Cowen C.J., Danielson P. E., Jablonski, P. D., "The microstructural evolution of Inconel alloy 740 during solution treatment, aging, ans Exposure at 760^0C", *Journal of Materials Engineering and Performance,* Vol. 20 (2011), pp. 1078-1083

[23] Oh J.-H., Choi I.-C., Kim Y.-J., Yoo B.-G., Jang J.-I., "Variations in overall- and phase-hardness of a new Ni-based superalloy during isothermal ageing", *Materials Science and Engineering A,* Vol. 528 (2011), pp. 6121-6127

INFLUENCE OF TEMPERATURE AND SURFACE TREATMENT ON STEAMSIDE OXIDATION

Satu Tuurna[1], Sanni Yli-Olli[1], Pertti Auerkari[1], Edgardo Coda Zabetta[2], Kyösti Vänskä[2]

[1]VTT Technical Research Centre of Finland, Espoo Finland; firstname.surname@vtt.fi
[2]Foster Wheeler Energia Oy, Varkaus Finland; firstname.surname@fwfin.fwc.com

Abstract

Steam oxidation has become an important issue for steam power plants as operating temperatures increase from current to 650°C and even higher. Apart from the chemical composition of the material, surface condition is a major factor affecting the oxidation resistance in steam and supercritical water. In this paper, stainless boiler steels (UNS S34710, UNS S31035) are investigated in elevated steam oxidation conditions. Tests were conducted in a supercritical water autoclave environment (250 bar, with 125 ppb dissolved oxygen and a pH of 7) at 625°C, 650°C and 675°C up to 1000 h. Materials were tested with different surface finishes shot peened, milled and spark eroded. The results show an influence of surface finish on the early stages of oxidation. Oxides formed on more rough surfaces were more adherent, and thinner than on a ground surface. To that extent that the oxide formed on the milled, most cold worked, surface of UNS S34710 (Cr 18 wt-%) was thinner than on the spark eroded and ground surface of S31035 (Cr 22 wt-%). More variation on oxidation rate could be seen with increasing temperature.

Keywords: steamside oxidation, surface treatment, superheater

1. Introduction

The efficiency of conventional power plants is elevated by increasing steam temperature and pressure. High efficiency in power generation is not only desirable because of economical reasons but also for enhanced environmental performance meaning reduced quantity of forming ash and emitted pollutants. In modern medium to large size plants, improvements require supercritical steam values meaning increasing material temperatures. Increasing temperatures will promote the growth rate of nearly all damage mechanisms. The rate of steamside oxidation is promoted by increasing temperature that will also continuously increase with the growth of the insulating oxide layer, when an approximately constant heat flow is extracted through the heat transfer surfaces. The loss of load-bearing wall thickness and the temperature increase resulting from decreased heat transfer due to forming oxides may lead to creep failures. Spallation of oxides can cause tube blockages leading to possible creep failures due local overheating and steam flow disturbances, and erosion damage in the turbines [1-4].

Oxidation rate depends on many variables; service conditions, surface treatment, alloy composition and microstructure. The protective behaviour of austenitic stainless steels in steam depends on the rapid development of a continuous chromium rich oxide layer. Generally 16-18 wt-% of chromium is considered to be sufficient to form the protective oxide [4,5]. Cold work increases the dislocation density of the material surface, which increases diffusion rates at the affected zone [6,7]. Shot peening has been reported to have a beneficial influence on oxidation resistance of lower alloyed as well as austenitic boiler steels [1,8]. Similarly, it has been shown that a fine grain size is often beneficial due to the high density of grain boundaries leading to fast outward Cr transport along the substrate grain boundaries [9,10]. In this paper, the effect of surface finish and exposure temperature on the steam

oxidation of austenitic stainless steels grades S34710 and S31035 was studied in supercritical water environment. Materials were tested with different surface finishes, shot peened, milled and spark eroded.

2. Materials and Methods

The test coupons (5 x 15 x 25 mm) were machined from tube samples. To evaluate the impact of surface finish on oxidation, the following types of surface finish were tested: milled, spark eroded and ground (to 1200 grit) and shot peened. The milled and spark eroded and ground surfaces represent the two extreme surface conditions, one with no additional cold work and the other with a high quantity. The surface quality of an actual boiler tube fits somewhere in between. The specimens were exposed to supercritical water (625°C, 650°C and 675°C, 250 bar) in the autoclave environment with 125 ppb dissolved oxygen and a pH of 7. The autoclave system is described in detail in [11]. The testing times were up to 1000 h. Table 1 and 2 show the test materials and the test matrix.

Table 1: Test materials chemical compositions (weight %)

Alloy	C	Si	Mn	Cr	Ni	Co	W	Nb	Cu
S34710	0.09	0.36	1.40	18.3	11.4	-	-	0.86	-
S31035	0.06	0.18	0.51	22.4	25.4	1.44	3.37	0.49	3

Table 2: Test matrix (M-milled, S+G-spark eroded and ground, SP-shot peened)

Material	Surface	625°C	650°C	675°C
S31035	M	100h, 1000h	100h, 300h, 1000h	100h, 300h, 1000h
S31035	S + G	100h, 1000h		100h, 300h, 1000h
S34710	M	100h, 1000h	100h, 300h, 1000h	100h, 300h, 1000h
S34710	S + G	100h, 1000h		100h, 300h, 1000h
S34710	SP		1000h	1000h

After exposures, surface appearance, oxide thickness and microstructure were characterised by 3D profilometry, light optical microscopy (LOM) and scanning electron microscopy (SEM) after oxidation testing. The surface composition profiles were determined by glow discharge optical emission spectroscopy (GDOES).

3. Results

3.1. 3D surface profiles

Figure 1 presents 3D surface profiles of the different surface finishes of S34710 after 1000 h exposure at 675°C. The characteristics of the milled and shot peened surfaces are still clearly visible, thus the spark eroded and ground surface shows that formed oxide nodules have grown together and formed a continuous net on the surface.
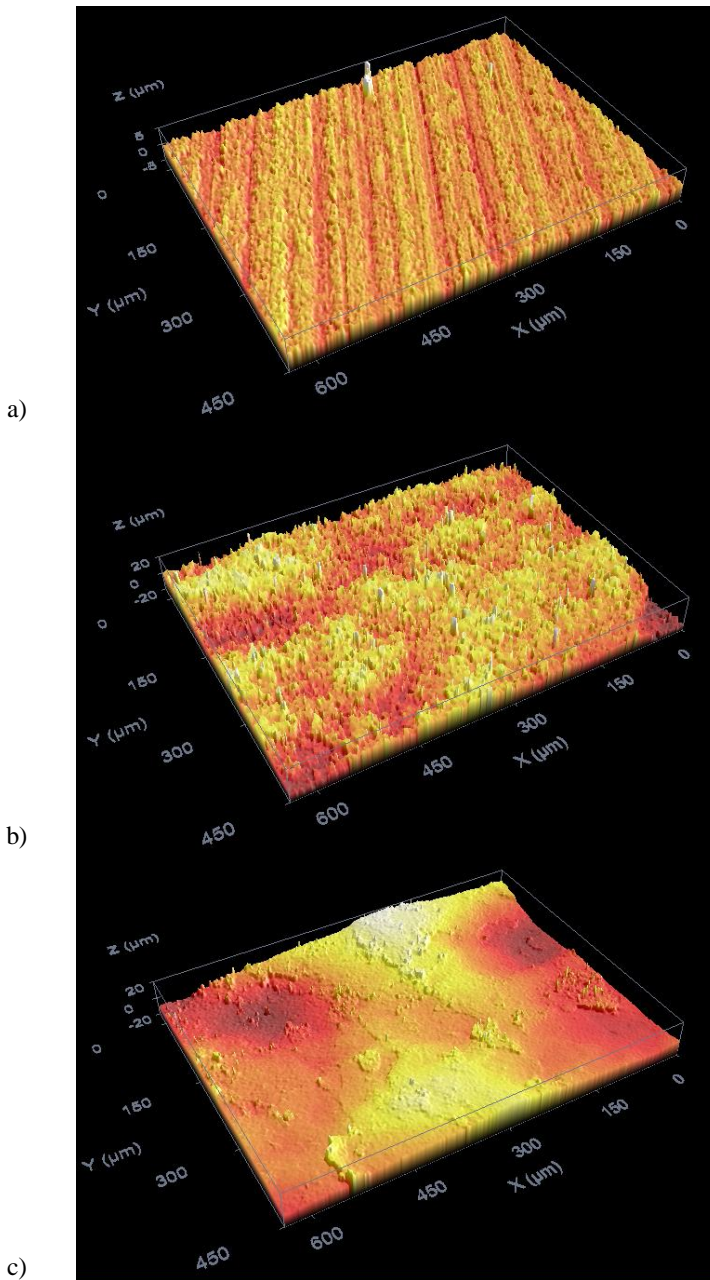
Figure 1: 3D surface profiles of a) the milled, b) the spark eroded and ground and c) the shot peened surface of S34710 after 1000 h exposure at 675°C. Note varying Z axis scaling to show oxide characteristics

Figure 2 presents the 3D surface profiles of the different surface finishes of S31035 after 1000 h exposure at 675°C. The characteristics of the milled surfaces are still clearly visible. The spark eroded and ground surface shows singular oxide nodules grown on the even surface.
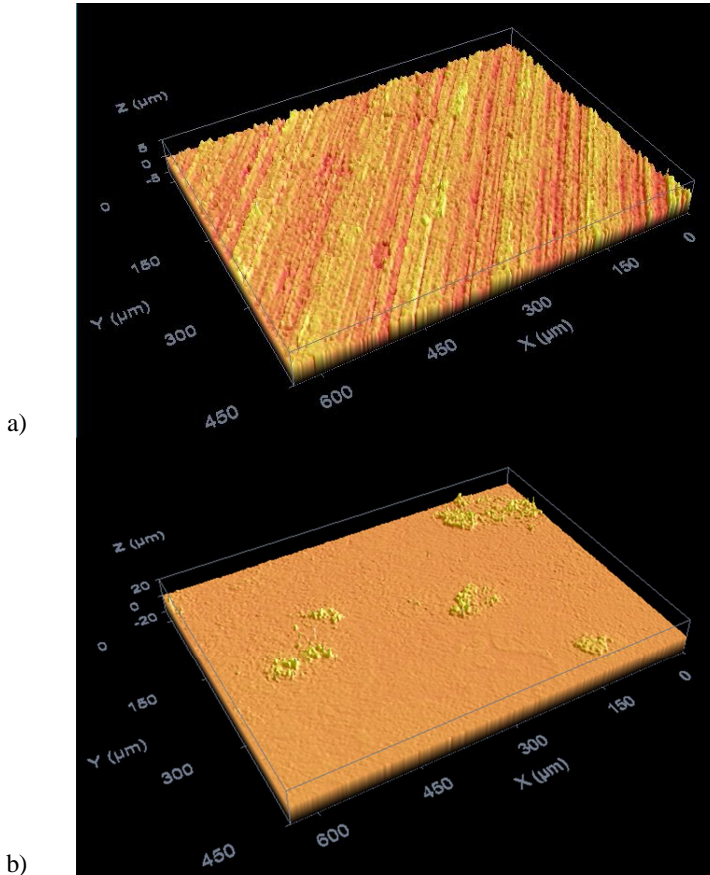
Figure 2: 3D surface profiles of a) the milled and b) the spark eroded and ground surface of S31035 after 1000 h exposure at 675°C. Note varying Z axis scaling to show oxide characteristics.

3.2. Surface cross-section studies with SEM

Figures 3 and 4 show the surface cross-sections of samples after 1000 h exposure at 675°C. Thin chromium rich oxides were formed on the milled and shot peened surfaces. Thicker oxide nodules with a layered structure were observed on spark eroded and ground surfaces. The nodular oxides composed of the outer iron rich oxide and inner chromium rich layers. Similar layered structure was observed in all test temperatures on the spark eroded and ground sample surfaces. With increasing test temperature the amount and thickness of oxide nodules increased, and after 1000 h at 675°C the scale covered most of the S34710 sample surface. Most of the S31035 sample surface was still covered with thin (~700 nm) Fe-Cr oxide with

some inward growing nodules, Figure 4b. Partial spallation of outer layers of thicker oxides formed on the spark eroded and ground surfaceswas observed in all test temperatures.

a)

b)

c)
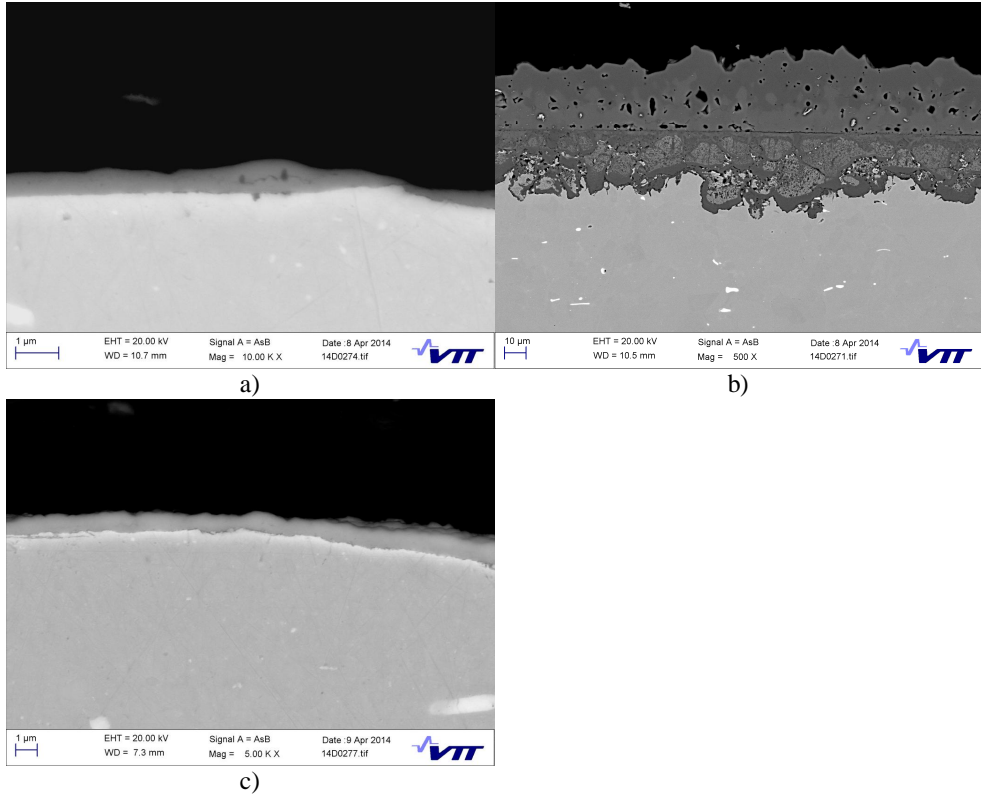
Figure 3: Oxides grown on a) the milled surface, b) the spark eroded and ground and c) shot peened surface of S34710 after 1000 h exposure at 675°C. Note varying magnification

a)

b)
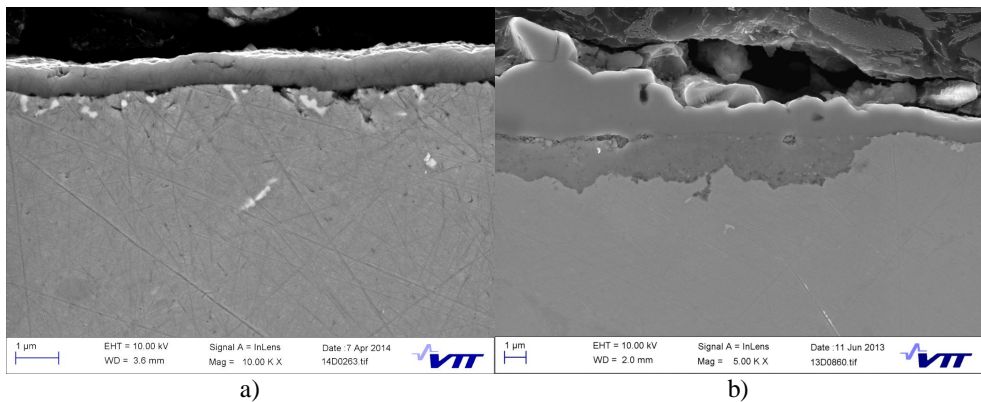
Figure 4: Oxides grown on a) the milled surface and b) the spark eroded and ground surface of S31035 after 1000 h exposure at 675°C. Note varying magnification

3.3. Oxide scale compositions

Figures 5 and 6 show the GDOES results for S34710 after 300 h at 625°C and 100 h at 675°C. The results show a chromium rich oxide formed on the milled surfaces, where as an iron oxide formed on the spark eroded and ground surfaces.

Figures 7 and 8 show the GDOES results for S31035 after 1000 h at 625°C and 675°C. The oxide on the milled surface was thin and chromium rich oxide on the top. The oxide on the spark eroded and ground surface had iron rich outer layer and chromium rich mixed oxide closer to metal.

a)   b)
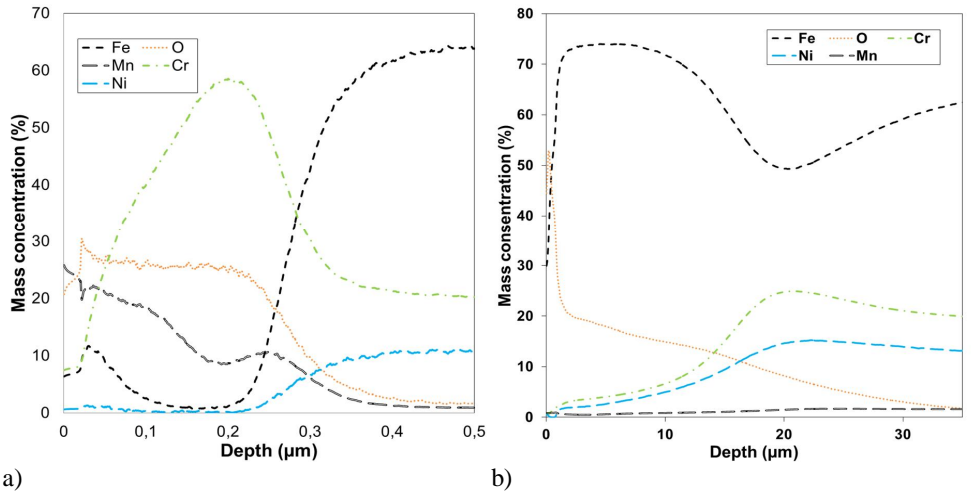
Figure 5: GDOES analysis of the oxide formed on a) the milled and b) the spark eroded and ground surface of S34710 after 300h at 625°C

a)   b)
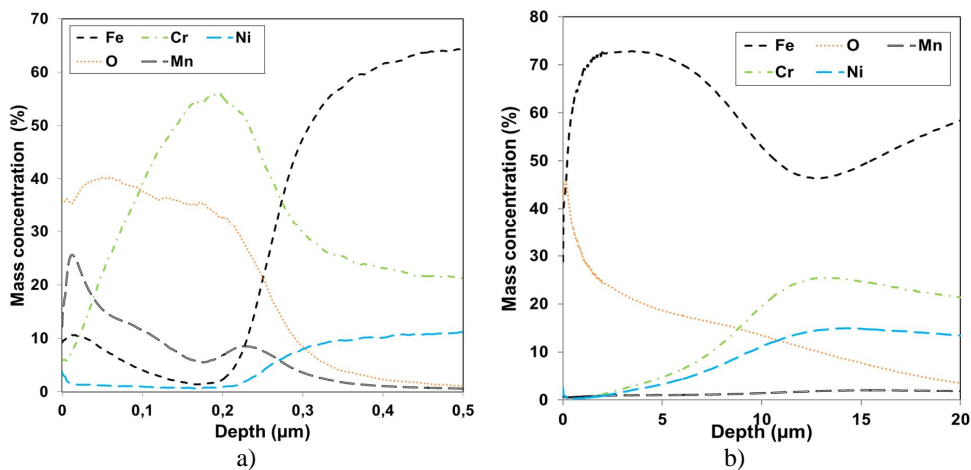
Figure 6: GDOES analysis of the oxide formed on a) the milled and b) the spark eroded and ground surface of S34710 after 100 h at 675°C

883
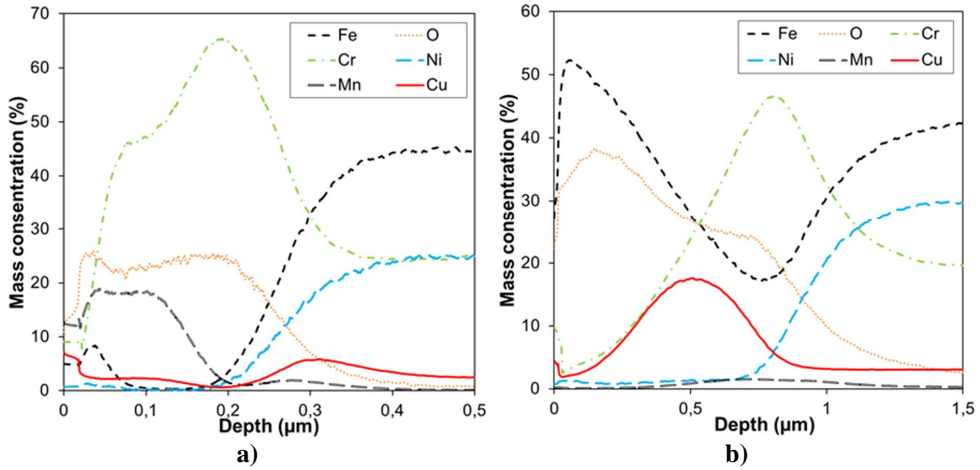
Figure 7: GDOES analysis of the oxide formed on a) the milled and b) the spark eroded and ground surface of S31035 after 1000 h at 625°C
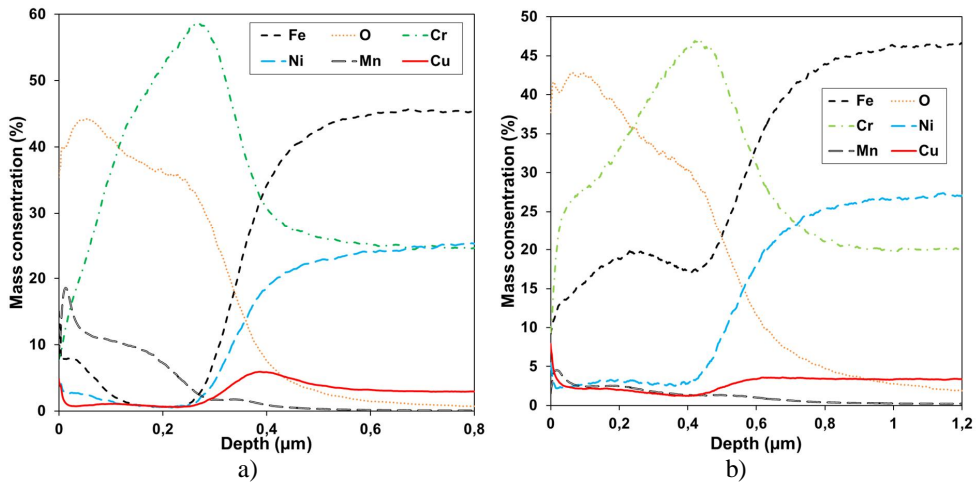
Figure 8: GDOES analysis of the oxide formed on a) the milled and b) the spark eroded and ground surface of S31035 after 1000 h at 675°C

3.4. Oxide thickness

Figure 9 shows an average inward grown oxide thickness of the tested materials, or in the cases of very thin oxides (< 1 µm) the whole oxide thickness. The results show that the milled surface retarded oxidation better than the spark eroded and ground surface. The shot peened S34710 located between the milled and spark eroded. The shot peened surfaces showed thin dense oxide growth, which did not seem to have temperature dependence in the range of 650°C to 675°C at least with used exposure times.
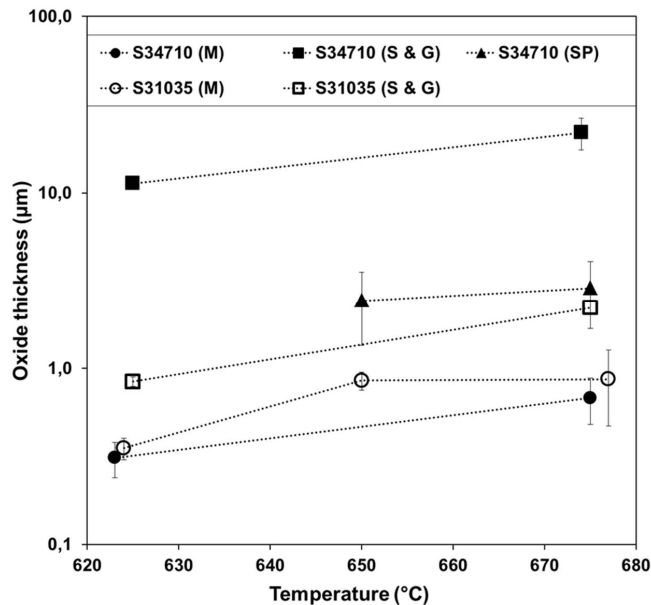
Figure 9: Average oxide thickness on the tested alloys (M-milled, S&G-spark eroded and ground, SP-shot peened) after 1000 h in SC water (250 bar), some data points have been slightly shifted horizontally for clarity

4. Discussion

As Figure 9 showed, in all cases the milled surface retarded oxidation better than the spark eroded and ground surface, and shot peened surfaces of S34710 showed thin dense oxide at 650°C and 675°C. On the spark eroded and ground samples S31035 showed clearly better oxidation resistance than S34710. The effect of temperature appears generally similar consistently for both materials and surface conditions. The impact of temperature to the resulting oxide thickness in the range of 625-675°C was clearly much less than that from the applied range of surface finish. It has been reported [12] that when going above 700°C the beneficial effect of cold work on oxidation resistance is lost, but as the results show at 675°C the positive effect is adequate at least for the test duration.

The effect of cold working on the forming oxide type was clearly seen. Iron rich oxide formation on the spark eroded and ground surfaces was seen already on the early stages of oxidation (100, 300 h) and accelerated oxidation rate can be predicted based on that. The temperature increase assists the formation of a protective oxide, which could be seen from the results of S31035. At 625°C iron rich scale was formed on the spark eroded and ground surface whereas at 675°C the oxide on S31035 alloy was chromium rich. With longer exposure times nodule formation starts when the protectiveness of the thin chromium oxide scale begins to disappear. Nodule formation is controlled by the outward and inward diffusion of metal and oxygen ions trough the oxide scale [4]. The tendency of oxide spallation in the

outer oxide layer was seen at locations with a two layer structure. Table 3 summarises the oxide formation after 1000 h exposures based on the GDOES and SEM inspections.

Table 3: Summary of the oxide formation on S34710 and S31035 after 1000 h exposure

Surface finish	625°C	650°C	675°C
S34710			
Milled	Thin (~300 nm) Cr + Mn rich oxide on top, Cr rich inside		Thin (~500 nm) Cr rich mixed oxide, traces of Fe oxide on top
S & G	Nodular, Fe-rich oxide on top, inner layers mixed Fe-Cr-Ni-oxides; Inward grown oxide depth[1] 30 µm. Some spallation observed.		Mainly uniform two layered oxide. Outer layer porous. Inward grown oxide depth[1] 30 µm. Some spallation observed.
Shot peened		Uniform thin oxide ~1.5 µm	Uniform thin oxide ~4.5 µm
S31035			
Milled	Thin (~400 nm) oxide, Cr- & Mn-rich on top	Thin (~400 nm) Cr rich scale, traces of Fe on top; some spallation of outer surface film	Thin (~350 nm) Cr rich mixed oxide, traces of Fe on top
S & G	Thin (~800 nm) layered oxide (outer Fe rich, inner Cr rich); some small nodules, inward depth[1] ~ 2 µm		Uniform thin (~700 nm) Fe-Cr mixed oxide; some small inward nodules, depth[1] ~3 µm

[1]Average maximum internal oxide thickness

5. Conclusions

The effect of surface treatment and exposure temperature on the oxidation performance of two austenitic stainless boiler steels (S34710 and S31035) in flowing supercritical water was studied. Testing was conducted in an autoclave environment (625-675°C, 250 bar, with 125 ppb dissolved oxygen and a pH of 7) for up to 1000 h, with three types of surface finish: shot peened, milled, and spark eroded and ground.

The results show a clear influence of the surface finish on the early stages of oxidation up to 1000 h. Oxides formed on strongly cold worked surfaces (milled or shot peened) were systematically much more adherent and thinner than on a spark eroded and ground surfaces. The oxide growth particularly on the spark eroded and ground surfaces was increasingly nodular and extensive with increasing time and temperature. More extensive oxidation was also seen with decreasing Cr content of the alloy, but this was also largely compensated by the cold work of milled or shot peened surface of S34710. Composition of the formed oxides indicates that the cold worked surface enables faster diffusion of chromium to the oxidising surface. Whereas on the surfaces with no addition diffusion paths iron oxidises first form a porous fast growing oxide.

The results indicate that the material surface condition can have a stronger influence than temperature (up to 675°C) or material composition (within the tested range) at the early stages on oxidation of austenitic boiler steels.

Acknowledgements

References

[1]   Sarver J.M., Tanzosh, J.M. Effect of temperature, alloy composition and surface treatment on the steamside oxidation / oxide exfoliation behavior of candidate A-USC boiler materials, *7th International Conference on Advances in Materials Technology for Fossil Power Plants*, October 22-25, 2013, Hawaii, USA.

[2]   Ennis, P.J., Quadakkers, W.J., Implications of steam oxidation for the service life of high-strength martensitic steel components in high-temperature plant, Pressure Vessels and Piping, Vol 84, pp. 82-87 (2007).

[3]   Lukaszewicz, M., Dudziak, T., Nicholls, J.R., Simms, N.J., Steam oxidation of superheater / reheater alloys: Impact of steam flow rates and specimen geometries, *EUROCORR 2011–Proceedings*, pp. 1788-1815 (2011).

[4]   Wright, I.G., Dooley, R.B. A review of the oxidation behaviour of structural alloys in steam, *International Materials Reviews*, Vol 55, pp. 129 – 167, (2010).

[5]   Young, D., High temperature oxidation and corrosion of metals, *Elsevier corrosion series* Vol. 1, UK, pp. 574 (2008).

[6]   Caplan, D., Effect of cold work on the oxidation of Fe-Cr alloys in water vapor at 600°C, *Corrosion Science*, Vol 6, pp. 509-512, (1966)

[7]   Khanna, A. S., Effect of cold work on the oxidation resistance of 2 ¼ Cr-1Mo steel, *Oxidation of metals*, 1985, Vol. 23, pp. 17-33

[8]   Naraparaju, R., Christ, H.-J., Renner, F.U., Kostka. A. Effect of Shot-peening on the oxidation behavior of boiler steels, *Oxidation of metals*, Vol. 76, pp. 233-245 (2011)

[9]   Ju-Heon Ki, Dong-Ik Kim, Satyam Suwas, Eric Fleury, Kyung-Woo Yi, Grain-Size Effects on the High-Temperature Oxidation of Modified 304 Austenitic Stainless Steel, Oxidation of Metals, Vol 79, pp. 239-247 (2013).

[10]   Trindade, V., Krupp, U., Hanjari, B., Yang, S., Christ, H.J. Effect of alloy grain size on the high-temperature oxidation behavior of the austenitic steel TP 347, *Materials Research,* Vol 8, pp. 371-375, (2005).

[11]   Toivonen, A. Penttilä, S. General corrosion and SCC tests on ODS steels in supercritical water, *Baltica IX. International Conference on Life Management and Maintenance for Power Plants*, Espoo, Finland, pp. 174 – 193, (2013).

[12]   Matsuo, H., Nishiyama, Y., Yamadera, Y., Steam oxidation property of fine-grain steels, Proceedings from the fourth international conference on advances in Materials Technology for Fossil Power Plants, South Carolina, USA, pp. 441-450, (2004).

BENCHMARKING OF CONVENTIONAL AND COMBINED CYCLE POWER PLANTS IN THE CYCLING REGIME
- *O&M TECHNICAL AND COST PERFORMANCE*

Authors: F Akther, S Hampson

fakther@etd-consulting.com

ETD Consulting, Fountain House, Cleeve Road, Leatherhead, Surrey KT22 7LX, UK

Abstract

The ongoing privatisation of the electricity industry worldwide, the ensuing market-driven competition and demand from shareholders for higher profits, as well as the overall increase in delivery of non-dispatchable renewable energy – have together resulted in an increasing requirement for electricity generators to have the ability to rapidly increase the supply of power on demand. This in turn, has lead to Conventional and Combined Cycle (CCGT) Power Plants being increasingly subjected to more varying modes of operation. Such modes of operation can result in new types and increased levels of damage, leading to loss of production, increased operation & maintenance (O&M) costs, increased forced outages, increased inspection frequency and in some cases reduction of plant life. No two plants are the same, and an understanding of the relative O&M technical and cost performance impacts due to cycling, with the intention of effective managing through improvements in operating, inspection and maintenance procedures is of vital importance - i.e. relatively small differences in costs and reliability can make a large difference in the station ranking.

This paper deals with the **technical & financial benchmarking** of conventional and CCGT plants in the cycling regime through statistical analysis, and assesses the relative impact of start-ups on a range of plant sizes and configurations. Much of the analysis is based on ETD's own work on North American, European and, to a lesser extent, Asian power plants.

Keywords: Benchmarking, Technical & financial, Cyclic operation, Planned & forced outage, Reliability.

1. Introduction

Benchmarking of power stations and other industrial plants is a very beneficial practice for plants trying to improve operation, maintenance, efficiency and other such factors and reduce costs. This can help the utilities to set targets for best achievable practices. The ongoing privatisation of the electricity industry the world over and the ensuing competition and demand by shareholders for higher profits, along with the increase of non-dispatchable renewable energy, has resulted in an increasing need to supply power on demand. As a result Conventional and Combined Cycle Gas Turbines (CCGTs) are increasingly being subjected to load following and/ or cyclic operation. However, cyclic operation can result in new damage types and thus in increased

inspection, repair and maintenance costs, as well as loss of production and penalties due to unplanned outages. Examination of the basic causes of these increased costs, with the intention of reducing them through improvements in operating, inspection and maintenance procedures is of vital importance. Relatively small differences in costs and reliability can make a large difference in the station ranking.

ETD has completed several projects which deal with operational and maintenance performance assessment of various conventional and CCGT plants in the cycling regime using a benchmarking methodology. The benchmarking study is conducted by carefully selecting a number of power plants (100 or more) from across Europe, North America and other countries for gathering data on their practices and then setting guidelines for best practices. The factors which make some plants more successful than others in terms of efficiency improvement and cost reduction have also been analysed to provide guidance for future planning and management. Benchmarking of power stations generally helps the utilities to know how their plants compare with other successful utilities in order to set achievable targets for significantly improving their plant performance and reducing costs.

It is clear that cyclic operation of power plant demands a closer understanding of the issues involved, better monitoring of the plant operation and behaviour of critical components, a strategy of component inspection and replacement and proper assessment of the costs involved. Assessment of the impact of cycling on the Operation & Maintenance (O&M) and cost performance of conventional and CCGT power plants was the most important aspect of this study. Major identifiable costs are envisaged to be due to component repair, replacement and plant overhauls. There are also other increased costs due to increased inspection, wear and tear, reduced unit efficiency due to component degradation and management complexity.

The assessed performance parameters in this project include: *Availability, Planned Maintenance, Forced Maintenance, Typology of Failures and Maintenance Costs*. During the course of this benchmarking project, the following tasks have been performed.

1. Operational, maintenance and costs data collection (questionnaire based) from project sponsors' individual plants and data review.
2. Selection of similar units from the ETD database for the benchmarking of various performance parameters, i.e. plant grouping.
3. Development of a performance model using statistical data analysis to determine upper and lower (range) levels of technical and financial performance from the database.
4. Superposition of the project sponsors' plant data onto the benchmarked data.
5. Analyse the performance and identify gaps (if any).

6. Identify the strengths and weaknesses of the plants in order to establish targets and provide recommendations for improvement in the performance (where and when necessary).

Performance Analysis
The performance analysis was classified into the following:

A. **Technical or Maintenance** performance which includes: Equivalent Forced Outage Factor (EFOF), Equivalent Planned Outage Factor (EPOF), Failure Typology (Failure Mechanisms) due to cyclic operation as a function of plant age and maintenance strategy in terms of Predictive (Pd), Preventative (PM) and Corrective (CM) Maintenance.

B. **Financial** performance which includes predicted annual maintenance O&M costs v. accumulated number of starts.

2. Data Base Grouping

The main task of the benchmarking study was to analyse several parameters that would help to select the most efficient plant in terms of operation, maintenance and cost. In order to attain reliable results, parameters involving all units and types of equipment from the power plant (e.g. steam turbines, gas turbines, conventional boilers, HRSGs, generators, transformers, auxiliary systems, etc.) are required to be analysed from a large number of power plants. Differences in plant design, age, size and components suggest that it is necessary to group the power plants in specific categories in order to be able to analyse and compare the performance of multiple plants at the same time.

One of the most important factors in a benchmarking statistical approach is the amount of data used to forecast maintenance and cost evolution. Based on ETD's past experience, it is clear that a minimum of 50-60 plants is normally required to obtain an acceptable amount of data to provide a reliable result [1].

The timeframe over which the data is available is also of much importance. Thus for a reliable benchmarking study it would be necessary to acquire a minimum of 7 years of operation & maintenance (O&M) data, since in some cases, especially for the newer plant, the impact of cycling does not appear to be immediate.

3. Considerations and Parameters for Benchmarking Methodology

There is now extensive experience of cyclic operation worldwide. Whilst there are potential risks and added wear and tear associated with two-shifting, with due care and application of sound

engineering and operational practices, economic two-shifting can be achieved with confidence. Economic two-shift operation requires that units are brought back on load and taken off load as quickly as possible [2]. This action has to be balanced against the obvious effects of induced thermal stresses which can result in costly plant failures.

Cyclic operation has become the most popular operating regime for old conventional plant and for new and old combined cycle plants. To analyse the impact of cyclic operation on O&M technical and costs performance, ETD has developed a methodology that allows collecting data from project sponsors' plants and inputting the data in a statistical model to generate O&M performance trends against the best practice benchmarked model. This helps with the comparing and understanding of the impact of cyclic operation on O&M costs and also on plant reliability and availability.

This section describes the parameters analysed, including the considerations made for the benchmarking study.

3.1. Modes of Operation

One of the first and principal steps of this study was to analyse the mode of operation since this is one of the most important parameters that helps to identify the real impact of plant operation in terms of thermal performance. Therefore, it is important to understand various cyclic operation regimes that have been considered for the benchmarking study.

Generally it should be recognised that "cyclic operation" or "cycling" is a wide-ranging term that covers the following or any combination of [3]:

- **Two-shifting** in which the plant is started up and shut down once a day (when the plant is started up and shut down twice a day it is considered as *Double two-shifting* which is a much less common form of cyclic operating regime).
- **Load-following** in which the plant is on for more than 48 hours at a time, but varies output as demand changes.
- **On-load cycling** in which, for example, the plant operates at base load during the day and then ramps down to minimum stable generation overnight.
- **Weekend shutdown** in which the plant shuts down at weekends. This is often combined with load-following and two-shifting**.**
- **Sporadic operation** for periods of less than two weeks followed by shutdown for more than several days.

"Two-shifting" is probably the most common form of cycling, indicating that a power plant is shut-down at night so that it only works over the period of the morning and afternoon shifts. As noted above, two-shifting also often implies, but not necessarily, that the plant will be shut-down from Friday night to Monday morning. Two-shifting is considered to be the most damaging form of cycling.

3.2 Equivalent Hot Starts

The study investigated the number of starts split in three types of start-ups - hot, warm and cold. The definitions in terms of time / component temperatures will vary from plant to plant. Often the definitions are driven by the declarations made to the grid company for times such as notice to synchronisation and start-up costs.

Starts are categorized as being hot, warm or cold, depending on the length of time that the unit has been offline and cooling before the start-up process begins. The amount of service life consumed by a stop/start cycle is a function of the range of temperature change, so the longer that a unit has been cooling from its operating temperature (for example, 540° C for a steam turbine), the more fatigue life is consumed when the next start-up cycle begins. The general approach adopted throughout the industry is that a **hot start** represents an overnight shutdown, or less than 8 hours offline (turbine metal temperatures >400°C); a **warm start** reflects a weekend shutdown of more than 8 hours and up to 48 hours (>200°C); and a **cold start** anything greater than 48 hours offline (<200°C) [4].

The accumulated number of starts is the parameter that measures the plant performance in terms of number of starts since the plant was first commissioned. Figure 3.1 shows an example of the number of accumulated starts per plant. The figure includes 20 conventional power plants arranged by type of fuel (solid fuel, fuel oil and gas).
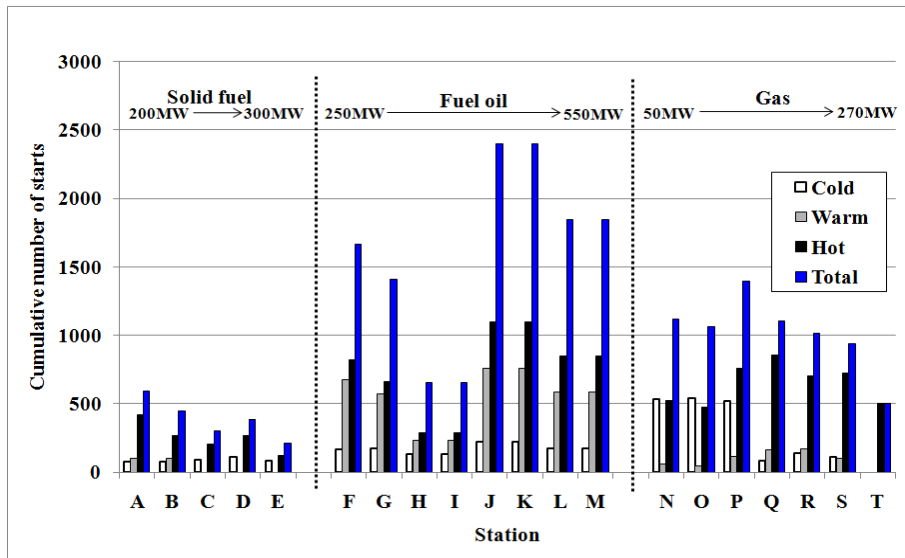
Figure 3.1: Cumulative number of starts for conventional power plants organised by type of fuel and plant size (20 plants)

Equivalent Hot Starts (EHS) have been calculated for conventional and CCGT plants to determine the impact of cycling on the plant performance and O&M costs. In terms of service life consumed by each type of start and its consequent cost, starting from a low temperature after a prolonged period offline is more damaging and therefore costly than starting after a few hours, when the metal components are still hot. The industry metric used to measure the performance and cost impact of each type of start is the Equivalent Hot Start (EHS), which ascribes a higher relative cost to warm and cold starts to reflect the additional damage caused. Different studies have reported varying cost impacts for each start category; however, ETD generally adopted the widely used ratio of 1:3:5 [Refs. 5, 6, 7] for hot, warm and cold start. Depending on how much care is taken over the various starts then the severity of the cold and warm starts can vary enormously, so the ratios could in reality be very different.

3.3 The Entire Life Cycle of a Plant

From the analysis, three distinct areas were identified for the entire life cycle of a power plant operating either in base load or cycling regime. These three areas characterise the different forced and planned outage levels, for the entire life cycle of the plant [6].

Commissioning period: This is identified to be approximately between the 1st to 6th years of operation.

Useful life period: This is considered to be the most important period for a plant since this is the period where the lower failure rate results in lower outages and where most of the generating profit is made. For a plant, this period is estimated to be located approximately between ~ 6 to 20 years of operational life.

Major component wear-out period: This period represents near the end of plant life, i.e. the period of time when the failure rate increases due to component life exhaustion. This period is identified to be approximately after 20 years of operation.

3.4 Equivalent Forced Outage Factor (EFOF)

Equivalent Forced Outage Factor (EFOF) is the fraction of a given operating period in which a plant or a unit *is not available due to forced outages*. This particular parameter is very useful in measuring forced outages in cycling power plants since it takes into account the derating hours. Furthermore, EFOF is also an important factor used during performance assessment, as it allows conducting a direct comparison with other similar generating units [9].

3.5 Equivalent Planned Outage Factor (EPOF)

Planned outages normally refer to the removal of a unit from service to perform work on specific components that is scheduled well in advance and has a predetermined duration such as annual overhaul, inspection, component testing etc. In general, increased routine maintenance is required due to increased levels of wear and tear when a plant moves from base load operation to cyclic mode [9]. Therefore, Equivalent Planned Outage Factor (EPOF) is useful to measure the planned outage performance which allows understanding of the impact of cycling on the plant availability.

ETD's analysis revealed that during the *commissioning period* the plant shows somewhat higher EFOF and EPOF values due to increased number of outages resulting from the installation problems. During the *useful life period* the EFOF and EPOF value starts to decrease and is at its lowest level between 10 to 20 years (for conventional plants) and 14 to 20 years (for CCGT plants) resulting from reduced number of installation problems and other related factors such as improvement of knowledge of operation, maturity of the technology, improvement of maintenance activities etc. During the *major component wear-out period* EFOF and EPOF values start to increase (assuming that the major components that are near or at end of life have not been replaced).

Some examples of ETD's previous studies on benchmarking analysis of the impact of cyclic operation on conventional and CCGT plants are provided in the following figures. Figure 3-2 represents the average EFOF values for the entire life cycle of CCGT plants operating in the cycling regime. Figures 3-3 and 3-4 represent the average EFOF and EPOF values v. EHS for conventional plants operating in the cycling regime.
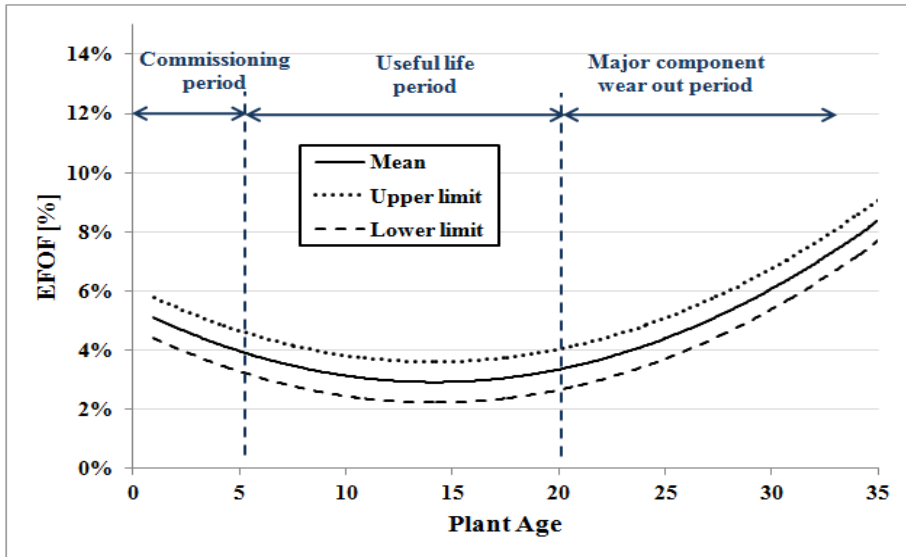
Figure 3-2: Life cycle EFOF v. Age for CCGT plants operating in the cycling regime
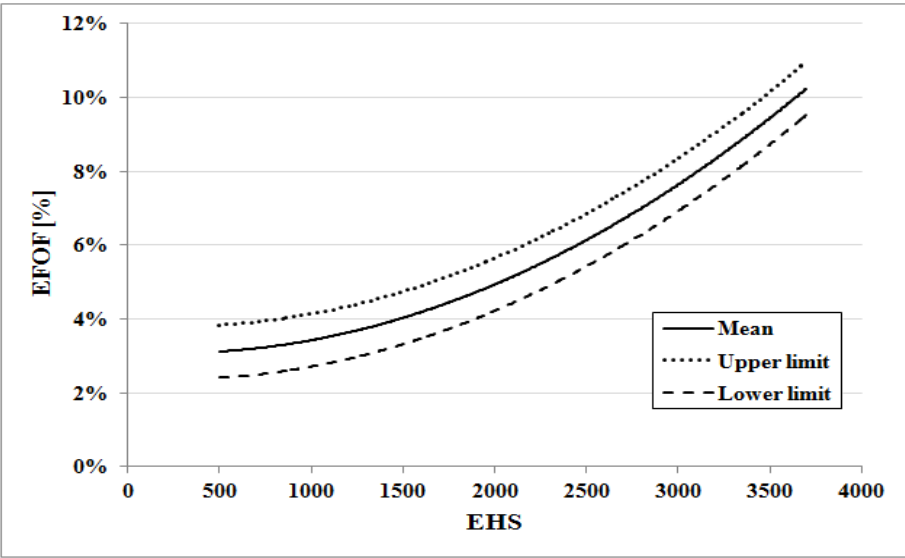
Figure 3-3: Average EFOF v. lifetime EHS for conventional plants operating in the cycling regime
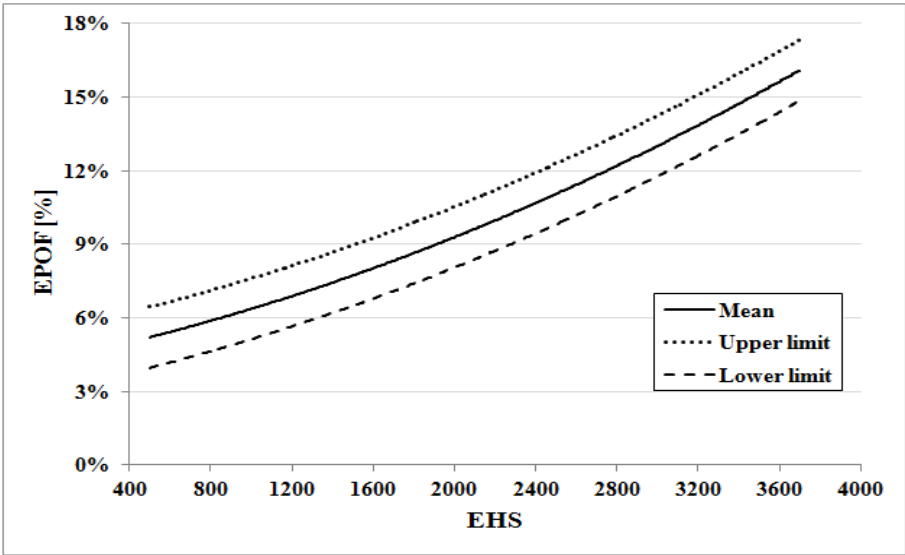
Figure 3-4: EPOF v. lifetime EHS for conventional plants operating in the cycling regime

3.6 Availability and Reliability

The *Availability* of a power plant is the percentage of time the plant is available to generate power in any given period.

The *Reliability* of a plant is the percentage of time between planned overhauls when it is available for service.

Availability and reliability have major impacts on the economics of plant operation. Reliability is essential in the sense that when the power is required the plant must be ready to generate instantly [9]. Planned outages are scheduled for non-peak periods. Peak periods are when the majority of the income is generated, as usually there are various tiers of pricing depending on the demand. Many power purchase agreements have clauses, which contain capacity payments, thus making plant availability critical in the economics of the plant.

4. Results of the Analysis

Studies carried out by ETD have shown that the older plant when subjected to cyclic operation exhibit new damage types at a relatively shorter time after the start of such operation compared with the newer plant. Thus the period over which significant increase in the inspection, repair, maintenance, modification and other related costs can appear may vary with the age (and size) of a plant.

The detailed analysis of the plant performance results shows that cyclic operation generates a considerable impact on the plant performance level. From the analysis, three distinct areas were identified for the entire life cycle of a power plant operating either base load or cycling regime and they form the classic 'bathtub' shape curve (typical of most plant equipment).

Analysis of Reliability (R) and Availability (A) revealed lower values during the earlier plant life and a steady increase from age 6 until age 20 years, achieving the maximum value possible between ~ 15 to 20 years of operating life. The A & R decrease abruptly during the later part of the plant life as the components of cycling conventional and CCGT plants will show an increase in failure rate and in downtime resulting in low Reliability and Availability.

Analysis of the breakdown frequency according to plant area (or component) revealed that the number of failures is generally higher in superheater tubes in boiler units for conventional plants and the highest levels in the GT section of CCGTs, with creep-fatigue being the dominant failure mechanism and the rotating blades of the hot gas path section having the highest frequency of failures within the GT in terms of critical components. The HRSG section with the highest

frequency of failures was the LP Economiser, and not unexpectedly FAC was the dominant culprit in terms of failure mechanisms. For the BoP the protection systems such as fire, lightning and breaker protection were the most frequent types of failure in CCGT plants in this study. A comparison between conventional and CCGT plants was also carried out which showed that the most frequent damage mechanism affecting plants operating in the cycling regime. According to the analysis, fatigue is the most damaging type of failure followed by wear and erosion in CCGT plants and corrosion-fatigue in conventional plants.

The *principal* damage mechanisms that could possibly affect the major components of HRSGs under cyclic operating conditions are summarised below [4]. This table includes the 'base-load' damage mechanisms, such as creep, that will be operative during the periods of steady state operation. Low cycle (thermal) fatigue damage to thick-section components (headers and drums) results from large through-wall temperature gradients during thermal transients. Most of the tube failures in cycling HRSGs are caused by low cycle fatigue (and creep-fatigue), flow assisted corrosion (FAC), corrosion-fatigue, corrosion pitting, and various forms of corrosion under deposits in the evaporators.

Component	Low Cycle Fatigue	Thermal Shock	Creep	FAC	Corrosion Fatigue	Deposits/ Corrosion	Oxidation/ Exfoliation	Gas-side Corrosion	Gas-side Erosion	Thermal Expansion
Superheater header	X	X	X							
Superheater tubes	X	X	X				X			
Reheater headers	X	X	X							
Reheater tubes	X	X	X				X			
Evaporator tubes	X			X	X	X		X		
Economiser headers	X	X		X	X	X				
Economiser tubes	X	X		X	X	X		X		
Drum	X	X		X	X	X				
Steam Piping	X	X	X							
Feed / connecting pipes	X			X	X					
Casing, liners, duct, etc	X	X	X					X	X	X

The cost analysis takes into account reported expenditure for each unit over a number of years to determine an annualized non-fuel O&M cost. Cost data were combined with each unit's historic operational data (online hours and unit starts) to develop a top-down statistical model of the O&M costs for a typical plant over its service life. The statistical relationship between Equivalent Hot Starts (EHS) and annual maintenance costs showed a positive correlation between the data. Also, the positive coefficient of the data trendline means that the upright bathtub curve is restored, conforming to the observation that O&M costs are usually higher in the early and late

stages of the unit's service life. Based on analysis of the units in this sample, therefore, it appears that the strongest indicator of annual O&M costs is the number of EHS that the unit has performed.

The example in the following figure (upright bathtub curve) represents the annual O&M costs v. EHS for the CCGT plants.
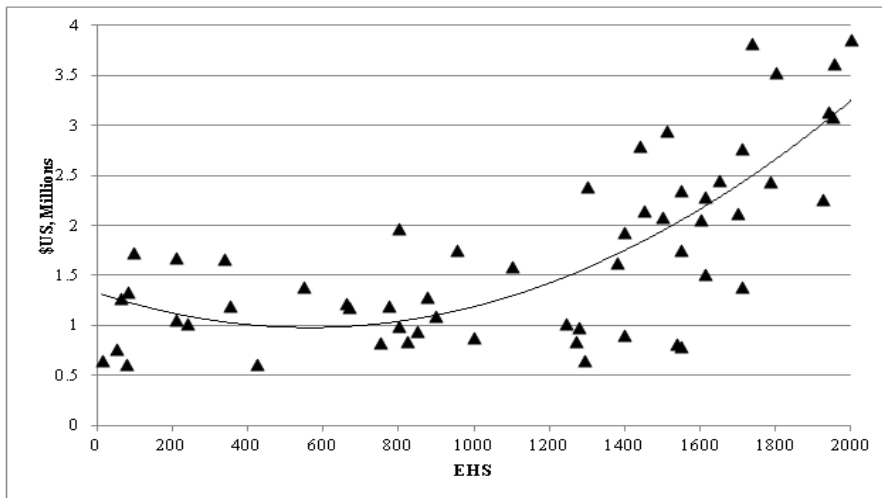
Figure 4-1: Annual O&M costs v. EHS for CCGT plants

5. Conclusions

Benchmarking of the plant helps to plan an appropriate maintenance programme. In order to minimize the economic impact due to cycling, it is crucial to create a maintenance plan with a well-balanced proactive maintenance, predictive maintenance and preventive maintenance through the plant life cycle. There are many excellent maintenance tools now available in the market and (if not already implemented) it would be extremely beneficial to conventional and CCGT plants to consider their implementation to achieve a well-balanced maintenance plan going forward.

A better damage/failure prediction methodology could help decision making during the planned outage which results in reduced forced outages; hence increase in the unit availability. Indeed ETD has developed its own Risk Based Maintenance (RBM) Procedure for power plants called 'Riskfit' and to date a number of plants (including some in the UK) have benefited from it. The

advantage is that with the predictive maintenance programme, costs can be reduced by reducing unnecessary inspection and maintenance.

6. References

[1] R. Taylor, Interpretation of the Correlation Coefficient: A Basic Review, *JDMS 1*, pp. 35-39, (February 1990).

[2] F. Starr, Potential Issues in the Cycling of Advanced Power Plants, *OMMI*. Vol.1, No.1, (April 2002).

[3] M. Jarvis and T. Raddings, Considerations for Alternative Configurations for Large Heavy Duty Industrial Combined Cycle Plant, *CCGT Plant Components- Development and Reliability, IMechE*, London, pp. 101-114, (1999).

[4] J. Ford, J. Fernandes, A. Shibli, Damage to Power Plant due to Cyclic Operation and Guidelines for Best Practices, *European Technology Development,* UK, Report no. 1096-gsp-81, (April 2009).

[5] Hoeft R., Janawitz J. and Keck R., Heavy-Duty Gas Turbine Operating and Maintenance Considerations, *GER-3620J*, pp. 19, (2003).

[6] A. Shibli, J. Gostling, and F. Starr, Damage to Power Plants Due to Cycling. Palo Alto, *CA: Electric Power Research Institute.* EPRI Tech. Report 1001507, pp. 6-11, (2001).

[7] J. Gostling, Private Communication, Central Electricity Generating Board (CEGB), (2013).

[8] E. Jeffs, Generating Power at High Efficiency – Combined Cycle Technology for Sustainable Energy Production, *Woodhead Publishing*, USA, (2008).

[9] IEEE Standard 762 – 2006.

[10] F. Fadipe, Maintenance Management of Gas Turbine Power Plant Systems, Lambert, USA, (2011).

[11] J. Fernandes, S. Simandjuntak, Operation & Maintenance Benchmarking Study: Technical and Cost, *European Technology Development*, UK, Report no. 1186-gsp135, (August 2011).

Materials issues for molten salt solar receivers

M. Spiegel and J. Mentz

Salzgitter Mannesmann Forschung GmbH, Ehinger Strasse 200,
47259 Duisburg, Germany, m.spiegel@du.szmf.de

Abstract

Solarthermic Power Plants (SPP) are an alternative energy source which uses concentrated sun-light for the production of steam which is converted to electrical power by a steam turbine. Especially tower receivers are most efficient in collecting sun radiation. However, a liquid medium is necessary to transport the heat to a heat exchanger and to store it overnight. According to the high heat capacity, molten nitrates are in use for the transport which occurs through thin walled metallic tubes. The requirements for the tube materials are reasonable resistance against thermo-cyclic fatigue at temperatures of 550 – 650 °C as well as an excellent stability in the presence of the molten salt. A selection of materials representing the classes of ferritic martensitic, austenitic and nickel alloys were exposed to a KNO_3-$NaNO_3$ eutectic mixture in air and nitrogen for 500 h at 600 °C in order to estimate the corrosion loss of the different classes of alloys and to evaluate the corrosion mechanisms.

Keywords: concentrated solar power, nitrate melts, oxidation, nitridation, hot corrosion

1. Introduction

The political requirement for enhanced usage of alternative power sources has driven the development of Solarthermic Power Plants (SPP) shown schematically in Figure 1 [1].
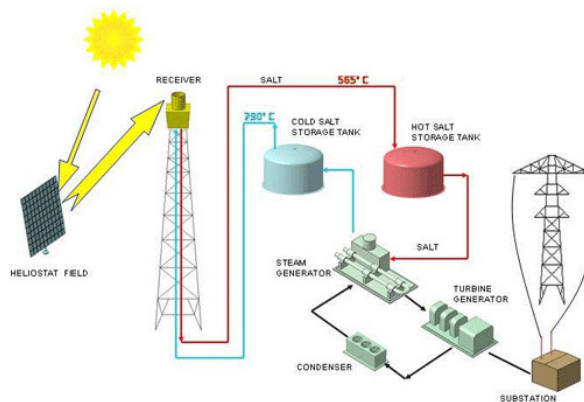
Figure 1: Schematic plot of a Solarthermic Power Plant, showing the heat loop, the salt storage tanks and the heat exchanger untits [1].

The SPP generates electricity with a steam turbine whereas the steam is generated in superheater tubes by heat produced by focused sun light instead of burning fossil fuel. The heat has to be transported from the central receiver units by a heat transfer medium to the steam turbines, however, due to the natural intensity changes of sun light, the heat has to be stored in tanks. Nowadays, the temperature of the heat storage medium is in the range of 550 – 600 °C. It is envisaged, to increase the temperature to 620 °C in order to increase the overall

efficiency of the plant and, therefore, lower their costs. An overview of the current technologies is given in [2]. Because of their high heat capacity, molten nitrates are the ideal heat transfer media with the additional advantage that they also can be used directly as the heat storage media over night and no additional storage medium is necessary as in the case of thermooil. This avoids additional heat losses. The main item by using molten nitrates is the stability of the transport tube and storage container material in contact with the molten salt. The stability of the nitrates used here has been calculated and stability diagrams are shown in figure 2 for $NaNO_3$ and figure 3 for KNO_3.
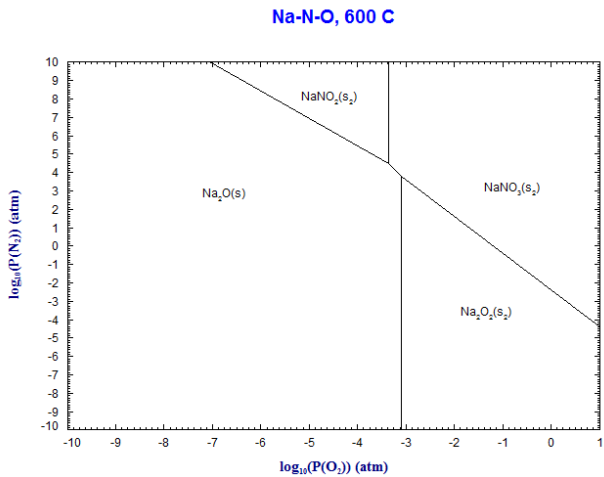
Figure 2: Stability diagram of the Na-N-O system at 600 °C. The nitrate is stable over a wide range of $p(O_2)$ and $p(N_2)$.
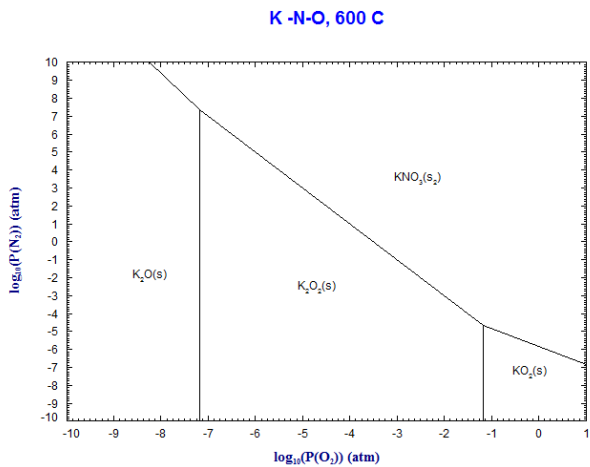
Figure 3: Stability diagram of the K-N-O system at 600 °C. The nitrate is stable over a wide range of $p(O_2)$ and $p(N_2)$.

The nitrates are stable over a wide range of $p(O_2)$ and $p(N_2)$, however, if $p(N_2)$ decreases significantly, the formation of oxide ions becomes possible. In general the stability of KNO_3 is higher than for $NaNO_3$. The nitrate melts are oxyanion melts and can, therefore, be classified as classical Lux-Flood bases, a concept which is known from sulfate melt, too [3]. The nitrate anion decomposes in the melt by giving:

$$NO_3^- = NO_2^- + \tfrac{1}{2} O_2(g) \quad (1)$$
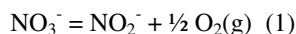
The concentration of the nitrite ion depends on $p(O_2)$ and temperature, as shown in figure 4 [4]. By decreasing the nitrogen content, the concentration of nitrite decreases. By increasing the temperature, the concentration of nitrite increases.
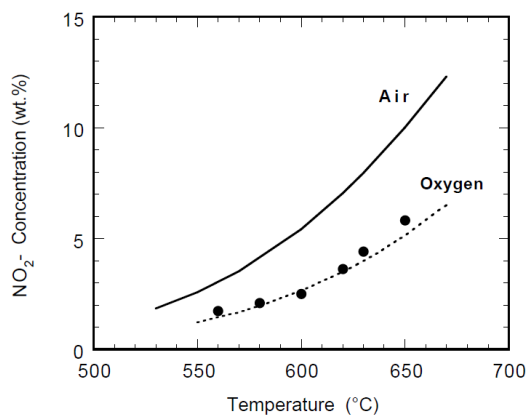
Figure 4: NO_2^- concentration in the nitrate melt as a function of temperature in oxygen and air. The concentration is higher in air than in oxygen [2].

If the temperature exceeds 600 °C the nitrate decomposes much faster and oxide ions are formed according to:

$$NO_3^- \text{ or } NO_2^- = O^{2-} + NO_x(g) \text{ or } N_2(g) \quad (2)$$
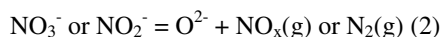
With this reaction, the basicity of the melt increases and nitridation may occur due to the formation of molecular nitrogen.
Corrosion studies beneath molten nitrates are rare in literature, however, most important papers can be found from US researchers, Figure 5 shows a plot about the corrosion rates of materials forming a duplex scale and a uniform chromia scale in steam, compared to corrosion in a molten $60\%Na_2SO_4\text{-}40\%K_2SO_4$ eutectic mixture. The corrosion rate is increased compared to uniform scales in steam and decreased compared to duplex scales in steam [4]. It was also found that increasing the chloride ion content of the salt leads to a increasing the corrosion rate of SS 304, figure 6. Studies were carried out on Fe-Cr-Ni alloys in molten NaNO3-KNO3 showing that basically austenitic stainless steels are quite stable up to 600 °C by the formation of a protective chromia layer showing parabolic growth rate. As 565 °C it

was also found that nickel-based alloy behaves quite well in contrast to low alloy steels with less than 9 % chromium. Silicon additions was beneficial for this materials.
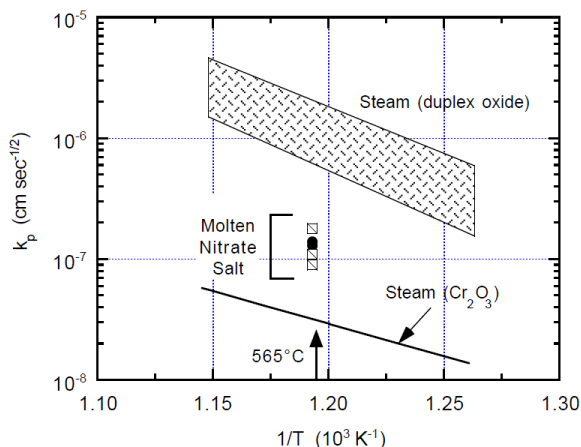
Figure 5: Parabolic rate constant of corrosion in steam for chromia scales and duplex scales compared to corrosion in molten nitrates as a function of temperature [3].
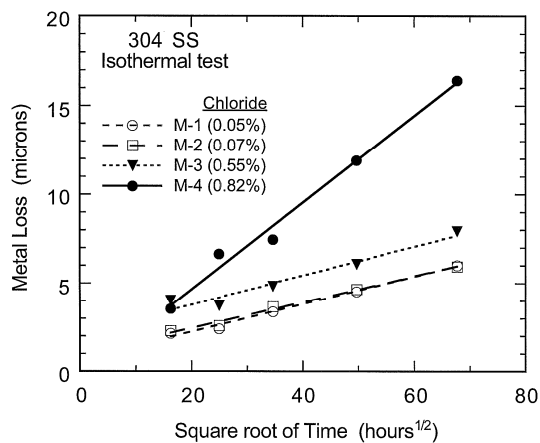
Figure 6: Influence of chloride ions in the molten nitrate on the corrosion rate on SS 304. As the chloride content increases, the corrosion rate increases [3]

The effect of thermal cycling was studied by the same authors. It was shown that thermal cycling increases the corrosion rate of stainless steels of about 25 %. The effect was found to be more pronounced if the melt contains more chloride ions [5].

2. Experimental

Samples of commercial alloys P 92, 310N, 304 HCu, Alloy 617 and C 263 (Table 1) were exposed in air and N_2, covered with 30mg/cm^2 of a binary eutectic mixture of 60%NaNO$_3$-40%KNO$_3$ for 500 h at 600 °C. After the experiments, the scale thickness was measured and sample analysis was performed by metallographic cross sections using Light Optical Microscopy (LOM), Scanning Electron Microscopy (SEM) with EDX and Electron Probe Micro Analysis (EPMA).

Table 1: Chemical composition of the materials used in this study.

	C	Si	Mn	Al	Cr	Fe	Ni	Mo	Ti	Nb	Co	N
617	0.05	0.08	0.06	1.3	22.1	1.9	53.1	8.7	0.40	<0.02	11.9	<0.01
C 263	0.05	0.10	0.17	0.57	20.8	0.48	49.8	5.8	2.05	<0.05	20.0	<0.01
310 N	0.06	0.75	2.0	-	24	Bal.	17	-	-	0.2	-	0.15
304	0.07	0.30	1.0	0.004	17	Bal.	7	-	-	0.45	-	0.05
P 92	0.07	0.5	0.43	0.04	8.7	Bal.	0.4	0.5	-	0.06	-	0.04

3. Results and Discussion

Figure 7 shows the results of scale thickness measurements after the experiment at 600 °C in air and nitrogen with 30mg/cm^2 of salt. The ferritic-martensitic steels P 92 exhibits the highest scale thickness in both atmospheres by forming an inner and an outer scale. The austenitic materials 310 N and 304 HCu are most stable in air and nitrogen. In N_2, they develop no separate inner layer. The nickel based alloys Alloy 617 show the lowest scale thickness in air, however, it is significantly increased in N_2, mainly due to the formation of an inner layer. The scale thickness of Alloy 263 is higher than of Alloy 617 and the austenitic materials. Also this alloy develops and outer and an inner scale.
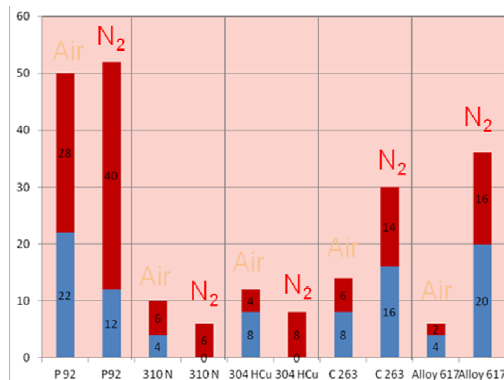
Figure 7: Scale thickness (blue:inner scale,red:outer scale) of commercial alloys in molten Na$_2$NO$_3$-K$_2$NO$_3$ at 600 °C after 500h of exposure in air resp. N_2 covered with 30mg/cm^2 with salt.

Scale analysis shows a thick oxide scale of about 50 µm thickness of porous iron oxide on P 92 in air with a low amount of chromium in the inner part next to the metal (Figure 8). The inner part is much more dense than the outer part. In N_2, the inner layer is much thinner, as the oxygen supply from the atmosphere is restricted
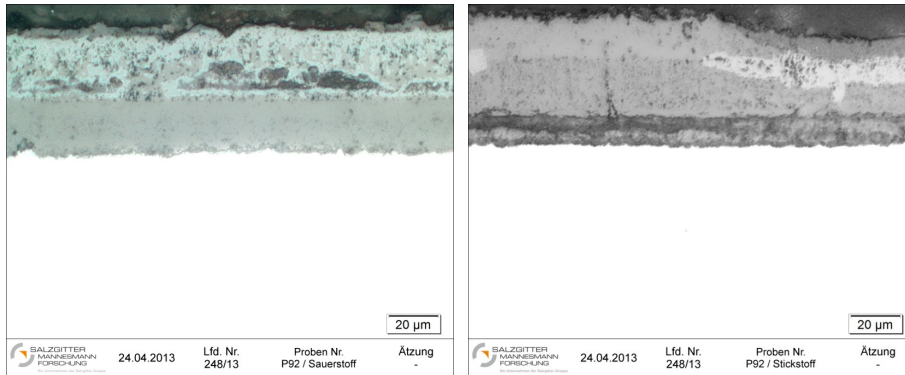
Figure 8: Metallographic cross section of the scale of P 92 after exposure in air (left) resp. N_2 (right) covered with 30mg/cm^2 salt.

The scale on the austenitic alloy 310 N is shown in Figure 9 in a LOM picture. The total scale thickness is around 10 µm in air and also some inward growing oxide is observed. By EDX analysis, a chromium rich scale was detected with increasing iron content from the metal/scale to the scale/melt interface. In N_2, no inward growing oxide scale has formed and the scale is much thinner,
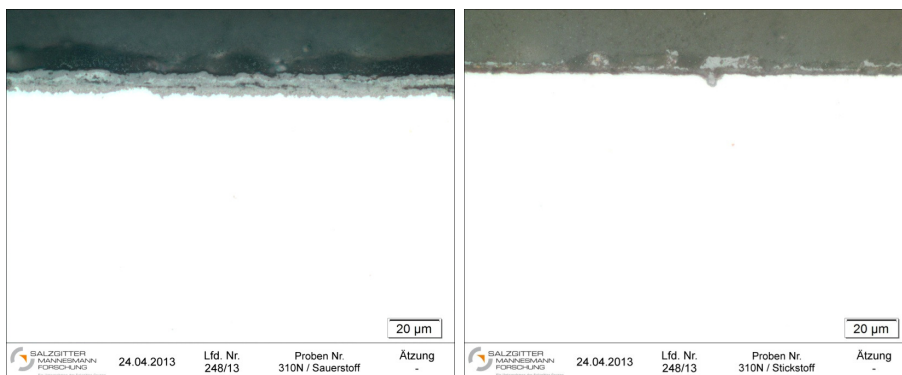
Figure 9: Metallographic cross section of the scale of 310 N after exposure in air (left) resp. N_2 (right) covered with 30mg/cm^2 salt.

Figure 10 shows a LOM picture of 304 HCu. This alloy has formed a thin scale of about 7 μm in thickness. The scale formed in air consists of an outer and an inner part, whereas the inner part is growing along grain boundaries. Like in the case of 310N, the inner part of the scale is rich in chromium and the iron content is increasing from the metal/scale to the scale/melt interface. In N_2, no inward oxide growth was observed.
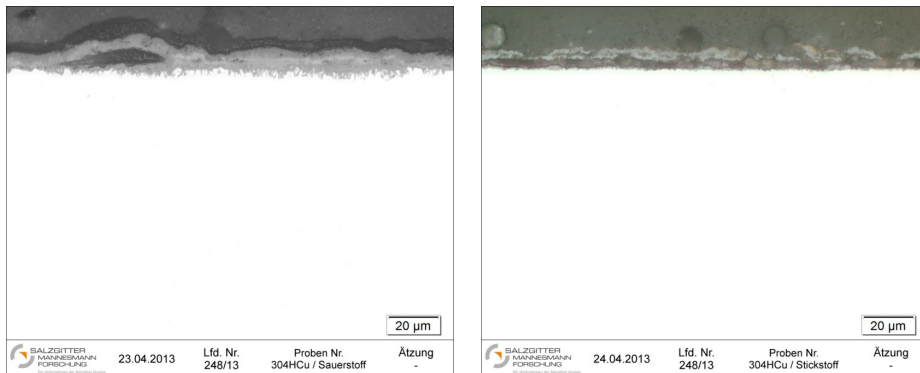
Figure 10: Metallographic cross section of the scale of 304HCu after exposure in air (left) resp. N_2 (right) covered with 30mg/cm^2 salt.
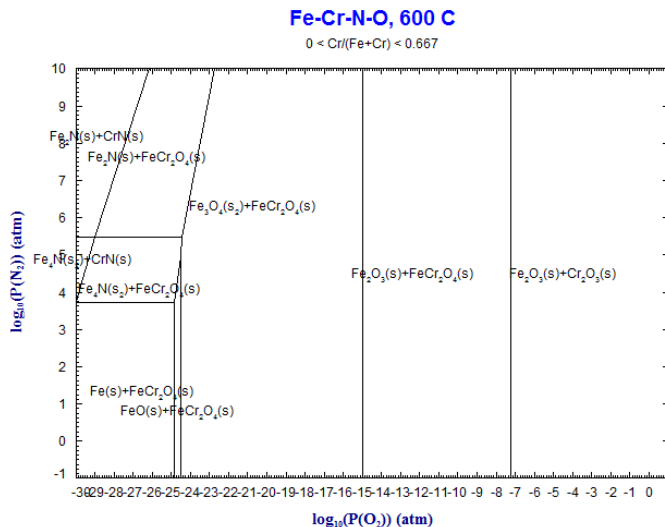
Figure 11: Stability diagramm of the Fe-Cr-N-O system at 600 °C. At reduced p(O$_2$), nitrides become stable in comparison to oxides

The situation for the ferritic-martensitic and also the austenitic alloys can be described with the thermodynamic stability diagram of the Fe-Cr-N-O system shown in figure 11. At high $p(O_2)$, corundum like oxides Fe_2O_3 and Cr_2O_3 are formed, with decreasing oxygen potential, spinel becomes more stable and if the oxygen potential decreases further, nitrides may be possible to form. It is interesting to note that the inner scale thickness decreases in N_2, which may have kinetic reasons as the oxygen supply is rather low.

Figure 12 shows a LOM picture of Alloy 617. A thin dual scale has formed in air, whereas the inner scale is thicker than the outer one. In N_2, the inner scale has grown significantly, by pushing out metal to the surface. This scale is rich in chromium and CrN could be detected.
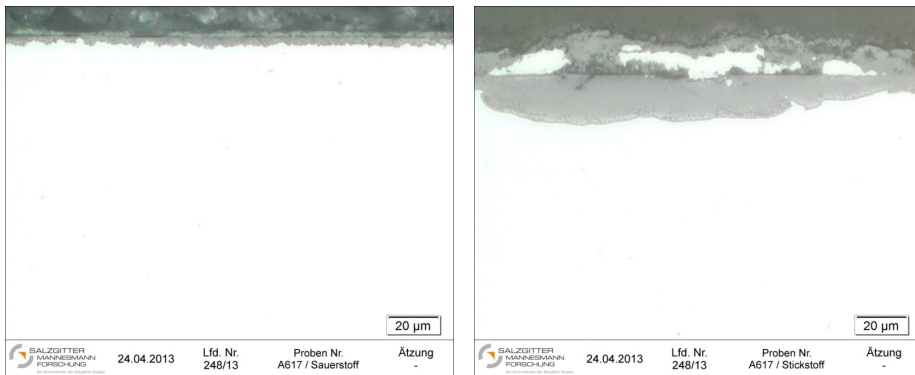
Figure 12: Metallographic cross section of the scale of Alloy 617 after exposure in air (left) resp. N₂ (right) covered with 30mg/cm² salt.

Alloy C 263 shows significant scale formation even in air (Figure 13). The major part of the scale is growing inward, whereas only a small part is an outward growing oxide. The inner part is rich in chromium, nickel and molybdenum with only small amounts of cobalt. In N_2, the inner part is much thicker than in air and in this case metal is pushed out from the matrix.
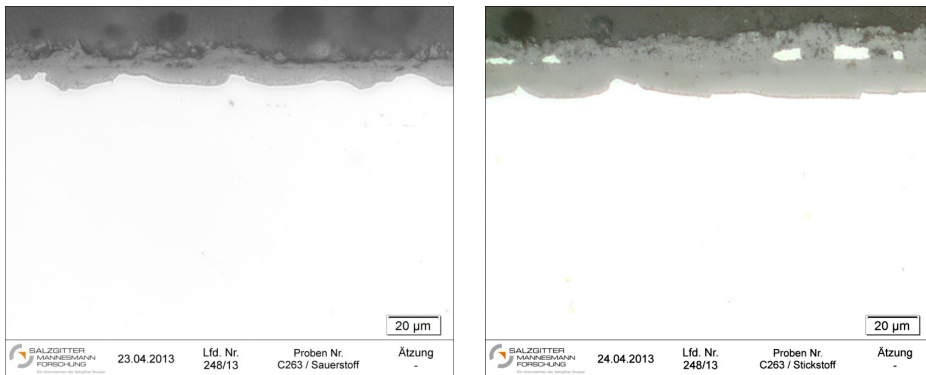
Figure 13: Metallographic cross section of the scale of Alloy C 263 after exposure in air (left) resp. N₂ (right) covered with 30mg/cm² salt.

908

Figure 14 shows the thermodynamic stability diagram for the nickel-based alloys. At high $p(O_2)$ NiO and spinel are stable. With increasing partial pressure of oxygen, chromia is formed and CrN becomes more stable in comparison to oxides.
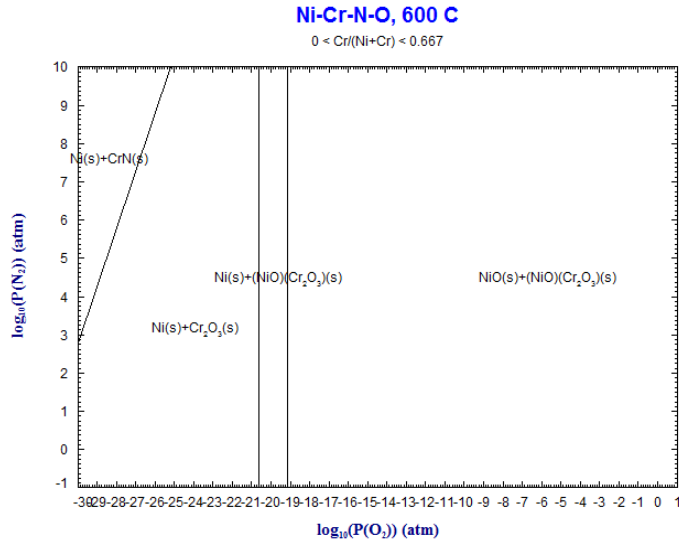
Figure 14: Stability diagramm of the Ni-Cr-N-O system at 600 °C. At reduced $p(O_2)$, chromium nitrides become stable in comparison to oxides

4. Summary

Samples of commercial alloys P 92, 310N, 304 HCu, Alloy 617 and C 263 (Table 1) were exposed in air and N_2, covered with 30mg/cm^2 of a binary eutectic mixture of 60%NaNO$_3$-40%KNO$_3$ for 500 h at 600 °C. After the experiments, the scale thickness was measured and sample analysis was performed by metallographic cross sections using Light Optical Microscopy (LOM), Scanning Electron Microscopy (SEM) with EDX and Electron Probe Micro Analysis (EPMA).

Ferritic martensitc materials (P 92) show the formation of a thick scale compared to the austenitic material (304 HCu and 310 N). The formation of an inner scale is more pronounced in air than in N_2 due to the lower oxygen concentration. The nickel-based alloys show different behavior. The inner scale is much thicker in N_2 and metallic protusions are included in the outer scale. This is due to the detrimental nitride formation. In general, austenitic materials seems to be more suitable for oxidation/nitridation in solar applications beneath molten KNO$_3$-NaNO$_3$ eutectic mixture at 600 °C than ferritic-martensitic materials and nickel-based alloys. Other properties like thermal expansion have to be proven and must be considered critically. Figure 15 shows the main features of scale formation for the different alloys.

Figure 15: Summary of scale formation of alloys investigated in this work, air (left) nitrogen (right)

References
[1] Deutsches Zentrum für Luft und Raumfahrt (DLR), Köln, Germany
[2] EASAC policy report 16, Concentrating solar power, **(2011)**
[3] H. Lux: Z. Elektrochem. Angew. Phys. Chem.**(1939)**, *45*, 303
[4] R.W. Bradshaw, S.H. Woods: Sandia Report, SAND2000-8727, **(2001)**
[5] R.W. Bradshaw, S.H. Woods: Sandia Report, SAND2001-8518, **(2001)**

MICROSTRUCTURE EVOLUTION OF NI-BASED ALLOYS IN617 IN740 NIM263 FOR POWER PLANT APPLICATIONS

Oriana Tassa [1, a], Susanna Matera[1b,], Fabio Di Martino [2c]; Joanna Zurek [3d]

[1]Centro Sviluppo Materiali, Via di Castel Romano 100-102, 00128 Castel Romano, Italy

[2]Loughborough University, Leicestershire LE11 3TU, Loughborough, United Kingdom

[3]Forschungszentrum Jülich, Wilhelm Johnen Strasse, 52425 Jülich, Germany

[a]o.tassa@c-s-m.it; [b]s.matera@c-s-m.it; [c] s.f.di-martino@lboro.ac.uk; [d]j.zurek@fz-juelich.de

Abstract

Ni-based alloys with high creep strength and oxidation resistance are candidates for applications in superheater tubes in Advanced Ultra-Supercritical (AUSC) coal fired power plants operating at 700/720°C. The use of this materials requires a deep investigation and understanding of the degradation mechanisms due to temperature/time/environment conditions. In this work the microstructural evolution of IN617, IN740 and C263 Ni alloys has been investigated after exposure in test loops as well as isothermal laboratory ageing treatments. The investigations have been performed in the framework of the ECSC project MACPLUS. They were carried out by means of Light Microscopy, Hardness Tests, Scanning Electron Microscopy (SEM), Transmission Electron Microscopy (TEM) equipped with Energy Dispersive Spectroscopy (EDS) combined with Selected Area Diffraction (SAD). Hardness measurements have been performed and related to precipitate status evolution. Primary MX ((Nb;Ti)(C,N)) are observed in all the materials. γ' ((Ni,Co(Nb))$_3$(Ti,Al)) phase is uniformly distributed within grains in all the samples, with near spherical morphology in IN617 and NIM263 and cubic in IN740. Coarsening of $M_{23}C_6$ (($Cr,(Mo))_{23}C_6$) precipitates located at grain/twin boundaries and within grains is observed in all the investigated alloys after long term aging. In IN617 alloy also Mo-rich M_6C (($Co,Ni)_3Mo_3C$), precipitates are observed. M_6C is unstable at the ageing temperatures and has been identified as possible precursor of Mo-rich μ phase, that it has only been observed at temperatures of 700°C, for long exposure times. Coarse particles of Si-rich G ($Ni_{16}Nb_6Si_7$) phase and η Ni_3Ti brittle phase are present only in alloy IN740. Alloy IN617 has shown lower hardness compared to alloy NIM263 and IN740.

Keywords: Ni base alloys, power plant, microstructure stability, precipitation

1. Introduction

The continuous trend in efficiency improvement in advanced ultrasupercritical (AUSC) coal-fired power plants for power generation needs an increasing in temperature and pressure in the critical components, namely boiler and turbine. The target is to reach efficiency up to 60% through an increase of steam temperature up to 750°C and pressure in the range of 350-375 bar. Therefore superheater tubes for boiler will be significantly stressed and steels and alloys with improved creep and corrosion-oxidation performances are required [1-5].

Nickel-based alloys, with higher creep rupture strength and better corrosion resistance against coal ash corrosion and steam oxidation compared to austenitic steels, have been recently applied in the hottest parts of superheater tubes of coal fired power plants operating at 720°C (test loops).

In Ni-based alloys the high temperature resistance and creep strength mainly depends on solid solution strengthening and the presence within the austenitic grains of age hardened alloys of the coherent intermetallic FCC precipitate γ' having composition $Ni_3(Al,Ti)$. Primary carbides, MX ((Nb;Ti)(C,N)), and chromium carbides, $M_{23}C_6$, can contribute to strengthening. Undesirable and brittle phases such as, μ, σ G and Laves phase can be formed during heat treatment and service exposure. These phases, indicated as TCP (Topologically Close-packed) phases can have an important role in the creep strength drop of the Nickel alloys [6]. The formation of TCP phases, rich in Mo, W, Ti and Nb, depletes the matrix of refractory elements and thus reduces the hardening solution provided by these elements.

Nowadays the Ni alloys have been widely developed for aeronautic application, where service times are limited: the use in power plant at 700/750°C opens several questions, particularly on their long-term microstructure stability, steam oxidation resistance, and fireside corrosion.

Long term microstructure stability of Ni-based alloys is related to the evolution of the precipitation state as a consequence of high temperature exposure [7-10]. Precipitation and/or coarsening of γ' phase and coarsening of carbides cause properties modification such as a hardness increase. In addition η formation for long term causes depletion of the gamma prime or makes gamma prime unstable thus reducing long-term strength,

The most dangerous microstructural modifications can be associated to TCP phases formation and coarsening which probably occur after long time, exceeding 10,000 hours. For these reasons the use of these materials require a deep investigation and understanding of the degradation mechanisms due to temperature/ time/environment conditions.

In this work the microstructural evolution, in term of hardness and precipitation state of IN617, IN740 and C263 Ni-base alloys has been investigated after exposure in test loops as well as laboratory isothermal ageing treatments. Precipitate characterization in terms of size, morphology, location (at grain boundary or within grains) and chemistry of the main phase (MX, $M_{23}C_6$, γ') has been used for monitoring relevant precipitation state modifications.

2. Materials and Methods

Samples from exposed tubes in test loops (COMTES 700 and ETR) and laboratory isothermally aged samples of Ni-based alloys have been used for microstructural assessment. The chemical compositions of some of the tube (T) and plate (P) as supplied condition of products in solutionized are presented in Table 1. The alloy compositions of investigated products fulfill the requirements of grade alloys.

In laboratory isothermal annealing temperatures were in the range 570-750°C for time from 1,000 up to 10,000 hours. In service, the exposure temperature was not constant, but the materials were subjected to a thermal cycle. For the analysis of results the high temperature exposure ranges are generally given, with the associated exposure time to explain, for a total

exposure time of 32000 hours, the sample was exposed at the highest temperature range for about 22,000 hours.

Metallographic investigations have been carried out on solutionized and aged samples. They were carried out by Light Microscopy, Hardness Tests, Scanning Electron Microscopy (SEM, SEM-FEG), Transmission Electron Microscopy (TEM-FEG) equipped with Energy Dispersive Spectroscopy (EDS) combined with Selected Area Diffraction (SAD). TEM observations were carried out on thin foils prepared from aged samples. TEM-EDS analysis on extraction replicas was also performed to estimate chemical composition and the quantitative assessment of geometrical parameters (size distributions, mean size) of phases.

Alloy	C	Si	Mn	Cr	Mo	Ti	Al	Co	Nb	Fe
617* Ref.	*0.05-0.10*	*<0.70*	*<0.70*	*20.0-23.0*	*8.0-10.0*	*0.20-0.60*	*0.60-1.50*	*10.0-13.0*	*<0.10*	*<20.*
T	0.051	0.14	0.03	21.7	8.6	0.40	1.25	11.2	<0.05	0.6
P	0.058	0.11	0.09	22.5	8.0	0.46	1.40	11.5	<0.05	1.2
740 Ref.	*0,03*	*<0.50*	*0.3*	*22.0-25.0*	*0,50*	*1,8*	*0,90*	*20,0*	*1.5-2.5*	*<0.7*
T	0.029	0.54	0.29	24.4	0.55	1.81	0.94	20.0	1.98	0.42
P	0.034	0.58	0.30	24.5	0.60	1.64	1.04	19.8	2.4	0.45
263 Ref.	*0.04-0.08*	*<0.40*	*<0.60*	*19.0-21.0*	*5.6-6.1*	*19.-2.4*	*<0.60*	*19.0-21.0*	*<0.10*	*<0.7*
T	0.050	0.09	0.15	20.00	5.90	2.1	0.45	19.8	<0.05	0.44
P	0.047	0.11	0.14	20.40	6.01	2.0	0.49	19.8	<0.05	0.10

*NiCr23Co12 Mo 2.4663

T*able 1: Chemical composition (wt%, Ni balance) of Ni alloys used in the investigations and Reference (Ref.) chemical composition of Ni grade alloys.*

3. Results

3.1. Microstructural Characterization

Light microscopy analysis showed an austenitic matrix constituted by equiaxed grains. Grain size have been measured on soluzionized materials, laboratory aged samples and on exposed tubes: some differences have been observed that can presumably be associated to previous different thermo-mechanical cycles of the tube/plate products. The average grain size was generally in the range 80-120 µm.
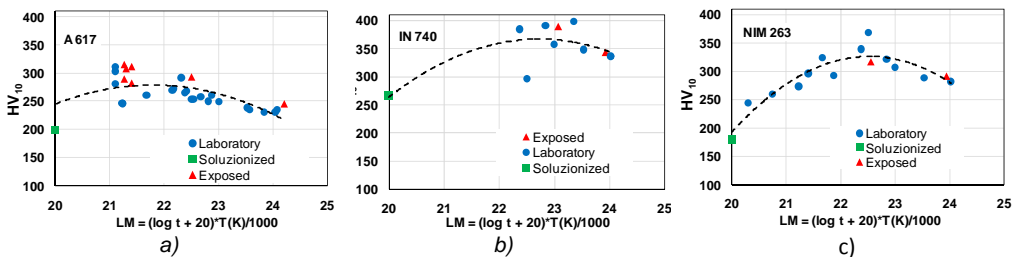
Figure 1 Hardness, HV_{10}, values in isothermal laboratory aged and exposed samples as function of Larson Miller (LM) parameter: a) IN617; b) IN740; c) NIM263

Hardness measurements (HV_{10}) have been performed on as received materials (soluzionized condition), laboratory isothermal aged samples and exposed tubes. In Figure 1, the hardness values are reported as function of Larson Miller parameter: $LM= (logt+20)T(K)/1000$, where t is time and T is temperature (K). Starting from material in the soluzionized condition, hardness initially increases and then decreases as LM increases. For Alloy IN617 (Figure 1a) the hardness increase is lower than those of alloy IN740 (Figure 1b) and NIM263 (Figure 1c).

3.2. Precipitation state

After solution treatment, the grain boundaries in the samples were found free of particles. Coarse spherical precipitates and elongated precipiates with sharp edges, having size in the range 0.2-1.0 µm were observed within grains. They were identified as MX precipitate, of type $(Ti,Mo)(C,N)$ carbo-nitrides, in IN617 and NIM 263 alloys and $(Nb,Ti)(C,N)$ carbo-nitrides in IN740 alloys. No γ' precipitates were observed in solution treated sample. With particularly reference to A617 alloy, SEM-FEG/EDS elemental maps, performed on aged samples, indicate the presence of complex carbides: at the particle centre a Ti rich carbide and at the particle periphery a Cr and Mo enrichment associated with $M_{23}C_6$ / M_6C carbides are observed. This suggests that primary MX precipitates act as preferential nucleation site for $M_{23}C_6$ (Figure 2).

Samples isothermally aged in laboratory and exposed tubes showed the grain boundaries (GB) continuously decorated by precipitates having elongated morphology with round edges and size 100-600 nm. They were identified as GB $M_{23}C_6$ carbides of type $(Cr,Mo)_{23}C_6$ in IN617 and NIM 263 alloys and $Cr_{23}C_6$ in IN740 alloy. $M_{23}C_6$ carbides having cuboidal, platelike and spherical morphology were also distributed within grains and on twin boundaries. Coarsening of $M_{23}C_6$ $((Cr,(Mo))_{23}C_6)$ precipitates located at grain/twin boundaries and within grains is observed in all the investigated alloys after long term aging.
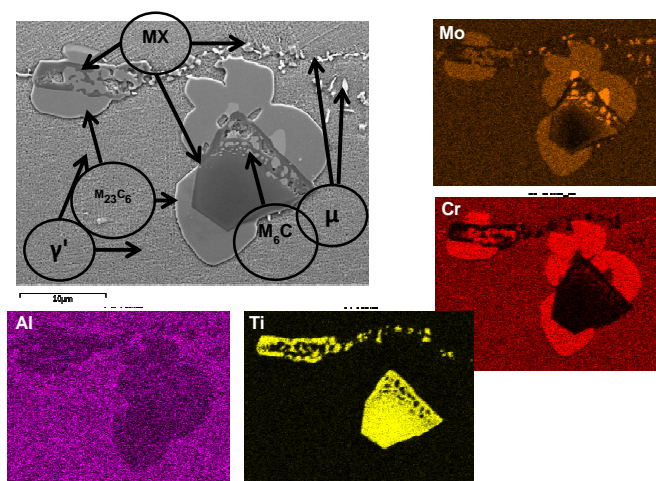
Figure 2 EDX map of IN617 specimen crept at 700°C for approximately 20,000 hours

Precipitates having mainly spherical morphology, whose representative micrographs are shown in Figure 3, were uniformly distributed within grains. They were identified as γ' (Ni_3,Co) (Al,Ti) phase in IN617 and NIM263 alloys and Ni_3,(Nb,Al,Ti) in IN 740 alloy on the base of their average chemical composition (at.%). In IN740 exposed sample (659-688°C ~22,000 hours) (Figure 3b) γ' precipitate morphology showed a slight tendency to cuboidal shape. There was a difference in γ' precipitation density: a roughly comparison reveals that 740 has the most precipitation density followed by 263 and much less in 617.

a)   *b)*   *c)*
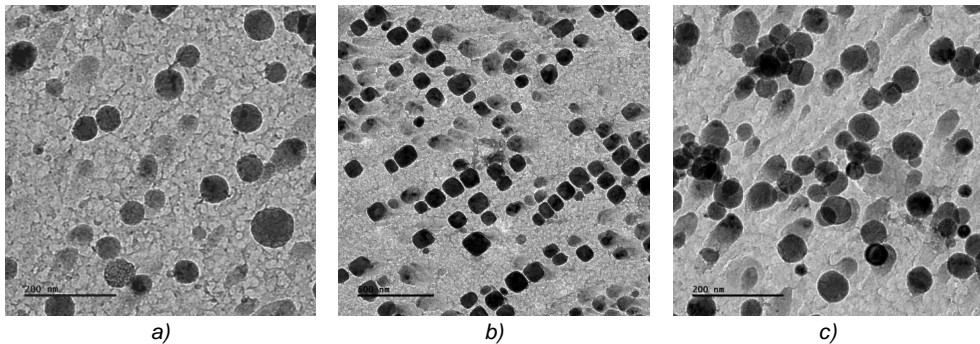
Figure 3 TEM micrograph showing extracted γ' precipitates from the austenitic (γ) matrix in the annealed samples: a) IN 617exposed 628-656°C ~22,000 hours; b) IN740 exposed 659-688°C ~22,000 hours; c) NIM 263 aged at 700 ° C for 10,000 hours.

The average diameter of γ' was measured on different samples (from test loop, isothermally aged), by using different techniques: TEM-FEG analysis on extraction replicas and SEM-FEG on bulk specimens: a relevant coarsening of γ' $Ni_3(Al,Ti)$ with increasing temperature and or ageing time was observed.

In IN617 and IN740 alloys, γ' size shows a relevant increase with increasing Larson Miller (LM) parameter (Figure 4). A linear relationship has been determined by regression analysis of data with acceptable correlation coefficient (R^2=0.92 and 0.79 for IN617 and IN740 respectively).

a)   *b)*
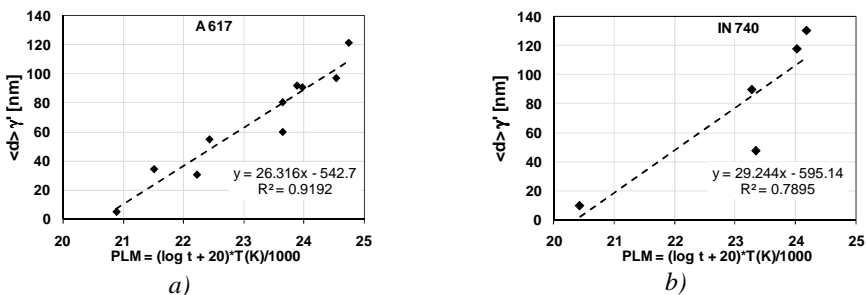
Figure 4 γ' precipitate average diameter in isothermal laboratory aged and exposed samples as function of Larson Miller (LM) parameter: a) IN617; b) IN740

In NIM263 alloy, quantitative γ' size assessment has been performed only on a limited number of samples and a relevant coarsening of γ' was observed at 700°C with increasing ageing time: after 10,000 hours the average diameter was of 90 nm, approximately three times larger than that after 3,000 hours ageing, with an average diameter of 30 nm. With increasing ageing time, the spherical morphology of γ', due to the limited γ/γ' mismatch (~0.2% as calculated by thermodynamic calculation), showed a slight tendency to change to cuboidal shape.

Coarse phases have been observed in exposed samples of IN617 and IN740 alloys under the most severe conditions, T>700°C for time> 20,000 hours. In IN617 alloy, Mo-rich M_6C (($Co,Ni)_3Mo_3C$) coarse precipitates having elongated morphology with quite sharp edges were observed (Figure 5a). M_6C is unstable at 700°C ageing temperatures and has been identify as a possible precursor of Mo-rich μ phase. Coarse particles of Si-rich G, ($Ni_{16}Nb_6Si_7$) phase (Figure 5b), and η Ni_3Ti phase were present IN740 (Figure 5c). G phase particles, with elongated morphology and round edges were the coarsest precipitates with size in the range of 1 to 5 μm. Thin foil TEM-FEG analysis(Figure 5c) showed needle like morphology of η phase located at grain boundaries and γ'-depleted zones surrounding η phase. This analysis indicates that η phase formed at the expense of γ' phase and caused a local matrix depletion of γ' phase. The presence of coarse η phase particles can be associated to a loss of strength and ductility [11].

a) IN617 b) IN740 c) IN740
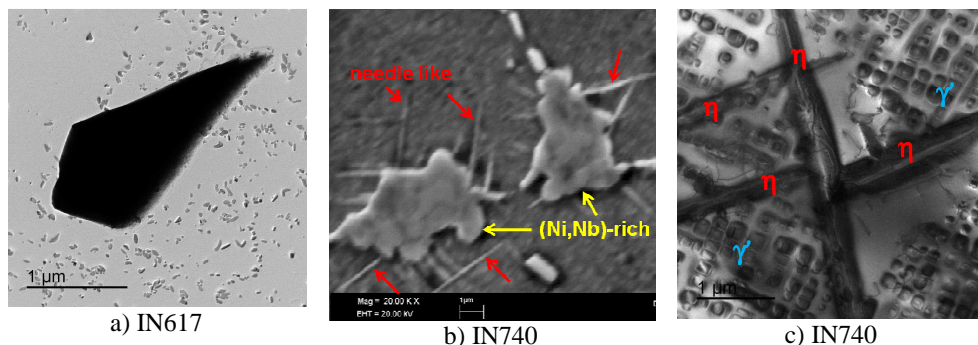
Figure 5 Coarse phase in exposed samples a) TEM image of extracted Mo-rich M_6C (($Co,Ni)_3Mo_3C$) in IN617exposed at T~706°C ~22,000 hours; b) SEM image of G phase (Ni,Nb)- and η phases in IN740 exposed at T~726°C ~22,000 hours; c)TEM image of η phase Ni_3Ti and γ' phase $Ni_3,(Nb,Al,Ti)$ on thin foil of the sample in Figure 5b).

In NIM 263 alloy ageing was limited to 10,000 and no η-phase and TCP such as μ, σ phases were observed. The chemical composition of the carbides is illustrated by the ternary diagrams in Figure 6: it can be observed that the fine (Ti,Mo)C observed on soluzionized material (size < 500nm by TEM) transforms into $M_{23}C_6$ with increasing ageing conditions.
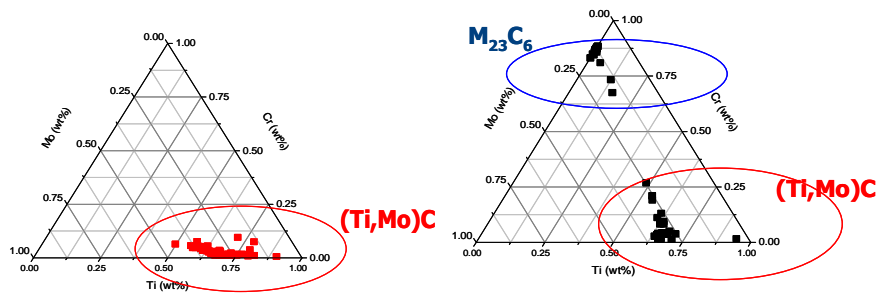
a) soluzionized   b) exposed sample T_{max} 661°C~22,000 hours

Figure 6: Ternary diagrams (Cr-Mo-Ni) for NIM 263

4. Discussion

The Ni_3Ti-η phase is expected from equilibrium calculations (Figure 7) in both alloys IN740 and NIM263.
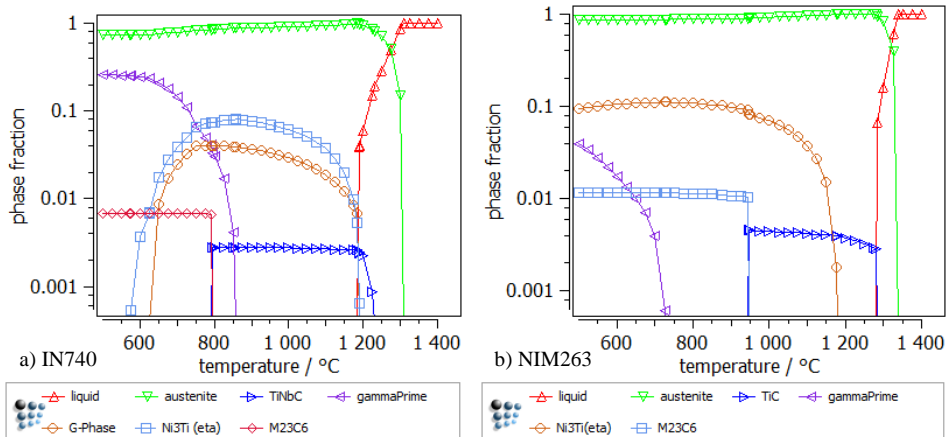
Figure 7 Equilibrium phases predicted by Thermocalc for alloy: a) IN740 ;b) NIM263.

Experimental results give evidence of its formation only in IN740 alloy, while, in NIM263 alloy, η phase does not form in the ageing conditions that have been investigated. Longer exposure times could allow precipitation of η phase at the expense of γ' also in this alloy. However, amounts of 2 to 3 pct of η phase do not affect the creep strength or ductility [4]. Literature data of TTP diagram of C263 alloy [10] are shown in Figure 8, in which η phase starts to precipitate after ~ 10^5 hours at 700°C and ~ 10^4 hours at 750°C.
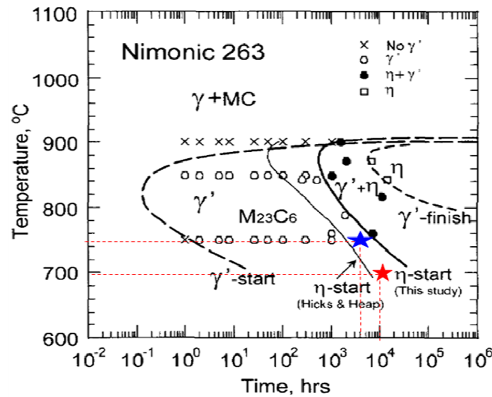
Figure 8 TTP Diagram of C263 [1] Ni based alloy

In the TTP diagram of Figure 8, current experimental annealing temperature /time conditions have been reported (red star at 700°C/10000h and blue star at 750°C/3000h). These points are on the left of the η-start curve and this result explains why η phase was not observed in the annealed samples 700°C/10000h and 750°C/3000h.

Microstructural modifications which can affect long term microstructure stability have been revealed in the present investigation in spite of the limited aging time: 22,000 hours for IN617 and IN740 alloys, 10,000 hours for NIM263 alloy. At the level of macroscopic investigation, all alloys showed quite similar hardness variations with increasing temperature and aging time. Starting from material in the as soluzionized condition, hardness initially increases and then decreases with increasing LM. For Alloy IN617 the hardness increase was lower than those of alloys IN740 and NIM263. Hardness behaviour can be mainly associated to precipitation state evolution, mainly γ' precipitation and coarsening for long term ageing. Precipitation state evolution in aged samples appeared to be very complex, especially for A617 and IN740 alloys. To summarise, the main phases observed in the Ni alloys are:

- γ' phase with near spherical morphology was uniformly distributed within grains and coarsening was observed with increasing temperature and ageing time. In IN617 and IN740, by plotting the γ' size as a function of the Larson-Miller Parameter a liner relationship has been determined showing a comparable coarsening kinetics;

- primary MX ((Nb,Ti)(C,N)) carbo-nitrides were observed in all the materials. They were identified as MX precipitate, of type (Ti,Mo)(C,N) carbo-nitrides, in IN617 and NIM 263 alloys and (Nb,Ti)(C,N) carbo-nitrides in IN740 alloys;

- grain boundary $M_{23}C_6$ carbides of $(Cr,(Mo))_{23}C_6$ type were commonly observed in all the investigated alloys. $M_{23}C_6$ carbide precipitation within grains and twin boundaries and coarsening with ageing were observed.

918

- in IN617 alloy also Mo-rich M_6C precipitates were observed, mostly located at grain boundaries. M_6C, probably obtained from the transformation of MC and $M_{23}C_6$, is unstable at the ageing temperatures and has been identified as a possible precursor of μ phase, that has only been observed at 700^oC and long exposure times (20000 hours) ; Possible sequences for the evolution of MX and $M_{23}C_6$ into M_6C are the following [2]:

$$Cr_{21}(Mo)_2C_6 + \gamma(Ni,Co,Mo) \rightleftarrows Mo_3(Ni,Co)_3C + Cr$$

$$(Ti,Mo)C + \gamma(Ni,Co,Al) \longrightarrow Mo_3(Ni,Co)3C + Ni_3(Al,Ti)$$
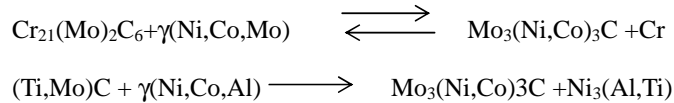
- coarse particles of Si-rich G ($Ni_{16}Nb_6Si_7$) (TCP) phase were present in aged samples of IN740 alloy. The role of such phase in the degradation mechanism is controversial. Its presence is generally accepted, but its absence is preferable;

- η Ni_3Ti phase precipitates were present in aged samples of IN740 under the most severe exposure conditions T>700°C for time> 20,000 hours. At 725^oC the η phase formed at grain boundaries and G interface and grew with needle-like morphology. The presence of γ'-free zones surrounding η phase gave evidence that η phase grew at the expense of γ' phase;

- the precipitation state of NIM263 alloy appeared more simple, for the investigated conditions, times ≤10000 hours, since only γ' phase, $M_{23}C_6$ and primary MX were observed. By considering the overall information the alloy NIM263 appeared more stable than the other two investigated Ni alloys, IN617 and IN740, even for long aging time [10].

5. Conclusion

The experimental results of this work gave evidence of relevant microstructural changes in Ni-based alloys after long term exposure up to 22,000 hours. Hardness behaviour has been associated to precipitation state evolution, mainly γ' precipitation and coarsening for long ageing times.

The precipitation and growth of Mo-rich M_6C (($Co,Ni)_3Mo_3C$) phases in IN617 alloy , Si-rich G ($Ni_{16}Nb_6Si_7$) and η Ni_3Ti in IN740 alloy appeared to be the most potentially detrimental microstructural modifications. These phases can affect microstructure stability and cause creep strength reduction.

In NIM263 alloy there was no evidence of η-phase and TCP such as μ, σ phases for the investigated conditions. Further inspections for longer time are needed to confirm long term microstructure stability of NIM263 alloy.

ACKNOWLEDGMENT

REFERENCE

[1] R. Blum, J. Bugge, The European perspective and advancements for the European Perspective and Advanecements for Advanced USC Steam Power Plants, *6th EPRI Conference on Advances in Materials Technology for Fossil Power Plants, August 31–September 3, 2010*; Santa Fe, MN, USA (EPRI 2010 Conf. Proc. S1-01-83).
[2] R. Viswanathan, J. Shingledecker, J. Hawk, S. Goodstine, Effect of Creep in Advanced Materials for Use In Ultrasupercritical Coal Power Plants: *ECCC Creep Conference, 21-23April 2009, Zurich-CH ECCC 2009 Conf. Proc. 04-Viswanathan-key).*
[3] T.U. Kern & others, Material and design solutions for advanced steam power plants, *5th Conference on Advances in Materials Technology for Fossil Power Plants, MARCKO Island FL, USA, September 2007.*
[4]. Y. Tanaka et al., Coal ash Corrosion Properties of Ni-Based Alloy for Advanced-USC-Boiler, *6th Int. Conf. on Advances in Mat. Tech. for fossil fuel Power Plant, 2010, Santa Fe, NewMexico (*EPRI 2010 Conf. Proc. S1B-10-86).
[5] J. P. Shingledecker. R. W. Swindeman, Q. Wu, V. K. Vasudevan, Creep strength of high temperature alloys for ultrasupercritical steam boilers, *4th EPRI Conference on Advances in Materials Technology for Fossil Power Plants, November 2-4 2004 Hilton Head Island SC USA (.*
[6] C. T. Sims, N. S. Stoloff, W. C. Hagel, "Superallys II", Ed. J. Wiley & Sons Inc., pag 1986.
[7] X. XIE et al., Structure stability study on fossil power plant advanced heat resistance steel and alloys in China: 6th EPRI Conference on Advances in Materials Technology for Fossil Power Plants, August 31–September 3, 2010; Santa Fe, MN, USA *(*EPRI 2010 Conf. Proc. S1-01-28).
[8] Zhao S., Xie X., Smith G. D., Patel S. J., Research and Improvement on structure stability and corrosion resistance of Nickel-base superalloy INCONEL alloy 740, *Materials and Design 27*, 1120–1127 (2006).
[9] W.Z. Wanga, H.U Honga., I.S. Kima, B.G. Choia, H.W. Jeonga, M.Y. Kimb, C.Y. Joa, Influence of γ' and grain boundary carbide on tensile fracture behaviors of Nimonic 263, *Mater. Sci. Eng., A 523* 242–245 (2009).
[10] J. C. Zhao, V. Ravikumar, A.M. Beltran, Phase Precipitation and Phase Stability in Nimonic 263, *Metall. Mater. Trans. A, 32A,* 1271-1282 (2001).
[11] C. T. Sims, N. S. Stoloff, W. C. Hagel, Superallys II, Ed. J. Wiley & Sons Inc., 1986 pp 178-179.

MICROSTRUCTURE AND PROPERTIES
OF IN 740 H NICKEL SUPERALLOY AFTER
WELDING AND AGEING AT 750 °C

Adam Hernas[1a], Barbara Kościelniak[1b], Stanisław Fudali[2c], Krzysztof Cieszyński[2d]

[1]The Silesian University of Technology, 40-019 Katowice, Poland
[a] adam.hernas@polsl.pl, [b] barbara.koscielniak@polsl.pl

[2]RAFAKO S.A., 47-400, Racibórz, Poland
[c] stanislaw.fudali@rafako.com.pl, [d] krzysztof.cieszynski@rafako.com.pl

Abstract

Since superheater and reheater tubes of ultra supercritical power plants are exposed to temperatures exceeding 650 °C, the choice of materials for this application falls on stainless steels and alloys due to their superior steam oxidation, hot corrosion and creep resistance. For these applications austenitic Sanicro 25 steel and nickel superalloys - IN 617, DMV617 mod., IN 625 and IN 740H are recommended. In this paper results of material investigations will be focused on welded joints of thin 4,8 mm wall tubes made of IN 740H in initial state and after long time annealing at 750 °C. The examination included tensile and notch toughness tests, transverse bend tests and hardness measurements. Microstructural investigations were carried out with LM, SEM and TEM. Also welding parameters and consumables used for welding are described.

Keywords: IN 740H nickel superalloy, welding, properties and microstructure

1. Introduction

Legal and environmental conditions, improvements in the performance parameters of power units and the need to increase the level of national energy security necessitate the construction of modern power units with supercritical parameters for high efficiency. Their construction requires the use of materials that comply with high standards regarding long-term creep resistance, resistance to oxidation in steam and resistance to high-temperature corrosion. Mastering the technology for the manufacturing and processing of thin-and thick-walled piping is also essential.

Trends in the development of boilers for ultrasupercritical power plants (Advanced Ultra Supercritical, A-USC) operating at steam temperatures from 650 to 760 °C and in a pressure range from 300 to 370 bar require the use of new materials from the group of Ni superalloys for the construction of critical elements. At steam temperature above 650 °C these requirements can be met by HR6W, Sanicro 25, IN 617, DMV 617mod. and IN 740H (Fig. 1) [1-3].

One of the latest materials designed for critical elements of the boiler, including piping headers and heating coils in A-USC boilers is IN 740. IN 740H nickel superalloy in its version with a modified chemical composition [1-4]. The superalloy was designed under the European Research Programme Thermie, aimed at the development of new materials offering high creep strength and corrosion resistance. The 740H alloy was supposed to have corrosion resistance to coal ash at temperatures above 700 °C and at these conditions have a creep rupture strength for 100 000 h of at least 100 MPa.
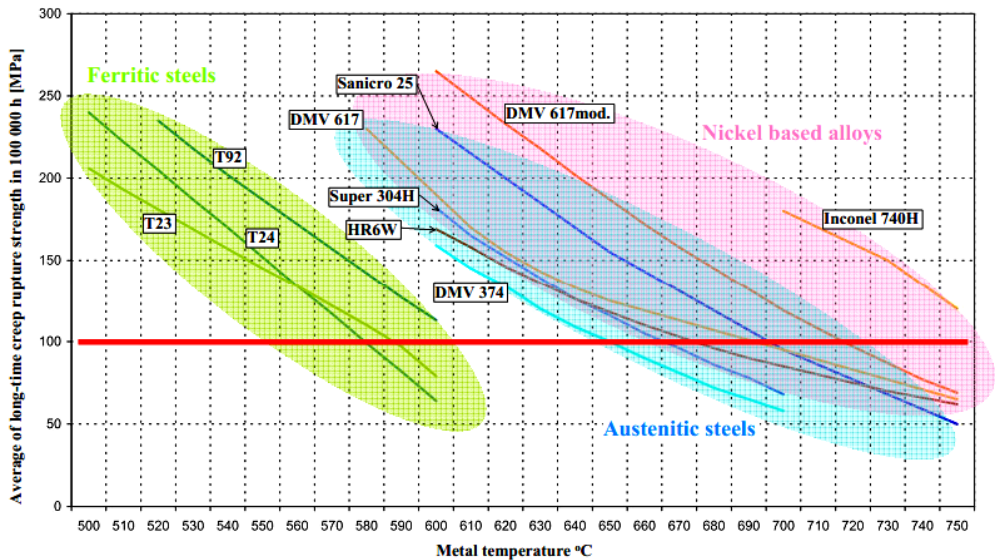
Figure 1: Mean creep rupture strength at 100 000 h for selected materials to be used in supercritical and A-USC- power units [done on the base of VdTÜV, GB5310:2008, PN-EN10216-2:2009].

Strengthening is mainly achieved through the large amount of precipitated particles of the γ' phase and solid-solution strengthening, mainly by the addition of cobalt. The chemical composition of the alloy provides good stability of microstructure and properties in the temperature range from 70 to 750 °C [4,5,8]. The low molybdenum content promotes good resistance to corrosion in contact with coal ash, while the content of chromium increased to 25% (in comparison to the IN 617 alloy) improves resistance to oxidation at 750 °C. Researchers analysing the effects of long term annealing in the temperature range from 700 to 750 °C on the stability of the microstructure described the precipitation of the γ' phase and carbides MC and $M_{23}C_6$ types [4,6]. In addition, depending on the temperature and time of annealing, the η phase (Ni_3Ti) may also be formed, often needle-shaped and present along the grain boundaries, as well as the G phase ($M_6Ni_{16}Si_7$). At the same time it was demonstrated that the volume of the strengthening phase γ' tends to increase rapidly, having a negative impact on the stability of properties [1,4]. The problem of the implementation of new creep-resistant materials is usually investigated in three types of studies focused on:

a) design of parameters for mechanical properties at room and elevated temperature,
b) understanding the mechanisms responsible for strengthening and stability of the microstructure and properties during prolonged exposure to high temperature,
c) mastering the technology of welding and tube bending, to develop the company's own know-how.

With regards to the IN 740 and IN 740H superalloys, the problems related to mechanical properties and precipitation processes have been extensively reported in literature. However, less information is available on the technological properties and relationships between the technology and microstructure or performance properties [1,6].

2. Research and Development in Poland

Since 2010 the Polish National Centre of Research and Development (NCBiR) has been carrying out a Strategic Research Programme aimed at the development of a technology for highly efficient zero-emission coal-fired power units with integrated CO_2 capture. Research on the technology and materials carried out by RAFAKO S.A. and the Silesian University of Technology has led to the development of starting requirements and preliminary design of an ultrasupercritical boiler with an efficiency above 45% [7,8]. The boiler would operate at live and reheated steam pressures and temperatures of 300 bar/653 ^{o}C/674 ^{o}C.

The materials chosen for application for critical pressure components of this boiler are listed in another paper of Liege Conf. 2014: Authors: A. Hernas, M. Staszewski, S. Fudali and J. Pasternak: Evaluation of welded joints properties and microstructure of new austenitic steels Sanicro 25 and HR6W.

The strength analysis for the concept of this boiler demonstrated that with the use of IN 740H and DMV 617 mod. superalloys the steam temperature on the base of 10 000 h creep strength can be increased up to about 700 ^{o}C (673 ^{o}C / 692 ^{o}C / 303 bar – Tab. 1), thus offering about 50 % net future boiler efficiency.

Table 1. Proposal of superalloys application, dimensions and steam parameters for coils of preliminary A-USC boiler

Primery steam parameters SH4: T_{medium}= 673 [°C]; p_{medium}= 30.3 [MPa]							
Type of component	Time of creep	Allowable stress	Material	Required calculated diameter x wall thickness		Design parameters T_{design}, p_{design}	
Coils	[h]	[MPa]		[mm]	C_1^* [%]	[°C]	[MPa]
0-100%	10 000	123,3	DMV 617mod.	φ 42.4 x 7.1	12,5	723	32,8
0-100%		194,3	Inconel 740H	φ 42.4 x 5.0			

$^*C_1$ – metallurgical allowance

3. Research material and preparation of welded joints

A thin-walled tube made of IN 740H superalloy, with an outer diameter φ 38 mm and wall thickness of 4.5 mm provided by Special Metal Corporation, Huntington (USA) was applied in this study. The chemical compositions of the material and the filler metal in the as-recieved conditionare presented in Tab. 2.

Table 2. Chemical composition of the tube and filler metal

Component	Alloy	Concentration of major elements (in wt.%)								
		C	Mn	Cr	Ni	Ti	Mo	Co	Nb	Al
Tube	IN 740H	0.03	0.10	24.41	51.86	0.81	1.65	20.19	0.49	1.35
Filler metal	IN 740H	0.03	0.24	23.39	52.86	1.08	1.61	20.15	0.19	1.38

Following the requirements established in the Pressure Equipment Directive, a series of welded joints was fabricated without heat treatment. Because the material was mainly intended for operation as a part of live and reheated steam superheaters, we chose two methods to fabricate weld joints [8,9]:

- automatic 141
- manual 141 GTAW, tungsten electrode W La15, φ =2.4 mm.

The paper presents the results from testing manually welded joints. Details of specimen preparation for manual welding method and the sequence of welding operations is presented in Fig. 2.
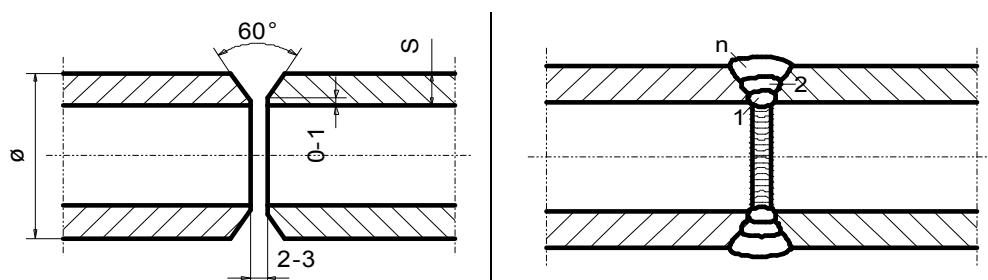
Figure 2: Details of the preparation for welding joints for manual 141-method (GTAW) and the sequence of the welding process.

Butt joints were welded manually (GTAW) under the following conditions:

- shielding gas: Argon I1,
- welding positions: PC and PH,
- filler metal: IN 740H (Tab. 2), diameter 1.14 mm,
- mean amperage for the root pass: (60÷90)A, for filling layers (70÷100)A,
- voltage: (11÷12.5)V,
- number of passes, runs: 3-4,
- maximum interpass temperature: 150 $^{\circ}$C.

4. Quality assessment of welded joints

Quality assessment of welded joints made of IN 740H superalloy for the purpose of the weld qualification procedure included NDT, testing mechanical properties (tensile strength, measurements of hardness and impact force for the joints) and analysis of macro- and microstructure.

Research on welding technology included both non-destructive and destructive testing:

- geometric measurements with visual inspection of joints after welding according to EN 970, EN ISO 17637 and EN ISO 5817-B standards, range of test: 100 % of surface area of joints,
- penetration tests for joints to detect superficial cracks according to the EN 571 standard, range of test: 100 % of surface area of joints, for the acceptance level according to the EN 23277 standard,
- radiographic examination of welded joints according to the EN 1435 standard, class B, range of test: 100 % of joint volume, including analysis of test results according to the EN 12517-1 standard.
- mechanical testing for tensile strength (acc. to EN ISO 4136 standard),
- measurement of hardness and impact strength for joints,
- bend tests for joints (acc. to PN-EN ISO 5173 standard),
- macroscopic and microscopic analysis of joints (acc. to EN ISO 3651-2 v.A) after welding and after annealing at 750 °C for 5, 100 and 500 h using LM, SEM and TEM examinations.

Assessment of tensile strength of the joints subject to qualification at room temperature was carried out according to EN 895 and EN PN 15614-1 standards. The results are as follow:

- Joint welded at position PH – **Rm = 695 MPa**, **A= 41%,** specimen broken at parent material
- Joint welded at position PC – **Rm = 682 MPa**, **A= 43%,** specimen broken at parent material

Specimens for bend tests, size 10 x 4.5 mm, were cut out from test joints and treated according to the requirements of the EN 910 standard – by stretching the root of the weld (2 specimens) and by stretching the face of the weld (2 specimens). The diameter of the bending mandrel (inner roll) was 4 times thicker then test specimen. Tests were positive and a 180° bending angle was attained.

Specimens for testing of impact strength at 20 ^{o}C with a size 10 x 2.5 mm, were prepared according to the EN 875 standard, with a Charpy's notch in the weld metal and HAZ. Impact energy was in the range from 24 to 37 J. The hardness of the joints was measured using the Vickers method with a load of HV10, according to the EN 1043-1 standard. Results from the measurements of hardness for the filler metal, HAZ and parent material are presented in Fig. 3. After undergoing the process of aging at 750 °C, the hardness of joint has been significantly increased (about 50%) in compared to the hardness of joint without heat treatment.
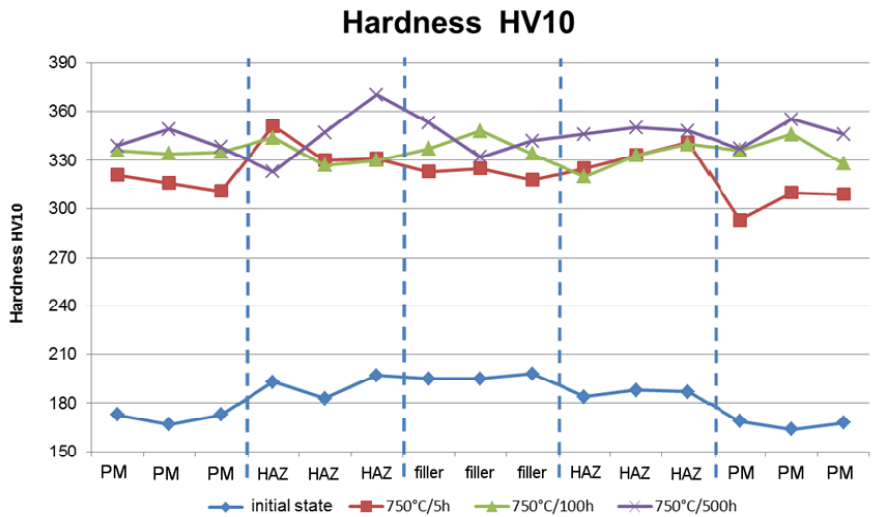
Figure 3: Distribution of hardness in joints before and after different times of annealing at 750 °C.

5. Results from the analysis of macro- and microstructure

The analyses of the macro- and microstructure of joints made of IN 740H tubes in delivery condition were designed and carried out according to EN 1321 standard. A slice and the macrostructure of the weld metal are presented in Figs. 4a and b, while the microstructure observed using LM at 200-fold magnification on etched microsections is presented in Figs. 4 c-e. The weld metal has a coarse-grained structure with evenly distributed precipitates of carbides. No excessive precipitation effects were observed in the area of the fusion line.
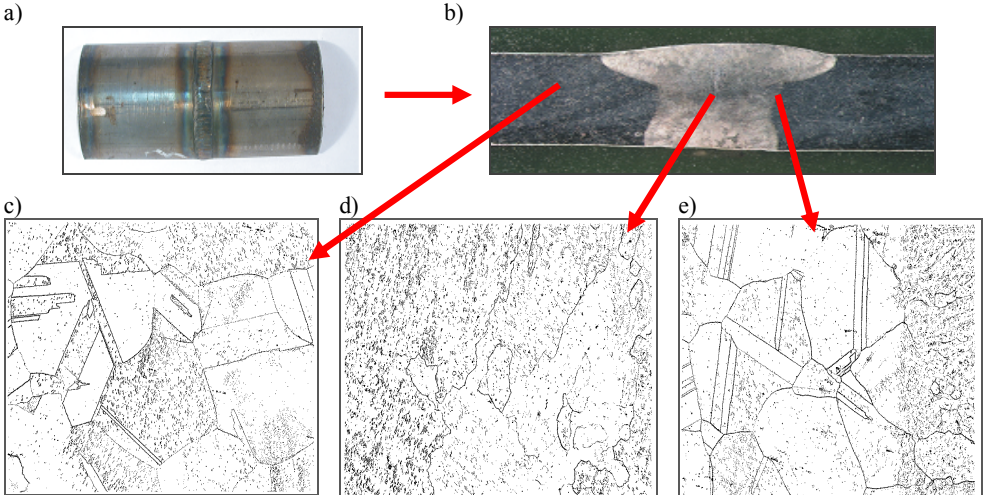
Figure 4:Weld joints made by IN 740H tubes: a, b) macro-; c) microstructure of PM, Mag 200-fold; d) microstructure of weld metal, Mag. 200-fold; e) microstructure of HAZ, Mag. 200-fold.

Weld joints were annealed at 750 °C for 5, 100 and 500 h, and then inspected using SEM (for annealing times of 100 and 500 h) and TEM techniques in order to detect signs of precipitation processes (for annealing times of 5 h).

The substructure of the weld metal and parent material after annealing at 750 °C/5 h in the area of the fusion line is presented in Fig. 5a and very fine coherent precipitates of the γ' phase are shown in Fig. 5b. Globular carbides $M_{23}C_6$ are present on the grain boundaries of the weld metal (Fig. 5c, d)

a)

b)

c)

d)
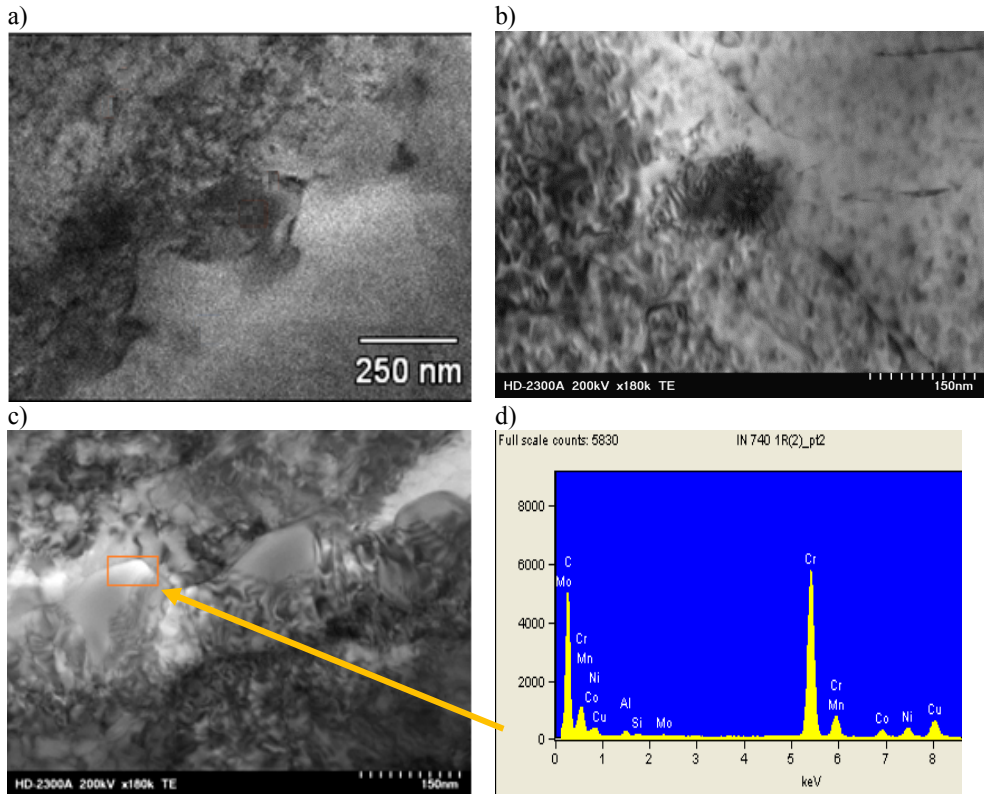
Figure 5: The substructure of welded joint material; a) HAZ; b) parent material;
c) weld metal and d) chemical composition of $M_{23}C_6$ carbide

Prolonged (100, 500 h) at 750 °C resulted in intensified precipitation and coagulation of both the γ' phase and carbides $M_{23}C_6$, which are mainly distributed along grain boundaries of austenite (γ phase) of the weld metal and parent material (Fig. 6-8). The arrangement of carbides is similar in the parent material and in the weld metal and they form a continuous network aligned with grain boundaries. In the HAZ area and the weld metal minor inhomogeneities, associated with the precipitates of the γ' phase, were found after 100 and 500 h of annealing (Fig. 7). High-resolution morphology of the γ' phase and $M_{23}C_6$ carbides in the parent material after 500 h of annealing is presented in Fig. 8.

a)

b)
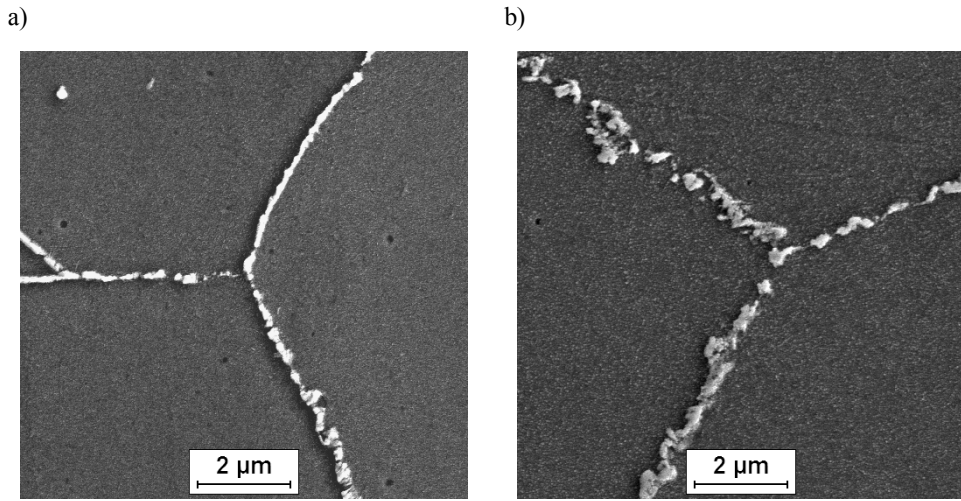
Figure 6: The microstructure of parent material in welded joint after: a) 75 0°C/100 h and b) 750 ^{o}C/500 h

a)

b)
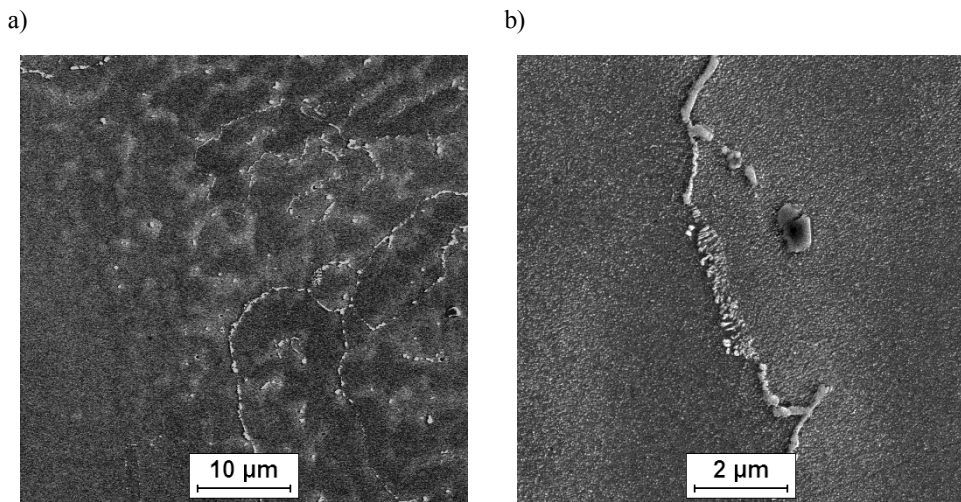
Figure 7: The microstructure of: a) HAZ after ageing at 750 °C/100 h and b) weld metal after ageing at 750 °C/500 h

a) b)
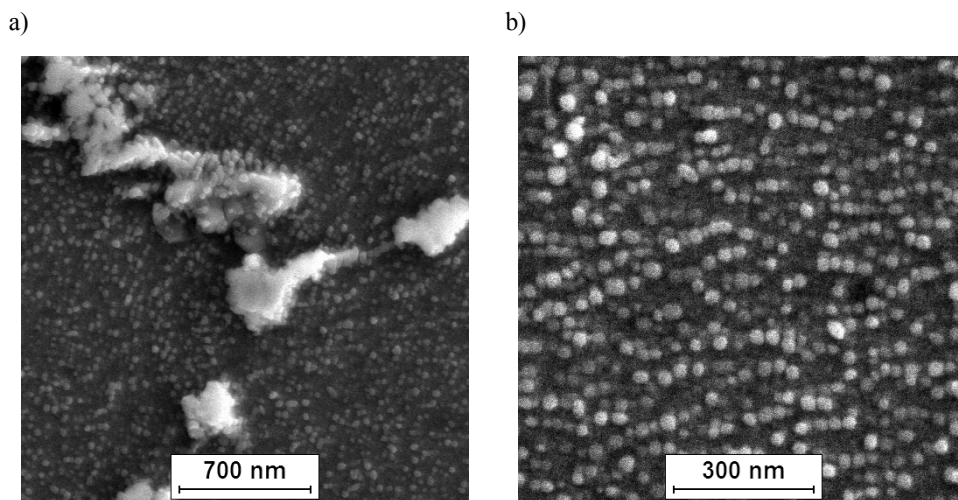
Figure 8: The morphology of $M_{23}C_6$ carbides and γ' phase in parents material after ageing at 750 ^{o}C/500 h.

Observation of precipitation processes taking place during annealing has led to findings similar to those reported by other authors [1-9].

Summary

- Butt joints made of IN 740H superalloy prepared for the purpose of the qualification procedure were thoroughly tested for their quality using non-destructive and destructive methods, tests for technological and structural properties. All results from NDT and destructive tests were positive.
- The joints have the correct macro- and microstructure of weld metal and the fusion line, and comply with the quality requirements for class B acc. to PN EN 5817 standard.
- The technology for welding IN 740H was successfully qualified by a notified body, TÜV NORD, according to a procedure compliant with the PN EN 15614 standard, in the range of mechanical properties and structure of the joints.
- Studies carried out on IN 740 H are pioneering for Poland, and improve knowledge and the researcher's own know-how.

Acknowledgments

References

[1] K. Coleman, R. Viswanathan, J. Shingledecker, JH. Sarver and others, Boiler materials for ultrasupercritical coal power plants, *First Quarterly Report October 1 – December 31* (2003), U.S. DOE NO.: DE-FG26-01NT41175

[2] G. D. Smith and H.W. Sizek, Introduction of an Advanced Superheater Alloy for Coal-Fired Boilers, *Corrosion 2000,* Paper 00256 © 2000 NACE International, TX.

[3] J. Sanders, J. Ramirez, B. Baker, Weldability of Inconel 740 for USC Boiler Applications, 5t*h Int. Conf.on Advances in Mater. Technol. for Fosil Power Plants*, EPRI, Floryda, USA (2007).

[4] Ch.Yan, L. Zhendong, A. Godfrey, L. Wei, W Yuqing, Microstructure evolution and mechanical properties of Inconel 740H during aging at 750^0C, *Mater. Sc. & Eng.*, A589 (2014), 153-164

[5] N. D. Evans, P. J. Maziasz, R. W Swindeman, G.D. Smith, Microstructure and phase stability in Inconel 740 during creep, *Scripta mater.*, 51 (2004) 503-507

[6] B. A. Baker, R. D. Gollihue and J. J. de Barbadillo, Fabrication and heat treatment of weld joints in Inconel Alloy 740H™ superalloy steam headers pipe and superheater tubing, *Special Metals*, a PCC Company 3200 Riverside Drive Huntington, WV 25720

[7] T.Y.Hwang, R. Banerjee, J. Tiley, R. Srinivasan, G.B. Visvanathan, H. Fraser, *Metall.Mater. Trans*, A40 (2009) 24-35

[8] S. Zhao, X. Xie, G.D. Smith, J. Patel, Microstructural stability and mechanical properties of a new nickel-based superalloys, *Mater. Sc & Eng.*, A355 (2003) 96-105

[9] J. P. Shingledecker, R. W. Swindeman, Q. Wu and V. K. Vasudevan, Creep Strength of High-Temperature Alloys for USC Steam Boilers, *Proc. to the 4th Int Conf. on Adv. in Mat. Technol. for Fossil Power Plants (Hilton Head, SC, Oct. 25-28, 2004)*, ASM-International, Materials Park, OH, 2005.

AUTHORS Index

KEYWORDS Index

Band / Volume 221
**Phenotyping Nannochloropsis gaditana under different conditions
in controlled photobioreactors in laboratory and upscaled
photobioreactors in greenhouse**
R. Braun (2014), III, 177 pp
ISBN: 978-3-89336-975-1

Band / Volume 222
**Fundamental processes of plasma and reactive gas surface treatment
for the recovery of hydrogen isotopes from carbon co-deposits
in fusion devices**
S. Möller (2014), 99 pp
ISBN: 978-3-89336-977-5

Band / Volume 223
**Analyse der Lichtstreuung zur Textur-Optimierung von Zinkoxid-
Frontkontakten für Silizium-Dünnschichtsolarzellen**
G. Jost (2014), viii, 203 pp
ISBN: 978-3-89336-978-2

Band / Volume 224
**Luftgestützte Messung von HOx-Radikalkonzentrationen mittels
Laser-induzierter Fluoreszenz auf einem Zeppelin NT: Untersuchung
der atmosphärischen Oxidationsstärke der unteren Troposphäre**
S. Gomm (2014), 5, iii, 205 pp
ISBN: 978-3-89336-981-2

Band / Volume 225
**Sorption, Transformation and Transport of Sulfadiazine in a loess
and a sandy Soil**
S. Sittig (2014), v, 121 pp
ISBN: 978-3-89336-982-9

Band / Volume 226
**A Lagrangian transport core for the simulation of stratospheric trace
species in a Chemistry Climate Model**
C. M. Hoppe (2014), vi, 112 pp
ISBN: 978-3-89336-984-3

Band / Volume 227
**Einfluss der Probengröße und der Kornorientierung auf die Lebensdauer
einer polykristallinen Ni-Basislegierung bei LCF- Beanspruchung**
T. Seibel (2014), II, 131 pp
ISBN: 978-3-89336-986-7

Schriften des Forschungszentrums Jülich
Reihe Energie & Umwelt / Energy & Environment

Band / Volume 228
Implementation of capillary electromigrative separation techniques coupled to mass spectrometry in forensic and biological science
T. N. Posch (2014), 264 pp
ISBN: 978-3-89336-987-4

Band / Volume 229
Mobile Messungen - Messung und Bewertung von Verkehrsemissionen
C. Ehlers (2014), VII, 136 pp
ISBN: 978-3-89336-989-8

Band / Volume 230
Data Processing and Trace Gas Retrievals for the GLORIA Limb Sounder
T. Guggenmoser (2014), xi, 111, XXVI
ISBN: 978-3-89336-993-5

Band / Volume 231
Assessment of Laser Induced Ablation Spectroscopy (LIAS) as a method for quantitative in situ surface diagnostic in plasma environments
N. Gierse (2014), 199 pp
ISBN: 978-3-89336-994-2

Band / Volume 232
Lattice-Boltzmann-Simulation in faserbasierten Mikrostrukturen
J. P. Brinkmann (2014), viii, 129 pp
ISBN: 978-3-89336-995-9

Band / Volume 233
Numerische Simulationen von Abfallgebinden aus der Wiederaufarbeitung von Kernbrennstoffen
S. Schneider (2014), 201 pp
ISBN: 978-3-89336-998-0

Band / Volume 234
Materials for Advanced Power Engineering 2014
J. Lecomte-Beckers, O. Dedry, J. Oakey, B. Kuhn (Ed.)
(2014), xxi, 930, viii pp
ISBN: 978-3-95806-000-5

Weitere *Schriften des Verlags im Forschungszentrum Jülich* unter
http://wwwzb1.fz-juelich.de/verlagextern1/index.asp

JÜLICH
FORSCHUNGSZENTRUM